CHEMICAL ENGINEERING RESEARCH

Reports of the 4th year research projects in the Department of Chemical Engineering at Imperial College London

VOLUME 4

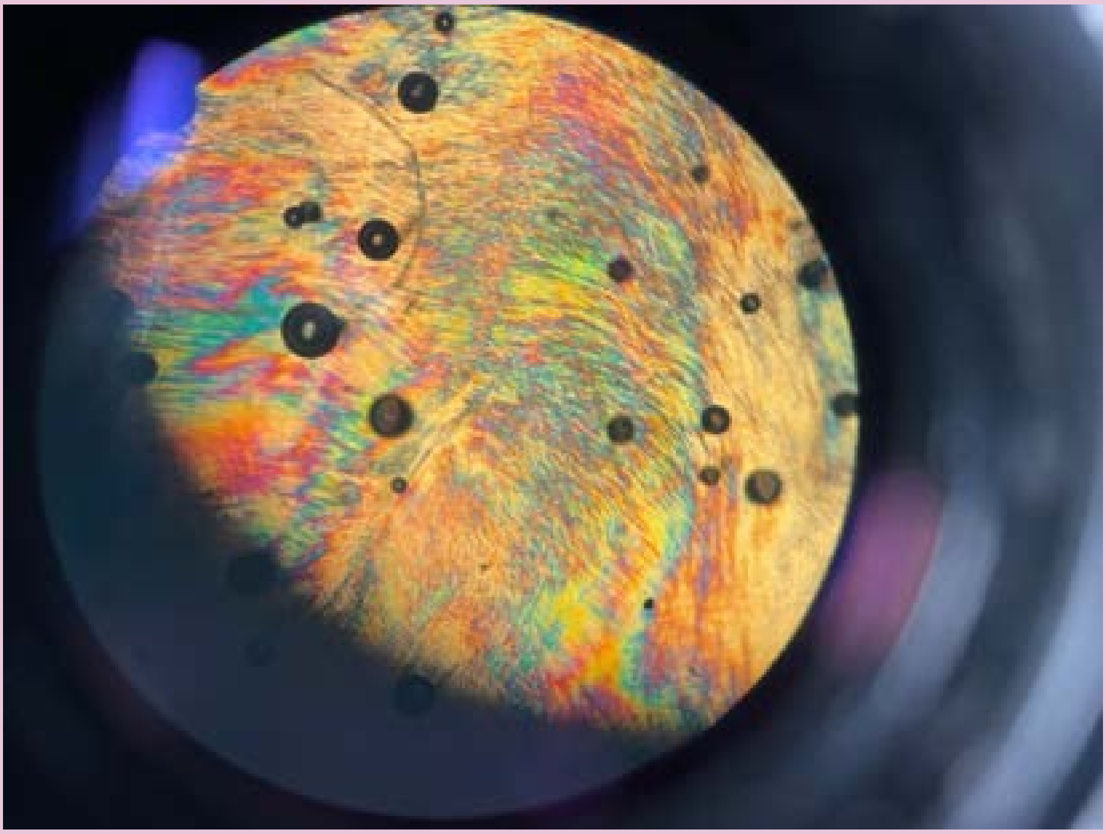

Edited by Erich A. Müller

February, 2022

CHEMICAL ENGINEERING RESEARCH

Reports of the 4th year research projects in the Department of Chemical Engineering at Imperial College London

Edited by Erich A. Müller

Volume 4

2022

9 781916 005037

Published by Imperial College London, London SW7 2AZ, UK
Contact details – e.muller@imperial.ac.uk

This book is a compilation of manuscripts created as part of a teaching assignment on the 4th year's Chemical Engineering CENG97005 course (Advanced Chemical Engineering Practice Research Project) . Copyright in each paper rests with its authors. The author of each paper appearing in this book is solely responsible for the content thereof; the inclusion of a paper in the book shall not constitute or be deemed to constitute any representation by Imperial College London that the data presented therein are correct or sufficient to support the conclusions reached or that the experiment design or methodology is adequate.

E-ISBN 978-1-9160050-3-7

First published in 2022

Preface

This volume of *Chemical Engineering Research* collects the unedited research project reports written by 4th year undergraduates (Class of 2022) of the M.Eng. course on Chemical Engineering in the Department of Chemical Engineering at Imperial College London. The research project spans for one term (Autumn) during the last year of the career and has an emphasis on independence, ability to plan and pursue original project work for an extended period, to produce a high quality report, and to present the work to an audience using appropriate visual aids. Students are also expected to produce a literature survey and to place their work in the context of prior art. The papers presented showcase the diversity and depth of some of the research streams in the department, but obviously only touch on a small number of research groups and interests. For a full description of the research at the department, the reader is referred to the departmental website[1].

The papers presented are in no particular order and they are identified by a manuscript number. Some papers refer to appendixes and/or supplementary information which are too lengthy to include. These files are available directly from the supervisors (see supervisor index at the end of the book). Some of the reports are missing, being embargoed as they contain confidential information. A few reports correspond to industrial internships, called LINK projects, performed in collaboration with Shell.

2022 continued to be challenging time, as many experimental facilities were either temporarily closed down and/or had restricted access as a consequence of the measures to mitigate the Covid-19 pandemic. This is reflected in a larger fraction of the research projects being theoretical or computational in nature.

Cover figure corresponds to an polarized microscopy image of an anionic polymer solution (taken from the work of Ho Maeng and Yesol Kim, manuscript 6).

London, February 2022

---

[1] https://www.imperial.ac.uk/chemical-engineering

Title Index

(*) These papers have been removed by request of the authors and/or supervisors

Author and Supervisor index at the end of the book.

Evaluation of Virtual Reality Training through a validated engagement index and subjective metrics

Caleb Sheng and Xiaozhou Feng
Department of Chemical Engineering, Imperial College London

Abstract

In recent years there have been an increasing number of studies into using Virtual Reality (VR) for training purposes due to reduced cost and increased convenience. Previous studies suggested using eye-tracking and heart rate monitoring as objective metrics and the Immersive Experience Questionnaire (IEQ) as the subjective metric to measure cognitive load. In this paper, engagement was assumed to be an indicator of the effectiveness of VR training platforms. This study developed a novel engagement index computed from eye-tracking, heart rate and body motion data to quantify engagement levels. 61 participants carried out a VR assembly task simulation, and their data were collected. The comparison of engagement between two demographic categories, namely those who require optical correction and those with previous VR experience, demonstrated a small enough statistical difference to conclude the training platform as non-selective towards those groups. The questionnaire adapted from IEQ provided similar findings to the engagement index, where the Assessment tasks generally scored higher. However, the usefulness of the subjective metric requires further investigation as it failed the Cronbach Alpha test. In addition, the engagement index was observed to change as a result of perceived difficulty and stimuli such as acoustic feedback and emotional involvement. Whilst a correlation was observed, due to limitations of the VR simulation, a robust relationship was not established. As a result, this paper recommends improvements to the simulation and further studies to be conducted.

***Keywords*—** Virtual reality, Engagement, Eye-tracking, ECG, Body Motion, IEQ

1 Introduction

Chemical Engineers often train on large pilot plants to familiarise themselves with operating and safety procedures. However, training on pilot plants is not only reliant on their availability and location but is also extremely costly. For example, Imperial College's Carbon Capture pilot plant costs approximately £2 million to build, with the capacity of teaching only 300 engineers a year [1][2]. In addition, the handling of dangerous chemicals on pilot plants also incurs safety risks, especially if operated by inexperienced engineers. Furthermore, the COVID-19 pandemic has resulted in increased working from home, thus reducing the opportunities for engineers to train in person. All these factors point towards alternative means of training chemical engineers. Interactive virtual reality (VR), primarily using head-mounted displays (HMD), has recently seen an enormous uptake in users, with 17.7% of the US population expected to have used VR monthly by the end of 2021 [3]. This is mainly due to the fast advancements of VR in fields such as gaming, allowing the creation of more detailed and immersive environments. Advancements in dynamic foveated rendering have improved headset framerates by up to 66 % and reduced shading loads up to 72% [4]. In addition, the onset of COVID-19 and social distancing has spurred increasing desire to use VR in social engagements, with 77% of survey respondents expressing interest in using VR to interact with one another [5]. As a result, there has been increasing enthusiasm for VR based training which can provide a more convenient, inexpensive, and safer alternative to conventional training methods [6][7].

2 Background

2.1 Engagement

Greater Engagement, along with immersion and presence, is frequently used within the field of VR as an indicator of success. Although McMahan [9] pointed out that engagement should only be classified as the first step towards immersion, the three concepts are often used interchangeably. Three key criteria have been identified to produce an engaging platform: matching the user expectation with the environment design, significant impact of user actions, and consistency in the virtual environment.

2.2 Objective Metrics

Eye-tracking has been identified as a critical indicator in estimating cognitive load, particularly the analysis of the pupil diameter [Foundations of Augmented. . .][Measuring cognitive load using]. Fluctuations in pupil diameter have been shown to directly relate to cognitive load through a metric known as the Index of Cognitive Activity (ICA) [foundations +IPA paper]. Despite this, the method to compute ICA is proprietary and not publicly available. A more recent study into the Index of Pupillary Activity (IPA) has shown similar relations to cognitive load. IPA was used in this study due to its non-proprietary nature and its thorough and detailed open-source documentation [18]. Moreover, there is evidence to suggest that IPA can distinguish between task difficulty[SOURCE]. Eye-tracking related metrics have not yet been established as an indicator of measuring engagement levels. Some studies have used Electroencephalogram (EEG) as a metric to measure engagement in VR systems [21][6]. However, a strong relationship between brain waves and engagement is yet to be established. Furthermore, there are many limitations to using EEG as a metric due to its intrusive nature and the requirement of direct scalp contact[5]. By implementing Electrocardiogram (ECG), the electrical signals generated from the heart is measured. This is usually achieved by placing electrodes close to the heart, and the intensity and timings of the signals are captured. The variability of heart rate specifically is a powerful indicator of stress [17]. As concluded by Meshkati [18], it is one of the most robust measurements of mental workload.

2.3 Subjective Questionnaire

Implementing a subjective metric allows the participants to self-assess their engagement level. In literature [8], various types of questionnaires have been proven to be effective, including Immersive Experience Questionnaire (IEQ), Game Experience Questionnaire (GEQ), Simulator Sickness Questionnaire (SSQ), and so on. The training used in this study was considered to be relatively stationary, hence SSQ was not considered. To measure the success of VR training, a few key psychological senses were identified: flow, cognitive absorption, presence, and immersion. Immersion refers to the dissociation with the real world, feeling the presence in the virtual environment. In order to achieve high levels of immersion, the virtual environment must reflect conventional expectations of action impact, and the conventions must remain consistent. Engagement, to be distinguished from immersion, refers more to the emotional connection of the user to the events within the virtual environment. An example is the urge to want to gain points during a quiz. [10] Lastly, motivation is important, especially for the purpose of teaching or training, to ensure the completion of modules. IEQ focuses on five metrics: challenge, control, real-world dissociation, emotional involvement, and cognitive involvement [8]. The questionnaire implemented in this study was adapted and condensed into 16 questions covering all five metrics, tailored to suit the application.

2.4 Platform Design Considerations

Within the last ten years, a wide range of studies have been conducted on the effectiveness of utilising VR, namely the extent of immersion and cognitive load. Studies have shown using an HMD produces a stronger sense of presence [11], which leads to higher engagement levels [10]. Moreover, first-person VR experiences greatly add to the sense of presence over third-person experiences [6]. The choice of graphic imagery is also crucial. The study from Li Y. shows that there is a notable and robust positive relationship between the mere presence effect of graphics and user engagement. However, the engagement enhancement of colours is shown to be inconsistent, as mental overload can occur. Within the field of VR, studies have confirmed the effectiveness of simple graphics, improving engagement by 21% (Peter Chapman). Moreover, as mentioned previously, engagement is high when the platform is consistent. Having simple imagery would result in less load on the hardware, allowing a smoother frame transition leading to higher engagement.

2.5 Statistical Comparison Methods

The primary method to determine whether two sample groups are statically different is the Mann-Whitney U test, which is a non-parametric test [13]. It evaluates the ranking of two independent groups from low to high and compares the sum of the rankings. Unlike the student T-test, it can analyse non-normally distributed data. This distribution is verified using the Shapiro-Wilk test [14], otherwise the student T-test should be implemented. The null hypothesis of the Mann-Whitney U test is that the two groups are not statistically different, which can be rejected if the p-value is less than 0.05. It also computes a U value, which is the lower of the two calculated Ui values as shown below:

$$U_i = R_i - \frac{n_i(n_i+1)}{2} \tag{1}$$

Where R_i is the sum of sample ranking, and n_i is the size of sample i In the development of IEQ, the internal consistency of the data set was assessed using Cronbach's Alpha ((Rigby, Brumby, Gould and Cox, 2019), which is also known as the tau-equivalent reliability. For k items, each with an associated score of Xi, the Cronbach's Alpha can be calculated with the following formula [15]:

$$\rho_T = \frac{k}{k-1}(1 - \frac{\sum_{i=1}^{k} \sigma_i^2}{\sigma_X^2}) \tag{2}$$

where σ represents the variance

The threshold of data reliability is 0.7, and any values below will deem the data set to be unreliable. In this study, the Cronbach's Alpha number was computed using SPSS 28.0.

2.6 Aim

This study aims to implement the strengths of previous studies and improve on their weaknesses, to develop more refined engagement measurements with a more robust methodology. In addition to eye-tracking, which is commonly used within this field, body motion and heart rate were monitored to provide a more reliable data set. The first-person user interaction is enhanced through a set of controllers, aiming to maximise engagement. Finally, this study intends to evaluate the effectiveness of a subjective engagement metric and define a non-biased engagement index.

3 Methods

3.1 Participants

For this study, 61 participants (39 males, 21 females and 1 non-binary) were selected between the ages of 18-61, primarily from Imperial College London. Participants were not expected to have any engineering background as the simulation required no prior knowledge. From a pre-experiment survey: 44.3% of participants had some prior experience in VR, 37.7% of participants wore glasses, and 18% wore contact lenses. The vast majority of participants, however, were from the younger age ranges of 20 (21.3%) and 21-30 (72.1%).

3.2 Materials

Eye-tracking data was recorded using a Pico Neo 2 Eye VR Headset due to its in-built eye-tracking capabilities and Qualcomm Snapdragon 845 processor, allowing for recordings to be taken from any location. In addition, the headset came with hand controllers allowing participants to interact with their environment. Both the headset and controllers were also capable of head and controller motion tracking, allowing IBA to be calculated. ECG data was recorded using a Polar H10 Heart Rate Sensor due to its industry-leading accuracy, ease of use and efficient data streaming capabilities. Statistical analysis was computed using SPSS 28.0 due to its wide usage within the field. [Nitesh Bhatia paper].

3.3 Simulation Outline

The Pre-Training simulation consisted of placing an empty box onto a table and closing it with a lid before placing the closed box onto a conveyor belt, all whilst under vocal and visual assistance. The purpose of Pre-Training was to familiarise participants with the VR controls and environment so that whilst undergoing Training and Assessment simulations, difficulties faced would be associated with the task at hand and not with using the controls themselves. The Training simulation consisted of an initial eye calibration test, followed by the box assembly task. The eye calibration test involved looking at both white and black screens and following a blue dot with your eyes in order to calibrate the participants eye psychometric data. The steps in the box assembly task are outlined in Table [5 column table with experienced difficulty] and a screenshot of the environment can be seen in Figure [Insert

Pic of VR simulation]. All of these steps were carried out under vocal and visual assistance. In the case of Print Label, this occurred automatically after the Start Process button was pressed and was accompanied by an audible printing sound. The Assessment simulation consisted of only the box assembly task as outlined in Table [5 column table with experienced difficulty], however this time with no vocal or visual assistance. It should be noted that in all simulations the tasks must be done in the right order to proceed.

3.4 Procedure

A play space of at least 3mX2m was initially set up to allow the participants to easily carry out the activities without obstructions. Before taking part in the study, participants first read through an information sheet detailing the activity they would be taking part in. They were then instructed to complete both a consent form and a Pre-Training Volunteer form. Participants were then instructed to wear the Polar H10 Heart Rate Sensor just below the chest with direct contact to the skin. Following this, participants put on the VR headset and carried out the Pre-Training. After the participants were comfortable with the grab and trigger controls, and overall movement in the environment, they took part in the Training. Once completed, a series of questions were asked about their experiences. It was made sure that the participants did not remove their headset when answering these to ensure the prior calibration and fit of the headset was still appropriate. Next, participants carried out the Assessment followed by a questionnaire asking about their experiences. In situations of difficulty, 20 seconds was waited before vocal assistance was given. Eye-tracking, ECG, Head and Motion Controller data was recorded for each participant in both the Training and Assessment simulations. The engagement index was calculated from three different metrics: IPA, Index of Body Activity (IBA) and Index of Heart Activity) IHA. IBA and IHA were calculated in the same way to IPA but using ECG and Motion data. These three metrics were then normalised relative to the participant population before being averaged to compute the engagement index. Task duration was seen as the primary indicator of task difficulty [Effectiveness of Virtual] as a more difficult task is expected to take longer to complete. In order to assess whether or not a participant found a task difficult, the Assessment task duration was compared to the Training. If the task took longer in the Assessment than Training, factoring in a 25% increase, then the participant was deemed to have experienced difficulty.

4 Results and Discussion

4.1 Procedure

Though 61 participants were selected for this study, the engagement index could only be computed for 32 participants. This was due to issues related to the hardware, physical environment and virtual simulation, such as poor room lighting leading to lost IBA data and the headset overheating leading to lost IPA data as outlined in Table XX [Table with IPA, IBA and IHA Metrics]. These issues were alleviated by switching rooms and procuring another identical headset for data collection. The largest problem was related to the heart rate sensor being unable to record ECG data for multiple participants in succession. Therefore, there were significantly fewer IHA metrics computed at only 34 for Training and 38 for Assessment. As it was desired to compare participant engagement across both Training and Assessment this resulted in only 32 common engagement indexes being calculated.

4.2 Demographic Findings

To evaluate the usability of the platform, two examples of the demographic features were isolated, and their statistical significances were computed using the Mann-Whitney U test. The first feature identified was the need for optical correction, namely glasses. Eye-tracking feasibility and comfort were concerns regarding wearing glasses inside the headset. Secondly, having previous VR experience can provide an advantage as those participants would be more comfortable with the gestures and environment. As seen in the table above, the participants who wore glasses are on average ranked lower in both Training and Assessment, implying that their engagement indices are higher numerically. As it was only expected that the glasses could hinder their performance, it can be concluded that this training platform is feasible for those who need optical correction. On the other hand, the participants with previous VR experiences performed better than the others in both modules, confirming the previously stated expectations. All four p-values computed are above the threshold of statistical difference, therefore the sample groups cannot be separated. This concludes that the two demographic characteristics should not hinder the training platform usability.

Category	Module	Criteria	Population Size	Mean Rank	Mann-Whitney U	P-value
Vision Correction (glasses)	Training	Yes	14	19.00	81.0	0.091
		No	18	13.29		
	Assessment	Yes	14	19.93	78.0	0.071
		No	18	13.83		
Previous VR Experience	Training	Yes	13	17.15	115.0	0.744
		No	19	16.05		
	Assessment	Yes	13	19.31	87.0	0.170
		No	19	14.58		

Table 1: Mann-Whitney U Test on Demographics

4.3 Statistical Analysis of Training compared to Assessment

By employing the Mann-Whitney U test, the difference in engagement between Training and Assessment can be determined

	Module	Mean Rank	Mann-Whitney U	p (2 tailed)
Questionnaire	Training	42.75	783.5	<0.001
	Assessment	72.25		
Engagement Index	Training	29.72	423.0	0.232
	Assessment	35.28		

Table 2: Training vs. Assessment Questionnaire Results

From both the questionnaire and computed engagement index, the Assessment showed a higher level of engagement. It is to be noted that the questionnaire result was obtained from a much larger population (57 valid data points); therefore, the higher U value has no statistical significance. By assessing the 2-tailed p-value of both metrics, the questionnaire suggests a statistical difference between the two modules, whereas the opposite is observed from the engagement index. The discrete scale of the questionnaire can be a contributing factor to the difference, as it will be more likely that the recorded scores are numerically further apart. Additionally, after computing the Cronbach's Alpha test on both metrics, the questionnaire failed the reliability threshold of 0.7, presenting a score of 0.570 for the sample population. Through implementing the "scaled if deleted" function on SPSS 28.0, the question that contributed most significantly to the unreliability is "How well do you think you performed in the training experience?", with the reliability index increasing to 0.678 after deletion. This is an indication that subjective views are influenced largely by the confidence level of individuals, which is an additional degree of freedom to the measurement. In order to utilise questionnaires as an effective engagement metric, further design refinement is necessary.

4.4 Engagement Index

Figure 1 a reveals that in most cases, higher levels of engagement were observed across the Assessment, with the exception of both Place Lid and End Process. This illustrates that participants felt more engaged in the Assessment, possibly due to the lack of both visual and vocal instructions, leading to a more realistic and immersive environment. Moreover, the challenge of recalling the correct task order has resulted in higher levels of engagement. Table [Wide table with 5 columns and some red text] reveals a larger standard deviation across the majority of tasks in the Assessment, with the exception of the Print Label and Move Box. This demonstrates how the engagement across participants greatly differed, possibly as a result of varying levels of difficulty experienced. Figure [Average Engagement Index] shows a higher engagement index in Print Label compared to Start Process, indicating a relationship between acoustic stimuli and engagement. The Print Label sound validated whether or not the Start Process button had been successfully pressed and thus enhanced engagement as the participants were sure they could proceed further. By dividing the participants into more engaged in Assessment and more engaged in Training for each task, the latter group can provide additional information on the effect of task design on engagement.

Figure **??** represents the population size who found the assessment module more engaging, with "0" depicting exactly half of the sample size (16 people). The three tasks with fewer than half of the population should be highlighted: Start Process, Place Lid, and End Process. This coincides with the most difficult tasks ranking by the participants:

Ranking of Task Difficulty	Training	Assessment
1	End Process	End Process
2	Start Process	Start Process
3	Grab Lid + Place Lid	Grab Label + Attach Label
4	Grab Label + Attach Label	Grab Lid + Place Lid

Table 3: Ranking of Most Difficult Tasks by Participants

Without vocal instruction, these difficult tasks seem to dissociate the users from the training platform, possibly due to the unintuitive or unrealistic task designs. For example, for the End Process step, the participants needed to recall the step which takes place before the packaging process finishes, as well as put their hand into the screen. This mismatch with their expectations of reality can be a significant source of disengagement. IPA, IHA, and IBA were assumed to all be equally weighted when calculating the engagement index. However, the validity of this weighting is yet to be confirmed. Furthermore, collecting more IPA, IHA, and IBA data from each participant would allow for normalisation relative to their own levels of engagement. This all would result in a more robust computation of the engagement index.

4.5 Task Duration

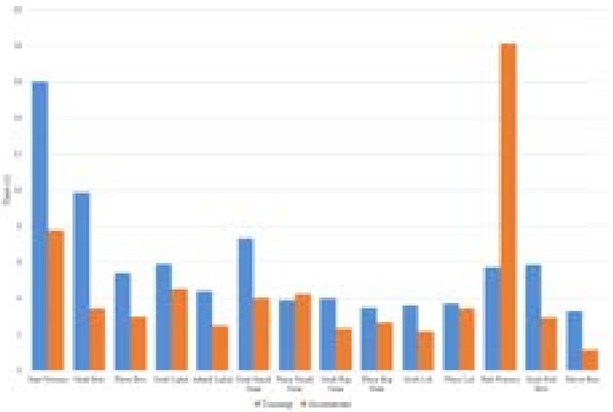

Figure [average task duration] reveals an opposite trend to that of the engagement index. As expected, task duration is lower in the Assessment than Training as participants were carrying out a task for the second time. However, in the case of End Process, the average task duration was 317% longer in the Assessment. It was observed from the data collection that the majority of participants forgot to click End Process before trying to move the full box onto the conveyor belt, preventing them from proceeding. In a few cases, this step was forgotten entirely, and vocal assistance had to be provided to ensure that the Assessment was completed. Table [5 column table with experienced difficulty] illustrates, in accordance with the average task duration, that End Process was the most difficult task with 16 participants experiencing difficulty. Table [5 column table with experienced difficulty] reveals that in 91.2% of cases where there was task difficulty, the participant's engagement index also dropped. Whilst this is the case, the magnitude of the difference in participant engagement is not reflected in the task duration, with values ranging from -0.12 to 0.01. It was initially thought that participants who showed low levels of engagement in Training would exhibit greater difficulty in the Assessment, reflected by a higher task duration. However, after this comparison, no clear relationship could be established. This perhaps shows the lack of a direct link between one's engagement levels and how much attention they paid during the Training. When comparing the engagement index in Assessment itself to the Assessment task duration, a greater correlation is revealed. Figure [Correlations in End Process] illustrates a slight negative correlation between the engagement index and task duration for the End Process task, showing that participants with lower engagement generally took longer to complete the task. However, it could not be established whether there was a linear or exponential relationship.

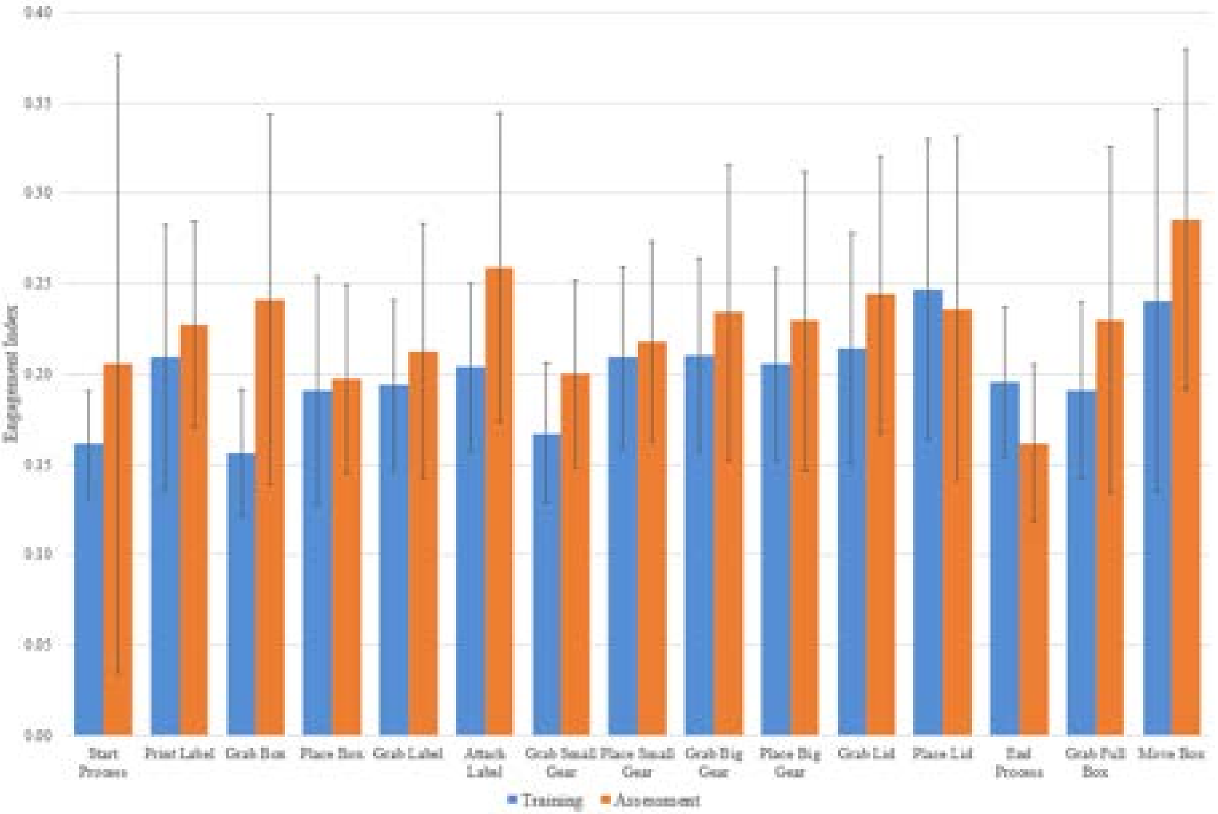

Figure 1: Average Engagement Index Per Task

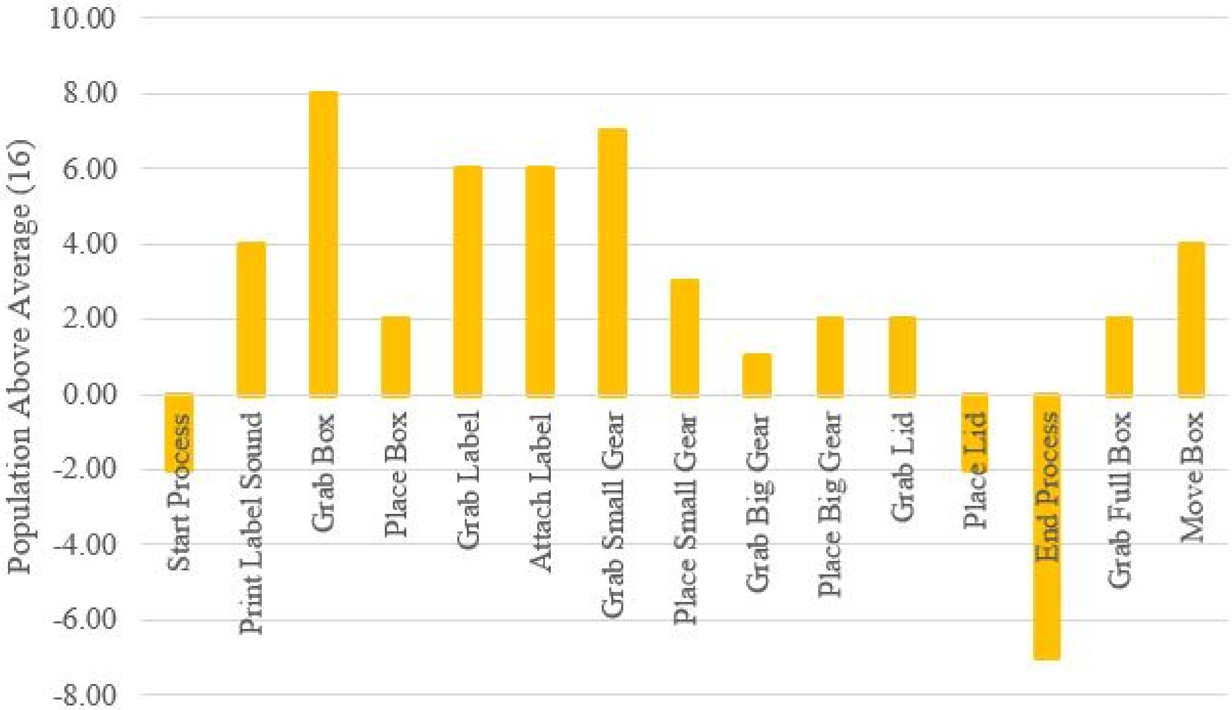

Figure 2: Population Compared to Average that Found Assessment More Engaging

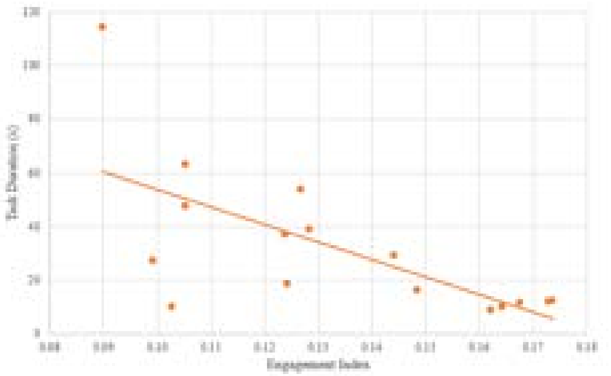

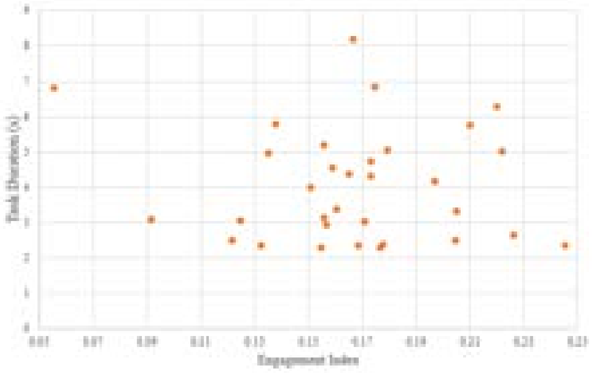

When observing a task that only 1 participant experienced difficulty in such as Grab Small Gear, Figure [Correlations in Grab Small Gear] illustrates little to no correlation between the engagement index and task duration. These findings illustrate how tasks with greater difficulty (End Process) exhibit a much stronger relationship with the engagement index than those with lower difficulty (Grab Small Gear). This is due to the greater range of task duration in more difficult tasks, and thus small variations in one's base task duration are less pronounced. Therefore, a limitation discovered was the lack of difficulty in the assembly procedure, pointing to the desire to implement harder tasks in order to compute a more robust relationship. Some limitations of this analysis were that there were multiple independent variables that could have caused the engagement index to lower, such as the increased difficulty in remembering tasks, the lack of vocal and visual instruction as well as the incurred boredom from task repetition.

5 Conclusions and Outlook

5.1 Conclusions

In this study, engagement level was quantified using both subjective metrics as well as a defined engagement index. The usefulness of each metric was evaluated, and the current training platform design was critically analysed. The engagement index computed from eye-tracking, heart rate, and body motion was found to be more reliable compared to the traditional questionnaire metrics, subject to the limitations of the current question designs. Engagement is found to be related to task difficulty, which in the study was shown through correlating engagement index to task duration. Despite the observed trend, no clear correlation was derived due to the uncontrolled independent variables. Further studies will be necessary to quantify a concrete relationship between them. Additionally, the strengths and weaknesses of the current platform design provide insights into possible improvements to enhance engagement, namely the implementation of stimuli. Finally, through statistical analysis of the performance variation across the participant demographics, the current platform is found to be suitable for users who need optical corrections and the ones without any previous VR experiences.

5.2 Outlook and Future Works

In order to take this study further, some improvements are suggested from both participant feedback as well as observations taken from conducting the procedure. The main suggestions include the implementation of more haptic and acoustic feedback, as well as allowing participants to proceed even if the tasks are not performed in the correct order. These changes would make the simulation reflect real life more accurately and ensure that participant engagement does not drop as a result of these flaws. A more diverse population should also be tested, particularly those that are older and from different educational and cultural backgrounds. In order to establish the effectiveness of the VR training itself, in-person data should be collected and use the performance as a benchmark to evaluate the VR training effectiveness. The questionnaire unreliability suggested by the low Cronbach's Alpha also requires further improvement in order to design robust future studies. The questions were answered on a scale of 1-5, which are very discrete quantities to obtain a continuous data distribution. Therefore it is recommended to implement larger scales such as maximums of 7 or 10. Secondly, some questions demonstrated significant response inconsistencies due to the varying confidence levels across participants. Questions requiring them to assess their own performance should be eliminated. Lastly, questionnaires are generally considered to be invasive methods of subjective data collection, often skewing the responses to the views of the investigators. Other survey forms such as focus groups and interviews are therefore recommended, and quantification techniques need to be developed. In the future, investigating the transferability of this study into other fields such as process plant training and surgery operations should be looked into, as frequently suggested by participants. In the field of education, the engagement index could be applied as a key indicator of one's reception to certain learning media. Therefore, allowing the future implementation of an automated learning delivery system that would provide one with information that exhibits the highest levels of engagement.

6 References

1. Facilities [Internet]. Imperial College London. 2021 [cited 14 December 2021]. Available from:https://www.imperial.ac.uk/chemical-engineering/discovery/facilities/

2. System 800xA for ABB pilot carbon capture plant at Imperial College [Internet]. Control Systems. 2021 [cited 14 December 2021]. Available from: https://new.abb.com/control-systems/industry-specific-solutions/oil-gas-and-petrochemicals/system-800xa-for-pilot-plant-at-imperial-college-london

3. US Virtual and Augmented Reality Users 2021 [Internet]. Insider Intelligence. 2021 [cited 14 December 2021]. Available from: https://www.emarketer.com/content/us-virtual-augmented-reality-users-2021

4. releases P, Tracking P. Tobii announces VR headset with native eye tracking [Internet]. Tobii.com. 2021 [cited 15 December 2021]. Available from: https://www.tobii.com/group/news-media/press-releases/2020/1/pico-interactive-and-tobii-announce-

worlds-first-commercial-standalone-vr-headset-with-native-eye-tracking/

5. Koetsier J. VR Needs More Social: 77% of Virtual Reality Users Want More Social Engagement [Internet]. Forbes. 2021 [cited 16 December 2021]. Available from: https://www.forbes.com/sites/johnkoetsier/2018/04/30/virtual-reality-77-of-vr-users-want-more-social-engagement-67-use-weekly-28-use-daily/?sh=1c74a78f18fc

6. Gavish N, Gutiérrez T, Webel S, Rodríguez J, Peveri M, Bockholt U et al. Evaluating virtual reality and augmented reality training for industrial maintenance and assembly tasks. Interactive Learning Environments. 2013;23(6):778-798.

7. Koumaditis K, Chinello F, Mitkidis P, Karg S. Effectiveness of Virtual Versus Physical Training: The Case of Assembly Tasks, Trainer's Verbal Assistance, and Task Complexity. IEEE Computer Graphics and Applications. 2020;40(5):41-56.

8. Jennett C, Cox A, Cairns P, Dhoparee S, Epps A, Tijs T et al. Measuring and defining the experience of immersion in games. International Journal of Human-Computer Studies. 2008;66(9):641-661.

9. [Internet]. Phil-fak.uni-duesseldorf.de. 2021 [cited 16 December 2021]. Available from: https://www.phil-fak.uni-duesseldorf.de/fileadmin/Redaktion/Institute/Kulturund Medien/MedienundKulturwissenschaft/Dozenten/Szentivanyi/ Computerspielanalyseausulturwissenschaftlicher Sicht/mcmahan.pdf

10. Kallinen, Kari Salminen, Mikko Ravaja, Niklas Kedzior, Ryszard Saaksjarvi, Maria. (2007). Presence and emotion in computer game players during 1st person vs. 3rd person playing view: Evidence from self-report, eye-tracking, and facial muscle activity data. Proceedings of the 10th Annual International Workshop on Presence. 11. i-Berthouze, W. W. Kim, and D. Patel.

12. Meshkati N. Heart Rate Variability and Mental Workload Assessment. Advances in Psychology. 1988;:101-115., pages 102–113. Springer, 2007.

13. Mann, H. and Whitney, D., 1947. On a Test of Whether one of Two Random Variables is Stochastically Larger than the Other. The Annals of Mathematical Statistics, 18(1), pp.50-60.

14. Sijtsma, K. and Emons, W., 2010. Nonparametric Statistical Methods. International Encyclopedia of Education, pp.347-353.

15. Cronbach L. Coefficient alpha and the internal structure of tests. Psychometrika. 1951;16(3):297-334.

16. Rigby, J., Brumby, D., Gould, S. and Cox, A., 2019. Development of a Questionnaire to Measure Immersion in Video Media.Proceedings of the 2019 ACM International Conference on Interactive Experiences for TV and Online Video,.

17. Murphy D, Higgins C. Secondary Inputs for Measuring User Engagement in Immersive VR Education Environments. [Internet]. 2019 [cited 15 December 2021];. Available from: https://arxiv.org/pdf/1910.01586.pdf

18. Meshkati N. Heart Rate Variability and Mental Workload Assessment. Advances in Psychology. 1988;:101-115.

19. Li Y, Xie Y. Is a Picture Worth a Thousand Words? An Empirical Study of Image Content and Social Media Engagement. Journal of Marketing Research. 2019;57(1):1-19.
20. Monteiro D, Liang H, Abel A, Bahaei N, Monteiro R. Evaluating Engagement of Virtual Reality Games Based on First and Third Person Perspective Using EEG and Subjective Metrics. 2018 IEEE International Conference on Artificial Intelligence and Virtual Reality (AIVR). 2018;.

21. P. Marshall S. Assessing Cognitive Engagement and Cognitive State from Eye Metrics. EyeTracking Inc. 2008

22. Zagermann J, Pfeil U, Reiterer H. Measuring Cognitive Load using Eye Tracking Technology in Visual Computing. Proceedings of the Beyond Time and Errors on Novel Evaluation Methods for Visualization - BELIV '16. 2016;.

23. Duchowski A, Krejtz K, Krejtz I, Biele C, Niedzielska A, Kiefer P et al. The Index of Pupillary Activity. 2021.

24. Mahmoud K, Harris I, Yassin H, Hurkxkens T, Matar O, Bhatia N et al. Does Immersive VR Increase Learning Gain When Compared to a Non-immersive VR Learning Experience?. Learning and Collaboration Technologies Human and Technology Ecosystems. 2020;:480-498.

Characterisation of Polyethylene Fibres as a Reference Hydrophobic Material for Chromatographic Separation of Peptides

Shivani Thangaraj and Irmantas Racaitis
Department of Chemical Engineering, Imperial College London, U.K.

Abstract: Reversed-phase chromatography on silica-based stationary phases is the most widely employed chromatographic technique for peptide purification. However, issues with silica-based resins arise due to the presence of residual silanols which interfere with the hydrophobic character of the stationary phase. This study investigates the potential of replacing conventional resins with Spectra 75 polyethylene fibres to create a column with exclusively hydrophobic interactions. A selection of established methods were employed to characterise the fibre stationary phase in comparison to a conventional silica-based column. The potential of the novel column was evaluated for uses in peptide separation and the development of a peptide hydrophobicity index with RP-HPLC through gradient elution of model peptides. The comparative performance of the Spectra 75 column revealed its limited separation power due to a significantly lower surface area within the column, resulting in greater resolution with the conventional column. Despite limited retention, a peptide hydrophobicity scale was successfully developed using elution concentrations in the Spectra 75 column and correlated with theoretical values and contact angles. This study has yielded demonstrable potential of Spectra 75 fibres for peptide separations with increased surface areas and a novel method for development of a peptide hydrophobicity scale to aid in separation processes.

Introduction

High-performance liquid chromatography (HPLC) is one of the most widely used analytical techniques in the pharmaceutical and biotechnological industries. It is used to separate the components in a mixture based on their physicochemical properties and affinities to the mobile and stationary phases of the HPLC system. Chromatographic separations are particularly relevant to pharmaceutical applications as they account for the largest fraction of separation costs for downstream processing of peptide-based drugs, such as insulin (Hardick et al., 2015).

Over the years, a variety of chromatographic modes have been developed, such as normal-phase (NP-HPLC), reversed-phase (RP-HPLC), size exclusion (SEC), and ion exchange (IE). By far, the most common is the reversed-phase technique, accounting for over 90% of all HPLC separations (Žuvela et al., 2019).

The commonly utilised chromatographic modes for peptide separation are size-exclusion (SEC), ion-exchange (IE) and reversed-phase (RP-HPLC) (Mant et al., 2007), the selection of which is governed by the properties of the target peptide analyte and its impurities.

In SEC, the separation is based on the hydrodynamic radii of the analytes. Although this technique is highly used in pharmaceutical applications and protein purification, it has a molecular weight cut-off of 5 kDa that only covers the maximum size range of peptides (generally between 0.1 to 6 kDa) (Mant et al., 2007). Additionally, if the target peptide is chemically synthesised, the by-products contain similar amino acid sequences as the main product; hence, the target peptide analytes are frequently of comparable molecular size to such impurities. As a result, the SEC technique can only be employed in a scarce subset of applications of peptide purification.

IE chromatography is based on the net charge and charge distribution of the molecules of interest. This technique is vastly utilised to separate proteins from biological debris due to its high selectivity (Stanton, 2004). However, the main disadvantage of this type of chromatography is that it requires extensive method development and elaborate fine-tuning. In addition, it is limited when the peptides in the mixture have similar isoelectric points.

On the other hand, RP-HPLC is by far the most relied upon mode for peptide separation due to its versatility and easier method development (Mant et al., 2007). Most importantly, this technique relies on the hydrophobic interactions between the stationary phase and the components of interest. Since peptide sequences are composed of amino acids which vary greatly in their hydrophobicity, these compounds are perfect candidate analytes for chromatographic separations based on hydrophobic interactions.

The majority of RP-HPLC columns are currently packed with silica supports. These silica-based resins are generally preferred to carbon- and polymer-based resins due to their well-understood and controllable pore structure and morphology, and physical stability which guarantee rapid mass-transfer, good loadability, and high reproducibility. In order to provide a hydrophobic character to silica supports, these are modified by chemically bonding of alkyl chains to their surface (Žuvela et al., 2019).

Despite alkyl-modified silica-based resins being the stationary phase of choice for most chromatographic applications, complex issues arise due to their surface chemistry. Even after the resin is chemically modified, a significant portion of its surface contains free silanol (Si-OH) groups. Since silanols are species that can participate in the formation of hydrogen bonds with its hydroxy group and electrostatic interactions with its ionised form, such can potentially affect separation of analytes

(Bocian and Buszewski, 2012). Many manufacturers pre-treat the silica with a mineral acid wash to ensure low silanol activity for stationary phase preparation (referred to as 'base deactivated silica'). It is also very common to employ an end-capping procedure in which the alkylated silica surface undergoes subsequent reactions with short alkyl chain silanes to reduce the amount of residual silanol groups. However, even after end-capping, more than 50% of silanol groups remain active (Borges, 2014).

Regarding the current techniques to overcome this problem, the addition of 0.1% TFA in the mobile phase suppresses the ionic interactions between peptides and surface silanols, however, it also interferes with and reduces the chromatographic signal, thus lowering sensitivity (Supelco, 2002). In addition, the issue of residual silanols led to the development of various hybrid silica adsorbents and silica-hydride materials, referred to as Type C silica. In Type C silica the surface is populated with silicon-hydride (Si-H) groups, which are less polar than silanol groups. (Borges, 2014).

Although methods to minimise the effects of residual silanols have been developed, they provide only a limited alleviation of the problem. A definitive approach would the complete substitution of silica-based resins with a different column packing material.

The material of interest in this study is ultra-high-molecular-weight polyethylene (UHMWPE) which was used to pack an HPLC column in the form of fibres. Due to the chemical composition of this polymer, the interactions between potential analytes and the PE stationary phase are hypothesised to be exclusively hydrophobic. Its highly crystalline structure also guarantees chemically robust and relatively uniform surface properties. As a result, the HPLC column could potentially prove useful for the separation of peptide-based drugs with regards to their hydrophobicity. In addition, the column could be employed as a new standard to evaluate the hydrophobicity of peptide molecules, as opposed to conventional techniques, such as modelling and contact angle measurements. Hence, the aim of this study is to propose and characterise polyethylene fibres as an alternative stationary phase and a hydrophobic reference material for chromatographic peptide separation.

To fully describe a stationary phase with regards to its main physico-chemical properties, suggested applications, and potential limitations, the column must first be characterised. This usually consists of, but is not limited to, a combination of chromatographic, thermal, spectroscopic, and computational methods. This study explores the application of a selection of these characterisation methods to the proposed Spectra 75 HPLC column.

Background

Over the years, there has been sporadic interest in the potential of polymer fibres for liquid chromatographic (LC) separations. The nature of research conducted has typically been limited to specific and unique applications of a single material; however, a more general two-part study was published in 2008–2009 by R Kenneth Marcus, discussing the physical and chemical rationale for polymer fibre stationary phases.

In this study, differently structured fibre phases in existing literature are reviewed. The most straightforward method uses aligned fibres extending along the flow axis of the column, in which the voids between fibres are effectively capillary channels. The capillary diameter and exposed surface area are dependent on the packing density and the individual fibre diameter. This method has been further developed with the use of capillary-channelled polymer fibres (C-CP), produced by melt-extruding typical polymer fibres to create continuous capillary channels running along the fibre axis. C-CP fibre phases have demonstrated the ability to separate a variety of organic compounds, including amino acids and proteins.

Studies have shown that higher efficiencies can be achieved with fibre phases compared to silica particles as linear velocities can be increased to much greater values. The primary trade-off is the very low specific surface area of around 1 m^2/g, compared to porous materials with a very wide range between 150–400 m^2/g. This decrease in the surface area reduces the potential loading capacity of columns (Marcus, 2009). While silica-based adsorbents are superior for small molecule separations, when it comes to macromolecules, the physicochemistry of polymer fibres allow for efficient mass transfer, low column back pressures with high mobile phase flow rates and chemical versatility. Therefore, polymer fibre-based separations can be developed as a means of complementing traditional methods in areas they prove to be superior rather than as a replacement.

Hydrophobic interaction chromatography (HIC) is a form of RP-HPLC, primarily employed for protein separations. It tends to use a less hydrophobic medium and thus weaker interactions to ensure the structural integrity and biological activity of the proteins is retained. In 2019, Wang and Marcus evaluated the separation of proteins using polyethylene terephthalate (PET) CC-P fibre phases, demonstrating that the PET C-CP column produced better separation efficiencies with much shorter analysis times compared to a commercially available HIC phase (Wang and Marcus, 2019). This was expanded on with a publication by a research group this year in which they presented a novel method of using a PET C-CP stationary phase to isolate lentiviruses with HIC (Huang et al., 2021).

The reliance on the hydrophobicity of proteins and peptides for separations has made the establishment of a hydrophobicity scale an important area of study. The grand average of hydropathicity (GRAVY) is a commonly used index which calculates the hydropathicity of an amino acid sequence by summing the experimentally determined hydropathicity values of each individual amino acid and dividing by the length of the sequence (Kyte and Doolittle, 1982). Since then, there have been several scales published to rank the hydropathicity of amino acids, typically obtained by partitioning in two immiscible liquid phases. However, this method does not consider the structural changes when amino acids are connected in a peptide. A group in 2016 tried accounting for this by simulating contact angle measurements of a water nanodroplet on a modelled peptide plane of unified amino acids (Zhu et al., 2016). Another method for characterising peptide hydrophobicity through RP-HPLC was developed by Krokhin and Spicer by correlating retention factors to the hydrophobicity of the peptides (Krokhin and Spicer, 2009).

Despite the recent additions to this field, there exists a gap in the literature worth exploring with regard to the use of pure PE fibres for evaluating hydrophobic interactions of peptides. In this study, properties of low-density PE fibre were characterised through different analytical techniques. Additionally, the potential uses of this material for peptide separations and as a reference for peptide hydrophobicity were assessed through inverse chromatography techniques.

Materials and Equipment

Materials

Spectra 75 polyethylene fibre was kindly provided by Honeywell (USA). The follwoing reagents were purchased from Merck (Germany): Uracil (99%), Ethylbenzene (anhydrous 99.8%), Propylbenzene (98%), Butylbenzene (99%), Pentylbenzene (99%), Hexylbenzene (97%), o-Terphenyl (99%), Tripenylene (98%), Caffeine (ReagentPlus, 99%), Benzylamine, Phenol (≥99%), Phosphoric acid (ACS reagent, ≥85 wt. %), Potassium phosphate monobasic (ACS reagent, ≥99.0%), Potassium phosphate dibasic (ACS reagent, ≥99.0%), Potassium hydroxide (ACS reagent, ≥85%, pellets), n-Hexane (99%), n-Heptane (99%), n-Octane (anhydrous, ≥99%), n-Nonane (99%), Ethyl acetate (≥99.5%), Dichloromethane (anhydrous, ≥99.8%), Diiodomethane (ReagentPlus, 99%). Other reagents were obtained from VWR International: Ethanol (99.8%), Acetone (pure), Hellmanex® III. All HPLC-grade organic solvents were purchased from Fisher Scientific: Methanol (99.9%, 2.5 L). , Acetonitrile (99.8%, 2.5 L). Peptides P1 (LGGGGGGDGSR), P2 (LGGGGGGDFR), P3 (LLGGGGDFR), P4 (LLGGGGDFR) and P5 (LLLLDFR), developed by Krokhin and Spicer, were chemically synthesised by GeneScript (Netherlands) with a minimum purity of 95% and no termini modification.

Equipment

HPLC analytical column (300 × 4.6 mm ID), analytical HPLC column Luna C18(2) (150 × 4.6 mm ID), Shimadzu Prominence LC20 modular HPLC system, Ohaus PX163 Pioneer Analytical Balance, Millex hydrophobic Fluoropore (PTFE) filter units from Merck, Millex hydrophilic Durapore (PVDF) filter units from Merck, Chromacol VAGK vials and caps from Thermo Scientific, 250 µl polypropylene inserts from Supelco, Micromeritics TriStar 3000 gas adsorption analyser, digital incubator INCU-Line from VWR International, 75 x 25 mm soda lime glass slides (1.0–1.2 mm thickness), 15 x 20 mm soda lime glass substrates with 20 nm ultra-flat quartz coating, adhesive tape, the spin coating machine, Krüss Drop Shape Analyzer, 1 mL syringes and 18ga Fisnar syringe dispense tips, silanised glass column (300 × 4 mm ID), iGC-SEA (Surface Measurement Systems, UK), JSM-6010 scanning electron microscope (Jeol, Japan)

Methods

A series of several analytical techniques was employed to gain a thorough understanding of the properties of Spectra 75 fibres and their behaviour as a stationary phase for liquid chromatography.

For all analytical techniques, Spectra 75 fibres were washed with water and ethanol in 5 cycles and dried in a 70 ˚C oven overnight. From here on, they will be referred to as cleaned Spectra 75 fibres.

Packing of the Spectra 75 HPLC Column

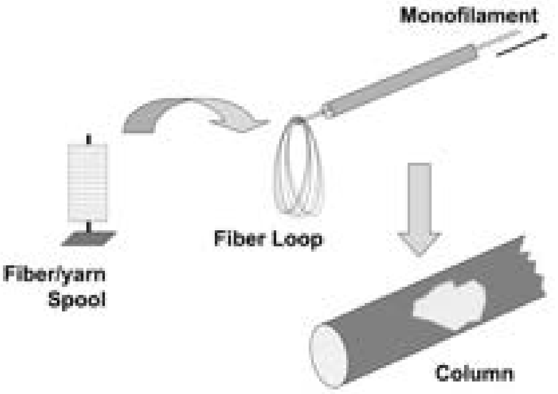

Figure 1*: Diagram taken from ‘Use of polymer fiber stationary phases for liquid chromatography separations: Part I – physical and chemical rationale’ (Marcus, 2008)*

The empty column (approx. 5 cm^3 in volume) was packed with Spectra 75 polyethylene fibres. The threads were carded to produce a loop of aligned

Table 1*: Tanaka Test conditions (Petersson and Euerby, 2005)*

	Run 1	**Expansion**	**Run 2**	**Run 3**	**Run 4**
Parameter	k'_{PB}, $\alpha_{(T/O)}$	$\alpha_{(CH2)}$	$\alpha_{(C/P)}$	$\alpha_{(B/P)}pH7.6$	$\alpha_{(B/P)}pH2.7$
Property tested	Hydrophobicity, Steric selectivity	Hydrophobicity	Hydrogen bonding capacity	Ion-exchange capacity at pH7.6	Ion-exchange capacity at pH2.7
Mobile phase composition	Methanol/H_2O 80:20	Methanol/H_2O 80:20	Methanol/H_2O 30:70	Methanol/Phosphate buffer 20 mM 30:70 pH = 7.6	Methanol/Phosphate buffer 20 mM 30:70 pH = 2.7
Flowrate	0.8 mL/min	0.8 mL/min	0.8 mL/min	0.8 mL/min	0.8 mL/min
Max. pressure	80 bar	80 bar	80 bar	80 bar	80 bar
Oven temp.	40°C	40°C	40°C	40°C	40°C
UV detection	254 nm	254 nm	254 nm	254 nm	254 nm
Inj. volume	10 µL	10 µL	10 µL	10 µL	10 µL
Sample	**In methanol:** Uracil (0.1 mg/mL) Butylbenzene (10 µL/mL) o-Terphenyle (1 mg/mL) Pentylbenzene (10 µL/mL) Triphenylene (0.1 mg/mL)	**In methanol:** Uracil (0.1 mg/mL) All 10 µL/mL: Ethylbenzene Propylbenzene Butylbenzene Pentylbenzene Hexylbenzene	**In water:** Uracil (0.1 mg/mL) Caffeine (0.5 mg/mL) Phenol (0.5 mg/mL)	**In water:** Uracil (0.1 mg/mL) Benzylamine (0.5 mg/mL) Phenol (0.5 mg/mL)	**In water:** Uracil (0.1 mg/mL) Benzylamine (0.5 mg/mL) Phenol (0.5 mg/mL)

fibres. An additional length of thread was tied through the loop and used to pull the fibres through the column. A diagram of the packing method is provided in *Figure 1*. The packed column contained approximately 2.6 g of fibre to obtain a packing volume of 50–60%. Afterwards, it was washed with water and ethanol for 50 minutes each at 1 mL/min (equivalent to approximately 10 column volumes).

Inverse Liquid Chromatography (ILC)

Tanaka Test

The Tanaka Test is commonly used as a characterisation method of stationary phases for liquid chromatography (McHale et al., 2021). A set of parameters obtained from the test can be used to estimate various characteristics of the columns of interest. The method, as carried out for the Spectra 75 and Luna C18(2) columns, is summarised in *Table 1*.

Run 1 was expanded to compare the hydrophobic selectivity with reference to the $-CH_2-$ (methylene) group.

A maximum safety limit for the pressure was imposed at 80 bar to avoid damage of UV detectors. In order to maintain a constant pressure within the safety range, the mobile phase flowrate was adjusted from the conventional values (1.0 mL/min and 0.6 mL/min) to 0.8 mL/min for all runs.

After the samples were prepared, they were filtered, transferred into 2 mL screwtop autosampler vials, and injected as triplicates. Hydrophobic filters were used for the Run 1 and expansion samples, whereas the hydrophilic filters were used for the Run 2, 3, and 4 samples.

Mobile Phase and Injection Volume Variation

The Tanaka method was modified after initial testing of the Spectra 75 column to improve the quality of the chromatograms produced. The methanol concentration of the mobile phase in the Spectra 75 column was varied between 0–60% to determine the percentage at which there was sufficient retention of the samples for calculation of all the required parameters. The flowrate was then increased to produce narrower peaks. The conditions decided upon for the mobile phase were a methanol concentration of 45% and a flowrate of 5 mL/min.

The behaviour of the column was analysed by injectiong Tanaka test samples at 50 µL and 100 µL.

Nitrogen Adsorption

The gas adsorption technique with nitrogen as the adsorbate was used to determine the surface area and, subsequently, the diameter of cleaned Spectra 75 fibres. The measurements were taken at room temperature and modelled with the Brunauer−Emmett−Teller (BET) theory.

Inverse Gas Chromatography (IGC)

Column Packing

A 4 mm ID glass column was packed with a bundle of cleaned Spectra 75 fibres using the same method as the HPLC column.

BET Surface Area Determination

A series of octane injections of decreasing volume were used to obtain an adsorption isotherm at 30°C, allowing for calculation of the BET specific surface area of the fibres using the SEA Analysis software.

Surface Energy Analysis

A number of polar (ethanol, ethyl acetate, acetonitrile, dichloromethane) and non-polar (hexane, heptane, octane, nonane) probes were injected into the column at 30°C to achieve fractional surface coverages over a range of 0.005 – 0.200. The dispersive, specific and total surface energy profiles and distribuitions were obtained directly from the SEA Analysis software.

Coating of Polyethylene and Peptides on Glass Substrates

Cleaning of Glass Slides and Substrates
The glass slides and substrates were sonicated in soap solution for 10 min. Inside a fume cupboard, the slides and substrates were rinsed twice with warm DI water before and after soaking them in 1% (v/v) Hellmanex solution for 5 min. Then, the glass was sonicated in acetone for 10 min and in DI water for 20 min. The slides and the substrates were dried in a 70 ˚C oven overnight.

Coating of Polyethylene Fibres
Double-sided adhesive tape was attached to cleaned glass slides. Cleaned Spectra 75 fibres were cut up into small pieces and pressed onto the adhesive part of the glass slide. An additional slide with adhesive only was used as a control sample.

Spin-coating of Peptides
A peptide layer was produced on cleaned glass substrates through spin-coating via the static dispense method at 1000 rpm for 30 seconds. A 50 µL aliquot of 1 mg/mL peptide sample dissolved in methanol was pipetted on to the centre of the substrates before spinning. To make control samples, the procedure was repeated with pure methanol.

Contact Angle Measurements

The advancing contact angle was measured on the spin-coated peptides, Spectra 75 coated glass slides, and the respective control samples. Measurements were performed with DI water and diiodomethane at room temperature and surface energies were determined via the Fowkes method.

HPLC of Peptides

Solutions of model peptides (P1–P5) were prepared for HPLC analysis with a concentration of 1 mg/mL in water with 25% acetonitrile (ACN). All methods used 1 µL injections of each sample.

The chromatographic runs for individual peptides were carried out with a linear gradient from 0% to 100% of ACN in H_2O (gradient slope of 0.5% ACN/min). Spectra 75 column was run at 2 mL/min flowrate, whereas the Luna C18(2) column was run at 1.6 mL/min due to maximum pressure safety restrictions in the HPLC system.

In addition, isocratic elution was carried out for the Spectra 75 column at 5, 8 and 10% ACN in H_2O.

The dead volumes of both columns were determined with acetone injections of 10 µL.

SEM Imaging

Scanning electron microscopy (SEM) was used to capture images of the cleaned Spectra 75 fibres to determine their shape and characteristic dimensions. A small sample of the fibres was prepared for SEM imaging by mounting onto a metal stub with double-sided carbon adhesive tape and sputter coating with gold.

Results & Discussion

Inverse Liquid Chromatography

Tanaka Test
The Tanaka test was carried out using the Luna C18(2) column as a means of comparing obtained parameters with database values from the ACD/Column Selector tool developed by Advanced Chemistry Development, Inc (Euerby and Petersson, 2005). Having confirmed the reproducibility of the results, the test was carried out on the Spectra 75 column.

However, it was found that the Tanaka method cannot be normalised for characterising this column due to the large difference in hydrophobicity and retention capacity of the stationary phase compared to the Luna C18(2) column. Under the standard conditions for the method, there was little to no retention of any solutes injected into the Spectra 75 column. A reduction of the methanol concentration in the mobile phase from 80% v/v to at least 45% v/v was required to achieve sufficient retention in the column, indicating that the hydrophobic interactions between Spectra 75 fibres and the analytes are weaker than those in the Luna C18(2) column, and likely also when compared with other commercial columns. The changes in chromatographic conditions make a direct comparison with database values for commercial columns invalid (Petersson and Euerby, 2005). Despite this, the nature of the samples injected in the Tanaka method do allow for a better understanding of the column characteristics.

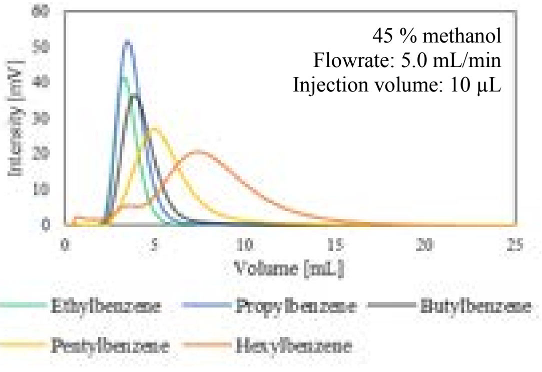

Figure 2: *Elution profiles of Tanaka test expansion compounds in Spectra 75 column under isocratic elution*

For the purpose of this study, the hydrophobic behaviour of the Spectra 75 column was particularly significant, therefore the hydrophobic retention capacity was of key interest. This parameter was

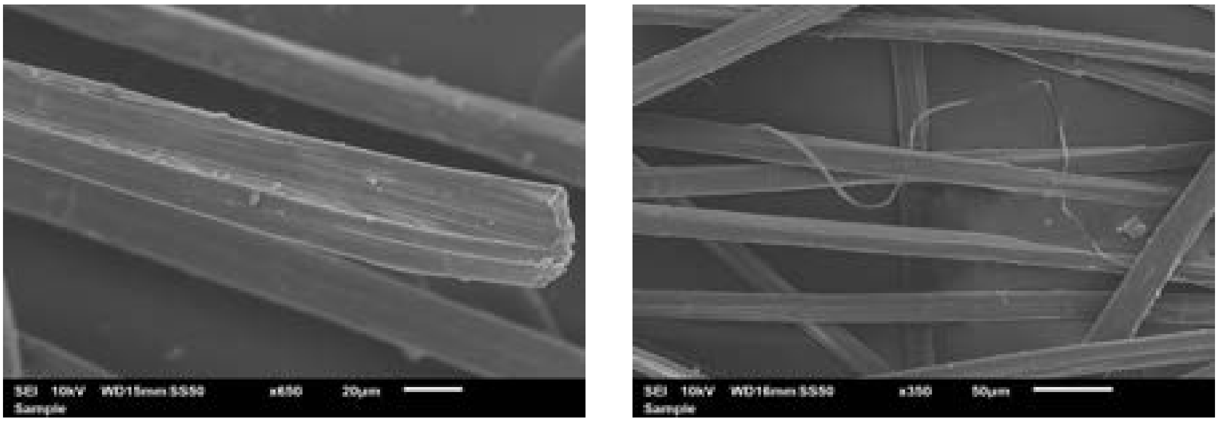

Figure 3: *SEM images of Spectra 75 fibres*

calculated from the expansion of Run 1 using the series of alkylbenzene injections. Uracil was injected as an indicator of the column void volume which was determined to be 3.15 mL. The retention time of uracil (t_M) was then used to calculate the retention factors of all samples with the equation:

$$k' = \frac{t_R - t_M}{t_M} \tag{1}$$

As shown in *Figure 2,* the column demonstrates a degree of hydrophobic retention as the retention volume increases with each subsequent alkylbenzene. However, retention factors are significantly lower than those obtained with the commercial column and the peak shapes deviate further from ideal Gaussian peaks with increasing molecule size. There is observably greater peak broadening and tailing. This can be attributed to the low surface area of the stationary phase.

The chemical structure of polyethylene ensures that the column does not have capacity for hydrogen bonding or electrostatic interactions with solutes and this is reflected in the results of runs 2, 3 and 4. All samples in these runs eluted at the column void volume as the interactions between the solutes and the stationary phase were much weaker than interactions with the more polar mobile phase. In a typical column, the parameters calculated from these runs ($\alpha_{C/P}$, $\alpha_{B/P}$ *pH 7.6,* $\alpha_{B/P}$ *pH 2.7*) are indicators of silanol activity in the stationary phase.

The results from the Tanaka test prove that the Spectra 75 column does exhibit retention of hydrophobic solutes without any charged interactions. They also highlight the significant limitation of the column's ability to separate components as a consequence of the very low packing surface area. This is demonstrated in the poor resolution of the chromatogram peaks.

Morphological & Chemical Properties of the Fibres

Surface Area

Initially, the surface area was estimated with the physical data of the Spectra 75 fibres (Honeywell). Since the column was packed with fibres extending throughout the whole column, this calculation was carried out while assuming a cylindrical filament shape and neglecting the base area of the cylinder (MiniFIBERS, 2018):

$$a = \frac{1}{2.9725 \cdot \sqrt{dpf \cdot \rho}} \ [m^2\, g^{-1}] \tag{2}$$

Using this equation, the surface area of the fibre was estimated to be 0.248 m^2 g^{-1}. This theoretical value was compared with the BET surface area acquired by two techniques: nitrogen adsorption and inverse gas chromatography (IGC). The acquired values were 0.3544 m^2 g^{-1} and 0.6897 m^2 g^{-1}, respectively. The BET surface area acquired by IGC was considerably larger than the theoretical or nitrogen adsorption values.

Even though there is a discrepancy of estimated surface area among the different techniques, it still reveals that the surface area of the Spectra 75 HPLC column is about 3 orders of magnitude lower than that of conventional reversed-phase column resins, such as Luna C18(2) with 400 m^2 g^{-1} (Phenomenex). As a result, the separation power of the Spectra 75 column is greatly reduced as the analytes have less interaction with the stationary phase due to its limited available surface. Since the Tanaka tests for the Spectra 75 column displayed low retention and resolution of analytes, this technical limitation necessitates an alternatively manufactured polyethylene fibre to obtain a higher surface area for improved retention and resolution.

Filament Diameter

The effective diameter of the fibres was also calculated from the surface areas obtained from the physical specifications, nitrogen adsorption experiments and IGC:

$$d = \frac{4}{a \cdot \rho} \tag{3}$$

The calculated values are shown in *Table 2*

***Table 2**: Spectra 75 filament diameter*

	Theoretical	N_2 Adsorption	IGC
Diameter [µm]	16.6	11.6	5.2

With the help of SEM images (see *Fig. 3*), the diameter of the Spectra 75 filaments was estimated to be 17.7 ± 1.9 µm. The SEM images revealed that the cross-section of the Spectra 75 filaments are of rectangular shape. This suggests a flat filament as opposed to the previously assumed cylindrical shape. This leads to the fibres being characterised by an *effective diameter* in place of a geometrical diameter.

When compared to other estimations, the SEM data suggest the largest diameter for the Spectra 75 filaments. This discrepancy is most likely linked to the aforementioned flat shape of the fibre, where the wider side of the fibres was seen more frequently in the SEM images. As a result, the SEM diameter estimations were skewed towards the longer dimension of the cross section and were not so useful, whereas other utilised methods (theoretical,N_2 adsorption, IGC) provided a more reasonable value (*effective diameter*).

Surface Energy

The surface energy of the Spectra 75 fibres was determined by contact angle measurements and inverse gas chromatography (IGC).

The advancing contact angles of water and diiodomethane on the Spectra 75 surface were measured at 131.0° and 9.7°, respectively. During experiments with diiodomethane, the liquid droplets would wet the surface completely. However, a very flat droplet would form just briefly before collapsing, so the whole measurement was recorded, and a value was taken at the frame where the droplet still held its shape. As a result, this one measurement was less precise than the other ones.

The dispersive and polar surface energy components were then estimated from contact angle data with the Fowkes method:

$$\sqrt{\sigma_l^D \cdot \sigma_s^D} + \sqrt{\sigma_l^P \cdot \sigma_s^P} = \frac{\sigma_l(1+\cos\theta)}{2} \qquad (4)$$

The calculated values were then compared to surface energies acquired by inverse gas chromatography (see *Table 3*).

It was observed that the surface energy components determined by the contact angle measurements are higher than those determined by IGC. Generally, for a rough surface, contact angles below 90° tend to appear lower than they are. This phenomenon might have occurred with diiodomethane on the Spectra 75 surface which would have led to a higher surface energy estimation than with IGC. In contrast, measurements of water would be affected too since contact angles above 90° tend to appear higher than they are. This could've contributed to the overestimation of the polar component of surface energy. The issue of surface roughness could be alleviated by modifying the fibre coating procedure, for example, using a hydraulic press to press down the fibres and/or evaluating the surface roughness by other techniques, such as white light interferometry or confocal microscopy.

***Table 3:** Surface energy of Spectra 75 fibres as determined by contact angle and IGC*

	Dispersive surface energy [mJ/m^2]	Polar surface energy [mJ/m^2]	Total surface energy [mJ/m^2]
Contact angle	50.1	8.2	58.3
IGC	42.8	3.6	46.4

All in all, contact angle measurements aren't as reliable as IGC and the latter technique provides more insight into the energetic heterogeneity of the Spectra 75 fibres, hence, the remaining part of this section will be focusing on this technique.

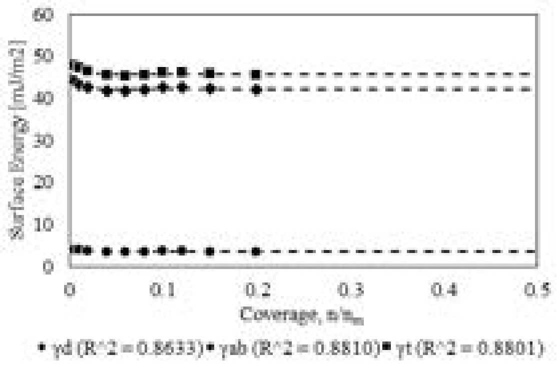

***Figure 4:** Surface energy profiles of Spectra 75 fibres*

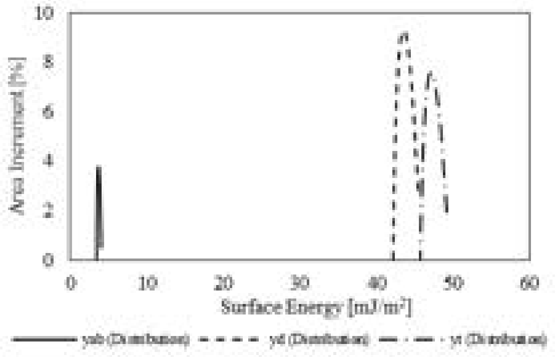

***Figure 5:** Surface energy distributions of Spectra 75 fibres*

The surface energy profiles and distributions obtained by IGC experiments are shown in *Figures 4* and *5*, respectively.

In *Figure 4*, the data were fitted with an exponential decay regression model in the form:

$$y = y_0 + a \cdot e^{-b \cdot x} \qquad (6)$$

In contrast with other regression models, such as linear, exponential, logarithmic, this one had the highest R^2 value and it, hence, shows that, as expected, the surface energy of the fibre sample decreases with coverage. Whereas this is a common feature of IGC analysis for all materials, it is the range of these surface energies (*table 6*) which is paramount in evaluating energetic heterogeneity.

Figure 5 depicts a relatively narrow surface energy distribution of the Spectra 75 fibres suggesting a quite energetically homogeneous surface which is consistent with the rigid crystalline structure of the fibre. In addition, it can be seen that the dispersive surface energy is the dominant component, accounting for over 90% of the total surface energy. This property of polyethylene fibres confirms that this resin would interact with analytes via mostly dispersive interactions and can be used as a hydrophobic reference. Further investigation by analysing an alkyl-bound silica resin would provide a better idea of how the surface properties of Spectra 75 compare to conventional resins.

Chromatographic Separation of Peptides

Finally, chromatographic tests were carried out to evaluate the Spectra 75 column for peptide separation and hydrophobicity scale development. Gradient elution of individual peptides with the Spectra 75 column are shown in *Figure 6*.

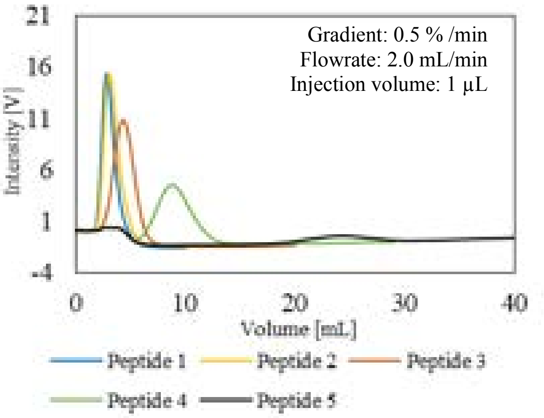

Figure 6: *Superimposed individual peptide runs with Spectra 75 column. Gradient elution from 0% to 100% acetonitrile in water.*

It was clear that the peptides could be ranked based on their retention times and, thus, a hydrophobicity scale was developed. A hydrophobicity index for each peptide was expressed as the concentration at which the peptide elutes. A similar approach can be found in the study by Krokhin and Spicer where isocratic elution was utilised to express the hydrophobicity index as the mobile phase composition at which the retention factor of the peptide is 10. This method, however, couldn't have been applied to the Spectra 75 column since there was insufficient retention of the analytes at higher acetonitrile concentrations. On the other hand, lowering the concentration resulted in extremely shallow peaks which were hard to analyse. Due to these limitations, this paper relies on gradient elution instead. The developed ranking was compared with modelled GRAVY (Grand average of hydropathicity index) values and water contact angles of the peptides. The GRAVY values were manually calculated by using the amino acid hydropathicity scale developed by Kyte & Doolittle.

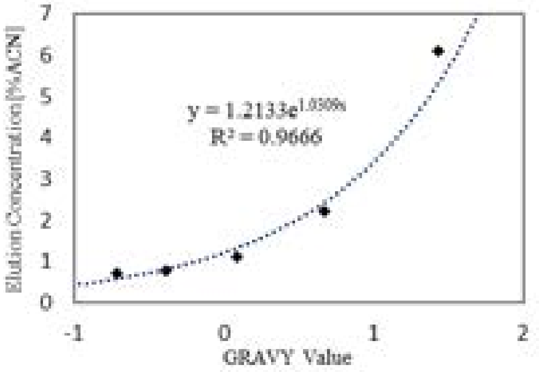

Figure 7: *Correlation between experimental elution concentration and peptide GRAVY values.*

The comparison between the three developed scales is shown in *Table 4*. As seen in the table, the rankings of the peptides with regards to their hydrophobicities match. However, after

Table 4: *Overview of three peptide hydrophobicity scales. GRAVY values were based on the Kyte-Doolittle amino acid scale. Contact angles were determined experimentally on spin-coated peptide films. %ACN values were determined for Spectra 75 column with gradient elution from 0% to 100% acetonitrile in water at 0.5 % /min, flowrate: 2 mL/min.*

Peptide	**Sequence**	**Hydrophobicity Measure**					
		GRAVY	**Normalised GRAVY**	**H_2O Contact Angle**	**Normalised Contact Angle**	**HPLC (%ACN)**	**Normalised %ACN**
P1	LGGGGGGDGSR	-0.71	0.000	26.5	0.000	0.71	0.000
P2	LGGGGGGDFR	-0.38	0.154	33.9	0.254	0.77	0.011
P3	LLGGGGDFR	0.09	0.374	46.3	0.680	1.11	0.073
P4	LLLGGDFR	0.67	0.645	49.5	0.790	2.20	0.277
P5	LLLLDFR	1.43	1.000	55.6	1.000	6.09	1.000

normalisation, these scales yield very different hydrophobicity values for the model peptides. As a result, a correlation was developed between the GRAVY values and elution concentration of the peptide (*Figure 7*).

This correlation could then be used to relate the experimental hydrophobicity indices with theoretical GRAVY values. For instance, a GRAVY value could be converted into an estimation of the mobile phase compositions at which the peptide would elute.

Quality of Separation

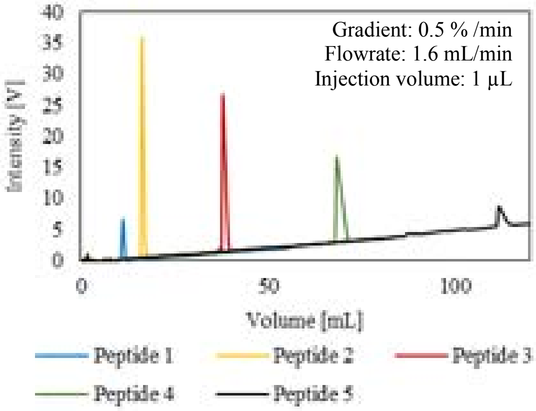

Figure 8*: Superimposed peptide runs with Luna C18(2) column. Gradient elution from 0% to 100% acetonitrile in water.*

Gradient elution was found to produce the greatest difference in retention of all five peptides in the Spectra 75 column and therefore the same method was used in the Luna C18(2) column for comparison.

Figure 8 displays the results of the gradient elution of each peptide run in the Luna C18(2) column. The elution volumes are significantly greater than in the Spectra 75 column. This large difference in retention capacity between the columns can be attributed primarily to the significant difference in surface area. As found through our material characterisation study, the specific surface area of the Spectra 75 fibre is less than 1 m^2/g compared to 400 m^2/g in the Luna C18(2) column. Another factor of note is the greater hydrophobicity of the stationary phase in the Luna column demonstrated by the previously conducted Tanaka test, and therefore, stronger interactions with the injected peptides.

Table 5: *Resolution between adjacent chromatographic peaks for Spectra 75 and Luna C18(2) columns*

Peptide pair	Resolution	
	Spectra 75	Luna C18(2)
P2/P1	0.10	4.32
P3/P2	0.46	15.54
P4/P3	0.97	13.41
P5/P4	2.00	14.94

The resolutions between adjacent peaks were calculated for both columns and listed in *Table 5*.

There was an improvement of resolution in the Spectra column with each pair of peptides. Between P4 and P5 there is sufficient resolution for a separation process, for which resolutions greater than 1.5 are acceptable to achieve good separation (Shimadzu).

Conclusions

In this study, the pure hydrophobic retention within the Spectra 75 fibre column was demonstrated. Compared to silica-based columns, the Spectra column displayed no capacity for polar interactions and the column behaviour is notably unaffected by changes in pH. However, issues of low separation capability arose due to the significantly lower surface area relative to conventional columns. The potential of a RP-HPLC column unaffected by the issues arising from free silanol groups is worth further study to improve separation power by increasing surface area within the column. This may be achieved by reducing the fibre diameter, developing capillary channels, increasing column size and packing fraction.

There was sufficient retention with gradient elution to establish a hydrophobicity scale for peptides based on elution concentration and correlate it with a GRAVY scale. This relationship could be used to estimate the optimal mobile phase composition for the separation of a peptide with a known GRAVY value. In addition, this novel scale could replace more conventional scales based on modelling, contact angle and silica-based RP-HPLC columns. This study could be expanded by investigating peptides with a wider hydrophobicity range and performing isocratic elution. To investigate the latter, the separation power of the column should be improved, as mentioned previously.

Although the separation power of Spectra 75 is low relative to conventional columns, it could be utilised in processes with large hydrophobicity differences between analytes with the benefit of high column throughput. In addition, implementation of alternative organic modifiers could be investigated, such as ethanol, to make the separations more environmentally friendly.

Acknowledgements

The authors would like to extend their gratitude to Oscar Mercado Valenzo (Imperial College London) for his continuous support and guidance throughout this research project.

References

Bocian, S. & Buszewski, B. 2012. Residual silanols at reversed-phase silica in HPLC – a contribution for a better understanding. *Journal of Separation Science,* 35**,** 1191-1200.

Borges, E. M. 2014. Silica, Hybrid Silica, Hydride Silica and Non-Silica Stationary Phases for Liquid Chromatography. *Journal of Chromatographic Science,* 53**,** 580-597.

Euerby, M. R. & Petersson, P. 2005. Chromatographic classification and comparison of commercially available reversed-phase liquid chromatographic columns containing polar embedded groups/amino endcappings using principal component analysis. *Journal of Chromatography A,* 1088**,** 1-15.

Hardick, O., Dods, S., Stevens, B. & Bracewell, D. G. 2015. Nanofiber adsorbents for high productivity continuous downstream processing. *Journal of Biotechnology,* 213**,** 74-82.

Honeywell. *Honeywell Spectra Fiber* [Online]. Honeywell. [Accessed 30 October 2021].

Huang, S., Bruce, T. F., Ding, H., Wei, Y. & Marcus, R. K. 2021. Rapid isolation of lentivirus particles from cell culture media via a hydrophobic interaction chromatography method on a polyester, capillary-channeled polymer fiber stationary phase. *Analytical and Bioanalytical Chemistry,* 413**,** 2985-2994.

Krokhin, O. V. & Spicer, V. 2009. Peptide Retention Standards and Hydrophobicity Indexes in Reversed-Phase High-Performance Liquid Chromatography of Peptides. *Analytical Chemistry,* 81**,** 9522-9530.

Kyte, J. & Doolittle, R. F. 1982. A simple method for displaying the hydropathic character of a protein. *Journal of Molecular Biology,* 157**,** 105-132.

Mant, C. T., Chen, Y., Yan, Z., Popa, T. V., Kovacs, J. M., Mills, J. B., Tripet, B. P. & Hodges, R. S. 2007. HPLC analysis and purification of peptides. *Methods in molecular biology (Clifton, N.J.),* 386**,** 3-55.

Marcus, R. K. 2008. Use of polymer fiber stationary phases for liquid chromatography separations: Part I – physical and chemical rationale. *Journal of Separation Science,* 31**,** 1923-1935.

Marcus, R. K. 2009. Use of polymer fiber stationary phases for liquid chromatography separations: Part II – applications. *Journal of Separation Science,* 32**,** 695-705.

Mchale, C., Soliven, A. & Schuster, S. 2021. A simple approach for reversed phase column comparisons via the Tanaka test. *Microchemical Journal,* 162**,** 105793.

Minifibers. 2018. *Fiber Measurement Conversions* [Online]. Available: www.minifibers.com/our-company/about-fibers/fiber-measurement-conversions/ [Accessed 30 October 2021].

Petersson, P. & Euerby, M. R. 2005. An evaluation of the robustness of the Tanaka characterization protocol for reversed-phase liquid chromatography columns. *Journal of Separation Science,* 28**,** 2120-2129.

Phenomenex. *Explore Luna HPLC Columns* [Online]. Available: www.phenomenex.com/ViewDocument?id=explore+luna+hplc+columns [Accessed 30 October 2021].

Shimadzu. *About Resolution, Part 1* [Online]. Available: https://www.shimadzu.com/an/service-support/technical-support/analysis-basics/basic/resol-1.html [Accessed 1 December 2021].

Stanton, P. 2004. Ion-Exchange Chromatography. *In:* AGUILAR, M.-I. (ed.) *HPLC of Peptides and Proteins: Methods and Protocols.* Totowa, NJ: Springer New York.

Supelco. 2002. Eliminate TFA and Improve Sensitivity of Peptide Analyses by LC/MS. Available: https://www.sigmaaldrich.com/deepweb/assets/sigmaaldrich/marketing/global/documents/129/989/11547.pdf.

Wang, L. & Marcus, R. K. 2019. Evaluation of protein separations based on hydrophobic interaction chromatography using polyethylene terephthalate capillary-channeled polymer (C-CP) fiber phases. *Journal of Chromatography A,* 1585**,** 161-171.

Zhu, C., Gao, Y., Li, H., Meng, S., Li, L., Francisco, J. S. & Zeng, X. C. 2016. Characterizing hydrophobicity of amino acid side chains in a protein environment via measuring contact angle of a water nanodroplet on planar peptide network. *Proceedings of the National Academy of Sciences,* 113**,** 12946-12951.

Žuvela, P., Skoczylas, M., Jay Liu, J., BąCzek, T., Kaliszan, R., Wong, M. W. & Buszewski, B. 2019. Column Characterization and Selection Systems in Reversed-Phase High-Performance Liquid Chromatography. *Chemical Reviews,* 119**,** 3674-3729.

Fabrication of PGO Hollow Fibre Membranes for Nanofiltration

YuChen Hu and Kantapat Tanjittasuwan
Department of Chemical Engineering, Imperial College London, U.K.

Abstract

In this study, we synthesised porous graphene oxide (PGO) nanosheets using a mild chemical etching approach. The structural and compositional changes of PGO nanosheets were observed by different characterisation techniques. A slight reduction in interlayer d-spacing of PGO was observed due to the partial chemical reduction. Raman spectra confirmed the chemical reduction of PGO samples as well. High-resolution TEM images also showed the generation of pores on the basal plane of PGO nanosheets. We fabricated PGO hollow fibre (HF) membranes by coating PGO nanosheets on alumina HF substrates. The permeance of PGO HF membranes was preferentially controlled by adjusting the coating time. PGO HF membrane with 3 mins coating time showed the best performance in terms of both water permeance and dye rejection. Interestingly, the water permeance of the PGO membrane was 12-fold higher than that of the GO membrane while showing similar rejection (100%) for protoporphyrin IX (PPI-hX) and erythrosin B (EB) dyes but smaller rejection (72.8%) for methyl red (MR). We believe that the PGO HF membrane showed much better potential than the GO membrane for nanofiltration application.

Keywords— Graphene oxide, Porous graphene oxide, Membrane, Nanofiltration, 2D materials, Hollow fibre membranes

1 Introduction

1.1 Importance of Membrane

Water scarcity crisis is an emerging concern and is expected to affect two-thirds of the world's population by 2025. Water is often thought to be plentiful, but only 3% of the world's water supply is fresh water and there is a growing demand for safe and drinkable water. Therefore, fresh and drinkable water needs to be produced using desalination of water and purification of wastewater. Purification of wastewater not only can provide a considerable amount of fresh water but also can preserve the environment from further pollution. Membrane technology has been widely considered as an energy and cost-efficient and environmentally friendly separation process for the purification of wastewater [1].

Numerous studies have been performed on nanofiltration (NF) membranes [2] to purify water especially in the fashion industry which contributes to about 20% of global wastewater. Wastewater from textile plants must be treated from chemicals such as dispersants, leveling agents and dyes prior to disposal due to significant environmental impacts [3]. Textile dyes have visual impacts on water bodies, they also reduce light penetration and decrease photosynthesis of aquatic plants [4]. Furthermore, some textile dyes are toxic and carcinogenic, causing serious health impacts [5]. Due to their small molecular weights, dye molecules are not separable by normal separation processes. Nanofiltration (NF) membrane has been widely used in industry for the separation of wastewater containing dyes.

1.2 Membrane Potential

Membrane technology has been widely used in different water separation applications such as reverse osmosis (RO), industrial wastewater purification, separating water from organic solvents using pervaporation process, etc. Based on pore sizes, membranes are classified into reverse osmosis (RO), nanofiltration (NF), ultrafiltration (UF), and microfiltration (MF) which can be used for different purposes [6]. Depending on the separation targets, pores should have an appropriate size to reject unwanted species in the feed and allow desired specie(s) to pass smoothly. Usually, the pore size of membranes is decided based on the molecular weight (kinetic diameter) of the molecules (ions) being separated. Molecular weight cut-off (MWCO), defined as the molecular weight of molecules which at least 90% of them can be retained, is a parameter used to indicate the rejection ability of membranes.

Figure 1 summarises the type of membranes used for a certain range of pore diameters [6]. The water separation performance of membranes is generally assessed using two parameters: (1) permeance which reflects the rate of transport of desired specie(s) through a membrane, and (2) rejection which indicates the sieving capability of the membrane towards unwanted specie(s). A desirable membrane should possess both high permeance and good rejection.

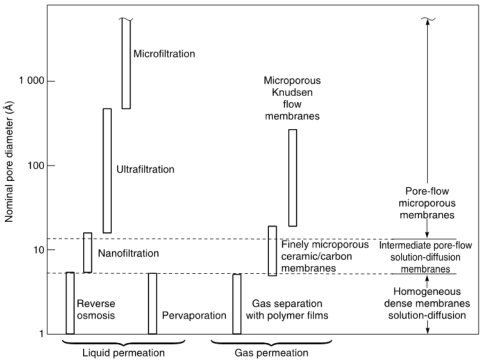

Figure 1: Schematic representation of the nominal pore size and theoretical model of transportation [6]

1.3 GO Membrane

Polymers are widely used material for the fabrication of water purification membranes. However, recently, much attention has been paid to two-dimensional (2D) nano-porous membranes, in particular graphene oxide (GO) membranes due to their good mechanical strength, chemical stability, tunable pore size, structural diversity, and surface functionalities [7, 8]. Indeed, GO nanosheets with atomic-scale thickness, rich surface chemistry conferred by oxygen functional groups like carbonyl, epoxy, carboxyl and hydroxyl groups, and high aspect (length/thickness) ratio are an ideal platform for the fabrication of graphene-based inorganic membranes [9, 10]. GO nanosheet has a hexagonal structure similar to the one of graphene but with oxygen-based functional groups on its basal plane and edges [11]. They are bonded by van der Waals forces and hydrogen bonding induced by oxygen moieties. Oxygen functional groups act as a spacer between nanosheets increasing the interlayer d-spacing from about 0.8 nm to 1-1.3 nm at dry and wet condition respectively [12, 13], as shown in Figure 2. This interlayer d-spacing (called nanogalleries) play the key role in separating species based on sized exclusion [14]. The oxygen functional groups also give a hydrophilic characteristic and correspondingly, stable dispersibility in water and in a wide range of organic solvents [15]. GO has shown excellent antimicrobial activity and great potential in the removal of radiochemical waste [16, 17].

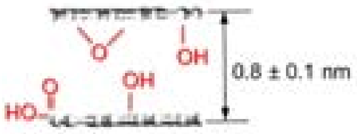

Figure 2: Cross-sectional view of adjacent GO sheets[18]

2D nanochannels between stacked GO nanosheets allow water to permeate through while retaining other unwanted solutes, making GO membranes highly suitable for water purification [19]. GO membranes showed high rejection of multivalent ions and organic dyes with a molecular weight cut-off about 250Da. According to Figure 3, there is a sharp cut-off for solutes with hydrate radii greater than 4.5Å, large molecules can be completely rejected by GO membrane, making it suitable for dye nanofiltration [13].

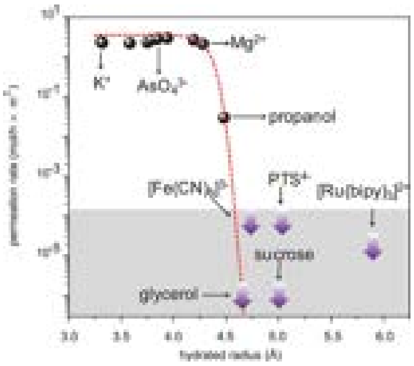

Figure 3: Permeance of Ions through GO membrane [13]

GO membranes are fabricated using different coating techniques such as vacuum filtration, dip coating, spray coating, spin coating and solution casting [7]. From a practical application standpoint, hollow fibre (HF) configuration is preferable to minimize the size of the separation unit. In fact, HF membranes with diameters usually less than 1mm are more favourable for membrane module assembly and will generate a much higher surface area to module volume ratios (9000 m^2/m^3), enabling more solvent to pass through the selective barrier and reducing the module size and operating costs [20].

1.4 Objective of This Study: Fabrication of PGO Membranes

The lamellar structure of GO membranes provides long and complex transport pathways leading to low permeance, a major problem impeding GO membranes for industrial wastewater purification [21]. In other words, due to the limited number of channels available for transport and the tortuous microstructure, water molecules require a longer time to pass through the GO membrane. Therefore, improving the water permeance of GO membranes based on scalable approaches is of importance. In this study, we aim to improve the permeance by synthesising PGO membrane through creation of pores on GO nanosheets, shortening permeation pathways while controlling rejection via pore size tunning. A mild pore generation approach was used to avoid the formation of nanoselective pores and severe chemical reduction of GO nanosheets, ensuring its dispersibility in water without forming precipitations. The structural changes of PGO nanosheets, compared to GO, were studied using characterisation techniques, including high resolution transmission electron microscopy (HR-TEM), X-ray diffraction (XRD), scanning electron microscopy (SEM) and Raman analysis. PGO membranes are coated on alumina HF substrate and water permeance was evaluated. In this study, ceramic support was used as substrate to make thin film HF composite GO and PGO membranes not only because of its better compatibility with the selective layer, preventing the formation of interfacial voids which may lead to poor rejection, but also due to its good chemical and mechanical stability [22]. To evaluate the sieving ability of the PGO membrane, the rejection of a neutral dye molecule was tested. As GO nanosheet is negatively charged, the use of a neutral dye ensures that the size exclusion determines the rejection rather than electromagnetic interaction [23].

2 Experimental

2.1 Ceramic Hollow Fibre Substrate Synthesis

2.1.1 Materials

Alumina powder (99.9% metals basis) purchased from Alpha Aesar was used for the HF substrate fabrication. 1-methyl-2-pyrrolidine (NMP) and poly (methyl methacrylate) (PMMA) were used as solvent and binder respectively. A mixture of ethanol/DI water (50/50 wt%) was prepared as bore fluid. Hydrogen peroxide and ammonia hydroxide were used to make porous GO (PGO).

2.1.2 Preparation of Ceramic Suspension

Firstly, a suspension composed of 3-4 g of dispersant, 180 g of NMP (solvent), and 150 g of alumina powder was prepared in a ceramic jar and mixed using a planetary ball miller for 48 hours, with a speed of 283 rpm. The polymer (PMMA) was then added, and suspension was rolled for a further 48 hours in a roll miller. The suspension was then degassed under vacuum for 3-4 hours to remove any bubbles before spinning.

2.1.3 Preparation of Hollow Fibre Substrate

After degassing, the suspension is transferred to a stainless-steel syringe. HF substrates were prepared based on a combined spinning/sintering method [24]. The suspension is extruded through the designated tube-in-orifice spinnerets into a coagulation bath that contains DI water. The rate of extrusion can be preferentially controlled by the syringe pumps, and in this experiment, bore and spinning fluid speeds were set to 26 mL.min^{-1} and 13 mL.min^{-1}, respectively. The diameter of the HFs can be determined by the gap between the spinneret and water bath, with a larger air gap, the produced HFs will have a smaller diameter and vice versa. In this study, zero air gap was used for the spinning process. It is worth mentioning that the bore fluid and ceramic dope flow rates have an impact on the diameter and thickness of HF substrates. The viscosity of ceramic dope also affects the structure and mechanical properties of HF substrate. Our experimental parameters were set based on the optimised values. The prepared alumina HF membranes were left in the DI water overnight to complete the phase inversion. Next, HF samples were straightened and dried at room temperature for one day. The last step was the sintering of HF substrates. The straightened HF samples were cut into 10 cm pieces and put into the furnace to be sintered at 1450 °C. The final HF substrates were mechanically strong enough to be used as support for the preparation of GO and PGO HF membranes as the molecules in the substrates are packed together very closely.

2.2 GO & PGO Synthesis

Graphene Oxide (GO) was synthesised using modified Hummer's method: First, 10 g of graphite was added to 380 mL of sulfuric acid (H_2SO_4) in a two-wall glass reactor at 5 °C and stirred for 10 min. Then, 50 g of potassium permanganate ($KMnO_4$) was added to the solution and stirred for 12 h at 35 °C. In the next step, 500 mL water was added dropwise to the solution at 5 °C and then stirred for about 1 h. The solution was poured into a beaker and further diluted by adding 2 L water. Hydrogen peroxide (H_2O_2) was added into the solution dropwise until the colour turned from dark brown to golden yellow and then stirred for about 30 min. The golden yellow dispersion was vacuum filtrated using a glass fibre filter, and the obtained cake layer was washed out using a 10 wt% hydrochloric acid (HCl) aqueous solution. The cake layer of GO was dried under dynamic vacuum at room temperature for more than two days. The dried powder was dispersed in acetone and sonicated (bath) for 10 min, followed by vacuum filtration through glass fibre filters. The cake layer was dried again for more than three days under the vacuum at room temperature to obtain GO powder. A homogeneous GO dispersion with concentration of 2 mg/mL was finally prepared [22, 25].

Porous graphene oxide (PGO) was obtained through mild chemical etching of GO dispersion [25]. Ammonia solution (30% in water) was added to the dispersion which leads to a better dispersion due to deprotonation of GO nanosheets and creation of repulsive forces between negatively charged GO nanosheets. H_2O_2 (30%) was added as an etchant which creates pores through oxidising graphitic domain of GO nanosheets. The ratio of GO to ammonia solution to H_2O_2 was 20:1:1. The dispersion was gently stirred in a double-walled reactor at 50 $^\circ$C for 3 hours. The resultant dispersion was then centrifuged at 12000 rpm for 1 hour to collect precipitated PGO nanosheets. Further purification was done using a dialysis membrane against DI water for at least 3 days to ensure no more H_2O_2 and ammonia was present in the dispersion. The concentration of PGO dispersion was determined by drying a 3 mL aliquot of dispersion at 40 $^\circ$C in a vacuum for at least a day and weighing the resulting powder.

2.3 Hollow Fibre Membrane Fabrication

GO and PGO HF membranes were prepared using the vacuum filtration method. The ceramic HF support was immersed in PGO dispersion with one end glued using epoxy and the other end connected to a vacuum pump. Under vacuum, water passes through the HF support pores while PGO nanosheets with a lateral size of more than 1 micron stick onto the surface, forming PGO membrane. The thickness of the PGO membrane can be adjusted by varying the concentration of PGO dispersion or the filtration time. In this study, GO (PGO) concentration was 0.1 mg/mL as lower concentration can lead to better stacking of nanosheets. The thickness of PGO membranes was adjusted by varying the filtration time. The prepared HF membranes were then dried at 40 $^\circ$C under vacuum for 3-4 hours to remove any remaining water in the membranes. The fabricated membranes are stored in DI water till usage.

2.4 Performance Evaluation

2.4.1 Pure Water Permeation Test

Due to the formation of micro-defects in GO membranes under the dry condition, HF membranes are immersed in water before pure water permeation tests [22]. The membrane attached to a tube-fitting using epoxy was mounted into a permeation cell (dead-end cell) which was filled up with water. The pressure of the dead-end permeation cell was controlled using the line connected to a N_2 gas cylinder. The pure water permeation tests were carried out at 10 bar. The permeated water was collected in a container and the weight change was monitored using a programmed balance. The steady-state permeation values were obtained once the rate of weight change remained constant. The permeance of membranes (LMHbar^{-1}) was calculated as following:

$$Permeance = \frac{\Delta M}{\rho * 1000 * \Delta t * A * p} \qquad (1)$$

where M, ρ, A, t, and p represent weight mass (gram), water density (g/cm^3), membrane area (m^2), time (h), and pressure (bar) respectively. Each reported value was the average of 4-5 different samples.

2.4.2 Rejection Tests

Along with water permeance, the rejection is another important parameter indicating the solute sieving ability of membranes. To avoid the impact of adsorption, HF membranes were first soaked in dye solution (preconditioning) to ensure that the rejection values are only due to the size exclusion effect. The concentration of the EB dye solution was 200 mg/mL. The rejection test was similar to the pure water permeation test. The HF membrane was fitted into the dead-end filtration cell containing the dye solution and pressure was set to 10 bar. Two batches of permeate were collected and the concentration of dye was measured using UV-VIS. The calibration curve of known intensities and concentrations was used to measure the concentration of the permeate samples. Rejection is then calculated as following:

$$R = \frac{C_0 - C_p}{C_0} \times 100\% \tag{2}$$

where R is the rejection of HF membrane, C_0 and C_p are the initial and permeate concentration of dyes. The rejection data reported for each membrane was the average of 4-5 samples.

2.5 Membrane Characterisation

The pores of PGO nanosheets were observed using high-resolution TEM (HR-TEM) (JEOL-2100F). XRD spectra of GO and PGO were collected in a 2θ range of 5° - 30° to measure the interlayer d-spacing of GO and PGO membranes using the Bragg's law as following:

$$\lambda = 2d \sin\theta \tag{3}$$

where λ is the wavelength of X-ray, θ is the diffraction angle and d is the interlayer d-spacing between adjacent nanosheets.

Similarly, the Raman spectra of GO and PGO samples were compared.

3 Results & Discussion

3.1 Membrane Characterisation

Interlayer d-spacings of GO and PGO membranes were calculated from XRD spectra using Bragg's law. The interlayer d-spacing slightly decreased from 0.836 nm to 0.828 nm from GO to PGO membrane which can be primarily due to the chemical reduction of PGO nanosheets and the removal of oxygen functional groups induced by ammonia and/or temperature (Figure 4). The removal of oxygen functional groups on the PGO nanosheets allows for more compact packing between the PGO nanosheets.

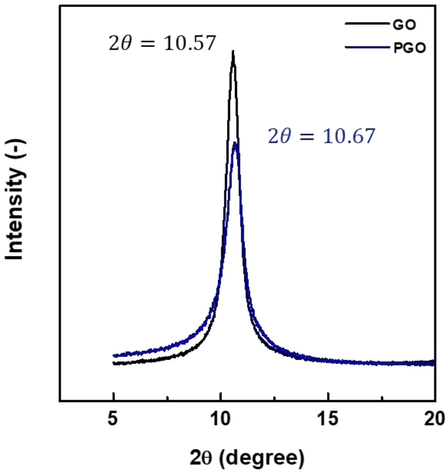

Figure 4: XRD spectra of GO and PGO sample

The Raman spectra is a proper analysis tool to monitor the oxidation degree and the extent of created pores of GO and PGO samples due to its high sensitivity to geometric structure and bonding within molecules. The intensity of G peak (I_G) represents the degree of graphitic domains (sp^2 hybridisation) in GO or PGO samples while D peak intensity (I_D) refers to amorphous (oxidised) domains. The D peak is also known as the disorder or defect band which can be due to structural missing of substituted atoms [26]. Therefore, generating pores on GO nanosheets with H_2O_2/ammonia increases I_D intensity. At the same time, the degree of graphitic domains was enhanced due to the chemical reduction of nanosheets. As shown in Figure 5, the I_D/I_G ratio decreased from 0.99 for GO to 0.96 for the PGO sample demonstrating the partial reduction of the PGO sample compared with GO. Both the G and D peak intensities are higher in the PGO sample than in GO. This describes the increase in both graphitic domains (G peak) and defects (D peak). The slight decrease in the ratio could be due to a greater increase in graphitic domain compared to the degree of defects.

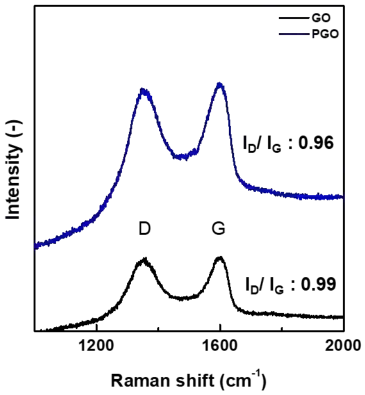

Figure 5: Raman Spectra of GO and PGO sample

Figure 6 shows the cross-sectional morphology and the surface of alumina HF substrates. The HF substrate contains two thin skin layers made of finger like structures originated from both the inner and outer surfaces of fiber (called sandwich morphology). A sponge-like region exists at the centre of fiber which provides enough mechanical strength [24]. The surface is very porous and imposes no additional resistance on transportation of species.

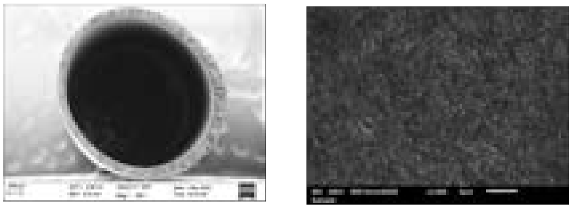
(a) Alumina-HF
(b) Surface

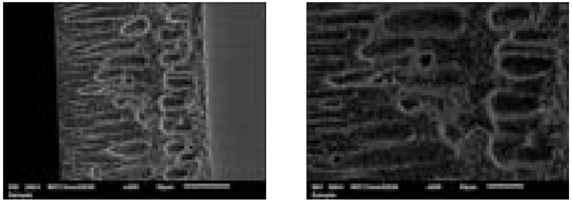
(c) Cross-section
(d) Cross-section

Figure 6: SEM images of Alumina HF. (a) Cross-sectional view of HF (b) Surface view of HF (c) and (d) Cross-sectional view of HF walls

Figure 7 exhibits the surface and cross-sectional images of PGO coated ceramic HF membranes with tightly packed layers. As the coating time was increased, the thickness of the PGO membrane also increased. The thickness of PGO membranes with 2 mins, 3 mins and 5 mins coating times were 401, 520 and 653 μm, respectively.

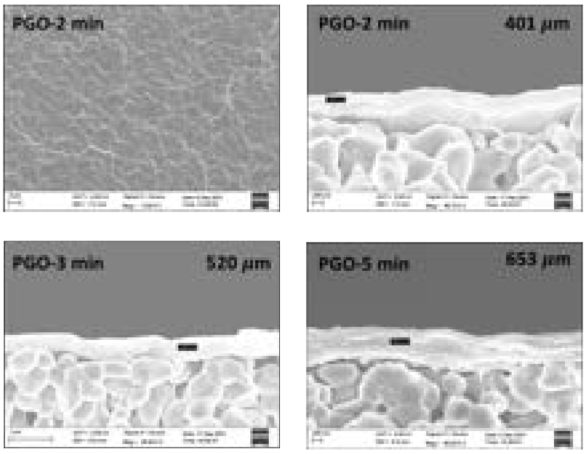

Figure 7: SEM images of PGO membranes. Surface view: (a) PGO-2 min coating Cross-sectional view: (b) PGO-2 min coating (c) PGO-3 min coating (d) PGO-5min coating

Figure 8 shows high-resolution TEM (HR-TEM) images of GO and PGO nanosheets. Pores with an average diameter of up to 10 nm were observed on PGO nanosheets. This confirms the successful generation of pores on the nanosheets. These pores provide additional and shorter transport pathways for water molecules, as will be discussed later. HR-TEM image shows that the generated pores have sizes of around 10nm, but in reality, due to high voltage ion beams, TEM spectroscopy will enlarge the pores and display larger pore sizes than they actually are [27].

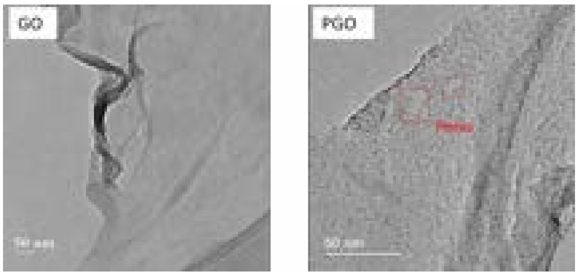

Figure 8: High-resolution TEM images of GO and PGO samples

3.2 Water Permeation Measurements

In industrial water treatment applications, it is always desirable to have pure water permeation rates as high as possible. During our experiments, initial water permeances were very high but they tend to decrease overtime before finally reaching a steady state. This is primarily due to the compaction behavior of PGO under high pressure. Pure water permeations rates of 4 different PGO membranes were tested, and the average permeation rate of each membrane was measured after 4-5 tests. As shown in Figure 9(a), the water permeance followed a reducing trend with respect to the coating time. The permeance dropped from 4.36 LMHbar^{-1} to 0.98 LMHbar^{-1} as the coating time increases from 1 min to 5 mins. This implies that as the membrane thickness increases, due to longer coating time, the water molecules need to transport through a longer tortuous path inside the selective layer, leading to a significant reduction in the permeation rates. This is also supported by the SEM images in Figure 7 showing the increasing thickness with coating time.

The increase in water permeance of PGO compared to GO membrane is mainly due to the additional created pores and hence less tortuous transport pathways. However, the EB dye rejection, which is primarily determined by the interlayer d-spacing in membrane, is retained due to negligible change in d-spacing. According to Figure 9(a), permeance decreases with increasing coating time, since PGO nanosheets are randomly stacked and as membrane thickens, some pores may be blocked off by adjacent nanosheets, decreasing water permeance.

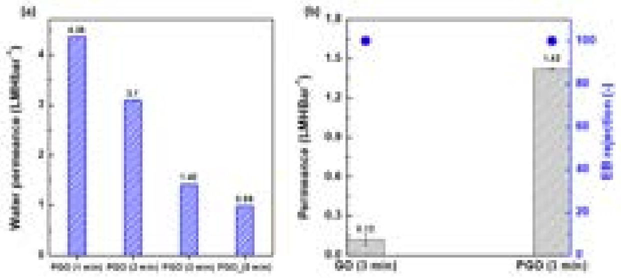

Figure 9: (a) Water permeance of PGO membranes as a function of coating time, and (b) water permeance and EB dye Rejection of GO and PGO membranes with 3 minutes coating time.

A comparison was made between GO and PGO samples with 3 mins coating time as even though we aim for membrane the highest permeance, the rejection of the membrane is equally important. PGO samples with 1 and 2 mins coating time have low rejections and were not suitable for the separation of dye molecules. Figure 9(b) compares the water permeance of GO and PGO membranes. The permeance of PGO membrane with 3 mins coating time is 1.42 LMHBar^{-1} which is almost 12-fold higher than that of GO membrane (0.12 LMHBar^{-1}). This confirmed a difference in the microstructure of GO and PGO membranes in good agreement with Figure 8 showing the additional pores on PGO nanosheets. Indeed, generated pores on the basal plane of the PGO nanosheets provide shorter and less tortuous pathways for the water molecules to permeate through the selective layer.

3.3 Rejection Tests

As mentioned before, the rejection is another important parameter in the overall evaluation of membrane performance. PGO with the coating time of 3 mins was chosen for the evaluation of membrane performance. Due to time limitation of the research project, we only managed to test the rejection of PGO membrane with EB dye. For a comprehensive rejection analysis, we were given rejection data for MR and PPI-hX dyes obtained from previous experiment conducted by Dr. Farhad Moghadam.

According to Figure 10, the PGO membrane showed 100% rejection to PPI-hX and EB dyes, similar to the values obtained for the GO membrane. This implies that though generated pores provide extra permeation pathways, the interlayer d-spacing still plays a determining role in the sieving ability of membranes. In other words, this shows that new interconnected channels formed from the generation of new pores are not only large enough for water molecules (M_w = 18.0 Da) to pass through smoothly but also small enough to completely retentate PPI-hX and EB dye molecules. On the other hand, the PGO membrane showed a lower rejection to the MR dye molecules (72.8%) than the GO membrane (97.5%). This suggests that generated channels are not small enough to completely exclude MR dye molecules. In summary, our membrane with 12-fold greater water permeance while still achieving 100% rejection to EB and PPh-IX dyes show great potential for usage in the separation of large dye molecules.

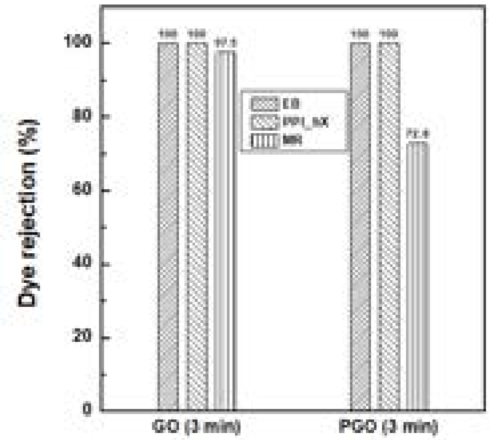

Figure 10: Rejection of dyes on GO and PGO hollow fibre membranes with 3 min coating time. Dyes used are: Methyl Red(MR), Erythrosin B(EB) and Protoporphyrin IX(PPh-IX)

4 Conclusion

In conclusion, we have successfully fabricated PGO HF membranes with improved permeance, compared with GO membrane, by generating pores on GO nanosheets. A slight decrease in the interlayer d-spacing from 0.836 nm to 0.828 nm was observed for the PGO membrane measured by XRD spectra. Similarly, Raman spectra showed a decrease in the I$_D$/I$_G$ ratio from 0.99 (GO) to 0.96 (PGO), signifying a partial reduction of the PGO membrane. The permeance of the PGO HF membrane was preferentially adjusted by controlling the thickness of the coated PGO layer. According to water permeation tests, the PGO HF membrane showed water permeance 12-fold higher than that of the GO HF membrane while retaining 100% rejection to PPI-hX and EB dyes, proving the potential of the PGO HF membrane in the nanofiltration for water purification.

5 Acknowledgements

We would like to express our utmost gratitude to Dr. Farhad Moghadam for his constant guidance and help during this period of time.

References

[1] Kim, S. Membranes for water, gas and ion separation. *Membranes* **11(5)** (2021).

[2] Tian, J., Zhao, X., Gao, S., Wang, X. & Zhang, R. Progress in research and application of nanofiltration (nf) technology for brackish water treatment. *Membranes* **11(662)** (2021).

[3] Singh, R., Singh, P., Gupta, R. & Singh, R. *Advances in Biological Treatment of Industrial Waste Water and their Recycling for a Sustainable Future* (Springer Nature Singapore Pte Ltd., 2019).

[4] Samchetshabam, G. *et al.* Impact of textile dyes waste on aquatic environments and its treatment (2017).

[5] Khan, S. & Malik, A. *Environmental and Health Effects of Textile Industry Wastewater* (Springer, Dordrecht, 2014).

[6] Baker, R. W. *Membrane Technology and Applications, 2nd Edition* (John Wiley Sons, Ltd, 2004).

[7] Moghadam, F. & Park, H. B. 2d nanoporous materials: membrane platform for gas and liquid separations. *2D Materials* **6(042002)** (2019).

[8] P Koenig, S., Wang, L., Pellegrino, J. & Bunch, J. S. Selective molecular sieving through porous graphene. *Nature Nanotechnology* **7(11)** (2012).

[9] Medhekar, N. V., Ramasubramaniam, A., Ruoff, R. S. & Shenoy, V. B. Hydrogen bond networks in graphene oxide composite paper: structure and mechanical properties. *ACS nano* **4(4)** (2010).

[10] Li, J. *et al.* Improved water permeability and structural stability in a polysulfone-grafted graphene oxide composite membrane used for dye separation. *Journal of Membrane Science* **595** (2020).

[11] Yang, H., Li, J. & Zeng, X. Correlation between molecular structure and interfacial properties of edge or basal

plane modified graphene oxide. *ACS Applied Nano Materials* **1(6)** (2018).

[12] Nair, R., Wu, H., Jayaram, P., Grigorieva, I. & Geim, A. Unimpeded permeation of water through helium-leak–tight graphene-based membrane. *Science* **335(6067)** (2012).

[13] Joshi, R. *et al.* Precise and ultrafast molecular sieving through graphene oxide membranes. *Science* **343(6172)** (2014).

[14] Liu, G., Jin, W. & Xu, N. Two-dimensional-material membranes: A new family of high-performance separation membranes. *Angewandte Chemie* **55(43)** (2016).

[15] Hu, X., Yu, Y., Zhou, J. & Song, L. Effect of graphite precursor on oxidation degree, hydrophilicity and microstructure of graphene oxide. *Nano* **9(3)** (2014).

[16] Azizi-Lalabadi, M., Hashemi, H., Feng, J. & Mahdi Jafari, S. Carbon nanomaterials against pathogens; the antimicrobial activity of carbon nanotubes, graphene/graphene oxide, fullerenes, and their nanocomposites. *Advances in Colloid and Interface Science* **284** (2020).

[17] Ma, F. *et al.* Potential application of graphene oxide membranes for removal of cs(i) and sr(ii) from high level-liquid waste. *Separation and Purification Technology* **188** (2017).

[18] Zheng, S., Tu, Q., Urban, J. J., Li, S. & Mi, B. Swelling of graphene oxide membranes in aqueous solution: Characterization of interlayer spacing and insight into water transport mechanisms. *ACS Nano* **11(6)** (2017).

[19] Sun, P. *et al.* Selective ion penetration of graphene oxide membranes. *ACS Nano* **7(11)** (2012).

[20] Chong, J. Y., NFD, A., Wang, B., Mattevi, C. & Li, K. Uv-enhanced sacrificial layer stabilised graphene oxide hollow fibre membranes for nanofiltration. *Scientific Reports* **5(15799)** (2015).

[21] Chong, J. Y., Wang, B., Mattevi, C. & Li, K. Dynamic microstructure of graphene oxide membranes and the permeation flux. *Journal of Membrane Science* **549** (2018).

[22] NFD, A., Chong, J. Y., Wang, B., Mattevi, C. & Li, K. Graphene oxide membranes on ceramic hollow fibers – microstructural stability and nanofiltration performance. *Journal of Membrane Science* **484** (2015).

[23] Miao, Y., Chen, K., Zhang, X., Xu, Z. & Yang, X. Water-mediated attractive interaction between negatively charged go nanosheets at the air–water interface. *The Journal of Physical Chemistry* **125(1)** (2021).

[24] Lee, M. Micro-channel enhanced alumina membranes - designing and tailoring their properties for widened applications. *PhD Thesis, Imperial College London* (2016).

[25] Moghadam, F., Lee, T. H., Park, I. & Park, H. B. Thermally annealed polyimide-based mixed matrix membrane containing zif-67 decorated porous graphene oxide nanosheets with enhanced propylene/propane selectivity. *Journal of Membrane Science* **603** (2020).

[26] Dimiev, A. M. & Eigler, S. *Graphene Oxide: Fundamentals and Applications* (John Wiley Sons, Ltd, 2016).

[27] Kemal, C. *et al.* Ultimate permeation across atomically thin porous graphene. *Science* **344(6181)** (2014).

Chemical Transport in Partially Saturated Porous Media

Zahra Deji-Abiola[1] and Oyekitan Oyeleke[2]

[1,2] *Imperial College London, Department of Chemical Engineering, London, UK*

Reception date of the manuscript: 15/12/2021

Abstract—The quantitative effects of residually trapped CO_2 on the diffusive flux of CO_2-brine systems in subsea geological formations were investigated in this report. In carbon capture and storage, the interactions between different trapping mechanisms is important as this is one of the factors governing the long-term storage stability of trapped CO_2. In particular, this report models the interaction between capillary trapping, where CO_2 is trapped by capillary forces and dissolution trapping, where CO_2 is trapped by dissolving in brine. This is done by modelling the trapping and transport mechanisms of the CO_2 in brine using OpenPNM, a Python-based modelling software. An invasion percolation model, governed by the Washburn equation was used to simulate the percolation sequence of brine through the pores, which is the process by which CO_2 is trapped. A Fickian diffusion model was then used to model the diffusive transport of the CO_2-brine solution, which was governed by a concentration gradient across the pore network. The results of the simulation were visualised using a combination of concentration outlet curves, concentration maps and diffusivity curves. The data from the simulation showed that the effective diffusivity of solutes in water decreased as the air saturation increased. When comparing the relationship between effective diffusivity and air saturation to Archie's law, a good fit was obtained at low air saturations. However, this relationship broke down at higher air saturations due to air clustering, which prevented complete randomisation of air pore occupancies. The results of this report are important in understanding the effect capillary trapping has on dissolution trapping, and consequently the overall storage stability of CO_2 in saline aquifers.

Keywords—Chemical transport, CO_2 trapping, Porous media, Diffusive transport, Carbon storage

I. INTRODUCTION

Interest in CO_2 reduction strategies have been increasing as CO_2 emissions continue to rise rapidly due to human activity [Program, 2020]. Policy and legislature regulations such as the EU's Fit for 55, which aims to reduce CO_2 emissions by 55% by 2030, have been created to ensure countries reduce their CO_2 emissions accordingly [Council, 2020]. Carbon capture and storage (CCS) has been identified as the most impactful way to reduce atmospheric CO_2 levels.

CCS involves a number of sequential steps. Firstly, the CO_2 emissions are captured, usually from exhaust pipes in post-combustion processes. This removes dilute CO_2 (5-15% CO_2 concentration) from flue gas streams at low pressures [Fanchi and Fanchi, 2017]. After this, the CO_2 is transported via pipelines or ships to use as feedstock in further processes, enhanced oil recovery or as discussed in this project, stored in underground geological formations at depths usually greater than 800m.

At such depths, CO_2 is present in a supercritical state as it is held above its critical temperature (32 °C) and pressure (72.8 atm). The supercritical CO_2 ($scCO_2$) is more buoyant than fluids such as brine or hydrocarbons present in the rock void space [Baban et al., 2021]. Therefore, to ensure the long-term stability of carbon capture, it is important that there are mechanisms in place to keep the buoyant $scCO_2$ underground and prevent it diffusing back into the atmosphere, negating the work done in CCS. There are four main $scCO_2$ storage mechanisms, namely structural trapping, capillary trapping, dissolution trapping and mineral trapping [Iglauer, 2011].

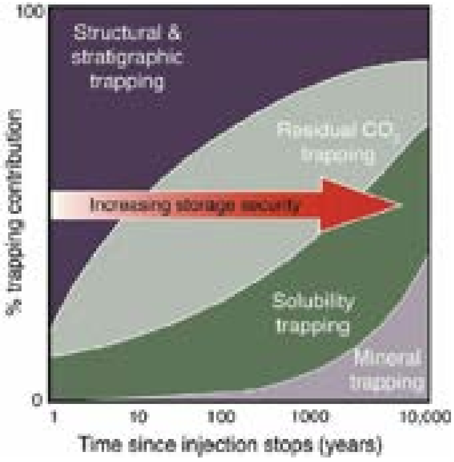

Fig. 1: Differing features of the various trapping mechanisms [Abidoye et al., 2015]

In structural trapping, an impermeable rock formation such as an anticline or sealing fault prevents the upwards migration of CO_2. In mineral trapping, a reaction of CO_2 and brine forms solid carbonate minerals, which are able to trap CO_2 efficiently. Although mineral trapping is considered the safest trapping mechanism as seen in Figure 1, it requires a long time scale (in the order of thousands of years) to come into effect. In dissolution trapping, CO_2 dissolves in the brine solution leading to an increase in CO_2-brine density and creating a dynamic gravity imbalance, triggering convection currents. This ensures that the trapping mechanism is secure, even in the absence of structural features such as cap-rocks.

Lastly, CO_2 can also be immobilised under capillary trapping, enhancing the security and capacity of CO_2 storage. This immobilisation is due to capillary forces, which hold the micrometer-sized CO_2 bubbles in the rock pore network through snap-off [Al-Menhali and Krevor, 2016]. Initially, the rock is assumed to be fully saturated with brine. In water-wet geological formations, when injected, the non-wetting phase (air, in this project) fills the large pores, while the wetting phase (water) fills the smaller pores and clings to the rock surface, minimising surface tension [Abdallah et al., 2007].

As the water (which forms the wetting layer) imbibes through the pore network, the water pressure rapidly increases, causing the wetting layers to swell [Vick et al., 2017]. At some point and at a critical air bubble radius, the air (non-wetting layer) loses contact with the rock's pores and the water moves rapidly into the throats, displacing the non-wetting layer. In capillary trapping, this usually occurs at the narrowest point of the throat with the smallest radius. Throats are then invaded in order of size in a percolation sequence, with the wetting phase in the throats and the non-wetting phase trapped in the pores.

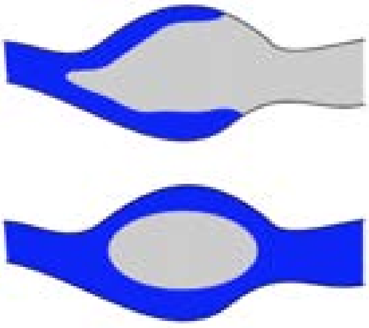

Fig. 2: Snap-off mechanism showing water (the wetting layer shown in blue) advancing and trapping air (the non-wetting layer shown in grey) [Kraus et al., 2015]

There are a few factors which affect the degree of trapping. Firstly, the wettability of the rock can influence the amount of CO_2 trapped. The wettability of the sub-sea rock has a significant impact on relative permeability, capillary pressure and CO_2-brine mass transfer [Al-Khdheeawia et al., 2016]. As a result, water-wet rocks such as sandstone or carbonate result in more trapping. The ratio of pore to throat size (larger pores relative to throats favour trapping) and network connectivity (more throat connections per pore can leads to less trapping) also affect the levels of trapping [Krevor et al., 2015]. Finally, the amount of CO_2 injected can also affect of trapping (more CO_2 injected, the more CO_2 is available to be trapped).

Importantly as this project explores, the presence of trapped CO_2 bubbles in the pores can affect the dissolution of CO_2 in brine by reducing the effective diffusivity. Acknowledging the different types of trapping and how they interact is essential to understanding the stability and long-term storage security of CO_2 in sub-sea geological formations.

Modelling techniques were employed to simulate the mass transport behaviour of CO_2 in porous rock partially saturated with brine. Water and air were used in place of brine and CO_2 when building the mass transfer models. This approximation was valid because the transport properties of air-CO_2 and water-brine were comparatively similar under the temperatures and pressures simulated. For the remainder of this project, water and air are used interchangeably for brine and CO_2.

An invasion percolation model was used in conjunction with the Fickian diffusion model to simulate the percolation of water through the porous rock. Here, viscous forces are assumed to have a negligible effect on fluid transport. Consequently, buoyancy and capillary forces are the primary factor in predicting the CO_2 plume migration [Mehana et al., 2020b]. The capillary pressures required to invade pores were calculated using the Washburn equation, which is explored below.

To characterise the diffusive behaviour of air in water, a 2-D Fickian diffusion model was employed. The Fickian diffusion model is a numerical method, which utilises volume-averaging, treating the pore space as homogeneous and restricting diffusion to the void space. This means the diffusion is influenced by the porosity and tortuosity of the network, impacting the total diffusive flux through the network. The effective and relative diffusivity of brine in CO_2 were calculated using Fick's first law as also explored in the section below.

II. Methods and Materials

Pore network simulations were carried out using OpenPNM, a Python-based modelling software. Firstly, pore network characteristics were determined by analysing different types of reservoir rock commonly used in carbon storage. Resulting rock features including number of pores, pore spacing and coordination number were then imported and modelled in OpenPNM.

Feature	Value
Number of pores	30
Lattice spacing (m)	1×10^{-5}
Lattice length (m)	30×10^{-5}
Coordination number	3
Shape	2-D

Table 1: Features of the porous network used in this project

The pore network was then modelled using a 2-D stick and ball network and the water and air phases introduced to observe the macroscopic transport behaviour in the rocks.

a. OpenPNM implementation

To simulate the different pore network models, OpenPNM was used. OpenPNM is an open source project providing network simulations, which can be used to simulate transport in porous materials such as reservoir rock. OpenPNM contains many key modules, which consist of various classes and methods.

These different modules can be used to specify the network, geometry, phases, physics, materials and algorithms used in the simulation. The geometry module was used to specify the stick and ball network in this project, which determined the pore and throat size distribution.

The phases module was used to introduce air and water into the network to simulate brine and CO_2 in the rock. This module was used to specify the thermophysical properties of the fluids present in the pore network [OpenPNM, 2018c]. Pore-scale models are included in the physics model and can be used to calculate physical properties of the fluids as functions of the relevant state variables. The object initialises at standard conditions of 298 K and 101325 Pa, but can be altered and thermophysical properties recalculated. The pore scale models for each fluid include the molar density, pore diffusivity, pore surface tension, pore thermal conducitivity and pore viscosity.

The physics module was used to calculate properties related to physical transport processes such as conductances and capillary effects. This module ensures that the different physical models will only have access to information on the network, geometry and phases to which they are assigned. In addition, models such as invasion percolation and Fickian diffusion, require information about the network, which is stored in the physics module. In this project, the physics model was used to compute the capillary entry pressure, modelling the throat in a cylindrical tube. The Washburn equation is used to determine the capillary entry pressure, which is suitable for non-wetting phases such as CO_2 [OpenPNM, 2018d].

The algorithms module was used to conduct transport simulations on pore networks. In this project, the invasion percolation simulation is run using the algorithms module. For invasion percolation, the algorithm uses a binary heap to store a list of all accessible throats (i.e. $P > Pc$), sorted according to entry pressure [OpenPNM, 2018a].

1. Use of pore network model (PNM)

PNM was used to model the transport processes that occur within the subsea rock's structure. A pore-scale simulation was chosen over experimental techniques for a number of reasons. Firstly, pore-scale simulations are able to mimic transport processes in a more cost-effective and efficient way. Secondly, variations in the rock's parameters (for example: porosity, coordination number, lattice size) can easily be altered, and the resulting effect on transport properties observed. Xiong et al. [2016]. This offers a way to measure chemical and transport properties, much easier than using experimental methods [Meakin and Tartakovsky, 2009].

PNM was also chosen over other pore-scale simulation techniques such as particle-based methods like the Lattice Boltzmann method. Firstly, unlike particle-scale models, PNM is adept in in intermediate-scale analyses involving tens or hundreds of pores [Tartakovsky et al., 2007]. In addition, PNM has quicker computational times, due to simplifications and approximations made in the simulations. This enables the algorithms to run faster, allowing a greater range of scenarios to be run in a given time-frame.

The accuracy of pore network modelling when predicting transport behaviour depends on how closely the PNM is able to represent the pore space being replicated. However, the intricacy of real pore networks with respect to the irregular pore distributions can make this hard to model.

b. Physics-based models

To model the transport behaviour, the percolation of water through the porous system and the resulting trapping of air was modelled using an invasion percolation algorithm. This was useful in simulating the capillary trapping sequence that occurs in porous media. After the percolation simulation, the diffusion of air in water was modelled using a Fickian diffusion algorithm. Finally, the effects of capillary trapping on the diffusion of CO_2 were studied, by calculating the effective diffusivity of CO_2 in brine as a function of air saturation.

1. Percolation algorithms

The migration of a CO_2 plume depends on a balance of buoyancy and capillary forces. The buoyancy forces are caused by density differences between the CO_2 and the surrounding brine. Conversely, the capillary forces represent the resistance to the invading fluid and depend on the pore structure, wettability and surface tension.

Darcy-based approaches can model plume migration by solving a set of partial differential equations (PDE's) to estimate the time and space distribution of pressure and saturation for both air and water phases [Mehana et al., 2020a]. When comparing invasion percolation and Darcy-based simulations, the computational efficiency of percolation simulations is greater, allowing for more advanced simulations.

As a result, plume migration and trapping was modelled using invasion percolation, which uses the balance between buoyancy and capillary forces to predict plume migration. The invasion simulation proceeds by identifying neighbouring elements of clusters and invading them one at a time.

This was also chosen over ordinary percolation for a number of reasons. Firstly, by invading clusters one at a time instead of all at once, a more accurate representation of transient flow and the related physics models are obtained [Wilkinson and Willemsen, 1983]. Secondly, as the invasion proceeds, some air clusters can become completely surrounded by the invading water phase due to capillary forces, leading to trapping and this can only be modelled using invasion percolation. The capillary pressures required to enter a pore/throat are calculated using the Washburn equation:

$$P_c = \frac{-2\sigma cos(\theta)}{r} \tag{1}$$

A range of pressures are defined and for each one the value is compared to the entry pressures of the throats. If the entry pressure is greater than the current threshold value, this element is considered invaded and can form part of an invading cluster [Guide, 2019].

2. Diffusion simulation

In this project, both steady-state and transient Fickian diffusion were used to measure transport properties. Transient Fickian diffusion was used to determine properties, such as the outlet concentrations of water, as a function of time. The diffusion equations are unsteady, and therefore require solutions in which position varies as a function of time. This was used to observe how these properties progressed over the course of the simulation.

The transient algorithm settings were updated to make the simulation more relevant to our investigations. Firstly, Dirichlet boundary conditions were implemented at the inlet, which were defined at the 'left' pores as specified by OpenPNM, to ensure the inlet solute concentration = 1 mol/m^3 while the outlet concentration of the 'right' pores varied. The time discretization scheme was set to Crank-Nicolson, which is second-order accurate in time. This involved the integration of every term in different equations over a time step (t=Δ1s). The final time step was also specified to ensure sufficient time for the simulation to reach steady-state.

The steady state Fickian diffusion was then run to determine the diffusion and therefore the effective diffusivity of the solute in water. This was done by applying controlled boundary conditions on opposing faces, calculating the diffusion rate, and inverting Fick's first law as seen in equation 4. The boundary condition were similar to the Dirichlet boundary conditions of the transient algorithm but with the 'right', outlet pores maintained at solute concentration = 0 mol/m^3.

$$D_{eff} = \frac{N_A \times L}{A \times \Delta C_A} \tag{2}$$

c. Porous framework modelling

After the relevant physics models were chosen, the porous network was replicated in OpenPNM. Porous systems are one of the most important characteristic of hydrocarbon reservoirs. Crude oil and/or natural gas are able to migrate through the rock's pores by displacing brine present in the voids. The pores exist as a distribution of sizes, with neighbouring pores connected to each other through throats. When modelling the porous network in 3-D, a stick and ball network was chosen, which represented the pores as perfect spheres, and the throats, cylinders.

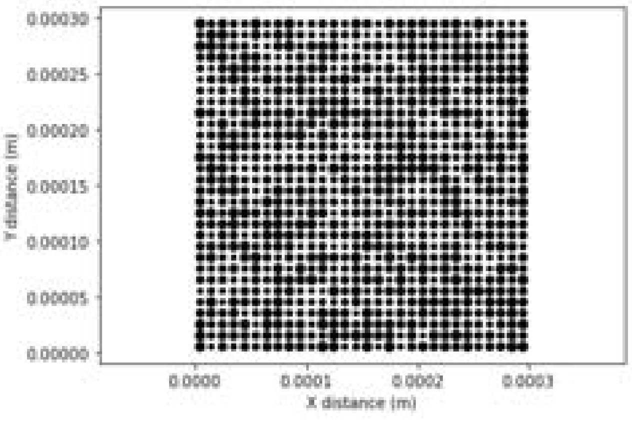

Fig. 3: 2-D pore network model showing pore size distribution

Pore sizes were determined by assigning diameters to each pore from a random distribution, spanning 0μm to 10μm. The upper limit matched the lattice spacing of the network, which was manually specified in the code. Throat diameters were then taken as half the size of the smallest pore they were connected to [OpenPNM, 2018b]. A porous network showing the pore size distribution can be seen in Figure 3, with darker dots representing larger pores.

Using this model, the mass and chemical transport of CO_2 were predominantly determined by the sizes and geometrical locations of the pores, as well as the connection of pores via throats [Xiong et al., 2016]. The interconnections of the pore-throat network allowed mass transport via a concentration gradient, where the water diffused from a region of high to low concentration. The porosity of the rock was calculated using:

$$\phi = \frac{V_p}{V_t} \tag{3}$$

where V$_p$ is the pore space volume filled with the wetting phase and V$_t$ is the entire volume of the rock. The porosity of the rock as well as other key features such as the coordination number were used to model the different rock samples examined.

1. Random seed averaging

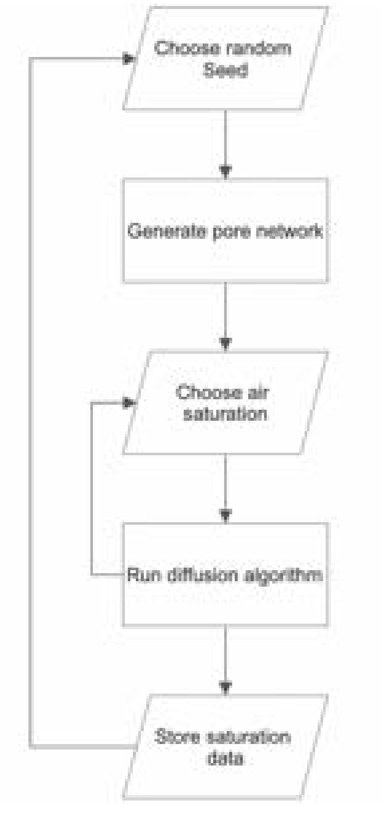

Fig. 4: Workflow showing sequential steps taken with circular loops for loop sequences

A different random pore network was generated each time the simulation was run at a given air saturation. This occurred due to the random assignment of pore and throat sizes affecting the capillary pressure required to invade the element. To ensure results were consistent, a random seed generator was implemented to ensure that the same random pore network was generated each time.

The inclusion of different random seeds generated porous networks, which consequently affected the mass and diffusive transport characteristics of CO_2 in the simulation. Therefore, extensive analysis had to be carried out to ensure that the appropriate number and values of random seeds were chosen to guarantee uniformity and replicability.

Figure 4 shows the workflow implemented when running the simulation. The random seed was used to generate the pore network and then the diffusion algorithm was run for a number of air saturations.

The number of random seeds included were varied from one to five values and the resulting effect on outlet water concentration observed to determine the optimum number of random seeds. Increasing the number of random seeds included changed the features of the outlet curves (such as time to reach concentration of 1 mol/m^3) in a random fashion, as can be seen in Figure 5. There was no observable pattern between the number of random seeds used and the resulting porous network. Therefore, the results from random seeds 10, 9 and 8 were taken and averaged to produce the porous network. This ensured randomness in the pore network generation, while optimising for speed and computational efficiency.

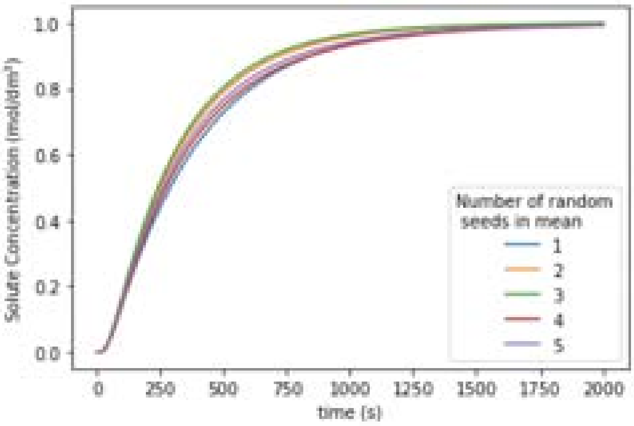

Fig. 5: Effect of the number of random seeds used on transport processes within the porous network, which effect the shape of the outlet curve

d. Phase introduction

After producing the porous network and selecting the relevant physics models, the fluid phases had to be introduced. The air phase was introduced into the pores, and then it was specified that any pores that didn't contain air must contain water, i.e. the pores had strict binary occupancies. Following this, a correction factor of $1x10^{-6}$ was applied to the diffusive conductance of all throats connected to at least one pore that contained air, restriction solute transport through them significantly.

In introducing the air phase, two different scenarios were modelled for comparison sake. In the first scenario, a manual random air-assignment was used, where a fraction of the pore volume = air saturation was randomly assigned with air. In the second scenario, there was no manual interference, and the air was allowed to occupy the pores based on the physics of the system, governed by the invasion percolation algorithm.

By simulating these two scenarios, the choice to use the percolation-based air assignment was justified. As seen in Figure 6a, the water represented in blue had no connected path from left to right, restricting flow. Conversely, as seen in Figure 6b, there is a path from left to right, which allows water flow and consequently diffusive transport.

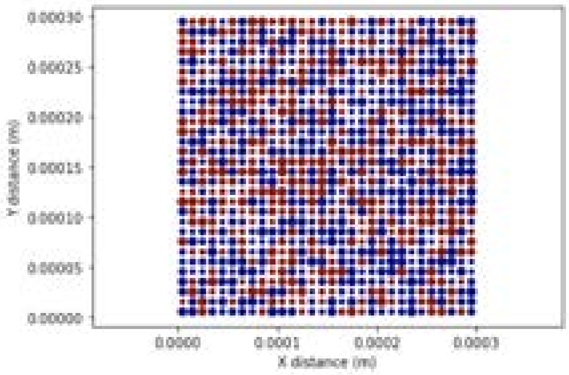

(a) Random air assignment

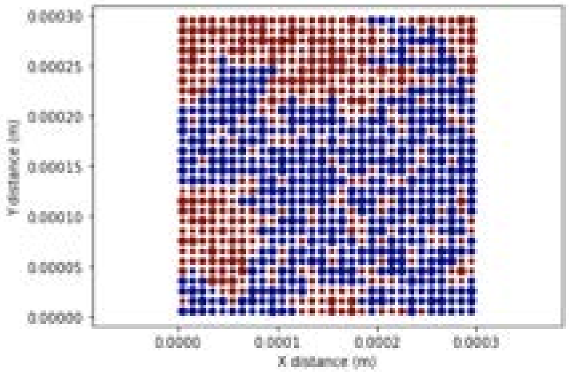

(b) Physics-based air assignment

Fig. 6: 2-D porous network showing air (represented in red) and water (represented in blue) occupancies

III. RESULTS

a. Concentration maps

In this section, the concentration of the solute in water was maintained at 1 mol/dm^3 in top part of the pore network and the fluid allowed to diffuse through the porous network. The resulting concentration maps depended on the air saturation being simulated, with differences in air saturation producing different results due to an increase in tortuosity. The concentration maps also varied temporally, as the solute took time to diffuse to regions of lower concentration.

1. Concentration maps as a function of saturation

As mentioned in the preceding section, the impact of the invasion percolation on the air pore occupancy of the porous network differed depending on the air saturation that was being modelled. At low air saturations, the pores that contained air were more uniformly distributed in the pore network and appeared random. However, as the saturation specification increased, the air-containing pores were more localised to sections of the pore network, forming clusters. This was as a result of smaller clusters joining to form larger aggregates. This meant entire sections of the pore network were inaccessible to water and therefore could not participate in diffusion.

With the impermeable, air-filled pores acting as obstacles to the diffusive flux, the solute molecules had a longer path around the barrier to travel in the partially saturated simulations. This increase in tortuosity was not equal in all sections of the pore network due to the clustering leading to a non-homogeneous mixture of the two phases. This inequality was

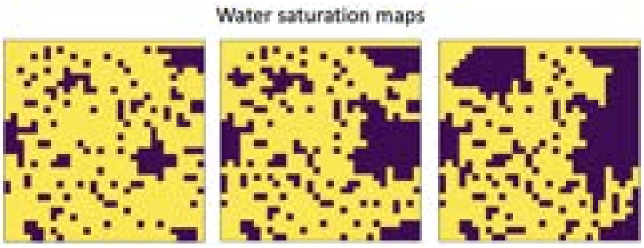

Fig. 7: Concentration maps at 10%, 20% and 30% air saturation. The yellow regions indicate 100% water, while the purple regions indicate 100% air. Higher air saturations exhibit higher amounts of air clustering - as seen by connected regions with 100% air

more pronounced at higher air saturations. This meant that the length of the paths that the solute molecules were exposed to differed depending on the extent of the tortuosity change in its vicinity.

2. Concentration progression over time

The phenomena described above is further illustrated with Figure 8, which presents snapshots of the concentration profile at given conditions of the pore network before steady state is achieved to compare the routes taken by the solute when air saturation is varied. In this simulation, the solute concentration was maintained at 1 mol/dm^3 at one end and the evolution of the concentration front was observed. The snapshots display the concentration profile when the average outlet solute concentration in the water-filled pores were 5%, 25% and 50% respectively.

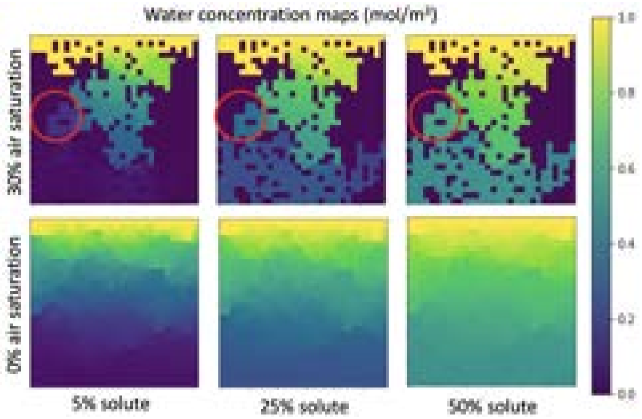

Fig. 8: Concentration progression maps at 0% and 30% air saturation for t at 5%, 25% and 50% average solute concentrations

Without any air, the concentration front was approximately perpendicular to the direction of diffusion at every point in the simulation as seen in Figure 8. There were also no dead zones along the concentration profile. This was due to the tortuosity being constant throughout the pore network. On the other hand, when air was introduced to the system, the concentration level curves had different features due to the dispersal of the solute being hindered by inaccessible air-filled pores which increased tortuosity.

This inaccessibility led to more tortuous paths for the solute to take to reach the outlet pores but this increase in tortuosity was not equally distributed in the pore network. This was evident from the areas of lower concentration with the highlighted area of Figure 8 being an example of one of these deadzones that were created. This area was just below a cluster of air. Thus, the solute was required to travel around this obstruction to reach this subset of low concentration pores. This was more tortuous than reaching most of the other pores at the same level. Consequently, the concentration front was no longer perpendicular and there were areas of lower concentration.

b. Outlet curves

The saturation had an effect on the concentration profile spatially but also how it evolved with time as can be observed in Figure 9. This monitored the mean concentration of the pores at the bottom which still contained water after the percolation process from time t=0 when a step change from 0 mol/dm^3 to 1 mol/dm^3 in the top pores' solute concentration was applied to and maintained for each system.

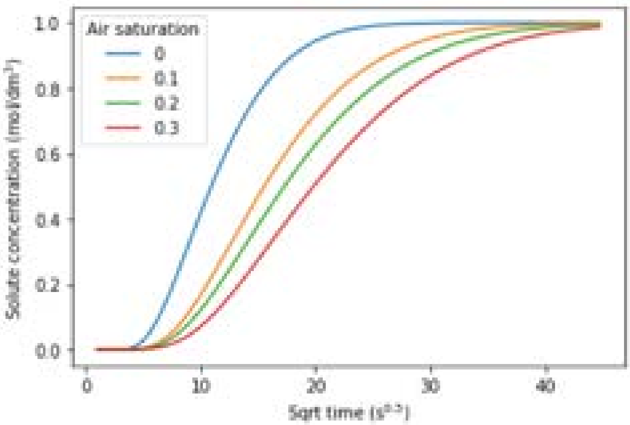

Fig. 9: Outlet curves at different air saturations

As can be seen in Figure 9, the increase in tortuosity at higher air saturation increased the time it took for the pore system to reach steady state during the Transient Fickian Diffusion experiment. This time corresponded to the point at which the mean outlet water concentration was 1 mol/dm^3. All the curves demonstrated behaviour that is characteristic of a step response change for a first order system. The initial gradient corresponds to the time constant which is characteristic of the system. With the same input change, a steeper initial gradient corresponds to a faster response of the system to a change. This meant that less air in the pore network gave a quicker response to changes in the system. This could once again be explained through the longer path the solute molecules must take to diffuse when faced with a more tortuous, obstacle-filled paths.

Furthermore, there was a more significant gap in the behaviour between 0% and 10% saturation than that of the 10% and 20% saturation. This trend was also observed with the subsequent interval. This showed that the rate of change of the steady-state time, and therefore the responsiveness, decreased as the saturation increases.

c. Diffusivity curves

In this section, the graphs were produced by averaging the pore network models produced from three different random seeds. The same trend in temporal and spatial behaviour of the pore networks' concentration profile can be encapsulated in the overall change in the diffusivity due to the presence of trapped air in the pore network.

1. Relative and effective diffusivity

The presence of air bubbles in the pore network due to trapping consequently led to an overall decrease in the diffusivity as seen in Figure 10 where the relative diffusivities were calculated using Fick's law. This diffusivity decrease was drastic following the initial inclusion of air with a 50% decrease in diffusivity when the air saturation was just below 10%.

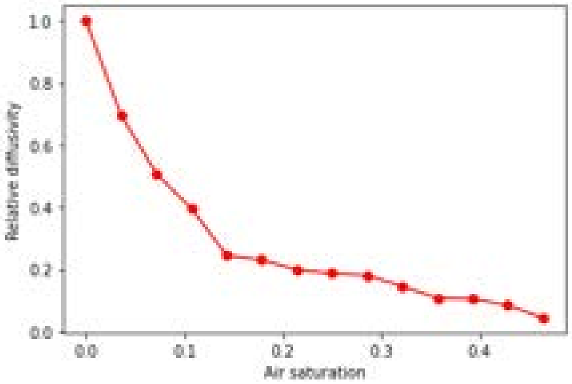

Fig. 10: Relative diffusivity as a function of air saturation. Relative diffusivity was determined by normalising effective diffusivity at a given saturation to the effective diffusivity at 0% air saturation

This decrease, however, became more moderate beyond an air saturation of 15%. This may have been due to the clustering as identified in Figure 7. The incremental change in the size of the clusters had a marginal effect on the level of obstruction for the solute compared to another path being blocked through the filling of pores with air in a separate area of the network.

At even higher air saturation, the diffusivity tended to 0. This could once again be explained through the clustering which made the water-filled pores capable of transporting the solute become disconnected. Thus, no diffusion could take place. This complete disconnection occurred at around 50% saturation at which point, the outlet curves, as seen in Figure 9, did not reach the steady state concentration.

2. Diffusivity modelling

Upon modelling the diffusion of CO_2 and brine percolation through the pore network, it was important to quantify the effects of trapped CO_2 on its diffusivity in brine. There are a number of empirical and mechanistical models quantifying the effective diffusivity (D_{eff}) to the level of water saturation (S). In this project, the most commonly used model - Archie's law was used [Archie, 1942]:

$$D_{eff} = S^n \times D_o \times \phi_{sat}^m \qquad (4)$$

The equation defines effective diffusivity as a function on saturation, porosity at complete water saturation (ϕ_{sat}) and molecular diffusion constant and two exponential constants - saturation exponent (n) and cementation exponent (m).

Upon fitting the data from our simulations to Archie's law as seen in Figure 11, a best-fit cementation exponent of 2.96 (± 0.30%) and saturation exponent of 6.59 (± 9.41%) were obtained.

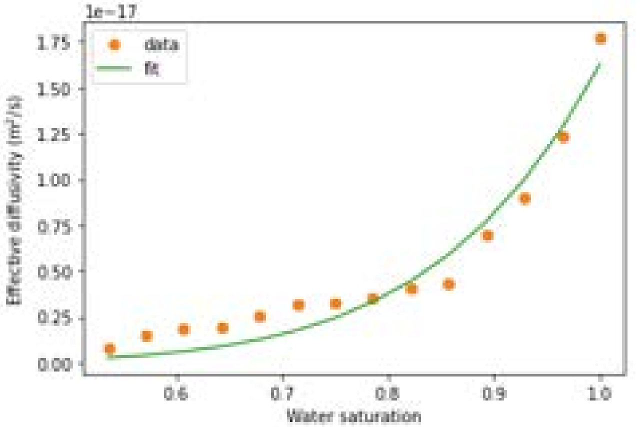

Fig. 11: Effective diffusivity curve fit to Archie's law

According to Hamamoto et al. [2010], the cementation and saturation exponents tend to vary between 1-3. This agrees with the value found for the cementation exponent however the saturation exponent deviates greatly from this range. This made this an interest of further investigation as explored in the section below.

IV. DISCUSSION

a. Deviations from Archie's law

The cementation exponent is related to the connectivity of the pore structure which is idealised and constant for this pore network model [Kennedy, 2015]. Thus, it is reasonable for the value obtained to be within the range seen in real rock samples.

Similarly, the deviation of the saturation exponent can be explained using an understanding of the theory that birthed the empirical correlation and acknowledging the shortcoming of the modelling technique. The saturation exponent is related to the wettability and a specific phenomena that occurs depending on this property. In actual water-wet rocks, even at high air saturation, it is found that there can be a thin, continuous film of water on the pore walls, encapsulating the air in the pores as seen in Figure 2. This allows for film diffusion to still take place in air-filled pores albeit with much higher resistance due to the decreased thickness. The more water-wet the pore body is, the lower the value of the saturation exponent is expected to take as the effect of the increased saturation is mitigated against by the fact that the pores can still maintain water connectivity.

OpenPNM models two-phase systems by assigning pores occupancy to a phase in a binary. This means that it doesn't have the capability to take into account a film of the second phase within the same pore. Moreover, to model diffusion, the throats connected to pores containing air were given a correction factor that dramatically reduced the diffusive conductance in the water phase to render them highly disconnected from the rest of the water phase. As such, the model is overall not able to take into account this potential for higher connectivity. As such, the saturation number is very high to accurately portray how highly effective changes in saturation is in reducing diffusivity.

With this in mind, the values for the saturation exponent may be better described in this experiment as more akin to the value of an oil-wet rock. For oil-wet rocks, that this value can increase to up to 25.2 [Tiab and Donaldson, 2012]. Although this is in relation to electrical conductance, this is more analogous to to the effect air had on solute diffusion in these simulations, making the value found more reasonable.

Another option to interpret this data is to utilise the corrections that have been made to Archie's Law over the years. Equation 4 does not take into account the saturated and unsaturated percolation threshold, ϕ_{th}^{*} and ϕ_{th} respectively. These represent the inactive water phase for the given transport process at complete water saturation and the water porosity at which the diffusive transport is rendered negligible due to the fluid becoming disconnected respectively [Hamamoto et al., 2010]. By writing the saturation in terms of porosity of the water phase at the saturation and at complete water saturation, Archie's Law can be rewritten as seen in Figure 5.

$$D_{eff} = D_o \times (\phi_{sat} - \phi_{th}^{*})^m \times \left(\frac{\phi - \phi_{th}}{\phi_{sat} - \phi_{th}} \right)^n \tag{5}$$

In approximating the unsaturated percolation threshold, the value corresponding to a water saturation of 0.5 was chosen as this is the point at which an outlet curve to steady state is no longer produced in the simulation. On the other hand, the saturated percolation threshold was kept at 0 as due to the simulation being idealised. Using this, a closer approximation when looking at high water concentration was found as seen in Figure 12. Consequently, the use of this gives a cementation and saturation exponent of 2.96 and 4 respectively. As expected, the value of the cementation exponent showed little change but the saturation exponent decreased significantly, fitting better with the initial research.

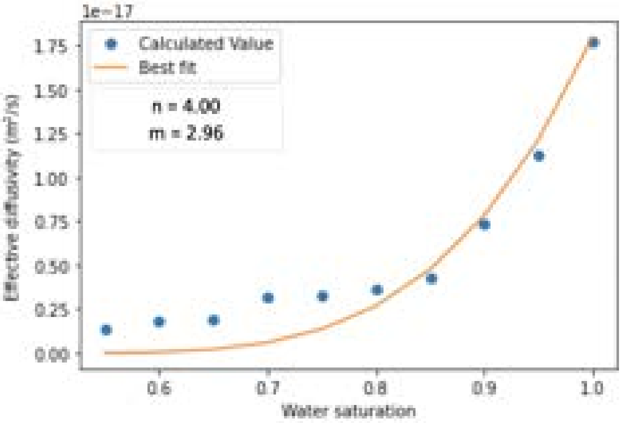

Fig. 12: Effective diffusivity curve fit to Archie's law when using the percolation threshold of 0.001

b. Lattice sizing

As seen in Figure 12, there is still some deviation from Archie's law at lower water saturations (or higher air saturations), which can be attributed to air clustering. At higher air saturations, the simulation becomes less able to randomly and evenly distribute air within the pore network. This becomes more obvious when the size of the air clusters increase and becomes similar to the lattice size as seen in Figure 7. Archie's law predicts the D_{eff} - saturation relationship based on complete randomisation of air occupancies, therefore in the absence of random distribution, a breakdown between research and our data exists at higher air saturations.

The relationship obtained is still relevant at lower air saturations as most capillary trapping processes have air saturations between 10-30% [Krevor et al., 2015]. Therefore, our data is still relevant especially given the scope of capillary trapping in CO_2 storage. Furthermore, the point at which the air saturation is high close to the injection point, it is unlikely for molecular diffusion to the main method of solute distribution due to the turbulence and it's effect could be neglected in modelling. However, if data at higher air saturations is required for future studies, a larger pore network could be utilised. This would increase the number of pores available for air occupation, which would enable the air bubbles to be more randomly placed.

c. Evolution of porous network

As the CO_2 dissolves in the brine, carboxylic acid (H_2CO_3) is produced, which reduces the pH of the brine, making it more reactive to the minerals it contains [Zhu et al., 2019]. This creates significant changes to the chemical, mineral and physical properties of the porous network.

This project assumed that the porous network stays constant over the lifetime of the simulation. However, this is not entirely accurate as the reactions mentioned above can lead to the evolution of the porous network, causing significant changes in larger-scale transport properties such as the calculated effective diffusivity. In future work, the effects of reactive transport on the pore network and consequently, transport properties can be observed, to get a more holistic view of the effects of trapped CO_2.

d. Evolution of saturation

This project also assumed that the air saturation stayed constant over the course of each simulation. However, the air saturation also changes from t = time of air injection. Over time, the trapped air bubbles dissolve in the water, reducing the air saturation. This could lead to a decrease in path tortuosity over time, which would affect the effective diffusivity of the air-water system. This effect is likely to be more pronounced at higher initial air saturations and at greater times since injection.

V. CONCLUSION

The research showed that the inclusion of capillary or residually trapped CO_2 led to the reduction of CO_2's diffusivity in brine, due to an increase in tortuosity caused by air-filled pores. As a result of these findings, it is recommended that the amount of capillary trapped CO_2, which is directly related to the amount of CO_2 injected intially, be limited to low CO_2 saturations (<30%). At low CO_2 saturation levels, there is still significant amounts of both capilllary and dissolution trapping. Above this saturation level, CO_2 clusters begin to form, which reduce the effective diffusivity of CO_2 in brine, significantly affect the amount of dissolution trapping that occurs. This should be avoided as dissolution trapping leads to more safely stored CO_2 than capillary trapping as can be seen in Figure 1.

The reduction in the CO_2 diffusivity in brine caused by residual capillary trapping of CO_2 followed the expected direction, agreeing with previous literature, which predicted the same trend [Gilmore et al., 2020], [Krevor et al., 2015], [Amarasinghe et al., 2020]. Quantitatively, the function relating effective diffusivity to CO_2 trapping was found to match research data from Archie's law at lower air saturations ($< 15\%$). This is still relevant as the amount of capillary trapping in porous networks is usually around this amount Krevor et al. [2015].

Given the rapid rise in atmospheric CO_2 levels over the years, climate mitigation techniques such as carbon capture and storage have seen a rapid increase in relevance and importance. It is imperative that the stored CO_2 is trapped safely underground and can not be released back into the atmosphere. Therefore, projects such as this which quantify the impact of one trapping mechanism on the other are important, as the safety of trapped CO_2 depends largely on the type and interactions between these different trapping mechanisms. This can be used to give further insight into the efficiency of carbon storage in porous subsea geological formations at different CO_2 injection levels. This project could also be relevant for enhanced oil recovery techniques, such as gas injection where CO_2 is injected not to be stored, but to enhance the flow of oil trapped within pores.

This work succeeds a growing field of research in simulation of transport processes in porous media. There is significant potential to extend this research to investigate the interplay between even more types of capillary trapping. For example, dissolution trapping (CO_2 reacts with brine to form solid carbonates) could reduce the CO_2 saturation and also lead to a change in the porous network, as the solid carbonates get deposited. This could influence the diffusivity relationship that we determined. This work could also be extended to include reactive transport of CO_2, where CO_2 reacts with the brine to form a weak carbonic acid. Finally, the same simulation could be run using different rock types and lattice sizes and the effects on transport properties quantified. These different revisions can be investigated in the context of carbon capture in porous media.

VI. ACKNOWLEDGEMENTS

Oyekitan Oyeleke and Zahra Abiola would like to express their sincere gratitude to Ronny Pini and Andrea Rovelli for their invaluable support and guidance throughout the entire duration of this project.

REFERENCES

Wael Abdallah, J.S. Buckley, A. Carnegie, J. Edwards, B. Herold, Edmund Fordham, Arne Graue, Tarek Habashy, N. Seleznev, C. Signer, Hassan Hussain, Bernard Montaron, and M. Ziauddin. Fundamentals of wettability. *Oilfield Review*, 19:44–61, 06 2007.

Luqman Abidoye, Diganta Das, and Kamal Khudaida. Geological carbon sequestration in the context of two-phase flow in porous media: A review. *Critical Reviews in Environmental Science and Technology*, 45:1105–1147, 03 2015. doi: 10.1080/10643389.2014.924184.

Emad A. Al-Khdheeawia, Stephanie Viallec, Ahmed Barifcania, Mohammad Sarmadivaleha, and Stefan Iglauera. Influence of rock wettability on co2 migration and storage capacity in deep saline aquifers. *13th International Conference on Greenhouse Gas Control Technologies*, 2017: 4357 – 4365, 2016.

Ali S. Al-Menhali and Samuel Krevor. Capillary trapping of co2 in oil reservoirs: Observations in a mixed-wet carbonate rock. *Environmental Science & Technology*, 50(5): 2727–2734, 2016. doi: 10.1021/acs.est.5b05925. PMID: 26812184.

Widuramina Amarasinghe, Ingebret Fjelde, Jan Åge Rydland, and Ying Guo. Effects of permeability on co2 dissolution and convection at reservoir temperature and pressure conditions: A visualization study. *International Journal of Greenhouse Gas Control*, 99:103082, 2020. ISSN 1750-5836. doi: https://doi.org/10.1016/j.ijggc.2020.103082. URL `https://www.sciencedirect.com/science/article/pii/S1750583619307856`.

Guatavus Archie. The electrical resistivity log as an aid in determining some reservoir characteristics. *Transactions of the AIME*, 146:1–9, 1942. doi: https://doi.org/10.2118/942054-G.

A. Baban, A. Al-Yaseri, A. Keshavarz, R. Amin, and S. Iglauer. Co2 – brine – sandstone wettability evaluation at reservoir conditions via nuclear magnetic resonance measurements. *International Journal of Greenhouse Gas Control*, 111:103435, 2021. ISSN 1750-5836. doi: https://doi.org/10.1016/j.ijggc.2021.103435.

European Council. Fit for 55. *European Green Deal*, 2020. URL `https://www.consilium.europa.eu/en/policies/green-deal/eu-plan-for-a-green-transition/`.

John R. Fanchi and Christopher J. Fanchi. *Energy in the 21st Century*. World Scientific Publishing Co, 4 edition, 2017.

K. A. Gilmore, J. A. Neufeld, and M. J. Bickle. Co2 dissolution trapping rates in heterogeneous porous media. *Geophysical Research Letters*, 47(12):e2020GL087001, 2020. doi: https://doi.org/10.1029/2020GL087001. URL `https://agupubs.onlinelibrary.wiley.com/doi/abs/10.1029/2020GL087001`. e2020GL087001 10.1029/2020GL087001.

OpenPNM User Guide. *Percolation Algorithm*, 2019.

Shoichiro Hamamoto, Per Moldrup, Ken Kawamoto, and Toshiko Komatsu. Excluded-volume expansion of archie's law for gas and solute diffusivities and electrical and thermal conductivities in variably saturated porous media. *Water Resources Research*, 46(6), 2010. doi: https://doi.org/10.1029/2009WR008424.

Stefan Iglauer. *Dissolution Trapping of Carbon Dioxide in Reservoir Formation Brine – A Carbon Storage Mechanism*, chapter 10, page 234. 2011.

Martin Kennedy. 8.1 introduction. *Developments in Petroleum Science - Practical Petrophysics*, 62, 2015. URL `https://app.knovel.com/hotlink/khtml/id:kt00UOLJ53/developments-in-petroleum/log-analys-introduction`.

David Kraus, Rainer Helmig, P. Nuske, and Yufei Cao. Two phase flow in homogeneous porous media - the role of dynamic capillary pressure in modeling gravity driven fingering, 06 2015.

Samuel Krevor, Martin J. Blunt, Sally M. Benson, Christopher H. Pentland, Catriona Reynolds, Ali Al-Menhali, and Ben Niu. Capillary trapping for geologic carbon dioxide storage – from pore scale physics to field scale implications. *International Journal of Greenhouse Gas Control*, 40:221–237, 2015. ISSN 1750-5836. doi: https://doi.org/10.1016/j.ijggc.2015.04.006. Special Issue commemorating the 10th year anniversary of the publication of the Intergovernmental Panel on Climate Change Special Report on CO2 Capture and Storage.

Paul Meakin and Alexandre M. Tartakovsky. Modeling and simulation of pore-scale multiphase fluid flow and reactive transport in fractured and porous media. *Reviews of Geophysics*, 47(3), 2009. doi: https://doi.org/10.1029/2008RG000263.

Mohamed Mehana, Seyyed a Hosseini, Timothy Meckel, and Hari Viswanathan. Modeling co 2 plume migration using an invasion-percolation approach that includes dissolution. *Greenhouse Gases: Science and Technology*, 10, 04 2020a. doi: 10.1002/ghg.1976.

Mohamed Mehana, Seyyed A. Hosseini, Timothy A. Meckel, and Hari Viswanathan. Modeling co2 plume migration using an invasion-percolation approach that includes dissolution. *Greenhouse Gases: Science and Technology*, 10(2): 283–295, 2020b. doi: https://doi.org/10.1002/ghg.1976.

OpenPNM. Overview of algorithm module, 2018a.

OpenPNM. Overview of geometry module, 2018b.

OpenPNM. Overview of phases module, 2018c.

OpenPNM. Overview of physics module, 2018d.

US Global Change Research Program. Atmospheric carbon dioxide. *Climate.gov*, 2020. URL `https://www.globalchange.gov/browse/indicators/atmospheric-carbon-dioxide`.

Alexandre Tartakovsky, Paul Meakin, Timothy Scheibe, and Rogene Eichler West. Simulations of reactive transport and precipitation with smoothed particle hydrodynamics. *Journal of Computational Physics*, 222:654–672, 03 2007. doi: 10.1016/j.jcp.2006.08.013.

Djebbar Tiab and Erle C. Donaldson. Chapter 6 - wettability. In Djebbar Tiab and Erle C. Donaldson, editors, *Petrophysics (Third Edition)*, pages 371–418. Gulf Professional Publishing, Boston, third edition edition, 2012. ISBN 978-0-12-383848-3. doi: https://doi.org/10.1016/B978-0-12-383848-3.00006-2. URL `https://www.sciencedirect.com/science/article/pii/B9780123838483000062`.

Mathias Vick, Mark Martinez, Duncan R. Hewitt, and Neil Balmforth. Imbibition with swelling: Capillary rise in thin deformable porous media. *PHYSICAL REVIEW FLUIDS*, 2, 2017.

D Wilkinson and J F Willemsen. Invasion percolation: a new form of percolation theory. *Journal of Physics A: Mathematical and General*, 16(3365):1–7, 1983.

Qingrong Xiong, Todor G. Baychev, and Andrey P. Jivkov. Review of pore network modelling of porous media: Experimental characterisations, network constructions and applications to reactive transport. *Journal of Contaminant Hydrology*, 192:101–117, 2016. ISSN 0169-7722. doi: https://doi.org/10.1016/j.jconhyd.2016.07.002.

Huixing Zhu, Tianfu Xu, Hailong Tian, Guanhong Feng, Zhijie Yang, and Bing Zhou. Understanding of long-term co2-brine-rock geochemical reactions using numerical modeling and natural analogue study. *Geofluids*, 2019: 16, 07 2019.

Exploration and Constraint Satisfaction in Trust Region Methods in Black-box Optimisation

R. Cortes-Monroy, F. Salim
Department of Chemical Engineering, Imperial College London, U.K.

Abstract

Optimisation problems in chemical engineering often take the form of expensive black-box optimisation problems, where the evaluation of any given set of input variables incurs significant computational cost. As such, the performance of an algorithm per point evaluated is of key interest to the study of Derivative-Free Optimisation (DFO). To this end, several modifications to the DFO algorithm CUATRO are described and investigated over a range of test functions and black-box case studies, the primary aim being to improve efficiency through better exploration. Key features of these modifications include a focus on safer exploration, improved trust-region sampling, as well as the incorporation of global solution heuristics for application in highly non-convex problems. The proposed safe exploration algorithm showed great promise in improving evaluation efficiency as well as reduced constraint violations. The proposed low-discrepancy sampling does not show significant improvement in the majority of 2-input variable problems but show potential improvement in problems with a greater number of input variables. The global heuristics are found to promote better exploration of a given problem's feasible region to locate several local optima. Hence, these are expected to provide a useful framework for global algorithms that could be used more generally.

1. Introduction

1.1 Black-box Optimisation

This study is concerned with black-box problems, which are defined as functions for which there is no explicit or analytical form. As such, the user can only rely on output data, which can often be expensive to compute. No derivative information is available, making derivative-based optimisation techniques inadequate.

This kind of problem is applicable to many chemical engineering situations (Eason & Biegler, 2018; Felton, Rittig & Lapkin, 2020). Two such situations are simulated – a Real-Time Optimisation and a Self-Optimising Reactor – and are used in this study for benchmarking.

1.2 Objectives

The objective of this study is to investigate the effect of implementing various strategies in CUATROg, a derivative free optimisation (DFO) algorithm developed by van de Berg et al. (2022) on the algorithms' efficiency and constraint violations. Each strategy uses different methods, but all aim to improve exploration in the algorithm. The performance is tested using various test functions and case studies.

The rest of the report is structured as follows. Section 2 looks at some of the theory behind nonlinear optimisation, types of surrogate models used in optimisation and discusses some examples of popular DFO algorithms and their strengths and weaknesses. Section 3 discusses in detail the methodology behind the strategies that are applied to CUATROg in this study and introduces the case studies on which they are tested. Section 4 describes the results of these tests and section 5 discusses the trends observed.

2. Background

2.1 Trust-region and line-search

Consider a simple description of an optimisation problem:

$$\begin{aligned} &\min_{\boldsymbol{x}} f(\boldsymbol{x}) \\ s.t.\quad & g(\boldsymbol{x}) \le 0 \\ & x_{l,j} \le x_j \le x_{u,j} \\ & \forall\, j = 1,2,\dots,n_x \end{aligned} \tag{1}$$

where $x_{l,j}$ and $x_{u,j}$ are the lower and upper bounds of the i^{th} element of $\boldsymbol{x}$ respectively, and n_x is the dimensionality of $\boldsymbol{x}$. The methods that one chooses to minimise the objective function $f(\boldsymbol{x})$ will depend on many factors, which includes the availability of derivative information to the user. Two common categories include *line-search* and *trust-region* (Nocedal & Wright, 2006).

The goal of line-search methods is to optimise along a specified search direction to find the optimal step-length α_k for every iteration k:

$$\alpha_k = \arg\min_{\alpha>0} f(\boldsymbol{x_k} + \alpha \boldsymbol{p_k}) \tag{2}$$

When derivative data is available to the user, the most obvious chose of $\boldsymbol{p_k}$ is the $-\nabla f(\boldsymbol{x_k})$ i.e. the direction of *steepest descent.* However, if $f(\boldsymbol{x})$ is twice differentiable, it is possible to instead approximate the model by a Taylor expansion up to the second degree:

$$\begin{aligned} f(\boldsymbol{x}+\boldsymbol{p}) = f(\boldsymbol{x}) + \nabla f(\boldsymbol{x})^T \boldsymbol{p} + \tfrac{1}{2}\boldsymbol{p}^T \nabla^2 f(\boldsymbol{x})\boldsymbol{p} \\ +H.O.T \end{aligned} \tag{3}$$

By negating higher order terms, the optimum can be estimated by setting $\nabla f(\boldsymbol{x}+\boldsymbol{p}) = 0$ and solving to find:

$$\boldsymbol{p} = -(\nabla^2 f(\boldsymbol{x})^{-1})\nabla f(\boldsymbol{x}) \tag{4}$$

as outlined by Nocedal & Wright (2006). For cases in which $\nabla^2 f(\boldsymbol{x})$ is positive definite at $\boldsymbol{x_k}$, this search direction is used as is the case with the Newton optimisation method. As deviations from the second order approximation worsen with $\mathcal{O}(\|\boldsymbol{p}\|^3)$, the estimated minimum will be less accurate for larger steps. Hence this process is iterated until convergence. In general this is more effective than following steepest descent as the model captures the curvature of the problem.

Line-search offers an effective framework for optimisation of problems with derivative information available to the user. Therefore, for expensive black-box optimisation, line-search is not an appropriate choice of algorithm. We look instead to a trust-region strategy where a model $m(\boldsymbol{x})$ of $f(\boldsymbol{x})$ is generated within a trust region in which the accuracy of $m(\boldsymbol{x})$ can be 'trusted' (Eason, 2018). More specifically, we enforce some radius Δ_k at iteration k for which:

$$\|\boldsymbol{x_{k+1}} - \boldsymbol{x_k}\| \leq \Delta_k \tag{5}$$

Similarly to the Newton line-search strategy, the model function (also called the surrogate model of $f(\boldsymbol{x})$) is commonly formulated as a quadratic approximation of $f(\boldsymbol{x})$:

$$m(\boldsymbol{x_k} + \boldsymbol{s}) = r + \boldsymbol{q}^T s + \tfrac{1}{2}\boldsymbol{s}^T P \boldsymbol{s} \tag{6}$$

for some step $\boldsymbol{s}$ within the trust region. Because derivative data is not available to the user, we instead define $\boldsymbol{q}$ and P as approximations to the gradient and Hessian matrix respectively. For the algorithms concerned in this paper, we impose the additional constraint that P is positive semi-definite so that optimising $m(\boldsymbol{x})$ becomes a convex problem. This ensures that a unique local minimiser exists within or at the boundary of the trust region. Though other surrogate model types can be used in trust-region model-based algorithms, quadratic surrogates have remained common in literature ever since being outlined by Winfield (1973) and further improved upon by Conn (1997) and Powell (2002).

2.2 Surrogate Models

The choice and formulation of a surrogate model to accurately represent a black-box function can be challenging. A variety of different methods are used with the main ones being polynomial, radial basis function and Kriging models (Forrester, Sóbester & Keane, 2008).

The first category of models, polynomial models, are conceptually the simplest. Forrester, Sóbester & Keane (2008) note that although higher order terms in the polynomial offer the potential for increasing the model's accuracy, they also run the risk of overfitting the data and modelling noise as part of the surrogate, indicating that high order polynomials are neither favourable nor indeed necessary.

When dealing with trust region-based methods, linear approximations ($n = 1$) can be useful as they are usually able to convey the general direction of the function's gradient and are extremely easy to minimise, owing to a constant gradient. Their shortcoming is in their inability to replicate any sort of curvature, which almost all nonlinear functions (and by extension black-box functions) used in this context have. They may also exhibit oscillatory behaviour, as is typical with steepest descent algorithms on problems with high curvature (Fletcher, 1964).

This is where quadratic approximations ($n = 2$) come in as they are curved and so can approximate non-convexity in functions much better (on a local scale), yet they do not carry much additional complexity and are therefore still easy to implement and minimise. It is because of these properties that they are especially useful in black box optimisation as mentioned before.

Radial basis function (RBF) and Kriging models can very accurately represent highly nonlinear functions to a much better degree than polynomial models (Forrester, Sóbester & Keane, 2008). That being said, in the application of trust region-based methods, surrogate models need to be updated at each iteration to represent new data in the current trust region. As such, the simplicity and ease of use associated with quadratic surrogate models makes them generally more attractive for these methods. There are, however, notable examples of algorithms that do not make use of them, such as ORBIT (Wild, Regis & Shoemaker, 2008), which uses RBF models. Their report points out that the number of samples needed to form quadratic approximations scales poorly with dimensions, thereby justifying the use of RBF models.

Additionally, surrogate models can be used to model the constraints of a black-box problem, which are typically unavailable to the user. These can be used as an alternative to penalty functions as a means approximating infeasibility (Forrester, Sóbester & Keane, 2008).

2.3 A review of DFO algorithms

When dealing with expensive black-box functions, derivative information is usually intractable to obtain, and can be further exacerbated by noise (Moré & Wild, 2009), hence there is a need for DFO algorithms.

Bayesian optimisation is one of the most notable examples, and has consistently demonstrated high efficiency (Turner et al., 2021; van de Berg et al., 2022). In short, it operates by first building a surrogate model of the function, then computing an acquisition function from this model, which takes into account exploration and finally evaluating the function at the minimum of this acquisition function before repeating the cycle (Frazier, 2018). A popular choice for the acquisition function is the Expected Improvement acquisition function (Schonlau, Welch & Jones, 1998). Although this method is effective, the models used are usually quite complex and this complexity only increases with each iteration, meaning it can be difficult to minimise the acquisition function and expensive to run in general (Ghanbari & Scheinberg, 2017; van de Berg et al., 2022).

The SIMPLEX algorithm – initially developed by Spendley et al. (1962) and subsequently improved upon by Nelder and Mead (1965) – is a famous example of a 'direct search' algorithm. Direct search algorithms do not aim to create and iterate on a model to minimise by proxy, but instead use heuristic strategies to generate the next point in a sequence of points (Lewis et. al, 2000). As a direct search algorithm, SIMPLEX does not approximate any gradient information such as the Hessian, and so performs well for areas in which curvature changes erratically. However, for neighbourhoods around local optima where curvature information is key, the algorithm struggles compared to model based approaches (Nelder & Mead, 1965).

The BOBYQA algorithm developed by Powell (2009), which builds on Powell's previous work on the NEWUOA algorithm, is a model-based algorithm using a quadratic surrogate bounded by a trust region. At each iteration k, n_s samples are generated in mutually orthogonal directions from the centre point $\boldsymbol{x_k}$. A quadratic model $m(\boldsymbol{x})$ is formed by interpolating sample points $\boldsymbol{x_s}$ such that

$$m(\boldsymbol{x}_{s,i}) = f(\boldsymbol{x}_{s,i}) \quad \forall \; i = 1,2,\dots,n_s \tag{7}$$

where $f(\boldsymbol{x})$ is the objective function. As such, the number of samples is limited by the maximum degrees of freedom for interpolation, which in this case is up to $\frac{1}{2}(n+1)(n+2)$ for an n-dimensional problem. At each iteration, the model is updated by minimising the following Frobenius norm:

$$\min_{P,\boldsymbol{q},r} \|\nabla^2 m_{k+1}(\boldsymbol{x}) - \nabla^2 m_k(\boldsymbol{x})\|_F \tag{8}$$

In doing so, the difference in the Hessian is minimised ensuring the stability of future iterations. The model, $m(\boldsymbol{x})$ is then minimised within the trust region to find the next local minimiser.

The CUATRO global (or CUATROg) algorithm developed by van de Berg et al. (2022) is the basis of the algorithms developed in this paper. It is similar in concept to BOBYQA, though it differs in a few crucial ways. As opposed to many other trust-region model-based approaches, the interpolation criteria in (7) are no longer imposed. Instead, the quadratic surrogate is generated by a least-squares regression of a set of randomly generated sample points within the trust region:

$$\min_{P,\boldsymbol{q},r} \sum_{i}^{n_s} \left(m_k(\boldsymbol{x}_{s,i}) - f(\boldsymbol{x}_{s,i}) \right)^2 \tag{9}$$
$$m_k(\boldsymbol{x}_{s,i}) = \tfrac{1}{2}\boldsymbol{x}_{s,i}^T P \boldsymbol{x}_{s,i} + \boldsymbol{q}^T \boldsymbol{x}_{s,i} + r$$

Additionally, it updates the trust region according to an approach outlined by Conn (1997). Namely, a variable ρ_k at iteration k is defined as the ratio of actual objective decrease over predicted objective decrease:

$$\rho_k = \frac{f(\boldsymbol{x_k}) - f(\boldsymbol{x_{k+1}})}{m_k(\boldsymbol{x_k}) - m(\boldsymbol{x_{k+1}})} \tag{10}$$

This value of ρ_k then decides whether or not to accept the x_{k+1} as the new centre and informs the size of the next trust region. For a detailed outline of the algorithm, the reader is referred to van de Berg et al. (2022).

CUATROg also focuses on a global search in its first iteration by generating a set of points across the problem bounds via a Latin Hypercube Sampling (LHS). The first step is therefore informed by the shape of the function to improve globality.

Compared to BOBYQA, CUATROg consistently performs better in stochastic problems where black-box evaluations are subject to noise. But BOBYQA is notably stronger at deterministic problems, where CUATROg is slower to converge (van de Berg et al., 2022). This paper is only concerned with deterministic problems.

A notable weakness of CUATROg is that the local samples are taken randomly from within the trust region, resulting in many samples forming 'clusters' where each new sample contributes little useful information to the model. We aim to resolve this weakness by implementing sampling that is random but well distributed to maximise the useful information contributed by each function evaluation.

Though CUATROg is initiated with LHS, subsequent steps take a local approach. As such we also aim to develop heuristics to locate other potentially global minima by exploring regions that do not necessarily guarantee good exploitation. Additionally we implement methods to minimise constraint violation so as to promote safe exploration, which is especially important in cases where the black-box problem is a real-life experimental system that must take safety constraints into consideration.

3. Methodology

3.1 Sampling improvements

Currently, CUATROg generates new sample points every iteration by randomly selecting points in a bounded box of length $2\Delta_k$. It first selects any points that have already been evaluated that fall within the trust bounds. If the number of points selected is less than the minimum number of samples required to generate a model, $n_{s,min}$, then the remaining samples are generated. At least one *new* sample is generated at each iteration to provide new information to the next model.

However, a set of randomised points will often produce clusters of locally nearby points, particularly for a large n_s. In these clusters, each additional point is contributing little information to the model. Additionally, there are often voids with no points where potentially useful information about the function is ignored. We propose that sampling in these voids would help generate a more comprehensive model.

The ideal distribution is one that is random but low-discrepancy. Techniques such as Sobol sequencing and LHS give satisfactory results, but what they lack is the ability to dynamically add points to a pre-existing collection. We propose an algorithm called Maximum Closest Distance (MCD) that is able to add a new point to a collection of pre-existing samples that are within the trust region. The Euclidian distance or L2 norm between the new point and its closest neighbour is maximised, provided that the trust region and bound constraints are respected:

$$
\begin{aligned}
&\max_{x}\left(\min_{x_s\in X_{s,k}} \|\boldsymbol{x}-\boldsymbol{x_s}\| - \alpha[\Delta_k - \|\boldsymbol{x}-\boldsymbol{x_k}\|]\right) \qquad (11)\\
&s.t. \qquad s.t\ \|\boldsymbol{x}-\boldsymbol{x_k}\| < \Delta_k\\
&\qquad\qquad x_{l,j} \le x_j \le x_{u,j}\\
&\qquad\qquad j = 1,2,\dots,n_x\\
&X_{s,k} = \{\boldsymbol{x_s} \in X_s \mid \|\boldsymbol{x_s}-\boldsymbol{x_k}\| < \Delta_k\}
\end{aligned}
$$

where X_s is the collection of all previous samples and α is a constant multiplying the repulsion from the trust-region boundary.

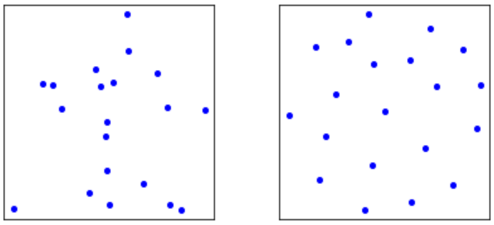

***Figure 1**: (a) Random sampling. (b) Samples generated with MCD*

This problem, particularly for large n_S, is highly non-convex as isolated regions in between groups of points will often have their own optima for MCD. We resolve this to some degree by generating a Sobol sequence of potential initial points. The Sobol point that is the farthest away from its nearest neighbouring sample point is selected as the initial point for MCD. As such, the solution to MCD is more likely to approach a suitably optimal point. We have implemented this in a modified version of CUATROg called CUATRO_base, which is used as the basis for all subsequent algorithms.

3.2 Local exploration heuristics

Several local exploration heuristics are proposed and implemented to aid in the exploration of local trust regions. In other words, these heuristics are not expected to direct the algorithm towards global optima, but rather, they are expected to aid in finding local optima more efficiently or with fewer constrain violations.

3.2.1 Sampling region

Currently, the CUATRO algorithm samples points at each iteration within the same region defined by the trust region. A modification is proposed to define a distinct sampling region of radius σ_k such that $\sigma_k < \Delta_k$. This strategy is inspired by the work done by Eason and Biegler (2018) for application in glass-box/black-box hybrid problems. The benefits are said to be twofold: firstly, that the algorithm can take larger steps near the optimum and secondly, that if a step is rejected, the model does not necessarily need to be recreated, as the sampling region may stay the same. Our method for updating the sampling region differs from that of Eason and Biegler due to the complete black-box nature of our problems, whereas Eason and Biegler update their sampling region based on glass-box information.

Our analogous system of updating the sampling region is simple; the user defines a maximum and minimum ratio of radii: α_l and α_u respectively where both parameters are within [0,1]. At each iteration, the following checks are made:

i) if $\sigma_k > \alpha_u\Delta_k$, set $\sigma_k \coloneqq \alpha_u\Delta_k$
ii) if $\sigma_k < \alpha_l\Delta_k$, set $\sigma_k \coloneqq \alpha_l\Delta_k$
iii) if $\|x_{k+1} - x_k\| < \sigma_k$, reduce σ_k by some user-defined constant. Update Δ_k if it falls out of the range of $[\sigma_k/\alpha_u\, , \sigma_k/\alpha_l]$

Check **(iii)** allows the algorithm to recognise that the sampling region is within the neighbourhood of the optimum point and therefore shrinks the sampling region to aid a more precise model of the function.

3.2.2 Feasibility sampling

This method looks at increasing safe exploration in CUATROg by focusing on reducing constraint violation. The way CUATROg currently handles inequality constraints on the objective function is through convex quadratic discrimination (van de Berg et al., 2022), which generates a quadratic approximation of the feasible region based on feasibility data of previous points. This approximation is then imposed during the minimisation of the surrogate to try and ensure that the minimum is itself feasible.

In this method, we impose the feasibility constraint during the sampling stage as well, meaning that new samples have to satisfy the inequality approximation generated from the previous iteration.

3.2.3 Exploit-Explore

This method takes inspiration from the acquisition functions in Bayesian optimisation, which take into account exploration (Frazier, 2018). The general idea behind this method is to make changes to the minimisation step in CUATROg so that it seeks not only to minimise the surrogate function within the trust region, but also to sample away from previously sampled points and thus combine both exploitation and exploration in the same step.

The exploration element is added by introducing a new variable α, which represents the Manhattan norm to the closest sample point inside the trust region. We want to simultaneously maximise this value as well as minimising the surrogate.

The closest distance maximisation is formulated in a way which allows it to be in the form of a mixed-integer linear problem, which is easier to solve than the equivalent nonlinear formulation. In this problem $y_{i,j}$ is a binary variable and M is a large constant, which is much larger than the trust region radius, Δ_k. These two variables force one of either $r^+_{i,j}$ or $r^-_{i,j}$ to be zero as neither one can be negative. The one which is positive takes the value of the 1 dimensional distance to the j^{th} dimension of the i^{th} sample, $x^s_{i,j}$. Finally, the first condition sets α to be lower than each of the Manhattan norms to all the sample points, meaning it has to be less than or equal to norm associated with the closest sample. As α is being maximised, it is forced to take the largest value, which indeed makes it equal to the norm between the optimum and the closest sample. The formulation is as follows

$$
\begin{aligned}
&\min_{x} \frac{\left(r + \boldsymbol{q}^T\boldsymbol{x} + \frac{1}{2}\boldsymbol{x}^T P\boldsymbol{x}\right)}{\max(10^{-4}, |f_k|)} - \frac{\alpha}{(\Delta_k)^2} \qquad (12)\\
s.t. \quad & \alpha \leq \sum_{j=1}^{n_x} r_{i,j}^{+} + r_{i,j}^{-}\\
& x_j - x_{i,j}^{s} = r_{i,j}^{+} - r_{i,j}^{-}\\
& r_{i,j}^{+} \leq M\left(1 - y_{i,j}\right);\; r_{i,j}^{-} \leq M y_{i,j}\\
& \alpha \geq 0;\; r_{i,j}^{+} \geq 0;\; r_{i,j}^{-} \geq 0\\
& \forall i = 0, \ldots, n_s;\; \forall j = 0, \ldots, n_x\\
& r_{ineq} + \boldsymbol{q}_{\boldsymbol{ineq}}^{T}\boldsymbol{x} + \frac{1}{2}\boldsymbol{x}^T P_{ineq}\boldsymbol{x} \leq 0\\
& x_{l,j} \leq x_j \leq x_{u,j}\\
& \|\boldsymbol{x} - \boldsymbol{x}_{\boldsymbol{k}}\| \leq \Delta_k
\end{aligned}
$$

where f_k is the value of the black-box function evaluated at the centre of the current trust region.

In the minimisation, the two contributing terms are normalised in an attempt to give each term a similar weighting and thus try to prevent either term from dominating the other.

3.3 Global exploration heuristics

In addition to better local exploration, we propose two algorithms that implement techniques to locate several optima and improve CUATRO's ability to solve globally. Neither algorithm fully guarantees globality, and tuning is often required for individual problems, but the following modifications will equip them with techniques to handle highly non-convex black-box problems more effectively.

3.3.1 Trajectories in Series (TIS)

One issue with the original algorithm is that it shrinks the trust region if the improvement for an iteration is deemed insufficient. Whilst this is useful at a large scale, it also makes it easy for it to get trapped at local minima, which not only hinders its performance, but can cause many unnecessary evaluations to be carried out. The idea behind this strategy is to prevent the original algorithm from getting stuck in local minima.

It builds on the original algorithm by enabling the trust region to suddenly expand by a large margin when any of the criteria from the following set are met, effectively 'restarting' and enabling more exploration. The criteria for initiating a 'restart' are aimed at defining convergence and are as follows:

i) The trust region radius falls below a certain radius.
ii) The current centre of the trust region does not move for a number of iterations.
iii) The overall improvement in the objective function from the past set of iterations is below a certain level.
iv) The current centre approaches a point from a previous trajectory (i.e. any point from before the most recent 'restart'). The threshold distance for this to occur is the smaller value of the trust region for the previous point or a pre-defined maximum convergence distance.

With criteria (ii) and (iii), the new algorithm only considers iterations since the last 'restart'. Moreover, all the criteria involve parameters that can be adjusted by the user.

This strategy is also designed so that the first iteration with the expanded trust region finds its new centre via MCD, as opposed to optimising a surrogate. The idea is to maximise exploration in this step.

Another slight difference is that, following the first 'restart', the algorithm will increase the factor of reduction for the trust region, meaning it can shrink more at each step. This is added due to the large trust regions caused by the 'restarts'.

3.3.2 Trajectories in Parallel (TIP)

TIP takes a more breadth-first approach by initiating a wide search of optima and subsequently eliminating trajectories based on selection criteria. The algorithm starts with a series of n_T initial points defined by the user, each of which will define its own trajectory. Ideally, these points will be as widely distributed across the feasible region as possible. For unconstrained problems, this can simply be a randomised set of points within the problem bounds. The following steps are then taken:

i) The trust regions of each initial point are determined such that they are as large as possible without overlapping the trust regions of other trajectories.
ii) For each trajectory t, samples are taken and a model $m_{k,t}(\boldsymbol{x})$ is generated. Minimisation within the current trust region proceeds as with CUATRO_base.
Each trajectory now has a new optimum and trust region. Selection criteria **(iii)** and **(iv)** apply:
iii) If the current optimum point of a trajectory is within the trust region of *any* point of *any* other trajectory, the two trajectories are compared. The one with the worse performing optimum is eliminated, and the other proceeds.
iv) If the trust region radius of a trajectory is less than the convergence radius defined by the user, it is deactivated, and its optimum is stored as a candidate for the global optimum.
v) The algorithm repeats from **(ii)** until all trajectories have either converged or been eliminated; or once the function evaluation budget has been exhausted. In the latter case, the optima in the remaining trajectories are stored as candidates.
vi) Of the global optimum candidates, the best performing one is selected as the final solution.

Step **(iii)** is motivated by the idea that if a trajectory has entered the 'domain' of another, proceeding would simply explore areas that have already been explored.

A key feature of TIP is the management of its evaluation budget. As opposed to running CUATRO individually on each initial point, TIP will divide its function evaluation budget among the remaining active trajectories. As such, each trajectory begins with very rough models which improve in accuracy as more trajectories are eliminated.

3.5 Test functions and case studies

Various case studies are used to test the algorithms, including both theoretical functions and simulations of real-life chemical engineering situations. The TIS and TIP algorithms are only carried out on Rastrigin as it is the only highly non-convex function. Similarly, the feasible sampling and sampling region algorithms are only tested on functions with constraints as they are developed specifically for handling constraints, therefore excluding Rastrigin.

3.5.1 Rosenbrock 2D

The Rosenbrock function is a commonly used test function for optimisation and takes the form:

$$f(\boldsymbol{x}) = 100(x_2 - x_1^2)^2 + (1 - x_1)^2 \tag{13}$$

for some 2-dimensional input variable $\boldsymbol{x}$. The following constraints are also used:

$$\begin{gathered}(x_1 - 1)^3 - x_2 + 1 \leq 0 \\ x_1 + x_2 - 1.8\end{gathered} \tag{14}$$

Though the Rosenbrock function only has one local minimum at (1,1), it creates a U-shaped valley with low curvature at the base which is notoriously difficult to solve.

3.5.2 Rosenbrock 4D

One way to generalise the Rosenbrock function for N dimensions is as follows:

$$f(\boldsymbol{x}) = \sum_{i=1}^{N-1} [100(x_{i+1} - x_i^2)^2 + (1 - x_i)^2] \tag{15}$$

with the constraints:

$$\begin{gathered}(x_i - 1)^3 - x_j + 1 \leq 0 \\ x_i + x_j - 1.8 \\ \forall\ j > i; \quad i, j = 1, 2, \ldots, N\end{gathered} \tag{16}$$

We use a 4-dimensional generalisation, which has 2 local minima.

3.5.3 Rastrigin

This function is a familiar test for the performance of optimisation algorithms. It has a highly non-convex and unique form, which in two dimensions presents itself as a series of regularly spaced, alternating local minima and maxima on a grid-like pattern. The global minimum is at the origin and each local minima gets gradually shallower the farther away they are from the origin. It takes the following form in 2D:

$$f(\boldsymbol{x}) = 20 + \sum_{i=1}^{2} [x_i^2 - 10\cos(2\pi x_i)] \tag{17}$$

3.5.4 Real Time Optimisation (RTO)

RTO deals with the minimising of 'plant-model mismatch' when modelling a plant that represents a complex system. In this case, the model represents the Williams-Otto benchmark problem in which a CSTR reactor produces two main products. Details can be found in section 3.3 of van de Berg et al. (2022).

3.5.5 Self Optimising Reactor (SOR)

As with RTO, this case study is the same as used in van de Berg et al. (2022). This relates to the optimisation of a flow reactor, inside which a Nucleophilic Aromatic Substitution reaction occurs. There are 2 independent variables, which correspond to the coolant temperature and inlet flow rate.

4. Results

The test functions and case studies outlined above are solved using the proposed CUATRO variations over several runs. The primary benchmark we analyse is the evaluation efficiency of each algorithm. The best evaluation is averaged over each run of every algorithm and is plotted over the number of evaluations made. These results are visible on Figure 3 and Figure 4

Contour plots have also been generated, as can be seen in Figure 2 and Figure 5 for a selection of case studies to observe the algorithms' ability to sample and follow an efficient path towards the global optimum. In addition, they provide a better intuition of the shape of each problem's objective function and constraints.

4.1 Rosenbrock 2D

When analysing the qualitative behaviour of the different strategies on Rosenbrock 2D as seen in Figure 2, one can note that all strategies successfully manage locate the global minimum. One can also see the difference in sampling distribution between *Global* and *Base*. In *Base;* samples are better distributed and do not form clusters like they do in *Global*. Plot (c) does not show much difference at all, suggesting little qualitative difference in the performance of *Sampling_region*. In plot (d), *Exploit_explore* takes a more indirect path towards the optimum, likely due to the conflict between exploitation and exploration. Finally, in plot (e), *Feasible_sampling* appears to take fewer infeasible samples, and those that it does take appear to violate the constraints less severely.

Figure 4 (a) reveals very little variation in performance between algorithms, less so than any other case study. All appear to converge after around 75 evaluations, except *Exploit_explore*, which takes a bit longer despite performing very well early on, and *Global*, which converges even earlier and performs the best.

4.2 Rosenbrock 4D

Figure 4 (b) exhibits a much wider range of performance compared to plot (a) for Rosenbrock 2D. *Sampling_region*, *Feasible_sampling*, and *Base* all show improved and similar efficiency compared to *Global* and *Exploit_explore*, with the latter performing the worst. Significant gains in efficiency are made in the *Sampling_region, Feasible_sampling*, and *Base* during the first 100 evaluations, with each algorithm plateauing thereafter.

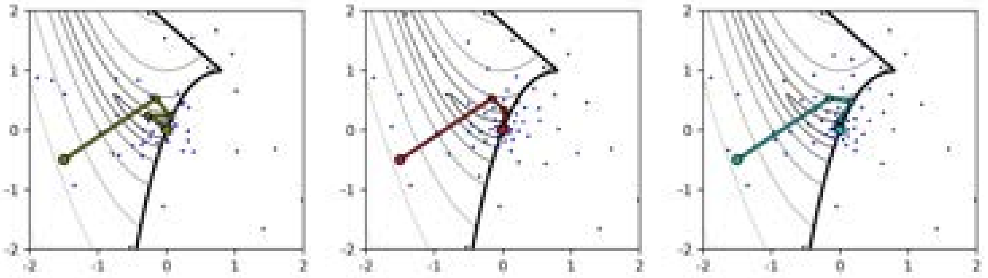

(a) CUATROg **(b) CUATRO_base** **(c) CUATRO_sampling_region**

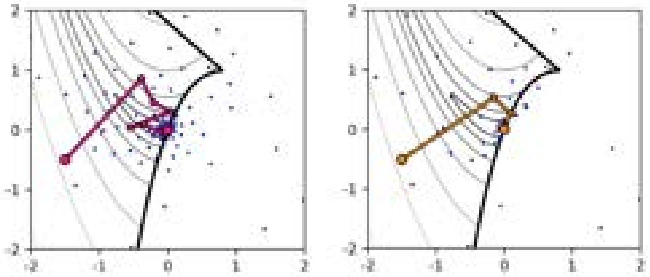

(d) CUATRO_exploit_explore **(e) CUATRO_feasible_sampling**

Figure 2: Contour plots with the 2D Rosenbrock function, showing the sample points and trajectory of each algorithm for a single run, starting from (-1.5, -0.5), in all cases. Start and end points are indicated with a larger dot.

4.3 Rastrigin

The plots in Figure 5 show a visual representation of each algorithm's behaviour. As is the case with Rosenbrock 2D, the low discrepancy sampling provided by MCD is apparent when comparing *Base* and *Global* in plots (a) and (b) respectively.

All methods display erratic behaviour, with each trajectory involving drastic changes in direction, which is to be expected considering the high non-convexity of Rastrigin. It is also worth noting that after first locating a local minima, *TIS* successfully manages to locate the global minima, which *TIP* also does. It is interesting to see the short length of each trajectory in *TIP*, each of which still manages to find a local minimum.

When looking at the overall performance of each strategy in Figure 3, *Global*, *Base* and *Exploit_explore* all seem to perform similarly, plateauing after around 50 evaluations. However, *TIS* and *TIP* show very different behaviour and their ability for global exploration is apparent. Both perform much better than the others after around 40 evaluations and show a continued decrease in the objective function across all 200 evaluations. It is also interesting to observe that *TIP* performs the best initially, while *TIS* is better in the long run.

4.4 Real Time Optimisation

As previously discussed, the shape of RTO in the solution space is simple and easy to approximate quadratically. This can be seen on contour plot (a) in Figure 6. As such, it is unsurprising that all local algorithms reach the constraints within 20 or so evaluations as seen on plot (c) on Figure 4. Algorithms *Global, Base, Sampling_region,* and *Exploit_explore* perform very similarly, as reflected by both the paths they take on Figure 6 and their evaluation efficiency on Figure 4. More remarkable is the performance of *Feasible_sampling* that appears to avoid the first constraint and manages to direct itself towards the global optimum of the problem situated between the two constraints.

4.5 Self Optimising Reactor

Similarly to RTO, the shape of this case study does not pose much difficulty when forming the surrogate. SOR, however, is particularly expensive to run and so the evaluation efficiency is of more importance. From Figure 6, it can be noted that all algorithms except *Exploit_explore* follow a similar path, with varying degrees of success in dealing with the constraint. *Exploit_explore* on the other hand, tends to take a more meandering path, but ultimately reaches the constraint farther up than other algorithms. Figure 4 plot (d) reveals that the differences in values along SOR's constraint ultimately do not vary significantly. Hence, constraint handling is not of great importance to this problem.

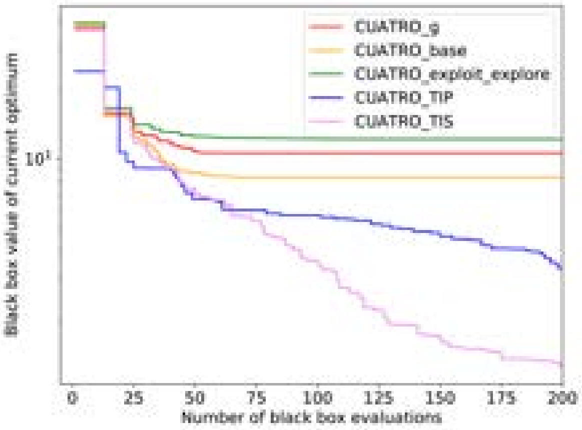

Figure 3: Average best black-box evaluations over total number of evaluations for Rastrigin, averaged over 20 runs, each with randomised starting points.

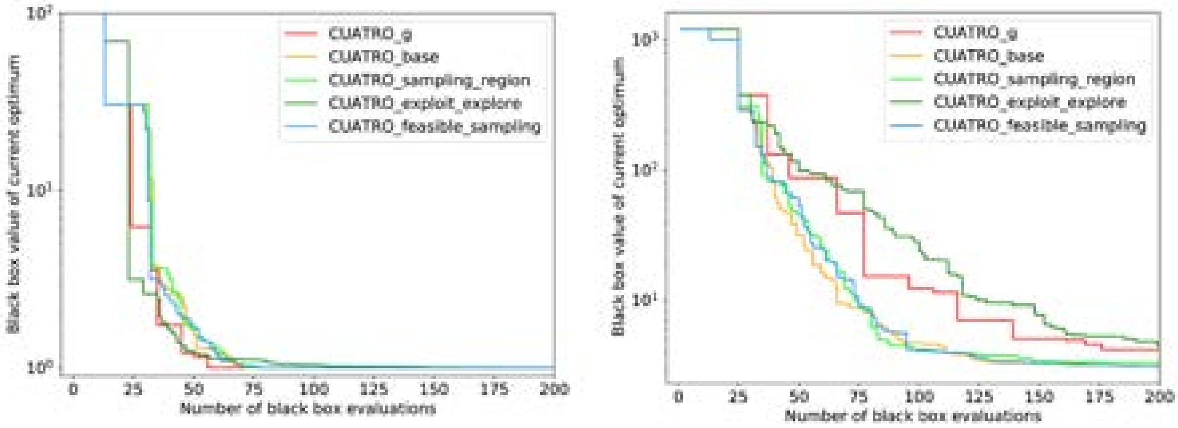

(a) Rosenbrock in 2D

(b) Rosenbrock in 4D

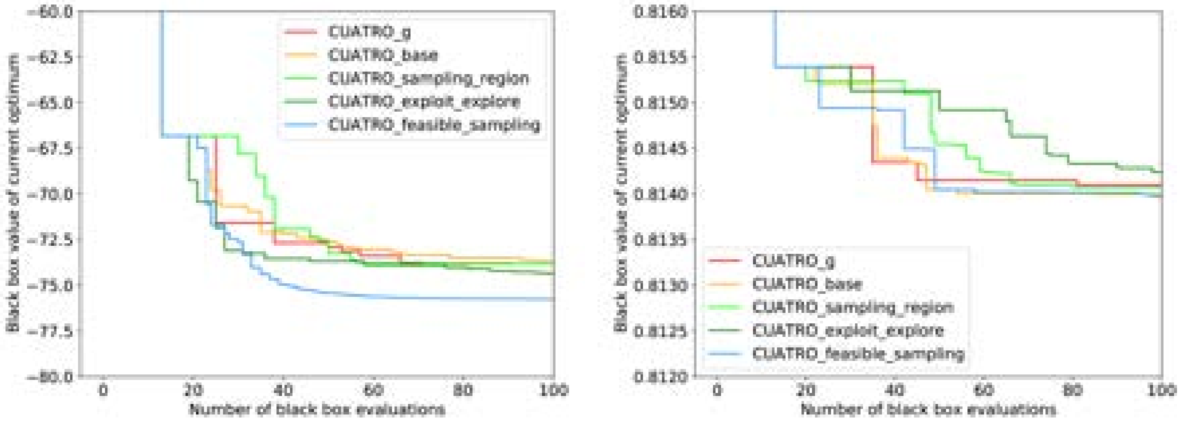

(c) Real-Time Optimisation

(d) Self-Optimising Reactor

Figure 4: Average best black-box evaluations over total number of evaluations. Values are averaged over several runs (10, 10, 5 and 3 respectively).

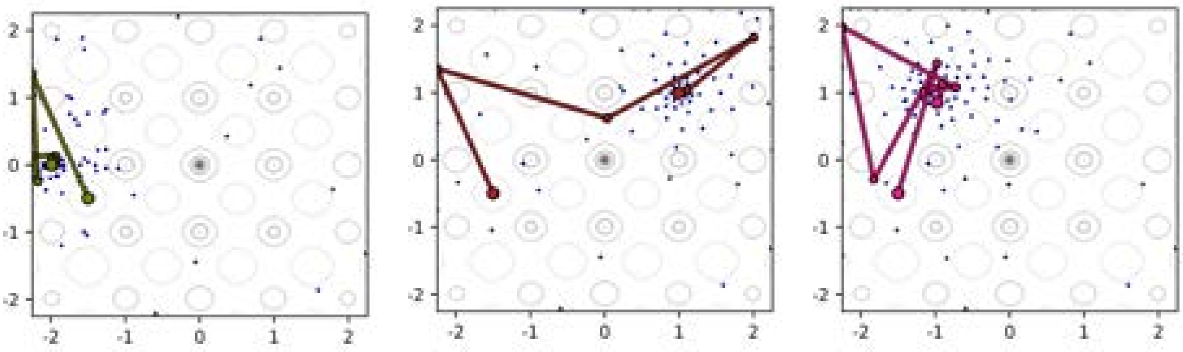

(a) CUATROg

(b) CUATRO_base

(c) CUATRO_exploit_explore

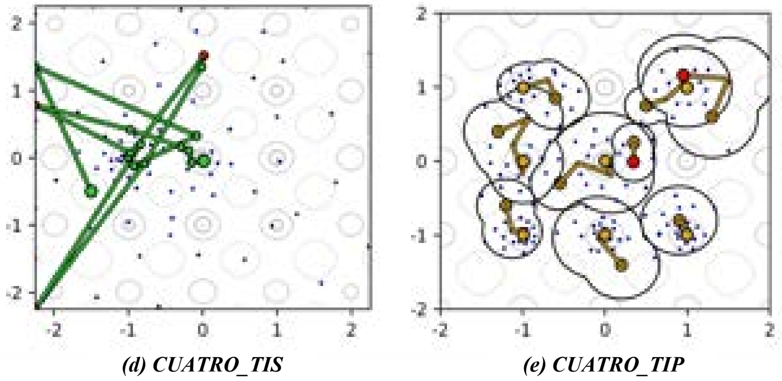

(d) CUATRO_TIS

(e) CUATRO_TIP

Figure 5: Contour plots with Rastrigin function, showing the sample points and trajectory of each algorithm for a single run, starting from (-1.5, -0.5), in all cases except (e). Start and end points are indicated with a larger dot. Red dots represent where the algorithm has 'restarted' in (d) and where a trajectory is terminated in (e). The black 'bubbles' in (e) show the combined area of the trust regions for each trajectory.

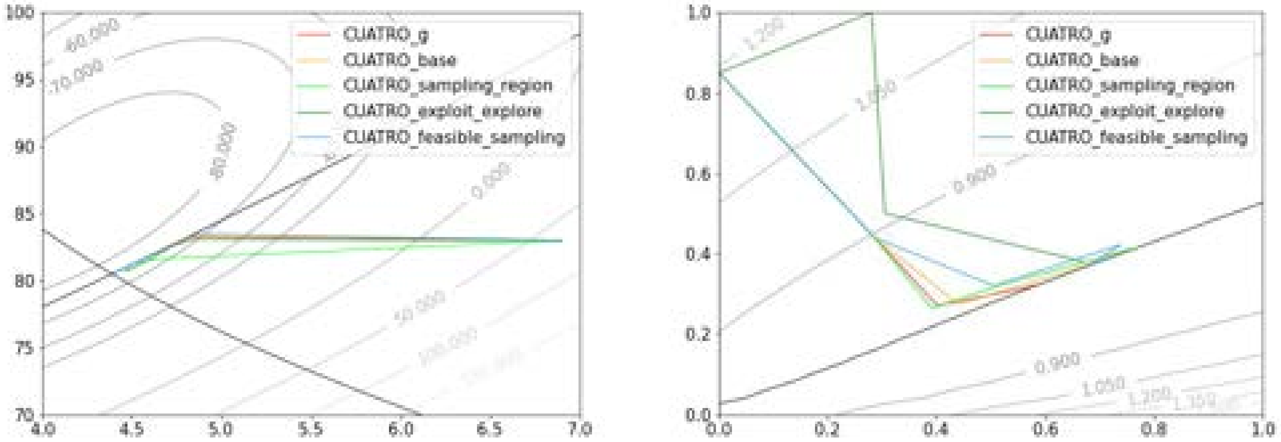

Figure 6: Contour plots showing the paths of each local algorithm for (a) Real-Time Optimisation and (b) Self-Optimising Reactor

Overall, *Global* and *Base* are slightly more efficient than the other algorithms during the first 50 evaluations, though *Base* and *Feasible_sampling* ultimately perform best by 100 evaluations, if but marginally.

4.6 Constraint violations

From Table 1, it is observed that Rosenbrock 2D, RTO and SOR case studies all exhibit a similar pattern. *Global* always has the most violations, while the lowest violations are with *Feasible_sampling* and *Exploit_explore*. It is surprising to see that *Exploit_explore* performs best having the least overall violations in Rosenbrock 2D and SOR – less still than *Feasible_sampling*, for which reducing constraint violations is the main objective.

It is also surprising that *Sampling_region* performs better than *Base*, given that the former allows larger steps to be taken at each iteration.

Rosenbrock 4D has a very different pattern, however, with *Global* performing the best and surpassing the others by a large margin. Amongst the other algorithms, there is a similar pattern to before, with *Exploit_explore* performing the best out of these, followed by *Feasible_sampling*, though all have much higher violations.

5. Discussion

The results are clear that *Feasible_sampling* has the best overall performance on case studies where constraints are present. Constraint violation is not always the lowest, although the violations are the less severe, as seen in Figure 2. However, no quantitative data on the severity is collected in this study and would be worth investigating in future studies. Although *Exploit_explore* appears to have fewer constraint violations, its performance is inconsistent and relatively poor. Thus, it is likely that because its path is more convoluted, a higher proportion of steps are taken far from the constraints resulting in fewer violations. However, it could be that more work needs to be done on tuning the weightings in the combined exploration-exploitation step, and so the potential of this strategy should not be ignored entirely. As for *Feasible_sampling*, there is room for potential improvement in its formulation. The inequality constraint approximation could instead be updated every time a new sample is evaluated, rather than using one approximation at each iteration. Although this may carry an additional expense, in the context of increasing safety for real life applications, this expense would be more than justified.

When comparing the *Base* algorithm with the original *Global*, the behaviour is very similar, except for in higher dimensions, where *Base* performs better, albeit with a much larger number of constraint violations. This hints at a potential trade-off between performance and violations, however more higher dimensional problems would need to be investigated before concluding this. It is also clear from the Rosenbrock 4D performance that a potential downfall with MCD is that it cannot handle constraints as well for higher dimensions, possibly because MCD pushes points away from previous points, that are likely feasible, into unexplored and potentially infeasible regions. For lower dimensions, MCD also does not seem to improve the model's accuracy, possibly due to the problems' simplicity.

Moreover, *Sampling_region* shows no consistent improvement. The formulation is admittedly simplified from Eason's original work and it may require new

Table 1: Average constraint violations for each algorithm and case study

Algorithm	RB 2D	RB 4D	RTO	SOR
CUATROg	43.7%	40.0%	55.0%	45.0%
CUATRO_base	37.6%	67.2%	52.2%	44.8%
CUATRO_sampling_region	36.8%	63.2%	49.8%	40.5%
CUATRO_exploit_explore	21.5%	53.8%	42.7%	26.4%
CUATRO_feasible_sampling	22.8%	57.9%	34.1%	30.4%

heuristics to better decouple the trust region and sampling region radii.

Finally, the algorithms with global exploration heuristics, TIP and TIS, show a notable improvement when applied to a highly non-convex problem. However, this advantage cannot be expected for convex problems that can be easily approximated, such as the RTO case study. One shortcoming of TIP is that it requires the user's knowledge of the feasible region when inputting the start points. This could be improved to allow initial exploration of the feasible region from one starting point, from which other feasible starting points can then be found. On the other hand, TIS requires many additional parameters that need to be fine-tuned for different problems which may be difficult to determine. Namely, those relating to 'restarting' conditions and the size of the 'restart' radius.

6. Conclusion

Several local and global heuristic-based modifications have been proposed for CUATRO. Of them, *Feasible_sampling* shows particular promise as the proportion of constraint violation is reduced. Efficiency is also improved on highly constrained problems. A low-discrepancy sampling algorithm MCD is also proposed. CUATRO modifications using MCD exhibit better evaluation efficiency for problems with more input variables, but possibly at the cost of higher constraint violations. Additionally, in 2D cases, the improvement in efficiency is not significant and may not justify the additional computational cost. Global heuristics are proposed that are equipped to handle highly non-convex problems. The formulations are admittedly simplistic and require many tuning parameters, but significant improvements in evaluation efficiency are observed. As such, they show promise as a framework for more rigorously defined algorithms.

Acknowledgements

We would like to express our gratitude for all the help and continued support that Damien van de Berg provided throughout this study.

References

Conn, A., Scheinberg, K. & Toint, P. (1997) Recent progress in unconstrained nonlinear optimization without derivatives. *Mathematical Programming*. 79 (1), 397-414.

Eason, J. P. (2018) *A Trust Region Filter Algorithm for Surrogate-based Optimization*.

Eason, J. P. & Biegler, L. T. (2018) Advanced trust region optimization strategies for glass box/black box models. *AIChE Journal*. 64 (11), 3934-3943.

Felton, K. C., Rittig, J. G. & Lapkin, A. A. (2020) *Summit: Benchmarking Machine Learning Methods for Reaction Optimisation*.

Fletcher, R. (1964) Function minimization by conjugate gradients. *Computer Journal*. 7 (2), 149-154.

Forrester, A., Sóbester, A. & Keane, A. (2008) *Engineering Design via Surrogate Modelling A Practical Guide*. West Sussex, Wiley. pp.1-106; 117-139.

Frazier, P. I. (2018) *A Tutorial on Bayesian Optimization*.

Ghanbari, H. & Scheinberg, K. (2017) *Black-Box Optimization in Machine Learning with Trust Region Based Derivative Free Algorithm.*

Lewis, R. M., Torczon, V. & Trosset, M. W. (2000) Direct search methods: then and now. *Journal of Computational and Applied Mathematics*. 124 (1), 191-207.

Moré, J. & Wild, S. (2009) Benchmarking Derivative-Free Optimization Algorithms. *SIAM Journal on Optimization*. 20 172-191.

Nelder, J. A. & Mead, R. (1965) Simplex method for function minimization. *Computer Journal*. 7 (4), 308-313.

Nocedal, J. & Wright, S. (2006) *Numerical Optimization*. Springer Series in Operations Research and Financial Engineering. Second edition. New York, Springer. pp.18-98.

Powell. (2009) The BOBYQA algorithm for bound constrained optimization without derivatives. *Department of Applied Mathematics and Theoretical Physics*.

Powell, M. J. D. (2002) UOBYQA: unconstrained optimization by quadratic approximation. *Mathematical Programming*. 92 (3), 555-582.

Schonlau, M., Welch, W. & Jones, D. (1998) Global versus local search in constrained optimization of computer models. *Institute of Mathematical Statistics Lecture Notes - Monograph Series*. 34, 11-25.

Spendley, W., Hext, G. R. & Himsworth, F. R. (1962) Sequential Application of Simplex Designs in Optimisation and Evolutionary Operation. *Technometrics*. 4 (4), 441-461.

Turner, R., Eriksson, D., McCourt, M., Kiili, J., Laaksonen, E., Xu, Z. & Guyon, I. (2021) *Bayesian Optimization is Superior to Random Search for Machine Learning Hyperparameter Tuning: Analysis of the Black-Box Optimization Challenge 2020.*

van de Berg, D., Savage, T., Petsagkourakis, P., Zhang, D., Shah, N. & del Rio-Chanona, E. A. (2022) Data-driven optimization for process systems engineering applications. *Chemical Engineering Science*. 248, 117135.

Wild, S., Regis, R. & Shoemaker, C. (2008) ORBIT: Optimization by Radial Basis Function Interpolation in Trust-Regions. SIAM J. *Scientific Computing*. 30 3197-3219.

Winfield, D. (1973) Function Minimization by Interpolation in a Data Table. *IMA Journal of Applied Mathematics*. 12 (3), 339-347.

Formation and Optimisation of Biosurfactant SAF-12 Synthesis Process

Ho Maeng and Yesol Kim
Department of Chemical Engineering, Imperial College London, U.K.

Abstract

Optimisation experiments of SAF-12 production synthesis is evaluated in this project. SAF-12 synthesis includes oxidation, esterification, and sulfonation. The formation of SAF-12 starts from furfural oxidation. Oxidation produces 2-furoic acid with the yield of 95.2% at 55°C using 50wt% hydrogen peroxide solution. In esterification, 2-furoic acid is esterified with 1-dodecanol to produce alkyl furoate. The reaction with 40 minutes gives a best clear color having below 1% of residual furoic acid percentage. Sulfonation of AF-12 is a final step to produce SAF-12. Rheology, solubility, and surface tension were tested at various SAF-12 to SDS ratio. 4:3 ratio is the most ideal since it is stable at room temperature without a help of non-ionic surfactant, forming lamellar phase at room temperature, and having lower critical micelle concentration at 460 ppm.
Key words : SAF-12, biosurfactant, critical micelle concentration

1. Introduction

Surfactant is essential in today's market. Currently most of detergents and personal care products are produced as formulation of different chemicals to meet certain targets for the final consumers. The study and elaboration of these formulations is complex, and it is often difficult to find a trade off between performances and price. The main surfactant which dominates the market nowadays is the oil derivative linear alkyl benzene sulfonate (LAS). Among many types of surfactants, LAS dominates the USA, Japan and western Europe market by taking 27% in 1984. [1] It has lots of advantages including a cheaper cost, easy to produce, and having high performance. However, its not highly biodegradable property results in toxicity in aquatic life. [2] Sodium dodecyl sulfate, SDS, is biobased and mild to environment, but relatively expensive and have low solubility.

In this project, the performance of SAF-12, a new class of biosurfactants belonging to the alkyl benzene furoate, was analysed. Formulations of different compositions of the surfactant from furfural, furoic acid, alkyl furoate and SAF-12, were evaluated to the optimum and the cleaning proprieties of the solution were tested.

---

2. Background

The production of SAF-12 starts from furfural oxidation. Furfural oxidation with hydrogen peroxide can produce furoic aicd, 2-hydroxyfuran, succinic acid, 2(5H)-furanone and maleic acid. [3] From the patent GB2188927A, the furfural oxidation was carried under triethylamine and the selectivity of 2-furoic acid was 100% with furfural conversion at 90%. [4] It is priority to react all furfural since furfural is considered as a skin, mucous membrane, and respiratory irritant. The main toxicity targets are respiratory system, nervous system, liver, and kidneys. [5] Furfural is not classified as toxic chemical to human, but it has potential to create cancer in aquatic species. Therefore it is better to remove it all from product. The oxidation rate of triethylamine by hydrogen peroxide is very low at 0.02 L/mol per minute. [6] The oxidation of furfural by hydrogen peroxide under triethylamine was followed in this project. Another CuCl catalyzed oxidation reaction under acetonitrile gives the yield of 91%. [7] This was simulated in the project.

After oxidation and esterification, AF-12 was formed. Chlorosulfonic acid was used equimolar to AF-12 as equimolar amount of reagents result in sulfonation and excess result in chlorosulfonation. In general, by using an amount corresponding to 1 mole of a reagent in an inert solvent such as chloroform, a large amount of sulfonyl chloride is prevented from being produced as a by-product in the case of sulfonation. Sulfonyl chloride is an intermediate of this reaction, but it can be converted to acid by hydrolysis and decrease pH even further than expected result. HCl is another by-product that appears during the reaction. It can be easily removed by connecting the reaction to distillation column or injecting nitrogen gas. Chlorofonic acid and chloroform are considered to be very toxic and corrosive. Thus, it is important to make sure the reaction is done completely. After the reaction, SAF-12 is produced with very low pH. It is important to neutralise it as soon as possible as the product is going to degrade with time.

Formulation is significant to test the effect of SAF-12. First thing to note is its stability. SAF-12 is a type of anionic surfactant which is characterized by a negatively charged hydrophilic polar group. It is most widely used surfactant between ionic surfactant as cation surfactant has potential to kill microorganisms and amphotheric surfactant has least potent in cleaning. Non-ionic surfactant is second most widely used surfactant as it is less skin irritable. Negative charge from anionic surfactant removes dirt or oils that are positive charge on the surface however, it doesn't mix with non-polar oils and tend to stick with dirt or oil. On the other hand, The non-ionic surfactant lowers the surface tension of water and covers more areas and acts easily to clean. It also helps non-ionic surfactant washes away all dirt and oil instead of just sitting on the surface or damage skin when used to human. In order to minimize damage, non-ionic surfactant and anionic surfactant are often used together in balance for effectivity and safety.[9] Rheology is another key concept in formulation. Anionic surfactants have both hydrophobic and hydrophilc part that they form aligned shape when they are dissolved in the water. This shape is most stable at lamellar phase. But above certain temperature, this lamellar phase is no more stable and shifts to cubic phase. Hence, polarised microscope should be used to observe this temperature point. Lastly, critical micelle concentration should be measured to test stable concentration. CMC is the surfactant concentration at which micelle is formed. SAF-12 and SDS which are anionic surfactant have two part: negatively charged hydrophobic head and hydrophilic tail. When it is dissolved in water, Surfactants tend to be adsorbed at an interface that finds the most energy favorable conditions due to their two-part structure. The decrease in interfacial tension by the surfactant becomes stronger as the surfactant is adsorbed more at the interface. Once the interface is saturated, adding more surfactants will no longer reduce the interfacial tension. Instead, the self-organisation of surfactant molecules takes place within the volume. Minimization of unfavorable contact between the non-polar surfactant chain and the polar solvent compensates for the loss of entropy due to micelle formation. Surfactant solutions can be determined by measuring surface tension at different concentrations. Under CMC, the surface tension decreases as the concentration of surfactants increases as the number of surfactants increases. On the other hand, since the surfactant concentration does not change any more over CMC, the surface tension of the solution is constant.[8] From economical and environmental aspects, the amount of cmc should be minimised. When the surface is saturated, micelles begin to form due to the bipolar surfactant. Above this point, additional surfactants no longer affect surface tension and are unnecessary.

3. Methods

3.1 Oxidation Before carrying out oxidation reaction, furfural was tested with HPLC (High-Performance Liquid Chromatography) in order to determine the purity. 20.9 mg of furfural was diluted with 19.7056 mL of water, and 1 mL of solution was prepared in HPLC vial. The result showed 1.190 mg/mL of furfural concentration which suggested furfural was pure.

Every oxidation reactions of furfural to furoic acid was done in 5 grams of furfural scale. The main basic reaction is shown in figure 1. Furfural reacts with hydrogen peroxide under triethylamine as solvent to produce 2-furoic acid. Furfural and triethylamine solution was prepared in a 50mL glass 3 neck flask then placed on hot plate. Thermometer was put at one neck for checking reaction solution temperature, a rubber stopper at another neck for needle syringe with hydrogen peroxide to be inserted, and an glass stopper at remaining neck. The reason of using 3 neck flask instead of 2 neck flask is because 3 neck flask is more stable to be used in rotary evaporator after the reaction finished. By using 3 neck flask from the start prevents loss of the solution during transportation. Together with triethylamine, tributylamine and acetonitrile was tested as a solvent.

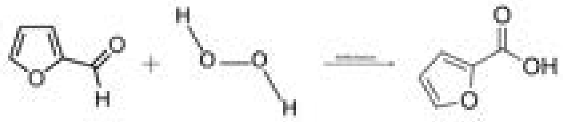

Figure 1: Chemical structural diagram of oxidation of furfural with hydrogen peroxide to form furoic acid under triethylamine

Oxidation is very exothermic reaction. Hence, hydrogen peroxide was injected with the syringe pump. 15 mm diameter and 10 mL volume syringe was used for injection. Before injection started, reaction solution was heated to desired temperature by hot plate. The desired temperature should not exceed 89.28 °C, which is the boiling point of triethylamine. After heating up, the heating was turned off and stirring at 200 rpm was turned on. The reaction kinetic is very high at first 30 minutes. The injection speed of 50µL/min was used for half hour and increased to 100µL/min for the remaining. Hydrogen peroxide should always stored in the refrigerator at 2-8°C. Both 30wt% and 50wt% hydrogen peroxide from Sigma-Aldrichwas used to determine the effect of water concentration on the reaction yield. In this experiment, stoichiometric ratio was mainly used which corresponds to 6 mL (30wt%) and 3.34 mL (50wt%). Tertbutyl hydroperoxide was also tested. As each samples reacted at desired reaction time, HPLC samples were prepared at 10 mg of solution to 1 mL of water ratio. To detect accurate data point, HPLC was calibrated with 5 standard levels, 4.0 mg/mL, 2.4 mg/mL, 1.6 mg/mL, 0.8 mg/mL, and 0.4 mg/mL. HPLC used PDA 210nm channel to detect furoic acid.

$$mass_{furoic} = (conc.)(volume)(dilution) \tag{1}$$

Produced furoic acid in mg can be calculated by multiplying 3 factors shown above; concentration read on HPLC in mg/mL, total volume of all reactants in mL, and sample dilution factor in mg/mL. Yield of furoic acid can be calculated with below equation.

$$Yield = \frac{mass}{MW_{furoicacid}}\left(\frac{1}{mole_{furfural}}\right) \tag{2}$$

After reaction, the solution was cooled down to room temperature. 12.5 mL of 15wt% NaOH solution was added. Addition of NaOH solution created two phases, top layer of amine and bottom layer of product. Separation of two phase was done with glass funnel and amine recovery was measured. Sulfuric acid was put to bottom aqueous solution, reaching pH under 3.12 (pKa of furoic acid) and left it in fridge for overnight. Crystalized furoic acid was filtered out.

3.2 Esterification 2-Furoic acid is esterified by 1-dodecanol to form alkyl furoate under surfuric acid at 150°C.

Figure 2: Chemical structural diagram of esterification of 2-furoic acid with 1-dodecanol to form alkyl furoate catalized by surfuric acid

In this project, 2-furoic acid was purchased from Aldrich Chemistry, 1-dodecanol from Merck KGaA. The first esterification test was done in 300 mg furoic acid scale in small glass vials. The effect of 1-dodecanol amount on residual furoic acid was tested. Five different molar ratio of fatty alcohol respective to furoic acid were used, stoichiometric (0.4978 g), 1.05 (0.5227 g), 1.1 (0.5476 g), 1.3 (0.6472 g), and 1.5 (0.7468 g). Each samples was added with 2.76 mg of sulfuric acid which acts as a catalyst. Samples were heat up to 150°C and ran for 1 hour and 30 minutes. Products were tested with HPLC to determine the residual furoic acid concentration. Since the furoic acid concentration is very low compared to oxidation HPLC test, HPLC furoic acid detector was re-calibrated with new standards, 0.4 mg/mL, 0.24 mg/mL, 0.16 mg/mL, 0.08 mg/mL, and 0.05 mg/mL.

The second esterification test was done in 5 g furoic acid scale. 5 grams of furoic acid and respective molar amount of dodecanol was added in a 50 mL glass flask. Condenser with chiller providing cooling water was connected with vacuum pump and another glass flask. Condenser is attached at the top of 50mL glass flask. By asset set up, the water, undesired side product, can exit from the reaction mixture. During the reaction run, samples were taken at desired time and residual furoic acid was tested via HPLC. The residual furoic acid percentage was calculated by the ratio between remaining furoic acid mass to initial furoic acid mass.

3.3 Sulfonation Sulfonation was done with mixing equimolar amount of chlorosulfonic acid(CSA) and Alkyl furoate (AF-12) as well as chloroform to produce SAF-12.

Figure 3: Chemical structural diagram of Alkyl furoate-12 with Chlorosulfonic acid to form SAF-12

Chloroform was used to decrease high viscosity and to avoid foaming. The reaction was done in the fume hood to avoid any spillage and to have proper ventilation since both CSA and chloroform are corrosive and toxic. The first experiment was done in 5 grams of AF-12 in 100 mL round bottom flask with three necks. In the fume hood, distillation column, thermometer and flow meter was connected in three different necks at heating plate. Distillation column sent out all the side product such as HCl that appears due to the reaction. Thermometer was used to make sure the reaction is set at proper temperature. Flow meter was used to send in nitrogen gas in order to remove heavier side products. After making sure that the reaction is completely sealed, ice bath was put below the flask. At temperature below 10 °C, 1 mL of chloroform was injected slowly to the reaction using 1ml syringe. And then, equimolar amount of CSA which is 1.2 mL was injected very slowly to maintain low temperature using 5ml syringe. Sulfonation reaction is highly exothermic thus dosing is important. It was ran for 30 minutes at below 10 °C. The reaction was then heated to 50 °C and ran for additional 60 minutes. There are two ways to know when the reaction is finished. First, check if there is no bubble, mostly HCl, coming out from distillation column. Second, the reaction becomes soluble in water so take out a very small amount of the product using 1ml syringe and mix it with deionised water. After the reaction was done, 40 mL of water was slowly injected directly into the flask using 50 mL syringe making sure the temperature does not go up. In 100 mL beaker, the product was poured and neutralised with 4.32 mL of sodium hydroxide. pH between 5-7 is most ideal for the neutralisation. The beaker was put in to the fridge for a day for precipitation. After 24 hours, the product was poured into 2 falcon tubes. cold water was added to balance both tubes. Then it was centrifuged for 5 minutes to separate supernatant. Supernatant was put back in the fridge to make sure that all SAF precipitated. Wet SAF-12 was collected together into 100 mL of round bottom flask and put into rotovap at 80 °C and 1 mbar pressure for 30 minutes. When the solid is totally dried, the weight was measured. The second sulfonation was done with 10 grams of AF-12 and respective molar amount of CSA. But only half amount of chloroform which was 1 mL of chloroform was used to test viscosity. One more experiments were repeated with this condition. The last sulfonation was done without chloroform. This trial was repeated once more.

3.4 Formulation The first formulation was done with mixing anionic surfactant which were SDS and SAF-12 to water to check solubility. 15% of anionic surfactant solutions were prepared with SDS and SAF-12 ratio of 0 to 1, 1 to 6, 2 to 5, 3 to 4, 1 to 1, and 1 to 0 and labelled from a to f. Sample a, b and c were mixed with non-ionic surfactant which was alcohol ethoxylate-7 (AE-7) as they were not soluble in the room temperature. 20% and 30% of same ratio anionic surfactant solutions were prepared. 150mg of AE-7 was added to the samples that are not soluble. To those that were stil not solube, 50 mg of AE-7 was added additionally. The second formulation was done with same anionic surfactant solutions. For those that were not soluble, 5% of $MgSO_4$ was added.

Detergents usually have enzymes which breaks ester bonds. To check if SAF is stable with the enzyme, 10% enzyme was injected to 15% anionic solution with 6:1 ratio. Then it was heated to 30°C for 60 minutes. Using 3ml of heptane, any decomposed chemicals were extracted.

Next, 40% anionic solution of SDS and SAF ratio of 3:4 were prepared to watch their phase at different temperature. Polarised microscope with temperature controller was used for watching different phases.

Lastly, the surface tension of different ratio surfactant solutions were measured to check the critical micelle concentration. Both economical and environmental reason, it is important to use minimum concentration of surfactant. Critical micelle concentration can be defined by measuring surface tension as a function of surfactant concentration. 50 mL of 3000 ppm SAF-12 and SDS solutions with ratio of 0 to 1, 1 to 6, 2 to 5, 3 to 4, 1 to 1, and 1 to 0 were prepared in 50 mL tube. And then it was diluted to 2000 ppm, 150 0ppm, 1000 ppm, 750 ppm, 500 ppm, 250 ppm, 150 ppm, 100 ppm, 50 ppm and 25 ppm. Water required for dilution was calculated with the following equation.

$$(molarity1)(volume1) = (molarity2) * (volume2) \quad (3)$$

Drop shape analyzer was used to analyse the surface tension of each samples. Using Kruss Advanced, pendant drop method was selected with setting of water as syringe phase and air as surrounding phase. Add procedure 1 with multiple measurement time 2 seconds, frequency 10fps. 1ml syringe and 1.25 mm needle was used for the whole experiment. All the surface tension results were collected in excel and analysed. With average value of each concentration, concetration versus surface tension graph were drawn. Another straight line was drawn using 4 to 5 surface tension values from 0ppm to get a linear equation in y=ax+b form. Average value of surface tension from 3000 ppm to 1000 ppm was put into the equation as y and x is the cmc value.

Results and Discussion

Oxidation The main and only focus of the oxidation reaction is to remove all furfural as much as possible. Total of 12 samples at different conditions were tested and their results are compiled in table 1. 30wt% hydrogen peroxide solution was used for sample 1 to 7, and 50wt% was used for sample 9 to 12. Under same temperature, amine molar ratio, peroxide molar ratio, and time, reactions with 50wt% hydrogen peroxide showed around 80 90% yield. Instead, 30wt% hydrogen peroxide reactions showed the yield around 60%. This suggests as the concentration of water molecules increase, hindrance on the oxidation is high.

To test the effect of amine content, 0.7 molar ratio and 1 molar ratio respective to furfural were used. Sample 1 and 3 used 0.7 molar of triethylamine and each showed 62.9% and 61.9%. On the another hand, sample 2 and 4 used 1 molar having greater yield of 68.9% and 62.6%. Sample 5 reaction was ran without triethylamine and showed only 0.03% of yield. This suggests triethylamine is actively influencing as a solvent and more amine, the better yield. Tributylamine was tested to see the difference. The reaction yield was half, at 37.2%. The shorter chain for amine was preferred.

Reactions were tested under two temperatures, 55°C and 70°C. By comparing yield of sample 1 and 2 to sample 3 and 4, reaction under 55°C showed higher yield. This trend applied same to the reaction with 50wt% hydrogen peroxide. Sample 9 had 80.1% furoic acid yield, but sample 11 had 95.2% which differs by 14.1%. Low temperature was preferred in fufural oxidation reaction. The oxidation reaction is exothermic. This suggests the increase in kinetic rate of forward reaction by the temperature is comparably smaller than the rate due to Le Chatelier's principle which push towards endothermic direction.

The time indicates the reaction time after all the injection of hydrogen peroxide was finished. The injection required total of 2 hours for 0.05208 mole of hydrogen peroxide. The only difference between sample 10 and 11 is the time reacted. Sample 10 was reacted for overnight (24hrs), and sample 11 was reacted for 1 hour. The result showed leaving the reaction overnight had a lower yield which indicates there is a degrading of furoic acid. Other types of oxidation reaction were tested. Sample 8 was an oxidation reaction by tertbutyl hydroperoxide, having an yield of 80.0%. Comparing to sample 10 with hydrogen peroxide, tertbutyl hydroperoxide is not a good oxidizing agent of furfural. Sample 12 is CuCl catalyzed oxidation reaction under acetonitrile as a solvent, but the yield was only 1.8%.

The best optimized reaction condition was using 50wt% hydrogen peroxide under stoichiometric ratio of triethylamine at 55 °C for 1 hour, which giving the yield of 95.2%. The furfural can be destroyed at the most.

There are few problems to be discussed. The first point is the recovery of triethylamine. When large amount of mole of furfural meets NaOH solution, the whole solution turns from orange color to non-transparent black. In result, observing two different layers was not possible. This phenomenon happened only when using 30wt% hydrogen peroxide which had lower conversion of furfural. This was not a case for reactions with 50wt%, but the average recovery of amine stay at 55%. Compared to literature value of 91%, it is very low recovery. Furoic acid yield was lower than literature value, which can be improved by using more concentrated hydrogen peroxide (70wt%). Relate to this, another problem was the difference between the real yield and HPLC recorded yield. After filteration, the measured furoic acid mass was higher than the mass calculated from HPLC. The crystalized furoic acid might contain impurities such as triethylamine which was not recovered at the first step. Running GC-MS to check the composition of mixture and seletivity of furoic acid could be helpful to analyse the reason of amine low recovery. Lastly, due to its nature of high exothermic, it

Table 1: Oxidation yield under corresponding conditions

Sample Number	Temperature (°C)	Amine molar ratio	H_2O_2 molar ratio	Type of peroxide	Time (hours)	Yield (%)
1	55	0.7	1	30wt% H_2O_2	1	62.9
2	55	1	1	30wt% H_2O_2	1	68.9
3	70	0.7	1	30wt% H_2O_2	1	61.9
4	70	1	1	30wt% H_2O_2	1	62.6
5	55	no amine	1	30wt% H_2O_2	1	0.03
6	70	1 (tributyl)	1	30wt% H_2O_2	1	37.2
7	55	1	2	30wt% H_2O_2	overnight	88.4
8	55	1	1	tertbutyl	overnight	80.0
9	70	1	1	50wt% H_2O_2	1	80.1
10	55	1	1	50wt% H_2O_2	overnight	93.9
11	55	1	1	50wt% H_2O_2	1	95.2
12	20	0 (1 mol% CuCl)	1	50wt% H_2O_2	overnight	1.8

was hard to control the constant temperature. The peak was occurring as hydrogen peroxide injected. In industry scale, batch with both heater and cooler is used to keep temperature constant. But in lab scale, only heating by hot plate is available which can lead to variation in temperature. The error in temperature condition could impact on kinetic of reaction.

Esterification The main objective is to optimize between product yield and the color. The decision in molar ratio amount of fatty alcohol was first variable to choose.

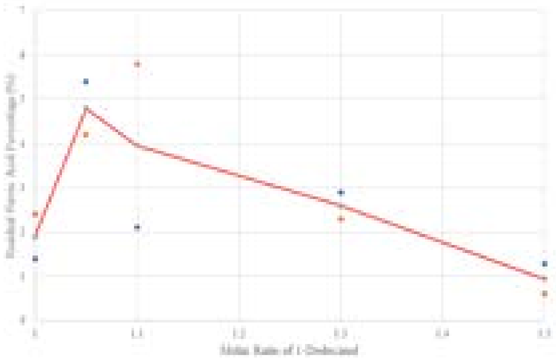

Figure 4: Residual 2-furoic acid percentage of various reaction condition by differing molar ratio of 1-dodecanol to 2-furoic acid under 1 mol% of H_2SO_4. Trial 1 and Trial 2 is represented by blue and orange symbols. The red line connects the average of two values at specific molar ratio.

Figure 4 shows the residual furoic acid content at different dodecanol ratio. The trendline first increases and decrease at 1.05 molar ratio. Stoichiometric, 1.3, and 1.5 ratio showed relatively high conversion of furoic acid. The inflection point was occuring between stoichiometric and 1.3 molar ratio. The same procedure with 3 mol% sulfuric acid was done.

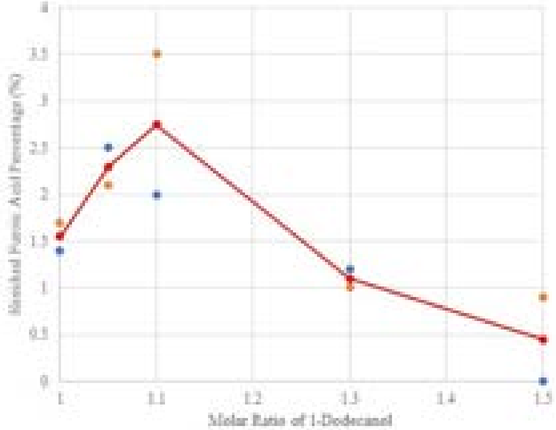

Figure 5: Residual 2-furoic acid percentage of various reaction condition by differing molar ratio of 1-dodecanol to 2-furoic acid under 3 mol% of H_2SO_4. Trial 1 and Trial 2 is represented by blue and orange symbols. The red line connects the average of two values at specific molar ratio.

The reaction under 3 mol% sulphuric acid is plotted in figure 5. This also results stoichiometric, 1.3, and 1.5 molar ratio of dodecanol giving less residual furoic acid percentage. The problem raised when experimenting in a small scale. Sulfuric acid needed to be diluted with water when using a small scale reaction leading water content to be too high. Water could not escape from the vial. Hence the reaction was carried in a 50mL glass flask. The pressure parameter for vacuum pump was adjusted. The pump was not turned on for first half hour since this drained both water and unreacted furoic acid. After half hour, the pump was turned on at 700 mbar. This drains all water produced from the flask.

Residual furoic acid percentage at different reaction time is shown in figure 6. The reaction with stoichiometric dodecanol molar ratio has minimum of 2.11%. However, both reactions with 1.3 and 1.5 molar ratio of dodecanol reaches under 1% in 1 hour. Since both reactions similarly reaches the furoic acid conversion, 1.3 molar ratio of dodecanol was chosen to be the optimum ratio. This uses less dodecanol, so the price of raw material and waste will be smaller.

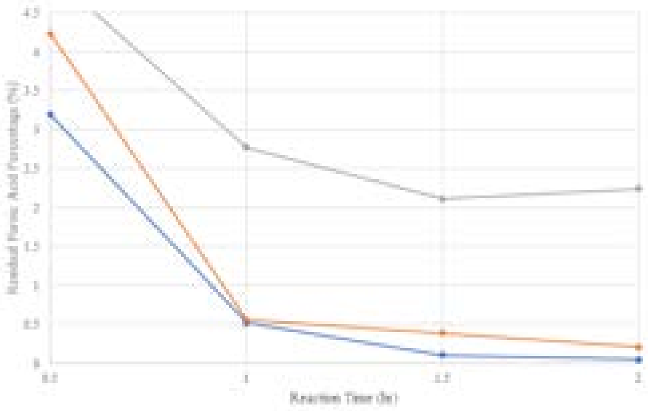

Figure 6: Residual 2-furoic acid percentage at corresponding reaction time in hours. Esterification reaction data at stoichiometric ratio (gray symbol), 1.3 molar ratio (orange symbol), and 1.5 molar ratio of 1-dodecanol (blue symbol) is taken at 0.5, 1, 1.5, and 2 hours of the reaction time

The reaction at 1.3 molar ratio of fatty alcohol was repeated, and the residual furoic acid percentage was checked every 5 minutes in order to get the time to reach below 1% residual content. From figure 7, 0.91% occurs at 40 minutes.

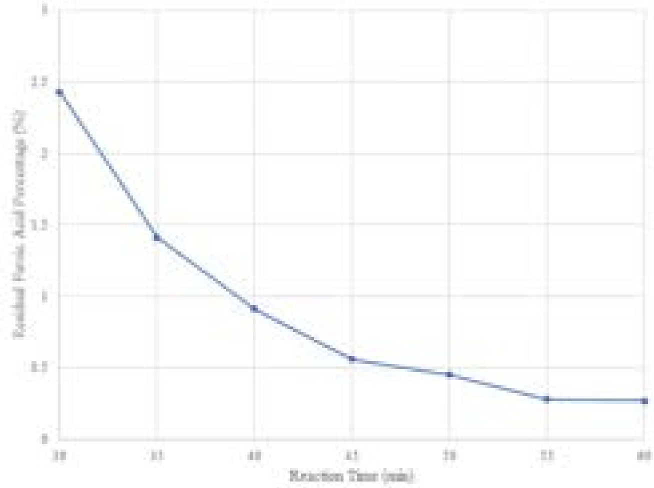

Figure 7: Residual 2-furoic acid percentage of the esterification reaction with 1.3 molar ratio of 1-dodecanol between the reaction time of 30 and 60 minutes with 5 minutes intervals.

The color of the solution is also important. This is not related to chemical property, but it is one of the variables in product characterisation. As brighter the surfactant and its product, the consumer are more likely to buy. Personal care product and detergents are focusing on cleaning aspect. Therefore if the product is clear and bright, it will possess clear and clean image and be successful in marketing. Figure 8 shows the color change of the esterification. The reaction after 1.5 hours have 0.27% residual furoic acid percentage but the color is dark brown. On the other hand, the reaction after 40 minutes has 0.91% residual percentage but has clear yellow and transparent color. The compensation between residual furoic acid and color exists. The project aimed for solution to have below 1% residual furoic acid. This project concludes the reaction at 40 mintues is the best optimum.

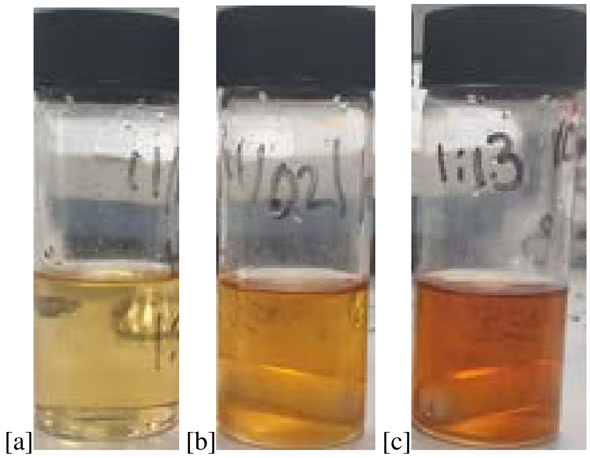

Figure 8: Color change of final product from esterification at (a) 40min (b) 1 hour (c) 1.5 hours

Sulfonation : Sulfonation reactions were done in different conditions and repeated few times to minimise error. The first sulfonation was done with 5 grams of AF-12 with 1.2ml of CSA and 1 mL of chloroform and repeated. The second sulfonation was done with 10 grams of AF-12 with 2.4 mL of CSA but 1ml of chloroform which was decreased by half of original amount and repeated. This was to discover how much chloroform is required to maintain low viscosity of the reaction. Viscosity is very significant since in high viscosity the reactant would not be mixed well. After using 1ml of chloroform, the third experiment was done without chloroform to see if the reaction without chloroform would actually works.

Table 2: Analysing 15% anionic solution with different ratios: A) pure SAF solution B) 6 to 1 of SAF to SDS solution C) 5 to 2 of SAF to SDS solution D) 4:3 of SAF to SDS solution E) 1:1 of SAF to SDS solution F) pure SDS solution

15% anionic solution	A	B	C	D	E	F
Soluble at room temp	X	X	X	O	O	O
Soluble after adding 150mg AE-7	X	X	O			
Soluble after adding 200mg AE-7	X	O				
Temp at 60 °C	O					

Reaction between 4.9839 g of AF-12, 1.2 mL of CSA and 0.9 mL of choloroform produced 2.3576 g of SAF-12. In neutralisation, 3.56 mL of 5M NaOH was calculated to be ideal amount. However, 7.21 mL of 5M NaOH was used to neutralise the product. Repetition was done for more accuracy with 5.0533 g of AF-12, 1.2 mL of CSA and

1ml of chloroform. 7.3 mL of 5M NaOH was required for the neutralisation and 2.5043 g of SAF-12 was produced. The next experiments were done with half of original amount of chloroform and double amount of AF-12 and CSA. With 10.1041 g of AF-12, 2.4 mL of CSA and 1 mL of chloroform, 8.58 mL NaOH solution was required in neutralisation and 6.0642 g of SAF-12 was produced. For the second trial, 8.64 mL of 5M NaOH was required and 8.2042 g of SAF-12 was produced. Last experiments were the reaction without using chloroform. 10.257 g of AF-12 was used and produced 8.0824g of SAF-12. 10.18 g of AF-12 produced 7.7289 g of SAF-12. The summary of the result is shown in table 3.

Few problems have raised during sulfonation including high viscosity of the reaction product and carbonisation during the reaction. Viscosity is the key to sulfonation since at very high viscosity, the reaction starts to be solidify or forms foaming and will not be done. Before the AF-12 and CSA got reacted, a little amount of chloroform was injected in order to decrease viscosity and avoid foaming. Dosing is also a key to maintain stable condition of the reaction. Thermometer was placed in one of the neck of the beaker to adjust temperature below 10°C when injecting both chloroform and CSA since the reaction with AF-12 with both chemicals are highly exothermic. Carbonisation is likely happened during the reaction when the beaker is not completely sealed. Thus, suba seal and adapter were used to completely seal the reaction. When the reaction is not completely sealed, side product can produced due to carbonisation. One example of the side products is HCl(g). During the reaction, nitrogen gas was injected direclty to the reaction to remove all the HCl. One way to know if side product still exist in the product is putting the reaction in rotary evaporator for 30 minutes to see the solid state. If the solid is still spongy or wet, ethyl acetate was used to remove the side product by washing the solid with it for several times. And rotary evaporator was used again at 80°C for 30 minutes to remove organic solvent.

Formulation 15%, 20% and 30% anionic surfactant solutions were prepared with various ratios. Table 2 shows that regardless with the concentration of anionic surfactant, pure SAF solution (A), SAF:SDS 6:1 solution(B) and SAF:SDS 5:2 solution (c) were all not soluble at room temperature. 15 % of Alcohol Ethoxylate-7 was additionally added to these solutions. Only C became soluble so additional 5% of AE-7 was added to A and B. Insoluble A was put into the oven at 60 textdegree C for 10 minutes. Another experiment was done with adding same 15% MgSO_4 and AE-7 to soluble solutions to increase viscosity. AE-7 did help increasing viscosity and solubility while MgSO_4 didn't show different.

Stability test to 6:1 solution was done with enzyme. Detergents usually have enzymes which breaks ester bonds. SAF has an ester bond that can be broken by enzyme so it was injected to the sample to check stability. If SAF hydrolysed, it would decompose in dodecanol and furoic acid. Heptane was added to extract the dodecanol.There was no dodecanol at the end, concluding the SAF is stable with the enzyme.

Polarised microscope with temperature controller was used to determine the rheology of 40 % anionic solutions with ratio of 4:3 of SAF-12 and SDS. The temperature was controlled by nitrogen gas. This ratio was chosen because it is soluble at room temperature without non-ionic surfactant with highest ratio of SAF-12. Figure 10 to 12 shows the photos of the phases with varying temperature. As temperature increased from 20 to 60, the phase shifted from lamellar phase to cubic phase. At lamellar phase, the particles are evenly dispersed while at cubic phase, the dark portion got enlarged and dispersed randomly.

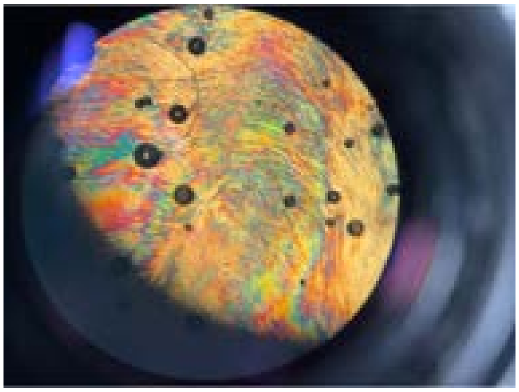

Figure 9: Phase of 40% 4 to 3 of SAF-12 to SDS solution at 20°C

Figure 10: Phase of 40% 4 to 3 of SAF-12 to SDS solution at 30°C

CMC is the minimum concentration of surfactants in which micelles are formed. It measures the effectiveness of surfactants. Micelles form above cmc, but are evenly dispersed below the CMC. Surface tensions for each concentration were measured with drop analyzer. These data were collected in excel to calculate cmc. In the first trial, calculated CMC values were too low. One of the examples of the graph from the first trial is be shown in figure 13.

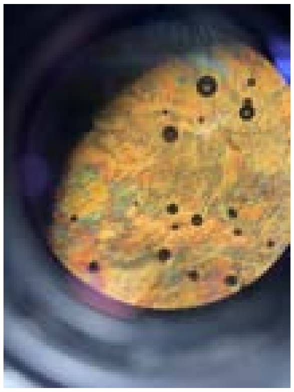

Figure 11: Phase of 40% 4 to 3 of SAF-12 to SDS solution at 40°C

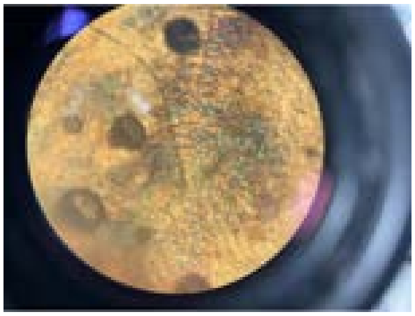

Figure 12: Phase of 40% 4 to 3 of SAF-12 to SDS solution at 60°C

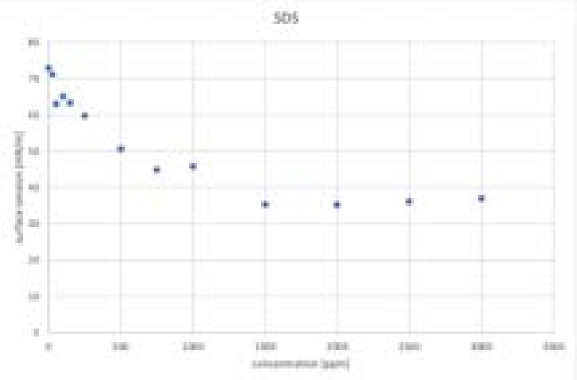

Figure 13: Surface tension versus concentration graph of SAF-12 solution for first trial

With this graph, the cmc of SDS solution was around 672.62ppm. This value was far below the tested value done by literature. To fix this problem, another trial was repeated with washed experimental equipment. All the equipment that were going to be used to measure cmc such as beakers, plastic pipets, and tubes were washed with soap, distilled water and ethanol. It was to get rid of salt remaining at any tools after washing them with tap water. Final result are shown from Figure 14 to 16.

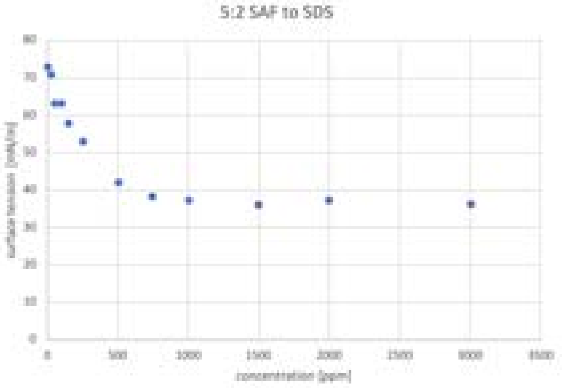

Figure 14: Surface tension versus concentration graph of 5:2 SAF-12 to SDS solution

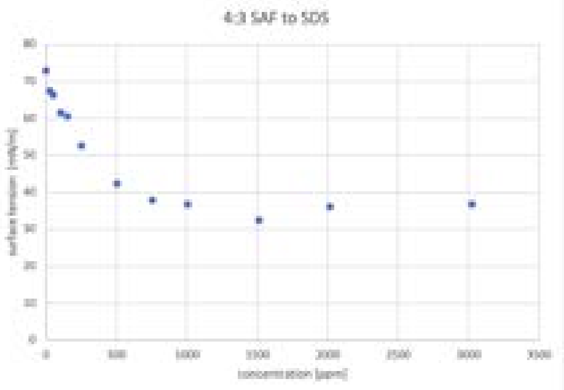

Figure 15: Surface tension versus concentration graph of 4:3 SAF-12 to SDS solution

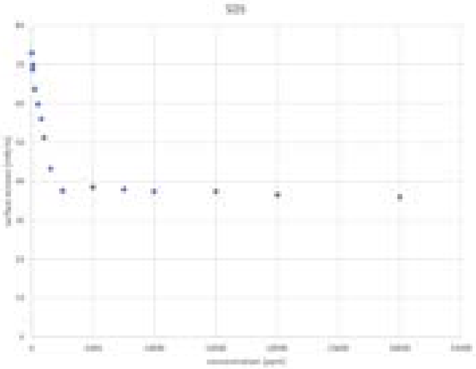

Figure 16: Surface tension versus concentration graph of pure SAF-12 solution

Table 3: Summary of Sulfonation done with AF-12 and Chlorosulfonic acid with Chloroform, amount of NaOH used to neutralise the product, pH and the yield

Sample Number	AF-12(g)	Chlorosulfonic acid (mL)	Chloroform (mL)	5M NaOH (mL)	pH	SAF-12 (g)	Yield (%)
1	4.9839	1.2	0.9	7.21	5-6	2.3576	47.3043
2	5.0533	1.2	1	7.3	5-6	2.5043	49.5577
3	10.0055	2.4	1	8.58	5.4	6.0642	60.6087
4	10.1041	2.4	1	8.64	6.14	8.2042	81.1967
5	10.2570	2.4	0	11.1	6.2	8.0824	78.7989
6	10.1800	2.4	0	10.9	6.55	7.7289	75.9224

SDS had its cmc around 1774.82 ppm which matched with the previous test done, 5 to 2 of SAF to SDS had its cmc around 432.18 ppm, 4 to 3 of SAF to SDS had its cmc around 459.82ppm. The calculations were done by excel. Other values provided by literature were SAF-12 at its cmc around 530ppm and 6 to 1 of SAF to SDS at its cmc around 330ppm. SDS and SAF have their cmc values very high when they are used separately. When mixed together, cmc values get much lower which means the ability to be used as surfactant has been increased.

Conclusion

Furfural to furoic acid oxidation at 55 °C, 1 hour reaction time, with 50wt% hydrogen peroxide gives best yield. By this furfural can be removed as much as possible. The optimum condition for esterification is at 150°C for 40 minutes with under 1% residual furoic acid percentage and bright yellow color.

Sulfonation was done with 5 grams of AF-12 and 10 grams of AF-12 with and without the help of side inert chloroform. For 5 grams of AF-12 the yield was low as traditional method of filteration was done with cotton filter that has a bigger hole than AF-12 powder that some AF-12 was lost during the filteration. 10 grams of AF-12 produced 60.6% and 81.2% yield of SAF-12 which was quite successful. The production of SAF-12 without chloroform went great and produced better yield around 78.8% and 75.9% but dosing is necessary.

In formulation, SAF-12 was mixed with SDS which is also an anionic surfactant for greater effect as surfactant. Adding AE-7 helped increasing stability of the solution and increase viscosity. 4 to 3 ratio of SAF-12 to SDS was most ideal at room temperature as it is soluble with highest volume of SAF-12. 40% of anionic solution was chosen for the rheology test with polarised microscope. From 20 °C to 50 °C showed lamellar phase while from 60 °C showed cubic phase. Lastly, the CMC value for SAF-12 provided by literature was around 530ppm and that of SDS was calculated at aroudnd 1774ppm. Therefore, it is better to mix both anionic surfactant to lower the CMC. Overall, 4 to 3 ratio of SAF-12 to SDS was determined to be most ideal ratio as it has proper viscosity, rheology, and the CMC at room temperature.

Further Research

Further possible research area is a financial analyse between a cost of purification process and revenue from the desired yield. In previous section, brighter color was chosen for better choice to consumers. If color was classified with colorimetry and corresponding revenue from each colored products in industry can be optained, the price can be compared with purification process, whether to purify 1% or even lower.

More sodium hydroxide was required in neutralising SAF-12 than the calculated value. One theory that might have increase acidity of the product is some unknown by-product has been formed during the reaction. It would be great to examine what by-product is forming and why. Further research can be made to proceed. First, rheology test can be done with more varying concentration such as 10%, 20% and 30% to draw 3D phase graph. With this graph, stable and unstable ranges with varying temperature and concentration can be known. Another improvement can be made in cleaning test. It can be done to test the efficiency and effectivity of SAF-12. Especially 4:3 Solution should be tested.

Acknowledgements

We first thank to Dr. Amir Al Ghatta for giving experimental directions and providing feedback on experiment procedures. We also thank to James and Raul for providing detailed procedures on using instruments including rotary evaporator and centrifuge. We thank Yanghong for providing instruction on HPLC, Pedro for giving safety induction of the lab. Lastly, we thank all Hallett research group members for understanding our usage of lab equipments and providing help on inquiries.

References

[1] Matthew J Scott, Malcolm N Jones, (2000), The biodegradation of surfactants in the environment, Biochimica et Biophysica Acta (BBA) - Biomembranes, Volume 1508, Issues 1–2, Pages 235-251, ISSN 0005-2736, https://doi.org/10.1016/S0304-4157(00)00013-7.

[2] HERA. (2013), LAS Linear Alkylbenzene Sulphonate Environmental Risk Assessment, Human and Environmental Risk Assessment on ingredeitns of household cleaning products, Page 26.

[3] Dmitry Yu. Murzin, Farhan Saleem, Johan Warnå, Tapio Salmi, (2020), Kinetic modelling of heterogeneous catalytic oxidation of furfural with hydro-

gen peroxide to succinic acid, Chemical Engineering Journal, Volume 382, 122811, ISSN 1385-8947, https://doi.org/10.1016/j.cej.2019.122811.

[4] Kenneth Thomas Rowbotto, David Ashton Cummerson (1987), Oxidation of furfural to 2-furoic acid, GB2188927A.

[5] N.R. Reed, E.S.C. Kwok. (2014), Furfural, Encyclopedia of Toxicology (Third Edition), Academic Press, Pages 685-688, ISBN 9780123864550, https://doi.org/10.1016/B978-0-12-386454-3.00147-0.

[6] Ross, S. D. (1946) The Rate of Oxidation of Thiodiglycol and Triethylamine by Hydrogen Peroxide. J. Am. Chem. Soc.68, 14841485.

[7] Sreedevi Mannam, G. Sekar. (2008), CuCl catalyzed oxidation of aldehydes to carboxylic acids with aqueous tert-butyl hydroperoxide under mild conditions, Tetrahedron Letters, Volume 49, Issue 6, Pages 1083-1086, ISSN 0040-4039, https://doi.org/10.1016/j.tetlet.2007

[8] Dataphysics-instruments.com. n.d. Surfactants critical micelle concentration (CMC) - DataPhysics Instruments. [online].

[9] Andrew. (2021). What are surfactants? Anionic and Non-ionic Surfactants, Millennial Homeowner.

CCD-NIPS Induced Membranes

Investigating the effects of dwell time and additive concentration on CCD-NIPS membrane performance and morphology

Faraaz Anjum and Emily Xu
Department of Chemical Engineering, Imperial College London, UK

December 16, 2021

Abstract

At present, the most common production methods of polymeric membranes for filtration are by phase-separation processes. Over the last ten years, the technological advancements in these methods have been limited. New methods, including CCD, would require a high capital cost to produce membranes with the appropriate UF capabilities. This reports shows that the new CCD-NIPS technique, inspired by the combined efforts of CCD and NIPS, utilises directional solvent freezing during immersion precipitation of the polymer. The membranes produced using PES polymer and DMSO solvent, have enhanced water permeance compared to its NIPS counterparts due to its superior connected structure and absence of dead volume. They also demonstrate small pore sizes and enhanced selectivity. The effects of pore-forming additives and dwell time are found to be influential on the performance and morphology of CCD-NIPS membranes. Essentially, the findings demonstrate the potential for an economic alternative to fabricating highly selective CCD-type membranes.

Key Words: CCD, NIPS, CCD-NIPS, immersion precipitation, directional freezing, dwell time and pore-forming additives, dead volume, water permeance, pore size

1 Introduction

In recent years, with the growing interest in wastewater treatment and recycling, polymeric membranes have proven to be a competitive and energy economic alternative to traditional thermally driven separation methods. Polymeric flat-sheet membranes have been used extensively in industrial separations since their invention via the phase inversion method in the 1960s [1]. This membrane-based filtration generates a business of tens of billions USD per year [2] with relevant applications in microfiltration (MF), ultrafiltration (UF), reverse osmosis and gas separation [3]. In most cases, the selectivity and permeability determine the effectiveness of the porous membrane, therefore, significant effort has been invested into improving the performance and morphology of existing membranes.

Multiple methods have been applied to fabricate polymeric membranes such as stretching, track etching, sintering and phase separation processes [3]. Each involves different fabrication principles which decide the final membrane geometry. Among these, controlled phase separation is the most common method due to its great tunability towards the membrane microstructure [3]. The polymer solution is separated into two phases: the polymer-rich and the polymer-lean phase. The polymer-rich solidifies after phase separation forming the membrane. The non-solvent induced phase separation (NIPS) method and the thermal-induced phase separation (TIPS) are fabrication techniques in the industry that utilise phase separation. Nevertheless, these techniques all possess intrinsic limitations which may affect the membrane morphology and performance.

NIPS involves a process whereby a polymer solution is cast onto a supporting plate which is then submerged in a coagulation bath containing a non-solvent [1]. Demixing occurs where the solvent phase is replaced by the non-solvent phase from the coagulation bath. The nature of these membranes are normally anisotropic or asymmetric [4]. Thus, the popularity of this fabrication technique stems from the simplicity of the process and the flexibility to manipulate membrane morphology [4]. However, the NIPS technique is susceptible to physical-chemical interferences, such as ambient temperature and humidity, inter-diffusion mechanisms, rheology of polymer solution and interfacial instabilities [2]. Due to the complexity and lack of understanding surrounding this, the NIPS technique falls short in terms of quality control and reliability of the membrane fabrication process. Consequently, it is difficult to achieve an optimal membrane morphology with minimised permeation resistance via the NIPS method.

The main disadvantage of the TIPS technique involves the absence of the tight-skin separation layer, characteristic of the NIPS method, as it lacks the solvent/non-solvent exchange. Therefore, the pore size of TIPS membranes lies within the MF range, which limits its application in UF scenarios. Attempts have been made to combine the respective advantages of TIPS and NIPS method using water-soluble diluents,[5] however, the competition that results between NIPS and TIPS creates an even more complicated fabrication process.

The combined crystallisation and diffusion (CCD) method is a simple freeze-drying approach that creates membrane pore structure through solvent unidirectional freezing. The solvent crystallisation is driven by a -30 °C cooling plate, where the precipitation of the polymer forms the membrane matrix. For this method, a solvent with a high freezing point (DMSO) is required. Thus, the resultant membrane structure exhibits aligned pore channels that minimise the transport resistance of water, giving rise to a high flux. Moreover, these membranes demonstrate superior mechanical properties and are much easier to control giving reproducible results [2].

Ideally, a CCD structure would be synthesised at a very low temperature (-30 °C), to extract the best possible membrane permeation and UF characteristics. In reality, such cryogenic temperatures are not preferred during the fabrication process as it would increase the membrane capital cost. Thus, the potential pore sizes of CCD membranes produced at economically viable temperatures will be significantly larger than the sizes produced by traditional NIPS methods.

This paper proposes an idealised fabrication technique where the CCD and NIPS methods are combined to produce an optimised membrane. It strives to present a viable economic alternative that can produce membranes with the high permeability and low pore size characteristic of the CCD and NIPS methods respectively, at a higher temperature.

In this study, the CCD-NIPS method is applied to polyethersulfone (PES), one of the most commonly used MF and UF materials. PES possess high mechanical strength, chemical resistance, and thermal stability, making it ideal for many industrial applications in waste-water treatment and bio-separations [6]. Literature suggests that DMSO demonstrates the appropriate solubility characteristics; its high melting point of 19°C enables the DMSO to freeze upon immersion, a step critical in CCD-induced separation [7]. An aluminium plate was chosen to provide high heat dissipation during cooling. Studies have shown that the permeation characteristics of membranes can be enhanced by the addition of additives like polyvinylpyrrolidone (PVP) [4]. This report will investigate whether the addition of PVP is beneficial to the performance of the CCD-NIPS induced membranes.

2 Theory

Each membrane consists of a separation and a supporting layer, where the separation layer is responsible for the selectivity properties, whilst the supporting layer provides mechanical stability and controls the permeation rate.

The CCD-NIPS membrane morphology is dependant on the polymer precipitation rate, which is controlled by two kinetic factors:

1. the diffusional exchange (demixing) of solvent with non-solvent in the polymer-lean phase, and
2. the DMSO crystallisation rate in the polymer-rich phase.

The first kinetic mechanism is characteristic of that found in the pure NIPS process, whilst the second is comparable to the mechanism in pure CCD.

2.1 NIPS Mechanism

In NIPS, the precipitation front is kinetically controlled by the diffusional exchanges associated with the liquid-liquid demixing of the DMSO solvent with the non-solvent water from the coagulation bath [8]. Upon immersion, the precipitation front travels inwards from the non-solvent bath-membrane interface [9]. Nuclei inception at the precipitation front is only possible once the solution overcomes an energy barrier and enters the metastable region (between the binodal and spinodal boundaries seen in Figure 1) [8]. In NIPS, the nucleation energy barrier is overcome by the concentration gradient, which arises once the membrane is submerged into the coagulation bath. Nucleation will continue until the diffusional driving forces can no longer overcome the mechanical strength of the vitrified nucleus wall.

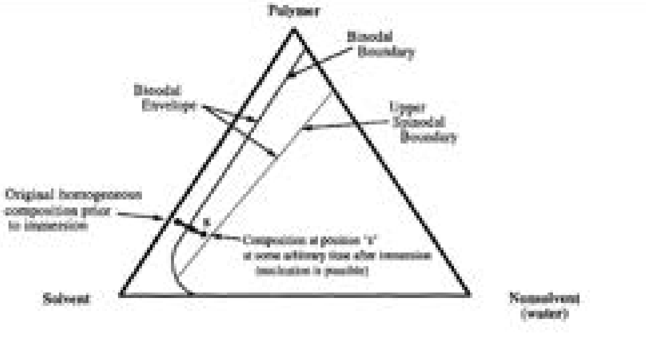

Figure 1: Ternary Diagram for Non-solvent (water), Solvent (DMSO) and Polymer (PES)[8]

The finger-like macropores are formed via viscous fingering from the top surface and grow inwards. These form under the separation layer, with their growth dependant on the concentration of polymer at the precipitation front. If the polymer concentration is low enough to sustain growth, the finger-like pores will continue to grow. Growth terminates once the precipitation front reaches the more viscous polymer-rich phase. The termination point is referred to as the glass transition point [10]. The research have also shown that these finger-like macropores are promoted by faster precipitation fronts and by rapid immersion [11].

The binary phase diagram in Figure 2 indicates the thermodynamic consideration of the demixing mechanism within the polymer solution. By lowering the temperature of the coagulation bath, the demixing behaviour of such solution shows three different patterns: the nucleation and growth of the polymer-rich phase, the bicontinuous morphology due to spinodal decomposition and nucleation and growth of the polymer-lean phase. Nevertheless, the transition between these regions is not sudden but rather a gradual change, and this is decided by the kinetics of demixing. A high demixing kinetic would promote the formation of a more continuous pore structure (bi-continuous or sponge-like pores). However, a delayed demixing would usually lead to the formation of isolated pores. These isolated pores, known as dead-volume, are prevalent in the bottom half of the NIPS membrane structure, exerting high transport resistance to the fluid.

The described NIPS morphology can be seen in Figure 4a.

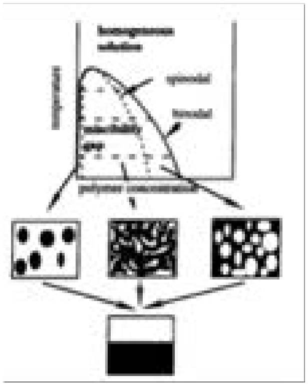

Figure 2: Phase Separation Mechanisms [12]

2.2 CCD Mechanism

In CCD, the topology of the pore is preserved by the crystallised solvent in the membrane solution which is replaced by a non-solvent when the membrane is immersed into an iced coagulation bath. The water needs to be at a lower temperature than the freezing point of the solvent so that it retains its crystalline structure.

The energy barrier for homogeneous and heterogeneous nucleation is dictated by the temperature difference between the cooling plate surface and the freezing point of the solvent, here and thereafter referred to as the undercooled temperature difference. The plate removes heat and enables fast cooling of the membrane solution pre-immersion. When the undercooled temperature difference is sufficiently high, the solvent will crystallise both homogeneously and heterogeneously. Homogeneous nucleation has a higher energy barrier to overcome and therefore occurs at a lower temperature than heterogeneous nucleation. Thus, it can be deduced that the rate of solvent crystallisation is also determined by the undercooled temperature difference[2]. The freezing mechanism explained above is unidirectional and is related to gelation. Gelation occurs when the solvent diffuses out of the solution to crystallise, gradually increasing the concentration of polymer in the solution. This subsequently increases the viscosity of the solution, forming a gel. Gelation is a temperature dependant phenomenon [13] that varies with distance from the cooling plate, a trend more apparent at lower temperatures and shorter contact times. In CCD, the gelation of the solution is fast due to the larger undercooled temperature difference. Once immersed, the DMSO crystallites are removed by solid-liquid demixing with the non-solvent.

The membrane morphology formed via CCD can be seen in Figure 4b. It can be seen that the pre-immersion solvent crystallisation determines the uniform lamellar structure present in CCD membranes.

2.3 CCD-NIPS Mechanism

Figure 4c demonstrates the membrane structure synthesized by a CCD-NIPS mechanism. Here, we observe the existence of a thin separation layer followed by long finger-like NIPS-induced structures that extend into a dense bicontinuous CCD-induced structure, with an apparent absence of dead volume. The top of the structure is formed via NIPS, whereas the bottom of the structure is formed via CCD. The structural properties of the CCD-NIPS membrane can be attributed to the fabrication mechanisms of both the NIPS and CCD processes.

The proposed CCD-NIPS mechanism utilises two kinetic mechanisms outlined in this section and will be further examined throughout the report.

3 Methodology

3.1 Chemicals

Polyethersulfone, PES, was used as a solute (18 wt.%) and dissolved in dimethyl sulfoxide, DMSO (MW. 78), to create the membrane solution. Polyvinylpyrrolidone PVP (MW. 3000) was used as an additive (1 wt.% and 4 wt.%), whilst isobutanol, hexane and ethanol were used in the drying process.

3.2 Membrane Fabrication

3.2.1 Membrane Preparation

During the investigation, each membrane was prepared using the same technique. The membrane solutions were prepared in 500ml batches. PES was first dried at 80 $^\circ C$ for 24h. PES was dissolved into DMSO to produce an 18 wt.% PES in DMSO solution, it was then placed on a rotating drum for sufficient mixing. Additionally, two separate batches of membrane solution with PVP additive were produced, with 1 wt.% and 4 wt.% PVP. The solutions were dried in the oven for 48h to remove any moisture and air bubbles. The solution was poured onto an aluminium casting plate of thickness 1.2mm and placed on the casting machine, ready to be formed using the method of choice as seen in Figure 3. It is worth noting that the time between casting the membrane and starting the synthesis method was minimised each time.

3.2.2 CCD Method

Immediately after the membrane was cast, the casting plate was moved to the cooling plate at -10 $°C$, well below the freezing point of DMSO, where it was left to freeze and form the membrane structure. After this, the plate was immersed into an iced coagulation bath to leach out the DMSO crystals and produce the final membrane structure.

3.2.3 NIPS Method

For the NIPS method, the solution film attached to the casting plate was immediately immersed into an iced coagulation bath to leach out the liquid DMSO from within the structure. The membrane had completely formed within a few minutes.

3.2.4 CCD-NIPS Method

In this method, the membrane on the casting plate is moved to an intermediate cooling plate where the membrane was cooled to 8 $°C$, below the freezing point of DMSO. The temperature of the cooling plate was much higher than that of the pure CCD method. It was important to ensure that the cooling plate was set at a temperature sufficient in changing the viscosity profile from the bottom of the solution, without freezing it. The dwell time is defined as the time spent by the solution film on the intermediate cooling plate. The dwell time was varied for experiments both with the PVP additive (for 20s and 60s) and without the additive (for 10s, 30s and 60s) to explore the significance of this constraint. After the desired dwell time had passed, the casting plate was swiftly transferred to an iced water coagulation bath at 0 $°C$ to leach out the DMSO from the solution. Figure 3 shows a set-up of the CCD-NIPS equipment.

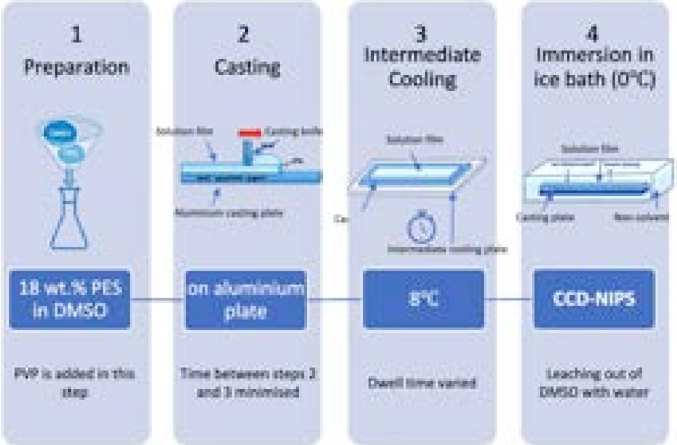

Figure 3: CCD-NIPS Fabrication Process Diagram

3.2.5 Membrane Storage

The membranes were stored in de-ionised water after casting to limit exposure to air and any subsequent damage. The de-ionised water was replaced every day to minimise effects of contamination.

3.3 Membrane Performance

3.3.1 Pure Water Permeance (PWP

The membrane permeability was determined through a series of pure water permeation (PWP) tests. A 500 ml dead-end filtration cell was connected to a compressed air pressure supply to dictate the feed flow rate into the cell. Each PES membrane was cut into circular samples which were then placed into the membrane holder attached to the dead-end cell. Within the membrane-holder was an O-ring, placed on top of the membrane for a tight seal, with an internal diameter of 2mm. At all points, the membrane was kept in de-ionised water and the time spent outside of water was minimised. All membranes were tested at a pressure of 1 atm for between 10 to 15 minutes, excluding NIPS (tested at 5 atm for 30 minutes). The PWP of each membrane was calculated using Equation 1.

$$J = \frac{V}{A \times t} \tag{1}$$

Where J is the pure water permeance ($Lhr^{-1}m^2$), V is the permeate volume (L), A is the effective membrane area dictated by the inner diameter of the O-ring (m^2) and t is the permeate collection time (hr).

3.3.2 Mean Flow Pore Diameter (MFPD

The mean flow pore diameter (MFPD) was calculated using a liquid-liquid porometer (PMI 1500A). The membrane was dried in two washes of ethanol followed by two washes of hexane each for 6 h to remove any water content from the mixture. Ethanol was needed as it was easily exchanged with the water, however, due to its slow evaporation rate, it was subsequently immersed in hexane (which has a faster evaporation rate). The hexane is immiscible with water and therefore an intermediate step using ethanol was needed. Once dried, the membrane was cut into samples the same as in the PWP experiment. The samples were wetted by an alcohol-rich isobutanol phase, produced from a water-isobutanol mixture. The wetted membrane was placed into the LLP where the water-rich phase from the mixture, replaced the isobutanol-rich phase. Since the two phases are immiscible, the interfacial tension between them was used to calculate the pore size in the LLP measurement. During the test, the pressure of the testing N_2 was increased from 0 to 180 psi, step by step to replace the wetting liquid. At each stage, the pressure and flow were stabilised and recorded. Each measurement produced a value that was representative of the bottleneck size of the open pores. Alongside the MFPD, a full pore size distribution was produced.

3.3.3 Membrane Contact Angle

To calculate the contact angle (CA) an optical contact angle machine (Rame-hart Model 590 Advanced Goniometer) was used. 5 microlitre drops of water were dropped onto the membrane surface from a microsyringe. Both the top (NIPS-induced) and bottom (CCD-induced) were tested. Multiple measurements were taken to calculate an average CA for each sample.

3.3.4 Scanning Electron Microscope (SEM) Sample Preparation

To examine the membrane morphology an SEM (LEO 1525) was used. The membranes were first wetted in ethanol for 30 mins to replace the water content within the pores. To obtain clear cross sections for the membrane the wetted membranes were frozen in liquid nitrogen before snapping the membrane to retain a clear cross-section structure. The membranes samples were covered in carbon tape to ensure conductivity before the SEM sampling.

2

4 Results and Discussion

4.1 Comparing Fabrication Methods on Membrane Performance and Morphology (NIPS, CCD, CCD-NIPS)

Table 1: Effect of Fabrication Method on PWP and MFPD

Fabrication Method	**NIPS**	**CCD**	**CCD-NIPS**
PWP ($Lhr^{-1}m^2$)	7.81	860	704
MFPD (nm)	11.7	30.0	13.3

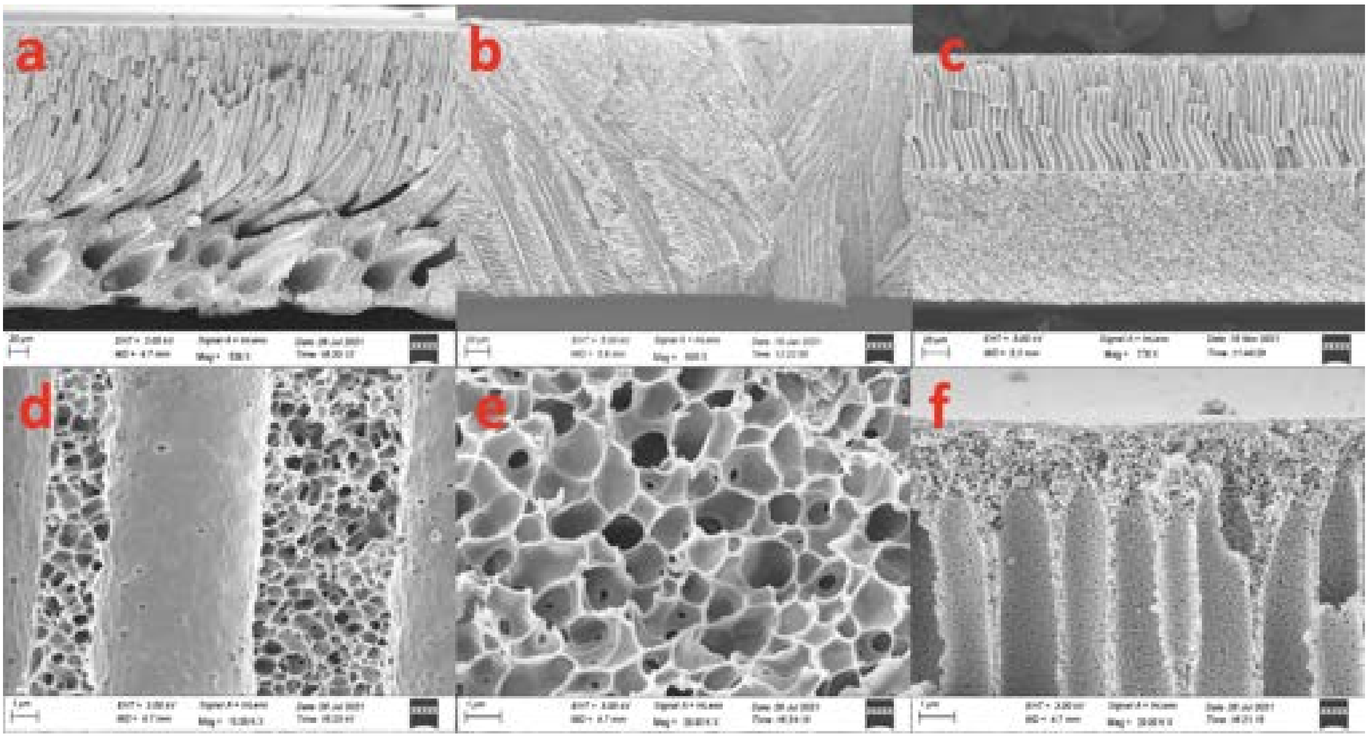

Figure 4: Effects of fabrication method SEM a) NIPS cross-section b) CCD cross-section c) CCD-NIPS cross-section d) NIPS finger-like macropore e) NIPS cellular discontinuous dead volume f) NIPS bincontiuous separation layer

4.1.1 Mean Flow Pore Diameter (MFPD) and Pure Water Permeance (PWP) Results

When comparing the different fabrication methods, it was found that the NIPS method had the smallest MFPD and the lowest PWP, at 11.7 nm and 7.81 $Lhr^{-1}m^2$ respectively. In contrast, the CCD method produced the largest MFPD and the highest PWP, of 30 nm and 860 $Lhr^{-1}m^2$ respectively [2]. CCD-NIPS produced a PWP of 704 $Lhr^{-1}m^2$ comparable to that of the CCD method whilst retaining a small MFPD of 13.3nm similar to that of the pure NIPS membrane.

4.1.2 Scanning Electron Microscope (SEM) Results

Figure 4 shows the SEM for the three fabrication methods. Each membrane consists of a separation layer that is attached to a supporting structure. The NIPS has a thin bicontinuous separation layer at the top of the membrane. This leads into the supporting structure, where finger-like pores develop into closed cellular regions of dead volume (volume where liquid cannot pass through). The cellular regions display a high tortuosity and were also found to be discontinuous. The NIPS membrane had a larger pore size distribution within its supporting structure.

By contrast, the CCD supporting structure demonstrated uniform lamellar pores, with negligible dead volume. A thin bicontinuous separation layer was observed at the membrane-solution/cooling-plate interface. Here the permeation paths were connected and much less tortuous.

Figure 4c shows the CCD-NIPS structure that forms. Here, we have the long finger-like NIPS structures that lead into an inter-connected and bicontinuous CCD-induced structure which has replaced the dead volume region present in the pure NIPS structure.

4.1.3 Discussion

The NIPS structure observed in the Figure 4a can be explained by the mass transfer attributed to the demixing of DMSO and subsequent intrusion of the non-solvent-based water from the coagulation bath into the membrane structure [8].

The discontinuous dead-volume found towards the bottom half of the membrane is formed via polymer-rich nucleation, whilst the tortuous bicontinuous intermediate region is formed via spinodal decomposition.

In CCD, the solvent (DMSO) begins to nucleate from the bottom and crystalise. The temperature gradient (driven by the undercooled temperature difference) is steep at the solution/cooling-plate interface and thus nucleation occurs quickly in this region forming a frozen front. Above the frozen front, the temperature gradient is flatter and thus alters the growth patterns due to the effect on nucleation mentioned in the theory. At this point, columnar and dendritic growth patterns are typically observed, as seen in Figure 4b. The separation layer consists of fine pores, whilst the supporting layer is composed of well-arranged interconnected lamellar microchannels which increase in size as they get further from the separation layer [2].

The principal interest in CCD-NIPS is to eradicate the effects of the dead-volume on membrane performance. We can see from the MFPD that the CCD-NIPS structure retains the selective nature associated with the small pore size of NIPS membranes. The PWP data demonstrates that the CCD-NIPS structure emulates the high permeance of the CCD structure. The fabrication technique for this membrane can explain these properties. From the SEM, it appears as though the top of the membrane (including the entirety of the separation layer) is NIPS-induced, whilst the bottom is CCD-induced. This is because as the membrane rests on the intermediate cooling plate, it does not freeze as it would via the traditional CCD method but instead is undercooled so that the viscosity increases. An increase in viscosity slows down the diffusional exchange highlighted in the theory section, causing the precipitation rate to decrease. Upon immersion, the formation of the NIPS-induced structure from the top is simultaneous with the formation of the CCD-induced structure from the bottom. Typically, for a fast precipitation rate, a steep temperature gradient is required. However, the lower temperature of the CCD-NIPS method at the cooling plate/membrane interface when compared to the CCD method causes a slower precipitation rate from the bottom of the membrane upon immersion. This is due to the smaller undercooled temperature difference in the CCD-NIPS method when compared to the pure CCD method. As a result, the kinetic and thermodynamic conditions in the CCD-NIPS mechanism are unfavourable for dead-volume formation as the slow precipitation rate enables the formation of a bicontinuous CCD-induced structure. This supports the trend in PWP and indicates that permeance is a function of the membrane supporting layer structure.

As mentioned above, the undercooled temperature difference for CCD-NIPS is considerably smaller than in pure CCD. This constrains the rate of homogeneous nucleation as the energy barrier is not exceeded. A lower rate of heterogeneous nucleation occurs and can explain the considerably larger pore sizes on the bottom surface of the membrane when compared to that produced by the CCD method.

4.2 Effects of Dwell Time on CCD-NIPS Membrane Performance and Morphology

Table 2: Effect of Dwell Time on CCD-NIPS on PWP, MFPD, Separation thickness and CA (3.s.f)

Dwell Time(s)	10	30	60
PWP ($Lhr^{-1}m^2$)	226	663	704
MFPD (nm)	9.60	12.1	13.3
Separation layer thickness (μm)	3.1	3.9	4.5
CA on CCD-induced side (°)	85.2	71.3	118
CA on NIPS-induced side (°)	51.3	57.8	59.8

4.2.1 Mean Flow Pore Diameter (MFPD) and Pure Water Permeance (PWP) Results

When exploring the effects of dwell time on the properties of the CCD-NIPS membranes, it was observed that the PWP increased with dwell time. The change in MFPD is marginal, though there is a slight increase with dwell time. Table 2 demonstrates the relationship between dwell time, PWP and MFPD. The pore size distribution was found to be consistent for all dwell times.

4.2.2 Scanning Electron Microscope (SEM) Results

The SEM images in Figure 5 show that as the dwell time increased, the ratio of NIPS-induced region (top side) to CCD-induced region (bottom side) in the supporting structure increased. The separation layer became thicker for longer dwell times. It can also be observed that the pore size on the bottom of the membrane structure increases as the dwell time increases.

4.2.3 Contact Angle (CA) Results

It can be seen in table 2 that the contact angle on the NIPS-induced side was smaller than that on the CCD-induced side for all dwell times. It was found that as the dwell time increased, so did the contact angle. An increase in dwell time from 10s to 60s saw a less significant change in contact angle on the NIPS-induced side (51.3° to 59.8°) when compared to the change on the CCD-induced side (85.2° to 118.4°).

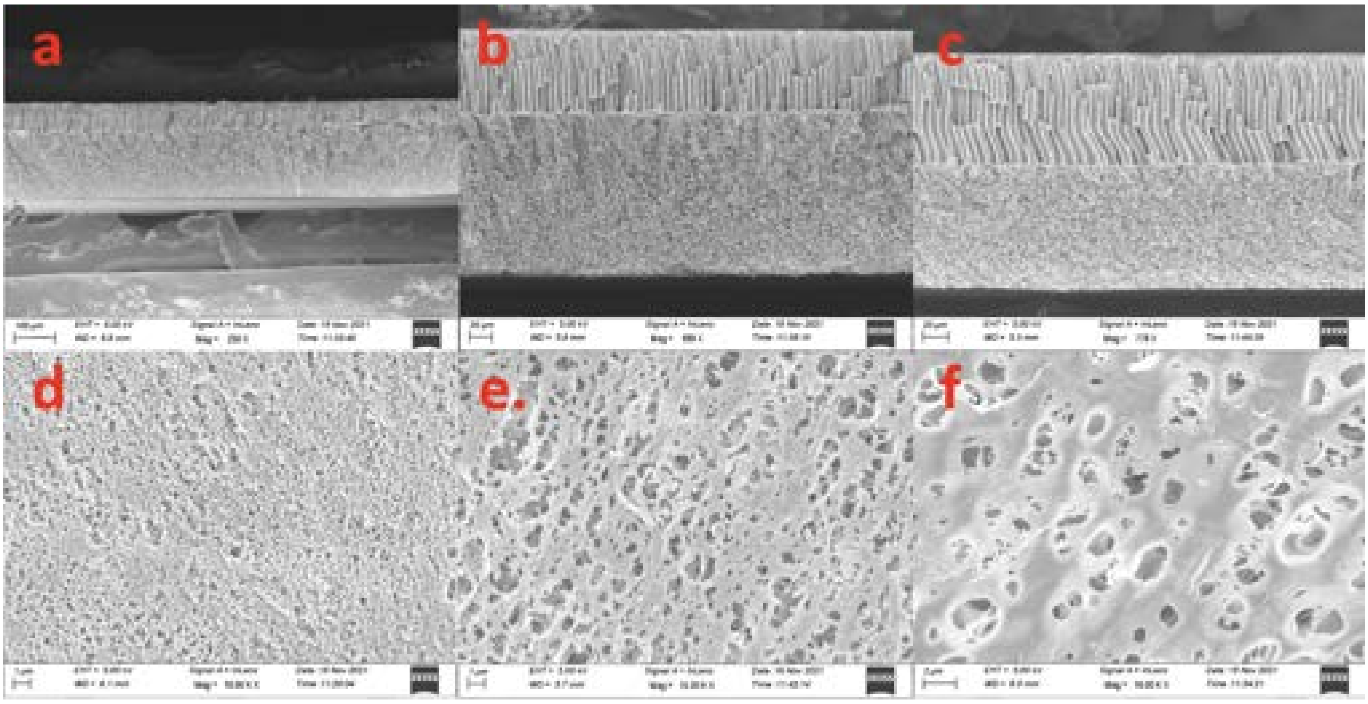

Figure 5: Effects of dwll time SEM a) 10s CCD-NIPS cross-section b) 30s CCD-NIPS cross-section c) 60s CCD-NIPS cross-section d) 10s CCD-NIPS plate/film surface e) 30s CCD-NIPS plate/film surface f) 60s CCD-NIPS plate/film surface

4.2.4 Discussion

The increase in PWP with dwell time can be attributed to the changes in the mass transfer that affect the DMSO crystallization rate. This, in turn, affects the polymer precipitation rate. The SEM pictures in Figure 5 can help explain the theory behind this. The visual trend in the ratio of NIPS-induced region to CCD-induced region (Figure 5a-c) in the supporting structure is derived from the effects of viscosity. The extension of the finger-like pores is limited by the precipitation rate of the polymer-rich region. The slower the precipitation of the polymer-rich region, the longer the water phase permeates through the supporting layer, forming the finger-like pores. As a result, as the dwell time increases, the further the finger-like pores can extend into the supporting layer, increasing the NIP to CCD-induced ratio and thus increasing the permeation rate.

Gelation can be used to explain this slower precipitation rate in the polymer-rich region. Gelation of the casting film can be observed at the cooling-plate/membrane-solution interface as the temperature difference increases the viscosity of the solution. Consequently, the level of gelation at the membrane-solution/casting-plate interface increases with dwell time. As the gelation increases, the viscosity start to build up from the solution-casting plate interface, and this propagates inside the polymer solution. This viscosity limits the diffusion of DMSO out of the polymer-rich phase, decreasing the DMSO crystallization rate, which in turn, slows down the polymer precipitation rate. As explained in the theory section, this results in longer finger-like pores which have penetrated deeper before reaching the glass transition boundary due to the abundant supply of solvent/non-solvent. Essentially, the freezing from the bottom of the membrane post immersion becomes slower as dwell time increases, yet the rate of the water intrusion remains unaffected. Slow precipitation of the PES also increases the pore size in the CCD-induced region. This can be seen in the SEM pictures in Figure 4 (d-f), where pore size increases as dwell time increases.

The insignificance of the effects of dwell time on the MFPD in Table 5 highlights that the separation layer is relatively unaffected by the induced concentration gradient. The relatively consistent MFPD demonstrates that the NIPS-induced region retains the selectivity of a pure NIPS membrane whilst enabling the larger CCD-induced pores channels to form in the supporting structure.

The contact angle is also reflective of the surface pore distribution and surface roughness – a measurement that was not calculated during the investigation. From the literature, it is apparent that the NIPS separation layer is hydrophilic and allows water to enter the membrane structure with ease. Conversely, the more hydrophobic tendencies of the CCD-induced surface are optimal for allowing water to exit the membrane structure. Thus, the two works in tandem to allow water to pass through the membrane [14].

Therefore, the CCD-induced surface for a dwell time of the 60s, can either be considered to have hydrophobic tendencies or low surface roughness. A conclusion cannot be drawn in regards to the hydrophilicity membrane surfaces due to the inconsistencies in the data collected. These inconsistencies can be attributed to the mishandling of the membrane when performing the contact angle test. Wenzel's equation suggests that contact angle is a function of the actual contact angle and surface roughness [14].

4.3 Effects of PVP Additive on CCD-NIPS Performance and Morphology

Table 3: Effect of Additive Concentration on CCD-NIPS on PWP, MFPD and CA (3.s.f)

Additive concentration (wt.%)	**0**	**1**	**4**
PWP ($Lhr^{-1}m^2$)	704	559	279
MFPD (nm)	13.3	18.8	10.1
CA on CCD-induced side (°)	118	75.4	51.3
CA on NIPS-induced side (°)	59.8	58.1	51.0

2

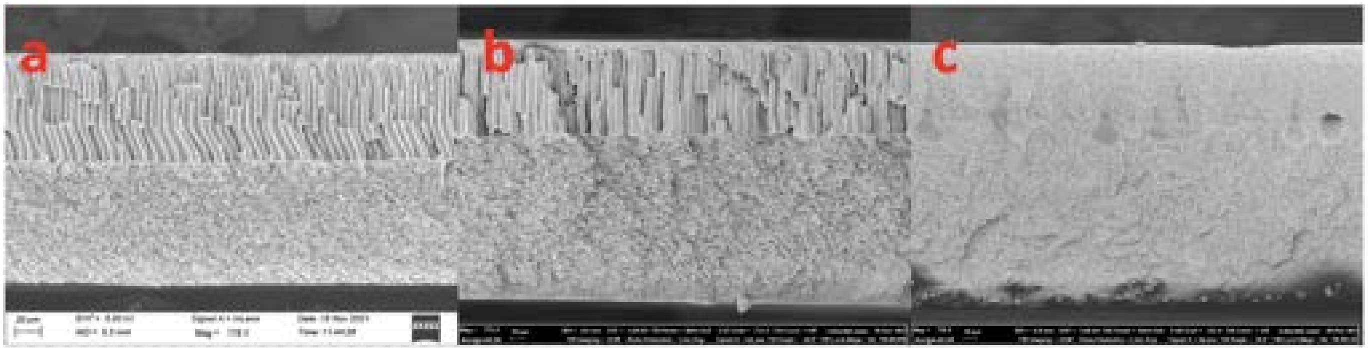

Figure 6: The effects of additive concentration on CCD-NIPS SEM a) 0wt.% b) 1wt.% c) 4wt.%

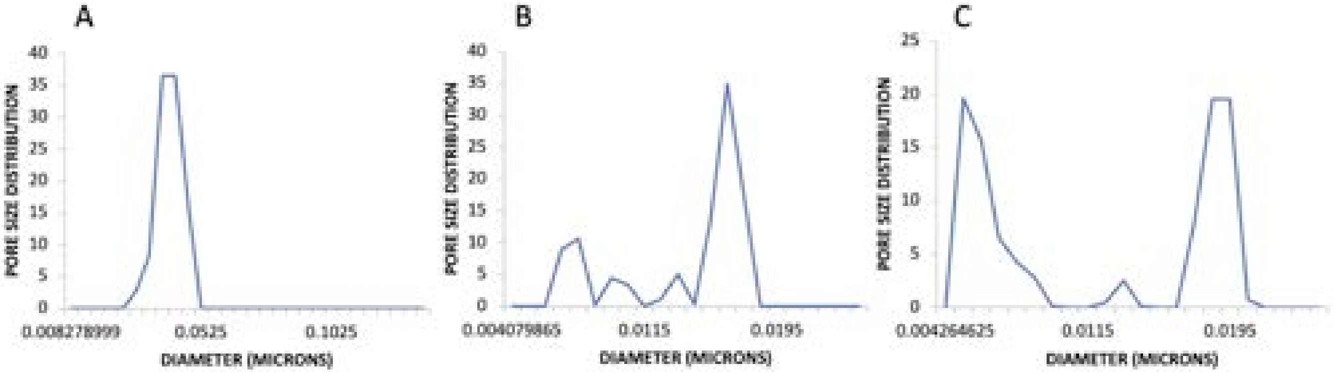

Figure 7: Pore Size Distribution vs Diameter (fitted) for CCD-NIPS membranes with additive a) 0wt.% PVP b) 1wt.% PVPc) 4wt.% PVP

4.3.1 Mean Flow Pore Diameter (MFPD) and Pure Water Permeance (PWP) Results

An inverse relationship was observed between the concentration of PVP additive in the membrane solution and the PWP. As PVP concentration increased from 1 wt.% to 4 wt.%, the PWP decreased form 559 $Lhr^{-1}m^2$ to 279 $Lhr^{-1}m^2$. An interesting relationship was observed for the MFPD, initially, an increase in additive from 0 to 1 wt.% saw MFPD rise from 13.3nm to 18.8nm. However, a subsequent increase in additive concentration to 4 wt.% saw the MFPD drop to 10.1nm. It is worth noting, that the pore size distribution was much less consistent when the membrane solution contained the PVP additive.

4.3.2 Pore Size Distribution

An increase in PVP addive results in a broader pore size distribution as seen in Table 7.

4.3.3 Scanning Electron Microscope (SEM) Results

The 1 wt.% PVP additive demonstrated similar structural properties as the membrane produced without PVP additive. The separation layer thickness decreased from 4.5nm (0 wt.% PVP) to 3.7nm (1 wt.% PVP). However, the increase of PVP additive to 4wt.% saw a deterioration in this regular structure: the NIPS-induced layer, CCD-induced layer and the separation layer were no longer distinguishable - instead a sponge-like cross-section was observed.

4.3.4 Contact Angle

Table 3shows that as contact angle decreases on both the NIPS-induced and CCD-induced surfaces, this effect is more significant on the CCD-induced side.

4.3.5 Discussion

Given the large molecular weight of PVP, even a small concentration can have a significant impact on the viscosity and subsequent mass transfers during phase separation. This increase in viscosity, however, is different to that caused by the effects of gelation and dwell time discussed in section 4.2. This change in viscosity is uniform throughout the cast-solution, not just at the cooling-plate surface.

Previously we have defined two main kinetic factors effecting the rate of polymer precipitation subsequent pore size. 1) The demixing rate of DMSO with water and 2) the DMSO crystallization rate in the bottom region. The increased viscosity throughout the entire solution hinders both of these factors.

For higher concentrations of PVP, larger residual PVP particles remain within the membrane post phase separation, altering the morphology. Therefore, upon addition of PVP we observe a shorter finger-like region as seen in Figure 6b). The shorter finger-like pores causes an increase in the permeation pathway and hence a decrease in permeability. The increased viscosity also causes both the NIPS and CCD-induced regions precipitates slower. This slower precipitation rate, as explained in the theory, promotes formation of larger pores. This explains the unusual trend from 0 wt.%- to 1 wt.% of an increased pore size from 13.3nm to 18.8nm but a decreased permeability from 703 $Lhr^{-1}m^2$ to 559$Lhr^{-1}m^2$.

When PVP is increased to 4% a drastic increase in viscosity is observed causing a complete deterioration of the CCD-NIPS typical structure. As a result, the two kinetic factors previously explained are both limited so much that an entirely new mechanism controls the morphology. The precipitation rate is so slow that it induces large regions of closed pores forming discontinuous pore structure. The effect of this can be seen in Figure 6c.

It is also worth noting that the addition of PVP additive leads to a broader pore size distribution which is undesirable. This can be seen in Figure 7.

As a side-note, it is known that PVP is a hydrophilic material, the effect of this can be seen by the decrease in contact angle as seen in Table 3 - an effect particularly amplified on the CCD-induced surface. Although this theory may support the findings, it neglects the effects of surface roughness on the contact angle. [14].

Overall, the addition of PVP additive hinders performance of our CCD-NIPS membranes.

5 Conclusion

In this study, a CCD-NIPS technique, inspired by the synergy of directional freezing during immersion precipitation of a polymer solution, was developed. Immersion precipitation created a tight UF-ranged top layer, and directional freezing aligned the membrane substructure. The resultant membrane showed excellent pore connectivity with the absence of dead-volume pores, yielding a water permeation rate a magnitude higher than its pure NIPS counterpart. The unique structure introduces versatile tunability to the final membrane performance. The influence of dwell time and pore-forming agent on the membrane performance was investigated. The results show that both variables are essential to alter the membrane pore size and permeance. The new membrane geometries demonstrated great potential to replace the current membrane fabrication techniques, namely the NIPS and TIPS methods, and to provide a more economically viable route to fabricate CCD-type membranes.

6 Outlook

Looking to the future, further investigation into the effects of surface roughness on the membrane surface will improve the current understanding of the significance that contact angle plays on CCD-NIPS membrane performance. Additionally, a further examination into the effects of dwell time on the mechanical stability of the structure will validate the commercial use of this method. The temperature dependence of the CCD-NIPS method was not tested during this investigation and thus, the economic benefits that may arise are yet to be discovered. Finally, a new proposed flash-freezing method could be explored, to see if a true CCD-like structure can be produced. A full cost-benefit analysis can be conducted to evaluate the industrial relevance that such a method could achieve. It is hypothesized that this flash-freezing method may in fact produce the best performance results.

7 Acknowledgement

The authors of this report would like to thank Professor Kang Li and Hao Peng for their continued support and guidance throughout the duration of this project. Special recognition is given to Imperial College London for allowing use of their facilities.

References

[1] Yutie Liu M.R. Moghareh Abed K. Li Fu Liu, N. Awanis Hashim. Progress in the production and modification of pvdf membranes. 2011.

[2] Jing Ji Kang Li Bo Wang. Crystal nuclei templated nanostructured membranes prepared by solvent crystallization and polymer migration. 2016.

[3] J.W.A. van den Berg J. Feijen P. van de Witte 1, p.j. Dijkstra. Phase separation processes in polymer solutions in relation to membrane formation. 1996.

[4] Congcong Chen K. Li Bo Wang, Jing Ji. Porous membranes prepared by a combined crystallisation and diffusion (ccd) method: Study on formation mechanisms. 2018.

[5] Xing Yang Xinhai Cai Ji Lu Tonghu Xiao, Peng Wang. Fabrication and characterization of novel asymmetric polyvinylidene fluoride (pvdf) membranes by the nonsolvent thermally induced phase separation (ntips) method for membrane distillation applications. 2015.

[6] T. Matsuura b G. Chowdhury b G. Pleizier c J.P. Santerre D.B. Mosqueda-Jimenez, R.M. Narbaitz. Influence of processing conditions on the properties of ultrafiltration membrane. 2003.

[7] Misgina Tilahun Tsehaye Bart Van der Bruggen Nicholas Evenepoel, Shufen Wen. Potential of dmso as greener solvent for pes ultra- and nanofiltration membrane preparation. 2018.

[8] William J. Koros Scott A. McKelvey. Phase separation, vitrification, and the manifestation of macrovoids in polymeric asymmetric membranes. 1996.

[9] J.W.A van den Berg A.J.Reuvers and C.A Smolders. Formation of membranes by means of immersion precipitation: Part i. a model to describe mass transfer during immersion precipitation. 1987.

[10] C. A. Smolders S.-G. Li, Th. van den Boomgaard and H. Strathmann. Physical gelation of amorphous polymers in a mixture of solvent and nonsolvent. 1996.

[11] Zhiping Lai Bo Wang. Finger-like voids induced by viscous fingering during phase inversion of alumina/pes/nmp suspensions. 2012.

[12] J.W.A. van den Berg J. Feijen P. van de Witte 1, p.j. Dijkstra. Phase separation processes in polymer solutions in relation to membrane formation. 1996.

[13] M. Mulder. Membrane preparation — phase inversion membranes. 2000.

[14] Robert N. Wenzel. Surface roughness and contact angle. 1949.

Optimisation of Nucleoside Modifications *in-vitro* transcribed mRNA

Ellson Chow and Darrel Lee
Department of Chemical Engineering, Imperial College London, U.K.

Abstract Nucleoside-modifications of *in-vitro* transcribed (IVT) mRNA can confer increased translational capacity and biological stability while diminishing immunogenicity, by preventing the induction of Type-I interferons (IFN-I). However, IFNs are essential to activate antigen presenting cells and elicit adequate T-cell immune responses for successful immunization. In this research, a firefly luciferase assay was used to transfect HEK293T.17 and HELA cell lines to find out the optimal ratio between unmodified and nucleoside-modified saRNA that provides the greatest vaccine efficacy, yield, and stability. Nucleoside modifications φ-GTP and Ʊ-*x*TP (*x* = A,G,C,U) displayed promising results as gene expression increases when they are incorporated into mRNA. The presence of a self-amplifying RNA (saRNA) cap structure and its effects on effective yield are also demonstrated, with it reducing mRNA manufacturing yield but increasing gene expression by multiple folds. However, capping and nucleoside modifications showed minimal differences between the functional half-lives of saRNA.

Introduction

Vaccinations currently prevent 4 to 5 million deaths a year, proving itself to be one of modern medicine's greatest successes. However, an additional 1.5 million deaths can be avoided if global vaccination coverage improves [1]. Not only does immunisation through vaccines help to prevent and control numerous infectious diseases, but they are also essential to ensuring quality education and protecting a healthier workforce for economic development. As the number and diversity of epidemics and pandemics gradually but inexorably increase, there is an urgent need to improve on conventional vaccine production methods to tackle these challenges quicker and more effectively. While conventional vaccine development takes an average of 8 to 14 years to commercialize and costs 0.55 to 1 billion USD, emerging RNA platform technologies, such as the messenger RNA (mRNA) and self-amplifying RNA (saRNA) platforms, can promote pre-clinical development at unprecedented speeds and expedite commercializing a new vaccine product to just 0.5 to 2 years [2].

Since conventional vaccines deliver live attenuated or inactivated pathogens into the body [3], manufacturing them requires inflexible, specifically catered single-product processes and facility development. However, RNA vaccines introduce genetic instructions for the vaccinated person's own cells to produce antigens and build immunity [4], thus only the RNA sequence encoding for a vaccine antigen needs to be known and changed, while the rest of the production process from equipment to quality control remains the same [2]. This is of paramount advantage as a facility dedicated to RNA platforms can rapidly manufacture vaccines against multiple viruses once the sequence encoding the immunogen is available [5].

To introduce heterologous mRNA into the cytoplasm of the cell, innate immune system receptors such as Toll-like receptors (TLRs) must be bypassed. TLRs are a natural line of defence against invading pathogens, preventing the translation of foreign mRNA. Activating RNA receptors such as TLR7 and TLR8 can greatly reduce cellular protein synthesis, induce cytokine production, and possibly lead to programmed cell death [6], thus initially rendering mRNA vaccines unfeasible due to its labile and immunogenic nature. However, studies have shown that the inflammatory nature of exogenous RNA can be mitigated by modifying the nucleosides in mRNA, where nucleoside-modified mRNA (modRNA) are produced either by incorporating naturally modified bases in eukaryotes or synthetic nucleoside analogs into transcripts [7]. For instance, transcribed mRNAs containing pseudouridine, instead of the standard nucleoside uridine, possess superior translational capacities and biological stability, while diminishing immunogenicity through the reduction of IFN-I produced both *in vitro* and *in vivo* [8]. To combat the COVID-19 pandemic, Pfizer-BioNTech lead mRNA vaccine candidate BNT162b2 also uses a type of nucleoside modification, N1-methylpseudouridine, in RNA synthesis to produce the active substance of single-stranded, 5'-capped mRNA that is translated into a codon-optimised sequence encoding the spike antigen of SARS-CoV-2 [9].

We report an optimal ratio of unmodified to nucleoside-modified saRNA that manages to bypass TLRs just enough to not invoke a potent immune response that renders the vaccine ineffective, while also ensuring that sufficient antigen presenting cells are activated to elicit ample T-cell responses for adaptive immunity. The proportion of unmodified to nucleoside-modifications of φ-GTP and Ʊ-*x*TP in mRNA are 75:25 and 25:75 respectively. We also report that the capping of saRNA results in higher gene expression albeit reducing manufacturing yield.

Quality by Design framework

Conventional development of process relies on empirical approach that pivots on inspection and constant end-product testing to determine the quality of the products. This process focuses on process reproducibility and creates fixed products which are difficult to change.

To improve the producer's ability to tailor their products and meet the needs of the consumer, QbD framework was selected. Quality by Design is a systematic approach which thoroughly analyse and optimise the development process to effectively identify quality issue before the finished product is developed [10]. This would save cost and time which are critical to ensure quick and wide roll out of vaccines. The whole QbD process consist of five major activities: 1. Define, 2. Discover, 3. Design, 4. Develop and 5. Deliver [11]. The information from this study contributes to the Design section of the QbD process where the product is researched on to gain an advantage over the competitors and existing products.

This study provides an optimal ratio of unmodified to modified ratio and an understanding of capping of the mRNA on in-vitro transcription and cell-based translation. This information can be applied in the vaccine development process in order to develop effective vaccines for the consumers.

Methods

All experiments were conducted by K. Samnuan and data in this research was obtained using the following protocol [12].

Plasmid DNA Synthesis and Purification

The plasmid DNA (pDNA) construct used for the synthesis of RNA replicons encodes for the non-structural proteins of Venezuelan Equine Encephalitis Virus (VEEV), wherein firefly luciferase (fLuc) gene (GenBank: AB762768.1) (GeneArt, Germany) was cloned into the plasmid right after the sub-genomic promoter using the restriction sites NdeI and MluI-HF. The pDNA was transformed into Escherichia coli and grown in 100 mL cultures in lysogeny broth (LB) media with 100 µg/mL carbenicillin (Sigma-Aldrich, U.S). Isolation and purification of the pDNA was done using a Plasmid Plus maxi kit (QIAGEN, UK) and a NanoDrop One Microvolume UV-Vis Spectrophotometer (ThermoFisher, UK) was used to measure the concentration and purity of the pDNA. The pDNA sequence was confirmed with Sanger sequencing (GATC Biotech, Germany). Prior to RNA IVT, pDNA was linearized using MluI for 3h at 37 °C, according to the manufacturer's instructions.

RNA Synthesis and Quantification

1 µg of linearized DNA template was used and kept constant across all IVT reactions with a final volume of 100 µL per reaction which were incubated at 37 °C for either 2, 4 or 6 hours. RNA yield was measured right after IVT using the Qubit RNA Broad Range Assay kit with the Qubit Fluorometer (Thermo Fisher, UK) according to the manufacturer's protocol.

RNA Purification and RNA Gel

After IVT, RNA was purified using MEGAclear™ Transcription Clean-up Kit (Thermo Fisher, UK) according to the manufacturer's protocol. To access the quality of the RNA, purified RNAs and the RNA Millennium Marker Ladder (Thermo Fisher, UK) were mixed with 2x RNA loading dye (Thermo Fisher, UK) and incubated at 50 °C for 30 min to denature the RNA. After purification, ScriptCap m7G Capping System and ScriptCap Ʊtransferase (CellScript) was used to introduce a Cap 1 system. Modified Nucleoside Triphosphates (NTPs) were obtained individually from Trilink. Each NTP concentration is maintained at 10nM. For example, if 75% Ʊ-GTP was used it would contain 7.5mM Ʊ-GTP and 2.5mM GTP. A 1.2 % agarose gel with 1x NorthernMax Running Buffer (Thermo Fisher, UK) was prepared. After incubation, the denatured ladder and samples were added to the gel and the gel was ran at 80 V for 45 min. The gel was then imaged on a GelDoc-It2 (UVP, UK).

Cells and In Vitro Transfections

HEK293T.17 cells (ATCC, USA) were cultured in complete Dulbecco's Modified Eagle's Medium (DMEM) (Gibco, Thermo Fisher, UK) containing 10 % fetal bovine serum (FBS), 1 % L-glutamine and 1 % penicillin-streptomycin (Thermo Fisher, UK). Cells were plated in a 6-well plate at a density of 1.08 x10^6 cells per well 48 h prior to transfection. Transfection of saRNAs encoding different GOIs and mRNA fLuc was performed using Lipofectamine MessengerMAX (Thermo Fisher, UK) according to the manufacturer's instructions.

Flow Cytometry

Transfected cells were harvested and resuspended in 1mL of FACS buffer (PBS + 2.5 % FBS) at a concentration of 1 x 107 cells /mL. 100 µL of the resuspended cells was added to a FACS tube and stained with 50 µL of Live/Dead Fixable Aqua Dead Cell Stain (Thermo Fisher, UK) at a 1:400 dilution on ice for 20 min. Cells were then washed with 2.5 mL of FACS buffer and centrifuged at 1750 rpm for 7 min. The cells that were transfected with a fLuc RNAs were permeabilized with Fixation/ Permeabilization solution kit (BD Biosciences, UK) for 20 min before washing them with 2.5 mL of FACS buffer and centrifuging at 1750 rpm for 7 min. Cells transfected with the fLuc RNAs were stained with 5 µL of anti-Luciferase antibody (C-12) PE: sc-74548 PE (Santa Cruz Biotechnology, US) while the MDR1 replicons were stained with 5 µL of PE antihuman CD243 (ABCB1) antibody clone 4E3.16 (Biolegend, US). After staining for 30 min on ice, cells were washed with 2.5 mL of FACS buffer, centrifuged at 1750 rpm for 7 min and resuspended with 250 µL of PBS. Cells were fixed with 250 µL of 3 % paraformaldehyde for a final concentration of 1.5 %. Samples were analyzed on a LSRFortessa (BD Biosciences, UK) with FACSDiva software (BD Biosciences, UK). Data were analyzed using FlowJo Version 10 (FlowJo LLC, Ashland, OR, USA).

Calculation methods

Data for post-capped (PC) mRNA with a ratio of 100:0 unmodified to nucleoside-modified bases will serve as a basis for normalisation calculations. Relative yield, Y_R, for each respective nucleoside-modification is thus calculated as:

$$Y_R = \frac{Y}{Y_{PC\ 100:0}} \tag{1}$$

Where Y is the yield and $Y_{PC\ 100:0}$ is the yield for post-capped (PC) mRNA with a ratio of 100:0 unmodified to nucleoside-modified bases.

The mRNA efficacy, E, was measured by the luciferase expression in the transfected cells after 24 hours. The efficacy of the post-capped sample with a 100:0 ratio of unmodified to modified bases, $E_{PC\ 100:0}$, was taken as a basis to measure relative efficacy, E_R, as shown:

$$E_R = \frac{E}{E_{PC\ 100:0}} \tag{2}$$

Effective yield, σ, is calculated by multiplying the relative yield and relative efficacy.

$$\sigma = Y_R E_R \tag{3}$$

The functional half-life of an mRNA was measured by following the luciferase expression at 24h, 48h, and 72h time points. Data is normalised to their respective luciferase expression at an initial time of 24h, thus a fractional change in amount of mRNA translated, and not an absolute change, is considered.

The mRNA functional half-life is defined as the amount of time it takes to reach 50% of its maximum luciferase activity, as shown in Equation 4:

$$\frac{E}{E_{max}} = 0.5 \tag{4}$$

Results

General overview

Data for five ratios of unmodified to nucleoside-modified mRNA were collected: 100:0, 75:25, 50:50, 25:75, and 0:100. ø-UTP, φ-dGTP, φ-GTP, η-UTP, Ʊ-*x*TP (*x*=A, C, G, U), ʌ-*x*TP (*x*=A, C, U, T) was analysed but only φ-GTP and Ʊ analogs displayed improvements in effective yield when they were incorporated into saRNA. Hence, they were selected for further analysis. All five datasets were available for the saRNA incorporated with φ-GTP but only the first four were available for Ʊ-*x*TP (with the ratio 0:100 dataset being omitted). All datasets include both uncapped and post-capped saRNA. In the comparison of manufacturing yield, efficacy yield and effective yield, values were normalised relative to post capped at 100:0 unmodified to modified base to cancel out noise in data provided.

Manufacturing yield

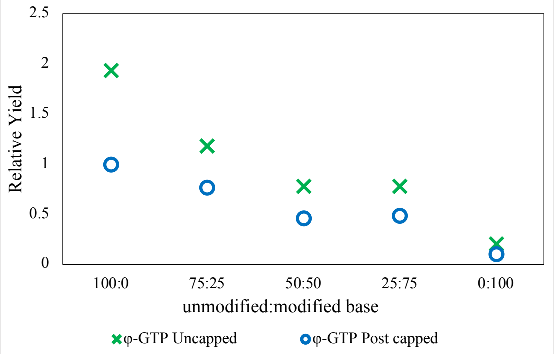

Figure 1. Relative manufacturing yield for φ-GTP

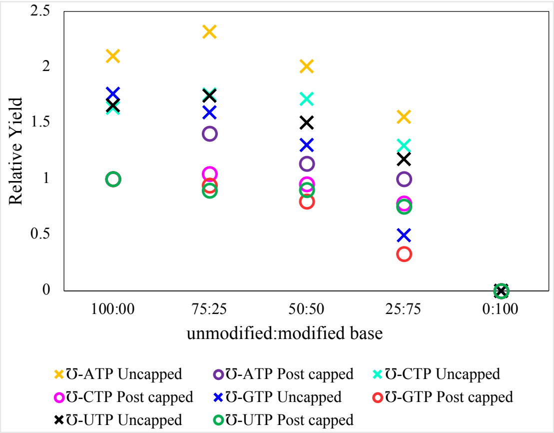

Figure 2. Relative manufacturing yield for Ʊ-*x*TP

Table 1. 2nd order polynomial coefficients for manufacturing yield. $y=ax^2+bx+c$, *where y is the manufacturing yield and x is the proportion of modified bases added*

Capping	Ʊ-	a	b	c
Post capped	ATP	-0.136	0.65	0.523
	CTP	-0.055	0.202	0.856
	GTP	-0.104	0.304	0.788
	UTP	-0.103	0.346	1.43
Uncapped	ATP	-0.167	0.64	1.65
	CTP	0.135	0.572	1.187
	GTP	-0.16	0.391	1.51
	UTP	0	-0.0725	1.07

Across all samples, there is a greater manufacturing yield for uncapped saRNA than for post-capped mRNA, ranging from about 1.5 to 2 times more as seen in figure 1 and 2. Independent of capping, manufacturing yield of saRNA decreases linearly with an increase in proportion of φ-GTP incorporated. A linear best fit line is plotted to calculate the gradient, m, to find the rate of decrease with respect to an increase in nucleoside modification incorporated. This decrease is strikingly more in mRNA incorporated with φ-GTP, where m = -0.389 for uncapped mRNA, with a peak relative manufacturing yield at 1.94 when no modified bases were added. For post-capped saRNA, m = -0.206, and the highest yield was also obtained when no modified bases were added. There was no standard deviation for manufacturing yield as only 1 data point was provided.

On the other hand, a second-degree polynomial model was used to describe the concave trend of Ʊ-*x*TP modified saRNA (Table 1) where the maximum manufacturing yield was achieved at a 75:25 ratio. The maximum relative manufacturing yield of Ʊ-ATP, Ʊ-CTP, and Ʊ-UTP respectively are 1.41, 1.04, and 1 for post-capped and 2.31, 1.75, and 1.74 for uncapped. The incorporation of Ʊ-GTP resulted in a general decrease in manufacturing yield.

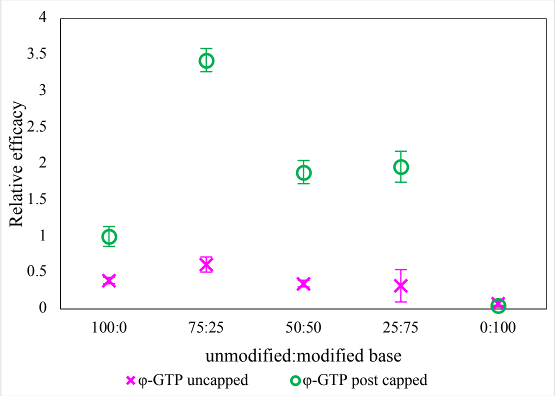

Figure 3. Relative efficacy for φ-GTP in HEK293T.17

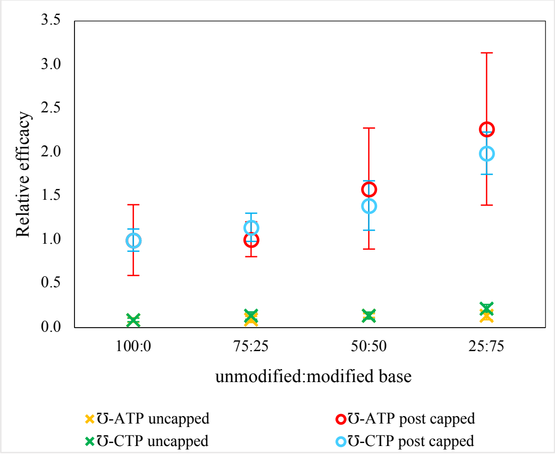

Figure 4. Relative efficacy for Ʊ-ATP and Ʊ-CTP

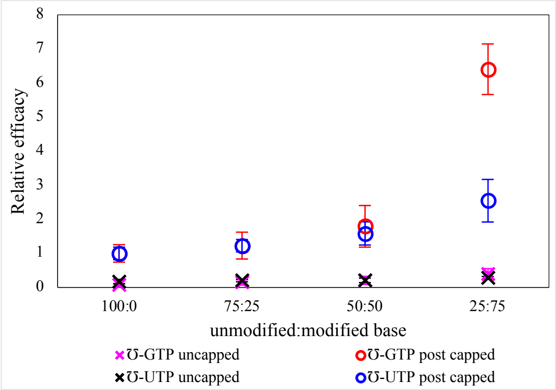

Figure 5. Relative efficacy for Ʊ-GTP and Ʊ-UTP

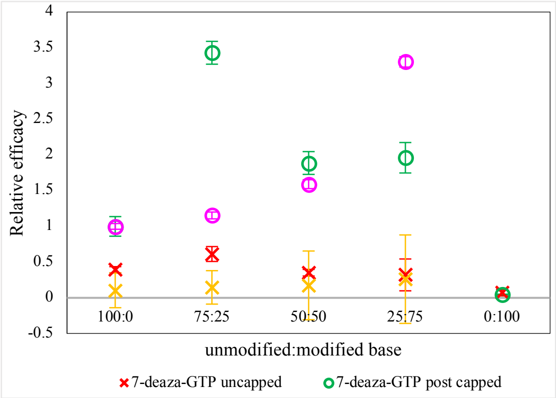

Figure 6. Indicative graph for Relative efficacy in HEK293T.17 cells

Table 2. 2nd order polynomial coefficients for relative efficacy. **y**=*ax*^{2}+*b***x**+*c, where y is the relative efficacy and x is the proportion of modified bases added*

HEK293T.17

Capping	Analog	a	b	c
Post capped	Ʊ-ATP	0.168	-0.4	1.21
	Ʊ-CTP	0.113	0.24	1.141
	Ʊ-GTP	1.09	-3.8	3.9
	Ʊ-UTP	0.183	0.42	1.26
	φ-GTP	-0.505	2.69	-0.857
Uncapped	Ʊ-ATP	0.0015	0.026	0.06
	Ʊ-CTP	0.008	0.0007	0.09
	Ʊ-GTP	0.027	0.03	0.078
	Ʊ-UTP	0.01	0.02	0.187
	φ-GTP	-0.050	0.209	0.28

HELA

Capping	Analog	a	b	c
Post capped	Ʊ-ATP	0.379	0.776	1.56
	Ʊ-CTP	0.3	0.9	1.64
	Ʊ-GTP	2.75	9.6	8.27
	Ʊ-UTP	0.27	0.8	1.5
	φ-GTP	-0.455	2.38	-0.68
Uncapped	Ʊ-ATP	0.0029	0.034	0.07
	Ʊ-CTP	0.03	0.095	0.16
	Ʊ-GTP	0.0039	0.024	0.076
	Ʊ-UTP	-0.1	0.55	0.13
	φ-GTP	0.1189	0.601	0.039

The efficacy, as calculated from Equation 2, will allow us to determine if the modification enhances the translation of the saRNA in both HEK293T.17 and HELA cells. A high efficacy means that there is large amount of translation of the saRNA into antigens which would trigger an immune response more effectively.

In general, efficacy of post-capped RNA is 5 to 17 times higher than uncapped RNA for Ʊ-XTP and 2 to 6 times for φ-GTP in both HEK293T.17 and HELA cells. This was especially clear at the 75:25 ratio where φ-GTP has relative luciferase expression of 0.61 in uncapped and 3.43 for post capped, a 6-fold increase in HEK293T.17 cells. The effectiveness of post capping was more drastic for Ʊ-XTP in HEK293T.17 cells where a maximum of 16-fold increase in luciferase expression was observed in 25:75 ATP to Ʊ-ATP ratio, where the post capped relative efficacy was 2.27 as compared to 0.14 in uncapped.

A ratio of 75:25 for GTP:φ-GTP and a ratio of 25:75 for *x*TP:Ʊ-*x*TP were found to produce the highest efficacy in both types of cells, as seen in Figure 6. The maximum point and its respective modified to unmodified base ratio is displayed in table 3.

Table 3. maximum relative efficacy for each nucleotides and the respective optimal unmodified to modified base ratio

Cell	Capping	Analog	Maximum effective yield	Peak ratio
HE293T.17	Uncapped	Ʊ-ATP	0.14	50:50
		Ʊ-CTP	0.22	75:25
		Ʊ-GTP	0.4	75:25
		Ʊ-UTP	0.29	75:25
		φ-GTP	0.61	25:75
	Post capped	Ʊ-ATP	2.27	25:75
		Ʊ-CTP	1.99	25:75
		Ʊ-GTP	6.4	25:75
		Ʊ-UTP	2.55	25:75
		φ-GTP	3.42	75:25
HELA	Uncapped	Ʊ-ATP	0.17	50:50
		Ʊ-CTP	0.27	25:75
		Ʊ-GTP	0.24	25:75
		Ʊ-UTP	0.98	50:50
		φ-GTP	0.9	75:25
	Post capped	Ʊ-ATP	4.69	25:75
		Ʊ-CTP	2.87	25:75
		Ʊ-GTP	14.4	25:75
		Ʊ-UTP	2.56	25:75
		φ-GTP	2.82	75:25

φ-GTP

Incorporation of φ-GTP during transcription results in saRNA with superior translation ability. The effective efficacy can be modelled using a 2nd order polynomial which can be found in Table 3. An average standard deviation (aSD) was 9% for post capped and 35% for uncapped in HEK293T.17 cells. The high average standard deviation of 31% and 46% for uncapped and post capped will affect the reliability of the φ-GTP model's prediction in HELA cells.

Ʊ-xTP

Ʊ-*x*TP exhibits the most positive results, with the results showing that 75% modified nucleotides achieved maximum translation. The relationship between modified base to relative efficacy is represented in a 2nd order polynomial as seen in table 2.

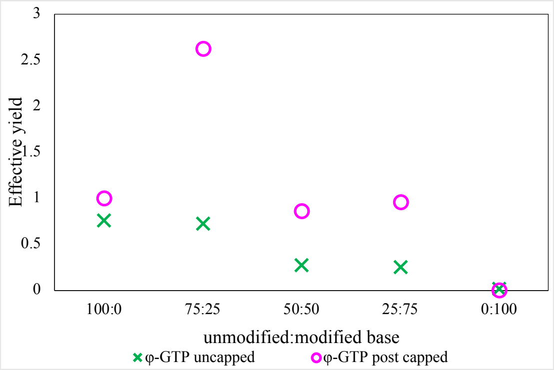

Figure 7. Effective yield of φ-GTP in HEK293T.17 cells

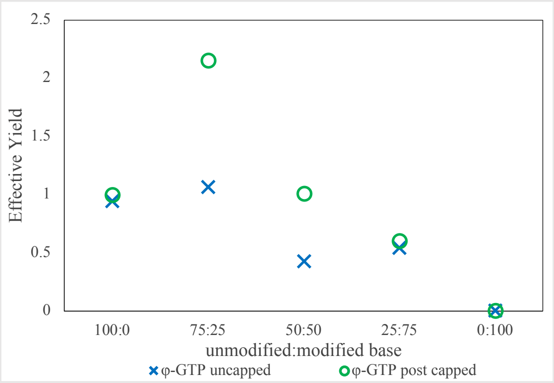

Figure 8. Effective yield of φ-GTP in HELA cells

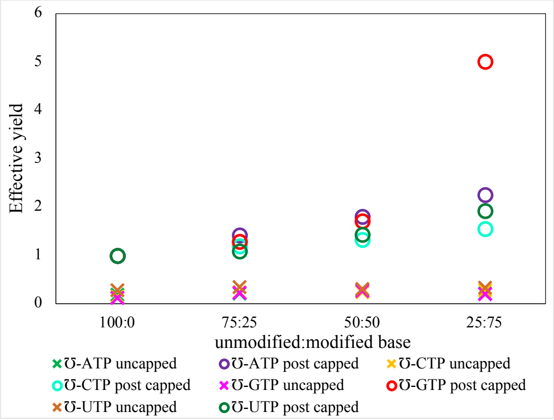

Figure 9. Effective yield of Ʊ-XTP in HEK293T.17 cells

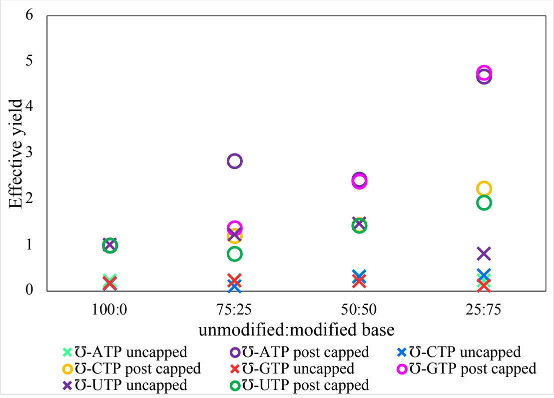

Figure 10. Effective yield of Ʊ-*x*TP in HELA cells

Table 4. 2nd order polynomial coefficients for Effective yield. **y**=*a***x**^{2}+*b***x**+*c*, *where y is the relative efficacy and x is the proportion of modified bases added*

HEK293T.17

Capping	Analog	a	b	c
Post capped	Ʊ-ATP	-0.024	0.136	0.0655
	Ʊ-CTP	-0.013	0.105	0.06
	Ʊ-GTP	-0.048	0.267	-0.1
	Ʊ-UTP	-0.012	0.072	0.23
	φ-GTP	0.002	-0.21	1.01
Uncapped	Ʊ-ATP	0.01	0.37	0.63
	Ʊ-CTP	0.006	0.151	0.85
	Ʊ-GTP	0.75	-2.51	2.9
	Ʊ-UTP	0.1	-0.18	1.08
	φ-GTP	-0.236	1.05	0.54

HELA

Capping	Analog	a	b	c
Post capped	Ʊ-ATP	-0.029	0.156	0.087
	Ʊ-CTP	0.023	-0.041	0.165
	Ʊ-GTP	-0.042	0.191	0.0263
	Ʊ-UTP	-0.224	1.08	0.104
	φ-GTP	-0.04	-0.002	1.042
Uncapped	Ʊ-ATP	0.099	0.57	0.575
	Ʊ-CTP	0.147	-0.335	1.214
	Ʊ-GTP	0.5	-1.26	1.8
	Ʊ-UTP	0.172	-0.52	1.3
	φ-GTP	-0.198	0.837	0.629

Table 5. Maximum point for each nucleotide and the respective optimal unmodified to modified base ratio

Cell	Capping	Analog	Maximum effective yield	Peak ratio
HE293T.17	Uncapped	Ʊ-ATP	0.28	50:50
		Ʊ-CTP	0.24	50:50
		Ʊ-GTP	0.27	50:50
		Ʊ-UTP	0.36	75:25
		φ-GTP	0.76	100:0
	Post capped	Ʊ-ATP	2.26	25:75
		Ʊ-CTP	1.56	25:75
		Ʊ-GTP	5.01	25:75
		Ʊ-UTP	1.93	25:75
		φ-GTP	2.62	75:25
HELA	Uncapped	Ʊ-ATP	0.34	50:50
		Ʊ-CTP	0.34	25:75
		Ʊ-GTP	0.24	75:25
		Ʊ-UTP	1.48	50:50
		φ-GTP	1.07	75:25
	Post capped	Ʊ-ATP	4.68	25:75
		Ʊ-CTP	2.25	25:75
		Ʊ-GTP	4.77	25:75
		Ʊ-UTP	1.94	25:75
		φ-GTP	2.16	75:25

Trends observed in the effective yield is similar to that of relative efficacy where φ-GTP achieved maximum effective yield at 75:25 unmodified to modified ratio while all the Ʊ analogs have a maximum at 25:75 ratio. Furthermore, the graphs also highlight the advantage of post capping where φ-GTP experience up to 4 times enhancement in effective yield while Ʊ experience up to a 16-fold increase in effective yield. Even though post capped has a lower manufacturing yield, it is multiplied with a large relative efficacy which leads to a high effective yield. The effective yield model for the various analogues studied can be seen in Table 3.

φ-GTP substitution shows promising improvement to the effective yield when 25% of the modified base is incorporated, achieving 3.43 times the effective yield of pure GTP saRNA in HEK293T.17 and 2.16 for HELA cells as seen in Table 4.

High levels of Ʊ-*x*TP substitution of ATP, CTP, GTP and UTP into the saRNA gave positive results with the maximum effective yield shown in Table 4.

Functional half-life

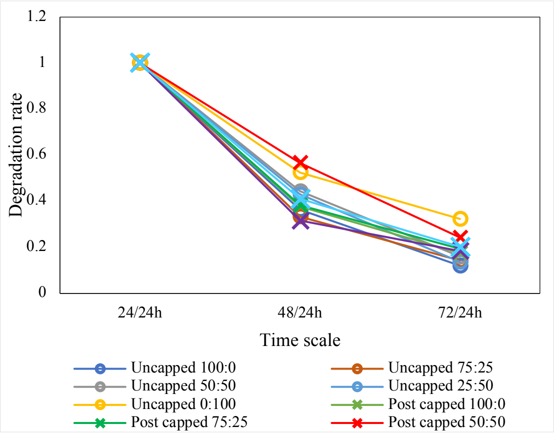

Figure 11. Luciferase expression of mRNA incorporated with φ-GTP from 24 to 72h

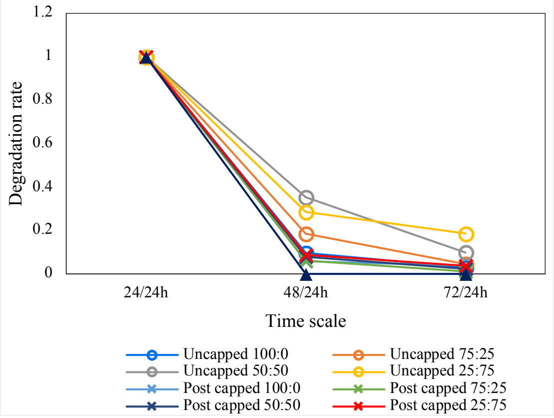

Figure 12. Luciferase expression of mRNA incorporated with Ʊ-*x*TP from 24 to 72h.

In general, luciferase expression decreases from 24h to 72h. The functional half-life for both post-capped and uncapped saRNA are similar for Ʊ analogs and φ-GTP modified bases; this trend is consistent across both HEK293.T7 and HELA cells. There is no clear trend between the amount of modified bases added and the functional half-life of the mRNA.

Discussion

Manufacturing yield

The linear decrease in manufacturing yield for φ-GTP could be explained using the kinetics of initiation. The T7 RNA polymerase prefers guanosine and sometimes adenosine as an initiation site for transcription [13]. The failure to incorporate φ-guanosine at the initiating or elongating position due to poor groove interaction will result in low yield. The N-7 and O-6 of GTP allows for correct positioning of the nucleotide during initiation and elongation. However, φ-GTP, which has CH at position 7, only retains part of the groove interaction, thus it is not favoured over GTP. As the proportion of φ-GTP increases, the misinitiation increases, resulting in less mRNA being synthesized [14]. The concave trend in the manufacturing yield as the percentage of Ʊ nucleotides increases is caused by the distinct inhibition behaviour. The slight increase in yield at 25% of Ʊ nucleotides could be the effect of less steric hindrance [15] and possibly competitive binding of the nucleotides. However, as the Ʊ nucleotide percentage increases, the modified nucleotide will hinder chain elongation through a reduction of binding probability of other nucleotide molecules, terminating the chain prematurely and reducing the yield [15].

The lower post-capped yield when compared to the uncapped yield is due to the low capping efficiency which could be caused by insufficient incubation time. This prevents all the RNA from undergoing Ʊation. Furthermore, there could be the formation of stable structures such as hairpins at the 5' end that obstruct the access of Ʊtransferase or capping enzyme [16].

Efficacy and effective yield

The cap structure present in all eukaryotic saRNA consists of Cap 0, an N7-methylated guanosine (m7G) moiety, linked to the first nucleotide of the transcript via a reverse 5'-5' triphosphate bridge. In this research, an additional methylation on the 2'-O position of the initiating nucleotide generates Cap 1 (m7GpppNm), where Nm denotes any nucleotide with a 2'O methylation, which serves to further increase translation efficiency of the saRNA [16]. This cap protects saRNA from exonuclease cleavage by 5' exoribonucleases and acts as a unique identifier for recruiting protein factors for pre-mRNA splicing, polyadenylation and nuclear export [17]. It is crucial in the initiation of protein synthesis and it enhances the stability of saRNA during translation as it establishes effective recognition by eukaryotic translation initiation factor 4E (eIF4E) [18]. In contrast, uncapped RNAs are more likely to be distinguished as nonself molecular structures and activate the innate immune system to produce interferons, thereby preventing translation [18].

Incorporating φ-GTP and Ʊ-*x*TP into the saRNA has resulted in an increase in luciferase expression of both transfected cell lines. This is because nucleoside-modified mRNA is known to improve translational capacity and stability as it diminishes the induction of Type-I Interferons (IFN-I) through the reduction of intracellular mRNA recognition by TLR3, TLR7, and TLR8 [19]. IFN-I play a central role in initiating antiviral pathways which programme the degradation of mRNA and inhibit their translation, as well as interfere with the generation of potent cytolytic T-cell responses, thereby hampering vaccine efficacy [20]. φ-guanosine has shown to increase translational efficiency and fidelity [21], while Ʊ-*x*TP play a critical role in regulating gene expression [22].

However, there are two sides of the coin regarding innate antiviral responses against mRNA vaccines. In addition to the detrimental effects of IFN-I on mRNA vaccines effectiveness, data is also provided for the positive effects of IFN-I mediated activation on an mRNA's 'self-adjuvant' property, which enhances immune response to an antigen. It is crucial for mRNA vaccines to elicit an adequate IFN-I response to effectively activate cytolytic CD8+ T-cells [23], as the induction of antigen-specific T-cell responses is necessary for successful immunization. The absence of IFN-I response also negatively impacts the ability to activate dendritic cells (DCs) [19], a type of antigen-presenting cell (APC) which processes and presents antigens on the cell surface for T-cells to capture. Furthermore, TLR7 signalling can also increase antigen presentation. These contrasting data encourages the need to strike a correct balance of IFN-I induction through an optimal ratio of unmodified to nucleoside-modified mRNA which the results in this paper have presented. mRNA vaccines engineered in this balanced manner will not only enhance translational capacity, but also capture the adjuvant effect required to improve overall efficacy.

Functional half-life

Changes in saRNA stability are reflected in the amount of protein produced, thus it is expected to see that the luciferase expressions over time generally decrease as the mRNA available for translation will naturally decay, with half-lives ranging from just a few minutes to more than 24 hours [24]. Another possible explanation for the decrease is that the limited availability of amino acids in the cell cultures leads to an accumulation of uncharged transfer RNAs (tRNAs), which bind and activate General Control Nonderepressible 2 (GCN2) kinase to reduce translation [25].

While it may seem superficial to directly relate the physical half-life of mRNA to the half-life of luciferase expression, D. R. Gallie discusses this in detail by differentiating the physical half-life of an mRNA from its functional half-life, which is defined as the time required to reach 50% of its maximum luciferase activity [26]. The functional half-life for both capped and uncapped mRNA in their paper showed minimal difference in animal cells, which corresponds to our results in HEK239T.17 cells. Studies have shown that functional half-life of mRNA depends on the ribosome spacing in the early coding region of the sequence [27], or a combination of specific sequence elements near the ribosome-binding sites [28]. Research also shows that incorporating modified nucleotides can affect the stability of base pairs and change the secondary structure of mRNA, which regulates protein expression through changes in functional half-life [29].

Conclusions

An optimal ratio of unmodified and nucleoside-modified saRNA found in this paper for several nucleoside modifications invites more exciting possibilities to further solidify our understanding on mRNA and saRNA vaccines and engineer more efficacious vaccines. The models developed can be incorporated into the Quality by Design process for vaccine development where the optimal ratio can be used to reduce cost and time in producing a vaccine. Performing multivariable analysis on the effects of simultaneously incorporating multiple nucleoside-modifications on vaccine efficacy would be an ideal pathway to continue this research on. Due to the highly complex interrelationships between the kinetics of translation, degradation, activating APCs, T-cell immune responses, as well as other factors such as capping and nucleoside-modifications, a data-driven approach may be more suitable for the optimisation of vaccine efficacy. Machine learning models will be able to better predict an optimal ratio of modified to nucleoside-modified RNA if given enough data, and possibly even shed light on certain areas we have yet to fully comprehend.

References

[1] World Health Organization, “Immunization,” 5 Deccember 2019. [Online]. Available: https://www.who.int/news-room/facts-in-pictures/detail/immunization. [Accessed 2021].

[2] Z. Kis, C. Kontoravdi, A. K. Dey, R. Shattock and N. Shah, “Rapid development and deployment of high-volume vaccines for pandemic response,” AlChE, 29 June 2020.

[3] N. Pardi, M. J. Hogan, F. W. Porter and D. Weissman, “mRNA vaccines — a new era in vaccinology,” Macmillan Publishers Limited, 2018.

[4] Pfizer UK, “Behind the Science: What is an mRNA Vaccine?,” Pfizer, 25 August 2020. [Online]. Available: https://www.pfizer.co.uk/news-and-featured-stories/behind-science-what-is-an-mrna-vaccine. [Accessed 2021].

[5] N. A. C. Jackson, K. E. Kester, D. Casimiro, S. Gurunathan and F. DeRosa, “The promise of mRNA vaccines: a biotech and industrial perspective,” npj Vaccines, 2020.

[6] Wikipedia, “Nuceoside-modified messenger RNA,” 29 November 2021. [Online]. Available: https://en.wikipedia.org/wiki/Nucleoside-modified_messenger_RNA. [Accessed 2021].

[7] L. Roncati and L. Corsi, “Nucleoside-modified messenger RNA COVID19 vaccine platform,” Wiley Journal of Medical Virology, 2021.

[8] K. Karikó, H. Muramatsu, F. A. Welsh, J. Ludwig, H. Kato, S. Akira and D. Weissman, “Incorporation of Pseudouridine Into mRNA Yields Superior Nonimmunogenic Vector with Increased Translational Capacity and Biological Stability,” NIH, 2008.

[9] Committee for Medicinal Products for Human Use, “Comirnaty Epar Public Assessment Report,” European Medicines Agency, 2021.

[10] DPT, “What is Quality be Design (QbD) - And why should you care?,” DPT, 2013. [Online]. Available: https://dptlabs.com/wp-content/uploads/2013/05/What-is-Quality-by-Design-QbD-and-Why-Should-You-Care.pdf. [Accessed 14 12 2021].

[11] Juran, “Quality by Design (QbD): An Overview,” Juran, 24 June 2019. [Online]. Available: https://www.juran.com/blog/quality-by-design-qbd-an-overview/. [Accessed 14 12 2021].

[12] K. Samnuan, A. K. Blakney, P. F. McKay and R. J. Shattock, “Design-of-Experiments In Vitro Transcription Yield Optimization of Self Amplifying RNA,” bioRxiv, 2021.

[13] T. Ohta, S. Sarkar and R. E. Thach, “The role of guanosine 5'-Triphosphate in the initiation of peptide synthesis. III. Binding of formylmethionyl-tRNA to robosomes,” *Proc Natl Acad Sci U S A,* vol. 58, no. 4, pp. 1638 - 1644, 1967.

[14] K. Iaroslav, G. A. Philip and M. T. Craig, “Binding of Priming Nucleotide in the Initiation of Transcription by T7 RNA Polymerase,” *The Journal of Biological Chemistry,* vol. 278, no. 5, p. 2823, 2002.

[15] C. Yuan, G. C. Eshani, U. C. Ilona and X. Huang, “Incorporation efficiency and inhibition mechanism of 2'-substituted nucleotide analogs agains SARS-CoV-2 RNA-dependent RNA polymerase,” *Royal Society of Chemisty,* vol. 23, pp. 20117-20128, 2021.

[16] CELLSCRIPT, “ScriptCap™ 2'-O-Methyltransferase Kit,” *C-SCMT0625,* pp. 1 - 6, 2021.

[17] A. Ramanathan, G. B. Robb and S.-H. Chan, “mRNA capping: biological functions and applications,” NCBI, 2016.

[18] E. Decroly, F. Ferron, J. Lescar and B. Canard, “Conventional and unconventional mechanisms for capping viral mRNA,” 2011.

[19] R. Verbekea, I. Lentacker, L. Wayteck, K. Breckpotc, M. V. Bockstald, B. Descampse, C. Vanhovee, S. C. D. Smedt and H. Dewittea, “Co-delivery of nucleoside-modified mRNA and TLR agonists for cancer immunotherapy: Restoring the immunogenicity of immunosilent mRNA,” Elsevier, 2017.

[20] A. D. Beuckelaer, C. Pollard, S. V. Lint, K. Roose, L. V. Hoecke, T. Naessens, V. K. Udhayakumar, M. Smet, N. Sanders, S. Lienenklaus, X. Saelens, S. Weiss, G. Vanham, J. Grooten and S. D. Koker, “Type I Interferons Interfere with the Capacity of mRNA Lipoplex Vaccines to Elicit Cytolytic T Cell Responses,” 2016.

[21] D. Iwata-Reuyl, “Biosynthesis of the 7-deazaguanosine hypermodified nucleosides of transfer RNA,” 2002.

[22] B. A. Elliott, H.-T. Ho, S. V. Ranganathan, S. Vangaveti, O. Ilkayeva, H. A. Assi, A. K. Choi, P. F. Agris and C. L. Holley, 2019.

[23] C. Iavarone, D. T. O’hagan, D. Yu, N. F. Delahaye and J. B., “Mechanism of action of mRNA-based vaccines,” Expert Review of Vaccines, 2017.

[24] H. Tourrière, K. Chebli and J. Tazi, “mRNA degradation machines in eukaryotic cells,” 2002.

[25] N. N. Pavlova, B. King, R. H. Josselsohn, S. Violante, V. L. Macera, S. A. Vardhana, J. R. Cross and C. B. Thompson, “Translation in amino-acid-poor environments is limited by tRNAGln charging,” 2020.

[26] D. R. Gallie, “The cap and poly(A) tail function synergistically to regulate mRNA translational efficiency,” 1991.

[27] M. Pedersen, S. Nissen, N. Mitarai, S. LoSvenningsen, K. Sneppen and S. Pedersen, “The Functional Half-Life of an mRNA Depends on the Ribosome Spacing in an Early Coding Region,” 2011.

[28] C. Peterson, “Multiple Determinants of Functional mRNA Stability: Sequence Alterations at Either End of the lacZ Gene Affect the Rate of mRNA Inactivation,” 1991.

[29] D. M. Maugera, B. J. Cabrala, V. Presnyaka, S. V. Sua, D. W. Reida, B. Goodmana, K. Linka, N. Khatwania, J. Reyndersa, M. J. Moorea and I. J. McFadyen, “mRNA structure regulates protein expression through changes in functional half-life,” 2019.

[30] C. Yuan, E. C. Goonetilleke, I. C. Unarta and X. Huany, “Incorporation efficiency and inhibition mechanism of 2'-substituted nucleotide analogs against SARS-CoV-2 RNA-dependent RNA polymerase,” *Royal Society of Chemisty,* vol. 23, pp. 20117-20128, 2021.

[31] H. Yoav, S. Nishat, Y. Elias, S. Mohammad Tofael Kabir, K. Keerat, C. Elena and Z. Lior, “Optimizing Modified M”.

[32] H. Yoav, S. Nishat, Y. Elias, S. Mohammad Tofael Kabir, K. Keerat, C. Elena and Z. Lior, “Optimizing Modified mRNA In Vitro Synthesis Protocol for Heart Gene Therapy,” *Molecular Therapy Moethods Clinic Development,* vol. 14, pp. 300-305, 2019.

[33] Y. V. Svitkin, Y. M. Cheng, T. Chakraborty, V. Presnyak, M. John and N. Sonenberg, “N1-methyl-pseudouridine in mRNA enhances translation through eIF2-dependent and independent mechanisms by increasing ribosome density,” Nucleic Acids Research, 2017.

[34] E. Schneider, M. Blundell and D. Kennell, “Translation and mRNA Decay,” 1978.

[35] B. Roy and A. Jacobson, “The intimate relationships of mRNA decay and translation,” 2013.

[36] T. Huang, S. Wan, Z. Xu, Y. Zheng, K.-Y. Feng, H.-P. Li, X. Kong and Y.-D. Cai, “Analysis and Prediction of Translation Rate Based on Sequence and Functional Features of the mRNA,” 2011.

[37] CELLSCRIPT, “ScriptCap 2'-O-Methyltransferase Kit”.

[38] B. R. Anderson, H. Muramatsu, B. K. Jha, R. H. Silverman, D. Weissman and K. Kariko, “Nucleoside modifications in RNA limit activation of 20 -50 -oligoadenylate synthetase and increase resistance to cleavage by RNase L,” 2011.

TiO_2 Inverse Opal/rGO/$CsPbBr_3$ Nanocrystal Composites for Improved Photocatalytic CO_2 Reduction

Adeoluwa Pearse and Aulia Rahmayanti
Department of Chemical Engineering, Imperial College London, U.K.

Abstract Titanium dioxide inverse opal structures (TIO) coupled with $CsPbBr_3$ nanocrystals and reduced graphene oxide (rGO) were synthesised for the design of a novel S-scheme photocatalyst with improved CO_2 photoreduction. Sol-gel method was used for TIO synthesis and high-energy ball milling for $CsPbBr_3$ nanocrystal synthesis. Characterisation of prepared samples included SEM, Raman, XRD, and UV-Vis diffuse reflectance spectrometry. Photocatalytic activity was investigated with gas-phase CO_2 reduction reaction in a 115 ml stainless steel reactor with a quartz glass window under simulated sunlight irradiation. It was found that there exists an optimal loading of $CsPbBr_3$ on TIO structures, with the TIO/rGO/8mg exhibiting a high yield of 41 μmol.g^{-1} of CO product within 2 hours, which was a nearly 5-fold enhancement compared to pure TIO. This study therefore further expands on perovskite-based heterojunctions on inverse opal structures with rGO.

1. Introduction

The direct conversion of solar energy into chemical fuels through photocatalytic reduction remains a challenge in sustainable energy research, pre-empting the need for better photocatalysts. Photoreduction of CO_2 to CO in the presence of semiconductors comprises the first step to this conversion. Anatase crystalline titanium dioxide (TiO_2) has been investigated extensively as a photocatalyst over the past 40 years owing to its favourable properties: low cost, high stability, low toxicity, good photocatalytic activity compared to its other crystalline phases, and highly oxidizing electron hole pairs [1, 2].

However, effective industrial-scale use of TiO_2 in photocatalysis is hindered by rapid electron-hole recombination and a large bandgap (3.2 eV) that significantly limits solar energy utilization to the UV-range (only 3-5% of total solar irradiation energy) [3].

Much work has therefore been done over the past 40 years to modify TiO_2 for slower charge recombination and visible light activation, and to discover new materials. Modification strategies have included doping with metals and non-metals, co-catalyst deposition, structural engineering, heterojunctions, and carbon-based material loading [4–6]. The tailored combination of these strategies poses an interesting opportunity to design better photocatalysts.

Photocatalytic activity of TiO_2 is affected by structural properties like crystalline size, crystal morphology, exposed lattice facets and surface area and thus many forms of TiO_2 have been investigated in literature. Of the 3D structures, inverse opals have attracted interest for their 'slow photon effect' that can enhance the absorption of visible light when tailored to the edges of semiconductor bandgaps, in addition to enhanced surface area and faster electron transmission [7, 8].

Further improvements are achievable through forming heterojunctions between TiO_2 and smaller bandgap semiconductors, such as ZnO, g-C_3N_4, CdS and Bi_2MoO_6 [9]. Over the past decade, halide perovskites have generated great interest due to the rapid improvement in quantum yield, facile and cheap synthesis, long charge carrier lifetimes, high absorption of UV light and tuneable bandgap [10–12]. Recently, nanocomposites of TiO_2/$CsPbBr_3$ have been synthesised with various morphologies in S-scheme heterojunctions, such as core/shell structure or $CsPbBr_3$ nanocrystals (NCs) on mesoporous TiO_2 [10, 13]. Studies on $CsPbBr_3$ NCs on inverse opal structures however remain limited and are not yet fully explored.

The addition of carbon-based sheets such as graphene or reduced graphene oxide (rGO) to photocatalysts is commended for improving photocatalytic activity due to its super-high surface areas, incredible charge transport properties for electron-hole separation, increased visible light absorption, increased CO_2 adsorption through π-π conjugation, and activation of CO_2 molecules for reduction [5, 8, 14]. A common method of integration seen in literature is to deposit TiO_2 nanoparticles and other co-catalysts onto graphene-based sheets [15] however only few recent studies have reported CO_2 photoreduction through incorporation of rGO onto TiO_2 inverse opal (TIO) structures[8, 16]

Herein, we investigate a new photocatalyst nanocomposite for CO_2 reduction through the synthesis and characterisation of TiO_2 inverse opal structures with $CsPbBr_3$ NCs nanocrystals and rGO as a charge carrying enhancer in the S-scheme heterojunction.

2. Background

2.1 Photocatalytic Mechanism

2.1.1 Semiconductor Catalysts

Semiconductor catalysts function through the promotion of an electron from a valence band (VB) to a conduction band (CB). If light incident on the catalyst has energy greater than or equal to the band gap energy of the difference in the VB and CB, then

VB electrons absorb energy and are promoted to an excited state in the CB. This leaves a positively charged 'hole' in the CB. Excited electrons can catalyse reduction reactions while the holes can catalyse oxidation reactions. However, excited electrons can also fall back to the hole in the VB in a process called hole recombination [1]. Recombination should be suppressed to ensure as many electrons as possible participate in reduction.

2.1.2 S-Scheme Heterojunction

Heterojunctions allow materials with different bandgaps to interact and produce a composite that can perform a previously unattainable desired catalysis or outperform a single material alone. For the pairing to function, one material (often metal oxides e.g. WO_3) must satisfy the conduction band requirement for the reduction reaction and the other must satisfy the valance band requirement for the oxidation reaction [1]. Each of the two materials can therefore straddle one boundary condition, rather than one material being called upon to do so.

S-scheme heterojunctions, similar to direct Z-scheme, consist of two semiconductors, the one with the more positive CB called the reduction photocatalyst (RP) and the one with the more negative VB called the oxidation photocatalyst (OP) **(Figure 1(a)**). Excited electrons in the CB of the OP combine with holes in the VB of the RP rather than holes in the VB of the OP (shown in **Figure 1(b)**). This leaves holes available for oxidation catalysis in the VB of the OP with the lowest electronic potentials. Due to the OP-RP recombination, high-potential electrons in the CB of the RP do not recombine with holes and are available for catalysing reduction reactions. The preservation of high potential electrons and low potential holes results in as strong a redox potential as possible and facilitates the photoreduction of CO_2 to CO – a reaction which is normally difficult due to the multi-step mechanism and large thermodynamic barrier [17].

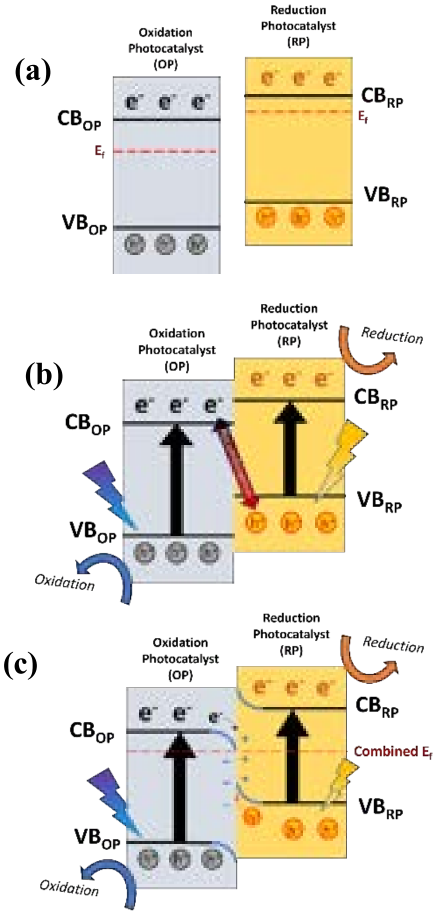

Figure 1. Schematic of the S-Scheme Heterojunction

The recombination of electrons in the CB of the OP and holes in the VB of the RP is driven by three main mechanisms: the electrostatic attraction between positive holes and negative electrons, the induced electric field, and the shifting of the Fermi levels [17]. The induced electric field is due to a phenomenon occurring when two photocatalysts are in contact and electrons diffuse from the RP to the OP, causing the formation of a positively charged 'electron depletion layer' on the RP and a corresponding negatively charged 'electron accumulation layer' on the OP. To neutralise this charge separation, there exists a pull for the electrons to return to the RP (where they can annihilate the holes). This mechanism is the shifting of Fermi levels (illustrated in **Figure 1(c)**). The Fermi levels of the OP and RP try to become closer as the materials are in contact, bending the VB of the RP and the CB of the OP closer to each other and easing the electron-hole recombination.

TiO_2 has a band gap of 3.26 eV (from -4.20 eV to -7.45 eV) and $CsPbBr_3$ has a band gap of 2.40 eV (from -5.85 eV to -3.45 eV) [18]. Therefore, in this study, the reduction photocatalyst would be the $CsPbBr_3$ and the oxidation photocatalyst would be the TiO_2.

2.2 Inverse Opal and Slow Light Effect

Photonic crystals of TiO_2 in their inverse opal form have highly ordered, periodic pores of often nanometre-scale diameter, promoting gaseous diffusion [19]. The propagation of certain wavelengths of light are forbidden deeper within these structures because of coherent Bragg diffraction. This causes the existence of 'stop-bands,' where certain ranges of wavelengths are not transmitted but reflected with increased path lengths through the material. For photons with wavelengths at the edges of these stop-bands, slow photon effects occur where photons propagate at greatly reduced velocities in solids and have an increased chance of being absorbed via the excitation of electrons from the VB to the CB. By varying pore diameter, tuning of stop-bands is achievable [19]. Matching this to the electronic bandgap of a semiconductor or co-catalyst can increase the material's absorbance and in turn, the number of generated electron-hole pairs, enhancing photocatalytic activity [2, 20, 21]. As the visible light utilisation of TiO_2 is targeted and $CsPbBr_3$ absorbs within the visible range, the tuning of TIO stop-bands to the $CsPbBr_3$ bandgap is can proomote photocatalytic activity. TiO_2 inverse opal structures are therefore further explored here with $CsPbBr_3$ nanocrystals.

The stop band position for TIO structures can be calculated using Bragg's Law:

$$\lambda_{max} = \frac{2D\sqrt{2}}{\sqrt{3}} \sqrt{n_{\mathrm{TiO_2}}{}^2 f + n_{\mathrm{air}}{}^2 (1-f) - \sin^2 \theta} \quad (1)$$

Where, λ_{max} is the stop band position for 1st order Bragg diffraction, D is IO pore size, $n_{\mathrm{TiO_2}}$ and n_{air} are refractive indices of the materials (2.5 and 1.0003 respectively), f is volume fraction of TIO (0.26 for FCC geometry) and θ is incident angle of light which is taken as 0° for these experiments [22].

2.3 Influence of rGO

Reduced graphene oxide is a beneficial addition to semiconductor catalysts, due to the fact that it is a good conductor and able to transfer electrons away from where they might recombine with holes. This is due to rGO's large specific surface area, which aids in this charge separation. One study suggested the electrons were redirected into the metal nanoparticles where co-catalysts are used [23]. Though metal nanoparticles (Au, Cu or otherwise) are not being used here, the charge separation properties of rGO will still benefit the reaction.

rGO is also able to adsorb and activate CO_2 molecules, as was previously discussed. There is also evidence that it increases the selectivity of the CO_2 reduction reaction [24], and due to CO_2 reduction being the investigated reaction the inclusion was rGO was thought to be beneficial.

One study suggested that the inclusion of graphite sheets placed on top of the perovskite benefitted the reaction as the holes were transferred into the graphite layer [25], reducing the amount of electron-hole recombination.

3. Methodology

3.1 TiO2 Inverse Opal (IO) Structure Synthesis and rGO Infiltration

5 ml of Titanium Isopropoxide precursor was mixed with 47 ml of ethanol. 2 ml of 37% HCl was then added and the whole stirred for 30 minutes. Pre-prepared colloidal polystyrene spheres of 380-400 nm on glass slides were dipped for 1 minute in this precursor solution and were left to dry in air for 24 hours [26]. The samples were then placed in an oven to calcine in air for 3 hours at 500 ℃ (ramp rate = 2 ℃.min^{-1}) and left to cool in overnight to form TIO slides.

An aqueous solution of graphene oxide pre-prepared via Hummer's modified method was exfoliated for 24 hours prior to each use. For rGO deposition, the TIO slides were first submerged in a 0.5 g.l^{-1} solution of poly-allylamine hydroxide for 2 hours. The slides were then washed with deionised water before being submerged in the rGO solution for 5 hours, after which the slides were calcinated in a furnace at 500 ℃ for 3 hours under nitrogen flow.

3.2 $CsPbBr_3$ Nanocrystal Fabrication

$CsPbBr_3$ nanocrystals (NCs) were manufactured using a high energy ball mill method at atmospheric conditions [27]. 0.212 g of CsBr and 0.367 g of $PbBr_2$ (i.e. 1 mmol of each substance) was added into a zirconia ball mill with 164 ceramic balls and milled at 500 rpm for 5 minutes. 0.1 ml of oleyl amine was added before returning to the ball mill at 500 rpm for 20 minutes. The ball mill was then washed with toluene to form a suspension of the NCs in toluene. The solution was centrifuged at 5000 rpm for 10 minutes and the NC supernatant decanted and collected, discarding the residue.

Three NC solutions were prepared in this manner. To determine each solution's concentration, the mass difference before and after the evaporation of 1 ml of each solution was taken.

To incorporate NCs to the TIO-rGO slides, various concentrations of NC solutions were prepared. An equivalent volume containing a desired mass of NC (2 mg, 4 mg, 8 mg and 16 mg) was added to a beaker and solution was then made up with toluene to 25 ml in total. TIO/rGO slides were submerged in these NC solutions for 2 hours and left to dry in a vacuum oven overnight. Henceforth, samples synthesised with NCs shall be referred to by their mass loading in the 25 ml toluene solution, most fully as TIO/rGO/2mg NCs or more simply as what was added to the TIO, i.e. rGO/2mg.

3.3 Photocatalytic Reaction

Fully synthesised samples were placed on a pedestal in a specially made 115 ml stainless steel reactor with quartz glass window, with 2 ml of deionised water injected at the base. The reactor was purged with CO_2 at a flowrate of 40 ml.min^{-1} for a minimum of 1 hour. Next, the CO_2 flowrate was changed to 3 ml.min^{-1}, whereupon gas chromatography was run to ensure the O_2 peak was less than 10,000 uV. Then the reactor was isolated from the system and a hot plate activated for 20s to evaporate some of the water in the reactor. A Xenon 500W lamp was then turned on and positioned 40cm above the window to ensure the illumination of the entire catalyst surface. The reaction was then left to progress for two hours, after which the lamp was switched off. The valves were opened to allow the throughflow of reacted gases to a Shimadzu gas chromatographer to determine the yield of CO.

3.4 Characterisation

The morphology of synthesised structures was inspected with scanning electron microscopy (SEM) using a Zeiss Leo Gemini SEM (EHT = 5.00 kV, WD = 5.2 - 6.6 mm, Signal A = InLens).

Raman spectra was obtained using a Senterra II confocal Raman spectrometer under 20x magnification and 785 nm laser excitation over a wavenumber range of 50-2500 cm^{-1}.

X-Ray Diffraction (XRD) measurements were performed using a PANalytical X'Pert Pro Diffractometer (Ni-Filtered Cu Ka, I=1.54 Å) at 40 kV and 40 mA. The 2θ range was 10º – 40º and steps of 0.05º were used. To fit and subtract the baseline, Highscore software was used to analyse the diffractograms.

For the Ultraviolet-Visible (UV-Vis) diffuse reflectance spectroscopy (DRS), a Shimadzu spectrometer was used over 1100-200nm range at medium scan speed for CsPbBr$_3$ NCs suspensions diluted in cuvettes with toluene and measured against a pure toluene standard. Transmittance was assumed negligible for the opaque samples. For solid photocatalyst samples, DRS was measured between 200-850 nm range against a standard of BaSO$_4$.

4. Results and Discussion

4.1 Scanning Electron Microscope (SEM)

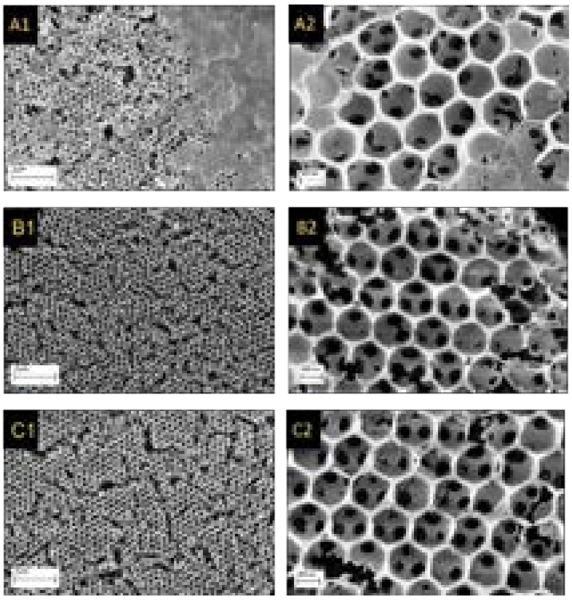

Figure 2. SEM images of (A1) TIO/rGO at 16.92k magnification and (A2) 104.7k magnification; (B1) TIO/rGO/4mg at 9.46k magnification and (B2) 98.17k magnification; (C1) TIO/rGO/8mg at 9.46k magnification and (C2) 104.49k magnification. Scale bar equals 2 μm (A1, B1, C1) and 200 nm (A2, B2, C2) respectively

Figure 2 shows the SEM images of TIO/rGO, TIO/rGO/4mg and TIO/rGO/8mg samples synthesised via the colloidal crystal template and sol-gel method, highlighting the structural features of TIOs with rGO and NCs of various mass loading. As seen from the SEM, regular hexagonal structures that are characteristic of inverse opals have been successfully synthesised. The inverse opal (IO) structure has an average pore diameter of 300 nm and were made with 380-400 nm PS spheres, therefore undergoing up to 25% shrinkage in pore size from the calcination. The IO structure exhibits some non-regularity in opal shape and cracking at the 200 nm and 1μm bar scale. Lower magnification showed larger cracks that segment the TIO into approximately 40 × 100 μm grid-like domains. These large cracks may be attributed to uneven infiltration of precursor solution into polystyrene sphere templates, that often disrupt the colloidal template structure and forms multiple domains [28]. Further, smaller defects can be explained by non-regularity of templates, uneven hydrolysis of precursor and stresses applied during the calcination step due to significant pore shrinkage. All TIO/rGO nanocomposites have smaller, somewhat irregular pores visible and extending deeper into the IO structure. Irregularity is likely because PS spheres had not been partially sintered prior to infiltration – a technique that normally strengthens the template structure [29] – which limits continuity of pores and weakens IO structure in the calcination step. This points to the importance of good template preparation in synthesis of high-quality IOs.

It has been reported that nanocomposites with rGO benefit from good transparency, and SEM images of TIO/rGO nanocomposites with 500nm IO pores obtained by Boppella et. al. [16] do demonstrate transparency and homogeneity. Large areas of rGO are visible on the surface of the TIO/rGO only sample as seen in **Figure 2(A1)**, however are not seen in other samples of TIO/rGO/HP NCs, pointing to uneven distribution of rGO. Additionally, rGO exhibits limited transparency and deeper layers of the macroporous structure are not visible through the rGO layer. Rather, some areas of rGO appear to block TIO pores suggesting that gaseous diffusion and incident light that could have entered deeper into the structure was limited to an extent. Although the GO synthesised had been exfoliated for 48 hours post-synthesis and for an additional 1 hour prior to any use, the thickness of rGO layers deposited and lack of transparency suggests the need for smaller-sized rGO precursors during synthesis for the smaller pore sizes (200nm) of IO that has been made here. Alternatively, Huo et. al [8] achieve homogenous distribution of transparent rGO on 250 nm pore-size TIO via ultrasonication of powder in rGO solution followed by membrane filtration and calcining, however this is a more complex method of separation compared to the thin film deposition employed here.

There is little visible difference in thickness of TIO wall structures when comparing the SEM images of TIO/rGO/4mg and TIO/rGO/8mg samples, as seen in **Figure 2(B2)** and **Figure 2(C2)** This indicates that deposited $CsPbBr_3$ NCs are significantly smaller than the characteristic width of the TIO wall structure that is approximately 40 nm. Indeed, according to the method of Wang et al. [27] $CsPbBr_3$ NCs synthesised by high energy ball milling have a mean size of 9.25 nm ± 0.8 nm which supports our observations. When inspected closely, some agglomerated NC particles can be seen, however are difficult to distinguish based solely on the SEM alone.

4.2 Raman Spectroscopy

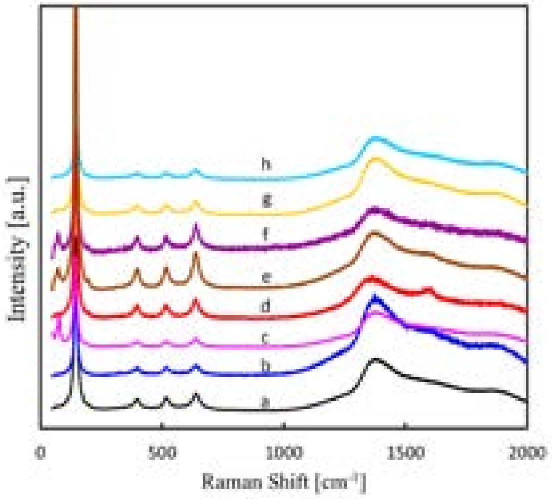

Figure 3. Raman Spectra of samples a) TIO, b) TIO/rGO, c) TIO/rGO/4mg, d) TIO/rGO/8mg, e) TIO/rGO/16mg(a), f) TIO/rGO/16mg (b), g) TIO/4mg and h) TIO/8mg

Raman spectroscopy of samples was undertaken to confirm the synthesis of TiO_2 in the IO structure and to attempt the identification of rGO on samples where large rGO layers were not clearly visible on the SEM. **Figure 3** shows the Raman spectra obtained. Peaks characteristic of anatase TiO_2 were observed in every sample, with the strong peak at 146 cm^{-1} ($E_{g(1)}$) caused by O-Ti-O symmetric bending vibrations, and those at 197 cm^{-1} ($E_{g(2)}$), 396 cm^{-1} (B_{1g}), 515 cm^{-1} (A_{1g}) and 637 cm^{-1} ($E_{g(3)}$) caused by Ti-O-Ti bending [8, 30].

An additional peak observed at 71 cm^{-1} on the TIO/rGO/4mg and TIO/rGO/16(a) and (b) samples may correspond to the vibrational mode of the $[PbBr_6]^{4-}$ octahedron and motion of Cs^+ cations as reported by Chen et al. and other studies on micro-Raman characterisation of $CsPbBr_3$ NCs [31]. The reason why this peak may not be prevalent for other $CsPbBr_3$ NC-containing samples may be due to the highly space-sensitive nature of sampling done with Raman spectroscopy and the fact that measurements are collected from specific points of the visible microscopic image as opposed to measuring across a larger area. If the deposition of NCs on the TIO structure is highly localised and not evenly distributed, some measurements may come upon the domain of $CsPbBr_3$ NCs and others may not. Improved consistency may be attained by altering the sampling method with a much greater number of randomly distributed Raman measurements, or by finding aggregates of $CsPbBr_3$ NCs, although the <10 nm nature of the NCs would pose a challenge for this. Micro-Raman spectroscopy would be beneficial to obtain low-wavenumber regions for additional identification of $CsPbBr_3$ peaks, however other characterisation methods such as UV-Vis proves to be sufficient to confirm the presence of $CsPbBr_3$ NCs as discussed in the next section.

It is of note that the characteristic D (1346 cm^{-1}) and G (1594 cm^{-1}) [32] peaks of rGO are not clearly seen due to significant glass interference between the 1000-1800 cm^{-1} ranges [33], however some samples did exhibit a peak at 1594cm^{-1} despite this (samples (d) and (e) of **Figure 3**) possibly indicating the presence of rGO. Intensity of glass interference varies across samples, which may correlate with the degree of large cracking of TIO domains that would expose more glass. Additional Raman measurements on fused quartz slides as opposed to microscopic slides and better uniformity of TIO via a crack-free synthesis method would reduce glass interference, however this was not achievable within the limited timeframe.

4.3. Ultraviolet-Visible Spectroscopy (UV-Vis)

Figure 4(a) shows that with the addition of the $CsPbBr_3$ NCs, there is increased absorbance (inferred from the decreased reflectance) between 370 – 530 nm. As the range of visible light is from 380 – 700 nm, the samples can effectively absorb over about half of the range of visible light. The addition of rGO alone appears to have improved the absorbance over most of the range, but not as dramatically as the NCs did. All the samples with NCs show a characteristic minimum at around 530 nm, which corresponds to the expected peak for $CsPbBr_3$ based on calculated bandgap. Using **Equation 1** with pore diameter of 300nm, a stop band of 750nm is calculated; within the reflectance spectra, the observed maximum in reflectance occurs at approximately 680nm and this reduced peak can be due to lower-than-expected solid volume fraction value f, due to dilution and condensation of precursors. Slow light effect absorption at the edge of this bandgap (500-600nm) is additionally seen [34].

Of all the samples, rGO/4mg displayed the greatest absorbance (i.e. the lowest percentage reflectance). Sample rGO/16mg(b) displayed better absorbance below about 460 nm but rGO/4mg had a more uniform absorbance after the initial drop. The next best sample was the rGO/8mg and the sample with the least absorbance was the rGO/16mg(a) sample. Though the spectrum curvature per sample remains the same, variances in the strength of absorption between samples may be due to variances in batches of $CsPbBr_3$ NCs used for different slides, as shown by the inset of **Figure 4(c)**.

Figure 4(b) displays how the reflectance varies with or without the addition of rGO and shows that for both the 4mg NC and the 8mg NC samples, the absorbance was increased with the addition of rGO, though less dramatically so for the 8mg sample. In fact, the reflectance of 4mg NC proved to be comparable to adding rGO alone, though lacking the characteristic peak of $CsPbBr_3$. Conversely to **Figure 3(a)**, the TIO/8mg NC slide displays better absorbance than the TIO/4mg slide, suggesting that the addition of the NCs does indeed improve the absorbance, which is now more clearly visible due to the absence of rGO.

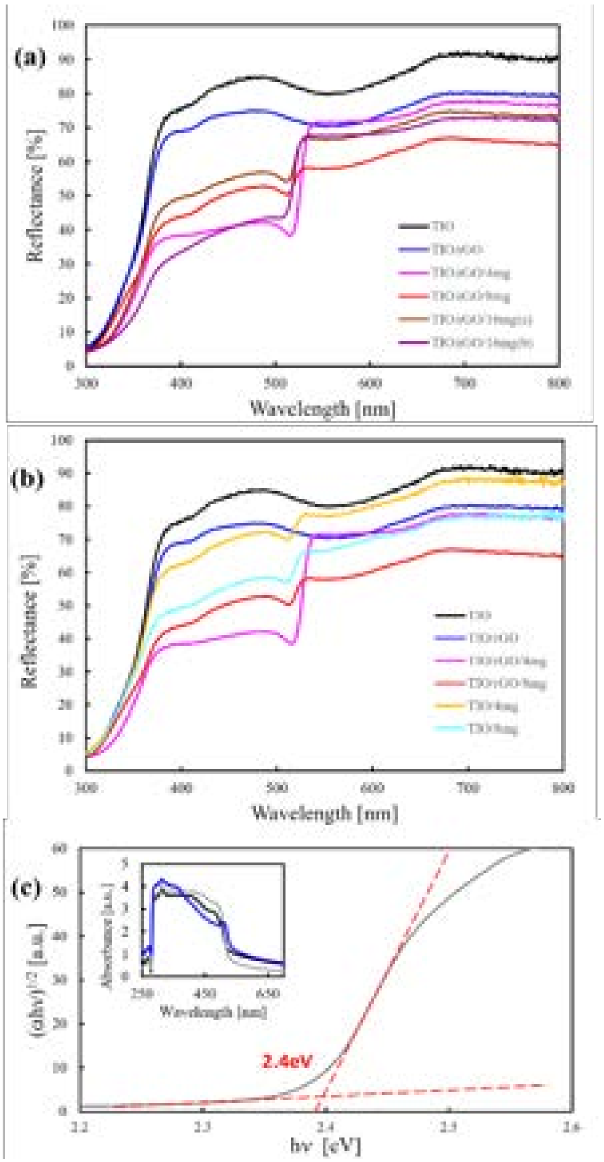

Figure 4. UV-Vis reflectance spectra of (a) TIO, TIO/rGO and all the rGO/NG slides and (b) the comparison of the 4mg and 8mg samples with or without rGO and (c) Tauc plot of $CsPbBr_3$ NC 1 mg.ml^{-1} liquid sample, with inset of the absorbance spectra of obtainable liquid samples

The insert in **Figure 4(c)** shows the spectra for the liquid $CsPbBr_3$ solutions. Three solutions were run, but these do not correspond to the three solutions mentioned earlier. Three solutions were prepared due to the need to do more experiments. The first solution produced about 25ml of solution, and this was subsequently found to not be enough for the desired number of experiments. The resulting three $CsPbBr_3$ solutions had concentrations of 1 mg.l^{-1}, 2 mg.l^{-1} and 2.5 mg.l^{-1}, designated solutions 1, 2 and 3, respectively. Unfortunately, in the course of the experiments solution 2 was completely used up, meaning there was not enough left to perform ultraviolet-visible spectroscopy on. Therefore, the first and third solutions were the only ones analysed. Solution 1 was analysed twice (the black and grey curves) with the second sample (the grey curve) being measured out with a more precise measuring tool.

The major graph of **Figure 4(c)** shows the Tauc plot of the 1 mg.ml^{-1} NC liquid sample. Superimposed on it is the absorbance spectra of the three measurements for the liquid solutions. The Tauc plot was plotted according to the method outlined in Johannes et al. [35]. The value for the exponent was taken as being ½, i.e. the value corresponding to direct allowed transitions. The band gap of $CsPbBr_3$ was experimentally determined to be 2.4 eV, a value corresponding with the literature values of 2.374 eV [36].

4.4 X-Ray Diffraction (XRD)

Figure 5(a) shows the XRD spectrum for the rGO/4mg NC sample. The spectrum shows a small $CsPbBr_3$ peak at 2θ equals 15 degrees. $CsPbBr_3$ peaks (purple dots) can also be seen at 2θ

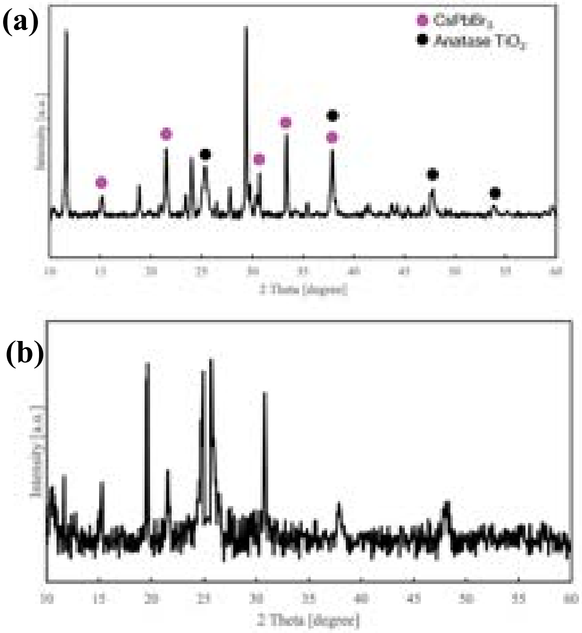

Figure 5. The X-ray diffraction pattern of (a) the rGO/4mg NC sample and (b) the 4mg NC sample

equals 21, 31, 34 degrees. Despite the noise, the spectrum shows a TiO_2 peak (black dots) at 2θ equals 25 degrees. The TiO_2 peak at 38 degrees is also clearly visible, while the peaks at 49 degrees and more so the peak 55 degrees are just barely discernible from the surrounding noise. Given that both $CsPbBr_3$ and TiO_2 have peaks 2θ equals 38 degrees, it is unknown which produced the peak shown on the spectrum, or indeed if the peak represents combination of both.

Due to the noise, it is unclear whether there are any rGO peaks in the sample. There should be a small peak at 2 theta equals 43 and while there appears to be one, it cannot be determined whether this is due to the presence of rGO or due to the surrounding noise. There should also be a broad peak at about 2 theta equals 23, but that is not visible on this spectrum.

Figure 5(b) shows the XRD spectrum for the 4mg NC sample. Due to the fact that it has more noise than **Figure 5(a)**, its peaks are less discernible. Most of the samples have a lot of noise so the peaks are not especially clear. This is likely due to the small amount of sample present on the slides, so most of the signal was coming from the glass slide. The XRD machine was set to take measurements of between 8 and 15 minutes, though if longer times were used (e.g. 1 hour) the peaks would be clearer.

Finer characterisation of the NCs would be beneficial where more resources and time were available, for example, X-ray Photoelectron Spectroscopy (XPS) to indicate the bonding of the NCs to the TIO or to the rGO; transmission Electron Microscopy with Energy Dispersive X-ray Spectroscopy (TEM-EDS) to confirm the homogenous dispersion of $CsPbBr_3$ nanocrystals and rGO.

4.5 Photocatalytic Reduction of CO_2 to CO

Figure 6 shows that there is a general positive correlation between the amount of $CsPbBr_3$ NCs and the CO yield. The clear optimum is the TIO/rGO/8mg NC sample, which had the highest CO yield of all the experimented samples producing 41 μmol.g^{-1} within 2h of light irradiation, which is a 5-fold improvement from base TIO. This in concordant with previous investigations, for example a study which investigated the effect of $CsPbBr_3$ NCs on porous g-C_3N_4 that concluded the CO yield increases with the addition of more $CsPbBr_3$ NCs but only up to an optimum point, after which it declines [10, 37]. This can be explained by excess $CsPbBr_3$ causing competition in light absorption with the TIO.

Initially, it was speculated that the 16mg sample had been overheated during the reaction, potentially decomposing the catalyst, and disallowing it to perform optimally. However, when a second 16 mg sample was prepared (designated 16b) it yielded an even lower value of CO. This is due to the fact that simply performing one experiment per specification may lead to experimental error and inaccuracies as there is no way to tell which samples may be anomalies. Therefore, repeat experiments would need to be carried out so that the CO yield for the repeat experiments could be averaged.

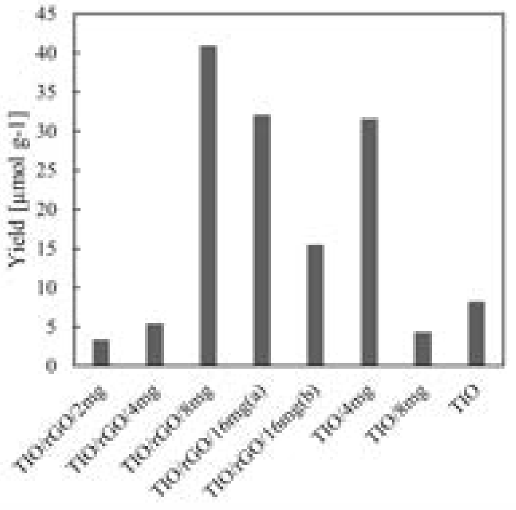

Figure 6. The yield of CO produced from the photocatalytic reduction of CO_2 as the inclusion of rGO and the $CsPbBr_3$ NC concentration is varied

The addition of rGO greatly worsened the CO yield for the 4mg sample but greatly improved the yield for the 8mg sample. This could be due to the high rGO/8mg value but considering that the 8mg did not even outperform the rGO/4mg, it probably would not have outperformed a lower rGO/8mg sample. This variation in whether the addition of rGO supports or inhibits CO yield could be due to the way the rGO solution was prepared or uneven distribution of rGO. The machine used to prepare the rGO flakes is optimised for large flakes, due to the other processes that this machine is required to be used for.

In an attempt to combat this, the rGO solution was sonificated for 48 hours before being first used in order to further its breakdown into smaller flakes. It was also sonificated for at least an hour before each subsequent use. However, this seems to not have been enough to break down the rGO to a size where it could infiltrate the inverse opal structure. rGO effects may inhibit light from reaching the inner layers of TIO and perovskite and thus potentially inhibiting rather than supporting the reaction [5]. Improvements could involve modifying GO synthesis method for smaller flakes for smaller pore sizes, not yet attempted here.

5. Conclusion

Titanium dioxide inverse opal structures were successfully synthesised with sol-gel method.

Additionally, the deposition of rGO and $CsPbBr_3$ nanocrystals onto TIO varying the mass loading of $CsPbBr_3$ in the infiltrating solution was undertaken. The nanocomposite photocatalyst was then characterised and tested for photoreduction efficacy, confirming the synthesis of mostly anatase titanium dioxide and demonstrating increased visible light absorbance of $CsPbBr_3$ loaded samples.

Nearly 5-fold improvement in CO yield is observed for the optimum sample synthesised within this study (TIO/rGO/8mg) compared to bare TIO indicating increased light harvesting and photocatalytic improvement with formation of the heterojunction with $CsPbBr_3$. In addition, some increased visible light absorbance is demonstrated in UV-Vis measurements, attributed to the inverse opal photonic bandgap and slow light effects.

Results of varying $CsPbBr_3$ loading suggests there is an optimum loading value of $CsPbBr_3$ due to competition in light absorption when overloading. Based on our results, a higher $CsPbBr_3$ loading may be needed for optimum performance with rGO compared to without rGO however due to experimental uncertainty this requires further investigation.

It is suggested that difficulty in obtaining a transparent layer of rGO may hinder reaction and reduces photocatalytic effectiveness due to light and pore-diffusion blocking, as it was observed that large layers were deposited on top of instead of within the IO structure and there is uneven rGO dieposition. Smaller GO flakes as a precursor would therefore need to be used for smaller pore sizes.

Moving forward, several repeat readings would need to be taken for the experiments to improve experimental uncertainty, especially for photocatalytic and Raman measurements.

6. Acknowledgements

The authors would like to thank Filipp Temerov for his continued guidance and support in the experimentation and assistance with the SEM measurements; Ed Rattner for his aid with the synthesis of the $CsPbBr_3$ nanocrystals; and Matyas Daboczi for his aid with the XRD measurements.

7. References

1. Regue M, Kumar S, Eslava S (2020) CHAPTER 4: Recent Advances in Photocatalytic Materials for Solar Fuel Production from Water and Carbon Dioxide. In: RSC Energy and Environment Series
2. Yu J, Lei J, Wang L, et al (2018) TiO2 inverse opal photonic crystals: Synthesis, modification, and applications - A review. Journal of Alloys and Compounds 769:740–757. https://doi.org/10.1016/J.JALLCOM.2018.07.357
3. Dong H, Zeng G, Tang L, et al (2015) An overview on limitations of TiO2-based particles for photocatalytic degradation of organic pollutants and the corresponding countermeasures. Water Research 79:128–146. https://doi.org/10.1016/J.WATRES.2015.04.038
4. Vu N-N, Kaliaguine S, Do T-O, et al (2019) Critical Aspects and Recent Advances in Structural Engineering of Photocatalysts for Sunlight-Driven Photocatalytic Reduction of CO2 into Fuels. Advanced Functional Materials 29:1901825. https://doi.org/10.1002/ADFM.201901825
5. Low J, Cheng B, Yu J (2017) Surface modification and enhanced photocatalytic CO 2 reduction performance of TiO 2 : a review. Applied Surface Science 392:658–686. https://doi.org/10.1016/j.apsusc.2016.09.093
6. Humayun M, Raziq F, Khan A, Luo W (2018) Modification strategies of TiO2 for potential applications in photocatalysis: a critical review. http://mc.manuscriptcentral.com/tgcl 11:86–102. https://doi.org/10.1080/17518253.2018.1440324
7. Ding Y, Huang L, Barakat T, Su BL (2021) A Novel 3DOM TiO2 Based Multifunctional Photocatalytic and Catalytic Platform for Energy Regeneration and Pollutants Degradation. Advanced Materials Interfaces 8:2001879. https://doi.org/10.1002/ADMI.202001879
8. Huo J, Yuan C, Wang Y (2019) Nanocomposites of Three-Dimensionally Ordered Porous TiO2 Decorated with Pt and Reduced Graphene Oxide for the Visible-Light Photocatalytic Degradation of Waterborne Pollutants. ACS Applied Nano Materials 2:2713–2724. https://doi.org/10.1021/ACSANM.9B00215/SUPPL_FILE/AN9B00215_SI_001.PDF
9. Peng C, Reid G, Wang H, Hu P (2017) Perspective: Photocatalytic reduction of CO2 to solar fuels over semiconductors. Journal of Chemical Physics 147:. https://doi.org/10.1063/1.4985624

10. Dong Z, Zhang Z, Jiang Y, et al (2021) Embedding CsPbBr3 perovskite quantum dots into mesoporous TiO2 beads as an S-scheme heterojunction for CO2 photoreduction. Chemical Engineering Journal 133762. https://doi.org/10.1016/J.CEJ.2021.133762
11. Jiang Y, Chen HY, Li JY, et al (2020) Z-Scheme 2D/2D Heterojunction of CsPbBr3/Bi2WO6 for Improved Photocatalytic CO2 Reduction. Advanced Functional Materials 30:. https://doi.org/10.1002/adfm.202004293
12. Huynh KA, Nguyen DLT, Nguyen VH, et al (2020) Halide perovskite photocatalysis: progress and perspectives. Journal of Chemical Technology and Biotechnology 95
13. Chen H, Li R, Guo A, Xia Y (2021) Highly fluorescent CsPbBr3/TiO2 core/shell perovskite nanocrystals with excellent stability. SN Applied Sciences 3:1–7. https://doi.org/10.1007/S42452-021-04648-8/FIGURES/8
14. Zhao Y, Wei Y, Wu X, et al (2018) Graphene-wrapped Pt/TiO2 photocatalysts with enhanced photogenerated charges separation and reactant adsorption for high selective photoreduction of CO2 to CH4. Applied Catalysis B: Environmental 226:360–372. https://doi.org/10.1016/J.APCATB.2017.12.071
15. Mondal A, Prabhakaran A, Gupta S, Subramanian VR (2021) Boosting Photocatalytic Activity Using Reduced Graphene Oxide (RGO)/Semiconductor Nanocomposites: Issues and Future Scope. ACS Omega 6:8734–8743. https://doi.org/10.1021/ACSOMEGA.0C06045
16. Boppella R, Kochuveedu ST, Kim H, et al (2017) Plasmon-Sensitized Graphene/TiO2 Inverse Opal Nanostructures with Enhanced Charge Collection Efficiency for Water Splitting. ACS Applied Materials and Interfaces 9:. https://doi.org/10.1021/acsami.6b14618
17. Xu Q, Zhang L, Cheng B, et al (2020) S-Scheme Heterojunction Photocatalyst. CHEMPR 6:1543–1559. https://doi.org/10.1016/j.chempr.2020.06.010
18. Liang J, Chen D, Yao X, et al (2020) Recent Progress and Development in Inorganic Halide Perovskite Quantum Dots for Photoelectrochemical Applications. Small 16:. https://doi.org/10.1002/SMLL.201903398/FORMAT/PDF
19. Wu M, Li Y, Deng Z, Su BL (2011) Three-Dimensionally Ordered Macroporous Titania with Structural and Photonic Effects for Enhanced Photocatalytic Efficiency. ChemSusChem 4:1481–1488. https://doi.org/10.1002/CSSC.201100082
20. Wu M, Jin J, Liu J, et al (2013) High photocatalytic activity enhancement of titania inverse opal films by slow photon effect induced strong light absorption. Journal of Materials Chemistry A 1:15491–15500. https://doi.org/10.1039/C3TA13574H
21. Zhang X, Liu Y, Lee ST, et al (2014) Coupling surface plasmon resonance of gold nanoparticles with slow-photon-effect of TiO2 photonic crystals for synergistically enhanced photoelectrochemical water splitting. Energy & Environmental Science 7:1409–1419. https://doi.org/10.1039/C3EE43278E
22. Temerov F, Pham K, Juuti P, et al (2020) Silver-Decorated TiO2Inverse Opal Structure for Visible Light-Induced Photocatalytic Degradation of Organic Pollutants and Hydrogen Evolution. ACS Applied Materials and Interfaces 12:. https://doi.org/10.1021/acsami.0c08624
23. Kumar S, Regue M, Isaacs MA, et al (2020) All-Inorganic CsPbBr3Nanocrystals: Gram-Scale Mechanochemical Synthesis and Selective Photocatalytic CO2Reduction to Methane. ACS Applied Energy Materials 3:. https://doi.org/10.1021/acsaem.0c00195
24. Jiang Y, Liao JF, Xu YF, et al (2019) Hierarchical CsPbBr3 nanocrystal-decorated ZnO nanowire/macroporous graphene hybrids for enhancing charge separation and photocatalytic CO2 reduction. Journal of Materials Chemistry A 7:13762–13769. https://doi.org/10.1039/C9TA03478A
25. Poli I, Hintermair U, Regue M, et al (2019) Graphite-protected CsPbBr3 perovskite photoanodes functionalised with water oxidation catalyst for oxygen evolution in water. Nature Communications 2019 10:1 10:1–10. https://doi.org/10.1038/s41467-019-10124-0
26. Pham K, Temerov F, Saarinen JJ (2020) Multicompound inverse opal structures with gold nanoparticles for visible light

photocatalytic activity. Materials and Design 194:. https://doi.org/10.1016/j.matdes.2020.108886

27. Wang L, Ma D, Guo C, et al (2021) CsPbBr3 nanocrystals prepared by high energy ball milling in one-step and structural transformation from CsPbBr3 to CsPb2Br5. Applied Surface Science 543:. https://doi.org/10.1016/j.apsusc.2020.148782
28. Hatton B, Mishchenko L, Davis S, et al Assembly of large-area, highly ordered, crack-free inverse opal films. https://doi.org/10.1073/pnas.1000954107/-/DCSupplemental
29. Míguez H, Tétreault N, Hatton B, et al (2002) Mechanical stability enhancement by pore size and connectivity control in colloidal crystals by layer-by-layer growth of oxide. Chemical Communications 2:2736–2737. https://doi.org/10.1039/B208805N
30. Frank O, Zukalova M, Laskova B, et al (2012) Raman spectra of titanium dioxide (anatase, rutile) with identified oxygen isotopes (16, 17, 18). Physical Chemistry Chemical Physics 14:14567–14572. https://doi.org/10.1039/C2CP42763J
31. Chen H, Guo A, Zhu J, et al (2019) Tunable photoluminescence of CsPbBr3 perovskite quantum dots for their physical research. Applied Surface Science 465:656–664. https://doi.org/10.1016/J.APSUSC.2018.08.211
32. Sun N, Ma J, Wang C, et al (2018) A facile and efficient method to directly synthesize TiO2/rGO with enhanced photocatalytic performance. Superlattices and Microstructures 121:1–8. https://doi.org/10.1016/J.SPMI.2018.07.017
33. Tuschel D (2016) Selecting an Excitation Wavelength for Raman Spectroscopy. Spectroscopy 31:14–23
34. Schroden RC, Al-Daous M, Blanford CF, Stein A (2002) Optical Properties of Inverse Opal Photonic Crystals. Chemistry of Materials 14:3305–3315. https://doi.org/10.1021/CM020100Z
35. Johannes AZ, Pingak RK, Bukit M (2020) Tauc Plot Software: Calculating energy gap values of organic materials based on Ultraviolet-Visible absorbance spectrum. MS&E 823:012030. https://doi.org/10.1088/1757-899X/823/1/012030
36. Zhang Q, Sun X, Zheng W, et al (2021) Band Gap Engineering toward Wavelength Tunable CsPbBr3Nanocrystals for Achieving Rec. 2020 Displays. Chemistry of Materials 33:3575–3584. https://doi.org/10.1021/ACS.CHEMMATER.1C00145/SUPPL_FILE/CM1C00145_SI_001.PDF
37. Shu M, Zhang Z, Dong Z, Xu J (2021) CsPbBr3 perovskite quantum dots anchored on multiwalled carbon nanotube for efficient CO2 photoreduction. Carbon 182:454–462. https://doi.org/10.1016/J.CARBON.2021.06.040

Microcapsule formation through the drying of colloidal suspensions using acoustic levitation

Deniz Aslan, Adrian Ize-Iyamu

DEPARTMENT OF CHEMICAL ENGINEERING, IMPERIAL COLLEGE LONDON, U.K.

Abstract

This document presents an investigation into the use of acoustic levitation to form microcapsules from silica nanoparticles (Ludox) and salt solutions. The drying regimes of these systems were investigated with optical microscopy and the resulting capsules were observed with Scanning Electron Microscopy to determine their surface morphology and internal structure. This study deduced a clear relationship between the concentration of colloidal suspensions within the mixtures, the drying profile and capsule structures; with higher concentrations of colloidal suspensions resulting in faster drying rates and smoother structures with higher aspect ratios (non-spherical shapes).

Introduction

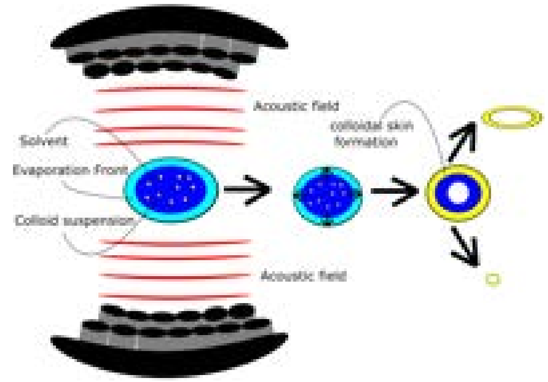

Fig. 1 Schematic illustration of droplet drying with acoustic levitation

Micro-capsules are useful in a wide range of areas which require specialised containers to protect, transport and deliver active, encapsulated materials, *e.g.* small molecules therapeutics. They are employed in fields such as drug delivery, paints & coatings and catalysis.[1–4] The shape, surface morphology and internal structure of these capsules can be designed to impart different functions such as large cargo capacity and tuneable release properties.[5] Due to the wide industrial applications of micro-capsules, understanding the mechanisms that govern micro-capsule formation and their optimisation is a thriving and exciting area of research.[6]

Traditionally, micro-capsules have been fabricated from 'bottom-up' synthetic techniques *e.g.* dispersion polymerisation or solvent removal from bulk emulsions.[7,8] More recently, techniques that combine the principles of microfluidics and directional solidification have been utilised to form precise capsules with prescribed release profiles related to the capsule internal microstructure.[9] For capsules formed by a solvent removal and directional solidification process, the capsule shape, size and internal structure are determined by the input mixture thermodynamics and the dynamic drying pathway undertaken.[10] Spray drying is the most common technique employed industrially to produce these capsules due to the throughput and versatility of the process to produce a variety of capsule structures.[11] Parameters such as temperature, pressure, feed flow rate and atomiser size can be optimised in the production process to meet different capsule specifications.[12] Additionally, spray drying can be operated as a batch and continuous process.[13]

For experimental evaluation of the drying of single droplets a spray dryer is impractical due to the droplets travelling at high velocities and fast drying times.[14] Alternative strategies, such as the glass filament technique, are employed.[15] However, acoustic levitation is being increasingly investigated as a potentially stronger technique to facilitate precise control over the formation of micro-capsules as it removes the need for mechanical contact between the droplet and the apparatus.[16] Since droplets are suspended in mid-air, drying can occur from all sides and the resulting capsules will be less hemispherical in nature.[17] Additionally, since the droplet is stationary it allows for pseudo-spray drying to be performed under a range of conditions in the laboratory. Acoustic levitation works by producing a standing wave between two surfaces; either by a transmitter and reflective surface, known as a Langevin Horn, or two emitting surfaces, known as a single-axis levitator.[18,19] Within the acoustic field a series of nodes is formed due to regions of constructive and destructive interference.[20] A droplet is able to be suspended within the nodes of the system with the gravitational force acting on the droplet being balanced by the vertical oscillatory pressure of the acoustic force.[21]

Experimental Procedure

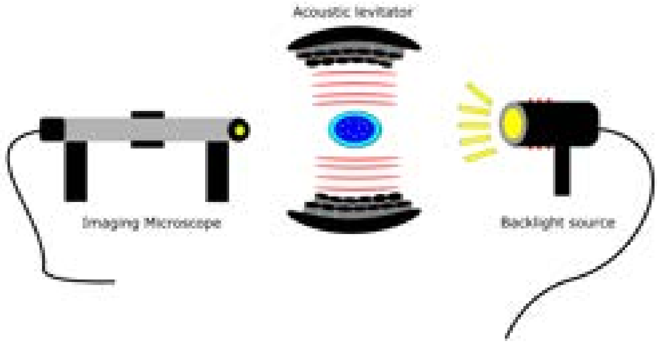

Fig. 2 Schematic illustrating the experimental set-up for the drying process including the camera to record the drying (shown on the left), the light source to ensure the images recorded are clear (shown on the right), the levitator with a depiction of the acoustic waves it emits and the droplet at the center

System

For this investigation micro-capsules were made of Ludox colloidal silica, which was selected as the material of choice due to its well established chemistry which includes thermodynamic stability at room temperature, low toxicity, and most importantly it forms stable colloidal suspensions in various conditions and mixtures.[22–24] The Ludox AS-40 colloidal silica was sourced from Sigma Aldrich; 40% (w/w) suspension in H_2O; with average molecular weight 60.08 g/mol. Our solvent of choice was water due to its thermodynamic stability, ability to carry colloidal silica suspensions, and its ability to evaporate at a relatively slow rate at room temperature - which is crucial to examine micro-capsule formation.[25] Distilled Water obtained from filtration system sourced from ThermoFisher Scientific - Nalgene labware. Sodium Chloride (NaCl) was selected to form ternary mixtures due to its ability to screen the surface charges on colloidal silica; providing the ability to tune the mixture thermodynamics and inter-particle interactions.[26,27] NaCl was sourced from VWR Chemicals with average molecular weight 58.44 g/mol. Binary solutions of Ludox with distilled water as solvent were used in Binary solutions with the concentrations (w/w) 1%, 5%, 10%, 20%, 30% and 40%. Salt (NaCl) was added to these mixtures to create ternary solutions with salt concentrations varying between 0.1%, 1% and 2%. Solutions were prepared gravimetrically to the concentrations using a balance - sourced from Balance Technology.

Experimental Setup

The acoustic drying process is very sensitive and can be influenced by minute changes in temperature, pressure, humidity and air flow around the system which may knock the droplet out of place.[20] To mitigate this the acoustic levitator was placed in a humidity controlled chamber, which allowed for precise control of these parameters. The temperature was set to 25°C and the humidity was set to 50%. The closed chamber also allowed for control of air flow around the acoustic levitator.

Droplets of the samples were injected with syringes into the central node of the acoustic levitator. The droplets were aimed to be as small as possible to prevent them from overlapping between regions of constructive and destructive interference as this would cause the droplets to vibrate violently until a stabilisation point is reached or until the droplets are ejected from the system. The droplets were backlit using a Thorlabs LED fitted with an Olympus condenser lens and images were acquired using a Mitutoyo 5X infinity-corrected objective and Basler acA2040-90uc camera; recording snapshots at 1 frame per second and yielding a spatial resolution of 1.10 μm/pixel. Once the droplets had fully dried and formed a solid capsule they were collected for further analysis.

Methods

The images were processed using the software ImageJ - which extracted droplet radii and areas; establishing relationships between sample concentrations and their drying rates and deformations in their shape.[28] The software MATLAB R2020b was also used in data analysis. Dry capsules were sputter coated with gold (EmiTech K575, 25mA for 25s) prior to imaging with scanning electron microscopy (SEM) with a JEOL6010LA operated at 10kV to visualise the surface morphology and internal structure of these particles.

Radii extracted from optical images were modelled using an adapted descriptive equation which had previously been used to model droplet solvent extraction.[29]

$$R(t) = R_\infty + (R_0 - R_\infty)(1 - \frac{t}{\tau})^{\alpha\sqrt{\frac{t}{\tau}}} \quad (1)$$

This equation was adapted by multiplying the exponent

α by a factor of $\sqrt{\frac{t}{\tau}}$. When testing the original empirical fit, it was found that for a given data set, higher alpha values fit the middle region of the drying process better while lower values were a better fit for the beginning and end. This makes it difficult to get a good quantitative fit with one alpha value. Based on this, it was deduced that rather than a constant exponent, a dynamic time-dependent one would be required to produce a closer fit to the data. R(t) is the radius of the droplet as a function of time (m); R_∞ is the final droplet radius (m); R_0 is the initial droplet radius (m) and τ is the solvent extraction time (s). For the original fit, α was an exponent which accounted for the Fickian (or otherwise) nature of the solvent removal, however it is unknown if this physical meaning is retained.[29] To compare the data to the empirical fit, the equivalent radius approximation was used to combine the major and minor axes into one radius:

$$R(t) = \sqrt[3]{R_{major}^2 R_{minor}} \tag{2}$$

where R_{major} and R_{minor} are the radii (m) of the droplet along the major and minor axes respectively.

During droplet drying the air-liquid interface starts receding due to evaporation and the colloids are brought to this interface by advective transport. Diffusive transport attempts to homogenise the system by transporting colloidal particles towards the centre of the droplet. The Péclet number, Pe, is used to determine which mechanism has more of an influence.[30]

$$Pe = \frac{Ru}{D} \approx \frac{R^2}{Dt} = \frac{advection\ rate}{diffusion\ rate} \tag{3}$$

where R is the characteristic radius (m) of the droplet and can be approximated by the equivalent radius from equation 3; u is the speed of movement of the bulk fluid ($m.s^{-1}$) and can be approximated by the change in equivalent radius over total drying time ($\frac{dR}{dt}$); D is the diffusion coefficient ($m^2.s^{-1}$). This allows a better picture to be illustrated of what occurs within the droplet as the drying occurs. D can be calculated through the Stokes-Einstein equation:

$$D = \frac{k_B T}{6\pi\eta r} \tag{4}$$

where k_B is the Boltzmann constant ($1.38x10^{-23} m^2.kg.s^{-2}.K^{-1}$), T is the absolute temperature (298K), η is the viscosity of the solvent - water ($8.9x10^{-4} Pa.s$) and r is the hydrodynamic radius of the colloid ($\approx 50nm$).

Results & Discussion

Drying of Water

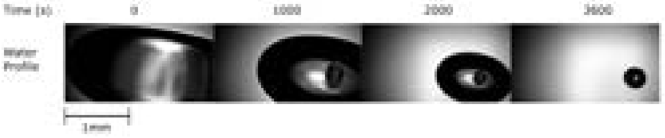

Fig. 3 Images showing the profile of a distilled water droplet as it dries over time

The solvent used in these experiments was distilled water and therefore it was necessary to observe the drying profile of water in the acoustic field. The profile above shows that water droplets dry over the course of approximately an hour and retain a mostly spherical shape throughout. An estimation of the Péclet number using equation 3 and 4 yields a value of 0.85 indicating that in this drying regime diffusive transport and advective transport both have significant roles in this system. Diffusive transport homogenises the water particles across the entire volume of the water droplet; preventing shape deformation, whereas advective transport brings the water particles to the evaporating interface.[31] A balance between advective and diffusive transport must be maintained because this is a single component system and water is evaporating, therefore, if advective transport dominates water particles would accumulate at the air-liquid interface forming a void in the centre of the droplet - which would lead to structural instability.[32]

Binary System

Shape of Particles and Evaporation Rate

Figure 4 shows the drying evolution of samples containing Ludox with the solvent water and the profile of its surface area and radius. Figure 4a shows the evaporation rate through the change in normalised surface area of the droplets over time. All of the concentrations follow a similar drying rate with 3 distinct stages. First there is a steady drying rate, where the droplet's surface area steadily decreases. At the second stage a transition stage is reached where the evaporation rate significantly decreases and the drop begins forming a solid skin, this transition state occurs at different times depending on the concentration of Ludox. In the last stage the evaporation rate is marginal and the normalised area of the surface area of the droplet levels off as there is minimal amounts of solvent present in the system. 4a shows that as the concentration of colloidal suspensions decreases the overall drying time decreases with 1% and 40% hav-

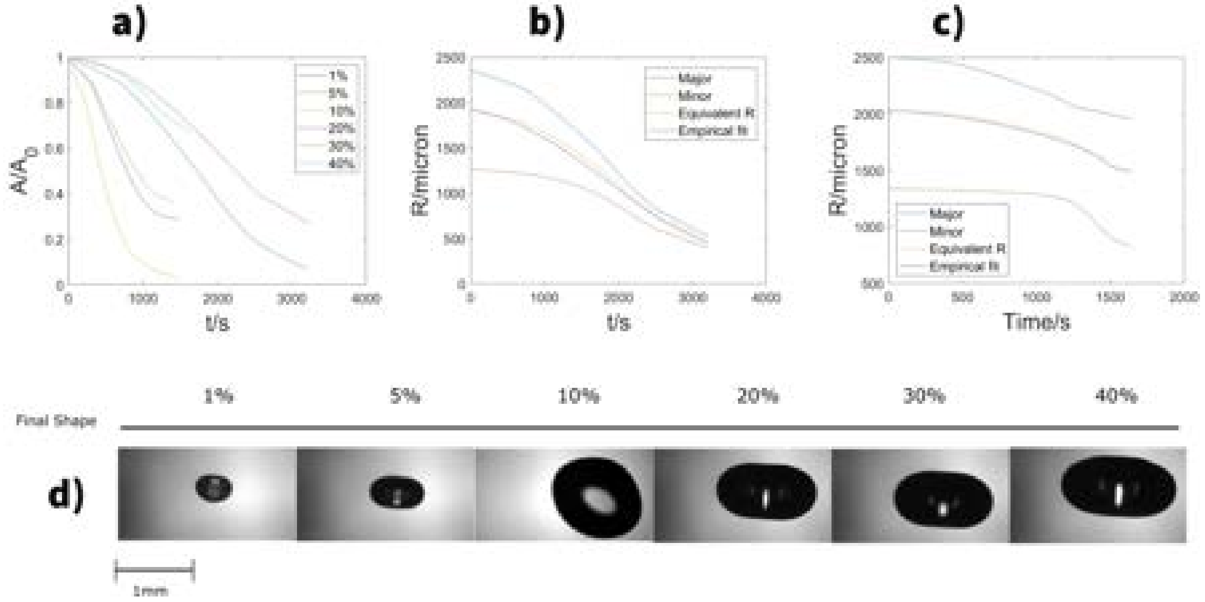

Fig. 4 Plots and graphs characterising the drying process for the Ludox solutions with a) Plot depicting the effects of Ludox concentration on the normalised cross-sectional area with respect to time b) Plot for 1% Ludox depicting the changes in major and minor radii and an equivalent radius with respect to time. c) Plot for 40% Ludox depicting the changes in major and minor radii and an equivalent radius with respect to time. d) A series of images taken from Image J depicting the final shape of capsule formed for all concentrations of Ludox.

ing a total drying time of ≈ 3200s and 1250s respectively. Furthermore, the transition state where a skin is beginning to form lasts a lot longer in lower concentration samples compared to their higher concentration counterparts - the 1% sample lasts nearly 600 seconds compared to 30% which forms its skin in about 200 seconds.

Additionally Figures 4b and 4c depict the change in major and minor radii over time for 1% and 40% Ludox samples, respectively. Divergences in the radii occur as the droplets dry within the acoustic field, because they are under the influence of various forces. There is a gravitational force acting downwards on the droplet, and an oscillatory pressure force acting upwards on the droplet. Hence, the greatest deformation comes from the vertical direction which creates elongated spheroids, with the horizontal axis forming the major radius and the vertical axis forming the minor radius. However, there are significant differences between the radii profiles in 1% and 40% samples. For 1% samples the radii converge to form a near spherical particle with an aspect ratio close to 1, while the 40% samples become more elongated with the major radius being more than twice that of the minor radius.

This elongation effect is most apparent in samples containing a larger concentration of Ludox - 20%, 30%, and 40% in particular - as can be seen in Figure 4d. The shapes formed from high concentrations of Ludox can be further explained by examining the drying mechanisms. The droplets initially start out with the micro-particles suspended within them. As drying progresses the micro-particles begin to drift towards the surface of the droplet and start packing at the interface. During this stage the evaporation rate is relatively constant as can be seen in Figure 4c. This process forms an internal void in the droplet with a rigid shell which slightly weakens the structure. As more colloidal particles are drawn to the surface a shell begins to form. This transition state can be observed in the graph, where the evaporation rate slows down significantly. Any remaining water solvent now has to diffuse through this shell - which is gradually becoming thicker; creating internal stresses. The particles that have accumulated at the evaporation front are drawn together by capillary forces, eventually being locked in place through van der Waals forces.[31,32] The vertical forces acting on the droplet coupled with the internal stresses, causes it to deform and cave inwards resulting in elongation. Ultimately a droplet with a high aspect ratio is formed.[33] This is observed in the divergence between the major and minor radius in 4c. This type of a system is characteristic of a drying regime where advective transport dominates, which is supported through an estimation of the Péclet number using equation 3 and 4, yielding a value of 163.2.[32]

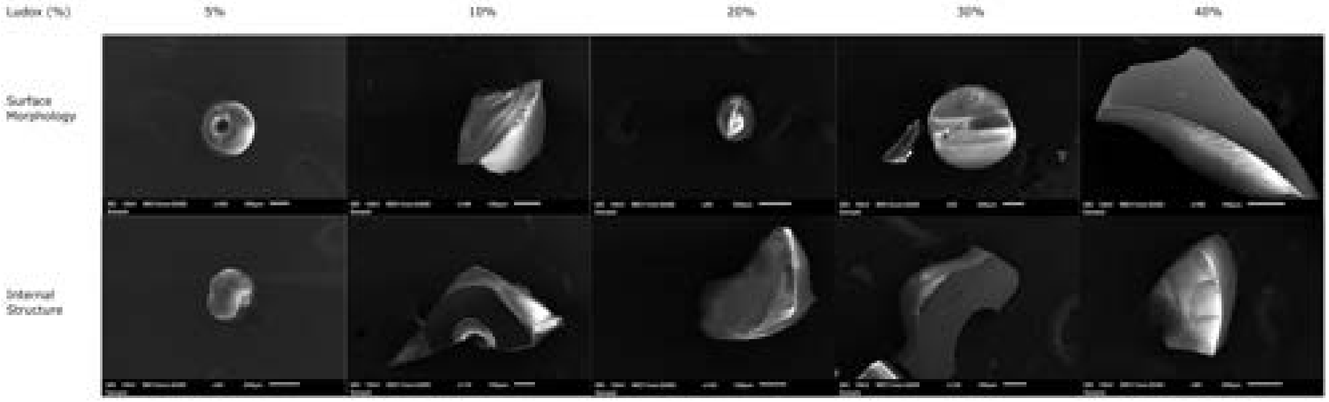

Fig. 5 Morphology diagram for the binary Ludox solutions

Lower concentrations of Ludox (1%, 5% and 10%) undergo a different drying process. From Fig 4a, it is seen that the transition state lasts for a far longer time; several minutes compared to their higher concentration counterparts. Furthermore, the droplets sizes for these concentrations are a lot smaller and a lot more spherical as indicated by the convergence of radii in Fig 4b. These systems are characteristic of those where the diffusive transport plays a much more significant role in the system, which is supported through an estimation of the Péclet number using equation 3 and 4, yielding a value of 15.6.[31].

The mechanism of this process is similar to the high concentration samples however, due to the slow rate of evaporation less colloidal particles are brought to the evaporation front through advective transport. Furthermore, as the diffusive transport component now plays a more significant role the colloidal particle concentration is more uniform throughout the droplet during its shrinking[31]. This leads to a more spherical shell which is as observed in Figure 4b as the radii are very similar. Thus it can be inferred that as the Ludox concentration decreases the aspect ratio tends to 1.[31]

Capsule Characterisation

Figure 5 shows a series of images from the various Ludox concentrations depicting the surface morphology and internal structures of these systems. It can be observed that all capsules have a smooth surface, this can be attributed to the drying regimes as estimated Péclet numbers are all greater than 1 indicating a regime dominated by convective transport. Therefore, inferring less colloidal clumping at the evaporation front.[31] Additionally, as the concentration of the Ludox increases, the general shape of the capsules becomes more elongated with a higher aspect ratio. This is most clearly observed in 30% images of Figure 5. It can be deduced that the deformations occurring in high concentration of Ludox are due to drying regimes with Péclet numbers much greater than 1. Which means there is preferential particle accumulation at the air liquid interface - making it susceptible to deformations.[34]

For lower concentrations, a more spherical shape is observed which is attributed to the isotropic drying profile due to the drying regime having a lower Péclet number, where the diffusive transport plays a more significant role in the system. Unfortunately 5% samples are to small to get an accurate depiction of surface characteristics; however, previous research has suggested a slightly more rough structure could be expected due to mechanical instability at small sizes and colloidal clumping due to a greater role of diffusive transport.[35].

The internal structure also varies between the concentrations, with higher concentrations tending to have thicker shells but a larger overall size - thus retaining a hollow internal structure. However, it is visible that there are regions of high stress on these capsules which is most clearly observed in the 40% image which puts the capsule at risk of breaking.

The lower concentration materials formed far smaller particles. The skins were relatively thin compared to the higher concentration samples, but due to the smaller volume of the capsules an overall denser structure was formed. Interestingly, the 5% sample formed a spherical toroidal structure, which is unusual given the samples concentration. A low Péclet number was calculated for this drying regime, which would expect to form a spherical particle.This formation could be explained through a variation between the flow regimes in the centre of the droplet and the outside of the droplet during levitation. If the centre of the droplet is more stagnant than the outside then the solvent would be carried out more rapidly on the outside edges.[36] If this drying regime occurred then the colloidal Ludox would be concentrated on the outside of the droplet. Thus, the centre of the droplet gets thinner until a breaking point is reached and a toroidal structure is formed.[36]

Unfortunately the 1% sample was extremely small and brittle and could not be transferred and mounted onto SEM stubs and placed under vacuum for imaging and was thus not pursued for further investigation. Overall, the 1% and 5% concentrations formed samples to small and brittle and were not pursued for further investigation.

τ distribution

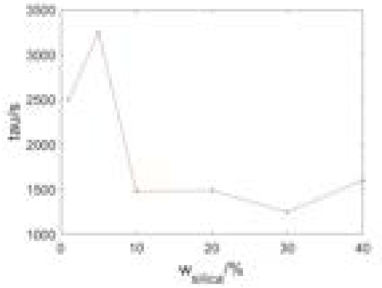

Fig. 6 Graph of droplet extraction time against concentration of colloidal silica

Looking in more detail at the τ distribution as seen in Figure 6, there isn't a strong correlation between drying time and silica concentration which is largely due to the volatile nature of the drying. This fact makes it difficult to pinpoint the exact time it takes for droplets of given concentration to dry. However, it can be seen that generally lower concentrations take a longer time to dry since they have more water in them. At 10% colloidal silica, τ falls significantly and remains low for higher concentrations, which represents an increased advection influence in the drying and makes the process significantly faster.

Ternary System

Shape of particles and evaporation rate

The impact of adding salt to the Ludox solutions is analysed through Figure 7 and its observed that the amount of NaCl in the system has a significant effect on the drying process. This is best illustrated by the 10% Ludox mixture in 7a,b,c graphs, which sees a significant increase in the time it takes for drying to occur from 0.1% to 1% salt before falling again at 2% salt. This could be attributed to the interaction between NaCl and Ludox; since Ludox is a charged colloid the salt screens the surface charges allowing for these particles to come closer together and potentially aggregate.[26,27] This impedes the evaporation of water molecules and increases the time it takes for the droplet to dry. The other phenomenon could be the salt acting as a drying agent and creating an osmotic gradient between the two sides of the droplet surface leading to a faster evaporation time.[37]

Analysing 7a,b,c shows no correlation between reduction in area and salt concentration for all concentrations apart from 10% - which displays an increase in the area reduction over time. This suggests that for 10% the concentration of salt can be used to design capsule size. Looking at the corresponding images in Figure 7d, an increase in salt concentration forms more spherical capsules - suggesting a regime where diffusive transport plays a more important role.

The graphs in 7 show that a similar drying profile to the binary solutions occurs, where there are 3 distinct drying stages (steady evaporation, skin formation, droplet settling). It is worth noting that the extent to which deformation occurs in the second stage is largely dependent on what drying regime the mixture droplet is within *i.e.* the value of the Péclet number. Looking at Figure 7a, it can be seen that the drying time increases as Ludox concentration goes from 10% to 20% to 30% while suddenly significantly decreasing at 40%. This suggests a much stronger influence of advective transport for the 40% concentration compared to its subsequent concentrations. This is further supported by calculating the Péclet numbers through equation 3 and 4, which yielded for the four solutions Péclet numbers of 43, 93.6, 36.7 and 264.7 in order of increasing Ludox concentration.

Comparing Figures 7b and 4a, it is observed that for the 10% binary Ludox mixtures, the 1% salt one takes significantly longer to dry in comparison to the 0.1% mixture which indicates that diffusive evaporation dominates over advective evaporation and that the drying is thus defined by a lower Péclet number. This is likely due to the aforementioned effect of salt seeding the surface charges of Ludox. NaCl also disolves in water and this chemical interaction may impede the diffusion of water out of the droplet. Additionally, the 40% drying process is strikingly similar to the 0.1% NaCl concentration. Therefore, it is likely that the higher the Ludox concentration, the more salt is required to make an impact on the drying process of the particle.

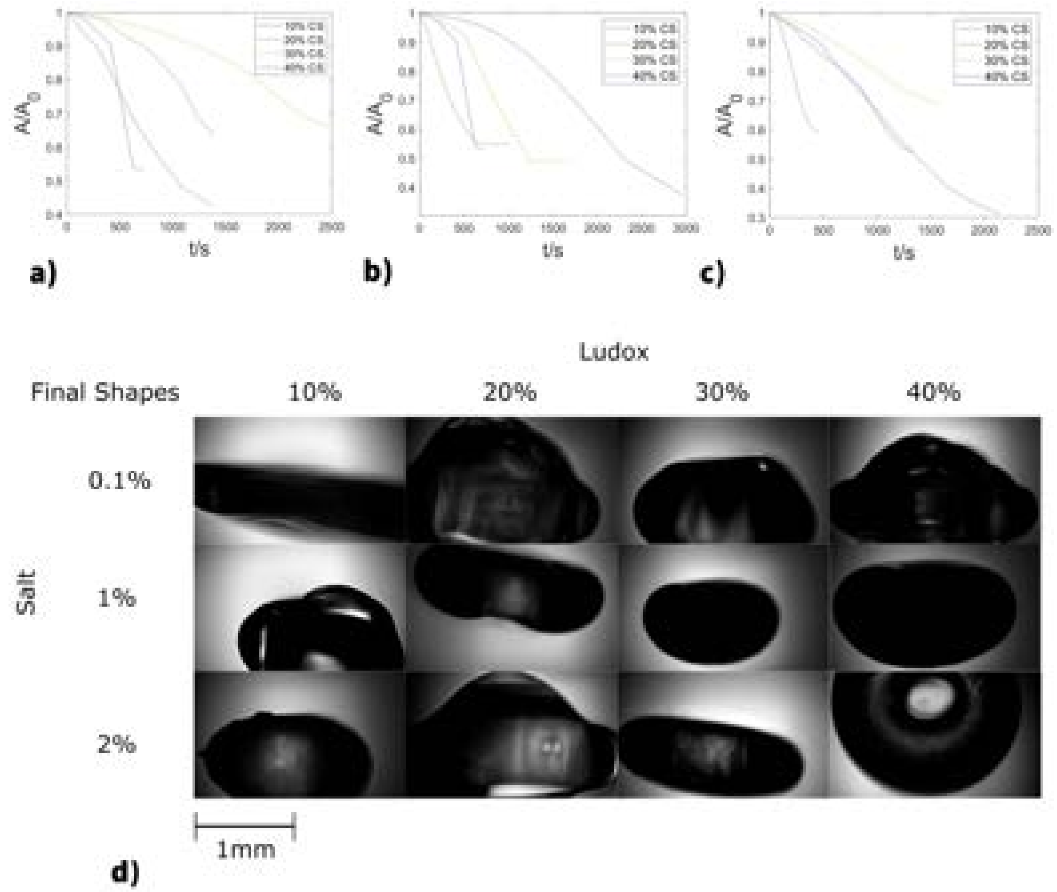

Fig. 7 Characterisation of the ternary solution droplets drying rate and mass transfer phenomena with graphs of cross-sectional area normalised by original area over time for a) 0.1% NaCl, b) 1% NaCl and c) 2% NaCl as well as d) the droplets for each mixture as they appear when the drying is complete to form capsules (Note: CS in the legends stands for colloidal silica)

Looking at Figure 7d for all salt concentration, there is a tendency towards sphericity as the Ludox concentration increases. However, since calculated Péclet numbers remain high for high Ludox concentrations (40% Ludox yields Péclet numbers of 264.7, 181.8 and 138.7 with respect to increasing salt concentrations.) a spherical structure is maintained - indicating a more exotic form of drying.

Additionally, it should be noted that as salt concentrations increase the solutions start jelling and pursuing concentrations beyond 2% was infeasible.

Capsule Characterisation

For the 0.1% NaCl row of Figure 8, one can see that the 10% capsule forms an ellipsoid shape with a depression observed in the middle. This has occurred due to significant advective transport in this droplet, leading to a greater deformation from sphericity. In the 0.1% row of Figure 8 capsules have formed with smooth surfaces with the stains observed likely resulting from gold sputter coating during the imaging process. This is similar to the binary Ludox solutions and thus it can be deduced that low salt concentrations don't significantly alter the surface structure of the capsule. The image of the 40% Ludox capsule at this percentage indicates that it was hollow with a shell which is in keeping with its fast solidification seen in 7a as it indicates that the solvent evaporated too quickly for the solution to properly mix leading to accumulation of salt and Ludox at its surface.[38]

For the 1% row, there is a clear shift from an ellipsoidal to a spherical shape as Ludox concentration increases. This result would imply that the Péclet number decreases with increasing Ludox concentration; however, after closer examination the Péclet numbers yielded for all 10% samples are 43, 44, 60 and 40% yields 264.7, 181.8, 138.7 (in order of increasing salt concentration) indicating an increase in Péclet number. This would suggest there is something else other than the drying regime which governs its shape - likely resulting from the interaction of salt with the other components in the system.

While the evaporation rates of the 30% and 40% droplets are faster than that of the 10% droplets, this

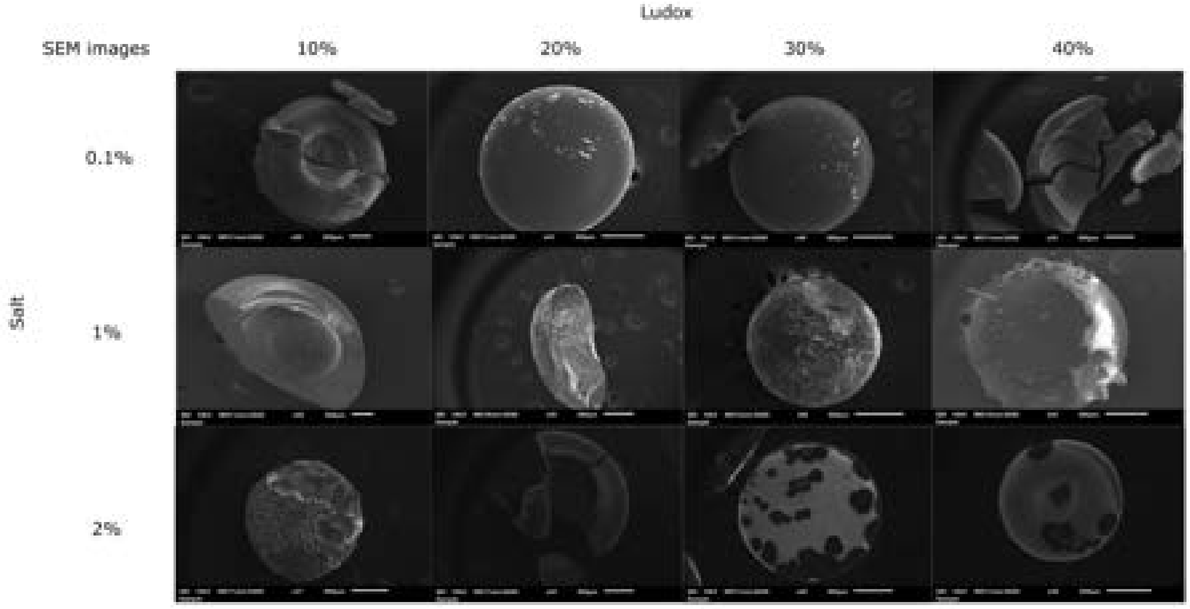

Fig. 8 Morphology diagram for the ternary solutions

trend means that this faster evaporation is predominantly caused by diffusive evaporation. This can be seen in the 20% capsule which appears to be solid. This is also the reason that the 10% droplet at this concentration displays a larger area reduction than the other mixtures. The surface of the capsules also become rougher as the concentration increases. This is due to the progressive dominance of diffusion over advection in the evaporation which means that colloidal clumping occurs as the solutes mix together.

For the 2% row, the capsules seem to show a reverse trend to the 1% row as in terms of structure as the 10% Ludox capsule is the only one that seems to have some kind of roughness. This is made stranger by the fact that it underwent a similar drying process to the 40% capsule. This further reinforces the point the morphology of a capsule is largely dependent on the drying regime the process occurs in rather than the actual drying rate itself. The 20% capsule in this row appears to be darker than in the other 11 capsules in Figure 8 which is likely to be an artefact from sputter coating. The 30% and 40% capsules appear to have growths on their surface which appear black in contrast to the white appearance of the rest of the surface. This could be a crystalline structure resulting from a change in the nature of the intermolecular interactions the salt and colloidal silica experience due to the former's higher concentration. This would then lead to a more ordered Ludox-NaCl complex forming in the shell and on the surface of the capsule making it significantly stronger than before. However, it should be noted that no control system was put in place for the nucleation of salt crystals.

τ distribution

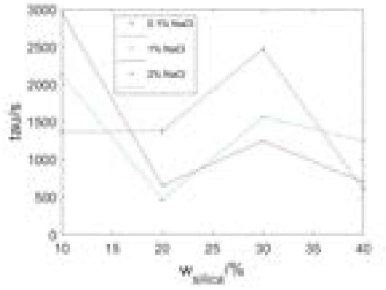

Fig. 9 Graph showing tau vs colloidal silica concentration at three different salt concentrations

As previously mentioned and seen in full detail in Figure 9, the extraction times tau do not have a strong correlation with either silica or salt concentration as seen by the erratic variance, which is explained by a strong interplay between salt-water and salt-silica interactions which work against each other in the drying process. However, for the 20% colloidal silica solutions, there appears to be a negative correlation with salt concentration which indicates that at this level, while for 40% colloidal silica solutions, there is a positive correlation between the two variables. Though the measurement of τ was extremely subjective, these two silica concentrations can be used as reference points to determine how the concentration of silica and salt impact the interactions that they have in the system.

Conclusions

This study investigates the use acoustic levitation to determine the impacts of concentration and composition on the shape, size, surface morphology and internal structure of capsules. It was found that concentration of these colloidal suspensions greatly influenced the drying kinetics in addition to the surface morphology and internal structure of the microcapsules formed. For binary mixtures, lower concentrations of Ludox tended to have much slower drying rates and skin formation often took several minutes; resulting in drying regimes with lower Péclet numbers. These concentrations yielded capsules of more spherical shapes, however greater surface roughness - due to greater particle agglomeration at the liquid/air interface. In contrast to this higher concentrations of Ludox had much faster drying regimes - and it can be therefore inferred that convective evaporation dominated in these systems. This is further supported by the fact that these regimes formed elongated particles with high aspect ratios in addition to smooth surfaces. All concentrations formed hollow structures with skin thickness and overall size of the capsule increasing with concentration.

For the case of ternary structures, there are more factors and mechanisms to consider when determining what mixture compositions are suitable for industrial use. Salt concentrations above 2% were discovered to form gel like solution and it was impossible to form droplets out of. For salt concentrations $\leq$ 2% it has been discovered that varying Ludox concentrations can control the shrinkage that the droplet experiences - with a higher amount of salt resulting to a greater area reduction. It was observed that diffusive evaporation tended to dominate at higher concentrations of Ludox for all salt solutions in contrast to the Ludox solutions as seen by the more spherical capsules on the right half of Figure 8. The drying rate of the droplets were less predictable due to being determined by factors that worked against each other which were the osmotic effect salt has on water and the enhanced solidification effect salt has on the solution. For specific control of the size of the droplet and relative control of morphology, it is recommended that droplets are made with around 10% Ludox and less than 5% salt to create the capsules.

Overall our results follow the trends in published in reports[31 34 36], which observed similar drying kinetics and similar characteristic formations when observed under SEM. For further investigation it is recommended to address the effects of temperature and humidity upon the drying regimes and final structures formed - as these parameters are believed to have a significant impact. Additionally, it is recommended to investigate the application of these concentrations and compositions in spray drying to determine whether or not the capsule characteristics are retained.

Acknowledgements

We thank William N. Sharratt and João T. Cabral for their help and guidance throughout the research.

Notes and references

1 M. A. Trojer, L. Nordstierna, J. Bergek, H. Blanck, K. Holmberg, and M. Nydén, “Use of microcapsules as controlled release devices for coatings,” *Advances in colloid and interface science*, vol. 222, pp. 18–43, 2015.

2 C. Thies, “Microcapsules as drug delivery devices.,” *Critical reviews in biomedical engineering*, vol. 8, no. 4, pp. 335–383, 1982.

3 T. Szabó, L. Molnár-Nagy, J. Bognár, L. Nyikos, and J. Telegdi, “Self-healing microcapsules and slow release microspheres in paints,” *Progress in Organic Coatings*, vol. 72, no. 1-2, pp. 52–57, 2011.

4 M. Buonomenna, A. Figoli, I. Spezzano, M. Davoli, and E. Drioli, “New pvdf microcapsules for application in catalysis,” *Applied Catalysis B: Environmental*, vol. 80, no. 3-4, pp. 185–194, 2008.

5 R. Jalil and J. Nixon, “Biodegradable poly (lactic acid) and poly (lactide-co-glycolide) microcapsules: problems associated with preparative techniques and release properties,” *Journal of microencapsulation*, vol. 7, no. 3, pp. 297–325, 1990.

6 E. Lintingre, F. Lequeux, L. Talini, and N. Tsapis, “Control of particle morphology in the spray drying of colloidal suspensions,” *Soft Matter*, vol. 12, no. 36, pp. 7435–7444, 2016.

7 R. Arshady, “Preparation of biodegradable microspheres and microcapsules: 2. polyactides and related polyesters,” *Journal of Controlled Release*, vol. 17, no. 1, pp. 1–21, 1991.

8 F. Khakzad, Z. Alinejad, A. R. Shirin-Abadi, M. Ghasemi, and A. R. Mahdavian, “Optimization of parameters in preparation of pcm microcapsules based on melamine formaldehyde through dispersion polymerization,” *Colloid and polymer science*, vol. 292, no. 2, pp. 355–368, 2014.

9 C. E. Udoh, J. T. Cabral, and V. Garbin, “Nanocomposite capsules with directional, pulsed nanoparticle release,” *Science advances*, vol. 3, no. 12, p. eaao3353, 2017.

10 S. SUZUKI, T. KONDO, and S. MASON, “Studies on microcapsules. i. preparation of polyurethane and polyphenolester microcapsules,” *Chemical and Pharmaceutical Bulletin*, vol. 16, no. 8, pp. 1629–1631, 1968.

11 E. Assadpour and S. M. Jafari, “Advances in spray-drying encapsulation of food bioactive ingredients: From microcapsules to nanocapsules,” *Annual review of food science and technology*, vol. 10, pp. 103–131, 2019.

12 X. Fang, M. Shima, and S. Adachi, “Effects of drying conditions on the oxidation of linoleic acid encapsulated with gum arabic by spray-drying,” *Food Science and Technology Research*, vol. 11, no. 4, pp. 380–384, 2005.

13 B. Long, K. M. Ryan, and L. Padrela, "From batch to continuous—new opportunities for supercritical co2 technology in pharmaceutical manufacturing," *European Journal of Pharmaceutical Sciences*, vol. 137, p. 104971, 2019.

14 S. Poozesh, S. W. Grib, M. W. Renfro, and P. J. Marsac, "Near-field dynamics of high-speed spray dryer coannular two fluid nozzle: Effects of operational conditions and formulations," *Powder Technology*, vol. 333, pp. 439–448, 2018.

15 B. Adhikari, T. Howes, B. Bhandari, and V. Truong, "Experimental studies and kinetics of single drop drying and their relevance in drying of sugar-rich foods: A review," *International Journal of Food Properties*, vol. 3, no. 3, pp. 323–351, 2000.

16 O. Kastner, G. Brenn, D. Rensink, and C. Tropea, "The acoustic tube levitator–a novel device for determining the drying kinetics of single droplets," *Chemical Engineering & Technology: Industrial Chemistry-Plant Equipment-Process Engineering-Biotechnology*, vol. 24, no. 4, pp. 335–339, 2001.

17 S. Santesson and S. Nilsson, "Airborne chemistry: acoustic levitation in chemical analysis," *Analytical and bioanalytical chemistry*, vol. 378, no. 7, pp. 1704–1709, 2004.

18 R. H. Morris, E. R. Dye, P. Docker, and M. I. Newton, "Beyond the langevin horn: Transducer arrays for the acoustic levitation of liquid drops," *Physics of Fluids*, vol. 31, no. 10, p. 101301, 2019.

19 A. Marzo, A. Barnes, and B. W. Drinkwater, "Tinylev: A multi-emitter single-axis acoustic levitator," *Review of Scientific Instruments*, vol. 88, no. 8, p. 085105, 2017.

20 H. Schiffter and G. Lee, "Single-droplet evaporation kinetics and particle formation in an acoustic levitator. part 1: Evaporation of water microdroplets assessed using boundary-layer and acoustic levitation theories," *Journal of pharmaceutical sciences*, vol. 96, no. 9, pp. 2274–2283, 2007.

21 P. Collas, M. Barmatz, and C. Shipley, "Acoustic levitation in the presence of gravity," *The Journal of the Acoustical Society of America*, vol. 86, no. 2, pp. 777–787, 1989.

22 A. Liberman, N. Mendez, W. C. Trogler, and A. C. Kummel, "Synthesis and surface functionalization of silica nanoparticles for nanomedicine," *Surface science reports*, vol. 69, no. 2-3, pp. 132–158, 2014.

23 A. Guerrero-Martínez, J. Pérez-Juste, and L. M. Liz-Marzán, "Recent progress on silica coating of nanoparticles and related nanomaterials," *Advanced materials*, vol. 22, no. 11, pp. 1182–1195, 2010.

24 J. Wang, Z. H. Shah, S. Zhang, and R. Lu, "Silica-based nanocomposites via reverse microemulsions: classifications, preparations, and applications," *Nanoscale*, vol. 6, no. 9, pp. 4418–4437, 2014.

25 T. Log, "Water droplets evaporating on horizontal semi-infinite solids at room temperature," *Applied Thermal Engineering*, vol. 93, pp. 214–222, 2016.

26 J. Laven and H. N. Stein, "The electroviscous behavior of aqueous dispersions of amorphous silica (ludox)," *Journal of colloid and interface science*, vol. 238, no. 1, pp. 8–15, 2001.

27 H. Ning, J. K. Dhont, and S. Wiegand, "Thermal-diffusive behavior of a dilute solution of charged colloids," *Langmuir*, vol. 24, no. 6, pp. 2426–2432, 2008.

28 J. Schindelin, I. Arganda-Carreras, E. Frise, V. Kaynig, M. Longair, T. Pietzsch, S. Preibisch, C. Rueden, S. Saalfeld, B. Schmid, *et al.*, "Fiji: an open-source platform for biological-image analysis," *Nature methods*, vol. 9, no. 7, pp. 676–682, 2012.

29 T. Watanabe, C. G. Lopez, J. F. Douglas, T. Ono, and J. T. Cabral, "Microfluidic approach to the formation of internally porous polymer particles by solvent extraction," *Langmuir*, vol. 30, no. 9, pp. 2470–2479, 2014.

30 K. A. Baldwin, M. Granjard, D. I. Willmer, K. Sefiane, and D. J. Fairhurst, "Drying and deposition of poly (ethylene oxide) droplets determined by peclet number," *Soft Matter*, vol. 7, no. 17, pp. 7819–7826, 2011.

31 A. Osman, L. Goehring, A. Patti, H. Stitt, and N. Shokri, "Fundamental investigation of the drying of solid suspensions," *Industrial & Engineering Chemistry Research*, vol. 56, no. 37, pp. 10506–10513, 2017.

32 N. Tsapis, D. Bennett, B. Jackson, D. A. Weitz, and D. Edwards, "Trojan particles: large porous carriers of nanoparticles for drug delivery," *Proceedings of the National Academy of Sciences*, vol. 99, no. 19, pp. 12001–12005, 2002.

33 A. Yarin, G. Brenn, O. Kastner, and C. Tropea, "Drying of acoustically levitated droplets of liquid–solid suspensions: Evaporation and crust formation," *Physics of Fluids*, vol. 14, no. 7, pp. 2289–2298, 2002.

34 J. Leng, "Drying of a colloidal suspension in confined geometry," *Physical Review E*, vol. 82, no. 2, p. 021405, 2010.

35 J. W. Hutchinson, "Buckling of spherical shells revisited," *Proceedings of the Royal Society A: Mathematical, Physical and Engineering Sciences*, vol. 472, no. 2195, p. 20160577, 2016.

36 B. Wang, H. C. Shum, and D. A. Weitz, "Fabrication of monodisperse toroidal particles by polymer solidification in microfluidics," *ChemPhysChem*, vol. 10, no. 4, pp. 641–645, 2009.

37 S. E. Skilhagen, J. E. Dugstad, and R. J. Aaberg, "Osmotic power—power production based on the osmotic pressure difference between waters with varying salt gradients," *Desalination*, vol. 220, no. 1-3, pp. 476–482, 2008.

38 Y. Sano and R. Keey, "The drying of a spherical particle containing colloidal material into a hollow sphere," *Chemical Engineering Science*, vol. 37, no. 6, pp. 881–889, 1982.

Effect of pelletisation routes on the physical and adsorption properties of ZIF-8

Iman Rezzag Salem & Serene Thomas

Department of Chemical Engineering, Imperial College London, U.K.

Abstract

The shaping of metal-organic framework (MOF) powders into mechanically stable bodies is paramount for their use in adsorption applications. Herein, this study reports the preparation of ZIF-8 crystals into resistant pellets under hydraulic pressing at 0.4 and 1 tonnes, with a selection of three binders and binder contents. Mechanical stabilities of the formed pellets were investigated and characterisation techniques were conducted on the materials using thermogravimetric analysis, Fourier-transform infrared spectroscopy, volumetric CO_2 adsorption and helium pycnometry. Following analysis of thermal and mechanical stabilities of each binder, methylcellulose/bentonite in a 1:1 ratio shows great promise as a binder to aid in the formation of robust ZIF-8 pellets for gas adsorption processes. With binder addition, adsorption experiments have highlighted that the pellets experience a decrease of CO_2 adsorption capacity, which is proportional to the reduction of ZIF-8 in the overall pellet. A 5% increase in binder content was shown to have negligible effect on the CO_2 adsorption capacity, but significantly improves the mechanical stability of the pellet. CO_2 isotherm plots demonstrated that increasing the pelletisation pressure has little effect on the microporosity of ZIF-8 within the pellet. Conversely, porosity data has indicated that methylcellulose/bentonite may contain macropores which are reduced under increased compression. From this experimental work, an optimal pelletisation route has been identified in line with the chosen parameters; the analyses indicate that a methylcellulose/bentonite binder content of 35% and pelletisation pressure of 1 tonne is a viable approach to shaping mechanically stable ZIF-8 particles suitable for use in industrial adsorption applications.

1. INTRODUCTION AND BACKGROUND

Porous materials, especially those that are thermally stable, are in great demand for many industrial processes, including but not limited to gas separation, adsorption, catalysis, conductivity, and biomedicine (Furukawa & Yaghi (2009); Morris & Wheatley (2008); Murray et al. (2009); Sai Bhargava Reddy et al. (2021); Smith et al. (2013)). Classification of porous materials is typically based on their pore diameter, ranging from microporous (smaller than 2nm), mesoporous (between 2 and 50nm) to macroporous (greater than 50nm) (Sing et al. 1985). These materials are widely available, exhibiting well-tailored physical and chemical properties, which can be designed to suit their specific uses.

Due to present day concerns surrounding global warming and the greenhouse effect, there has been an emphasis on the development of these materials as adsorbents for CO_2 capture (Achiou et al. 2020). These solid adsorbents comprise of metal-organic frameworks (MOFs), clay, silica, activated carbon and zeolites, which have different physiochemical interactions with adsorbates (Chan Wai et al. 2013).

As a class of promising porous materials, MOFs have opened new avenues for adsorption applications. MOFs are microporous crystalline structures consisting of metallic ions that are coupled with organic ligands or 'cross-linkers', displaying favourable characteristics in the field of gas separations (Batten et al. 2013). Zeolitic imidazolate frameworks (ZIFs), a sub-family of MOFs, have been of particular focus in recent research due to their tuneability, high porosities, chemical and thermal stability, as well as large surface areas, and have been of particular focus in recent research studies (Bergaoui et al. (2021); Chan Wai et al. (2013)). ZIFs are strong contenders for several applications relying on controlled adsorption of molecules, such as gas storage, catalysis, and water purification, due to their high selective adsorption of a variety of gases (Petit 2018). ZIF-8 is a classic member of this family and exhibits particularly interesting characteristics including the gate-opening effect, which refers to its structural flexibility when exposed to external stimuli, resulting in enlarged pore apertures and increased pore volume (Muñoz-Gil & Figueiredo 2019). Whilst zeolites also exhibit flexibility, the conditions required to trigger a change are much harsher than that for ZIFs (Petit 2018).

Despite its significant potential, ZIF-8 is yet to be commercially employed in industrial applications, partly due to the challenges faced in its shaping. A common challenge facing the shaping of ZIF-8 is its general lack of cohesive properties, meaning that it cannot easily be shaped to form a mechanically stable pellet without the addition of an adhesive, formally known as a binder. Binders are paramount in imparting mechanical integrity and overall adherent characteristics, but their integration with the ZIF-8 powder generally results in reduced adsorptive performance (Cousin-Saint-Remi et al. 2020). The incorporation of an inactive binder dilutes the active component, the porous powder, which causes a reduction in performance of the structured adsorbent (Akhtar et al. 2014). The binder essentially covers the powder surface leading to pore blockages. In the case of gas separation and storage applications, research into the stability and porosity of structured adsorbents are of high importance, where electronic structure is less decisive of these characteristics (Hendon et al. 2017).

The utilisation of porous materials in adsorption applications requires shaping of the fine powder into a macroscopic body, such as pellets or tablets. This is undertaken to minimise the issues associated with using powders, namely difficulty in handling, high pressure-drop, and low mechanical stability, which are issues typically found in packed bed applications. Pressure drop is significantly impacted by the adsorbent size; the smaller the particle diameter, the higher the pressure drop, which is undesirable as it results in poor system performance and excessive energy consumption (Koekemoer & Luckos 2015). In large-scale adsorption processes, it is essential to use relatively large adsorbent particles, with typical diameters ranging from 1-3mm (Ruthven 1984). The structured adsorbent should exhibit chemical and mechanical stability, with high heat and mass transfer rates, to combat the aforementioned issues. The shaping of porous materials into larger structures has been extensively researched over the past decades, and is often attained via a variety of methods, including granulation, spray-drying extrusion, and pressing (Akhtar et al. (2014); Liu et al. (2020)).

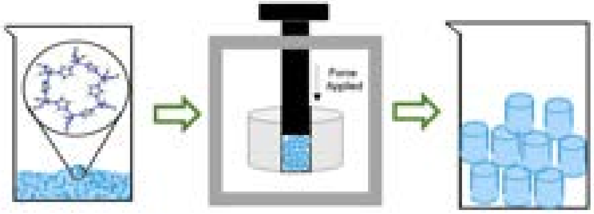

Figure 1: *Schematic showing the process of hydraulic pressing for the pelletisation of MOFs.*

Granulation is a widely used method of shaping, whereby the adsorbent power is integrated into large spheres using a centrifuge. Spray-drying is a rapid and scalable process also extensively used in industrial applications (Morris & Wheatley 2008). A suspension of the material is sprayed into tiny droplets, accelerating the drying process by exposing a larger wet sample surface area in hot air (Liu et al. 2020). Due to its high efficiency and low operational costs, extrusion is a method that is commonly used in industry. The adsorbent is shaped by applying pressure over the cross-section (Liu et al. 2020). Similar to extrusion, pressing executes shaping by means of mechanical or hydraulic pressing, as shown in Figure 1. This method allows for manipulation of pellet size, by the selection of an appropriate die diameter. In pressing, the properties of the pellet such as weight uniformity, density, mechanical strength, and disintegration rate are affected by the amount of powder inserted into the die before compaction (Baserinia 2016).

Based on their composition, binders can be classified as two types: organic and inorganic. Examples of commonly used organic binders comprise cellulose, methylcellulose and polyvinyl alcohol (PVA), and are practical in that they can be removed after shaping to eliminate any excess binder that would result in macropore congestion (Liu et al. 2020). Inorganic binders, including silica and bentonite clays are also commonly used in industry as they are inexpensive and are more thermally stable than organic binders. Combinations of organic and inorganic binders are prevalent as they combine the desired characteristics from their respective structures.

The phenomena of adsorption using MOFs can be explained by the same mechanisms followed by other adsorbents, such as activated carbon or zeolites. The two main mechanisms are chemisorption and physisorption, with the latter being the most prevalent mechanism for most adsorption separation processes (Ruthven 1984). Physisorption refers to the physical bonding of molecules onto the surface of an adsorbent via physical forces, namely Van der Waals forces and electrostatic interactions (Ruthven 1984). This type of separation relies on the adsorbent and adsorbate having different surface properties, such as polarisability or quadruple moment, thus achieving strong electrostatic interactions between both (Wanigarathna et al. 2020). Chemisorption occurs through chemical bonding between the adsorbate and either the MOF unsaturated metallic sites or functional group, such as amines. For example, ZIF-8 exhibits strong interactions between its open Zn metal sites and CO_2, as CO_2 is an electrophile (Hayashi et al. 2007). In addition, the pore size of MOFs can be tuned to induce steric effects. As the diameter of the adsorbate approaches the diameter of the pores, it can enter the pores, whereas larger molecules are prevented from entering. This form of separation is particularly useful for small gas molecules.

The shaping of MOFs, particularly ZIF-8, into pellets and the effect of the pelletisation route on the intrinsic properties of the resultant pellet has been investigated only recently. Tsalaporta & MacElroy (2020) demonstrated the effects of pelletisation of four commercial MOFs (ZIF-8, ZIF-67, HKUST-1 and UiO-66) with a binder made of methylcellulose and bentonite in a 1:1 ratio. The obtained pellets showed similar hardness for each of the different MOFs. ZIF-8 showed small structural collapse and 7% pore volume per mass decrease. The other three MOFs were extremely sensitive to the pelletisation process, resulting in a major loss in the surface area and collapse of the porous network, indicating that they may not be suitable for pelletisation with this binder. Delgado et al. (2017) investigated the extrusion of HKUST-1 and ZIF-8 with polyvinyl alcohol (PVA). The obtained extrudates exhibited low reduction of surface area and pore blocking effect of the binder was not observed, suggesting potential for applications within gas separation.

Compression of MOF Basolite C300 at pressures of 55.9, 111.8 and 186.3 MPa was studied by Ursueguía et al. (2020). The rigid crystalline material exhibited dramatic loss of crystallinity, surface area and pore volume, implying a lower adsorption capacity owing to this pore collapse. In another study, Ribeiro et al. (2019) examined the effect of compression on MIL-53(Al) and ZIF-8, showing that mechanical compression had a greater effect on the crystalline structure of MIL-53(Al) than on ZIF-8. It was found that the higher the mechanical pressure applied to the respective MOF, the greater the losses in specific surface area and pore volume in their pelletised form.

Building on previous work regarding the shaping of MOFs, this work aims to investigate the physical and adsorptive effects of varying more than one parameter at a time and develop a successful pelletisation route, specifically for ZIF-8. Identifying an appropriate pressure and suitable binder is paramount when formulating a mechanically stable pellet to avoid structural collapse under compression and pore blocking. The physical and adsorption properties of the formed pellets were then investigated via various analytical techniques.

2. Materials and Methods

2.1. Materials

Basolite Z1200 (2-methylimidazole zinc salt), commonly known as ZIF-8 was purchased from Sigma-Aldrich and synthesised by BASF SE. The various binders tested were methylcellulose and bentonite in a 1:1 ratio, silica gel 60 (0.032-0.063mm, 230-450 mesh) from Alfa Aesar and 87-90% hydrolysed polyvinyl alcohol (PVA). For preparation of the binder paste, solvents were required; ethanol absolute was used in the case of PVA and methylcellulose/bentonite, and water was used for silica.

2.2. Methods I: Formulation

Binder-free pellets were produced by pressing the powder using two hydraulic presses: the Specac Manual Hydraulic Press and the Specac 15 Ton model (Specac Limited, United Kingdon), to test pelletisation under two different pressures. The pellets, made up of binder alone, were produced by mixing the powder with solvent until a paste was formed. Approximately 80 mg of the paste was inserted into a 5mm die which was introduced into the hydraulic press. The pressure was manually increased to the desired value and maintained for 20 seconds before pressure release and removal of the pellet. The solvent was changed depending on the binder type. Methylcellulose and bentonite were combined in a 1:1 ratio and mixed with ethanol, as was the PVA. For silica, the powder was mixed with water until a paste was formed, as suggested by Rivera-Torrente et al. (2021).

ZIF-8 pellets with binder were produced in a similar manner. Ethanol was first added to each of the binders in a ratio of 1.5g of binder to 2ml of ethanol to form a paste, which was then added to a beaker with the ZIF-8 powder. The contents of the beaker were mixed for 2 minutes until a uniform paste was formed. Following the aforementioned pelletisation step, the pellets were held overnight in a vacuum oven at 70°C. The binder fraction (relative to the total mass of ZIF-8 and binder in the pellet) was varied from 10% to 30% (see section 2.2.2 for further detail).

2.2.1. Binder Type

A selection of binder types was tested to determine the optimal material for the combination with ZIF-8 specifically. The four binders mentioned in section 2.2 are used in many MOF-shaping processes and were therefore considered suitable binders for the shaping of ZIF-8 (Cousin-Saint-Remi et al. 2020). Silica (SO_2) displays desirable adsorption properties, whereby the pore sizing can be controlled by varying its synthesis conditions (e.g. pH and solvent content) (Narayan et al. 2018). Bentonite clay is commonly used as a binder, absorbent, and catalyst, particularly in the milling industry (Jasra et al. 2003). It is inexpensive and highly resistant to thermal degradation. The organic binders tested, PVA and methylcellulose, are well-established organic polymeric binders and are both hydrophilic due to the presence of hydroxyl and carboxyl groups .

2.2.2. Binder Content

Varying the binder content typically results in a trade-off between mechanical stability and adsorption capacity (Tian et al. 2021). Different mass ratios were examined to test the compatibility of the binder to ZIF-8. The prepared mass ratios were ZIF-8:binder equivalent to 70:30, 80:20 and 90:10. Previous works have successfully pelletised MOF/binder mixtures at a ratio of 70:30 (Jasra et al. (2003);Whiting et al. (2016)). Two ZIF-8:binder ratio mixtures of 80:20 and 90:10 were formulated to determine the minimum requirement of binder content for each pellet, in terms of pellet stability. The binder content of the pellets used in the CO_2 adsorption experiments was verified by thermogravimetric analysis (see section 3.3 for further detail).

2.2.3. Pelletisation Pressure

There is no universal pelletisation route that can encompass the shaping of all MOFs, and thus research and experimentation must be undertaken for the case of ZIF-8 alone. Due to the mechanical fragility of some MOFs, immense compaction may lead to collapse of porous structure or amorphization of the material, limiting the exertion of high pelletisation pressures whilst shaping (Wu et al. 2013). In the case of ZIF-8, pressurisation above 3400 bar would lead to irreversible structural transition and amorphise accordingly (Tan & Cheetham 2011). This pressure limit was too high to use for research and potential applicability in industry, so the pelletisation pressures selected in this work were 0.4 and 1 tonnes to determine the minimal pressure sufficient to successfully pelletise ZIF-8.

2.3. Methods II: Characterisation Techniques

2.3.1. Thermogravimetric Analysis (TGA)

TGA is a destructible analytical technique used to determine the thermal stability of the ZIF-8 combined pellets, as well as the binders themselves. The mass percentage change is measured over time as the temperature changes. Increasing the temperature can result in decomposition of solids either by combustion, oxidation, reaction with a gas or pyrolysis, and in the case of thermogravimetry the gaseous by-products are removed (Coats & Redfern n.d.). The TGA system used was the NETZSCH TG 209 F1 Libra model, using air with a flowrate of 80mL/min and protective gas purge made up of nitrogen of 20mL/min, from 30°C to 1000°C, with a heating rate of 10°C NETZSCH (n.d.). A minimum of 15 mg of each sample was placed in a ceramic crucible for analysis.

TGA was also used for the confirmation of composition of the samples at a later stage. This is of high importance especially since there is a potential scope of error in measuring and transferring of the different mixtures in sample preparation. Differential thermogravimetric curves were plotted to determine the composition of materials.

2.3.2. Fourier-Transform Infrared (FTIR) Spectroscopy

FTIR is a technique used to obtain an infrared spectrum of absorption or emission of a crystalline structure. It helps in identifying compounds, and to determine if the crystalline structure of a sample changes when subject to any changes (Fisher Scientific n.d.).

An FTIR works by using interferometry – a technique used where light from a single source is split into two beams that travel in different optical paths and then superimpose to cause interference. This interference is used to record information about the sample placed in the IR beam, resulting in spectra that can be used to identify characteristic compounds within the material. The Cary 630 FTIR Spectrometer from Agilent Technologies was used for these measurements (Fisher Scientific n.d.).

2.3.3. Single-component CO_2 adsorption

CO_2 adsorption isotherms were measured using a Autosorb iQ (Quantachrome Instruments, United States) at 298 K up to a pressure of 1 bar. The samples were degassed ex-situ using the in-built degassing stations on the instrument by heating the sample to 393 K and maintaining this temperature under vacuum (a minimum pressure of $4e{-4}$ mbar) for 19 hours. For the data analysis, only the adsorption branch of the measurement was used.

2.3.4. Helium Pycnometry

Porosity is the measure of the void or empty spaces in a material and is a fraction of the volume of voids over the total volume, as shown in Equation 1. Helium Pycnometry is therefore a useful technique, in which displacement is used to measure the volume and porosity to accurately determine the skeletal density of the sample i.e. the density of the sample alone. It works by filling the voids in the powder or pellet with helium gas to measure the volume taken up by the pores.

$$\phi = V_V / V_T \tag{1}$$

Where V_V is the void volume and V_T is the total volume, and ϕ is the porosity (Espinal 2012). Sample degassing in order to remove any adsorbed gases, particularly any trapped moisture is important and was done following the same degassing technique outlined in section 2.3.3. Subsequently, the sample was placed in a helium pycnometer and measurements at 298 K were taken. The pycnometer used was the AccuPyc II 1340 model, accompanied by a $1cm^3$ cell (Merlin Powder Characterisation n.d.).

3. Results and Discussion

3.1. Comparison of Binder Type

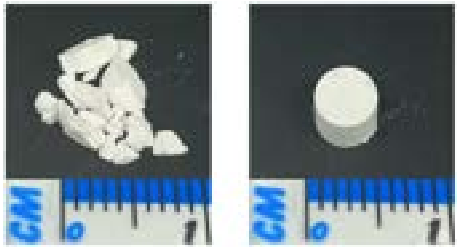

Figure 2: *Pelletised binderless ZIF-8 vs well-formed ZIF-8 pellet.*

Pelletisation of ZIF-8 without binder was unsuccessful as the powder showed no strong agglomeration to itself, resulting in the pellet falling apart whilst being removed from the die. Figure 2 above shows that the incorporation of a binder at these pelletisation pressures is a prerequisite for the successful formation of a mechanically resistant pellet, ensuring its usability for industrial applications.

3.1.1. Selection of suitable binders according to mechanical strength

Figure 3: *Binder-only pellets, from left to right, methylcellulose/bentonite, PVA and silica pelletised at 1 tonne.*

Binder-only pellets were formed to assess their mechanical strength under the selected pelletisation pressures. Images of the binder-only pellets pressed at 1 tonne are presented in Figure 3. Both the methylcellulose/bentonite (MCB) and PVA binders formed mechanically resistant pellets and were able to withstand regular handling, indicating that these binders would be suitable to produce hard, well-formed ZIF-8/binder pellets. The pellets formed with MCB binder appear to yield the best mechanical strength, but were significantly more compact compared to PVA, suggesting compression may significantly affect the physical properties of MCB.

Unlike PVA and methylcellulose/bentonite, the silica gel did not form a mechanically stable pellet, and was unable to maintain its shape under a small applied force. This indicates that silica was not suitable as a binder to form pellets stable enough for regular handling in an industrial setting. Furthermore, if the pellet crumbles or sheds powder, the instruments in a real system may be damaged. Following this analysis, silica was eliminated from the selection of potential binders.

3.1.2. Comparison of thermal stability of the binders

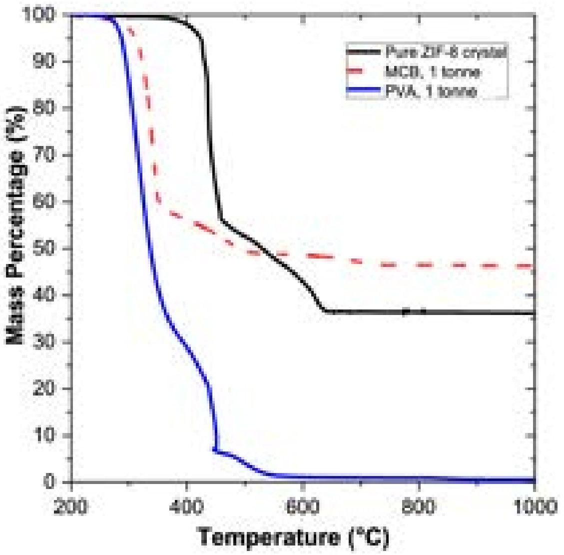

Figure 4: *Comparison of TGA results for varying binder type in pellet form.*

Mass loss profiles from thermogravimetric analysis (TGA) of PVA and methylcellulose/bentonite pellets were measured and are presented in Figure 4. The first stages of degradation (up to c. 100°C) are discarded as it likely represents water loss due to evaporation. It is observed that there is little weight loss of ZIF-8 between the temperature range of 200-400°C, indicating ZIF-8 is stable up to 400°C. ZIF-8 is observed to begin decomposing at around 427°C, consistent with reported decomposition temperature (T_d) values, which generally lie in the 400°C to 450°C region (Tran et al. 2011). The mass loss, amounting to 63.8% of its original mass, corresponds to the removal of all organic material, including the evaporation of any gas molecules within the pores (Healy et al. 2020).

Complete degradation of PVA is observed, with a T_d of approximately 350°C. The severe thermal decomposition pattern (300°C to 440°C) gives rise to the release of water from the polymer matrix of PVA. This step resulted in the largest mass loss of PVA, followed by a further smaller step (440°C to 520°C), owing to the cracking of the polymer chain and ultimately the removal of the sample via combustion (Taghi Taghizadeh & Sabouri 2013). The thermal instability of PVA signifies that it is not a suitable binder for pellets to be used in adsorption applications, as regeneration of the pellets is typically performed at higher temperatures under vacuum. Thus, PVA binder was excluded for further examination from this work.

3.2. Analysis of pelletisation routes for ZIF-8/MCB

Table 1: *Overview of pelletisation outcome for ZIF-8/MCB mixtures with varying binder content and pressure.*

ZIF-8:MCB Mass Ratio	Pelletisation Pressure (tonne)	Did a pellet form?
90:10	0.4	No
	1	No
80:20	0.4	No
	1	Yes
70:30	0.4	Yes
	1	Yes

The three binder contents investigated were the ZIF-8:methylcellulose/bentonite ratios of 70:30, 80:20 and 90:10 under tonnages of 0.4 and 1 tonnes. A summary of the pelletisation routes investigated and their outcomes is summarised in Table 1. Out of the 6 routes tested, only 3 resulted in the formation of mechanically stable pellets. With the proposed 90:10 mass ratio, the pellets produced were lacking in hardness and crumbled when taken out of the hydraulic press, indicating that the binder content of 10% was too low to have a significant impact on the pellet's mechanical stability. The pellets containing the highest binder content were considerably more mechanically stable and able to withstand regular handling, suggesting that binder content has a significant impact on the overall robustness of the pellet – more specifically, the higher the binder content the more structurally integral the pellet. This is expected as binders assists pellet formation by imparting strength to the pellet. Thus the pellets with a 90:10 ratio were not considered for further analyses.

As shown in Table 1, the applied pressure of 1 tonne yielded pellets with adequate hardness for the proposed 80:20 and 70:30 mass ratios, whereas the pellet produced at 0.4 tonnes for the 80:20 ratio was not structurally sound. A lower pelletisation pressure of 0.4 tonnes was not high enough to compress the mixture with a lower binder content effectively, indicating that the pressure whilst shaping has a significant impact on the mechanical strength of the pellet. The hardness of the pellets can be further tested with a manual pellet hardness tester and compared using the Rockwell B hardness scale to better distinguish between the formed pellets, however this analysis is outside the scope of this study (Tsalaporta & MacElroy 2020).

3.3. Determination of true binder composition

Having formed three mechanically stable pellets, the TGA results were used to confirm the true composition of the ZIF-8/binder pellets. Figure 5 shows the degradation of the combined 70:30 pellet (in blue) alongside the individual powder components. The mass percentages for all the samples were normalised at 200°C (to account for water loss before 120°C) and plotted. A system of mass balance equations was formulated to determine the compositions of methylcellulose, bentonite, and ZIF-8:

Determination of methylcellulose (MC) composition:

$$x_{MC} = \frac{\%\ Mass\ loss\ in\ pellet}{\%\ Mass\ loss\ in\ pure\ MC\ powder} \tag{2}$$

Determination of ZIF-8 and bentonite compositions:

$$x_{ZIF8} + x_{Bentonite} + x_{MC} = 1 \tag{3}$$

$$\%\ Mass\ loss\ in\ pellet = \sum_i x_i * (\%\ Mass\ loss\ of\ i) \tag{4}$$

Where i = ZIF-8, bentonite, MC.

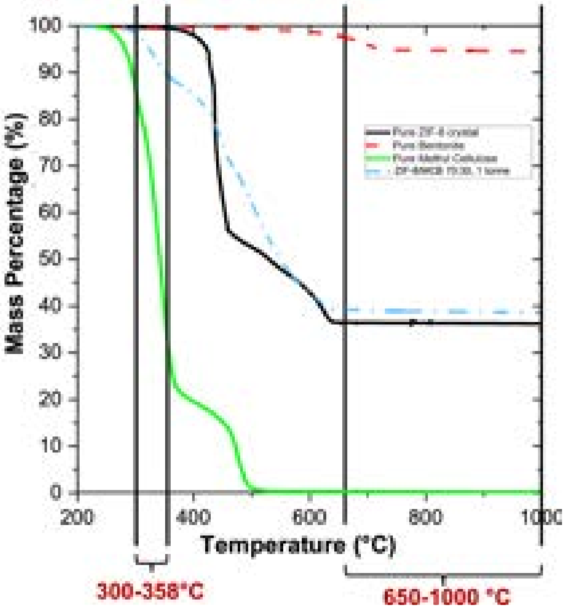

Figure 5: *TG graph of ZIF-8/MCB of the proposed 70:30 ratio at 1 tonne, along with pure ZIF-8, bentonite and methylcellulose.*

It is observed that the decomposition of the combined pellet is dependent on the decomposition of each individual component, as expected. Due to its organic nature, only methylcellulose deteriorated between 300°C and 358°C, shown in Figure 5. This indicates that any mass loss in the combined pellet resulted from the degradation of methylcellulose alone. Thus, between 300°C and 358°C, Equation 2 was used to compute the composition of methylcellulose in the combined pellet, and an average value was found.

Between 650°C and 1000°C, it is observed that methylcellulose has completely degraded and both ZIF-8 and bentonite have reached a stable mass. This implies that the remaining mass of the combined pellet is the sum of the ZIF-8 and bentonite masses only. Therefore, between these temperatures, the composition of ZIF-8 and bentonite were calculated using Equations 3 and 4 above, and an average value was found.

Following the TG analysis for each combination, the true compositions of each pellet were found, and have been summarised in Table 2. The true compositions of the 80:20 pellet at 1 tonne and 70:30 pellet at 0.4 tonnes were different from the proposed binder content. The error observed in binder content possibly originates from the difficulty in controlling exactly how much of the binder clusters with the ZIF-8 crystals, resulting in discrepancies between the batches of mixture produced. In addition, it is likely that powder mixture was lost in transfer between formulation and pelletisation. To avoid these errors in the future, it is proposed that the mixtures are formed in larger batches and mixed for a longer duration to obtain better homogenisation of the mixture.

3.4. Chemical structure of the formed pellets

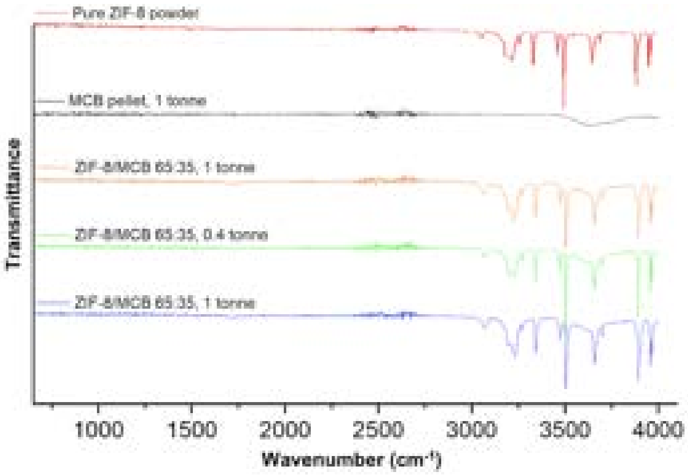

Figure 6: *FTIR analysis showing functional groups of each material.*

Figure 6 shows the infrared spectrum analysis of each combination pellet alongside the ZIF-8 and binder (highlighted in red and black respectively). All FTIR spectra reveal no distinct changes in the chemical structure of the ZIF-8 or methylcellulose before and after mechanical compression and addition of binder.

The methylcellulose in the binder contributes to the broad peak between 4000 and 3500 cm^{-1}, indicating the presence of hydroxyl bonds. On the other hand, ZIF-8's absorption spectrum is more populated and presents sharper peaks, showing the presence of secondary amines (3350-3310 cm^{-1}), and alkene groups (3100-3000 cm^{-1}) (Sigma Aldrich n.d.). The combined pellets display merged spectra (of ZIF-8 and binder), with a noticeable broad dip in transmittance at 4000-5300 cm^{-1} showing the incorporation of the binder without any chemical reactions having taken place (as no new peaks were present).

Table 2: *True compositions of each pellet calculated using the mass balance Equations 2, 3 and 4, and their new names for further analyses.*

Pelletisation Pressure (tonne)	Proposed Mass Composition (ZIF-8:MCB)	True Calculated Composition (ZIF-8:MCB)	Pellet Name
1	70:30	70:30	ZIF-8/MCB 70:30, 1 tonne
0.4	70:30	65:35	ZIF-8/MCB 65:35, 0.4 tonne
1	80:20	65:35	ZIF-8/MCB 65:35, 1 tonne

3.5. Effect of binder content

3.5.1. Mechanical strength

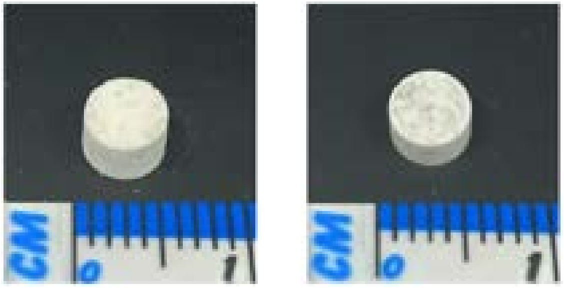

Figure 7: *ZIF-8/MCB pellets - from left to right, ZIF-8/MCB 70:30 and ZIF-8/MCB 65:35, both pelletised at 1 tonne.*

Figure 7 shows images of the ZIF-8 pellets pelletised with both 30% and 35% methylcellulose/bentonite. It was observed that as the binder content increased from 30% to 35% there was an increase in pellet strength, following expected trends. This is a result of the methylcellulose/ bentonite working as a glue to hold the ZIF-8 crystals together, thus imparting strength onto the pellet. These results further substantiate the notion that increasing binder content will ensure a stronger pellet, however, the effect on CO_2 uptake is also of great importance in determining the optimum content for adsorption purposes, as identified in section 3.5.2.

To understand the impact of binder addition on a microscopic scale, Scanning electron microscope (SEM) imaging and X-ray diffraction (XRD) could be undertaken to assess any changes to crystal structure, pore-blocking, or cross-linking and interactions between binder and ZIF-8. In this way, the effect of varying binder content can be better evaluated, but this is beyond the scope of the current work.

3.5.2. Adsorption properties

After the degassing process, volumetric CO_2 adsorption isotherms at 298 K were obtained for the formed pellets containing ZIF-8 and methylcellulose/bentonite binder, as displayed in Figure 8. Comparing the 70:30 1 tonne and 65:35 1 tonne, it is observed that both pellets display a decrease in adsorption capacity compared to the ZIF-8 powder. The drop in uptake compared to pure ZIF-8 is correlated to the amount of binder added, suggesting that at pressures below 1 bar, the adsorption equilibrium properties of ZIF-8 crystals within the combined pellets remains unaltered. The decrease in CO_2 capacity is therefore a result of low CO_2 uptake by additional methylcellulose/bentonite binder present, not pore blockage.

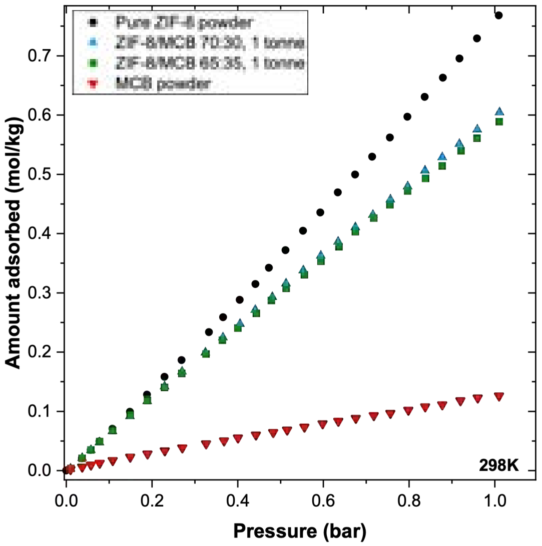

Figure 8: *Comparison of CO_2 isotherms for varying methylcellulose/bentonite binder content.*

It is worth noting that (as shown by the red scatter in Figure 8), the methylcellulose/bentonite binder exhibits CO_2 adsorption capabilities. This is expected as bentonite is a known adsorbent of CO_2. The CO_2 adsorption on the binder is non-negligible and contributes to the adsorption capacity of the pellets, proving its compatibility with ZIF-8 in adsorption applications.

At pressures below 0.7 bar a 5% increase in binder content does not have a significant effect on CO_2 adsorption, as the ZIF-8/MCB 70:30 and ZIF-8/MCB 65:35 plots are almost identical. However, as the pressure increases to 1 bar, the two curves seem to deviate, and it is observed that the 70:30 pellet adsorbs more CO_2 than the 65:35 pellet (around 2.6% more at 1 bar).

This implies that at higher CO_2 pressures, the difference in the micropore volume between the two pellets will result in a larger variation of CO_2 uptake. With an addition of 5% of binder, it is expected that more of the pores will be blocked by binder, thus inhibiting the CO_2 uptake. This can be explained as adsorption will decrease with decreasing micropore volume due to fewer sites being accessible and a lower diffusion rate through the framework. To confirm this proposition, high pressure CO_2 adsorption measurements must be undertaken.

3.5.3. CO_2 sorption in the theoretical vs observed case

To determine whether the observed adsorption curves aligned with the expected, theoretical graphs were plotted, via linear combination of ZIF-8 and binder. The isotherms for the combined pellets for each composition (70:30 and

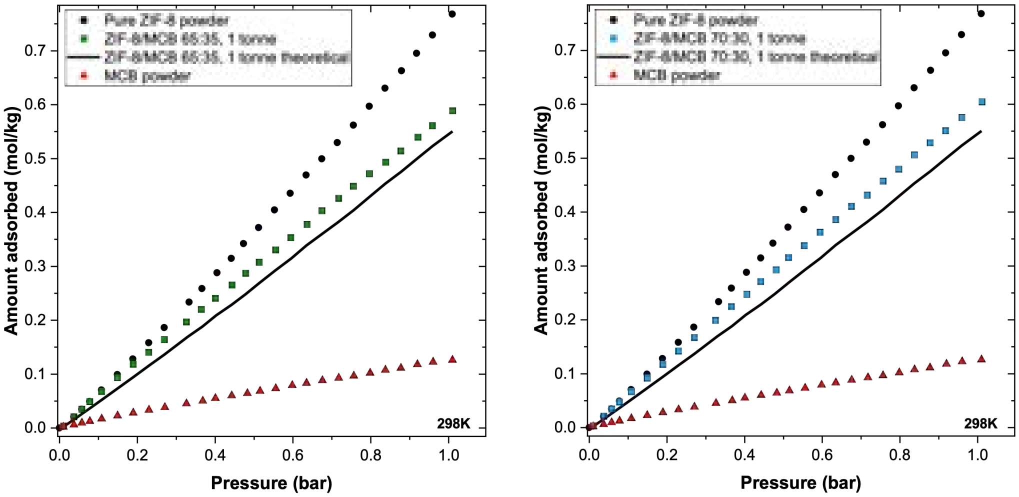

Figure 9: *11 a) and b): Comparison of CO_2 isotherms of the observed and the theoretical ZIF-8/MCB pellets compositions of 70:30 and 65:35 ratios respectively.*

65:35) are displayed in Figure 9, and the theoretical lines have been plotted for both pellet compositions. A slight discrepancy between the scatters and lines can be seen – the observed CO_2 uptake is greater than the theoretical CO_2 uptake. This deviation could be explained by the error in the composition of the binder present in each pellet, such that methylcellulose and bentonite were not in a 1:1 ratio, resulting in a higher adsorption capacity than anticipated.

3.5.4. Porosity

To identify the effect of binder content on the porosity of the combined pellets, helium pycnometry was undertaken and the results are displayed in Table 3. The ZIF-8 exhibits a skeletal density of 1.44 g/cm^3, consistent with literature (Giang et al. 2019). The porosity measurements show that the combination of 1:1 methylcellulose/bentonite powder has a 9% higher porosity than pure ZIF-8, despite the binder having a significantly lower CO_2 adsorption capacity.

Table 3: *Table of porosities with varying binder content, from pure ZIF-8 powder to pure methylcellulose/bentonite.*

Pellet	Porosity [%]
Pure ZIF-8 powder	30.59
ZIF-8/MCB, 70:30, 1 tonne	34.37
ZIF-8/MCB, 65:35, 1 tonne	33.35
Pure MCB powder	39.67

It has been reported that CO_2 sorption is not governed by total pore volume, but instead by pores smaller than a certain diameter (Presser et al. 2011). The study noted that at lower pressures, micropores contribute the most to CO_2 uptake. This indicates that the high porosity of the methylcellulose/bentonite binder is a result of larger macropore volume as opposed to micropore volume, which would not contribute to its adsorption capacity. The porosity difference between the two pellets is negligible at this pressure range, indicating that for a 5% increase in binder, there is no significant pore blockage of ZIF-8, which supports the earlier hypothesis. Nitrogen sorption and mercury intrusion tests could be carried out to determine complete porosity distribution encompassing micropore to macropore regions, to better quantify how additional binder content effects the porous network of ZIF-8.

3.6. Effect of pelletisation pressure

3.6.1. Mechanical strength

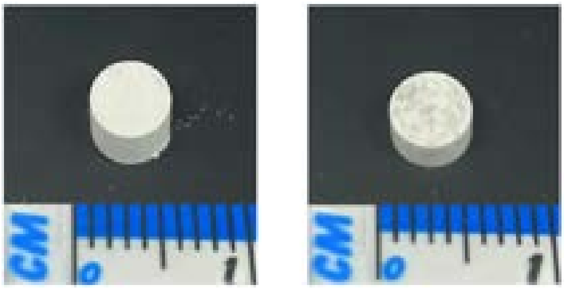

Figure 10: *From left to right ZIF-8/MCB 65:35 at 0.4 tonne and 1 tonne.*

Figure 10 shows images of the pellets formed at different pelletisation pressures. It was observed that increasing pelletisation pressure resulted in a more mechanically stable pellet. The pellet formed at 1 tonne pellet was more compact and less prone to crumbling than the 0.4 tonne pellet, thus it was able to better withstand regular handling. This suggests that mechanical resistance is improved with increasing pressure, likely due to the densification of the particles causing both the binder and ZIF-8 particles to better agglomerate together.

3.6.2. Adsorption properties

Figure 11 illustrates the CO_2 adsorption isotherms measured to evaluate the effect of pelletisation pressure on performance of the pellets. It is apparent that increasing pelletisation pressure has little impact on the CO_2 uptake, as there is a negligible reduction in CO_2 sorption between the two pellets. This indicates that within the pressure range measured, the micropore structure of ZIF-8 is still conserved with additional compression, despite the observable compaction.

These results suggest that a higher pelletisation pressure of 1 tonne is preferred to ensure a mechanically stable pellet without compromising its adsorption properties. To further identify variations in porosity and pore size distribution with increasing pelletisation pressure, N_2 sorption can be undertaken, and higher tonnages can be tested.

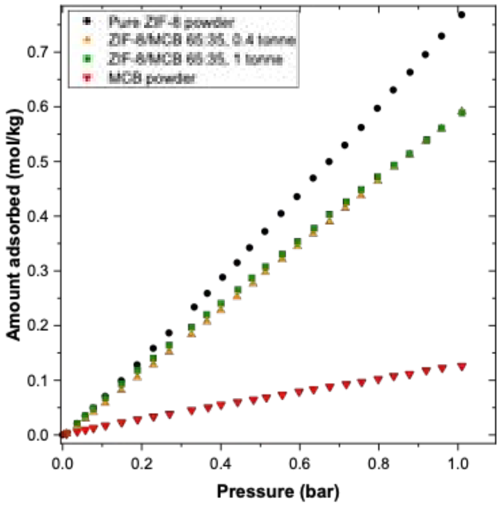

Figure 11: *Comparison of CO_2 isotherms for varying pelletisation pressure.*

3.6.3. Porosity

Table 4: *Table of porosities with varying pelletisation pressure, from pure ZIF-8 powder to pure methylcellulose/bentonite.*

Pellet	Porosity [%]
Pure ZIF-8 powder	30.59
ZIF-8/MCB, 65:35, 1 tonne	33.35
ZIF-8/MCB, 65:35, 0.4 tonne	34.52
Pure MCB powder	39.67

The sample pressed at 1 tonne has a 1.17% lower porosity than the sample pressed at 0.4 tonnes. This decrease in porosity may be explained by the pore structure collapse caused by compaction, resulting in a decrease of overall pore volume. Along with the results from CO_2 adsorption, this indicates that the reduction of macropores under compression is more significant than the reduction of micropores. This is supported by literature which suggests the reason for this is because the deformation in larger pores is greater and hence their volume reduction is more notable than that of smaller pores (Malekian et al. 2019). As volume is a function of the radius, the same percentage decrease in radius for both larger and smaller pores will result in a greater volume decrease for larger pores.

To identify macroporosity within the samples and better assess how compression affects the microscopic structure of the formed pellets, mercury intrusion and SEM experiments should be undertaken in future studies.

4. CONCLUSION

In this work, various pelletisation routes to shape ZIF-8 crystals into mechanically stable pellets have been investigated, and the resultant shaped bodies have been characterised to analyse their physical and adsorption properties. Three different binders, binder fractions and two pelletisation pressures were evaluated with mechanical and thermal stability tests, adsorption and porosity measurements. ZIF-8 displayed potential for successful pelletisation with the aid of specific binders and hydraulic pressing. Methylcellulose and bentonite in a 1:1 ratio has been identified as a promising binder to formulate mechanically and thermally stable pellets with ZIF-8 crystals for adsorption applications.

Within the parameters tested, the optimal pelletisation route was found to be a methylcellulose/bentonite binder content of 35% and a pelletisation pressure of 1 tonne. Adsorption experiments indicated that ZIF-8 has retained its microporous structure and adsorption capability within the shaped pellet.

There is significant potential for further investigation, such as a more comprehensive understanding of how the parameters varied will affect:

i Adsorption capacity at a higher pressure using high pressure CO_2 sorption,
ii BET surface area and complete pore size distribution using N_2 sorption and mercury intrusion porosimetry,
iii Crystalline structure using XRD and SEM imaging.

Further work testing a wider range of binder types, binder content and pelletisation pressures is crucial in optimising these parameters for pelletisation of ZIF-8. Finally, investigation of pellet size, effects of temperature and the reusability of the pellets for several adsorption cycles will reduce the knowledge gap and improve issues in the effective shaping of ZIF-8 for adsorption applications.

5. ACKNOWLEDGEMENTS

We would like to express our immense gratitude and appreciation to our supervisors, **Dr Camille Petit** and **Dr Ronny Pini** for their guidance and assistance throughout the project; **Hassan Azzan** for all the time dedicated to train, guide and aid us in this work; **Patricia Carry** and **Kaho Cheung** for training us in the analytical laboratory.

REFERENCES

Achiou, B., Karunakaran, M., Tchalala, M. R. & Belmabkhout, Y. (2020), MOF mixed matrix membranes for CO2 separation, *in* 'Advances in Carbon Capture', Elsevier, pp. 331–355.

Akhtar, F., Andersson, L., Ogunwumi, S., Hedin, N. & Bergström, L. (2014), 'Structuring adsorbents and catalysts by processing of porous powders', *Journal of the European Ceramic Society* **34**(7), 1643–1666.

Baserinia, R. (2016), Flow of Fine and Cohesive Powders under Controlled Air Pressure Conditions, Technical report.

Batten, S. R., Champness, N. R., Chen, X.-M., Garcia-Martinez, J., Kitagawa, S., Öhrström, L., O'Keeffe, M., Paik Suh, M. &

Reedijk, J. (2013), 'Terminology of metal–organic frameworks and coordination polymers (IUPAC Recommendations 2013)', *Pure and Applied Chemistry* **85**(8), 1715–1724.

Bergaoui, M., Khalfaoui, M., Awadallah-F, A. & Al-Muhtaseb, S. (2021), 'A review of the features and applications of ZIF-8 and its derivatives for separating CO2 and isomers of C3- and C4-hydrocarbons', *Journal of Natural Gas Science and Engineering* **96**, 104289.

Chan Wai, H., Mazlee, M. N., Ahmad, Z. A., Jamaludin, S. B., Mohd Ishak, M. A. & Jusoh, M. S. (2013), 'Sustainable Porous Materials for Gas Adsorption Applications; A Concise Review', *Advanced Materials Research* **795**, 96–101.

Coats, A. W. & Redfern, J. P. (n.d.), Thermogravimetric Analysis A Review*, Technical report.

Cousin-Saint-Remi, J., Finoulst, A. L., Jabbour, C., Baron, G. V. & Denayer, J. F. (2020), 'Selection of binder recipes for the formulation of MOFs into resistant pellets for molecular separations by fixed-bed adsorption', *Microporous and Mesoporous Materials* **304**, 109322.

Delgado, J. A., Águeda, V. I., Uguina, M. A., Brea, P. & Grande, C. A. (2017), 'Comparison and evaluation of agglomerated MOFs in biohydrogen purification by means of pressure swing adsorption (PSA)', *Chemical Engineering Journal* **326**, 117–129.

Espinal, L. (2012), POROSITY AND ITS MEASUREMENT Ã, Technical report.

Fisher Scientific (n.d.), 'FTIR Spectroscopy Basics | Thermo Fisher Scientific - UK'.

Furukawa, H. & Yaghi, O. M. (2009), 'Storage of hydrogen, methane, and carbon dioxide in highly porous covalent organic frameworks for clean energy applications.', *Journal of the American Chemical Society* **131**(25), 8875–83.

Giang, H., Nguyen, T., Horn, J. C., Bleakney, M., Siderius, D. W. & Espinal, L. (2019), 'Understanding Material Characteristics through Signature Traits from Helium Pycnometry'.

Hayashi, H., Côté, A. P., Furukawa, H., O'Keeffe, M. & Yaghi, O. M. (2007), 'Zeolite A imidazolate frameworks', *Nature Materials* **6**(7), 501–506.

Healy, C., Patil, K. M., Wilson, B. H., Hermanspahn, L., Harvey-Reid, N. C., Howard, B. I., Kleinjan, C., Kolien, J., Payet, F., Telfer, S. G., Kruger, P. E. & Bennett, T. D. (2020), 'The thermal stability of metal-organic frameworks', *Coordination Chemistry Reviews* **419**, 213388.

Hendon, C. H., Rieth, A. J., Korzyński, M. D. & Dincă, M. (2017), 'Grand Challenges and Future Opportunities for Metal–Organic Frameworks', *ACS Central Science* **3**(6), 554–563.

Jasra, R. V., Tyagi, B., Badheka, Y. M., Choudary, V. N. & Bhat, T. S. G. (2003), 'Effect of Clay Binder on Sorption and Catalytic Properties of Zeolite Pellets', *Industrial & Engineering Chemistry Research* **42**(14), 3263–3272.

Koekemoer, A. & Luckos, A. (2015), 'Effect of material type and particle size distribution on pressure drop in packed beds of large particles: Extending the Ergun equation', *Fuel* **158**, 232–238.

Liu, X.-M., Xie, L.-H. & Wu, Y. (2020), 'Recent advances in the shaping of metal–organic frameworks', *Inorganic Chemistry Frontiers* **7**(15), 2840–2866.

Malekian, A., Salari, S., Stumper, J., Djilali, N. & Bahrami, M. (2019), 'Effect of compression on pore size distribution and porosity of PEM fuel cell catalyst layers', *International Journal of Hydrogen Energy* **44**(41), 23396–23405.

Merlin Powder Characterisation (n.d.), 'True Density | Gas Pycnometry and Helium Pycnometry | Merlin PC'.

Morris, R. & Wheatley, P. (2008), 'Gas Storage in Nanoporous Materials', *Angewandte Chemie International Edition* **47**(27), 4966–4981.

Muñoz-Gil & Figueiredo (2019), 'High Surface Proton Conduction in Nanostructured ZIF-8', *Nanomaterials* **9**(10), 1369.

Murray, L. J., Dincă, M. & Long, J. R. (2009), 'Hydrogen storage in metal–organic frameworks', *Chemical Society Reviews* **38**(5), 1294.

Narayan, R., Nayak, U., Raichur, A. & Garg, S. (2018), 'Mesoporous Silica Nanoparticles: A Comprehensive Review on Synthesis and Recent Advances', *Pharmaceutics* **10**(3), 118.

NETZSCH (n.d.), 'Thermogravimetric Analysis - NETZSCH Analyzing & Testing'.

Petit, C. (2018), 'Present and future of MOF research in the field of adsorption and molecular separation', *Current Opinion in Chemical Engineering* **20**, 132–142.

Presser, V., McDonough, J., Yeon, S.-H. & Gogotsi, Y. (2011), 'Effect of pore size on carbon dioxide sorption by carbide derived carbon', *Energy & Environmental Science* **4**(8), 3059.

Ribeiro, R. P., Antunes, C. L., Garate, A. U., Portela, A. F., Plaza, M. G., Mota, J. P. & Esteves, I. A. (2019), 'Binderless shaped metal-organic framework particles: Impact on carbon dioxide adsorption', *Microporous and Mesoporous Materials* **275**, 111–121.

Rivera-Torrente, M., Kroon, D., Coulet, M., Marquez, C., Nikolopoulos, N., Hardian, R., Bourrelly, S., De Vos, D., Whiting, G. T. & Weckhuysen, B. M. (2021), 'Understanding the Effects of Binders in Gas Sorption and Acidity of Aluminium Fumarate Extrudates', *Chemistry – A European Journal* .

Ruthven, D. M. (1984), *Principles of Adsorption and Adsorption Processes*, John Wiley & Sons, Inc.

Sai Bhargava Reddy, M., Ponnamma, D., Sadasivuni, K. K., Kumar, B. & Abdullah, A. M. (2021), 'Carbon dioxide adsorption based on porous materials', *RSC Advances* **11**(21), 12658–12681.

Sigma Aldrich (n.d.), 'IR Spectrum Table'.

Sing, K., Everett, D., Haul, R., Moscou, L., Pierotti, R., Rouquérol, J. & Siemieniewska, T. (1985), Reporting physisorption data for gas/solid systems-with special reference to the determination of surface area and porosity, Technical report.

Smith, D. S., Alzina, A., Bourret, J., Nait-Ali, B., Pennec, F., Tessier-Doyen, N., Otsu, K., Matsubara, H., Elser, P. & Gonzenbach, U. T. (2013), 'Thermal conductivity of porous materials', *Journal of Materials Research* **28**(17), 2260–2272.

Taghi Taghizadeh, M. & Sabouri, N. (2013), 'Thermal Degradation Behavior of Polyvinyl Alcohol/Starch/Carboxymethyl Cellulose/ Clay Nanocomposites', *Universal Journal of Chemistry* **1**(2), 21–29.

Tan, J. C. & Cheetham, A. K. (2011), 'Mechanical properties of hybrid inorganic–organic framework materials: establishing fundamental structure–property relationships', *Chemical Society Reviews* **40**(2), 1059.

Tian, T., Hou, J., Ansari, H., Xiong, Y., L'Hermitte, A., Danaci, D., Pini, R. & Petit, C. (2021), 'Mechanically stable structured porous boron nitride with high volumetric adsorption capacity', *Journal of Materials Chemistry A* **9**(22), 13366–13373.

Tran, U. P. N., Le, K. K. A. & Phan, N. T. S. (2011), 'Expanding Applications of MetalOrganic Frameworks: Zeolite Imidazolate Framework ZIF-8 as an Efficient Heterogeneous Catalyst for the Knoevenagel Reaction', *ACS Catalysis* **1**(2), 120–127.

Tsalaporta, E. & MacElroy, J. D. (2020), 'A comparative study of the physical and chemical properties of pelletized HKUST-1, ZIF-8, ZIF-67 and UiO-66 powders', *Heliyon* **6**(9), e04883.

Ursueguía, D., Díaz, E. & Ordóñez, S. (2020), 'Densification-Induced Structure Changes in Basolite MOFs: Effect on Low-Pressure CH4 Adsorption', *Nanomaterials* **10**(6), 1089.

Wanigarathna, D. K. J. A., Gao, J. & Liu, B. (2020), 'Metal organic frameworks for adsorption-based separation of fluorocompounds: a review', *Materials Advances* **1**(3), 310–320.

Whiting, G. T., Chowdhury, A. D., Oord, R., Paalanen, P. & Weckhuysen, B. M. (2016), 'The curious case of zeolite–clay/binder interactions and their consequences for catalyst preparation', *Faraday Discussions* **188**, 369–386.

Wu, H., Yildirim, T. & Zhou, W. (2013), 'Exceptional Mechanical Stability of Highly Porous Zirconium Metal–Organic Framework UiO-66 and Its Important Implications', *The Journal of Physical Chemistry Letters* **4**(6), 925–930.

Modelling of Cellulose Pyrolysis in a Wire-Mesh Reactor

Cameron, Few and Yi Xian, Koh

Department of Chemical Engineering, Imperial College London, U.K.

ABSTRACT

Cellulose pyrolysis is a key process for biomass conversion, but its study is complicated by secondary reactions. Primary pyrolysis reactions can be better studied in a wire-mesh reactor (WMR), which suppresses secondary reactions. This study set out to model the pyrolysis of a cellulose particle in a WMR. Modelling efforts focused on high heating rates (up to 1000 K/s), which are currently less well understood. Three models of increasing complexity were built in MATLAB. Model 1 predicted the product yields from a uniformly heated cellulose particle based on the Broido-Shafizadeh model of reaction pathways and was shown to generally agree with experimental trends. Model 2 restricted direct heating to the particle surface and assumed that conduction dominated intraparticle heat transfer. The results showed negligible intraparticle temperature gradients, assuming a uniform particle surface heating profile. The heats of reaction had no significant effect on the temperature profile. Model 3 therefore neglected reactions and focused on conductive, convective, and radiative heat transfer at the particle surface with a modified 3-D particle design. The results showed that homogeneity of the particle surface temperature depended on particle geometry, particularly mesh contact area.

Keywords: Wire mesh reactor, WMR, cellulose, pyrolysis, model

Background

Pyrolysis is the process of thermal decomposition of materials at high temperatures in the absence of oxygen. Pyrolysis provides an attractive pathway for converting biomass to high-energy-density products with simple handling, storage, and refining. With cellulose being the most abundant polymer on Earth and accounting for approximately 40% of biomass [1], understanding cellulose pyrolysis is key to understanding biomass pyrolysis as a whole.

Cellulose pyrolysis has primarily been described by the Broido-Shafizadeh (B-S) model [2]–[4], where cellulose is initially converted to an intermediate “active cellulose”. This intermediate then further decomposes via two competitive pathways: one producing non-condensable gases and biochar, and the other producing condensable vapours. The main volatile product of cellulose pyrolysis is levoglucosan (LGA), with lighter volatile products including pyrans, furans and light oxygenates [5].

To better understand primary pyrolysis reactions, experimental work has been done using wire mesh reactors (WMRs). Research groups from numerous institutes around the world have been involved in developing this reactor since the first electrically heated WMR was developed in 1964 [6].

In a WMR, a single layer of particles is held between two wire meshes to which precise and rapid heating rates (>1000 K/s) can be applied. The monolayer setup prevents interparticle reactions. An inert sweep gas (e.g. helium) is also passed through the sample to enable rapid product separation and suppression of secondary reactions. The preserved primary products are then swept through a liquid nitrogen-cooled cold trap, which condenses volatile products to liquid (tar). Full descriptions of the experimental setup can be found in other papers in the literature [7] [8].

There has been experimental work done on pyrolysis of fuel materials in WMRs, including cellulose [9] [10], and modelling of cellulose pyrolysis in other reactors such as fluidised bed and fixed bed reactors [11]. However, comparatively little research has been conducted into modelling cellulose pyrolysis specifically in a WMR.

This study aims to model the pyrolysis of a cellulose particle in a WMR via a variety of computational methods. Model parameters were obtained from literature, and results were compared primarily with experimental results from Yu et. al [12] using the WMR at Imperial College London. Three models of increasing complexity were built, with the latter two models accounting for heat transfer and aspects of particle geometry.

The methodologies and results from each model are presented in their order of implementation, as each model design was informed by the results from the previous one.

General Methods

Modelling software

Modelling was primarily done using MATLAB. SolidWorks was also used for designing 3-D particle geometry and AutoCAD was used to visualize the 2-D configuration of the particle and wire mesh.

Internal structure

Literature values for cellulose porosity range from 30-80% [13]–[15]. However, during pyrolysis, cellulose fibres will be consumed, making porosity a function of residence time. For model simplicity, the cellulose was modelled as a rigid non-porous particle, the implications of which are discussed in Model 2.

Mass transfer limitations

Previous papers modelling cellulose pyrolysis [16][17] have assumed that diffusive mass transfer within the particle is negligible compared to convection, since any volatiles formed can (be assumed to) travel easily to the particle surface due to the porosity of cellulose. Since a WMR also makes use of an inert sweep gas to aid mass transfer within and away from the particle, there were assumed to be no mass transfer limitations for gaseous products.

Particle and mesh geometry

A spherical particle geometry was primarily assumed, except for in Model 3, with a particle radius of 79 µm based on an average from the 106–150 µm experimental particle size range [12]. A wire mesh aperture (diagonal) of 63 µm, and wire diameter of 40 µm were used [18]. A 2-D layout of the mesh and particle is shown in Figure 1.

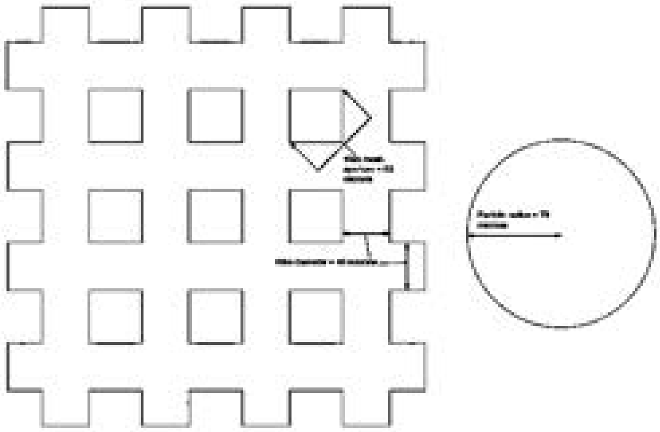

Figure 1: 2-D layout of wire mesh and cellulose particle, drawn in AutoCAD

Heating process

The particle is heated from room temperature (298 K), with heating applied to different parts of the particle in each model. Due to the instrument-particle contact area being relatively large, it was assumed that there was no thermal lag from instrument-particle resistances [19]. Thus, it was assumed that the wire mesh and the particle surface in contact with it were at the same temperature.

The WMR referenced for this study utilised a very precise temperature control system with only slight deviations [20]. Thus, the wire mesh temperature (T_{mesh}) profile was modelled as a linear ramp with a gradient equal to the heating rate and ending at a constant setpoint, as shown in Figure 2.

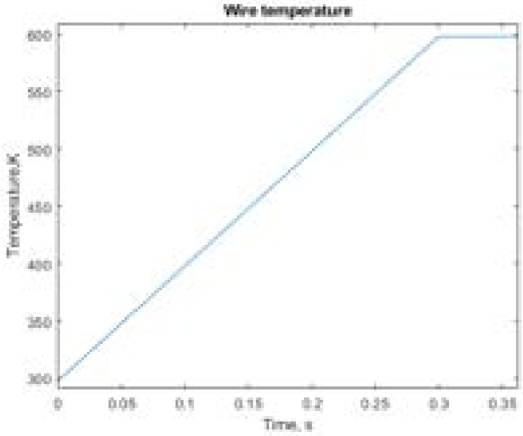

Figure 2: Temperature-time heating profile of WMR, with a heating rate of 1000 K/s and a setpoint temperature of 598 K

Heating rates were varied between 1 K/s (low) and 1000 K/s (high), and setpoint temperatures were varied between 598 K, 723 K, and 798 K so the effects of these parameters on product yields and heat transfer could be explored.

Model 1 - Methods

$$(C_6H_{10}O_5)_n(s) \xrightarrow{r_1} (C_6H_{10}O_5)'_n \tag{1}$$

$$(C_6H_{10}O_5)'_n \xrightarrow{r_2} 4.7n\ C(s) + 1.3n\ CO_2(g) + 2.4n\ H_2O(g) + 2.6n\ H_2(g) \tag{2}$$

$$(C_6H_{10}O_5)'_n \xrightarrow{r_3} n(C_6H_{10}O_5)(g) \tag{3}$$

Cellulose pyrolysis was modelled on the B-S reaction scheme, as introduced in the background section of this report, and seen in equations (1) - (3) [21]: Reaction (1) for the conversion of cellulose to an intermediate state; Reaction (2) for the decomposition of the intermediate to gases and biochar (carbon); and Reaction (3) for the competitive pathway to condensable volatiles. LGA was assigned as the sole condensable vapour due to it being the main component produced in reaction 3. Competitive pathways for cellulose to decompose to lighter derivatives were not included in this model. All reaction rates r_i are first order with respect to reactants, with A_i and i=1,2,3, and referring to the reactants of the respective reactions:

$$r_i = k_i C_{A_i} \tag{4}$$

Rate constants k_i follow Arrhenius behaviour:

$$k_i = k_{0,i} e^{-\frac{E_{a,i}}{RT}} \tag{5}$$

Kinetic data was taken from Bradbury et.al [4], shown in

Table 1, along with thermodynamic data from Cho et.al [21].

Table 1: Kinetic and thermodynamic data taken from literature

Reaction	$\log_{10} k_0$[4] (mol^{-1})	E_A [4] (kJ mol^{-1})	ΔH [21] (kJ mol^{-1})
1	19.45	242.67	-0.75
2	10.12	153.13	-170.17
3	14.50	197.90	121.38

Mass balance equations are shown:

$$\frac{dn_{(C_6H_{10}O_5)_n}}{dt} = -r_1 \tag{6}$$

$$\frac{dn_{(C_6H_{10}O_5)'_n}}{dt} = r_1 - r_2 - r_3 \tag{7}$$

$$\frac{dn_{products,r_{2,3}}}{dt} = r_{2,3} v_{2,3} \tag{8}$$

With $v_{2,3}$ referring to the stoichiometric coefficients of the products in Reactions 2 and 3.

Equations (6) to (8) were solved computationally using the Runge-Katta method (MATLAB ode45 solver) to model a particle of pure cellulose as a single reacting “block”. The temperature of the whole particle was assumed to follow the T_{mesh} temperature profile exactly, with no intraparticle temperature gradients.

Results from this model were compared with experimental results [22] showing the weight percentages at certain holding times after the setpoint temperature was reached, with the species classified as seen in Table 2 below.

Table 2: Classification of reaction species according to states of matter

States of matter	Species
Solid	Cellulose, Active cellulose, Char
Liquid	LGA
Gas	CO_2, H_2O, H_2

Active cellulose was classified as a “solid” product because it is a short-lived transition species that very rapidly decomposes to other products. LGA is initially produced in gaseous form, but it was assumed in the model that all LGA is condensed to liquid by the cold trap, which is at liquid nitrogen temperature (between 609 K and 624 K) [23], which is below the boiling point of LGA of 658 K [24].

Model 1 - Results

Table 3 shows the model results (shaded) and experimental results (non-shaded) Generally, the model agreed with experimental trends, but there were minor discrepancies with certain results.

Table 3: Composition results from Model 1 (shaded) compared with experimental results from Yu. et al [12]

			Solid residue (wt%)		Liquid (wt%)		Gas (wt%)	
Setpoint Temperature (K)	Heating rate (K/s)	Holding time (s)	Model 1	Experiment [12]	Model 1	Experiment [12]	Model 1	Experiment [12]
598	1	15	98.7	81.5 ± 1.8	1.1	10.1 ± 2.4	0.2	8.4
723	1	15	5.1	4.6 ± 0.3	85.4	85.5 ± 0.8	9.5	9.9
798	1	15	0.5	2.5 ± 0.4	85.4	86.0 ± 0.6	9.5	11.5
723	1000	15	2.3	3.7 ± 0.3	93.5	85.0 ± 0.3	4.3	11.3
798	1000	15	1.4	1.2 ± 0.2	96.0	86.7 ± 1.2	2.6	12.1
598	1000	15	99.5	96.1 ± 0.7	0.4	–(**)	0.1	–(**)
598	1000	300	56.9	53.7 ± 1.3	35.6	36.3 ± 2.2	7.6	10.0
598	1000	1200	13.5	19.6 ± 1.4	71.3	69.7 ± 2.4	15.2	10.7

When heating to 723 K and 798 K, with both low and high heating rates, Model 1 agreed closely with experimental data after 15 s of holding time: a high degree of solid decomposition, with most of the original mass converted to liquid, and a small amount to gaseous products. However, at high heating rates, Model 1 slightly overpredicts liquid production (~95 wt% predicted vs ~86 wt% experimentally) and underpredicts gaseous production (~3% predicted vs ~10% experimentally). A possible explanation for this is that at high temperatures and heating rates, the model fails to account for large cellulose fragments at the surface of the particle that could have broken off and been carried away by the sweep gas before complete decomposition into volatiles could occur. This behaviour has been described in previous studies [25][26] and would have negatively impacted experimental liquid yields. Since experimental gas yields were calculated by difference, this phenomenon could explain both differences between Model 1 and Yu et al. results.

With slow heating to 598 K, Model 1 shows significantly less solid decomposition (98.7 wt% residue), and practically zero gas products. A possible explanation for this is that the study in which the model parameters were developed [4] had different experimental conditions to Yu et al., with larger particles and a less efficient reactor setup. This could have led to higher instrument-particle thermal resistance, which in turn would have resulted in higher measurements for activation energy. Using this kinetic data would then cause Model 1 to underpredict solid decomposition when applied to a more efficient experimental setup, which would be especially pronounced at low heating rates and temperatures.

For fast heating to 598 K, after 1200 s holding time, Model 1 predicts more solid decomposition to gases than the experimental results show. This indicates that conversion of cellulose to gases happens predominantly on the particle surface and early in the heating process [25]. Amorphous surface cellulose undergoing decomposition to char and gases before being depleted was hypothesized by Yu et al. to be why experimental gas yields stayed about the same (~10 wt%) regardless of holding time. Model 1 failing to account for this may explain why it predicts solid decomposition to gases to proceed longer than it should.

Model 2 - Methods

Model 2 considered the cellulose particle as a rigid solid sphere with an unchanging internal and external structure. It was assumed that only the particle surface temperature ($T_{surface}$) followed the T_{mesh} heating profile. Heat transfer to the centre of the particle was assumed to be dominated by conduction through cellulose nanofibers, the conductivity λ_{CNF} of which was modelled using equation (9) [27]:

$$\begin{aligned}\lambda_{CNF} = (0.0787 + (2.73 \times 10^{-3})T \\ - (7.6749 \times 10^{-6})\,T^2 \\ + (8.4637 \times 10^{-9})\,T^3)\left(\frac{\rho}{\rho_0}\right)^2\end{aligned} \tag{9}$$

For the purposes of this study, $\rho = \rho_0 = 1350\ kg/m^3$ so that $\frac{\rho}{\rho_0} = 1$

Isobaric heat capacity for cellulose was modelled using equation (10) [28]:

$$C_P = 6.0T - 657.8 \tag{10}$$

Equation (12) was added to account for the energy balance for each component i respectively:

$$\rho C_P \frac{\partial T}{\partial t} = \frac{\partial}{\partial x}\left(\lambda_{CNF} \frac{\partial T}{\partial x}\right) - \sum_{i=1,2,3} \Delta H_i r_i \tag{11}$$

with x *denoting the radial direction, and* $\Delta \mathrm{H_i}$ *taken from Cho et. al* [21]

Equations (1) - (11) were solved as a system of PDEs at each small slice in the radial direction. An even distribution of cellulose within the initial particle was assumed. The final composition was taken as the average composition across all the slices at each point in time, as instantaneous mass transfer of gaseous products was assumed. The difference between $T_{surface}$ and the particle centre temperature (T_{centre}) was calculated across the heating period to observe the effect of intraparticle temperature gradients.

No-flux boundary conditions were implemented at the particle centre for heat and each chemical species to ensure conservation of mass and energy.

Model 2 - Results

Model 2 was built to investigate if intraparticle temperature gradients could better explain the minor discrepancies in Model 1. To illustrate this, the difference between $T_{surface}$ and T_{centre} , $\Delta T_{\ s-c}$, was plotted.

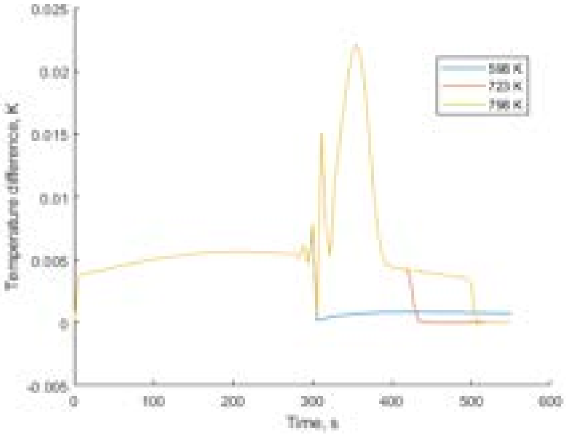

Figure 3: Plot of $\Delta T_{\ s-c}$ *against time for slow heating (1 K/s) to setpoint temperatures of 598 K, 723 K, and 798 K*

For slow heating, the low rate of heat transfer resulted in negligible intraparticle temperature gradients, with a peak $\Delta T_{\ s-c}$ of 0.025 K, shown in Figure 3. Conversely, for fast heating, $\Delta T_{\ s-c}$ was in the range of 4-10 K during the temperature ramp-up period, as seen in Figure . For both slow and fast heating rates, $\Delta T_{\ s-c}$ was only positive for as long as it took for T_{mesh} to reach the setpoint before quickly subsiding to zero.

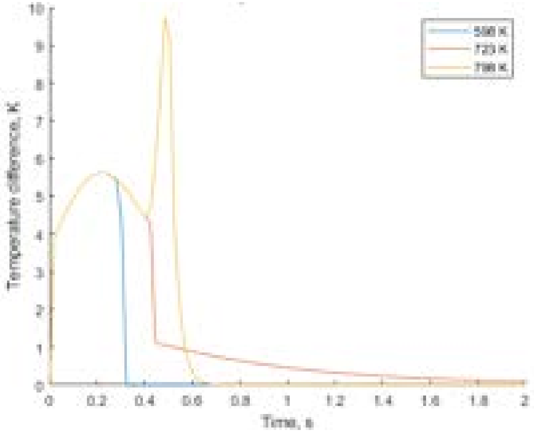

Figure 4: Plot of $\Delta T_{\ s-c}$ *against time for fast heating (1000 K/s) to setpoint temperatures of 598 K, 723 K, and 798 K*

The highest $\Delta T_{\ s-c}$ reached was 9.7 K, for a setpoint of 798 K. However, this did not cause a noticeable difference in reaction rates inside the particle, as Model 1 and Model 2 composition results were essentially the same for all heating rates and setpoints (Table A 1 in the Supplementary Material) Heats of reaction were also removed from the model, and no significant change was seen in the resultant temperature profile and compositions. This indicates that intraparticle conduction is sufficient to ensure a near-homogeneous temperature profile within the particle throughout the heating process.

It should be noted that λ_{CNF} and C_p have not been experimentally validated for the full temperature range of this study. λ_{CNF} has only been validated up to 300 K [27] and C_p up to 433 K [28], as those studies investigated properties of cellulose below the range for pyrolysis. In general, however, thermal conductivities and heat capacities of solids increase with temperature due to additional contributions from rotational and vibrational energies. In addition to that, Model 2 has not accounted for the changing internal structure of cellulose during pyrolysis. Decomposition of cellulose fibres would lead to reduced conduction, but an increase in intraparticle radiation via the pores [16].

Model 3 - Methods

Based on previous results, Computer-Aided Design (CAD) was used to model a solid cellulose particle, allowing more complex geometry to be shown.

2-D layouts of the particle and wire mesh were modelled in AutoCAD based on experimental data, as shown in Figure 1. These were overlayed in different positions to approximate the contact areas between the particle and mesh, samples of which are shown in Figure 5. These areas were averaged, then a spherical particle compressed at both ends was modelled using SolidWorks, with its non-curved surfaces having an area equal to the average contact area (Figure 6). These surfaces were modelled as the surfaces heated by the two wire meshes. Other solid models with decreasing contact areas were built from this baseline model and applied in Model 3 to investigate the effect of particle geometry. Two examples are shown in Figure 7.

A heat flux boundary condition was added on the particle surface not in contact with the mesh. The flux (q_{gain}) was defined in terms of the heat loss from convection $(q_{convection})$, heat loss from particle radiation to the surroundings $(q_{particle\,rad})$ and heat gained from mesh radiation to the particle surface $(q_{mesh\,rad})$, as shown in Equation (12). $q_{convection}$ and $q_{particle\,rad}$ were defined with Equations (13) and (14).

$$q_{gain} = q_{mesh\,rad} - q_{particle\,rad} - q_{convection} \tag{12}$$

$$q_{convection} = h\left(T_{surface} - T_{amb}\right) \tag{13}$$

$$q_{particle\,rad} = \sigma\varepsilon_{cell}\left(T_{surface}^4 - T_{amb}^4\right) \tag{14}$$

An attempt was made to analytically find $q_{mesh\,rad}$ by integrating the flux contributions to infinitesimal particle surface elements, but this proved computationally infeasible. Instead, it was assumed that the radiation from a given double-layer mesh area $2L^2$was distributed evenly over the exposed particle surface A_p, giving Equation (15):

$$q_{mesh\,radiation} = \frac{2L^2\sigma\varepsilon_{mesh}{T_{mesh}}^4}{A_p} \tag{15}$$

A full description of the analytical attempt can be found in the Supplementary Material.

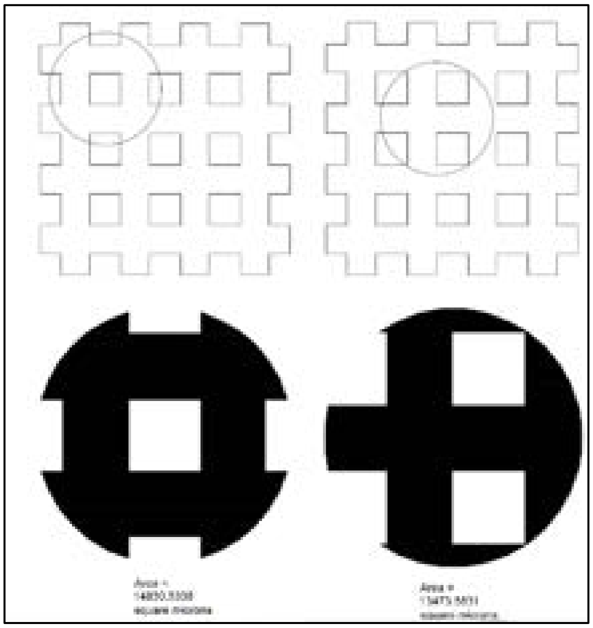

Figure 5: Sample particle-mesh contact area approximated from overlaying 2-D layouts

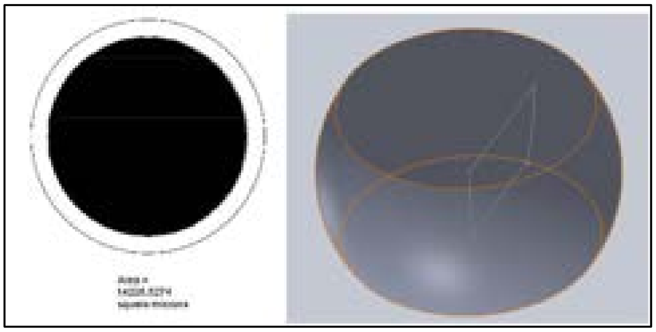

Figure 6:
(shown left) Average mesh-particle contact area (shaded) overlayed on particle cross-section and (shown right) “Compressed 1” solid model built in Solidworks

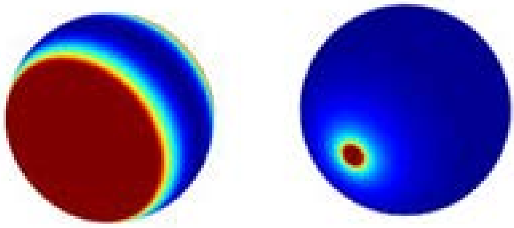

Figure 7: (Shown left) Compressed 1 (baseline) and (shown right) Point source solid models

Model 3 - Results

The key parameter ΔT_s was calculated from the Model 3 predictions. ΔT_s is the difference between T_{mesh} and the surface temperature on the particle equator (which is defined as the line around the widest part of the exposed surface) at any given time.

ΔT_s was found to be heavily dependent on the chosen particle geometry (Figure 8): The peak ΔT_s (designated $\Delta T_{s,max}$) ranged from 64.7K for the point source model to 2.3 K for Compressed 1 model.

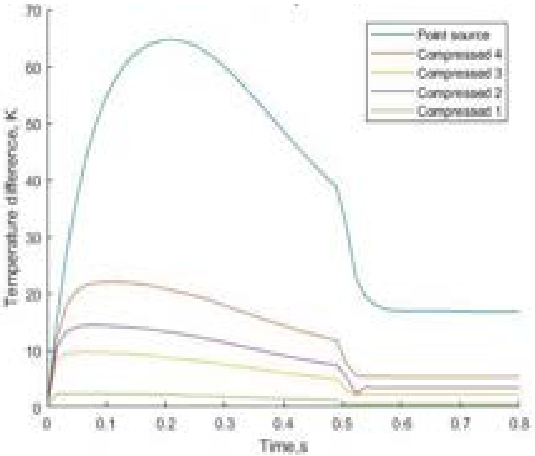

Figure 8: ΔT_s for different compressed models for fast heating (1000K/s) to 798K

This trend is due to two complementary effects. Firstly, a greater contact area with the mesh increases the conductive heat flux into the particle. The particle then heats faster and $\Delta T_{s,max}$ decreases. Secondly, the more compressed models have a reduced distance between the flat conducting surfaces and the particle equator. This gives a steeper temperature gradient, which results in faster conduction due to Fourier's law and thus reduces $\Delta T_{s,max}$.

As shown in Figure 8, the initial increase of ΔT_s is equal to the mesh heating rate (1000˚C/s) for all model geometries apart from Compressed 1. This is because the heating of the particle equator is negligible over the first solver timestep, apart from with the geometric setup that optimizes conduction.

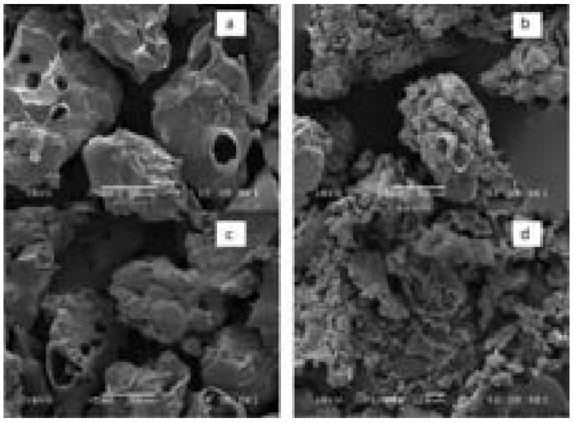

Figure 9: SEM micrography of cellulosic biomass particles [29]

Scanning electron microscopy from Yu et al. (Figure 9) shows that cellulose particles actually have irregular, non-spherical geometries. The rough surfaces would give a larger area for contact with individual wires within the mesh than would be possible with flat surfaces on a particle of similar radius. The proportion of the surface area available for conduction will be greater than that of the point-source model (0.5%), particularly when the mesh is modelled as individual wires rather than a plane. The particle would be better modelled by one of the compressed models, which predict a value of $\Delta T_{s,max}$ of 22.0K for Model 4 and smaller values for the more compressed models.

After the mesh has reached the setpoint (at 0.5s in Figure 8), $\Delta T_{s,max}$ reaches different non-zero value at steady-state. This is because of the balance of fluxes at the equator, as shown for Compressed Model 1 at 798 K setpoint in Table 4.

Table 4: Heat fluxes in Model 3 on the equator (non-heated surface) of Compressed 1

	Flux (W/m^2)
$q_{mesh\ rad}$	4698
-$q_{particle\ rad}$	-21365
-$q_{convection}$	-7827
q_{gained}	**-24494**

q_{gained} is dominated by the outgoing heat flux $q_{particle\ rad}$ rather than the incoming heat flux $q_{mesh\ rad}$ because $\varepsilon_{cell} \gg \varepsilon_{mesh}$. If the mesh were to be coated by the reaction products, ε_{mesh} could increase until q_{gained} was positive. However, the assumption that there are sufficiently many reflections between the plates with negligible absorption to scatter the radiation evenly over the particle surface would no longer be valid due to Kirchoff's law of thermal radiation.

The effective wire mesh surface area assigned to each particle for radiation $(2L^2)$ is sensitive to the density of cellulose particles in the monolayer and the percentage of the wire mesh plane occupied by wires and gaps.

Conclusion

Model 1 agreed very well with experimental values if the temperature within the particle could be considered homogeneous throughout the heating process, and Model 2 indicated that this is achievable if the entire particle surface is heated equally. Model 3 indicates that good particle-mesh contact area would allow for a homogeneous surface temperature.

However, there are multiple areas for improvement. Better characterisation of the different regions in a cellulose particle (amorphous surface vs crystalline body) and the respective reaction phenomena in each region would offer better insight into composition differences. Modelling changing intraparticle structures and porosity, as well as intraparticle radiation would give a better understanding of temperature gradients within the particle. With more experimental data, a more accurate solid model could be built that accounts for geometric irregularities including surface roughness. Lastly, an analytical model for reflections of the mesh radiation between the mesh surfaces would give a better approximation of particle surface temperature effects. Integration of the reaction modelling from Model 1 & Model 2 with the geometry and heat transfer modelling of Model 3 would offer a more comprehensive view of the process.

[1] N. W. Y. Ho, M. R. Ladisch, M. Sedlak, N. Mosier, and E. Casey, "Biofuels from Cellulosic Feedstocks," *Comprehensive Biotechnology, Second Edition*, vol. 3, pp. 51–62, Jan. 2011, doi: 10.1016/B978-0-08-088504-9.00155-0.

[2] A. Broido, A. C. Ouano, and E. M. Barrall, "Molecular Weight Decrease in the Early Pyrolysis of Crystalline and Amorphous Cellulose," 1973.

[3] A. Broido and M. A. Nelson, "Char yield on pyrolysis of cellulose," *Combustion and Flame*, vol. 24, no. C, pp. 263–268, Feb. 1975, doi: 10.1016/0010-2180(75)90156-X.

[4] A. G. W. Bradbury, Y. Sakai, and F. Shafizadeh, "A kinetic model for pyrolysis of cellulose," *Journal of Applied Polymer Science*, vol. 23, no. 11, pp. 3271–3280, Jun. 1979, doi: 10.1002/app.1979.070231112.

[5] W. Yin, R. H. Venderbosch, and H. J. Heeres, "Recent developments in the catalytic hydrotreatment of pyrolysis liquids," *Direct Thermochemical Liquefaction for Energy Applications*, pp. 249–292, Jan. 2018, doi: 10.1016/B978-0-08-101029-7.00007-2.

[6] C. Zeng *et al.*, "Advances in the development of wire mesh reactor for coal gasification studies," *Review of Scientific Instruments*, vol. 79, no. 8, p. 084102, Aug. 2008, doi: 10.1063/1.2968714.

[7] C.-Z. Li, K. D. Bartle, and R. Kandiyoti, "Characterization of tars from variable heating rate pyrolysis of maceral concentrates," *Fuel*, vol. 72, no. 1, pp. 3–11, Jan. 1993, doi: 10.1016/0016-2361(93)90368-C.

[8] L. Gao, L. Wu, N. Paterson, D. Dugwell, and R. Kandiyoti, "The use of wire mesh reactors to characterise solid fuels and provide improved understanding of larger scale thermochemical processes," *International Journal of Oil, Gas and Coal Technology*, vol. 1, no. 1/2, p. 152, 2008, doi: 10.1504/IJOGCT.2008.016737.

[9] X. Gong, Y. Yu, X. Gao, Y. Qiao, M. Xu, and H. Wu, “Formation of anhydro-sugars in the primary volatiles and solid residues from cellulose fast pyrolysis in a wire-mesh reactor,” *Energy and Fuels*, vol. 28, no. 8, pp. 5204–5211, Aug. 2014, doi: 10.1021/ef501112q.

[10] E. Hoekstra, W. P. M. van Swaaij, S. R. A. Kersten, and K. J. A. Hogendoorn, “Fast pyrolysis in a novel wire-mesh reactor: Decomposition of pine wood and model compounds,” *Chemical Engineering Journal*, vol. 187, pp. 172–184, Apr. 2012, doi: 10.1016/J.CEJ.2012.01.118.

[11] T. Lin, E. Goos, and U. Riedel, “A sectional approach for biomass: Modelling the pyrolysis of cellulose,” *Fuel Processing Technology*, vol. 115, pp. 246–253, Nov. 2013, doi: 10.1016/j.fuproc.2013.03.048.

[12] J. Yu, N. Paterson, and M. Millan, “The primary products of cellulose pyrolysis in the absence of extraparticle reactions,” *Fuel*, vol. 237, pp. 911–915, Feb. 2019, doi: 10.1016/j.fuel.2018.10.059.

[13] L. F. Chen and G. T. Tsao, “Physical characteristics of porous cellulose beads as supporting material for immobilized enzymes,” *Biotechnology and Bioengineering*, vol. 18, no. 11, pp. 1507–1516, Nov. 1976, doi: 10.1002/bit.260181103.

[14] F. P. Morais, A. M. M. S. Carta, M. E. Amaral, and J. M. R. Curto, “An innovative computational strategy to optimize different furnish compositions of tissue materials using micro/nanofibrillated cellulose and biopolymer as additives,” *Polymers*, vol. 13, no. 15, Aug. 2021, doi: 10.3390/polym13152397.

[15] J. M. R. Curto *et al.*, “The importance of optimizing the 3D structure when developing cellulosic materials for medical applications: the case of drug delivery systems (DDS),” Dec. 2016.

[16] P. O. Okekunle, T. Pattanotai, H. Watanabe, and K. Okazaki, “Numerical and experimental investigation of intra-particle heat transfer and tar decomposition during pyrolysis of wood biomass,” *Journal of Thermal Science and Technology*, vol. 6, no. 3, pp. 360–375, Aug. 2011, doi: 10.1299/jtst.6.360.

[17] L. J. Curtis and D. J. Miller, “"Upgrading of Coal Liquids for Use ‘Capillary Column Gas Chromatography with Sulphur-and Nitrogen-specific Hall Detectors for Determination of Kinetics of Hydroprocessing Reactions of Individual Com-pounds in Coal-liquid Fractions’ Transport Model with Radiative Heat Transfer for Rapid Cellulose Pyrolysis,” 1988. [Online]. Available: https://pubs.acs.org/sharingguidelines

[18] R. C. Messenböck, “Rapid Pyrolysis and Gasification of Coal in a High Pressure Wire-Mesh Reactor,” 1998.

[19] Y. C. Lin, J. Cho, G. A. Tompsett, P. R. Westmoreland, and G. W. Huber, “Kinetics and mechanism of cellulose pyrolysis,” *Journal of Physical Chemistry C*, vol. 113, no. 46, pp. 20097–20107, 2009, doi: 10.1021/jp906702p.

[20] J. R. Gibbins and R. Kandiyoti, “The effect of variations in time-temperature history on product distribution from coal pyrolysis,” *Fuel*, vol. 68, no. 7, pp. 895–903, Jul. 1989, doi: 10.1016/0016-2361(89)90127-0.

[21] J. Cho, J. M. Davis, and G. W. Huber, “The intrinsic kinetics and heats of reactions for cellulose pyrolysis and char formation,” *ChemSusChem*, vol. 3, no. 10, pp. 1162–1165, 2010, doi: 10.1002/cssc.201000119.

[22] J. Yu, N. Paterson, and M. Millan, “The primary products of cellulose pyrolysis in

the absence of extraparticle reactions," *Fuel*, vol. 237, pp. 911–915, Feb. 2019, doi: 10.1016/j.fuel.2018.10.059.

[23] NIST Webbook, "Nitrogen." https://webbook.nist.gov/cgi/cbook.cgi?ID=C7727379&Mask=4#Thermo-Phase (accessed Dec. 09, 2021).

[24] T. Shoji, H. Kawamoto, and S. Saka, "Boiling point of levoglucosan and devolatilization temperatures in cellulose pyrolysis measured at different heating area temperatures," *Journal of Analytical and Applied Pyrolysis*, vol. 109, pp. 185–195, Sep. 2014, doi: 10.1016/j.jaap.2014.06.014.

[25] J. Lédé, "Cellulose pyrolysis kinetics: An historical review on the existence and role of intermediate active cellulose," *Journal of Analytical and Applied Pyrolysis*, vol. 94, pp. 17–32, Mar. 2012, doi: 10.1016/j.jaap.2011.12.019.

[26] J. Lédé, F. Blanchard, and O. Boutin, "Radiant flash pyrolysis of cellulose pellets: products and mechanisms involved in transient and steady state conditions," *Fuel*, vol. 81, no. 10, pp. 1269–1279, 2002, doi: https://doi.org/10.1016/S0016-2361(02)00039-X.

[27] M. Antlauf, N. Boulanger, L. Berglund, K. Oksman, and O. Andersson, "Thermal Conductivity of Cellulose Fibers in Different Size Scales and Densities," *Biomacromolecules*, vol. 22, no. 9, pp. 3800–3809, Sep. 2021, doi: 10.1021/acs.biomac.1c00643.

[28] C. Qi, S. Hou, J. Lu, W. Xue, and K. Sun, "Thermal characteristics of birch and its cellulose and hemicelluloses isolated by alkaline solution," *Holzforschung*, vol. 74, no. 12, pp. 1099–1112, Nov. 2020, doi: 10.1515/hf-2019-0285.

[29] J. Yu, N. Paterson, J. Blamey, and M. Millan, "Cellulose, xylan and lignin interactions during pyrolysis of lignocellulosic biomass," *Fuel*, vol. 191, pp. 140–149, Mar. 2017, doi: 10.1016/J.FUEL.2016.11.057.

[30] K. Bikane, J. Yu, X. Long, N. Paterson, and M. Millan, "Linking char reactivity to structural and morphological evolution during high pressure pyrolysis of Morupule coal," *Chemical Engineering Science: X*, vol. 8, p. 100072, Nov. 2020, doi: 10.1016/J.CESX.2020.100072.

Ionic Liquids Waste Treatment Modelling and Optimization

Wai Lun Tsang, Jin Yu Zheng

Department of Chemical Engineering, Imperial College London, U.K.

Abstract The scientific researcher was driven by the challenge of water scarcity to develop efficient wastewater treatment systems for reuse. Although ionic liquids have been used in a variety of industrial and analytical separation processes, their use in wastewater treatment, particularly for the removal of organic contaminants, has yet to be fully investigated. In this report, we are focusing on separating organic components from the households and industrial dyes factory wastewater using ionic liquid. Three main parameters which affect the efficiency of the extraction process are being discussed in the report. The target of this project is to develop a simulation model of an ionic liquid liquid-liquid Extraction process using software Aspen Plus V.11 and assess its feasibility of VOC reduction at an industrial scale. The final model setup can achieve a VOC reduction rate of 87.6 %. The Techno-Economic Analysis (TEA) led to a unit operating cost of \$1.9 /m^3. A sensitivity analysis was performed to identify parameters that could affect operation cost and VOC removal efficiency of the process. Moreover, the simulation result of ILs liquid-liquid extraction is compared with two other popular treatment methods to justify the IL LLE performance.

Content

1. **Introduction**
2. **Background**
   - **2.1. Parameter definition**
   - **2.2. Extraction mechanism**
     - **2.2.1. Effect of Temperature and the Transfer Thermodynamic Properties**
     - **2.2.2. Effect of pH of Aqueous Phases**
     - **2.2.3. Effect of Extraction phase ratio**
   - **2.3. Toxicity**
3. **Methodology**
   - **3.1. Model setup**
   - **3.2. Economic Evaluation**
4. **Result**
   - **4.1. Systematic Process model analysis**
   - **4.2. Process Design and Model setup**
   - **4.3. OPEX and TCI**
5. **Comparison with Existing Technology and Sensitivity analysis**
   - **5.1. Comparison with Existing Technology**
   - **5.2. Sensitivity analysis**
6. **Conclusion**
7. **Reference**
8. **Appendix**

1.Introduction

To satisfy people's future needs, it has become necessary to treat and purify wastewater. Various treatment techniques have been used to transform wastewater into a usable form, with the combination of an innovative technology-oriented approach and a traditional process proving to be effective. In comparison to other materials, the use of ionic liquid for the treatment of wastewater containing organic pollutants has shown positive results, demonstrating strong selectivity, stability, and adsorption capabilities.[1] Therefore, the usage of ionic liquid in wastewater treatment is proven to be worthy. On the other hand, the application of ionic liquid to the traction process is affected by several factors which we will discuss these key findings in detail. Ionic liquids, on the other hand, are possible persistent aquatic contaminants due to their water solubility and limited biodegradability. They may also be transferred to deeper soil layers and pollute groundwater, including drinking water, due to their poor sorption to soil particles. As a result of their limited biodegradability and toxicity, which are unfavourable compared to conventional chemicals if left untreated, there are certain worries concerning their disposal and end of life. To better understand their environmental characteristics, there is a need to model their end-of-life fate and exposure to quantify their environmental impact at the end of their life cycle. In addition, since they are disposed of at some point after their use, the waste contaminated with ILs needs to be treated using waste-treatment technologies before they can be discharged to the environment. In this report, we will focus on exploring and modelling waste-treatment systems involving ionic liquids and evaluating their Techno-economic.

1. Background

Ionic liquid (IL) is defined as a salt in the aquae state below certain arbitrary temperatures, such as 100 °C (212 °F). While ordinary liquids such as water and petrol are predominantly made of electrically neutral molecules, ionic liquids are largely made of ions. They are organic salts with unique physicochemical properties, including low melting points, negligible vapour pressure, high thermal and chemical stability, and high solubility in both water and lipids (amphiphilic). The special characteristic of the ILS in removing volatile organic pollutants (VOCs) has shown potential for new wastewater treatment technologies. Between 2012 and 2018, 900–1100 papers on "ionic liquids" were recorded in PubMed, with the great majority focusing on technical and chemical issues. Ionic liquids have been dubbed a "silent revolution in material science," and their use, emission to the environment, and human exposure are all projected to skyrocket in the near future. (IL advantage /Industrial background relating to Wastewater treatment)

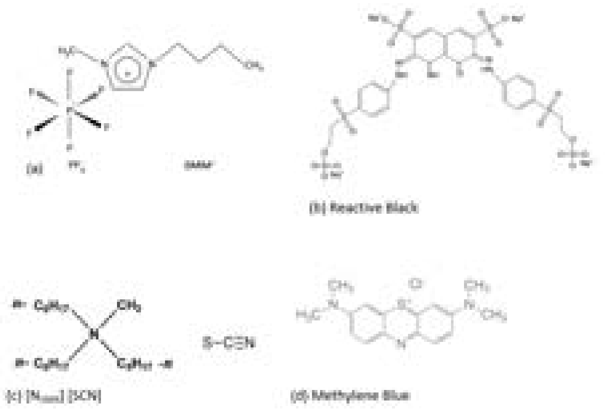

Figure 1 The structure of the ionic liquid and the typical dyes in this study: (a) ionic liquid [BMIM][PF_6]; (b) Reactive Black; (c) ionic liquid [N_{1888}] [SCN];(d) Methylene Blue.

1.1. Parameter definition

To understand how different parameter affects the performance of wastewater treatment, there are several important variable and definition to introduce.

Removal efficiency (R, %) and experimental distribution coefficient (D) values of dyes between ionic liquid and aqueous phases were calculated using the following equations:

$$R = \frac{C_{aq,o} - C_{aq}}{C_{aq,o}} \times 100 \qquad (1)$$

$$D = \frac{(C_{aq,o} - C_{aq}) \times V_{aq}}{C_{aq} \times V_o} \qquad (2)$$

$$= \frac{V_{aq}}{V_o} \times \frac{R}{100-R} = K \times \frac{R}{100-R} \qquad (3)$$

Where $C_{aq,o}$ and C_{aq} is the concentration of dyes in the aqueous phase before and after extraction. and V_{aq} and Vo are the aqueous and organic phase volumes, respectively. Denote K= V_{aq}/Vo, where V_{aq}/V_o(extraction phase ratio) is the volume ratio of aqueous and organic phases.V_{aq}/Vo, where

V_{aq}/V_o(extraction phase ratio) is the volume ratio of aqueous and organic phases.

1.2. Extraction mechanism

The Extraction mechanism can be taken as a transfer of extracted Cation and anion dissolved in water. The process is accompanied by an equal number of counter-ions which is ANI for anion and CAT for cation. The equations are listed below.

$$Ani_{aq}^{-}+DYE_{aq}=Ani_{org}^{-}+DYE_{org}^{-} \qquad (4)$$

$$Cat_{aq}^{+}+DYE_{aq}^{+}=Cat_{org}^{+}+DYE_{org}^{+} \qquad (5)$$

Here is an example:

$$KN_{aq}^{-}+PF6_{org}^{-}=KN_{org}^{-}+PF_{6aq}^{-} \qquad (6)$$

$$G_2RC_{aq}^{+}+BMIM_{org}^{+}=G2RC_{org}^{+}+BMIM_{or}^{+} \qquad (7)$$

After thorough research on the organic compound extraction process, the efficiency is found to be determined by three main factors which are temperature, PH and treat ratio.

1.2.1. Effect of Temperature and the Transfer Thermodynamic Properties

The extraction efficiency of the dyes increases as the temperature rises. The extraction of a dye from the aqueous phase into a specific IL may be thought of as a dye transfer from the aqueous to the IL phases from the standpoint of thermodynamics. As the solubility of IL increase as the temperature rise, we can be certain that the dye transfer process is endothermic.[17]

1.2.2. Effect of pH of Aqueous Phase

The relationship of pH value and the partitioning of dyes (Methylene Blue and Reactive Black) is illustrated in Fig. 2 as an example. The partition coefficient of Reactive Black rises to its summit around pH 6. That of Methylene Blue is not influenced by the adjustment of pH.[17]

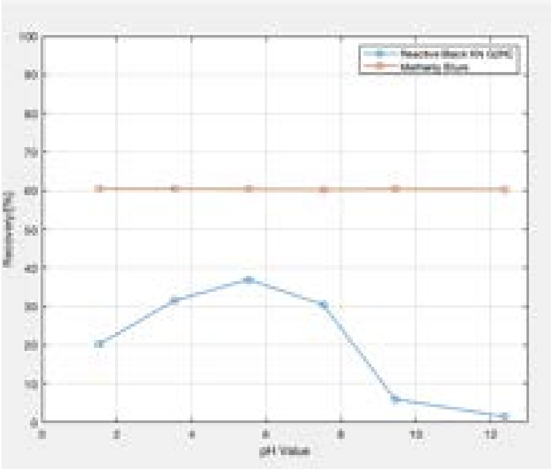

Figure 2 Effect of pH of the aqueous phase on removal efficiency of dyes.[19]

As Methylene Blue possesses an electro-symmetrical structure, charge transfer in the Methylene Blue moiety does not modify its anionic nature whether the acid or alkali is present. Therefore, its removal efficiency is not influenced by the adjustment of pH value. In neutral solutes, Reactive Black is in a neutral zwitterionic state, favouring the RTIL phase. The charge distribution of the Reactive Black molecule, however, changes under acidic or basic circumstances. In the aqueous phase, it has a higher tendency to dissolve.

1.2.3. Effect of Extraction phase ratio

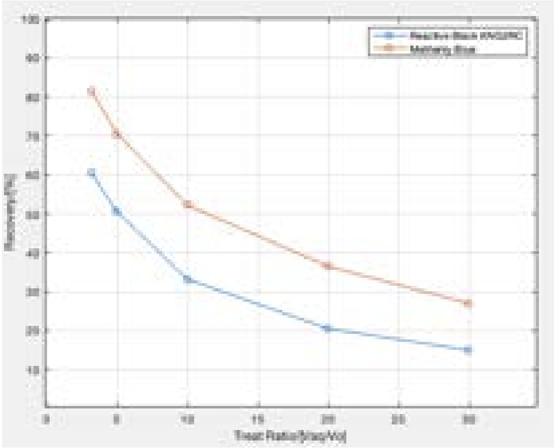

Figure 3 Effect of extraction phase ratio on removal efficiency of dyes[19]

In general, when the phase ratio (Vaq/Vo) increases, the dye removal efficiency falls. The ideal extraction phase ratio, on the other hand, must be established based on the outcomes of experiments. The removal efficiency of dyes after extraction decreases with the increase of phase ratio Vaq/Vo. The appropriate phase ratio was chosen in order to obtain the greatest balance of the largest distribution coefficient, best dye extraction efficiency, and shortest amount of ionic liquids needed. Figure 2 shows two example experiments on the effect of extraction phase ratio on the removal efficiency of dyes.[17]

1.3. Toxicity

Despite the growing usage of ionic liquids and the potential for contamination, the negative impacts on human health have not been examined, and their designation as "green solvents" is not based on any toxicological risk assessment. Various research has been conducted to confirm the green character of ionic liquids, with data released indicating that, due to their relatively high toxicity and limited biodegradability, these substances might have a significant detrimental influence on the environment.

The sorption, biodegradability, and toxicity of ILs, as well as their degradation products, are critical for their environmental impact and final fate. The toxicity of ILs is often assessed in a variety of test organisms (in vivo) or tissues, animal cells, and cell fractions (in vitro). Recently, the toxicity of ILs was comprehensively investigated and assessed on different test organisms such as bacteria, yeast, algae, nematode, water snail, water flea, kelp, invertebrates, fish, plants, as well as in different mammalian and fish cell cultures. Different test systems have exhibited varying degrees of sensitivity to ILs, implying that a test system's trophic level impacts its susceptibility to ILs.[5]

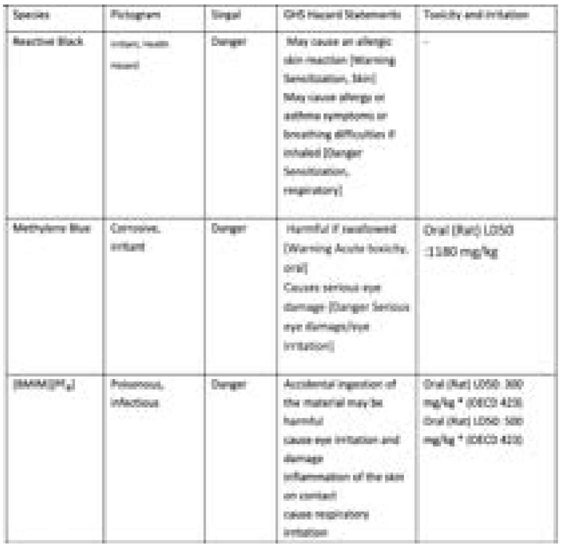

Species	Pictogram	Singal	GHS Hazard Statements	Toxicity and irritation
Reactive Black	Irritant, Health Hazard	Danger	May cause an allergic skin reaction [Warning Sensitization, Skin] May cause allergy or asthma symptoms or breathing difficulties if inhaled [Danger Sensitization, respiratory]	–
Methylene Blue	Corrosive, irritant	Danger	Harmful if swallowed [Warning Acute toxicity, oral] Causes serious eye damage [Danger Serious eye damage/eye irritation]	Oral (Rat) LD50 :1180 mg/kg
$[BMIM][PF_6]$	Poisonous, infectious	Danger	Accidental ingestion of the material may be harmful cause eye irritation and damage inflammation of the skin on contact cause respiratory irritation	Oral (Rat) LD50: 300 mg/kg * (OECD 423) Oral (Rat) LD50: 500 mg/kg * (OECD 423)

Figure 4 Chemical safety of ionic liquid $[BMIM][PF_6]$; Reactive Black; Methylene Blue.

3. Methodology

1.1. Model setup

Based on the ionic liquid LLE mechanism, a Systematic Process model analysis on recovery efficiency of liquid extraction column is first pursued. The model can help predict the system behavior of ionic liquid extraction columns responding to changes in operate parameters. As mentioned in the extraction mechanism section, operation variables Treat ratio K, pH, Temperature, and metal salt concentration can affect the recovery efficiency. To reduce the complexity and DOF in the systematic model. The temperature and metal salt concentration are set to be fixed. And the pH value and the treat ratio are selected as the independent variables. From the supplemented experimental data, the effect of pH and treat ratio K on the removal efficiency of dye can be precisely estimated by using the polynomial regression method. With additional correlation, the attained pH and treatment ratio profiles can be converted into a systematic numerical in MATLAB. Once the model has been set up, it can help to generate removal efficiency for any selected pH and K value inside the optimal domain.

By using the recovery efficiency data and the breakdown of the process, a simulation of the Ionic liquid LLE process is constructed in Aspen Plus V11. Although, it has been reported that the ionic liquid might be capable of removing organic pollutants. Other organic compounds might remain in the waste stream. Since the discharge wastewater meet appropriate COD (Chemical Oxygen Demand) the emission standard. An anaerobic digestion reactor needs to be integrated into the model setup to full remove the organic contents.

The treatment capacity for the simulation model was estimated based on literature research. In the model setup, an industrial waste stream combined with household wastewater and food waste is used. The selection of combined waste stream aims to generalize the feed conditions, thus, to make the simulation closer to reality. The major VOC present in the waste stream Reactive black KNG2RC which is a dye in textile coloring industry, structure can be found in figure 1. The total VOC removal efficiency is calculated by the reduction of over the total amount of Reactive black. Detailed feed waste stream composition can be found in appendix 1.

The process design and simulation aimed to create a feasible set-up to conduct a successful VOC reduction, as well as understand the technical feasibility to scale up a Room temperature ionic liquid (RTIL) liquid-liquid extraction process. The allowance discharge COD concentration for treated water is <16mg/l>. Given the ionic liquid might be toxic to creatures in the waterbody, ionic liquid concertation also needs to be monitored at the stream exit. The detailed simulation design is included in the result and discussion section, with a stream table describing the final discharged stream composition.

1.2. Economic Evaluation

To perform economic analyses on the Aspen model, the Aspen Simulation Workbook tool was used in combination with Microsoft Office Excel 2013. The Techno-Economic Analysis (TEA) was done by estimating the capital cost and operating cost using the book (Warren D. Seider, 2018)[23]. Three significant variables were calculated to justify the economic potential of the RTIL liquid-liquid extraction process. TCI refers to the total capital investment cost, where OPEX stands for the operating expenditure. UPR represents the unit process revenue. Among the three, TCI and FCI were determined based on the estimated sizing and costing of each process instrument. Where OPEX is mainly contributed by the quantity of reagents, utilities, selling of products and byproducts. The equations for calculating OPEX and TCI are given below.

Total Capital Investments (TCI)= Direct Costs + Indirect Costs + Working Capital

Operating Expenditure (OPEX)= Raw Materials Costs + Utilities Costs + General Expenses + Labor

4. Result

4.1. Systematic Process model analysis

In order to investigate the system behavior of the ionic liquid LLE process and determine the optimal operating point. A systematic process model is conducted in MATLAB. The model is constructed based on the description of the extraction mechanism, pH value and Treat ratio are the selected parameters.

The static extraction efficiency response surface is illustrated in figure 5. The optimal recovery efficiency of 83.3% is achieved at a pH of 3.53 and treat ratio of 1.8, approximately. It is well supported by experimentally data, that the recovery efficiency is close to zero at high pH region. Therefore, pH control is necessary to achieve an optimal recovery. Generally, the removal efficiency prefers a low treat ratio and low pH value. However, in the actual setup, an unnecessary low treat ratio will require an impractically large tank and a considerable amount of ionic liquid which will increase the operating cost dramatically. Therefore, a slightly high treat ratio should be considered to balance the raw material cost and extraction efficiency.

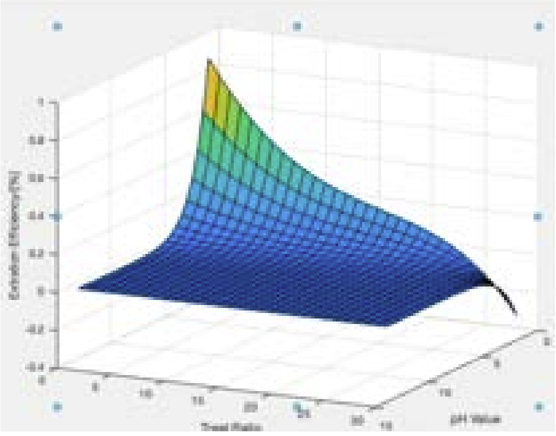

Figure 5 A systematic model according to the extraction mechanism. Selected Variable pH value and Treat ratio

4.2 Process Design and Model setup

Ionic liquid LLE Column

Based on literature and primary data profile, an RTIL LLE column integrated with an anaerobic digestor is simulated in Aspen Plus V11. The extraction process is carried out in a single channel multiple-stage liquid-liquid extraction column. The treat ratio is selected to be 10 in order to balance the operation cost and the wastewater residual time inside the column. The wastewater and food waste stream composition are taken from the 2018 BIE annual report with a flowrate of 2450kg/hr and 395500kg/respectively. To justify the capability of applying ionic liquid in a more general wastewater treatment process. An industrial waste stream is combined with household wastewater and food waste and feed to the condensation tank. The final flowrate of the combined waste stream is 505m^3 per hour with a COD and VOC concentration of 100mg/l and 70mg/l.

The design overview is presented in figure 6, the composition of treated water and product biogas stream is also included at the bottom. On the left of the figure6, food waste (food waste) and domestic wastewater (wastewater) enter the 5-column. To generalise the simulation and make the scenario more universal and typical, both types of wastewaters are treated in the same model. Both forms of wastewater have pipelines that lead to a mixer. The blended substance is then transferred to a new mixer with the ionic liquid of choice. The newest content reaches the separator unit after passing through the pre-treatment tank and heat exchanger to guarantee consistent temperature and PH. Figure 4 shows the output of ionic liquid from the separator, which may be reused in the process, in the top pipe on the right. The separator's other output will be purified further in the anaerobic digestion process before being released into the environment. The extracted VOC and ionic liquid mixture with feed will then feed to separation column for IL recycling. Separation can be done in a flash column. The low volatile nature of IL can ensure an easy separation with VOC pollutant. This separation efficiency is set to be 98%. The IL will leave at the bottom of the separation unit and ready to be rejointed with the new feed stream. The final discharge rate of the treated wastewater stream is 616.72m^3/hr, the COD concentration is 13.3mg/l. The recovery ratio of Ionic liquid is calculated to be 98%, with a Reactive black KNG2RC concentration of 12.888ppm. Since the allowance emission COD concertation is 16mg/l, the process can fit the performance criterion. The total removal efficiency of VOC by ILLLE is 87.6%. According to an MDPI report in 2019, an average 82.50% BOD5, 88.29% COD reduction rate is being suggested for 23

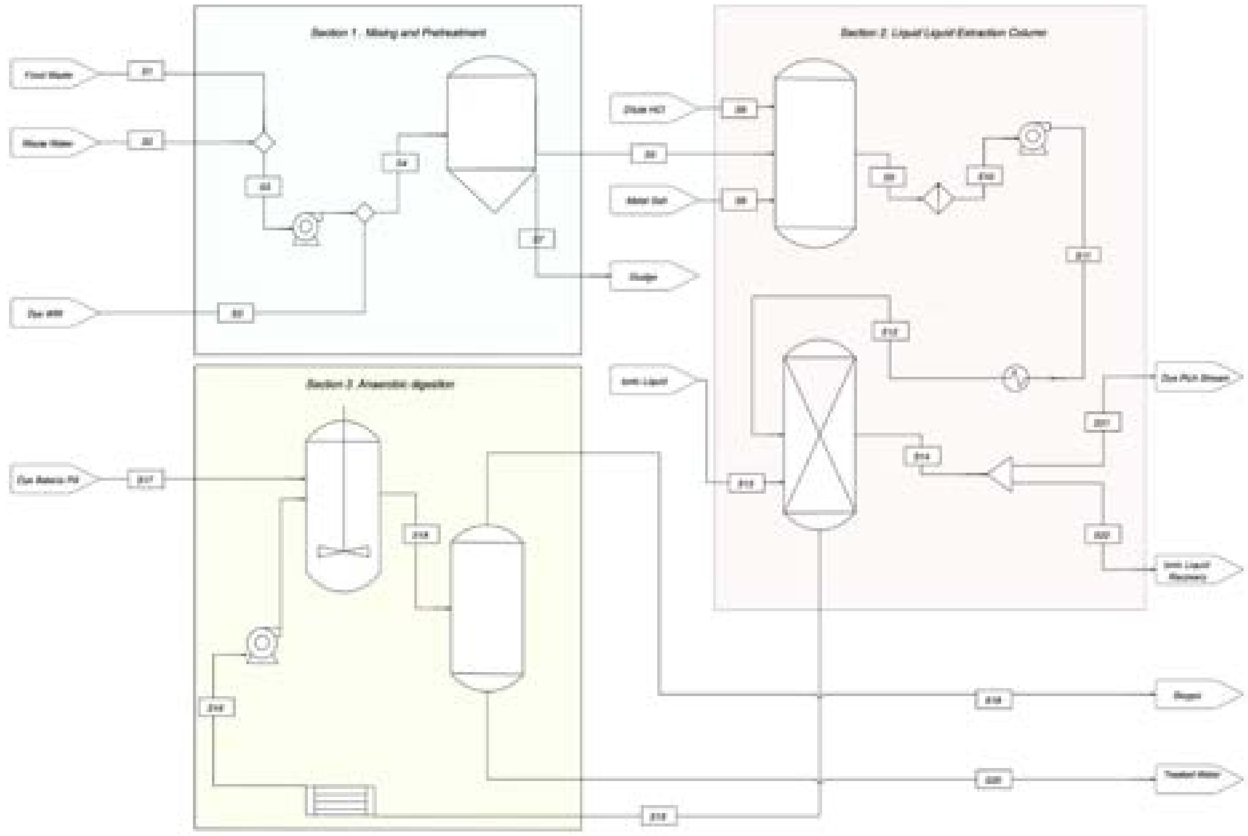

Figure 6 Process Design and Simulation Model setup

CO2	H2O	O2	N2	AMMONIA	HCL	CH4	KCL	NA2S	BIOMASS	NAOH	RB5	MB	IL	Volume Flow	Temperature	Pressure
735.129469	0	0	0	0	0	461.082627	0	0	0	0	0	0	0	1152.24562	37	1

Figure 7 Biogas output composition

H2O	NA+	H3O+	K+	NH4+	AMMONIA	HCL	OH-	CL-	NAOH	RB5	MB	IL	Mass Flows	Volume Flow	Temperature	Pressure
[illegible]	[illegible]	2.42E-08	0	4.85E-05	4.38E-08	[illegible]	[illegible]	[illegible]	[illegible]	[illegible]	0	[illegible]	[illegible]	[illegible]	31	1

Figure 8 Treated water output composition

can be linked with the remain of ionic liquid in the treat stream. In the simulation model ionic liquid is recovered by reaction with sodium hydroxide. However, since this process is mainly targeted to remove VOC pollutants in water. The slightly lower COD removal rate might still consider to be acceptable.

Anaerobic digestion Reactor

An Anaerobic digestion reactor is integrated into the system to complete the ionic liquid LLE process. After the effluent can still be discharged to the environment after separation from the ionic liquid since there are still organic substances present. Microorganisms break down biodegradable material in the absence of oxygen through a series of processes known as anaerobic digestion. The reaction system inside the Anaerobic digestion is shown in Fig.9.Notice the complex biomass compound do not have defined chemical formular, the number of elements in the biological formula is in fact a relative ratio of element mass over the total molecule mass. A detailed table for all compound involved in the system is attached in appendix.2. The column's output is subsequently sent via flash column to separate gas phase. After CO2 and CH4 have been removed from the liquid content, the treated water can be discharged. Both compounds are considered process by-products that might be sold to reduce operational costs. The result for biogas production in this section is 1152 kg/h with a composition of 61% CO_2 and 38% CH_4. The target composition for the biogas production stream was 65 w%CH_4 and 35 w%CO_2. Low CH_4 concentration might lead to extra cost on separation. Therefore, the biogas stream is suggested to be sold as electricity.

Stoichiometry	Component	Fractional conversion
Starch→2.592CO_2(MIXED)+2.99CH_4(MIXED)	Starch	1
Palmitic→1.648CO_2(MIXED)+11.4969CH_4(MIXED)	Palmitic	1
Protein→0.3325CO_2(MIXED)+0.5098CH_4(MIXED)	Protein	1
NH_4Cl→NH_3(MIXED)+HCl (MIXED)	NH_4Cl	1
2C+2H_2O→CO_2(MIXED)+CH_4(MIXED)	C	1

Figure 9 Reactions in Anaerobic digestion reactor column

4.3 OPEX and TC

Total Capital Investment (TCI)

The Capital cost is consisted of three component which are the direct cost, indirect cost, and work Capital. The total capital investment for this process as selected operation condition is $6066720.The percentage breakdown of all costs contributing to TCI is shown in Figure 10.

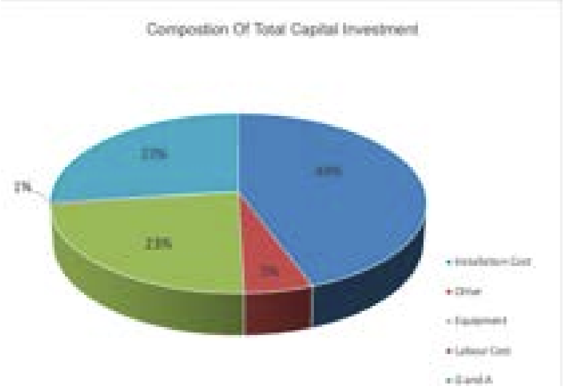

Figure 10. composition of Total Capital cost (TCI)

Amount the five sections, The installation is recognized as the main contributor which account for 44% of the total capital investment. The equipment cost and General and Administrative cost can combine as the direct capital cost which is equivalent to 50% of the total TCI. The remain 6% is the indirect cost.

Total Operation Cost (OPEX)

The calculated OPEX is $84434004.61, which can be divide into 7 components. The percentage breakdown of all costs contributing to OPEX is shown in Figure 11.

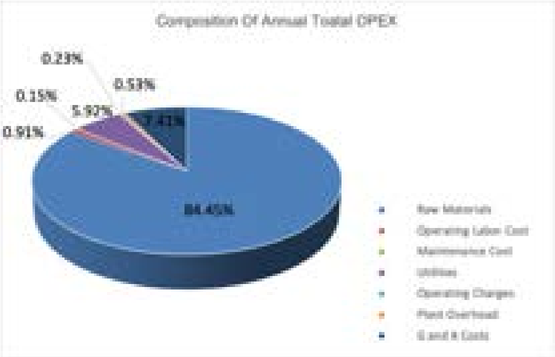

Figure 11. Composition of Total operation cost (OPEX)

Raw material cost is contributed to 84.45% of total OPEX and is recognized to be the major contributor. The OPEX calculated for per unit wastewater is $1.906. Based on the Number of municipalities and amount paid for WWT ((€/m³) estimated by the MDPI [11] Total revenue is calculated between -$1.759 to -$1.1802. Total average revenue calculated for this simulation process is - $ 1.49/m³.

Average Unit Revenue/[$/m3]	Maximum Unit Revenue/[$/m3]	Minimum Unit Revenue/[$/m3]	Coefficient of variation
0.419	0.726	0.147	0.349

Figure 12. Paid rate of 1-unit wastewater being treated

5.1 Comparison with Existing Technology

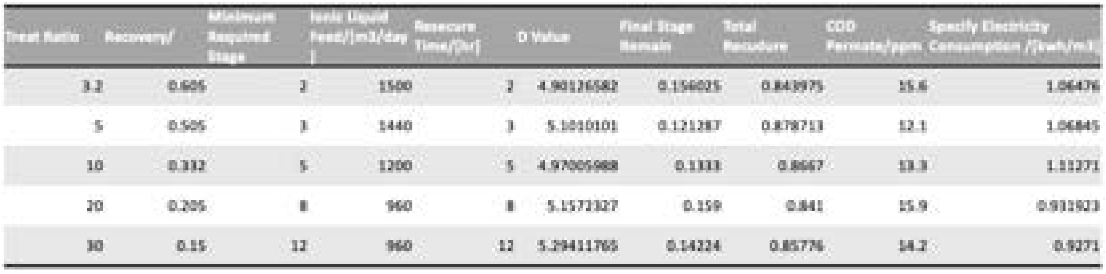

Treat Ratio	Recovery/	Minimum Required Stage	Ionic Liquid Feed/[m3/day]	Resecure Time/[hr]	D Value	Final Stage Remain	Total Recudure	COD Permeate/ppm	Specify Electricity Consumption /[kwh/m3]
3.2	0.605	2	1500	2	4.90126582	0.156025	0.843975	15.6	1.06476
5	0.505	3	1440	3	5.1010101	0.121287	0.878713	12.1	1.06845
10	0.332	5	1200	5	4.97005988	0.1333	0.8667	13.3	1.11271
20	0.205	8	960	8	5.1572327	0.159	0.841	15.9	0.931923
30	0.15	12	960	12	5.29411765	0.14224	0.85776	14.2	0.9271

Figure 13 Data of ionic liquid liquid-liquid extraction

Method	COD Concentration/[mg/l]	Running Time/[hr]	Removal Efficiency
SF-FWS plant	100-120	14	82.45
SF-FWS control	100-120	14	76.3

Figure 14 Data of artificial wetland [25]

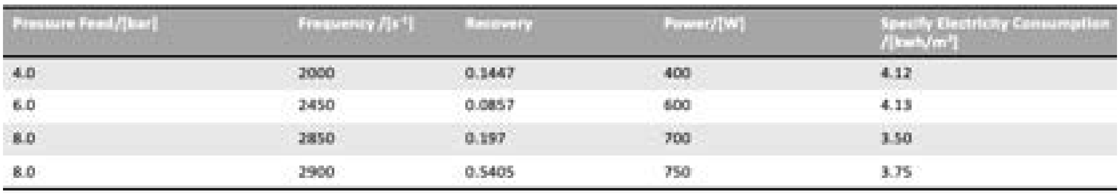

Pressure Feed/[bar]	Frequency /[s^{-1}]	Recovery	Power/[W]	Specify Electricity Consumption /[kwh/m³]
4.0	2000	0.1447	400	4.12
6.0	2450	0.0857	600	4.13
8.0	2850	0.197	700	3.50
8.0	2900	0.5405	750	3.75

Figure 15 Data of nano-filtration[24]

When comparing the recovery efficiency of Artificial wetland with ILs liquid-liquid extraction, the recovery efficiency of Artificial wetland is typically greater than ILs. The disadvantages of time and land consumption, on the other hand, are evident. Artificial wetlands take far more time and space to cleanse the same volume of water, so it is not an easy task to scale the process up.

Nano-filtration [24] shares the advantage of ILs liquid-liquid extraction process which can be easily scaled up. However, Nano-filtration only has a high recovery efficiency at high pressure, 8 bar. Such high-pressure poses safety risks and heavy maintenance-fee burden to the process. Besides, the power required for the compressor to achieve such high pressure is significant. As a result, the energy consumption of the process is 3-4 times of ILs liquid-liquid extraction.

Although, IL liquid-liquid extraction does not show the best recovery efficiency. The low specifies electricity consumption and capability of handling high wastewater flow led to a general low energy intensity and less land consumption. These characteristics can reduce the difficulty when pursuing a scale up. In general, the number instrument, utility consumption and size of an IL LLE process will be smaller compared with other two technology achieving the same treat capacity.

5.2 Sensitivity analysis

Sensitivity of operating cost was assessed to determine the most dominant factor. A +/- 25% variant in selected parameters is conduct through the model and the respond of OPEX to the system is shown in Table In addition, the effect of treat ratio on OPEX and TCI is also evaluated, results shown in the following figure.

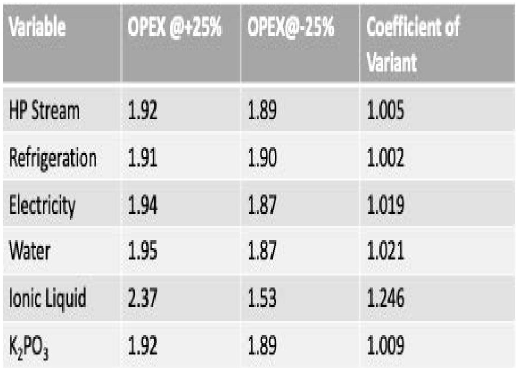

Variable	OPEX @+25%	OPEX@-25%	Coefficient of Variant
HP Stream	1.92	1.89	1.005
Refrigeration	1.91	1.90	1.002
Electricity	1.94	1.87	1.019
Water	1.95	1.87	1.021
Ionic Liquid	2.37	1.53	1.246
K_2PO_3	1.92	1.89	1.009

Figure 16 Sensitivity analysis of OPEX

The sensitivity analysis indicated the variation in ionic liquid price give most significant impact to OPEX. This value is significantly higher than other substrates and operation utilities. Calculation illustrated that ionic liquid accounts for 76% of operating costs.

The trend of change in operational costs OPEX (in blue) and capital costs CAPX (in red) when the treat ratio is altered from 3 to 30 can be seen in figure 17.

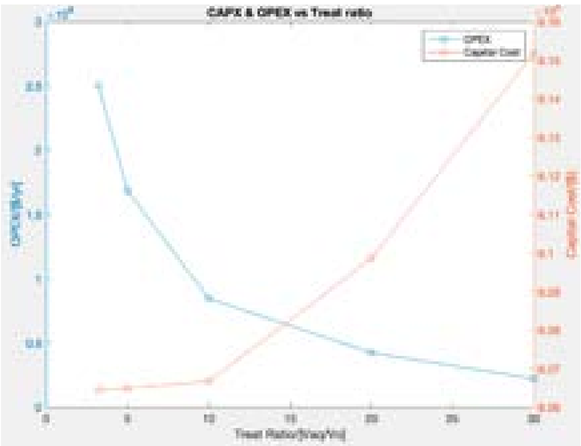

Figure 17 Change in OPEX & CAPX with treat ratio

The data shows that when the treat ratio rises, the capital cost rises at a faster pace. It's logical since the lower the treat ratio, the more stages there are in the extraction process, necessitating a bigger extractor. On the contrary, when the treat ratio increases, the operational cost decreases at a decreasing rate. The two analyses result generally support with each other, where the high expense of ionic liquid might be the key reason of an extremely high operation cost.

6. Conclusion

Due to the special characteristic of ionic liquid to absorb organic pollutant, ionic liquid liquid-liquid extraction is introduced to one of the plausible methods to treat wastewater. There are several pros and cons in choosing ionic liquid extraction over artificial wetland and nano-filtration which we have discussed previously. The main dilemma of this technology is the exceptionally high cost of ionic liquid. It shows immaturity in the current technology over production or usage of ionic liquid. In recent future, it is expected that the technological advancement in the field will lead to universalization of ionic liquid usage and hence reduce the cost. Until then, the process of ionic liquid liquid-liquid extraction is considered not worthy as the cost out weight the benefit that comes with it. In terms of future aspect, more research and experiment can be done to investigate what other factors are concerned in the recovery efficiency. Moreover, there are voices saying ionic liquid pre-treatment has a positive impact on the Anaerobic digestion process which is yet to be proved so we look forward to investigating further on such matter.

7. Reference

[1] Isosaari, P., Srivastava, V. and Sillanpää, M., 2021. Ionic liquid-based water treatment technologies for organic pollutants: Current status and future prospects of ionic liquid mediated technologies.

[2] Stepnowski, P. and Zaleska, A., 2021. *Comparison of different advanced oxidation processes for the degradation of room temperature ionic liquids*.

[3] Blake, D., 2021. *Bibliography of Work on the Heterogeneous Photocatalytic Removal of Hazardous Compounds from Water and Air--Update Number 4 to October 2001*.

[4] Banić, N., Abramović, B., Šibul, F., Orčić, D., Watson, M., Vraneš, M. and Gadžurić, S., 2021. *Advanced oxidation processes for the removal of [bmim][Sal] third generation ionic liquids: effect of water matrices and intermediates identification*.

[5] Zhao, D., Liao, Y. and Zhang, Z., 2021. *Toxicity of Ionic Liquids*.

[6] Upcraft, T., Tu, W., Johnson, R., Finnigan, T., Van Hung, N., Hallett, J. and Guo, M., 2021. *Protein from renewable resources: mycoprotein production from agricultural residues*.

[7] Yaseen, D. and Scholz, M., 2021. *Textile dye wastewater characteristics and constituents of synthetic effluents: a critical review*.

[8] Carmen, Z. and Daniel, S., 2021. *Textile Organic Dyes – Characteristics, Polluting Effects and Separation/Elimination Procedures from Industrial Effluents – A Critical Overview*.

[9] Sun, Y., Wang, D., Tsang, D., Wang, L., Ok, Y. and Feng, Y., 2021. *A critical review of risks, characteristics, and treatment strategies for potentially toxic elements in wastewater from shale gas extraction*.

[10] Avlonitis, S., Poulios, I., Sotiriou, D., Pappas, M. and Moutesidis, K., 2021. *Simulated cotton dye effluents treatment and reuse by nanofiltration*.

[11] Moral Pajares, E., Gallego Valero, L. and Román Sánchez, I., 2021. *Cost of Urban Wastewater Treatment and Ecotaxes: Evidence from Municipalities in Southern Europe*.

[12] Kocyıgıt, H. and Ugurlu, A., 2021. *Biological decolorization of reactive azo dye by anaerobic/aerobic-sequencing batch reactor system.*. [online] Cabdirect.org. Available at: <https://www.cabdirect.org/cabdirect/abstract/20153361383> [Accessed 16 December 2021].

[13] Hussein, A. and Scholz, M., 2021. *Treatment of artificial wastewater containing two azo textile dyes by vertical-flow constructed wetlands*.

[14] Aschenbrenner, O., Supasitmongkol, S., Taylor, M. and Styring, P., 2021. *Measurement of vapour pressures of ionic liquids and other low vapour pressure solvents*.

[15] Vijayaraghavan, R., Vedaraman, N., Surianarayanan, M. and MacFarlane, D., 2021. *Extraction and recovery of azo dyes into an ionic liquid*.

[16] Mittal, A., Malviya, A., Kaur, D., Mittal, J. and Kurup, L., 2021. *Studies on the adsorption kinetics and isotherms for the removal and recovery of Methyl Orange from wastewaters using waste materials*. [online] Academia.edu. Available at: <https://www.academia.edu/56772143/Studies_on_the_adsorption_kinetics_and_isotherms_for_the_removal_and_recovery_of_Methyl_Orange_from_wastewaters_using_waste_materials> [Accessed 16 December 2021].

[17] Pei, Y., Wang, J., Xuan, X., Fan, J. and Fan, M., 2021. *Factors Affecting Ionic Liquids Based Removal of Anionic Dyes from Water*.

[18] Temimi, M., 2021. *Adsorption of Reactive Black 5 dye onto two kinds of Poly (vinyl imidazole) in aqueous solutions. – Journal of Basrah researches sciences*. [online] Bjrs.uobasrah.edu.iq. Available at: <http://bjrs.uobasrah.edu.iq/?p=495> [Accessed 16 December 2021].

[19] Li, C., Xin, B., Xu, W. and Zhang, Q., 2021. *Study on the extraction of dyes into a room-temperature ionic liquid and their mechanisms*.

[20] Stepnowski, P. and Zaleska, A., 2021. *Comparison of different advanced oxidation processes for the degradation of room temperature ionic liquids*.

[21] Hendrickx, I., 2021. *Pollution prevention studies in the textile wet processing industry*. [online] Vtechworks.lib.vt.edu. Available at: <https://vtechworks.lib.vt.edu/handle/10919/41081> [Accessed 16 December 2021].

[22] Chen, X., Li, F., Asumana, C. and Yu, G., 2021. *Extraction of soluble dyes from aqueous solutions with quaternary ammonium-based ionic liquids*.

[23] Seider, W., Lewin, D., Seader, J., Widagdo, S., Gani, R. and Ng, K., n.d. *Product and process design principles*.

[24] Avlonitis, S., Poulios, I., Sotiriou, D., Pappas, M. and Moutesidis, K., 2021. *Simulated cotton dye effluents treatment and reuse by nanofiltration*.

[25] Cumnan S, Yimrattanabovorn J (2012) The use of constructed wet- land for azo dye textile wastewater. Int J Civil Eng Build Mater 2:150–158

Metal electrodeposition to mitigate resistive losses associated with scale up of photoanodes in photo-electrochemical reactors

Authors: Euichul Jeong & Chris Lawrence

ABSTRACT

Photo-electrochemical (PEC) reactors are potential technology for green hydrogen synthesis. In this paper, the problems that arise from scale-up of PEC reactor photoanodes consisting of semiconductors, namely WO_3 and $BiVO_4$, deposited on a fluorine-doped tine oxide, FTO, substrate are highlighted. Metal electrodeposition is explored as a technique to mitigate resistive losses of the FTO substrate upon reactor scale-up. In particular, the suitability of molybdenum over nickel to this semiconductor pairing using band theory is described. Molybdenum, however, is difficult to deposit on FTO and has not been thoroughly tested in the literature. Therefore, experience developed from nickel electrodeposition on FTO is applied to molybdenum deposition. A pretreatment surface reductive procedure, originally intended to increase the adhesion of nickel deposits on FTO, was found to form an intermetallic layer consisting of iron and tin on the substrate. The presence of iron improved subsequent molybdenum electrodeposition by: i) catalysing the deposition of molybdenum on FTO and ii) increasing the adhesion of molybdenum deposits. An optimum molybdenum depositing current density was found to be ~5 mA cm^{-2} for 2 hours through SEM and EDS analyses. At these conditions, carrying out the pretreatment procedure doubled the observed molybdenum deposits compared to depositing on untreated FTO.

Keywords: Electrodeposition, Molybdenum, Nickel, FTO, Catalysis, Pretreatment

---

1 INTRODUCTION

Photo-electrochemical (PEC) reactors are a promising technology with potential to support a green hydrogen economy. In order to reach 5 GW capacity of low carbon hydrogen by 2030, as declared in “The Prime Minister’s Ten Point Plan for a Green Industrial Revolution”, green hydrogen production methods need to be developed (HM Government, 2020). Currently, a PV-powered electrolyser setup can deliver hydrogen at a cost of \$6.22/kg, compared to a recent figure for PEC reactors of \$8.43/kg (Bellini, 2020). However, there is a strong argument for further development of PEC reactors: they require no platinum, which is a scarce resource (EU Science Hub, 2020), and could potentially deliver initial lower capital costs, which will decrease the level of risk investors may associate with the technology (Grätzel, 2001).

2 BACKGROUND

2.1 PEC REACTORS

The function of a PEC reactor depends strongly on a particular characteristic of semiconductors. Owing to the energy separation of a semiconductor’s conduction and valence bands, electrons, given enough solar energy, can ‘jump’ up from the valence to the conduction band. They leave behind a positively charged hole, h^+, which promote the oxidation of water into oxygen and hydrogen ions. These hydrogen ions are then reduced to from hydrogen gas. The equation for the photon absorption and electron + hole generation process is as follows:

$$hv \xrightarrow{\text{Semiconductor}} e^- + h^+ \quad (1)$$

$$4h^+ + H_2O \xrightarrow{\text{Photooxidation}} O_2 + 4H^+ \quad (2)$$

$$4H^+ + 4e^- \xrightarrow{\text{Reduction}} 2H_2 \quad (3)$$

Figure 1 describes how this reaction procedure commences at the semiconductor-electrolyte interface. Energy from the sun, hv, strikes the semiconductor and excites the electron from the valence to the conduction band (2). The electron will travel across a series of materials before it enters the circuit and journeys to the counter electrode to reduce hydrogen (3). It is this journey that is of concern; problems with energy loss immediately arise as a result of scale-up owing to the fundamental properties of the materials involved.

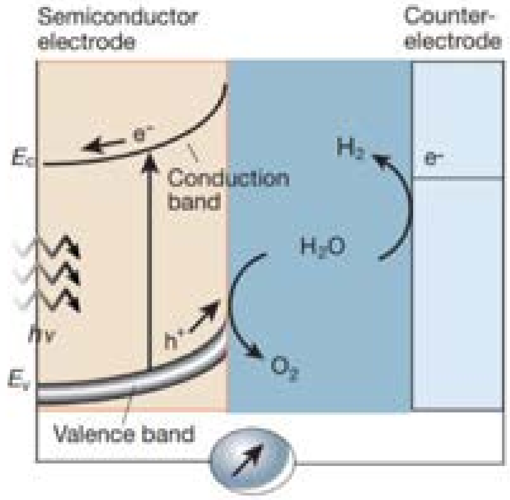

Figure 1: Water oxidation and reduction reactions at the semiconductor-electrolyte interface and metal-electrolyte interface, respectively. (Grätzel, 2001)

2.2 PROBLEMS WITH SCALE-UP

The semiconductors need to be deposited - via chemical vapour deposition - onto an adequate surface. This surface most be both transparent and conductive to maximise the sunlight that strikes the semiconductors, as well as be mechanically robust.

Transparent conductive oxides (TCOs) are regularly selected as suitable substrates onto which the semiconductors can be deposited. Indium tin oxide (ITO) and fluorine-doped tin oxide (FTO) are readily available as transparent coatings applied onto glass. Although ITO has a greater electronic conductivity, FTO is cheaper and allows for quicker metal deposition. The latter of these two advantages is deemed relevant due to problems that arise from scaling up.

As electrode dimensions increase, voltage losses as a result of substrate resistance drastically increase (Abdi, 2020). Previous studies have confirmed the necessity of depositing metal on FTO, which will contact the semiconductor to minimise resistive losses upon scale-up. However, a metal coating will drastically reduce transmissivity of the overall photoanode. Therefore, this system may be thought of as subject to two contrasting constraints. Through COMSOL Multiphysics modelling, and optimum structure has emerged. This optimum structure consists of a series of horizontal lines, 5 mm in width spaced 7 mm apart (Zhang, 2021).

When a metal is in contact with a semiconductor, the Fermi energies of both materials need to equilibrate. This equilibration can deliver an additional energy barrier for an electron travelling from the electrolyte.

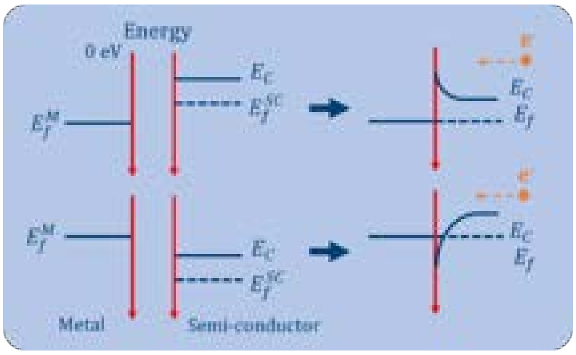

Figure 2: Conduction band bending at the semi-conductor-metal interface

If the Fermi energy of the metal, E_f^M, is higher in potential energy (lower along the energy axis in Figure 2) than the conduction band of the semiconductor, E_C, an energy barrier will have an inhibitory effect on the incoming electron. This will hinder the improvement of efficiency for the overall PEC reactor. The energy barrier is caused by the bulk tendency of the semiconductor to maintain the difference between its Fermi and conduction band energy. However, at the interface, the conduction band maintains its original energy level, causing band bending (Lüth, 2010). The semiconductor of interest is WO_3, which has a conduction band energy of -5 eV. Molybdenum, with a Fermi energy of -4.5 eV would thus be suitable to act as a contact metal.

Nickel, which has a Fermi energy of -5.3 eV, would conversely deliver an energy barrier. As a deposition metal, however, nickel has been used extensively and thus the experience gained will be applied to molybdenum deposition. Both a suitable current density and a reproducible procedure that can be adopted to increase the adhesion of molybdenum to FTO will be investigated. Results will be discussed from nickel deposition, and a coupling of quantitative spectroscopic data and qualitative adhesion testing will be used to confirm certain FTO pre-treatment methods (Mittal, 1975).

Potentiostatic electrodeposition of molybdenum on FTO will be optimised experimentally. A range of different current densities will be attempted and deposits will be inspected. Galvanostatic electrodeposition of molybdenum will be carried out using an electrochemical quartz crystal microbalance (EQCM) device. The EQCM device can use frequency to measure small changes in mass on an electrode (K. Chiang, 2008).

$$\Delta f = -C_f \, m \tag{3}$$

Sauerbrey's equation can used to calculate mass accumulation, m, knowing changes in frequency, Δf and the calibration constant, C_f (Gamry Instruments, 2014). Faraday's first law of electrolysis will be used throughout this study where the depletion of ions in solution is of concern. It connects the current applied and metal deposited as follows:

$$m = \frac{MIt}{nF} \tag{4}$$

This equation can be used to calculate the theoretical mass of deposited species, m (g), from equivalent weight, M (in g/mol), the current, I (A), the time, t (s), the electron stoichiometry, n, and the Faraday's constant, F, given as 96500 C/mol.

3 METHODOLOGY

The research was divided into three main components: the deposition of two metals, Ni and Mo, and a pre-treatment process to improve metal adhesion and deposition rate. When required, Kapton® tape was used to mask the FTO substrate to deliver grid line metal deposits. To analyse the deposition quality, EDS (Energy-Dispersive x-ray Spectroscopy) with SEM (Scanning Electron Microscope) were used to analyse the substrate surface. Furthermore, the 'scotch tape method' - tape is applied to a deposited surface and peeled off to see how much of the deposition is removed - was used to test the adhesivity of the metal deposited. Subject to practical inaccuracies, a multi-meter was used as a quick test of conductivity. This provided a relative comparison between FTO before and after metal deposition. In addition, Nova software was used in tandem with a 500ml electrochemical glass cell to perform the electrodepositions. Nova software was similarly used to retrieve the EQCM results.

3.1 NICKEL DEPOSITION

An in-house electrochemical glass cell was used for electrodeposition of Ni. The materials used for electrodes are Pt (Asynt Ltd) and Ag/AgCl (Metrohm Ltd) for counter electrode and reference electrode respectively the potentiostat used was Autolab PGSTAT302N. The setup used is shown in Figure 3.

Figure 3: Electrodeposition setup involving an Ag/AgCl reference electrode (blue wire), FTO substrate as working electrode (red wire) and platinum counter electrode (black wire).

The prepared FTO substrate (TEC 15, Pilkington Perkin-Elmer), which acted as the working electrode that has the dimensions of 2cm by 2cm, was immersed in Watt's bath solution whilst varying current densities were applied for different times. The Watt's bath is a solution composing of 0.1M $NiSO_4.6H_20$, 0.04M H_3BO_3 and 0.04M Na_2SO_4 (Sigma Aldrich). After the deposition process had commenced, the glass was rinsed with acetone, ethanol and deionised water.

3.2 TREATMENT OF FTO GLASS

In order to improve the adhesion of metals on the FTO, a surface reductive process was used (Ahmet, 2019). This method delivered the formation of an intermetallic layer on the FTO surface. In preparation, the FTO was rinsed with ethanol, acetone and deionised water. Thereafter, the glass was immersed, FTO side upwards, in a solution containing 1.0 M glycine, 0.5 M $FeSO_4.7H_2O$ in deionised water, adjusted to pH 3.0 with H_2SO_4. After leaving the glass for 30 seconds, Zn powder (mesh 30~100), ground with a mortar and pestle, was sprinkled uniformly on the glass and left for 2 hours. The aim of this process was to obtain a shiny, metallic layer on the unmasked regions. This layer consists of Fe_xSn_y metal. The reaction mechanism is as follows: Fe^{2+} reduces SnO_2 on the FTO surface to SnO and Sn, sequentially. During the reduction, Fe^{2+} gets oxidized to Fe^{3+} but gets reduced to Fe^{2+} back again by zinc.

3.3 MOLYBDENUM DEPOSITION

The setup was identical to that used for Ni deposition, except a different electroplating bath was used. A pH 4 solution containing 0.042 M $Na_2MoO_4.2H_2O$, 0.2 M $NiSO_4.7H_2O$ and 0.3 M H_3BO_3 was used. The immersed substrate was exposed to constant current densities for different lengths of time. Again, after the deposition

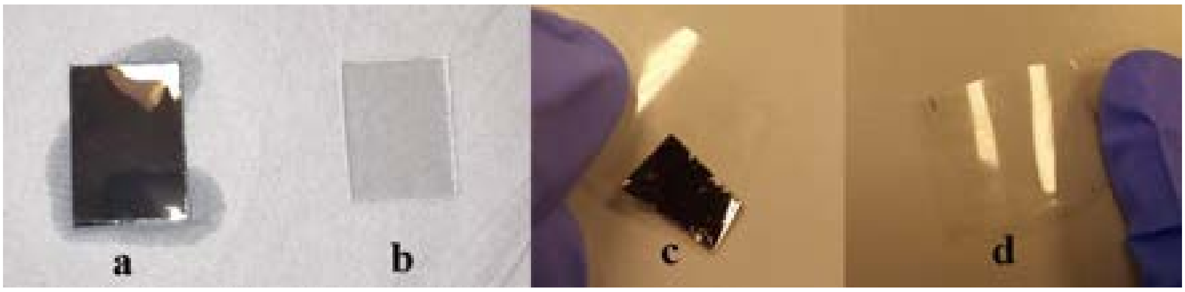

Figure 4: (a) Treated (2cmx3cm) FTO glass. (b) FTO glass without treatment. (c) Nickel deposits removed from FTO using the 'Scotch tape' test. (d) Nickel deposits on the scotch tape (i.e. almost none) with FTO pre-treatment

process had commenced, the glass was rinsed with acetone, ethanol and deionised water. Importantly, the bath contains nickel ions, which will also be deposited.

4 RESULTS AND DISCUSSION

4.1 NICKEL DEPOSITION

The effects of varying current density and electrodeposition time were investigated. The main points of interests were the adhesivity and the uniformity of Ni deposition, as well as the suitability of the surface morphology. When the current density is too small, the electrodeposition rate is very slow, requiring long deposition times. The drawback of this is that as deposition time increases, and the thickness of the deposited layer increases, the adhesivity decreases (Mittal, 1975).

After carrying out the experiment at different conditions, the conditions that resulted in the most adhesive, conductive layer was applying current density of approximately 5 mA cm^{-2}, for 10 minutes. However, even in this condition, the deposited Ni did not fully pass the 'Scotch tape' test, where small portions of the Ni peeled off with the tape. When a multimeter was used to measure the resistance between two end points of the FTO glass, the glass with deposited Ni had significantly lower resistance, around 25 Ω, compared to 35 Ω of pure FTO glass. It was possible to achieve a gridline deposition, as can be seen from Figure 5. The main difficulty placing the Kapton® tape in equal distances, and therefore the distance between gridlines was not exactly 7 mm apart (Zhang, 2021). However, the gridline provides improved conductivity relative to pure FTO glass.

Figure 5: Nickel deposited on (2cmx4cm) FTO in grid structure as optimised by previous studies (Zhang, 2021).

4.2 TREATMENT OF FTO GLASS

The goal of the treatment process was to coat the FTO layer with a Fe-Sn compound, as metal to metal adhesion is much stronger in bond energy compared to that of metal to oxides.

Table 1: Compositions of different elements on the FTO surface, pre- and post- treatment

Element	**Composition (mass %)**	
	Pre-treatment	Post-Treatment
O	17.79	17.05
Si	15.96	11.39
Fe	0	11.45
Sn	66.24	60.11

Having a shiny, intermetallic appearance, as seen in Figure 4(a), the treated FTO was run with EDS to confirm the success of the process. Table 1 shows that the Fe^{2+} ions in solution had successfully been reduced to metallic Fe on the substrate, as seen by the presence of elemental Fe. Furthermore, when nickel was deposited onto the treated surface, it passed the scotch tape test; no metal peeled off with the tape, as seen in Figure 4(d). After repeatedly trying, smears of nickel deposits were removed. This was, however, a notable improvement from nickel deposits on un-treated FTO (see Figure 4(c)).

4.2.1 SENSITIVITY OF ZINC PARTICLE SIZE

Different conditions in the treatment process were attempted to optimise the results. Although the literature suggested that a lower $FeSO_4$ concentration may aid reaction speed, this was not found to be true in the investigations carried out. Furthermore, although the literature suggests the use of Zn powder mesh 100, it was not available at the time of experiment. Therefore, a mortar and pestle were used to grind relatively big zinc powders.

Without grinding the zinc, the treatment process resulted in a patchy metallic layer, where areas covered with coarser zinc particles had a slower rate of reaction, exemplified by the visibly lighter patches. This phenomenon can be explained by the role of Zn in the pre-treatment reaction mechanism. It acts as a key component as a reducing agent of Fe^{3+} ions to Fe^{2+} ions. Furthermore, the bigger particle size inhibits access of the said ions to the FTO surface, therefore slowing down the reaction.

4.2.2 SENSITIVITY OF N_2 PURGING

The original literature does not mention purging the solution with N_2 or Ar. However, the Fe^{2+} solution quickly oxidized to brown Fe^{3+} solution if no purging was done. Therefore, the solution was purged with N_2 to displace dissolved O_2 for 30 minutes before the process, and throughout the process. This prevented the oxidisation of Fe^{2+} ions and resulted in expected shiny, intermetallic layer.

The importance of N_2 as a component of the overall reaction mechanism was quantified through EDS testing of samples with and without N_2 purging. It was found that N_2 increases the iron content on the surface by a factor of 3.5. One can go even so far as to say N_2 purging delivers a favourable intermetallic morphology for metal deposition, shown in Figure 6. With N_2, a much smoother surface is observed. This would allow a more uniform deposition of metal. Due to the availability of the SEM machine during the period of this study, it was not possible to obtain images at an equal magnification, thus the differences in scale between the two images.

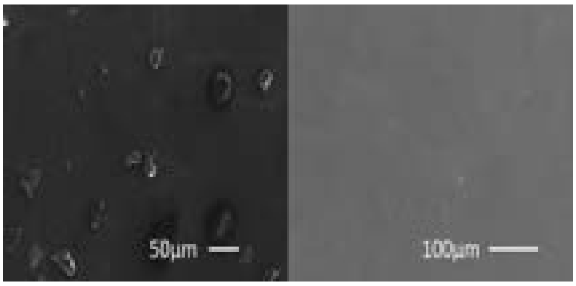

Figure 6 : SEM imaging of pre-treated surface without N_2 purging (left) and pre-treatment surface with N_2 purging (right)

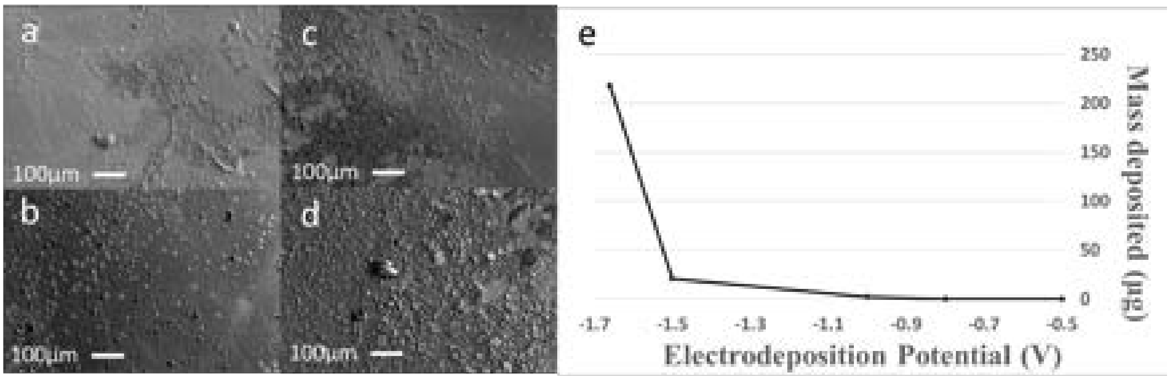

Figure 7: SEM images of molybdenum and nickel deposited on (a) 7mA cm^{-2} with no pre-treatment, (b) 7mA cm^{-2} with pre-treatment, (c) 5mA cm^{-2} with no pre-treatment, (d) 5mA cm^{-2} with pre-treatment. (e) Mass deposited on EQCM electrode vs electro-deposition potential

---

4.3 MOLYBDENUM DEPOSITION

In conventional electrodeposition, the main effect of high current density is the lower energy efficiency due to energy used to create H_2 on the surface. In deposition on FTO glass, however, not only does the energy efficiency decrease but also the deposition only occurs near the top of the substrate, as electrons tend to travel along the path of least resistance. This is primarily because of the low conductivity of FTO glass and therefore the electrons will prefer to travel towards the metal layer formed near the surface and react with H_2O to produce H_2.

4.3.1 GALVANOSTATIC CONDITIONS

After verifying that nickel can be deposited on FTO, the metal of interest was changed to molybdenum. Again, the solution was kept the same while varying the current density and deposition duration. Unlike the case with nickel, the deposition was not uniform in all current density ranges investigated. Furthermore, even the deposited Mo could not pass the scotch tape test. One possible solution towards uniform deposition was to improve the adhesion of FTO by treating it with Fe and Zn. The non-uniformity of the deposition resulted in inconsistent resistance reading of the glass. However, taking the mean range of resistivity showed that it increased compared to clean FTO. Out of the mixture of current densities and deposition durations experimented, 5 mA cm^{-2} for 2 hours and 7 mA cm^{-2} for 1 hour gave the most uniform deposits.

4.3.2 POTENTIOSTATIC CONDITIONS

EQCM results were obtained and used to derive an optimum voltage. Using a value for the calibration constant, C_f, of 0.0815, frequency changes were detected from the EQCM device and the graph from Figure 6(e) was obtained using Sauerbrey's equation (4). Therefore it was determined that the voltage should be lower than -1.5 V for successful deposition, as a value less negative than this would result in poorer deposition.

4.3.3 DEPOSITION WITH PRE-TREATMENT

When pre-treated FTO was used to deposit molybdenum, carrying out the procedure under the same conditions resulted in a more uniform deposition, indicating that an intermetallic layer does indeed improve molybdenum deposition.

Table 2: EDS results for both 5mA cm^{-2} and 7mA cm^{-2} electro-deposition current densities with and without pre-treatment carried out on the FTO. The pre-treatment results in the formation of an intermetallic layer consisting of iron and tin, which acts as a catalyst for the deposition of molybdenum.

Element	**7 mA cm^{-2} composition (mass%)**		**5 mA cm^{-2} composition (mass%)**	
	No pre-treatment	Pre-treatment	No pre-treatment	Pre-treatment
O	81.90	85.46	70.78	40.17
Ni	4.75	0.65	18.77	1.29
Mo	3.66	10.15	8.17	14.99
Sn	9.70	3.12	1.32	3.02
Fe	0	0.62	0	0.64

Both SEM imaging and EDS analysis were used to discern the effect of pre-treating FTO on molybdenum deposition. Table 2 shows that the iron acts as a catalyst for the electrodeposition of molybdenum. For 7 mA cm^{-2}, iron on the surface can increase molybdenum deposition by a factor of ~3. Whereas for 5 mA cm^{-2}, molybdenum deposits are increased by a factor of ~2. This finding could in part be due to the presence of iron, but effects of ion (Ni^{2+}) depletion in the electrochemical bath are could also be influential. If overall nickel deposition was less, a greater percentage of molybdenum on the surface would be observed. But this would not necessarily correlate with a greater rate of molybdenum deposition. Additionally, the cracks in the depositions, seen in Figure 7(c) and (d) and was suspected to be due to the depletion of molybdenum in the solution.

Therefore, a calculation using Faraday's law was used to confirm the mass of the deposited material relative to the amount of metal in the solution. The deposited mass was calculated to be 1.38% of metal ions present in the solution. Hence, it can be deduced that the crack is not due to the depletion of ions. This value was calculated through the use of Faraday's first law of electrolysis (4), with a total of 1.2g of molybdenum present in a 0.042 M solution. As the Mo used, $Na_2MoO_4.2H_2O$, has a charge of +6 in solution, E becomes 96 / 6 = 16 g/mol. With 7 mA cm^{-2} charge for 3600 seconds across an area of 4cm^2, this delivers a depleted mass of 0.0167g.

The circular crater-like areas in Figure 7(b) suggest a non-uniform deposition. This is highly likely to be due to the formation of hydrogen bubbles on the electrodeposition surface inhibiting a uniform deposition. As the deposited molybdenum accelerates the generation of hydrogen, hydrogen generation during the process is inevitable (Morley, 2012). Therefore, a further investigation on possible hydrodynamic systems, for example stirred reactors, is required.

5 CONCLUSION & OUTLOOK

Electrodeposition of two metals, nickel and molybdenum, was carried out on FTO glass to improve its electrical conductivity. Further to overall plating, electrodeposition in the shape of gridlines were alco achieved. This is important as when FTO is used in the PEC reactor, the transmissivity of the photoanode will need to be maximised to ensure as much light strikes the semi-conductors as possible. Furthermore, theoretical optimum results were confirmed to be true for nickel; a 5 mm thick gridline approximately 8 mm apart provides greatly improved conductivity relative to pure FTO glass (Zhang, 2021).

Nickel deposition is relatively easier than molybdenum, although molybdenum in theory provides a better conductivity enhancing effect. In both cases however, the adhesion on FTO was very poor, and did not pass the 'Scotch tape' test. Previous investigations have been made into the pre-treatment of FTO to improve the adhesion of nickel deposits; the investigation has been extended confirm its effectiveness on molybdenum, and the results along with EDS and SEM confirm that not only the adhesion improves, but so does the overall deposition quality. The optimum conditions for nickel deposition were a current density of 5 mA cm^{-2} for 3 minutes, and for molybdenum, 5 mA cm^{-2} for 2 hours, as this delivers the highest surface composition of molybdenum.

The ultimate objective of the electrodeposition was to improve the conductivity of FTO glass. Although previous theoretical work has been carried out to calculate the conductivity, a more robust method of measuring conductivity is required. Another interesting area for further investigation is the effectiveness of molybdenum. Although molybdenum has a more suitable Fermi energy, its raw material cost is higher and from this research, it can be seen that its electrodeposition is much more challenging than that for nickel. The efficiency of molybdenum's conducting capabilities should be compared to its raw material costs, and hence the overall impact in PEC reactor efficiency. Finally, the SEM images of molybdenum deposition shows that the current treatment process is not sufficient for a uniform, smooth deposition. Cracks and circular areas of non-deposition existed on the surface, and although stirring the solution may resolve the latter, a new pre-treatment process will be required for a complete uniform deposition as in the case of nickel.

6 CONFLICTS OF INTEREST

There are no conflicts to declare.

7 ACKNOWLEDGEMENTS

We would like to express our sincere thanks to Dr Anna Hankin and Jatuporn Banjong. This project wouldn't have been possible without their help. Furthermore, we would also like to thank Dr. Ibbi Ahmet for the helpful advice that he gave us during such a short period.

8 REFERENCES

Abdi, F. F., 2020. Mitigating voltage losses in photoelectrochemical cell scale-up. *Sustainable Energy Fuels.*

Ahmet, D. I., 2019. Demonstration of a 50 cm2 BiVO4 tandem photoelectrochemical-photovoltaic water splitting device. *Sustainable Energy and Fuels.*

Bellini, E., 2020. *Photo-electrochemical cells vs. PV electrolysis.* [Online]
Available at: https://www.pv-magazine.com/2020/08/12/photo-electrochemical-cells-vs-pv-electrolysis/

EU Science Hub, 2020. *Raw Materials Information System.* [Online]
Available at:
https://rmis.jrc.ec.europa.eu/?page=crm-list-2020-e294f6

Gamry Instruments, 2014. *Basics of an eQCM.* [Online].

Grätzel, M., 2001. Photoelectrochemical cells. *Nature.*

HM Government, 2020. *The Ten Point Plan for a Green Industrial Revolution,* s.l.: s.n.

K. Chiang, T. M., 2008. *Techniques for Corrosion Monitoring,* s.l.: s.n.

Lüth, H., 2010. *Solid surfaces, interfaces and thin films,* s.l.: s.n.

Mittal, K. L., 1975. *Adhesion measurement of thin films,* s.l.: Gordon and Breach Science Publishers Ltd..

Morley, T. J., 2012. The deposition of smooth metallic molybdenum from aqueous electrolytescontaining molybdate ions.

Zhang, Y., 2021. *Optimisation of photoelectrode substrate structures for up-scaled photoelectrochemical reactors via kinetic modelling,* s.l.: s.n.

Pathways to concurrently achieving decarbonisation and other development goals in the Kenyan cooking sector through agent-based modelling

Mia McLachlan, Avinasshini Seran
Department of Chemical Engineering, Imperial College London, SW7 2AZ London

16th December 2021

The widespread adoption of clean cooking in Kenya is an integral step in achieving net-zero CO_2 emissions by 2050. This study was motivated by the potential to identify target demographics and leverage this for the synergic achievement of other development goals alongside decarbonisation through focused policy development. Impactful development areas drove the narrative of independent scenarios translated into MUSE, making particular use of its novel capabilities for complex agent-based modelling. Crucial socioeconomic insights from the social sciences were integrated within MUSE to accurately characterise the Kenyan consumer investment portfolio and bridge the knowledge gap within energy planning models. The results alert that following the current trajectory, consumers will continue to choose solid biomass stoves to meet their demand. The introduction of a carbon tax as well as forest conservation laws will discourage solid biomass stove uptake, but are insufficient to meet emissions targets. Targeted HAP awareness programmes show the most promise in accelerating cleaner stove adoption, leading to the concurrent achievement of vital health and environmental goals. This study has reaffirmed the historical targeting of (rural) women for clean cooking incentives and highlighted that energy planning in the developing world is just as much a socially-driven issue as it is environmental.

1 Introduction

Consumer adoption of clean cooking technologies is vital to counteract a growing population which would lead to increased cooking demand and consequent carbon emissions.

Within various envisioned scenarios, this study highlights the possibility of achieving decarbonisation in parallel to other development goals through the adoption of clean cooking technologies. Existing barriers contributing to the slow uptake of clean cooking stoves beyond economic factors include preconceptions regarding clean cookstoves and their dissemination rates, insufficient awareness of the importance of safe and sustainable cooking as well as electrification and infrastructure development rates [1].

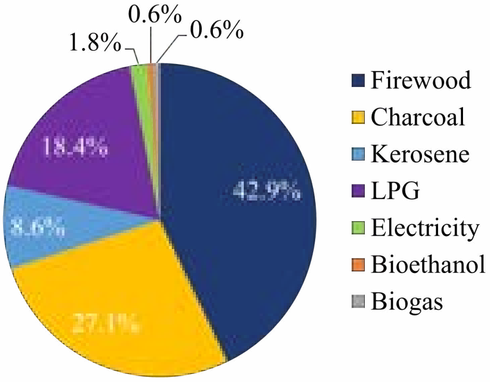

Figure 1: Pie chart representing the proportion of total existing cooking capacity accessible through use of each technology

Traditional cooking fuels like firewood and charcoal have been used for generations and are ingrained in Kenyan cooking culture, as illustrated in Figure 1. These cookstoves are still used by more than 75% of Kenyan households (and 90% of rural Kenyan households) as either of their two dominant cooking appliances [2]. Beyond ease of availability and tradition, the persistence of these preferences could be attributed to higher fuel and capital costs for alternative stoves and the associated fuels, with these factors taking precedence over environmental sustainability and arguably most importantly, health [3]. The idea that clean cooking only denotes lower or negligible GHG emissions is dated as there is also a significant importance placed on lower particulate matter ($PM_{2.5}$) emission rates.

Particulate matter has long been documented as harmful to health, but exposure to the finest, $PM_{2.5}$, poses the greatest health risk and is deadly when inhaled either outdoors or indoors. 14,000 deaths were attributed to the latter alone in Kenya in 2017 [4]. The hotspot for indoor household air pollution (HAP) is typically the kitchen, with different levels of emissions associated with stove choice. Women overwhelmingly shoulder the burden of cooking in Kenya, and have historically been targeted by incentives as the most significant stakeholders in clean cooking. However, the tendency of men to have the final say in household purchase decisions introduces complexity in the ease of adoption of clean cooking technologies as a result of even these targeted incentives [5].

The impact of gender and socioeconomics on household energy choices are important factors to be considered in energy models. Most major household decision-making is likely to be made either jointly or dominated by men whereas day-to-day decisions, including those regarding meals, are almost autonomously made by women [6],[7]. However, on average, men are still more likely to decide on the type of device to buy and use, and to pay for said device, despite women almost solely undertaking the major domestic tasks requiring these appliances [5]. This is stark in the context of cooking. Furthermore, there are employment and educational differences between rural and urban women which affect their level of input into decisions [8],[9],[10], as well as differing economic outlooks in rural and urban Kenyans [11]. Therefore, to accurately characterise the population, geo-economics and gender must be taken into account simultaneously [12].

The last decade has seen Kenya experience a rapid growth in electricity access, with more than a 200% increase across the population between 2009 and 2019 [13]. Universal access to electricity and other clean cooking solutions is currently targeted for 2028, ahead of the global 2030 milestone, within the Sustainable Energy for All (SEforALL) initiative [14] as well as the Kenyan National Electrification Strategy (KNES) [15]. Although constrained by accessibility issues, energy sustainability can and must be considered simultaneously by Kenya to align with the global push towards this end. Rural electrification has historically been less prioritised as the infrastructure development for these sparsely populated regions was considered too costly [16]. In 2020, the rural and urban electricity access rates were 56.3% and 90.8% respectively, bringing the national average to only 69.8% [1]. It is likely that grid connection will only diversify choices instead of causing a direct transition towards electric stoves [17].

There have been legislative efforts to reduce reliance on dirtier traditional technologies, particularly charcoal and firewood, as well as programmes to push for the adoption of cleaner stoves which have informed the development of scenarios in this study. Kenya's Ministry of Energy has identified the need for more data collection and specifically gender disaggregated data in the context of clean cooking. Segmenting the population into 4 distinct agents (rural men, rural women, urban men, and urban women) encompassing geo-economic differences between rural and urban agents in addition to gendered differences allowed the determination of 'target' demographics. This study aims to aid critical decision making for policy, financial incentives, awareness programmes and identify how initiatives can synergetically solve multiple development goals within the Kenyan residential cooking sector.

2 Background

There is a need for well-characterised energy modelling in the context of the developing world. The knowledge gaps lie within the context upon which these models are developed and their technical robustness.

The majority of energy planning models have been created in and for developed countries. Debnath et al [18] state that substituting correct data is insufficient as the models also contain biases and assumptions within their formulation which are unsuitable for developing countries. Several key issues lacking representation include suppressed demand due to lack of infrastructure or grid connection, complex socioeconomic characteristics such as corruption and political unrest and the extent of climate change impacts [18]. Perhaps the most pressing of all would be the lack of high quality, accessible and validated data as a result of insufficient R&D activity [18].

Pfenninger et al [19] remark that previous work within energy systems optimisation models has endeavoured to maximise spatial and temporal resolution with the data available while maintaining computational tractability. This trade-off between feasibility and resolution, coupled with the often inaccurate assumptions to account for the resolution loss is similarly being improved upon within power systems and electricity market models [19]. Development within energy systems simulation models has progressed through more formal approaches towards presenting uncertainty analyses as well as increased transparency through accessible documentation [19].

MUSE is an agent-based energy system simulation model which addresses the aforementioned concerns [20],[21],[22]. It allows for complete characterisation of an energy system in terms of regions, sectors, service demands, technologies, commodities and agents. MUSE makes use of a market-clearing algorithm (MCA) to match the demand with a supply, then models investment decisions for each agent. The former is either input exogenously or through appropriate correlations with a population or GDP. It is particularly novel because it is able to model investment decisions of multiple agents with heterogenous objectives. MUSE also accommodates both temporal and spatial resolution through options to specify multiple regions and 'timeslices' respectively.

A particularly difficult challenge to overcome in the realm of energy models is the capturing of socio-economic and other qualitative factors. In the interest of maintaining model robustness, variables which are easier to model accurately are favoured over potentially more insightful variables which are harder to ascribe to a simple mathematical relationship. This aligns well with widespread consensus on the importance of collaboration with social scientists to ensure that these variables are correctly represented in models highlighted by Trutnevyte et al [23]. Multiple strategies on effective combinations of work have been proposed, with the merging strategy showing the most promise [23]. This approach relies on the assumption that crucial social factors are possible to model and social scientists' results are then used to either alter preexisting models or build improved new models.

The misrepresentation of the global south and the opportunity to shed light on a historically gendered service demand motivated the study to be set within the Kenyan cooking sector. The influence of socioeconomic factors on energy choices are typically acknowledged, but not explicitly included within energy modelling. Several studies have highlighted that ([10],[8],[12],[9],[11]) these factors cannot be overstated in the context of household energy choices for cooking. This study integrates the socioeconomic landscape of Kenya into MUSE, allowing the resulting investment outlook to highlight 'target' demographics for better-informed decision-making for policy, incentives and awareness programmes. The Kenyan population was split into 4 distinct agents with complex objectives driven by statistics and sociological studies [7],[3],[6], [24],[25],[26] for several scenarios highlighting various focus areas. These areas each correlate to existing and potential policies on CO_2 emissions, HAP reduction, and forest conservation. This study has sought the use of MUSE with its agent-based capabilities combined with the incorporation of insights from the social sciences to bridge the current knowledge gap in energy models.

3 Methods

3.1 Overview

MUSE requires a variety of technical and economic data and makes use of a market-clearing algorithm to match the demand with a supply. These inputs were found either directly from sources or through correlations fueled by data-driven assumptions. These included the techno-economic parameters [2],[27],[28],[29],[30],[31],[32],[33],[34],[35],[2],[36] of each technology considered, with projections required for certain parameters in five-year intervals through to 2050 [37]. Several scenarios were developed and embedded within MUSE using its functionalities, including capacity growth constraints for certain technologies and the introduction of a carbon price. These inputs contribute to modelling the overall technology uptake, in addition to independently-modelled distinct agent behaviours within each scenario.

3.2 Technology selection

Technologies were selected to reflect the available cookstoves in the Kenyan residential sector and are summarised in Table **??**. In this study, stoves were considered independently of any potential external improvement technologies such as ventilated cookstove interventions.

It was recognised that firewood and charcoal, collectively known as solid biomass, are often collected for free but even purchasing is affordable as these fuels are locally-sourced and exempt from VAT. These stoves have the highest CO_2 and $PM_{2.5}$ emissions, but are invariably steeped in Kenyan culture. Biogas fuel, which is typically agricultural residue, is also either very cheap or free. Electric stoves, unlike the others, have a prerequisite of grid access which is the largest barrier to its adoption, especially in rural areas.

3.3 Techno-economic assumptions and calculations

3.3.1 Technical

MUSE required technology-specific data to forecast the trajectory of the corresponding capacity uptake. Some of these are highlighted as follows, with further information available within the **Supplementary Information**.

Utilisation factor

The utilisation factor (UF) describes the maximum obtainable output from installed capacity for each technology. Reliable data to describe the amount of time each technology would have to be offline due to maintenance and repair could not be identified so this was not taken into account. Differences in UF among technologies were therefore only dependent on fuel accessibility. This was only relevant for electric stoves where grid reliability is a noted issue [28].

Annual household capacity

The 2020 average cooking energy demand was calculated as described in Section 3.3.2 [2]. For each technology, the estimated minimum capacity required to meet the demand of a household was the ratio of average energy demand for a single household to the UF.

Scaling size

This minimum capacity required to meet the demand of a single household was taken to be the ‘scaling size’ which discretises a minimum capacity addition which can be proposed by MUSE.

Existing capacity

The total existing capacity of each technology was the product of the scaling size and the estimated number of households in possession of the technology in 2020 [29], [27].

Decommissioning profile

To identify the trajectory beyond 2020, the existing capacity was decommissioned linearly based on the average lifetime of each technology [30]. A minimum existing capacity was added for technologies with announced targets for the relevant year(s). For example, the National Climate Change Action Plan (NCCAP) has announced targets for 2 million households to use LPG or bioethanol and 6500 biodigesters (biogas-fuelled stove) for domestic use by 2022 [2].

Table 1: Summary of techno-economic inputs for each technology with all costs in millions and annual 2020 terms

Type	Technology	Stove cost (US\$/PJ)	Fuel cost (US\$/PJ)	Emission factor ($kgCO_2/kWh$)	$PM_{2.5}$ conc. ($\mu/gm3$)	Thermal efficiency
Traditional	Firewood	4.84 [27]	15.99 [2]	0.36 [32]	356 [34]	0.30 [2]
	Charcoal	5.95 [27]	9.10 [36]	0.36 [32]	356 [34]	0.43 [2]
	Kerosene	1.78 [27]	26.75 [36]	0.26 [31]	117 [34]	0.57 [2]
Modern	LPG	39.31 [27]	55.35 [36]	0.23 [31]	72 [34]	0.62 [2]
	Electricity	103.44 [27]	58.02 [36]	No direct emissions	55 [34]	0.90 [2]
	Bioethanol	14.54 [35]	61.03 [2]	0.16×10^{-2} [31]	99.68 [33]	0.55 [2]
	Biogas	209.12 [27]	0.05 [38],[39]	$0.02 \times 10-2$ [31]	99.68 [33]	0.50 [2]

Carbon emission factor
Carbon emission factors were identified for each technology to inform MUSE of their CO_2-producing potential. It should be noted that carbon emission factors were adjusted to consider the sustainability of fuel production. Solid biomass is unsustainable because its collection requires continued deforestation which will not be feasible in Kenya [2] in the near future. Therefore, MUSE was informed with the absolute CO_2 emission factor which only accounts for emissions produced from burning the fuel. In Kenya, biogas and bioethanol production are considered sustainable such that MUSE was informed with the $CO_{2,e}$ emission factor which considers the CO_2 required to grow the biomass as offsetting negative emissions.

3.3.2 Cooking demand projection

An estimation for the average annual cooking demand was calculated assuming 0.91 MJ per meal, 2.5 cooked meals per person daily and 4.4 Kenyans per household to reach an average daily energy demand of 9.9 MJ per household [2]. It is evident the service demand for cooking will not be split equally throughout the day as households are unlikely to cook during typical hours of sleep. To account for this, six equally proportioned timeslices were registered in MUSE to represent six different sections of the day with markedly different demands: morning, afternoon, early-peak, late-peak, evening, and night. The annual demand was then divided across these timeslices based on the typical daily demand profile in Kenya [2]. The demand profile for 2050 was then projected using the forecasted population growth between 2020 and 2050 [37]. MUSE then calculated the demand profile for each year within this range using linear interpolation.

3.3.3 Economic

MUSE required certain economic data to determine agent decisions through calculations of various objective functions. Some of these are highlighted as follows, with further information available within the **Supplementary Information**.

Fuel price
The historical average retail prices of charcoal, kerosene, LPG and electricity [36] were converted to the base year and currency required by MUSE. These prices were then projected into the future using moving averages. As a result of insufficient data reporting, firewood and bioethanol were assumed to have a constant price [2]. This was due to the unregulated nature of the former and the poor uptake of the latter. Fuel for biogas stoves was assumed to be either collected or purchased agricultural waste, the price of which was estimated using values of maize residue [38],[39].

The projection of fuel price detailed here could be subject to variation explored in Section 4.5.

Capital, fixed and variable costs
The capital costs of each type of stove were recorded, using averages of different models [27],[35] and converted to 2020 terms. Fixed and variable costs constituted maintenance and labour costs respectively. The former was estimated as 10% of the capital cost while the latter was assumed to be negligible as cooking is typically the responsibility of household members.

Interest rate
It was found that effectively all stoves, either primary or secondary, were bought completely through upfront cash payment [27]. To reflect this, an interest rate of 0% was used for traditional stoves and LPG as these stoves have already sufficiently penetrated the sector. However, owing to the high capital costs of the clean stoves, an interest rate of 10% was used in line with the Jiko Safi Fund's loans to Savings and Credit Cooperatives (SACCOs) within the umbrella organisation, Kenya Union of Savings and Credit Cooperatives (KUSCCO) [40].

Carbon price
To date, there have been no announcements of a carbon price by the Kenyan government [41] and the only country on the continent with an established carbon price is South Africa, standing at US$8.09/tonne before potential allowances or exemptions [42]. This value was assumed to be an appropriate estimate for a carbon tax that Kenya may introduce in the future.

3.4 Scenario development

Scenario narratives were developed based on the policy landscape in Kenya and the consequent envisioned paradigm shift in consumer behaviour. Policies were used as a baseline for growth constraints within MUSE and the resulting agent behaviour was modelled through changes in priority among decision-making objectives, and is described further in Section 3.5.

3.4.1 Scenario 1: Business-As-Usual (BAU)

This scenario was characterised using initiatives either in effect or coming into effect in Kenya across various development areas for the corresponding technologies, as described in Section 3.3. Agent characteristics reflected current decision-making patterns, with certain objectives having a pronounced gender skew. The subsequent scenarios each represent particular focus on a specific development area.

3.4.2 Scenario 2: Carbon price focus (CAR)

This scenario entailed the introduction of a carbon price by the Kenyan government and an accompanied increase in prioritisation of minimising carbon emissions across all agents. Within MUSE, consumers are impressed upon this carbon price through its influence on the emission cost objective which is a function of the price and amount of a pollutant produced, with CO_2 being the pollutant in this case. Sensitivity analysis was carried out, as outlined in 4.5 to examine the effects of additional financial penalties through increases in fuel price, capital stove costs and the carbon price on resulting CO_2 emissions.

3.4.3 Scenario 3: Household air pollution focus (HOU)

This scenario investigates improved consumer health literacy, achieved through awareness programmes. This scenario discourages technologies associated with excessive household air pollution (HAP) through the use of the 'comfort' function in MUSE. Each technology was ranked based on the typical $PM_{2.5}$ concentration in kitchens, with a lower emission rate corresponding to greater comfort, and the agents' objective share was scaled up to reflect the increased awareness across all agents.

3.4.4 Scenario 4: Forest conservation focus (FOR)

This scenario introduces strict conservation laws which restrict uptake of solid biomass stoves due to enforced removal of fuel access. This was modelled within MUSE by significantly constraining the growth of firewood and charcoal capacity in line with gradual forest conservation policy permeation.

3.5 Agent characterisation

Across all scenarios, the Kenyan population was divided into four agents consisting of urban men (UM), urban women (UW), rural men (RM), and rural women (RW) to fully describe the influence of gender and geo-economics on household decision-making. Agent objectives are complex [3] and were grouped into financial, environmental and health drives. Each agent was modelled to have a maximum of three objectives with different weightages depending on their priorities in each scenario [7],[3],[6],[24],[25],[43],[26], in line with MUSE's capabilities. The objectives of interest to the agents were found to be the capital cost of stoves, cooking fuel consumption cost, lifetime levelised cost of energy (LCOE), emission cost, and comfort, all of which were registered on MUSE and set to be either minimised or maximised.

Urban agents considered the LCOE which is a cost calculated by MUSE accounting for all associated costs for producing cooking energy, levelised across entire forecast period. However, rural agents considered the capital, fuel consumption and emission costs separately. These costs were not levelised such that the agents sought to minimise the individual costs every year rather than over the entire forecast. The discrepancy between rural and urban agents was identified through literacy rates [26], supplemented by the likelihood of rural agents to be limited by high initial costs more so than their urban counterparts due to lower economic status. The gender difference was accounted for using studies documenting the likelihood of women to have agency in decision-making for large household purchases [7],[24].

The environmental objective of emissions cost minimisation was only considered for CAR and agent weightages were calculated based on environmental literacy [43]. As described in Section 3.4, a greater preference was modelled across all agents for minimised emission costs for CAR. Rural men were modelled to give a higher weightage to emission costs over other financial costs compared to rural women due to their higher literacy rates [26]. This gender disparity in literacy was assumed to affect environmental awareness which would contribute to differences in decision-making. Urban agents still show the trend in higher literacy among men, but have significantly higher literacy rates to begin with [26], so this was deemed to be less important and both men and women were modelled identically in their relative weightage of LCOE and emission costs.

Health objectives, related to $PM_{2.5}$ concentration, were modelled through the comfort objective. For BAU, comfort objective weightages were calculated using sociological studies which reported the awareness of HAP amongst each agent [3], [25]. These values were scaled based on the average time spent in the kitchen by each agent, correlating to how invested they were in reducing the pollution. It was found that all women spend significantly more time in the kitchen than men [6], leading to a negligible consideration of comfort by men. Rural agents considered higher prioritisation of comfort to reflect the increased perceived health risk resulting from lower ventilation in indoor rural kitchens [43]. These comfort weightages were then scaled up for the scenario which considered accelerated health literacy, HOU.

3.6 Data collection

Output parameters of interest included capacity uptake of each technology by each agent as well as the CO_2 emissions attributed to each agent over the time horizon. Installed capacity uptake is driven by demand growth which is directly linked to population expansion. The uptake of each technology is primarily driven by the objectives of the agents but must fulfil the decommissioning profile of existing capacity and the minimum targets of technology growth set out in policy. Both cumulative and agent-normalised CO_2 emissions were determined and benchmarked against the average emissions produced per person in BAU.

4 Results and Discussion

4.1 Scenario 1: Business-As-Usual (BAU)

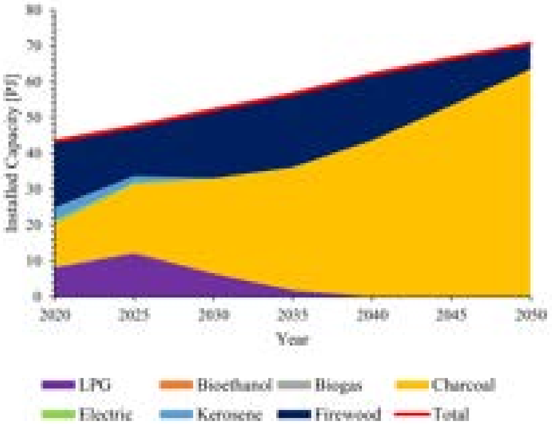

Figure 2: Installed capacity in PJ across the time horizon for the BAU scenario represented as a stacked area graph demonstrating the uptake of technologies

In this scenario, both solid biomass technologies continue to increase in capacity due to the prioritisation of cost objectives among all agents, as seen in Figure 2. All modern fuels as well as kerosene decline in capacity owing to their high fuel and stove costs. By 2040, the entire cooking demand is served only by solid biomass cookstoves. The initial increase in LPG and decrease in firewood followed by opposing trends are due to enforced minimum capacity additions and decommissioning profiles respectively. Charcoal ultimately predominates over firewood as it is the cheapest and most thermally efficient fuel and stove, aligning with all agents' cost-minimising objectives.

Each agent contributes equally to the gradual re-adoption of traditional cookstoves and retiring of modern cookstoves. Neither rural nor urban men select comfort as an objective. Although comfort is preferred by both rural and urban women, it is inconsequential over their cost objectives thus explaining the persistence of the shift to solid biomass in the population-averaged results seen in Figure 2. The differences in agent characterisation can be seen in contributions of individual agents to the installed capacity, with urban men prioritising only LCOE minimisation resulting in purely charcoal adoption. Contrastingly, the other agents choose a minor share of firewood in addition to charcoal due to firewood being the next cheapest choice to meet demand. Rural agents have a slightly lower share of firewood than urban women due to the difference in modelling financial cost objectives for the rural population.

Consequently, each agent also individually produces the same amount of CO_2 emissions due to zero adoption of clean cooking technologies and each individual having the same cooking demand. In 2050, this corresponds to approximately 50 $kgCO_2$ per person annually, which is used as a benchmark for subsequent scenarios.

4.2 Scenario 2: Carbon price focus (CAR)

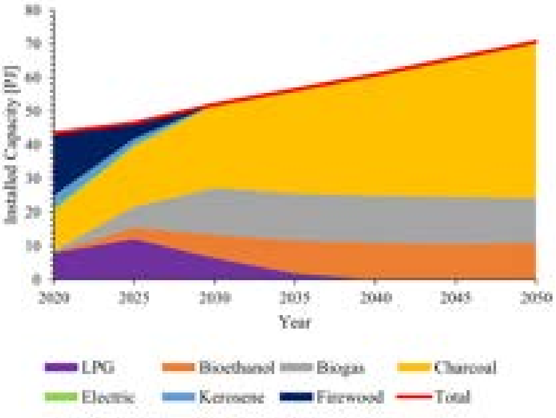

Figure 3: Installed capacity in PJ across the time horizon for the CAR scenario represented as a stacked area graph demonstrating the uptake of technologies

In contrast to BAU, Figure 3 demonstrates a notable increase in adoption of clean fuels, biogas and bioethanol, across the population in this scenario. This is due to the added objective of minimising emission costs for all agents. This is also aided through the introduction of a carbon price which translates into higher costs for higher emissions within the model. Emission costs were prioritised separately from other cost objectives to isolate the effects of environmental awareness in agents. Charcoal stoves persist with the highest share of installed capacity, similarly to BAU, due to existing cost minimisation objectives across all agents still having a higher weightage than emission costs. Electric stoves do not manage to penetrate the sector due to their relatively lower UF as a result of both electricity access and reliability issues in Kenya [28] which are not experienced by other stoves.

However, unlike BAU, all agents adopt a clean fuel supplementarily to charcoal, with rural agents choosing biogas due to it being the cheapest fuel and urban agents choosing bioethanol as it has the lowest LCOE. Rural agents do this because the highest weightage given for lower fuel consumption in addition to the introduction of the emission costs objective, which are both satisfied optimally by the cheapest clean fuel, biogas. There is a slightly lower adoption of biogas amongst rural women compared to men due to their agent characterisation considering emissions costs less than men as a result of lower literacy [26]. Both urban agents yield identical adoption shares due to their overall higher literacy rate having a negligible gender skew.

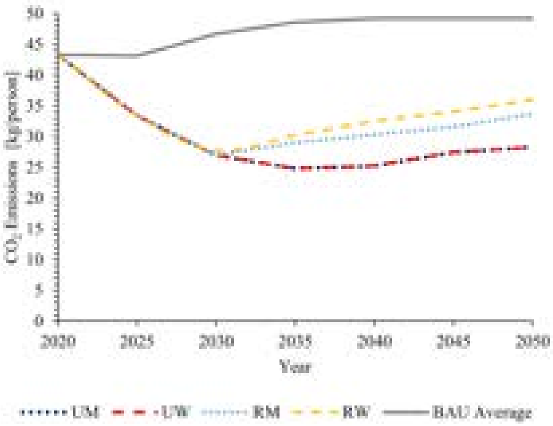

Figure 4: Annual individual CO_2 emissions in kg/person across the time horizon for the CAR scenario represented as a lined graph demonstrating differences among agents

This straightforwardly correlates with the result that both urban agents individually contribute the same CO_2 emissions with rural women producing more emissions than men, as seen in Figure 4. Although decarbonisation is not achieved, every agent in this scenario contributes less emissions than the average BAU agent, illustrating the impact of employing a carbon price and higher environmental awareness.

4.3 Scenario 3: Household air pollution focus (HOU)

Figure 5 shows that electric and LPG installed capacities increase to make up effectively the entire share of technologies adopted by 2030. This is due to comfort being an objective considered by all agents in this scenario, along with cost minimisation objectives. Solid biomass fuels decline quickly despite being cheap due to having the highest $PM_{2.5}$ emissions. Bioethanol and biogas make up an insignificant share mainly due to their higher $PM_{2.5}$ emissions compared to LPG and electric stoves, as well as the low existing capacity. Therefore, the agents' objectives are most effectively satisfied by electric and LPG stoves.

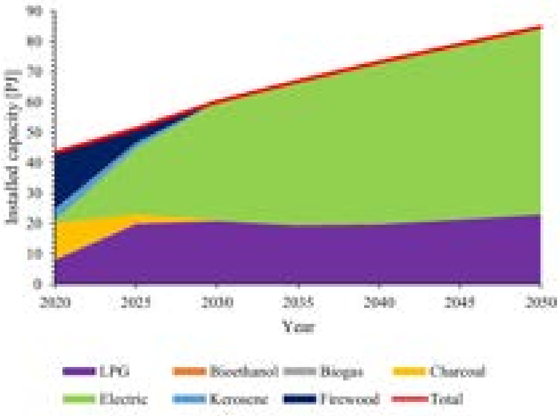

Figure 5: Installed capacity in PJ across the time horizon for the HOU scenario represented as a stacked area graph demonstrating the uptake of technologies

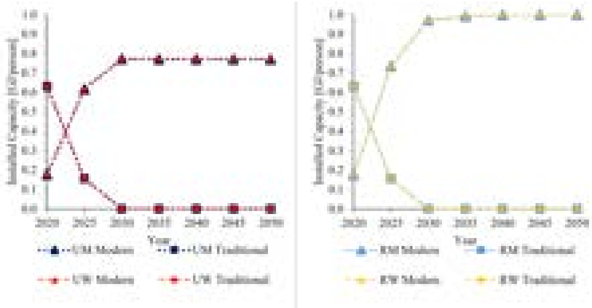

Figure 6: Installed capacity in PJ across the time horizon for the HOU scenario represented as a lined area graph demonstrating the differences in uptake of technologies among agents

As demonstrated in Figure 6, urban and rural agents exclusively choose LPG and electricity respectively, with no difference on a gender basis. Traditional technologies decrease to zero in line with Figure 5 and the opposite trend is seen for modern technologies. An interesting distinction here, is that a markedly greater installed capacity is required to meet demand amongst the rural agents who choose electricity because of a lower UF as a result of grid unreliability [28]. Electricity is selected by rural agents due to their higher prioritisation of comfort to reflect the increased perceived health risk resulting from lower ventilation in indoor rural kitchens.

This aligns with trends in individual agent CO_2 emissions in Figure 7 which are higher for both urban agents, owing to the significant CO_2 emission factor of LPG. Rural agents' preference towards electricity is an unexpected outcome due to grid accessibility challenges. Decarbonisation is achieved for rural agents by 2040 which offers the best potential for net-zero. For this outcome to materialise, the Kenyan government must accelerate rural grid accessibility in conjunction with advanced health education programmes particularly focused on the dangers of HAP.

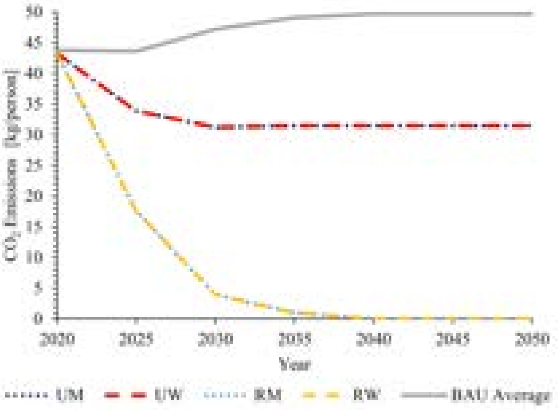

Figure 7: Annual individual CO_2 emissions in kg/person across the time horizon for the HOU scenario represented as a lined graph demonstrating differences among agents

4.4 Scenario 4: Forest conservation focus (FOR)

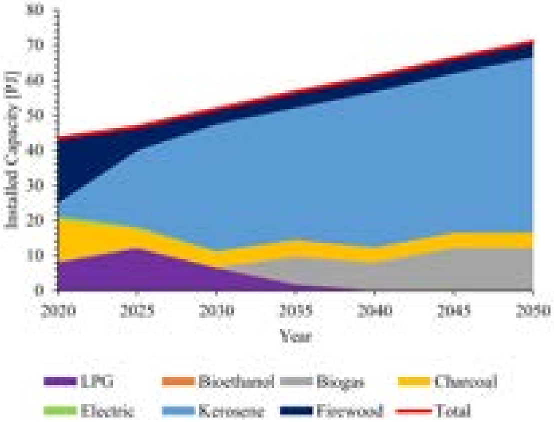

Figure 8: Installed capacity in PJ across the time horizon for the FOR scenario represented as a stacked area graph demonstrating the uptake of technologies

In this scenario, the Kenyan population chooses to adopt kerosene majorly due to strict constraints placed on capacity additions of solid biomass fuels as well as identical agent characterisation as BAU. This is satisfied best by the next cheapest fuel, kerosene. This explains the gradual decline of solid biomass observed in Figure 8 which still presents as a small share equivalent to the maximum allowable capacity additions modelled. Biogas is adopted as the next best choice to fulfil demand due to its low fuel costs, which is the objective given the highest weightage among rural agents.

However, only rural women choose biogas due to their comfort prioritisation, with biogas being both cheap and low in $PM_{2.5}$ emissions. This is a significant observation as it identifies the market demographic most likely to first shift towards cleaner technologies with the phasing out of solid biomass. Rural men still choose mostly kerosene, although less so than the urban agents. Urban agents allow for more solid biomass and therefore slightly less kerosene than their rural counterparts due to differences in their cost minimisation. Similarly to BAU, there is no perceivable gender skew between the urban agents due to the inconsequential preference given to comfort by women.

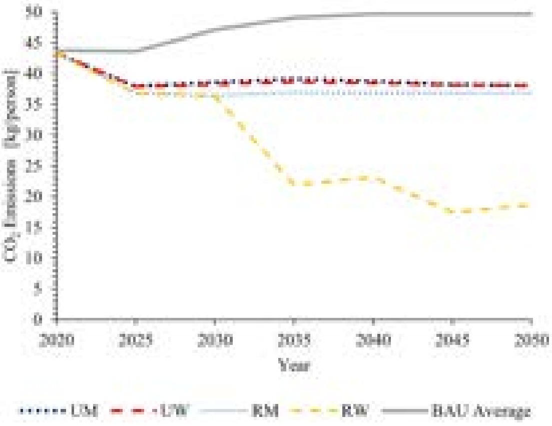

Figure 9: Annual individual CO$_2$ emissions in kg/person across the time horizon for the FOR scenario represented as a lined graph demonstrating differences among agents

In line with these observations, rural women are the only agent with markedly less individual CO$_2$ emissions due to their adoption of biogas. The slight variations seen in Figure 9 among the three other agents arise from their individual relative share of tradition stove adoption. This demonstrates that a targeted education programme to discourage the selection of solid biomass stoves to rural women would aid both forest conservation efforts and push towards decarbonisation but this alone would not be sufficient to drive the other agents to this end.

4.5 Sensitivity analysis

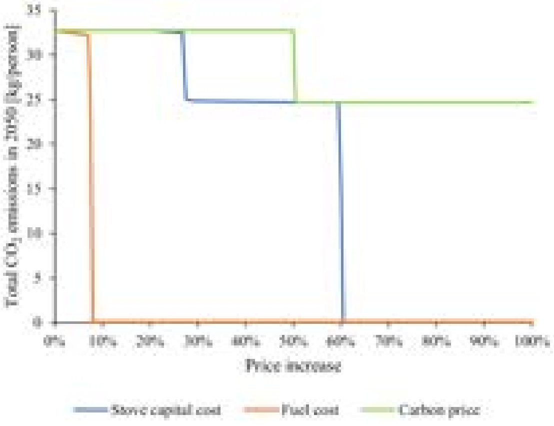

Figure 10: Total CO$_2$ emissions in 2050 by percentage increase in stove capital cost, fuel cost and carbon price

Since CAR was unable to achieve decarbonisation by 2050 with existing stove and fuel costs, there was potential for achieving decarbonisation by applying further financial penalties to discourage the uptake of dirtier technologies. The capital costs of dirtier stoves could be taxed relative to cleaner technologies. Similarly, fuel costs with higher associated carbon emissions could be increased relative to cleaner fuels. A higher carbon price was also conjectured. Percentage increases were applied to the values used in CAR and their effects were quantified through observing changes in annual CO$_2$ emission in order to determine which variable was more effective in emission reduction.

It is observed in Figure 10 that fuel cost is the most sensitive and achieves the goal with the least price increase. However, it was noted that increasing price of solid biomass fuels could prove challenging as households may choose to collect the fuel themselves rather than paying the increased fee. The price change would have to be introduced very gradually or through increased deforestation regulation to prevent households from switching to self-collection. Directly taxing the stoves promises the next best route towards decarbonisation with emissions dropping to 25kgCO$_2$ per person with a 27% price increase and complete decarbonisation achieved upwards of a 60% increase. The model was found to be the least sensitive to changes in carbon price, where decarbonisation could not be achieved within a range of +100%.

5 Conclusions

The results of the BAU scenario show that without further action, consumers will continue to choose dirtier, traditional stoves to meet their demand. Therefore, CO$_2$ emissions will continue increasing. The introduction of a carbon price to tax CO$_2$ emissions will discourage dirty stove uptake but this will not be enough to decarbonise the sector. Targeted HAP awareness and health literacy programmes show great potential to encourage the uptake of cleaner technologies leading to both improved health and reduced CO$_2$ emissions. Forest conservation laws alone are insufficient to encourage Kenyans towards modern stoves but their implementation would still work in favour of decarbonisation. Rural women were identified to be the demographic most likely to first shift towards cleaner technologies with the phasing out of solid biomass stoves.

Electric stoves struggle to penetrate the sector in general due to a lower UF as a result of grid reliability issues. The aforementioned finding [17] that disproves the direct translation between electricity access and shifts towards electricity use and instead serves to widen the range of technology choices possible was reaffirmed. This helps explain the interesting result in HOU that rural agents exclusively choose electric stoves despite facing significant grid-related issues whilst urban agents who do not experience these circumstances as severely choose LPG instead.

Women have also historically been targeted by incentives as the most significant stakeholders in clean cooking. Women have therefore accurately been historically targeted by incentives for clean cooking. However, the tendency of men to have the final say in household purchase decisions introduces complexity in the ease of adoption of clean cooking technologies despite already isolating the target demographic, and is an understated barrier in the ease of adoption. This study has demonstrated the potential of agent-based energy planning models in determining policy decisions, however, its accuracy relies of the quality and granularity of data available.

6 Limitations and Further Research

This study has demonstrated the potential of agent-based energy planning models in determining policy decisions, however, its accuracy relies of the quality and granularity of data available. Weighted averages according to population splits were used to distinguish between rural and urban populations where only population-average values were found. The sample sizes used in certain data sources were also sometimes small or relating to niche demographics [24],[4]. A truer representation of agents' decision-making would also extend beyond MUSE's capabilities of a maximum of three objectives per agent.

Future fuel prices are difficult to predict, especially for a 30-year time horizon. In the interest of taking a conservative view on these projections, historical values were extrapolated using moving averages to represent typical fluctuations in commodity prices instead of applying a set growth or shrinkage percentage on historical prices, which itself would be subject to scrutiny. However, certain fuels were subject to data gaps which lead to either a constant value to be used across the time horizon or fewer values to be included in the moving averages.

Stove prices were modelled to be static in this study, but the introduction of more players in the future stove market, particularly clean fuels, would mean these prices are also subject to change. This limitation was addressed by using data with rural and urban granularity on retail prices transformed into a weighted average for MUSE as well as average prices for multiple stove models where possible.

Although data on $PM_{2.5}$ emissions specific for Kenyan kitchens and typical Kenyan cooking styles/meals were scarce, only the relative values amongst stove technologies [33], [34] were used to describe the comfort objective which would be similar regardless of meal types.

The UF for electric stoves was calculated using the current grid reliability data [28] but this is subject to change as electricity infrastructure improves.

Targeted data collection with more granularity on the contrast between rural and urban men and womens' attitudes is required. Agents could be characterised even better by collecting more specific data relating to the exact agent objectives available on MUSE. The comfort objective was utilised in MUSE as a proxy for $PM_{2.5}$ emissions but $PM_{2.5}$ emissions should be modelled directly within MUSE in the future in the same way as CO_2 emissions. The model could also be used as a trial-and-error to determine exact future policy figures for carbon price, technology interest rate, or fuel tax percentages by observing values which create the desired change in the agent adoption.

Acknowledgements

We would like to thank Dr Alexander Kell and Dr Sara Giarola of the Sustainable Gas Institute for their continued support and guidance in the completion of this study.

7 Supplementary Information

The supplementary information pertaining to this study can be found at the end of this report.

References

[1] Kenya Ministry of Energy. *Kenya National Energy Efficiency and Conservation Strategy*. 2020. URL `https://energy.go.ke/wp-content/uploads/2021/03/2020_06-Kenya-Strategy-EE_LOW-1-1.pdf`.

[2] Anna Nilsson, Tessa Schiefer, Marie-Jeanne Kurdziel, Murefu Barasa, and Daniel Wanjohi. *The Kenyan Cooking Sector: Opportunities for Climate Action and Sustainable Development*. 2021. URL `https://ambitiontoaction.net/wp-content/uploads/2021/07/A2A_Kenya_CleanCookingStudy_July2021.pdf`.

[3] Michael U Treiber, Lars Kåre Grimsby, and Jens Bernt Aune. Reducing energy poverty through increasing choice of fuels and stoves in kenya: Complementing the multiple fuel model. *Energy for Sustainable Development*, 27:151–159, 2015. doi: https://doi.org/10.1016/j.esd.2015.04.004.

[4] State of Global Air. *State of Global Air 2019: Kenya*, 2019. URL `https://www.stateofglobalair.org/sites/default/files/2019-08/soga_fact_sheet_kenya.pdf`.

[5] Tanja Winther, Kirsten Ulsrud, Margaret Matinga, and Govindan. In the light of what we cannot see: Exploring the interconnections between gender and electricity access. *Energy Research & Social Science*, 60:101334, 2020. doi: 10.1016/J.ERSS.2019.101334.

[6] John Musalia. Household decision making among married women in kenya: A latent class analysis. *Sex Roles*, 78:182–193, 2018. doi: 10.1007/s11199-017-0788-1.

[7] Njeri Kagotho and Michael G Vaughn. Women's agency in household economic decision making in kenya. *International Social Work*, 61:767–780, 2018. doi: 10.1177/0020872816663291.

[8] Vikas Menghwani, Hisham Zerriffi, and Puneet Dwivedi. Determinants of Cookstoves and Fuel Choice Among Rural Households in India. *ECOHEALTH*, 16, 2019. doi: 10.1007/s10393-018-1389-3.

[9] S E T Muneer and E W M Mohamed. Adoption of biomass improved cookstoves in a patriarchal society: an example from sudan. *SCIENCE OF THE TOTAL ENVIRONMENT*, 307, 2003. doi: 10.1016/S0048-9697(02)00541-7.

[10] Farai Kapfudzaruwa, John Fay, and Tiago Hart. Improved cookstoves in africa: Explaining adoption patterns. *DEVELOPMENT SOUTHERN AFRICA*, 34, 2017. doi: 10.1080/0376835X.2017.1335592.

[11] Caroline A Ochieng, Yabei Zhang, and John Kennedy Nyabwa. Household perspectives on cookstove and fuel stacking: A qualitative study in urban and rural kenya. *ENERGY FOR SUSTAINABLE DEVELOPMENT*, 59, 2020. doi: 10.1016/j.esd.2020.10.002.

[12] Edwina Fingleton-Smith. Smoke and mirrors-the complexities of cookstove adoption and use in kenya. *ENVIRONMENT DEVELOPMENT AND SUSTAINABILITY*. doi: 10.1007/s10668-021-01595-7.

[13] The World Bank. *Access to electricity (% of population - Kenya*, n.d. URL `https://data.worldbank.org/indicator/EG.ELC.ACCS.ZS?end=2019&locations=KE&start=2009`.

[14] Sustainable Energy for All Africa Hub. *Kenya - SEforALL Africa Hub*, 2021. URL `https://www.se4all-africa.org/seforall-in-africa/country-data/kenya/`.

[15] Kenya Ministry of Energy. *Kenya National Electrification Strategy: Key Highlights 2018*. 2018. URL `https://pubdocs.worldbank.org/en/413001554284496731/Kenya-National-Electrification-Strategy-KNES-Key-Highlights-2018.pdf`.

[16] Mathilde Pedersen, Walter Wehrmeyer, and Ivan Nygaard. Commercial yet social: The practices and logics of bringing mini-grid electricity to rural villages in kenya. *Energy Research Social Science*, 68:101588, 2020. doi: 10.1016/j.erss.2020.101588.

[17] Meron Tesfamichael, Clifford Bastille, and Matthew Leach. Eager to connect, cautious to consume: An integrated view of the drivers and motivations for electricity consumption among rural households in kenya. *Energy Research Social Science*, 63:101394, 2020. doi: 10.1016/j.erss.2019.101394.

[18] Kumar Biswajit Debnath and Monjur Mourshed. Challenges and gaps for energy planning models in the developing-world context. *Nature Energy*, 3:172–184, 2018. doi: 10.1038/s41560-018-0095-2.

[19] Stefan Pfenninger, Adam Hawkes, and James Keirstead. Energy systems modeling for twenty-first century energy challenges. *Renewable and Sustainable Energy Reviews*, 33, 2014. doi: https://doi.org/10.1016/j.rser.2014.02.003.

[20] Iván García Kerdan, Sara Giarola, and Adam Hawkes. A novel energy systems model to explore the role of land use and reforestation in achieving carbon mitigation targets: A brazil case study. *Journal of Cleaner Production*, 232, 2019. doi: https://doi.org/10.1016/j.jclepro.2019.05.345.

[21] Julia Sachs, Yiming Meng, Sara Giarola, and Adam Hawkes. An agent-based model for energy investment decisions in the residential sector. *Energy*, 172, 2019. doi: https://doi.org/10.1016/j.energy.2019.01.161.

[22] Sara Giarola, Anahi Molar-Cruz, Kathleen Vaillancourt, Olivier Bahn, Luis Sarmiento, Adam Hawkes, and Maxwell Brown. The role of energy storage in the uptake of renewable energy: A model comparison approach. *Energy Policy*, 151, 2021. doi: https://doi.org/10.1016/j.enpol.2021.112159.

[23] Evelina Trutnevyte, Léon F Hirt, Nico Bauer, Aleh Cherp, and Hawkes. Societal transformations in models for energy and climate policy: The ambitious next step. *One Earth*, 1:423–433, 2019. doi: https://doi.org/10.1016/j.oneear.2019.12.002.

[24] Jessica Osanya, Rahma I Adam, and Otieno. An analysis of the respective contributions of husband and wife in farming households in kenya to decisions regarding the use of income: A multinomial logit approach. *Women's Studies International Forum*, 83:102419, 2020. doi: https://doi.org/10.1016/j.wsif.2020.102419.

[25] Thaddaeus Egondi, Remare Ettarh, Catherine Kyobutungi, and Ng. Exposure to outdoor particles (pm2.5) and associated child morbidity and mortality in socially deprived neighborhoods of nairobi, kenya. *Atmosphere*, 9, 2018. doi: 10.3390/atmos9090351.

[26] KNBS. *Kenya Development Indicators, 2012*. 2015. URL `https://kenya.opendataforafrica.org/tginbk/kenya-development-indicators-2012`.

[27] CCAK Republic of Kenya Ministry of Energy. *Kenya Household Cooking Sector Study-Assessment of the Supply and Demand of Cooking Solutions at the Household Level*. 2021. URL `https://eedadvisory.com/wp-content/uploads/2020/09/MoE-2019-Kenya-Cooking-Sector-Study-compressed.pdf`.

[28] Payce Madden. *Figure of the week: Progress toward reliable energy access in Africa*, 2019. URL `https://www.brookings.edu/blog/africa-in-focus/2019/12/12/figure-of-the-week-progress-toward-reliable-energy-access-in-africa/`.

[29] Statista. *Kenya - number of households 2017 - 2025*, 2021. URL `https://www.statista.com/statistics/1229987/number-of-households-in-kenya/`.

[30] *The State of the Global Clean and Improved Cooking Sector*, 2015.

[31] Energy Industrial Strategy Department for Business. Government conversion factors for company reporting of greenhouse gas emissions, 2021. URL `https://www.gov.uk/government/collections/government-conversion-factors-for-company-reporting`.

[32] Carla; Pappis Ioannis; Cervantes Barron Allington, Lucy; Cannone. *CCG Starter Data Kit: Kenya*, 2021. URL `https://zenodo.org/record/5013943#.YapNxvHP3BL`.

[33] Jessica Lewis, John Hollingsworth, Ryan Chartier, Ellen Cooper, and Foster. Biogas stoves reduce firewood use, household air pollution, and hospital visits in odisha, india. *Environmental Science Technology*, 51, 2016. doi: 10.1021/acs.est.6b02466.

[34] Amod K Pokhrel, Michael N Bates, Jiwan Acharya, and Valentiner-Branth. Pm2.5 in household kitchens of bhaktapur, nepal, using four different cooking fuels. *Atmospheric Environment*, 113, 2015. doi: https://doi.org/10.1016/j.atmosenv.2015.04.060.

[35] BloombergNEF. *Africa's $40B Market for Cooking Fuel Is Being Cleaned Up: QA*, 2019. URL `https://about.bnef.com/blog/africas-40b-market-cooking-fuel-cleaned-qa/`.

[36] KNBS. *Consumer Price Indices (CPI) and Inflation Rates of Kenya: National Average Prices of Selected Commodities*. 2017. URL `https://kenya.opendataforafrica.org/ltziiob/consumer-price-indices-cpi-and-inflation-rates-of-kenya`.

[37] Statista. Kenya - total population forecast 2020 - 2050, 2021. URL `https://www.statista.com/statistics/1229652/forecast-of-the-total-population-of-africa/`.

[38] Julia Berazneva. *Economic value of crop residues in African smallholder agriculture*. 2013. URL `https://ageconsearch.umn.edu/record/150367/?ln=en`.

[39] Frank Place Julia Berazneva, David R. Lee and George Jakubson. *Allocation and valuation of non-marketed crop residues in smallholder agriculture: the case of maize residues in western Kenya*. 2016. URL `https://pages.vassar.edu/lacdevconf2016/files/2016/08/Allocation-and-Valuation-of-Non-marketed-Crop-Residues-in-Smallholder-Agriculture.pdf`.

[40] Winrock International USAID. *KUSCCO'S Jiko Safi Clean Cookstove Fund*. n.d. URL `https://winrock.org/wp-content/uploads/2017/09/KUSCCOProfile.pdf`.

[41] OECD. *Taxing Energy Use for Sustainable Development-Country Notes: Kenya*. n.d. URL `https://www.oecd.org/tax/tax-policy/taxing-energy-use-kenya.pdf`.

[42] Carbon Pulse. *South African carbon tax could be too low, too limited to cut emissions -report*, 2021. URL `https://carbon-pulse.com/120970/#:~:text=South%20Africa's%20carbon%20tax%20started,use%20of%20offsets%2C%20PwC%20noted`.

[43] Sydney Oluoch, Pankaj Lal, Andres Susaeta, and Neeraj Vedwan. Assessment of public awareness, acceptance and attitudes towards renewable energy in kenya. *Scientific African*, 9, 2020. doi: https://doi.org/10.1016/j.sciaf.2020.e00512.

[44] Kirstie Jagoe, Madeleine Rossanese, and Charron. Sharing the burden: Shifts in family time use, agency and gender dynamics after introduction of new cookstoves in rural Kenya. *Energy Research & Social Science*, 2020. doi: 10.1016/J.ERSS.2019.101413.

[45] Statista. *Kenya - urbanization 2020*, 2021. URL `https://www.statista.com/statistics/455860/urbanization-in-kenya/`.

IMPERIAL COLLEGE LONDON
DEPARTMENT OF CHEMICAL ENGINEERING
ADVANCED CHEMICAL ENGINEERING PRACTICE RESEARCH PROJECT

DEVELOPMENT OF A SINGLE-STEP MECHANISTIC MODEL TO PREDICT PRODUCT DISTRIBUTION OF PYROLYSIS

AUTHORS: AKANSHA GOYAL, SOHAN GWALANI

Abstract

Plastic waste poses a significant threat to the environment. Shifting to a circular polymer economy necessitates the use of chemical recycling techniques such as pyrolysis, which is the thermal breakdown of long chain hydrocarbons into shorter ones. The main objective of this work is the formulation and development of a mechanistic model to predict the product distribution of low-density polyethylene (LDPE) pyrolysis using MATLAB. Due to the complex kinetics of the free radical mechanism, a first-order random scission model governed by an overall kinetic constant is presented as a viable solution. Despite pyrolysis modelling being extensively studied, this simplification allows the model to be applicable to any polymer which undergoes random scission, such as polypropylene and polystyrene. Experimental data of semi-batch and non-ideal batch LDPE pyrolysis was obtained from the Department of Chemical Engineering at Imperial College London. Model fitting to this data was conducted using statistical regression analysis and resulted in best-fit kinetic constants of 0.33 ± 0.03min^{-1} for semi-batch operation between 440-460°C, and 0.60 ± 0.05min^{-1} for non-ideal batch operation at 440°C. The main finding was that the model best represented an ideal batch reactor and could not perfectly simulate pyrolysis experiments conducted in different modes of operation. To be of particular industrial relevance, the model could be refined to establish process parameters which maximise the recovery of high-value product fractions, increasing process profitability.

Keywords: low-density polyethylene, pyrolysis, MATLAB, kinetic constant, first-order, scission, batch, semi-batch

1. Introduction

With the unprecedented rise in plastic demand showing no sign of abatement, polymer waste management remains one of the most challenging environmental issues facing society today. It is estimated that over 130 million metric tons of single-use plastics were disposed in 2019, with 35% of this being incinerated, 31% ending up in landfills and 19% accumulating on land or in the ocean as pollution. (Charles, et al., 2021). With public scrutiny primarily aimed at the accumulation of polymer waste in aquatic bodies, there is also a growing concern regarding the industry's impact on global carbon emissions. Wood Mackenzie predicts polymers could contribute to as much as a third of total energy-related emissions by 2040 (Wood Mackenzie, 2021). Due to the versatility and utility of plastic, it is irreplaceable, however steps must be taken to find a sustainable solution.

The top 100 polymer producers have in the past depended almost exclusively on virgin, fossil-fuel based feedstocks, with production of recycled polymers from plastic waste accounting for less than 2% of output in 2019 (Charles, et al., 2021). There is an urgent need to commit to a 'circular' plastics value chain, incorporating sustainable practices across polymer manufacturing, disposal, waste collection and recycling. As new sustainability legislations are being introduced, several consumer good firms have shifted focus from a linear to a circular polymer economy. Unilever, like many other global corporations, has committed to halving their use of virgin plastic by 2025, through accelerated adoption of recycled plastic (Unilever, 2020).

Therefore, the use of recycled polymer, through both mechanical and chemical means, is expected to rise exponentially. Mechanical recycling has been the industrial norm to date, however recent technological advancements has allowed chemical recycling to complement this process. Chemical recycling has a lower carbon footprint in comparison to current end-of-life practices, such as landfilling and incineration. There are three main chemical recycling routes: dissolution, which involves the use of solvents, depolymerisation, where monomers are formed as a secondary raw material and finally conversion, which includes pyrolysis and gasification processes (European Chemical Industry Council, 2020).

Pyrolysis is the high-temperature thermal degradation of long-chain polymer molecules, creating smaller hydrocarbon molecules which can be used as fuels, in the absence of oxygen (Zhao, D et al., 2020). Pyrolysis technology has huge commercial potential, and many large-scale projects are already in the pipeline. Global chemical company, INEOS, is currently developing several advanced pyrolysis plants in collaboration with technology developer Plastic Energy, with production targeted for 2023 (INEOS, 2020). By simultaneously reducing the required volume of carbon-intensive virgin feedstocks and preventing harmful emissions from post-consumer plastic waste that would have otherwise been incinerated, pyrolysis can play a significant role in the decarbonisation of polymer value chains.

This paper focuses on thermal pyrolysis of low-density polyethylene (LDPE), a non-biodegradable polymer, widely used for plastic bags and several packaging purposes. The primary objective of this study is to develop a mechanistic model which predicts the product distribution of the thermal LDPE pyrolysis process, using MATLAB. Models to computationally simulate pyrolysis are becoming of increased relevance as it provides opportunity for process optimisation (product distribution and reactor configuration) before operating the real-life process. Simulations can be run to generate the expected product chain length distribution, depending on the length of the original polymer, operating temperature, and residence time in the pyrolysis reactor. Appropriate kinetic constants can be determined by fitting the model to data from batch and semi-batch mode experimental runs between 440-460°C. The use of the model should be extendable to several different polymer types and could potentially be refined to predict pyrolysis products of mixed plastic waste material. Additionally, this model could be further developed to be applicable in scenarios where process operating conditions need to be determined to achieve a targeted product distribution. For example, if a certain firm desires their pyrolysis product primarily in the gasoline range, the model can be refined to recommend process parameters which maximise liquid product recovery between C4 and C12 (Marques & Almeida, 2016).

2. Background

2.1 Literature review

The product yield and composition in the pyrolysis process depend predominantly on factors such as type of reactor (batch, semi-batch, fluidised bed, fixed-bed, CSBR), type of polymer (PET, PP, PVC, HDPE, LDPE, PS), process conditions (temperature, pressure, residence time, catalysts), as well as factors that influence the reaction kinetics which depend on the reaction mechanism, reaction phase, and heat and mass transfer resistances (Marongiu, A et al., 2007).

Various pyrolysis studies have been conducted in which one or more of these factors have been investigated to optimise product yield. Sezgi et al. (1998) used a two-phase plastics-pyrolysis process occurring in the polymer melt. Molecular weight distributions were determined from the pyrolysis products, which were then used to compute the rate coefficients for the chain-end scission step in the free radical mechanism for HDPE. However, rate coefficients for random scission and repolymerization could not be determined due to model limitations. The mathematical models were developed purely on experimental data obtained at temperatures 370-410°C (Sezgi, N. A et al., 1998).

By contrast, Zhao et al (2020), estimated the intrinsic kinetic parameters of two first order random scission steps using Thermogravimetric Analysis (TGA) analysis. The experiment was conducted in a fluidised bed reactor for temperatures 500-600°C at 12.4-20.4s with PE4000. A key outcome of the experiments was the observation of the carbon yield product distribution with changes in temperature and residence time. Gaseous products included hydrogen, C1–C4 paraffins, C2–C4 olefins, and 1,3-butadiene. Liquid products included C4–C60 n-paraffins, iso-paraffins, mono-olefins, cycloalkanes/alka-dienes and aromatics. It was observed that as temperature and residence time increased, the yield of gaseous products increased, while the yield of liquid products decreased (as shown in Figure 1) (Zhao, D et al., 2020).

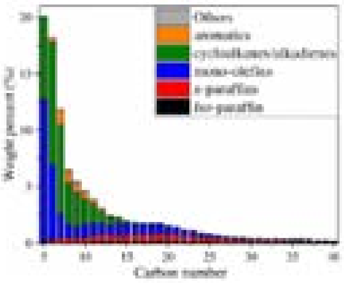

Figure 1: Spectroscopic analysis of liquid product (C5-C40) from PE4000 pyrolysis at 550°C with a residence time of 17.9s in a fluidised bed reactor (Zhao, D et al., 2020)

Ghasr and Abedini predicted the distribution of thermal pyrolysis of high-density polyethylene (HDPE) products using a mechanistic model based on the free radical mechanism. Several kinetic rate expressions and differential expressions were developed for each of the initiation, scission, hydrogen abstraction, aromatic formation, and radical combination steps. These equations were solved on MATLAB software and then compared with experimental results, obtained from a conical spouted bed reactor (CSBR) at temperatures 500–900°C and residence times 0.016–0.032s. However, the kinetic parameters for the model were estimated from existing literature, leading to considerable differences between predicted values and experimental data (Ghasr & Abedini, 2017; Mastral, J. F et al., 2007).

Due to lack of sufficient knowledge of pyrolysis kinetics, many studies have developed isolated kinetic models on lumped reactions, however, the models were unable to establish a confidence interval of 95% to the experimental data (Nejad, S., 2021).

As seen from literature, the complexity involved in the pyrolysis process of plastics makes it difficult to design a full factorial experiment and ascertain the exact kinetics of the various reaction steps that take place. Thus, this prevents successful reactor design and optimisation, which hinders the industrial uptake of plastic pyrolysis. As a result, this paper aims to develop a simplistic model that consolidates the multi-step free radical mechanism into a single-step kinetics model.

2.2 Mechanism of LDPE pyrolysis

Thermal pyrolysis of LDPE proceeds through a free radical mechanism, leading to a wide distribution of hydrocarbon products mainly between the C5-C80 range, depending on the residence time and temperature in the reactor (Marques & Almeida, 2016). The main kinetic stages are outlined below.

2.2.1 Initial scission

Initial scission, also known as chain fission, involves the formation of free radicals from the breakdown of paraffins, olefins and diolefins, as illustrated below:

$$P_n \xrightarrow{K_I} R^{\cdot}_{Pm} + R^{\cdot}_{P(n-m)} \tag{1}$$

$$O_n \xrightarrow{K_I} R^{\cdot}_{Pm} + R^{\cdot}_{O(n-m)} \tag{2}$$

$$D_n \xrightarrow{K_I} R^{\cdot}_{Om} + R^{\cdot}_{O(n-m)} \tag{3}$$

Homolytic cleavage of the C-C bond occurs, in which each of the two radical products receives one of the shared electrons. The chain scission is a random process and each C-C bond in the hydrocarbon chain has an equal probability of breakage (Ghasr & Abedini, 2017).

When a chain is broken, the free radical formation occurs at the two extremities of the new smaller carbon chains. It is important to note that chain fission does not solely occur during the initial stages of pyrolysis, rather throughout the process (Khawaja, et al., 2018).

2.2.2 Hydrogen abstraction

Hydrogen is transferred between radical molecules and hydrocarbons (paraffins, olefins and diolefins), which has a positive stabilising effect on the radicals, as secondary radicals form (Ghasr & Abedini, 2017). An example of hydrogen abstraction between an olefin radical and paraffin, producing a paraffin radical and an olefin, is shown as follows:

$$R^{\cdot}_{Om} + P_n \xrightarrow{K_H} R^{\cdot}_{Pn} + O_m \tag{4}$$

2.2.3 B-scission

The propagation phase of the mechanism is called β-scission, and this is the main reaction of the pyrolysis process. The intermediate radicals formed in hydrogen abstraction allow for C-C bond scission within a paraffin, olefin or diolefin radical chain. A new shorter chain radical and unsaturated hydrocarbon form. Possible β-scission reactions are displayed as follows; however, it is important to note that there are other possibilities:

$$R^{\cdot}_{Pn} \xrightarrow{K_\beta} O_m + R^{\cdot}_{P(n-m)} \tag{5}$$

$$R^{\cdot}_{On} \xrightarrow{K_\beta} D_m + R^{\cdot}_{P(n-m)} \tag{6}$$

$$R^{\cdot}_{Dn} \xrightarrow{K_\beta} D_m + R^{\cdot}_{O(n-m)} \tag{7}$$

2.2.4 Termination

Termination involves the radicals in the reactor recombining into paraffins, olefins and diolefins. Essentially termination reactions are the opposite of what occurs in the initial scission, as indicated below:

$$R^{\cdot}_{Pm} + R^{\cdot}_{P(n-m)} \xrightarrow{K_T} P_n \tag{8}$$

$$R^{\cdot}_{Pm} + R^{\cdot}_{O(n-m)} \xrightarrow{K_T} O_n \tag{9}$$

$$R^{\cdot}_{Pm} + R^{\cdot}_{D(n-m)} \xrightarrow{K_T} D_n \tag{10}$$

$$R^{\cdot}_{Om} + R^{\cdot}_{O(n-m)} \xrightarrow{K_T} D_n \tag{11}$$

2.2.5 Aromatic Formation

Secondary reactions, including the formation of polyaromatics can occur. A considerably higher production rate of aromatic hydrocarbons is expected when a metal-impregnated zeolite catalyst is used, compared to metal-free catalytic pyrolysis or thermal pyrolysis (Akubo, et al., 2019). It is also suggested that aromatization reactions have a strong temperature dependence and only become important at temperatures above 800°C (Mastral, J. F et al., 2007). Since thermal pyrolysis at lower temperatures is being investigated, aromatic formation will not be considered in development of the model.

2.2.6 Product Generation

The main products from LDPE pyrolysis are liquid (hydrocarbon) oil, gas and solids (char). Thermal pyrolysis at temperatures between 300-500°C can lead to high amounts of fuel oil, with the liquid making up around 80% of the products by weight (Setiawan, et al., 2021). The gas fraction includes all paraffins and olefins whose molecule has four carbon atoms or less (Li, 2017). At high temperatures, hydrogen is formed as a by-product.

3. Methods

3.1 Theoretical model development

3.1.1 Multiple stage free radical model

As per literature, an attempt was made to develop a four-step free radical mechanistic model, encompassing initial scission, hydrogen abstraction, beta-scission, and termination. A system of first order differential equations (ODEs) was developed to model each of the four steps in the free radical mechanism, following the methodology that Mastral et al. adopted (Mastral, J. F et al., 2007). Each stage has its unique kinetic parameters determined experimentally which take the form of the Arrhenius equation, signifying a temperature dependence. However, implementation of kinetic parameters from Mastral's high density polyethylene (HDPE) pyrolysis experimental set-up between 500-1000°C was deemed inappropriate to model LDPE pyrolysis between 440-460°C. Due to lack of accurate kinetic models for LDPE pyrolysis for the desired operating conditions, a mathematical construct of the time-dependent system using this complex mechanism was not viable. The efficacy of the free radical mechanism model in scenarios where the exact kinetics of any stage is unavailable will be low, and hence its applicability would be severely limited.

Furthermore, due to the large number of species that would need to be considered across all stages, the solution of multiple complex systems of ODEs would be required. This is because the reaction stages in the free radical mechanism run sequentially, as well as in parallel once termination occurs (looped process). If the model is run for long-chain polymers, significantly long computational times would be expected, making the model intractable.

For this model to be widely applicable in an industrial setting, it should be easy to run and compatible with different polymer types, operating conditions and reactor configurations. Thus, a more simplistic model is desired, where a single kinetic constant can be matched to a unique pyrolysis process.

3.1.2 Model simplification

An attempt was made to model the LDPE pyrolysis process as a single-step process, governed by an overall kinetic constant. Therefore, the pyrolysis process is treated as the continual breakdown of larger hydrocarbon chains into smaller ones.

Certain assumptions had to be taken to allow for this simplification. The model does not differentiate between the different types of products (olefins, paraffins, radicals, etc) and works purely based on number of carbon atoms in the chain. Therefore, each hydrocarbon molecule with n carbons (Cn) represents n CH_2 units, corresponding to a molar mass of 14 n $gmol^{-1}$. Additionally, the model does not automatically differentiate between solid, liquid and gas products. Further calculations are required to determine liquid yields separately. All C1-C4 products are considered to be gaseous and C5 and above are assumed to be liquid product. The solid fraction and any hydrogen formed is neglected, as experimental results deem these to be insignificant in the temperature range of consideration. Resistances to heat and mass transfer in the kinetic model and the effects of pressure are neglected.

3.1.3 Development of first-order random scission model

The simple model built illustrates the LDPE pyrolysis process described by a first-order random-scission mechanism. This assumes that the cleavage of the C-C bonds is random along the polymer chain and has equal probability of breakage at any point to form shorter hydrocarbon chain-lengths. As opposed to chain scission which can occur at selective sites, random scission occurs in polymers which have equi-reactive repeat units. This confirms the suitability of the model applied to LDPE as it is made up of CH_2 repeating units (Benzarti, K. et al, 2013). Moreover, it also conforms to literature findings where it is known that plastics such as polyethylene, polypropylene and polystyrene undergo random scission (Sherratt, n.d.).

Since every C-C bond has equal probability of breakage, it is a reasonable assumption that the rate of random-scission is proportional to the number of bonds that can be broken (analogous to initial scission). The assumption that the decomposition of the starting polymer only generates saturated hydrocarbons can be explained by observation from experimental data, which showed paraffins and olefins dominated the product mixture. The yield ratio of paraffins: olefins obtained was close to 1:1 for each Cn, while no formation of diolefins or aromatics were observed at the specific reaction conditions. This is due to olefins having boiling points very similar to paraffins with the same number of carbon atoms (Chemistry LibreTexts, 2020). As a result, the mathematical model was simplified to consider only repeating units of CH_2.

In the developed model, the generation of each species is described by mass balance equations which form a system of first-order ODEs, entailing probability rate expressions. An example of how the probabilities were assigned and the ODEs were formulated is discussed.

Assuming PE10 (C10) to be the starting polymer, the possible reaction pathways are as follows:

$$C10 \rightarrow C9 + C1 \quad (12)$$
$$C10 \rightarrow C8 + C2 \quad (13)$$
$$C10 \rightarrow C7 + C3 \quad (14)$$
$$C10 \rightarrow C6 + C4 \quad (15)$$
$$C10 \rightarrow C5 + C5 \quad (16)$$
$$C10 \rightarrow C4 + C6 \quad (17)$$
$$C10 \rightarrow C3 + C7 \quad (18)$$
$$C10 \rightarrow C2 + C8 \quad (19)$$
$$C10 \rightarrow C1 + C9 \quad (20)$$

Therefore, the consumption of C10 has 9 reaction pathways, with each species forming with a probability of 2/9. It is important to note that two molecules of C5 are formed (Equation 16). Consequently, taking the stoichiometry into account, the overall probability of C5 forming from C10 is 1/9 + 1/9 = 2/9.

A similar approach was used to compute probabilities for the decomposition of all the intermediate products formed from C10, until all the species eventually breakdown to form C1. An extract from the system of ODEs for PE10 is as follows:

$$\frac{dx(10)}{dt} = -k * x(10) \quad (21)$$

$$\frac{dx(9)}{dt} = \frac{2}{9} * k * x(10) - k * x(9) \quad (22)$$

$$\vdots$$

$$\begin{aligned}\frac{dx(2)}{dt} &= \frac{2}{9} * k * x(10) + \frac{2}{8} * k * x(9) + \frac{2}{7} * k * x(8) + \frac{2}{6} * k * x(7) \\ &+ \frac{2}{5} * k * x(6) + \frac{2}{4} * k * x(5) + \frac{2}{3} * k * x(4) + \frac{2}{2} * k * x(3) \\ &- k * x(2) \quad (23)\end{aligned}$$

$$\begin{aligned}\frac{dx(1)}{dt} &= \frac{2}{9} * k * x(10) + \frac{2}{8} * k * x(9) + \frac{2}{7} * k * x(8) \\ &+ \frac{2}{6} * k * x(7) + \frac{2}{5} * k * x(6) + \frac{2}{4} * k * x(5) + \frac{2}{3} * k * x(4) \\ &+ \frac{2}{2} * k * x(3) + \frac{2}{1} * k * x(2) \quad (24)\end{aligned}$$

A set of generalised mass balance equations (ODEs) was formulated, which can be solved for any n number of carbons in the starting polymer:

$$\frac{dx(n)}{dt} = -k * x(n) \quad (25)$$

$$\frac{dx(j)}{dt} = \sum_{i=j}^{n-1} \frac{2}{i} * k * x(i+1) - k * x(j)$$

$$for\ j = 2\ to\ n - 1 \quad (26)$$

$$\frac{dx(j)}{dt} = \sum_{i=j}^{n-1} \frac{2}{i} * k * x(i+1)\ for\ j = 1 \quad (27)$$

Here, i and j are increasing integers. x represents the number of moles of each carbon species, n represents the number of carbons in the starting polymer, j represents the chain-length of a hydrocarbon species, i is the variable which forms the probability series for each ODE, and k represents the first order kinetic constant. The terms in the

ODEs which are summed represent production of certain species and the terms that are subtracted represents the consumption of a species through further decomposition.

As illustrated above, each hydrocarbon species (Cn) in the model has a corresponding ODE assigned to it, which is solved by MATLAB by computing a numerical integration over time, using MATLAB solver ode23s.

Operation of the MATLAB model necessitates the selection of three process parameters which are input variables: (1) the chain-length of the starting polymer that needs to be pyrolysed, (2) an estimation of the overall first order kinetic constant (min^{-1}) which does not change during the process assuming isothermal pyrolysis, and (3) the chosen reaction residence time. These parameters can be altered between successive model runs.

3.2 Fitting to experimental data

Experimental data was obtained from a third-party research group in the Department of Chemical Engineering at Imperial College London. The 65mL reactor used in the experimental set-up can be operated in both batch and semi-batch modes and was constructed in-house. The reactor was heated by a vertical tube furnace which operates at a temperature up to 490°C at 30bar. Gas chromatography-mass spectrometry (GC-MS) equipment from Shimadzu (GCMS-QP2020 NX) was utilised for liquid analysis.

All semi-batch mode data used was from LDPE pyrolysis experiments which were conducted at 5 bar with a constant N_2 flow of 0.16 $Lmin^{-1}$, between 440-460°C. In the semi-batch process, once the reaction was allowed to proceed, the gaseous products generated were continuously removed by N_2 and condensed at room temperature. At the end of the reaction only char remained in the vessel and the liquid product was collected in the condenser. The total run-time of all semi-batch runs was 60 minutes, however, as a rule of thumb approximation the reaction was taken to be complete at 30 minutes.

Data from a single batch mode run was also available. LDPE pyrolysis was conducted at a temperature of 440°C for one hour, with a peak pressure (gauge) of 29psi. In the batch process, all the starting LDPE PE2000 reactant was fed at the beginning of the process, and the products were only recovered when the reaction was complete at 60 minutes, and then analysed. However, the batch reactor was also connected to the condenser, taking away the volatile products from the vapour-liquid equilibrium achieved in the reactor, and condensing them in the condenser (this indicates non-ideal batch operation). At the end of the run, liquids from both the reactor and condenser were collected and analysed.

Statistical regression analysis was utilised to fit the results from the MATLAB model to both semi-batch and batch experimental data. The model was run multiple times varying kinetic constants, however keeping the starting polymer length and residence time constant to match the experimental conditions. The sum of squared residuals (SSR) method was used to measure the discrepancy between the data and the mechanistic model for different kinetic constants, using the following equation:

$$SSR = \sum_{i=1}^{n} (y_i - x_i)^2 \qquad (28)$$

Here y_i represents the model prediction, x_i represents the experimental results and i refers to the carbon number of the product, which is summed to the longest chain hydrocarbon product that can be determined experimentally, Cn. The range of k-values that resulted in the smallest SSR, indicating smallest deviation from data, was identified for each experimental run. The experimental data was provided in weight % of liquid product. Therefore, the product yield computed by the model had to be converted to in terms of purely the liquid product (weight % in liquid), by disregarding C1-C4 yields, which are treated as gaseous products. An assessment of which of the two modes of operation was more accurately represented by the mechanistic model could be made.

4. Results and Discussion

4.1 MATLAB original model for C2000

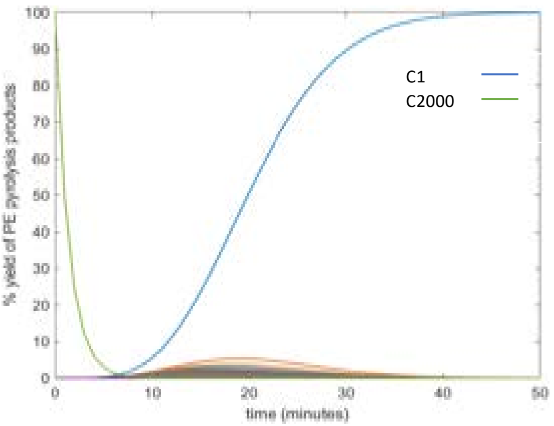

Figure 2: Model for pyrolysis of PE2000 displaying % yield as a function of time. The input parameters of this run were: (1) starting polymer of PE2000, (2) kinetic constant, k = 0.7min^{-1} and (3) residence time of 50 minutes.

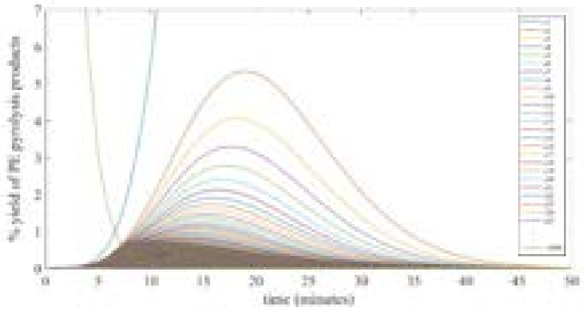

Figure 3: Model (zoomed) for pyrolysis of PE2000, displaying % yield as a function of time. The input parameters of this run were: (1) starting polymer of PE2000, (2) kinetic constant, k = 0.7min^{-1} and (3) residence time of 50 minutes.

The MATLAB model operates based on the carbon number of the starting LDPE. The number average molecular weight (Mn) of the LDPE sample used by the research group was 34797 $gmol^{-1}$ with a corresponding carbon number of 2485. The Mn corresponds to the statistical average molecular weight of all polymer chains in the sample (Agilent Technologies, 2015). Therefore, a starting LDPE chain of 2485 carbons was initially envisioned as an input to the MATLAB model. It should be noted that computational times for pyrolysis simulation above 2000 carbons were considerably longer and therefore PE2000 was determined as a suitable choice for fitting the available experimental data.

Figure 2 displays the % yield of all hydrocarbons in the simulated pyrolysis reactor as a function of time. The rapid decomposition of C2000 can be observed, with complete consumption predicted within 15 minutes. The model predicts the rate of C2000 consumption to be much faster than C1 production, which itself depends on the decomposition of intermediate hydrocarbon products; this is in line with what occurs experimentally. There is a gradual production of C1, reaching a yield of 100% at 50 minutes, as all other intermediate hydrocarbons have been completely broken down.

Figure 3 displays the behaviour of the intermediate hydrocarbon products (C2 – C1999), which follow a symmetrical bell curve distribution. Each hydrocarbon product has a maximum yield at a certain time, with longer chain products peaking earlier in the process. Additionally, the shorter the carbon chain of the product, the larger the maximum possible % yield, as there is a greater number of reaction pathways (hence a higher probability) that can lead to its formation.

After determining the appropriate kinetic constant, this plot can be used to decide on optimum operating times if the recovery of a certain product needs to be prioritised. For example, if C8 production needs to be maximised, the model recommends for C2000 to pyrolyse for approximately 17 minutes, as can be determined from Figure 3.

4.2 Experimental semi-batch and batch results

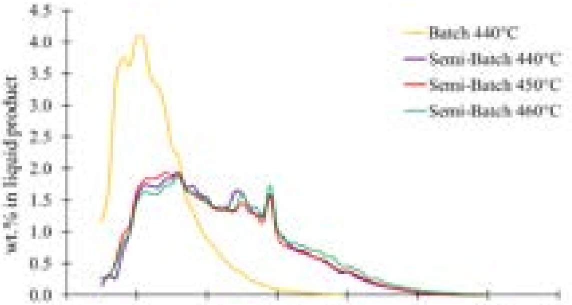

Figure 4: Experimental data for aliphatic compounds (paraffins and olefins) displaying % yield in liquid phase for C5-C60 for batch and semi-batch operation

Figure 4 showcases the liquid product yield distribution of LDPE PE2000 pyrolysis from the batch and semi-batch process. Experimental measurement error was not applicable for this analysis.

The analysis of the liquid product wt.%, produced irregular shaped distribution curves. C1-C4 have boiling points lower than room temperature, and so remain in the gaseous phase during the condensation process (Chemistry Reference, 2021). As a result, C1-C4 do not appear on these experimental graphs. Additionally, aliphatic compounds with boiling points above 300°C may not be detected. The aliphatic concentrations (paraffin and olefin) were determined by GC-MS. Hydrocarbon products with higher boiling points than the maximum injector temperature (~300°C), may result in them not being injected into the GC-MS column (Chemistry Reference, 2021). Hence the longer carbon chain molecules, C60 and above, were not detected.

In general theory at a constant reactor temperature, as the residence time increases, the gas product yield also increases, while the liquid product yield decreases (Zhao, D et al., 2020). This is due to the continuous decomposition of heavier compounds into lighter compounds, shifting the carbon-number distribution towards lower molecular weights. This behaviour is confirmed by the downward sloping trends observed between C10-C60. Moreover, higher temperatures should lead to an increased rate of chain-fission, resulting in a steeper decrease in the liquid product yields due to faster kinetics (Zhao, D et al., 2020). From Figure 4, despite increasing temperatures from 440°C to 460°C (semi-batch process) this behaviour is not observed, and instead shows the same product yield distribution with mild deviations. This may be because a narrow temperature range was investigated.

In Figure 4 an unusual upward trend is observed from C5-C10, compared to Figure 1 which indicates a monotonically decreasing trend is expected in this region. An interpretation for this is that the vapour phase products are continuously removed from the reactor by N_2 and condensed during the experiment in the semi-batch process. Aliphatic compounds smaller than C26 having boiling point temperatures <420°C (Chemistry Reference, 2021). These are highly volatile at the reactor operating temperatures (440-460°C) used in the experiment, and so would vapourise. Moreover, the constant removal of the vapour products would reduce the vapour pressure of all the compounds in the reactor, forcing vapourisation of the heavier species. Once the vapour products are condensed in the condenser at room temperature, further decomposition cannot take place to smaller compounds including C5-C10, resulting in their lower yield.

The experimental results from the batch process also give an irregular shaped distribution yield curve, which was run for 60 minutes at 440°C. This could be explicated from the non-ideal operation of the batch reactor. The small amounts of volatile products (from the vapour-liquid equilibrium achieved) that diffused from the hot region of the reactor and condensed during the experiment do not undergo further decomposition to form smaller compounds. This may have resulted in the lower liquid yields for C5-C10 than was theoretically expected and hence, the upward increase in the curve as shown in Figure 4. Another conjecture could be loss due to the vapourisation of C5-C10 after removal from the condenser for GC-MS analysis, since they are volatile compounds (boiling points are close to room temperature) (Chemistry Reference, 2021).

Therefore, for both batch and semi-batch processes the model fitting was only performed for C10 and above, as experimental data follows the expected decreasing trend in liquid product yield with increasing carbon-number, as decomposition of heavier compounds occur to form smaller compounds.

Another graphical observation from Figure 4, is that the liquid product yield obtained for C10 is almost doubled in the batch process compared to the semi-batch process for the same temperature (440°C). The batch process yield curve is much steeper than the semi-batch process curve, with a greater shift in yield towards the lower molecular weight compounds. This is because in the batch process the products are not continuously removed from the reactor compared to the semi-batch process during pyrolysis. The larger compounds have greater opportunity to cleave and form smaller compounds in the batch process.

4.3 Model fitting for 440°C semi-batch process

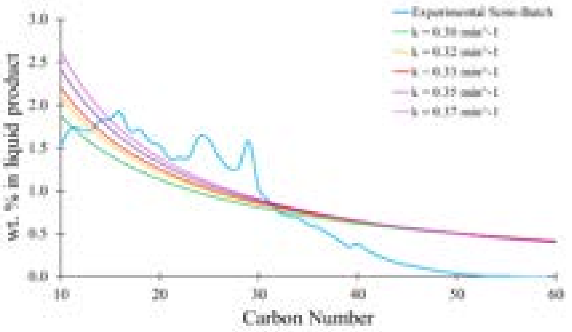

Figure 5: Model fitting for 440°C semi-batch reactor at 30 minutes for different values of the single 1st order kinetic constant between 0.30 – 0.37 min^{-1}

Table 1: SSR analysis for semi-batch run at 30 minutes at 440°C

	Liquid yield, wt. %	**Gas yield, wt. %**	**Solid yield, wt. %**	**SSR**
Experimental Semi-batch at 440°C	80.7	17.7	1.6	-
k = 0.30min^{-1}	77.0	23.0	0.0	7.61
k = 0.32min^{-1}	72.4	27.6	0.0	6.97
k = 0.33min^{-1}	70.0	30.0	0.0	6.85
k = 0.35min^{-1}	65.2	34.8	0.0	6.94
k = 0.37min^{-1}	60.1	39.9	0.0	8.75

Model fitting for the semi-batch experimental run at 440°C was conducted and is displayed in Figure 5. The MATLAB model was used to simulate this pyrolysis process for 30 minutes, accounting for the run-time approximation, with different kinetic constants ranging between 0.30-0.37min^{-1}.

The kinetic constant that best fits the semi-batch 440°C run is k=0.33min^{-1}, as it results in the minimum SSR of 6.85, indicating closest fit to the experimental data from the kinetic constants that were simulated. Table 1 indicates the SSR is increasing for constants both smaller and greater than 0. 33min^{-1}, thus the most suitable kinetic constant for this data must lie between 0.32 and 0.35min^{-1}. Allowing for a margin of error, the optimum kinetic constant for this run is taken to be 0.33 ± 0.03min^{-1}.

Higher kinetic constants increase the rate of the pyrolysis process, hence more gas product will be formed (as indicated on Table 1), as short-chain hydrocarbons are present at higher yields. The recovery of gas in the experimental run (17.7%) is less than what the model predicts at k=0.33min^{-1} (30.0%). A possible explanation for this is that since gas products are continuously removed from the semi-batch reactor and subsequently condensed, further decomposition to smaller hydrocarbons (C1-C4) is limited. Therefore, k=0.33 ± 0.03min^{-1} is deemed appropriate.

The experimental yields are greater than what is predicted by the model between C15-C30. In the semi-batch system, continuous removal of vapour products throughout the pyrolysis process means that products do not undergo decomposition for equal lengths of time. This may result in the irregular yield distribution in this region, which is not observed in the model distribution.

The model seems to overpredict the liquid yield after C32, in comparison to the experimental results. This, however, can be rationalised through the fact that aliphatic compounds larger than C30 have boiling points above 300°C (Chemistry Reference, 2021) and hence may only be partially detected by GC-MS. This leads to lower-than-expected experimental yields after C32, with the model behaving more consistent with what is expected in this region.

The experimental results for runs at 450°C and 460°C showed little deviation to the run at 440°C (Figure 4), and model-fitting resulted in identical optimum rate constants. Therefore, k=0.33 ± 0.03min^{-1} is applicable as the best kinetic constant to describe semi-batch operation in the 440-460°C range.

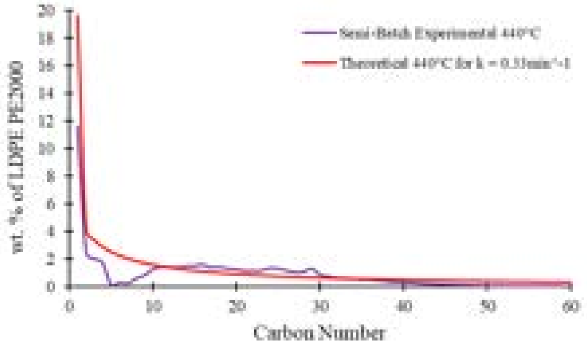

Figure 6: Experimental and theoretical yield distribution for combined liquid and gas phase at 440°C using best-fit k = 0.33min^{-1}

For the best fit k=0.33min^{-1}, the model prediction of the product yield as a % of the starting LDPE PE2000 was tested against the experimental data for C1-C60, combining gas and liquid yields (as shown in Figure 6). The 440°C run was used, and the lumped gas yield of 17.7% provided was used to predict the C1-C4 % yield in the overall system.

From Figure 6, the overall model trend is deemed to have a reasonable match to the experimental trend. The lower experimental yield for C1-C10 compared to the model prediction reasoning can be reiterated from the active removal and condensation of the vapour products, which also contain heavier species. As a result, the continuous decomposition to C1-C10 compounds with time is hindered, as also previously explained.

4.4 Model fitting for 440°C batch experimental data

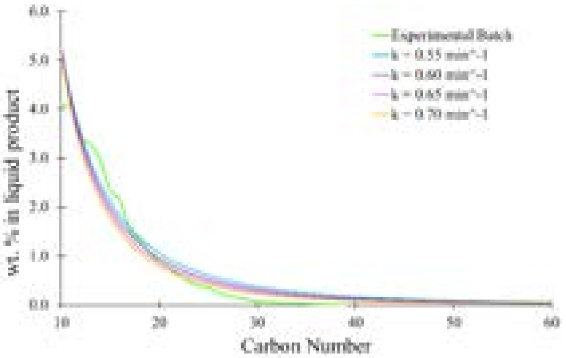

Figure 7: Model fitting for 440°C batch reactor at 60 minutes for different values of the single 1st order kinetic constant between 0.55 – 0.70min^{-1}

Table 2: SSR analysis for batch process at 60minutes at 440°C

	Liquid yield, wt. %	Gas yield, wt. %	Solid yield wt. %	SSR
Experimental Batch at 440°C	81.8	16.6	1.6	-
k = 0.55min^{-1}	0.06	99.94	0.0	3.18
k = 0.60min^{-1}	0.02	99.98	0.0	2.94
k = 0.65min^{-1}	0.004	99.996	0.0	3.08
k = 0.70min^{-1}	0.001	99.999	0.0	3.53

Model fitting using SSR minimisation was conducted for batch operation at 440°C, for 60 minutes, and is displayed in Figure 7. The optimum kinetic constant for this run is found to be 0.60 ± 0.05min^{-1}. The minimum SSR of 2.94 indicates a much tighter fit compared to semi-batch operation. The best-fit kinetic constant is approximately twice that from semi-batch operation, despite LDPE pyrolysis occurring at the same temperature. The model has not been developed to consider any removal of products during operation, and hence behaves as an idealised batch process. Therefore, the model is expected to be more suited to this experimental batch process, despite its non-ideal nature.

However, there is significant deviation between the liquid/gas yield weight % obtained from the model and what was determined experimentally. The gas yield (wt.%) from the model is expected to have risen, as the input residence time of pyrolysis is doubled compared to the semi-batch scenario (the 60 minutes semi-batch process was modelled for 30 minutes), leading to increased decomposition to short chain products. Simulations predict the products to be almost completely in the gaseous phase at these conditions (Table 2). However, the experimental lumped gas and liquid weights do not agree with the model and are notably similar in magnitude to the experimental semi-batch run at 440°C. A possible source of this discrepancy could be from the manual splitting of the liquid and gas yields, that the model necessitates. It is advisable that the model is fitted to more experimental batch data to validate the experimental lumped yields.

4.5 Model behaviour at different residence times

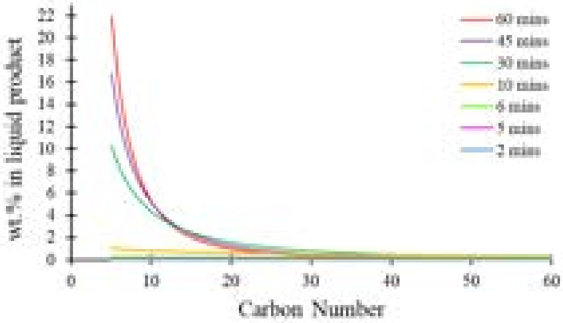

Figure 8: Model run for k=0.6min^{-1} for different residence times between 2 – 60 minutes

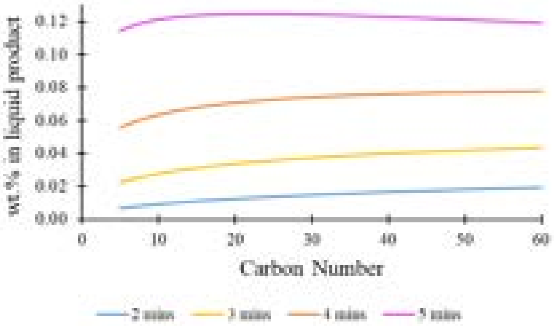

Figure 9: Model run for k=0.6min^{-1} at smaller residence times between 2 – 5 minutes

The carbon-number distributions for pure random scission can follow one of two options. For high conversions, a monotonically decreasing distribution with increasing carbon number is expected, whereas for low conversions the distribution displays a single maximum (Zhao, D et al., 2020). The model was run for different residence times, at k=0.6min^{-1} (optimum kinetic constant for batch-mode operation at 440°C) to investigate this behaviour. Product distributions obtained are shown in Figures 8 and 9, confirm the findings by Zhao et al.

At short times (0-5 minutes), one can identify a carbon distribution that peaks at a particular carbon number. The weight % of C1-C60 hydrocarbons is small (<0.15%) in the first five minutes. This is because there has been insufficient time for pyrolysis reactions to progress to an extent where the shortest hydrocarbon chain is the dominant product. After 6 minutes, C1 has the greatest yield, hence the decreasing distribution curves are justified.

Once a kinetic constant has been identified for a certain run of a pyrolysis process, the model can generate product distributions for a range of operating times, without the need for more experimental runs.

4.6 Model limitations

Despite the model-fitting for LDPE batch and semi-batch experimental data both being conducted at 440°C, different best-fit rate constants were found. The intrinsic kinetics of the polyethylene pyrolysis process should not depend on the type of reactor. Therefore, this signifies that the model is not perfectly suited to simulate different modes of operation currently.

Product yield distributions obtained simulate C1 to be the shortest hydrocarbon chain formed, due to the assumptions made. However, literature highlights that C2 would be shortest paraffin (ethane) and olefin (ethene) products derived from polyethylene pyrolysis, as methyl radicals recombine (Ghasr & Abedini, 2017). Additionally, it was found that the independent liquid phase and gas phase kinetic constants for hydrocarbon pyrolysis are similar. However, the model does not correct the kinetic constant to account for diffusion limitations from the liquid phase into the gas phase. Since the breakage of C-C bonds in the random scission process requires high activation energy, diffusion limitations become more significant. This further contributes to the model's inability to accurately project the actual gas and liquid yields (most impacted in the C1-C10 region) (Marongiu, A et al., 2007).

There is no applicability of the model to polymers that decompose through end chain scission (e.g., PMMA), chain stripping (e.g., PVC) and cross linking (polyacrylonitrile), as the inherent model assumption is based on random scission.

5. Conclusions and Outlook

Development of a first-order random scission MATLAB model, based on LDPE pyrolysis, was successful. The proposed model is a simple approach which does not take into consideration all the steps in the pyrolysis free-radical mechanism. However, it is presented as a useful tool to predict product distributions from knowledge of polymer chain length, residence time and a single kinetic constant. The model was found to simulate an ideal batch reactor after a fitting was conducted for semi-batch (440-460°C) and non-ideal batch (440°C) experimental data. The best-fit kinetic constants for the two modes are k=0.33 ± 0.03min^{-1} and k=0.60 ± 0.05min^{-1} respectively. The non-ideal batch run at 440°C displayed a stronger fit than semi-batch operation at the same temperature. Future possible refinements could include the introduction of 'mode of operation' as a fourth variable, where the model can automatically adjust the product yield distribution to correctly simulate a specific type of reactor behaviour, which is currently cannot.

The developed kinetic model is not restricted to the use of LDPE and may be appropriately applied to simulate any polymer which is shown to undergo random scission, such as HDPE, polypropylene, and polystyrene. Literature suggests a scission kinetic model for the prediction of pyrolysis curves of polystyrene from its chain structure has previously been proposed (Perez-Maqueda, et al., 2014). Experimental fitting of these other polymers to the MATLAB model is recommended to establish strength of correlation.

Future work on the presented model could include testing its performance in the C5-C10 region, which is not considered in this study, due to the limitations of analytical equipment. Model fitting to a wider range of temperatures is recommended to obtain a relationship between temperature and best-fit kinetic constants. This correlation can be linked to an Arrhenius relationship, where activation energies and pre-exponential factors for pyrolysis of specific polymers can be determined.

The model has significant industrial relevance. Reversing the model to recommend operating parameters as output variables, as opposed to being input variables, may be beneficial. If the model can be enhanced to differentiate between paraffin and olefin yields, parameters to maximise yield of C5-C20 olefins based on the starting polymer, can be computed. These are the highest-value pyrolysis product fractions and are worth up to \$1700t^{-1} (Greiner, et al., 2013).

6. Acknowledgement

The authors would like to specially thank Xiangyi Long for her continuous guidance and support throughout this project.

7. Nomenclature

Abbreviations	
CSBR	Conical Spouted Bed Reactor
GC-MS	Gas Chromatography–Mass Spectrometry
HDPE	High Density Polyethylene
LDPE	Low Density Polyethylene
ODE	Ordinary Differential Equation
PEn	Polyethylene with n carbons atoms
PET	Polyethylene Terephthalate
PMMA	Polymethyl Methacrylate
PP	Polypropylene
PS	Polystyrene
PVC	Polyvinyl Chloride
SSR	Sum of Squared Residuals
TGA	Thermogravimetric Analysis
Terminology	
Cn	Hydrocarbon chain with n CH_2 units
D_n	Diolefin with n carbon atoms
K_β	kinetic constant of β-scission reaction (min^{-1})
K_H	kinetic constant of H-abstraction reaction (m^3/mol min)
K_I	kinetic constant of initial scission reaction (min^{-1})
K_T	kinetic constant of termination reaction (m^3/mol min)
O_n	Olefin with n carbon atoms
P_n	Paraffin with n carbon atoms
$R^{\cdot}_{Dn}$	Diolefin radical with n carbon atoms
$R^{\cdot}_{On}$	Olefin radical with n carbon atoms
$R^{\cdot}_{Pn}$	Paraffin radical with n carbon atoms
k	Single overall first-order kinetic constant (min^{-1})

References

Agilent Technologies, 2015. *Polymer Molecular Weight Distribution and Definitions of MW Averages,* s.l.: s.n.

Akubo, K., Nahil, M. A. & Williams, P. T., 2019. Aromatic fuel oils produced from the pyrolysis-catalysis of polyethylene plastic with metal-impregnated zeolite catalysts. *Journal of the Energy Institute,* 92(1), pp. 195-202.

Benzarti, K. et al, 2013. 12 - Understanding the durability of advanced fibre-reinforced polymer (FRP) composites for structural applications. *Woodhead Publishing Series in Civil and Structural Engineering,* pp. 361-439.

Charles, D., Kimman, L. & Saran, N., 2021. *The Plastic Waste Makers Index,* s.l.: Minderoo Foundation.

Chemistry LibreTexts, 2020. *Physical Properties of Alkenes.* [Online]
Available at: https://chem.libretexts.org/Bookshelves/Organic_Chemistry/Supplemental_Modules_(Organic_Chemistry)/Alkenes/Properties_of_Alkenes/Physical_Properties_of_Alkenes
[Accessed 13 December 2021].

Chemistry Reference, 2021. *ALKANES - PROPERTIES AND TRENDS.* [Online]
Available at: http://chemistry-reference.com/alkanes/
[Accessed 13 December 2021].

Eidesen, N et al., 2018. Simulation of the HDPE Pyrolysis Process. The International Journal of Multiphysics. *The International Journal of Multiphysics,* pp. 79-88.

European Chemical Industry Council, 2020. *Chemical Recycling: Making Plastics Circular.* [Online]
Available at: https://cefic.org/a-solution-provider-for-sustainability/chemical-recycling-making-plastics-circular/
[Accessed 10 December 2021].

Ghasr, S. F. & Abedini, H., 2017. Predicting the distribution of thermal pyrolysis of high density polyethylene products using a mechanistic model. *Modeling Earth Systems and Environment.*

Greiner, E., Blagoev, M. & Yamaguchi, Y., 2013. Linear alpha-Olefins.

INEOS, 2020. *INEOS and PLASTIC ENERGY to collaborate on new advanced plastic recycling facility.* [Online]
Available at: https://www.ineos.com/news/shared-news/ineos-and-plastic-energy-to-collaborate-on-new-advanced-plastic-recycling-facility/
[Accessed 10 December 2021].

Jude, A et al., 2009. Composition of products from the pyrolysis of polyethylene and polystyrene in a closed batch reactor: Effects of temperature and residence time. *Journal of Analytical and Applied Pyrolysis,* 86(2), pp. 293-303.

Khawaja, H., Eidesen, H. & Jackson, S., 2018. Simulation of the HDPE Pyrolysis Process. *The International Journal of Multiphysics,* Volume 12.

Li, H., 2017. *Applications of Lumping Kinetics Methodology to Plastic Waste Recovery via Pyrolysis,* s.l.: Institute of Mechanical, Process, and Energy Engineering - Heriot-Watt University.

Marongiu, A. et al., 2007. Detailed kinetic modeling of the thermal degradation of vinyl polymers. *Journal of Analytical and Applied Pyrolysis,* 78(2), pp. 343-362.

Marques, M. d. F. & Almeida, D., 2016. Thermal and catalytic pyrolysis of plastic waste. *Polimeros,* 26(1).

Mastral, J. F et al., 2007. Theoretical prediction of product distribution of the pyrolysis of high density polyethylene. *Journal of Analytical and Applied Pyrolysis,* 80(2), pp. 427-438.

Nejad, S., 2021. *An Examination of Pyrolysis Kinetics of Waste Plastics,* London, United Kingdom: Department of Chemical Engineering, Imperial College London.

Perez-Maqueda, L. A. et al., 2014. Scission kinetic model for the prediction of polymer pyrolysis curves from chain structure. *Short communication: property modelling.*

Setiawan, A., Setiani, V. & Mazdhatina, O. S., 2021. Characterization of fuel oil from pyrolysis waste light density polyethylene (LDPE) and polypropylene (PP). *IOP Conference Series: Materials Science and Engineering.*

Sezgi, N. A et al., 1998. Polyethylene pyrolysis: Theory and experiments for molecular-weight-distribution kinetics. *Ind Eng Chem Res,* 37(7), pp. 2582-2591.

Sherratt, J., n.d. *The effect of thermoplastic melt flow behaviour on the dynamics of fire growth,* Scotland: University of Edinburgh .

Unilever, 2020. *Unilever makes progress on its sustainable packaging goals.* [Online]
Available at: https://www.unilever.com/news/press-and-media/press-releases/2020/unilever-makes-progress-on-its-sustainable-packaging-goals/
[Accessed 10 December 2021].

Wood Mackenzie, 2021. *The plastics industry must go under the knife for a more sustainable future.* [Online]
Available at: https://www.woodmac.com/press-releases/the-plastics-industry-must-go-under-the-knife-for-a-more-sustainable-future/
[Accessed 10 December 2021].

Zhao, D et al., 2020. The Chemistry and Kinetics of Polyethylene Pyrolysis: A Process to Produce Fuels and Chemicals. *Published in ChemSusChem,* 13(7), pp. 1764 - 1774.

Imperial College London

Department of Chemical Engineering

Development of a Machine Learning Framework in Predicting Protein Glycosylation Profiles

Authors:
Monika Kaminska, Stefan Michev

Supervisor:
Professor Cleo Kontoravdi

Abstract

Monoclonal antibodies (mAbs) constitute a major part of the biopharmaceuticals market, due to their potential in the diagnosis and treatment of various diseases, including cancer. As protein products, mAbs undergo N-linked glycosylation, one of the most common post-translational modifications that can influence safety and efficacy of the final product. In this work, two data-driven frameworks for predicting glycan distribution in mAbs were introduced and evaluated: an Artificial Neural Network created and optimised in Python 3.8 using Keras and TensorFlow, and a Partial Least Squares Regression framework designed in Unscrambler X. The analysis was performed using 17 datasets, each containing 13 NSD and nucleotide concentrations as the inputs, and 7 glycan distributions as the outputs. The datasets originated from experiments with varying conditions, such as cell lines, temperatures and feeding strategies. In most cases, the ANN models were found to perform better than the PLS counterparts. However, the accuracy in both approaches was limited by insufficient volume of data available for some experimental conditions. Here, the benefits and limitations of data-driven models were discussed, and a detailed description of the models and experimental systems was provided.

Keywords: Machine Learning, Artificial Neural Network, Partial Least Squares Regression, N-linked Glycosylation, Monoclonal Antibodies.

1 Introduction

A biopharmaceutical is defined as a medical drug produced, extracted or semi-synthesised using biological means. It can be a macromolecule, a cell, or a cellular component.[1] The global biopharmaceuticals market is projected to reach $526 billion by 2025, with a CAGR of 13.8% from 2018 to 2025.[2] Currently, the monoclonal antibody (mAb) segment dominates the global biopharmaceuticals market, and this tendency is expected to continue.[2,3] The importance of monoclonal antibodies and growth in this sector can be attributed to the various uses of mAb in treatment and diagnostics of some infectious diseases, as well as non-infectious ones, such as cancer, or immune diseases.[4]

N-linked glycosylation is one of the most common, and most complex post-translational modifications in proteins.[1] It results in a number of structurally varied carbohydrate forms attached to the protein, called glycans. Glycan heterogeneity stems from various factors, such as availability of nucleotide sugar donors (NSDs), or enzyme availability and activity.[5]

NSDs consist of a nucleotide mono-/di-phosphate and a sugar molecule. They are metabolites that act as precursors for the glycosylation process.[6] The process starts in the Endoplasmic Reticulum, where a precursor oligosaccharide is attached to the protein backbone site. Then, in the Golgi apparatus, the oligosaccharide is enzymatically modified by the addition of sugar residues provided by the NSDs.[6] Therefore, nucleotide and NSD concentrations are frequently used as inputs into models predicting glycosylation patterns. Intracellular NSD levels were previously found to depend on conditions that impact the cell metabolism, such as temperature, pH, carbon source availability and dissolved oxygen.[5] Their concentrations can also be impacted by feeding the cell culture with relevant substrates, such as sugars and nucleosides.[7]

Moreover, temperature and pH also influence glycosylation because they affect enzyme activity levels. For instance, it has been shown that mild hypothermia contributes to downregulating of glycosylation enzyme expression levels and may result in pre-matured glycan structures.[3] The choice of host cell line used to produce the glycoprotein can also have a strong impact on glycosylation as different host cells express different glycosylation enzymes and transporters which will be reflected in different glycan profiles. Types of mammalian cells used to produce approved bio-therapeutics include Chinese hamster ovary (CHO) cells, baby hamster kidney (BHK) cells, NS0 myeloma and Sp2/0 hybridoma mouse cell lines, human embryonic kidney cells 293 (HEK293) and HT-1080 human cells.[8]

Glycosylation is a complex phenomenon which can significantly impact product efficacy and safety. Depending on the individual case, it may influence biological activity, complement dependent and antibody dependent cellular cytotoxicity, product half-life and immunogenicity.[9] Quality by Design (QbD), a new approach taken in therapeutic protein development, assumes that product quality is ensured by appropriate design, rather than tested for. It requires that potential Critical Quality Attributes (CQAs), that may have an impact on product efficacy and safety, are at least identified. They can be then linked to Critical Process Parameters (CPP) to determine optimal process conditions.[9] Due to the high variability of glycan distributions and its importance in product quality, it is crucial to have accurate models in place that will predict glycan distribution under particular process conditions.

Mechanistic models have been developed to predict the impact of precursor feeding on glycan distribution. Kotidis et al. investigated the impact of galactose and uridine feeding on NSD concentrations and, subsequently, glycan profiles.[7] The model developed was able to successfully predict the glycosylation patterns. However, a disadvantage of this type of model is that it requires detailed knowledge of cell metabolism and the values of the parameters that describe it. Obtaining these parameters requires numerous measurements and significant effort, and the accuracy of the model can be affected by the accuracy of the parameters used.

This limitation may be overcome by using data-driven models, such as Support Vector Machines or Artificial Neural Networks (ANNs). They are less computationally expensive than kinetic models, can be readily developed using off-the-shelf software and do not require extensive knowledge of the biological system, which is useful in cases where the underlying mechanisms are poorly understood. A limitation of these models is the large amount of experimental data needed to ensure that the model predictions are accurate. A hybrid approach can also be used, that links the benefits of the two approaches: computational efficiency of data-driven models and mechanistic components that support transferability across the experimental system.[10]

A hybrid kinetic/ANN model has been previously developed to predict protein glycosylation for galactose and uridine feeding, as well as for manganese chloride, galactose and fucose addition. It used concentrations of metabolites and certain amino acids in the cell culture as inputs and fed them into the kinetic CHO metabolism module, which calculated the specific growth rate and the specific antibody production rate. They were then fed to the kinetic NSD synthesis module which calculated the intracellular NSD concentrations. The NSD concentrations were used as inputs into the ANN model which outputs the glycosylation profile. This hybrid model was shown to outperform a fully kinetic model.[6]

In this work, two models were developed that take NSD and nucleotide concentrations as inputs and output the predicted glycan distribution of the product. One was an Artificial Neural Network (ANN) developed in Python 3.8, using Tensofrlow and Keras, and optimised using Hyperas and Hyperopt libraries. The other one was based on Partial Least Squares regression and developed in Unscrambler X, Version 10.4. The goal of this work is to investigate the relative ability of the two approaches to predict the glycan distributions, especially if very limited data is available. Moreover, the ability of the models to perform on combined data from different datasets (cell lines, feeding strategies and temperatures) was also assessed.

2 Framework Development

2.1 Experimental Data Used

The datasets used in this investigation, as shown in Figure 1, were collected from three works on IgG-producing cells.

In all datasets (DSs) the nucleotides and NSDs used as inputs to the model were: AMP, ADP, ATP, CTP, UTP, GTP, UDPGalNAc, UDPGlcNAc, UDPGal, UDPGlc, GDPMan, GDPFuc and CMPNeu5Ac. Overall, 17 datasets were used with 13 inputs each. For each of the datasets 1-13 and 16-17, there were 6 glycans which constituted outputs for the model: Man5, G0, G0F, G1F, G2 and G2F. For the hybridoma cell line datasets (14-15), Man5 glycan was not reported, however, an additional glycan, G1, was. In all cases, 'Day' corresponds to the cell culture day at which the measurement was taken. The data did not require significant pre-processing, however, in a small number of cases NSDs data was not available for 2 species for Low Guanosine(LG) experiments. The data was, therefore, interpolated, by averaging between values for the respective days in High Guanosine (HG) and Control groups (Control).

Figure 2. provides an overview of how the two frameworks were developed.

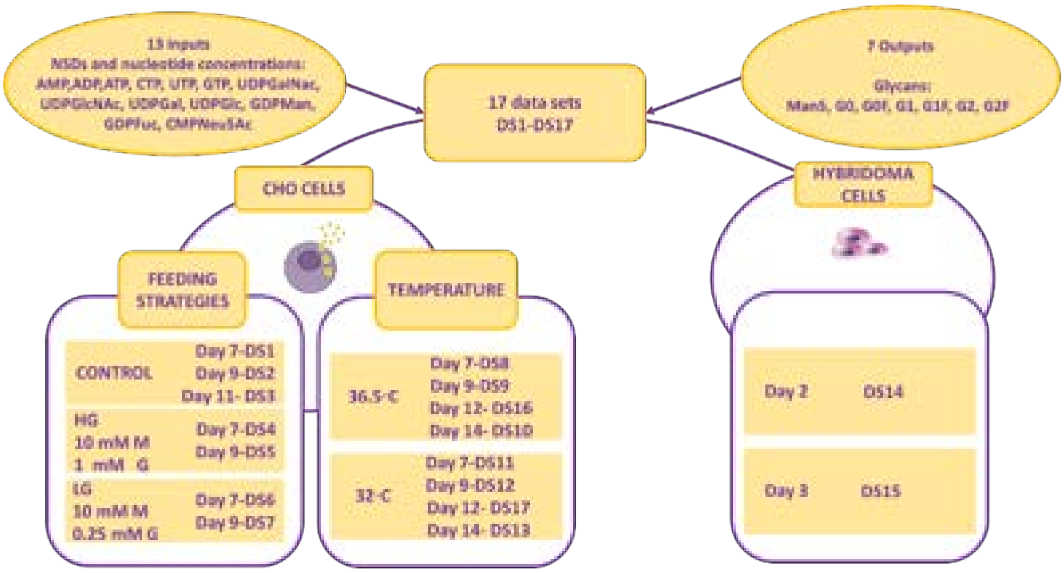

Figure 1: Datasets breakdown. Datasets (DSs) 1-7: experiments on CHO cells with three different feeding strategies at 36.5°C.[1] Control group - supplied with 32.5 mM (0.25% v/v) DMSO; High Guanosine group - 10 mM Mannose and 1 mM Guanosine; Low Guanosine group – 10 mM Mannose and 0.25 mM Guanosine. DSs 8-13 and 16-17: experiments on CHO cells that investigated cell metabolism under mild hypothermia (32°C) as compared to normal conditions (36.5°C). Datasets 14-15 investigated glycosylation patterns in murine hybridoma cell line.[11]

2.2 Artificial Neural Network (ANN)

An ANN is a type of data-driven model which has been shown to find applications in predicting antibody glycosylation patterns, often in combination with mechanistic models.[6,10] It consists of sequential, interconnected layers of nodes. It is composed of an input layer, a number of hidden layers (HLs) with varying number of nodes (or 'neurons') and an output layer.[12] A node assigns a weight to each of its input connections. When the network is active, a node transforms the sum of inputs multiplied by their respective weights into outputs via an activation function. The last layer in the network is the output layer, which ultimately predicts the desired results.[13]

The model was produced in Python 3.8 using TensorFlow – a machine learning library, and Keras, its neural network API. Hyperopt library and Hyperas wrapper were used for model optimisation. The data was split into train and test sets. Different combinations of datasets were assigned into train and test sets in various models investigated, as discussed in the following sections. An explicit train-validation-test split was not used, as k-fold cross-validation was implemented, as discussed further.

The network was optimised with respect to the number of nodes in each layer, activation functions associated with the hidden layers, optimiser, learning rate and dropout value in each of the hidden layers. The choice of optimisers was between Adagrad, which works well with sparse data, RMSprop, which has been shown to converge quickly, and Adam, which is believed to combine advantages of the other two.[14,15] The choice of activation functions in the hidden layers was between Rectified Linear Unit (ReLU), Sigmoid and Hyperbolic Tangent (TanH), which are widely used in neural networks.[13] In the output layer, the Softmax activation function was used, to ensure that the outputs sum up to 1. The number of neurons in the output layer was 6, as there are 6 outputs (glycans) for each dataset. In the models that also included DS14 and DS15, the number of neurons in the output layer was 7, as an additional glycan was observed.

Dropout was introduced in both hidden layers to prevent overfit and optimised within a linear range between 0 and 0.5 as higher values could limit learning ability.[16] The metric used to evaluate the model was Mean Absolute Error (MAE), commonly used in regression problems.[17] The number of hidden layers was kept at two, as introducing a third one did not result in much improvement in accuracy, and instead increased complexity and computation time. The number of epochs was tuned by inspection and fixed at 300. Validation accuracy would usually increase up to approximately 300 epochs and then plateau. Increasing epochs further could increase the computational time and risk of overfit. The network optimisation choices are summarized in Figure 2a.

K-fold cross-validation was performed to reduce the bias that could occur if an explicit train-validation-test split was implemented. Due to the small volume of data used here, Leave-One-Out Cross-Validation (LOOCV) was performed.[18] In LOOCV, one dataset is withheld from the train set and used for validation. The process is repeated for all datasets and model performance is averaged. Hyperopt enables use of Tree-structured Parzen Estimator (TPE) algorithm for optimisation, which has been shown to outperform the random search method.[19] As TPE requires many iterations to converge to an optimal solution, the number of iterations was set to 200.[20] The model with best average performance on validation sets was run on the test set. A random seed was set to ensure a reproducible result.

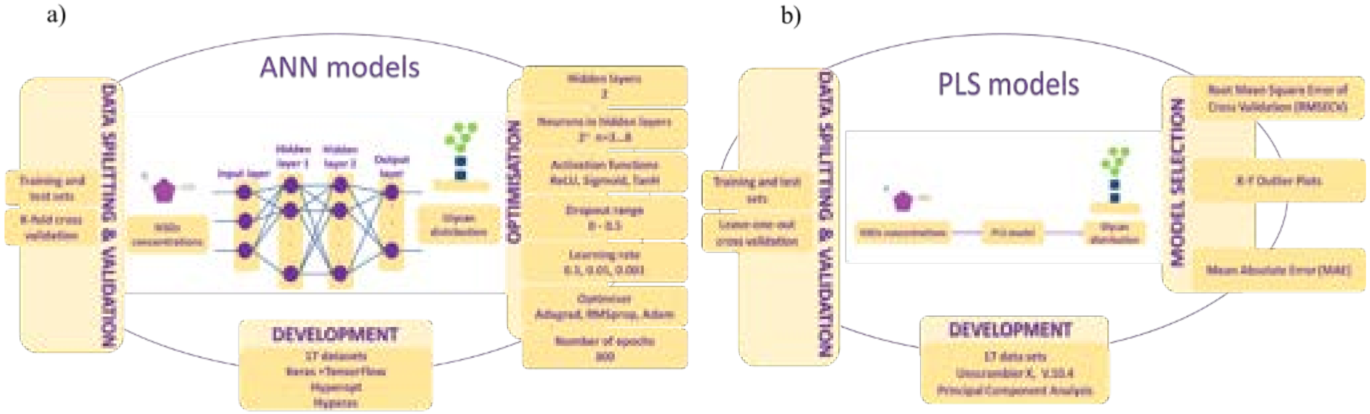

Figure 2: Model construction overview. a) Artificial Neural Network (ANN) was developed using TensorFlow, Keras, Hyperopt and Hyperas libraries in Python. Different combinations of training and testing sets were used, and K-fold cross validation was implemented. Optimisation was conducted with respect to number of neurons in hidden layers, activation functions, dropout rate, learning rate and optimisers.The number of epochs used was 300. The ANN models were evaluated using Mean Absolute Error (MAE). b) Partial Least Squares (PLS) models based on Principal Component Analysis were developed using Unscrambler X, Version 10.4. Combinations consistent with the ANN training and testing sets were used, using Leave-One-Out-Cross Validation (LOOCV). Selection of the model was made based on RMSECV and X-Y Outlier Plots. The ANN and PLS models were then compared using MAE.

2.3 Partial Least Squares (PLS) Models

The alternative approach compared to the ANN was a multivariate regression framework developed using Unscrambler X, Version 10.4. Partial Least Squares regression based on PCA (Principal Component Analysis) was performed using the same datasets as in case of ANN models. When fed with NSD concentrations, each model provides glycan distribution as the output.

The X-data was normalised – between 0 and 1. The validation was conducted using LOOCV. The optimum number of principal components was determined from the minimum value of the average Root Mean Square Error of Cross-Validation (RMSECV).[21] Six different combinations of training and testing datasets were compared. A suggestion for which PLS model might perform the best on the test sets was made by comparing the RMSECV, and the relevant X-Y outlier plots from Unscrambler X. Finally, combinations of train and test sets consistent with the ANN models were used to compare the two approaches on the basis of MAE.

3 Results and Discussion

3.1 ANN Results and Discussion

Table 1 shows that although the optimal hyperparameters for each model were different, there were a few similarities across them. All three activation functions appeared as optimal choices, however, most commonly it was the TanH function, especially in HL1. This may be due to the fact that the TanH function is zero-centered, and it thus facilitates the learning for the next hidden layer.[22] The number of neurons and dropout rates differed vastly across the models.

Most frequently, the optimiser leading to the best results was RMSprop. It is worth noting that the instances where RMSprop was chosen also correspond to the lowest MAE, i.e., highest accuracy. To investigate this further, Models 2 and 5 were re-run, but changing the optimisers manually to RMSprop. In Model 5, MAE increased slightly, but in Model 2, performance improved significantly, as MAE fell to 0.037760. A more optimal solution (implementing RMSprop instead of Adagrad in Model 2) was, therefore, not found, which might be due to the nature of the search algorithm. As TPE is informed by past evaluations, it may converge into a local optimum with a higher MAE than the other optima.[23] The optimal learning rate was always found to be 0.01, the intermediate value from the options provided. This is expected, as too small of a learning rate might result in slow learning, but too large might result in the model converging to a sub-optimal value.[24]

Table 1: Summary of ANN optimisation

	Model 1	Model 2	Model 3	Model 4	Model 5
Train DSs	1-5, 8-13	1-5, 8-13, 16	1-5, 8-10	1-5, 8-10, 14-15	1-5, 8-10
Test DSs	6, 7, 16, 17	6, 7, 17	6, 7, 16	6, 7, 16	6, 7, 14-16
No. of neurons (HL1, HL2)	(32, 32)	(32, 32)	(8, 16)	(64, 256)	(256, 128)
Activation function (HL1, HL2)	(TanH, ReLU)	(TanH, TanH)	(TanH, Sigmoid)	(TanH, Sigmoid)	(ReLU, ReLU)
Dropout rate (HL1, HL2)	(0.393533, 0.262315)	(0.193434, 0.007517)	(0.138715, 0.091648)	(0.111387, 0.124942)	(0.001581, 0.065180)
Optimiser	RMSprop	Adagrad	RMSprop	RMSprop	Adam
Learning rate	0.01	0.01	0.01	0.01	0.01
MAE	0.023735	0.088774	0.018855	0.022521	0.072371

3.2 PLS Model Results and Discussion

PLS model selection is summarised in Table 2.

Table 2: Summary of PLS model selection

Model	Train DSs	Test DSs	Optimum PC	Average RMSECV
1	1-5, 8-13	6, 7, 16, 17	3	0.0414
2a (DS3 included)	1-5, 8-13, 16	6, 7, 17	1	0.0377
2b (DS3 excluded)	1,2 4, 5, 8-13, 16	6, 7, 17	1	0.0364
4	1-5, 8-10, 14, 15	6, 7, 16	3	0.0506
3a/5a (DS3 included)	1-5, 8-10	6, 7, 16, 14, 15	1	0.0419
3b/5b (DS3 excluded)	1,2, 4, 5, 8-10	6, 7, 16, 14,15	1	0.039

To rule out some of the combinations, the values of RMSECV, X-Y outliers plots (Figure 3) and MAE were compared. DSs 14 and 15 did not cluster with the rest of the data which implies that these datasets should not be included in the training. A possible explanation is that the data for DS14 and DS15 belongs to a different cell line. Hence, Model 4 can be omitted. Upon further examination, it was noticed that DS 3,6 and 7 also do not cluster with the rest of that data and instead, DS6 and DS7 were used for testing. While excluding DS3 generally decreased the RMSECV, it increased the mean average error by 1.86% for PLS Model 2b. Since the PLS and ANN models are later compared based on MAE, it was decided to keep DS3 within the training set and thus Model 2b was omitted. Moreover, datasets DS1, DS2, DS4 and DS5 also appear to be outliers, however removing them from the training significantly worsened the RMSECV values. Thus, they were kept in the training set.

Finally, Models 3a, 5a, 3b and 5b were created for consistency with the ANN models and to compare the performance of the models without including 32°C data. They were eliminated for having a higher RMSECV than other models. Comparing between the remaining combinations, Model 2a was chosen as the best PLS model in cross validation as it gave a lower RMSECV than Model 1. Model 2a was anticipated to perform the best on the test set basing on the approach outlined. The predictive abilities of Models 1, 2a, 3a, 4 and 5a (referred to, respectively, as Models 1, 2, 3, 4 and 5 in the subsequent section) were evaluated by calculating the respective mean absolute error (MAE). The values were then compared to the corresponding ANN models as discussed further.

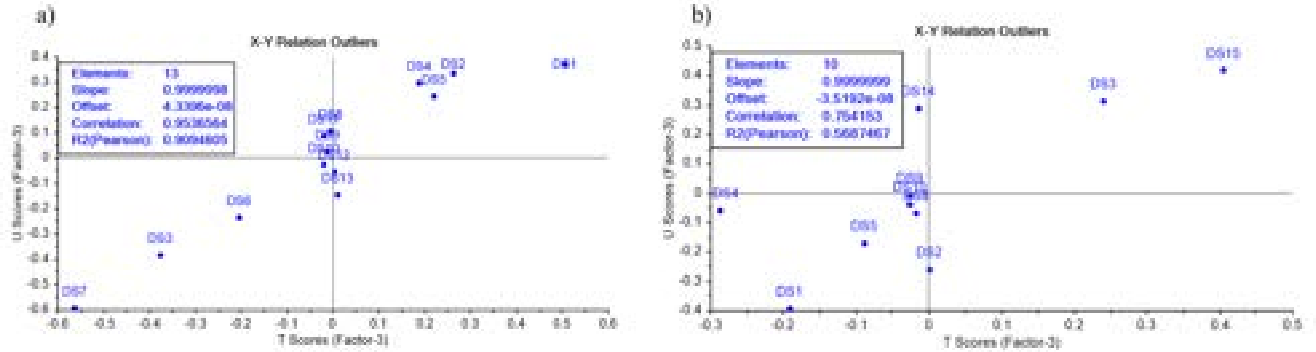

Figure 3: X-Y Outlier plots used for the selection of the best performing PLS model in cross-validation. a) PLS Model 1; b) PLS Model 4.

3.3 ANN and PLS Models Comparison

As shown in Figures 4a and 4b, the Mean Absolute Error tends to be the highest in Models 2 and 5. Those correspond to test sets including 32°C data and hybridoma data, respectively. In most situations, ANN models performed better than the corresponding PLS models, as measured by the value of MAE. The exception was Model 2, where MAE was significantly larger for the ANN model.

After altering the optimiser from Adagrad to RMSprop in Model 2, the MAE for the ANN model was also lower than that of the PLS one. This suggests that the ANN approach was able to make more accurate predictions than PLS in most cases; however, in some instances the algorithm might not find the optimal hyperparameters – either a better performing algorithm or higher number of evaluations could be implemented, which would significantly increase computational time.

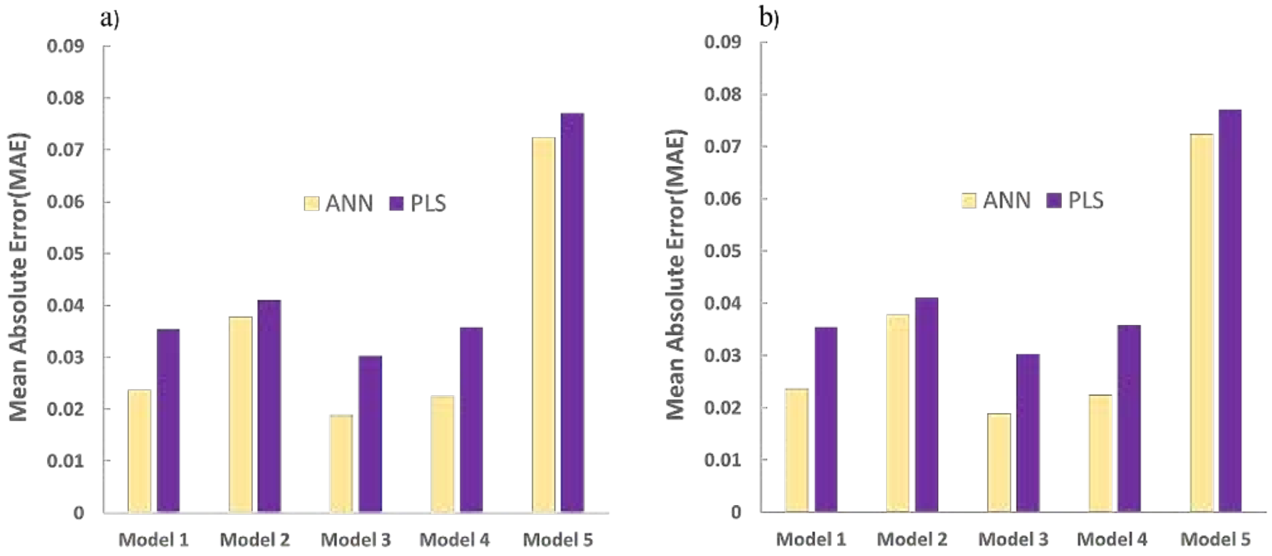

Figure 4: Comparison of Mean Absolute Error (MAE) between the ANN and PLS models for a) Adagrad optimiser used in ANN, Model 2; b) RMSProp optimiser used in ANN, Model 2.

Another insight that can be drawn from these results is that both types of models give good predictions when the conditions under which test data was gathered (especially the temperature and cell line used) are also represented in the training set. The impact is most clearly seen in the ANN models, although both approaches follow a similar trend. In both cases, the model with the lowest error was Model 3, which only included datasets from experiments on CHO cells at 36.5°C. The models with the highest errors are Model 2 for ANN and Model 5 for PLS. However, after changing the optimiser in Model 2 to RMSprop, Model 5 yielded the highest error in both models (it would not respond to an optimiser change; the change in MAE was negligible) and Model 2 resulted in the second highest.

This is consistent with the analysis of MAE for the individual datasets. Taking test datasets of Model 5 as an example, the individual MAE values for datasets corresponding to hybridoma cells are significantly higher than for CHO datasets for both ANN and PLS models, as shown in Figure 5a.

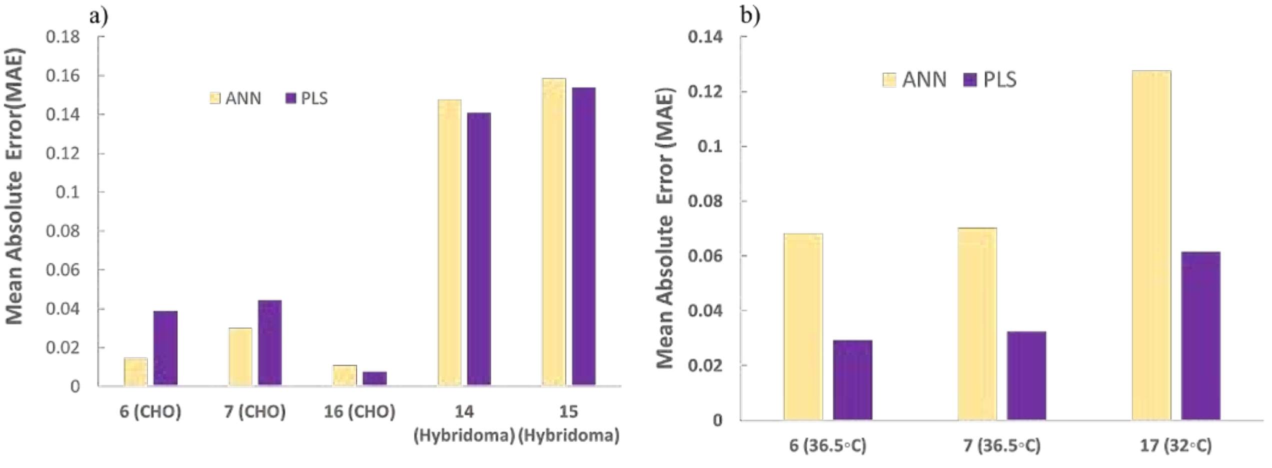

Figure 5: Comparison of the MAE values of the ANN and PLS models for individual datasets in a) Model 5; b) Model 2.

A similar trend was noticed in Model 2 between datasets corresponding to 36.5°C and to 32°C. although the effect was less pronounced than that in Model 5. The individual MAE values for datasets corresponding to 32°C are higher than for 36.5°C datasets, and are shown in Figure 5b. This may be explained by the variation in host cell metabolism. Mild hypothermia affects the expression levels of key enzymes related to glycosylation.[3] Different host cell lines also express different profiles of glycosylation enzymes.[8] Therefore, there might be different dependencies between the NSDs and nucleotide profiles and glycan distributions for different temperatures and host cell lines which the model might not grasp if the volume of data available is small.

Figure 6 shows the glycan distributions predicted by the ANN and PLS models. It is apparent that the predictions made for hybridoma datasets by both models have much more similarity to the experimentally determined CHO glycan distributions than to the experimental results for hybridoma cells.

It is also worth noting that the ANN predictions were identical for DS14 and DS15 (hybridoma cell datasets). This indicates that the algorithm is unable to yield meaningful predictions when the data available for building the model is not similar in nature to the distribution to be predicted. This is one limitation of data-driven models. However, in Model 4, the MAE was relatively small for both models. This implies that the presence of highly different datasets in the training set still allows the models, especially the ANN model, to perform well. This is valid, as long as the majority of data exhibits similar patterns to the data in test set.

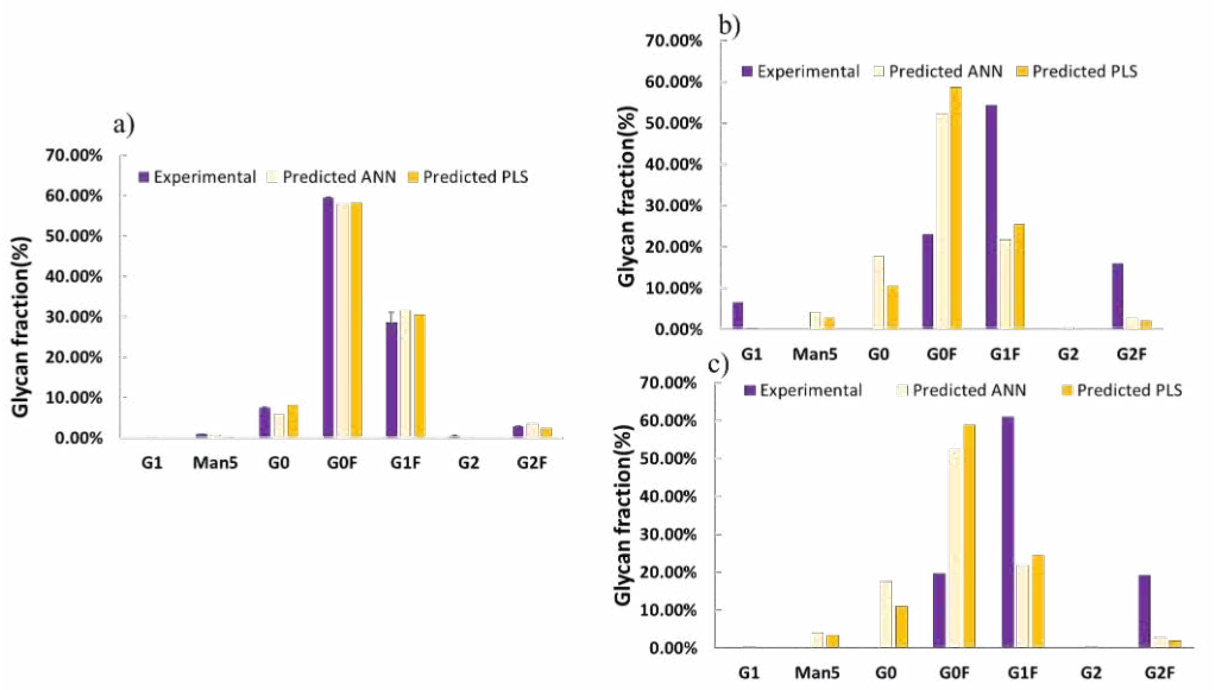

Figure 6: Glycan distributions for various datasets predicted by PLS Model 5 and ANN Model 5, compared to experimental results. a) DS16, corresponding to Day 12 CHO cells at 36.5°C; b) DS14, corresponding to Day 2 hybridoma cells; and c) DS15, corresponding to Day 3 hybridoma cells.

Ultimately, the choice between using either of the two approaches may depend on the circumstances. As mentioned above, the ANN model usually gives more accurate predictions than the PLS equivalent. However, it may take several hours to optimise even a relatively small neural network, while setting up and running an equivalent PLS model takes several minutes. In both cases, in order to ensure accurate predictions of the glycan profiles, previous experimental data gathered for the same cell line and temperature is necessary. Lastly, randomness embedded in the ANN approach should be considered. Although random seed was set to ensure reproducible results for model testing, this is not the case for model optimisation. Therefore, the optimal hyperparameters obtained may vary between optimisation runs and depend on the search algorithm and the number of evaluations used.

4 Conclusion

Two modelling frameworks - one using an Artificial Neural Network and the other one using Partial Least Squares regression were proposed for predicting glycan distribution in CHO and murine hybridoma cells. The approaches used NSD and nucleotide concentrations as the inputs. On average, the ANN models performed better than the PLS equivalents, the only exception being Model 2. However, manually altering the optimiser lead to the ANN framework performing better in all instances.

A higher Mean Absolute Error was observed for test data associated with hybridoma cells and at 32°C compared to those in CHO cells and at 36.5°C. This is attributed to insufficient hybridoma and 32°C information available for training. Hence, the models in both frameworks provided accurate predictions when the testing datasets were similar in nature to the training ones. However, when some of the dissimilar datasets (e.g hybridoma cells data) are used for training, the frameworks still yield accurate predictions provided that test datasets are sufficiently represented in the training.

Finally, other factors, e.g. computational time and stochastic nature of the ANN models also need to be considered when selecting the appropriate framework.

5 Future Directions

Firstly, the experiments described could be reimplemented over a range of temperatures, with various feeding strategies that include relevant metabolites (e.g uridine and galactose). This approach would be especially beneficial for the hybridoma cell line, due to low volume of data currently available. Moreover, the effect of factors such as pH and electrolyte concentrations (e.g $MnCl_2$) on glycan distribution can be added to increase the volume of the data available. This could improve the accuracy of the predictive models and establish new and relationships between the cell lines and their respective glycan distributions.

Moreover, the performance of the ANN models could be further explored by implementing alternative search algorithms (for example, Adaptive TPE, recently added to Hyperopt) or hyperparameter optimisation libraries (e.g. Optuna).[25,26]

Finally, while this report focused on performance of ANN and PLS models, other modelling techniques such as Gaussian Processes (GP) Regression can be introduced. This would allow to obtain an insight into other, potentially better predictive techniques. Additionally, as the trained ANN model is a deterministic one, it outputs an array of single values for each glycan distribution, without accounting for the uncertainty. Previous research demonstrated an advantage of a model based on Gaussian Processes over ANN due to comparable prediction ability and, additionally, incorporating uncertainty.[27] Hence, GP regression could be employed to obtain a probabilistic model that accounts for the uncertainty in the glycan distribution profiles.

References

[1] Jedrzejewski, P. (2015) *A Platform for the Optimisation of Metabolic Pathways for Glycosylation to Achieve a Narrow and Targeted Glycoform Distribution.*[Online]. Chemical Engineering, Imperial College London. Available from: http://hdl.handle.net/10044/1/53386

[2] Shaikh, S. & Jaiswal, P. (n.d.) *Biopharmaceuticals Market By Type (Monoclonal Antibody, Interferon, Insulin, Growth & Coagulation Factor, Erythropoietin, Vaccine, Hormone, and, Others) and Application (Oncology, Blood Disorder, Metabolic Disease, Infectious Disease, Cardiovascular Disease, Neurological Disease, Immunology, and Others) - Global Opportunity Analysis And Industry Forecast, 2018-2025.* [Online]. Available from: https://www.alliedmarketresearch.com/biopharmaceuticalbiopharmaceutical-market.

[3] Sou, S.N., Sellick, C., Lee, K., Mason, A., et al. (2015) *How does mild hypothermia affect monoclonal antibody glycosylation?* [Online] 112 (6), 1165–1176. Available from: doi:10.1002/bit.25524.

[4] Mahmuda, A., Bande, F., Kadhim Al-Zihiry, K.J., Abdulhaleem, N., et al. (2017) *Monoclonal antibodies: a review of therapeutic applications and future prospects.*[Online] 16 (3), 713. Available from: doi:10.4314/tjpr.v16i3.29.

[5] Papathanasiou, M.M. & Kontoravdi, C. (2020) *Engineering challenges in therapeutic protein product and process design.* [Online] 16 (3), 713. Available from: doi:10.4314/tjpr.v16i3.29.

[6] Kotidis, P. & Kontoravdi, C. (2020) *Harnessing the potential of artificial neural networks for predicting protein glycosylation.* [Online], Metabloic Engineering Communications.,vol.10 Available from: doi:10.1016/j.mec.2020.e00131.

[7] Kotidis, P., Jedrzejewski, P., Sou, S.N., Sellick, C., et al. (2019) *Model-based optimization of antibody galactosylation in CHO cell culture.* [Online] 116 (7), 1612–1626. Available from: doi:10.1002/bit.26960.

[8] Goh, J.B. & Ng, S.K. (2018) *Impact of host cell line choice on glycan profile.* [Online] 38 (6), 851–867. Available from: doi:10.1080/07388551.2017.1416577.

[9] Eon-Duval, A., Broly, H. & Gleixner, R. (2012) *Quality attributes of recombinant therapeutic proteins: An assessment of impact on safety and efficacy as part of a quality by design development approach.* [Online] 28 (3), 608–622. Available from: doi:10.1002/btpr.1548.

[10] Antontonakoudis, A., Strain, B., Barbosa, R., Jimenez del Val, I., et al. (2021a) *Synergising stoichiometric modelling with artificial neural networks to predict antibody glycosylation patterns in Chinese hamster ovary cells.* [Online] 154. Available from: doi:10.1016/j.compchemeng.2021.107471.

[11] Jedrzejewski, P.M., del Val, I.J., Constantinou, A., Dell, A., et al. (2014) *Towards Controlling the Glycoform: A Model Framework Linking Extracellular Metabolites to Antibody Glycosylation.* [Online] 15 (3), 4492–4522. Available from: doi:10.3390/ijms15034492.

[12] Hardesty, L. (2017) *Explained: Neural networks.* [Online]. Available from: https://news.mit.edu/2017/explained-neural-networks-deep-learning-0414.

[13] Brownlee, J. (2021a) *How to Choose an Activation Function for Deep Learning.* [Online].
Available from:
https://machinelearningmastery.com/choose-an-activation-function-for-deep-learning/.

[14] Kingma, D.P. & Ba, J. (2014) *Adam: A Method for Stochastic Optimization.* [Online] Available from: https://arxiv.org/abs/1412.6980.

[15] Doshi, S., (2019) *Various Optimization Algorithms For Training Neural Network.* [Online]. Available fom: https://towardsdatascience.com/optimizers-for-training-neural-network-59450d71caf6 [Accessed 05 December 2021].

[16] Srivastava, N. et al. (2014) *Dropout: A Simple Way to Prevent Neural Networks from Overfitting.* [Online] 15 (2014) 1929-1958 Available from: https://www.cs.toronto.edu/ rsalakhu/ papers/srivastava14a.pdf

[17] Brownlee, J. (2021b) *Regression Metrics for Machine Learning.* Available from: https://machinelearningmastery.com/regression-metrics-for-machine-learning/.

[18] Brownlee, J. (2020) *LOOCV for Evaluating Machine Learning Algorithms.* [Online]. Available from: https://machinelearningmastery.com/loocv-for-evaluating-machine-learning-algorithms/.

[19] Bergstra, J., Bardenet, R., Bengio, Y. & Kégl, B. (2011) *Algorithms for Hyper-Parameter Optimization. In: Advances in Neural Information Processing Systems.* [Online]. Neural Information Processing Systems Foundation Available from: https://hal.inria.fr/hal-00642998.

[20] Anon (n.d.) *Tree-Structured Parzen Estimator (TPE).* [Online]. Available from: https://docs.openvino.ai/latest/ pot_compression_optimization_tpe_README.html.

[21] Sokolov, M., Ritscher, J., MacKinnon, N., Souquet, J., et al. (2017) *Enhanced process understanding and multivariate prediction of the relationship between cell culture process and monoclonal antibody quality.* [Online] 33 (5), 1368–1380. Available from: doi:10.1002/btpr.2502.

[22] Omkar,N. (2019) *Activation Functions with Derivative and Python code: Sigmoid vs Tanh Vs Relu* [Online]. Available from: https://medium.com/@omkar.nallagoni/activation-functions-with-derivative-and-python-code-sigmoid-vs-tanh-vs-relu-44d23915c1f4.

[23] Koehrsen, W. (2018) *A Conceptual Explanation of Bayesian Hyperparameter Optimization for Machine Learning.* [Online]. Available from: https://towardsdatascience.com/a-conceptual-explanation of-bayesian-model-based-hyperparameter-optimization-for-machine-learning-b8172278050f.

[24] Brownlee, J. (2019) *Understand the Impact of Learning Rate on Neural Network Performance.* Online]. Available from: https://machinelearningmastery.com/understand-the-dynamics-of-learning-rate-on-deep-learning-neural-networks/.

[25] Arsenault, B. et al (2020) *GitHub - electricbrainio/hypermax: Better, faster hyperparameter optimization* [Online] GitHub. Available from: https://github.com/electricbrainio/hypermax [Accessed 5 December 2021].

[26] Optuna (2021) *Optuna - A hyperparameter optimization framework.* Online] Available from: https://optuna.org/ [Accessed 5 December 2021].

[27] Bradford, E., Schweidtmann, A.M., Zhang, D., Jing, K., et al. (2018) *Dynamic modeling and optimization of sustainable algal production with uncertainty using multivariate Gaussian processes.* [Online] 118, 143–158. Available from: doi:10.1016/j.compchemeng.2018.07.015.

Densities and GERG-2008 Equation of State for Binary Mixtures of Iso-octane with M, P and O-xylene from 283.15K to 463.15K at Pressures up to 60 MPa

Man Tang & Yujia Wang
Department of Chemical Engineering, Imperial College London, U.K.

Abstract In this paper, densities were measured for binary mixtures of iso-octane with m, p, and o-xylene at temperatures from 283.15 K to 463.15 K and pressures up to 60 MPa. This was done by measuring period of oscillations τ using a vibrating tube densimeter and applying a physically-based model which calculates density as a function of T, p and τ. The model was fitted through calibration using vaccum and water, and corrections were made on system deviations to improve data quality. The resulting experimental densities were used together with data from literatures to optimise the Helmholtz Equation of State, GERG-2008, for both iso-octane and n-octane mixtures with xylene isomers. It was found that the performance of the model generally improves with increasing number of model parameters tuned and amount of input data. The average sum of squares reduced error has been used as the objective function for optimisation. Excess volumes calculated from the density data were plotted and were compared with those calculated using the Helmholtz models. Uncertainties of input and output quantities were carefully investigated throughout the study, with an overall expanded uncertainty of density of 0.59 kg/m^3.

1. Introduction

Accurate information of thermodynamic properties and relevant prediction models of complex fluid mixtures are of particular importance in the basic engineering process in many industries. These areas include aerospace science, geoscience, geothermal field, and chemical process plant where high-quality thermodynamic data is the key to determine the economic value of the process [23].

Density is a crucial intensive thermodynamic property for engineers and scientists to understand how fluids expand and contract at different temperatures and pressures [3]. Thus, this research aims to obtain accurate density data and use it together with data from literatures to optimize an Equation of State (EoS) model for thermodynamic property predictions. Excess volume was calculated as a supporting property that evaluates the quality of the density data, while at the same time expanding the understanding of the interactive behaviour between molecules of the sample mixtures.

Alkanes and aromatics are common hydrocarbons extracted from crude oil, petroleum, and coal tar, among which iso-octane and xylenes are widely used as non-polar industrial solvents for purification, recrystallisation, and washing in various industries, for example, pharmaceuticals [21,30]. In real life, they are also commonly found in paintings, paint thinners, polishes, varnishes, cleaners, and adhesives [8,21]. As the process of oil refinery might be subject to high-pressure high-temperature (HPHT) conditions, for instance, hydrocracking process can achieve a temperature at about 673 K and pressure over 30 MPa [4], it is important to understand the thermodynamic behaviours of iso-octane-and-xylene binary mixtures at HPHT. Within the current field of study, despite the thermodynamic properties of various hydrocarbon mixtures were studied by many researchers, there is still a shortage of highly accurate data under HPHT conditions, especially for the iso-octane-and-xylene mixtures. In this work, liquid binary mixtures of iso-octane respectively with m-xylene and o-xylene were studied at temperatures between 283.15 K to 463.15 K and pressures up to 60 MPa; mixtures of iso-octane with p-xylene were only measured at temperatures from 288.15 K to 463.15 K and pressures up to 30 MPa to avoid solidification of p-xylene in the equipment. Mole fractions at x = 0, 0.25, 0.5, 0.75 and 1 of iso-octane were investigated for each xylene. The resulting density data obtained from the vibrating tube densimeter (VTD) was then used for the improvement of thermodynamic properties prediction models.

2. Background

In the past 30 years, there has been an increase in the precision of density measurements through the development in the designs and the corresponding models of vibrating tube densimeters (VTD) by manufacturers [32,33] and researchers [15]. A procedure of how a VTD measures density will be described in Section 3.3. Generally, its eventual objective is to allow density ρ to be calculated from measured temperature T, pressure p, and resonance period τ. The working equation of VTD, including parameters fitted using calibration fluids and vacuum, is the determining factor of the accuracy of density measurements. A physically-based model was used in this work, which was initially developed by Holcomb and Outcalt [11], expanded by Bouchot and Richon [5], and finally simplified by May et al [16] through comparing the 6 different types of VTDs that the model is applicable to. This model takes the material and geometry of the VTD tube into account when determining the model parameters. Also, it does not require the calibration condition to exactly match the pressure and temperature of the sample fluid of interest. If a fixed ratio between pressure resonance coefficients β_V / β_τ

is used [16], the calibration data of vacuum and only one reference fluid are needed rather than two calibration fluids, and the experimental work needed at the preparation stage will be reduced.

A popular type of model used to predict thermodynamic properties is Equation of State (EoS) [19]. There are hundreds of forms of EoS proposed by different researchers. Among these, the most common form used in the oil and gas industry is the cubic EoS by Peng and Robinson (1976) [20]. Although these cubic EoS are easy to implement and not very computationally demanding, they tend to be poor in accuracy and deviate from the real values significantly under HTHP conditions. Another commonly applied form of EoS in the natural gas industry is the AGA8-DC92 EoS by Starling and Savidge (1992) [1], but it is only limited to being used for the gas phase. More recently, Trusler et al (2003 & 2004) [9,10] extended EoS models for natural gases and relevant mixtures. In the same year, Kunz et al [12] proposed a new EoS model based on non-dimensionalised Helmholtz energy – GERG-2004. This broadened the application of EoS as all fundamental thermodynamic properties of fluids can be calculated by combining various derivatives of Helmholtz energy. The multi-fluid mixture model chosen in this work is the most accurate EoS currently available – GERG-2008, which was expanded from GERG-2004 by Kunz & Wagner [13]. It was then implemented in a state-of-the-art thermophysical property library – REFPROP, to carry out calculations for the modification and optimisation of GERG-2008 model parameters.

3. Materials and Method

3.1 Chemicals

Chemicals used in this study are m-xylene, p-xylene, o-xylene and iso-octane provided by companies listed in Table 1. Purities for the specific batches of chemicals used were also found in Certificates of Analysis (COA) from the official websites of the manufaturers:

Table 1: A list of chemicals used.

Chemical	Source	CAS no.	Batch purity
m-xylene	Sigma-Aldrich	108-38-3	99.8%
p-xylene	Sigma-Aldrich	106-42-3	99.8%
o-xylene	Sigma-Aldrich	95-47-6	99.2%
iso-octane	Supelco	540-84-1	≥ 99.8%

3.2 Solution Preparation

Initially, calibration was carried out using water as calibration fluid. Details of calibration can be found in Section 3.5. For mixtures at $x = 0$, pure xylene data obtained from Uko's previous study [27] were directly used. Binary mixtures of iso-octane with m, o and p-xylenes at iso-octane mole fractions of $x = 0.25, 0.5, 0.75$ were prepared gravimetrically. Masses required for each pure substance for 60 ml of solution were calculated at each desired mole fraction, using the following equation

$$x_2 = \frac{\left(\frac{m_2}{M_2}\right)}{\left(\frac{m_1}{M_1} + \frac{m_2}{M_2}\right)} \tag{1}$$

where 1 and 2 stand for iso-octane and xylene isomers respectively. m and M are the measured mass and molar mass of a pure substance. Pure iso-octane was directly used for mesurements at $x = 1$.

Mixtures were then prepared using a Mettler Toledo mass balance (XPE5003S). The balance was re-zeroed initially with a 200-ml glass bottle on it. Iso-octane was then added and m_1 was recorded before the balance was re-zeroed again to measure m_2. Due to the high-volatility nature of the solution, even though the measurement was done quickly, unavoidable mass loss of solution due to evaporation by ≤ 0.01 g was observed. Therefore, ± 0.005 g, which is half of this largest possible mass loss, was taken as the mass uncertainty $u(m)$ instead of the resolution of the balance which is 0.01 mg. The mass loss, however, would not have a large influence on the molar ratios as both chemicals evaporate at similar speeds.

The actual mole fraction after mixture preparation was calculated again using Eq. (1), and its uncertainty was calculated in Section 3.6 using Gaussian error propagation.

3.3 Equipment and Procedures

Figure 1 is a schematic diagram of the experimental setup. The primary equipment used in this study is Anton Paar vibrating tube densimeter (DMA-HP) on the left-hand side of the diagram, with a measurement capacity from 0 to 70 MPa for pressure and -10 to 200 °C for temperature. At a set temperature and pressure, it measures the period of oscillations (τ) of the sample solution contained inside the hollow U-tube which is fitted within the DMA HP cell of the VTD. Values of temperature can be directly set and read from Anton Paar DMA-5000 densimeter master instrument which controls temperature through an integrated thermostat. A parallel temperature sensor (Fluke 1502A Thermometer Readout) was calibrated and installed by inserting its probe into the thermowell of the VTD, to monitor any temperature deviation read by the Anton Paar master instrument. Pressures were set on the controller of Teledyne Isco syringe pump (Model 100DM), which is shown on the righ-hand side of the diagram. At the start of a measurement, sample solution was firstly filled into the syringe pump which generates pressures up to 69.5 MPa through injecting certain amounts of solutions into the U-tube of the VTD. Pressures measured by (Keller, model 33X) pressure sensor with an upper limit of 70 MPa can be read from the corresponding software (Control Center Series 30). Uncertainties of T, p and τ readings from the apparatus are listed in Section 3.6 Table 3. The system was closed during measurements, i.e. V1 and V6 were closed.

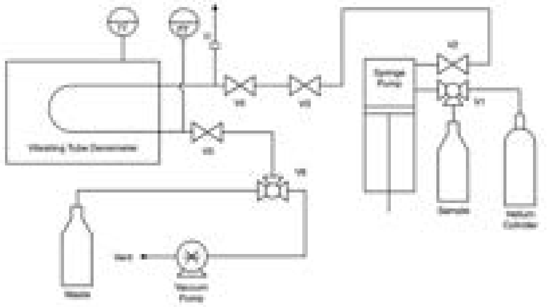

Figure 1: Schematic diagram of experimental setup.

After the preparation of solutions, they were well mixed through adequate swirling and flicking. For pure substances, solution was degassed through direct pumping to create a vacuum environment above the solution within the glass bottle. Mixtures were degassed using Fisherbrand$^{\text{TM}}$ S-Series Ultrasonic Cleaning Bath.

Right after degassing, approximately 35 ml of solution was filled into the syringe pump with a maximum capacity of 100 ml. The initial pressure was set at 1 bar, and after pressing "run", V2 was opened automatically, and solution was then fed into the U-tube until the set pressure was reached. V6 was opened manually to flush the system, to further ensure that there was no residue left and the U-tube has been uniformly filled with the sample fluid. After that, for m-xylene and o-xylene mixtures, measurements were carried out incrementally throughout the pressure range of (10, 50, 100, 200, 300, 400, 500 and 600 barg), at each isotherm (283.15, 313.15, 343.15, 373.15, 403.15, 433.15 and 463.15 K). For p-xylene mixtures, due to its higher freezing point (i.e. higher feezing temperature and lower freezing pressure) compared to other xylenes [6], the lowest isotherm was adjusted to 288.15 K, and the highest pressure was changed to 300 barg, to prevent the formation of solid. After the maximum pressure was reached at each temperature, it was lowered to 1, 1, 1.5, 2, 3.5, 5.5 and 8.5 barg for 283.15, 313.15, 343.15, 373.15, 403.15, 433.15 and 463.15 K respectively. These pressures were the lowest values used in this study, and were obtained by adding around 2 bars of safety margin onto the boiling pressure [31] at each isotherm to prevent the formation of gas. At each isotherm, quality check was done in the end by repeating measurements at 10 barg to double-check the system was working properly. After all measurements were finished for one mixture composition, a final quality check was also one by repeating conditions at 283.15 K and 10 barg to verify the consistency and repeatability of the data. The system was flushed by Helium and vacuumed alternatively several times. Vacuum condition was kept overnight for the system to fully evaporate any residues left. External walls of the pipes were heated by an external heating device (Thurlby Thandar Instruments TS3510P) at a constant voltage of 20 V to improve evaporation efficiency.

3.4 Theories

3.4.1 Physically Based Model

Experimental densities of each mixture can be calculated from measured T, p and τ using an existing model of the VTD. The working equation of a VTD relates density of a fluid to its period of oscillation as follows:

$$\rho = A\tau^2 - B \tag{2}$$

where A and B are in terms of temperature, pressure, and parameters depending on the type of VTD used. May et al [16] demonstrated a robust physically-based model for VTDs including the type used in this study, in which A and B are consisted of T, p and seven adjustable apparatus parameters S_{00}, τ_{00}, $\varepsilon_{\tau 1}$, $\varepsilon_{\tau 2}$, β_τ, α_V and β_V,

$$A = \left(\frac{\rho_M}{S_{00}\tau_{00}^2}\right)\left[\frac{(1+\beta_\tau p)}{(1+\varepsilon_{\tau 1}T+\varepsilon_{\tau 2}T^2)^2(1+\alpha_V T+\beta_V p)}\right]$$
$$= B(1+\beta_\tau p)/\tau_0^2 \tag{3}$$

where T, p are temperature and pressure, and

$$\tau_0 = \tau_{00}(1+\varepsilon_{\tau 1}T+\varepsilon_{\tau 2}T^2) \tag{4}$$

$$B = \frac{\rho_M}{S_{00}(1+\alpha_V T+\beta_V p)} \tag{5}$$

The model was validated for temperatures from 273 to 472 K, and for pressures up to 140 MPa.

To obtain the seven model parameters, calibration data of vacuum and two calibration fluids with known equations of states, i.e. known density, was needed. In this work, only one calibration fluid was used instead of two. Therefore, β_V/β_τ was fixed at -3.87 [15] to accommodate the one extra additional degree of freedom, reducing number of parameters required to be fitted from seven to six.

3.4.2 Multi-Fluid Helmholtz Energy Approximation

The GERG-2008 EoS was developed based on the approximation method explicit in dimensionless Helmholtz energy [13]. The function is split into two parts – the ideal-gas part α^o and the residual part α^r.

$$\alpha(\delta,\tau,\bar{x}) = \alpha^o(\rho,T,\bar{x}) + \alpha^r(\delta,\tau,\bar{x}) \tag{6}$$

where the reduced Helmholtz energy, the reduced mixture density and the inverse reduced mixture temperature are

$$\alpha = \frac{a}{RT}, \quad \delta = \frac{\rho}{\rho_r(\bar{x})}, \quad \tau = \frac{T_r(\bar{x})}{T} \tag{7}$$

with ρ_r and T_r which are the composition-dependent reducing functions for mixture density ρ and temperature T.

The ideal part α^o is only dependent on ρ, T, and molar composition $\bar{x}$

$$\alpha^o(\rho, T, \bar{x}) = \sum_{i=1}^{N} x_i[\alpha_{oi}^o(\rho, T) + \ln(x_i)] \qquad (8)$$

where N is the number of components in a mixture, α_{oi}^o is the dimensionless Helmholtz energy in the ideal-gas state of component i.

The residual part α^r is given by

$$\alpha^r(\delta, \tau, \bar{x}) = \sum_{i=1}^{N} x_i \alpha_{oi}^r(\delta, \tau) + \Delta\alpha^r(\delta, \tau, \bar{x}) \qquad (9)$$

where the first term of Eq. (9) is the summation of residual part of the reduced Helmholz free energy of component i, α_{oi}^r, which only depends on the state of the mixture. The second term is called the departure function $\Delta\alpha^r(\delta, \tau, \bar{x})$ which sums over all binary specific or generalized (for a group of binary mixtures) departure functions $\alpha_{ij}^r(\delta, \tau, \bar{x})$

$$\Delta\alpha^r(\delta, \tau, \bar{x}) = \sum_{i=1}^{N-1} \sum_{j=i+1}^{N} x_i x_j F_{ij} \alpha_{ij}^r(\delta, \tau, \bar{x}) \qquad (10)$$

The adjustable factor $F_{ij} = 0$ when there is no departure function developed for the binary mixture; $F_{ij} = 1$ when there is a binary specific departure function for the binary mixture. To fit F_{ij}, it would require a large amount of experimental data [2]. Since the departure functions for the mixtures investigated here were not designed in the REFPROP thermophysical library, and due to the paucity of experimental data especially for iso-octane mixtures, the departure term was not considered in this work.

The latest formulation, implemented in all of the state-of-the-art libraries including REFPROP, calculates δ and τ (see Eq. (13)) by

$$Y_r(\bar{x}) = \sum_{i=1}^{N} x_i^2 Y_{c,i} + \sum_{i=1}^{N-1} \sum_{j=i+1}^{N} 2x_i x_j \frac{x_i + x_j}{\beta_{Y,ij}^2 x_i + x_j} Y_{ij} \qquad (11)$$

where Y indicates the variables of interest, which are temperature T and specific volume v. Variables and parameters from Eq. (11) are expanded in Table 2, in which v_r can be expressed by $1/\rho_r$.

Table 2: Expressions for the variables and parametrs of Eq. (11)

Y_r	$Y_{c,i}$	$\beta_{Y,ij}$	Y_{ij}
T_r	$T_{c,i}$	$\beta_{T,ij}$	$\beta_{T,ij}\gamma_{T,ij}\left(T_{c,i}T_{c,j}\right)^{0.5}$
v_r	$\frac{1}{\rho_{c,i}}$	$\beta_{v,ij}$	$\beta_{v,ij}\gamma_{v,ij}\frac{1}{8}\left(\frac{1}{\rho_{c,i}^{1/3}} + \frac{1}{\rho_{c,i}^{1/3}}\right)^3$

Bell & Lemmon [2] claimed that $\beta_{T,ij}$ and $\gamma_{T,ij}$ are the two most important parameters when fitting bubble-point data. Therefore, isobaric VLE data of each mixture was retrieved from the Internet using DETHERM [26] and other literature resources [28] to be included in the parameter tuning process in order to achieve a better description of the thermodynamic behaviour of the mixture.

The detailed expressions for α_{oi}^o, α_{oi}^r and α_{ij}^r are not given in this paper but can be found in the literature [12,13]. They include all the ideal and residual coefficients and exponents for both pure components and binary pairs. Ideal Helmholtz energy function - α_{oi}^o and α_{oi}^r have been well-established and optimised in the past. The departure function α_{ij}^r was neglected. Therefore, the parameters in these functions are considered to be non-adjustable thus not discussed in this work.

The benefit of the non-dimensionalised multi-fluid Helmholtz model is that all thermodynamic properties of a mixture or pure substance can be calculated from a combination of different derivatives of Eq. (6) [13]. For detailed information on calculating other thermodynamic properties using derivatives of Helmholtz energy, there is much literature available [12,13,24].

In this work, to optimise the interaction parameters of the Helmholtz model, the objective function was set to be the average sum of squares reduced error, and was minimized

$$\Delta_{ASSRE}(X) = \frac{1}{N} \sum_{i=1}^{N} \left(\frac{X_i - X_{i,fit}}{u(X)}\right)^2 \qquad (12)$$

where X is the property input - density ρ or mole fraction x at vapour-liquid equilibrium, and $u(X)$ is the uncertainty of the property.

The goodness of the fit on density was assessed using average absolute relative deviation and maximum absolute relative deviation

$$\Delta_{AARD}(\rho) = \frac{1}{N} \sum_{i=1}^{N} \left|\frac{\rho_i - \rho_{i,fit}}{u(\rho)}\right| \qquad (13)$$

$$\Delta_{MARD}(\rho) = max\left|\frac{\rho_i - \rho_{i,fit}}{u(\rho)}\right| \qquad (14)$$

where ρ_i is the experimental density of the mixture at a state point i, and $\rho_{i,fit}$ is the calculated density from the fitted model.

3.4.2 Excess Volume

In order to justify the validity of experimental measurements, excess volumes were also calculated, for their trends to be assessed by physical chemistry knowledge or to be compared with existing literature.

All experimental data were firstly interpolated or extrapolated to exact round values of pressure, using three-point Lagrangian interpolation [22]. The excess volume for each mixture at a specific temperature and pressure is calculated from

$$V_E = V_{mix} - x_1 V_1 - x_2 V_2 \qquad (15)$$

where V_E is excess molar volume, V_{mix} is molar volume of a mixture, x_i and V_i $[i \in 1,2]$ are mole fraction and molar volume of pure substances. Molar volumes can be calculated from measured densities as follows

$$V_{mix} = \frac{x_1 M_1 + x_2 M_2}{\rho_{mix}} \tag{16}$$

$$V_i = \frac{M_i}{\rho_i} \tag{17}$$

The two mole fractions are dependent, and x_1 can be replaced by $(1 - x_2)$ for the uncertainty calculation of excess molar volume in Section 3.6.

3.5 Calibration and Corrections

3.5.1 Calibration

The VTD was calibrated using vacuum and water as the calibration fluid (Section 3.4) to span a large range of densities from 0 to 1000 kg/m^3. In 2020 calibration, τ of water was measured at temperatures between 10C to 200 C and pressures from 1 MPa to 65MPa. In this work, τ of water was measured again under the same conditions. Since the deviation of τ from last year is 10^{-5} times of τ value itself, it was decided to make a correction by adding a modification function onto the original physically-based model instead of refitting the parameters. The modification equation was found to be linear with respect to temperature:

$$\Delta\tau = 1.7906 \times 10^{-4}\, T - 0.1548 \tag{18}$$

3.5.2 System Error Corrections

As suggested by Tay & Trusler [25] in 2018, in which sudy the same apparatus was used, there was a system error in density when comparing toluene densities calculated from the physically-based model with the ones calculated from NIST correlations developed by McLinden and Splett [17]. Therefore, system errors $\Delta\rho$ need to be added onto Eq. (2), which gives the follows

$$\rho = A\tau^2 - B + \Delta\rho \tag{19}$$

In this study, iso-octane densities obtained from experiment was also compared with that calculated from NIST reference correlation [18]. The blue dots in Figure 2 are the plotted system deviations in densities for both toluene and iso-octane against experimental densities.

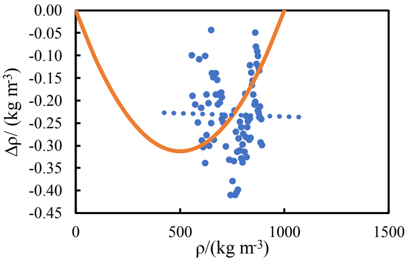

Figure 2: System error of ρ against experimental ρ for both toluene and iso-octane measurements where blue dots denote experimental data, orange curve was fitted with Eq. (20), and the dashed blue line is the linear trendline of experimental data.

It was considered to be more practical to have the system error go to zero at the two bounds of the valid range of density measurements where $\rho = 0$ and $\rho = \rho_w = 1000\ kg/m^3$. Therefore, the data was initially fitted using Eq. (20), assuming deviation is a function of density only

$$\Delta\rho = C[\rho(\rho_w - \rho)] \tag{20}$$

where C is a constant parameter fitted by the data and ρ_w is water density.

The resulting orange curve was plotted in Figure 2. However, since data available did not cover the full density range of the fitted curve, it cannot be considered to be a accurate representation of the deviation. For the density interval studied in this work, it was decided to use a linearly fitted trendline of the data (the blue dotted line) for simplicity, which is nearly horizontal with $\Delta\rho$ approximately = $-0.2209\ kg/m^3$. For future improvement, data of samples with lower densities can be added to the plot to explore the full picture of the deviation trend.

3.5.3 Temperature Corrections

Deviations in temperature readings were observed between the two thermometers. This was because the integrated thermostat of VTD measured the upstream T of the U-tube, which measurement would be influenced by temperature gradient as well as the stagnant fluid within the sensor, while the parallel thermometer was newly calibrated and directly measured T of fluid within the U-tube. Therefore, the latter was taken as the standard temperature reference. The deviations are consistent at each isotherm (see Figure 3), and this allows corrections to be made for all of the temperatures measured in this work and those measured in 2020 [27].

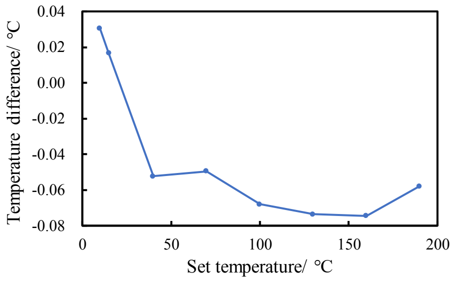

Figure 3: Temperature difference (temperature reading from the parallel thermostat minus temperature reading from Anton Paar master instrument) against set temperatures.

3.6 Uncertainties

The overall combined expanded uncertainty of measured densities is given by

$$U_c(\rho) = k\ \{\ u^2(\rho) + \left[\left(\frac{\partial\rho}{\partial p}\right)_{T,x} u(p)\right]^2 + \left[\left(\frac{\partial\rho}{\partial T}\right)_{p,x} u(T)\right]^2 + \left[\left(\frac{\partial\rho}{\partial x}\right)_{p,T} u(x)\right]^2 \}^{\frac{1}{2}} \qquad (21)$$

where $u(p)$, $u(T)$, and $u(x)$ are standard uncertainties of pressure, temperature, and the mole fraction of the more volatile component – iso-octane, respectively, and k is the coverage factor with approximately 95% of confidence level of the density distributions.

The density standard uncertainty is split into two parts

$$u^2(\rho) = u_A^2(\rho) + u_B^2(\rho) \qquad (22)$$

where $u_A(\rho)$ is Type A error produced by deviations of measured values, and $u_B(\rho)$ is Type B error caused by system deviations.

The standard uncertainty of density was evaluated differently in this work compared to previous works. For the previous work on n-octane [27], the Type A standard uncertainty of measured density $u_A(\rho)$ was calculated using the partial differentials of density with respect to τ and ρ of the two calibration fluids based on Gaussian error propagation [14] and Tay & Trusler's method [25].

In this work, only one calibration fluid was used as mentioned in Section 2 & Section 3.4.1. Therefore, the Type A uncertainty of the density measurements was assessed using Monte Carlo Simulations instead.

This was done by introducing disturbances to the calibration data on each temperature, pressure, and period of oscillations input data point as well as on the beta ratio. Random variables were extracted from normal distributions, with a mean of zero and standard deviations which are equal to the standard uncertainties of the variables as the disturbances. The standard uncertainties are either obtained from equipment specifications or previous studies [16] as shown in Table 3.

Table 3: Standard uncertainties of Monte Carlo variable inputs.

	T	p	τ	ε	β_τ/β_τ
unit	K	MPa	μs	-	
u	0.0025	0.020	0.01	0.0001	0.02

Moreover, the densities of the calibration fluid - water, that were used to fit the physically-based model parameters, were calculated from a highly accurate EoS which is a smooth mathematical function. Therefore, the uncertainties of these calibration densities calculated from the EoS were shifted by a common ratio ε [29], which was also extracted from a normal distribution with a standard deviation of ε.

By using the disturbed calibration data, a set of newly fitted parameters for the physically-based model were obtained. Then, several representative state points from the measurements of the sample mixtures were selected, i.e. data points at the lowest, medium and the highest pressures for each isotherm, to be substituted into the new model thus calculating a new density at each of these state points. Via repeating this process for 1000 times, a distribution of densities can be obtained at each state point. After that, an average standard deviation of these density distributions at each isotherm for different mixtures was calculated to represent the Type A uncertainty $u_A(\rho)$. This computationally demanding process was carried out in MatLab. Type B uncertainty $u_B(\rho)$ was calculated by taking the root-mean-square difference between densities of pure iso-octane measured and those calculated from McLinden and Splett's reference correlation from NIST [18].

To obtain $U_c(\rho)$, $u(x)$ was also calculated by applying Gaussian error propagation [14]

$$\sigma_q^2 = \sum_{i=1}^{n} \left(\frac{\partial q}{\partial x_i}\sigma_{xi}\right)^2 \qquad (23)$$

onto Eq. (1) for x_2 in Section 3.2 (the uncertainty of x_1 would be equivalent).

$u(x)$ is then expressed in terms of follows

$$u^2(x_2) = \left[\left(\frac{\partial x_2}{\partial m_1}\right)u(m_1)\right]^2 + \left[\left(\frac{\partial x_2}{\partial m_2}\right)u(m_2)\right]^2 \qquad (24)$$

where standard uncertainty for the mass measured $u(m)$ was estimated to be ±0.005 g as mentioned in Section 3.2. The resulting $u(x)$ value for each mixture can be found in Appendix B, Table B.1-B.3.

Gaussian error propagation was also applied to Eq. (15) to obtain standard uncertainty of excess volume

$$u^2(V_E) = \left[\left(\frac{\partial V_E}{\partial \rho_{mix}}\right)u(\rho)\right]^2 + \left[\left(\frac{\partial V_E}{\partial \rho_1}\right)u(\rho)\right]^2 + \left[\left(\frac{\partial V_E}{\partial \rho_2}\right)u(\rho)\right]^2 + \left[\left(\frac{\partial V_E}{\partial x_2}\right)u(x_2)\right]^2 \qquad (25)$$

The resulting $u(V_E)$ values for all mixtures at different conditions are tabulated in Table B.4-B.6.

4 Experimental Results and Discussions

4.5 Density

The experimental results of density are tabulated in Appendix B, Table B.1-B.3.

Type A error estimated via Monte Carlo Simulation and Type B symtatic error are 0.0718 kg/m^3 and 0.2847 kg/m^3, respectively. This shows that the Type B error dominates the expanded uncertainty of density $U_c(\rho)$ which equals to 0.59 kg/m^3. This value is similar to the uncertainty calculated by the previous user of the equipment, which is 0.53 kg/m^3 [27].

4.6 GERG-2008 Equation of State

Optimisations and analysis of GERG-2008 EoS were carried out on both Uko's n-octane data [27], and data from this experimental work. The model parameters were tuned using both the density data and the VLE data obtained from the literature [26]. It is important to note that there is a severe deficiency in the VLE data available for iso-octane-and-xylenes mixtures, whereas n-octane-and-xylenes mixtures have an abundance of experimental data for VLE. Thus in this research, most of the characteristics of the GERG-2008 Helmholtz model were investigated using Uko's n-octane mixture data [27]. Two large sets of isobaric VLE data were used for n-octane-and-xylenes mixtures with more than 20 data points in each set, while only one small set of isobaric VLE data were found for both iso-octane with m and p-xylenes mixtures with only 12 data points in each set. No VLE data was found for the iso-octane-and-o-xylene mixture, thus the model for this mixture was purely tuned based on density data, which will be addressed later in this paper. The number of data points significantly influence the optimisation quality and the value of Δ_{ASSRE}.

A comparison of different numbers of tuned parameters of the Helmholtz model with different sets of VLE data is shown in Table A.2 of Appendix A with the average and maximum absolute relative deviations of densities. Table 4 shows that there is a great enhancement in the accuracy of density prediction by tuning the model parameters and by including more VLE data, especially when all four binary interaction parameters were optimised using all data prepared - density data and 2 sets of VLE data. The Δ_{AARD} of density were reduced to less than 0.088%. It also can be noticed that the tuned models sometimes failed to predict the mole fractions of components at VLE. This happened mostly when no or less VLE data was present while tunning the model. Although the models for iso-octane with m and p-xylenes with no VLE data did successfully generate T,x,y diagrams of VLE, the accuracy was still poor with Δ_{ASSRE} greater than 2000. The iso-octane-o-xylene mixture seems to give an incredibly small Δ_{ASSRE} in comparison to the other two, but this was because there was no VLE data included thus no contribution of errors from the failure of VLE prediction in this case. Hence, there was no point in continuing with tuning 4 parameters when information is lacking. However, this does not mean the models developed by only density data or a few VLE data should be abandoned. Despite their failures in estimating VLE, they still demonstrate highly-accurate predictions of densities only. For example, iso-octane and o-xylene mixtures as shown in Figure 5 and Figure 6. The models tuned by 4 optimised parameters with as much VLE data as possible are generally more robust and able to predict a broader range of thermodynamic properties, hence they were considered to be the best ones for application.

In summary, there were four main discoveries during the optimisation of the Helmholtz model:

- The more experimental data points used, in terms of both amounts and types, the better the prediction can be achieved by tunning the Helmholtz model parameters. Certainly, there will be a limit where an increase in the amount of data does not improve accuracy anymore.
- To predict VLE properties, experimental VLE data is indispensable to fit Helmholtz model parameters.
- With the same data set, the more parameters are tuned, the better the predictions in general, and more importantly, the model is less likely to fail to predict VLE.
- More parameters tuned does not necessarily mean that there must be a more accurate prediction, especially when data is lacking.

Table 4: A simplified version of Table A.2 in Appendix A with the uncertainties of densities calculated by the original and various of optimised Helmholtz model. All mixtures of n-octane or iso-octane with each xylene were compared, and only the maximum deviations are shown. Δ_{ASSRE} shown here is not the objective function used, instead, it evaluates the accuracy of fitting all available data no matter how much has been used as the optimisation inputs. Δ_{AARD} and Δ_{MARD} only assess the goodness of fit for density data only. '$-$' under Δ_{ASSRE} means that the model failed to generate a VLE graph in some cases.

	Original Parameters + 2 VLE	**2 Tuned Parameters + 0 VLE**	**2 Tuned Parameters + 1 VLE**	**2 Tuned Parameters + 2 VLE**	**4 Tuned Parameters + 1 VLE**	**4 Tuned Parameters + 2 VLE**
$\Delta_{ASSRE}(\rho)$	$\leq$ 3533.140	$-$	$-$	$-$	$\leq$ 480.521	$\leq$ 29.475
$\Delta_{AARD}(\rho)$	$\leq$ 0.531%	$\leq$ 0.490%	$\leq$ 0.430%	$\leq$ 0.350%	$\leq$ 0.151%	$\leq$ 0.088%
$\Delta_{MARD}(\rho)$	$\leq$ 1.185%	$\leq$ 0.835%	$\leq$ 0.785%	$\leq$ 0.760%	$\leq$ 0.447%	$\leq$ 0.344%

There are several defects while fitting the model parameters, some of which were also addressed in Bell & Lemmon's paper [2]:

- The Excel Solver uses Generalized Reduced Gradient (GRG) algorithm which gets stuck at a local optimum without finding the global optima. It also stops the search early if it finds the objective function improves slowly [34]. This is a possible reason why some models failed to predict VLE and their parameters stayed unchanged even when more data is included.

- The objective function is not continuously differentiable with respect to the parameters.
- The accuracy of the VLE experimental data and the uncertainties given by the literature authors are doubtful. Therefore, the uncertainties that were too idealised were adjusted beforehand.

An example of T,x,y diagram of n-octane-and-o-xylene fitted with Helmholtz models is shown below in Figure 4.

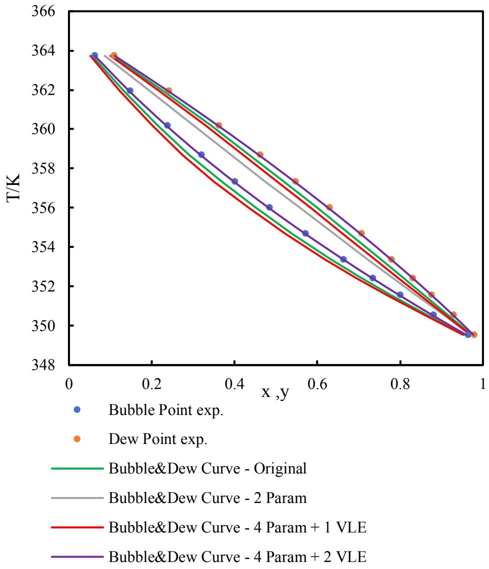

Figure 4: T,x,y phase equilibrium diagram for n-octane-and-o-xylene mixture. The bubble and dew curves that were fitted by the same number of parameters and VLE data sets have the same color, while the grey line was the results of failed models.

By viewing Figure 4 and Table A.2 together, readers can perceive that for the iso-octane-and-o-xylene mixture, the model (the grey line) failed to predict when only two parameters were tuned no matter how much VLE information was included. Also, the most accurate discription of the VLE data was indeed made by the model optimised with 4 parameters and 2 sets of VLE data. This demonstrates the third point emphasized in the four main discoveries that by tuning 4 parameters rather than 2 the model was generally better and less likely to fail. On the other hand, as shown by the red lines in Figure 4, the optimised model with 4 parameters and 1 sets of VLE data was actually worse than the original model which also matches the fourth discovery mentioned before.

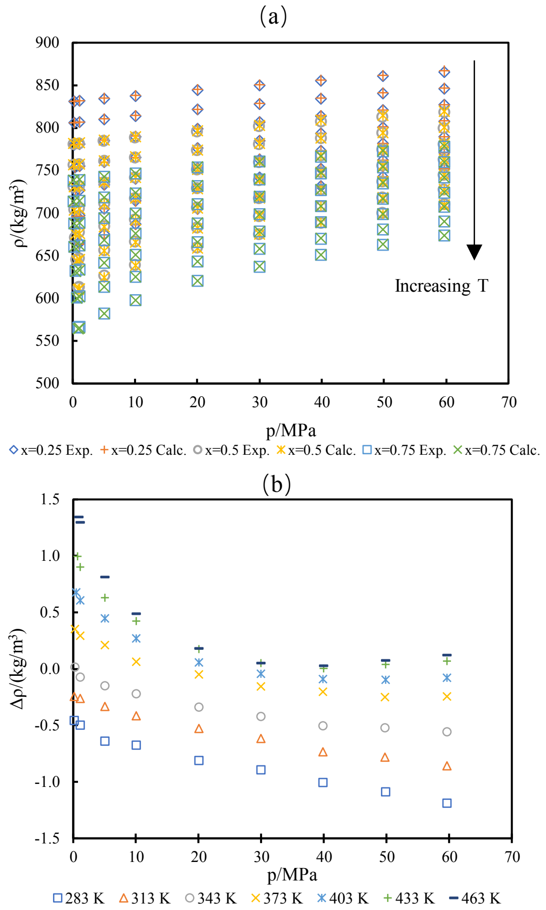

Figure 5: Comparisons of experimental and calculated densities. (a) density against pressure (b) density deviations of the fitted Helmholtz model from the experimental densities for iso-octane + o-xylene mixtures.

Figure 5.a & 5.b are example graphs of how much Helmholtz-predicted density deviates from the experimental values even when there was no VLE data to tune the model. The calculated densities overlap the experimental densities well in Figure 5.a., and the absolute deviations are very systematic at each isotherm which are within ±1.5 kg/m^3.

4.7 Excess Volume

The calculated excess volumes and their uncertainties can be found in Appendix B Table B.4-B.6. Graphs of excess volumes were plotted against mole fractions for all mixtures' intermolecular behaviours to be observed and reliability of density measurements to be assessed. An example graph for iso-octane-and-o-xylene mixture at 373.15 K is given in Figure 6, where dots represent the excess volumes calculated from experimental density data, and curves represent those densities predicted by the best Helmholtz model optimised for the mixture, which were drawn using Redlish-Kister polynomials [7].

Example graphs for the other iso-octane and o-xylene mixtures at all the other isotherms are provided in Appendix B, Figure B.1.

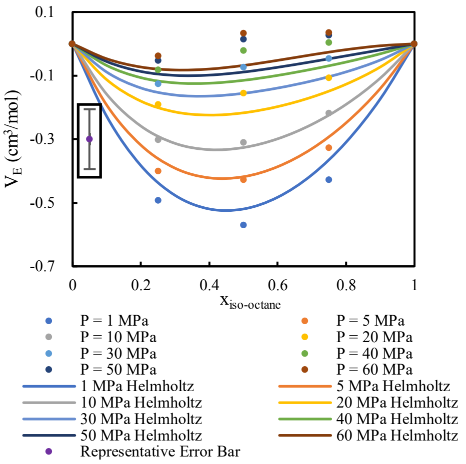

Figure 6: Comparison of excess volumes calculated from experimental density data (data points), with those predicted by the best Helmholtz model optimised for the mixture (curves), for iso-octane-and-o-xylene mixtures at 373.15 K.

By looking at the shape formed by the dots in Figure 6, convex parabolas were generally observed, which means that there are attractions between the molecules. This parabolic shape is less obvious at lower temperatures (Appendix B, Figure B.1) since the excess volumes are smaller. As the error bars are relatively large in comparison to the size of these curves at lower temperatures, the shape deviates more from a normal parabola.

The attractive behaviour is possibly due to the London force and a good packing efficiency between the two nearly non-polar molecules. Unfortunately, studies on excess volumes of iso-octane-and-xylene mixtures are scarce. Therefore, more investigations are needed in the future to further prove the trend obtained in this study. However, the regular and consistent trend is good proof of the reliability of the measured data.

By drawing the curves in Figure 6 and Figure B.1 using the Helmholtz model, their deviations from experimental data are shown graphically. These deviations are generally smaller than the representative error bars, which again shows a good density prediction by the model.

5 Conclusion

Iso-octane-and-xylene mixtures are useful in many industries, for example, oil industries, which makes it crucial for their thermodynamic properties to be accurately predicted, especially under HPHT conditions. So far there have been numerous EoS models developed for thermodynamic property predictions including density, but most of them are not applicable at HPHT. GERG-2008 EoS (based on Helmholtz energy) was considered as a suitable and accurate model, in which the binary interaction parameters can be adjusted for mixtures of iso-octane or n-octane with xylenes to predict thermodynamic properties. Therefore, in this study, a VTD was used for density measurements. At various iso-octane mole fractions, densities were calculated in terms of T, p, and τ using the working equation of the VTD. M-xylene and o-xylene mixtures were both studied at temperatures from 283.15K to 463.15K and pressure up to 60 MPa, while for p-xylene mixtures, the lowest temperature and highest pressure were adjusted to 288.15K and 30 MPa respectively to prevent solidification. Then, the Helmholtz model was optimized using the experimental density data and VLE data from literature. An investigation of how the number of parameters and number of VLE data sets influence the model was conducted. Several key conclusions were drawn from the trial optimisations. In general, by increasing the number of tuned parameters and the amount of input data, the goodness of fit was improved. The amount of input VLE data holds more importance in improving accuracy, while the number of parameters tuned is more helpful in preventing the model to fail to predict VLE. Graphs of excess volumes against mole fractions were plotted using measured densities. A regular and consistent trend of convex parabolas was obtained, which verified the reliability of the density data, and at the same time helped with learning more about the interactions between the molecules.

6 Future Improvements

Several improvements can be made to this study in the future.

First of all, highly accurate boiling experiments can be conducted to obtain more VLE data for iso-octane-and-xylene binary mixtures to expand the database for tuning the Helmholtz model, preventing the model from failing to predict VLE properties.

Secondly, better software and methods such as Matlab Global Optimization Toolbox, GAMS (BARON Solver), LINDO, and ANTIGONE, can be used to fit parameters rather than Excel Solver. However, as the deviations of predictions from the measurements are already small, using a more rigorous optimizer would not make a big difference to the results of this research.

Furthermore, it is also helpful to gather data for other thermodynamic properties in order to both test and improve the model's robustness, versatility, and applicability. For example, sound speed is a valuable property to be measured [25].

When the Helmholtz model optimised by tuning 4 parameters is unable to predict thermodynamic properties with an acceptable range of deviations (the expanded uncertainty of the data), even when enough data is available, it is necessary to include and design a departure function for the Helmholtz model. Although this did not happen on the mixtures of iso-octane and xylenes which are nearly ideal, this can happen in the future when people try to tune the Helmholtz model for other non-ideal mixtures. This will make the tuning process more computationally demanding, where better software might be needed.

Nevertheless, the same departure function α_{ij}^{r} is expected to work for a family of mixtures (e.g. iso-octane with all xylenes) due to their similar intermolecular behaviours, and only F_{ij} needs to be adjusted for each binary pair.

7. References

[1] I. Bell, A. Jäger, Helmholtz Energy Transformations of Common Cubic Equations of State for Use with Pure Fluids and Mixtures, Journal of Research of the National Institute of Standards and Technology. 121 (2016) 238.

[2] I.H. Bell, E.W. Lemmon, Automatic Fitting of Binary Interaction Parameters for Multi-fluid Helmholtz-Energy-Explicit Mixture Models, Journal of Chemical and Engineering Data. 61 (2016) 3752–3760.

[3] D. Blankschtein, Lectures in Classical Thermodynamics with an Introduction to Statistical Mechanics, 1st ed., Springer International Publishing, Cham, 2020.

[4] D. Bose, Design Parameters for a Hydro desulfurization (HDS) Unit for Petroleum Naphtha at 3500 Barrels per Day, World Scientific News. (2015).

[5] C. Bouchot, D. Richon, An enhanced method to calibrate vibrating tube densimeters, Fluid Phase Equilibria. 191 (2001) 189–208.

[6] N.R. Council, Xylene, in: Emergency and Continuous Exposure Limits for Selected Airborne Contaminants: Volume 2, The National Academies Press, Washington, DC, 1984: pp. 113–113.

[7] D. Das, Z. Barhoumi, N. Dhouibi, M.A.M.K. Sanhoury, N. Ouerfelli, The reduced Redlich–Kister equations for correlating volumetric and viscometric properties of N,N-dimethylacetamide + dimethylformamide binary mixtures at temperatures from 298.15 to 318.15 K, Physics and Chemistry of Liquids. 50 (2012) 712–734.

[8] D.J. Dotson, Uses of Xylene, Sciencing.Com. (2018).

[9] J.F. Estela-Uribe, M.A. De, J.P.M. Trusler, Extended corresponding states model for fluids and fluid mixtures II. Application to mixtures and natural gas systems, FLUID PHASE EQUILIBRIA. 216 (2004) 59–84.

[10] J.F. Estela-Uribe, J.P.M. Trusler, Extended corresponding states model for fluids and fluid mixtures I. Shape factor model for pure fluids, FLUID PHASE EQUILIBRIA. 204 (2003) 15–40.

[11] C.D. Holcomb, S.L. Outcalt, A theoretically-based calibration and evaluation procedure for vibrating-tube densimeters, Fluid Phase Equilibria. 150–151 (1998) 815–827.

[12] O. "Kunz, R. "Klimeck, W. [Ruhr-U.B. (Germany)]" "Wagner, M. [E. O.R.A.G. "Jaeschke Dorsten (Germany)]," The GERG-2004 wide-range equation of state for natural gases and other mixtures, VDI-Verlag, Duesseldorf (Germany), Germany, 2007.

[13] O. Kunz, W. Wagner, The GERG-2008 Wide-Range Equation of State for Natural Gases and Other Mixtures: An Expansion of GERG-2004, Journal of Chemical & Engineering Data. 57 (2012) 3032–3091.

[14] E. Lo, GAUSSIAN ERROR PROPAGATION APPLIED TO ECOLOGICAL DATA: POST-ICE-STORM-DOWNED WOODY BIOMASS, Ecological Monographs. 75 (2005) 451–466.

[15] V. Majer, A.A.H. Padua, Measurement of density with vibrating bodies, in: A.R.H. Goodwin, K.N. Marsh, W.A. Wakeham (Eds.), Measurement of the Thermodynamic Properties of Single Phases: Experimental Thermodynamics. Volume VI, Elsevier, Amsterdam ;, 2003: pp. 149–168.

[16] E.F. May, W.J. Tay, M. Nania, A. Aleji, S. Al-Ghafri, J.P. Martin Trusler, Physical apparatus parameters and model for vibrating tube densimeters at pressures to 140 MPa and temperatures to 473 K, Review of Scientific Instruments. 85 (2014) 095111.

[17] M. McLinden, J. Splett, A Liquid Density Standard Over Wide Ranges of Temperature and Pressure Based on Toluene, (2008).

[18] M.O. McLinden, J.D. Splett, Certification Report for SRM 2214: Density of Iso-octane for Extended Ranges of Temperature and Pressure, Boulder, CO, 2016.

[19] M. Mesbah, A. Bahadori, Chapter Two - Equations of State, in: A. Bahadori (Ed.), Fluid Phase Behavior for Conventional and Unconventional Oil and Gas Reservoirs, Gulf Professional Publishing, Boston, 2017: pp. 65–116.

[20] D.-Y. Peng, D.B. Robinson, A New Two-Constant Equation of State, Industrial & Engineering Chemistry Fundamentals. 15 (1976) 59–64.

[21] S. Rulhoff, iso-Octane, Haltermann Carless. (2021).

[22] K.N. Saniee, A Simple Expression for Multivariate Lagrange Interpolation, in: 2008.

[23] J. v. Sengers, M. Klein, eds., The Technological Importance of Accurate Thermophysical Property Information, in: Proceedings of a Session of the Winter Annual Meeting of the American Society of Mechanical Engineers Held in New York, NY, December 6, 1979, The National Bureau of Standards, New York, 1979.

[24] R. Span, Multiparameter Equations of State, 1st ed., Springer Berlin Heidelberg, Berlin, Heidelberg, 2000.

[25] W.J. Tay, J.P.M. Trusler, Density, sound speed and derived thermophysical properties of n-nonane at temperatures between (283.15 and 473.15) K and at pressures up to 390 MPa, (2018).

[26] The PSDS Team, "We wish to acknowledge the use of the EPSRC funded Physical Sciences Data-science Service hosted by the University of Southampton and STFC under grant number EP/S020357/1.," (n.d.).

[27] D. Uko, Density and Equation of State model for mixtures of binary mixtures of n-octane with m-xylene, p-xylene and o-xylene from 283.15 K to 463.15 K at pressures up to 60 MPa, London, 2020.

[28] T.E. Vittal Prasad, N. Sriram, A.N. Raju, D.H.L. Prasad, (Vapor+liquid) equilibria of binary mixtures formed by iso-octane with a variety of compounds at 95.8kPa, The Journal of Chemical Thermodynamics. 38 (2006) 119–122.

[29] W. Wagner, A. Pruß, The IAPWS Formulation 1995 for the Thermodynamic Properties of Ordinary Water Substance for General and Scientific Use, Journal of Physical and Chemical Reference Data. 31 (2002) 387–535.

[30] L.B. Young, What Is Xylene Used For, ReAgent. (2021).

[31] NIST Reference Fluid Thermodynamic and Transport Properties Database (REFPROP): Version 10, NIST. (2013).

[32] Anton Paar USA Inc. Homepage, (2021).

[33] CHANDLER ENGINEERING Homepage, (2021).

[34] STANDARD EXCEL SOLVER - LIMITATIONS OF NONLINEAR OPTIMIZATION, Frontline Solvers. (2021).

Imperial College London

Department of Chemical Engineering

Sulphur-doped Hard Carbons as Sodium-Ion Battery Anodes

Author:
Will Cahill

Supervisor:
Prof. Magda Titirici
Maria Crespo Ribadeneyra
Jesus Barrio Hermida

December 2021

Abstract

Previous work has shown that hard carbons hold considerable promise as an anodic material for sodium-ion batteries (SIB). Short graphitic domains, defects, edges, enlarged interlayer spacing and the presence of pores give hard carbons significant potential in terms of sodium storage capacity. A new and exciting way of tuning the electrochemical characteristics of these hard carbons, is *via* heteroatom doping. In recent years, work has been done presenting sulphur-doped hard carbons as sodium-ion battery anodes, showing that doped sulphur can considerably increase the activity towards sodium ions, and hence increase the specific capacity of hard carbons. It has also been shown that sulphur atoms will interconnect the pore structure of the carbon, while also enlarging interlayer distances that connect the pores, which is crucial for sodium-ion storage. This report focuses on a new sulphur-doped hard carbon material, synthesised from pure sulphur and hexaketocyclohexane (HKH). This material was characterised using XPS, and these results were then used to develop a reaction mechanism and to suggest a structure of the carbon material. Electrodes were then formed from this new material, and were tested in half-cells utilising sodium metal as the counter-electrode. The surface area and the conductivity of the materials was varied, and the effect that these variables had on its electrochemical performance was measured. It was predicted that sulphur doping these hard carbons would increase their specific capacity as anodes, and that the introduction of porosity and conductivity into these materials would also have a positive effect on their specific capacity. It was shown that this new hard carbon material can reach a significantly large specific capacity of 953.4 mAh.g^{-1} in the case where both porosity and conductivity were introduced, but there are significant issues with irreversibility and solid-electrolyte interphase (SEI) formation.

1 Introduction

Global warming and the impending climate crisis mean that traditional, unsustainable forms of energy - such as coal, oil and gas - will need to be phased out, and replaced with new, sustainable energy sources - such as wind and solar power. Due to the inclemency of these energy sources, demand for large-scale energy storage for "load-levelling" is going to increase considerably within the next few years [1].

Lithium-ion batteries (LIB) have been the leading energy storage system in portable electronic devices and electric vehicles for a number of years, but concerns have been raised over its sustainability - lithium supplies are short and are often found in remote and politically sensitive places [2][3]. This therefore means that LIB are not an attractive solution to large-scale energy storage.

Recently however, there has been a renewed interest in sodium-ion batteries (SIB) as a possible solution to this problem. Sodium has similar chemical properties to lithium, as well as a greater abundance and lower cost, meaning that SIB hold considerable promise for large-scale energy storage applications.

In standard electrolytes sodium cannot intercalate into graphite - the traditional anodic material used in LIB - to any useful extent [4]. Because of this, research efforts in the field of SIB have focused mainly on synthesising new and effective anode materials. In 2000, Stevens and Dahn showed that sodium can intercalate effectively into hard carbons with two suggested mechanisms [5]. They suggested that a sloping region in the galvanostatic charge/discharge curve was due to intercalation of sodium ions into the interlayers of graphitic domains, and that a plateau region was formed due to insertion of sodium ions within nanopores. More recently, it has been shown that there is a relationship between the size of the nanopores and interlayer distance, dependent on the pyrolysis temperature [4].

An exciting way of tuning the physicochemical properties of these promising hard carbons is heteroatom doping [6]. Doping with atoms such as sulphur will significantly improve the sodium-ion storage capacity in hard carbon anodes, and can be used to tune interlayer distances in graphitic domains, contributing to a longer cycling performance in SIB [6].

Z. Hong et al. [7] used a molten salt method of doping to show that sulphur-doping hard carbons with fewer defects results in a hard carbon with a larger interlayer distance as sulphur will favourably dope within the interlayer of the graphitic domains. It was also shown that when doping in a hard carbon with lots of defects, sulphur will favourably dope at defect sites, forming a hard carbon with a shorter interlayer distance. Here is was shown that the interlayer distance and pore inter-connectivity of hard carbons can be carefully controlled by choosing suitable hard carbons - these factors begin of prime importance for sodium-ion interstion. This sulphur-doped hard carbon had a stable reversible capacity of 200 mAh.g^{-1} after 400 cycles at 1 A.g^{-1}, showing an incredible improvement to the cycling performance of SIB which Z. Hong et al. [7] attributed to the increased activity towards sodium-ions due to sulphur doping, as well as an enlarged interlayer distance between graphitic domains.

Yu Zhang et al. [6] also synthesised sulphur-doped hard carbons *via* a molten salt method for use in potassium-ion batteries (KIB). It was shown that a hard carbon with a high sulphur content (25.8 wt%) was synthesised, showing a high specific capacity of 361.4 mAh.g^{-1} during the first cycle, and of 317.7 mAh.g^{-1} during the 100th cycle at 0.05 A.g^{-1}.

This study will investigate a new, direct method to synthesise sulphur-doped hard carbons for use as SIB anodes, exhibiting a high sulphur loading at relatively low experimental temperatures. This method involves melting hexaketocyclohexane (HKH) together with sulphur to form a sulphur-bridged precursor, and then a subsequent pyrolysis step to form the sulphur-doped hard carbon. The effect of surface area/porosity of these materials on their electrochemical performance was evaluated by adding a magensium chloride template before pyrolysis, and the effect of conductivity was evaluated by adding carbon black to some samples. This new material was characterised and then electrochemically tested.

2 Experimental Section

2.1 Materials Synthesis

Control samples (i.e. no sulphur doping) were synthesised by pyrolising HKH at 800 °C, at a heating rate of 5 °C.min^{-1}, under an atmosphere of nitrogen. Throughout this report, these samples are referred to as HKH materials. CS-1 materials (sulphur-doped hard carbons) were synthesised by first melting together a 1:1 molar ratio of HKH and sulphur until a homogeneous liquid mixture is formed. This mixture was then left to cool overnight before being pyrolised at 800 °C. All materials synthesised with the magnesium chloride template were thoroughly ground together with magneisum chloride before being pyrolysed. After pyrolysis, the templated materials were then washed thoroughly overnight overnight with a 2M hydrochloric acid solution to remove any excess magnesium chloride, before being filtered and dried overnight at 80 °C in a vacuum oven.

-	**Without $MgCl_2$**	**With $MgCl_2$**
No Sulfur	HKH-800	HKH-800-$MgCl_2$
With Sulphur	CS_1-800	CS_1-800-$MgCl_2$
No S + Carbon Black	HKH-800-CB	HKH-800-$MgCl_2$-CB
S + Carbon Black	CS_1-800-CB	CS_1-800-$MgCl_2$-CB

Table 1: Table of synthesised materials and nomenclature

2.2 Materials Characterisation

XPS analysis was conducted using a Thermo Fisher K-Alpha XPS system and the resulting spectra were analysed using Avantage software. To account for charging effects, all spectra were calibrated relative to the carbon C1s peak at 284.8 eV.

2.3 Electrochemical Characterisation

Electrodes were prepared from slurries of 90 wt% hard carbon and 10 wt% carboxymethyl cellulose (M_w 250,000 Sigma Aldrich) in water. Electrodes with a conductive additive were prepared from slurries of 85 wt% hard carbon, 5 wt% carbon black (99.9% Sigma Aldrich) and 10 wt% carboxymethyl cellulose binder. The slurry was then spread evenly (2 mg.cm^{-2}) over aluminium foil (conductive carbon coated, 18 μm, MTI Corporation). Electrodes were cute using a template and a scalpel to 1 cm^2 and then placed in a vacuum oven to dry overnight at 80 °C, before being placed in a glovebox for final assembly.

The preparation of coin cells for testing was carried out in an argon-filled glovebox. A previously assembled carbon anode and a glass fibre separator (Whatman GF/A glass microfibre, 18 mm diameter) that was saturated with $NaPF_6$ electrolyte (150 μL), were placed in a CR2032 coin cell along with a circular sodium metal sheet (Sodium ingot, 99.8% metal basis, Alfa Aesar).

Galvanostatic charge/discharge curves and the rate capability of the cells were measured using a BaSyTec CTS battery testing system in the potential window of 0.005-2.5 V, at C-rates from 0.1-2 c.

3 Results and Discussion

3.1 Materials Characterisation

Firstly, after analysing XPS results, it was shown that there is up to 8 wt% sulphur incorporation into hard carbons using this technique. Figure 1 a shows the C1s spectrum of HKH before any chemical reaction, and Figure 1 b shows the C1s spectrum of the HKH-Sulphur precursor (the material formed when HKH and sulphur are melted together). Figures 1 c and d show the C1s and S2p spectra of the CS-1-800 sulphur-doped hard carbon respectively.

Figure 1 a shows an expected C1s spectrum of pure HKH. When HKH is melted together with sulphur, it forms what is referred to in this report as the HKH-S precursor, and it is shown in Figure 1 b will start to form C-S bonds as shown via a peak at 287.5 eV. As well as sulphur-carbon bonds, the C1s spectrum of the HKH-S precursor exhibits peaks at 289 eV and 285 eV, corresponding to C=O and C-C bonds respectively. This suggests that there is a cross-linking of HKH molecules through diphenyl-sulphide bridges.

Figure 1 c shows the C1s spectrum of the HKH-S precursor after it has been ground together with $MgCl_2$ (which serves as a pore template during the carbonisation of the precursor), and pyrolysed at 800 °C. This spectrum shows that the peak at 298 eV - corresponding to C=O bonds- has decreased considerably in intensity, while the peak at 285 eV has increased in intensity. As well as this, a peak at 287.5 eV, and a

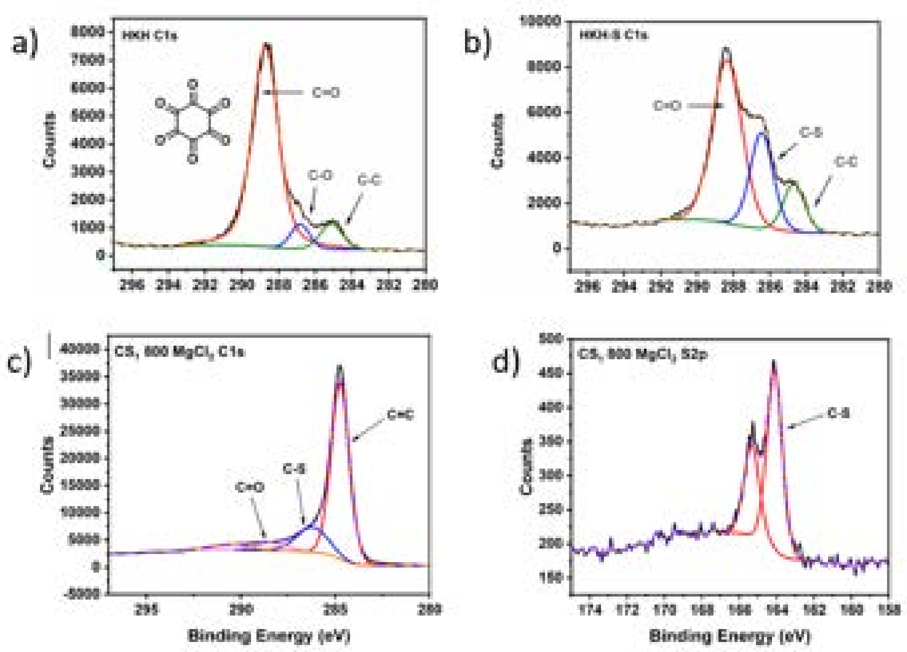

Figure 1: XPS Spectra for a) Hexaketocyclohexane (HKH), b) HKH-S precursor, c) C1s spectrum for CS1-800, d) S2p spectrum for CS1-800

strong peak at 164 eV in the S2p spectrum of CS1, suggest that C-S bonds are still present in the final material. This suggests a possible mechanism for the formation of the CS1 material. When the HKH-S precursor is pyrolysed, the disordered matrix of sulphur-bridged HKH molecules will start to form a more regular structure, the C=O bonds being broken and replaced with C-C bonds, forming short, graphitic domains, interspersed with doped sulphur atoms. Figure 2 shows a chemical diagram of the suggested CS1 formation mechanism, provided by Jesus Barrio Hermida.

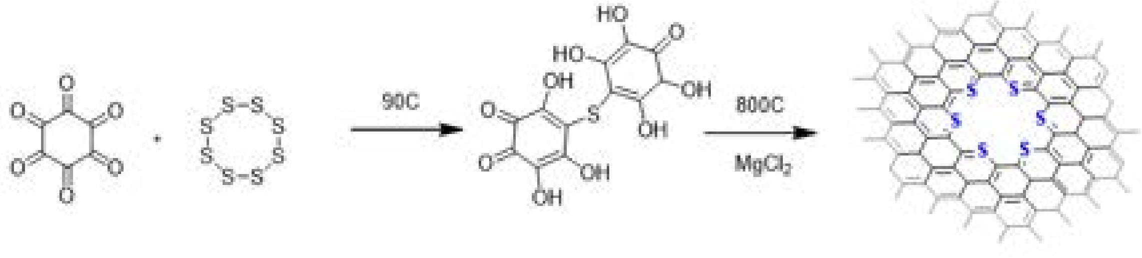

Figure 2: Chemical diagram of suggested mechanism for the formation of CS1

3.2 Electrochemical Performance

The electrochemical performance of the sulphur-doped carbon materials was carried out in a half-cell, using sodium metal as the counter electrode. Shown in Figure 3 are the galvanostatic charge/discharge curves for all the tested carbon materials. These profiles were obtained in a voltage window of 0.005-2.5 V and at a c-rate of 0.1 c.

Figures 3 a) and b) show the galvanostatic charge/discharge curves for HKH and CS-1 pyrolysed at 800 °C respectively. In the case of HKH (i.e. no doped sulphur), the 1^{st} cycle reaches a specific capacity of 341 mAh.g^{-1}, dropping down to a specific capacity of 158.7 mAh.g^{-1} during the 5^{th} cycle. For CS-1 (the sulphur doped carbon material), the specific capacity during the 1^{st} cycle is 363 mAh.g^{-1}, while during the 5^{th} cycle it drops to 167.1 mAh.g^{-1}. Although the increase in specific capacity between the two samples is not significantly large, this increase may be attributed to the greater activity towards sodium ions caused by sulphur doping. In both cases, the majority of the capacity is seen to be slope capacity, and there is significant irreversibility in the 1^{st} cycle. Since pyrolysis of hard carbons at a lower temperature results

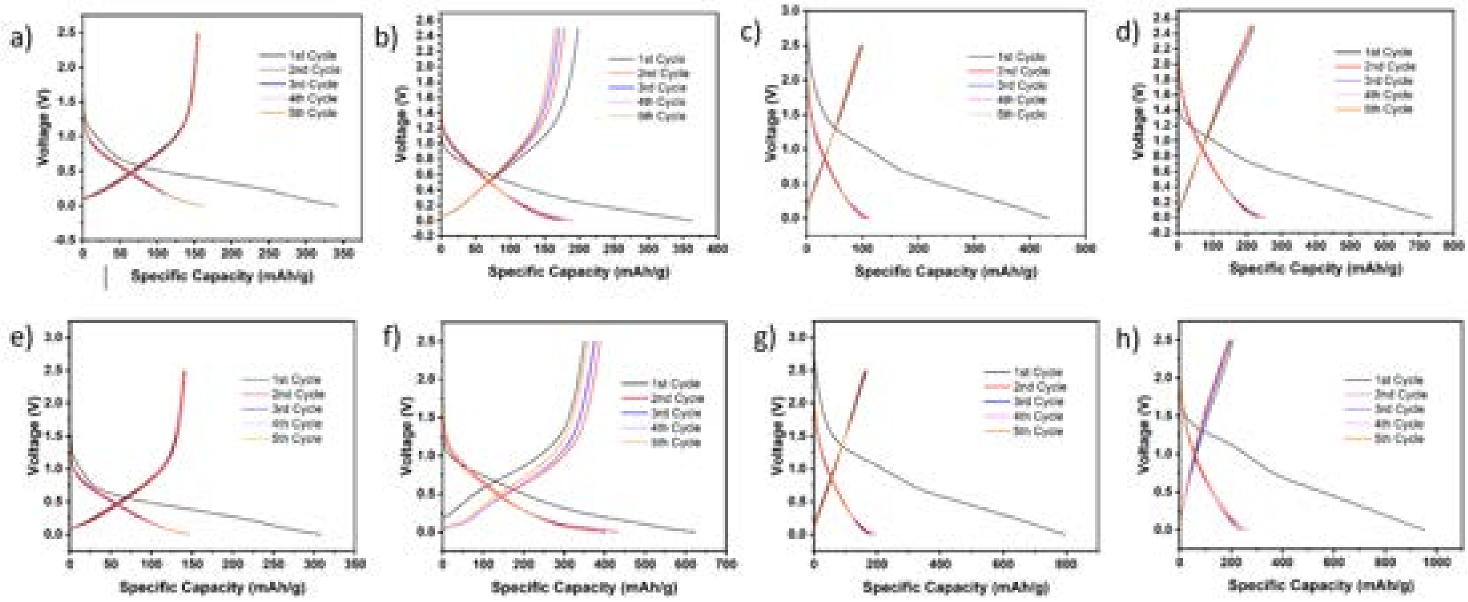

Figure 3: Fig. X Galvanostatic charge/discharge profiles for a) HKH-800, b) CS-1-800, c) HKH-800-$MgCl_2$, d) CS-1-800-$MgCl_2$, e) HKH-800 + Carbon Black, f) CS-1-800 + Carbon Black, g) HKH-800-$MgCl_2$ + Carbon Black, h) CS-1-800-$MgCl_2$ + Carbon Black

in a carbon with a less ordered structure and a higher surface area for solid-electrolyte interphase (SEI) formation[4], this result is expected.

Figures 3 c) and d) show the galvanostatic charge/discharge profiles of the HKH and CS-1 materials, but with a magnesium chloride template added before pyrolysis. The 1^{st} cycle specific capacity of the CS-1 material and the HKH material is 736.5 mAh.g^{-1} and 434.8 mAh.g^{-1} respectively, dropping down to 223.8 mAh.g^{-1} and 101.4 mAh.g^{-1}. This shows a large increase in capacity compared to the carbon materials *without* the magnesium chloride template. This increase can be attributed to an increase in surface area due to the addition of magnesium chloride. A larger surface area creates a larger amount of surface that can react with sodium ions, increasing the sodium ion storage and hence the specific capacity. There is also an increase in specific capacity between the HKH and CS-1 materials in this instance which can once again be attributed to an increase in activity of the carbon material due to doped sulphur. The irreversibility in this case is much higher. This can also be attributed to the increased surface area formed through the magnesium chloride template, which would have increased SEI formation and sodium ion trapping at defect sites during the 1^{st} cycle. The irreversibility and the slope capacity can also be partially attributed to the low pyrolysis temperature, for reasons discussed previously.

Figures 3 e) and f) show the galvanostatic charge/discharge profiles of the HKH and CS-1 materials *without* the magniesum chloride template, but with carbon black added to increase the conductivity of the carbon material. The 1^{st} cycle specific capacity of the CS-1 material is 623.3 mAh.g^{-1}, dropping to a specific capacity of 378 mAh.g^{-1} during the 5^{th} cycle. This shows an expected increase in specific capacity compared to the CS-1 material without a conductive additive. The conductive additive allows sodium ions and electrons to move more quickly and freely through the carbon material, allowing for a greater amount of sodium storage, and hence a larger capacity. The 1^{st} cycle specific capacity of the HKH material is 308.2 mAh.g^{-1}, a lower capacity than the HKH material *without* a conductive additive. This is an experimental anomaly, most likely caused by the very small amount of HKH material - and hence carbon black - used to synthesise the electrodes. The increase in capacity between the HKH and CS-1 material in this case, can be attributed to doped sulphur within the CS-1 material. Once again, the irreversibility and the slope capacity can be partially attributed to the low pyrolysis temperature, for reasons didcussed previously.

Finally, Figures 3 g) and h) show the HKH and CS-1 materials with the magnesium chloride template *and* the carbon black conductive additive. As shown in both of these figures, the 1^{st} cycle specific capacity of both of the carbon materials is the highest, the specific capacity for CS-1 and HKH reaching 953.4 mAh.g^{-1} and 795.9 mAh.g^{-1} respectively. This is to be expected as the materials benefit from the increased surface area from the magnesium chloride template, and also the increased conductivity from the carbon black additive, both contributing to a large increase in the specific capacity. However in both cases, the irreversibility is high, the specific capacity dropping to 258.8 mAh.g^{-1} and 171.7 mAh.g^{-1} for the CS-1 and HKH material respectively. This can once again be attributed to the high surface area, causing a large amount of SEI formation and sodium ion trapping in the first cycle. As before, there is an increase in the specific capacity between the HKH and CS-1 material in this case, attributed to sulphur doping.

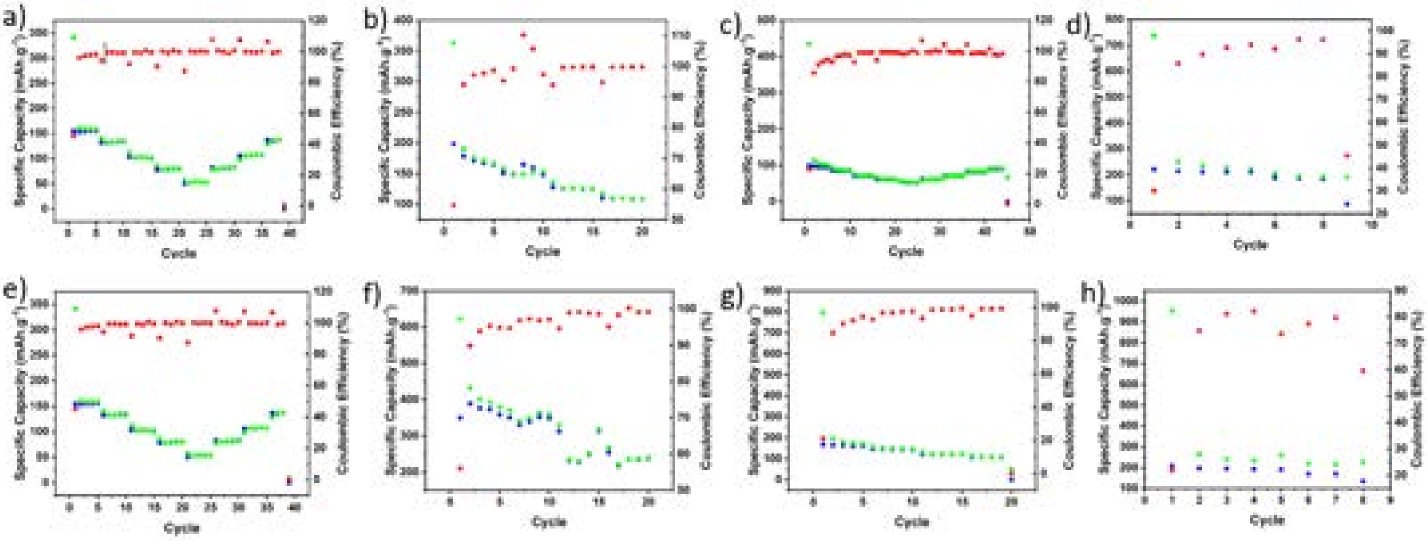

Figure 4: Rate capability plots for a) HKH-800, b) CS-1-800, c) HKH-800-MgCl$_2$, d) CS-1-800-MgCl$_2$, e) HKH-800 + Carbon Black, f) CS-1-800 + Carbon Black, g) HKH-800-MgCl$_2$ + Carbon Black, h) CS-1-800-MgCl$_2$ + Carbon Black

	HKH-800	CS$_1$-800	HKH-800-MgCl$_2$	CS$_1$-800-MgCl$_2$
1^{st} Cycle Discharge Capacity (mAh.g^{-1})	341	363	434.8	736.5
5^{th} Cycle Discharge Capacity (mAh.g^{-1})	158.7	167.1	101.4	223.8
Coulombic Efficiency (%)	47	46	23	30

Table 2: Summary of 1^{st} and 5^{th} cycle specific capacities and coulombic efficiencies

	HKH-800-CB	CS$_1$-800-CB	HKH-800-MgCl$_2$-CB	CS$_1$-800-MgCl$_2$-CB
”	308.2	623.3	795.9	953.4
”	144.7	378	171.7	258.8
”	47	61	22	27

Table 3: Summary of 1^{st} and 5^{th} cycle specific capacities and coulombic efficiencies

Figures 4 a-h, and Tables 2 and 3 show the rate capabilities of all the materials synthesised, and a summary of the 1^{st} and 5^{th} cycle specific capacities and the coulombic efficiency. As has been discussed previously, it is shown here that doping sulphur into the hard carbon will increase its specific capacity overall. The specific capacity of the hard carbons can then be further increased by adding magnesium chloride and carbon black, however, there are significant issues regarding the irreversible capacity of the electrodes - the coulombic efficiency of the best performing electrode being only 27 %.

4 Conclusions

A sulphur-doped hard carbon was synthesised by melting together hexaketocyclohexane (HKH) and sulphur together at 100 °C and then being pyrolysed further at 800 °C. The porosity of this material was tuned by grinding the HKH-S precursor together with a magnesium chloride template prior to pyrolysis, and the conductivity was tuned by adding carbon black during electrode preparation. This material was then characterised via XPS, and from this, a mechanism for the formation of this carbon material was suggested.

After synthesis and materials characterisation, the electrochemical performance of the hard carbon anodes was then characterised. From electrochemical tests, it was shown that the capacity of the 1^{st} to the 5^{th} cycle was increased by the introduction of sulphur as a dopant. It was also shown that the capacity of the 1^{st} cycle was significantly increased by the introduction of porosity through a magnesium chloride template, and was even further increased by the introduction of a conductive additive - the highest capacity reaching 953.4 mAh.g^{-1}. However, a significant irreversible capacity is seen in these materials, which can be attributed to the high surface area and therefore, enhanced formation of the irreversible solid-electrolyte interphase (SEI).

5 Further Work

Suggested further work includes the synthesis, characterisation and electrochemical testing of CS1 materials, pyrolysed at 1300 °C. Pyrolysing these carbon materials at a higher temperature will form a more ordered, graphite-like structure[4], decreasing the intrinsic surface area of the resulting CS1 materials. It can then be hypothesised that the irreversible capacity of this material will be decreased, as the reduction in surface area will inhibit the formation of the SEI. As well as a smaller intrinsic surface area, this material will also benefit from being more conductive, owing to its more ordered structure. This may also increase the capacity somewhat. However, pyrolysis at higher temperatures will decrease the amount of sulphur in the CS1 material, and so the capacity benefits of sulphur-doping may be lost. Also, the introduction of porosity through a magnesium chloride template may also introduce a large irreversible capacity in this material, making the effect of the higher pyrolysis temperature negligible. In any case, any future work should have a focus on removing the irreversibility from the best performing anode materials.

References

[1] B.L. Ellis and L.F. Nazar. Sodium and sodium-ion energy storage batteries. *ChemInform*, 44(46):168–177, 2013.

[2] F. Risacher and B. Fritz. Origin of salts and brine evolution of bolivian and chilean salars. *Aquatic Geochemistry*, 15(1-2):123–157, 2008.

[3] A. Yaksic and J.E. Tilton. Using the cumulative availability curve to asses the threat of mineral depletion: The case of lithium. *Resources Policy*, 34(4):185–194, 2009.

[4] Alptekin H. Jensen A.C.S. Olsson E. O'Keefe C.A. Smith T. Crespo-Ribadeneyra M. Headen T.F. Grey C.P. Cai Q. Drew A.J. Au, H. and M. Titirici. Correction: A revised mechanistic model for sodium insertion in hard carbons. *Energy Environmental Science*, 14(5):3216, 2021.

[5] D.A. Stevens and J.R. Dahn. High capacity anode materials for rechargeable sodium-ion batteries. *Journal of The Electrochemical Society*, 147(4):1271, 2000.

[6] Li L. Xiang Y. Zou G. Hou H. Deng W. Zhang, Y. and X. Ji. High sulfur-doped hard carbon with advanced potassium storage capacity via a molten salt method. *ACS Applied Materials Interfaces*, 12(27):30431–30437, 2020.

[7] Zhen Y. Ruan Y. Kang M. Zhou K. Zhang J.-M.-Huang Z. Hong, Z. and M. Wei. Rational design and general synthesis of s-doped hard carbon with tunable doping sites toward excellent na-ion storage performance. *Advanced Materials*, 30(29):1802035, 2018.

Benchmarking the performance of the SAFT-γ Mie approach to model oxygen solubility for improved fuel-cell design

Roopali Hothi, Malavika Raman
Department of Chemical Engineering, Imperial College London, U.K.
December 2021

This paper investigates oxygen solubility in C_8F_{18}-O_2, C_8H_{18}-O_2, C_6F_{14}-O_2 and C_6H_{14}-O_2 binary mixtures to explore the scope for their application in ionic liquids used to form catalytic ionic layers in fuel-cells, as a replacement for high-priced platinum alloy. The investigation involved estimating new unlike binary interaction parameters for CH_3-O_2, CH_2-O_2, CF_3-O_2 and CF_2-O_2 using gSAFT optimization software. Subsequently, the pre-existing databank was extended to include these interactions and theoretical SAFT-γ Mie calculations describing two phase VLE behaviour of the mixtures were then performed. This report's main findings conclude the favourable enhancement of O_2 solubility through use of shorter chain compounds and substitution of hydrogen in *n*-alkanes with fluorine functionalised groups. The theoretical phase coexistence region was identified to be in a similar range of temperatures for each *n*-alkane O_2 mixture when compared with its equivalent *n*-perfluoroalkane. Conversely, a significant difference manifested in the range of pressures observed for the VLE of the C_8H_{18}-O_2 system when compared to its counterpart C_8F_{18}-O_2. The promise of gSAFT optimization software in building feasible thermodynamic models, validating SAFT-γ Mie theory, is also highlighted.

Keywords: SAFT-γ Mie, perfluoroalkane, alkane, PEMFC, optimization, oxygen solubility, ORR, electrochemistry

1. Introduction

The alarming acceleration of climate change in recent years has acted as a catalyst for the development and employment of more environmentally benign power generation technologies. Moreover, with economies set out to find a post-COVID normal, countries worldwide plan to utilise the low-carbon pollution conditions initiated by widespread shutdowns during the pandemic, augmenting demand for clean-fuel alternatives. One such emergent is hydrogen which, shows promise to decarbonize hard-to-abate industry sectors.

Fuel-cells have been long recognized as a key growth driver of the nascent global hydrogen generation market with a CAGR of 9.2% [1].This technology is gaining visibility in sustainable energy production across automotive industries due to its high energy density, fast refueling time, and low carbon intensity. The vast deployment of Fuel-cell Electric Vehicles (FCEVEs) that are found to be cleaner and more efficient than conventional internal combustion engine vehicles, is causing a surge in demand for fuel-cells in the market. Such developments have changed the calculus for hydrogen and are paving way for the world to reduce its fossil fuel dependence.

Fuel-cells are electrochemical devices that generate electricity through an important oxygen reduction reaction (ORR) in which, oxygen is split into its ions and combined with protons to form water. The relatively slow speed of this reaction dampens the efficiency of fuel-cells, thus necessitating large amounts of platinum alloy catalyst to speed up its sluggish kinetics. The high cost of platinum, however, limits the commercialization of this technology. For large-scale uptake of fuel-cells, a catalytic alternative to platinum is imperative.

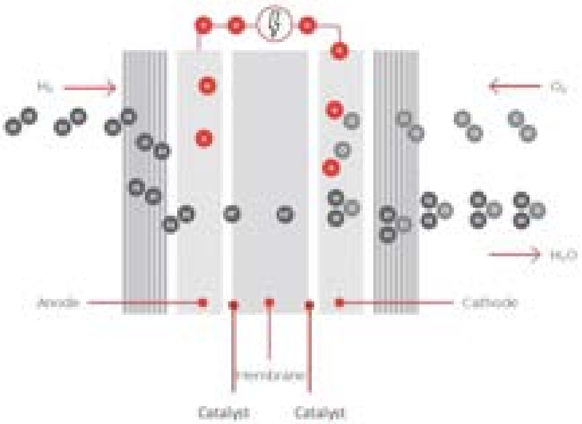

Figure 1. Conventional proton-exchange membrane fuel-cell (PEMFC), showing relevant electrochemical reactions with the ORR contained in the right half cell *[2]*

There have been recent efforts in the scientific community to utilize ionic liquids (ILs) as ORR catalyst modifiers in traditional proton exchange membrane fuel-cells. Ionic liquids (ILs) are solvents consisting entirely of ions with melting points typically below 100 °C [3]. Their "designer" properties of high thermal and chemical stability, tunable solubility of gases, and intrinsic ionic conductivity, compared to traditional volatile solvents and/or catalysts make them desirable.

This investigation looked at developing a SAFT (Statistical Associating Fluid Modelling Theory)- γ Mie model to examine the solubility of oxygen in a variety of oxygen–*n*-alkane and oxygen–*n*-perfluoroalkane mixtures relevant to the ILs of interest in the design of ionic layers. PSE [4] has commercialised an extensive databank, which can perform calculations based on a predefined model and input theory. The thermodynamic properties of a variety of pure components and mixtures can thus, be predicted. Specific objectives of this paper include utilising and building upon a separate, internal databank to define the interactions existing in a range of binary mixtures and thus accurately predict their fluid phase behaviour. This study also looked at establishing sensitivity of Mie parameters for different binary mixtures and adapting the gSAFT optimization procedure to enhance the quality of predictive thermodynamic calculations.

2. Background

2.1. SAFT-γ Mie

Previously, the SAFT-γ Mie software has been utilised to build an extensive databank, defining both like and unlike binary pair interaction parameters. One such databank found in literature specifies 58 separate groups [5]. Several variations of the input theory over the years have given rise to different iterations of the software such as PC-SAFT, SAFT-VR, SAFT-VR Mie, all of which make use of different EoS. The iteration of relevance to this work, SAFT- γ MIE makes use of the Mie potential to describe intermolecular interactions. The Eos in use sums different contributions of Helmholtz energies together to get the total Helmholtz free energy, A, of a mixture [6]:

$$A = A^{ideal} + A^{mono} + A^{chain} + A^{assoc} + A^{Born} + A^{ion} \quad (1)$$

Where; A^{ideal}: Helmholtz free energy contribution of an ideal gas

A^{mono}: Contribution due to repulsion & dispersion of interacting segments, in reference to the monomeric system

A^{chain}: Contribution of energy due to formation of monomers into chains from Mie segments

A^{Assoc}: Contribution to the free energy from association interactions

A^{Born}: Contribution to free energy due to insertion of all ions in the dielectric medium

A^{ion}: Contribution due to electrostatic interactions between charged species

SAFT considers molecules to be comprised of groups. These groups are defined as segments, as depicted in Figure 2. Through the assumption that one pair of interacting groups between two adjacent molecules is independent of all other interactions in the system, SAFT combines all possible interactions to attribute an overall thermodynamic property to the system, in what is known as the Group Contribution (GC) Method [5].In such a way, it is possible to make physico-chemical predictions on a variety of mixtures that differ only by the number of groups. For instance, hexane-oxygen (C_6H_{14}-O_2) phase behavior is predicted using the same parameters as for an octane-oxygen (C_8H_{18}-O_2) system; both dependent on solely CH_2-O_2 and CH_3-O_2 interactions, with octane comprising of two more CH_2 segments than hexane.

A balance of repulsive and attractive Van Der Waals (VDW) dispersion forces, as a function of the separation of two segments, is well defined using the Mie potential, depicted in Figure 3.

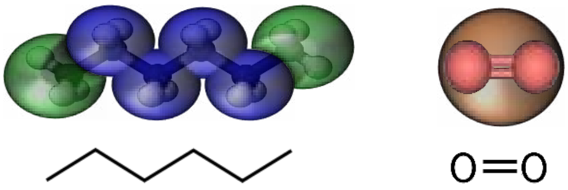

Figure 2. Hexane molecule (left) and its constituent segments, comprising of 4 CH_2 groups, in blue, and 2 CH_3 groups, in green. Oxygen molecule (right) displaying one segment of homonuclear nature (group O_2)

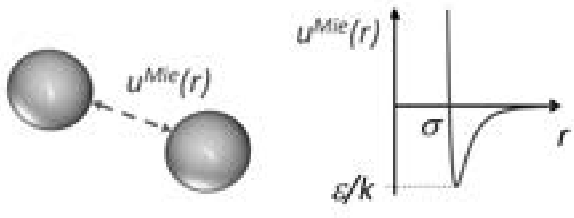

Figure 3. Mie dispersion energy of two interacting segments (u), as a function of their separation (r). Points of interest highlighted are on the potential well, such as the minimum dispersion energy (ε) and diameter of segment (σ). *[4]*

The relationship of segment separation and dispersion energy is characterized in the following way:

$$u_{kl}^{Mie}(r_{kl}) = C_{kl}\varepsilon_{kl}\left[\left(\frac{\sigma_{kl}}{r_{kl}}\right)^{\lambda_{kl}^{r}} - \left(\frac{\sigma_{kl}}{r_{kl}}\right)^{\lambda_{kl}^{a}}\right] \quad (2)$$

Where, k denotes group one and l denotes group two in the interaction pair, and C_{kl} is found through the following:

$$C_{kl} = \frac{\lambda_{kl}^{r}}{\lambda_{kl}^{r} - \lambda_{kl}^{a}}\left(\frac{\lambda_{kl}^{r}}{\lambda_{kl}^{a}}\right)^{\frac{\lambda_{kl}^{a}}{\lambda_{kl}^{r} - \lambda_{kl}^{a}}} \quad (3)$$

Where, λ_{kl}^{r} and λ_{kl}^{a} are the attractive and repulsive constants, which determine the shape of potential well shown in Figure 3. For the purposes of this work, λ_{kl}^{a} is set at a constant default value of 6. Conversely λ_{kl}^{r} is accounted for in some mixtures, particularly those containing polar halogenated groups, due to their highly non-ideal behaviour. ε_{kl} quantifies the depth of potential well, as shown in Figure 3. This value is proportional to the attractive constant ‘a’ which appears in the VDW equation. σ_{kl} is the segment diameter. This parameter is used as a measure of the repulsive force experienced between two interacting segments: proportional to repulsive constant ‘b’ in VDW equation.

Moreover, S_k, the shape factor, which informs of the level of overlap between two interacting segments. It is related to the number of interacting segments (μ^*) through the following equation:

$$\mu^* \times S_k \geq 1 \quad (4)$$

S_k is assigned a value of one to describe a spherical segment.

Additional Mie parameters beyond the scope of this report include association energies and bonding volumes, accounting for extra interactions arising through the presence of H and e$^-$ sites on the segments.

2.2. Ionic Liquids

Ionic liquids are defined as salts consisting of organic cations and inorganic ions, with the ability to maintain liquid state at RTP. They are a promising fuel-cell catalyst due to their low volatility and flammability and high thermal stability and conductivity. Electrochemical window is in reference to the operable potential range in which undesirable redox reactions do not occur. This accounts for the typical potential range of fuel-cells, being below 1V [7]. Thus, it is easier to tailor ILs in order to adhere to the operating conditions of fuel-cells, due to their larger electrochemical window. Currently the IL class comprises of more than 200 ions, with a possible expansion to more than 10^{14} ions [8].

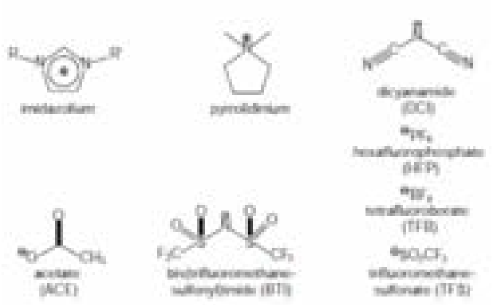

Figure 4. Typical ions found to constitute current ionic liquids *[19]*

Such ions require more theoretical phase characterisation due to the limited physical data that is pre-existing in literature. One type of compound for forming ILs, *n*-perfluoroalkanes, has proven previously in literature to dissolve a larger quantity of gas than its alkane equivalent, which is of importance in catalysing the ORR of a conventional PEMFC fuel-cell using hydrogen fuel [9].

3. Methodology

3.1. Combining Rules

To conduct a study on binary mixtures, unlike cross-interaction parameters were considered. Combining rules were employed to obtain appropriate estimates of σ_{kl}, ε_{kl}, and λ_{kl}. These cross-interaction parameters describe the unlike-segment diameter, unlike dispersion energy, and unlike repulsive constant respectively, for two hard spheres, k and l.

$$\sigma_{kl} = \frac{\sigma_{kk} + \sigma_{ll}}{2} \tag{5}$$

$$\varepsilon_{kl} = \frac{\sqrt{{\sigma_{kk}}^3 {\sigma_{ll}}^3}}{{\sigma_{kl}}^3} \sqrt{\varepsilon_{kk}\varepsilon_{ll}} \tag{6}$$

$$\lambda_{kl} = 3 + \sqrt{(\lambda_{kk} - 3)(\lambda_{ll} - 3)} \tag{7}$$

Based on the Lorentz arithmetic-mean rule (5), σ_{kl} was computed using the like-diameters, σ_{kk} ad σ_{ll}, obtained from relevant literature. In cases where $\sigma_{kl} = \sigma_{ll}$, a simple geometric mean combining rule can be employed. However, due to size asymmetry in this investigation i.e., $\sigma_{kl} \neq \sigma_{ll}$, the unlike dispersion energy was calculated using an augmented geometric-mean rule (6).

The values obtained using these combining rules were defined as initial guesses for the Mie parameters. They were however further refined by conducting a parameter estimation on *gSAFT* using experimental data, as described in Section 3.2. This method is used to ensure greater accuracy, particularly while studying solubility with respect to mixtures where dispersion and/or association energies become important.

3.2. Parameter estimation

An executable gSAFT programme requires specifications from three separate input files: i. experimental binary mixture VLE data, ii. initial guesses and bounds for the Mie parameters to be fitted as defined in Section 2.1 and iii. a configuration file creating a placeholder for such parameters.

i. Existing experimental data on the dew and bubble conditions of the mixture was obtained from DETHERM and plotted, to identify the region of phase coexistence to be theoretically replicated. Where input data was specified for several properties (indexed *N*) (being T_{Bub}/P_{Bub}, T_{Dew}/P_{Dew}) Eq.8 was used to assign weights (*w*). This instructed gSAFT to place greater importance on fitting to whichever data had the higher number of experimental points (*n*). This weight is a factor which scales the objective function that quantities the error associated with the theoretical calculation.

$$\frac{w_1}{n_1} = \frac{w_2}{n_2} = \cdots = \frac{w_N}{n_N} \tag{8}$$

The isothermal/isobaric data was selected from several years and a maximum number of data points was utilised. Where possible newer data was favoured to decrease experimental uncertainty. Data at intermediate temperatures and pressures were opted for, to avoid both the critical conditions (up to 90% of the critical point), and extremely low *T/P*, remaining as close to ambient conditions as possible.

ii. The optimal MIE interaction parameters were not known a priori. Knowledge of typical values of these parameters was drawn from those already defined in the pre-existing databank and was used to set the bounds for parameter estimation as first approximation (e.g., 50-1000 for ε, 10-30 for ${\lambda_{kl}}^r$).

Thus, values of these parameters, as calculated by combining rules mentioned in Section 3.1, are utilised as an initial starting point for gSAFT, and specified in the parameter estimation input file. A cursory analysis of the effects of ε alone, λ_{kl}^{r} alone, and both ε and λ_{kl}^{r} on the mixture was conducted. This was to establish an understanding of the sensitivity of the involved groups towards these interaction parameters, as well as indicate how meaningful the starting values are.

An iterative process on the parameter estimation was then carried out, each time tuning the initial guess values for the specified parameters to achieve greater congruence between experimental and theoretical values. For instance, if the experimental data points were consistently higher than the theoretical ones in a *T-x, y* diagram, this was indicative of ε, the interaction energy, being too low. Furthermore, in this work a low number of sobol points (100) was used for ease of computation, as it often provided a close to optimal solution in a relatively short run-time. The uncertainty of optimized parameters depended on this value. Where initial guess values of parameters caused computational issues, they were reassigned the value of the midpoint of the upper and lower bound. This allowed more even coverage of the feasible solution region for the given number of sobol points. Once a functional optimal solution set was found, it was transferred into the main databank and used to theoretically calculate T_{Bub}/P_{Bub}, T_{Dew}/P_{Dew}.

3.3. Thermodynamic calculations

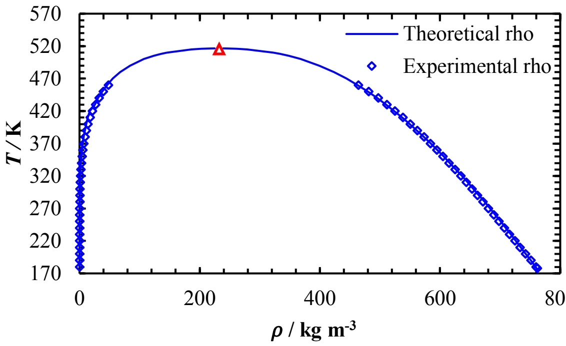

Figure 5. *T-ρ* phase envelope of pure *n*-hexane. The symbols/markers represent experimental data obtained from NIST [10]. The red symbol represents the critical point

Thermodynamic calculations were initially carried out for pure compounds (Figure 5) to establish confidence with the gSAFT software for the purpose of this investigation. This also allowed for a study of the phase behavior of the relevant pure compounds prior to building models of their binary mixtures with oxygen. NIST thermodynamic webbook was the database of choice to obtain experimental values of pure compounds. Beyond the critical point, gSAFT was unable to accurately predict theoretical values, indicating that there is no physical meaning to gSAFT calculations outside the two-phase envelope. This was accounted for while building on the desired models in further studies of oxygen solubility as elaborated in Section 4.

For binary mixtures, throughout the investigation, theoretical phase envelopes were developed for the entire range of compositions from 0-1. This can be seen through the continuous range of values returned in the *T-x, y* (Figure 6a) for an oxygen-hexane mixture. Limited availability of experimental data however, meant that %AAD calculations and model verification were conducted for a smaller range of data. Based on the theoretical values computed in gSAFT, the process was repeated iteratively as detailed in Section 3.2 until the model was optimized and error was as low as practicably possible. This decision was based on the absolute average deviation which, is a summary statistical dispersion or variability.

$$\%AAD = \frac{1}{N_X}\sum_{1}^{N_X}\frac{\left|X_{Theoretical} - X_{Experimental}\right|}{X_{Theoretical}} \times 100 \quad (9)$$

The %AAD Eq. 9 was the metric used to quantify the difference in fit between the SAFT-γ Mie computational model and experimental data.

3.4. Average Relative Solubility

Solubility ratios were computed to quantify the differences in oxygen solubility observed between different mixtures. Eq.10 defines this ratio where, ${x_{O_2}}^{i}$ is the composition of oxygen in mixture i, ${x_{O_2}}^{j}$is the composition of oxygen in mixture *j*, p_n is a given pressure with n = 1,2,3…n at which, the two compositions are compared. An average was taken by summing together all the ratios and dividing by *N*, the total number of composition-pressure points.

$$Average\ Relative\ Solubility = \frac{\sum_{1}^{n}\frac{{x_{O_2}}^{i}{}_{p_n}}{{x_{O_2}}^{j}{}_{p_n}}}{N} \quad (10)$$

4. Results & Discussion

4.1. Optimized Parameters

Table 1. Final optimized parameters obtained from parameter estimation

Group *k*	Group *l*	(ε_{kl}/k_B) / K	λ_{kl}^{r}
O_2	O_2	128.33	13.399
CH_2	O_2	200.00	21.482
CH_3	O_2	219.12	14.000
CF_3	CF_2	390.00*	31.300
CF_3	O_2	272.79	20.564
CF_2	O_2	232.97	27.185

** Literature value* [11]

The optimized Mie parameters of the final model for each mixture are summarized in Table 1. In most binary pairs studied, both λ_{kl} and ε were fitted for in the end. The parameters were compared to other pre-existing binary interaction parameters to judge whether a sensible range of values was observed.

4.2. Model verification

4.2.1. Absolute Average Deviation (AAD)

Table 2. %AAD values quantifying deviation of the theoretical calculation from experimental points, using optimized parameters

Mixture	Thermodynamic Property	%AAD
$O_2 + C_8H_{18}$	T_{bub}	1.19
$O_2 + C_8F_{18}$	P_{bub}, P_{dew}	4.50-40.0
$O_2 + C_6H_{14}$	T_{bub}	0.982
$O_2 + C_6F_{14}$	T_{bub}	0.282

The thermodynamic property studied was chosen based on available experimental data. Overall, temperatures were predicted better than pressures and exhibited lower %AADs.

4.2.2. Oxygen – *n*-alkane

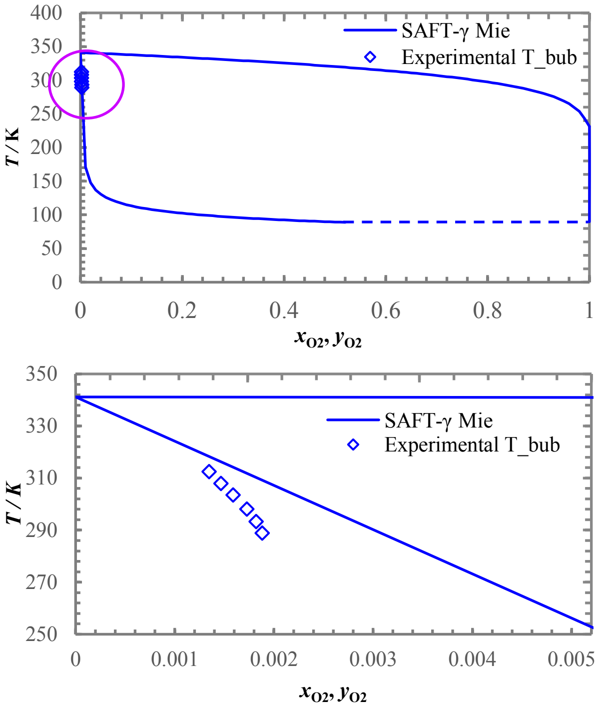

Figure 65. (a) (Top) *T-x,*y diagram depicting theoretical VLE phase envelop of an O_2-C_6H_{14} mixture at an isobar of 1 atm. Experimental bubble temperatures obtained from DETHERM (b) (Bottom) Limited axis of Figure 6a, from x_{O2} values of 0 to 0.005;

The discrepancies (Figure 6b) between the SAFT-γ Mie predictions and DETHERM values were not very significant. A %AAD of ~ 0.982 % was obtained for this oxygen-hexane mixture. An observation worth noting is that at high temperatures the %AAD is lower i.e., the theoretical model shows a better fit at higher temperatures. The oxygen-octane model was similarly validated, returning a reasonable %AAD of 1.19 %. This could indicate that the oxygen-hexane model generated was marginally more robust than that of the latter. The room for uncertainty in the comparative model with respect to the unique sets of experimental data exploited for each binary mixture, is however an important factor to be considered.

4.2.3. Oxygen – *n*-perfluoroalkane

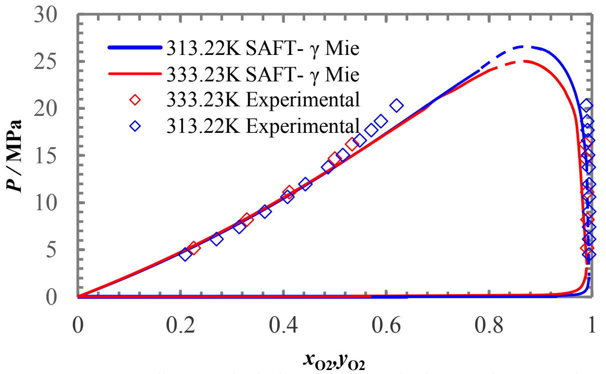

Figure 76. *P-x,y* diagram depicting the theoretical VLE phase envelop of an O_2-C_8F_{18} mixture at two isotherms of 313.22K and 333.23K

Any compositions for which a theoretical phase boundary calculation could not be executed, a manual extrapolation of the curve was made, as seen in the VLE envelop of Figure 7. At both dew and bubble conditions, lower %AAD was observable at the higher temperature isotherm. The optimized parameter set replicated the bubble pressures well for the C_8F_{18}-O_2 oxygen system with the theoretical curve obtaining close congruence with experimental data points in the composition range ~0.2-0.6. For 313.22K and 333.23K respectively, %AAD was quantified as 17% and 5%. On the other hand, experimental dew pressures existing in the x_{O2} composition range of ~0.98-1, were consistently underpredicted. This yielded a large %AAD of 40% and 30% at the 313.22K and 333.23K isotherm respectively. The larger error may be attributed to the increased uncertainty of experimental data points obtained under dew conditions, due to the difficulty in fixing precise compositions of the vapour phase to measure the corresponding liquid phase component compositions. An artefact of note is the turning point of the dew curve, for both isotherms at an x_{O2} value of ~0.98. For both isotherms it is apparent that the theoretical curve does not intersect the pure component axis where x_{O2}, y_{O2} are equal to one, as should be the case. This point of intersection would be indicative of the saturation temperature of oxygen at 313.22K and 333.23K. However, at x_{O2} near unity theoretical dew pressures computed appeared anomalous and were consequently not featured in the plot. A finer increment approach to the pure O_2 condition would be needed to feasibly solve this part of the curve.

4.3. Factors affecting oxygen solubility

A summary of the solubility trends, as calculated using Eq. 10, is featured below.

Table 3. Average relative solubility values

Comparison	Average relative solubility
$O_2 + C_6H_{14} : O_2 + C_8H_{18}$	1: 1.36
$O_2 + C_6F_{14} : O_2 + C_8F_{18}$	1: 1.22
$O_2 + C_6H_{14} : O_2 + C_6F_{14}$	1: 2.34
$O_2 + C_8H_{18} : O_2 + C_8F_{18}$	1: 2.54

4.3.1. Chain Length

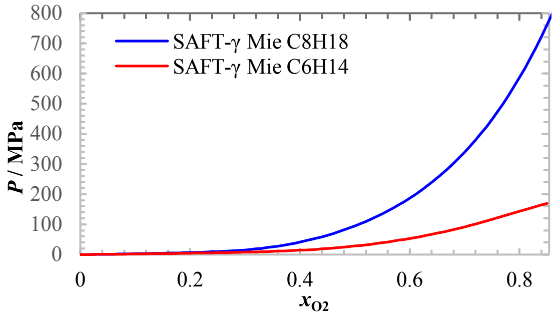

Figure 87. *P-x* diagram depicting theoretical bubble pressure of an O_2-C_6H_{14} mixture, in comparison to the O_2-C_8H_{18} mixture, both at an isotherm of 200 K

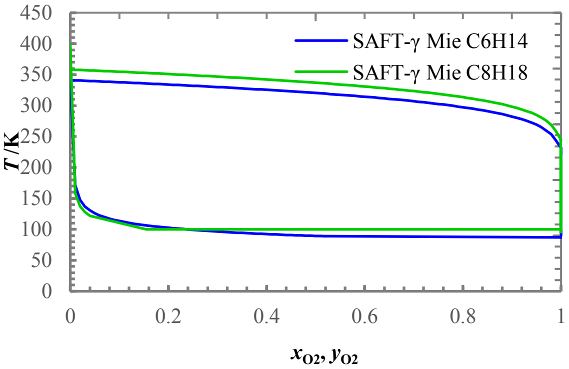

Figure 98. *T-x,y* diagram depicting the theoretical VLE phase envelop of O_2-C_6H_{14} mixture, in comparison to the O_2-C_8H_{18} mixture, in comparison to mixture, both at an isobar of 1 atm

Thermodynamic models were built for binary mixtures of oxygen with hexane and octane at a constant pressure of 1 atm. For any given pressure along the bubble curves in Figure 8, where two-phase coexistence holds, the compositions of O_2 in C_6H_{14} are greater than that in C_8H_{18}. This is indicative of higher oxygen solubilities in shorter chain alkanes in the liquid phase, as was established in previous literature [12]. With an increase in chain length, there is an increase in surface area and in turn, VDW forces. For oxygen to dissolve in either alkane, the intermolecular VDW dispersion forces holding the alkane together need to be overcome i.e., the amount of energy released during formation of new bonds needs to compensate for the energy required to weaken the alkane's intermolecular forces. Resultantly, at any specified thermodynamic condition, there is a greater energy demand for longer chain alkanes, developing a greater barrier to solubility, as evidenced in the model built.

In the complete phase envelop (Figure 9) for a range of temperatures, there was a focus on the liquid phase and bubble curves given the objective of evaluating oxygen solubility in ILs. Typically, ionic liquids have a melting point lower than room temperature with some entering the liquid phase only below 0°C (273 K). Within a temperature range where most IL substances would potentially be in liquid phase, it is evident that the conclusion of shorter chain alkanes showing better oxygen solubility still holds. In the range of ~ 0.25-0.90 x_{O_2}, the graphs pan out almost horizontally. This resulted from the fact that gSAFT calculations for minute temperature increments i.e., hundredths of 1K, were not carried out. The input temperatures at which, these phase boundary calculations were performed were all a minimum of ~ 2 K apart. The preliminary nature of the phase envelope suggests potential to further refine these thermodynamic calculations to ensure greater precision and accuracy.

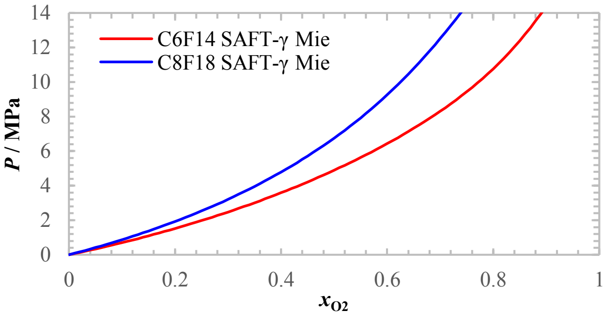

Figure 109. *P-x* diagram depicting theoretical bubble pressure of an O_2-C_6F_{14} mixture, in comparison to the O_2-C_8F_{18} mixture, both at an isotherm of 200 K

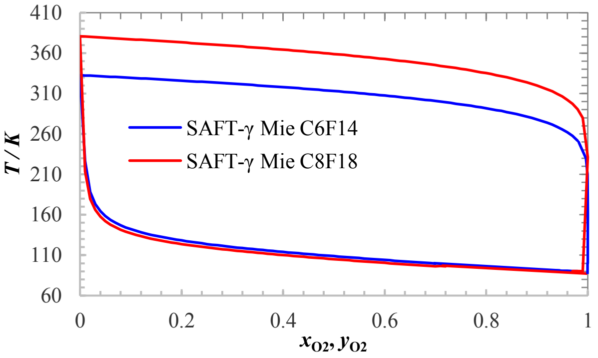

Figure 1110. *T-x,y* diagram depicting the theoretical VLE phase envelop of O_2-C_6F_{14} mixture, in comparison to the O_2-C_8F_{18} mixture, in comparison to mixture, both at an isobar of 1 atm

The equivalent fluorine-functionalized alkanes were similarly compared in Figures 10 and 11. Given that the carbon chain is intact between alkane and perfluoroalkane, with hydrogen to fluorine being the only substitution or change made to the chemical structures of the fluorinated counterpart, the same observation of improving oxygen solubility by reducing chain length resulted.

Solubility ratios were computed to quantify the solubility differences seen between C_6H_{14}-C_8H_{18} and C_6F_{14}-C_8F_{18}. Relative solubilities of 1:1.36 and 1:1.22 respectively were obtained making oxygen 1.36 times more soluble in hexane than in octane, and 1.22 times more soluble in perfluorohexane than in perfluorooctane.

4.3.2. Fluorination

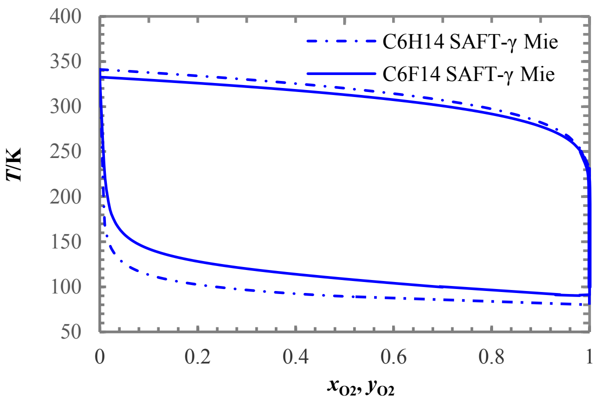

Figure 1211. *T-x,*y diagram depicting the theoretical VLE phase envelop of an O_2-C_6H_{14} and an O_2-C_6F_{14} mixture at an isobar of 1 atm

At any temperature specified in the range 90K-340K (Figure 12), it was predicted that C_6F_{14} will dissolve oxygen to a higher degree than C_6H_{14}. This favourable enhancement in solubility becomes more apparent as the temperature is further decreased to the predicted O_2 saturation temperature of 90K, indicated by the intercept with the pure component axis (where x_{O2} is equal to one). Thus, the solubility gap of O_2 between C_6H_{14} and C_6F_{14} is best exploited for lower temperatures. Conversely, the dew curves as depicted at the top of the *T-x, y* diagram show a reversal in trend of solubility with fluorination, with oxygen appearing more soluble in C_6H_{14} than C_6F_{14}. Experimental dew pressure data for the two mixtures would be required to validate this prediction and allow for further analysis.

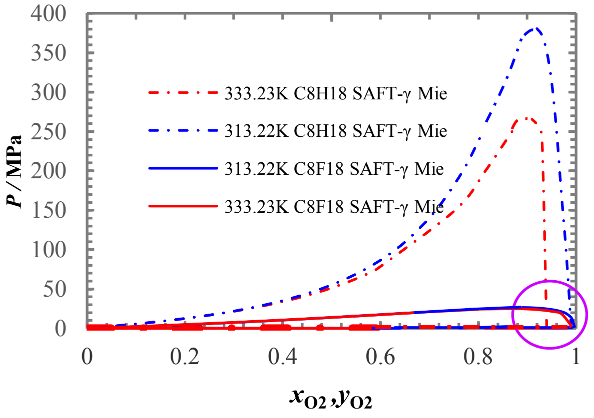

Figure 13a12. *T-x,*y diagram depicting the theoretical VLE phase envelop of an O_2-C_6H_{14} and an O_2-C_6F_{14} mixture at two isotherms of 333.23 K and 313.22 KK

For both the 313.23K and 333.23K isotherm, theoretical calculations predicted a VLE phase envelop spanning over a much larger pressure range for the octane-oxygen system than the perfluorooctane-oxygen system. Over most of the composition range, the bubble pressure curves lie at very low pressures and are virtually indistinguishable for both mixtures. However there exists a solubility gap at high x_{O2} compositions in excess of 0.9. Thus, a scaled axis yielding Figure 13b is presented.

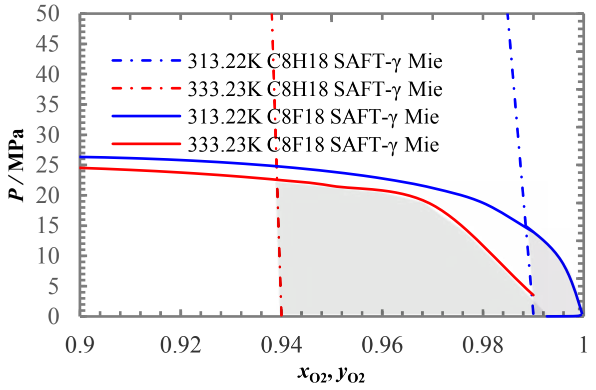

Figure 13b. Limited axis of Figure 13a, from x_{O2} values of 0.9 to 1; where shaded green or purple highlights the favourable enhancement in O_2 solubility observed in O_2 – C_8F_{18} compared to O_2 -C_8H_{18} at 333.23K and 313.22K respectively

For both isotherms it was observed that the expected trend of increased solubility in the oxygen-perfluorooctane system, in comparison to the oxygen-octane system, existed after a certain mole fraction. This finding is supported by previous literature [13]. These are indicated by the shaded regions in Figure 13b. At the 333.23K isotherm a higher x_{O2} of ~0.99 must be achieved to exploit the favourable enhancement of O_2 solubility through addition of fluorine. Conversely this x_{O2} lies at a lower value of 0.94 for the 313.22K isotherm. In both cases, the average solubility ratio is extremely small, concluding the little effect of fluorination of octane under these thermodynamic conditions.

Predictions for upper critical solution pressures, indicated as the maxima of the *T-x-y* curves in Figure 13a, are reported in Table 4. This shows a 14-fold increase in critical pressure when comparing O_2 +C_8H_{18} P_c with its counterpart O_2 +C_8F_{18} mixture. For both mixtures, at both isotherms, critical x_{O2} values appear to be similar. More experimental data on the two mixtures is required in order to assess %AADs of these values and validate the model.

Table 4. Upper critical solution pressure (UCSP) predicted from theoretical VLE phase envelop of O_2+C_8H_{18} and O_2+C_8F_{18}, at two different isotherms

Mixture	$T_{isothermal}$ /K	P_c/MPa	$x_{O_2,c}$
O_2 +C_8H_{18}	313.22	380.59	0.92
	333.23	265.37	0.91
O_2 +C_8F_{18}	313.22	26.43	0.89
	333.23	25.0	0.87

In summary, as reported in Table 3, the average solubility ratio of O_2 + C_6H_{14} : O_2 + C_6F_{14}, and O_2 + C_8H_{18} : O_2 + C_8F_{18} is 1:2.34 and 1:2.54 respectively, suggesting increased solubility in O_2 resulting from fluorination of the alkane. This effect is more apparent in substitution of octane than hexane.

5. Conclusion

gSAFT optimization software was utilized to study oxygen solubility in C_8F_{18}-O_2, C_8H_{18}-O_2, C_6F_{14}-O_2 and C_6H_{14}-O_2 mixtures. Through the investigation, gSAFT was validated as a powerful predictive tool in building practicable thermodynamic models based on SAFT-γ Mie studies.

Overall, close agreement was observed between available experimental data points and the theoretical calculations, as reflected by low %AAD values (ranging 0.282-1.19%). This was with exception to one dataset, for which higher %AAD was observed; both the dew and bubble pressure of the C_8F_{18}-O_2 mixture, at 16% and 40% respectively.

The effect of chain length on solubility was evaluated to find that oxygen was more soluble in short chain *n*-alkanes and *n*-perfluoroalkanes, with a focus on the liquid phase. Looking at the relationship between fluorinating alkanes and solubility, it was observed that oxygen solubility improved in the fluorine-functionalized counterparts of hexane and octane. Thus, it can be suggested that shorter chain, fluorinated alkanes the more suitable choice for IL application in forming ionic layers in fuel-cells.

Furthermore, while assessing the effect of fluorination, it was identified that for every oxygen-*n*-alkane mixture studied in comparison to its corresponding oxygen-*n*-perfluoroalkane, its theoretical two phase region existed in a comparable range of temperatures. More specifically, there was a considerable deviation in the range of theoretical dew and bubble pressures obtained for the oxygen-octane binary mixture from that of oxygen-perfluorooctane system. The former assumed an apparent critical pressure showing a 14-fold sizeable increase from the critical pressure of the latter.

6. Limitations & Outlook

Results identified the shortfall of SAFT in correctly predicting VLE phase properties of the O_2-C_8F_{18} mixture, particularly its bubble and dew pressure, with a more significant %AAD in the former. Despite several runs of parameter estimation, little could be done to alleviate this error, whilst still maintaining good agreement between theoretical calculation and experimental points within other datasets (O_2-C_6F_{14} dew temperature). As such, future work into SAFT theory of dew and bubble pressure should be carried out, allowing for extension or modification terms to account for any unexpected behaviour in the system of interest. This observation of error may perhaps be attributed to the method of data gathering; in dew condition (for which there was greater %AAD), it is difficult to fix the gas composition and measure the corresponding liquid compositions. Vice versa proves to be more experimentally attainable, thus improved VLE data gathering methods could be further investigated.

Overprediction of critical point for pure components was observed when executing theoretical calculations of *n*-hexane and oxygen, a limitation of SAFT to be wary of.

To place less computational strain on SAFT and collate results more efficiently, parameter estimation ran with a smaller number of sobol points, set at 100. Repeats of these estimations would yield different results, highlighting the randomness of the initial guess value of the fitted parameters in each sobol point. As such, it is important to run parameter estimation in a longer time period, with greater number of sobol points (from 1000-10,000). This will ensure the ultimately optimal parameter set is obtained, enforcing a reproducible estimation and far more predictive theoretical calculations.

The scope of this report was limited by the available experimental data of *n*-alkane and *n*-perfluoroalkane O_2 mixtures. Further work on gathering data for more of these compounds, and over a larger pressure and temperature range, should be carried out. Resultantly parameter fitting will be contingent on a larger number of experimental points, greatly buffering out the effect of any spurious data points, and increasing the certainty in the obtained parameters, thus producing more accurate phase predictions. Moreover, characterisation of other IL O_2 mixtures of interest in addition to perfluoroalkanes will be helpful in aiding the development of fuel-cells. Lastly, a direct continuation of this work would investigate the effect of branched perfluoroalkanes on O_2 solubility.

Trialling the success of SAFT theory in predicting other two-phase systems, such as LLE and SLE may be of future interest, to make more use of the available data.

Implementing more extensive VLE data (spanning over a larger T/P range) into parameter estimation will also provide a more robust thermodynamic prediction for other pressures and temperatures not yet encountered in experimental data for the mixtures of interest. This report's work has not considered the optimized parameter sets dependence on the isobar or isotherm of input data, providing a possible research opportunity.

The 3D solution space presents the issue of multiple optima, thus causing for several output parameter sets (degree of degeneracy). A more consolidated approach is needed to cement the most optimal solution set, therefore further work should focus on heuristics guiding the optimization algorithm, and when it should terminate.

A key limitation in SAFT methodology is the requirement for a well-informed initial guess of the relevant Mie parameters describing the system, accompanied by a fully rationalised upper and lower bound. As mentioned, combining rules were utilised to achieve this. However, averaging properties like so fails in capturing the joint behaviour of two segments that are chemically and size wise differing. Despite this there is no way of knowing the general location of the feasible solution space. This implicated the need for successive estimations before achieving a functional parameter set. To reduce this time intensive activity, more research into heuristics for initial guesses and bounds should be conducted. In group contribution, a simplified representation of the molecules, modelled as a series of segments was assumed. Interactions may differ when taking a higher order view of the molecule and defining segments which claim more atoms. Future parameter estimation exercises should account for the possible interaction effects of higher order groups.

Lastly, the optimized parameters obtained may not be of physical significance when describing the binary mixture; instead, being utilised to fit theoretical calculation to the available data. Therefore, a careful consideration of the accuracy of SAFT computation, vs how predictive of the system it is, should be considered and seen as limitation.

Acknowledgements

We would like to thank Professor Amparo Galindo and Dr Andrew J. Haslam, Malak Wehbe and Felipe Antonio Perdomo Hurtado for their continual guidance and support in this work.

Bibliography

[1] [Online]. Available: https://www.marketsandmarkets.com/Market-Reports/hydrogen-generation-market-494.html.

[2] [Online]. Available: https://new.abb.com/marine/systems-and-solutions/electric-solutions/fuel-cell.

[3] [Online]. Available: https://www.sciencedirect.com/topics/nursing-and-health-professions/ionic-liquid.

[4] PSE, gSAFT Material Modeller (gSAFTmm) Overview, 2018.

[5] e. a. Haslam, “Expanding the Applications of the SAFT-γ Mie Group-Contribution Equation of State: Prediction of Thermodynamic Properties and Phase Behavior of Mixtures”.

[6] [Online]. Available: https://www.semanticscholar.org/paper/New-reference-equation-of-state-for-associating-Chapman-Gubbins/490a9d45ea7151c9677e2996d8d62c7bfccfdd0d .

[7] H. Y. Huan L., “Ionic liquids for electrochemical energy storage devices applications,” Elsevier, 2018.

[8] C. Chiappe, “Ionic liquids: solvent properties and organic reactivity,” Journal of Organic Physical Chemistry, 2004.

[9] J. e. a. Xu, “The study on fuel-cell performance by using,” IOP, 2019.

[10] [Online]. Available: https://webbook.nist.gov/chemistry/fluid/.

[11] J. Martinez, “Master’s Thesis; Development of a SAFT-γ Mie group-contribution approach to modelling d process design of ORCs,” Imperial College London, 2020.

[12] T. S. A. Hai Ngo, “Oxygen Absorption into Stirred Emulsions of n-Alkanes,” International Journal of Chemical Engineering, 2012.

[13] V. G. e. al., “Fluorine-functionalized ionic liquids with high oxygen solubility,” Royal Society of Chemistry, 2017.

[14] F. C. Ltd, “Perfluoro-n-octane,” 3 November 2021. [Online]. Available: https://www.f2chemicals.com/perfluoro-n-octane.html.

[15] J. S. Martínez, “MASTER'S THESIS Development of a SAFT-γ Mie group-contribution,” Imperial College London , 2020.

[16] V. A. F. d. Santos, Instituto Superior Técnico, Lisbon, Portugal, 2016.

[17] [Online]. Available: https://new.abb.com/marine/systems-and-solutions/electric-solutions/fuel-cell.

[18] [Online]. Available: https://www.semanticscholar.org/paper/New-reference-equation-of-state-for-associating-Chapman-Gubbins/490a9d45ea7151c9677e2996d8d62c7bfccfdd0d .

[19] [Online]. Available: https://www.sigmaaldrich.com/GB/en/technical-documents/technical-article/materials-science-and-engineering/batteries-supercapacitors-and-fuel-cells/ionic-liquids-for.

Carbamazepine hydrate vs. anhydrate: A crystal structure prediction and stability investigation

Siyu Guo and Xie Wing Chan

December 2021

Abstract

Organic molecules are able to crystallise into different structures, called polymorphs. These structural differences are of significant importance due to its impact on its attributes such as solubility, stability, and rheological behaviour during downstream processing. In the pharmaceutical industry, solubility is an important property as it affects the bioavailability of a solid. Thus, accurately predicting and controlling the formation of crystal structures could avoid possible legal and economic consequences. This study investigates the applicability of crystal structure prediction (CSP) methods on the flexible Carbamazepine (CBZ) molecules, specifically on its anhydrates and dihydrates, thus determining the relative stability ranking of the polymorph forms based on its lattice energies. The CSP method first uses Crystal Structure Optimisation for Flexible Molecules (CSOFM) algorithm to conduct local lattice energy minimisations. Then, the CrystalPredictor programme is used to generate possible crystal structures in global search followed by a refinement stage using CSOFM. The performance of repulsion/dispersion parameters: FIT and DB2020 are also assessed in combination with the level of theory used. By comparing energy rankings and $RMSD_{15}$ values, it is concluded that DB2020 performs slightly better than FIT when used with level of theory PBEPBE6-31G(d,p), hence it is subsequently used to determine the relative stability ranking of the polymorphs. The relative stability ranking of CBZ polymorphs was found to be dihydrate P21/C as most stable, followed by anhydrate type III, IV, V and II, where anhydrate type II is the least stable.

Keywords: Carbamazapine, Crystal Structure Predictor, Crystal Predictor, Crystal Structure Optimiser for Flexible Molecules, flexible molecules, relative stability

1 Introduction

Crystallisation of organic molecules have been a topic of research by fine chemical industries such as pharmaceutical and agrochemical industries. This is due to the polymorphic behaviour of organic molecules, which influences their solid-state properties including solubility, stability, and rheological behaviour during downstream processing. It is also worth mentioning that in the pharmaceutical industry, solubility of a crystal affects its bioavailability [1]. Thus, predicting and controlling the formation of crystal structures are essential in preventing chemical products from losing its effectiveness and/or changing its attributes altogether, avoiding possible legal and economic consequences. A famous example would be Ritonavir, an antiretroviral drug used in combination with other medications to treat HIV [2]. The drug underwent temporary market withdrawal due to the formation of a more stable polymorph that exhibits lower solubility, resulting in lower bioavailability [2]. Eventually, the problem was solved by reformulating the capsule with a refrigerated gelcap. This example proves the importance of predicting possible crystal structures, which is where crystal structure prediction (CSP) becomes useful.

CSP is a theoretical tool used to identify the thermodynamically most stable crystal structure at 0 K temperature and 0 bar pressure setting, based on 2D molecular formula of all species in a crystal or co-crystal [3]. It is also used to determine other crystal structures that are likely to occur in nature in correct order of decreasing stability. The stability of crystal structure is determined by Gibbs free energy, where the lowest Gibbs free energy at a given pressure and temperature represents the most stable structure. Hence, prediction of a stable crystal structure requires the minimisation of Gibbs free energy:

$$minG = min(U + pV - TS) \tag{1}$$

where U is the internal energy, V the volume, and S the entropy. The work term, pV is neglected as it only becomes significant at very high pressures, while the thermal and entropy term, TS is typically omitted as it cannot be readily and accurately computed at low computational cost. This term is also approximated to have a small magnitude at low temperatures [3]. The energy function thus simplifies to the lattice internal energy, U at a temperature of 0 K. The CSP methodology uses this function to find all low-energy local minima in the lattice energy surface, identifying most stable crystal structures.

The organic molecule studied in this paper is Carbamazepine (CBZ). Sold under the trade name Tegretol, it is a drug commonly used to treat epilepsy and neuropathic pain [4]. It is available on the market as a generic medication and listed on the World Health Organisation's Essential Medications [5]. In 2019, over 2.8 million prescriptions of CBZ are given in the United States alone [**usage**], making it the 204^{th} most commonly prescribed medication in the country [6].

The CSP approach used in this study is developed by CPSE at Imperial College London. In this approach, a local lattice energy minimization algorithm, Crystal Structure Optimisation for Flexible Molecules (CSOFM) is used before generating possible structures at the global search step (CrystalPredictor) followed by the refinement of low energy ranking structures using CSOFM. The purpose of this study is to test the applicability of this multi-stage methodology and repulsion/dispersion parameter sets FIT and DB2020 for pure CBZ crystals and dihydrate polymorphs both:

- Geometrically
- Low Energy Rankings

with level of theory PBEPBE6−31G(d,p) employed. Another objective of this study is to give a relative stability ranking among the available CBZ polymorphs (anhydrate type II, III, IV, V, and dihydrare monoclinic P21/C) based on the output optimal lattice energy from CSOFM step.

2 Methodology

The relative stability of each CBZ polymorph and evaluation of performance of DB_2020 and FIT repulsion/dispersion parameter sets are completed using Imperial College London's High Performing Computer (HPC). The process mainly require the following programs:

- CSOFM V.1.2
- CrystalPredictor V.2.4.4
- Mercury

CSOFM is used in the optimisation process of molecular structure. The program will output the optimal crystal structure and its corresponding lattice energy (kJ/mol) and density (g/cm^3).

CrystalPredictor is used to generate a crystal energy landscape (density vs lattice energy) for a molecule given its 2D molecular formula. CrystalPredictor then identifies and lists feasible polymorph structures in terms of lattice energies. These structures are then further refined using CSOFM.

After the refinement stage, the structures are then compared against the experimental structure in Mercury by computing the $RMSD_{15}$ value. The lower the $RMSD_{15}$ value, the similar the generated structure is to the experimental structure.

2.1 Polymorph identification

The research on possible polymorph forms of CBZ is completed through the CCDC database. The criteria of choosing feasible polymorphs for CSP are:

- Z' =1.
- Fully identified .res file.
- For polymorphs that have multiple structures, the one with lowest R-factor were chosen, where R-factor is a formula for estimating error in data set [7]

Five possible polymorphs, which includes four anhydrate polymorphs and one dihydrate polymorph are selected for further investigation. The corresponding CCDC code, R-factor [7] and Z' number are summarised in Table 1.

Polymorph	CCDC code	Z'	R-factor
II	CBMZPN03	1	6.9%
III	CBMZPN18	1	1.08%
IV	CBMZPN12	1	3.57%
V	CBMZPN16	1	4.50%
P21/C	FEFNOT09	1	4.41%

Table 1: CBZ polymorph studied

A total of five anhydrate polymorphs and three dihydrate CBZ polymorphs are identified. However, following the criteria outlined above, anhydrate type I and both othorhombic dihydrates were excluded, with reasons listed in Table 2.

Polymorph code	Reason
I	Z' > 1
Orthorhombic Cmca	Incomplete experimental structure file
Orthorhombic Abam	Incomplete experimental structure file

Table 2: Excluded polymorphs and reasons

2.2 Gas phase energy calculation

The gas phase energy of CBZ and water molecules is a crucial input of CSOFM and CrystalPredictor. Gas phase energy was calculated using the CrystalSetup program, by inputting the selected experimental structure of CBZ anhydrate (polymorph type III structure with lowest R-factor was used), bond interaction information, and CrystOpt.input containing the relevant settings, maximum valid range for intramolecular, intermolecular and electrostatic LAM calculations. By using the Gaussian09 program, the gas phase energy was calculated and recorded in mol.input file, which is used then used in CSOFM and CrystalPredictor step.

2.3 Identifying degrees of freedom

CBZ is considered as a rigid molecule overall due to the presence of tricyclic structure. However, the overall structure ($R - CONH_2$) in which the bond connecting the tricyclic component and amide functional group, and the bond connecting NH_2 with C are considered as flexible, as the bonds can perform torsion and rotation movement. A figure illustrating the flexibility of CBZ molecule is shown below.

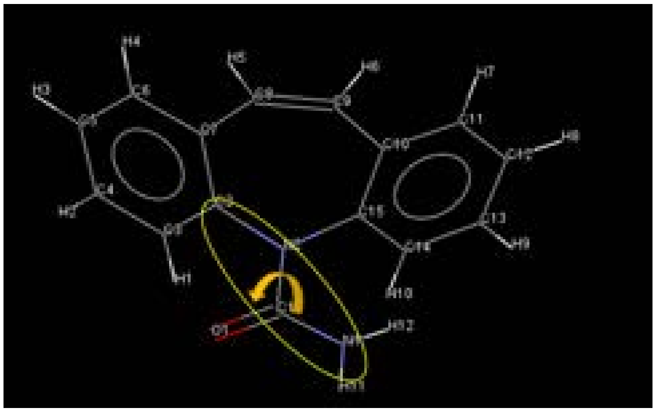

Figure 1: Torsion and rotation movement

Each flexible degree of freedom is defined by a dihedral, which consists of 4 consecutive atoms. When determining a dihedral, the following rule of thumb is used:

- The flexible bond is defined by the 2^{nd} and 3^{rd} atom.
- Avoid using double bond (in this case , the $C-O$ bond), as there is no relevant specification for π bond for QM calculations.

The following table summarises the dihedral used in calculations:

No.	Dihedral
1	C-N-C-N
2	H-N-C-N

Table 3: Dihedral identification

2.4 CSOFM trial run

Structure identified above were used as input for a trial CSOFM run. This step is aimed to evaluate the whether the combination of level of theory PBEPBE6−31G(d,p) and repulsion/dispersion parameter sets (FIT and DB2020) used are suitable for this study. The performance of these combinations are evaluated based on two indicators:

- $RMSD_{15}$ value [8]
- The optimal lattice energy

The optimal lattice energy of each polymorph given by the output file, CSO_FM.output was recorded to determine the relative stability ranking of CBZ polymorphs. The optimal structure was then extracted and compared against the original input (experimental) structure using the Crystal Similarity Packing tool in Mercury which gives the $RMSD_{15}$ value, indicating how much the optimal structure has deviated from the experimental structure.

It is generally regarded that an $RMSD_{15}$ value below 0.8 suggests the generated and experimental structures are considered identical.

2.5 Crystal Structure Prediction

The crystal structure prediction step employed CrystalPredictor V.2.4.4 developed by the Centre of Process Engineering (CPE). The program utilised the 2D molecular formula and gas phase energy of the CBZ molecule, as well as information on empirical repulsion/dispersion interactions for each different atomic type (this information were stored in file potential.in). An existing LAM-database from CPE database generated by the previous research group was also used. [9]

CyrstalPredictor V.2.4.4 then uses the molecular information submitted to generate a series of feasible structures, where the number of output dihydrate structures were specified in this study to be 200,000, while the anhydrate structures used were generated by CPE previously. A energy cut-off of 20 kJ/mol above the global minimum was then applied to filter out unstable structures.

The top 1,000 most stable structures are then selected for further refinement.

2.6 Structure refinement

The purpose of this step is to obtain the optimal lattice energy and corresponding density of the generated structures. The structures undergo CSOFM with combinations of level of theory PBEPBE6-31G(d,p) with both DB_2020 and FIT repulsion/dispersion parameters. The optimal structures (output.res) are then analysed using Crystal Similarity Packing tool, giving $RMSD_{15}$ values respectively. The structure with the lowest $RMSD_{15}$ value was then selected. The difference in lattice energy between the experimental structure and global optimal (in the refined landscape) determines its energy ranking. The energy ranking is indicative of the performance of the repulsion/dispersion parameter used.

3 Results and discussion

This section provides key findings of each step listed in the methodology above. The performance of FIT and DB_2020 parameters are also evaluated in this section from the following two perspectives:

- Geometric resemblance.
- Energy ranking and optimal lattice energies.

Geometric resemblance was analysed through $RMSD_{15}$ values in the same fashion as previously discussed. On the other hand, a lower the energy ranking suggests that the experimental structure are closer to the global optimal, where structures with lower lattice energy are more stable.

3.1 Optimisation of experimental structures

The experimental structure was optimised using CSOFM, producing optimal lattice energy and corresponding generated structure as output. The results show that both DB2020 and FIT repulsion/dispersion parameter sets work well with level of theory PBEPBE6-31G in terms of geometric optimisation. All output structures have $RMSD_{15}$ value less than 0.8, implying that the optimal structure has negligible deviation from the initial experimental structure. The general trend is that the FIT parameter has lower $RMSD_{15}$ values compared to DB2020, hence it can be inferred that FIT has slightly more accurate structure prediction than DB2020 with the exeption ofdihydrate P21/C and anhydrate IV where FIT has a higher $RMSD_{15}$, hence less accurate. In the case of anhydrate polymorph type III, both DB2020 and FIT parameters show similar performance, while for anhydrate polymorph II and V, $RMSD_{15}$ value from FIT is significantly lower than that of DB2020.

$RMSD_{15}$ Value			
Polymorph	Reference Structure	DB2020	FIT
II	CBMZPN03	0.229	0.208
III	CBMZPN13	0.400	0.387
IV	CBMZPN12	0.192	0.214
V	CBMZPN16	0.516	0.490
P21/C	FEFNOT09	0.300	0.312
III (2)	CBMZPN17	0.403	0.403

Table 4: $RMSD_{15}$ values of optimal structures

Anhydrate type III and IV inherit the same space group as dihydrate P21/C, which is categorised as monoclinic. Multiple studies have shown that CBZ crystals under this space group exhibit high stability [10]. Polymorph II is in a trigonal form and polymorph V in an orthorhombic form, where both are metablestable structures. An additional CSOFM job was done for another polymorph III structure which has the second lowest R-factor. The result shows that both DB2020 and FIT output the same $RMSD_{15}$ value, confirming that FIT and DB2020's geometric prediction capability have negligible deviation with structure that is highly stable. Overall, both sets of parameters provide good representation on the experimental structures based on the $RMSD_{15}$ values in the results. With monoclinic P21 space group, DB2020 has better geometric prediction than FIT whereas FIT has better geometric optimisation for structures that are less stable (CBZ crystrals with trigonal and othorhombic space groups).

Another factor to consider is the optimal lattice energy output, which will be discussed in further detail in a later section. The output optimal lattice energy gives the relative stability ranking shown in Table 5. Both parameter sets agree that polymorph III is the most stable structure while II is the least stable among the existing anhydrate polymorphs. However, there is a disagreement between the stability ranking of polymorphs IV and V, with IV having an optimal lattice energy 1.27 kJ/mol higher than V based on FIT parameter. As for DB2020, the optimal lattice energy of IV is significantly lower than V by 6.55 kJ/mol [11].

Optimal Lattice Energy (kJ/mol)		
Polymorph	DB2020	FIT
II	-108.91	-110.88
III	-120.43	-121.80
IV	-118.62	-117.07
V	-112.08	-118.33
P21C	-69.36	-70.81
III (2)	-120.23	-121.72

Table 5: Optimal lattice energy from CSOFM step

Limited amount of studies have been conducted on the relative stability between polymorphs IV and V due to few reasons. Firstly, although polymorph IV has similar space group as polymorph III, the discovery of form IV was quite recent in 2017 [12]. This polymorph form can be only produced via spray drying on small scale as it is extremely thermal sensitive [13]. Form V is in a similar scenario and due to its instability, there is only one experimental structure submitted to the CCDC database. Given these conditions, the relative energy ranking found from CrystalPredictor will be used to decide the parameter set that is more reliable on determining the stability ranking of the polymorphs.

Overall, both parameter sets optimised the structures well and returned optimal lattice energies giving relative stability ranking that matches with literature. Therefore, either parameter set could be used in structure refinement after the CSP step.

3.2 Crystal Structure Prediction

In this step, CrystalPredictor V.2.4.4 performs a global search on global landscape [14] and generated 200,000 feasible structures, where each feasible structure is represented by a global optimal on the energy landscape. Clustering was then applied to get rid of redundant or repetitive structures, while the remaining structures undergo a single iteration of CrystalOptimizer to output the optimal lattice energy. This was followed by a energy cut-off of 20 kJ/mol above the global optimal as outlined in the methodology. The energy landscape was then visualised in Figure 2.

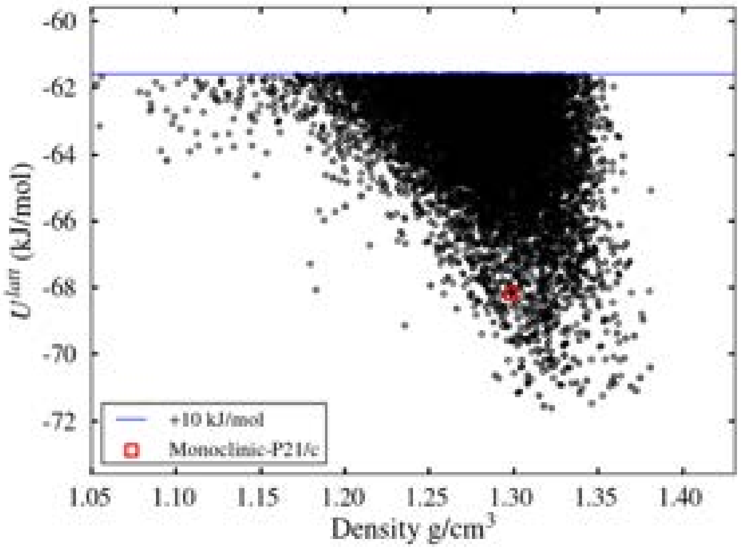

Figure 2: Energy landscape - CrystalPredictor

After the energy cut-off was applied, 15,285 structures remain, which is 7.5% of the total number of searches. The number of remaining structures is likely to increase by increasing the number of searches - by relaxing the constraint. From the figure, we can see that the optimal lattice energy (kJ/mol) and density (g/cm^3) are not directly correlated. Rather it shows a shape resembling a normal distribution curve, where the global optimum is located somewhere close to the average (or median) density.

This trend could be explained using the density is an indicator of how close the molecules are packing in a unit cell (where Z' = 1 represents 1 molecule in 1 unit cell). The closer the packing, the larger the dispersion/repulsion interaction. The stability of a structure has a certain amount of trade off between increase in intramolecular energy caused by deformations of vacuo conformations and the energy decrease due to attractive and repulsive intermolecular interactions [14]. The global minimum has a density between 1.3-1.35 g/cm^3, which from the chart, is on the larger side. To calculate the lattice energy, CrystalPredictor V.2.4.4 uses the following formula sets at 0 K and 0 bar, the lattice energy is partitioned into the intramolecular and intermolecular contributions [3].

$$\underset{x,\theta}{\mathrm{Min}} E^{latt} = \underset{x,\theta}{\mathrm{Min}}[\Delta E^{intra}(\theta) + U^{inter}(x,\theta,\Omega(\theta))] \quad (2)$$

where descriptions of each variable could be found in the nomenclature. Intramolecular energy is usually small and decrease with decreasing temperature[15]. Therefore, the intermolecular energy, which is mainly composed by the electrostatic interaction between each isolated molecule's charge density through closed packing, is the dominant term. This is further proven by the results from the optimisation of experimental structures. A figure that visualises the difference between intermolecular and intramolecular contributions could be found in the Appendix, where the intramolecular contribution is nearly negligible compared to the intermolecular contribution.

The aim in this step is to capture the monoclinic P21/C structure from the set of remaining structures. These structures were compared against experimental structure FEFNOT09 on Mercury and the structure with the lowest $RMSD_{15}$ value is identified, with the results reported in Table 6.

Generated structure : 951-1				
ρ	$RMSD_{15}$	Global Optimum	E^{latt}	Ranking
1.30	0.42	-72.000	-68.187	+3.813

Table 6: Experimental structure from CP.V.2.4.4

The output structure from CrystalPredictor with the lowest $RMSD_{15}$ value among the 200,000 generated structures is ranked 951^{st}. The refinement process allows a structure with an even lower lattice energy to be found, better representing the experimental structure. The density of the output structure was 1.3 g/cm^3, fairly similar to the global optimum value, whereas the energy ranking was +3.813 kJ/mol, indicating that the prediction is less precise in energy optimisation. The $RMSD_{15}$ value found was 0.42, which compared to the value from the previous optimisation step, lacks accuracy in terms of geometric prediction.

The structure that was 'refined' once by the CrystalOptimizer [16] uses *ab inito* Gaussian Investigations to calculate the intramolecular contributions, while GDMA and empirical repulsion/dispersion parameters were used for computing intermolecular contributions. However, the empirical repulsion/dispersion parameter sets employed by CrystalOptimizer might not be optimal with the level of theory used. Hence, with the aim of determining the suitability of parameter, and while following the standard procedure of CSP, CSOFM is employed in the refinement stage for the first 1,000 (low-energy) structures [17], allowing a more accurate structure prediction.

3.3 Refinement Stage

In this stage, the use of DB2020 and FIT parameter sets were each tested with level of theory PBEPBE6-31G(d,p). The performance of each parameter were assessed based on the energy ranking and $RMSD_{15}$ value of the output structures, with low energy ranking and $RMSD_{15}$ value being classified as good. The accuracy of geometric prediction are evaluated through the $RMSD_{15}$ value of the predicted experimental structure.

Both refinements (using DB2020 and FIT) show significant improvement in the accuracy of geometric prediction. A possible explanation could be that the level of theory used is more suitable for molecules with two or more flexible DoFs (torsion angles) compare the default level of theory used by CrystalOptimizer. PBE series are known for its calculation capacity of molecules with multiple DoFs, using GAUSSIAN09. For example, one study shows that the PBE level of theory demonstrated high accuracy when using it as a intermediate step to estimate free energy of structures [18]. Another example is a study conducted on the sixth blind test of molecule (XXVI) using PBE1PBE, which is similar to level of theory PBEPBE. It produced an output of conformational multipoles and intramolecular energy, demonstrating that it could handle molecules with up to 7 torsion angles [19].

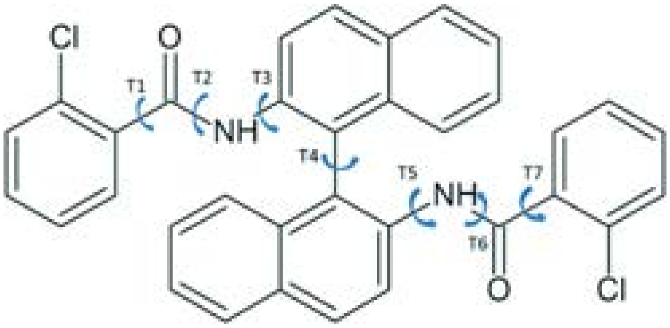

Figure 3: Highly flexible molecule (XXXVI)

However, there is a deviation between FIT and DB2020 in terms of lattice energy optimisation and energy ranking decrements. The reasons for this will be discussed in further detail in sections 3.3.1 and 3.3.2

3.3.1 DB2020 parameter

Figure 4 shows the refined energy landscape of the top 1,000 low-energy structures while the summarised results can be found in Table 8, it is shown that the optimal generated structure is much closer to the global optimum in both density and lattice energy.

The generated structure after the CSOFM step shows significant improvement geometrically and energy ranking wise. The $RMSD_{15}$ value decreased from 0.42 to 0.307 while the energy ranking decreased 42% from +3.81 to +2.210. It is worth mentioning that the density only changed by 0.01 g/cm^3 after CSOFM, implying that the structural density will not change much regardless of the level of theory and parameter set used.

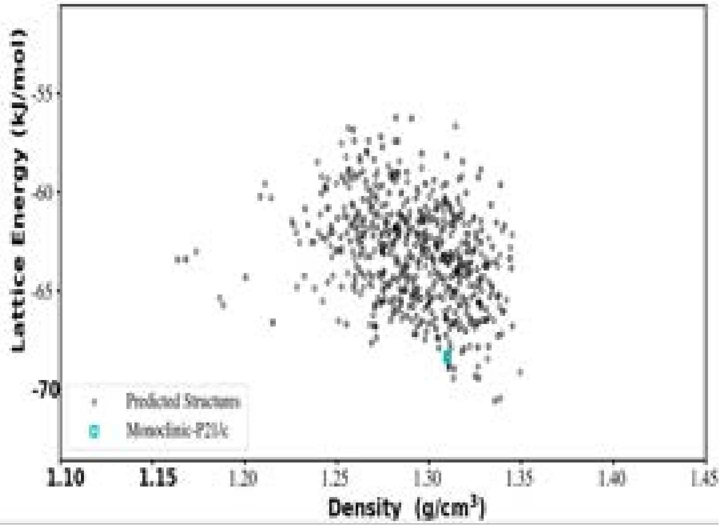

Figure 4: Refined energy landscape for DB2020

DB2020 - Structure 367−1				
$RMSD_{15}$	Global Optimal	Lattice Energy	Energy Ranking	Density
0.307	-70.554	-68.344	+2.210	1.310

Table 7: Refined structure

3.3.2 FIT parameter

In contrast to DB2020, the FIT parameter has optimal generated structure further away from the global optimum. The structures optimised by FIT parameter is also less than DB2020 with 811 structures refined, whereas DB2020 had 856 structures refined.

From the figure above, it can be seen that the optimal generated structure is well above the global optimum and the density is smaller than the DB2020's experimental structure. The numerical information is summarised in Table 9.

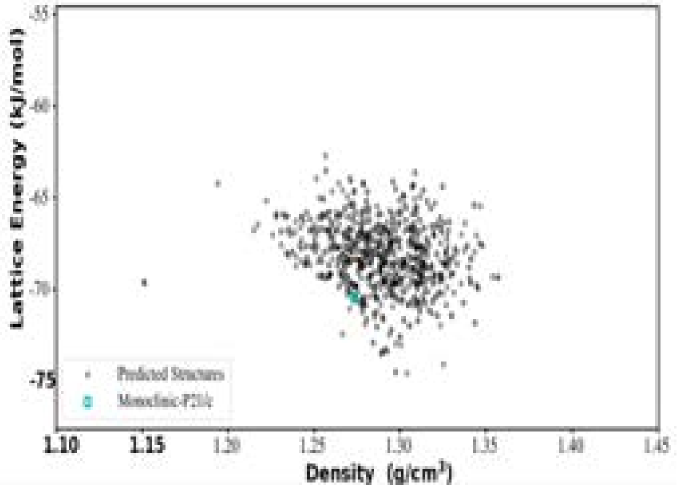

Figure 5: Refined energy landscape for FIT

FIT - Structure 648−1				
$RMSD_{15}$	Global Optimal	Lattice Energy	Energy Ranking	Density
0.300	-74.101.	-70.501	+3.600	1.277

Table 8: Refined structure using FIT

The experimental structure shows a significant improvement in terms of geometric prediction. The $RMSD_{15}$ value of the refined experimental structure decreased from 0.42 to 0.3, corresponding to a 28.57% decrease. The improvement in energy ranking, however, is not as significant as in DB2020. The energy ranking is +3.6 kJ/mol compared to the initial 4.2 kJ/mol energy ranking, only a 14% decrease in energy ranking.

3.4 Performance analysis

The performance of each parameter are analysed by two aspects:

- Geometric prediction
- Energy ranking

From the refined results, FIT has slightly better geometric prediction than DB2020 when working with level of theory PBEPBE6−31G(d,p). The average $RMSD_{15}$ value of the top 1,000 low-energy structures, and the $RMSD_{15}$ value of experimental structures are lower in FIT than DB2020. A graphical illustration comparing the capacity to predict geometrically is shown in Figure 6.

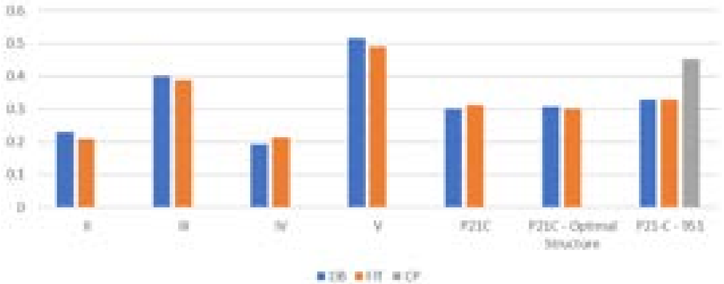

Figure 6: $RMSD_{15}$ results

Both DB2020 and FIT can to capture the geometrical structure with $RMSD_{15}$ value well below 0.8, where the reference structure and experimental structure could be considered as identical. The generated structures using FIT and DB2020 parameters have significantly better performance than empirical repulsion/dispersion parameters (grey in Figure 6). Therefore, it is insufficient to just use geometrical factors to assess the performance of dispersion/repulsion parameter sets. The energy ranking from the refinement stage should also be used to determine this [20].

Energy ranking measures how far the experimental structure deviates from the global optimum, thus it is proportional to instability. A predicted crystal structure with high energy ranking infers that the structure is more unstable. To predict a better structure that is more stable and closer to the optimal structure, the constraint of searching might have to relaxed,such as increasing the number of searches, energy cut-off, or number of structures for refinement; else additional iterations of crystal optimisation using the generated LAM databases from previous runs as input. However, doing this is not advisable as it will drastically increase computing resources, hence finding the parameter set output lower energy ranking in a single crystal optimisation iteration is beneficial. The energy ranking comparison between DB2020 and FIT are summarised below:

	CSOFM with DB2020 (kJ/mol)	CSOFM with FIT (kJ/mol)
Global minimum	-70.5542	-74.10065
Experimental lattice energy	-68.3441	-70.50075
Energy ranking	+2.2101	+3.5999

Table 9: Compare energy ranking DB2020 and FIT

The energy ranking output by DB2020 is lower than FIT by 38%, this figure is calculated by

$$Diff_{RMSD_{15}} = \frac{RMSD_{15FIT} - RMSD_{15DB2020}}{RMSD_{15FIT}} \tag{3}$$

The energy ranking of DB2020 is significantly lower than FIT, which means that the predicted structure by DB2020 resembles more with the global optimum solution compared to FIT with only one CSOFM iteration. Although the global optimum could vary between different molecules, in this case, DB2020 is more efficient than FIT and therefore, a parameter set better suited with level of theory PBEPBE6-31G(d,p) when performing CSP. Although both parameter sets use multipoles to model electrostatic interactions, the reason that this is the case could be because DB2020 parameter set is specially fitted to PBE level of theory.

Thus, the optimal lattice energy outputs by CSOFM using repulsion/dispersion parameter set DB2020 is used to determine the relative stability of available polymorph in this study.

3.5 Stability ranking of polymorphs

3.5.1 Anhydrates

The relative stability ranking of CBZ polymorphs were determined by the lattice energy output from CSOFM. The following figure visualises the absolute value of optimal lattice energy output (kJ/mol) for the four anhydrate polymorphs. The dihydrate polymorph P21/C is excluded as additional steps are required to calculate the energy contribution of water molecules in the dihydrate.

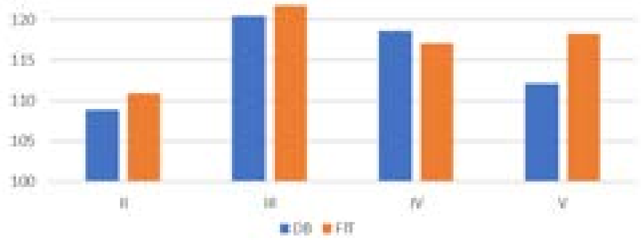

Figure 7: Optimal lattice energies of anhydrate polymorphs in absolute values

Figure 7 shows that both FIT and DB2020 parameters deem polymorph III as the most stable while polymorph II the least stable based on their lattice energies. However, the parameters each rank the relative stability of polymorph IV and V differently. Furthermore, on the optimisation of polymorph V, there is a large difference in optimal lattice energy output (approximately 6.3 kJ/mol) between the two parameters.

As found in section 3.4, DB2020 performs better than FIT with the chosen level of theory. Therefore, the energy ranking computed based on DB2020 was used. In order of decreasing stability, the relative stability ranking for anhydrates are as follows: polymorph III > IV > V > II.[21] This order matches with literature which states that CBZ crystals in space group monoclinc P21/C (polymorph III) and monoclinic P21/n (polymorph IV) are relatively more stable than other space group types. Among the two, monoclinic P21/C is more stable, proven by comparing their solubility and thermo-sensitivity data. The stability of polymorph III and IV have been tested experimentally by dissolving both crystals in multiple solvents, with results showing that anhydrate polymorph IV has higher dissolution rate than III [1] while it is also more thermo-sensitive. This would explain why polymorph III is used on a large scale in the pharmaceutical industry, whereas the usage of IV is quite limited. A figure illustrating the relative stability ranking of four available anhydrate polymorphs are shown below.

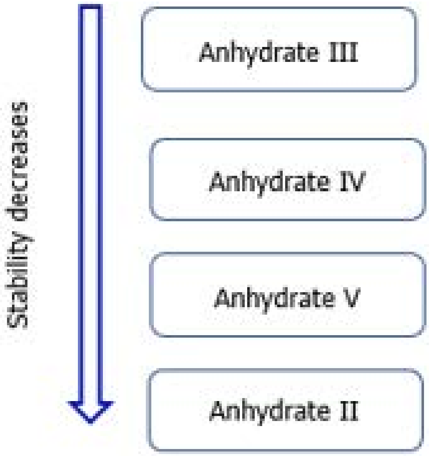

Figure 8: Stability ranking of CBZ anhydrates

3.5.2 Stability of dihydrate

Multiple studies have found that CBZ dihydrate in monoclinic P21/C space group is one of the most stable polymorphs. The high stability of the dihydrate could be contributed by water molecules filling up the vacant spaces within the crystal structure, thus improving its structural integrity and introduces extra dipole-dipole interactions which affects its intermolecular energy. This further decreases the overall lattice energy, making the crystal structure more stable.

To take into account the contribution of water molecules on the overall lattice energy of the dihydrate, a mathematical relation was proposed:

$$E^{Latt}_{CBZ} + 2E^{Latt}_{H_2O} \geq E^{Latt}_{Dihydrate} \geq 3E^{Latt}_{Optimal} \tag{4}$$

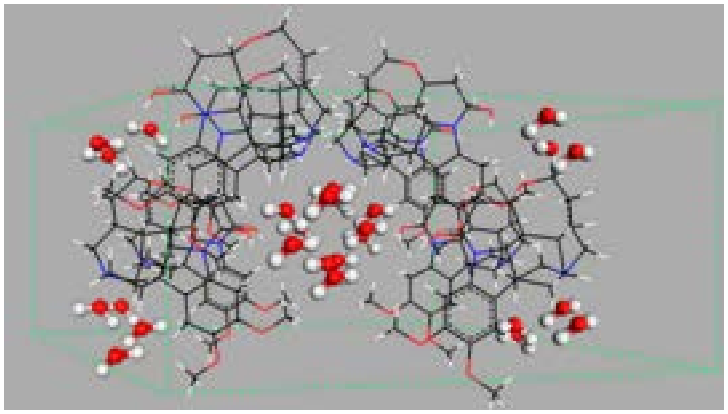

Figure 9: Dihydrate stability illustration

where $E^{Latt}_{Optimal}$ is the output from CSOFM, corresponding to the average lattice energy contribution of each molecule in the dihydrate (3 molecules in total: 1 CBZ and 2 H_2O molecules).

The lattice energy of the isolated water molecule was calculated using cubic ice structure through a single iteration of CSOFM utilising DB2020 repulsion/dispersion parameter. The lattice energy of individual water molecule was then calculated to be -48.63 kJ/mol and the average lattice energy contribution was -69.36 kJ/mol.

Hence, the resulting lattice energy of dihydrate P21/C is within the following range:

$$-166.62kJ/mol \geq E^{Latt}_{Dihydrate} \geq -208.89kJ/mol \tag{5}$$

Dihydrate P21/C is the most stable polymorphs in this study. The relative stability ranking is now:

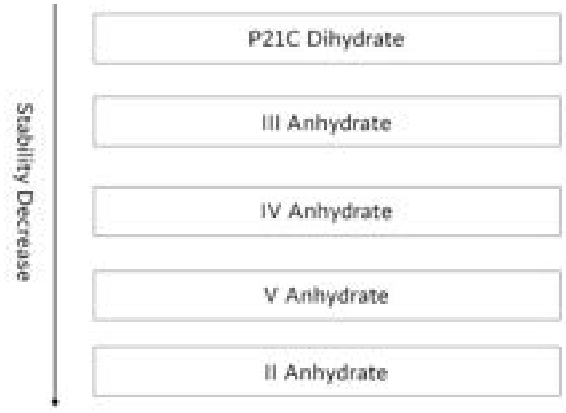

Figure 10: New stability ranking of CBZ polymorphs

4 Conclusion

In this report, we studied the feasibility of repulsion/dispersion parameter sets, DB2020 and FIT with level of theory PBEPBE6-31G(d,p) and assessed which parameter sets work better in predicting the potential structure of CBZ anhydrate and dihydrate. Thus, giving a relative stability ranking of CBZ polymorphs. The experimental structures selected for this study are anhydrates II, III, IV, V and dihydrate P21/C.

After running the experimental structures through a single iteration of crystal optimisation using CSOFM, it was found that both DB2020 and FIT geometrically optimised the CBZ crystal structure well enough that the $RMSD_{15}$ values are well below 0.8. Indicating that both parameter sets are feasible for crystal optimisation. To further assess the performance of both parameters, CrystalPredictor is used to generate 200,000 possible structures while applying an energy cut-off of 20 kJ/mol. Here, results show that the lowest $RMSD_{15}$ value is 0.42 with energy ranking +3.813 kJ/mol. However, as CrystalPredictor employs empirical repulsion/dispersion parameter to perform the cluster step, it might not be the best suit for level of theory. Hence, further iteration of crystal optimisation on the top 1,000 low-energy structures were done using CSO-FM to identify the parameter that can further improve the geometric prediction and energy rankings of structures.

The predicted experimental structures using DB2020 has $RMSD_{15}$ value of 0.307 and the energy ranking of 2.210 kJ/mol above the global optimum, whereas FIT had $RMSD_{15}$ value of 0.3 and energy ranking of

3.6 kJ/mol above the global optimum. As the energy ranking of DB2020 is much lower than FIT given their similar performance on geometric prediction, results from DB2020 is used to determine the relative stability ranking of the polymorphs, which has the following order:

$P21/C_{dihydrate} > III_{anhydrate} > IV_{anhydrate} > V_{anhydrate} > II_{anhydrate}$

5 Outlook

To gain a better understanding on how well the parameter sets perform in CSP, while also to test the reliability of DB2020 parameter sets, the same analysis could be conducted using different combinations of DFT and basis sets that are also popular in CSP of flexible molecule, such as PBE1PBE6-31G and BELY+aug-cc-pvtz level of theory [22][23].

To be more time efficient in the early setup process, and to help future research groups work more efficiently with the CSP programs developed by CPE, a standard procedure for CSO-FM/CSO-RM could be written.

In order to save computational resources, a relatively smaller number of predicted structures were generated by CrystalPredictor in our study. However, to obtain a more integrated energy/density landscape, as well as have better assessment on the performance of parameters based on energy rankings, up to 1 million predicted structures can be generated, and all structures below the energy cut-off of 20 kJ/mol refined to identify the new predicted experimental structures.

6 Acknowledgement

We would like to express our sincere gratitude to Mr. Yizu Zhang and Professor Claire Adjiman for their invaluable support, guidance and feedback throughout the project. We would also like to thank Mr. Issac Sugden and Mr. Stefanos who kindly provided us with the relevant database and files for this project.

References

[1] Roberta Censi and Piera Di Martino. “Polymorph Impact on the Bioavailability and Stability of Poorly Soluble Drugs”. In: *Molecules* (2015). DOI: `https://www.mdpi.com/journal/molecules`.

[2] *Ritonavir*. URL: `https://www.drugs.com/monograph/ritonavir.html`. (accessed: 19.12.2021).

[3] C Adjiman P Karamertzanis and C Pantelides. “Efficient Handling of Molecular Flexibility in Lattice Energy Minimization of Organic Crystals”. In: *Journal of Chemical Theory and Computing* (2011). DOI: `https://pubs.acs.org/doi/pdf/10.1021/ct100597e`.

[4] *Carbamazepine*. URL: `https://www.nhs.uk/medicines/carbamazepine`. (accessed: 19.12.2021).

[5] World Health Organization. “World Health Organization model list of essential medicines: 21st list 2019”. In: *World Health Organization Model List of Essential Medicines* (2019). DOI: `https://apps.who.int/iris/bitstream/handle/10665/325771/WHO-MVP-EMP-IAU-2019.06-eng.pdf`.

[6] *The Top 300 of 2019 Provided by the ClinCalc DrugStats Database*. URL: `https://clincalc.com/DrugStats/Top300Drugs.aspx`. (accessed: 19.12.2021).

[7] Y Andreev. “R-Factor”. In: *Encyclopedia of Materials: Science and Technology, 2001* (2001).

[8] *Supplementary Data: Details of Predictions located during post-analysis*. URL: `chrome-extension://efaidnbmnnnibpcajpcglclefindmkaj/viewer.html?pdfurl=https%5C%3A%5C%2F%5C%2Fjournals.iucr.org%5C%2Fb%5C%2Fissues%5C%2F2011%5C%2F06%5C%2F00%5C%2Fbk5106%5C%2Fbk5106sup4.pdf&clen=339531&chunk=true`. (accessed: 19.12.2021).

[9] Imperial College London Centre of Process Engineering. *Crystal Predictor v2.4.3 Manual*. (accessed: 06.12.2020).

[10] Aurora J. Cruz Cabeza. *Amide Pyramidalization in Carbamazepine: A Flexibility Problem in Crystal Structure Prediction*. URL: `https://pubs.acs.org/doi/full/10.1021/cg0601756`. (accessed: 20.12.2021).

[11] Sarah L. Price Jean-Baptiste Arlin Louise S. Price and Alastair J. Florence. “A strategy for producing predicted polymorphs: catemeric carbamazepine form V”. In: *Chemical Communication* (2011). DOI: `https://pubs.rsc.org/en/content/articlelanding/2011/CC/c1cc11634g`.

[12] Adam J. Matzger Meidong Lang Jeff W. Kampf. “Form IV of Carbamazepine”. In: *Journal Of Pharmaceutical Science* (2002). DOI: `https://doi.org/10.1002/jps.10093`.

[13] Rajni M.Bhardwaj Rebecca A.Halliwell. “Spray Drying as a Reliable Route to Produce Metastable Carbamazepine Form IV”. In: *Journal of Pharmaceutical Sciences* (2017). DOI: `https://www.sciencedirect.com/science/article/pii/S0022354917302460`.

[14] Claire S. Adjiman Constantinos C. Pantelides and Andrei V. Kazantsev. “General Computational Algorithms for Ab Initio Crystal Structure Prediction for Organic Molecules”. In: *Top Curr Chem* (2014). DOI: `https://link.springer.com/chapter/10.1007/128_2013_497`.

[15] John C. Stephenson and C. Bradley Moore. “Temperature Dependence of Nearly Resonant Vibration-Vibration Energy Transfer in CO2 Mixtures”. In: *The Journal of Chemical Physics* (1972). DOI: `https://aip.scitation.org/doi/10.1063/1.1677362`.

[16] Imperial College London Centre of Process Engineering. “CrystalOptimizer Manual”. In: (2017).

[17] Claire S. Adjiman Manolis Vasileiadis Constantinos C. Pantelides. “Prediction of the crystal structures of axitinib, a polymorphicpharmaceutical molecule”. In: *Chemical Engineering Science* (2015). DOI: `https://www.sciencedirect.com/science/article/pii/S0009250914004904`.

[18] Sarah L.Price Luca Iuzzolino Patrick McCabe and Jan Gerit Brandenburg. “Crystal structure prediction of flexible pharmaceutical-like molecules: density functional tight-binding as an intermediate optimisation method and for free energy estimation”. In: *Chemical Engineering Science* (2018). DOI: `https://pubs.rsc.org/en/content/articlehtml/2018/fd/c8fd00010g`.

[19] Claire S. Adjiman Isaac Sugden and Constantinos C. Pantelides. “Accurate and efficient representation of intramolecular energy in ab initio generation of crystal structures. I. Adaptive local approximate models”. In: *Acta Crystallographica Section B* (2016). DOI: `https://www.ncbi.nlm.nih.gov/pmc/articles/PMC5134761/`.

[20] Marcus A.Neumann Johannes Hoja Hsin-Yu Ko. "Reliable and practical computational description of molecular crystal polymorphs". In: *Science Advances* (2019). DOI: `https://www.ncbi.nlm.nih.gov/pmc/articles/PMC6357866/`.

[21] Horst Puschmann Robin K. Harris Phuong Y. Ghi. "Structural Studies of the Polymorphs of Carbamazepine, Its Dihydrate, and Two Solvates". In: *Organic Process Research and Development* (2015). DOI: `https://pubs.acs.org/doi/10.1021/op0500990`.

[22] *Density Functional (DFT) Methods*. URL: `https://gaussian.com/dft/`. (accessed: 19.12.2021).

[23] *CHEM6085: Density Functional Theory*. URL: `https://www.southampton.ac.uk/assets/centresresearch/documents/compchem/DFT_L8.pdf`. (accessed: 19.12.2021).

Development of a Reversible Fluorescent Ca^{2+} Biosensor for Contact Lens Diagnosis

Fhai Gunavibool and Temilola Olapade-Ayomidele
Department of Chemical Engineering, Imperial College London, U.K.

Abstract: Detection of calcium concentration outside of the physiological range within the body can be an indication of different diseases such as dry eye disease and ocular cancers. For early detection, wearable devices with ion sensors are currently being developed. With the aim to create a non-invasive point-of-care diagnostic device, this study sought to produce a sensitive, selective and reversible Ca^{2+} hydrogel based contact lens biosensor. It is composed of four main components: a monomer (hydroxyethyl methacrylate, HEMA), a luminogen (acrylated berberine chloride, BBR chloride), a crosslinker (N,N'-Methylenebisacrylamide, MBA) and Ca^{2+} receptor (methacrylic acid). The project was split into two phases; the first was to create the hydrogel sensor and the second to optimise the sensor. A microplate reader was used to measure the emissivity of the hydrogel and an optical microscope was used to measure the swelling ratio. The optimal hydrogel sensor consisted of a 1:9 HEMA:MAA ratio, 0.05 mol% MBA, 15 mM acrylated BBR chloride and 1:1 v/v isopropanol as a solvent.

Keywords: Hydrogel, biosensor, Ca^{2+} receptor, luminogen, crosslinker, contact lens

1 Introduction

Calcium is vital in the functioning of life, being among the top five most common elements on Earth and the most abundant metallic ion in most biological systems (Erulkar, 1981). Its integral role within the cells of a human body makes it crucial to be able to monitor and detect its concentration with ease and accuracy. Calcium cations are situated in intercellular, intracellular, and extracellular sites, providing a great scope for detection through various sampling methods. Within the human body, calcium signalling uses calcium ions as a driver for signal transduction, where it acts as a key secondary messenger and facilitates in the regulation of important physiological activities such as muscle contractions, fertilization, intestinal microbial activity, and the neuronal excitability (Song et al., 2019).

Abnormal concentrations of calcium in the body can cause hypercalcemia (ionised calcium in blood >1.30 mmol/L). This is when the concentration of calcium ions in the blood is in excess, causing weakened bones, kidney stones and interference with the normal functioning of the heart and brain (MayoClinic). Hypercalcemia affects 1 in 1000 people (Turner, 2017) and up to 30% of all people with cancer will develop a high calcium level as a side effect (Cancer.net, 2020). Early detection of the changes in calcium levels has great potential to help many patients. Hypocalcaemia (ionised calcium in blood <1.17 mmol/L) is a state in which there is insufficient calcium in the blood, and leads to neurological and psychological deterioration, as well as muscle related issues. These diseases are currently diagnosed by blood tests (III, 2021).

The use of contact lenses to detect calcium levels will cause minimal disruption to the wearer. In addition, it will reduce the burden on our healthcare system as the first diagnostic stage is done at home. With the rise in popularity of wearable health-tracking devices such as smart watches and smart jackets, there is growing demand for reversible, sensitive, and selective sensors. These three characteristics are particularly important in wearable health devices for biomarkers like calcium cations. Reversibility refers to the ability for the sensor to revert to the original state after collecting and measuring the relevant parameters; sensitivity refers to whether the sensor can detect minute changes in dilute concentrations; and selectivity refers to whether the sensor can accurately select the calcium ions out of a sample that is rich with many other biomarkers present, as this could skew the measured concentrations. The development of these wearable sensors and the advancement of technologies in predictive and preventative medicine, makes it possible for rapid diagnosis and screening to improve patient treatment, reduce cost of healthcare, and alleviate the burden on the healthcare systems.

Currently, there are other calcium cation detection methods available, such as calcium imaging, electrochemical sensors, and fluorescent sensors. However, calcium imaging is unsuitable for extracellular detection as the commercial dyes that are used such as fura-2, indo-1, fluo-2, and fluo-4 are dyes that only bind to intracellular calcium (Wikipedia, 2021). Electrochemical sensing technology is not compatible with the contact lens application and is also critically dependent on pH, which would be difficult to maintain with the desired sampling method using tears (Bazydlo et al., 2014). Fluorescent ion sensors work in such a way that takes advantage of the changing fluorescent properties of the luminogen. When a change in its chemical structure occurs, it can also be incorporated into a multitude of platforms due to its versatility, selectivity, and sensitivity, such as hydrogels to form fluorescent hydrogel sensors.

Several types of devices were considered and compared with traditional blood sampling. All wearable devices that were investigated allowed for less (or non) invasive sampling, although some are not continuous. Some of these devices include: microneedles (Esfandyarpour et al., 2013), patches (Orwar et al., 1999), mouth guards

(Arakawa et al., 2020) and contact lenses, where interstitial fluid, sweat, saliva and tears are used as the sampling fluids respectively. Although the use of microneedles with interstitial fluid would give the closest relationship to blood, the sampling method is still somewhat invasive when compared to using a contact lens as the patient's skin needs no penetration. The use of an iontophoretic patch biosensor by sampling sweat is less advantageous since there are many factors that affect the quality as it is heavily dependent on external environmental factors such as ambient temperature, activity, and diet. Moreover, sample collection is slow and tedious, as sweat is secreted at low volumes and can be evaporated quickly, which may not be effective or sufficient for detection (Park et al., 2021). Finally, the main considerations for using a mouthguard stem from production challenges, as each mouthguard must be fitted to each specific patient's mouth. Additionally, a mouthguard cannot always be worn, and current published literature has only investigated use for sporting applications, which means it may not be viable for everyday continuous use. Furthermore, the sensor must be very selective as the constituents of saliva can vary greatly depending on the patient's diet or daily activities (Seshadri et al., 2019).

Tears have been increasingly popular in investigations for the diagnosis of ocular diseases, such as dry eye disease (DED), vernal conjunctivitis, diabetic retinopathy, Graves' ophthalmopathy, ocular tumours and glaucoma (Hagan et al., 2016). This is due to its close relationship with blood caused by the continuous leakage of plasma from the blood to tears through the blood-tear barrier. In addition to this, contact lenses are relatively easy to produce using biocompatible hydrogels, which can integrate the fluorescent hydrogel sensors. This allows for the scope of detection to include other crucial biomarkers that can be found in tears for future development (Tseng et al., 2018). The contact lens is the most suitable platform.

Fluorescent hydrogel sensors can be integrated onto a contact lens (March et al., 2006). For the application to contact lenses, hydrogels should possess the following key characteristics: good oxygen permeability, transparency, flexibility, strength and low reactivity to chemicals on the eye surface (Royal Society of Chemistry, 2021). The calcium receptors must be a chemical species that can reversibly bind to ions, such as calcium, enabling the 'on-off' quality of the sensor. Luminophores are functional groups of a chemical species that are responsible for the fluorescent characteristics, which are the backbone of the sensor's mechanism - these compounds are referred to as luminogens. These luminogens can exhibit Aggregation-Induced Emission (AIE) (Wang et al., 2015) or Förster Resonance Energy Transfer (FRET) characteristics (Herman et al.; LibreTexts). The objective is to create a reversible, selective, and sensitive biosensor for point-of-care diagnosis advancements of divalent calcium ions within tear fluid.

2 Background

2.1 Hydrogels and Crosslinking

Hydrogels are a three-dimensional system of polymer chains that are held together with physical or chemical crosslinkers. They can swell and absorb large amounts of water while maintaining a gel-like structure (Bahram et al., 2016). For a system to be classified as a hydrogel, water must constitute at least 10% of the total weight volume. This hydrophilic nature of the network is owed to the existence of hydrophilic groups such as -NH_2, -OH and COOH. Depending on the properties of the specific hydrogel, it can undergo significant volume changes subject to external physical or chemical stimuli, which can be quantified by the swelling ratio of the gel. This response is largely determined by the nature of the monomer used and cross linker density.

Within this hydrogel, there are four key components to form the structure - monomer, Ca^{2+} receptor, crosslinker and luminogen. The first component is the monomer, hydroxyethyl methacrylate (HEMA), which is typically used as a basis of contact lens formation. The second component is the Ca^{2+} receptor, methacrylic acid (MAA), which is required for the adsorption of divalent calcium ions in tear fluid onto the hydrogel structure. Existing literature suggested acrylic acid as a calcium receptor as Ca^{2+} induces the single chain aggregation of polyacrylic acid through [COO^-–Ca^{2+}–^-OOC]-type ion binding (Ishiwari et al., 2016). Therefore, MAA should exhibit the same ion binding behaviour and thus was chosen to investigate as a novel receptor. The third component is the crosslinker, N,N'-Methylenebisacryl-amide (MBA) , which is a crucial player in the mechanism of the biosensor as it determines how much the hydrogel swells and contracts in response to the stimuli. The final component is the aggregation induced emission (AIE) luminogen, acrylated berberine (BBR) chloride, which is the component that underpins the fluorescence detection mechanism that the sensor relies on.

2.2 Aggregation Induced Emission Luminogens

Luminogens are atoms or molecules that when added to a solution cause it to fluoresce or luminesce (Wikitionary, 2016). AIE is a characteristic of a molecule that when excited in its isolated molecular state, does not release energy as light but releases energy through the molecule's freely rotating groups. When aggregation occurs, the molecule has restricted rotation and therefore emits light. There are three main mechanisms which describe the different ways AIEgens work: through-bond conjugation, which is the restriction of intramolecular rotation or vibration; through-space conjugation, which is the restriction of intramolecular motion; and through-bond & space conjugation, which can be the restriction of intramolecular motion or rotation. AIEgens are weakly or non-emissive in dilute solutions however when the molecules aggregate or are in solid state, they fluoresce (Zhu et al., 2018). Extensive research has been done into using tetraphenylethene (TPE) as the AIEgen in calcium sensors (Ishiwari et al., 2016). The synthesis of the PAA-TPE$_x$ was complex and therefore this report explores berberine chloride as it is naturally occurring in many herbal plants such as Rhizoma coptidis, Hydrastis canadensis and Cortex Phellodendri (Gu et al., 2018). This compound exhibits the AIE phenomenon and is biocompatible and therefore is the chosen AIEgen. The BBR chloride was acrylated so that it could be incorporated into the hydrogel matrix.

2.3 Sensor Mechanism

When the hydrogel matrix is placed into a calcium solution the methacrylic acid receptors bind to the Ca^{2+} ions. This binding causes the aggregation of the AIEgen and subsequently the hydrogel matrix fluoresces. A schematic of the sensor mechanism can be found in section A of the supplementary document.

3 Materials

For luminogen synthesis, BBR chloride of purity 98% from Meryer Chemical Technology, acryloyl chloride (≥ 97.0%), triethylamine (≥ 99.0%), diethyl ether (≥ 97.5%) from Sigma-Aldrich and absolute ethanol from VWR chemicals were used. For the preparation of glass slides, acetone (≥ 99.9%) and 3-(trimethoxysilyl)propylmethacrylate (98.0%) from Sigma-Aldrich were used. The monomers, methacrylic acid (MAA) of purity 99.0% and 2-hydroxyethyl methacrylate (HEMA) of purity 97.0% and remaining components Methylenebis-(acrylamide) (MBA) (99%), BBR chloride, 2-Hydroxy-2-methylpropio-phenone (HMPP) (97.0%), and isopropanol were procured from Sigma-Aldrich. To test the AIE phenomenon, tetrahydrofuran (≥ 99.9%) from Sigma-Aldrich was used. For solvent selection process, dimethyl sulfoxide (≥ 99.9%) was used alongside deionised (DI) water and isopropanol. For the solutions, Tris hydrochloride (99.0%) from Merck Millipore, Tris base (99.9%) from Roche, calcium chloride (≥93%), potassium chloride (≥99%), magnesium chloride (≥96%) and sodium chloride (≥99.5%) from Sigma-Aldrich were used.

4 Methods

4.1 Luminogen Synthesis (Acrylated Berberine Chloride)

The AIE luminogen was synthesised using 0.500 g of BBR chloride that was heated at 190°C for 15 minutes under vacuum in a bath of paraffin oil to form berberrubine as a dark purple solid. The berberrubine was dissolved by injecting 10 mL dichloromethane, 0.54 mL acryloyl chloride and 0.934 mL triethylamine, and subsequently degassed by nitrogen bubbling for 30 minutes. Reaction was left to proceed for 1 hour at room temperature. Once the reaction was completed, the reaction mixture was added dropwise in stirring diethyl ether. The precipitate was collected by filtration under vacuum. The purification process was repeated by dissolving the filtered solid in ethanol. The mixture was added dropwise, to stirring diethyl ether and filtered under vacuum once again and resulted in a yellow solid product and stored at 4°C. The product was characterised by mass spectra and NMR spectroscopy, the characterisation data can be found in section B of the supplementary document.

4.2 Hydrogel Preparation

Prior to hydrogel preparation, glass slides were silanised. Microscopic glass sides were immersed in a silane solution containing 3-(trimethoxysilyl)propylmethacrylate and acetone (1:50, v/v, 50 mL) in an aluminium tray for 24 hours. At the end of this period, most of the solvent had evaporated and slides were gently wiped and dried. The slides were stored in the dark.

The monomer mixture of 2-hydroxyethyl methacrylate (HEMA) and methacrylic acid (MAA) was pipetted into a small glass vessel in the desired ratio. Desired amounts of N,N′-Methylenebis(acrylamide) (MBA), acrylated BBR chloride and 2 mol% 2-Hydroxy-2-methylpropio-phenone (HMPP) were added and then diluted in a 1:1 ratio (v/v) of isopropanol. The solution was shaken until all the solids were completely dissolved.

On a polyester side of a flat polyester aluminised film, 350 μL of monomer solution was pipetted and a silanised slide was carefully placed on to the droplet, ensuring not to trap air pockets. The aluminised film had tracks of tape to support the weight of the glass slide to ensure even film distribution. It was exposed to UV light for 60 minutes in a UVP CX-2000 L Ultraviolet Crosslinker. Once the gels set, the slides were peeled off the aluminised film and soaked in DI water. The DI water was changed three times to ensure that the unreacted monomer and solvent was completely washed.

4.3 Hydrogel Optimisation

4.3.1 Varying MBA Concentration

The MBA concentration was varied to investigate the effect of crosslinker density on the performance of the hydrogel. The investigated concentrations were: 0.05 mol%, 0.10 mol%, 0.3 mol% and 0.5 mol%. The change in luminescence intensity due to calcium ions was detected in the microplate reader and the hydrogel with the MBA concentration that provided the greatest change was selected as the optimal MBA concentration.

4.3.2 Varying HEMA:MAA ratio

The HEMA:MAA ratio was varied to investigate the effect of Ca^{2+} receptor density on the performance of the hydrogel. The investigated ratios were: 0:10, 1:9, 3:7 and 5:5. The change in luminescence intensity due to calcium ions was detected in the microplate reader and the hydrogel with the MBA concentration that provided the greatest change was selected as the optimal HEMA:MAA ratio.

4.3.3 Varying AIE luminogen concentration

The luminogen concentration was varied to investigate its effect on the emissivity of the hydrogel. The effect of luminogen concentration in solution and hydrogel phase was investigated from 0.01 mM to 25 mM. The change in luminescence intensity due to calcium ions was detected in the microplate reader and the hydrogel with the luminogen concentration that provided the greatest change between low and high calcium states was selected as the optimal luminogen concentration.

4.4 Solution Preparation

4.4.1 Tris Buffer

A tris buffer of pH 7.4 was prepared by making a 100 mL solution of a 50 mM basic tris buffer and then adding a 50 mM acidic tris buffer until a pH of 7.4 was reached. The chemical mechanism is shown section D of the supplementary document. A Mettler Toledo LE438 pH probe was used to measure the pH. A tris buffer was used to stabilise the pH and ionic strength of the solutions.

4.4.2 Calcium Concentration

Solutions of varying calcium concentration were prepared to investigate the sensitivity of the receptor. The investigated concentrations were 0.001 mg/mL, 0.005 mg/mL, 0.01 mg/mL, 0.03 mg/mL, 0.05 mg/mL, 0.07 mg/mL, 0.09 mg/mL, 0.11 mg/mL, 0.13 mg/mL, 0.15 mg/mL and 1 mg/mL. These concentrations were chosen to see if the receptor could detect to the calcium concentration in tear fluid in the normal physiological and the diseased range.

4.4.3 pH

The pH of tear fluid tends to fluctuate throughout the day and therefore the functionality of the hydrogel in different pH solutions was investigated. The investigated pHs were 5.5, 6, 6.5, 7, 7.5, 8, 8.5, 9. Using the pH probe, the solution's pH was measured when adding acidic tris buffer to the basic tris buffer.

4.4.4 Ionic Strength

Solutions of varying ionic strength were made by dissolving varying amounts of acid tris, basic tris and sodium chloride (NaCl) in 25 mL of DI water. The investigated strengths were 50 mM, 100 mM, 150 mM and 200 mM. Ionic strength was a factor that was investigated as calcium is not the only ion present in tear fluid. Sodium is the most abundant ion and therefore it was important to see if the hydrogel was still functional in an environment with other ions present.

4.5 Hydrogel measurements

To use the prepared slides for measurements, the slides were cut using a glass cutting tool into 1x1cm pieces. These pieces were subsequently soaked in appropriate solutions and used with the following equipment.

4.5.1 Microplate Reader

A Varioskan Lux microplate reader in conjunction with the SkanIt RE 6.1 program were used to measure the emissivity of the hydrogels. Samples of the tested hydrogels were placed in wells filled with 1 mL DI water, tris buffer or calcium solution. It was imperative that the hydrogel samples were placed in the centre of the wells so that the microplate could take an accurate reading. Using the SkanIt RE 6.1 program, the correct plate configuration was chosen and the wells that were occupied with hydrogels were then selected on the program. A fluorescence spectrum with a range of 440 – 600 nm at an excitation wavelength of 405 nm was used to conduct our analysis.

4.5.2 Optical Microscope

A Leica DMC 4500 optical microscope in conjunction with the Las core software was used to measure the thickness of the hydrogels. The objective lens with a magnification of x5 was used to see the hydrogel clearly. The fine and coarse adjustment wheels were used to bring the hydrogel into focus. Using the software, the image was captured and measurements of the thickness of the hydrogel at 3 different points was recorded and averaged.

5 Results & Discussion

This section conveys all observations and measured results gathered through variations in formulation of the calcium sensing hydrogels and their response to stimuli such as calcium ion concentration, pH, temperature, and ionic strength.

5.1 Testing AIE Phenomenon

In this study, acrylated BBR chloride was used so that the luminogen could be incorporated into the matrix. However, because the structure of BBR chloride was changed it was imperative to test the AIE phenomenon of the molecule. Following the procedure (Gu et al., 2018), the AIE characteristic of the modified BBR chlride was tested by studying its photoluminescence behaviour in water/tetrahydrofuran (THF) mixtures. THF is a non-polar solvent therefore increasing the THF fraction in the solutions causes the AIE to precipitate out and aggregate on a microscopic scale. Figures 1 and 2 show that as the THF fraction increases, the emission intensity increases, confirming that acrylated BBR chloride exhibits the AIE phenomenon. The large error bars at the high concentrations of THF could be due to the fact that THF could dissolve the apparatus that was used to measure emissivity.

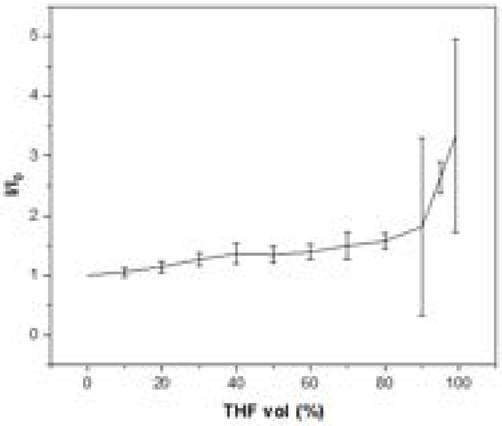

Figure 1: I/I$_0$ Ratio vs vol% of THF

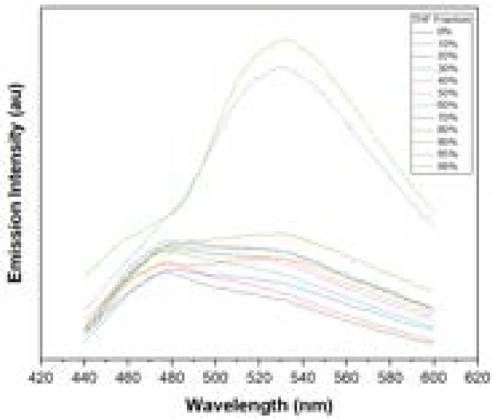

Figure 2: Photoluminescence (PL) spectra of acrylated BBR chloride in water/THF mixtures with different % of THF. Slit width: 12 nm

5.2 Hydrogel Optimisation

5.2.1 Solvent Selection

Figure 3: Comparison of hydrogels using different solvents, left: isopropanol, right: water

Before varying any other component of the hydrogel, the solvent used to dissolve the monomer solution was investigated. Three hydrogels of identical monomer formulation were dissolved using water, isopropanol and dimethyl sulfoxide (DMSO) and slides were prepared according to the aforementioned method. However, slides prepared by DMSO showed a cloudy film compared to slides prepared by water and isopropanol. This was beneficial, as DMSO would have been the least ideal solvent due to its toxic properties. The experiment was repeated to come to a conclusive decision with the results shown in figure 3. This experiment showed much more distinctive differences between the two slides; thus isopropanol was chosen as the solvent as it resulted in consistently transparent films. This is due to the solubility properties of the monomer mixture and how they interact with the solvent once crosslinking has occurred.

5.2.2 Effect of crosslinker (MBA) concentration

The effect of crosslinker concentration on hydrogel performance was investigated by varying the concentration of MBA for a 1:1 HEMA:MAA ratio, 2 mol% initiator (HMPP) and 0.1 mol% AIEgen. The results in figure 4 were obtained from the microplate reader. The results show the comparison of emissivity between the hydrogel in water and a high calcium concentration buffer solution. Figure 4a) shows the greatest difference of 9.84 au between the spectra peak for water and high calcium concentration solution, whilst figures 4b) ,c) and d) show progressively smaller differences in the spectra peak. This shows that the lower concentration of MBA enables the hydrogel to swell and contract more drastically due to a lower crosslinker density, thus causing a starker difference between the swollen, zero-calcium state and the contracted, high calcium saturated state. A lower concentration of MBA was not further investigated due to limitations of the accuracy of measuring equipment, but also the hydrogel in the swollen state at a lower crosslinker concentration is likely to cause it to be too fragile and therefore not fit for practical use. Considering the obtained results, 0.05 mol% of MBA was selected as the optimum concentration of crosslinker for the hydrogel formulation.

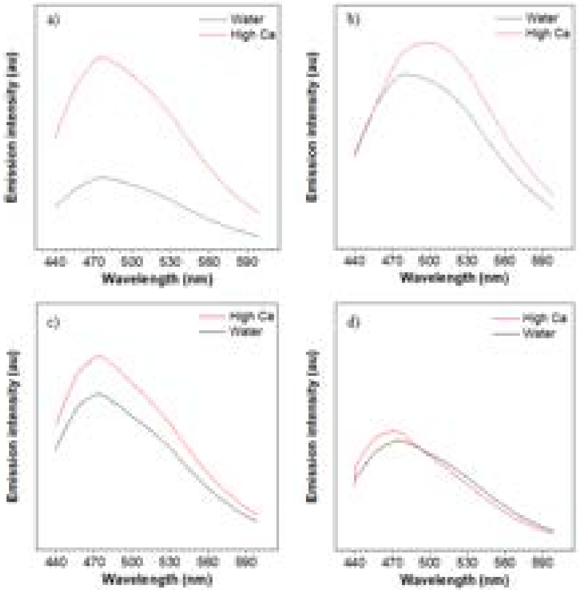

Figure 4: Effect of varying MBA concentration a) 0.05mol% b) 0.1mol% c) 0.3mol% d) 0.5mol%

This value was reverified using 0.05 mol% and 0.25 mol% of MBA, once the HEMA:MAA ratio was determined at 1:9, to ensure that this hadn't impacted the previous decision. The results showed similar trends as before, as seen in figure 5, whereby the lower MBA concentration exhibited a greater difference in emissivity between the zero-calcium state and the high calcium state.

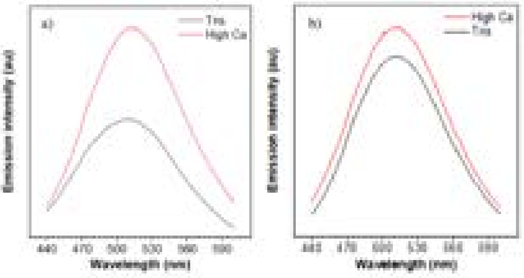

Figure 5: Reverification at 1:9 HEMA:MAA between a) 0.05 mol% MBA and 0.25 mol% MBA

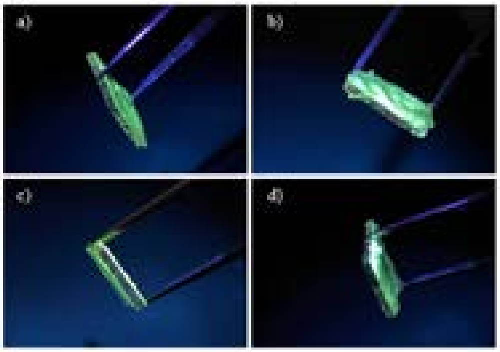

Figure 6: Observable differences between a) 0.05 mol% MBA in high concentration b) 0.05 mol% MBA in pure tris c) 0.25 mol% MBA in high concentration d) 0.25 mol% MBA in pure tris

Figure 6 show the observable differences in swelling between the two MBA concentrations, where the hydrogel containing 0.05 mol% MBA shows a more drastic change in its thickness.

5.2.3 Effect of HEMA:MAA ratio

The effect of HEMA:MAA ratio on hydrogel performance was investigated by varying the molar ratio of HEMA, the monomer, to MAA, the calcium receptor monomer for a 0.05 mol% MBA, 2 mol% initiator and 0.1 mol% AIEgen. It was observed that, in the dry state, the gels looked very similar, except for the 0:10 slide exhibiting slightly more translucent and opaque corners. However, once soaked in DI water, the absorption process caused the gels to swell up significantly and turn transparent. The gels with higher proportions of HEMA were harder and less fragile compared to those with lower proportions. This would be beneficial in terms of the practical application as durability is a desired property in contact lenses. However, since MAA is the calcium receptor, a higher proportion would mean that there would be more receptors available to detect the calcium ions and therefore would have greater sensitivity between different calcium concentrations, resulting in a more sensitive sensor.

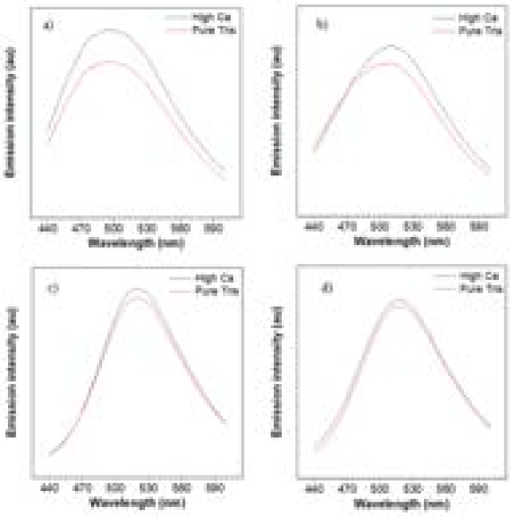

Figure 7: Effect of varying HEMA:MAA ratio a) 0:10 b) 1:9 c) 3:7 d) 5:5

These results are shown in figure 7, comparing the difference between the maximum peak height between the different ratios. It can be observed in figure 7a), that 0:10 hydrogel exhibited the largest difference of 5.01 au between peaks in a low calcium state compared to a high calcium state, with the differences becoming progressively smaller with decreasing proportions of methacrylic acid. As a compromise between the two considerations, the selected ratio of HEMA:MAA was 1:9 as the gels are significantly more durable than the 0:10 gels, but still exhibit considerable sensitivity to changes in calcium concentration. Figure 8 shows that, for low molar ratios (3:7, 5:5) of MAA there is blue shift in the emission intensity curves whereas with large concentrations of MAA (0:10, 1:9) there is red shift. This occurs because of the increase of the concentration of MAA within the matrix, which increases the polarity and affects the behaviour of the luminogen as it is polar.

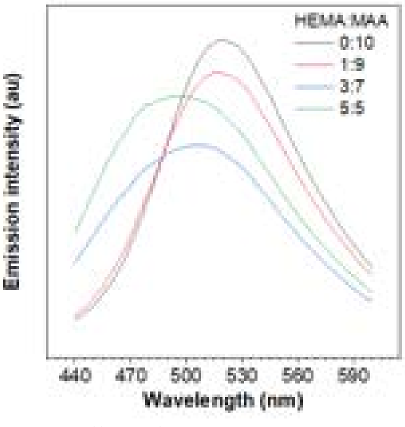

Figure 8: Effect of varying HEMA:MAA ratio

5.2.4 Effect of AIE luminogen concentration

5.2.4.1 Solution phase

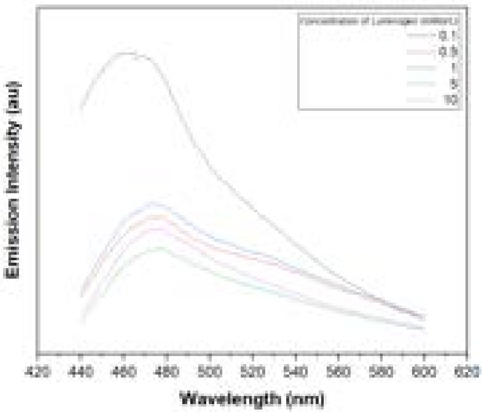

Figure 9: PL spectra of different concentrations of luminogen in tris buffer

To decide the concentration of luminogen in the hydrogel, different concentrations of the luminogen were dissolved in tris buffer (pH 7.4) and the emission intensity was measured. Figure 9 shows at low concentrations there is enhanced fluorescence. This contradicts the AIE phenomenon of acrylated BBR chloride as discussed in section 5.1. This could be due to the other ions present in the tris buffer which affect the behaviour of the luminogen and hence why the luminogen must be chemically bonded in the matrix.

5.2.4.2 Hydrogel phase

Following on from the solution phase results, initially low concentrations of luminogen were tested within the hydrogel. However, this resulted in very low emissions. Subsequently, the larger concentrations were investigated as shown in figure 10. The chosen concentration was 15 mM as this showed the greatest emission change of 2.77 au between tris buffer and the high Ca solution.

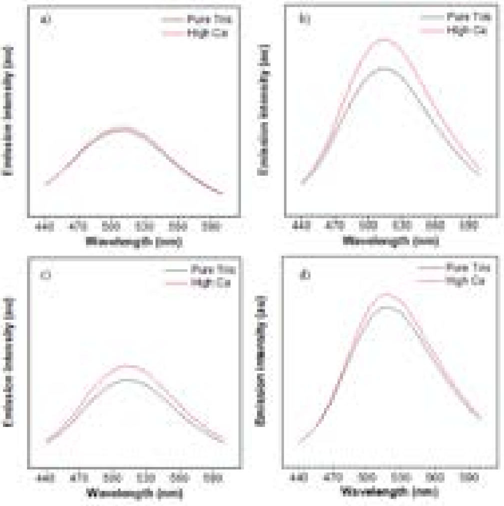

Figure 10: Effect of varying luminogen concentration in hydrogel state, a) 10mM b) 15mM c) 20mM d) 25mM

5.3 Hydrogel Functionality

5.3.1 Sensitivity

5.3.1.1 Calibration curve

Figure 11 shows the calibration curve used to indicate the relationship between emissivity and calcium ion concentration. Using this figure, the emissivity reading can be correlated with a corresponding concentration, which would indicate whether the calcium ion concentration in the patient's tears are at the healthy physiological value of 0.8mM.

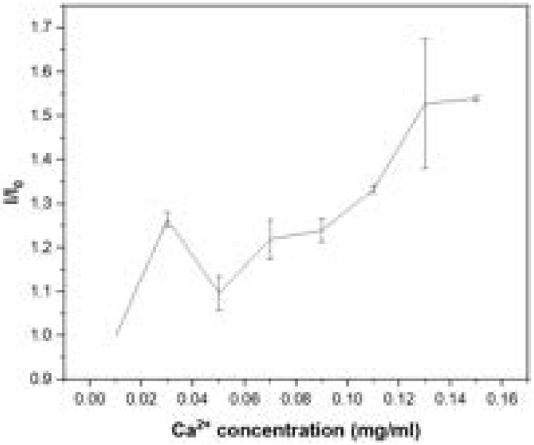

Figure 11: Calibration Curve

Figure 11 shows that, as the calcium concentration increases the emission intensity of the hydrogel matrix also increases. This was to be expected because there are more Ca^{2+} ions to bind with the receptors, which causes more aggregation within the matrix. The calibration curve shows only around a 54% increase in emission intensity ratio whereas other literature, (Mank et al., 2006) using different luminogens show a 400% increase, suggesting the AIE phenomenon may not be the greatest characteristic to aid in the detection of Ca^{2+}. There is an anomaly at 0.03 mg/mL and therefore more repeats would be necessary to explain this data point.

5.3.1.2 Swelling ratio

Figure 12 was obtained from using an optical microscope. They show the functional hydrogel soaked in a zero calcium and a high calcium tris buffer solution respectively. These figures demonstrate that the gels behave as theory suggests, as the zero-calcium state is almost three times as swollen as the high calcium state, with a thickness of 294.902 µm, compared to 103.634 µm, which results in a swelling ratio of 0.373, where the swelling ratio is the ratio of the average thickness of high calcium state to the zero-calcium state.

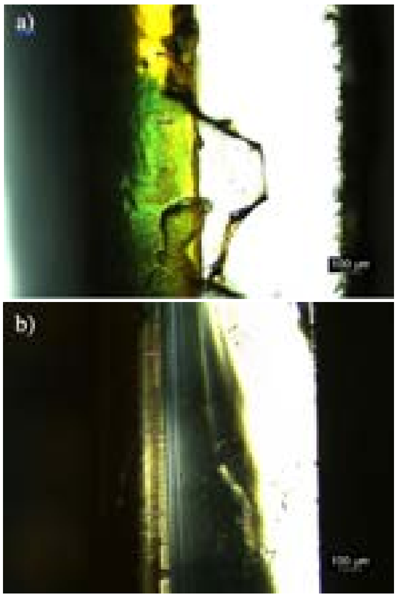

Figure 12: Microscope pictures of a) zero-calcium hydrogel b) high calcium hydrogel

5.3.2 Reversibility

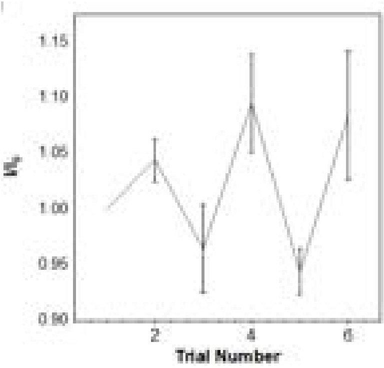

Figure 13: Investigating reversibility of the final functional hydrogel

To test the reversibility of the hydrogel, the slide is soaked in alternating concentrations of low and high calcium six times. Figure 13 shows the emissivity change between each time the solutions are switched, where trials 1,3 and 5 are low calcium solutions and trials 2, 4 and 6 are high calcium solutions. The oscillating emissivity indicates that the hydrogel is reversible between low and high calcium states. However, the relative differences between each trial are quite small, so further work should be conducted to improve the hydrogel. From figure 13, it is clear that the hydrogel does not return to its original state but this could be due to procedural errors when the glass slides shift within the microplate.

5.3.3 Selectivity

To test the selectivity of the hydrogel, the slide was soaked in a pure calcium solution with the same calcium concentration as the typical physiological value and a mixed ion solution containing calcium (0.8 mM), magnesium (0.6 mM), potassium (24 mM), and sodium (132 mM) (Badugu et al., 2018). Figure 14 shows that the hydrogel system is selective towards only calcium ions, since the emissivity spectrum remains relatively the same for both environments, showing that the presence of other ions has not affected the contraction of the hydrogel. This is likely due to the conformational change of the receptor chain that is triggered by the presence of only Ca^{2+} ions (Ishiwari et al., 2016).

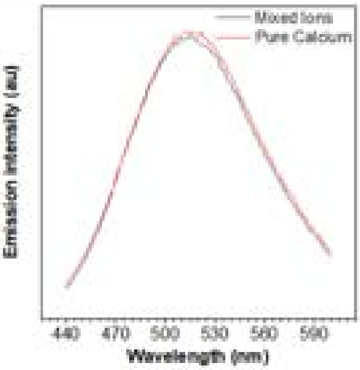

Figure 14: Investigating selectivity of the final functional hydrogel

5.4 Effect of other stimuli

5.4.1 pH

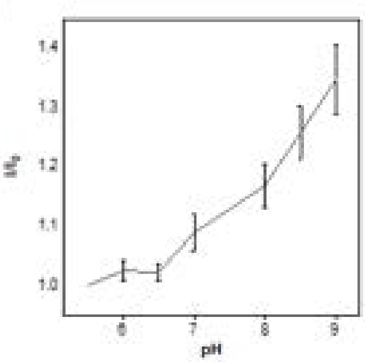

Figure 15: Effect of pH on emissivity

Figure 15 shows a clear upward trend, as pH increases, peak average emissivity increases. However, looking at the relative scale, the increase is not too significant. Despite this, it should still be a factor to consider when taking readings from the hydrogels with tear samples, as results could be skewed. To explain this trend, there are two competing factors that need to be considered when looking at the effect of pH on emissivity. The first factor is that as pH increases, there are more dissociated carboxyl groups, which means there is a steady decrease in osmotic pressure. This causes the hydrogel to swell and the increase in swelling reduces the emission intensity. The second factor is that at high pH, the COO^- on the hydrogel network binds to the positive charge on the luminogen. This causes restricted intramolecular motion, which is the mechanism for aggregated induced emission. This increase in restricted motion causes greater emission intensity. From figure 15, it is clear that the leading factor is the latter.

5.4.2 Ionic strength

At first glance, figure 16 shows that emissivity varies with ionic strength, however, looking at the scale, the relative difference is miniscule. For instance, for a 250% increase in ionic strength, there is only a 16% change in emissivity. Thus, implying that there is little to no relationship between the ionic strength of the solution and the emissivity of the hydrogel. This is beneficial, as there is a wide range of ionic strengths within healthy tears (Badugu et al., 2018) due to the multitude of ionic components present. Knowing that there is little effect gives more weight to the results. The overlapping error bars suggest that the difference in results are not statistically significant and more trials would need to be conducted to ensure reliability.

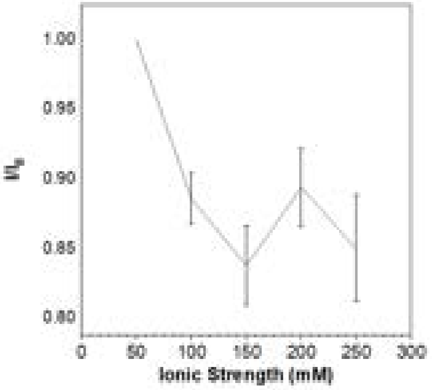

Figure 16: Effect of ionic strength on emissivity

5.4.3 Temperature

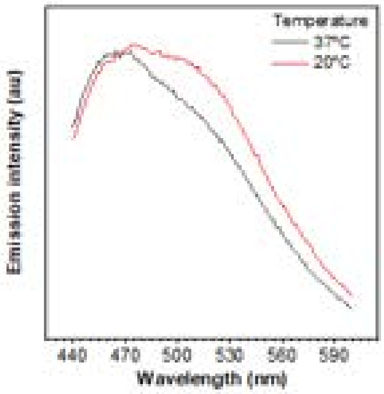

Figure 17: Effect of temperature on emissivity

Since the typical body temperature is regulated at 37°C, it was important to investigate whether the hydrogel would react differently in these conditions, as the experiments were conducted at room temperature (20°C). Figure 17 shows that there is very little difference between the maximum peak value for both temperatures, therefore the results and discussions in the aforementioned sections are valid for the applications in the tears and the human body. Further investigation on a wider range of temperatures would confirm the application of the sensor as the human body is not always regulated at 37°C due to other factors like fevers.

6 Conclusion

There is great scope and potential for this technology which can greatly benefit the medical world for a variety of eye-related diseases. This will lead to faster, less invasive, more effective point-of-care diagnosis and treatment, but also provide an immense amount of new information and understanding of human physiology. This study established an effective hydrogel formulation for the detection and measurement of divalent calcium ions in solution. This can be attained by synthesising hydrogels with the following components: 1:9 HEMA:MAA ratio, 0.05 mol% MBA, 15 mM luminogen (acrylated BBR chloride), and 1:1 v/v Isopropanol as solvent. With this functional hydrogel, different levels of emissivity can be correlated to relevant calcium ion concentrations, thus used for diagnosis in patients. To account for different analysis methods, the graphs were displayed as I/I_0 ratios to facilitate in easier comparison. This work proposes a further investigation of other receptors or luminogens with greater emission ranges for calcium ions to improve sensitivity of the hydrogel matrix. In addition to this further investigation into the effect of more extreme temperatures on the hydrogel sensor.

7 Outlook

7.1 Further Improvements

To measure the emissivity, the glass slides with the hydrogel were cut scoring the glass with a glass cutter. However, the cut slides were rarely of the exact same dimensions due to the glass sometimes breaking unevenly. This would have had an impact on emissivity readings, for example larger glass slides would give greater emissivity because they would have more luminogen. To avoid this problem in the future, an automatic glass cutting table could be purchased as this would cut the slides more accurately.

This experiment worked with very small masses, which means that any experimental error is more significant. In the future, conduct experiments on a larger scale so that such small quantities are not needed but it is important not to be wasteful as this is harmful to the environment. The error calculations in this report can be found in section E of the supplementary document.

It was found that sometimes the distribution of luminogen in the gel was inconsistent. One way to improve this would be to grind the luminogen into fine particles so that it is evenly dispersed within the gels.

7.2 Further Experiments

Progressing beyond the optimisation of hydrogels, the next stage of the development is to embed the functional hydrogel into contact lens by using the FOBA laser cutter to create suitable microcavities and microchannels in silica sheets for the gel. There would be many factors that should be taken into consideration when incorporating the sensor into the contact lens. For example, the placement of the microcavities, how the swelling would affect the functionality of the lens itself and the volume of hydrogel required for a functional sensor. Subsequently, further testing for clinical applications with artificial tear fluid would be necessary to evaluate the full extent of the feasibility of using this device in clinical, day-to-day applications.

Acknowledgements

We would like to express our gratitude to the members of the Yetisen Biosensors group for their valuable words of wisdom and continuous support. Particular thanks to Yubing Hu and Dr Ali K. Yetisen, for their feedback and guidance throughout this project.

References

Arakawa, T., Tomoto, K., Nitta, H., Toma, K., Takeuchi, S., Sekita, T., Minakuchi, S., & Mitsubayashi, K. (2020). A Wearable Cellulose Acetate-Coated Mouthguard Biosensor for In Vivo Salivary Glucose Measurement. *Analytical Chemistry*, *92*(18), 12201-12207. https://doi.org/10.1021/acs.analchem.0c01201

Badugu, R., Jeng, B. H., Reece, E. A., & Lakowicz, J. R. (2018). Contact lens to measure individual ion concentrations in tears and applications to dry eye disease. *Anal Biochem*, *542*, 84-94. https://doi.org/10.1016/j.ab.2017.11.014

Bahram, M., Mohseni, N., & Moghtader, M. (2016). An Introduction to Hydrogels and Some Recent Applications. In. https://doi.org/10.5772/64301

Bazydlo, L. A. L., Needham, M. A., & Harris, N. S. (2014). Calcium, Magnesium, and Phosphate. *Labmedicine*, *45*.

Cancer.net. (2020). *High Calcium Levels or Hypercalcemia*. Cancer.Net Editorial Board. https://www.cancer.net/coping-with-cancer/physical-emotional-and-social-effects-cancer/managing-physical-side-effects/high-calcium-levels-or-hypercalcemia#:~:text=When%20you%20have%20more%20calcium,if%20you%20experience%20any%20symptoms.

Royal Society of Chemistry. (2021). *Polymers in Everyday Things - Contact Lens* http://chemistry.pixel-online.org/files/ed_pack/03/info21/contact%20lenses.pdf

Erulkar, S. D. (1981). The Versatile Role of Calcium in Biological Systems. *Interdisciplinary Science Reviews*, *6*(4), 322-332. https://doi.org/10.1179/isr.1981.6.4.322

Esfandyarpour, R., Esfandyarpour, H., Javanmard, M., Harris, J. S., & Davis, R. W. (2013). Microneedle Biosensor: A Method for Direct Label-free Real Time Protein Detection. *Sensors and actuators. B, Chemical*, *177*, 848-855. https://doi.org/10.1016/j.snb.2012.11.064

Gu, Y., Zhao, Z., Su, H., Zhang, P., Liu, J., Niu, G., Li, S., Wang, Z., Kwok, R. T. K., Ni, X.-L., Sun, J., Qin, A., Lam, J. W. Y., & Tang, B. Z. (2018). Exploration of biocompatible AIEgens from natural resources. *Chemical science*, *9*(31), 6497-6502. https://doi.org/10.1039/c8sc01635f

Hagan, S., Martin, E., & Enríquez-de-Salamanca, A. (2016). Tear fluid biomarkers in ocular and systemic disease: potential use for predictive, preventive and personalised medicine. *The EPMA journal*, *7*(1), 15-15. https://doi.org/10.1186/s13167-016-0065-3

Herman, B., Frohlich, V. E. C., Lakowicz, J. R., Fellers, T. J., & Davidson, M. W. *Fluorescence Resonance Energy Transfer (FRET) Microscopy*. https://www.olympus-lifescience.com/en/microscope-resource/primer/techniques/fluorescence/fret/fretintro/

III, J. L. L. (2021). *Hypocalcemia - Endocrine and Metabolic Disorders - MSD Manual Professional Edition*. https://www.msdmanuals.com/en-gb/professional/endocrine-and-metabolic-disorders/electrolyte-disorders/hypocalcemia?query=Hypocalcemia%20(Low%20Level%20of%20Calcium%20in%20the%20Blood)

Ishiwari, F., Hasebe, H., Matsumura, S., Hajjaj, F., Horii-Hayashi, N., Nishi, M., Someya, T., & Fukushima, T. (2016). Bioinspired design of a polymer gel sensor for the realization of extracellular Ca2+ imaging. *Scientific Reports*, *6*(1), 24275. https://doi.org/10.1038/srep24275

LibreTexts. (2021/8/16/). *Fluorescence Resonance Energy Transfer*. https://chem.libretexts.org/@go/page/2012

Mank, M., Reiff, D. F., Heim, N., Friedrich, M. W., Borst, A., & Griesbeck, O. (2006). A FRET-Based Calcium Biosensor with Fast Signal Kinetics and High Fluorescence Change. *Biophysical Journal*, *90*(5), 1790-1796. https://doi.org/https://doi.org/10.1529/biophysj.105.073536

March, W., Lazzaro, D., & Rastogi, S. (2006). Fluorescent measurement in the non-invasive contact lens glucose sensor. *Diabetes Technol Ther*, *8*(3), 312-317. https://doi.org/10.1089/dia.2006.8.312

MayoClinic. *Hypercalcemia*. https://www.mayoclinic.org/diseases-conditions/hypercalcemia/symptoms-causes/syc-20355523

Orwar, O., Jardemark, K., Farre, C., Jacobson, I., Moscho, A., Shear, J. B., Fishman, H. A., Lillard, S. J., & Zare, R. N. (1999). Voltage-clamp biosensors for capillary electrophoresis. *Methods Enzymol*, *294*, 189-208. https://doi.org/10.1016/s0076-6879(99)94012-0

Park, H., Park, W., & Lee, C. H. (2021). Electrochemically active materials and wearable biosensors for the in situ analysis of body fluids for human healthcare. *NPG Asia Materials*, *13*(1), 23. https://doi.org/10.1038/s41427-020-00280-x

Seshadri, D. R., Li, R. T., Voos, J. E., Rowbottom, J. R., Alfes, C. M., Zorman, C. A., & Drummond, C. K. (2019). Wearable sensors for monitoring the physiological and biochemical profile of the athlete. *npj Digital Medicine*, *2*(1), 72. https://doi.org/10.1038/s41746-019-0150-9

Song, Z., Wang, Y., Zhang, F., Yao, F., & Sun, C. (2019). Calcium Signaling Pathways: Key Pathways in the Regulation of Obesity. *International journal of molecular sciences*, *20*(11), 2768. https://doi.org/10.3390/ijms20112768

Tseng, R. C., Chen, C.-C., Hsu, S.-M., & Chuang, H.-S. (2018). Contact-Lens Biosensors. *Sensors*, *18*(8), 2651. https://www.mdpi.com/1424-8220/18/8/2651

Turner, J. J. O. (2017). Hypercalcaemia - presentation and management *Clin Med (Lond)*, *17*(3), 270-273. https://doi.org/10.7861/clinmedicine.17-3-270

Wang, H., Zhao, E., Lam, J. W. Y., & Tang, B. Z. (2015). AIE luminogens: emission brightened by aggregation. *Materials Today*, *18*, 365-377.

Wikipedia. (2021, 9/12/2021). *Calcium Imaging*. https://en.wikipedia.org/wiki/Calcium_imaging

Wikitionary. (2016). *Luminogen*. https://en.wiktionary.org/w/index.php?title=luminogen&action=history

Zhu, C., Kwok, R. T. K., Lam, J. W. Y., & Tang, B. Z. (2018). Aggregation-Induced Emission: A Trailblazing Journey to the Field of Biomedicine. *ACS Applied Bio Materials*, *1*(6), 1768-1786. https://doi.org/10.1021/acsabm.8b00600

EAM. v4 2020

Predicting the Joule-Thomson Properties of a Lennard-Jones Fluid Using Artificial Neural Networks

Chingis Idrissov[1] and Revash Ramtahal[1]

[1] *Department of Chemical Engineering, Imperial College London, U.K.*

Publication date: 16/12/2021

Abstract— Machine Learning has been successfully applied to a wide range of forecasting and classification problems leading to unique insights and efficiency improvements in the broader areas of application. This type of predictive modelling has potential to aid scientific research in areas where empirical data collection is challenging. This study presents a data-driven approach using molecular and Monte-Carlo simulation data to train Artificial Neural Networks (ANNs) that predict the Joule-Thomson (JT) coefficient (μ_{JT}^*) of the Lennard-Jones (LJ) fluid, as opposed to the traditional, theoretical-based correlation through Equations of State (EOS). The ANN was used to correlate the thermodynamic state properties in reduced units (p^*, T^*, ρ^*) of the LJ fluid to predict the JT coefficient and locate the JT inversion curve in the T^*, ρ^* and T^*, p^* planes. The ANN performed similarly to the EOS of Lafitte et al. [1] in predicting the locus of the JT inversion curve, indicated by $R^2 = 0.9608$ and $R^2 = 0.9604$ respectively. Predictive capability for real fluids is limited as the model was trained on LJ fluid data, creating relatively good predictions of μ_{JT}^* for Ar and N_2, while the level of accuracy faltered for CO_2 and C_3H_8. It was found that the ANN performs best when the training dataset is well populated throughout the entire phase space as it struggles to extrapolate where data is sparse.

Keywords—Joule-Thomson Coefficient, Joule-Thomson Inversion, Lennard-Jones Fluid, Equation of State, Machine Learning

1 Introduction

The Joule-Thomson (JT) coefficient describes the rate of change of temperature (T) with pressure (p) at constant enthalpy (H) and is formally defined as:

$$\mu_{JT} = \left(\frac{\partial T}{\partial P}\right)_H \tag{1}$$

This relation is particularly useful when considering the practical application of throttling of fluids through a nozzle. Hence, the effect has relevance for use in several industries, such as valve operation in the oil & gas industry.

For real gases, JT coefficient will be equal to zero at some point within the phase space, called the inversion point. The locus of these points (at $\mu_{JT} = 0$) maps the region of the phase space where isenthalpic expansion and compression can occur. Since there is no temperature change during the expansion of an ideal gas through a throttling device, all non-zero values for the JT coefficient refer to real gases [2]. The JT coefficient and the inversion curve are important parameters used to evaluate the performance of fluids that involve the vapour-compression refrigeration cycle. Applications include refrigeration, air conditioning, gas separation and gas liquefaction [3].

Developing an accurate correlation is challenging due to insufficient availability of quality data around the phase space. This is due to the difficulties in gathering empirical data as measuring μ_{JT} of a fluid requires extremely high pressures and highly sensitive equipment to detect the very small temperature change. This is particularly challenging at the JT inversion point. Typically, at the upper end, large changes in pressure result in a very small temperature change as $\mu_{JT} \to 0$.

To address the current data problem, molecular simulations have been introduced. Molecular simulation is a computational method used in science and engineering that simulates the thermophysical properties of molecules. The accuracy and reliability of the simulated data is relies heavily on the applied conditions (T, p, etc) [4]. The usual approach in molecular simulation is as follows [5]:

1. Select a system containing N particles.
2. Choose an appropriate force field for the system (Lennard-Jones potential in this case).
3. Solve Newton's equations of motion for each particle. This is done until the system properties no longer change with time (reach equilibrium).
4. Calculate instantaneous properties of the system. Average that property over some time interval.
5. If measurements are subject to statistical noise, then increasing the time-span for the average provides a more accurate measurement.

The LJ potential describes the interactions between two particles on a molecular level using the following equation:

$$V_{LJ}(r) = 4\varepsilon\left[\left(\frac{\sigma}{r}\right)^{12} - \left(\frac{\sigma}{r}\right)^{6}\right] \tag{2}$$

where ε is the depth of the potential well (energy parameter), σ is the hard-sphere radius (size parameter) and r is the distance between the two particles. The LJ fluid is studied extensively in thermodynamics, due to its applicability in developing soft-matter physics models as well as computational methods. The LJ fluid model adequately describes the interactions in simple inert fluids, such as Argon.

The LJ model provides microscopic level data which can be linked in a point-wise basis (i.e. at a given T or ρ), allowing molecular simulations to be performed on ensembles of particles where the collective behaviour of the species can be interpreted on a macroscopic level [5]. These thermodynamic and structural properties are extracted as T, p, ρ and so on.

Molecular simulation has several benefits over experimentation. Empirical data is usually poorly distributed as a large proportion of it lies at the 'easier' conditions (i.e. close to ambient conditions). This makes the dataset inappropriate for correlation [6]. Use of in-silico data provides quality control over the dataset, which would in theory, produce a more accurate model. Additionally, the challenges associated with experimentation are removed.

An equation of state (EOS) is an expression that relates thermodynamic properties (p, v, T) to describe the fluid phase behaviour under certain conditions [7]. EOS have major applications in fields where thermodynamics and fluid mechanics are key in solving problems, such as the in oil & gas [8] and pharmaceuticals industries [9].

Developing EOS for the LJ fluid is a problem which has attracted significant effort, leading to the development of many EOS [10]. The EOS are generally classified as empirical and theoretically-based. The aim of empirical EOS is to correlate the simulation data, which is done through a mathematical form using a large number of parameters. The theoretically-based EOS use theoretical consideration as the basis and adjust parameters using empirical correction terms from simulation data [11].

In their investigation, Stephan et al. [11] used the following criteria to evaluate the performance of each EOS:

a EOS has to represent data well for most of the properties.

b EOS has to show no unphysical behaviour in the two-phase region.

c EOS has to be well-behaved for extrapolations in extreme conditions.

Despite the simple nature of the LJ fluid and the number of EOS developed, only the semi-theoretical LJ EOS of Kolafa and Nezbeda [12] met all criteria to a good degree and was found to be the most robust. It also gave a good description of μ_{JT}, so the EOS can be used for comparison. Other popular EOS that can be used for comparison include: Johnson et al. [13], Lafitte et al. [1] and Stephan et al.[14]

Machine learning (ML) enables the extraction of complex and hidden correlations directly from the dataset, encapsulating them in a mathematical form. All ML algorithms can be broadly classified into supervised, unsupervised, semi-supervised and reinforcement learning algorithms. In supervised learning, the model learns by example from a labelled dataset, i.e. a dataset containing features (inputs) and labels (outputs) is provided to the model with the task of determining the best correlation between the two [15].

Supervised learning algorithms can be applied to classification, regression and forecasting problems. The problem at hand is a regression problem since both the features and the labels are continuous in their nature. Therefore, popular supervised learning algorithms, such as artificial neural networks (ANNs) and support vector machines (SVMs), can be used for modelling the JT coefficient.

The use of ML to model LJ fluid properties has been investigated in the past by Craven et al. [10], who modelled the radial distribution function (RDF) of the LJ fluid. They found that ML models, namely kernel ride regression algorithms, are able to reproduce the RDF more accurately than the traditional EOS. Other investigations, discussed in the study by Ding et al. [16], have successfully correlated the liquid densities and viscosities of hydrocarbons through SVM and ANN models by using real fluid data with molecular descriptors as features. This further reinforces the applicability of supervised ML models to this problem. Finally, ML methods have never been applied to modelling the JT coefficient of the LJ fluid before, so their implementation for the purpose of this investigation looks promising.

This investigation aims to answer the following questions:

1. Is it possible to fit the ANN model on the phase space defined by the available data?
2. Is it possible to define the JT inversion point locus, i.e. where $\mu_{JT} = 0$?
3. How does the performance of the ANN model compare to that of the EOS?
4. Is it possible to predict μ_{JT} of real fluids (such as CO_2 and Ar) using the ANN model for the LJ fluid?
5. How does the size and distribution of the training dataset affect the model's performance?

2 Methodology

2.1 Data

Stephan et al. [14] have compiled a database of thermophysical properties for the LJ fluid. The data was obtained from previous molecular and Monte-Carlo simulation experiments found in the literature. All of the datasets were digitised, evaluated and compiled into a single database consisting of around 35,000 data points [14]. The database contains data for various thermodynamic properties for the LJ fluid. The Excel version of the database can be found in the supplementary materials in the source [14]. All of the data points are reported in LJ reduced units, denoted by the asterisk (*). When referring to thermophysical properties throughout this report, the asterisk is dropped.

The Excel sheets of interest for this investigation are: JT inversion curve (aka Charles) dataset, μ_{JT} dataset and the p, T, ρ (or p, v, T) dataset.

The first was used in Section 2.6 to model the JT inversion curve. This dataset contains 106 points with T and p values reported for all points of the JT inversion (aka Charles) curve. Some data points also have ρ (density) values reported.

The second was used for training the ANN in Section 2.9.1. This dataset contains 1723 data points with ρ, T and

μ_{JT} values reported for each data point.

The third dataset contains 5254 datapoints of corresponding p, T, ρ values and it also incorporates most of the values from the second μ_{JT} dataset. The p column in the second dataset was removed from the Excel sheet. Therefore, the third dataset was used to match the ρ, T values in the second dataset to their corresponding p value from the third dataset. This was done through a Python script, which compares the dataset sources, fluid region and ρ, T values. This new compiled dataset was then used to train the ANNs in Section 2.9.2. The dataset contains 1620 values (100 less than dataset 2).

For simplicity, these datasets will be referred to as datasets 1,2 and 3 respectively. Additionally, it should be noted that data points from dataset 1 (JT inversion locus points) are not present in datasets 2 or 3.

2.2 Data Cleaning & Pre-processing

The quality of input data has a major effect on the ANN model's ability to learn and produce accurate predictions [17].

Since the data was already in reduced LJ units, no additional transformation was needed. All parameters have the following ranges:

Table 1: Parameter Ranges in Datasets 2 and 3 for the LJ Fluid

	p	T	ρ	μ_{JT}
max	3442.65	90.000	2.500	8.741
min	0.0038	0.694	0.005	-0.466

p has the largest range and it scales logarithmically. Therefore, the values were converted to $ln(p)$ for training the ANNs in Section 2.9.2.

Additionally, the effects of normalisation (min-max scaling) and standardisation on ANN performance were investigated, with the results outlined in Section 3.1. Scikit-learn's MinMaxScaler and StandardScaler were used [18]. Scikit-learn's Local Outlier Factor (LOF) was used to identify any possible irregularities within dataset 1 (see Appendix A.1).

Stephan et al. [14] have also provided labels for outliers in their dataset (1 = confirmed points; 0 = outlier). These labels were used to filter outliers in datasets 2 and 3.

2.3 Artificial Neural Network (ANN)

ANNs are models inspired by the interconnection of neurons in the brain. They have a wide array of use cases and can correlate large amounts of multidimensional data [19]. The most common type of ANN is the feedforward neural network which consists of an input layer, a hidden layer and an output layer. Each node within the network accepts input represented by the vector **x**, where the weighted sum is computed and a bias vector, **b** is added as described by equation 3.

$$\mathbf{y} = \mathbf{W}\mathbf{x} + \mathbf{b} = \begin{bmatrix} w_{1,1} & w_{1,2} & \cdots & w_{1,n} \\ \vdots & \vdots & \ddots & \vdots \\ w_{m,1} & w_{m,2} & \cdots & w_{m,n} \end{bmatrix} \begin{bmatrix} x_1 \\ \vdots \\ x_n \end{bmatrix} + \begin{bmatrix} b_1 \\ \vdots \\ b_m \end{bmatrix} \tag{3}$$

The linear output is passed through an activation function to integrate non-linearity into the system as it assists the neural network in recognising the complex features of the data. The absence of an activation function would effectively make the ANN a linear regression model. The activation function is responsible for creating back propagation in the network as the weights and biases are updated based on the error at the output.

The Reactified Linear Unit function (ReLU) is the most commonly used activation function in deep neural networks today, mainly implemented in the hidden layers of the network. The ReLU activation function is described by equation 4 where x is the input to each neuron.

$$f(x) = x^+ = \max(0, x) \tag{4}$$

ReLU has the advantage of being able to learn faster than other activation functions such as sigmoid and tanh, however suffers from the problem of producing zero outputs for negative inputs, causing nodes to become unable to learn [20]. To combat this, Leaky ReLU introduces the adjustable α parameter shown in equation 5. This ensures that the slope remains positive and also speeds up the model training as the mean activation is near zero [21].

$$f(x) = \max(\alpha x, x) \tag{5}$$

Considering all of the aforementioned factors, a mathematical and visual description of a N-layered neural network is given by equation 6 and figure 1 respectively.

$$\mathbf{y} = f_N\left(\mathbf{W}_N \ldots f_2\left(\mathbf{W}_2 f_1\left(\mathbf{W}_1\mathbf{x} + \mathbf{b}_1\right) + \mathbf{b}_2\right) \ldots + \mathbf{b}_N\right) \tag{6}$$

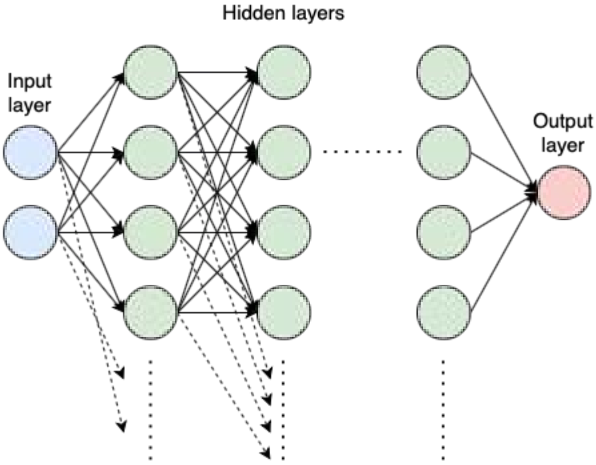

Fig. 1: Visual representation of a N-layered ANN

Training of the ANN requires suitable input data (features) to produce predictions, which are compared to the output data (labels). The training process involves the optimisation of the weights for each node and bias term for each layer in an effort to minimise the error function. The function used in this investigation is the Mean Squared Error (MSE).

The derivatives of the error function with respect to all adjustable parameters are computed and multiplied by the learning rate. This produces adjustment constants for all parameters, that are added or subtracted to the parameters. This is the process by which the network trains and is called backpropagation. The ideal neural net setup would be the one that achieves the smallest validation set error.

When using ANNs, caution must be exercised when developing the model architecture as the problem of overfitting may arise. Increasing the number of layers usually tends to gives rise to a regularisation effect, causing the parameters to learn the general features of the dataset [22]. However, increasing the number of layers past a certain extent will force the model to learn unique features of the training dataset which will result in the model having difficulties correlating unseen data.

Dropout is a common regularisation method in ANN training. Randomly selected neurons are ignored or 'dropped-out' during training, which temporarily stops downstream neurons from contributing to the forward pass. Hence, weight updates are not applied to those neurons in the backward pass. This reduces the chance of overfitting to the training data and improves the ANN's ability to generalise [23]. The effect of dropout on ANN performance is outlined in Section 3.1.

2.4 Hyperparameters Optimisation

Experimentation on the combination of different learning rates, optimisers (Adam, Adagrad, RMSprop) and various network configurations (varying number of layers and nodes) was done using Optuna [24]. Optuna is a hyperparameter optimisation framework that searches through possible parameter combinations (defined by the user) and finds a global minimum in the error or a global maximum in R^2.

2.5 Statistical Metrics

Unadjusted R^2 was used as the main performance metric for model evaluation and comparison. It is defined as:

$$R^2 = 1 - \frac{SS_{\text{res}}}{SS_{\text{tot}}} = 1 - \frac{\sum_i (y_i - \hat{y}_i)^2}{\sum_i (y_i - \bar{y})^2} \tag{7}$$

where y_i is an observed data point, $\bar{y}$ is the observed mean of the data set and $\hat{y}_i$ is the predicted data point. SS_{res} and SS_{tot} are the sums of squares of residuals and totals respectively.

Root Mean Squared Error (RMSE) and Mean Absolute Error (MAE) were used as the main error metrics and are defined as follows:

$$\text{RMSE} = \sqrt{\frac{\sum_{i=1}^{N} (y_i - \hat{y}_i)^2}{N}} \tag{8}$$

where i = variable i, N = total number of observations y_i = actual value and $\hat{y}_i$ = forecasted value

$$\text{MAE} = \frac{\sum_{i=1}^{n} |y_i - \hat{y}_i|}{N} \tag{9}$$

where N = total number of observations, y_i = actual value and $\hat{y}_i$ = forecasted value

Both performance metrics RMSE and MAE describe the average prediction error in terms of the target variable, without considering the direction of the error. They are both negatively-oriented which means that smaller values of error are more desirable. RMSE takes the square of the error before it is averaged and then square rooted. This means that RMSE gives greater weighting to larger margins of error and will be more useful where larger errors are undesirable. MAE gives the average of the error which implies that the error value is relative to the actual values. MAE is useful as an alternative error metric to the RMSE.

2.6 Preliminary Study: Modelling the JT Inversion Curve

For preliminary investigation, Polynomial Regression and Support Vector Regression (SVR) models were explored for the initial attempt in modelling the JT inversion curve. Polynomial regression with Lasso (L1) regularisation was used, with the polynomial degree varying between 3 and 15.

For SVR, parameters were produced using a grid search algorithm (GridSearchCV in sklearn). The best combination of parameters was $C = 100$, $\gamma = 0.1$ and Radial Basis Function (RBF) kernel.

Finally, regression was also performed using an ANN where T was used as the input to predict values of μ_{JT}. The parameters used for the ANN architecture setup are shown in Table 4 in Appendix A.2.1.

Each model used the processed dataset 1 (JT inversion dataset) shown in Appendix A.1, Figure 8 to predict the location of the inversion curve.

2.7 Predicting JT Coefficient

Since the ANN was found to be the best tool for correlating the relevant data, it was used to predict values for JT coefficient in the phase space of the LJ fluid. The architecture of the ANN was adjusted as described by Table 5 in Appendix A.2.2, to accept two inputs to predict JT coefficient.

The relevant JT coefficient data compiled by Stephan et al. [14] was used as input using parameters T and ρ. The dataset used consisted of 1729 points, already classified as confirmed points or outliers.

2.8 Predicting JT Coefficient at "Easy Conditions"

Since gathering empirical data is difficult around the region of the JT inversion curve, the question of using a reduced dataset to predict the entire phase space arose. It is most convenient to accurately record data at the "easy conditions" (near ambient conditions), so the network was trained on data around ambient T and p within the range the range of $T \in [0, 1.5]$ and $p \in [0, 0.2]$, both in LJ units. The dataset was then increased incrementally in intervals of $T = 1.5$ and $p = 0.2$ to test the effect on the performance of the network by analysis of the accuracy of predictions.

2.9 Calculating the JT Inversion Curve

2.9.1 Calculating JT Inversion from ρ, T using bisection

The inversion curve in T, ρ space closely resembles a linear function with every T value corresponding to a unique ρ value (a one-to-one function of $\rho = f(T)$). Additionally, the data points are well populated around the expected region of inversion curve ($T \in [0,7]$ and $\rho \in [0,1]$), so bisection can be used in order to calculate the JT inversion curve from the ANN in Section 2.7.

The bisection model in Python iterates through a list of ρ values between $[0.001, 1]$. Each ρ value is assigned a T_{min} of 0.01 and T_{max} of 10, for instance: $(\rho, T_{min}) = (0.001, 0.01)$ and $(\rho, T_{max}) = (0.001, 10)$. The two sets of values are then evaluated by function $\mu_{JT} = f(\rho, T)$, which is the ANN. The algorithm then compares the two μ_{JT} values to make sure that they are of opposite sign, consequently recording the midpoint. This midpoint is then used as a lower or higher limit for further bisection. The algorithm eventually finds a combination of (ρ, T_{min}) and (ρ, T_{max}) (opposite signs in μ_{JT}) that produces a difference in μ_{JT} within a specified tolerance (10^{-5} in this case). A final midpoint of (ρ, T_{mid}) is hence found. This point is recorded as the location of the inversion point. The procedure is then repeated for further ρ values.

2.9.2 Calculating JT Inversion in p,T

Since the form of the inversion curve relating density is not used in practice, the ANN was adjusted to produce predictions in the T, p plane. However, the inversion curve in T, p is non-linear in nature and closely resembles an inverted parabola, with 2 T values for each p value. When plotted on a 3D diagram $(x,y,z) = (ln(p), T, \mu_{JT})$, the surface was seen to be highly non-linear. This makes bisection non-viable because it is hard to define a region where μ_{JT} on opposing sides would have negative signs.

Therefore, an alternative approach was developed. The ρ, T data produced from the bisection method outlined in Section 2.9.1 can be used to convert the JT inversion curve into T, p space. Therefore, an additional ANN that can predict p with ρ, T as inputs (i.e. $p = f(\rho, T)$ where f is the ANN) was trained on dataset 3. The inversion curve exists within $T \in [0,7]$ and $\rho \in [0,1]$, therefore, only those data points and their corresponding p values were used for training the new ANN.

Additionally, another ANN configuration was investigated. Here, the inputs into the ANN are ρ, T, μ_{JT} (i.e. $p = f(\rho, T, \mu_{JT})$). The addition of μ_{JT} as an input was thought to have the potential of improving the accuracy of conversion from ρ, T to p.

2.9.3 Addition of Pseudo-data

In order to produce a more accurate inversion curve by conversion to the p, T space, the points from dataset 1 can be added to dataset 3 when training the $p = f(\rho, T)$ and $p = f(\rho, T, \mu_{JT})$ ANNs. However, most points in dataset 1 only had p and T values, with only 25 out of the 106 points having corresponding ρ values as few sources for the JT inversion data reported ρ values. This problem was solved by the generating pseudo-data points in order to complete the set of missing ρ values in dataset 1.

The pseudo-data points were generated by training a new ANN with p, T as inputs to predict ρ (i.e $\rho = f(p, T)$). The same restricted dataset as in Section 2.9.2 was used for training. When testing the performance of this network, it was found that the network predicts the existing 25 ρ values in dataset 1 with $R^2 \approx 0.99$. Hence, the new pseudo-data was seen to be of a satisfactory standard for addition to dataset 3.

2.9.4 ANN Matrix

The conversion of ρ, T to p using the two network configurations (Section 2.9.2) and the new dataset with added pseudo-data (Section 2.9.3) produce different combinations for converting the ρ, T inversion curve to p, T.

Additionally, the pseudo-data points can be added to dataset 2 to train the ANN used to predict μ_{JT} from ρ, T inputs (Section 2.7). This would improve the quality of the ρ, T inversion curve calculated from bisection (Section 2.9.1).

The different methods outlined above can be combined in various ways. The combinations that were investigated can be seen below:

Table 2: ANN Matrix (* denotes the addition of pseudo-data for training)

	$\mu_{JT} = f(\rho, T)$	$\mu_{JT} = f^*(\rho, T)$
$p = f(\rho, T)$	ANN 1	ANN 5
$p = f(\rho, T, \mu_{JT})$	ANN 2	ANN 6
$p = f^*(\rho, T)$	ANN 3	ANN 7
$p = f^*(\rho, T, \mu_{JT})$	ANN 4	ANN 8

In Table 2, the different combinations each represent an effective model that is used to produce the JT inversion curve in p, T space. For instance, ANN 5 denotes the following sequence:

1. Train $\mu_{JT} = f(p, T)$ ANN with pseudo-data.
2. Produce the ρ, T inversion curve (series of ρ_{inv} and T_{inv} values) by bisecting with the ANN in step 1.
3. Train $p = f(\rho, T)$ ANN with pseudo-data.
4. Predict the p_{inv} from ρ_{inv} and T_{inv} values using ANN in step 3, thus obtaining the inversion curve in p, T.

2.9.5 EOS & ANN Performance Comparison

The JT inversion curves generated through ANN combinations in Table 2 were compared against JT inversion curves obtained from 4 different EOS: Lafitte et al. [1], Kolafa & Nezbeda [12], Johnson et al. [13] and Stephan et al [25]. All EOS inversion curves were generated from MATLAB versions of each (provided by Stephan).

Dataset 1 (JT inversion curve dataset) with the addition of pseudo-data was used as a benchmark for the performance of all EOS and ANNs. The data points from all models were matched with the data points from dataset 1 by mapping equivalent T values (within a tolerance of 1×10^{-5}). This generated 102 points for comparison (same as in dataset 1). R^2, RMSE and MAE relative to the data were then calculated for all models. The curves were also examined visually to assess their relative smoothness and location within the p, T and ρ, T spaces.

2.10 Comparison to Real Data

The thermodynamic properties (p, T, ρ, μ_{JT}) at saturation and isobaric (p = 0.1, 1, 5, 10, 50, 100, 500 MPa) conditions for different compounds were extracted from the NIST Fluid Webbook [26]. The substances of interest were: Argon (Ar), Carbon Dioxide (CO_2), Nitrogen (N_2) and Propane (C_3H_8).

Each species is dominated by the same type of intermolecular forces being London Dispersion Forces and are considered to be electronically neutral. Ar was used as it is well described by the LJ fluid model. CO_2 was chosen as a larger, linear molecule which is highly inert. N_2 was chosen as it is a small non-spherical particle and an inert fluid. C_3H_8 is a common household refrigerant which has relevance to this study.

The data was converted to LJ units as seen in Appendix A.5 and compared to the ANN predictions in terms of μ_{JT} using the metrics R^2, RMSE and MAE. LJ parameters (hard-sphere radius σ and the potential well depth ε) used in the conversion are reported in Table 7 of Appendix A.5.

3 Results & Discussion

3.1 ANN Setup and Parameters

As discussed in Section 2.2, the effects of normalisation and standardisation were investigated. Both techniques were applied to the ρ, T data from dataset 2 when training the $\mu_{JT} = f(\rho, T)$ ANN. It was seen that the performance with both methods was worse than without, regardless of model architecture. This was shown by the lower R^2 value of around 0.96 as opposed to the higher value shown of 0.9968 shown in Figure 4. Similarly, it was seen that using dropout worsens the predictive ability of ANNs. Therefore, none of these techniques were used when training subsequent models.

Different hyperparameter combinations were tested as per the discussion in Section 2.4. It was found that the best optimiser was Adam with a learning rate of 0.001. The study on layers and nodes from Optuna showed that most combinations of layers and nodes above 2 layers provide R^2 values of above 0.9 (see Appendix A.3). However, the study was mostly inconclusive as the optimum architecture produced by Optuna performed worse than the original network architecture outlined in Section 2.7. Therefore, the original architecture was used for all subsequent ANNs.

3.2 Preliminary Study: Modelling the JT Inversion Curve

The performance of models discussed in Section 2.6 was analysed. The results for the polynomial and SVR models can be found in Figures 10 and 11 of Appendix A.4 respectively.

Polynomial regression with a degree 8 polynomial produced the best result out of all polynomials that were tested with respect to dataset 1 with $R^2 = 0.9547$ and $RMSE = 0.0058$. However, it failed to capture the correlation as well as the SVR and ANN models, especially within regions containing less data points. Great importance was placed on model performance in areas where data was sparse as the ability of the models to extrapolate accurately was vital to this study. SVR was able to perform slightly better, achieving values of $R^2 = 0.9590$ and $RMSE = 0.0056$. Qualitative analysis of the curve indicates that SVR attempts to fit through most of the points resulting in a very smooth curve.

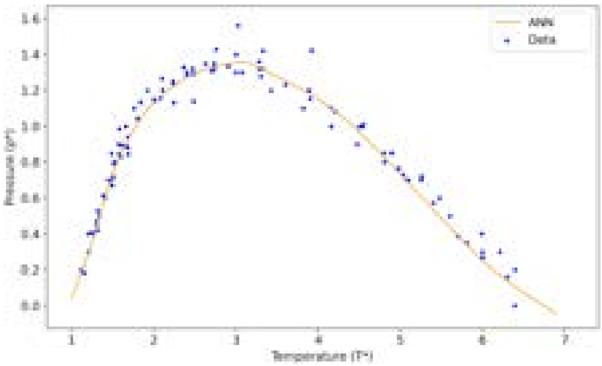

Fig. 2: ANN Preliminary Prediction of JT Inversion Curve

The ANN produced the best fit to the data based on the statistical performance indicators, achieving $R^2 = 0.9627$ and $RMSE = 0.0051$. Good qualitative performance in sparsely populated regions of data was also seen. The curve produced in Figure 2 is comparable to that of the SVR model. This preliminary study therefore confirms that ANNs are adequate for modelling the JT inversion curve.

3.3 Predicting the JT Coefficient

The ability of the model to prediction μ_{JT} was measured and results were plotted on Figure 3. The heat map feature shows the absolute error between the prediction and the actual data points. Percentage error was not used as small deviations where $\mu_{JT} \approx 0$ lead to large percentage errors, which may be misleading. It can be seen that there is a higher degree of error between $\rho = 0 - 0.7$. This can be attributed to the fact that a large number of data points lie within that region and thus, the ANN struggles to identify which combination of points corresponds to the correct points. The ANN produced relatively accurate predictions for the majority of points, however, larger error values are seen at the phase space boundaries. This behaviour was expected in areas where data is sparse.

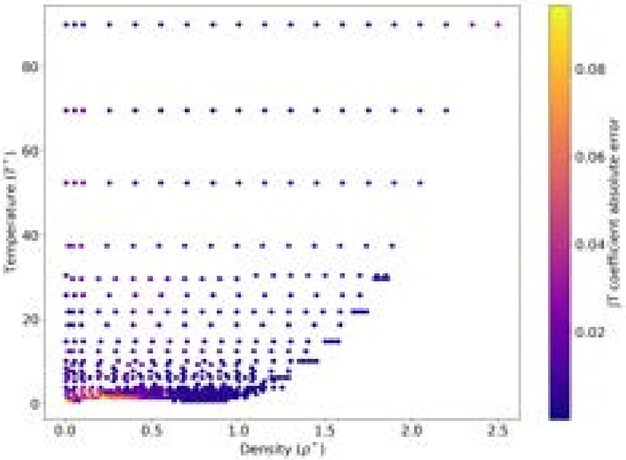

Fig. 3: Absolute Error in JT Coefficient (μ_{JT})

The parity plot in Figure 4 depicts the relationship between the actual and predicted values for the JT coefficient. It can be seen that the ANN produced relatively accurate predictions as the majority of points lie on or close to the line $y = x$.

Upon closer inspection, it was seen that the points around $\mu_{JT,Actual} = 6.5$ have the same values of T, but have slightly differing ρ values. The ANN classifies these points as having equal μ_{JT} when in actuality, they should vary slightly. Additionally, this disparity between the predicted values and actual values in the lesser populated regions can be attributed to the lack of data. ANNs are unable to generalise data and extrapolate well when the testing points are not well represented within the training set [6]. During training, the ANN was not able to "see" enough data points and therefore learn the corresponding effect of the slight variation of μ_{JT} at higher values, which explains why the ANN struggles somewhat in this region. Thus, it can be inferred that the quality of results achieved from ANN models are highly dependent on the training data.

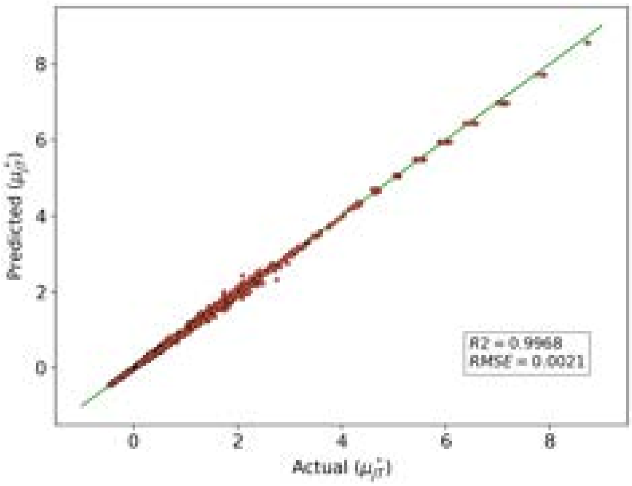

Fig. 4: Parity Plot showing the relationship between predicted and actual values of JT coefficient

3.4 Predicting the JT Coefficient at 'Easy Conditions'

The effect of varying the training data size was tested using MAE as the main performance indicator. The general trend displayed by Figure 5 clearly shows that increasing the size of the training dataset has a positive impact on the quality of result produced as MAE is minimised. The dataset at "easy conditions" contained the least amount of data points and as expected, produced the worst predictions. The size of the error produced decreased dramatically as the range of the training dataset increased to 4× the range of the "easy conditions" dataset and continued to show gradual improvement as the amount of training data was increased. This is exactly the type of result that was expected in terms of the general trend as it is widely accepted that ANNs are not good at fitting data far outside of the testing set.

There are several noticeable points that do not follow the trend, which can be explained by the incremental increase of data. As the training set increased, the ANN potentially overfitted to the known points and did not predict the newly introduced data very well, resulting in an increase in the error. However, this effect occurred to a much lesser extent as the dataset size increased further.

It can also be deduced that data needs to be well distributed around the entire phase space to produce good predictions using the ANN. This is supported by the general trend shown by Figure 5 as the upper regions of the dataset are filled in, the MAE reduces accordingly.

Based on these results, it is clear that a well populated training dataset that is also large enough to capture the empirical relationship is needed to achieve optimal performance for predictive modelling using ANNs.

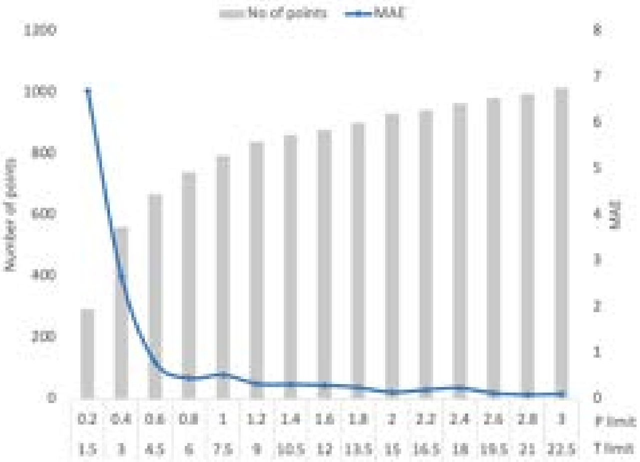

Fig. 5: The effect of increasing the training dataset on MAE

3.5 Calculating the JT Inversion Curve

3.5.1 T, ρ JT Inversion Curve by Bisection

Bisection on the ANN was able to predict the location of the inversion curve with an absolute deviation of 4.5×10^{-6} from the actual value of zero. Figure 6 shows that the network was able to generate a relatively smooth curve, which encapsulates the shape of the actual inversion curve on the ρ, T plane. All of the points shown have μ_{JT} very close to zero with the largest absolute errors occurring at the high ρ - low T region. The general error trend displayed by the heat map shows that the error increased with increasing ρ, which is in accordance with the distribution of the dataset. This provides more evidence that lacking data is responsible for the larger error values seen at higher ρ.

The method used for calculation of the true inversion curve is inherently different to methods used in past studies. Since empirical measurements of $\mu_{JT} = 0$ are infeasible, several approaches have been taken in the past. For example the study by Colina and Müller [27] used thermodynamic relations to correlate volumetric data as well as Monte-Carlo simulations to predict the location of the curve. Since all of the required data was provided for this investigation, a numerical approach, using bisection was taken to calculate the location of the inversion curve from the ANN predicted data. Bisection of the ρ, T graph produced a smooth curve which was expected, however this particular form of the inversion curve, relating density is not readily used in practice. Thus, the ANN was adjusted to produce predictions on the $T - p$ plane.

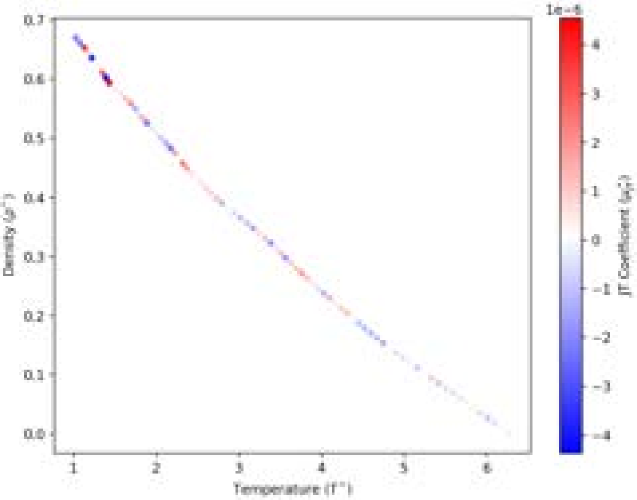

Fig. 6: T,ρ Inversion Curve with JT Coefficients Values

3.6 EOS & ANN Model Performance

As mentioned in Section 2.9.2, bisection could not be carried out on the T,p inversion curve. Instead, the combinations of different ANNs (from the ANN Matrix in Section 2.9.4) were used.

The ANN and EOS models p predictions were all compared against the p values in dataset 1. The ρ predictions were compared to the pseudo-data for ρ discussed Section 2.9.3. The results are summarised as statistical metrics in Tables 8 and 9 of Appendix A.6 respectively. All T,ρ and T,p JT inversion curves can be found in Appendix A.7.

3.6.1 Performance of ANN Models

The performance of all ANN models is similar for ρ predictive ability. ANNs 1 to 4 have the same performance metrics at R^2 of 0.9957 and RMSE of 0.0122. ANNs 5 to 8 perform marginally better with R^2 of 0.9961 and RMSE of 0.0117. The same neural network was used to predict μ_{JT} for ANNs 1 to 4, hence the metrics are equivalent. The neural network for ANNs 5 to 8 was trained using the pseudo-data (ρ values), hence the slightly enhanced performance.

The performance of all ANNs in predicting p is again very similar in terms of the statistical metrics, with R^2 values ranging from 0.9480 for ANN 5 to 0.9608 for ANN 8. From the results, it can be seen that ANNs 1 and 3 have matching performance metrics. The same can be said for ANNs 2 and 4. The p-predicting neural networks in ANNs 3 and 4 were trained with pseudo-data while ANNs 1 and 2 were trained without it. Additionally, all of these models had their μ_{JT}-predicting networks trained without pseudo-data. Therefore, it can be concluded that the addition of pseudo-data for training p-predicting neural nets does not impact the predictions when the μ_{JT}-predicting network is trained without pseudo-data. The reason for this could be that the values generated from bisection with the μ_{JT}-predicting networks did not activate the nodes responsible for memorisation of the pseudo-data in the p-predicting network.

The relative performance of ANN models 5 to 8 are all different, with ANNs 6 and 8 having marginally higher R^2 values than ANNs 5 and 7. This shows that the addition of μ_{JT} as an additional input for determining p improves the predictions. This also shows that the addition of pseudo-data to p-predicting networks only has a noticeable improvement when those networks are combined with μ_{JT}-predicting networks, which were also trained on pseudo-data. In other words, memorisation of the pseudo-data needs to take place in both neural networks for the inversion curve to be predicted with higher accuracy. The same nodes in both networks could potentially be responsible for this effect, hence the mismatch in ANN model performance.

3.6.2 Performance of EOS Models

When analysing the relative performance of the four EOS in terms of predicting p, it can be seen that R^2 values increase in the following order: Stephan et al. [25], Johnson et al. [13], Kolafa & Nezbeda [12] and Lafitte et al. [1]. Similarly, RMSE and MAE values decrease in the same order. It should be noted that the latter three EOS have relatively small differences in R^2, RMSE and MAE. They also significantly outperform the EOS of Stephan et al. [25] at predicting the JT inversion curve than , as the R^2 value is lower by 0.0843 than that of Johnson et al. [13] (third best EOS).

The order in terms of performance is the same for predicting ρ. The Johnson et al. [13], Kolafa & Nezbeda [12] and Lafitte et al. [1] EOS all have very similar R^2 values at 0.99 when considering 2 significant figures. In this case, the Stephan et al. [25] EOS performs significantly better at predicting ρ, with a difference of only 0.0083 to the Johnson et al. EOS.

3.6.3 EOS & ANN Comparison

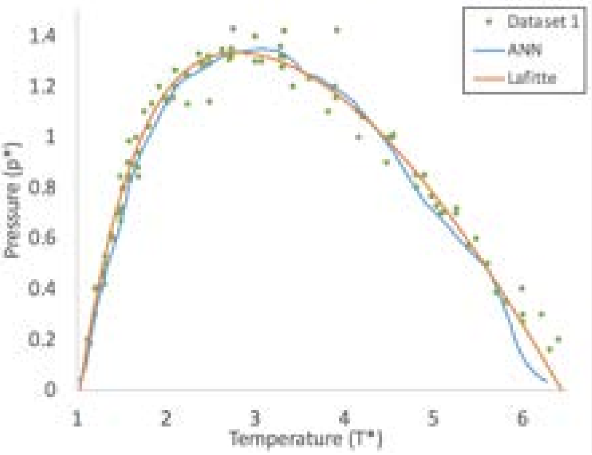

Fig. 7: Comparison of T,p JT Inversion Curves of ANN 1, Lafitte EOS and Dataset 1

The statistical metrics for all ANN models indicate that the predictions of the T,ρ inversion curve are very similar to those of the Lafitte et al. [1], Johnson et al. [13] and Kolafa & Nezbeda EOS [12], as R^2 values are all within a range of 0.9957-0.9964. When examining the curves visually, it can be seen that the ANNs all have very slight kinks in the T region of 3-4. However, all ANN models produce smooth curves that are comparable to the Lafitte [1] and Kolafa & Nezbeda [12] EOS in terms of how well they fit the data points. ANNs 5 to 8 all have slightly smoother curves than their counterparts as their μ_{JT}-predicting networks were trained using the added pseudo-data, hence the points' locations were memorised better. Despite this, ANNs 1 to 4 provide satisfactory curves, which shows the robustness of ML models.

In terms of the p predictions, the metrics show that ANN models again fit the data as well as the EOS. R^2 values for ANNs 2,4,6 and 8 are marginally higher than that of the Kolafa & Nezbeda [12] EOS. Only ANN 8 'outperforms' the Lafitte et al. [1] EOS, but the R^2 difference is very small (only 0.004). The visual examination of the T, p curves, such as the one in Figure 7, shows that all ANNs curves are not very smooth due to the slight kinks and oscillations along the curves. On the other hand, the JT inversion curves produced by all EOS are completely smooth, with the Lafitte [1] curve having the best visual fit to the data.

The curve oscillations increase as T increases past the maximum (at $T \approx 3$). This effect occurs due to the sparse distribution of data in those regions so the curves have to predict the behaviour. ANN models 7 and 8 produce the least oscillatory behaviour as both the μ_{JT} and p-predicting networks in those models were trained with the pseudo-data included. ANN 8 also has the added μ_{JT} input parameter in the p-predicting network, thus generating the smoothest p, T curve out of all ANN models.

The oscillatory aspects of the ANN-produced curves represent the neural networks' dependency on the quality of data input. Data needs to be plentiful and evenly distributed across the entire p, T, ρ space for ANNs to perform at their best. Additionally, it was not expected that the smooth T, ρ curve would produce oscillatory behaviour in the T, p curve. The μ_{JT}-predicting networks and the p-predicting networks were trained independently of each other, which could explain the predictive mismatch between the two. This presents a possibility of a more complex architecture, which combining both networks and training them together.

3.7 Comparison to Real Data

Comparison to data for real fluids was necessary to test the robustness of the ANN in predicting μ_{JT}. The R^2 values for Ar and N_2 are relatively high at 0.972 and 0.987 respectively, which shows that the ANN model predicts μ_{JT} well for both compounds. The fit for N_2 is slightly better than for Ar, which is confirmed by the lower RMSE and MAE. This result was unexpected as the LJ potential model is traditionally thought to provide a better description of the pair interactions in mono-atomic inert gases, such as Ar, rather than diatomic gases, such as N_2. However, it should be noted that LJ parameters vary from source to source, so the performance with respect to N_2 can change if different parameters are used.

CO_2 is a linear molecule with a bond length of 1.16Å [28], which makes it non-spherical. The results for CO_2 confirm that the LJ model is not ideal for describing non-spherical molecules. However, CO_2 is electronically neutral and inert, hence the LJ model provides a somewhat adequate description. Finally, the results for propane further confirm the LJ model's inadequacy for predicting longer chain fluid properties. The application of the traditional LJ potential model is inappropriate for propane since it cannot be described as an attracting hard sphere. The σ and ε LJ parameters are not sufficient for defining the pair potential function of propane. Instead, a more sophisticated EOS, such as the ones based on SAFT, can be applied.

Table 3: Results from Comparison of ANN Predictions to Real Data

Compound	R^2	RMSE	MAE
Argon	0.972	0.373	0.284
Carbon Dioxide	0.802	0.861	0.697
Nitrogen	0.987	0.085	0.199
Propane	0.416	75.410	11.966

4 Conclusions

This investigation has proven that it is possible to predict the thermophysical properties of fluids as the models were able to predict μ_{JT} and the location of the JT inversion curve in terms of T, ρ and T, p. The analysis has shown that ANNs are purely data-driven and hence the quality of results produced is heavily dependant on the input data used for training. Distribution of data was also found to be extremely important for the development of good working models as the ANN is unable to extrapolate far outside the region of the input data, hence is unlikely to create accurate predictions where data is few and far between. This was supported by all results showing that error values increase for predictions made in sparsely populated regions of the phase space.

The results also showed that the despite the lack of data around the boundaries, the ML models are able to perform similarly to the EOS by Lafitte et al. [1], which is the most accurate EOS based on the comparisons made. This implies that ML can create a good alternative to the traditional EOS, which can increase efficiency in terms of computational time by reducing the need for empirical data collection through molecular simulation. However, these models are not backed by underlying thermodynamic theories, hence, the lacking data will continue to be a limitation of basic ANNs for this use case. The model also struggled to produce good results for fluids that are not well described by the LJ model in terms of size of particles and shape, even though the molecules are dominated by the same type of intermolecular forces and are all non-polar. This highlighted the effect of the molecular shape on the LJ fluid model as it fails to accurately describe longer chain molecules.

The disadvantage of the proposed method for generating the T, p JT inversion curve is that the p-predicting and μ_{JT} predicting networks were trained independently (see Section 3.6), which could be a source of the non-smoothness in the curve. In order to improve this, one might consider building a larger ANN model that incorporates both of these networks and trains them together, in order to optimise their combined performance. Alternatively, residual ANNs (RNNs) & convolutional ANNs (ANNs) have had proven success in regression problems, due to their ability to memorise complex and intricate shapes and patterns that regular fully connected networks miss out on. Therefore, their use can be investigated to improve performance and generalisation ability.

Another area of improvement could be to use more input features to predict μ_{JT}, such as the fluid region for more accurate predictions in terms of μ_{JT} or the LJ parameters σ and ε for predicting real fluid LJ properties. A more thermodynamics-based approach could be to model the Helmholtz energy a, from which a range of different properties, including μ_{JT}, can be calculated directly by computing derivatives.

References

[1] T. Lafitte, A. Apostolakou, C. Avendaño, A. Galindo, C. S. Adjiman, E. A. Müller, and G. Jackson, "Accurate Statistical Associating Fluid Theory for Chain Molecules Formed From Mie Segments," *The Journal of Chemical Physics*, vol. 139, no. 15, p. 154504, 2013. [Online]. Available: https://doi.org/10.1063/1.4819786

[2] Y. Demirel and V. Gerbaud, *Nonequilibrium Thermodynamics (4th Edition)*, University of Nebraska, 2019. [Online]. Available: https://doi.org/10.1016/B978-0-444-64112-0.00001-0

[3] Neutrium, "Joule-Thomson Effect," Sep 2015, Accessed 12/12/2021. [Online]. Available: https://neutrium.net/fluid-flow/joule-thomson-cooling/

[4] F. Cailliez, P. Pernot, F. Rizzi, R. Jones, O. Knio, G. Arampatzis, and P. Koumoutsakos, *Bayesian Calibration of Force Fields for Molecular Simulations*, 2020. [Online]. Available: https://msse.gatech.edu/publication/UQMMM_chapter1.pdf

[5] E. Müller, "Molecular Simulation Approaches," *Imperial College London, Molecular Modelling of Fluids, Lecture Slides*, 2021.

[6] K. Zhu and E. A. Müller, "Generating a Machine-Learned Equation of State for Fluid Properties," *The Journal of Physical Chemistry B*, vol. 124, no. 39, pp. 8628–8639, 2020. [Online]. Available: https://doi.org/10.1021/acs.jpcb.0c05806

[7] E. M. Mansour, "Equation of State," in *Inverse Heat Conduction and Heat Exchangers*, 2019. [Online]. Available: https://www.intechopen.com/chapters/71295

[8] I. Ashour, N. Al-Rawahi, A. Fatemi, and G. Vakili-Nezhaad, "Applications of Equations of State in the Oil and Gas Industry," 2011. [Online]. Available: https://www.intechopen.com/chapters/20175

[9] E. Sheikholeslamzadeh and S. Rohani, "Prediction of Solubility of Active Pharmaceutical Ingredients in Single Solvents and Their Mixtures — Solvent Screening," in *Recent Advances in Thermo and Fluid Dynamics*, M. Gorji-Bandpy, Ed. Rijeka: IntechOpen, 2015, ch. 1. [Online]. Available: https://doi.org/10.5772/60982

[10] G. T. Craven, N. Lubbers, K. Barros, and S. Tretiak, "Machine Learning Approaches for Structural and Thermodynamic Properties of a Lennard-Jones fluid," *The Journal of Chemical Physics*, vol. 153, no. 10, p. 104502, 2020. [Online]. Available: https://doi.org/10.1063/5.0017894

[11] S. Stephan, J. Staubach, and H. Hasse, "Review and Comparison of Equations of State for the Lennard-Jones Fluid," *Fluid Phase Equilibria*, vol. 523, p. 112772, 2020. [Online]. Available: https://www.sciencedirect.com/science/article/pii/S0378381220303204

[12] J. Kolafa and I. Nezbeda, "The Lennard-Jones Fluid: An Accurate Analytic and Theoretically-Based Equation of State," *Fluid Phase Equilibria*, vol. 100, pp. 1–34, 1994. [Online]. Available: https://www.sciencedirect.com/science/article/pii/0378381294800014

[13] J. K. Johnson, J. A. Zollweg, and K. E. Gubbins, "The Lennard-Jones Equation of State Revisited," *Molecular Physics*, vol. 78, no. 3, pp. 591–618, 1993. [Online]. Available: https://doi.org/10.1080/00268979300100411

[14] S. Stephan, M. Thol, J. Vrabec, and H. Hasse, "Thermophysical Properties of the Lennard-Jones Fluid: Database and Data Assessment," *Journal of Chemical Information and Modeling*, vol. 59, no. 10, pp. 4248–4265, 2019. [Online]. Available: https://doi.org/10.1021/acs.jcim.9b00620

[15] K. Wakefield, "A Guide to the Types of Machine Learning Algorithms," Accessed 05/11/2021. [Online]. Available: https://www.sas.com/en_gb/insights/articles/analytics/machine-learning-algorithms.html

[16] J. Ding, N. Xu, M. T. Nguyen, Q. Qiao, Y. Shi, Y. He, and Q. Shao, "Machine Learning for Molecular Thermodynamics," *Chinese Journal of Chemical Engineering*, vol. 31, pp. 227–239, 2021, frontiers of Chemical Engineering Thermodynamics. [Online]. Available: https://www.sciencedirect.com/science/article/pii/S1004954120307333

[17] D. Kumar, "Introduction to Data Preprocessing in Machine Learning," Accessed 10/09/2021. [Online]. Available: https://towardsdatascience.com/introduction-to-data-preprocessing-in-machine-learning-a9fa83a5dc9d

[18] F. Pedregosa, G. Varoquaux, A. Gramfort, V. Michel, B. Thirion, O. Grisel, M. Blondel, P. Prettenhofer, R. Weiss, V. Dubourg, J. Vanderplas, A. Passos, D. Cournapeau, M. Brucher, M. Perrot, and E. Duchesnay, "Scikit-learn: Machine Learning in Python," *Journal of Machine Learning Research*, vol. 12, pp. 2825–2830, 2011.

[19] Y.-S. Park and S. Lek, "Chapter 7 - Artificial Neural Networks: Multilayer Perceptron for Ecological Modeling," in *Ecological Model Types*, ser. Developments in Environmental Modelling, S. E. Jørgensen, Ed. Elsevier, 2016, vol. 28, pp. 123–140. [Online]. Available: https://www.sciencedirect.com/science/article/pii/B9780444636232000074

[20] S. Tiwari, "Activation Functions in Neural Networks," Accessed 20/09/2021. [Online]. Available: https://www.geeksforgeeks.org/activation-functions-neural-networks/

[21] D. Liu, "Activation Functions in Neural Networks," Accessed 20/09/2021. [Online]. Available: https://medium.com/@danqing/a-practical-guide-to-relu-b83ca804f1f7

[22] J. Rocca, "A Gentle Journey from Linear Regression to Neural Networks," Accessed 20/09/2021. [Online]. Available: https://towardsdatascience.com/a-gentle-journey-from-linear-regression-to-neural-networks-68881590760e

[23] J. Brownlee, "Dropout regularization in deep learning models with keras," 2020, Accessed 10/09/2021. [Online]. Available: https://machinelearningmastery.com/dropout-regularization-deep-learning-models-keras/

[24] T. Akiba, S. Sano, T. Yanase, T. Ohta, and M. Koyama, "Optuna: A Next-Generation Hyperparameter Optimization Framework," in *Proceedings of the 25th ACM SIGKDD International Conference on Knowledge Discovery Data Mining*. Association for Computing Machinery, 2019, p. 2623–2631. [Online]. Available: https://doi.org/10.1145/3292500.3330701

[25] S. Stephan, J. Staubach, and H. Hasse, "Review and Comparison of Equations of State for the Lennard-Jones Fluid," *Fluid Phase Equilibria*, vol. 523, p. 112772, 2020. [Online]. Available: https://www.sciencedirect.com/science/article/pii/S0378381220303204

[26] National Institute of Standards and Technology (NIST), U.S. Department of Commerce, "Thermophysical Properties of Fluid Systems; NIST Chemistry WebBook, SRD 69," Accessed 17/11/2021. [Online]. Available: https://webbook.nist.gov/chemistry/fluid/

[27] C. Colina and E. Müller, "Joule-Thomson Inversion Curves by Molecular Simulation," *Molecular Simulation*, vol. 19, no. 4, pp. 237–246, 1997. [Online]. Available: https://doi.org/10.1080/08927029708024153

[28] G. Glockler, "Carbon–Oxygen Bond Energies and Bond Distances," *The Journal of Physical Chemistry*, vol. 62, no. 9, pp. 1049–1054, 1958. [Online]. Available: https://doi.org/10.1021/j150567a006

[29] M. P. Allen and D. J. Tildesley, *Computer Simulation of Liquids*, 1989. [Online]. Available: https://oxford.universitypressscholarship.com/view/10.1093/oso/9780198803195.001.0001/oso-9780198803195

[30] G. V. Belov, "Real-Gas Equations of State Based on the Lennard-Jones Potential," *Mathematical Models and Computer Simulations*, vol. 1, no. 6, p. 677, Nov 2009.

[31] B. M. Mognetti, L. Yelash, P. Virnau, W. Paul, K. Binder, M. Müller, and L. G. MacDowell, "Efficient Prediction of Thermodynamic Properties of Quadrupolar Fluids from Simulation of a Coarse-Grained Model: The Case of Carbon Dioxide," *The Journal of Chemical Physics*, vol. 128, no. 10, p. 104501, 2008. [Online]. Available: https://doi.org/10.1063/1.2837291

[32] R. Tahery and H. Modarress, "Lennard-Jones Energy Parameter for Pure Fluids from Scaled Particle Theory," *Iranian Journal of Chemistry & Chemical Engineering - International English Edition*, vol. 26, pp. 1–9, 06 2007, Accessed 29/11/2021. [Online]. Available: https://www.ijcce.ac.ir/article_7647.html

Development of compressor efficiency maps for the techno-economic modelling of small-scale heat-pumping applications

Aleksander Ziolkowski and Vethalingam Siva Shanmugam

Department of Chemical Engineering, Imperial College London, U.K.

Abstract This paper presents a data-driven heat pump design and optimization approach focusing on the analysis of four compressor types in small scale heat pump systems. Performance maps were developed by collecting compressor performance data for a multitude of small-scale rotary, scroll and piston compressors using a variety of common working fluids into a database. To implement these into an existing data-driven thermodynamic performance, costing correlations were developed to accurately design and optimize heat pump techno-economic performance. The model was then run at specific heat pump scenarios, including normal and wide range design conditions. The model was capable of accurately determining the performances of all compressors, including screw compressors for reference from the original model. Rotary compressors resulted in the best techno-economic performance at all considered design conditions due to their relatively good coefficient of performance (COP) at a relatively cheap cost. While scroll compressors offer a better COP of 3.22 at normal design conditions compared to 3.09 for rotary compressors, they did come at a much higher price. Meanwhile, piston and screw compressors resulted in the worst performance in almost all cases except for the largest temperature difference case where the screw compressor outperformed the techno-economic performance of the scroll compressor. Lastly, it was shown with wide range efficiency and COP maps that the compressors generally follow an expected trend of better performance with smaller temperature differences. While the objectives of this paper were met by delivering a data-driven compressor techno-economic and performance analysis related to heat pumps, the models could be improved in future work to investigate variable temperatures at specific design points to reflect performance across a range of real-life variable temperatures with a single compressor design.

Keywords: *Domestic, Heat pumps, Thermodynamic modelling, Data-driven, Optimisation, Compressors*

1 Introduction

Space heating is a crucial element required in every part of the world to keep homes at comfortably warm temperatures. Globally, heating accounts for nearly half of all energy consumption and is one of the highest contributors of individual carbon footprints. 40% of carbon dioxide emissions are stemmed from heating homes, with the proportion being significantly higher for colder climates.

Residential housing contributes to 38% of greenhouse gas emissions in the US, while the UK has a significant 19% emission from heating buildings, with three-quarters of that from domestic buildings. Since natural gas is relatively cheap, 85% of UK homes still utilise gas boilers for heating which is the 2nd highest CO_2 emitter after oil boilers[1].

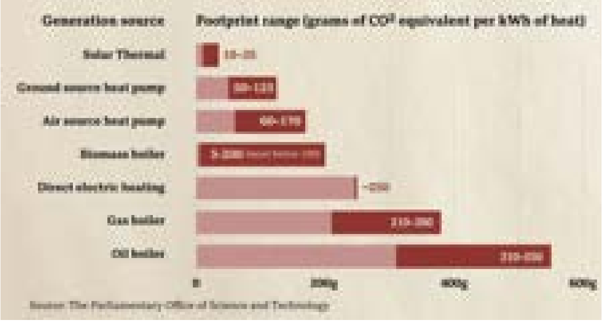

Source: The Parliamentary Office of Science and Technology

Figure 1: Heating options from different sources[2]

However, there are several less carbon-intensive alternatives that can be adopted by householders such as district heat networks, heat pumps and electrical resistance heating. The common types of heating systems include central and district heating systems. Heat pumps classified as central heating systems were focused on in this investigation due to the vast potential they offer with their environmentally friendly footprint as shown in figure 1. Furthermore, heat pumps only demand one-quarter of the energy required by traditional gas boilers.

Although the main drawback of heat pumps is that the current high electricity prices compared to natural gas makes it less favourable, but the lower energy requirement, net-zero target and a relatively long lifespan[3] allows investors to lean towards heat pumps.

Heat pumps are slowly gaining popularity on a global scale and are projected to grow from US$ 54. 34 billion in 2018 to US$ 94.42 billion by 2023 – CAGR of 11.68% from 2018 to 2023[4]. The increasing investments in domestic and commercial sectors accompanied by rising industrial demand in Europe and Asia Pacific is the main driving force for the heat pump market during this period[5].

Evidently, heat pumps play a significant role in heat decarbonisation. Choosing heat pumps involves various sources of heat (air or ground), components design (compressors, expansion valves, heat exchangers) and working fluid options which can all then affect the performance and cost.

This project focuses on the development of an extended data-driven model through generation of a database comprising major types of small-scale compressors available on the market. This was performed through analysis of commercially available compressors from different UK manufacturers involving data collection for performance parameters. Previous studies have been done in this area using a similar model, such as that of Astolfi[6]. However, these models concentrated on either fixed or maximum isentropic efficiencies which tend to introduce errors. Hence, this investigation was aimed to improve on this work by developing better data-driven models with variable isentropic efficiencies focusing on small domestic compressors

Curve-fitting techniques were used to identify relationships between key variables and projected for ranges outside the working conditions used. The data-driven model could help in diminishing simulation uncertainties in future work. The second part of this investigation applied the obtained correlations to a thermodynamic and component-costing model of a domestic-scale electric heat pump. The model was then run for normal and wide range heat pump operating condition scenarios. Additionally, this project aims to make the analysis more applicable to selecting compressors for heating applications by performing a techno-economic analysis to determine the cost efficiency performance of compressors in various conditions.

2 Background

Heat pumps work by capturing heat from outside and transferring it into the required space, with electricity being delivered to the pump cycle to generate heat[7]. However, the quantity of heat produced is much greater than the electricity required, which is then represented as a coefficient of performance (COP) to evaluate the heat pump. Heat is naturally transferred from a hot region to a colder region but to heat homes the process is reversed, hence requiring work to be done.

Two most common heat pumps are air source heat pump (ASHP) and ground source heat pumps (GSHP). The mutual feature of both pumps is heat being transferred between refrigerant and outer fluid. However, cold air is the outer fluid for ASHP and cold water is circulated in underground pipes in GSHP[8]. The cold water mixed with brine, which has antifreeze properties passes through the heat exchanger and transfers heat to the refrigerant. ASHP's are more commonly installed and was the focus of this project. The higher capital costs and maintenance requirements for GSHP's results in it being less favourable in the energy market.

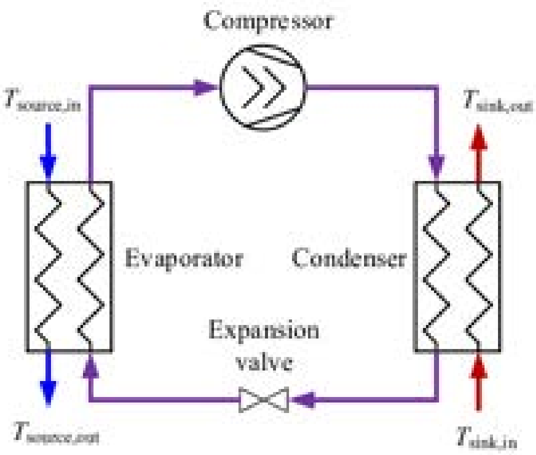

Figure 2: Schematic diagram of a heat pump system[9]

The fluid, which is usually gas, is fed to the heat exchangers and are called refrigerants. Cold air from outside passing through the evaporator increases the temperature of the refrigerant. The refrigerant is then pressurised through the compressor where the corresponding fluid temperature rises. The condenser receives the high temperature fluid which is used to heat up the temperature inside the building. The refrigerant is then allowed to expand to cool even further and is now cold enough to absorb more heat from the surroundings and then the cycle repeats.

The core component in a heat pump is the compressor. A number of variables need to be considered before selecting a compressor, such as evaporating and condensing temperatures, efficiency values, working fluids, and other factors. The compressor increases both pressure and temperatures of the passing refrigerant. An electric motor is powered by the power grid and integrated into the compressor. In comparison to heat production through burning of fossil fuels, electrically operated compressors offer a more attractive solution when the COP has a reasonable value.

2.1 *Working fluids*

Refrigerant choices for heat pumps are crucial and there are various options depending on working conditions. R410a works very well for high pressure and low temperature settings, however, has a very high global warming potential (GWP) of 2088[10]. GWP of gas reflect the total contribution to global warming from emission of one unit of gas relative to one unit of CO_2, which has an assigned value of 1. R22 is one of the most common refrigerant available but has a significantly high GWP of 1810. One of the better options being applied in industry in recent years is R32 which has a lower GWP of 675 and portrays a better performance in heat pumps[11]. R134a has a good working condition at low outdoor temperatures, -5 ^{0}C to 5 ^{0}C in ASHP although the GWP is not favourable[12]. In a study comparing propane (R290) and butane (R600) with R134a as a baseline, both hydrocarbons had higher heating capacities and much lower GWP's but their COPs were significantly lower than that of R134a[13]. Hence, a perfect balance of COP, heating capacity and GWP needs to be considered to determine the optimal refrigerant as a working fluid.

2.2 Rotary compressor

Rotary compressors, also referred to as rotary vane compressors, are considered positive displacement machines. Unlike reciprocating compressors, they do not have valves to drive gas around the compressor. High speed obtained from direct-connect motors is required from most rotary compressors[14]. The major exception is the helical lobe type as it needs a speed-increasing gear and operate above motor speed. Major advantages of rotary compressor are relatively light, experience less vibration and do not require having foundations.

2.3 Scroll compressor

Scroll compressors are also classified as positive displacement compressors. A scroll compressor uses two interleaving scrolls to pressurise fluids where one scroll is fixed and the other orbits eccentrically without rotating[15]. When the orbiting scroll moves, gas is absorbed on the outer circumference of the scroll. The decrease in space between the two scrolls results in compression occurring. A thin layer of lubricant film is present between the scrolls and act as a sealing element[16]. In comparison to piston compressors, scroll compressors have fewer moving parts, smaller in size, lower vibration, and increased service life.

2.4 Piston compressor

Reciprocating compressor or otherwise referred to as piston compressor operates based on cycles of suction, discharge, and extrusion of water vapour of working factor. Change of volume is observed due to the piston movement in an enclosed cylindrical space. The major element is the presence of a crankshaft which converts rotary motion into reciprocating motion of the piston. Piston compressors can be classified based on number of valves, number of cylinders, construction of closure of compressor body and the number of compression stages and refrigeration type. Some positives of piston compressors are relatively low maintenance cost, ability to have high pressure and high power and significant product life[17].

2.5 Screw compressor

The major structural elements of screw compressors involve two helical rotors with varying teeth number and notches. These are arranged in parallel to each other and enclosed with two lids. A lubricant film is used during compressor operation to seal the backlash, which is maintained between rotors and the hull[18]. The working fluid is passed through the suction chamber and extruded through the pressure side. Screw compressor is a great option in heat pumps since it has no working valves, no flow pulsation and possibility of variable heating power between 20-100% of maximum power.

3 Methods

3.1 Compressor Modelling

The creation of databases was key focus for this project. This was then applied during the later stages of the model. The databases were created in the exact same way for three different types of compressors namely rotary, scroll and piston compressors. Two major websites were used to extract data including Bitzer[19] and Area Cooling Solutions[20]. Data for different compressor models and series were compiled for cooling capacity (Q), power input (P), mass flow [kg/h] (m) and current [A] (I). This data was stored by adopting the *Ten Coefficient Polynomial*, shown below.

$$y = c_1 + c_2 * t_o + c_3 * t_c + c_4 * t_o^2 + c_5 * t_c * t_o$$
$$+ c_6 * t_c^2 + c_7 * t_o^3 + c_8 * t_c * t_o^2 + c_9 * t_o * t_c^2 + c_{10} * t_c^3$$

Where c_1 to c_{10} represent compressor-specific coefficient values obtained from the references for Q, P, m and I while t_o and t_c represent the evaporating and condensing temperatures respectively.

All the collected data are stored in a MATLAB database representing the company, compressor model, working fluid and type of series. The database formed also corresponds to a specific working fluid for every compressor model.

Using the REFPROPM extension available on MATLAB, the pressure, enthalpy, entropy and density of fluids were evaluated for both the inlet and outlet conditions. The following key parameters were calculated to aid the analysis section.

$$\dot{V}_{in}\ [m^3/s] = \frac{\dot{m}_{in}}{\rho_{in}}$$

$$\dot{V}_{out}\ [m^3/s] = \frac{\dot{m}_{out}}{\rho_{out}}$$

$$\text{Volume flowrate ratio} = \frac{\dot{V}_{in}}{\dot{V}_{out}}$$

$$\text{Isentropic Efficiency} = \frac{\dot{m}}{w_{in}}\left(H_{out,isen} - H_{in}\right)$$

Where $\dot{m}$ is the mass flowrate, ρ is the fluid density, $\dot{V}_{in}$ is the volume flowrate inlet, $\dot{V}_{out}$ is the volume flowrate outlet, $H_{out,isen}$ is the compressor outlet isentropic enthalpy and H_{in} is the compressor inlet enthalpy.

3-D performance maps were plotted to represent volume flowrate inlet, volume ratio and isentropic efficiency in the same graph. MATLAB's curve fitting tool was used to then create the 3-D performance map based on the data for each compressor. The resulting polynomial correlation can then be used in the heat pump model to calculate the isentropic efficiency at any point for any compressor.

3.2 *Heat pump model*

To implement our databases and performance curves to model heat pumps, the thermodynamic performance model developed by Olympios et al was used[21]. This model is based on the heat pump cycle and uses a "spatially lumped thermodynamic model of a low-temperature heat pump with a single-stage-compressor.[22]" The heat pump cycle can be split into four stages as described below, with corresponding stages shown on a temperature-entropy diagram in figure X.

- 1-2: Compression of the working fluid
- 2-3: Heat rejection to hot water
- 3-4: Isenthalpic expansion
- 4-1: Heat addition from the heat source

Furthermore, the model assumes no pressure loss across pipes, steady-state operation of components and isenthalpic expansion across the expansion valve.

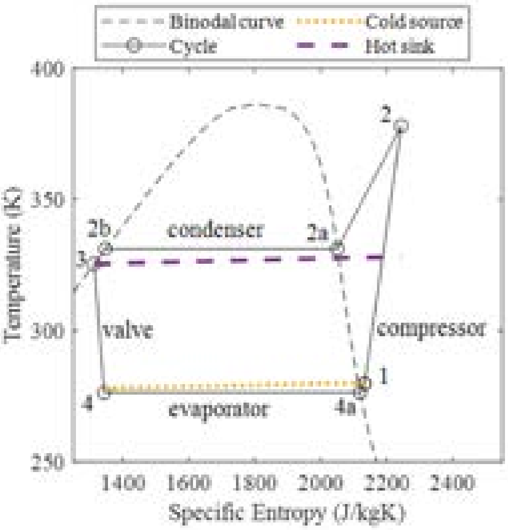

Figure 3: T-s diagram, taken from Olympios et al.[23]

The initial model developed by Olympios et al. used compressor efficiency maps for a screw compressor and R32 fluid adapted from the works of Astolfi[24]. However, it has been adapted to use updated compressor efficiency maps for the different compressors developed from our database. Furthermore, the model uses multiple cost correlations for all the components in the heat pump/ However, it has been further adapted to use specific cost correlation curves developed based on market research done by the CEP Laboratory on small sized refrigeration compressors. The correlations were done by creating lines of best fit from volume flowrate against price plots.

The detailed description of the model can be found in the paper written by Olympios et al. However, for the purpose of this paper, the model uses optimization to design an optimal heat pump with maximum COP for the specified temperature and power conditions. Given the temperature conditions, it is then able to size the heat exchangers and heat pump components `optimally given the performance maps to give all the output conditions.

3.3 *Heat pump scenarios*

While the model can theoretically be run for any temperature ranges, design conditions need to be chosen to design and optimise the heat pumps for. There are two main temperatures to be considered when working with heat pumps: the air temperature and the heat sink temperature. The air temperature is defined as the source temperature that goes into the heat pump and is referred to as *T-in*. Whereas the sink temperature is the outlet temperature that goes out of the heat pump for heating, referred to as *T-out*. The analysis considers normal design conditions and also wide range conditions.

3.3.1 *Normal design conditions*

The design air temperature was chosen to be 7°C since it is the industrial standard for specifying ASHP efficiency[25] and aligns well with the average temperatures in the UK. Whereas the design sink temperature was chosen to be 55°C as it is the minimum temperature required for hot water and in modern radiators for heating in spaces[26].

3.3.2 *Wide range design conditions*

Realistic boundary conditions must be defined for the wide range design conditions for the analysis to have practical meaning. Therefore, the heat sink temperature lower boundary condition was chosen to be 35°C, which is considered as the design water temperature for floor heating systems as specified in the European standard[27]. The upper boundary condition was set at 55°C, the required temperature for hot water. On the other hand, boundary conditions for the air temperatures of -10°C and 20°C were considered as they are temperature ranges one may expect in the UK.

It should be noted that all the scenarios considered in this paper use the same constant power output of 10kW, which is considered to be a normal size for the average household in the UK. This therefore results in the specific price always being equal to a tenth of the total price.

4 Results

4.1 *Databases*

As mentioned in 3.1, three major databases were generated for rotary, scroll and piston compressors. The number of compressors stored in the database for different working fluids are as follows:

Table 1: Breakdown of generated database

Type of compressor	Number	Working fluids
Rotary	25	R32, R134a, R407c, R410a, R290
Scroll	66	R22, R32, R134a, R407c, R410a
Piston	30	R32, R134a, R407c

Figures visualizing the databases can be found in the supplementary information section.

4.2 *Performance Maps*

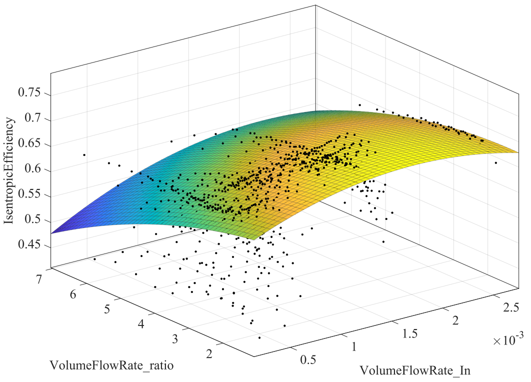

Figure 5: Performance map for rotary compressor

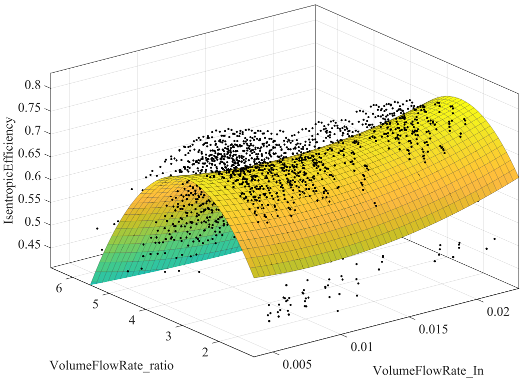

Figure 6: Performance map for scroll compressor

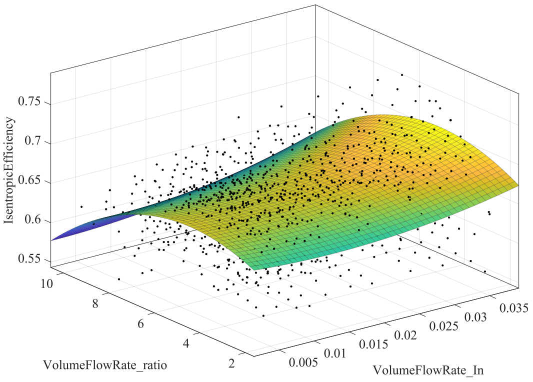

Figure 7: Performance map for piston compressor

From the generated compressor database, isentropic efficiencies and other key parameters were evaluated. These values were vital in plotting the performance maps for rotary, scroll and piston compressor. By applying the curve fitting tool in MATLAB, a polynomial fit of 2nd order to form a correlation was obtained from the best fit. Other polynomial fits of orders 1 to 5 and some non-polynomial fits were attempted but these formed very steep curves which were outside the working range. It can be noted that these performance maps were plotted to analyse the fit of average compressor performances. Hence, a 2nd order polynomial was finalised to be the best representative of the aforementioned average values. As observed from figure 4 and figure 6, both rotary and piston compressors have a flatter average 2nd order fit compared to scroll compressor in figure 5 which forms maximum isentropic efficiencies in the region of 2.5-4 for the volume ratio. This could be analysed as scroll compressors having a more specific optimal working range. All the correlations generated followed the same polynomial equation as follows and their respective coefficients described in table 2.

$$f(x,y) = p00 + p10 * x + p01 * y + p20 * x^2 + p11 * x * y + p02 * y^2$$

Table 2: Polynomial map equation coefficients

Compressor	p00	p10	p01	p20	p11	p02
Rotary	0.637	87.1	-0.005	-26800	4.52	-0.002
Scroll	0.369	-5.05	0.268	368.1	-1.11	-0.046
Piston	0.625	-1.09	0.0222	36.9	0.0897	-0.003

4.3 *Cost correlations*

As described in the methodology section, cost correlations were developed to create equations relating the volume flowrate of compressors to their price using data collected by the CEP Laboratory. As can be seen below in figure 7, both rotary and scroll compressors have a linear trendline with R^2 values of 0.43 and 0.82, respectively. The data for rotary compressors was scattered and did not fit the trends well, hence the low R^2 value. Whereas the piston compressors fit a power curve to a high extent, with an R^2 value of 0.95. All equations for the lines of best fit are displayed on figure 7 below. These were then used in the heat pump design and optimisation model to replace a similar costing correlation, developed originally by the CEP Lab, to calculate costs for the small compressors used in heat pumps.

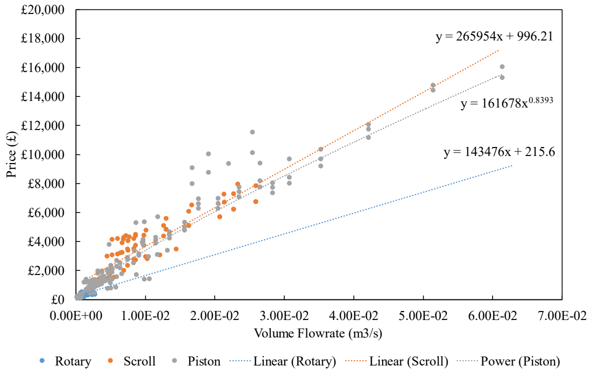

Figure 7: Costing correlations for compressors

4.4 *Normal design condition results*

The data-driven heat pump design and optimisation model was run for each compressor type with normal design conditions of air temperature 7°C and heat sink temperature of 55°C. The model produced temperature-entropy and pressure-enthalpy diagrams for each design point, however these were almost identical for all compressor types and are thus omitted from the results. The temperature-entropy graphs are equal to that shown earlier in figure 3, but with slightly varying slopes of the compression step (1-2) accounting for the change in isentropic efficiency. The results for the COP, isentropic efficiency and heat pump specific prices are shown below in table 3, along with the Astolfi screw model results for reference.

Table 3: Model results

Compressor	Rotary	Scroll	Piston	Screw
COP	3.09	3.22	3.06	2.93
Isentropic Efficiency	0.682	0.725	0.67	0.627
HP Specific Price (£/kWth)	390.7	433.1	489.7	431.1

Based on the results shown in table 3, it can be observed that the scroll compressor displays the best coefficient of performance and isentropic efficiency values out of all the compressor types. However, it comes at a relatively high specific cost compared to the rotary and piston compressors, which have lower coefficients of performance and isentropic efficiencies. Meanwhile, the screw compressor shows the lowest performance results, while also occurring at a price similar to that of the scroll compressor. Overall, judging by performance and price, the scroll and rotary compressors display strong results in this section.

To further analyse what drives the difference in prices, a costing breakdown was performed by extracting prices of each component from the heat pump model. Figure 8 below shows a proportionate cost breakdown of all the components in the rotary compressor-based heat pump, including additional non-component related costs such as tax, profit, and hardware. Furthermore, figure 9 shows a cost breakdown comparison of all the compressor types, with the compressor associated costs highlighted in red.

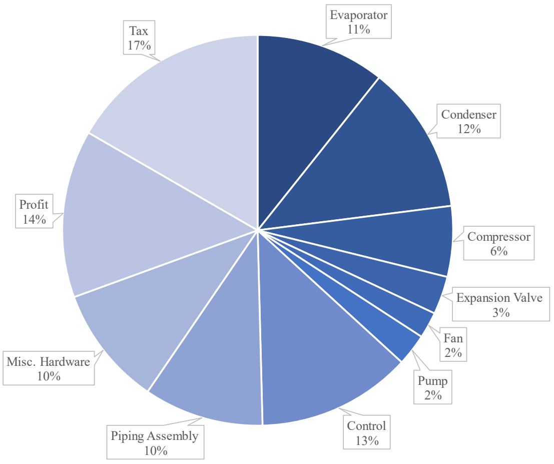

Figure 8: Cost breakdown of rotary compressor

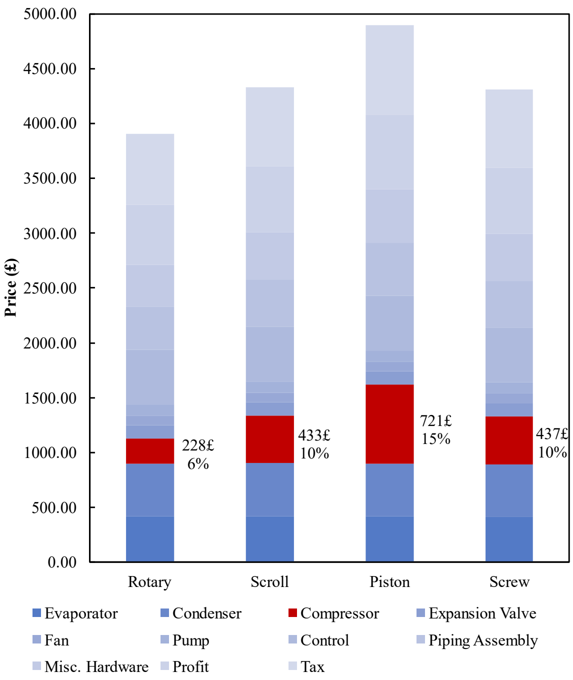

Figure 9: Compressor cost breakdown comparison

As can be seen in figures 8 and 9, compressors account for between 6% to 15% of total heat pump costs, which is enough to drive the total price to change to favour different heat pumps depending on the compressor costs. The cheapest compressor cost is 228£, which is roughly only a third of the cost of the most expensive piston compressor at 721£. With domestic applications and residents purchasing these heat pumps, such price differences are likely to affect consumer's choices. Hence the costs of the compressors would be a relatively significant consideration when designing heat pumps.

However, to assess the performance and cost of compressors, a techno-economic ratio was introduced which calculates the cost per COP of each compressor. Thus, leading to a better understanding of whether the additional costs may be worth the expensive if they provide additional performance, since COP performance also varies between compressors. The results are below in table 4, along with specific price, total heat pump price and compressor cost for reference. The lower the techno-economic ratio the better.

Table 4: Heat pump cost summary

Compressor	Rotary	Scroll	Piston	Screw
Compressor cost	228.40	432.50	721.07	437.20
Total HP price	3907	4331	4897	4311
HP Specific Price (£/kWth)	390.7	433.1	489.7	431.1
Techno-economic ratio (£/COP)	1263	1345	1601	1470

The analysis shows confirm the previous results that the rotary compressor heat pump offers the best value for performance, with scroll compressors coming second. Hence, it provides a clear advantage over piston and screw compressors, which have a noticeably higher ratio. It should also be noted that in this measure, the piston compressor has the worst performance rather than the screw compressor, which is due to the high specific price of piston compressors.

4.5 Wide range design condition results

To further evaluate the usefulness of the optimisation model at various conditions, the model was run using the wide range design conditions as defined in the methodology. Figure 10 depicts a comparison of all compressor types using the techno-economic price at the wide range boundary conditions, in addition to the normal design conditions for reference. The graph has 6 design points, labelled using the air temperature (e.g. A-10 is equivalent to air T-in at -10°C) and water temperature (e.g. W35 is equivalent to water T-out at 35°C).

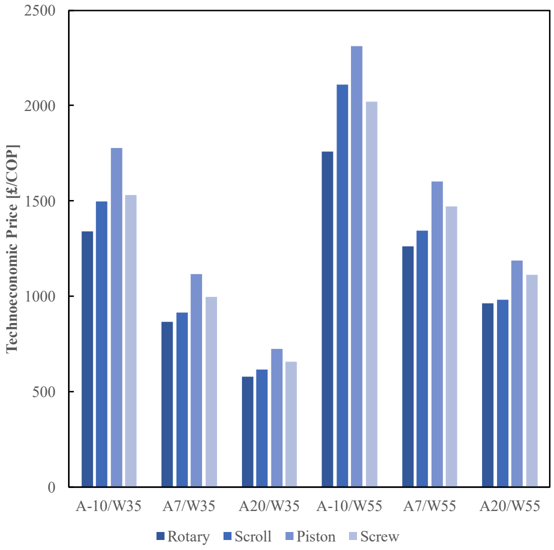

Figure 10: Techno-economic heat pump price comparison with wide range temperature values (A = Air, W = Water)

Analysing the general performance of all compressor types, it can first be observed that as the temperature difference between T-in and T-out is decreased, the techno-economic price decreases significantly. This is an expected trend explained by the fact that as the temperature difference is smaller, less work is required to achieve by the heat pump cycle. Thus, the A20/W35 design point offers the best techno-economic price value. However, in real life this is an unrealistic scenario as heat pumps would not be designed to work optimally for such small temperature differences, especially in the UK.

Comparing the performance of specific compressors at each design point, the rotary and piston compressor-based heat pumps respectively have the best and worst techno-economic performance again at all points. This is the same case as in the normal design conditions. However, the trends are different with the scroll and screw compressor-based heat pumps. Between the two, the scroll outperforms the screw compressor at all design points except for A-10/W55. This point corresponds to the largest temperature difference, suggesting that for cold regions with hot water heating, the screw compressor could be more economical compared to the scroll compressor. However, this would have to be verified in a more thorough investigation specific to those two compressors where a rotary compressor cannot be used. Since otherwise the rotary compressor still comes out as the superior one.

Next, performance maps were created to analyse the isentropic efficiency and COP across the whole range of temperatures within the boundary conditions. Maps are shown for rotary, scroll, piston and screw compressors in figures 11 to 18.

The trends are also generally as expected and confirmed by the previous boundary condition analysis, confirming that lower temperature differences give higher efficiency and COP. However, while the COP trends are consistent across all compressor types, the isentropic efficiency trends in the maps are flipped for scroll and piston compressors but the same for rotary and screw. The trends for isentropic efficiency for scroll and piston compressors are illustrated in figures 13 and 15; showing that as the air temperature increases, the isentropic efficiency decreases in a non-linear manner. The variation in trends is most likely due to the data and maps being different for the compressors, but also potentially due to physical reasons, which were not investigated as part of this data-driven research.

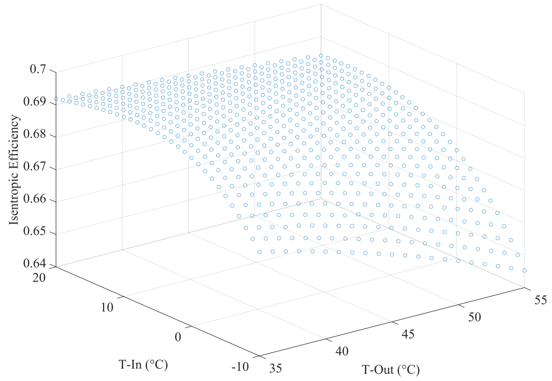

Figure 11: Rotary compressor wide range isentropic efficiency map

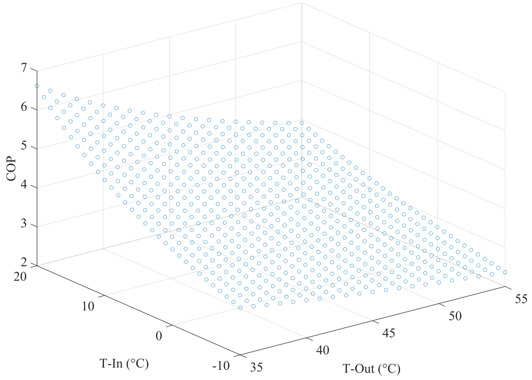

Figure 12: Rotary compressor heat pump wide range COP map

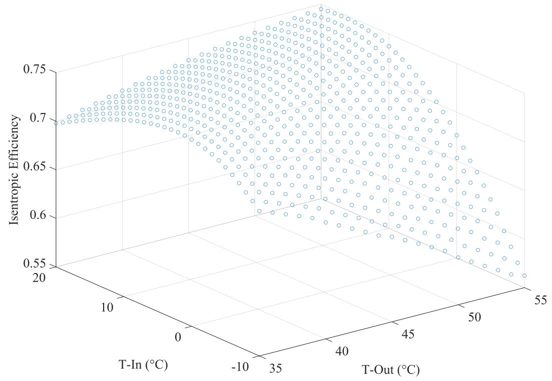

Figure 13: Scroll compressor wide range isentropic efficiency map

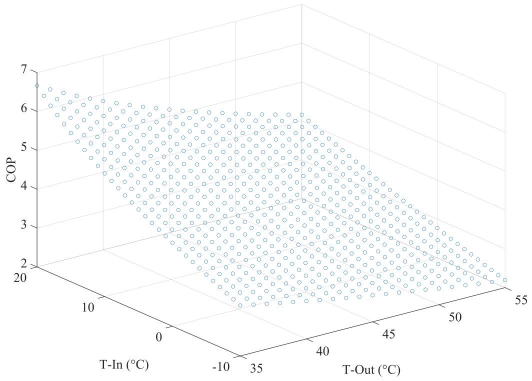

Figure 14: Scroll compressor heat pump wide range COP map

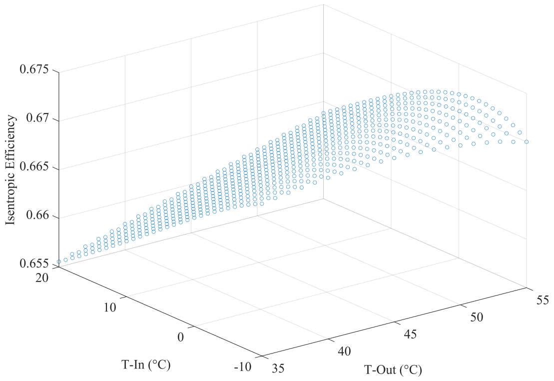

Figure 15: Piston compressor wide range isentropic efficiency map

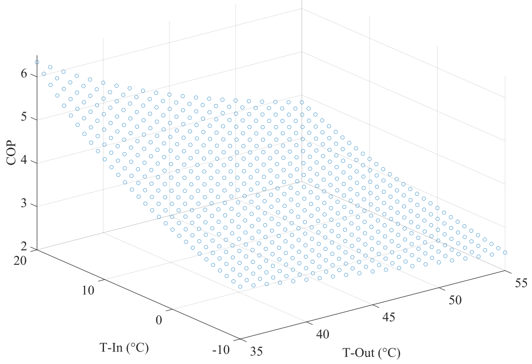

Figure 16: Piston compressor heat pump wide range COP map

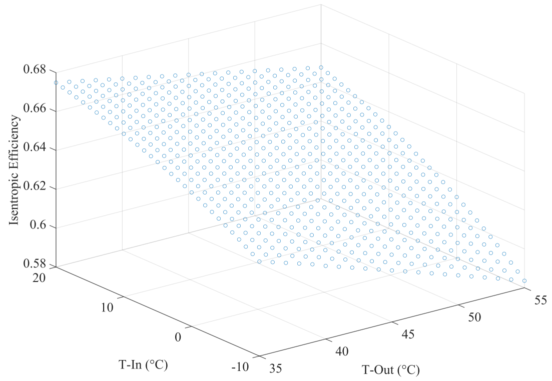

Figure 17: Screw compressor wide range isentropic efficiency map

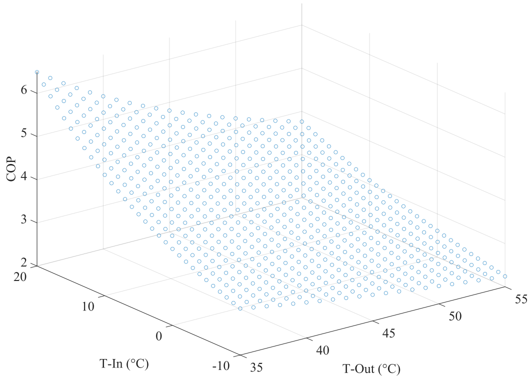

Figure 18: Screw compressor heat pump wide range COP map

5 Conclusions

The primary objectives of this investigation were creating a compressor database and adapting a data-driven heat pump design and optimisation model to use the created performance maps and correlations. These objectives have been met since a reliable compressor database has been generated as aimed with functioning and efficient MATLAB codes. This data-driven model accurately predicts isentropic efficiencies for various compressor types at specific design conditions, calculating isentropic efficiency, COP, and cost data at those specific points. The performance maps can then be used for development of heat pumps and other small-scale systems by research groups. They will be able to expand on the maps created to design and optimise heat pumps with various types of compressors.

The integrated heat pump model was able to accurately design and optimise heat pumps based on the performance maps and costing correlations obtained from the compressor database. Based on the techno-economic analysis performed, rotary compressors were favourable due to optimal results. The COP of 3.09 for rotary compressors were competitive to that of 3.22 for scroll compressors. The much lower cost for rotary compressor will make it a more favourable option based as shown in the results of this model. However, in a real-life setting, other than COP and cost, variable design conditions will need to be considered since the required operations are not always the same temperature range. Hence, a trade-off will need to be achieved.

6 Outlook

Possible directions for future work include generating a much larger compressor database by adding more datapoints. More websites and compressor manufacturers could be consulted to populate the database. This could be further expanded to other compressor types as well as large-output compressor models. Venturing into larger compressors would be beneficial to be applied to the commercial and industrial sectors where more heat output is required. Since industries have a high heating duty, analysing and optimising compressor models could have a substantial energy-savings in the long run.

It is also possible to carry out analysis on various working fluids to determine optimal choices during heat pump operations. One of the critical parameters for choice of refrigerant is the global warming potential (GWP). This would need to be compared for different refrigerants together with their effect on compressor performance and ability to work for range of conditions.

A short maximum isentropic efficiency study was performed in this research where the best working condition was selected for every compressor model and similar performance curves were plotted. However, due to insufficient datapoints, significant trends could not be observed but this has a great potential for further investigation in the future. If the maximum isentropic efficiency can be evaluated accurately, it is very valuable for efficient compressor choices.

Since this study aimed at analysing optimum design for specific conditions, the investigation can be propagated to heat pumps which works on various ranges. This would lead to a comprehensive model that could be potentially applied in a real-life setting. All of this is only feasible and practical if large advancements in electricity production is accomplished especially through more renewable energy sources as well as large-scale energy storage.

7 Acknowledgements

The authors of this paper would like to express their appreciation towards Jian Song and Andreas Olympios, members of the CEP Laboratory, for their guidance and comprehensive support throughout the project.

8 References

---

[1] Energy Systems Catapult. (n.d.). *A Guide to Decarbonisation of Heat*. [online] Available at: https://es.catapult.org.uk/guide/decarbonisation-heat/.

[2] Cole, L. (2021) *How to cut carbon out of your heating*. [Online]. 2021. Bbc.com. Available from: https://www.bbc.com/future/article/20201116-climate-change-how-to-cut-the-carbon-emissions-from-heating.

[3] EDF. (n.d.). *Air Source Heat Pumps: A Complete Guide*. [online] Available at: https://www.edfenergy.com/heating/advice/air-source-heat-pump-guide.

[4] Markets and Markets. (n.d.). *Heat Pump Market Size, Share, Growth, Industry Report - 2023*. [online] Available at: https://www.marketsandmarkets.com/Market-Reports/heat-pump-market-153294991.html.

[5] Markets and Markets. (n.d.). *Heat Pump Market Size, Share, Growth, Industry Report - 2023*. [online] Available at: https://www.marketsandmarkets.com/Market-Reports/heat-pump-market-153294991.html.

[6] Astolfi M. Techno-economic optimization of low temperature CSP systems based on ORC with screw expanders. Energy Procedia 2015;69:1100‑12.

[7] Smarterhouse.org. (2016). *Types of Heating Systems | Smarter House*. [online] Available at: https://smarterhouse.org/heating-systems/types-heating-systems.

[8] Energy Saving Trust. (n.d.). *In-depth guide to heat pumps*. [online] Available at: https://energysavingtrust.org.uk/advice/in-depth-guide-to-heat-pumps/.

[9] Hindsgaul, Claus & Hulgaard, Tore & Houbak, Niels. (2018). Biomass and Waste sections in Technology Data.

[10] Bellos, E. and Tzivanidis, C. (2019). Multi-objective optimization of a solar assisted heat pump-driven by hybrid PV. *Applied Thermal Engineering*, [online] 149, pp.528–535. Available at: https://www.sciencedirect.com/science/article/abs/pii/S1359431118322300

[11] Ca.gov. (2018). *High-GWP Refrigerants | California Air Resources Board*. [online] Available at: https://ww2.arb.ca.gov/resources/documents/high-gwp-refrigerants.

[12] TamdemirS. and KilicarslanA. (2014). Thermodynamic analysis of a heat pump for different refrigerants. *Hittite Journal of Science and Engineering*, [online] 1(1), pp.27–36. Available at: https://dergipark.org.tr/en/pub/hjse/issue/59673/860067.

[13] Energy, Exergy, and Environmental (3E) Analysis of Hydrocarbons as Low GWP Alternatives to R134a in Vapor Compression Refrigeration Configurations

[14] Stewart, M. (2019). *11 - Rotary compressors*. [online] ScienceDirect. Available at: https://www.sciencedirect.com/science/article/pii/B9780128098950000119.

[15] Ushimaru, K. (1990). *Japanese and American competition in the development of scroll compressors and its impact on the American air conditioning industry*. [online] www.osti.gov. Available at: https://www.osti.gov/servlets/purl/6952508.

[16] Butrymowicz, D., Baj, P., Śmierciew, K., 2014, Cooling technique, PWN, Warszawa, in Polish.

[17] Ash Air. (n.d.). *5 Benefits of a Reciprocating (Piston) Compressor*. [online] Available at: https://www.ashair.co.nz/blog/benefits-of-a-reciprocating-compressor/

[18] Butrymowicz, D., Baj, P., Śmierciew, K., 2014, Cooling technique, PWN, Warszawa, in Polish

[19] www.bitzer.de. (n.d.). *BITZER Software*. [online] Available at: https://www.bitzer.de/websoftware/.

[20] Area Cooling Solutions. (n.d.). *Industrial compressors*. [online] Available at: https://areacooling.com/c/compressors/.

[21] Olympios, A. V., Pantaleo, A. M., Sapin, P. & Markides, C. N. (2020) On the value of combined heat and power (CHP) systems and heat pumps in centralised and distributed heating systems: Lessons from multi-fidelity modelling approaches. Applied Energy. 274 10.1016/j.apenergy.2020.115261.

[22] Olympios, A. V., Pantaleo, A. M., Sapin, P. & Markides, C. N. (2020) On the value of combined heat and power (CHP) systems and heat pumps in centralised and distributed heating systems: Lessons from multi-fidelity modelling approaches. Applied Energy. 274 10.1016/j.apenergy.2020.115261.

[23] Olympios, A. V., Pantaleo, A. M., Sapin, P. & Markides, C. N. (2020) On the value of combined heat and power (CHP) systems and heat pumps in centralised and distributed heating systems: Lessons from multi-fidelity modelling approaches. Applied Energy. 274 10.1016/j.apenergy.2020.115261.

[24] Astolfi M. Techno-economic optimization of low temperature CSP systems based on ORC with screw expanders. Energy Procedia 2015;69:1100‑12.

[25] National Fire Protection Association. Standard system for the identification of the hazards of materials for emergency response; 2017.

[26] Van Kenhove E, De Vlieger P, Laverge J, Janssens A. Towards energy efficient and healthy buildings: trade-off between Legionella pneumophila infection risk and energy efficiency of domestic hot water systems. In: 12th REHVA world congress, Aalborg, Denmark; 2016.

[27] CEN (1994) EN 1264: Floor Heating — Systems and Components. European Committee for Standardization

Solar Combined Cooling, Heating, and Power Systems Based on Spectral Splitting PV-Thermal Collectors for the Food Processing Industry

Alice Mokrousov* and Tom Newnham†

Department of Chemical Engineering, Imperial College London, London SW7 2AZ

December 16, 2021

Abstract

In this study a methodology is developed to model the energy usage in a food processing factory, and then apply novel Perovskite solar cell-photo voltaic thermal (PVSC-PVT) collectors intended to satisfy some, if not all, of the energy demands. The energy demands consist of electricity, high temperature heating, low temperature heating, and cooling provided by a single effect absorption cooling system with cooling energy provided by hot oil. The facility investigated is a theoretical chocolate factory based in Argentina producing 12200 tonnes/yr of chocolate. It is found that on the day simulated a total of 43.7% of the total energy required can be satisfied by incorporating a network of 200 PVSC-PVT collectors. This consists of 63.9%, 62.8%, and 4.2% of cooling, heating, and electric demands being satisfied, respectively. It is calculated that carbon emissions and costs are reduced by 21.1% and 9.3% respectively. Clearly these collectors provide large environmental and economic incentive and this methodology can be applied to many specific processes in the food industry. It is suggested that further research can be conducted surrounding physical lab and pilot scale instances of the collectors, to corroborate results with simulation data, as well as expand the scope of the model to determine yearly, and lifetime, benefits. A further avenue for investigation consists of a hybrid system where both PV and PVSC-PVT are used, to satisfy a much larger proportion of the electricity demand without majorly impacting the other two energy streams.

Nomenclature

Abbreviations

COP	Coefficient of performance
HH	High temperature heating
LH	Low temperature heating
PV	Photo voltaic
PVSC	Perovskite solar cell
PVT	Photo voltaic-thermal
SS	Spectral splitting

Symbols

$\bar{T}_i$	Mean temperature of fluid i in collector
$\dot{m}_i$	Mass flow rate of i
η_i	Collector efficiency for channel i
COP_i	Coefficient of performance for exchange i
G	Solar irradiance
$Q_{C,DEM}$	Total cooling demand
$Q_{H,DEM}$	Total heating demand
Q_i	Energy for i provided to process by solar system
T_a	Ambient temperature
T_{C_n}	Temperature out of cooling stage n
T_{H_n}	Temperature out of heating stage n
$T_{i,j}$	Temperature of fluid i at position j, relative to collector
$c_{p,i}$	Specific heat capacity of i
TR_i	Reduced temperature in channel i

---

[*] alice.mokrousov18@imperial.ac.uk

[†] tom.newnham18@imperial.ac.uk

1 Introduction

1.1 Motivation

Food production is an essential industry which currently accounts for over a third of the total greenhouse gas emissions worldwide, producing around 17.3 billion tonnes $CO_{2,e}$ annually [1]. In order to move towards a cleaner environment it is clear that this number needs to reduce drastically. Industrial scale food processing plants can have a large energy demand, estimated to be between 10 and 15MJ/kg product [2], including energy considerations from both the electricity and fuel demands. Currently around the world industrial electricity use indirectly leads to greenhouse gas emissions, with 34% of final energy consumption being electricity [3] yet 40% of energy use related $CO_{2,e}$ emissions coming from the production of the electricity [4]. Food processing consumes both thermal energy (through fired heaters/electrically driven heaters and coolers) and electrical energy for mechanical processes such as mixing and transporting along a production line. According to Ladha-Sabur, Bakalis, Fryer, and Lopez-Quiroga remaining (and hence majority) of energy demand in the context of food processing is satisfied by fuel usage [2]. This makes conventional methods of reducing energy related emissions such as implementing photo voltaic solar cells, hydro-electric power production, and wind power production less desirable. Because of this, alternative methods that target a reduction of both grid electricity demand and fossil fuel usage have to be found.

1.2 Hybrid solar collectors

Utilising solar energy is no new concept, and recently huge strides have been made in this field including novel methods to increase efficiency using spectral splitting (SS) in hybrid photo voltaic-thermal (PVT) collectors [5]. This approach involves splitting the incident wavelengths of light in order to improve both electrical and thermal efficiency, providing a source of electricity and thermal energy. Spectral splitting technology works by separating incoming sunlight into higher and lower frequency bands, which are then absorbed, transferring energy into different parts of the collector. The higher frequency band being used to generate electrical power and the lower band being used to generate thermal energy. In the present study this SS is performed by utilising special semi-transparent cells, where the higher frequency photons are absorbed by the top PV layer and the other photons are allowed to pass through to the thermal energy generation channel. This allows for more efficient conversion of energy, as there is no longer a constraint of operating at a single temperature. Since electric power generation is most efficient at lower temperatures, there is an additional layer of flowing air in between the two channels which collects excess heat, creating a channel of its own. The resulting three energy channels can then be utilized for appropriate use. Figure 1 shows a novel approach which can provide electricity along with both high and low temperature heating demands using oil and air respectively.

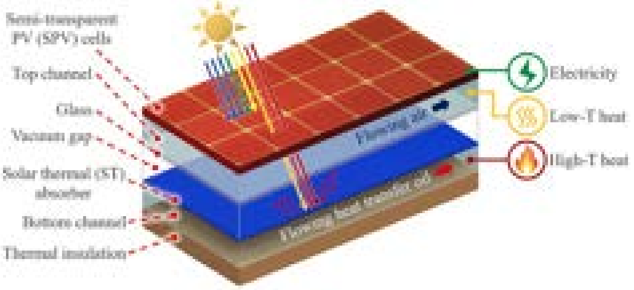

Figure 1: Schematic of a PVSC-PVT solar collector taken from Huang and Markides [5]. Semi-transparent solar cells on top, air channel in the middle, oil channel at the bottom.

1.3 Application to food production

Running multiple instances of this type of collector could help satisfy demands for energy in food processes, as many food production processes require close temperature control at various levels. The hot oil is useful for providing energy for both refrigeration and various cooking processes, with the hot air being used to either carefully dry moisture out of a process stream or carefully bring a process temperature up or down. The present study focuses specifically on the application of these collectors to the manufacture of chocolate. This was chosen due to various temperatures stages being required for tempering [6]. Tempering is crucial in the manufacturing process and ensures a quality 'glassy' finish to the surface of the bar and ensures the final chocolate bar doesn't melt whilst kept in proper storage. [7]. Cacao butter in chocolate can form six different types of stable crystals depending on the temperature at which it solidifies, and it is desired that on at least the surface level the crystals formed are type V [7]. First the chocolate mixture is brought up to a temperature such that all crystals are melted and then it is slowly, and precisely, cooled forming type IV and V crystals before the temperature is raised which destroys the type IV crystals leaving only type V in the final cooling. In the present study the collector in figure 1 is considered for providing the thermal energy for this tempering process, utilising the various levels of heating (and cooling via absorption cooling) available.

1.4 Absorption Cooling

Absorption cooling technology is applied in a heat-activated cooling system based on a solution absorption process. For this investigation, the absorption cooler was modelled after the Yazaki SINGLE-EFFECT absorption chiller [8] which uses a solution of lithium bromide and water as the working fluid. Water acts as a refrigerant whilst lithium bromide is the absorbent. The absorption cycle is energized by the SYLTHERM 800 Heat Transfer Fluid [9] which acts as the heating medium from the PVT collector heat source. The cooling cycle is summarised by figure 2.

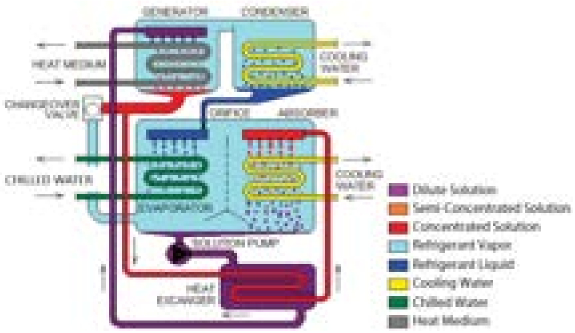

Figure 2: Yazaki SINGLE EFFECT chiller flowsheet. Taken from MAYA [8]. Heat medium (top left) is hot water, which is to be heated by the Syltherm 800 from the collector

Within the generator, as the heating medium inlet temperature exceeds a threshold value, the solution pump feeds in dilute lithium bromide solution. As the solution boils on the surface of the generator tubing bundle, refrigerant vapour is released. The vapour then rises up to the condenser, making the solution more concentrated. The concentrated solution then drops into the generator sump where its is drained down through a heat exchanger before entering the absorber section.

Inside the condenser, the refrigerant vapour is condensed on the surface of the cooling coil. The resulting latent heat is removed by the cooling water into a cooling tower. Refrigerant liquid accumulates in the condenser sump, eventually passing through an orifice that leads to the evaporator.

Within the evaporator, the refrigerant liquid is exposed to a vacuum. As it flows over the surface of the evaporator coil, it boils into a vapour, which results in heat being removed from the chilled water circuit. The recirculating chilled water cools to the selected set temperature, after which the refrigerant vapour is attracted to the absorber.

The absorber is also operated under a vacuum, which is maintained by the affinity of the concentrated solution from the generator to the refrigerant vapour formed in the evaporator. The refrigerant vapour is absorbed by the concentrated lithium bromide solution. Cooling water removes the heat of condensation and dilution into a cooling tower. The resulting dilute solution is then heated by a heat exchanger and returned back to the generator. The cycle is then repeated.

2 Methodology

Multiple SSPVT collectors, modelled by Huang and Markides [5], were implemented on the top of a theoretical chocolate manufacturing facility in Argentina. The outputs of the model, with inputs being environmental conditions, were then analysed to produce values of heating, cooling and electricity that could be covered. A schematic for the complete system is depicted in figure 3.

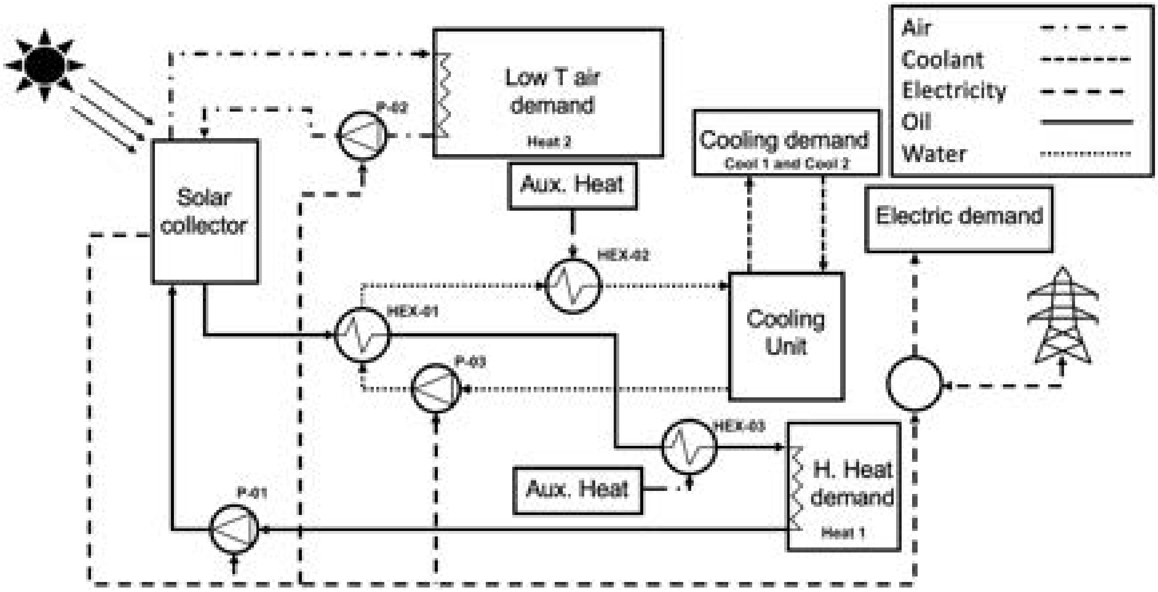

Figure 3: Solar system process flow diagram. Heat 1 is 'H. Heat demand'. Heat 2 is 'Low T air demand', energy for Cool 1 and Cool 2 is provided by HEX-01.

2.1 Environmental Conditions

The percentage of the energy demand that can be met is extremely dependent on certain environmental conditions, namely the ambient temperature and the solar irradiance. Hourly measurements for these data were taken from the Europeans Commission's Joint Research Centre [10] with coordinates 31°04'58.8"S 58°56'49.2"W. The data used was taken from the day with greatest average solar irradiance, the trend is shown by figure 5. It follows a parabolic shape, the maximum at hour 17.

2.2 Energy Demands

The theoretical plant in Argentina was assumed to have a production rate of 12200 tonnes$_{choc}$/yr (1kg/s for 261 days at 13 hours per day), electricity demand data was taken from Wojdalski et al. [11] at the rate of 184.1kWh/Mg$_{choc}$, assumed constant throughout the year.

The thermal energy demands considered were associated with tempering, the tempering process, with specific temperatures, is shown in figure 4.

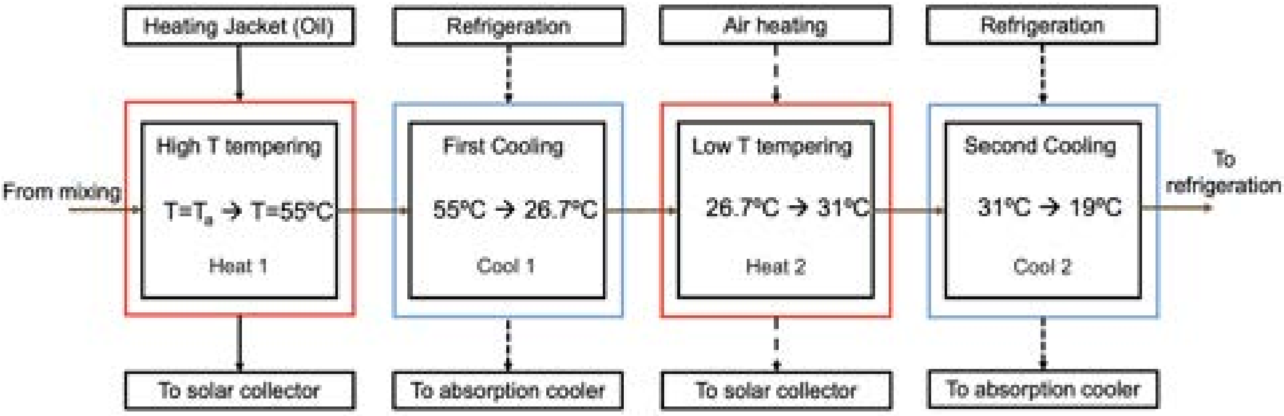

Figure 4: Block diagram of tempering process. From left to right Heat 1, Cool 1, Heat 2, Cool 2. Heat 1 energised using oil, Heat 2 energised with air. Cool 1 and 2 satisfied by absorption cooler.

The heating and cooling demands were calculated using simple heat transfer equations as follows.

2.2.1 Cooling Demand

The chocolate must have its temperature lowered twice, the total cooling energy demand is calculated using equation 1

$$Q_{C,DEM} = \dot{m}_{choc}c_{p,choc}(T_{H_1} - T_{C_1} + T_{H_2} - T_{C_2}) \tag{1}$$

This cooling demand is to be satisfied by using the heated oil to drive the absorption cooling cycle mentioned in section 1.4. At any time interval where the solar collector is not able to provide the required energy an auxiliary heater is used to meet the cooling demand. The temperatures of tempering are fixed due to the process, however the mass flow of chocolate changes and as such the cooling demand is a function of $\dot{m}_{choc}$ only.

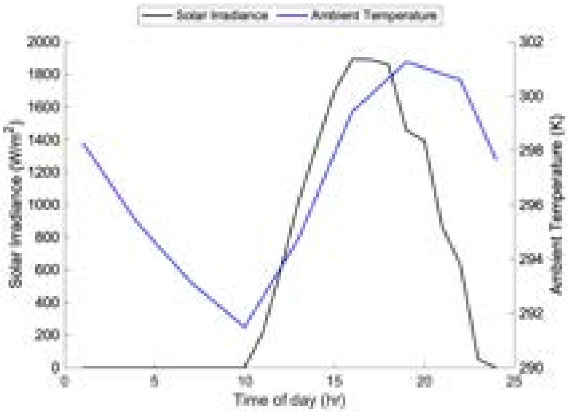

Figure 5: Environmental conditions, taken from the European commission [10]. Left axis solar irradiance, right axis ambient temperature. Plotted hourly

2.2.2 Heating Demand

As above, the chocolate has to be heated twice during the process. This is done by using both the heated air and oil outputs from the collectors. The first heating (T_a to 55ºC) is completed by running the hot oil (which has already exchanged some energy with water for cooling) through a heating jacket surrounding the chocolate flow. This oil is then pumped back through the solar collector to be used again.

The second heating utilises the hot air from the top channel of the solar collector and is counter-currently fed over the chocolate flow, slowly bringing it up to the desired temperature of 31ºC. Similar to before, these demands are again a function of $\dot{m}_{choc}$, however the heating demand is also a function of the ambient temperature, T_a. The total heating demand is given by equation 2. LH is considered as the energy associated with Heat 2 (T_{C_1} to T_{H_2}), with HH being the energy associated with Heat 1 (T_a to T_{H_1}).

$$Q_{H,DEM} = \dot{m}_{choc}c_{p,choc}(T_{H_1} - T_a + T_{H_2} - T_{C_1}) \tag{2}$$

Given the ambient temperature from [10] and a chocolate production rate of 1kg/s (while the factory is open) the energy demands are demonstrated by figure 6

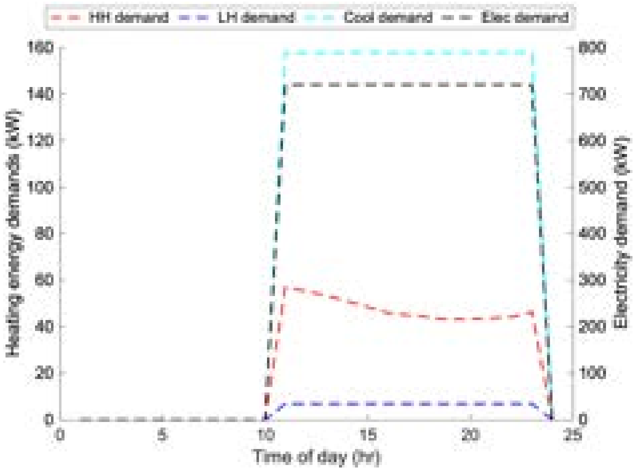

Figure 6: Energy demand for each energy type throughout the day based on environmental conditions. Left axis heating power, right axis electrical power. Plotted hourly

2.3 Modelling the system

A MATLAB model of figure 3 was created to calculate the percentages of each type of demand that was covered, and hence the percentage reductions in cost and $CO_{2,e}$ emitted.

2.3.1 Process calculations

The model calculated efficiencies for the energy transferred to electricity, oil and air by iterating until the equations 3 and 4 were true.

$$\dot{m}_{oil}c_{p,oil}[T_{oil,out} - T_{oil,in}] = \eta_{oil}(\bar{T}_{oil}, \bar{T}_{air}, G)G \quad (3)$$

$$\dot{m}_{air}c_{p,air}[T_{air,out} - T_{air,in}] = \eta_{air}(\bar{T}_{air}, \bar{T}_{oil}, G)G \quad (4)$$

Efficiencies of the collector are dependent on the average reduced temperatures $TR = (\bar{T} - T_a)/G$ and Huang and Markides [5] produced the efficiency maps in figure 7. The mass flow rates of air and oil were determined by adjusting the flow rate until the upper limit of each energy coverage each collector could satisfy had been reached.

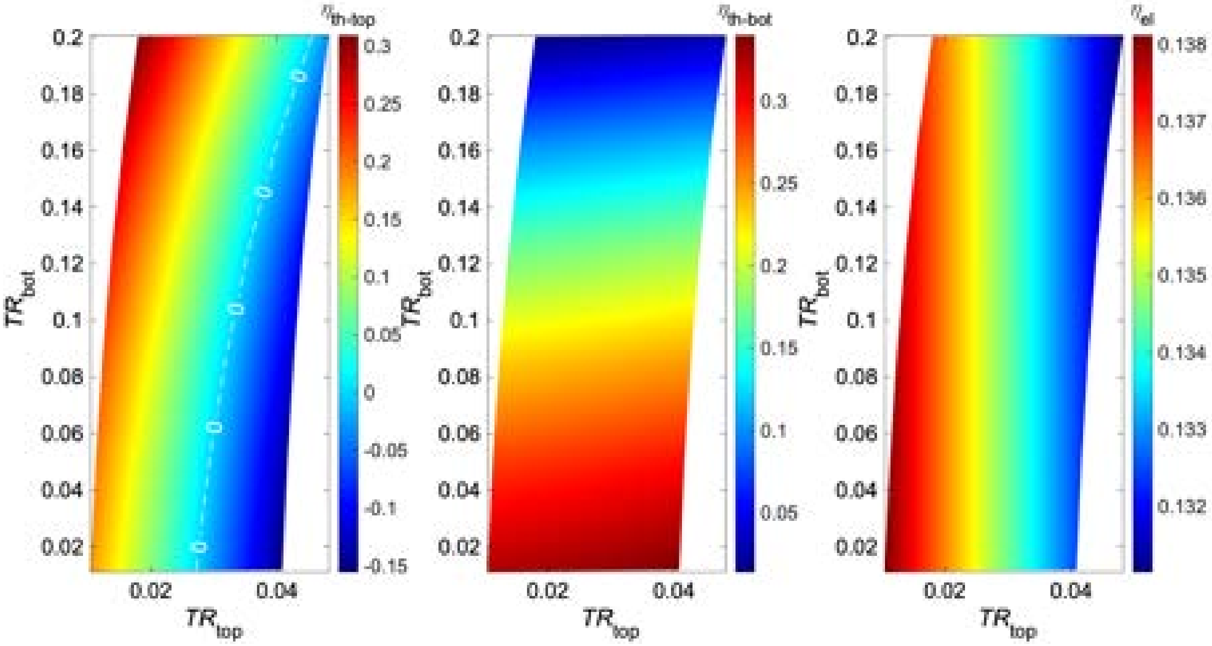

Figure 7: Performance maps of the PVSC-SSPVT collector. Left: Thermal efficiency of the top channel, Centre: thermal efficiency of the bottom channel, and Right: electrical efficiency; here $TR_{top} = \frac{\bar{T}_{top}-T_a}{G}$, $TR_{bot} = \frac{\bar{T}_{bot}-T_a}{G}$. [5]

Once efficiencies, and hence collector output temperatures had been determined, the energy balance calculations were performed to quantify the proportion of the demands that could be covered. These all took the form of equation 5 where COP_i represented individual heat exchange efficiencies, which were estimated for each specific case using COMSOL for the heating and a COP value for the absorption chillers [8]. The MAYA units chosen were the SC 5 cooling units due to their cooling capacity of 17.6kW with a heat input of 25kW. Eight of the units ran at the nominal capacity with the final one running at 96% of this capacity, within the operational bounds and yielding the same COP.

$$Q_i = COP_i \dot{m}_i c_{p,i} \Delta T_i \quad (5)$$

The return temperatures of the oil and air were calculated using equation 5, with $Q_{Oil/air} = Q_i/COP_i$. The process is assumed to reach a steady state in each hour and as such the return temperatures from hour $t-1$ are assumed to be the inlet temperatures for hour t. Once the amount of usable energy had been calculated these data were compared to the demands to give the required amount of auxiliary heating/electricity per hour.

2.3.2 Economical and environmental factors

Using average $CO_{2,e}$ and cost values for gas and electricity the cost and $CO_{2,e}$ reduction in each hour could be determined. These were summed to give a daily percentage reduction.

A minimum payback time was also estimated, this utilised data from Herrando et al [12], this case study focused on collectors already established and hence less novel than those detailed in the present study and thus are estimated to be less expensive than commercial versions of the semi-transparent solar collectors discussed here.

2.3.3 Key variables and model parameters

The model required certain fixed inputs, these, along with fixed process parameters, are listed in table 1.

Table 1: Key variables and model parameters used for simulations, with units

Parameter/Variable	Value	Unit	Description & reference
$c_{p,oil}$	1.9	kJ/mol.K	Specific heat capacity of oil [9]
$c_{p,air}$	1	kJ/kg.K	Specific heat capacity of air
$c_{p,choc}$	1.6	kJ/kg.K	Specific heat capacity of chocolate [13]
$c_{p,w}$	4.18	kJ/kg.K	Specific heat capacity of water
$\Delta h_{lat,choc}$	46	kJ/kg	Chocolate specific latent heat of fusion [13]
$T_{Heat,1}$	328.15	K	Process temperature downstream of heater 1
$T_{Heat,2}$	304.15	K	Process temperature downstream of heater 2
$T_{Cool,1}$	299.85	K	Process temperature downstream of cooler 1
$T_{Cool,2}$	292.15	K	Process temperature downstream of cooler 2
$T_{Absorption,start}$	361.15	K	Water temperature required to start absorption cycle [8]
$T_{Absorption,end}$	356.15	K	Water temperature at outlet of absorption cycle [8]
ΔT_{HEX}	5	K	Minimum temperature difference in HEXs
COP	0.7	-	COP for absorption cooling cycle [8]
n_{Cool_units}	9	-	Number of parallel MAYA SC 5 cooling units
$n_{Collector\_modules}$	200	-	Number of 1x1m solar collectors installed
$\dot{m}_{choc}$	1	kg/s	Chocolate production rate while open
$\dot{m}_{oil,per\_collector}$	0.0028	kg/s	Oil flowrate per collector
$\dot{m}_{air,per\_collector}$	0.001	kg/s	Air flowrate per collector
$Cost_{gas}$	0.009	£/kWh	Local cost per unit energy for natural gas [11]
$Cost_{elec}$	0.029	£/kWh	Local cost per unit energy for electricity [11]
$Cost_{Collector}$	449.8	£/m$^2_{\text{installed}}$	Cost per m^2 of installed collector [12]
$CO_{2,gas}$	0.227	kg/kWh	Local CO_2 emitted per unit energy for gas [14]
$CO_{2,elec}$	0.17	kg/kWh	Local CO_2 emitted per unit energy for electricity [15]
COP_{HH}	0.855	-	COP of high heating exchange
COP_{LH}	0.371	-	COP of air heating exchange

3 Results and discussion

3.1 Collector performance

The heat transfer fluid temperatures coming out of the collector systems have been plotted in figure 8. Clearly they follow the same trend as the solar irradiance, as expected, with greater energy incident leading to higher outlet temperatures. The high outlet temperatures have a negative influence on the electricity production efficiency, as is expected for a PV panel [16], this in part leads to the result that a lower proportion of the electric demand being covered as discussed later.

The average efficiency throughout the day of each collector channel is shown by table 2. The efficiencies of the high temperature and electricity streams are at the high end of the range determined by Huang and Markides. The result of this is that the low temperature stream has a very low efficiency so very little of the sun's energy is utilised to heat the air. This helps to keep the air temperature stream slightly cooler such that the electrical efficiency is large enough that a non negligible amount of the demand is covered.

The total percentage of the sun's energy converted to useful heat/electricity in the collector is 43.9%, compared to the (electric) efficiency of 20-25% in the popular PV-Si solar panels [17]. This is a vast improvement and implies great application potential for processes with multiple medium to high temperature phases.

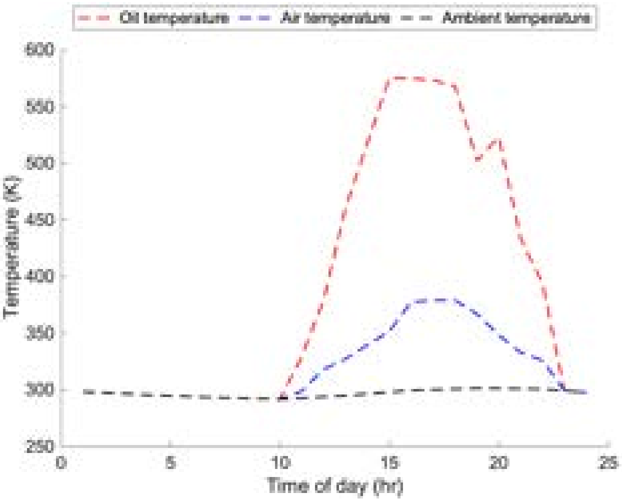

Figure 8: Temperature profiles through the day. Plotted hourly

Table 2: Collector average efficiencies

Channel	Avg. efficiency
Air channel	3.27%
Oil channel	27.1%
Electricity channel	13.5%

3.2 Analysis on demands satisfied

For each hour throughout the day, the amount of each type of energy demand satisfied was calculated. These have been plotted in figures 9,10, and 11. As the day begins there is no potential to cover any demand, and also no demands to cover as the factory is closed. When the sun rises and $G(t)$ increases, the energy is absorbed and hence some of the factory energy demands are covered. At hour 11 there is enough irradiance that the air stream can meet some of the demand but the oil temperature is only raised to 329K which is not above the threshold value for the counter current heat exchange of $T_{Heat,1} + \Delta T$ =333.15K and as such none of the cooling, or high heat demand is met. The next hour the temperature has exceeded this value and has reached a value above the threshold at which some cooling can be covered. The temperature of the oil is not great enough that the entire cooling demand is met and therefore the high heat demand met is equal to equation 6 which is a constant. This is, therefore, the same coverage achieved in hours 13, 19, 21 and 22.

$$m_{oil}\dot{c}_{P,oil}(T_{Absorption,start} + \Delta T - T_{Heat,1} + \Delta T) \quad (6)$$

When the oil outlet temperature from the collector is greater than 449.2K the entire cooling demand is met. When the outlet temperature is higher than this there is an excess energy which is fed downstream and this allows a greater proportion of the heating demand to be met. This demand is fulfilled for hours 15 to 18 inclusive.

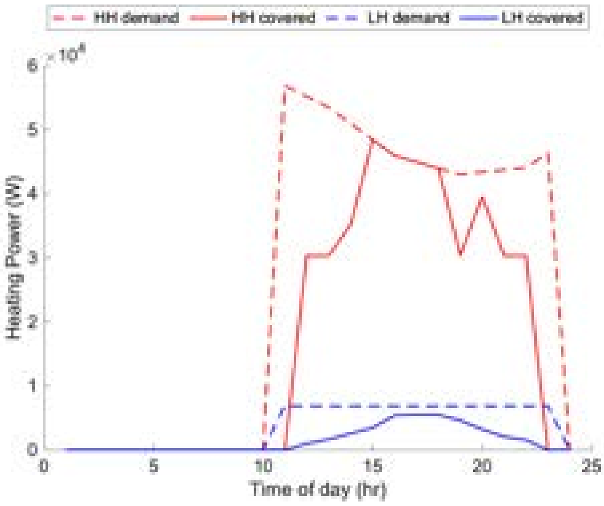

Figure 9: Heating covered compared to the demand. Plotted hourly time

The air stream is not able to fully meet the demand at any point in the day, this is due to the heat exchange between the air and chocolate having a low efficiency (37%) as well as a low efficiency in the air channel of the solar collector. This leads to a maximum of 80% being covered for the peak hours of sunlight during the day, before the coverage declines as the sun recedes.

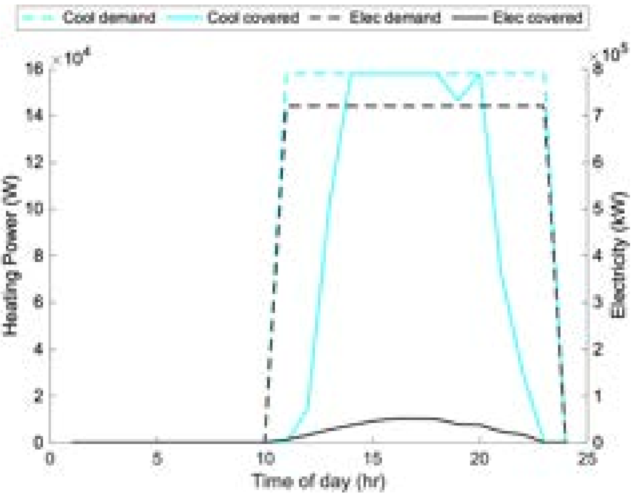

Figure 10: Energy demand and amount covered. Left axis: Cooling covered compared to the demand. Right axis: Electricity covered compared to the demand. Plotted hourly

The cooling coverage is met for much of the middle of the day, at hour 19 $G(t)$ has started to dip and the cooling demand is not fully met, however the carry over energy from the process is large enough that the next hour full cooling is satisfied again by the collectors alone. This means that over the whole day 63.9% of the cooling demand is met. The electricity coverage is very low in comparison to the other demands, with a maximum coverage of 7% in the peak hours. This coverage is so low due to the large electrical demand of this process as a whole, and the low electrical efficiency of the PV collector.

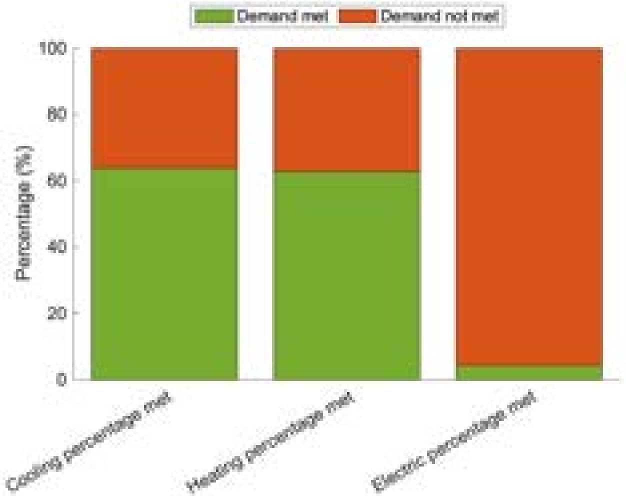

Figure 11: Total proportion of demand met in the day for Cooling (left) Heating (centre) Electric (right)

These data give the result that a total of 43.7% of the combined tempering and electric energy demands for the day are met by the solar system. Covering almost half of the process energy demands further indicates that these semi transparent solar cells could prove very promising in real world applications where multiple differing energy demands are to be satisfied. As the technology is developed it is expected that this percentage will only increase, resulting in greater benefits for the same costs.

3.3 Quantifying the benefits

3.3.1 Environmental benefits

With the solar energy providing 43.7% of the considered energy demands there is a drastic reduction in the negative environmental footprint of the process. Conventionally the process produces upwards of 160kg/hr of $CO_{2,e}$ and with the network of 200 solar collectors and 9 absorption units this is reduced to less than 115kg/hr in the hours of maximum sunlight. Over the entire day the emissions are reduced by 21.1%. This is clearly a significant reduction in carbon footprint, however it is not the only measure required to be put in place to offset or eliminate the carbon footprint of a large scale food production plant.

It is considered this is the maximum reduction that feasibly could be achieved, due to it being a simulation ran for the day with maximum solar irradiance. When running the model for the average day a reduction of 4.2% was found. This is due to the irradiance and ambient temperature being much lower in the colder months leading to less power available and the heating demand being larger. Using the summer value the amount of $CO_{2,e}$ removed yearly is calculated to be 143 tonnes/yr. Accounting for the lower irradiance figures over the year the minimum predicted yearly carbon reduction is 30 tonnes/yr.

3.3.2 Monetary benefits

Another motivation behind implementing combined solar systems is that they can lead to a cost reduction. In the summer months this reduction is a significant 10%, with winter months accounted for this drops to around 3%. The cost in this instance is reduced due to less resources having to be purchased. Naturally this makes the idea of retro-fitting a factory less appealing. The pay back time, calculated using the average yearly value for cost reduction, is 38.1 years before the costs associated with purchase and installation of collectors are offset. If the summer value is used this reduces to 8.97 years. If the factory were placed even closer to the equator, hence seasonal effects would be minimised, the pay back time would decrease significantly from 38.1 years. This is suggested as a route for further investigation.

4 Conclusions

In this study a chocolate production process implementing 200 novel semi-transparent solar cell collectors was modeled and simulated over a single day in the summer months in northern Argentina. It was found that on this day a total of 43.7% of all energy demands could be covered by renewable solar energy, this reduced the daily carbon footprint by 21.1% and costs by 10%.

An average day was also simulated to give a more realistic scenario, this resulted in total demand coverage of 11%, emission reduction of 4.2% and a cost reduction of 2.2%.

In both scenarios the proportion of electricity demand covered was much less than the cooling and heating. This is because much of this particular process is electrically driven, with natural gas only being required for the tempering and maintaining environmental conditioning for workers in the factory. Also a factor is the lower electrical efficiency of the PVSC-SSPVT collector compared to conventional PV collectors. The low electric coverage is the main drawback of this system in the current models, implementing multiple types of collectors such as a 50:50 split of PVSC-SSPVT to PV could allow further demand coverage.

For the system considered under the present study, in the summer months it was found that the payback time was as low as 8.97 years, this is below the lifetime of a PV solar collector (25 years) [18], considering the environmental data throughout the year this value increased to close to 40 years, well over the expected lifetime for the panels meaning retrofitting an existing location would result in a loss of money overall.

5 Recommendation and Outlook

Judging from the findings of this study, it is clear that hybrid PVT collectors create both monetary and environmental incentives as sustainable forms of renewable energy, and have potential to partially offset electric and heating demand for confectionery and other food processing manufacturers. To further verify these conclusions, it is vital to repeat the study for a wider range of scenarios and conditions described below.

5.1 Location and Climate

To more accurately record average solar energy captured by the PVT collectors, it is important to account for a variation in climate. Given that the weather data for our study only accounted for a summer climate in Argentina, further studies can be repeated using data from Argentina's winter months. Similarly, the study can be repeated using weather data from countries with different climates. This would allow for comparison of results, which could then be used confirm the effectiveness of the use of PVT panels in different weather conditions.

5.2 Manufacture Simulation

Though it was concluded that, energetically, some manufacturing steps could be partially powered using energy derived from PVT panels, practical results derived from more detailed manufacture simulations would yield more accurate values from which better conclusions can be drawn. Precisely, the heat exchange between the chocolate mixture and the heating/cooling mediums can be better simulated by accounting for factors such as conveyor shape and size, heating/cooling medium contact area and temperature distribution.

Secondly, substitutions for other steps within the manufacture process can be explored for heat substitution, as only the tempering process has been studied so far. Processes such as melting and storage also require a substantial amount of heating/cooling which PVT panels can provide.

5.2.1 Modelling other components

As this study has investigated a process assuming a single collector type and single commercial absorption cooling type, there is scope to investigate using other similar components to determine which are most effective. This model has treated these key components as black boxes, and thus can be easily replaced provided data can be found/simulated yielding an efficiency or COP factor. For the majority of commercial units this will be readily available, for novel devices these will however have to be calculated.

5.3 Other Processing and Manufacture

Similar heating/cooling requirements exist in many industrial food manufacturing processes which allows for expansion of PVT substitution into those industries. For example, milk powder production requires heating for pasteurisation and evaporation as well as refrigeration for storage. Other processes include confectionery, snacks and animal food manufacture.

Acknowledgments

The authors would like to thank Dr Gan Huang for his advice and assistance throughout the study, as well as the Clean Energy Processes Laboratory, Department of Chemical Engineering, Imperial College London.

References

[1] Krista Charles. Food production emissions make up more than a third of global total. new scientist. https://www.newscientist.com/article/2290068-food-production-emissions-make-up-more-than-a-third-of-global-total/, Sep 2021.

[2] Alia Ladha-Sabur, Serafim Bakalis, Peter J. Fryer, and Estefania Lopez-Quiroga. Mapping energy consumption in food manufacturing. https://www.sciencedirect.com/science/article/pii/S0924224417303394, 2019.

[3] IEA. World energy use, data and statistics. https://www.iea.org/data-and-statistics, 2021.

[4] World Nuclear Association. Carbon dioxide emissions from electricity. https://www.world-nuclear.org/information-library/energy-and-the-environment/carbon-dioxide-emissions-from-electricity.aspx, May 2021.

[5] Gan Huang and Christos N. Markides. Spectral-splitting hybrid pv-thermal (pv-t) solar collectors employing semi-transparent solar cells as optical filters. https://www.sciencedirect.com/science/article/pii/S0196890421009523, 2021.

[6] manufacturing.net. Temperature: Chocolate's secret ingredient. https://www.manufacturing.net/operations/article/13162755/temperature-chocolates-secret-ingredient, Aug 2018.

[7] Cacao Cacao Magazine. Tempering chocolate: Everything you need to know -. https://readcacao.com/eating-chocolate/the-ultimate-guide-to-tempering-chocolate-why-how-and-everything-you-need-to-know/, Sep 2020.

[8] MAYA. Water fired absorption chillers wcf series. https://maya-airconditioning.com/eng/pdf/WFC%20Series%20LD_001_EN.pdf, 2018.

[9] DOW Chemical Company. Syltherm 800 heat transfer fluid product technical data. https://www.npl.washington.edu/TRIMS/sites/sand.npl.washington.edu.TRIMS/files/manuals-documentation/syltherm-800-product-brochure.pdf, October 1997.

[10] European Comission Joint Research Centre. Photovoltaic geographical information system. https://re.jrc.ec.europa.eu/pvg_tools/en/#DR, Jan 2016.

[11] Janusz Wojdalski, Józef Grochowicz, Bogdan Dróżdż, Katarzyna Bartoszewska, Paulina Zdanowska, Adam Kupczyk, Adam Ekielski, Iwona Florczak, Aleksandra Hasny, and Grażyna Wójcik. Energy efficiency of a confectionery plant – case study. https://www.sciencedirect.com/science/article/pii/S0260877414003574, 2015.

[12] María Herrando, Antonio M. Pantaleo, Kai Wang, and Christos N. Markides. Solar combined cooling, heating and power systems based on hybrid pvt, pv or solar-thermal collectors for building applications. https://www.sciencedirect.com/science/article/abs/pii/S0960148119306561, May 2019.

[13] Stephen T. Beckett. Industrial chocolate manufacture and use. 667-668. https://onlinelibrary.wiley.com/doi/pdf/10.1002/9781444301588.oth1, 2009.

[14] Department for Environment Food & Rural Affairs. 2012 greenhouse gas conversion factors for company reporting. https://www.gov.uk/government/publications/2012-greenhouse-gas-conversion-factors-for-company-reporting, Oct 2013.

[15] Hannah Ritchie and Max Roser. Argentina: Energy country profile. https://ourworldindata.org/energy/country/argentina?country=~ARG, Nov 2020.

[16] Swapnil Dubey, Jatin Narotam Sarvaiya, and Bharath Seshadri. Temperature dependent photovoltaic (pv) efficiency and its effect on pv production in the world – a review. https://www.sciencedirect.com/science/article/pii/S1876610213000829, 2013. PV Asia Pacific Conference 2012.

[17] Fahhad H. Alharbi and Sabre Kais. Theoretical limits of photovoltaics efficiency and possible improvements by intuitive approaches learned from photosynthesis and quantum coherence. https://www.sciencedirect.com/science/article/pii/S136403211401048X, Dec 2014.

[18] Md. Shahariar Chowdhury, Kazi Sajedur Rahman, Tanjia Chowdhury, Narissara Nuthammachot, Kuaanan Techato, Md. Akhtaruzzaman, Sieh Kiong Tiong, Kamaruzzaman Sopian, and Nowshad Amin. An overview of solar photovoltaic panels' end-of-life material recycling. https://www.sciencedirect.com/science/article/pii/S2211467X19301245, 2020.

Investigating the Universality of Viscosity Prediction Models for Non-Newtonian Suspensions

Shyana Gopy and Raza Naqvi
Department of Chemical Engineering, Imperial College London, U.K.

Abstract

Non-Newtonian suspensions are widely used in today's society, from everyday yoghurts and shower gels to industrial drilling fluids, but they are as complex as they are versatile. Manipulating the viscometric properties of these solutions is vital for manufacturing and applicative purposes, hence highlighting the importance of accurate prediction models. The Einstein, Batchelor and Krieger-Dougherty models are well-known relations used to describe the relative viscosity of suspensions in Newtonian fluids, however based on our research, there are no studies modelling their effectiveness in non-Newtonian fluids. This study tests the agreement of these models with empirically obtained data for inherently non-Newtonian suspensions, as the latter are common base mediums in industrial applications. The shear-thinning behaviour of fluids Xanthan (polymer) and Sepiolite (clay) were investigated under varying volume fraction of dispersed glass Ballotini particles and various shear stresses in a serrated rheometer. The Krieger-Dougherty equation was effective in predicting the viscosity of suspensions in dilute Xanthan solutions, whilst the Batchelor equation showed little compatibility with the investigated suspensions. Meanwhile, Einstein's formula typically outperformed the other models at dilute particle concentrations. The nature of the non-Newtonian medium has a clear influence as the models were less effective at predicting relative viscosity in the Sepiolite suspensions. Trends observed in the clay agreed with the models over brief shear rate periods, though diverged greatly outside of these domains.

1. Introduction

Non-Newtonian fluids are ubiquitous in society. From medicines and foodstuffs to industrial substances such as cement and drilling fluid, they have an extensive and vast range of applications. Xanthan is a widely used non-Newtonian fluid in the upstream oil and gas industry, commonly used as a viscofier in flooding and drilling due to its pseudoplastic behaviour, high viscosity, and high resistance to shear-degradation [1]. As the drill tip shears through the ground, the viscosity of Xanthan decreases, thus the drill-tip requires less energy to rotate, and when the drill shearing ceases, the viscosity increases and prevents hole cave-ins.

Altering the viscometric properties of fluids through the addition of suspended particles is another common technique employed to achieve target product characteristics. For example, pharmaceutical particles are suspended in solution for child medicine to allow for easier consumption [2]. Knowledge on the behaviour of non-Newtonian fluids with suspended particles can be useful in product design and manufacturing for both household and industrial performance.

The Einstein equation provides a simple relationship associating the apparent viscosity of a Newtonain fluid (η) with the volume fraction (φ) of the suspended particles in that fluid. However, this relation is typically only valid for low volume fractions of the suspended particle, ($\varphi < 0.02$) [3]. The Batchelor equation is typically relevant for $\varphi < 0.20$ [4], whilst the Krieger-Dougherty equation (1) is effective up to the maximum packing fraction of suspended particles:

$$\eta_r = \frac{\eta}{\eta_{medium}} = \left(1 - \frac{\varphi}{\varphi_{max}}\right)^{-[\eta]\varphi_{max}} \qquad (1)$$

This relationship was derived on a semi-empirical basis and is highly applicable to predict the apparent viscosity of a solution with suspended particles given the viscosity of the underlying fluid medium (η_{medium}), the volume fraction of suspended particles (φ), the maximum packing fraction (φ_{max}) and the intrinsic viscosity of the particles ($[\eta]$).

The basis of this report is to determine whether the existing models are relevant to determine the viscosity of suspended-solid solutions where the base medium is a non-Newtonian rather than a Newtonian fluid. The papers used to derive these equations do not indicate whether the relationships would hold for non-Newtonian fluids, and it is unknown whether the hydrodynamic, structural, and thermodynamic interactions in the non-Newtonian base medium may impair the effectiveness of the relation [5][6]. Therefore, it is useful to investigate from an empirical standpoint whether the Einstein, Batchelor and Krieger-Dougherty relations are applicable to solutions with a non-Newtonian base medium.

2. Background

Newton's law of viscosity defines the relationship between the shear stress and shear rate for simple shear where the viscosity μ is the effective constant of proportionality as in equation (2). This relation is linear for Newtonian fluids. For non-Newtonian fluids, the shear rate is raised to the n^{th} power with a new constant of proportionality, k, to distinguish between Newtonian and non-Newtonian fluids. Equation (3) illustrates this 'power-law' model which approximates the Cross model [7]. The apparent viscosity is defined as the shear stress divided by shear rate as in (4).

$$\tau = \mu \dot{\gamma} = \mu \frac{du}{dy} \quad (2)$$

$$|\tau| = k \, |\dot{\gamma}|^n \quad (3)$$

$$\eta = \frac{|\tau|}{|\dot{\gamma}|} \quad (4)$$

Non-Newtonian fluids where $n < 1$ are pseudoplastic or shear-thinning fluids, whilst fluids with $n > 1$ are known as dilatant or shear-thickening fluids. The mechanism for non-Newtonian behaviour can be understood by acknowledging that the very act of deforming a material can cause a rearrangement of the material microstructure which results in flow decreases or increases with shear rate.

Considering how the viscosity of the fluid changes once particles are added to form suspensions, Einstein [8] derived a simple formula showing the viscosity of a liquid (η) as a function of the phase volume (φ) of the suspended particles:

$$\eta_r = \frac{\eta}{\eta_{medium}} = 1 + \frac{5}{2} \varphi \quad (5)$$

The key assumption to derive this equation is that the spherical particles are regarded as alone in infinite fluid, this typically limits the validity of the equation to $\varphi < 0.02$ [3]. All subsequent studies of dispersed suspensions essentially extend this equation so that the charge, particle shape and the hydrodynamic interactions that occur when one particle is within the locality of another are accounted for.

Work by Batchelor [3] exhibited an analytically derived relationship to consider higher order terms of φ to account for the hydrodynamical interactions between interacting hard spherical particles, producing equation (6) which is valid up to 20% phase volume fraction of the suspended particles. Equation (7) displays the more general form for suspensions of differing particles and geometries.

$$\eta_r = 1 + \frac{5}{2} \varphi + 6.2 \, \varphi^2 \quad (6)$$

$$\eta_r = 1 + \alpha \, \varphi + \beta \, \varphi^2 \quad (7)$$

To account for higher phase volumes of the suspended particles, the semi-empirical Krieger-Dougherty equation (8) [6] for monodisperse suspensions exhibits a relation between the viscosity and phase volume, based on two dimensionless parameters: the intrinsic viscosity [η] and the maximum packing fraction φ_{max}. Ball and Richmond [9] derived the same relation based on an averaging technique through a modification to equation (5):

$$\eta_r = \left(1 - \frac{\varphi}{\varphi_{max}}\right)^{-[\eta]\varphi_{max}} \quad (8)$$

The intrinsic viscosity [η] is based on particle shape and taken as $[\eta] = 2.5$ for hard spheres [10]. The maximum packing fraction φ_{max} is based on the concept that as particles are added to the base fluid, a solution will develop where there is a network of three-dimensional contact between the spheres throughout the system, therefore flow would be impossible, and the viscosity tends to infinite. The phase volume at which this occurs is represented by φ_{max}. The value of φ_{max} is typically reported between values of 0.52 and 0.74, where the φ_{max} value increases as the shear rate tends to infinite due to the solution particles orientating to a more efficient packing structure [11]. This relation is found to be an effective predictor of viscosity up to the maximum packing fraction for Newtonian fluids [5].

A gap in the literature is identified when considering the relevance of the existing models to inherently non-Newtonian fluids. The basis of this report is to determine whether the Einstein, Batchelor and Krieger-Dougherty equations are effective predictors of viscosity in suspended particle solutions where the base medium is non-Newtonian. Many polymers and all clays are shear-thinning non-Newtonian fluids; therefore, Xanthan and Sepiolite were selected to represent these two categories respectively. The Newtonian fluid glycerol was also investigated to serve as a basis medium to provide an objective evaluation of the agreement between experimental and model predicted values. These suspensions were exposed to a range of shear rates from 0.001s^{-1} to 1900s^{-1} - in a rheometer whilst varying the phase volume of the hard-shell spherical suspended particles glass Ballotini. This provided ample data to determine whether Xanthan with glass Ballotini followed model predictions whilst varying dispersed phase volumes at a low, medium, and high shear-rate. The permutations using the other materials served to corroborate the results obtained and verify that the conclusions achieved from Xanthan with glass Ballotini are not unique to that particular system.

3. Methods

To analyse the rheometric behaviour of the dispersed particles in non-Newtonian continuous phases, base mediums of 0.5%, 1% and 1.5% Xanthan by weight and 5% Sepiolite by weight were prepared. Appropriate masses of the suspended particles of glass Ballotini were added to achieve the desired phase volume of suspended particles. These solutions were subjected to a controlled stress rheometer to obtain their viscometric properties over the range of shear rates 0.001s^{-1} to 1900s^{-1}.

3.1 Materials

Xanthan is a long-chain polysaccharide molecule. Particles are short, rod shaped and relatively flexible in solution [13]. Powdered Xanthan gum was mixed into distilled water to form 0.5, 1.0 and 1.5 wt.% solutions. Commercial grade Xanthan from ALDRICH Chemistry with Lot # SLBN1080V sourced from Spain was used.

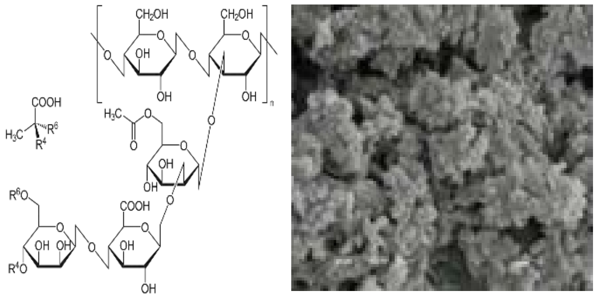

Figure 1: Structure of Xanthan. Left: molecular structure. Right: electron microscopy at 10,000x magnification [12]

Sepiolite is a shear-thinning clay with applications in pharmaceuticals and drilling [14], much like Xanthan. The Sepiolite ($Si_{12}O_{30}Mg_8(OH)_4(OH_2)_4 \cdot 8H_2O$) investigated in this study was used as a powder and dissolved in distilled water to form a 5 wt.% solution. The macroscopic structure of the Sepiolite is visualised as fibres immersed in aqueous solution, unlike typical clays that have a platy morphology [15]. Commercial grade Sepiolite from ALDRICH Chemistry with Lot # BCBP5247V sourced from Spain was used.

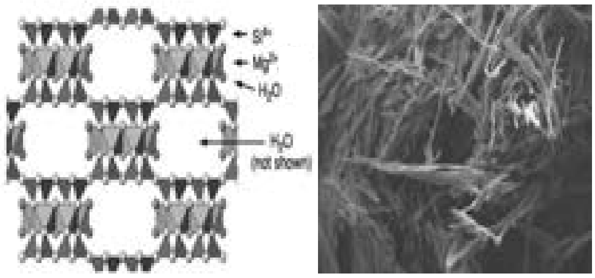

Figure 2: Structure of sepiolite. Left: molecular structure. From Dixon JB and Schulze DG (2002) Soil Mineralogy with Environmental Applications, pp. 1-35. With permission. Right: electron microscopy at 20,000x magnification [16]

Commercial spherical glass Ballotini particle with diameter 0.15mm to 0.25mm sourced from Jencons was used as the suspened particle in all solutions, with cat. # 136-002 and grade 5215 [17].

Glycerol is a Newtonian, colourless, odorless polyol compound. Glycerol prepared in situ at Imperial College London, Chemical Engineering Department with 99.5% purity was used.

3.2 Solution preparation

The Xanthan and Sepiolite base solutions were prepared in a similar fashion. An electronic balance ($m \pm 0.00005g$) was utilised to add the correct mass of solvent to the correct mass of distilled water. The IKA® EUROSTAR 60 overhead stirrer was used to mix the Xanthan powder into the water to prepare the base solution. The standard procedure followed involved submersing the rotor-head approximately 75% into the water volume and slowly increase the revolutions per minute (RPM) of the rotor to 330RPM. The Xanthan powder was gradually added over the course of 2 minutes to prevent clumping.

A magnetic stirrer was used for homogenisation of the Sepiolite solution. As with Xanthan, Solute clay powder was added to the lip of the water vortex and the solution left to stir for 24 hours or until the solution was absent of clumps and of uniform consistency.

3.3 Addition of spherical particles

From the base solutions of Xanthan, Sepiolite, and glycerol, 30ml samples were extracted to create suspended particle solutions. Volume fractions of suspended particles ranging from 5% to 45% were prepared. The appropriate masses of particles to add were computed based on the simple density relation in (9).

$$\rho \; (kg\; m^{-3}) = \frac{m\; (kg)}{V\; (m^3)} \qquad (9)$$

The IKA® overhead stirrer assisted in homogenising the suspended particle solutions to achieve uniform distributions of suspended particle throughout the viscous mediums.

Difficulties were encountered with volume fractions above 30%, 35% and 40% of glass Ballotini in glycerol, Sepiolite and Xanthan respectively. The glass Ballotini began sedimenting above these concentrations, thereby infringing on the requirement of homogenous solutions. Therefore, these results were excluded from analysis to maintain the integrity of the study.

3.4 Rheological measurement

The viscometric properties were obtained using a controlled stress rheometer. A Haake Mars Rheometer, equipped with a coaxial cylinder geometry CC33/PR/XL and serrated rotor were used for measurements. The serrated geometry for the rotor was selected to prevent wall-slip. Wall-slip occurs due to a concentration gradient developing between the wall and the suspension bulk leading to a lubrication layer at the wall surface [18][19].

The rheometric data was obtained at 25ºC ($T \pm 0.00001$℃) by increasing the shear rate (ascending ramp) and then decreasing the shear rate (descending ramp), over a period of 15s at each shear rate, using the step shear rate mode of the rheometer across the rheometer's maximum range of 0. 001s^{-1} to 1900s^{-1}. A total of 40 data points were collected for each ramp. Initially, repeats were carried out for all data sets for 1 wt. % Xanthan with glass Ballotini, the viscometric data were within 3 percentage points difference. For the other solvent-solute combinations, at least one repeat was carried out to confirm the 3% error range, otherwise a single set of results were acquired without repeats. The linear section of the log-log axis in apparent viscosity (η) against shear rate ($\dot{\gamma}$) was identified as the focal point of comparison to predicted results from the existing models discussed.

3.5 *Performance Metrics*

Two statistical measures are used to quantify the performance of the models at estimating true viscosity. R^2 is mainly used as an indicator of linearity, whilst the root mean square error (RMSE) is computed to evaluate the effectiveness of the models against experimental values. The RMSE is between the experimental and predicted values for relative viscosities across N number of samples using the following formula:

$$RMSE = \sqrt{\frac{\sum_{i=1}^{N}(\eta_{r,experimental} - \eta_{r,predicted})^2}{N}} \qquad (10)$$

The errors are squared before being averaged in the RMSE calculation, giving a relatively high weighting to large errors. This helps accentuate where the models are ineffective, and the RMSE is directly interpretable in terms of the measured units.

Glycerol is a Newtonian fluid. The RMSE analysis on glycerol's solutions provided the basis for an objective evaluation of the effectiveness of the Einstein, Batchelor, and Krieger-Dougherty models when they were applied to the Xanthan and Sepiolite solutions.

4. Results

Figure 3 shows the general decrease in viscosity of a Xanthan gum suspension with increasing shear, confirming the fluid's non-Newtonian nature. Two datasets are plotted depicting the changes in viscosity: the first over an ascending ramp and the second over a descending ramp. The pseudoplastic drop is easily identifiable across both curves. This region is of particular interest as Xanthan's shear-thinning characteristics determine the extent of usability in industry.

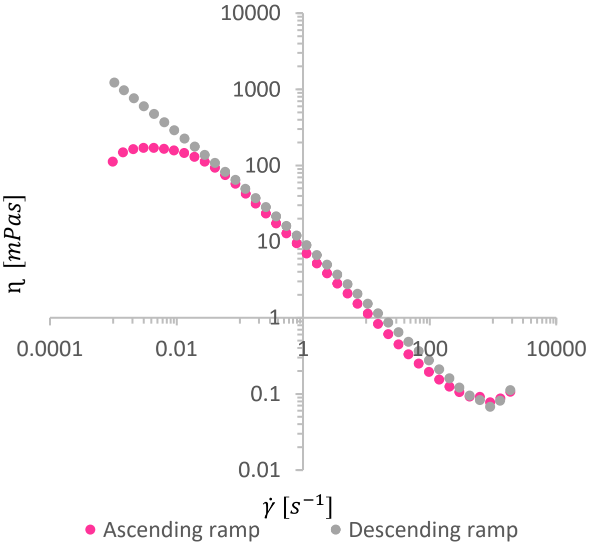

Figure 3: Experimental data for viscosity against shear rate in a 1% Xanthan solution with 30% volume fraction glass Ballotini particles

At low shear, there is a clear disparity between curved and straight lines for the first and second dataset respectively. Whilst suspensions are expected to plateau at low shear when reaching the limiting zero-shear viscosity, the plateau over the ascending ramp is clearly inconsistent with the descending ramp, suggesting that the non-linearity is not indicative of a Newtonian plateau. Instead, this deviation can be linked to the inertial effects of the rotor upon starting the rheometer strongly influencing and thereby disturbing the viscometric data collected. Elsewhere, apparent viscosity results were on average within 5% of each other for the ascending and descending. At high shear, both curves begin to show a positive relationship between viscosity and shear (shear-thickening). This behaviour is typically observed past the second Newtonian plateau at a large shear rate, the critical shear. Critical shear decreases in magnitude as the concentration of the dispersed phase increases. Given that the opposite is true across the obtained data for all volume fractions (see Appendix A), and that this shift is seen at a relatively low shear value than expected [11], this deviation is instead attributed to turbulence within the rheometer when the ramp changes direction.

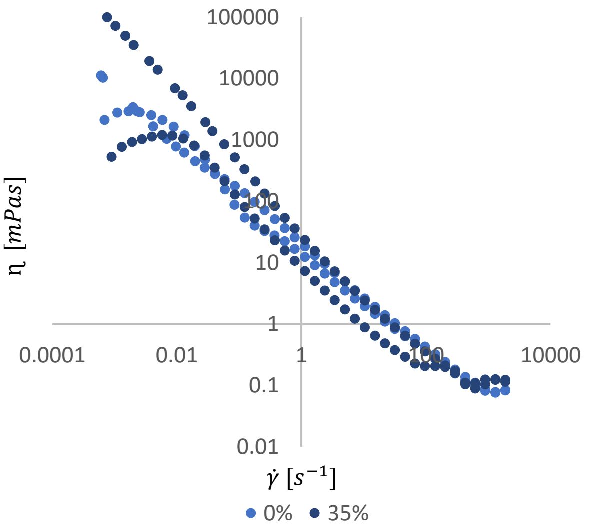

Figure 4: Experimental data for viscosity against shear rate in 5 wt.% Sepiolite solution with 0% and 35% volume fraction glass Ballotini

To avoid the prominent non-linearity across the ascending ramp and at the extremes of the tested shear, the study focuses on a narrowed range of $0.0134\ to\ 97.9\ s^{-1}$ from high to low shear. Note that the values 0.0134, 1.15 and 97.9 are referred to as low, medium, and high shear respectively in the following sections. Viscosity-shear relationships within this shear range exhibit linearity close to unity, with suspensions at all tested volume fractions returning $R^2 > 0.99$.

Similar observations were made across the viscosity measured for all Xanthan gum suspensions of varying particle and continuous phase concentrations, as well as all Sepiolite suspensions, as detailed in Appendix A. Figure 4 illustrates the viscometric measurements in Sepiolite with suspened particles solutions at 0% and 35% by volume fraction. At lower shear rates around $0.001 s^{-1}$ the higher viscosity of the suspended solution is significantly higher than that of the pure sepiolite solution, by almost an order of magnitude, highlighting the significant effect of the addition of suspended particles on the solution viscosities.

Note that the smoothness of the curves indicates that the serrated geometry is successful at negating wall-slip effects. The viscometric results obtained from the glycerol-glass Ballotini suspensions can also be found in Appendix A.

5. Discussion

It is established that correctly predicting the viscosity of suspensions is critical to many industries. Dilute and non-dilute suspensions of non-Brownian hard spheres have been adequately modelled by several equations on the basis of the Einstein relation but there is no such study on whether these apply when the continuous phase itself is non-Newtonian.

5.1 Model Evaluation

In this study, the Einstein, Batchelor, and Krieger-Dougherty equations have been used to assess the applicability of existing models to experimental values for suspensions of non-Newtonian continuous phases. Table 1 outlines the individual model predictions at the empirically measured volume fractions. An intrinsic viscosity of 2.5 was used to account for the spherical shape of the glass Ballotini particles, as determined by Einstein. At $\varphi_{max} = 0.74$, the Krieger-Dougherty model was found to provide the best overall fit, indicating a hexagonal close-packed or face-centred cubic sphere stacking scheme within the Xanthan-glass Ballotini suspensions. A value of $\varphi_{max} = 0.65$ was selected for the Sepiolite-glass Ballotini system after trial and error to find the value that yielded the lowest average RMSE within the range $0.60 \leq \varphi_{max} \leq 0.74$.

Table 1: Predictions for relative viscosity at 5% increments of particle volume fraction shown to 4 decimal places with φ_{max}=0.65 and 0.74

φ	$\eta_{r,Einstein}$	$\eta_{r,Batchelor}$	$\eta_{r,KD\ 0.65}$	$\eta_{r,KD\ 0.74}$
0%	1.0000	1.0000	1.0000	1.0000
5%	1.1250	1.1405	1.1389	1.1382
10%	1.2500	1.3120	1.3119	1.3081
15%	1.3750	1.5145	1.5316	1.5206
20%	1.5000	1.7480	1.8177	1.7912
25%	1.6250	2.0125	2.2011	2.1440
30%	1.7500	2.3080	2.7345	2.6163
35%	1.8750	2.6345	3.5129	3.2705
40%	2.0000	2.9920	-	4.2154

The three models agree up to a volume fraction of 10%, after which the Batchelor and Krieger-Dougherty predictions increase at a faster rate that Einstein's, largely owing to their additional additive terms. Both the Batchelor and Krieger-Dougherty models exhibit general agreement until a volume fraction of ~30%. Beyond this, the Krieger-Dougherty model makes much larger predictions for viscosity as the equation rapidly tends towards an asymptote at the infinite-viscosity at φ_{max}. Note that the predicted viscosities increase more rapidly when a smaller φ_{max} is used.

Results from the glycerol-glass Ballotini experiments were analysed to produce RMSE data detailing the fit of the Einstein, Batchelor, and Krieger-Dougherty models to the solutions of the Newtonian base medium (Appendix B). The range of RMSE for the Krieger-Dougherty model across 0% to 30% volume fraction was 0.16 - 0.43. The Krieger-Dougherty model displayed the lowest RMSE across all shear rates. Since the glycerol solutions were prepared and investigated with the same methodology and equipment, it can be reasoned that where the RMSE is less than 0.4, the experimental data can be said to be following the modelled predictions. This provides a baseline indicator for evaluating whether the inherently non-Newtonian base medium suspensions are being effectively predicted by the models.

5.2 Polymer suspensions

Figure 5A shows the evolution of viscosity with increasing concentration of glass Ballotini particles in a 0.5% Xanthan gum solution. It is apparent that the measured viscosities across all shear rates follow the same overall trend as the Krieger-Dougherty model. Surprisingly, however, at low volume fractions (5 - 15%) the relative viscosity over low and medium shear dip below 1, implying a decrease in suspension viscosity at dilute particle concentrations. It is unclear why this is observed. On the other hand, high shear viscosities seem to be independent of volume fraction over the range of 0 - 15%, implying that the interactions between particles are not significant enough at this low concentration to influence viscosity.

The accuracies of the models have a clear dependence on the concentrations of the dispersed particles. Despite a general fit to Krieger-Dougherty, low, medium, and high shear viscosities are much closer to Einstein's model below volume fractions of 20%, with RMSE values of 0.1865, 0.1506 and 0.1124 respectively. Einstein's model is typically applicable in infinitely dilute suspensions of Newtonian fluids, which are characteristically independent of the effects arising from Brownian motion. Therefore, it can be inferred that the dispersed glass Ballotini particles have negligible particle-particle hydrodynamic interactions at low volume fractions and do not interfere with the flow pattern significantly. However, it is worth noting that the low RMSE between Einstein's model and the experimental data for these suspensions at low volume fraction could instead be due to Einstein's model producing the least of an overestimation for the viscosities compared to the Batchelor and Krieger-Dougherty equations.

Above a volume fraction of 20%, viscosity increases much more non-linearly with increasing volume fraction and the Krieger-Dougherty model correctly predicts this dramatic increase in viscosity. The greater resistance to flow observed can be linked to increased multi-particle hydrodynamic interactions. This effect becomes increasingly pronounced with more concentrated suspensions due to increased compactness which further restricts fluid flow [20]. By accounting for φ_{max}, the Krieger-Dougherty model is able to produce predictions close to the actual values.

Investigating the viscosity of suspensions in relatively dilute concentrations of Xanthan is especially relevant to the food industry. Xanthan gum is used at concentrations of 0.5% primarily as a thickening-agent [21]. Correctly predicting the viscosity of these suspensions is imperative to achieving the correct texture of product, with increasing importance on the use of Xanthan to regulate food for those with swallowing disorders. These findings show that the Krieger-Dougherty and Einstein models can be used to make accurate predictions for viscosity at high and low volume fractions of particles respectively in suspensions with more dilute continuous phases.

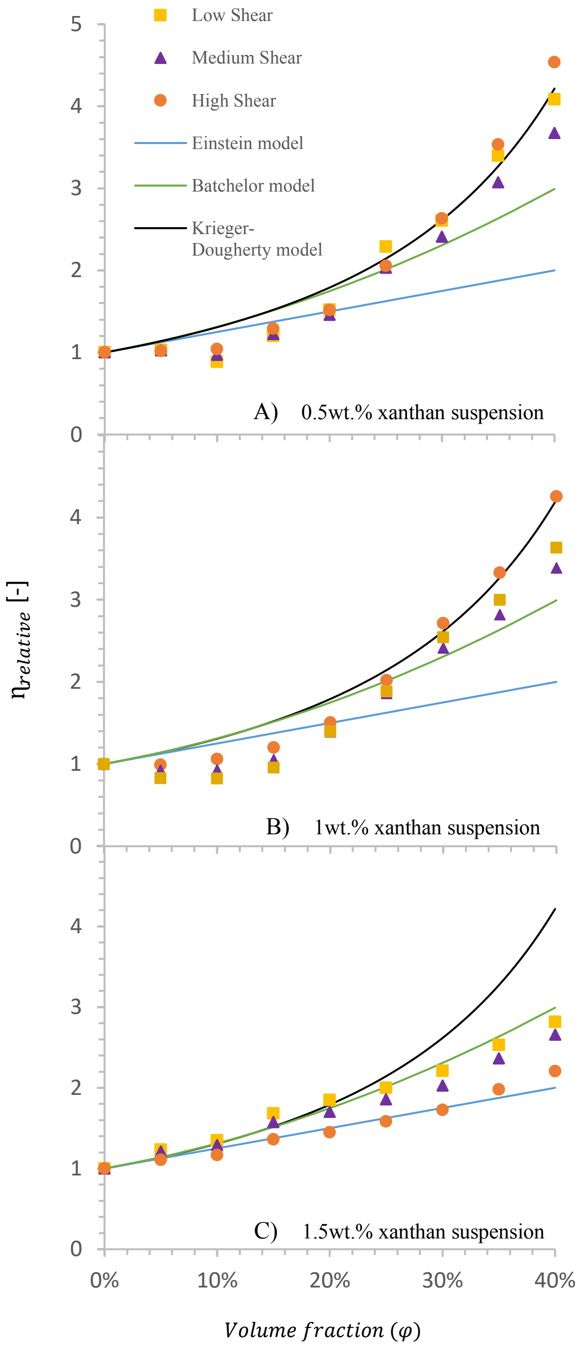

Figure 5: Relative viscosities against volume fraction of glass ballotini A) in 0.5 wt.% xanthan solution B) in 1 wt.% Xanthan solution C) in 1.5 wt.% xanthan solution

To further examine the universality of these models, the relative viscosities of suspensions in 1wt.% and 1.5wt.% Xanthan gum solutions were analysed across the volume fraction range: $0\% < \varphi < 40\%$.

The 1.0% Xanthan-glass Ballotini suspensions show similar behaviour to that seen in the 0.5% solution. Fig 5B shows the same overestimation of viscosity at high, medium, and low shear over the volume fractions of 0 - 20% by all three models. At these glass Ballotini concentrations, the Einstein model is again shown to have the greatest agreement with experimental values across all shear rates. It is also apparent that viscosities at high and low shear have greatest overall fit to the Krieger-Dougherty model, whilst medium shear viscosities closely fit Batchelor's predictions. This is in line with literature as the Krieger-Dougherty equation is best suited to high and low shear [11]. Additionally, the points tend to show greater agreement with Krieger-Dougherty at higher volume fractions. The RMSE between the Krieger-Dougherty model and the true values is lowest at high shear, closely followed by low shear then medium shear, further supporting the greater applicability of Krieger-Dougherty at high and low shear (Appendix B). Relative viscosity is also generally lowest at medium shear. It is clear that both the shear rate and volume fraction have a large influence on the suitability of a model when using a 1% Xanthan continuous phase.

Conversely, the concentrated 1.5% Xanthan suspensions are more accurately represented by the Batchelor model at low and medium shear. The suspensions exhibit a very different trend to those in the relatively dilute Xanthan base mediums, as seen in figure 5C. The linearity typically observed at volume fractions below 20% is maintained up to the highest tested volume fraction of 40%. This Newtonian behaviour is unexpected as the suspensions otherwise display explicit shear-thinning characteristics as previously discussed. The R^2 values of 0.9902, 0.9797, and 0.9709 for low, medium, and high shear respectively, suggest that this linearity breaks down with increasing shear. Another notable variation can be seen in the magnitudes of viscosity across different shear rate.

Unlike in the 0.5 and 1wt% Xanthan solutions, a higher shear applied to the 1.5wt.% Xanthan solution relates to a lower relative viscosity across all volume fractions. The high shear viscosity is noticeably overestimated by Krieger-Dougherty at higher volume fractions, nearing a 50% overestimate of viscosity at 40% concentration of glass Ballotini. High shear viscosities are almost perfectly predicted by Einstein's equation with an RMSE of 0.0863 over the range of volume fractions, suggesting that hydrodynamic particle-particle interactions are not prominent within the suspensions. It is possible that in relatively highly viscous fluid mediums, the increasing presence of particles begins to break down the fluid structure. In such a case that the structural integrity of the continuous phase is compromised, the space between the particles would increase, reducing the extent of hydrodynamic interactions and lowering overall viscosity. The counteracting effects described are a potential source of reasoning behind the continuing linear trend observed across low to high shear, as opposed to a non-linear increase.

In 1.5wt.% Xanthan, low and medium shear viscosities are most accurately predicted by Batchelor's equation overall, with the exception of low shear at 0 - 20% where the Krieger-Dougherty model performs marginally better than the Batchelor model by an RMSE difference of 0.0087. Relatively higher concentrated Xanthan solutions (1 - 1.5%) are becoming increasingly relevant as a cheaper and environmentally friendly alternative to traditional building materials, as well as use in soil treatment. As such, it is imperative to be able to predict suspension viscosities to facilitate the development of these processes [22].

Tabulated values for RMSE across the different models and experimental data across $0\% < \varphi < 40\%$ at different shears can be found in Appendix B.

5.3 Clay Suspension

Experimental data up to a 35% volume fraction of glass Ballotini in Sepiolite was obtained, as above this volume fraction the Ballotini was seen sedimenting in the solution container.

Figure 6 illustrates how experimental values obtained for the relative viscosity at different shear rates compare with the relative viscosities predicted by the Einstein, Batchelor, and Krieger-Dougherty models. It is apparent that at high and medium shear rates, the relative viscosity is almost independent of the volume fraction of glass Ballotini. The relative viscosity at high shear has a mean and sample standard deviation of 0.78 and 0.16 respectively, whilst at medium shear that of 1.08 and 0.15 respectively. Perhaps the relative viscosity is less than unity at high shear due to the particles interfering with and breaking down the sepiolite fibres, resulting in a lower resistance to flow. It can be reasoned from Figure 6 that as the shear rate decreases, the solution becomes more sensitive to the suspended solids in solution and the curve tends towards the Krieger-Dougherty predictions, as seen with medium-low shear at a shear rate value of 0.0594s^{-1}. Whilst the shear rate continues to decrease, the relative viscosity demonstrates values above that predicted by the Krieger-Dougherty equation. It can be inferred that there is a range of shear values for which the Krieger-Dougherty equation is an appropriate predictor of relative viscosity for glass Ballotini in Sepiolite solvent.

The RMSEs comparing the experimental and predicted values from the Einstein, Batchelor and Krieger-Dougherty models are plotted against shear rate at all shear rate values within the linear region considered in Figure 7. The motivation for this plot stems from the high dependence on shear rate observed in Figure 6. Therefore, investigating over which shear rates the experimental values and predicted values converge would provide greater insight into whether specific models are more appropriate predictors of relative viscosity dependent on shear rate.

At shear rates above 1s^{-1} the relative viscosity is practically independent of volume fraction of suspended particles, where an average can be taken at that particular shear rate to describe relative viscosity. At these higher shear rates, the RMSE is lower for Einstein's model not because the Einstein and experimental viscosities match, but because Einstein's equation predicts lower relative viscosity values at higher volume fractions compared to Batchelor and Krieger-Dougherty, as seen in Figure 6. As the shear rate decreases, the accuracy of the models increases. Figure 7 illustrates the dips at which the model accuracies reach their maxima, centred at 0.178s^{-1}, 0.0862s^{-1} and 0.0594s^{-1} for the Einstein, Batchelor, and Krieger-Dougherty models respectively. Below the 0.05s^{-1} to 0.5s^{-1} window, in which the relative viscosities are predicted effectively with $RMSE < 0.4$, the relative viscosity is significantly underestimated by all the models though the same form of the Krieger-Dougherty curve is seen.

The clay sepiolite is a complex material in solution, as could be inferred from its non-Newtonian status and the structure illustrated in Figure 2. The mechanism for why the relative viscosity is apparently independent of phase-volume of particles at high shear is unclear from literature [23][24][25]. It is known that at higher shear rates the stiff, rod-shaped sepiolite fibres organise themselves to minimise resistance to flow resulting in

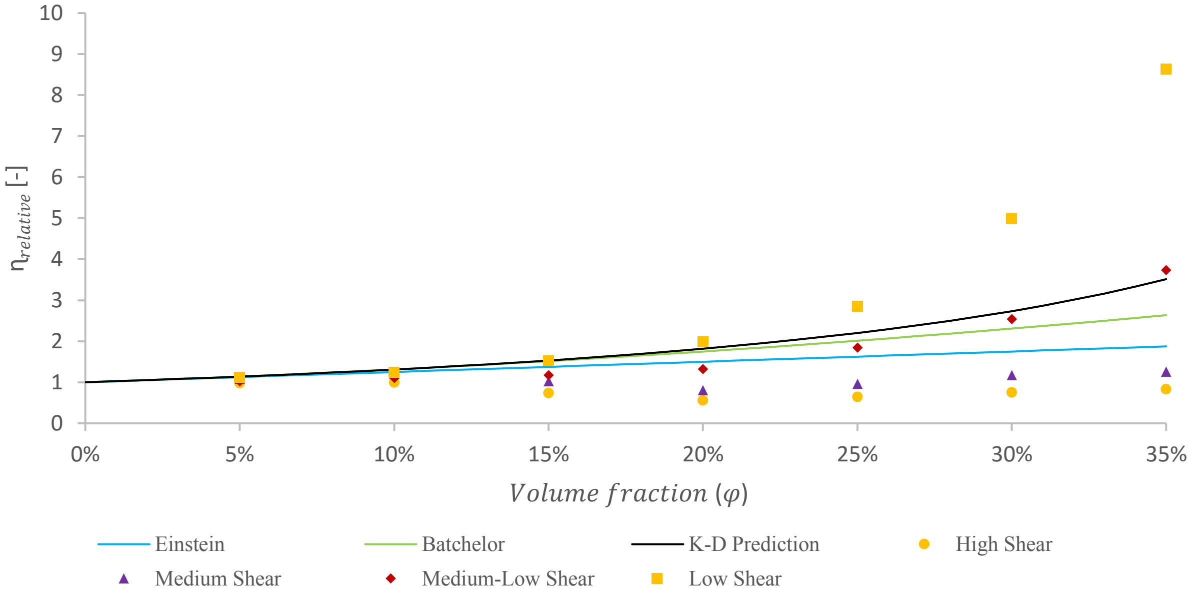

Figure 6: Relative viscosity against volume fraction of glass ballotini in Sepiolite

shear-thinning behaviour [5]. At medium and high shear, the mechanism for the solution's relative viscosity being independent of volume fraction of suspended particles could be due to the imposed velocity gradient arranging the suspended particles with high efficiency in particle layers. It is known that for Newtonian suspensions at high shear the particles form layers separated by clear layers of the continuous phase, (confirmed by light diffraction) [11]. The Sepiolite solution's particle layers may have a high capacity such that relative viscosity remains constant. This results in a solution independent of volume fraction of suspended particles at medium and high shear. This underlines a potential advantage of using sepiolite as a drilling fluid: the viscous properties would remain constant independent of the volume fraction of cuttings being incorporated into solution at high shear [14].

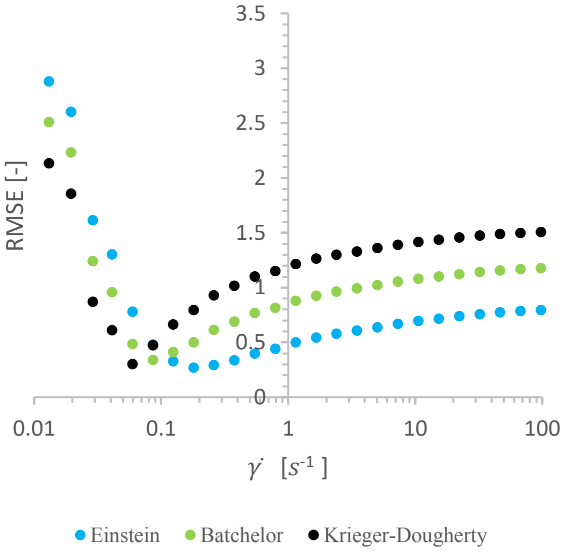

Figure 7: Root Mean Square Error (RMSE) against Shear Rate ($\dot{\gamma}$) for Glass Ballotini suspended in Sepiolite

At shear rates below $0.05s^{-1}$, the solution is less organised and apparent viscosity increases such that experimental and modelled values diverge significantly. The relative viscosity against phase-volume trend at low shear rate follows the same general shape as that predicted by the Krieger-Dougherty model, although the experimental values are significantly higher than predicted. A higher value of [η] in the index of the Krieger-Dougherty equation would provide a better fit to the experimental data, however the value of [η] is based on the suspended particle geometry and determined as 2.5 for spherical particles [7], thus it would be illogical to alter this value. Therefore, the Krieger-Dougherty equation is an ineffective predictor of relative viscosity in Sepiolite at lower shear rates.

6. Conclusion

The predictive performance of existing viscosity models for suspensions of non-Brownian hard spheres is evaluated using true values for the viscosity of non-Newtonian polymer and clay suspensions. The Krieger-Dougherty equation is found to accurately describe the viscosity of concentrated glass Ballotini suspensions in relatively dilute Xanthan mediums by accounting for multi-particle hydrodynamic interactions.

Predictions from Einstein's model closely follow the observed viscosity in dilute polymer suspensions, implying that Brownian motion and hydrodynamic interactions can be safely ignored at low volume fractions of up to 20% across high to low shear.

Meanwhile, Batchelor's model proves to be inapplicable to non-Newtonian suspensions.

The relative viscosity of suspended glass Ballotini in Sepiolite proved independent of volume fraction at shear rates above $1s^{-1}$. There was a shear range centred at $0.06s^{-1}$, over which the Krieger-Dougherty model briefly applied, before returning to vast overestimations below this shear rate.

For the Sepiolite suspension, the mechanism of the shear velocity gradient arranging the suspended particles with extreme efficiency in particle layers is suggested to justify why relative viscosity is independent of volume fraction at medium and high shear rates. At lower shear rates, there were narrow shear rate ranges over which the Krieger-Dougherty, Batchelor and Einstein models briefly applied. More research into the interactions between the suspended particle and Sepiolite fibres across the range of shear rates is required to understand this phenomenon. Investigation of different clay fluids such as bentonite would be insightful to determine whether these existing models are only effective predictors across an optimal shear range and to help develop a more suitable mechanism for use in industry.

7. Acknowledgements

We offer our thanks to Professor Paul Luckham for his continuous support and insights, without which this paper would not have been possible.

Citations

[1] Wei, B., Romero-Zerón, L. & Rodrigue, D. (2014) Mechanical properties and flow behavior of polymers for Enhanced Oil Recovery. *Journal of Macromolecular Science, Part B*. [Online] 53 (4), 625–644. Available from: doi:10.1080/00222348.2013.857546.

[2] Carolina, V.J., Woerdenbag, H., Reinier, V., Wouter, H., et al. (2018) Comparison of Rheological and Sedimentation Behavior of Commercially Available Suspending Vehicles for Oral Pharmaceutical Preparations. *International Journal of Pharmaceutical Compounding*. 22 (3), 247–251.

[3] Batchelor, G.K. (1977) The effect of Brownian motion on the bulk stress in a suspension of spherical particles. *Journal of Fluid Mechanics*. [Online] 83 (1), 97–117. Available from: doi:10.1017/s0022112077001062.

[4] Tadros, T.F. (2017) Chapter 9: Rheology of Suspensions. In: *Suspension concentrates: Preparation, stability and Industrial Applications*. De Gruyter. pp. 195–196.

[5] Mooney, M. (1951) The viscosity of a concentrated suspension of spherical particles. *Journal of Colloid Science*. [Online] 6 (2), 162–170. Available from: doi:10.1016/0095-8522(51)90036-0.

[6] Krieger, I.M. & Dougherty, T.J. (1959) A mechanism for non-Newtonian flow in suspensions of rigid spheres. *Transactions of the Society of Rheology*. [Online] 3 (1), 137–152. Available from: doi:10.1122/1.548848.

[7] Cross, M.M. (1965) Rheology of non-Newtonian fluids: A new flow equation for pseudoplastic systems. *Journal of Colloid Science*. [Online] 20 (5), 417–437. Available from: doi:10.1016/0095-8522(65)90022-x.

[8] Einstein, A. (1906) Eine Neue Bestimmung der Moleküldimensionen. *Annalen der Physik*. [Online] 324 (2), 289–306. Available from: doi:10.1002/andp.19063240204.

[9] Ball, R.C. & Richmond, P. (1980) Dynamics of colloidal dispersions. *Physics and Chemistry of Liquids*. [Online] 9 (2), 99–116. Available from: doi:10.1080/00319108008084770.

[10] Barnes, H.A. (2000) Chapter 15. In: *A Handbook of Elementary Rheology*. Aberystwyth, University of Wales, Institute of Non-Newtonian Fluid Mechanics. p. 120.

[11] Barnes, H.A., Hutton, J.F. & Walters, K. (2005) Chapter 7: Rheology of Suspensions. In: *An introduction to rheology*. Amsterdam, Elsevier.

[12] de Mello Luvielmo, M., Borges, C.D., de Oliveira Toyama, D., Vendruscolo, C.T., et al. (2016) Structure of xanthan gum and cell ultrastructure at different times of alkali stress. *Brazilian Journal of Microbiology*. [Online] 47 (1), 102–109. Available from: doi:10.1016/j.bjm.2015.11.006.

[13] Li, X., Lu, Y., Adams, G.G., Zobel, H., et al. (2020) Characterisation of the molecular properties of scleroglucan as an alternative rigid rod molecule to Xanthan gum for oropharyngeal dysphagia. *Food Hydrocolloids*. [Online] 101105446. Available from: doi:10.1016/j.foodhyd.2019.105446.

[14] Alvarez, A. (1984) Sepiolite: Properties and uses. *Developments in Sedimentology*. [Online] 253–287. Available from: doi:10.1016/s0070-4571(08)70044-x.

[15] Shainberg, I. & Levy, G.J. (2005) Flocculation and dispersion. *Encyclopedia of Soils in the Environment*. [Online] 27–34. Available from: doi:10.1016/b0-12-348530-4/00363-5.

[16] Alves, L., Ferraz, E., Santarén, J., Rasteiro, M.G., et al. (2020) Improving colloidal stability of sepiolite suspensions: Effect of the mechanical disperser and chemical dispersant. *Minerals*. [Online] 10 (9), 779. Available from: doi:10.3390/min10090779.

[17] Jencons (2021) *Ballotini Specifications*. [Online]. Ballotini. Available from: https://uk.vwr-cmd.com/ex/downloads/jencons/pdf/catalogue/Ballotini.pdf [Accessed: 2021].

[18] Malvern Instruments Worldwide (2015) *Understanding yield stress measurements introduction*. [Online]. 2015. WHITEPAPER. Available from: https://cdn.technologynetworks.com/TN/Resources/PDF/WP120416UnderstandYieldStressMeas.pdf [Accessed: 2 December 2021].

[19] Barnes, H.A. (1995) A review of the slip (wall depletion) of polymer solutions, emulsions and particle suspensions in viscometers: Its cause, character, and cure. *Journal of Non-Newtonian Fluid Mechanics*. [Online] 56 (3), 221–251. Available from: doi:10.1016/0377-0257(94)01282-m.

[20] Pal, R. (2020) New generalized viscosity model for non-colloidal suspensions and Emulsions. *Fluids*. [Online] 5 (3), 150. Available from: doi:10.3390/fluids5030150.

[21] Hublik, G. (2012) Xanthan. *Polymer Science: A Comprehensive Reference*. [Online] 221–229. Available from: doi:10.1016/b978-0-444-53349-4.00262-4.

[22] Chang, I., Im, J., Prasidhi, A.K. & Cho, G.-C. (2015) Effects of xanthan gum biopolymer on soil strengthening. *Construction and Building Materials*. [Online] 7465–72. Available from: doi:10.1016/j.conbuildmat.2014.10.026.

[23] Hamid, Y., Tang, L., Hussain, B., Usman, M., et al. (2021) Sepiolite Clay: A review of its applications to immobilize toxic metals in contaminated soils and its implications in soil–plant system. *Environmental Technology & Innovation*. [Online] 23101598. Available from: doi:10.1016/j.eti.2021.101598.

[24] HILLEL, D. (2005) Chapter C: Clay Minerals: Palygorskite and Sepiolite. In: *Encyclopedia of Soils in the environment*. Oxford; Boston, Elsevier/Academic. pp. 252.

[25] Alves, L., Ferraz, E., Santarén, J., Rasteiro, M.G., et al. (2020) Improving colloidal stability of Sepiolite suspensions: Effect of the mechanical disperser and chemical dispersant. *Minerals*. [Online] 10 (9), 779. Available from: doi:10.3390/min10090779.

Graphene liquid-exfoliation in Cyrene: An evaluation of solvent performance, shear rate and centrifugation parameter effects on graphene production

Natalia Neocleous and Anastasios Tsimpidaros
Department of Chemical Engineering, Imperial College London, U.K.

Abstract

Graphene is an upcoming nanomaterial that has the potential for many applications ranging from electronic devices to inks, due to its extraordinary properties. The growing interest in graphene-based materials requires large-scale production of graphene, which remains unfeasible to this day due to economic and environmental considerations. The performance of Cyrene, a novel, and environmentally friendly solvent, as a dispersant for liquid-phase exfoliation of graphite was assessed in a Taylor-Couette high-shear device. The effects of shear rate, processing time, centrifugation time and Relative Centrifugal Force on the concentration and average layer number, $\langle N \rangle$, of the produced graphene dispersions were examined and compared against NMP, a common high-performing, but toxic solvent. It was found that both shear rate and processing time had a positive impact on the final product concentration but no influence on $\langle N \rangle$. However, Cyrene produced up to 160% higher graphene concentrations than NMP and lower $\langle N \rangle$, in the range of 5 to 7. Contrarily, Cyrene was a poorer solvent for storage of graphene dispersions. Moreover, the concentration of graphene over the centrifugation cycle appeared to initially decrease by an average of 15%, before reaching a plateau. The centrifugation time did not affect $\langle N \rangle$. Separation was revealed to be more effective in the higher RCF centrifuge, producing higher final product concentrations within the reported range of average layer numbers. The results obtained in this study provide useful insight for both the potential up-scale of graphene production and the graphene LPE research field.

1 Introduction

Graphene has been gaining popularity over the last few years as a new and exciting nanomaterial owing to its unique features, such as high tensile strength and high thermal and electrical conductivity. Quite remarkably, this material only consists of the fourth most abundant element in the universe, carbon. Graphene is the two-dimensional (2D) form of carbon. It forms a planar structure of carbon atoms that are fully conjugated in the sp^2 state with a bond angle of 120° forming a honeycomb lattice [1]. Graphite, the three-dimensional (3D) form of carbon, is essentially a structure composed of monolayers of graphene stacked on top of each other that are held together by (weak) Van der Waals (VdW) forces.

There are different types of graphite precursors and graphene products. The graphite precursor properties can drastically affect the exfoliation process as well as the quality of the graphene product. Graphite can either be natural or synthetic, and can be found in many varieties such as flake graphite, expanded graphite, highly oriented pyrolytic graphite (HOPG), Kish graphite, etc. [2]. Different varieties are characterised by different particle lateral size, thickness, morphology, and purity. Wu et al. [3] used artificial graphite, flake graphite powder, Kish graphite, and natural flake graphite as precursors to chemical exfoliation and suggested that the lateral size and the crystallinity of the starting material is directly proportional to the number of graphene layers obtained. Knirsch et al. [4] in a study testing graphite flakes, graphite powder and spherical graphite, concluded that larger graphite particles undergo partial exfoliation because of their higher intrinsic lattice energy and that powder graphite yields graphene with the highest functionalisation. Moreover, it was shown that smaller graphite particles are more easily dispersed in a solvent, form a more stable dispersion, and can be used to produce Few Layer Graphene (FLG) more efficiently, in comparison to larger graphite particles [5] [6].

The first breakthrough in graphene research was made by Novoselov et al. in 2004 [7], when graphene, previously thought to be unstable in its free state, was successfully produced with a thickness of a few atomic layers. Originally, it was produced as a new and non-traditional material to be used in semiconductors, and it was the first ever material of that thickness to be continuous and metallic. Thanks to its unique properties, such as high resistance to gas permeation, high transmittance, and high modulus of elasticity, graphene is a potential candidate for applications in electronic devices, sensors, energy storage, solar cells, paints, coatings, inks, and many other fields. [8] [9]. Since the Nobel Prize-winning paper by Novoselov et al. (2004) [7], the research into production of graphene has been increasing by a factor of $\sim t^3$ each year [1].

2 Background

Currently, the main limitation in the implementation of graphene in the aforementioned applications is the lack of mature large-scale production routes. There are two main production pathways of graphene: "bottom-up" and "top-down". Bottom-up methods involve producing graphene via chemical manipulation of hydrocarbon precursors, and usually produce monolayer and multilayer graphene (MLG) with $2 < \langle N \rangle < 10$, where $\langle N \rangle$ is the average number of layers. Top-down methods produce graphene from a graphite precursor by breaking-up the VdW forces that hold the individual graphene monolayers together through various physical mechanisms outlined further below. A minimum energy of 2 eV nm^{-2} must be provided for this to happen [10]. Typically, top-down methods also produce MLG but with a broader distribution in $\langle N \rangle$ than the former approach. Whilst bottom-up methods typically produce higher quality graphene sheets than top-down methods, the production rates are well below the demand for such graphene products. Since the applications that require higher quality graphene are quite specific, it is believed that mass production of graphene will be dominated by top-down methods despite its limitations [1].

Top-down methods usually employ Liquid-Phase Exfoliation (LPE) methods, where graphene sheets are exfoliated from the graphite precursor in a liquid medium. The three main mechanisms of LPE are the following: mechanical, chemical and electrochemical. Mechanical exfoliation is performed by mechanically overcoming the VdW forces between the graphite layers. Chemical mechanisms often rely on oxidising graphite to graphite oxide, which is then delaminated to give graphene oxide (GO), and subsequently, reduced graphene oxide (rGO). Electrochemical methods capitalise on the conductivity of graphite, using it in as a positive or negative electrode, allowing oppositely charged ions to intercalate between graphite layers and trigger exfoliation [1].

Sonication, is one of the many examples of LPE. It involves blasting the liqiuid media with high intensity ultrasonic waves, which creates cavitation bubbles that distribute around the graphite flakes. When these bubbles finally become unstable, they burst, and the resulting micro jets and shock waves produce tensile stresses on the graphite flakes, resulting in fragmentation and exfoliation to graphene. High-shear mixing is another potential LPE method that has potential for scale-up production. An LPE study by Paton et al. [11] concluded that a minimum shear rate ($\dot{\gamma}_{min}$) of 10^4 s^{-1} is required, regardless of the degree of turbulance. Similarly, Varrlon et al. [12] demonstrated that a large quantity of defect-free graphene can be produced using a conventional kitchen blender and Fairy liquid as a dispersant. High-shear forces can also be induced by Taylor-Couette devices, where the graphite dispersion is sheared between a rapidly spinning inner cylinder and a stationary outer cylinder as demonstrated in experimental and modelling work by Stafford et al. [13]. Above a critical rotational speed, counter-rotating tortoidal vortices start forming. This type of flow is called Taylor Vortex flow which causes exfoliation of the graphite on the inner cylinder walls.

The selection of an appropriate solvent is pivotal to the efficient LPE of graphite. A solvent would ideally be able to form stable dispersions of graphene by balancing the attractive potentials with repulsive potentials, and thus, preventing the aggregation of graphene sheets [1]. Moreover, suitable solvents can be identified by minimizing the energetic cost of exfoliation or the enthalpy of mixing, ΔH_{mix} [14]. Effectively, matching the surface tension of the solvent to that of graphene would minimize ΔH_{mix}. Hernandez et al. [14] recommended that the solvent should have a surface energy of 40 – 50 mJ m^{-2}. Another way to represent the energetic cost of exfoliation is through the Flory-Huggins interaction parameter, χ [15]. By matching the Hilderbrand and Hansen solubility parameters for dispersion (δ_D), polarity (δ_P) and hydrogen bonding (δ_H) of the solvent to those of graphene, the Flory-Huggins parameter would be minimised [14] [15]. A study by Hernandez et al. [15] recommended that for a solvent to perform well it must have Hansen solubility parameters of around δ_D = 18.0 $MPa^{1/2}$, δ_P = 9.3 $MPa^{1/2}$, δ_H = 7.7 $MPa^{1/2}$.

Shih et al. [16], produced a thermodynamic model to describe the mechanism of stabilization of graphene in five different solvents. They calculated the potential mean force between two dispersed graphene sheets for varying interplanar distances. N-Methyl-2-pyrrolidone (NMP) was ranked as the best solvent because of the high energy barrier of sheet aggregation and the shallower VdW well in comparison to the two graphene sheets in a vacuum. From a kinetic point of view, a higher energy barrier leads to a slower aggregation rate, and thus, a more stable dispersion. A shallower VdW well means that the attractive potential between the graphene sheets is effectively balanced by the solvent, resulting in much lower aggregation (restacking) of the exfoliated graphene sheets.

Apart from these thermodynamic and kinetic considerations, one should also consider the level of 'greenness' and toxicity of the solvent, and the sustainability of the overall process. While NMP offers excellent properties as a dispersing solvent, it is highly toxic, non-sustainable, and has high boiling point, which makes it very difficult to separate from the graphene product without influencing the quality of the latter. Recently, an alternative solvent Dihydrolevoglucosenone, termed as Cyrene, was developed to tackle the aforementioned issues caused by high-performing solvents such as NMP. Cyrene is considered a 'greener' substitute of NMP for graphene dispersions. It is non-toxic, biodegradable, not mutagenic, and during biodegradation it only yields carbon dioxide and water. Moreover, it has a low acute toxicity (LD_{50} > 2000 mg kg^{-1}) and aquatic toxicity (EC_{50} > 100 mg L^{-1}) [17]. Due to these advantageous characteristics of Cyrene, a study by Salavagione et al. [17] was conducted in which graphite exfoliation was achieved by ultrasound treatment, and the performance of various solvents including Cyrene and NMP was directly compared. The results allowed to conclude that Cyrene is an excellent solvent for sustainable graphene production and processing.

Previous notable work on shear exfoliation of graphite with Taylor-Couette flow include the work done by Stafford et al. [13]. NMP was used as a solvent to create a graphite dispersion with an initial graphite concentration C_i = 10 g/L, which yielded graphene at concentration of C_g = 0.2 g/L at an inner cylinder rotational speed (ω) of 175 rad/s.

This study built on this work and focused on the performance of Cyrene, as a potential new, environmentally friendly solvent for the shear-assisted exfoliation of graphite to graphene. A centrifugation study was also performed to evaluate the effect of centrifugation parameters, in particular processing time and relative centrifugal force (RCF) on both the resulting concentration and the average layer number of graphene produced.

3 Methodology

3.1 Materials

Graphite flakes from Sigma Aldrich (part no. 332461) and Cyrene (Dihydrolevoglucosenon, purity $\geq$ 98.5%) purchased from Sigma Aldrich were used for exfoliation.

3.2 Experimental Procedure

Cyrene dispersion of 1.5 L and initial graphite concentration of 10 g/L was exfoliated for a total of 3 hours using three different exfoliation conditions, i.e., cylinder rotational speeds of 102 rad/s, 122 rad/s and 175 rad/s. These parameters are identical to those used by Stafford et al. [13] and Farooq [18] allowing for direct comparison of results for NMP. Regular sampling (2 per hour) was performed by taking 30 mL of exfoliated product. Post 3 hours processing period, the final product from Reservoir A (Figure 1) was also collected. All collected samples were left overnight to settle prior to further processing. Following this, solutions of 54 mL were prepared from the final product supernatant and were centrifuged in two different centrifuges; Centrifuge 1 ($RCF = 290g$, accuSpin 400, Fisher Scientific, 15-45 minutes) and Centrifuge 2 ($RCF = 190g$, Sorvall Legend X1, Thermo Scientific, 120-200 minutes). Time samples were diluted with Cyrene by a factor of 3 to form 54 mL samples (18 mL of supernatant and 36 mL cyrene), which were ran through Centrifuge 2. This was performed to separate any unexfoliated graphene from the samples. After centrifugation all samples were diluted with Cyrene by a total factor of 30, and were analysed using UV-Vis-nIR spectroscopy (UV-2600, Shimadzu).

3.3 Cyrene dispersion performance

Before looking into data measurements, it was helpful to assess the solvent properties to understand its capabilities as a graphene dispersant. For this, the surface energy of Cyrene was firstly determined through the Pendant drop method, where the Young-Laplace equation is fitted to an experimental image (Krüss ADVANCE software, setup of: light source, camera, needle attached to syringe). Additionally, the Hansen solubility parameters were considered. The enthalpy of mixing (ΔH_{mix}) and Flory-Huggins parameter (χ) can then be determined [14] [15] [19] [20]:

$$\frac{\Delta H_{mix}}{V_{mix}} \backsimeq \frac{2}{T_{flake}}(\delta_g - \delta_c)^2\phi \tag{1}$$

$$\chi = \frac{v_0}{kT}R^2 \tag{2}$$

where $R = \sqrt{(\delta_{D,c} - \delta_{D,g})^2 + (\delta_{P,c} - \delta_{P,g})^2 + (\delta_{H,c} - \delta_{H,g})^2}$ and $\delta_i = \sqrt{E_{surface,i}}$. V_{mix} is the total volume of the mixture, T_{flake} is the graphene thickness, ϕ is the graphene volume fraction, $E_{surface,i}$ is the surface energy of species i, v_0 is the molecular volume of the solvent, δ_D, δ_P, δ_H are the Hansen solubility dispersive, polar and hydrogen-bonding components respectively. The g and c subscripts denote graphene and Cyrene, respectively.

3.4 Shear-assisted exfoliation of graphite

Exfoliation of the graphite flakes was performed using an in-house built high-g shear LPE rig (Figure 1). Previous work of Stafford et al. [13] on the rig showed that it is best described by the Taylor-Couette flow, and can be approximated by Large-Eddy simulations (LES) [1] [13]

As can be seen in Figure 2(a) the flow is generated in the gap between two concentric cylinders, with the outer cylinder held stationary. At sufficiently high Reynolds number (Re), the local shear rate generates Taylor vortices which facilitate the exfoliation process. These vortices are intensified closer to the wall of the device where most of the exfoliation occurs.

At low inner cylinder rotational speeds, or low Re, the flow between the two cylinders is laminar, and it is called Couette flow. As the rotational speed increases, the flow experiences different regimes such as Taylor Vortex Flow (TVF), Wavy Vortex Flow (WVF), Modulated Wavy Vortex Flow (MWV), Chaotic Wavy Vortex Flow (CWV) and Turbulent Taylor Vortex Flow (TTV) [21]. TTV has two distinguished phases: soft turbulence and hard turbulence. For the purposes of this study, the critical Reynolds numbers for the transitions to soft and to hard turbulence are denoted as Re_{ST} and Re_{HT} respectively.

The transitional Reynolds numbers between these regimes are usually given normalised to the critical Reynolds number, Re_c. Above Re_c, one enters TVF, which is characterised by pairs of counter rotating toroidal vortices. The next important Reynolds number in the calculations that follow is the hard turbulence Reynolds number, Re_{HT}. Equation (10) was used to calculate

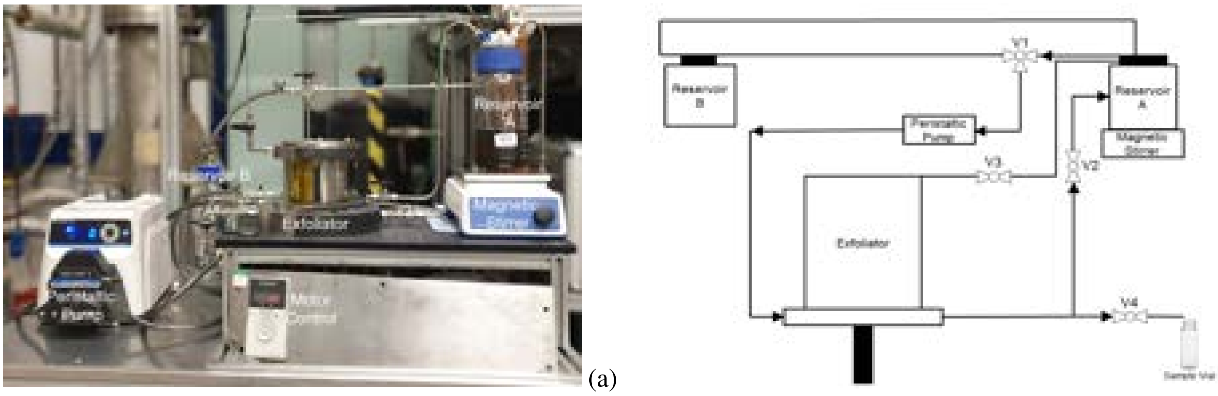

(a) (b)

Figure 1: (a) Exfoliation experimental setup. From left to right: Peristaltic pump to adjust flow rate, Exfoliator device with motor control of rotational speed, final product reservoir with magnetic stirrer residing on a magnetic plate. (b) Schematic of graphene rig.

Re_c. Table 1 shows the relative Re for each transition. The relative Re for the onset of soft and hard turbulence is simply Re_{ST}/Re_c and Re_{HT}/Re_c respectively, where $Re_{ST} = 707/\eta(1-\eta)^{1/2}$ and $Re_{HT} = 4472/\eta(1-\eta)^{1/2}$.

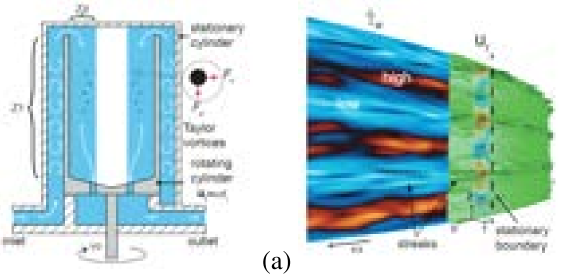

(a) (b)

Figure 2: (a) Depiction of flow inside exfoliation device. Z1 is the exfoliation zone. (b) Exfoliation zone shear rate ($\dot{\gamma}_w$) distribution. Topology of shear stress (green) and positive (red) and negative (blue) fluid vortices are depicted. Both images adapted from Stafford et al. (2020) [13].

Table 1: Flow regimes in Taylor-Couette flow.

Flow Regime Transition	Relative Re	Ref.
TVF	1	[22]
WVF	1.2	[22]
MWV	10.1	[22]
CWV	12	[21]
Soft Turbulence	17.13	-
Hard Turbulence	111.1	-

To identify the dependence of the shear rate, $\dot{\gamma}$, on the Reynolds number, the torque was determined through the properties of the flow (Reynolds number), properties of the solvent (viscosity) and vessel size (inner and outer cylinder radius). Here, a dimensionless torque, G_i, is calculated for the different flow regimes, which is then used to calculate the shear rate as a function of the overall Reynolds number, Re [23] [24].

Couette flow ($Re < Re_c$):

$$G_i = \frac{2\pi}{(1-\eta)^2}\eta Re \tag{3}$$

Transitional regime ($Re_c \leqslant Re \leqslant Re_{HT}$):

$$G_i = \frac{(3+\eta)^{1/4}(\eta Re)^{3/2}}{(1-\eta)^{7/4}(1+\eta)^{1/2}} \tag{4}$$

Hard turbulent regime ($Re > Re_{HT}$):

$$G_i = 0.33\frac{(3+\eta)^{1/2}}{(1-\eta)^{3/2}(1+\eta)}\frac{(\eta Re)^2}{(\ln[M(\eta)(\eta Re)^2])^{3/2}} \tag{5}$$

$M(\eta)$ is defined as:

$$M(\eta) = 0.0001\frac{(1-\eta)(3+\eta)}{(1+\eta)^2} \tag{6}$$

The overall Reynolds number, Re, was obtained through the following expression, where the outer cylinder Reynolds number, Re_{o}, was set to zero since the outer cylinder remained stationary:

$$Re = \frac{2}{1+\eta}|\eta Re_0 - Re_{\mathrm{i}}| \tag{7}$$

Re_{i} is the inner cylinder Reynolds number, which was varied by varying the cylinder rotational speed, Ω_i:

$$Re_{\mathrm{i}} = r_i\Omega_i d/\nu \tag{8}$$

where, η is the ratio of the inner to outer cylinder radius ($\eta = r_i/r_o$), d is the gap between the two cylinders and ν is the kinematic viscosity of the dispersion. Here, the kinematic viscosity of the solvent was used as an approximation, since the effect of the presence of graphene on the kinematic viscosity of the dispersion was deemed to be negligible. Finally, the shear rate was obtained for each Reynolds number:

$$\dot{\gamma} = \frac{G_i \nu}{2\pi r_o^2} \tag{9}$$

The value of Re_c was calculated using an expression proposed by Esser et al. [25] and applying the small gap approximation ($\eta \to 1$) [24]:

$$Re_c = \sqrt{\frac{1708}{-R_\Omega(R_\Omega + 1)}} \tag{10}$$

where $R_\Omega = (1-\eta)(Re_\mathrm{i} + Re_\mathrm{o})/(\eta Re_\mathrm{o} - Re_\mathrm{i})$

The corresponding calculated results and flow regimes can be seen in Figure 3 The three experimental rotational speeds with *Re* 1277, 1483, 2128 fell into the WVF regime. In this regime, the flow is time-dependent due to the presence of an azimuthal wave, and the vortices deform. One could visualise WVF as pairs of counter-rotating toroidal vortices, whose intersections form waves. Higher Reynolds numbers result in better mixing and hence, higher mass transfer coefficients [26], which could be very advantageous in the exfoliation of graphite.

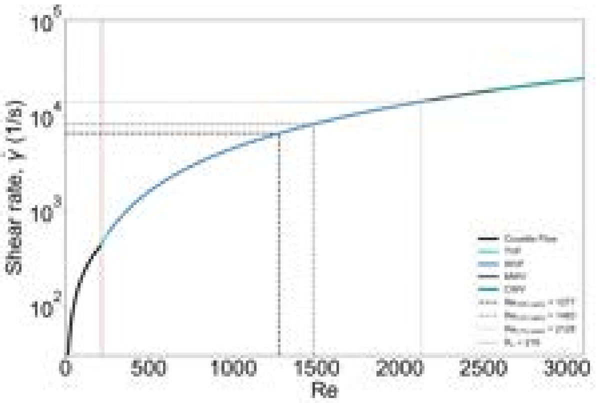

Figure 3: Shear rate, $\dot{\gamma}$ as a function of Reynolds number, *Re*. The different colours indicate the different flow regimes inside the Taylor-Couette device.

3.5 Centrifugation of samples

Exfoliated samples were centrifuged to remove any unexfoliated graphite. Centrifugation is a mechanical process of speeding up natural sedimentation, where heavier particles (graphite) tend to settle at the bottom of the centrifugation tube due to gravitational forces. The relative centrifugal force (RCF) of the centrifuges is given by:

$$RCF = (RPM/1000)^2 \times r \times 1.118 \tag{11}$$

where *RPM* is the rotational speed of the centrifuge (rotations per minute) and *r* is the centrifugal radius in mm.

3.6 UV-Vis-nIR spectroscopic measurements

To assess the concentration of the produced graphene, samples underwent UV-vis-nIR spectroscopic analysis. Recent work has shown that spectroscopic data can be used directly to determine the concentration of graphene by using the appropriate parameters in the Beer-Lambert law [17] [27]

$$E = \varepsilon C_g l \tag{12}$$

where C_g is the graphene concentration, E is the measured absorbance intensity, l is the length of the cuvette used (= 10 mm), and ε is the extinction coefficient taken as 398 g/L [17].

In addition, empirical correlations have been deduced to determine the average layer number, $\langle N \rangle$, using absorbance measurements [27].

$$\langle N \rangle = 40.5 \times \alpha_{550}/\alpha_{390} - 25.5 \tag{13}$$

where α_{550} is the absorbance intensity at 550 nm, where the spectra of Cyrene dispersion has a gradient of approximately zero, and α_{390} is the absorbance intensity at the $\pi - \pi^*$ region (taken at $\sim$ 390 nm). This equation was modified compared to what Backes et al. [27] presented. In their work, the $\pi - \pi^*$ region occurs around 325 nm, whereas in this study, it was found to occur closer to 390 *nm*. This was the point where absorbance effects due to the presence of Cyrene were minimal and the signal due to the presence of graphene was most distinguishable. The error of 20% suggested by Backes et al. [27] was taken into account for these calculations.

4 Results and Discussion

4.1 Effect of shear rate on graphene production yield

The concentration of graphene dispersion obtained demonstrated a positive dependence on the processing time, as seen in Figure 4. This was to be expected, as the more time the graphite flakes spend inside the system, the higher the probability there is that they will get exfoliated, which is in agreement with the work of Stafford et al. [13]. For the lowest rotational speed, i.e., 105 rad/s, the graphene concentration increased monotonically and linearly with respect to the processing time. The concentration profiles for the other two operating conditions, however, exhibited two distinct phases. The graphene concentration increased linearly with time up to a certain point, i.e., t_{sat}, after which concentration plateaued. This is the point of saturation, thereafter exfoliation is no longer productive. From qualitative observations, this occured in the Taylor-Couette device due to deposition of graphitic material on the inner cylinder walls, which effectively decreased the overall graphite concentration and provided less available particles for exfoliation. Deposition itself occurred due to the centrifugal force that the particles experience inside the rapidly rotating inner cylinder. At higher rotational speeds, one would expect the deposition of graphite to be more pronounced, due to higher centrifugal forces and thus, a decrease in t_{sat} [18]. However, this was not the case here. Saturation was reached after $\sim$ 2.1 hours at 175 rad/s, and $\sim$ 1.7 hours at 122 rad/s (see Figure 4). Nevertheless, this was still within the depicted error bounds.

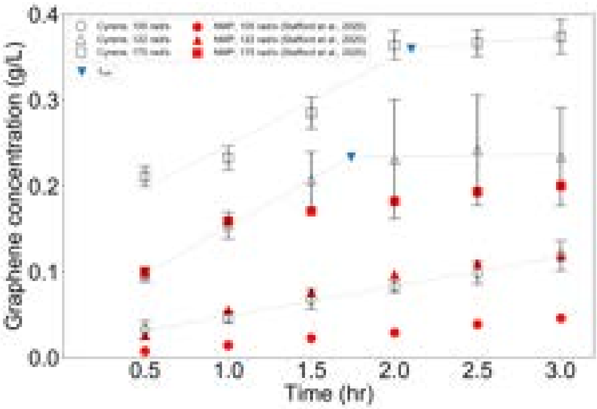

Figure 4: Graphene concentration as a function of processing time for varying speeds of exfoliation for cyrene and NMP. NMP data extracted from Stafford et al. [13].

As previously mentioned, a minimum shear rate requirement has to be fulfilled before exfoliation can occur [11]. Given Equations (3) - (9), it could be concluded that the simplest way to increase the shear stress is to increase the rotational speed of the inner cylinder. As mentioned in Section 3.4, the flow regime inside the exfoliator was WVF, meaning that a power law relationship exists between the shear rate and the rotational speed, i.e., $\dot{\gamma} \sim \omega^{3/2}$. Therefore, a higher shear stress would be forced upon the particles making exfoliation more likely, and thus, resulting in higher graphene concentration. This trend can be evidently seen in Figure 4.

Nevertheless, the end-goal of this study was not only to assess the performance of Cyrene relative to NMP, but to also assess the scalability of this process. A trade-off can be identified between higher graphene concentrations and continuous operating time. On the one hand, higher rotational speeds lead to higher product concentrations, but on the other hand, saturation was reached much faster. In a large-scale graphene production plant, this could mean that operation would be halted more frequently to remove the deposited graphite from the inner cylinder walls and thus, more maintenance would be required. Therefore, costs could potentially increase and production would not be as efficient.

Stafford et al. [13] obtained similar trends to what was observed here, using an identical exfoliation rig and rotational speeds. Interestingly, Cyrene seems to have significantly outperformed NMP, as for the same energy input, one could obtain up to 160% higher graphene concentrations with Cyrene as a working solvent. This was attributed to the closer-matching Hansen solubility parameters of graphene and Cyrene (discussed below in detail) that effectively minimise the Flory-Huggins interaction parameter, χ and in turn, the energetic cost of exfoliation. Apart from this, a major difference between the two solvents was the kinematic viscosity. Salavagione et al. [17], rationalise the higher concentration of dispersed graphene in Cyrene through an increase in kinematic viscosity relative to NMP. Cyrene has a kinematic viscosity of 8.47 $\mu\text{m}^2/\text{s}$, which is more than 5 times greater than that of NMP, i.e., 1.65 $\mu\text{m}^2/\text{s}$ [17]. Therefore, graphene flakes in the dispersion have a lower settling velocity, which contributes to a higher concentration of graphene after centrifugation. Yet, the estimated thickness of graphene particles are within the same range as for those obtained using NMP [13].

In spite of that, a lower concentration of graphene in Cyrene dispersion was expected, due to the nature of the flow inside the Taylor-Couette exfoliator. The relationship between the shear rate and the kinematic viscosity in the WVF regime is $\dot{\gamma} \sim \nu^{-0.5}$ (see Equation (4)), and so, for the same rotational speed, the shear rate in an NMP dispersion is greater, due to lower kinematic viscosity. As such, a higher graphene concentration with NMP would be anticipated. Since this was not the case, it could be concluded that the resulting concentration is dominated primarily by the centrifugation process, since sedimentation rate of particles is proportional to liquid viscosity and difference between the particle and liquid densities. For instance, the density of NMP is lower than that of Cyrene by $\sim$ 20% .

Noteworthy was also the fact that for processing times above 2 hr at ω = 175 rad/s, the produced graphene concentration also surpassed the ones reported by Salavagione et al. [17] ($C_{g,i} = 0.24$ g/L), which is one of the few reported works with Cyrene as a solvent. It should be noted, however, that the exfoliation method used in their work was ultrasonication.

4.2 Effect of shear rate on graphene thickness

Evident from the increasing graphene concentration with shearing rate and processing time, it is valid to claim that $\dot{\gamma} > \dot{\gamma}_{min}$, yet the estimation of $\dot{\gamma}_{min}$ requires data on graphene lateral size, which can be acquired using AFM analysis, but was outside the scope of this present study. In addition, evidence from UV-Vis spectroscopic measurements also proved the exfoliation of graphite to graphene with $\langle N \rangle < 10$ (Figure 5(c) - (d)). The range of average layer numbers acquired, i.e., $5 \leq \langle N \rangle \leq 7$, is lower than what was previously reported by Farooq [18], who followed an identical exfoliation procedure and centrifu-

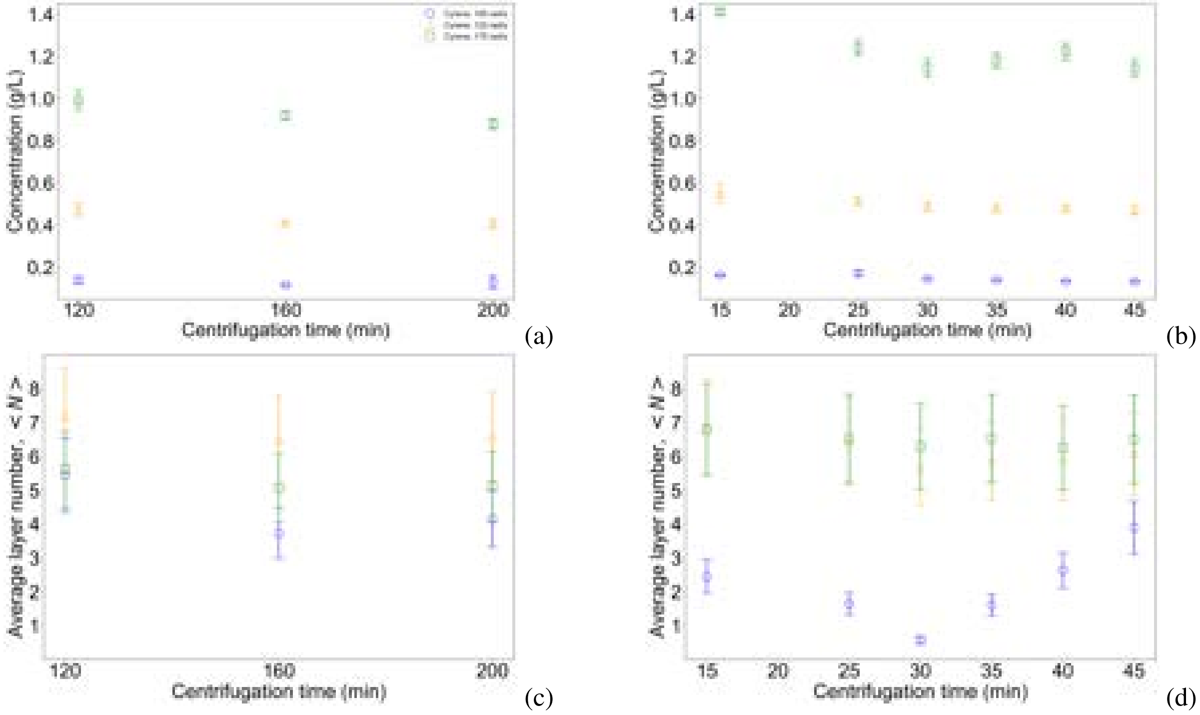

Figure 5: (a) Concentration of final product against centrifugation time for varying rotational speeds in centrifuge of 190g RCF (b) 290g RCF (c) Average layer number $\langle N \rangle$ of final product against centrifugation time for varying rotational speeds in centrifuge of 190g RCF (d) 290g RCF.

gation protocol. However, it should be noted that here, a different expression was used to calculate $\langle N \rangle$ (see Equation (13)).

Nevertheless, no substantial trend was observed between the different rotational speeds, as there was significant error ($\sim$ 20%) in the calculation of $\langle N \rangle$. The average $\langle N \rangle$ produced by 105 rad/s, 122 rad/s and 175 rad/s was 3.58, 6.35 and 5.85, respectively. Interestingly, the lowest rotational speed produced the smallest $\langle N \rangle$ and the intermediate rotational speed produced the highest $\langle N \rangle$. This observation was also made by Farooq [18].

4.3 Separation of graphene by centrifugation

The effect of centrifugation for separation of the final product was assessed. As indicated in Figure 5(a) - (b), similar trends for both centrifuges were observed, with an initial average decrease of 13% in the low RCF centrifuge (from 120 to 160 minutes) and 15% in the high RCF centrifuge (from 15 to 30 minutes). Concentration values then remained relatively constant with an overall change of 4% in both centrifuges (from 160 min and 30 min onward). Additionally, the 290g (high) RCF centrifuge produced higher concentrations in the final product with an average increase of 15.0% for both 105 rad/s and 122 rad/s, and 27.3% for 175 rad/s, relative to the values obtained from samples processed in the 190g (low RCF) centrifuge.

An analogous trend was noted for $\langle N \rangle$ (Figure 5(c) - (d)) wherein the average layer number initially decreased on average by 17% for both centrifuges (at 160 min and 30 min). After these points, for both centrifuges, the average layer number values stabilised with an overall change of 4%. No difference in produced graphene layer number was noticed between the two centrifuges ($5 \leq \langle N \rangle \leq 7$ in the 190g centrifuge, and $6 \leq \langle N \rangle \leq 7$ in the 290g centrifuge).

Overall, the similar behaviours of concentration and $\langle N \rangle$ were attributed to two factors. Firstly, it was believed that the higher kinematic viscosity and density of Cyrene relative to NMP would have impeded the effects of centrifugation. The second factor which justified the behaviour was the fact that the samples reached their isopycnic points during centrifugation. At this point the working solvent (Cyrene) and dispersed particle densities are matched. Separation will therefore, not depend on size differences but will be achieved through differences in densities of particles in the dispersion. As graphene and graphite have almost identical densities, separation will become extremely slow and changes in concentration will be minimal. Furthermore, the matching densities will in turn lead to graphene and graphite particles mixing and begin restacking, thus slightly increasing $\langle N \rangle$ after the isopycnic point is reached. Comparing all results in Figure 5, it was determined that the isopycnic point occurred close to 160 minutes for the low RCF centrifuge, and at around 30 minutes for the high RCF one.

Additionally, the error of 20% reported in Equation (13) used for establishing the average layer number was clearly higher than that of the concentration values ($\leq$ 4.5%). Taking this into account, it was also possible to deduce that no significant trend was identifiable as values of $\langle N \rangle$ would overlap for all operating conditions in both centrifuges. Even so, the values obtained here had insignificant variation between them, therefore the establishment of a specific trend would have no effect in the overall picture presented.

Overall, centrifugation time did not seem to affect results due to the stabilisation noticed for both properties. The RCF of centrifuge was found to affect the final concentrations of graphene produced, with the $290g$ centrifuge outperforming the $190g$ one. This occurred because of the higher intensity of centrifugation present in the former, caused by the larger g forces. Here, the important outtake was that using a centrifuge of higher intensity could produce better results in concentration, with similar layer numbers for a significantly shorter processing time (15 minutes compared to 120 minutes). This was a crucial observation which could largely benefit both the industry in case of a scale-up of the process and any future experiments.

4.4 Evaluation of cyrene dispersion and storage performance

Looking at the equations presented in Section 3.3 an appropriate solvent would be one that minimises the enthalpy of mixing and χ through matching of the δ parameters [1] [14] [15]. Values for these parameters were obtained as shown in Table 2.

Table 2: Hansen solubility parameters and surface tensions [17].

Component	Graphene	NMP	Cyrene
δ_D $(MPa^{1/2})$	18	18	18.8
δ_P $(MPa^{1/2})$	9.3	12.3	10.6
δ_H $(MPa^{1/2})$	7.7	7.2	6.9
E (mN/m)	38.2	40.7	31.3
R	-	3.0	1.7
$(\delta g - \delta i)^2$	-	6.2	47.3

It became evident from this theoretical analysis that Cyrene outperformed NMP in the Hansen parameters, since it had almost half the value of R, which indicated that it would be a more suitable dispersion solvent than NMP. As seen from the experimental results of the exfoliation process in Section 4.1, Cyrene was proven to produce higher concentrations than NMP for the same operational parameters, confirming this prediction.

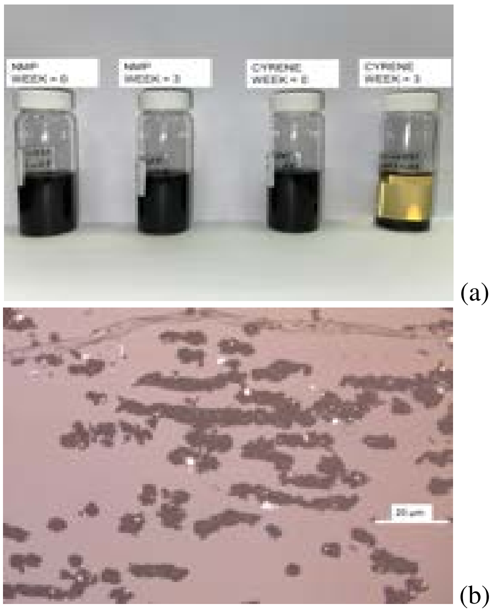

Figure 6: (a) Cyrene and NMP graphene dispersions freshly made and after settling for 3 weeks. (b) Image of Raman spectroscopy showing carbon nanotube (top) and agglomerates of cyrene dispersion.

This was, however, not the case for the surface tensions. NMP has a surface tension which is significantly closer to graphene's than Cyrene and this was expected to also have an effect in some aspect of the results. Although the graphene produced seemed to be unaffected by this inferior result, a visual observation was made; Figure 6 compares the behaviour of the graphene dispersion in Cyrene and NMP. It was clear that in the case of Cyrene, graphene particles separated and agglomerated more significantly (at the bottom of the solution) when compared to NMP after 3 weeks of storage. It is believed that this effect can be justified by the larger surface tension difference between Cyrene and graphene in comparison to NMP, causing graphene to be less soluble in the Cyrene solution and leading to its sedimentation. This also alluded to Cyrene being a poor solvent for graphene dispersion storage. Nevertheless, surface tension is not a sufficient property on its own for a terminal decision to be made, as it typically influences the solubility of a component in combination with the dipole moment and Hilderbrand parameter of the solvent in which the component is dispersed [28].

5 Conclusions and Outlook

Overall, this study achieved the predetermined aims discussed previously. Cyrene, a new and sustainable solvent, was assessed as an alternative to NMP, a conventional, high-performing but toxic solvent, to be used in LPE of graphite. This entailed running experiments on a bench-scale Taylor-Couette device, patented by Imperial College London, followed by a strict centrifugation protocol and UV-Vis-nIR characterisation. Information on the average layer number and graphene concentration were obtained.

The increase in shear rate exerted on the graphite flakes, significantly increased the likelihood of exfoliation and gave higher graphene concentrations. The same conclusion was made with an increasing processing time. However, for higher rotational speeds, the dispersion eventually reached saturation and the concentration plateaued, after about 2 hours. Comparing the performance of Cyrene to that of NMP, it was found that Cyrene provided an increase in graphene concentration of up to 160% after centrifugation. Moreover, it was established that to obtain a desired graphene concentration, one would need a lower rotational speed, and hence a lower energetic input. Conversely, for the same rotational speed and product concentration, Cyrene cut down the required processing time by up to 3 times. Yet, graphene in Cyrene dispersions were qualitatively observed to agglomerate more readily than NMP after 3 weeks of storage, suggesting that Cyrene may not be suitable for long-term storage.

In addition, the effect of varying centrifugal parameters on the graphene product was investigated. It was found that the higher the relative centrifugal force, the higher the concentration of graphene produced with an increase of up to 27% between $290g$ and $190g$. An initial decrease followed by a stabilisation of both concentration and average layer number of the product was noted over the course of the centrifugation period. The latter was found to be unaffected by the relative centrifugal forces and remained within the range of $5 \leq \langle N \rangle \leq 7$.

The implications of these observations on the large-scale applicability of LPE of graphite are major. They also indicated the possibility of optimisation of the production process. Exfoliation time should not continue longer than the saturation time, otherwise the inner cylinder should be cleaned at regular time intervals so as to delay saturation. Regardless, this study showed that continued operation beyond the point of saturation is unfruitful. On top of that, it was shown that centrifugation times can be minimised significantly by switching to a higher-RCF centrifuge. The same degree of separation was achieved in 15 minutes with RCF = $290g$, as opposed to 120 minutes with RCF = $190g$. Lastly, Cyrene, apart from its environmental advantages, has strong potential in making the process more efficient and scalable, by remarkably cutting down costs and energy requirements.

With regards to possible future work it is advised that centrifugation experiments should be run for shorter times ($<$ 120min, $<$ 15min) to examine the possibility of any trends arising in the shorter range. A further look into the physical properties of Cyrene would be beneficial, allowing for justification of certain of the trends observed, especially in the storage aspect. Samples produced could also be analysed by Raman spectroscopy, Atomic Force Microscopy (AFM) and Transmission Electron Microscopy (TEM) technologies to verify the average layer number reported and gain additional data about flake size and the defects of the graphene produced. During experiments, a lot of human labour was required. For this, the usage of automated sampling could be introduced to ensure that collection is performed identically throughout and the human error can be minimised. Finally, the optimisation of the procedure can be enhanced in any future experiments by utilizing the shorter time results using the higher RCF centrifuge.

Acknowledgements

The authors would like to thank Prof. Omar Matar, Prof. Camille Petit and Dr. Jason Stafford for their continual support during this project. Thanking is also expressed towards Dr. Andrius Patapas for providing his essential insight and assistance that helped this project progress, and Dr. Usmaan Farooq for providing the methodology for this work in his PhD thesis.

Supplementary Information

A supplementary document is provided which includes raw data from the UV-Vis measurements.

References

[1] Jason Stafford et al. "Towards scale-up of graphene production via nonoxidizing liquid exfoliation methods". In: *AIChE Journal* 64.9 (2018), pp. 3246–3276.

[2] Mathis Wissler. "Graphite and carbon powders for electrochemical applications". In: *Journal of Power Sources* 156.2 (2006), pp. 142–150.

[3] Zhong-Shuai Wu et al. "Synthesis of high-quality graphene with a pre-determined number of layers". In: *Carbon* 47.2 (2009), pp. 493–499.

[4] Kathrin C. Knirsch et al. "Screening of the chemical reactivity of three different graphite sources using the formation of reductively alkylated graphene as a model reaction". In: *Chemical Communications* 49.92 (2013), pp. 10811–10813.

[5] Nina V. Kozhemyakina et al. “Effect of the Structure and Morphology of Natural, Synthetic and Post-processed Graphites on Their Dispersibility and Electronic Properties”. In: *Fullerenes, Nanotubes and Carbon Nanostructures* 21.9 (2013), pp. 804–823.

[6] Yoshihiko Arao et al. “Efficient solvent systems for improving production of few-layer graphene in liquid phase exfoliation”. In: *Carbon* 118 (2017), pp. 18–24.

[7] Konstantin S. Novoselov et al. “Electric field in atomically thin carbon films”. In: *Science* 306.5696 (2004), pp. 666–669.

[8] Dimitrios G. Papageorgiou et al. “Mechanical properties of graphene and graphene-based nanocomposites”. In: *Progress in Materials Science* 90 (2017), pp. 75–127.

[9] Min Yi et al. “A review on mechanical exfoliation for the scalable production of graphene”. In: *Journal of Materials Chemistry A* 3.22 (2015), pp. 11700–11715.

[10] Ying Wei et al. “Liquid-phase exfoliation of graphite for mass production of pristine few-layer graphene”. In: *Current Opinion in Colloid Interface Science* 20.5 (2015), pp. 311–321.

[11] Keith R. Paton et al. “Scalable production of large quantities of defect-free few-layer graphene by shear exfoliation in liquids”. In: *Nature Materials 2014 13:6* 13.6 (2014), pp. 624–630.

[12] Eswaraiah Varrla et al. “Turbulence-assisted shear exfoliation of graphene using household detergent and a kitchen blender”. In: *Nanoscale* 6.20 (2014), pp. 11810–11819.

[13] Jason Stafford et al. “Real-time monitoring and hydrodynamic scaling of shear exfoliated graphene”. In: *2D Materials* 8.2 (2021), p. 025029.

[14] Yenny Hernandez et al. “High-yield production of graphene by liquid-phase exfoliation of graphite”. In: *Nature Nanotechnology 2008 3:9* 3.9 (2008), pp. 563–568.

[15] Yenny Hernandez et al. “Measurement of multicomponent solubility parameters for graphene facilitates solvent discovery”. In: *Langmuir* 26.5 (2010), pp. 3208–3213.

[16] Chih Jen Shih et al. “Understanding the stabilization of liquid-phase-exfoliated graphene in polar solvents: Molecular dynamics simulations and kinetic theory of colloid aggregation”. In: *Journal of the American Chemical Society* 132.41 (2010), pp. 14638–14648.

[17] H. J. Salavagione et al. “Identification of high performance solvents for the sustainable processing of graphene”. In: *Green Chemistry* 19.11 (2017), pp. 2550–2560.

[18] Usmaan Farooq. “Exploring graphene exfoliation using thin film and Taylor Couette flow in a rotating cylinder device”. In: *Thesis, Imperial College London* (2021).

[19] Shane D. Bergin et al. “Multicomponent solubility parameters for single-walled carbon nanotube-solvent mixtures”. In: *ACS nano* 3.8 (2009), pp. 2340–2350.

[20] Chih Jen Shih et al. “Understanding the stabilization of liquid-phase-exfoliated graphene in polar solvents: Molecular dynamics simulations and kinetic theory of colloid aggregation”. In: *Journal of the American Chemical Society* 132.41 (2010), pp. 14638–14648.

[21] Yasushi Takeda. “Quasi-periodic state and transition to turbulence in a rotating Couette system”. In: *Journal of Fluid Mechanics* 389 (1999), pp. 81–99.

[22] P. R. Fenstermacher et al. “Dynamical instabilities and the transition to chaotic Taylor vortex flow”. In: *Journal of Fluid Mechanics* 94.1 (1979), 103–128.

[23] B Dubrulle et al. “The European Journal B: Momentum transport and torque scaling in Taylor-Couette flow from an analogy with turbulent convection”. In: *Eur. Phys. J. B* 26 (2002), pp. 379–386.

[24] B Dubrulle et al. “Stability and turbulent transport in Taylor-Couette flow from analysis of experimental data ”. In: *Physics of Fluids* 17 (2005), p. 1814.

[25] Alexander Esser et al. “Analytic expression for Taylor–Couette stability boundary”. In: *Physics of Fluids* 8.7 (1998), p. 1814.

[26] Marouan Nemri et al. “Experimental and numerical investigation on mixing and axial dispersion in Taylor–Couette flow patterns”. In: *Chemical Engineering Research and Design* 91.12 (2013), pp. 2346–2354.

[27] Claudia Backes et al. “Spectroscopic metrics allow in situ measurement of mean size and thickness of liquid-exfoliated few-layer graphene nanosheets”. In: *Nanoscale* 8.7 (2016), pp. 4311–4323.

[28] Dimitrios Konios et al. “Dispersion behaviour of graphene oxide and reduced graphene oxide”. In: *Journal of Colloid and Interface Science* 430 (2014), pp. 108–112.

Analysis of Data-Driven and Hybrid Modelling Techniques for Online State-of-Charge Estimation in Lithium-Ion Batteries

D. W. Adams and P. de Metz

Department of Chemical Engineering, Imperial College London, South Kensington Campus, London SW7 2AZ, United Kingdom

16th December 2021

Abstract

As a consequence of multinational pledges of net-zero agenda and improving consumer awareness of the dangers posed by climate change, the adoption of electric vehicles is expected to accelerate throughout this decade. This trend will be a key driver for growth in the lithium-ion battery market, which is projected to expand at a compound annualised growth rate (CAGR) of 12.3% to reach USD 116.6 bn by 2030. To prevent overheating during battery operation, quick and accurate estimation of State-of-Charge (SoC) is of paramount importance. Since the turn of the millennium, data-driven techniques such as Artificial Neural Networks (ANNs) have drawn increasing attention in the literature for their ability to estimate SoC. The nonparametric character of data-driven models enables them to capture small perturbations in SoC that are inaccessible to more traditional reduced-order mechanistic models. However, it has been shown that data-driven models struggle to maintain prediction quality when extrapolating to discharge cycles with unfamiliar characteristics. In recent literature, hybrid modelling techniques combining elements of mechanistic and data-driven models have demonstrated superior prediction quality over their standalone constituent components. Their data-driven component can improve the accuracy of the mechanistic model without significantly increasing computational load. On the other hand, the mechanistic component can improve generalisation over lone data-driven models.

This study encompasses a thorough analysis of data-driven techniques for SoC estimation. The best performing model, a NARX fitted on a Support Vector Regressor (SVR), is then incorporated in two parallel hybrid architectures with an Equivalent Circuit Model (ECM). Within the hybrid structures, the constituent NARX-SVR predicts the error (ΔSoC_{NARX}) in the ECM's prediction (SoC_{ECM}). ΔSoC_{NARX} is then summed with SoC_{ECM} to yield a final prediction. These architectures are demonstrated to improve the accuracy of SoC estimation over the standalone NARX and ECM, achieving an average improvement in RMSE of 90% - a strong endorsement of their suitability for online applications.

Keywords: Hybrid model, Data-driven model; Mechanistic model; State-of-charge; NARX; Equivalent circuit model; Support Vector Regression

1. Introduction

Lithium-ion batteries (henceforth, “Li-ion batteries”) were first developed in 1985 by Akira Yoshino based on research from John Goodenough and M. Stanley Whittingham - a feat worthy of the 2019 Nobel Prize in Chemistry.

Characterised by their relatively high energy density, low cost and ease-of-maintenance, Li-ion batteries quickly captured the dominant market share in transport, consumer electronics and stationary storage applications (Electronics Notes, 2021). The market for Li-ion batteries is projected to grow at a compound annualised growth rate (CAGR) of 12.3% to USD 116.6bn by 2030 (PRNewswire, 2021). This expansion will primarily be driven by growth in the electric vehicle market - a trend driven by multinational pledges of net-zero agenda and improving consumer awareness of the dangers posed by climate change (Lu & Frith, 2019).

Battery discharge is achieved by moving lithium ions from the anode to the cathode through an electrolyte where the ions subsequently recombine with their electrons and electronically neutralise (University of Washington, 2021).

State-of-charge (SoC) is a key measure of Li-ion battery performance and is readily defined as,

$$SoC = \frac{Q_{curr}}{Q_{max}} \tag{1}$$

where Q_{max} is the maximum charge that can be stored in the battery and Q_{curr} is the current charge of the battery (Biologic, 2021). Therefore, SoC is a measure of the remaining energy stored in the battery, defined relative to the maximum storage capacity (Bhattacharjee et al., 2021).

Battery performance is affected by a plethora of internal and external phenomena including battery chemistry, internal and ambient temperature, cycle frequency and current loads applied (Xiong, 2019). As SoC is not directly measurable, it is critical that Li-ion batteries are integrated with a battery management system (BMS) that can estimate it from observable parameters (Bhattacharjee et al., 2021). The BMS is critical in preventing “overcharging” and “trickle charging” - continuing to apply current even when the battery is at maximum capacity and the perpetual topping up of the battery to 100%, respectively. If left unchecked, these phenomena can generate undesirable excess heat, potentially leading to a fire or explosion (Bian et al., 2020). Therefore, it is paramount that the BMS can quickly and accurately estimate the SoC Li-ion batteries in online applications. The following study encompasses:

- Generation of dynamic driving cycles with the LIONSIMBA simulation toolbox (Torchio et al., 2016)
- An evaluation of a range of data-driven modelling techniques for SoC prediction trained and tested on the generated dynamic driving cycles
- Integration of the best performing data-driven model with a reduced-order mechanistic model to produce hybrid models for SoC estimation

2. Background

The most accurate modelling technique for Li-ion batteries is pseudo-two-dimensional (P2D) models. P2D models utilise a large number of partial differential equations (PDEs) and exhaustive parameter sets to accurately capture the dynamics of Li-ion batteries (Torchio et al., 2016). Though, in online applications, this methodology is prohibitively expensive from a computational perspective. Thus, there exists a need to develop lightweight models for estimation of SoC in online settings.

2.1 Literature review of SOC estimation methods

In recent literature, a number of methodologies for predicting SoC have been explored. These include:

a) **Mechanistic methods** include the aforementioned P2D model; the Single Particle Model (SPM), in essence a reduced-order P2D model; and Equivalent Circuit Models (ECMs), which utilise individual electronic components to represent the desired cell. Each of these methods leverage known parameters of the battery to accurately predict properties such as Voltage, Current and SoC. These predictions are facilitated via a range of algorithms, the most popular of which is the Kalman filter (henceforth, "KF"). With the exception of the P2D model, mechanistic methods tend to offer a good compromise between accuracy and complexity (Rzepka, 2021).

Significant attention has been paid to mechanistic models in the literature. Torchio et al. (2016) introduced a finite volume P2D model by means of a series of partial differential equations (PDEs). The model, commonly referred to as "LIONSIMBA", is suitable for Li-ion battery design, simulation and control. Liu et al. (2014) proposed an adaption of the ECM, introducing electrolyte dynamics to more effectively capture complex internal phenomena. Similarly, Moura et al. (2017) developed a SPM which accounted for electrolyte effects. Kalman filtering is a recursive method to estimate unknown states in a process. While Kalman filtering is not a new methodology, there continues to be a number of interesting developments surrounding it. Pan et al. (2017) presented a "grey extended KF" for SoC prediction which draws on a combination of prior process data and defined model parameters. Building on work of Pan et al. (2017) and others, Shen (2018) proposed an "adapative extended KF" to circumvent issues posed by weak initial guesses. In a more significant break from traditional extended KFs, Cong Jiang (2021) utilised a similar adaptive technique to introduce an "adaptive square-root KF". By removing rounding errors, this further strengthened prediction accuracy, particularly in more severe discharge cycles.

b) **Coulomb counting methods** predict the current flowing in and out of the battery to determine the amount of energy which has entered or left the battery. A notable drawback of this method is its requirement for initial values to be provided. This, alongside an inability to capture more complex internal dynamics, hinders its viability in BMSs.

There have been several attempts to counter these drawbacks in the literature. Kim et al. (2013) introduced an enhanced Coulomb counting method utilising a SoC compensator in tandem with a particle swarm optimisation algorithm. The initial SoC is provided via hybridising with an ECM. Other approaches have employed "look-up tables", which detail known relations between measurable quantities and SoC. Haq et al. (2016) demonstrated the use of look-up tables in initial SoC estimation to complement a coulomb counting system.

c) **Data-driven estimation methods** include Artificial Neural Networks (ANNs) and other learning algorithms. Examples of these include Recurrent Neural Networks (RNNs) and Long Short-Term Memory networks (LSTMs). These models are "trained" with known battery data and in-tern "learn" a series of weights and biases that can effectively predict SoC. As they do not require prescriptive parameter definitions, data-driven models benefit from reduced computational load and development time (M.S. Hossain Lipu, 2020). One caveat is the sheer quantity of data required to perform the initial training. Moreover, prediction quality can rapidly decline when predicting the SoC of drive cycles with unfamiliar characteristics.

In recent years, there has been a significant increase in the prevalence of data-driven methods for SoC estimation sin literature. In a recent publication, Li et al. (2021) presented an RNN architecture achieving less than 3% prediction error. This approach also incorporated corrections for battery degradation. LSTMs, which differ to RNNs through their ability to carry "weights" throughout the full length of the network (detailed in Section 3.2), have also been successfully employed. Oyewole et al. (2021) proposed an LSTM architecture which leverages the predictions of other ANNs in series. This was demonstrated to be particularly effective for batteries with significantly depleted capacity. Sidhu et al. (2019) presented an architecture with a random forest regressor and a Gaussian filter. Gaussian filters are commonly employed to combat the "zig-zagging" phenomenon that can arise from use of non-zero-centered activation functions such as the sigmoid. In a more creative approach, Ordás et al. (2021) successfully demonstrated the use of ANNs in tandem with k-Means and agglomerative clustering for SoC estimation. Lipu et al. (2018) utilised a recurrent NARX neural network model-based lightning search algorithm. NARX's have been widely employed for SoC estimation due to their strength in handling nonlinear data. They are explored in more detail in Section 3.2.

d) **Hybrid models** combine two or more modelling techniques into one predictive model with the goal of using each component's strengths to cover the drawbacks of the other. Common hybrid configurations can broadly be categorised as "series" or "parallel", though more bespoke architectures have been explored (von Stosch et al., 2014).

While hybrid modelling techniques are not a new concept, it is only more recently that their application in online BMSs has gained significant prevalence in literature. Chang (2013) proposed a hybrid method combining a radial bias function (RBF) neural network, an orthogonal least-squares (OLS) algorithm and an adaptive genetic algorithm (AGA). Feng et al. (2020) introduced a hybrid electrochemical-thermal hybrid architecture composed of a SPM, a lumped thermal model and an ANN. Predictions were then fed to an unscented KF. Caliwag & Lim (2019) utilised a hybrid vector auto-regressive moving average VARMA-LSTM model. Son et al. (2020) proposed a hybrid of an unscented particle filter and a least-square support vector machine.

A common theme in the literature is the combination of mechanistic and data-driven models. The parametric character of the mechanistic model enables the system to generalise more strongly than standalone data-driven models. Though, as reduced-order mechanistic models struggle to predict smaller perturbations in SoC, data-driven models serve as a useful supplement to improve prediction accuracy.

3. Methodology

3.1 Data generation

3.1.1 LIONSIMBA

The LIONSIMBA Toolbox is a MATLAB framework based on a finite volume P2D model suitable for Li-ion battery design, simulation, and control (Torchio et al., 2016). Compared to commercial software such as COMSOL MultiPhysics, the toolbox provides satisfactory performance for the simulation of Li-ion batteries by means of 59 internal and external parameters. Therefore, it is considered a suitable framework to generate the discharge cycle data for this study.

3.1.2 Real-world datasets & characteristic drive cycles

When generating synthetic data to mimic experimentally-generated data, utmost care should be taken to ensure the representation is accurate. To maximise the validity of the P2D-generated discharge cycles, real-world datasets were first analysed to extract their characteristic features. A wide range of experimental battery datasets are publicly available, among the most heavily referenced are the "Randomised Battery Usage Datasets" (Lee et al., 2007). These datasets, compiled at NASA, contain drive cycles for Lithium Cobalt-Oxide (LCO) 1850 cells operated continuously for 50 discharge cycles. In each cycle, the cells are charged and discharged within a discharge distribution table (dos Reis & Li, 2020). Another popular dataset is that of Steinstraeter et al. (2020), where data for 72 discharge cycles in BMW i3 cars is provided.

To ensure the training data accurately represented real-world data, drive cycles were enhanced with the characteristics of the battery datasets from Lee et al. (2007) and Steinstraeter et al. (2020). Cox (2020) found that the variance in the current densities input to the battery in Steinstraeter et al. (2020) can be characterised by a normal distribution. This normal distribution takes the same parameters as the NASA battery usage dataset 6: $\mu = -8.4Am^{-2}$ and $\sigma = 21.6Am^{-2}$ (B. Bole & Daigle, 2014). To reduce the influence of anomalous drive cycles on model predictions, the normal distribution was truncated within the range -6C and 3C.

For each driving cycle the initial SoC was varied between 10% and 90%. This wide range of initial values will provide sufficient diversity to the training dataset to equip the model to perform well in real-world use cases. In addition, the depth of discharge (DoD) of each discharge cycle was varied randomly between 0% and the initial value of the SoC.

Half of the generated cycles maintain a fixed ambient temperature of $25°C$ to facilitate an initial evaluation of model performance. In the other half, initial ambient temperature was randomly varied between $-10°C$ and $50°C$. The varied temperature datasets enable study of model performance in conditions more representative of real-life, where ambient temperature naturally varies.

Lastly, to ensure consitency with Lee et al. (2007) and Steinstraeter et al. (2020), and to increase the resolution of predicted SoC, a constant timestep of 0.5s was chosen.

To adequately assess the ability of the models to generalise, a number of "testing" cycles were also generated. Two characteristic discharge cycles detailed by the US Environmental Protection Agency (EPA) were utilised. These include the EPA Urban Dynamometer Driving Schedule (UDDS) and the New York City Cycle (NYCC) (United States Environmental Protection Agency, 2021). To supplement this, two constant current discharge cycles were generated, one with a high rate of discharge ($-6C$) and one with a low rate of discharge ($-1C$), where a negative sign indicates the discharge of the battery in line with Cox (2020). In doing this, it is indirectly assumed that input currents to the battery are proportional to the acceleration of the car - the maximum car acceleration corresponding to the maximum possible discharge current ($-6C$). Lastly, a complete discharge-only cycle was generated from 90% to 0% with a discharge current randomly varied between $-6C$ and $-3C$ at each timestep. Maximum SoC is limited to 90% as LIONSIMBA cannot generate cycles above this threshold.

Lastly, a degree of "regenerative breaking" is incorporated in the cycles. Regenerative breaking is a process by with cars convert kinetic energy back into stored electrical energy while breaking. For the purposes of this study, this value is set at 40% in line with (Björnsson & Karlsson, 2016). This assumption is a significant simplification of reality, though it is useful for exploratory studies, as noted in (Cox, 2020).

3.2 Review of Data-Driven Models

The introduction of, and subsequent democratisation of access to, Artificial Neural Networks (ANNs) marked the start of a Cambrian Explosion of seminal computational studies. ANNs are a collection of connected nodes capable of "learning" a series of weights to predict the characteristics of target variables. Each node can be represented as its own linear regression model governed by,

$$\sum_{i=1}^{m} w_i x_i + bias = w_1 x_1 + ... + w_m x_m + bias. \tag{2}$$

High weights contribute more significantly to final predictions (Dasaradh, 2020). ANNs are typically composed of an input layer, followed by one or more hidden layers and then an output layer.

Recurrent Neural Networks (RNNs) are a type of ANN introduced by Rumelhart et al. (1985) that are commonly employed for predicting time series data. RNNs differ from traditional ANNs as they allow previous outputs to be used as inputs whilst utilising hidden states. For each time state, t, the activation and output of an RNN are defined as,

$$a^{<t>} = g_1 \left(W_{aa} a^{<t-1>} + W_{ax}^{<t>} + b_a \right), \tag{3}$$

$$y^{<t>} = g_2 \left(W_{ya} a^{<t>} + b_y \right) \tag{4}$$

where $W_{ax}, W_{aa}, W_{ya}, b_a, b_y$ are temporally-dependent coefficients and g_1, g_2 are activation functions (Rumelhart et al., 1985). A notable limitation of RNNs is their inability to handle long-term temporal dependencies, a problem often referred to as the "vanishing gradient problem". More explicitly, the error back-propagating in the network vanishes (Hochreiter, 1998).

The Long Short-Term Memory network (LSTM) was specifically developed to counter the vanishing gradient problem (Hochreiter & Schmidhuber, 1997). The addition of a "cell state", which flows almost uninterrupted through the entire network, enables the LSTM to handle longer-term temporal dependencies. The information stored in the cell state is managed by a series of "gates" which actuate by means of a sigmoid function - a 0 deletes the piece of information entirely and a 1 keeps it in its entirety. Illustrated in Figure 1(b), the leftmost "forget" gate decides if any stored information should be removed from the cell state. The central "input" gate governs what information should be added to the cell state. The rightmost gate governs the output by filtering the information stored in the cell state. This filtering is achieved by passing the information through a hyperbolic tangent activation function (tanh) and multiplying it with the output of a sigmoid gate.

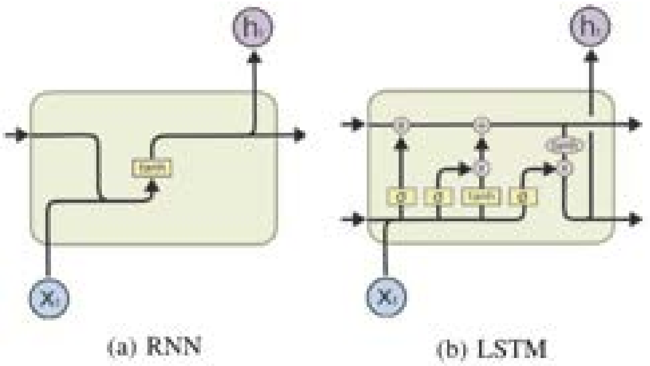

(a) RNN (b) LSTM

Figure 1. A comparison of the structures of RNNs and LSTMs. The cell state is the horizontal line running across the top of the LSTM. The gates manage updates to the cell state and its relevant outputs. Image adapted from Stanford University (2015).

Another popular class of algorithms is the "gradient boosted decision tree". Boosted trees are defined mathematically through,

$$\hat{y}_i = \sum_{k=1}^{K} f_k(x_i), \quad f \in \mathcal{F} \tag{5}$$

where K is the number of trees, f is a function in the functional space $\mathcal{F}$, and $\mathcal{F}$ is the set of all possible classification and regression trees (CARTs) (Brownlee, 2020). "Boosting" refers to the combination of a learning algorithm in series to yield a robust learning system from a series of weak learners. A commonly used boosted tree algorithm is "XGBoost" (Chen & Guestrin, 2016).

Nonlinear Auto-Regressive models with Exogenous inputs (NARX models) are commonly employed prediction of time-series data. NARX models predict the current value of a series based on the previous values of the series and the current and previous values of the exogenous series influencing the predicted series (Mathworks, 2020). Given the output series to predict $y(t)$ and exogenous inputs $X(t)$, the NARX will predict the next step as,

$$\begin{aligned} y(t+1) &= f(y(t), y(t-1), ... \\ &..., y(t-p+1), X(t-d), X(t-d-1), ..., X(t-d-q+1)) \end{aligned} \tag{6}$$

where p is the autoregression order, q is the exogenous input order and d is the exogenous decay. The function, f, is a non-linear function such as a Support Vector Regressor (SVR) upon which the NARX is fitted (Mathworks, 2020).

Each of the aforementioned data-driven models - RNN, LSTM, XGBoost and NARX - were evaluated in this study.

RNN and LSTM models were implemented in python utilising Google's TensorFlow and Keras (Abadi et al., 2015; Chollet, 2015). A range of different architectures were analysed. Bayesian tuning was used to find optimum hyperparameter sets. Bayesian tuning differs from the more traditional grid search by using a probability model of the objective function to determine the most promising hyperparameters to evaluate via a surrogate function. This makes it more computationally efficient than grid search or random search. XGBoost was also implemented in python utilising its native library (Chen & Guestrin, 2016). Similarly, Bayesian tuning was utilised to determine optimum hyperparameter sets. Bayesian tuning was performed with the HyperOpt package (Komer, 2021).

Two NARX architectures were implemented in python with the FireTS library (FireTS, 2020). The first NARX was fitted on a linear regression model and the second on an epsilon-support vector regressor (SVR). Linear regression models fit a linear model with coefficients $w = (w_1, ..., w_p)$ to minimise the residual sum of squares between the observed targets in the dataset and the targets predicted by linear approximation (Scikit-learn, 2021). A contratio, a SVR fits a best line on the the continuous variables within a threshold of values called the "epsilon-insensitive tube" (Bakshi, 2020). The SVR will try to fit as many points in the region of tolerance on either side of the hyper plane and within the boundary lines located at a distance epsilon, $\pm\varepsilon$.

3.3 Mechanistic Model Selection

With respect to mechanistic model selection, the equivalent circuit model (ECM) and the single particle model (SPM) represent the two "fundamental" choices in battery modelling.

ECMs employ basic electrical components to reflect the terminal voltage output under a current profile. They are frequently deployed in real-time cases for their simplicity and low computational load. However, the structure of ECMs are usually empirically-based and cannot reflect the electrochemical process during charge and discharge well. A notable limitation of ECMs, as highlighted by Yang et al. (2017) and others, is their high prediction uncertainty in low SoC regions.

SPMs calculate terminal voltage and SoC from knowledge of the electrochemical processes within the cell. The SPM, a direct reduction of the P2D model, views the dynamics of the electrode particles and current density as identical within an electrode. As such, each electrode is modelled as a “single particle”. SPMs have the potential to capture more information about the battery dynamics than ECMs at the cost of increased computational demand. Consequently, ECMs can be more suitable for applications where computational load highly limited, as is the scope of this study. Therefore, an ECM was chosen for hybrid model formulation. The ECM presented by Reiter et al. (2019) was implemented in MATLAB 2021b using Simulink. Minimal modification was required to bring the ECM in line with the LIONSIMBA model. The battery parameters used are detailed in Appendix 3. ECM predictions were produced for all P2D-generated drive cycles to facilitate training of data-driven models to predict the error in ECM predictions.

3.4 *Hybrid model assembly*

The highest-performing data-driven model was chosen as the base to begin hybridising the ECM. von Stosch et al. (2014) provides an excellent overview of hybrid modelling techniques in process engineering and their respective advantages. The most common hybrid model architecture sees the data-driven model predict the difference between the mechanistic model prediction and the true value. The mechanistic model’s prediction and the error term are then summed to yield the final hybrid prediction. In line with its popularity and generally strong performance, this model architecture is explored in this study. In this study, two variations of this model are considered. In each case the ECM takes the input $x(t) = [V(t), I(t), T(t)]$. However, the models differ in their inputs to the data-driven model. In the first model, the data-driven element takes the input $y(t) = [V(t), I(t), T(t)]$. In the second model, the input to the data-driven model takes the form $y(t) = [V(t), I(t), T(t), \mathrm{SoC}_{ECM}]$, where SoC_{ECM} is the SoC prediction of the ECM. The model architectures are illustrated below:

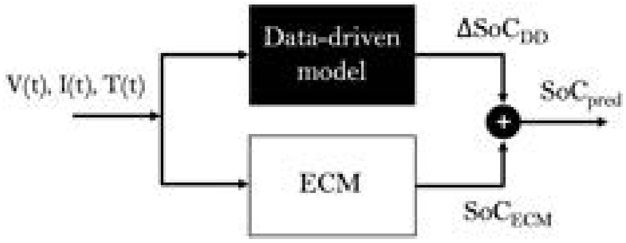

Figure 2. Hybrid model 1.

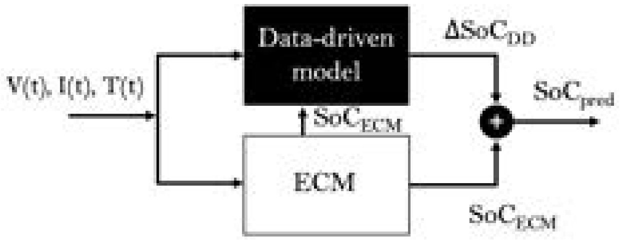

Figure 3. Hybrid model 2.

3.5 *Error metrics*

The Mean Absolute Error (MAE) and Root Mean Squared Error (RMSE) are used to assess the SoC estimation methods. They are defined respectively as,

$$MAE = \frac{\sum_{i=1}^{n} |\hat{y}_i - y_i|}{n} \tag{7}$$

$$RMSE = \sqrt{\sum_{i=1}^{n} \frac{(\hat{y}_i - y_i)^2}{n}} \tag{8}$$

where $\hat{y}_i$ is the predicted value and y_i is the actual value. The overall objective was to minimise these errors. The RMSE differs from the MAE in that the difference between the prediction and the real value is squared. Consequently, the larger the magnitude of the error, the more weight will be associated to it. As such, RMSE can be said to “punish” large errors more severely than MAE. In addition to the MAE and RMSE, metrics such as the maximum error are considered in model evaluation.

4. Results & Discussion

4.1 *Data-Driven Model*

The optimum number of epochs was explored for the RNN and LSTM models, with training cycles conducted for 1, 3, 5, 10, 15 and 20 epochs. It was found that training for 10 epochs yielded the best results, appearing to find a healthy optimum between underfitting and overfitting. The degree of overfitting was evaluated by comparing the training loss to the testing loss. In instances where the training loss was significantly lower than the testing loss, the network was deemed to have overfitted on the training set. Therefore, subsequent RNN and LSTM training cycles were conducted for 10 epochs. The learning rate represents another key parameter for tuning. The learning rate is the step size taken per iteration while moving towards the minimum in a loss function. A range of learning rates were evaluated through Bayesian optimisation, which considered the range of $\eta = 0.001$ - 0.05. As before, the effect on model loss and the degree of overfitting were considered and the optimum learning rate was found to be $\eta = 0.01$. The “Adam” optimiser was implemented due to its computational efficiency and low memory requirements (Kingma & Ba, 2017).

Tuning the number of nodes in the network presented a number of useful trends. It can be seen that increasing the number of nodes in a layer generally resulted in a lower loss, both on training cycles and generalised testing. Though, the ideal architecture varies significantly between the RNN and LSTM. For example, in the case of the RNN, the optimum architecture for the UDDS cycle utilises a single layer of 10 nodes (MAE : 0.22, $RMSE$: 0.26). Whereas for the LSTM, the optimum architecture is two layers of 10 nodes each (MAE : 0.23, $RMSE$: 0.28). Full results from the tuning of the number of nodes can be found in Appendix 1.

In the case of the NARX models, the key metric to tune is the length of the exogenous inputs. In a NARX, exogenous inputs enable the model to consider current and past values of

Table 1. MAE and RMSE values for data-driven models trained and tested on drive cycles at constant ambient temperature

	Training Data		UDDS		NYCC		Constant discharge (low)		Constant discharge (high)		Complete discharge	
	MAE	*RMSE*	*MAE*	*RMSE*	*MAE*	*RMSE*	*MAE*	*RMSE*	*MAE*	*RMSE*	*MAE*	*RMSE*
NARX-SVR	0.041	0.172	0.071	0.082	0.033	0.051	0.041	0.049	0.121	0.244	0.111	0.114
NARX-LinReg	0.090	0.174	0.153	0.156	0.058	0.069	0.212	0.267	0.201	0.231	0.132	0.156
RNN	0.275	1.041	0.224	0.262	0.334	0.415	2.442	2.778	1.851	2.287	2.671	3.394
LSTM	0.202	1.024	0.236	0.282	0.622	0.891	3.986	4.623	2.232	2.567	3.325	9.143
XGBoost	0.541	0.708	0.452	0.565	1.419	2.968	5.193	5.684	4.897	4.952	2.791	3.023

the exogenous series when making the current prediction. To illustrate: an exogenous input of 5 would allow the network to consider up to y_{t-n} and X_{t-n}, where $n = 1, ..., 5$. Notation is consistent with that presented in Equation 6. Again, Bayesian tuning was utilised to find the optimum length of exogenous inputs over a range of 3 to 20. A strong positive correlation with increasing length of exogenous input and reduced loss was observed, though this benefit became negligible for any increase beyond $n = 10$. Therefore, in the interest of optimising the trade-off between improved loss and increased computational cost, $n = 10$ was chosen as the length of exogenous inputs.

The last model that was tuned was XGBoost. As an accelerated boosted-tree algorithm, there is a wide variety of hyperparameters to tune, ranging from maximum tree depth to regularisation parameters. Again, Bayesian optimisation was utilised to tune these hyperparameters. The optimal hyperparameters were found to be (in the naming convention of XGBoost): colsample_bytree = 0.85, gamma = 0, learning_rate = 0.09, max_depth = 40, min_child_weight = 7, n_estimators = 175, reg_alpha = 0.01, reg_lambda = 1.6.

Lastly, it can be observed the ratio of RMSE:MAE for training data predictions in Table 1 and Table 2 is considerably higher than on testing cycles. This may seem counter-intuitive, though is readily explained by the characteristics of the training dataset. As detailed in Section 3.1.2, the training data has randomised input currents. This introduces considerable variance in the data. In contrast, the observed variance in characteristic discharge cycles is generally lower. It appears that this variance increases the likelihood of a large error in prediction for the training cycles.

4.1.1 Constant Ambient Temperature

Firstly, the constant ambient temperature case was tested. Therefore, in each cycle, the initial temperature of the battery was set at a constant 25°C. The rest of the parameters, such as SoC and depth-of-discharge, were set as detailed previously. Before training, each set of 100 discharge cycles was split into a training and testing set with a split of 80 and 20, respectively.

The most immediate observation from the results presented in Table 1 and in Figure 4 is the excellent performance of each NARX configuration relative to the other architectures. This observation holds true across all discharge cycles, and is especially pronounced in the case of the constant current discharge cycles. While the losses of the NARX-LinReg and the NARX-SVR are generally similar, upon closer inspection the NARX-SVR can be seen to outperform the NARX-LinReg across all drive cycles. This is expected, as SVRs are strongly suited to the nonlinear character of discharge time-series data. More granularly, while there is a general negative gradient associated with battery discharge, fluctuations arise from small perturbations within the battery - for example, from electrolyte effects - and from the normal distribution that was applied to current inputs in data generation. By virtue of its epsilon-tube, SVRs are less susceptible to the effects of these outliers in the data.

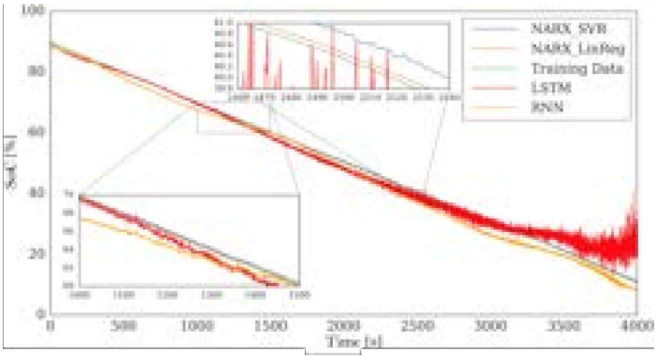

Figure 4. Plot of SoC predictions [%] against Time [s] for NARX-SVR, NARX-LinReg, LSTM and RNN for a complete discharge cycle.

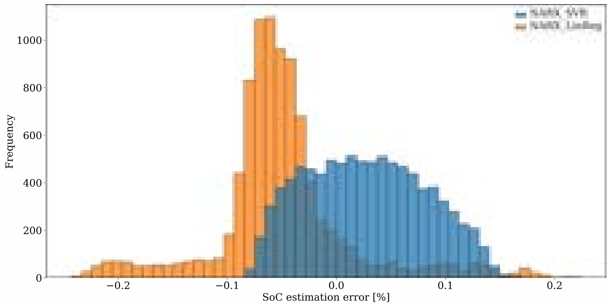

Figure 5. Error histogram of NARX models on the constant discharge-only at constant ambient temperature

Analysis of Figure 5 highlights another advantage of the NARX-SVR over the NARX-LinReg. Illustrated in orange, the NARX-LinReg appears to consistently underestimate the true SoC. This contrasts the more balanced estimations of the

Table 2. MAE and RMSE values for data-driven models trained and tested on drive cycles at varying ambient temperature

	Training Data		UDDS		NYCC		Constant discharge (low)		Constant discharge (high)		Complete discharge	
	MAE	*RMSE*	*MAE*	*RMSE*	*MAE*	*RMSE*	*MAE*	*RMSE*	*MAE*	*RMSE*	*MAE*	*RMSE*
NARX-SVR	0.043	0.172	0.043	0.052	0.053	0.074	0.021	0.028	0.063	0.067	0.111	0.134
NAR-LinReg	0.113	0.174	0.051	0.064	0.083	0.088	0.511	0.561	0.039	0.055	0.313	0.384
RNN	0.612	1.244	1.061	1.295	0.554	0.737	2.778	3.318	2.393	2.892	1.292	1.544
LSTM	0.295	1.055	0.532	0.624	0.415	0.539	4.422	5.193	2.641	2.892	3.598	9.345
XGBoost	0.836	1.336	1.255	1.635	1.832	3.159	6.434	7.036	6.433	7.064	3.825	4.274

NARX-SVR. This discrepancy likely arises from "regression attenuation" (also referred to as "regression dilution") which is caused by errors in independent variables. In this case, the error is thought to stem from variance in the current profiles – a product of the normal distribution applied during data generation. This variance introduces bias in the prediction. By definition, this variance is non-negative, producing a regression coefficient that is lower that the desired value. This leads to consistent underestimation in the target variable. The NARX-SVR is less susceptible to regression attenuation due to its epsilon-tube, though the figure demonstrates its presence to a smaller degree.

Further inspection of Figure 4 highlights an accumulation of error in SoC prediction over time in all models. In each case, the accumulation of error is likely the result of information about previous predictions in the series being used to make the current prediction. Through this mechanism, errors in the previous predictions are incorporated into subsequent predictions, producing increasingly large errors as time progresses. In the case of the RNN and LSTM, this results in significant maximum errors of 14% and 13%, respectively.

Lastly, from Table 1 we observe that XGBoost also fails to deliver strong performance on the training or testing cycles.

This analysis has demonstrated that the NARX-SVR and NARX-LinReg models provide superior prediction quality to the RNN, LSTM and XGBoost models in a constant ambient temperature environment.

4.1.2 Varied Ambient Temperature

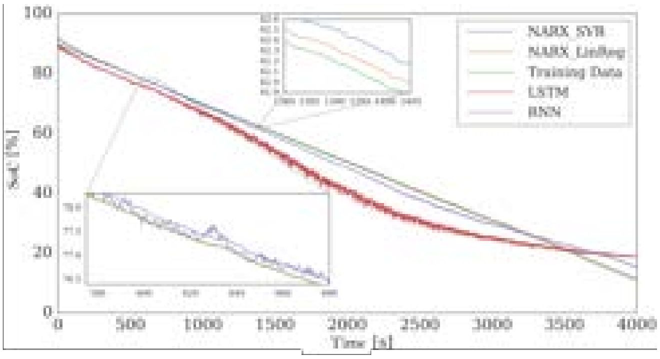

Figure 6. Graph displaying the SOC[%] against seconds [s] for a range of networks - Complete Discharge Cycle

The varied temperature case differs from the previous section as the initial ambient temperature of the cell was varied between -10°C and 50°C, rather than held constant at 25°C. All other parameters were as previously detailed, and, as before, each set of 100 discharge cycles was split into training and testing sets of 80 and 20, respectively. Inspection of Table 2 and Figure 6 tells a similar story to the constant temperature case. Once again, the NARX-SVR and NARX-LinReg significantly outperform the other models. Showing similar symmetry, the NARX-SVR consistently outperforms the NARX-LinReg. Again, these trends hold true for all discharge cycles and are more pronounced in the constant discharge cycles. When analysing relative performance between the constant and varied temperature cases, presented in Table 1 and Table 2 respectively, the NARX-SVR and NARX-LinReg models are shown to perform similarly well. Therefore, their predication quality does not suffer when the ambient temperature of the battery is changed. This is a strong endorsement of their suitability for online applications, as varied ambient temperature better mimics real-use conditions. In contrast, the XGBoost, RNN and LSTM models demonstrate a less favourable trend – the models tend to perform worse on the varied temperature case than in the constant temperature case. As another example of poor predictive ability, this would further limit their suitability for online applications. As before, full results for all architectures tested are presented in Appendix 2.

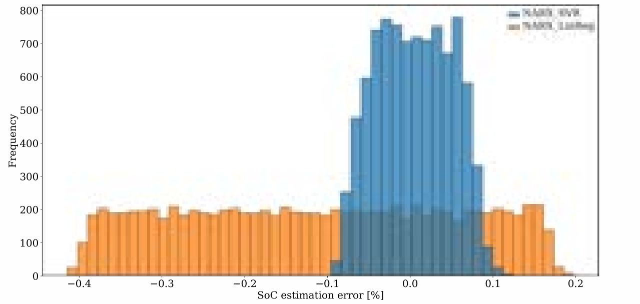

Figure 7. Error histogram of NARX models on the complete discharge-only cycle at varying ambient temperature

As before, analysing Figure 7 highlights a flaw in the performance of the NARX-LinReg model – it consistently underestimates the SoC. This again contrasts the more balanced predictions of the NARX-SVR. Once again, this error stems from the aforementioned regression attenuation.

Table 3. MAE and RMSE values for hybrid mechanistic-ML models trained and tested on drive cycles with constant ambient temperature. Note that the "ECM only" row is blank as the model is not trained, therefore general performance is equal to the self-test column.

	Training Data		**UDDS**		**NYCC**		**Constant discharge (low)**		**Constant discharge (high)**		**Complete discharge**	
	MAE	*RMSE*	*MAE*	*RMSE*	*MAE*	*RMSE*	*MAE*	*RMSE*	*MAE*	*RMSE*	*MAE*	*RMSE*
NARX-SVR alone	0.043	0.172	0.043	0.052	0.053	0.074	0.021	0.028	0.063	0.067	0.111	0.134
Hybrid structure 1	0.009	0.023	0.005	0.007	0.006	0.008	0.003	0.004	0.006	0.008	0.026	0.030
Hybrid structure 2	0.005	0.014	0.007	0.007	0.006	0.008	0.004	0.005	0.009	0.010	0.035	0.040
ECM alone	0.099	0.121	-	-	-	-	-	-	-	-	-	-

The data presented in Table 1 and Table 2 points towards the NARX-based models as the most suitable candidates to carry forward to hybridisation. Their prediction quality is overall much stronger than that of the RNN, LSTM and XGBoost models. Moreover, they maintain a consistently strong predictive quality in the varied temperature case, which is important for success in online applications. In addition to marginally better losses, the NARX-SVR is demonstrated to be superior to the NARX-LinReg by Figure 5 and Figure 7. Here, it is shown that the NARX-LinReg suffers from a larger degree of regression attenuation, which manifests in consistently larger underestimations of SoC. This highlights the NARX-SVR model as the best model to proceed with for hybridisation.

4.2 Hybrid Models

Analysis of the hybrid model is conducted with varied ambient temperature to most effectively evaluate the suitability for online application. The recommendations presented in von Stosch et al. (2014) for evaluation criteria for hybrid modelling were utilised. Firstly, the predictive quality of the hybrid models are evaluated as before, utilising the MAE and RMSE of the predictions to compare performance to the standalone mechanistic and data-driven models. Secondly, the ability of the hybrid models to maintain strong predictive quality in areas with little training data for the data-driven model is assessed using the same loss metrics.

As detailed in Section 3.4, two hybrid architectures are evaluated. In each, the ECM receives input $x(t) = [V(t), I(t), T(t)]$. Though, the models differ in their inputs to the data-driven model. In the first model, the data-driven element takes the input $y(t) = [V(t), I(t), T(t)]$. In the second, the input takes the form $y(t) = [V(t), I(t), T(t), \text{SoC}_{ECM}]$, where SoC_{ECM} is the SoC prediction of the ECM.

4.2.1 Hybrid model performance

The results for the training and testing of the hybrid models are presented in Table 3 alongside losses from standalone ECM and data-driven models. Performance on a complete discharge cycle is illustrated in Figure 8. Both hybrid architectures demonstrate significantly improved predictive ability over the the standalone NARX-SVR and ECM in the training data case. Inspection of the subplots on Figure 8 clearly demonstrates how the inclusion of the NARX-SVR in parallel enahnces the prediction quality of the ECM. Each of the hybrid models are successfully capturing small deviations in SoC.

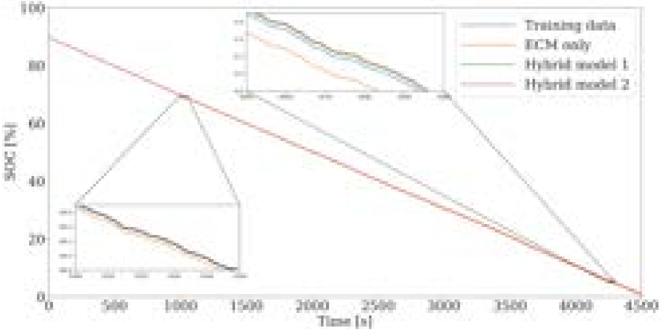

Figure 8. Plot of SoC predictions [%] against Time [s] for the ECM alone and the two hybrid model architectures alongside the P2D-generated cycle for reference.

In contrast, the ECM produces quite a smooth curve, absent of any of these deviations. The manifestation of this improvement is particularly stark in the case of the RMSE where we see an 87% and 92% improvement over the NARX alone for hybrid models 1 and 2, respectively. As RMSE "punishes" large errors more severely than MAE, this indicates that the hybrid architectures are particularly effective at removing these larger errors - something that would prove useful in online applications. In this respect, the second hybrid structure outperforms the first by around 39% in RMSE. This is likely due to the fact that the second model benefits from a richer training set as it makes use of SoC_{ECM} before predicting the error. Therefore, it demonstrates a stronger ability to interpret training data and apply this to cycles with similar characteristics.

To fully evaluate the strengths of each hybrid configuration, their ability to extrapolate from training data to unseen cycles is assessed. On every standalone data-driven cycle, there is a negative ratio between the MAE of training cycle predictions and the testing cycle predictions. This means that the data-driven models perform worse on testing cycles. As would be expected, the hybrid model demonstrates a strong ability to generalise. Though, there is a notable performance gap between the two hybrid models. While hybrid model 2 performs strongly on the testing cycles relative to the standalone data-driven model, it still demonstrates a depleted performance capacity relative to the training cases. On the other hand, hybrid model 1 boasts a positive ratio between MAEs on training cycles and those on testing cycles. This means it actually performs better when extrapolating, with the exception of the full discharge cycle. This strong extrapolative performance would be particularly useful in online applications, where users would be expected to fully deplete their battery's charge on occasion. Of course, the variance in the testing cycles is lower than in the training case in this study, but this remains a clear display of the model's strength in extrapolation.

A notable area of under-performance for both hybrid models is the complete discharge cycle. This is demonstrated both by the relatively high MAE and RMSE values presented in Table 3. This error has two root explanations. Firstly, ECM performance is notoriously poor at low SoC values, as noted by Yang et al. (2017). In this instance, the MAE and RMSE of the ECM on SoC values below 20% on the high constant current discharge cycle are 0.21 and 0.24, respectively. These losses increase further as SoC goes to 0%. The poor quality of SoC_{ECM} appears to have a detrimental impact on overall model performance in the complete discharge case. This error can also explain the relatively larger differential between the performance of hybrid model 1 and 2 on this cycle type. As model 2 considers SoC_{ECM} more strongly, errors in this value will manifest more strongly in the final SoC prediction. This error is then supplemented by the accumulation of error over time in the NARX-SVR, leading to significantly poorer prediction quality towards the end of the cycle. This is illustrated in the two subplots within Figure 8. In the first subplot, captured early in the cycle, the prediction quality provided by all models is strong, even in the case of the ECM. However, by the second subplot, captured towards the end of the cycle, this picture has significantly changed. By this point, the prediction quality of all models can be seen to have declined somewhat.

This analysis has demonstrated the strength of hybrid modelling techniques for SoC estimation. In all instances, the hybrid models outperform their standalone counterparts. What is less clear is which of the two proposed hybrid models is stronger in absolute terms. One the one hand, hybrid model 2 demonstrates a better ability to interpret trends in training data. Though, it demonstrates a slightly reduced extrapolative ability when compared to hybrid model 1, especially in complete discharge cycles.

5. Outlook and concluding remarks

Several areas of study demonstrate significant potential for improvements in continuations of this work. Firstly, the ECM utilised could be upgraded with an "Enhanced ECM" or SPM with electrolyte (Liu et al., 2014; Moura et al., 2017). By including electrolyte effects in the mechanistic model, prediction error at low SoC can be reduced. Secondly, increasing the training dataset size would further improve predictive accuracy in the NARX-SVR. If sufficient training set diversity was achieved, the second hybrid model's extrapolative ability may improve relative to the first. Thirdly, as this study is concerned with online applications, it would be interesting to investigate the drop-off in loss with NARX-SVRs of reduced complexity. Ideally, model complexity can be reduced while maintaining strong performance. There is also a need to expand the study to include SoC values above 90%. This was, unfortunately, outside of the scope of this study as LIONSIMBA cannot generate cycles above this threshold. Finally, alternate hybrid structures should be explored. One such configuration would be the so-called "stacked semi-parametric models". Stacked models combine the output of multiple data-driven or hybrid models to produce a final prediction.

This study has provided a range of useful insights into the performance of data-driven and hybrid models in SoC estimation. Firstly, recapping the data-driven section, it was demonstrated that the NARX-LinReg and NARX-SVR outperform other data-driven models with this training methodology. This was true in absolute terms, and by their consistent prediction quality across constant- and varied-ambient temperature cycles. Upon closer inspection, through analysis of their respective losses and of where errors arose in the system, the NARX-SVR was chosen to progress to hybridisation.

Two hybrid architectures were then investigated. In each, data-driven and hybrid models were deployed in parallel, with the data-driven component predicting ΔSoC_{DD}, the difference between SoC_{ECM} and the true SoC value. In hybrid model 2, SoC_{ECM} was passed to the NARX-SVR before it made its error prediction. Whereas in hybrid model 1 the prediction is made independently. Both hybrid models demonstrated a significant improvement in accuracy over the standalone models. Hybrid model 2 demonstrated a stronger ability to interpret the features of training data, producing 40% lower MAE and RMSE scores than model 1. In contrast, hybrid model 1 performed better when extrapolating to unseen cycles.

It was clear that the hybrid models' constituent NARX-SVR enables it to capture more small perturbations in SoC than the standalone ECM. Moreover, the hybrid models extrapolate much better than the standalone NARX-SVR. Overall, this analysis serves as a strong endorsement of the strength of hybrid modelling techniques and their suitability for online SoC estimation.

References

Abadi, M., Agarwal, A., Barham, P., et al. 2015, TensorFlow: Large-Scale Machine Learning on Heterogeneous Systems, software available from tensorflow.org

B. Bole, C. K., & Daigle, M. 2014, Adaptation of an Electrochemistry-based Li-Ion Battery Model to Account for Deterioration Observed Under Randomized Use, doi:10.1.1.658.2112

Bakshi, C. 2020, Support Vector Regression, https://medium.com/swlh/support-vector-regression-explained-for-beginners-2a8d14ba6e5d

Bhattacharjee, A., Verma, A., Mishra, S., & Saha, T. K. 2021, Estimating State of Charge for xEV Batteries Using 1D Convolutional Neural Networks and Transfer Learning, doi:10.1109/TVT.2021.3064287

Bian, X., Liu, L., Yan, J., Zhou, Z., & Zhao, R. 2020, An open circuit voltage-based model for state-of-health estimation of lithium-ion batteries: Model development and validation, doi:https://doi.org/10.1016/j.jpowsour.2019.227401

Biologic. 2021, Battery states: State of charge (SoC), State of Health (SoH)

Björnsson, L.-H., & Karlsson, S. 2016, Applied Energy, 168, 75

Brownlee, J. 2020, A Gentle Introduction to the Gradient Boosting Algorithm for Machine Learning, https://machinelearningmastery.com/gentle-introduction-gradient-boosting-algorithm-machine-learning/

Caliwag, A. C., & Lim, W. 2019, Hybrid VARMA and LSTM method for Lithium-ion Battery State-of-Cahrge and output voltage forecasting in electric motorcycle applications, doi:10.1109/ACCESS.2019.2914188

Chang, W.-Y. 2013, Estimation of the state of charge for a LFP battery using a hybrid method that combines a RBF neural network, and OLS algorithm and AGA, doi:https://doi.org/10.1016/j.ijepes.2013.05.038

Chen, T., & Guestrin, C. 2016, in Proceedings of the 22nd ACM SIGKDD International Conference on Knowledge Discovery and Data Mining, KDD '16 (New York, NY, USA: ACM), 785–794

Chollet, F., . o. 2015, Keras, https://github.com/keras-team/keras

Cong Jiang, Shunli Wang, B. W. C. F. X. X. J. C.-K. 2021, A state-of-charge estimation method of the power lithium-ion battery in complex conditions based on adapative square root extended Kalman filter, doi:https://doi.org/10.1016/j.energy.2020.119603

Cox, J. 2020, Data-driven state of charge estimation in Li-ion batteries under dynamic operating conditions

Dasaradh, S. K. 2020, A Gentle Introduction To Math Behind Neural Networks, https://towardsdatascience.com/introduction-to-math-behind-neural-networks-e8b60dbbdeba

dos Reis, G., S. C. Y. M., & Li, S. 2020, Lithium-ion battery data and where to find it, doi:https://doi.org/10.1016/j.egyai.2021.100081

Electronics Notes. 2021, Lithium Ion Battery Advantages & Disadvantages

Feng, F., Teng, S., Liu, K., et al. 2020, Co-estimation of lithium-ion battery state of charge and state of temperature based on a hybrid electrochemical-thermal-neural-network model, doi:10.1016/j.jpowsour.2020.227935

FireTS. 2020, fireTS, https://github.com/jxx123/fireTS

Haq, I. N., Saputra, R. H., Edison, F., Kurniadi, D., & Leksono, E. 2016, State of charge (SoC) estimation of LiFePO4 module using support vector regression, doi:10.1109/ICEVTIMECE.2015.7496640

Hochreiter, S. 1998, International Journal of Uncertainty, Fuzziness and Knowledge-Based Systems, 6, 107

Hochreiter, S., & Schmidhuber, J. 1997, Long Short-Term Memory, doi:https://doi.org/10.1162/neco.1997.9.8.1735

Kim, T., Qiao, W., & Qu, L. 2013, Real-time state of charge and electrical impedence estimation for lithium-ion batteries based on hybrid battery model, doi:10.1109/APEC.2013.6520266

Kingma, D. P., & Ba, J. 2017, Adam: A Method for Stochastic Optimization, arXiv:1412.6980

Komer, B. 2021, hyperopt, https://github.com/hyperopt/hyperopt

Lee, J., Qiu, H., Yu, G., Lin, J., & Services, R. T. 2007, "Bearing Data Set", NASA Ames Prognostics Data Repository

Li, S., Ju, C., Li, J., et al. 2021, State-of-Charge Estimation of Lithium-Ion Batteries in the Battery Degradation Process Based on Recurrent Neural Network, doi:https://doi.org/10.3390/en14020306

Lipu, M. S. H., Hannan, M. A., Hussain, A., et al. 2018, State of charge estimation for Lithium ion battery using recurrent NARX neural network model based lightning search algorithm, doi:10.1109/ACCESS.2018.2837156

Liu, G., Lu, L., Fu, H., et al. 2014, A comparitive study of equivalent circuit models and enhanced equivalent circuit models of lithium-ion batteries with different model structures, doi:10.1109/ITEC-AP.2014.6940946

Lu, S., & Frith, J. 2019, Will the Real Lithium Demand Please Stand Up? Challenging the 1Mt-by-2025 Orthodoxy

Mathworks. 2020, Design Time Series NARX Feedback Neural Networks, https://www.mathworks.com/help/deeplearning/ug/design-time-series-narx-feedback-neural-networks.html

Moura, S. J., Argomedo, F. B., Klein, R., Mirtabatabaei, A., & Krstic, M. 2017, Battery state estimation for a single particle model with electrolyte dynamics, doi:10.1109/TCST.2016.2571663

M.S. Hossain Lipu, M.A. Hannan, A. H. A. A. M. H. S.-T. F. K. D. N. H. 2020, Data-Driven state of charge estimation of lithium-ion batteries: Algorithms, implementation factors, limitations and future trends, doi:https://doi.org/10.1016/j.jclepro.2020.124110

Ordás, M. T. G., del Blanco, D. Y. M., Aveleira-Mata, J., et al. 2021, Hybrid model to calculate the state of charge of a battery

Oyewole, I., Savargaonkar, M., Chehade, A., & Kim, Y. 2021, A hybrid long short-term memory network for state-of-charge estimation of Li-ion batteries, doi:10.1109/ITEC51675.2021.9490188

Pan, H., Lu, Z., Lin, W., Li, J., & Chen, L. 2017, State of charge estimation of lithium-ion batteries using a grey extended kalman filter and a novel open-circuit voltage model, doi:10.1016/j.energy.2017.07.099

PRNewswire. 2021, Global Lithium-Ion Battery Market (2021 to 2030) - Declining Prices of Lithium-Ion Batteries Presents Opportunities.

Reiter, C., Wildfeuer, L., Wassiliadis, N., et al. 2019, in 2019 Fourteenth International Conference on Ecological Vehicles and Renewable Energies (EVER), 1–17

Rumelhart, D. E., Hinton, G. E., & Williams, R. J. 1985, Learning Internal Representations by Error Propagation

Rzepka, B.; Bischof, S. 2021, Implementing an Extended Kalman FIlter for SoC Estimation of a Li-ion Battery with Hysteresis: A Step-by-Step Guide

Scikit-learn. 2021, sklearn.linear_model.LinearRegression, http://scikit-learn.org/stable/modules/generated/sklearn.linear_model.LinearRegression.html

Shen, Y. 2018, Adaptive extended kalman filter based state of charge determination for lithium ion batteries, doi:10.1016/j.electacta.2018.07.078

Sidhu, M. S., Ronanki, D., & Williamson, S. 2019, State of charge estimation of lithium ion batteries using hybrid machine learning technique, doi:10.1109/IECON.2019.8927066

Son, Y., Liu, D., Liao, H., & Peng, Y. 2020, A hybrid statistical data-driven method for on-line joint state estimation of lithium-ion batteries, doi:10.1016/j.apenergy.2019.114408

Stanford University. 2015, Understanding LSTM networks

Steinstraeter, M., Buberger, J., & Trifonov, D. 2020, Battery and Heating Data in Real Driving Cycles, doi:10.21227/6jr9-5235

Torchio, M., Magni, L., Gopaluni, R. B., Braatz, R. D., & Raimondo, D. M. 2016, LIONSIMBA: A Matlab Framework Based on a Finite Volume Model Suitable for Li-Ion Battery Design, Simulation, and Control, doi:10.1149/2.0291607jes

United States Environmental Protection Agency, E. 2021, Dynamometer Driving Schedules, https://www.epa.gov/vehicle-and-fuel-emissions-testing/dynamometer-drive-schedules

University of Washington. 2021, What is a lithium-ion battery and how does it work?

von Stosch, M., Oliveira, R., Peres, J., & Feyo de Azevedo, S. 2014, Computers Chemical Engineering, 60, 86

Xiong, S. 2019, A study of the factors that affect lithium ion battery degradation

Yang, S., Deng, C., Zhang, Y., & He, Y. 2017, State of charge estimation for Lithium-ion battery with a temperature-compensated model, doi:10.3390/en10101560

Comparative Study of the Synthesis, Optimisation & Performance of Fe-Substituted MFI and MEL Zeolites

Mahad Abdi
Department of Chemical Engineering, Imperial College London, SW7 2AZ, U.K.

Abstract

A series of Fe-substituted ZSM-5 and ZSM-11 catalysts were prepared at different crystallisation temperatures, times, and iron weight loading (%). The influence of oxalate ligand functionalisation on the synthesis procedure and metal dispersion within the MFI zeolites was also investigated. These parameters were optimised to achieve the greatest purity and yield of crystalline material. The synthesised catalysts were calcinated and evaluated by N_2O decomposition. In summary, batch synthesis runs of iron substituted ZSM-5 catalysts demonstrated an increase in yield obtained by up to 20 % and an increase in crystallinity by up to 10% as the concentration of oxalic acid precursor was increased during the impregnation step. UV-vis spectroscopy highlighted that the increase in oxalic acid concentration had no bearing upon the nuclearity of the as-synthesised Fe-species present, however, the intensity of the relevant absorbance bands diminished indicating less iron uptake in the zeolite framework. N_2 adsorption results demonstrated iron oxalate supported enhanced textural properties, displaying an increase in BET surface area and N_2 adsorption. From nitrous oxide decomposition, the catalytic activity of the ZSM-5 catalyst was found to be slightly lower than the ZSM-11 catalysts, however, the ZSM-5 synthesis approach achieved a high yield, high crystallinity, and a significantly developed catalytic material within timescales of the order of hours in comparison to the days currently adopted within industrial practices for both MFI and MEL synthesis, offering a competitive pathway in zeolite synthesis, avoiding the basic pH and high OSDA content required in ZSM-11 synthesis.

Keywords: Oxalic Acid, Zeolite, MFI, MEL, Iron, XRD, BET, Nitrous Oxide Decomposition

1 Introduction

Zeolites are microporous crystalline materials, that encompass a vast group of aluminosilicate materials, in which aluminium/silicon atoms bond to four other oxygen atoms in a tetrahedral geometry, where each oxygen atom can bond to one other aluminium/silicon atom in a wide variety of arrangements. Zeolites are routinely utilised in a variety of applications ranging from gas separation, ion-exchangers, and adsorbents, where the global zeolite market size is projected to reach $6.19 billion by 2027, exhibiting a CAGR of 4.7% in the forecast period of 2021-2027; however, they are most widely deployed as catalysts in petrochemistry due to their numerous pores, active sites, thermal stability, and shape-selective properties [1] [2]. Zeolites can confine molecules in small spaces, which in turn changes their structure and reactivity. To date, over 250 unique zeolite frameworks have been identified, and for the purpose of this study, the MFI and MEL frameworks were focused on:

The MFI (Mobil-type five) zeolites were firstly synthesised in 1972, which compromise 4, 5, 6, & 10 membered ring structures and can allow the diffusion of molecules of up to 4.7 Å of diameters. The resulting porous structures consist of intersecting straight and sinusoidal channels. ZSM-5 is an established representative of the MFI class zeolites with intensive industrial applications. It is a synthetic zeolite that contains silica (Si) and alumina (Al), with the ratio of silica greater than the alumina by at least 5. The existence of aluminium and the Si:Al ratio of the zeolite causes ZSM-5 to exhibit acidic properties. MEL is also a member of the high-silica zeolite family. The crystal lattices of this zeolite family are based on double secondary building units which form linear chains, these linear chains subsequently link into layers via 4, 5, 6, 8, & 10 membered rings. The MEL structures allow the diffusion of molecules of up to diameters of 5.19 Å.

Although MEL & MFI zeolites share a comparable structural framework, morphology, pH, and textural properties, studies have shown that due to the subtle differences in pore topology, ZSM-11 demonstrates improved diffusion and catalytic performances compared to ZSM-5 across several mediums and reactions. A study by Kustova et al. found that copper substituted ZSM-11 based catalysts outperformed similar ZSM-5 based catalysts in gas decomposition [3]. This result is largely attributed to the difference in aluminate distribution in the frameworks; ZSM-11 has only straight microporous channels, allowing for more rapid intra-crystalline diffusion [4]. On the contrary, MEL synthesis presents significant industrial production challenges and environmental limitations, most notably, many ZSM-11 production processes require organic structure-directing agents, otherwise crystalline seeds are the only other viable option [5]. Reducing the cost and environmental hazards of zeolite synthesis is essential from both an academic and industrial perspective.

The purpose of this study was to systematically examine the crystallisation process of MFI and MEL-type zeolites, inferring the optimal conditions in which the greatest yield and purity could be achieved. The parameters that were investigated were time, temperature, and concentration of reagents in the batch synthesis. The properties of the synthesised zeolites were evaluated through analytical techniques such as x-ray diffraction, UV-vis spectroscopy, and BET *(Brunauer–Emmett–Teller)* surface analysis. Finally, the materials were calcinated and evaluated based on their stability and activity in catalysing NO_X decomposition reactions.

2 Background

Metal-support interactions in heterogeneous catalysts significantly influence the metal dispersion within the catalyst framework, in turn affecting the catalytic performance. The impregnation step has been shown to be critical to the activity of the synthesised zeolites [7]. Studies related to the suitability of precursors in facilitating high concentrations of active metal sites are limited. Kuwait Institute for Scientific Research studied the modification of the impregnation step of metal-substituted catalyst synthesis via ethylenediaminetetraacetic acid (EDTA) as a chelating agent, where they concluded that EDTA significantly reduced strong interactions between the metal species and the support [8]. More recently, a study conducted by Ayodele assessed the viability of oxalic acid (OA) as a precursor in the synthesis of cobalt substituted ZSM-5, the findings concluded that cobalt oxalate supported the ZSM-5 catalyst, highlighting an increase in the surface area and pore volume [9]. Oxalate, the conjugate base of oxalic acid, is an excellent ligand for metal ions such as iron. Oxalate is a bidentate ligand, whereby only two of the four lone pairs are utilised when forming a coordination compound. Oxalate is also regarded as a chelating agent which provides more stability to the complex.

Extensive studies have investigated the influence of several parameters that can affect the performance of N_2O decomposition, such areas of research included the topology of zeolites, calcination/synthesis conditions, reaction mechanisms and kinetics. The work of Richards, N., Nowicka, E., Carter, J.H. et al. demonstrated that iron species are an essential component in NOx decomposition, due to the increase in active sites [10]. The nature of active Fe-sites (alpha sites) is still a matter of debate. The difficulties in determining the nature of active Fe-sites can be attributed to the following reasons: The issue of coexistence in several iron substituted species adds a layer of complexity, the difference in the relative number of iron species present within frameworks lead to varying performances in catalytic activity, and the role of extra framework species following treatment has shown to improve catalytic activity but is still elusive.

Iron substituted species may exist in the following arrangements: Bulk FeO_x particles, small FeO_x nanoparticles, framework Fe^{3+}, isolated Fe^{3+}/Fe^{2+} anchored to the zeolite framework via Si-O-Fe or Al-O-Fe bridges, dinuclear Fe-O-Fe species anchored to the framework and confined in the zeolite channel, and atomically (oligomerically) dispersed Fe-oxo species anchored at framework Al sites (α-oxygen) [11] [12] [13]. Although the optimal activation conditions depend on the composition of the zeolite framework, Pirngruber et al. showed that the activity of different Fe species follows the sequence of *monomer* Fe^{3+}*, dimeric* Fe^{3+} *> oligomeric Fe species >* Fe_xO_y *type species*. These findings were also supported by Prins et al. in which the activity sequence followed: *monomeric* Fe^{3+} *> dimeric* Fe^{3+} *> oligomeric Fe species >* Fe_2O_3 *type species* [14].

The N_2O decomposition reaction mechanism can be described as adsorption of N_2O at the active catalytic site which then decomposes forming N_2 and surface oxygen, O. The desorption of surface oxygen is facilitated by combination with another surface oxygen atom, forming O_2. The scientific community have unequivocally substantiated that the rate-limiting step is the recombination of an oxygen atom to form O_2. The rate of this step can be accelerated via a reductant which promotes catalytic activity, allowing for lower reaction temperatures. Although Fe-substituted zeolites catalyse N_2O decomposition, high reaction temperatures ($T>450$ °C) are required. A study by Xie et al. reported a conversion of 100% beyond 450 °C where the Fe loading weight (%) in the ZSM-5 catalyst was 7.46 wt % [15]. A similar study by Wood et al. reported a much lower conversion of 84 % at 500 °C, however, the Fe loading weight in the ZSM-5 catalyst was 0.57 wt % [16]. By contrast, copper or cobalt substituted ZSM-11 catalysts were shown to be more active in N_2O decomposition than their ZSM-5 counterparts by Xie et al.; this was due to the enhanced reducibility and accessibility of active species and sites [17]. Xie et al. expanded this study to Fe-substituted ZSM-11 and found that the activity was higher than other Fe-substituted zeolite catalysts such as BEA, FAU, MOR and FER [18].

This study expands on the work of Xie et al. and Ayodele, synthesising iron oxalate via the functionalisation of iron nitrate nonahydrate, where oxalic acid was deployed as a chelating agent. The Fe-OA precursor was incorporated within the MFI zeolites. The parameters of iron weight loading (%), time and temperature were studied. Ultimately, the performance of the synthesised MFI catalysts was compared to synthesised MEL catalysts in NO_X decomposition.

3 Materials

Table 1: Synthesis of MFI zeolites

SiO_2 Source	Structure Directing Agent	Al Source	Fe Source	Si:Al	Crystalline Phase
TEOS	TPAOH	$NaAlO_2$	$Fe(NO_3)_3.9H_2O$	45-90	ZSM-5

Table 2: Synthesis of MEL zeolites

SiO_2 Source	Organic Structure Directing Agent	Al Source	Fe Source	Crystalline Phase
LUDOX AS-30	DAO	$Al_2(SO_4)_3·18H_2O$	$Fe(NO_3)_3.9H_2O$	ZSM-11

3.1 Reagents

The reagents used in this study include tetraethyl orthosilicate (TEOS, Sigma Aldrich, 99.99% trace metal basis); tetrapropylammonium hydroxide (TPAOH, 15.0 g, Sigma Aldrich, 1.0 M in water); iron nitrate nonahydrate ($Fe(NO_3)_3·9H_2O$, Sigma Aldrich, 98 %); oxalic acid (Sigma Aldrich, 98 %); $NaAlO_2$ (Sigma Aldrich, 50-55 wt % Al_2O_3); aluminium sulphate octadecahydrate ($Al_2(SO4)_3·18H_2O$); LUDOX-AS30; 1,8-Diaminooctane (DA); potassium hydroxide (KOH 1N). Note that none of the aforementioned materials was further purified before usage.

3.2 Synthesis of Fe substituted ZSM-5 (MFI)

A series of Fe-substituted MFI samples were synthesised at varying levels of Fe substitutions, as well as varying concentrations of oxalic acid. In a typical synthesis procedure, 10.24 g of TEOS were added dropwise to a 15.0 g solution of TPAOH, the mixture was left to homogenize for two hours at 60 °C *(Solution A)*. Simultaneously, a 5 ml solution of iron nitrate nonahydrate and oxalic acid was synthesised and left to homogenize for two hours *(Solution B)*. Lastly, a 5 ml solution of sodium aluminate was prepared *(Solution C)*. The compositions of solutions B and C were varied throughout the experiment. Solution B was added dropwise to solution A, followed by solution C. The subsequent gel was left to homogenise at 60 °C for 16 hours, after which the gel was transferred into several reactor types including a microwave reactor and ½ inch stainless steel tube reactor. The liquid volume to reactor volume ratio within the reactors was maintained at 1:1.32. After the crystallization, the crystalline product was removed from the mother liquor by four cycles of centrifugation and washed with deionized water. The material was dried overnight at 90 °C.

3.3 Synthesis of Fe substituted ZSM-11 (MEL)

Due to the high-silica zeolite nature of MEL, an organic template is required. This is a key difference between MEL and MFI zeolites, which can be synthesized from template-free sodium aluminosilicate gels [19]. For our synthesis of the MEL, a 2 ml solution of iron nitrate nonahydrate and oxalic acid was synthesised and left to homogenize for two hours. Aluminium sulphate octadecahydrate was added to a mixture of KOH solution, dropwise. To this solution was added DAO, followed by colloidal silica (LUDOX AS-30). Finally, the iron nitrate solution prepared prior was added dropwise. The resulting mixture was stirred at room temperature for 21 h, and the gel was crystallised in a Teflon lined stainless-steel autoclave at various temperatures. The crystalline product was removed from the mother liquor by three cycles of centrifugation and washed with deionized water.

3.4 Characterization of Catalysts

Powder X-ray diffraction (XRPD) was performed using a PANalytical X'PertPRO X-ray diffractometer, with a Cu Kα radiation source (40 kV and 20 mA). Diffraction patterns were recorded between 5° and 60° 2θ (Total Runtime = 8 minutes). UV-vis spectra of the samples were collected using a Shimadzu UV-2450 UV-vis spectrometer in the 200–800 nm range at a scan rate of 600 nm min^{-1}, this was performed such that the nature and distribution of the iron substituted species in the zeolites at the different concentrations of Fe could be assessed. The calcinated catalysts were degassed twice, firstly at 300 °C for 6 hours, followed by degassing in situ nitrogen overnight. Nitrogen adsorption-desorption isotherms were collected on a Micrometrics 3-Flex analyser. From the N_2 adsorption isotherms, the BET surface area was calculated. Additionally, the Barrett-Joyner-Halenda (BJH) method was used to determine average pore size and relevant pore volumes.

3.5 Evaluation of Catalysts Performance

Due to the environmental concerns associated with nitrogen oxides, a potent pollutant that produces photochemical smog, acid rain, and a cause of our ozone's destruction, there is a need to reduce the nitrogen oxides emission levels in the environment [20]. An aptitude of studies have investigated the viability of several pathways in nitrogen oxide emission mitigation such as highly efficient adsorption and non-selective catalytic reduction, however, selective catalytic reduction (SCR) has been shown to be the most effective method [21]. Consequently, the catalytic activities of the Fe/ZSM-5 and Fe/ZSM-11 samples were evaluated and compared for NO_X decomposition. Nitrous oxide (N_2O) was fed over the catalyst, where the catalyst was packed into a quartz tube and placed into a furnace that was heated up to 900 °C. Zeolites are resistant to thermal deactivation in this reaction temperature range [22]. The as-synthesized powders were calcined prior to reaction, at 550 °C from room temperature at a rate of 1 °C per minute; This was achieved in a flow of nitrogen (5 hr) followed by air (3 hr) in order to burn off the structure-directing agent.

The decomposition of nitrous oxide takes place through dissociation into oxygen and nitrogen.

$$2N_2O \rightarrow 2N_2 + O_2 \qquad (1)$$

4 Results & Discussions

4.1 MFI Synthesis Optimisation

The reproducibility of these experiments was tested by synthesising selected crystallisations repeatedly. The average range of error in yield obtained was found to be 1.22 %, whilst the greatest difference in yield between any two points was found to be 4 %. Thus, we conclude the following yield results are acceptable within an error range of 4 %.

4.1.1 Influence of Crystallisation Time on Fe/ZSM-5 Synthesis

The synthesis times for the ZSM-5 catalysts in the ½ inch stainless tube batch-reactors were studied. Literature had outlined the significant effect that time had on the crystallisation kinetics, which in turn affected the associated yield and overall crystallinity of the catalysts [23].

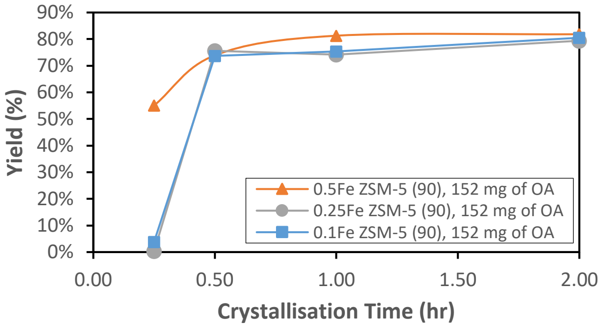

Fig. 1 Yield obtained in isothermal synthesis of ZSM-5 catalyst, at 175 C

Figure 1 highlighted a consistent trend that as the crystallisation time spent in the furnace increased, where the temperature was constant at 175 °C, the yield obtained from the synthesis had also increased. The maximum yield obtained fluctuated around 80%, this was mainly due to the experimental limitations associated with the batch process. Moreover, in synthesis runs where the Fe loading percentages were greater, a much greater yield of material was synthesised. For example, at 15 minutes, the catalyst at 0.5 wt % Fe demonstrated a yield 40% greater than either 0.1 wt % or 0.25 wt % Fe loading.

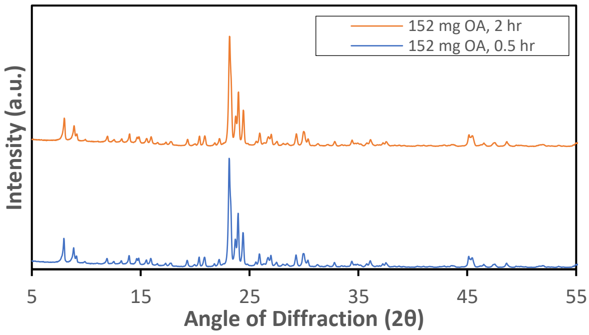

Fig. 2: XRD pattern for 0.25Fe ZSM-5 (90) catalysts at varying crystallisation times

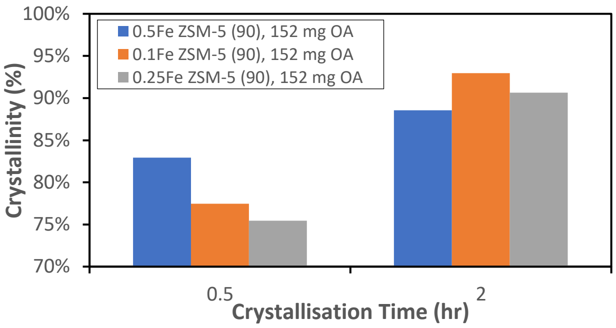

Fig. 3: Crystallinity of MFI zeolites as crystallisation time increases, where the reaction occurred at 175 C

From XRD analysis of the catalysts, *figure 3* demonstrated that the purity of the catalysts produced showed a positive correlation with crystallisation time, where the extent of this trend was most significant for lower Fe weight loading (%). The crystallinity of 0.5 Fe weight loading weight (%) ZSM-5 showed high crystallinity at shorter time scales, however, the crystallinity of the 0.1/0.25/0.5 zeolites agreed after two hours within a range of 5 %. *Figure 2* highlights the general XRD pattern found for all MFI synthesised materials in this study; the intensity of the peaks located between 2θ degree [7.86°, 8.78°] (doublet peaks) and [23.10°, 23.78° and 24.38°] (triplet peaks) were indicative of an MFI structure. A subtle trend that was observed was that the peak intensities had decreased as the iron content of the catalysts increased. This decrease was expected as iron-substituted compounds demonstrate higher x-ray absorption coefficients, demonstrating iron was incorporated within the zeolite framework. In reference to current industry standards, ZSM-5 synthesis is typically carried out in batch reactors as well, however, the order of crystallisation timescales are days or even weeks, which facilitate high crystallinity (>98%) [18]. In this study, we achieved yields of up to 80 % within 2 hours, and an acceptable crystallinity of up to 93 %.

4.1.2 Influence of Oxalate Ligand Functionalization on Fe/ZSM-5 Synthesis

The concentration of the oxalic acid incorporated in the batch synthesis of ZSM-5 catalysts was studied, as there was a research gap regarding the effect of this ligand in Fe/ZSM-5 synthesis during treatment, furthermore, the effect of oxalic acid concentrations on the textural properties of the catalysts was of interest:

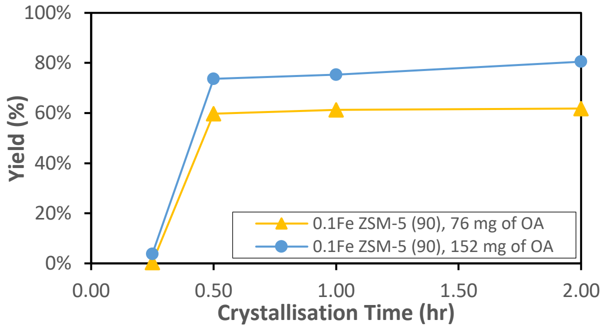

Fig. 4a: Yield (%) vs crystallisation time (hr) for 0.1 wt. % Fe Loading, at 175 C crystallisation temperature

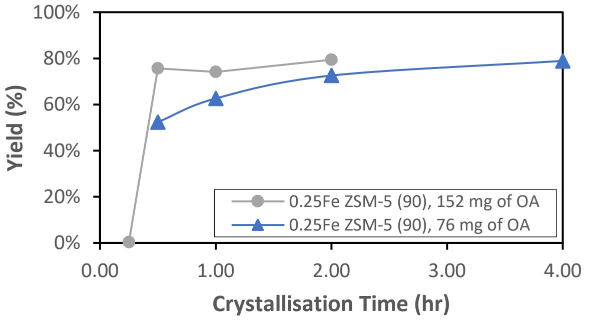

Fig. 4b: Yield (%) vs crystallisation time (hr) for 0.25 wt. % Fe Loading. at 175 C crystallisation temperature

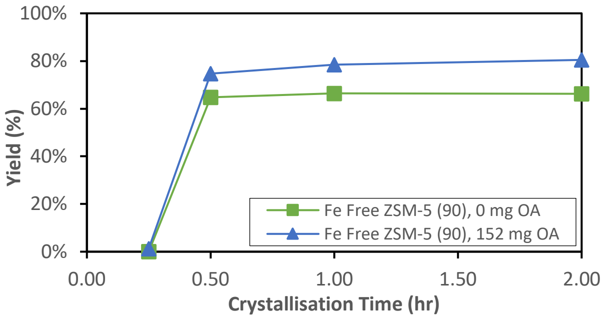

Fig. 4c: Yield (%) vs crystallisation time (hr) for Fe free ZSM-5 synthesis, at 175 C crystallisation temperature

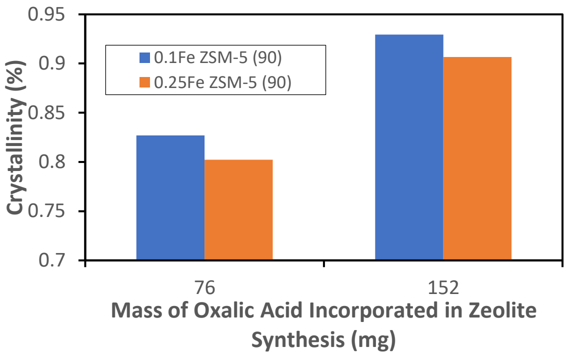

Fig. 5: Crystallinity of synthesised ZSM-5 as oxalic acid content varies, where crystallisation time and temperature were 2 hours and 175 C, respectively

From *figures 4a* and *4b* we can clearly see that as the concentration of oxalic acid had increased, the yield of the corresponding synthesis had also increased. In the instances where the loading weight (%) of Fe was greater, the effect of oxalic acid ligand functionalisation was less evident. For example, at a crystallisation time of 2 hours, the yield of 0.1Fe/ZSM-5 crystalline material increased by 20% as the oxalic acid content doubled. Whereas, in the case of 0.25 Fe loading weight (%), the yield only increased by 9%. This trend is understandable as the relative amount of iron ions in excess of OA was less during the impregnation step. The trend associated with *figure 4c* is quite remarkable, as literature has outlined the ideal condition for iron-free ZSM-5 synthesis is under high pH conditions [24]; on the contrary, as the pH of the batch was reduced *(i.e. increasing OA concentration)*, the yield of the iron-free ZSM-5 material increased by almost 15% for a crystallisation time of 2 hours indicating that oxalic acid may be also supporting the ZSM-5 synthesis via other mechanisms. Finally, from the XRD analysis of the Fe-substituted zeolites, *figure 5* demonstrates the crystallinity of both 0.1 and 0.25 Fe loading weight (%) zeolites increased by 10% as the mass of oxalic acid within the batch mixture doubled. Asides from the chelating effect of OA, oxalic acid may also be extracting residual non-crystallised Fe^{3+} ions, which has been shown to hinder catalytic performance.

4.1.3 Physical and Chemical Characterisation of Fe/ZSM-5 Synthesis

The nuclearity of Fe species in the Fe-substituted ZSM-5 samples is investigated through UV-vis spectroscopy, where the spectra are shown in *supplementary figure A* for 0.1Fe/ZMS-5 and supplementary *figure B* for 0.25Fe/ZSM-5. In summary, the oxalic acid content did not influence the nuclearity of the as-synthesised Fe species present. A consistent conclusion that was drawn from UV-vis spectroscopy was that the MFI catalysts demonstrated two strong absorbance peaks at 215 nm and 240 nm, indicating the presence of tetrahedral Fe^{3+} sites [25]. There was significant absorbance at 280 nm indicating (possibly isolated) octahedral Fe^{3+} sites at extra-framework positions [26]. There were weak absorbances in the region of 300 nm – 400 nm, which is attributed to the presence of oligomeric tetrahedrally coordinated Fe_xO_y clusters within the MFI zeolite micropores [27]. Relatively, there was no absorption past 400 nm, which suggested there was little to no presence of Fe_2O_3 nanoparticles. Finally, samples with higher Fe concentrations showed a broader high-intensity absorption band, indicating a higher portion of oligonuclear/pseudotetrahedrally coordinated Fe^{3+} sites.

With regards to OA content; the trends outlined by UV-vis spectroscopy of the samples showed that the intensity of the peaks at different crystallisation times were more compact as the oxalic acid contents in the batch mixture increased, demonstrating a significantly developed framework even at shorter crystallisation timescales. Although the absorbance intensity increased as the crystallisation time increased, it was found that the maximum absorbance intensity generally decreased when the oxalic concentration in the batch increased. This indicates a decrease in the uptake concentration of the tetrahedral/octahedral Fe^{3+} sites within the MFI catalysts at longer time scales, relative to lower OA concentrations. The poor exchange may be related to the crystal sizes of the Fe/Ox precursor, resulting in an increase in diffusion length for the iron species within the zeolite channel**.**

To assure further that indeed crystalline ZSM-5 had been synthesised. The porosity and surface area were investigated through nitrogen adsorption-desorption isotherms. The isotherm plots and textural properties of the samples are found in supplementary *figure C* and *table A*, respectively. A consistent trend observed in all MFI zeolites was that there was a high uptake of N_2 adsorbed in the region of $P/P_0 < 0.1$, indicating the micropore volumes in the zeolites were being filled, furthermore, the materials followed a mixed type I and II isotherms. There was also a very slight hysteresis loop of type IV present within the 0.1 and 0.25 Fe weight loading (%) samples, indicating the presence of mesoporosity. 0.1Fe/ZSM-5 synthesised at 2 hours with 152 mg OA demonstrated the greatest average volume of N_2 adsorbed, BET surface area, total pore volume and micropore volume *(to 3 s.f.)* of any MFI catalyst. On the contrary, the average pore diameter increased relative to the same catalyst that was synthesised with 76 mg of OA instead, indicating an increase in mesopore volume within the zeolite framework. The effect of OA ligand functionalization was also noticeable at shorter timescales, wherein the case of 0.25Fe/ZSM-5 synthesised at 0.5 hours, the BET surface area had increased by 10% as the OA content of the synthesis increased from 76 mg to 152 mg.

0.25Fe/ZSM-5 and 0.5Fe/ZSM-5 zeolites synthesised with 152 mg of OA demonstrated similar textural properties and quantity of nitrogen adsorbed. However, the amount of nitrogen adsorbed relative to 0.1Fe/ZSM-5 was far lower indicating a partial blockage of nitrogen, this may be due to an increasing concentration of iron clusters forming outside of the zeolite channels. Remarkably, as seen in 0.5Fe/ZSM-5 synthesised at 15 minutes, for a high iron content within the zeolites, the material is developed even at very short time scales. All in all, these results supported the findings from XRD and UV-vis spectroscopy, where the crystallinity of 0.1Fe/ZSM-5 at 152 mg OA was greatest, demonstrating enhanced catalyst properties could be achieved as the concentration of OA within the batch synthesis increased and a reduction in Fe weight loading (%).

In relation to the conventional synthesis of Fe-ZSM-5, even at 2 hours, the BET surface area found in this study was found to be 93% of the conventional ZSM-5 synthesised material's BET surface area in the case of 0.5Fe/ZSM-5. This is remarkable noting that the catalyst synthesised in this study had spent a 1/60th of the time crystallising in comparison to the conventional synthesis method [27].

4.2 MEL Synthesis Optimisation

4.2.1 Influence of Crystallisation Temperature on Fe/ZSM-11 Synthesis

Identifying suitable crystallization temperature allows for an effective crystallisation synthesis, however, this is especially important in MEL synthesis. Research has highlighted that with appropriate variations of synthesis temperature several physicochemical properties can be controlled including the morphology and acidic properties of the crystallization products [28]. MEL crystallizations are generally carried out in the temperature ranges of 150 – 180 °C, for the purpose of this study the temperature range studied was 175 – 190 °C:

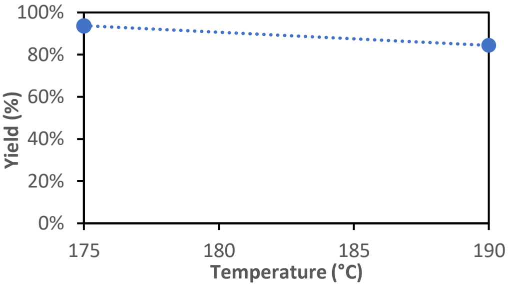

Fig. 6: Yield (%) vs Crystallisation Temperature (°C) for 0.1Fe ZSM-11 (45) catalyst

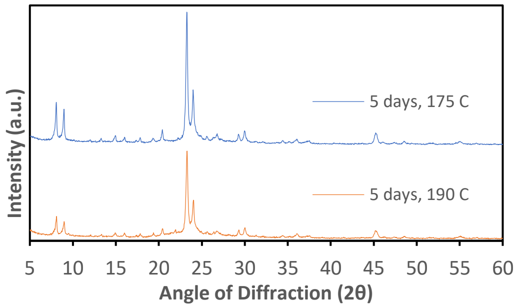

Fig. 7: 0.1Fe ZSM-11 (45) X-Ray Diffraction Pattern for 175 °C and 190 °C

The MEL catalysts were synthesised for 5 days in Teflon-lined stainless steel batch autoclaves. As seen in *figure 6*, as the crystallisation temperature increased from 175 °C to 190 °C, no conclusive trend could be drawn with regards to yield obtained; within an error range of approximately 10%, the yield had not increased, nor decreased. On the contrary, studies have shown that a decline in MEL synthesis temperature slows down the crystallization process [29]. In f*igure 7*, the ZSM-11 (MEL) catalysts were characterised in XRD; the analysis showed intense peaks at [7.88°, 8.80°] (doublet peaks), [23.22°, 23.84°] (doublet peaks) [45.10°] (singlet), this was representative of a MEL structure. However, the catalyst that had been synthesised at the lower temperature of 175 °C showed to be slightly more crystalline, where the peaks integrated were between 23.22° - 23.84°. This trend was unexpected, as previous studies had outlined the required crystallization time for fully crystalline MEL decreased with the increase of temperature because the induction period is prolonged at lower crystallisation temperatures, thus more nuclei were needed for nucleation and crystal growth. The reason for the observed trend may have been due to the inhomogeneity between the two autoclave reactors in which the MEL catalysts were synthesised, resulting in varying crystallisation processes.

4.2.2 Physical and Chemical Characterisation of Fe/ZSM-11 Synthesis

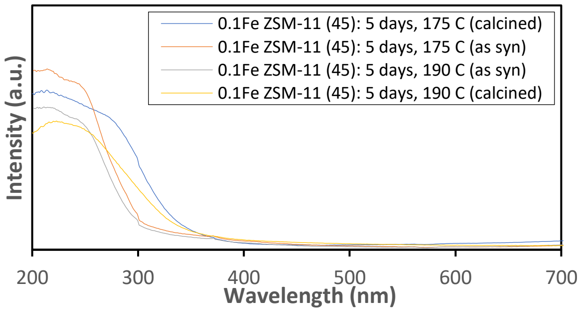

Fig. 8: UV-vis spectroscopy of MEL Zeolites synthesised for 5 days at 175 °C and 190 °C

The UV-Vis spectrum for the MEL crystals is presented in *figure 8*. Before calcination, the UV-vis spectra for the ZSM-11 catalysts demonstrated intense absorbance between 200 – 300 nm. Studies have agreed that bands within this region can be attributed to ligand-to-metal charge-transfer transitions of isolated Fe^{3+} species in three possible scenarios; octahedrally coordinated in framework positions, tetrahedrally coordinated in the framework or extra-framework positions [17].

Calcination facilitated the removal of the template which was essential to achieve higher catalytic activity when performing NO_x decomposition. From the UV-vis spectra, the band intensity diminished significantly and encompassed a larger region of absorbance [200 - 350 nm], this can be due to the migration of the Fe ion from the framework to extra-framework positions. This result was expected as UV-vis spectra studies within literature confirmed the migration of iron ions upon heat-treatment, demonstrating an increasing extra framework component. This result is the key driver for better catalytic activity [30].

From the 3-flex analysis of the MEL samples, the catalyst synthesised at 175 °C demonstrated greater catalytic properties in comparison to that synthesised at 190 °C. Namely, the BET surface area, total pore and total micropore volume had increased. Both catalysts demonstrated similar average pore diameters. The quantity of N_2 absorbed by 0.1Fe/ZSM-11 (45) synthesised at 175 °C was found to be greater than the same catalyst synthesised at 190 °C. However, both catalysts demonstrated type I isotherms, with the presence of a hysteresis loop past 0.45 P/P_0 *(Supplementary Figure D & Table B)*.

4.3 Catalysts Activity & Evaluation

4.3.1 Reaction Tests

The performance of the zeolites synthesised was quantified in NO_X decomposition via a fixed-bed flow reactor, where 50 mg of catalyst were packed into a quartz tube, sandwiched between two layers of quartz wool. Initially, the catalyst was pre-treated in Helium to 900 °C at a rate of 10 °C min^{-1} and held for 2 hours. The catalyst was then cooled in the same gas to the starting reaction temperature (350 °C). A step-response experiment was performed, where the catalyst was heated from 350 °C to 810 °C, where ZSM-5 and ZSM-11 are stable within these temperature ranges [31] [32]. The final test was a stability test where the catalyst was held at 570 °C. Both catalyst materials were synthesised for 5 days.

The total flow to the reactor was set to 20.1 [ml/min], the weight hourly space velocity (WHSV) was maintained at 1415, the concentration of N_2O in the gas feed to the reactor was set to 5.1 v/v %. Helium was used to dilute the gas feed. The gaseous mixture leaving the reactor was periodically measured using the Agilent Technologies 7820A gas chromatograph (GC) system.

The metrics used in quantitively describing the performance of the catalysts are listed below:

$$Yield\ of\ Nitrogen = \frac{Outlet\ Nitrogen\ Flowrate}{Inlet\ N_2O\ Flowrate} \quad (2)$$

$$Yield\ of\ Oxygen = \frac{Outlet\ Oxygen\ Flowrate}{Inlet\ N_2O\ Flowrate} \quad (3)$$

$$Turnover\ Freuqency = \frac{Rate\ of\ N_2O\ Converted\ [molar]}{Total\ Amount\ of\ Fe\ [molar]} \quad (4)$$

The yield highlighted the conversion rate of the NO_x decomposition, furthermore, both equations (2) & (3) were required to validate the postulated reaction mechanism. The turnover frequency (TOF) was defined with respect to the total moles of iron present in our catalysts, allowing for the determination of the concentration of surface-active sites. Note that the calculated TOF would only provide an estimation of the 'real' concentration of surface-active sites due to the presence of spectator iron species within the zeolite framework.

4.3.2 Reaction Tests – MFI & MEL

The step response curve and steady-state response on the stream for the Fe-substituted MFI and MEL zeolites can be seen in *figures 9* and *10*, respectively. Below the temperature of 450 °C, both catalyst families were unable to increase the decomposition of N_2O, within this region the conversion plateaued at ~7 %. As the temperature increased beyond 450 °C, both MEL and MFI calcinated zeolites demonstrated significant catalyst activity. The conversion of N_2O to nitrogen and oxygen continued to increase, till the reaction temperature exceed ~670 °C, corresponding to a conversion of ~94 % in the case of the 0.1Fe/ZSM-11 (45) synthesised for 5 days, and ~90 % in the case of 0.25Fe/ZSM-5 (90) synthesised for 5 days. The TOF peaked at 0.546 (min^{-1}) and 0.544 (min^{-1}) for ZSM-11 synthesised at 175 °C and 190 °C, respectively. The TOF peaked at 0.224 (min^{-1}) in the case of the ZSM-5 catalyst. Although the crystallinity of both materials was similar, BET analysis of the materials clearly demonstrated the enhanced catalytic properties of 0.1Fe/ZSM-11 (45) which were a consequence of the differences in topology. Furthermore, due to the difference in Si/Al ratio; literature has highlighted the poor catalytic behaviour of ZSM-5 (90) in comparison to ZSM-5 (45) as a lower Si:Al ratio can facilitate a higher concentration of active sites, this is because active sites have been observed to form on the Al moiety in the zeolite framework [11].

The conversion rate of the catalysts was stable for both materials as time spent on-stream increased. Thus, there was no catalyst degradation. However, the steady-state conversion of the catalysts was noticeably lower at 570 °C, compared to that of the step response experiment; this result was more evident in the case of the MEL catalysts compared to the MFI catalysts. A subtle trend that was noticed which supported the theory that surface-oxygen dissociation in N_2O decomposition was the rate-limiting step, was that the concentration of nitrogen leaving the furnace reactor in comparison to oxygen was greater than double, indicating significant amounts of oxygen was still bound to the active site of the catalysts.

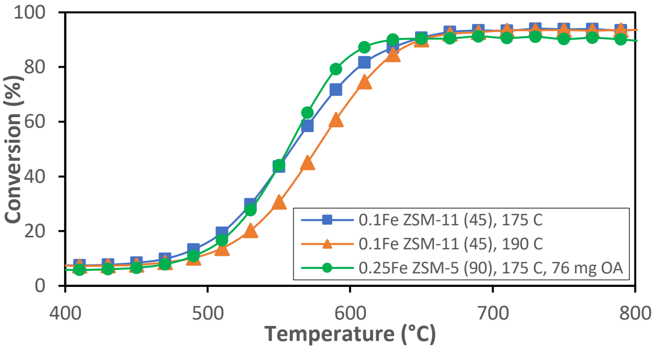

Fig. 9: N20 conversion for calcined MEL zeolites (5 days) and MFI zeolite (5 days) as temperature increases

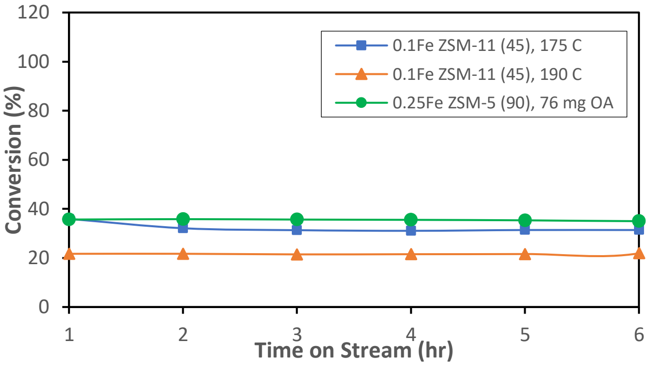

Fig. 10: N20 conversion for calcined MEL and MFI zeolites where reaction temperature is held constant at 570 C, and time spent on stream increases

5 Conclusions

A series of iron substituted MFI and MEL catalysts were synthesised successfully, where the properties of the materials were characterised by XRD, UV-Vis, and N_2 adsorption via the 3-Flex analyser. The influence of oxalate ligand functionalization on the ZSM-5 catalyst was studied; it was found that for a higher concentration of oxalic acid present during the impregnation step of the metal within the zeolite framework, the obtained yield of catalytic material in batch synthesis runs increased by up to 20%. These findings were acceptable within an error range of 4%. The effect of the OA precursor on material yield was most significant in scenarios where the iron weight loading (%) were lower.

Furthermore, characterisation results demonstrated iron oxalate supported enhanced textural and crystallinity properties: From XRD analysis, the crystallinity of the synthesised catalysts increased by 10% as the mass of the oxalic acid content was doubled in the reaction with iron nitrate nonahydrate. Similarly, the BET surface area and N_2 adsorbed increased significantly. From UV-vis spectroscopy, the increase in oxalic acid concentration had no bearing upon the nuclearity of the as-synthesised Fe species present. A consistent conclusion that was drawn from UV-vis spectroscopy was that the MFI catalysts demonstrated two strong absorbance peaks at 215 nm and 240 nm, indicating the presence of tetrahedral Fe^{3+} sites [25]. There was significant absorbance at 280 nm indicating (possibly isolated) octahedral Fe^{3+} sites at extra-framework positions [26]. There were weak absorbances in the region of 300 nm – 400 nm, which is attributed to the presence of oligomeric tetrahedrally coordinated Fe_xO_Y clusters within the MFI zeolite micropores [27]. Relatively, there was no absorption past 400 nm, which suggested there was little/to no presence of Fe_2O_3 nanoparticles.

The performance of the MFI and MEL catalysts were evaluated in N_2O decomposition. Although the variation in preparation methods and Si:Al ratio highlight difficulty in quantitatively comparing the performance of the catalysts, the results were summarised to put the results in this paper in perspective. In conclusion, the calcinated 0.1Fe/ZSM-11 (45) catalyst demonstrated similar catalytic activity to the calcinated 0.25Fe/ZSM-5 (90) catalyst. As the reaction temperature increased between 450 °C and 630 °C, the conversion of N_2O increased significantly from 7 %. The MEL catalyst series demonstrated a maximum conversion of ~94 %. Conversely, the calcinated 0.25Fe/ZSM-5 (90) catalyst achieved a maximum conversion of ~90%. Similarly, the TOF of the MFI zeolites were found to be lower than their MEL counterparts. These results can be attributed to the increased active site availability due to more rapid intracrystalline diffusion within the less tortuous straight channels of the MEL catalysts.

In comparison to current industrial applications, our synthesis approach achieved a high yield (%) of ZSM-5 material within hours in comparison to the long time-scale of days currently utilised in industry. The materials synthesised in this study were significantly developed even at 30 minutes in some instances, offering an economical and environmental benign strategy for synthesizing Fe-substituted ZSM-5 without the need for seeds or high concentrations of OSDAs. Furthermore, the preparation method in synthesising the MEL zeolites was far more arduous as long timescales and high content of organic structure-directing agents (OSDA) were required, this posed limitations in developing larger-scaled production techniques due to the economic burden incurred because of the prohibitively high costs. The MFI catalyst offers similar catalytic activity in nitrous oxide decomposition, offering a competitive synthesis pathway.

6 Outlook

To achieve enhanced catalytic properties and yield of catalytic material, oxalic acid should be incorporated within the impregnation step of the synthesis. All in all, this approach offers a competitive pathway, avoiding the basic pH and high OSDA content required in ZSM-11 synthesis.

Although the performance of both zeolite families has been evaluated by N_2O decomposition, the quartz wool required to perform further reactions was limited. Thus, the influence of oxalate ligand functionalisation has not been studied kinetically. Similarly, due to reagent limitations, a limited range of synthesis conditions was tested: The Si:Al ratio of the synthesised catalysts could not be adjusted, nor other reagent conditions. As such, further experimental studies can be carried out to synthesis ZSM-5 (45) at different oxalic acid concentrations to achieve a fair and comprehensive comparison to the standard ZSM-11 (45) catalyst. Similarly, repeat experiments and analyses should be conducted to strengthen these findings.

Work has commenced in the development of a semi-continuous synthesis approach, in which the quantity of ZSM-5 material synthesised can be increased to a large scale, bypassing the limitations associated with the batch process approach.

To verify the uptake of iron within the zeolite framework, inductively coupled plasma-optical emission spectroscopy (ICP-OES) should be deployed. In which the Si/(Al + Fe) molar ratios can be calculated and compared to the expected values. This will give a better understanding of the crystallisation process.

References

[1] B. R and S. S, "Selective catalytic reduction of nitric oxide with ethane and methane on some metal exchanged ZSM-5 zeolites," 24 May 1994. [Online]. Available: https://doi.org/10.1016/0926-3373(94)0004X-9.

[2] A. Corma and J. Martínez-Triguero, "The Use of MCM-22 as a Cracking Zeolitic Additive for FCC," 1 January 1997. [Online]. Available: https://doi.org/10.1006/jcat.1997.1474.

[3] M. Y. Kustova, A. Kustov, S. E. Christiansen and K. T. Leth, “Cu-ZSM-5, Cu-ZSM-11, and Cu-ZSM-12 catalysts for direct NO decomposition,” 2006.

[4] Y. Shen, T. T. Le, R. Li and J. D. Rimer, “Optimized Synthesis of ZSM-11 Catalysts using 1,8-Diaminooctane as a,” Department of Chemical and Biomolecular Engineering, University of Houston, 2018.

[5] K. Itabashi, Y. Kamimura, K. Iyoki, A. Shimojima and T. Okubo, “A Working Hypothesis for Broadening Framework Types of Zeolites in Seed-Assisted Synthesis without Organic Structure-Directing Agent,” 2012.

[6] T. W. v. Deelen, C. H. Mejía and K. P. d. Jong, “Control of metal-support interactions in heterogeneous catalysts to enhance activity and selectivity,” 2019.

[7] K. Al-Dalama and A. Stanislaus, “Temperature programmed reduction of SiO2–Al2O3 supported Ni, Mo and NiMo catalysts prepared with EDTA,” 2011.

[8] O. B. Ayodele, “Influence of oxalate ligand functionalization on Co/ZSM-5 activity in Fischer Tropsch synthesis and hydrodeoxygenation of oleic acid into hydrocarbon fuels,” 2017.

[9] N. Richards, E. Nowicka, J. Carter and e. al., “Investigating the Influence of Fe Speciation on N2O Decomposition Over Fe–ZSM-5 Catalysts”.

[10] J. WANG, H. XIA, X. JU, F. FAN, Z. FENG and Can LI, “Catalytic performance of different types of iron zeolites in N2O decomposition,” 2013.

[11] G.I.Pannov, V.I.Sobolev and A.S.Kharitonov, “The role of iron in N2O decomposition on ZSM-5 zeolite and reactivity of the surface oxygen formed,” 1990.

[12] E. Starokon, K. Dubkov, L. Pirutko and G. Panov, “Mechanisms of Iron Activation on Fe-Containing Zeolites and the Charge of α-Oxygen,” 2003.

[13] G. Pirngruber, P. Roy and R. Prins, “The role of autoreduction and of oxygen mobility in N2O decomposition over Fe-ZSM-5,” 2007.

[14] N. Richards, E. Nowicka, J. H. Carter, D. J. Morgan, N. F. Dummer, S. Golunski and G. J. Hutchings, “Investigating the Influence of Fe Speciation on N2O Decomposition Over Fe–ZSM-5 Catalysts,” 2018.

[15] B. R.Wood, J. A.Reimer and A. T.Bell, “Studies of N2O Adsorption and Decomposition on Fe–ZSM-5,” 2002.

[16] P. Xie, Z. Ma, H. Zhou, C. Huang and Y. Yue, “Catalytic decomposition of N2O over Cu-ZSM-11 catalysts,” 2014.

[17] P. Xie, Y. Luo, Z. Ma, C. Huang, C. Miao, Y. Yue, W. Hua and Z. Gao, “Catalytic decomposition of N2O over Fe-ZSM-11 catalysts prepared by different methods: Nature of active Fe species,” 2015.

[18] S. Narayanan, A. Sultana, K. Krishna, P. Mériaudeau and C. Naccache, “Synthesis of ZSM-5 type zeolites with and without template and evaluation of physicochemical properties and aniline alkylation activity,” March 1995. [Online]. Available: https://doi.org/10.1007/BF00808329.

[19] K. Skalska, J. S. Miller and S. Ledakowicz, “Trends in NOx Abatement: A Review,” 2010.

[20] M. Kim and K. Yang, “The Role of Fe2O3 Species in Depressing the Formation of N2O in the Selective Reduction of NO by NH3,” 2018.

[21] D. Kwon, K. Park, H. Ha and S. Hong, “ The role of molybdenum on the enhanced performance and SO2 resistance of V/Mo-Ti catalysts for NH3-SCR,” Appl. Surf. Sci., 2019.

[22] G. T. KOKOTAILO and D. C. A. FYFE, “ZEOLITE STRUCTURE ANALYSIS WITH POWDER,” Department of Chemistry, University of British Columbia, 1995.

[23] S. P. Shylesh, I. R. Shaikh, R. A. Shaikh, A. A. Shaikh and et.al, “H-ZSM-5 Zeolite Synthesis by Sourcing Silica from the Wheat Husk Ash: Characterization and Application as a Versatile Heterogeneous Catalyst in Organic Transformations including Some Multicomponent Reactions,” 2015.

[24] M. S. Kumar, M. Schwidder, W. Grünert and A. Brückner, “On the nature of different iron sites and their catalytic role in Fe-ZSM-5 DeNOx catalysts: new insights by a combined EPR and UV/VIS spectroscopic approach,” 2004.

[25] E. HENSEN, Q. ZHU, R. JANSSEN, P. MAGUSIN, P. KOOYMAN and R. VANSANTEN, “Selective oxidation of benzene to phenol with nitrous oxide over MFI zeolites - On the role of Iron,” 2005.

[26] G. D. Pirngruber, P. K. Roy and R. Prins, “On determining the nuclearity of iron sites in Fe-ZSM-5—a critical evaluation,” 2006.

[27] J. G. A. B. M. K. U. B. M. D. L. V. J. Pérez-Ramírez, “Evolution of isomorphously substituted iron zeolites during activation: comparison of Fe-beta and Fe-ZSM-5,” 2005.

[28] H. L. Chen, J. Dinga and Y. M. Wang, “One-step synthesis of mesoporous ZSM-11 composites through a dual-template method,” 2013.

[29] H.-J. Li, X.-D. Zhou, Y.-H. Di, J.-M. Zhang and Y. Zhang, “Effect of Si-ATP/CTAB ratio on crystal morphology, pore structure and adsorption performance of hierarchical (H) ZSM-11 zeolite,” 2018.

[30] C. Prestipino, M. Rivallan, S. Bordiga, C. Lamberti and A. Zecchina, “Behavior of extraframework Fe sites in MFI and MCM-22 zeolites upon interaction with N2O and NO,” 2006.

[31] K. Sun, H. Xia, E. Hensen, R. v. Santen and C. Li, “Chemistry of N2O decomposition on active sites with different nature: Effect of high-temperature treatment of Fe/ZSM-5,” 2006.

[32] M. S. Renzini, L. C. Lerici, U. Sedran and L. B. Pierella, “Stability of ZSM-11 and BETA zeolites during the catalytic cracking of low-density polyethylene,” 2011.

[33] K. Jíša, J. Nováková, M. Schwarze, A. Vondrová, S. Sklenák and Z. Sobalik, “Role of the Fe-zeolite structure and iron state in the N2O decomposition: Comparison of Fe-FER, Fe-BEA, and Fe-MFI catalysts,” 2009.

Acknowledgements

The author would like to express his sincere appreciation to Dr C Hammond, but especially Dr G Tarantino for their support and guidance offered throughout this research project. The author is also sincerely grateful to the whole of Hammond Group, for hosting him in their facilities for over 4 months, where they offered amazing professional and moral support throughout the past semester that was spent together in the lab.

Supplementary Material

Supplementary material for this report can be found in the supporting document attached.

Computer-Aided Design of Optimal Adhesive Mixture Formulations of Medical Nail Patches

Farah El-Hamri and Sumaiyah Jiffry
Department of Chemical Engineering, Imperial College London, U.K.

Abstract Onychomycosis is a fungal infection of the nail and is the most common nail disorder globally. Adhesive medical patches can be applied topically to the nail, releasing a therapeutic drug to the infected area. The pressure sensitive adhesive (PSA) is formulated from a blend of the adhesive polymer, solvents, and the medical drug. Computer Aided Mixture/Blend Design (CAMbD) provides a framework to systematically solve for optimal mixture formulations by optimising a Mixed Integer Non-Linear Program for a predefined objective function. The sensitivity of the CAMbD optimal adhesive formulations to changes in the nail plate surface energy, and the robustness of the model to a range of nail plate scenarios are unknown. Additionally, the relationships between multiple competing objective functions have not been previously investigated. The present work will show that the efficacy of a medical nail patch relies heavily on the surface energy of the nail plate substrate, which at low values can limit both the solubility of the loading drug in the adhesive polymer and the thermodynamic work of adhesion between the PSA film and the nail. In the development of a robust solution, only 2 feasible formulations were found which could satisfy the required surface energy and variance constraints, each corresponding to a unique adhesive polymer, showing that there are limited optimal formulations over a range of nail plate surface energies. The objective functions of the solubility parameter distance, toxicity, and thermodynamic work of adhesion were all found to be competing with respect to each other. Thus, indicating that improving one objective causes a worsening of the other. The results of this assay provide a foundation for more refined models for the computational design of medical nail patches.

1. Introduction

Onychomycosis is a fungal infection of the nail caused by dermatophytes, yeasts, and non-dermatophyte molds [1]. It is the most common nail disorder, affecting a substantial 14-18% of the global population [2]. Depending on the clinical classification, onychomycosis can attack the hyponychium, nail plate and nail bed, or the proximal nail folds [3], causing discolouration, thickening, and splitting of the nail.

There are a number of treatment methods available for onychomycosis. Systemic oral therapies are the most common approach [1]. However, the liver toxicity of oral drugs is a major concern [4]. In chronic cases, the infected area of the nail may be treated by surgical or device-based therapies. However, surgical methods are less patient-friendly, and the rate of reinfection is higher than in other treatment approaches [5].

Another effective treatment method is that of topical therapies. These include solutions, lacquers, films, gels, and medical adhesive nail patches. Topical treatment is more desirable than other methods, as it avoids negative systemic effects and drug interactions. However, maintaining a drug concentration in the nail that is high enough for effective treatment can be a key limitation, and analysing drug penetration can be a complex task [6]. In general, combinations of topical and oral therapies have been employed for more effective treatment.

Medical adhesive nail patches present a promising alternative therapy for onychomycosis. The nail patches are applied to the infected area and release the drug in a controlled dosage to the nail over the period of application [7]. Whilst numerous patch types are commercially available, this work will focus on the drug-in adhesive matrix type, where a pressure sensitive adhesive acts as a carrier for the drug. The adhesive layer is positioned between a backing membrane and release liner [8]. This formulation is regarded to be the most advanced and easiest to apply. These patch types offer improved bioavailability of the drug, as first-pass metabolism in the liver and GI tract are avoided [9], in addition to being relatively painless, with minimal side effects.

The pressure sensitive adhesive is formulated from a blend of component chemicals, including solvents, the polymeric adhesive, the medical drug, and traces of additives. Generating an optimal formulation poses a numerical challenge as the identities, numbers, and compositions of the components must be determined combinatorically, and in accordance with mechanical and rheological requirements [10]. The common approaches for developing product formulations include experimental or empirical methods that utilise database searches. However, these methods are often inefficient and produce relatively small design spaces due to time and cost constraints [11].

Therefore, there is a clear need for a computer-based systematic tool that combines with property models to identify product attributes, the selection of components, and an evaluation of the final product [11]. Computer Aided Mixture/Blend Design (CAMbD) provides a framework to systematically and resourcefully solve for optimal adhesive formulations. The primary objective of CAMbD is to generate a design space of theoretically feasible formulations, which can be further developed through experiments.

The CAMbD framework makes use of an MINLP problem, subject to constraints on the properties of the mixture, to develop a formulation that optimises a predefined objective function [12]. The aim of this work is to develop and investigate a comprehensive CAMbD model of a drug-in- adhesive matrix nail patch. The objective of the model is to optimise the mixture formulation of the polymer and solvent compounds in the adhesive. Ingredient properties are optimised simultaneously, such as to satisfy imposed constraints and to minimise the chosen objectives.

2. Background

The pressure sensitive adhesive is a polymer-solvent matrix, and is defined to be a material that, under light pressure, adheres to the substrate and does not leave behind any residue once removed [10]. It consists of a formulated polymer-solvent mixture containing the drug of interest. The solvent is then evaporated, leaving behind a sticky adhesive residue. Critically, the adhesive polymer must be stable and functional in the patch, be biocompatible with the drug and excipients, and facilitate sufficient drug diffusivity [8]. It functions as both a mechanism for adhesion and a drug carrier [13] and thus the drug must dissolve well in the adhesive. The choice of drug was selected such that it would not alter the properties of the patch formulation.

The drugs terbinafine-HCl, amorolfine-HCl, ciclopirox olamine and efinaconazole are commonly used in onychomycosis treatments [14]. In 2014, prior to approval by the FDA of Kerydin® and Jublia®, amorolfine-HCl was widely used as a nail lacquer, as it demonstrated great efficacy as a topical treatment [7]. This work will focus on the modelling of amorolfine-HCl as the drug of choice in the nail patch formulation.

The literature on nail patch design is relatively limited. Previous work has involved investigating the influence of the nail patch components on ungual drug permeation [15], testing the use of nail patches in the photo-dynamic therapy of onychomycosis [16], investigating sertaconazole nail patches in a study on human volunteers [17], and developing a systematic approach to formulating anti-onychomycotic nail patches [10]. The limited sphere of work is mainly due to the difficulties of estimating possible formulations of an adhesive over a large design space, due to the complicated chemical structures of the polymers and solvents [18]

There remains a significant scope to develop efficient computer-based approaches for the design of multicomponent mixtures and adhesive formulations. There have been several reviews on computer-aided methodologies and their applications. Several CAMbD studies have been conducted on integrating health, safety, and environmental parameters into the design of pharmaceutical and fine chemical products [19]. Other work has presented a review of a range of product categories, by their classification into molecular, formulated, and functional products [20]. Most of the existing methodologies of CAMbD follow a hierarchical approach, where the polymer is chosen first, followed by the choice of a corresponding solvent or binary solvent mixture [18]. A general computer-aided methodology was developed [11], where the choices of integer design variables, the main product properties, and imposed environmental constraints were optimised simultaneously, rather than in a hierarchical manner. This study has presented promising results that may be relevant to the case of medical adhesive nail patches.

Limited research has been done on the application of CAMbD to nail patch design. However, in a previous study, the use of CAMbD in the direct design of adhesive nail patches was investigated [7]. The study developed a single-objective model to solve for locally optimal adhesive formulations. It examined different case studies of drug choices, and polymer and solvent choices to investigate the efficacy of the model and obtained results. This work aims to expand upon existing research contributions [7] and previously developed generic methodologies [11] by investigating 3 interconnected objectives.

The first objective was motivated by the fact that in a clinical setting, different patients will have nails in a range of different conditions, but the nails should still be treated effectively by the same nail patch. The main parameter for modelling different nail plates is the surface energy, as it is a key variable influencing the compatibility of the nail and adhesive polymer. This work aims to investigate the sensitivity of the model to changes in the individual surface energy parameters. The sensitivity analysis is then expanded to investigate the response of the model to changes in surface energy over a 3D feasible region.

The second objective builds upon the sensitivity analysis, with the aim of developing a robust adhesive formulation that is a feasible optimum over a range of nail surface energies.

The third objective of the project involved applying a new methodology to CAMbD design; that of multi-objective optimisation. This involves solving the problem to optimise 2 objectives, which are often conflicting, such that improving one objective will cause a worsening of the other. In CAMbD, it is common practice for 2 objective functions to be combined into one, such that a single, combined function is minimised only [7]. In this work, multi-objective optimisation was used to optimise individual competing functions together, to investigate the relationship between the variables, and analyse their trade-offs.

3. Methods

3.1 Building the CAMbD framework

In CAMbD, chemically feasible molecular structures are generated from a set of functional groups, and specific properties can be estimated by group contribution methods.

The general mathematical programming representation of a CAMbD problem is outlined below:

$$\begin{gathered} min_{x,y}\, f_{OBJ}(\boldsymbol{x},\boldsymbol{y}) \\ h(\boldsymbol{x},\boldsymbol{y}) = 0 \\ g(\boldsymbol{x},\boldsymbol{y}) \leq 0 \\ \boldsymbol{x} \in [\boldsymbol{x}^L, \boldsymbol{x}^U]^m \\ \boldsymbol{y} \in [0,1]^n \end{gathered}$$

where $f_{OBJ}(\boldsymbol{x},\boldsymbol{y})$ is the objective function, $\boldsymbol{x}$ is the vector of continuous variables, $\boldsymbol{y}$ is the vector of binary variables, $h(\boldsymbol{x},\boldsymbol{y})$ is the set of equality constraints and $g(\boldsymbol{x},\boldsymbol{y})$ is the set of inequality constraints.

The CAMbD framework developed in this study was implemented in the General Algebraic Modelling System (GAMS), by way of an MINLP formulation that was adapted to each stage of the study.

The design space of the problem is the space of all loading drugs, polymers and solvents being considered as candidates, which is detailed in the Supplementary Material. The choice of drug was fixed as amorolfine-HCL. Sixteen candidate polymers were selected, building on previous work [7], that have been proven to be feasible in transdermal design systems.

Thirty-four organic solvents were chosen as candidates on account of their ability to enhance ungual drug permeability [10], and suitability from a health, safety, and environmental perspective, based on the GlaxoSmithKline solvent guide [21].

Key features of the CAMbD framework include the use of group contribution methods to estimate rheological properties such as the Hansen Solubility Parameters, which predict drug-nail affinities, and mechanical properties such as elastic constants and tensile properties of the polymer. The objective functions in this study are the solubility parameter distance between the polymer and drug (R_a), the thermodynamic work of adhesion between the polymer and nail-plate ($\psi_{jj,m}$) and the objective function *z*, which are described by the following equations. The subscripts *jj*, *d* and *m* denote the chosen polymer, drug and the nail plate respectively):

$$R_a^2 = 4\left(\delta_{jj}^d - \delta_d^d\right)^2 + \left(\delta_{jj}^p - \delta_d^p\right)^2 + \left(\delta_{jj}^h - \delta_d^h\right)^2 \qquad (1)$$

$$\psi_{jj,m} = 2\sqrt{\gamma_{jj}{}^d\,\gamma_m{}^d} + 2\sqrt{\gamma_{jj}{}^p\,\gamma_m{}^p} \qquad (2)$$

$$z = \frac{R_a}{\psi_{jj,m}} \qquad (3)$$

where δ^d, $\delta^p$and δ^h are dispersive, polar and hydrogen bonding Hansen Solubility Parameters.

The objective of the design problem was to choose the best formulation of a polymer and solvent mixture to maximise adhesive-drug compatibility (minimising R_a), whilst maximising the thermodynamic work of adhesion, to minimise *z* overall.

The key model constraints included minimum allowable mole fractions of components in the formulation and the limit on toxicity of the solvent mixture. The governing constraint in this study was found to be the following:

$$\gamma_{jj} \leq \gamma_m \qquad (4)$$

which states that the total surface energy of the liquid film (PSA) must be less than that of the solid substrate (nail plate) for good intrinsic adhesion [22].

3.2 Testing sensitivity of objective functions to polar/dispersive surface energies of the nail plate

The surface energy of the human nail plate is a key parameter affecting the efficacy of adhesion and drug permeation of medical nail patches. Whilst essential to the choice of final formulation, the surface energy is expected to vary widely from patient to patient, depending on the state of the nail [23].

3.2.1 Determination of Surface Energy Component Ranges

The total surface energy of the human nail plate (γ_m) comprises polar ($\gamma_m{}^p$) and dispersive ($\gamma_m{}^d$) components, and is described by the Fowkes model [24]:

$$\gamma_m = \gamma_m{}^p + \gamma_m{}^d \qquad (5)$$

The average polar and dispersive surface energies of the human nail plate are 8 mJm^{-2} and 24 mJm^{-2} respectively, as reported in literature [25]. The measured uncertainty in the total surface energy value was reported to be ±3 mJm^{-2}. These values were calculated using the mathematically rigorous Wu method [26] using human nail clippings. To assess the sensitivity of the objective function to deviations in the surface energy, a suitable range of values for the individual polar and dispersive components was determined.

In a previous study, the Van Oss model using the Lifshitz–van der Waals/acid–base (LW-AB) approach was employed to determine the polar acid–base ($\gamma_m{}^{AB}$) and apolar Lifshitz–van der Waals ($\gamma_m{}^{LW}$) surface energy components of human nails in three different states: untreated, hydrated and abraded [23]. The untreated nail represents a baseline scenario, and its surface energy can change upon hydration or abrasion. Hydration may result from the application of topical nail medicines. Abrasion is clinically significant in practice, as patients abrade their nail plates prior to applying medicines to increase ungual drug permeation [23].

Although the polar acid-base and the apolar Lifshitz–van der Waals components of surface energy are not equivalent to the polar and dispersive components discussed in the current study, they account for similar types of intermolecular forces of attraction and are comparable in magnitude relative to the total surface energy. Hence, they were considered to be suitable surrogates to inform the limits of uncertainty.

Accounting for the uncertainties in experimental data across the three possible nail states [23], the lower and upper bounds of $\gamma_m{}^{AB}$ were calculated to be 0 mJm^{-2} and 6.1 mJm^{-2}, and the corresponding values for $\gamma_m{}^{LW}$ were 29.8 mJm^{-2} and 41.2 mJm^{-2}. Advocates of the LW-AB theory have demonstrated that when experimentally measuring the $\gamma_m{}^{AB}$ component, slight measurement errors or 'noise' in the data can cause negative values to be reported [27]. In addition to the imperfect knowledge of the behaviour of the $\gamma_m{}^{AB}$ components, it is common practice to take the lower bound as zero [28], discounting the negative values. The same approach was employed in this work.

In view of the calculated bounds of $\gamma_m{}^{AB}$and $\gamma_m{}^{LW}$ as well as the uncertainty in measured average values for polar and dispersive surface energies of nail clippings, the ranges of uncertainty of $\gamma_m{}^p$ and $\gamma_m{}^d$ were set to be 0-9 mJm^{-2} and 22-37 mJm^{-2}.

3.2.2 MINLP Solver Methods

The elasticity of the optimised objective functions with respect to variations in $\gamma_m{}^p$ was investigated, holding $\gamma_m{}^d$ constant at 24 mJm^{-2}. The model was run using two independent MINLP local solvers. The first was the local solver SBB, and the second was the BARON solver with use of the *FirstLoc* option. The *FirstLoc* option terminates the search for a feasible solution at each value of $\gamma_m{}^p$ once the first local optimum has been found, irrespective of solution quality. In the current study, both local solvers were used to increase the accuracy of the recorded solutions, as each solver utilises a different algorithm. The SBB solver is highly sensitive to the choice of initial conditions, whereas the Baron *FirstLoc* option reports the first-found local optimum.

The results of the two different algorithms, SBB and BARON with *FirstLoc*, were compared and the best local optima were recorded in sensitivity plots. In a similar manner, the elasticity of the objective functions with respect to changes in ${\gamma_m}^d$ was also explored, holding ${\gamma_m}^p$ constant at 8 mJm^{-2}.

Irregularities in the optimised objective functions were investigated by applying the *CompIIS* option to the BARON solver. The model was re-run in the regions of non-uniformity, imposing equality constraints on the polymer and solvent choices of the solution to investigate the model infeasibilities which caused irregularities in the objective function. *CompIIS* allowed for the identification of the set of constraints that were made infeasible. A second approach involved using the SBB solver, also setting equality constraints on the polymer and solvent choices, and manually analysing the *GAMS* report to ascertain constraints that changed in activity in the neighbourhood of the non-uniformity.

Sensitivity analysis was repeated for ${\gamma_m}^p$ over the full range of ${\gamma_m}^d$(22-37 mJm^{-2}). The results were plotted on a 3-dimensional (3D) surface using MATLAB.

3.3 Constructing a robust model to simultaneously optimise objectives in different scenarios

The first step in developing a robust polymer/solvent blend that could be used by patients regardless of the condition of their nail-plate surface, was to produce a Sobol sequence using the scientific computation library *SciPy* in *Python*. A Sobol sequence is a quasi-random, low-discrepancy point set that fills space in a highly uniform manner [29]. Hence, this was used to generate five scenarios capturing different combinations of ${\gamma_m}^d$ and ${\gamma_m}^p$ which were representative of the overall design space. These scenarios are depicted in Table 1.

Table 1. ${\gamma_m}^p$, ${\gamma_m}^d$, γ_m values in different Sobol scenarios

Scenario Number	**${\gamma_m}^p$ [mJm^{-2}]**	**${\gamma_m}^d$ [mJm^{-2}]**	**γ_m [mJm^{-2}]**
1	2.12	34.55	36.67
2	8.36	28.5	36.86
3	4.84	31.71	36.55
4	3.09	23.86	26.95
5	4.01	30.74	34.75

The surface energies in each scenario were encoded in a *GAMS* model built to minimise the averaged objective function $\bar{Z}$, given by:

$$\bar{Z} = \frac{\sum_{i=1}^{5} z_i}{5} \tag{6}$$

in which *i* denotes the scenario number. In addition, a strict constraint on the variance, σ^2, was introduced:

$$\sigma^2 = \frac{\sum_{i=1}^{5}(z_i - \bar{Z})}{5-1} \leq 0.02 \tag{7}$$

The problem could be approached by two methods. In the first, BARON was used with the *NumSol* facility, which is a powerful tool that enables enumeration of all feasible solutions in the design space.

In the alternative method, the BARON solver was used with two integer cuts added to the model. In each integer cut, the chosen optimal polymer of the previous solution was excluded from the feasible design inputs. Thus, global optima could be found in an increasingly restricted design space.

3.4 Multi-objective optimisation to explore the trade-offs between competing objective functions

The design problem in this study consists of multiple potentially conflicting variables, which cannot be concurrently optimised. In multi-objective optimisation, the trade-off between objective functions of interest can be investigated, and an appropriate operating point may be chosen by engineering judgement.

The trade-offs between three pairs of objective functions - $R_a$and $\psi_{jj,m}$, $\psi_{jj,m}$ and *τ*, and R_a and *τ* - were analysed. The toxicity of the nail patch is given by *τ*, which follows a linear mixing rule:

$$\tau = x_{a_1}\tau_{jj} + x_{s_1}\tau_{s_1} + x_{s_2}\tau_{s_2} \tag{8}$$

where a$_1$, s$_1$ and s$_2$ represent the optimal choices of polymer and solvents, respectively.

Using the SBB solver in GAMS, the *ε*-constraint scalarisation technique was applied due to its suitability for non-convex problems. In this method, a single function f_1 in a given pair of objective functions f_1 and f_2 is minimised whilst the other is expressed as an inequality constraint:

$$f_2 \leq \varepsilon_2 \tag{9}$$

The minimisation of f_1 is repeated over the full range of ε_2, $[\varepsilon_{2,min}, \varepsilon_{2,max}]$. $\varepsilon_{2,max}$ is given by the maximum value of f_2 which occurs when f_1 is minimised as a single-objective function with no restriction on f_2. $\varepsilon_{2,min}$ is the minimum value of f_2, and this occurs when f_2 is minimised with no restriction on f_1.

The same procedure is applied to minimise f_2 subject to a constrained f_1. The two sets of results can be combined to generate a Pareto frontier, which consists of all feasible and efficient combinations of f_1 and f_2.

The main controlled variables in multi-objective optimisation were the polar and dispersive energies of the nail plate, and these were held constant at values informed by the results of sensitivity analysis.

4 Results and Discussion

4.1 Single-objective sensitivity analysis

4.1.1 Individual surface energy parameters

The sensitivity of the objective function, *z*, to independent variations in the surface energy dispersive, ${\gamma_m}^d$ and polar, ${\gamma_m}^p$ components of the nail plate was investigated.

The results for the sensitivity analysis of the objective function, *z*, for the polar component of surface energy, ${\gamma_m}^p$, are displayed in Figure 1.

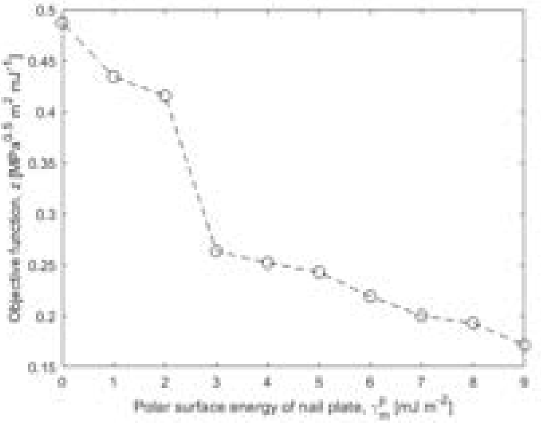

Figure 1. Variation of *z* with respect to ${\gamma_m}^p$

In both cases, as the component of surface energy increases, the thermodynamic work of adhesion between the polymer and nail plate, $\psi_{jj,m}$ increases, as described by Equation 2. The solubility parameter distance R_a was observed to decrease in a discrete fashion, directly determined by the choice of polymer in the optimal solution combination. At higher values of the total surface energy, the upper bound on the inequality constraint described by Equation 5 is relaxed, thus increasing the number of feasible polymer choices. This allows the model to solve for an improved adhesive combination with a more minimal R_a. This inequality constraint models the requirement that the surface energy of the polymer adhesive should be less than or equal to that of the nail plate substrate for the achievement of good intrinsic adhesion, as reported by [22]. The graphical results of $\psi_{jj,m}$ and R_a can be found in the attached Supplementary Material, in addition to the sensitivity results for the dispersive component of surface energy, ${\gamma_m}^d$.

The combined effects of the individual trends in $\psi_{jj,m}$ and R_a resulted in an overall decreasing value of z for an increase in the surface energy component. It was observed that there was a greater sensitivity of the objective function at lower values of both ${\gamma_m}^d$ and ${\gamma_m}^p$. This is primarily due to the behaviour of the solubility parameter distance, R_a, due to discrete changes in the choice of optimal polymer. At lower values of surface energy, the polymer feasible space is more restricted, and there are larger differences in the corresponding R_a values of each polymer, thus causing larger changes in the value of z when the choice of polymer is changed. Whereas at higher surface energies, the polymer feasible space is larger, and there are more available polymer choices with similar R_a values. Thus, the value of z exhibits a less sensitive response, decreasing in a steady and predictable fashion.

In the region of high sensitivity, discrete jumps in the value of the objective function, z were observed, indicating that the model solution is less robust to changes in the surface energy of the nail plate. There are 2 factors that contribute to these changes. The first is the changing value of the surface energy component itself, which directly determines the thermodynamic work of adhesion, affecting the objective function, z. The second factor is due to changes in the polymer choice of the optimal formulation.

The results for changes in ${\gamma_m}^p$ from 1 to 4 are as displayed in Table 2. A significant jump in the value of z can be seen from 0.4155 to 0.2634, when the polymer choice changes from PIB to PMAA.

Table 2. Sensitivity of key variables for ${\gamma_m}^p$ ranging from 2-3 mJm^{-2}

${\gamma_m}^p$ [mJ m^{-2}]	${\gamma_m}^d$ [mJ m^{-2}]	z [MPa$^{0.5}$m^2 mJ^{-1}]	R_a [MPa$^{0.5}$]	$\psi_{jj,m}$ [mJ m^{-2}]	**Optimal formulation** ***(a_1, s_1, s_2)***
2	26	0.4155	17.25	41.52	(PIB, Trimethylpentane, Octanol)
3	27	0.2634	12.30	46.71	(PMAA, Toluene, Acetone)

Changes in the polymer occur due to the requirement to satisfy Equation 5. In this case, the total surface energies of PMAA and PIB are 26.9 and 17.7, respectively. PMAA provides the most optimal objective function when ${\gamma_m}^p$ is 3, however, it cannot satisfy the necessary conditions when ${\gamma_m}^p$ is 2 and is thus an infeasible option. If PMAA were to be chosen in the latter formulation, the intrinsic adhesion of the medical nail patch would be too poor for effective drug permeation. Therefore, a jump is observed as the model is required to choose PIB instead, leading to an overall worsening of the optimal objective function.

4.1.2 3D feasible region

As the investigation into the sensitivity of the model was expanded across the full range of values for both the dispersive and polar components, a feasible region was generated containing locally optimal formulations for a range of combinations of surface energies. The aim was to model the response of the medical nail patches to different patient nails and the corresponding uncertainties in their surface energies.

Figure X displays the results of the analysis in a 3D plane. It provides a visual representation of the behaviour of the objective function over the region of interest. The point corresponding to the surface energy of human nail clippings is plotted in a magenta colour on the graph for reference.

The results obtained for the objective function, z clearly indicate that at higher levels of ${\gamma_m}^d$ and ${\gamma_m}^p$, the feasible region is smoother, and the results are less sensitive to variations in the parameter values. Whereas, at lower values of both variables, z is more sensitive to uncertainty, as there are more observed jumps and discontinuities.

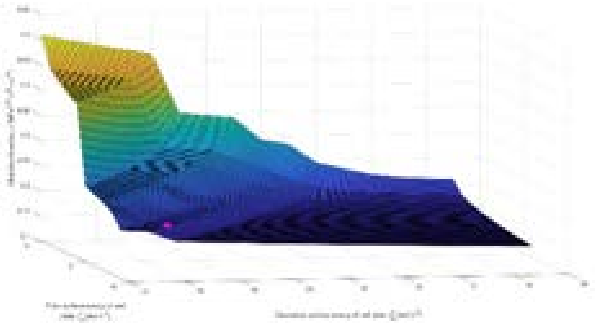

Figure 2. 3D surface showing the synergistic effects of ${\gamma_m}^d$ and ${\gamma_m}^p$ on z

The discontinuities can occur due to 2 major effects. For relatively flat regions of $\psi_{jj,m}$, the discontinuities occur due to constraint requirements, causing a necessary change in the choice of polymer.

Thus, a discontinuity will be observed in R_a and in turn, in z. This occurs in the region where the values of both ${\gamma_m}^p$ and ${\gamma_m}^d$ are low.

It was found that a discontinuity can also occur solely due to the change in surface energy such that the polymer choice remains the same, but there is nevertheless a relatively large change in z. This was observed in the region of low values of ${\gamma_m}^p$ and relatively high values of ${\gamma_m}^d$. In this region, a diagonal ridge from left to right can be observed in Figure 2. The ridge lies along the locus of points where there is a discrete increase of 1 unit of the total surface energy, γ_m. In this case, the feasible region is relaxed, causing an improvement in the objective function without a change of formulation.

Previous work has shown that the nail plate, a solid, must have a higher surface energy than the polymer component of the adhesive formulation, a liquid, for the solid to attract the liquid molecules with more force than they attract each other [22]. Hence, lower values of the surface energy components do not facilitate strong adhesion. They show a poor compatibility, in agreement with the presented results from this work, as depicted by higher values of R_a and a lower thermodynamic work of adhesion. These individual effects combine synergistically to produce higher values of the objective function z, which are influenced more strongly by changes in the optimal formulation, and relaxations of the feasible region, explaining the greater sensitivity response of the model at lower values of surface energy.

CAMbD functions as a tool to generate a design space of feasible formulations, which can be further developed through experiments. A designer or experimentalist testing the effectiveness of adhesive formulations could use the results of the sensitivity analysis to better identify the suitable range of nail surface energies, which would provide the most optimal compatibility with the formulation.

4.2 *Single-objective robustness analysis*

4.2.1 *Comparison of alternative methodologies*

The Sobol sequence was used to generate 5 individual scenarios, capturing different combinations of ${\gamma_m}^p$and ${\gamma_m}^d$, as a representation of 5 randomly chosen patient nails. These scenarios were representative of the overall design space.

Using the Baron solver with the *NumSol* option in the GAMS model to investigate robustness, the feasible region of polymer-solvent combinations was found to be extremely large. Yet, despite the large space of feasible solutions, only two unique values were obtained for the optimal averaged objective function, $\bar{Z}$. Each one of the two solutions corresponded to a distinct polymer choice in the pressure sensitive adhesive formulation, leading to a large difference in the values of the objective functions.

The large number of feasible solutions is due to the fact that R_a and $\psi_{jj,m}$ are independent of solvent choices. Hence, solvents are easily interchangeable in the optimal formulation, leading to a wide range of combinations, all with the same polymer choice. Tables 3 and 4 depict examples of some feasible formulations for each of the two optima, which were taken from the feasible region obtained via Baron *NumSol*.

Table 3. Individual scenario objectives and feasible formulations corresponding to the global optimum: $\bar{Z}$=0.2332 MPa$^{0.5}$m^{2}mJ^{-1}, R_a=12.30 MPa$^{0.5}$, σ^2= 0.04066%

Scenario Number	z [MPa$^{0.5}$m^{2}mJ$^{-1]}$	$\psi_{jj,m}$ [mJm^{-2}]	**Feasible formulations** (*a₁, s₁, s₂)*
1	0.2406	51.15	(PMAA, Acetic acid, Chlorobenzene) (PMAA, Butanone, Butanol) (PMAA, Butanone, Benzyl alcohol)
2	0.2092	58.81	
3	0.2223	55.34	
4	0.2628	46.82	
5	0.2313	53.20	

Table 4. Individual scenario objectives and feasible formulations corresponding to the second-best optimum: $\bar{Z}$=0.3583 MPa$^{0.5}$m^{2}mJ^{-1}, R_a=17.25 MPa$^{0.5}$, σ^2= 0.06491%

Scenario Number	z [MPa$^{0.5}$m^{2}mJ$^{-1]}$	$\psi_{jj,m}$ [mJm^{-2}]	**Feasible formulations** *(a₁,s₁, s₂)*
1	0.3537	48.78	(PIB, Octanol, p-Xylene) (PIB, 2-Propanol, p-Xylene) (PIB, Trimethylpentane, Octanol)
2	0.3378	51.07	
3	0.3437	50.20	
4	0.4022	42.90	
5	0.3541	48.73	

In the alternative methodology employed, two integer cuts were used to evaluate robustness. Only two unique feasible solutions were obtained, corresponding to the results of the original model and the first integer cut, whilst the second integer cut was infeasible. The two feasible solutions were in agreement with the results obtained from using the Baron *NumSol* feature, giving the same parameter values as reported in Tables 3 and 4.

The infeasibility of the third integer cut was also in agreement. The results using Baron *NumSol* indicate that the two unique reported values of $\bar{Z}$ are the only solutions in the feasible space. Hence, the entire design space had been searched, causing the reported infeasibility.

Further optimal solutions could not be found in the design space because of the constraint imposed by Equation 5. This constraint must be satisfied by each individual Sobol point. Thus, it forces the selected polymer of the robust solution to have a total surface energy below that of the lowest value of γ_m from the five individual Sobol points. Further, there is a tight imposed constraint on the variance. The above criteria were only met by the polymers PMMA and PIB, corresponding to the two feasible unique optima.

4.2.2 *Assessment of robustness*

The original GAMS model was solved to optimise each of the Sobol scenarios independently of the others, for comparison with their individual solutions corresponding to the two optima in the model for robustness analysis.

It was Scenario 4 in which ${\gamma_m}^p$=3.09 and ${\gamma_m}^d$ =23.86, which constitute the lowest overall surface energy (γ_m =26.95) that lead to the worst objective value - z=0.2628. This was to be expected, as it was previously illustrated that low values of surface energies show poor performance.

In the robust model, the individual objective value of the worst-case scenario remains identical to that of the original model but drives up the averaged objective function $\bar{Z}$ as well as the individual objectives of the other scenarios, due to the constraint that the variance relative to the average must be less than or equal to 2%.

Owing to their sufficiently high surface energies, individual solutions from the original model lie in the robust region on the 3D surface, except for that of Scenario 4 which lies at the onset of the steep, elastic region. Solutions corresponding to the global optimum from the robust model were plotted on the same surface, and all such points lie above their counterparts from the original model, except in the worst case where the two solutions coincide, as demonstrated in Figures 3 and 4.

Any one of the feasible formulations presented in Tables 3 and 4 may produce a high-performing nail patch that is applicable to all five scenarios. However, in practice it is advisable that patients increase the surface energy of their nails, for instance by abrasion, so as not to risk falling into the sensitive region of the 3D domain where slight decreases in surface energy can induce a dramatic increase in the objective function value (such as in the case of Scenario 4), as this may reduce the effectiveness of the patch and its compatibility with the nail.

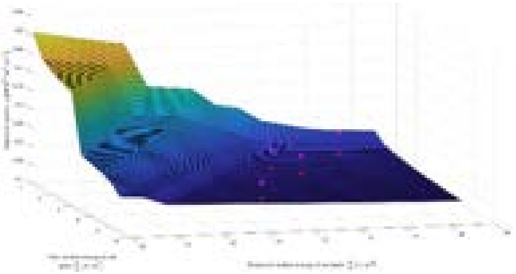

Figure 3. Positions of Sobol scenario solutions on 3D sensitivity surface (Angle 1)

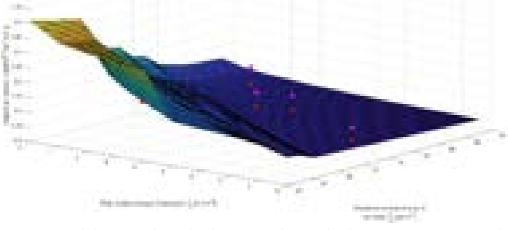

Figure 4. Positions of Sobol scenario solutions on 3D sensitivity surface (Angle 2)

4.3 *Multi-objective optimisation*

In multi-objective optimisation, the subset of all non-dominated feasible points is called the Pareto optimal set. The Pareto set forms a Pareto frontier, which represents the frontier for which no single objective can be improved without sacrificing the second objective. Therefore, the Pareto frontier visually represents the trade-off between the two objective functions under study.

The multi-objective optimisation analysis was performed to explore the 3 main objective functions, as the nature of their relationships to each other were previously unknown and ambiguous. The objective functions that were investigated were the solubility parameter distance, (R_a), the thermodynamic work of adhesion ($\psi_{jj,m}$), and the toxicity of the formulation, τ.

The investigation was performed for constant values of the surface energy parameters of the nail plate. Thus, the MOO analysis was for a given nail, and its corresponding constant parameters. The values of ${\gamma_m}^d$ and ${\gamma_m}^p$ were 37 and 2, respectively. They were chosen as such to be in the most robust region of the feasible space, as determined in Section 4.1 on sensitivity analysis. This enlarged the feasible design space such that the interplay between objective functions could be explored with no limiting effects brought about by the lack of appropriate polymer and solvent choices, that would have otherwise caused anomalies or non-uniformities in the Pareto frontiers.

4.3.1 *Multi-objective optimisation of R_a and $\psi_{jj,m}$*

As seen by the Pareto frontier in Figure 5, there is an inverse relationship between R_a and the negation of $\psi_{jj,m}$; this is intuitive as a shorter solubility parameter distance would give rise to stronger attractive forces between the adhesive and nail plate, and hence a greater thermodynamic work of adhesion.

No horizontal or vertical regions in the Pareto frontier are permissible due to the nature of the model formulation as, for any given nail plate, R_a and $\psi_{jj,m}$ depend only on the choice of polymer. Therefore, when one of the two objectives is varied (by changing the polymer), the other must also change.

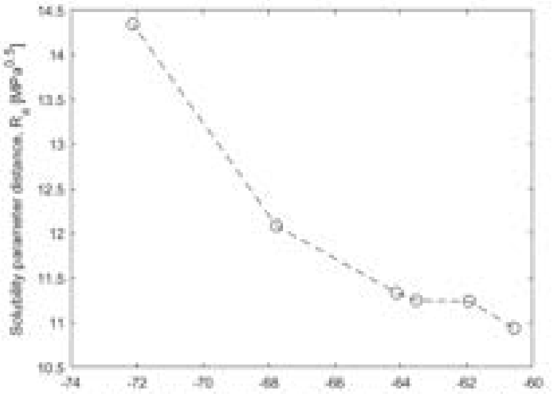

Figure 5. Pareto frontier of $R_a$versus $\psi_{jj,m}$

4.3.2 *Multi-objective optimisation of R_a and τ*

Figure 6 displays the Pareto frontier for R_a and τ. The toxicity level is governed by the polymer and solvent combination, and thus can be varied by changing the solvent mixture and fixing the polymer, leaving R_a unaffected (as it only depends on the polymer). This gives rise to a series of discrete feasible combinations, but it is only the solution associated with the lowest toxicity that is desirable. This said to dominate the other points (in red), as they display the same value of the solubility parameter, R_a, but higher, less desirable toxicities.

The Pareto frontier consists of two unique optimal values of R_a, corresponding to two different polymer choices in the adhesive formulation. The curve appears to be downwards-sloping due to the exclusion of dominated solutions, which in isolation define flat regions where there is no correlation between R_a and τ. There are two distinct flat regions on the frontier, separated by a jump in the R_a value due to a change in polymer. The R_a value is lower at higher toxicities, as there has been a relaxation of the constraint on toxicity, allowing for an enlarged design space of feasible polymers, which have more minimal values of R_a.

Within each flat region of dominated points, it appears that there is no trade-off between the two objective functions. Due to the ambiguity in this region, it cannot be concluded that R_a and τ are inversely related, and future work will be required to determine if there exists a cause-and-effect relationship between the two variables. In this regard, the frontier fails to capture the exact relationship between the two objective functions, however, it serves as a proxy to find the best possible solvent combination for a chosen polymer.

By scrutiny of the frontier, an optimal mix of decision variables can be inferred, corresponding to point A, where the solubility parameter distance is 11.09, and the toxicity is at its minimum level of 0.6395. Point B is associated with a solubility parameter distance of 10.94 and a toxicity of 0.7396. Point A is preferred, because moving from point B to A represents a considerable 13.53% decrease in toxicity for a minimal 1.37% increase in R_a, which is desirable from a biocompatibility standpoint.

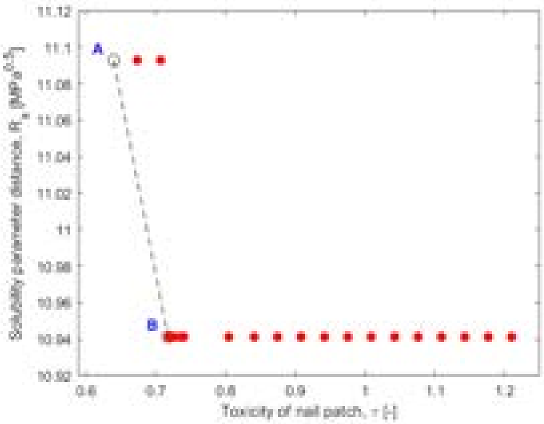

Figure 6. Pareto frontier of R_a versus τ

4.3.3 Multi-objective optimisation of $\psi_{jj,m}$ and τ

It was observed that there was an overall trade-off between the nail patch toxicity, τ, and the thermodynamic work of adhesion. The objective was to minimise toxicity, τ, and minimise the value of $-\psi_{jj,m}$.

As the toxicity was increased, the thermodynamic work of adhesion was found to increase. At higher values of toxicity, the constraints on the design space are relaxed, allowing for more polymers, with worse individual toxicity contributions, to be allowed in the feasible formulation. Thus, there are more polymers with a higher surface tension that can be chosen from the feasible region, allowing for lower values of $-\psi_{jj,m}$.

Furthermore, it has been reported [30] that the greater the surface tension of a polymer, the more easily it will spread over a solid substrate, and the higher its surface activity. In this way, a polymer that exhibits a higher thermodynamic work of adhesion, will be more toxic, as it can react more readily with biological membranes. This vindicates the negative relationship found between $-\psi_{jj,m}$ and τ.

Nonetheless, this relationship does not depict a perfect trade-off between the two variables, and a clear change in curvature in Figure 7 can be observed. This is due to the highly nonlinear nature of the problem, the numerous variables at play, and the fact that polymer choices are discrete which leads to a jagged frontier.

Additionally, there are a number of locally optimal points in this region which are considered to be dominated, depicted in red. These points represent formulations of the same polymer choice, but with different solvent combinations. Due to substitution of the solvents, the toxicity of the formulation varies, whilst the value of the thermodynamic work of adhesion is constant. This is because after the solvents have evaporated, the surface energy of the adhesive is determined by the polymer, as reflected in the model equations. Judgement should be exercised to discount the dominated points, and the point on the Pareto frontier should instead be chosen for the optimal formulation, representing the minimal toxicity for a given thermodynamic work of adhesion.

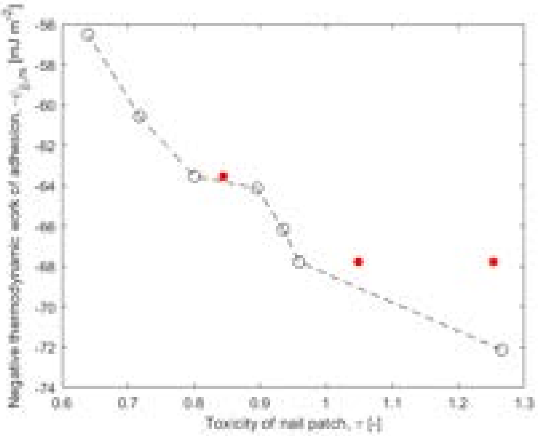

Figure 7. Pareto frontier of $\psi_{jj,m}$versus τ

5 Conclusions and Outlook

Several conclusions can be drawn from the analysis of the obtained results.

It was found that at low values of surface energy parameters, the model solutions were highly sensitive, due to changes in the optimal polymer choice of the adhesive formulation. Whereas, at higher values of the surface energy parameters, the model solutions were far less sensitive.

It is recommended that in a practical setting, nail patches should be developed with a formulation determined by the results obtained for low surface energy parameters. In this way, the formulation is guaranteed to be feasible over the majority of nail plates, although it may be sub-optimal for nails with higher surface energies. Alternatively, intervention could be made to increase the surface energy of the patient's nail before treatment. This may be most easily performed by the mechanical abrasion of the nail, although roughening, drying, or priming may also be possible.

In future work, the model formulation may be adapted to account for manual increases in the surface energy prior to treatment. The constraint for good intrinsic adhesion would be relaxed by increasing γ_m, to separate out the limiting effects that it has on the feasible design space of polymer choices. Investigations could be conducted to determine a correlation between the required level of mechanical abrasion of the nail, and the required increase in the surface energy parameters for the nail plate to be in the less-sensitive region.

The development of a robust solution was also investigated to better represent the function of a real nail patch. Only 2 feasible formulations were found which could satisfy the imposed constraints, namely that of the polymer surface energy, and that of the imposed variance. Each formulation corresponded to a unique choice of polymer, and there were no other formulations possible in the feasible space.

A future improvement to robustness analysis could include partitioning the full range of the surface energy values, and optimising the averaged objective function, $\bar{Z}$ for each partition. The number of feasible robust solutions in each division can be explored, as well as their relative positions on the 3D sensitivity plot. This could have important applications in a clinical setting, where the nail plate of a patient could be classified as either high or low in surface energy and assigned the suitable robust solution from the relevant partition. This would produce optimised results for individual patients.

Multi-objective optimisation was performed for the three most significant objective functions. The results indicated an inverse trend between R_a and $\psi_{jj,m}$. It may be concluded that for smaller R_a values, there are stronger attractive forces between the adhesive and the nail, causing a greater thermodynamic work of adhesion. A negative relationship was also observed between R_a and toxicity. However, there were many dominated solution formulations providing sub-optimal toxicity values. Further investigation would be required to confirm the observed trend. Additionally, there was an overall inverse relationship observed between $\psi_{jj,m}$ and toxicity. Higher values of toxicity led to an enlarged space of polymer choices, and higher values of $\psi_{jj,m}$ lead to greater inherent biological toxicity.

In future work, multi-objective analysis can be repeated over a variety of combinations of ${\gamma_m}^d$ and ${\gamma_m}^p$, for example those of the Sobol scenarios, to evaluate the effect of surface energy on the shape of the Pareto frontiers. This would allow for a more rigorous investigation of the interactions between key objective functions, particularly that between R_a and toxicity. Additionally, the individual scenario solutions from robustness analysis can be plotted on the relevant Pareto graphs to assess whether they are Pareto optimal.

Acknowledgements

The authors would like to thank Tanuj Karia and Lingfeng Gui who provided much appreciated assistance with the modelling tools used and insights into the results.

References

[1] A. K. Gupta, M. Paquet and F. C. Simpson, "Therapies for the treatment of onychomycosis," *Clinics in Dermatology,* vol. 31, no. 5, pp. 544-554, 2013.

[2] P. Rich and R. k. Scher, An Atlas of Diseases of the Nail, London: The Parthenon Publishing Group, 2003.

[3] O. Welsh, L. Vera-Cabrera and E. Welsh, "Onychomycosis," *Clinics in Dermatology,* vol. 28, no. 2, pp. 151-159, 2010.

[4] S. Murdan, "Nail disorders in older people, and aspects of their pharmaceutical treatment," *International Journal of Pharmaceutics,* vol. 512, no. 2, pp. 405-411, 2016.

[5] A. Kushwaha, R. N. Murthy, S. N. Murthy, R. Elkeeb, X. Hui and H. I. Maibach, "Emerging therapies for the treatment of ungual onychomycosis," *Drug Development and Industrial Pharmacy,* vol. 41, no. 10, pp. 1575-1581, 2015.

[6] A. A. Shirwaikar, T. Thomas, A. Shirwaikar, R. Lobo and K. S. Prabhu, "Treatment of Onychomycosis: An Update," *Indian Journal of Pharmaceutical Sciences,* vol. 70, no. 6, pp. 710-714, 2008.

[7] E. Kakoulidis, "Computer-aided design of pressure sensitive adhesives for medical nail patches," Centre for Process Systems Engineering, Department of Chemical Engineering, Imperial College London, London, 2020.

[8] H. S. Tan and W. R. Pfister, "Pressure-sensitive adhesives for transdermal drug delivery systems," *Pharmaceutical Science & Technology Today,* vol. 2, no. 2, pp. 60-69, 1999.

[9] M. B. Brown, G. P. Martin, S. A. Jones and F. K. Akomeah, "Dermal and transdermal drug delivery systems: Current and future prospects," *Drug Delivery: Journal of Delivery and Targeting of Therapeutic Agents,* vol. 13, no. 3, pp. 175-187, 2006.

[10] K. Rizi, I. Mohammed, K. Xu, A. Kinloch, M. Charalambides and S. Murdan, "A systematic approach to the formulation of anti-onychomycotic nail patches," *European Journal*

of Pharmaceutics and Biopharmaceutics, vol. 127, pp. 355-365, 2018.

[11] S. Jonuzaj, J. Cui and C. S. Adjiman, "Computer-aided design of optimally environmentally benign solvent-based adhesive products," *Computers and Chemical Engineering,* vol. 130, no. 106518, 2019.

[12] S. Jonuzaj, P. T. Akula, P.-M. Kleniati and C. S. Adjiman, "The formulation of optimal mixtures with generalized disjunctive programming: A solvent design case study," *AIChE Journal,* vol. 62, no. 5, pp. 1616-1633, 2015.

[13] S.-S. Baek and S.-H. Hwang, "Preparation and adhesion performance of transparent acrylic pressure-sensitive adhesives containing menthyl acrylate," *Polymer Bulletin,* vol. 73, pp. 687-701, 2016.

[14] M. Ameen, J. T. Lear, V. Madan, M. F. M. Mustapa and M. Richardson, "British Association of Dermatologists' guidelines for the management of onychomycosis," *British Journal of Dermatology,* vol. 171, no. 5, pp. 937-958, 2014.

[15] Y. Myoung and H.-K. Choi, "Permeation of ciclopirox across porcine hoof membrane: effect of pressure sensitive adhesives and vehicles," *European Journal of Pharmaceutical Sciences,* vol. 20, no. 3, pp. 319-325, 2003.

[16] R. F. Donnelly, P. A. McCarron, J. M. Lightowler and A. D. Woolfson, "Bioadhesive patch-based delivery of 5-aminolevulinic acid to the nail for photodynamic therapy of onychomycosis," *Journal of Controlled Release,* vol. 103, no. 2, pp. 381-392, 2005.

[17] R. Susilo, H. C. Korting, W. Greb and U. P. Strauss, "Nail Penetration of Sertaconazole with a Sertaconazole-Containing Nail Patch Formulation," *American Journal of Clinical Dermatology ,* vol. 7, pp. 259-262, 2006.

[18] E. Conte, R. Gani and K. M. Ng, "Design of formulated products: A systematic methodology," *AIChE Journal,* vol. 57, no. 9, pp. 2431-2449, 2011.

[19] C. Capello, U. Fischer and K. Hungerbühler, "What is a green solvent? A comprehensive framework for the environmental assessment of solvents," *Green Chemistry,* vol. 9, no. 9, pp. 927-934, 2007.

[20] R. Gani and K. Ng, "Product design – Molecules, devices, functional products, and formulated products," *Computers & Chemical Engineering,* vol. 81, pp. 70-79, 2015.

[21] C. Adler, J. Hayler, R. Henderson, A. Redman, L. Shukla, L. Shuster and H. Sneddon, "Updating and further expanding GSK's solvent sustainability guide," *Green Chemistry,* vol. 18, no. 13, pp. 3879-3890, 2016.

[22] H. Plasma, "Adhesion and Surface Energy," Henniker Plasma, 2021. [Online]. Available: https://plasmatreatment.co.uk/pt/plasma-technology-overview/adhesion-and-surface-energy. [Accessed 16 12 2021].

[23] S. Murdan, C. Poojary, D. R. Patel, J. Fernandes, A. Haman, P. S. Saundh and Z. Sheikh, "In vivo measurement of the surface energy of human fingernail plates," *International Journal of Cosmetic Science,* vol. 34, no. 3, pp. 257-262, 2012.

[24] F. F.M., "Additivity of Intermolecular Forces at Interfaces. I. Determination of the Contribution to Surface and Interfacial Tensions of Dispersion Forces in Various Liquids," *Journal of Physical Chemistry,* vol. 67, no. 12, pp. 2538-2541, 1963.

[25] F. Laube, A. Poupon, P. Zinck, C. Muller-Goymann, S. Reichl and V. Nardello-Rataj, "Physicochemical investigations of native nails and synthetic models for a better understanding of surface adhesion of nail lacquers," *European Journal of Pharmaceutical Sciences,* vol. 131, pp. 208-217, 2019.

[26] S. Wu, Polymer Interface and Adhesion, Wilmington: CRC Press, 1982.

[27] C. J. V. Oss, R. F. Giese and W. Wu, "On the Predominant Electron-Donicity of Polar Solid Surfaces," *The Journal of Adhesion,* vol. 63, no. 1-3, pp. 71-88, 1997.

[28] H. v. d. Mei, H. Busscher and R. Bos, "A reference guide to microbial cell surface hydrophobicity based on contact angles," *Colloids and Surfaces B: Biointerfaces,* vol. 11, no. 4, pp. 213-221, 1998.

[29] A. Savine, "Sobol Sequence Explained by Antoine Savine," Medium, 18 December 2018. [Online]. Available: https://medium.com/@antoine_savine/sobol-sequence-explained-188f422b246b. [Accessed 16 December 2021].

[30] L. Pro, "Surface Tension," ChemSafetyPro, 13 1 2016. [Online]. Available: https://www.chemsafetypro.com/Topics/CRA/Surface_Tension.html. [Accessed 16 12 2021].

Identifying Mutation Patterns in PDAC via Machine Learning

Zachary Jenkins, Stefan Opiola
Department of Chemical Engineering, Imperial College London

Abstract

Pancreatic cancer has one of the lowest 5 year survival rates of all cancers at 10%; moreover, its mortality rate has increased at 0.3% a year since 2000. Hence, any means of development surrounding the cancer are vital. The scale and depth of modern genetic data-sets coupled with the gene based nature of cancer development makes machine learning an ideal tool for analysis. This paper covers an array of different methods to enrich the current knowledge base surrounding the development, treatment and processes within pancreatic ductal adenocarcinoma (PDAC). Analysis of the Cancer Cell Line Encyclopedia (CCLE) data-set aided in developing understanding behind: cell-line dose response, the most commonly mutated PDAC genes, gene expression relationships and data-set restriction methods. The findings of which allowed for development of methods for checking PDAC network accuracy and data-set restriction for efficient and effective network generation. In this work we have concentrated on a number of proof of concept approaches, thereby highlighting the possibility of further research into: the development of a pathway based kinetic model, improved data restriction methods and methods of improving drug selection.

Keywords: PDAC, Expression, Mutation, Cell-lines, Pathway, Network

1 Introduction

1.1 Motivation

Over 2021, pancreatic cancer was the leading cause of death of over 60,000 people in the USA[1]. The 5 year survival rate for pancreatic cancer is at 10%, the lowest of all cancers[1]. Moreover, pancreatic cancer mortality has continued to increase at a rate of 0.3% annually since 2000 despite the decline in other cancer related deaths over the same period[1]. All these metrics show a clear need for the improvement of the pancreatic cancer prognosis.

The most frequent sub-type of pancreatic cancer is pancreatic ductal adenocarcinoma (PDAC), which originates in the ductal epithelial cells of the exocrine part of the pancreas[2]. PDAC can be identified by its abnormally aggressive behavior and poor response to various therapies[3].

In order to improve the prognosis of PDAC, machine learning techniques can be utilised to gain a better understanding of the disease. Such approaches have previously been effective in approaching other types of cancers, such as: imaging based breasts cancer detection[4,5], a prognosis predictor for stage 3 colon cancer from tissue slides[6] and a cancer classifier for leukemia, lymphoma and colon cancer utilizing micro-array genomics data[7].

1.2 Biological background

1.2.1 Gene expression and pathways:

Genes govern cells via the transfer of information from DNA to RNA to proteins which then undertake the cells desired function. Such function is coordinated and regulated via the type and amount of proteins it manufactures. Gene expression may be increased or decreased via the up or down regulation of a gene in response to changes within the cell. Generally, regulation is prompted by the proteins of other genes produced in response to an external stimulus.

Linking the consequential up or down regulation of genes leads to the formation of pathways. Pathways are composed of a number of networks which themselves are composed of a number of genes, the expression of which is dependent on upstream genes within the same network. Certain stimuli are required for the activation of certain networks and pathways. The networks that make up the main PDAC pathway are triggered by mutations in key cancer driver genes such as KRAS, TP53 and CDKN2A[8].

1.2.2 Tumour formation and cancer progression:

The cell cycle comprises four main stages: G1, S, G2 and M. Progression through the stages is driven by a number of genes such as KRAS. KRAS specifically causes G1/S phase progression via the production of RAS proteins which must be activated by an associated transcription factor to promote progression[9]. Mutations within the KRAS gene can lead to the production of pre-activated RAS proteins, which may lead to uncontrolled growth and tumour formation. For this reason KRAS is known as an oncogene.

The transition between each growth phase is marked with a checkpoint allowing for the arrest of abnormal cells such as tumour and other cancerous cells. These checkpoints stop any damaged cells from reproducing and passing on their damaged DNA thereby halting the progression of cancers. The fate of these damaged cells is controlled by tumour suppressor genes such as TP53, APC and MAD2L1[10]. Mutations within these tumour suppressor genes can result in inhibited function leading to replication of damaged DNA and tumour formation.

1.3 Introduction to CCLE data-set

Human cancer-derived cell-lines have historically had a very important role in the discovery and development of new cancer therapies[11,12]. cell-line panels annotated with both genetic and pharmacologic data have been used in numerous studies[13–22]; however, these have often been limited in their depth of genetic characterization or quantity of cell-lines.

The Cancer Cell Line Encyclopedia (CCLE) is a large scale data-set consisting of 1825 cell-lines spanning over 35 primary diseases[23]. Each cell-line is genetically characterized in multiple ways including: SNP array copy number profiling, RNA sequencing, whole exome & genome sequencing, reverse-phase protein arrays, reduced representation bisulfite sequencing, global histone modification profiling and microRNA expression profiling[24]. Furthermore, pharmacologic profilings were conducted for 24 compounds across over 500 of these cell-lines[25]. The CCLE therefore allows for an in depth investigation into the causes and correlations corresponding to numerous cancer types and their responses to various drugs.

1.4 Prior research into the area

A sizable amount of research has already been conducted with large scale human cancer cell-line data-sets. Numerous studies have applied machine learning algorithms to effectively predict the dose response of cell-lines for a variety of compounds[26–29]. Barretina et el. utilised the CCLE data-set to accurately predict drug response to 24 compounds using both elastic net analysis and naive Bayes classifiers[25]. In addition to known predictors from regression models[16,19,20,30–33], their results uncovered many new indicators of response, such as AHR expression associated with MEK inhibitor efficacy in NRAS mutant lines, as well as SLFN11 predicting sensitivity to topoisomerase inhibitors.

Numerous studies have shown how cell-lines can be utilised to improve patient outcomes[34–36]. These 3 papers all show that a model trained with cell-line data once combined with relevant patient data, could be used to effectively and efficiently predict whether patients would respond well to certain drugs.

Due to the increase in available large scale data-sets, there have been numerous recent developments in computational approaches to help understand this data. These work in a variety of ways, including methods that: use pre-existing pathways, are based on existing biological network data and that predict cancer pathways de novo based on their combinatorial patterns of occurrence[37]. A variety of these tools were used throughout the analysis covered in this paper, specifically ARACNE, an algorithm for the reconstruction of gene regulatory networks using gene expression data[38].

1.5 Overall goals

Overall, 3 goals were set for the exploration of the CCLE PDAC data-set. Firstly, we aimed to identify key driver gene mutations present in aggressive pancreatic cancer cell-lines. We also aimed to improve current drug response models, defining key drivers related to treatment response. Finally, we explored relationships between gene expression and known gene pathways. We aimed to understand these relationships which may aid the development of a dynamic kinectic model than can monitor up and down regulation of the gene pathways.

2 Methodology

2.1 Data collection

The data was retrieved from the Broad Institutes DepMap portal. When available, the 2021 Q4 release was used[39]. In total five data-sets from the CCLE were utilised in our investigation. These included:

Cell-line Sample Info[39]: Cell-line information including cell-line name, sample collection site and primary disease.

Gene Level Expression[39]: Matrix of gene expression of protein coding genes for each cell-line.

Gene Level Copy Number[39]: Matrix of gene level copy number data for protein coding genes for each cell-line.

Gene Mutations[39]: List of mutations for each cell-line, including gene, variant classification (nonesense, missense, silent), reference and alternate alleles, codon change, and protein change.

CCLE Drug Response[23,25]: List of response metrics for each cell-line for a variety of chemical compounds. Metrics include EC50 (half the drug concentration at maximum inhibition), IC50 (drug concentration required for 50% relative growth inhibition), Amax (the maximum relative growth inhibition) and Activity Area (area under the response curve). Each metric is illustrated in figure 1.

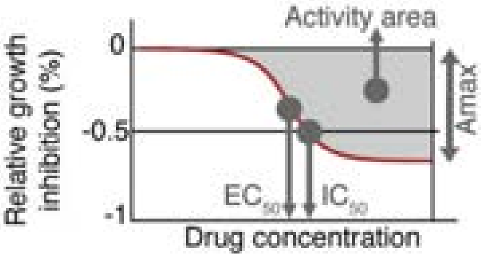

Figure 1: Diagram of metrics used to measure drug dose response[25]

2.2 Data cleaning

All data-sets underwent a variety of cleaning stages within Python Pandas before they could be aggregated for analysis. Very little cleaning was required as the data was provided precleaned by the CCLE.

The data was checked for structural errors such an inconsistent naming conventions. None were found.

Next, to avoid wasting computational power on unnecessary calculations, any irrelevant observations were removed from the data-set. The cell-line sample info was filtered to only contain cell-lines with a primary disease of PDAC. These cell-line ID's were then used to filter down the remaining 4 data-sets.

The data was then checked for any duplicate cell-lines in every data-set. None were found.

The data then underwent a further reduction. For the majority of the analysis information on both the expression and copy number of genes, as well as their mutation status is required. Therefore, any cell-lines that were not included in all 3 of these data-sets were excluded from the analysis. After filtering, the final cell-line count came to N=33.

The data was then analysed for any unexpected or missing data points. Within the CCLE Drug Response data-set, cell-lines with a constant or linear response curve (instead of sigmoidal) had 'NA' EC50 values. Furthermore, some cell-lines were not tested for certain drugs. These were all marked as N/A within Pandas to exclude them from the analysis. Within the mutations data-set, many entries were missing data within their cDNA change or codon change columns. These entries were filled in by inference from each other as well as the reference allele, tumor allele and genome change columns. No further data-points of interest were found.

2.3 Data aggregation

The data was then aggregated in a variety of ways for further analysis. The majority of data aggregation was completed using Python's Pandas data analysis package.

2.3.1 Dose Response

To assess patterns in dose response across cell-lines, matrices of metric value for each drug and cell-line were constructed for each of the 4 metrics (EC50, IC50, Amax and Activity Area). This was done by first filtering the drug response data-set to only its cell-line ID, chemical compound and metric columns, and then performing a pivot for each metric separately. These matrices were then used to construct heat maps of the dose response metric values using Python's Seaborn graphing package.

2.3.2 Key Gene Mutations

To assess the mutations most common within PDAC, an analysis of the mutations data-set was conducted to obtain a list of how many cell-lines had certain mutations. Firstly, the mutations data-set was reduced to only contain the gene and cell-line ID columns. All duplicates were then removed; these were present due to some cell-lines having multiple mutations of the same gene. This list was then grouped by gene, before the final frequency percentage was calculated.

2.3.3 Common Mutation Combinations

To find common mutation combinations within the data-set, the Apriori Algorithm from the Mlxtend Python library was utilised. The Apriori Algorithm is a bottom up algorithm where frequent subsets are extended one item at a time. It utilises a breadth first search, where candidate combinations are pruned if they do not reach a minimum amount of occurrence (also known as support)[40].

$$\text{support}(A \rightarrow C) = \text{support}(A \cup C) \tag{1}$$

To reduce computational load when conducting the algorithm, the data-set was first reduced to only contain genes with a mutation frequencies of above 15%. The algorithm was then conducted with a minimum support of 10%, giving a list of common mutation combinations within the data-set.

Once a list of common combinations was obtained, association rules for these combinations would then be produced. Two further statistical metrics were calculated for these combinations.

Confidence: The probability of seeing a consequence giving that the antecedent has happened. This has a range from 0 to 1, with 0 representing an impossible combination and 1 representing a certain combination.

$$\text{confidence}(A \rightarrow C) = \frac{\text{support}(A \rightarrow C)}{\text{support}(A)} \tag{2}$$

Lift: A measure of how much more often the antecedent and consequent of a rule occur together than we would expect if they were statistically independent. This has a range from 0 to ∞. If A and C are completely independent, the lift would be 1, if the occurred less often than independent, the lift would be < 1, and if they occurred more often, it would be > 1.

$$\text{lift}(A \rightarrow C) = \frac{\text{confidence}(A \rightarrow C)}{\text{support}(C)} \tag{3}$$

All these calculations were conducted using the association rules function from the Mxltend Python library.

2.3.4 Clustering of Mutations

The location of mutation sites was graphed to investigate clustering within frequent mutations. First, the location of the mutation had to be extracted from the mutations data-set. The location was extracted by splicing the changed nucleotide number from the cDNA change column. For mutation variations with multiple changed nucleotides, e.g frame shift deletion, the middle location was taken.

These mutations were then graphed for the top mutated genes using Python's Seaborn package. The opacity of points was reduced and a random jitter was applied to both the x and y axis to make clustering clearer.

2.3.5 Gene expression changes

To analyse changes within gene expression due to mutations, the gene expression and mutations data-sets had to be merged. First, the mutations data-set was reduced to a list of cell-line id's with a mutation within the gene of question and all duplicates were removed. These were labelled as ”Mutated” in an additional mutations occurrence column. This DataFrame was then merged with the gene expression DataFrame using an outer join. Rows unlabeled in the mutations occurrence column were then labeled ”Not-Mutated”.

A density distribution was then plotted using Python's Seaborn package normalised kde displot method. The two separate distributions for ”Mutated” and ”Non-Mutated” were plotted on the same graph for comparison. This process was repeated for a variety of known cancer driver genes at the start of the pancreatic cancer pathway networks.

2.3.6 Preparation of networks

Gene expression correlation was analysed for a variety of known PDAC networks. These networks were obtained from KEGG Pathway, an online database resource of manually drawn biological pathways[8]. Firstly, the mutations data-set was utilised to generate a list of cell-line ID's with the mutation required at the start of each pathway. The gene expression data-set was then reduced to this list of cell-lines; moreover, the gene columns were reduced to only contain the genes in each given pathway.

A combination of graphical and computational approaches were used to assess the pairwise correlation between the relevant genes. The correlation was graphically assessed by using a Python Seaborn pairplot. In addition to this, the Pearson correlation coefficent (PCC) was calculated for each gene pair in the network using Python's Pandas library correlation function. This is a measure of linear correlation as is defined by equation 4[41]. A PCC of +1 indicates a strong positive correlation, a PCC of -1 indicates a strong negative correlation and a PCC of 0 means there is no correlation.

$$PCC = \frac{\sum_{i=1}^{n}(x_i - \overline{x})(y_i - \overline{y})}{\sqrt{\sum_{i=1}^{n}(x_i - \overline{x})^2}\sqrt{\sum_{i=1}^{n}(y_i - \overline{y})^2} \tag{4}$$

These correlation values were then compared to the known PDAC networks. For activating relationships, a strong positive correlation close to 1 was expected, whereas for inhibiting relationships, a negative correlation close to -1 was expected. A new correlation value was then assigned to each edge in the network depending on whether it was as expected.

2.3.7 ARACNE Pathway Development

In addition to using gene correlation, the ARACNE algorithm was also utilised to evaluate known networks. ARACNE is an algorithm for the reconstruction of gene regulatory networks in a mammalian cellular context[38]. ARACNE creates edges between nodes of genes that can only be explained by an irreducible statistical dependency between gene expression profiles. It constructs the network as if the effect of loops in the network topology were negligible.

The ARACNE algorithm was deployed and used as an extension to the Cyni Toolbox app via Cytoscape, a network data integration, analysis and visualization tool[42–44]. To prepare the gene expression data for the algorithm, the genes were reduced to only contain the genes in the whole PDAC known pathway. The matrix was then transposed and imported into Cytoscape. The ARACNE inference algorithm was then run using the naive bayes mutual information algorithm, with a mutual information threshold of 0.8. Next, the output node network was visualised in Cytoscape and compared to known networks. This process was repeated for a variety of cases, including genes restricted to one network at a time and cell-lines restricted to contain only those with driver mutations of a network.

3 Results and Discussion

3.1 Dose response assessment

Cancer severity is usually gauged via the symptoms of the patients experiencing the disease, with a number of measured variables such as pain, tumour size and fatigue building up the entire picture[45]. Due to the nature of cell-line data, these metrics cannot be assessed. Hence it was hypothesised that PDAC severity of the cell-lines may be measured via drug response, with some cell-lines having good responses to most drugs, and some having bad.

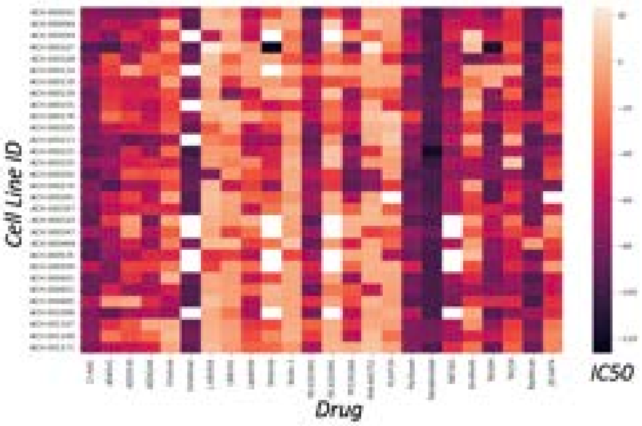

Figure 2: Dose response of cell-lines to an array of anti-cancer drugs

Figure 2 demonstrates that drug response may not be used to assess disease severity, given the lack of any consistent response to drugs. If severity were to scale with drug response, horizontal bands should be present in figure 2 denoting a generally higher or lower response for certain cell-lines against all the anti-cancer drugs. General cell-line responses were most likely not present due to the varying drug mechanisms, with each drug targeting certain areas of gene networks. Therefore each drug likely correlates with an array of mutation combinations rather than the overall cell-line.

3.2 Most commonly mutated genes

Table 1: Frequency of gene mutations in PDAC CCLE data

Gene	Cell Line Freq	Expected Freq[46]	Pathway Starter[8]	Known Cancer Gene[47]
KRAS	97%	70-95%	YES	YES
TP53	82%	20-76%	YES	YES
TTN	73%	-	NO	NO
MUC16	51%	-	NO	YES
LRP1B	33%	-	NO	YES
SMAD4	33%	19-50%	YES	YES
CDKN2A	27%	49-98%	YES	YES
BRCA2	6%	3.6-7.5%	YES	YES
ERBB2	0%	-	YES	YES

The frequency of mutations throughout the whole CCLE PDAC data-set was explored and is summarised in table 1. The PDAC CCLE data was concordant with literature[46] frequencies of KRAS and SMAD4, with the percentage frequency remaining within the experimental bounds. TP53 was shown to be slightly more frequent in the cell-line data compared to literature values. While CDKN2A mutation frequency was expected to be in the region of 49-98%, the CCLE data contained mutated versions of the gene in only 27% of samples. These variations are most likely attributable to the inherent biological difference between cell-line and human PDAC cells and the relatively small sample size of 33 cell-lines.

Mutations in known cancer driver genes BRCA2 and ERBB2 were relatively rate, with mutated genes present in only 6% and 0% of cell-lines respectively. However, these lower mutation rates still agree with literature. The lower mutation rate is anticipated due to the driver gene mutation occurring further down the cancer life-cycle in the PDAC pathway[8]. These 2 mutations are driven first by mutation tumor suppressor genes such as TP53.

3.3 Common mutation combinations

Generally, it was noted that common cancer driver genes such as TP53, KRAS, MUC16, CDKN2 and SMAD4 were more likely to occur in groups than on their own as shown in table 2.

Table 2: Common mutation combinations

Gene Mutation Combination	Support
TP53, KRAS	0.77
TP53, KRAS, MUC16	0.32
TP53, KRAS, CDKN2A	0.23
TP53, KRAS, SMAD4	0.23
TP53, KRAS, SMAD4, CDKN2A	0.13
MUC16, CDKN2A	0.12

TP53 and KRAS mutations had the highest support value of 0.77. Such high support is likely due to their high prevalence in PDAC cases, with KRAS present in 70-95% and TP53 in 20-70% of PDAC cases[46].

Table 3: Significant lift values

Antecedents	Consequents	Lift
MUC16	CDKN2A	0.75
MYO18B	TP53, KRAS, SMAD4	2.87
PCLO	TP53, KRAS, SMAD4	2.54

While MUC16 and CDKN2A mutations are present in 52% and 27% of cell-lines respectively, they have a low support value of 0.12 alongside a lift value 0f 0.75, which is below 1. These values indicate some kind of mutual exclusivity, not yet discovered in literature. While such a direct link has not as of yet been explored, a better understanding of the gene specific biology must be understood to confirm such a relationship, something deemed beyond the scope of this paper.

MYO18B and PCLO mutations shared some of the highest lift values, both in excess of 2.5 indicating a significant increase in the mutation of TP53, KRAS and SMAD4 genes following a mutation in either of the genes in question. Such a relationship is as of yet undocumented, with MYO18B mainly playing a role in muscle function and PCLO functioning as part of the presynaptic cytoskeletal matrix[48]. Nevertheless the implications of such a link could lead to use of MYO18B and PCLO mutations as early detection biomarkers of those at risk of developing PDAC.

3.3.1 Mutation Clustering

Previous studies have been conducted surrounding the link between drug sensitivity and frequency of gene mutations, with the status of mutations contributing to 68% of the model weighting[25]. It was hypothesised that the introduction of further granularity via the integration of mutation location within genes could improve model accuracy. In order to do this, the length of each gene would need to be split into numerous buckets of fixed width, centered around clustered mutation locations.

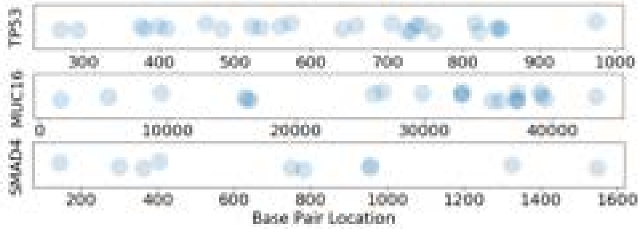

Figure 3: Mutation locations within the genes showing no clustering

The vast majority of genes show mutation distributions akin to those shown in figure 3, with a seemingly random and unconnected mutation locations.

Figure 4: Mutation locations within genes showing clustering

The strongest clustering was observed within the KRAS gene, with a clear hot spot towards the left of the KRAS distribution in figure 4. The hot spot is present due to the G12C driver mutation which is adjacent to a shallow binding site predisposing the position to mutation and the hereditary G12D mutation both of which occur at the same location[49].

The results highlighted in figures 4 and 3 indicate little hope for improving model accuracy as mutations are shown to be either randomly distributed throughout a gene or wholly concentrated at a single spot. While a finer data resolution is required to conclude the lack of mutation hot spots present in the majority of genes, results such as TTN hint at the possibility of a slight increase in model accuracy as mutation locations are neither wholly distributed nor wholly concentrated at a single location.

3.4 Network analysis

The CCLE expression data was employed to construct PDAC networks to compare and contrast to those present in literature[8].

3.4.1 Gene expression analysis

Analysis of CCLE expression data allowed for comparison of mutated and non mutated gene expression levels. Such comparison was necessary prior to network construction, as a significant change in expression is required to facilitate effective analysis of up or down regulation further down PDAC networks.

The majority of gene expression profiles were similar to those of TP53 and KRAS depicted in figure 5. The mutated gene expression levels fell within the distribution of the equivalent non mutated genes. This signifies no significant change in the expression of mutated genes. The lack of change in oncogenes could be linked to their biology. KRAS as an example, creates a pre-activated RAS protein once mutated. Figure 5 hence indicates that while mutations alter the RNA-sequence of the proteins, the overall number of RNA-sequences is conserved throughout mutation.

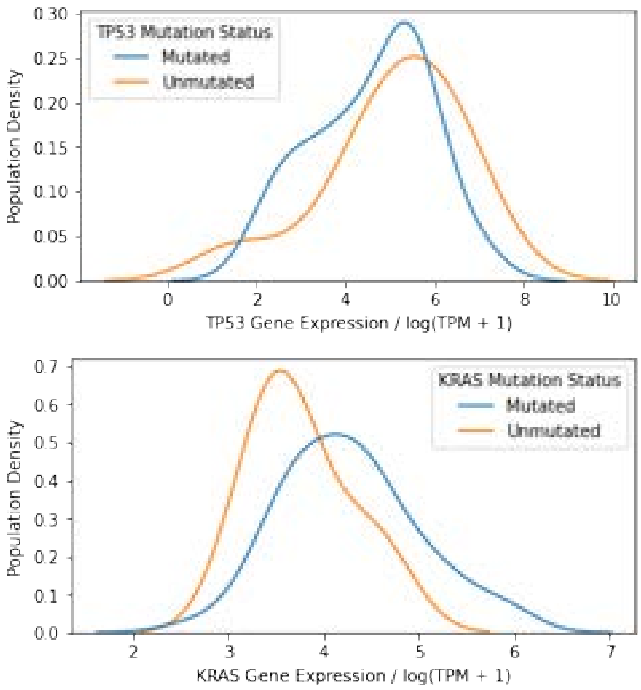

Figure 5: TP53 and KRAS expression profiles

TP53 and other tumour suppressor genes must produce certain proteins such as p53 to promote cell repair and apoptosis of the relevant mutated cells. Therefore figure 5 again indicates the production of different RNA-sequences which are unable to maintain normal function; however are produced at the same rate as before.

While there was no significant change in expression is was possible that other downstream effects were occurring despite the low expression change hence network comparison was still attempted with KRAS and TP53.

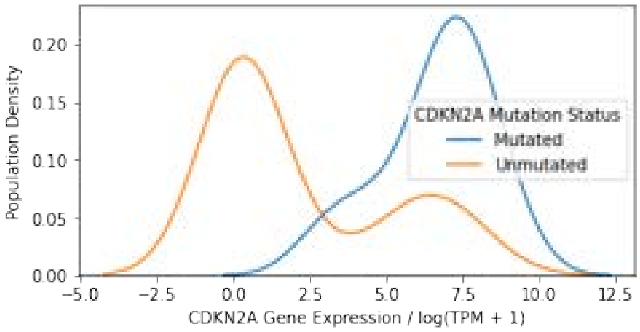

Figure 6: CDKN2A expression profiles

CDKN2A was the only gene with any significant change in expression post mutation as shown in figure 6. The presence of two peaks within the unmutated distribution indicates a minority of cell-lines have been activated as part of a gene network or regulatory loop. The fact that far more cell-lines containing mutated CDKN2A genes were present at the higher expression value, indicates that the aforementioned gene network or regulatory loop is activated by CDKN2A mutation. Further analysis via machine learning classification of the 2 peaks given cell-lines labeled with mutations led to no further explanation of the separation. Hence more data, a better understanding of the biological background and further study is required to uncover the relationship.

The presence of a change in gene expression does however present the opportunity for effective gene network reconstruction due to the clear mutation based up-regulation.

3.4.2 Network comparison

Gene expression values were then used to compare up or down regulation with known PDAC networks[8]. Figure 7 shows a comparison to the known N00104 PDAC network, it can be seen that there is little agreement. Most of the networks generated were similar to that in figure 7, with little correlation.

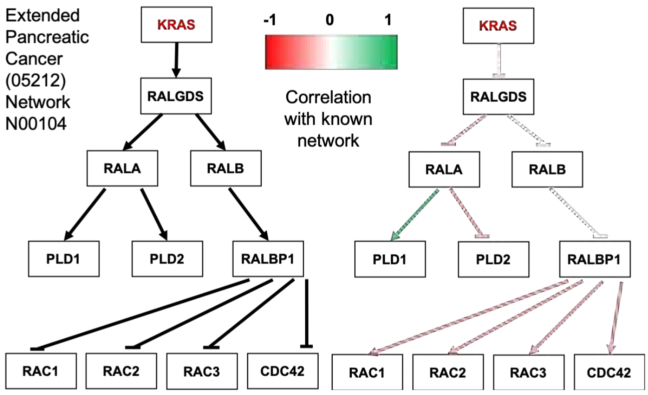

Figure 7: Comparison of known KRAS network to that implied from CCLE data

The lack of concordance is likely due to a number of factors. Firstly the aforementioned lack of expression change following mutation which will thereby narrow the range of gene expression. This narrow corridor of expression further exposes the data to distortion from other effects.

Relationships with a weak correlation in either direction, are most likely due to the presence of phosphorylation steps and other non-regulation based processes. While these aren't present in the network in figure 7 such steps are prevalent in a number of other networks. Moreover, the variance of expression is intrinsic to each gene, hence random variation can cloud results. Finally, the TPM (transcripts per million) metric used to measure the gene expression hides the nature of the gene expression, with a number of genes producing a variety of RNA-sequences for a multitude of other competing networks both healthy and PDAC related.

Strong opposite correlations such as those shown in dark red may have been caused by the presence of hidden feedback loops and other gene regulation networks. These feedback loops may only be uncovered via analysis of more complete data-sets with step changes, using a method similar to that used by Teije et al[50]. However, so far this method has only been used on very basic biological creatures such as Caenorhabditis Elegans (Roundworms), hence it would be extremely difficult to replicate such methods with human cell-lines.

The N00070 PDAC network had the highest correlation with CCLE expression data, as shown in figure 8. The only different links being CDK4-RB1 and Cyclin D-RB1. These two links however, are shown to be phosphorylation steps in the known network, hence are not expected to align well with expression data. Moreover, further complications and skew may have arisen due to the binding of CDK4 and CyclinD related proteins[8].

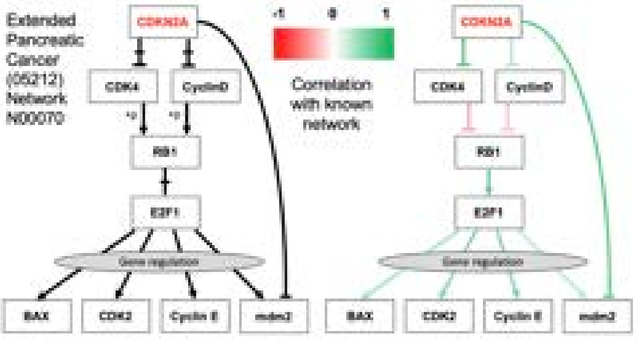

Figure 8: Comparison of known CDKN2A network to that implied from CCLE data

We can attribute much of the concordance with the known network to the differing expression profiles of mutated and non mutated cell-lines shown in figure 6. Moreover, the N00070 network has limited overlap with other healthy cell processes and PDAC pathways leading to less noise surrounding the data, something which is especially apparent in the KRAS-centric networks.

The data highlights the lack of any hidden feedback loops and confirms the accuracy of the known network as well as the further interactions which propagate through the gene regulation step, something which hasn't been directly measured in literature[8]. The CDKN2A network thereby confirms the possibility of using expression data to test known networks, identify networks where unknown feedback interactions could be occurring and identify effects downstream of the network through steps such as gene regulation.

3.5 ARACNE Network Construction

Several methods of data restriction were trialed using the ARACNE network generation algorithm. Each data restriction method was applied to the CCLE data-set before a network was generated, using the known networks shown in figures 9 and 10 to gauge the effectiveness of the restriction. The degree of removal, or degrees of separation of a gene in question from the PDAC driver gene, are colour coded to allow for easy comparison with the following generated networks shown in figures 9 and 10.

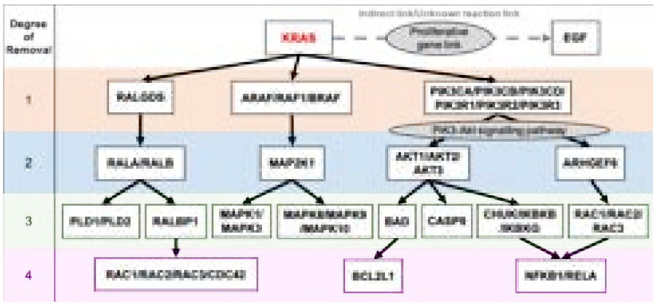

Figure 9: Known KRAS network [8]

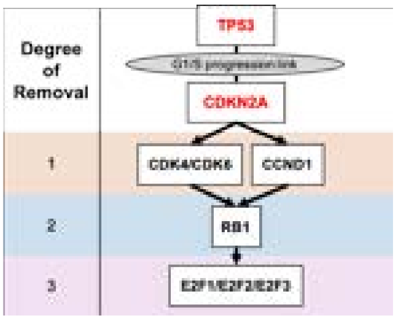

Figure 10: Known CDKN2A network [8] and links to TP53 network

3.5.1 Known PDAC related genes and all cell-line data

Firstly, only the expression values for known PDAC pathway related genes were used from all cell-lines. The resulting network shown in figure 11 details the interactions surrounding KRAS. While the network formed differs from the known PDAC KRAS pathway, almost all genes within the vicinity of KRAS mirrored those present in the vicinity of the known network. It can be concluded that the known PDAC pathway gene restriction was effective in narrowing the data-set. Conversely the structure of the generated network doesn't correlate to that of the known network, as shown by the mix in degrees of removal. Inaccuracies in the network structure can be attributed to the low variation in expression data as well as the existence of hidden feedback loops and interactions.

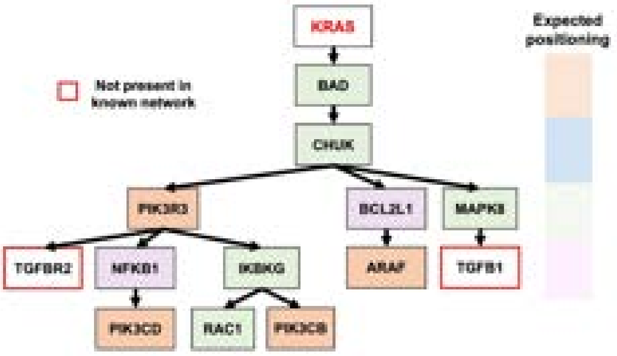

Figure 11: ARACNE generated KRAS related network from unrestricted gene and cell-line data

Conversely, the same restrictions applied to the CDKN2A network had far less success as shown in figure 8. Only the RB1 gene was present within the generated and known network. Moreover, the strength of the correlations are the lowest of any other network, highlighting that the data-set was too small to discern any meaningful network.

Figure 8 does however, highlight a link between CDKN2A and RB1 which is shown to be a phosphorylation step in known PDAC network N00070. The link highlighted could refer to an undiscovered feedback loop. More analysis and data would be required to confirm as such.

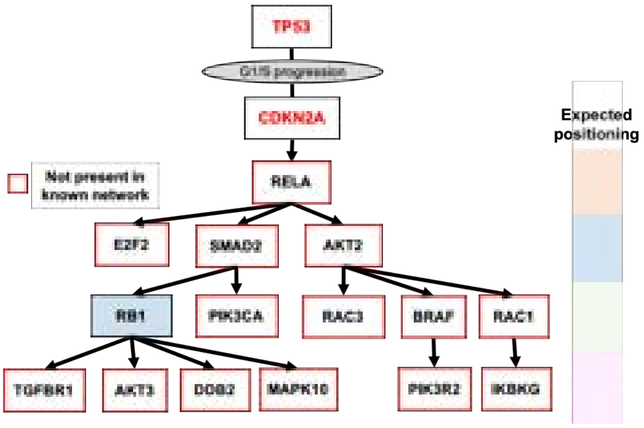

Figure 12: ARACNE generated TP53 and CDKN2A related network from unrestricted gene and cell-line data

Overall it may be concluded that the restriction of a data-set to just genes present in known PDAC pathways is effective in producing networks containing the correct genes with the caveat that there is a lower bound to the data-set size. Such restriction does not however allow for effective prediction of network order and general structure. Larger samples and expression variation could improve results.

3.5.2 Known KRAS network related genes and all cell-line data

The results of the network generated, following a restriction to genes present in the known KRAS network are presented in figure 13.

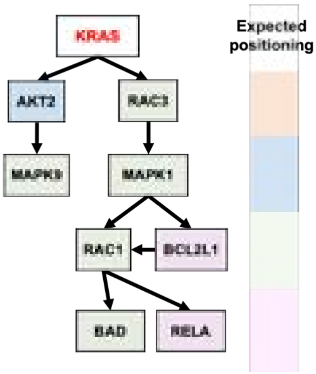

Figure 13: ARACNE generated KRAS related network from restricted gene and unrestricted cell-line data

The structure of the network presented in figure 13 does not correlate with that of the known network. There are also no meaningful or insightful relationships highlighted by the generated network.

It can be concluded that the restriction to genes present in the known network was not an effective method of network construction. Moreover, such restriction leaves little scope for the discovery of unknown interactions. It may be possible that the sample size was too small, or that there are too many unknown feedback loops and interactions which are skewing the structure.

3.5.3 Known PDAC related genes and mutated cell-line data

Figure 14 was generated using all known PDAC pathway related genes with expression data from only cell-lines which contain a mutated KRAS gene.

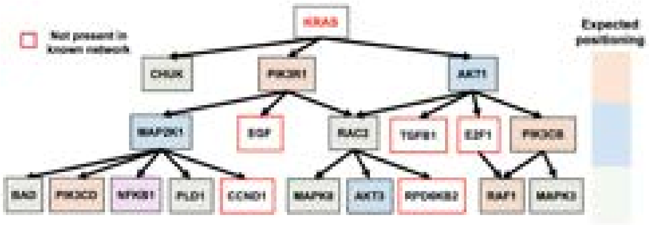

Figure 14: ARACNE generated KRAS related network from unrestricted gene and mutation restricted cell-line data

The types of genes present in the network are again concordant with those in the known network. Moreover, the degree of removal from KRAS correlates relatively well with most genes only one degree or less from its corresponding position in the known network.

The ARACNE network shown in figure 14 indicates a network linking KRAS and EGF. Such a link has been hypothesised; however, the direct network relationship is currently branded an unknown connection via a proliferative gene link[8]. More data concerning the link would be required to support the conclusion. The presence of such a link in the data-set restricted to mutated cell-lines further supports the conclusion as activation of such a link should only occur following the driver mutation of the KRAS gene.

This method results in concordant network genes, with a somewhat concordant structure. Moreover, such restriction still leaves scope for the discovery of unknown interactions. Overall it may be concluded that restriction of the CCLE data to all known PDAC pathway related genes with expression data from only cell-lines which contain a mutated version of the driver gene of the network in questions serves as the best preparation of data for network generation using the ARACNE algorithm. The same may be true for other algorithms however further testing would be required to confirm as such.

4 Scope for future work

4.1 Alternate data-sets

While the CCLE data-set used throughout this paper provided significant insight, further analysis was stunted due to the limited data-set size and data variety. Alternate data-sets may overcome these limitations and provide greater insight into the underlying relationships governing PDAC and its progression.

4.2 Kinetic model

The results discussed throughout this paper could be used to aid the development of a kinetic model of gene expression. Given a data-set containing step change expression data for key driver genes, the aforementioned correlation methods may be used to assess the downstream regulation strength. Adaptation of current computation network generating algorithms such as ARACNE could be used to form a kinetic network comprising nodes representing genes and edges representing regulation strengths.

4.3 Improvement of expression data restriction methods

The findings in this paper may also be used to improve alternative current expression data restriction methods such as Oncofinder. Oncofinder assigns weightings of [-1, -0.5, 0, 0.5, 1] to each network edge dependent on the type and strength of regulation, before calculating the relevance of downstream genes to upstream changes by assigning a numerical relevance cutoff. Such methods reduce noise for improved machine learning applications. The correlation methods discussed in section 3.4 could be used to apply more accurate network weightings thereby improving the data restriction and consequent results.

4.4 Improve drug selection via deeper understanding of mutation pathways

Following further study and possible confirmation, the newly discovered network links and relationships identified within this paper may be used to deepen the current understanding of PDAC progression, as well as providing scope for novel early detection and cancer therapy methods.

5 Conclusions

This paper has assessed a number of methods and approaches to reduce the impact of PDAC. The approaches identified the most commonly mutated genes in PDAC such as KRAS, TP53, CDKN2A and MUC16, providing a select few genes for deeper study. Further understanding behind these mutations may unlock the ability to create newer more effective gene targeting treatments. This report also identifies a number of possible PDAC bio-markers such as MYO18B and PCLO which indicate underlying relationships with known cancer driver genes. These relationships may be utilised to serve as a method of early detection for PDAC and those pre-disposed to it.

Gene expression analysis highlighted how different genes react to mutations, indicating that while most genes are not significantly up or down-regulated directly due to their own mutations, some such as CDKN2A are, thereby confirming their suitability for use in network reconstruction. While most of the networks reconstructed did not corroborate with known networks, the CDKN2A pathway did correlate strongly with the known N00070 PDAC pathway. Furthermore, the CDKN2A analysis confirmed the presence of further as of yet hypothesised links past the gene regulation step.

The method of restricting gene expression data-sets via PDAC pathway related genes and cell-lines containing mutated driver genes proved the best method of data restriction for the ARACNE algorithm. While there is plenty of scope for improvement, the methods highlighted key heuristics to follow such as the inclusion of genes not known to be present in the network allowing for the discovery of unknown interactions. Moreover, the ARACNE generated networks demonstrated a pathway link between KRAS and EGF via regulation of the PIK3R1 gene, a relationship which was known to exist with a previously unknown pathway sequence. Overall this paper has outlined a number of areas and methods for future study to improve our understanding of PDAC, its development and its regulatory processes.

References

[1] Rebecca L Siegel, Kimberly D Miller, Hannah E Fuchs, and Ahmedin Jemal. Cancer statistics, 2021. *CA: a cancer journal for clinicians*, 71(1):7–33, 2021.

[2] Mohadeseh Fathi, Soudeh Ghafouri-Fard, Atefe Abak, and Mohammad Taheri. Emerging roles of mirnas in the development of pancreatic cancer. *Biomedicine & Pharmacotherapy*, 141:111914, 2021.

[3] Trevor J Grant, Kevin Hua, and Anurag Singh. Molecular pathogenesis of pancreatic cancer. *Progress in molecular biology and translational science*, 144:241–275, 2016.

[4] Essam H Houssein, Marwa M Emam, Abdelmgeid A Ali, and Ponnuthurai Nagaratnam Suganthan. Deep and machine learning techniques for medical imaging-based breast cancer: A comprehensive review. *Expert Systems with Applications*, 167:114161, 2021.

[5] Satish Chand et al. A comparative study of breast cancer tumor classification by classical machine learning methods and deep learning method. *Machine Vision and Applications*, 31(6):1–10, 2020.

[6] Dan Jiang, Junhua Liao, Haihan Duan, Qingbin Wu, Gemma Owen, Chang Shu, Liangyin Chen, Yanjun He, Ziqian Wu, Du He, et al. A machine learning-based prognostic predictor for stage iii colon cancer. *Scientific reports*, 10(1):1–9, 2020.

[7] Sung-Bae Cho and Hong-Hee Won. Machine learning in dna microarray analysis for cancer classification. In *Proceedings of the First Asia-Pacific Bioinformatics Conference on Bioinformatics 2003-Volume 19*, pages 189–198, 2003.

[8] KEGG. Kegg pathway database. https://www.genome.jp/kegg/pathway.html, 2021.

[9] Jianguo Fan and Joseph R Bertino. K-ras modulates the cell cycle via both positive and negative regulatory pathways. *Oncogene*, 14(21):2595–2607, 1997.

[10] Geoffer M Cooper. The cell: a molecular approach 2nd edition, 2000.

[11] Sreenath V Sharma, Daniel A Haber, and Jeff Settleman. Cell line-based platforms to evaluate the therapeutic efficacy of candidate anticancer agents. *Nature reviews cancer*, 10(4):241–253, 2010.

[12] Jean-Pierre Gillet, Sudhir Varma, and Michael M Gottesman. The clinical relevance of cancer cell lines. *Journal of the National Cancer Institute*, 105(7):452–458, 2013.

[13] William M Lin, Alissa C Baker, Rameen Beroukhim, Wendy Winckler, Whei Feng, Jennifer M Marmion, Elisabeth Laine, Heidi Greulich, Hsiuyi Tseng, Casey Gates, et al. Modeling genomic diversity and tumor dependency in malignant melanoma. *Cancer research*, 68(3):664–673, 2008.

[14] Richard M Neve, Koei Chin, Jane Fridlyand, Jennifer Yeh, Frederick L Baehner, Tea Fevr, Laura Clark, Nora Bayani, Jean-Philippe Coppe, Frances Tong, et al. A collection of breast cancer cell lines for the study of functionally distinct cancer subtypes. *Cancer cell*, 10(6):515–527, 2006.

[15] Martin L Sos, Kathrin Michel, Thomas Zander, Jonathan Weiss, Peter Frommolt, Martin Peifer, Danan Li, Roland Ullrich, Mirjam Koker, Florian Fischer, et al. Predicting drug susceptibility of non–small cell lung cancers based on genetic lesions. *The Journal of clinical investigation*, 119(6):1727–1740, 2009.

[16] Jonathan R Dry, Sandra Pavey, Christine A Pratilas, Chris Harbron, Sarah Runswick, Darren Hodgson, Christine Chresta, Rose McCormack, Natalie Byrne, Mark Cockerill, et al. Transcriptional pathway signatures predict mek addiction and response to selumetinib (azd6244). *Cancer research*, 70(6):2264–2273, 2010.

[17] Levi A Garraway, Hans R Widlund, Mark A Rubin, Gad Getz, Aaron J Berger, Sridhar Ramaswamy, Rameen Beroukhim, Danny A Milner, Scott R Granter, Jinyan Du, et al. Integrative genomic analyses identify mitf as a lineage survival oncogene amplified in malignant melanoma. *Nature*, 436(7047):117–122, 2005.

[18] Joel Greshock, Kurtis E Bachman, Yan Y Degenhardt, Junping Jing, Yuan H Wen, Stephen Eastman, Elizabeth McNeil, Christopher Moy, Ronald Wegrzyn, Kurt Auger, et al. Molecular target class is predictive of in vitro response profile. *Cancer research*, 70(9):3677–3686, 2010.

[19] Ultan McDermott, Sreenath V Sharma, Lori Dowell, Patricia Greninger, Clara Montagut, Jennifer Lamb, Heidi Archibald, Raul Raudales, Angela Tam, Diana Lee, et al. Identification of genotype-correlated sensitivity to selective kinase inhibitors by using high-throughput tumor cell line profiling. *Proceedings of the National Academy of Sciences*, 104(50):19936–19941, 2007.

[20] David B Solit, Levi A Garraway, Christine A Pratilas, Ayana Sawai, Gad Getz, Andrea Basso, Qing Ye, Jose M Lobo, Yuhong She, Iman Osman, et al. Braf mutation predicts sensitivity to mek inhibition. *Nature*, 439(7074):358–362, 2006.

[21] Jane E Staunton, Donna K Slonim, Hilary A Coller, Pablo Tamayo, Michael J Angelo, Johnny Park, Uwe Scherf, Jae K Lee, William O Reinhold, John N Weinstein, et al. Chemosensitivity prediction by transcriptional profiling. *Proceedings of the National Academy of Sciences*, 98(19):10787–10792, 2001.

[22] John N Weinstein, Timothy G Myers, Patrick M O'Connor, Stephen H Friend, Albert J Fornace, Kurt W Kohn, Tito Fojo, Susan E Bates, Lawrence V Rubinstein, N Leigh Anderson, et al. An information-intensive approach to the molecular pharmacology of cancer. *Science*, 275(5298):343–349, 1997.

[23] Cancer Cell Line Encyclopedia Consortium, Genomics of Drug Sensitivity in Cancer Consortium, et al. Pharmacogenomic agreement between two cancer cell line data sets. *Nature*, 528(7580):84–87, 2015.

[24] Mahmoud Ghandi, Franklin W Huang, Judit Jané-Valbuena, Gregory V Kryukov, Christopher C Lo, E Robert McDonald, Jordi Barretina, Ellen T Gelfand, Craig M Bielski, Haoxin Li, et al. Next-generation characterization of the cancer cell line encyclopedia. *Nature*, 569(7757):503–508, 2019.

[25] Jordi Barretina, Giordano Caponigro, Nicolas Stransky, Kavitha Venkatesan, Adam A Margolin, Sungjoon Kim, Christopher J Wilson, Joseph Lehár, Gregory V Kryukov, Dmitriy Sonkin, et al. The cancer cell line encyclopedia enables predictive modelling of anticancer drug sensitivity. *Nature*, 483(7391):603–607, 2012.

[26] Robert H Shoemaker. The nci60 human tumour cell line anticancer drug screen. *Nature Reviews Cancer*, 6(10):813–823, 2006.

[27] Wanjuan Yang, Jorge Soares, Patricia Greninger, Elena J Edelman, Howard Lightfoot, Simon Forbes, Nidhi Bindal, Dave Beare, James A Smith, I Richard Thompson, et al. Genomics of drug sensitivity in

cancer (gdsc): a resource for therapeutic biomarker discovery in cancer cells. *Nucleic acids research*, 41(D1):D955–D961, 2012.

[28] Amrita Basu, Nicole E Bodycombe, Jaime H Cheah, Edmund V Price, Ke Liu, Giannina I Schaefer, Richard Y Ebright, Michelle L Stewart, Daisuke Ito, Stephanie Wang, et al. An interactive resource to identify cancer genetic and lineage dependencies targeted by small molecules. *Cell*, 154(5):1151–1161, 2013.

[29] Brinton Seashore-Ludlow, Matthew G Rees, Jaime H Cheah, Murat Cokol, Edmund V Price, Matthew E Coletti, Victor Jones, Nicole E Bodycombe, Christian K Soule, Joshua Gould, et al. Harnessing connectivity in a large-scale small-molecule sensitivity dataset. *Cancer discovery*, 5(11):1210–1223, 2015.

[30] Lloyd R Kelland, Swee Y Sharp, Paul M Rogers, Timothy G Myers, and Paul Workman. Dt-diaphorase expression and tumor cell sensitivity to 17-allylamino, 17-demethoxygeldanamycin, an inhibitor of heat shock protein 90. *Journal of the National Cancer Institute*, 91(22):1940–1949, 1999.

[31] Gottfried E Konecny, Mark D Pegram, Natarajan Venkatesan, Richard Finn, Guorong Yang, Martina Rahmeh, Michael Untch, David W Rusnak, Glenn Spehar, Robert J Mullin, et al. Activity of the dual kinase inhibitor lapatinib (gw572016) against her-2-overexpressing and trastuzumab-treated breast cancer cells. *Cancer research*, 66(3):1630–1639, 2006.

[32] Christoph R Müller, Erik B Paulsen, Paul Noordhuis, Florence Pedeutour, Gunnar Sæter, and Ola Myklebost. Potential for treatment of liposarcomas with the mdm2 antagonist nutlin-3a. *International journal of cancer*, 121(1):199–205, 2007.

[33] Gromoslaw A Smolen, Raffaella Sordella, Beth Muir, Gayatry Mohapatra, Anne Barmettler, Heidi Archibald, Woo J Kim, Ross A Okimoto, Daphne W Bell, Dennis C Sgroi, et al. Amplification of met may identify a subset of cancers with extreme sensitivity to the selective tyrosine kinase inhibitor pha-665752. *Proceedings of the National Academy of Sciences*, 103(7):2316–2321, 2006.

[34] Paul Geeleher, Nancy J Cox, and R Stephanie Huang. Clinical drug response can be predicted using baseline gene expression levels and in vitro drug sensitivity in cell lines. *Genome biology*, 15(3):1–12, 2014.

[35] Balázs Györffy, Violeta Serra, Karsten Jürchott, Rula Abdul-Ghani, Mitch Garber, Ulrike Stein, Iver Petersen, Hermann Lage, Manfred Dietel, and Reinhold Schäfer. Prediction of doxorubicin sensitivity in breast tumors based on gene expression profiles of drug-resistant cell lines correlates with patient survival. *Oncogene*, 24(51):7542–7551, 2005.

[36] Artem Artemov, Alexander Aliper, Michael Korzinkin, Ksenia Lezhnina, Leslie Jellen, Nikolay Zhukov, Sergey Roumiantsev, Nurshat Gaifullin, Alex Zhavoronkov, Nicolas Borisov, et al. A method for predicting target drug efficiency in cancer based on the analysis of signaling pathway activation. *Oncotarget*, 6(30):29347, 2015.

[37] Christos M Dimitrakopoulos and Niko Beerenwinkel. Computational approaches for the identification of cancer genes and pathways. *Wiley Interdisciplinary Reviews: Systems Biology and Medicine*, 9(1):e1364, 2017.

[38] Adam A Margolin, Ilya Nemenman, Katia Basso, Chris Wiggins, Gustavo Stolovitzky, Riccardo Dalla Favera, and Andrea Califano. Aracne: an algorithm for the reconstruction of gene regulatory networks in a mammalian cellular context. 7(1):1–15, 2006.

[39] Broad DepMap. Depmap 21q4 public. 10.6084/m9.figshare.16924132.v1, 2021.

[40] Rakesh Agrawal, Ramakrishnan Srikant, et al. Fast algorithms for mining association rules. In *Proc. 20th int. conf. very large data bases, VLDB*, volume 1215, pages 487–499. Citeseer, 1994.

[41] David Freedman, Robert Pisani, and Roger Purves. Statistics (international student edition). *Pisani, R. Purves, 4th edn. WW Norton & Company, New York*, 2007.

[42] ARACNE. Aracne version 1.0.0.beta1. https://apps.cytoscape.org/apps/aracne, 2021.

[43] Cyni Toolbox. Cyni toolbox version 1.0.0.beta6. https://apps.cytoscape.org/apps/cynitoolbox, 2021.

[44] Cytoscape. Cytoscape version 3.9.0. https://cytoscape.org/, 2021.

[45] Barbara Given, Charles W Given, Alla Sikorskii, Sangchoon Jeon, Ruth McCorkle, Victoria Champion, and David Decker. Establishing mild, moderate, and severe scores for cancer-related symptoms: how consistent and clinically meaningful are interference-based severity cut-points? *Journal of pain and symptom management*, 35(2):126–135, 2008.

[46] Jonas Cicenas, Kotryna Kvederaviciute, Ingrida Meskinyte, Edita Meskinyte-Kausiliene, and Aiste Skeberdyte. Kras, tp53, cdkn2a, smad4, brca1, and brca2 mutations in pancreatic cancer. *Cancers*, 9(5):42, 2017.

[47] John G Tate, Sally Bamford, Harry C Jubb, Zbyslaw Sondka, David M Beare, Nidhi Bindal, Harry Boutselakis, Charlotte G Cole, Celestino Creatore, Elisabeth Dawson, Peter Fish, Bhavana Harsha, Charlie Hathaway, Steve C Jupe, Chai Yin Kok, Kate Noble, Laura Ponting, Christopher C Ramshaw, Claire E Rye, Helen E Speedy, Ray Stefancsik, Sam L Thompson, Shicai Wang, Sari Ward, Peter J Campbell, and Simon A Forbes. COSMIC: the Catalogue Of Somatic Mutations In Cancer. *Nucleic Acids Research*, 47(D1):D941–D947, 10 2018.

[48] Weizmann Institute of Science. Genecards - the human gene database. https://www.genecards.org, 2021.

[49] Frank McCormick. Progress in targeting ras with small molecule drugs. *Biochemical Journal*, 476(2):365–374, 2019.

[50] Ni Ji, Teije C Middelkoop, Remco A Mentink, Marco C Betist, Satto Tonegawa, Dylan Mooijman, Hendrik C Korswagen, and Alexander van Oudenaarden. Feedback control of gene expression variability in the caenorhabditis elegans wnt pathway. *Cell*, 155(4):869–880, 2013.

Design and Construction of Recombinant Plasmid with Spliced *HAC1* Gene for VLP Production in *Pichia Pastoris*

Erica Christofi and George Muir
Department of Chemical Engineering, Imperial College London

Abstract

Virus like particles (VLPs) are a key component in modern day vaccine production and as a result, exploration of efficient VLP production methods carries great value. One particularly effective approach of VLP production is protein expression in the methylotropic yeast *Pichia pastoris* (*P. pastoris*). However, a considerable disadvantage of this process is the high amounts of unfolded proteins which are not secreted and remain within the cell. A potential solution to address this issue is to speed up the cell's own remedial action, the unfolded protein response (UPR), through the use of spliced DNA containing the *HAC1* gene. In this study, several methods were used to firstly, verify the low yield of secreted proteins and its causes, and then to produce a recombinant plasmid containing the *HAC1* spliced gene. Example methods include western blotting, polymerase chain reaction (PCR) and Gibson assembly. The PCR conditions to produce pKanB$_{v2}$ backbone, *HAC1* 3' and *HAC1* 5' fragments were optimised to best aid the Gibson assembly reaction that followed. Then, the plasmid backbone was spliced with the *HAC1* gene fragments and successfully transformed into *Escherichia coli* (*E. coli*) competent cells with 1 in 5 colonies containing the recombinant plasmid. This result was confirmed through colony PCR, commercial sequencing and MAFFT alignment on the Benchling platform. It was found that there were no mutations within the *HAC1* section of the sequence. It would therefore be appropriate for transformation into *P. pastoris* and could be tested to determine its effectiveness in promoting the UPR.

Keywords - VLP, HAC1, P. pastoris, E. coli, Gibson Assembly, Cloning, PCR

1 Introduction

Virus like particles (VLPs) are viral proteins, which self-assemble to form a structure of similar size and form of viruses, without any genetic material (Vicente et al., 2011). This makes them excellent candidates for vaccine production, as they are considered safer alternatives to traditional inactivated or live attenuated viruses. This is because they can generate both the antibody and cell-mediated immune responses, but are unable to infect host cells (Nooraei et al., 2021).

The expression and self-assembly of VLPs can occur in a number of expression systems, but the use of the methylotropic yeast *P. pastoris* offers great promise due to its ability to grow to high cell densities and express proteins with the correct folding and post-translational modifications (PTMs). An additional advantage is the very low amounts of endogenous proteins secreted in the supernatant together with the VLP components (Mastropietro, Aw, and M.Polizzi, 2021), which simplifies the downstream purification process.

Despite its potential, the yields of recombinant proteins expressed in *P. pastoris* can be low. This can be attributed to an accumulation of unfolded proteins in the endoplasmic reticulum (ER), causing a bottleneck in the secretory pathway. While this accumulation triggers the unfolded protein response (UPR), the mediation response is slow, as the UPR in *P. pastoris* requires splicing of a non-conventional intron in the HAC1 mRNA, consistent with other eukaryotes (Whyteside et al., 2011).

This paper explores the use of Gibson Assembly in cloning the spliced HAC1 gene into a synthetic plasmid derrived from *E. coli*, as well as transformation protocols. The extracted recombinant plasmid can then be linearised, and integrated into the *P. pastoris* genome, to potentially speed up the UPR.

2 Background

Both Mastropietro, Aw and Polizzi as well as Ahmad et al discuss the great potential *Pichia pastoris* presents for the expression of proteins. *P. pastoris* has gained a large amount of popularity due to its relative simplicity as well as high-cell densities, reaching up to 130g/L of dry cell mass. Additionally, compared to other eukaryotic systems, it is one of the most productive with protein expression yields reaching 20g/L. However, it is important to note that yields of this magnitude are not achieved for every protein.(Ahmad et al., 2014)(Mastropietro, Aw, and M.Polizzi, 2021)

One way in which this protein yield can be further optimised is by using the *HAC1* gene to trigger the unfolded protein response (UPR), as proposed by Guerfal et al. The UPR is a remedial action within the cell, activated by the accumulation of unfolded and misfolded proteins. It is a linear signaling pathway regulating the transcription of UPR target genes encoding chaperones, foldases, and proteins involved in lipid metabolism, glycosylation, *etc.* During this signaling pathway, the *HAC1* mRNA is spliced at two specific sites. *HAC1* mRNA is constitutively expressed, but, no protein is produced when the mRNA remains unspliced, due to the secondary structure of the intron. The translational block in the *HAC1* mRNA is released by the removal of the intron. Hac1p is then translocated to the nucleus, where it binds to UPR responsive elements (UPRE) in the promoter of UPR target genes. From the evaluation of inducible and constitutive UPR induction, it was shown that whenever the hac1p affected protein expression levels, the effect was always greater when hac1p expression was inducible rather than constitutive. Therefore, the introduction of the *HAC1* gene to *P. pastoris* via genetic modification, inducing the expression of hac1p, will lead to greater amplification of protein expression. It is important to note that the increase in heterologous protein production will need to be evaluated on a case by case basis, as for some proteins there was actually a decrease in production rather than an increase.(Guerfal et al., 2010)

To effectively design and produce cloned DNA containing the *HAC1* gene within the given time-frame, an appropriately fast and efficient method of cloning would be required. Gibson et al develop a great solution to this with a single stage method that allows for multiple overlapping DNA molecules to be assembled. When one of the assemblies studied in the Gibson et al. paper was transformed into *E. coli*, 5 out of 10 colonies screened contained the correct insert size, proving it to be an effective method of DNA cloning. Additionally, the error rate during *in vitro* recombination was shown to be very low with only about one error per 50 DNA molecules.(Gibson et al., 2009)

3 Methods

3.1 Media Preparation

A range of different media were prepared as needed following the below recipes:

Buffered Glycerol Complex Medium (BMGY)

1% yeast extract, 2% peptone, 100mM potassium phosphate (pH 6.0), 1.34% yeast nitrogen base (YNB), 0.00004% biotin, 1% glycerol in water.

Buffered Methanol Complex Medium (BMMY)

1% yeast extract, 2% peptone, 100mM potassium phosphate (pH 6.0), 1.34% YNB, 0.00004% biotin, 0.5% methanol in water.

Yeast Extract Peptone Dextrose Medium (YPD) Broth

1% yeast extract, 2% peptone and 2% dextrose in water. The mixture was sterilised at 121°C for 15 minutes in an autoclave without dextrose, which was instead filtered for sterilisation. The dextrose was then added, under sterile conditions, once the medium had cooled.

Lysogeny Broth (LB) Broth and Agar

1% tryptone, 0.5% yeast extract, 1% sodium chloride in water. The mixture was autoclaved at 121°C for 15 minutes for sterilisation. For agar plates, 15g/L bacteriological agar was added before autoclaving.

Super Optimal Broth with Catabolite-Repression (SOC)

2% tryptone, 0.5% yeast extract, 10 mM sodium chloride, 2.5 mM potassium chloride, 10 mM magnesium chloride, 10 mM magnesium sulfate, and 20 mM glucose.

A list of all other reagents that were used throughout the methods can be found in Appendix A.1.

3.2 Culture Preparation, Glycerol Stocks and Plasmid Extraction

***P. Pastoris* Overnight Culture Preparation**

Working next to a blue flame for sterility, a sterile pipette tip was used to streak a colony of *P. pastoris* from an agar plate, to pick up some cells. The tip was then dropped in a 50mL falcon tube containing 5ml of YPD or BMGY. The cap was left slightly loose, to ensure adequate aeration and the tube was incubated whilst shaking at 30°C overnight.

***E. Coli* Overnight Culture Preparation**

Working next to a blue flame for sterility, a sterile pipette tip was used to streak a colony of *E. coli* from an agar plate, to pick up some cells. The tip was then dropped in a 15mL culture tube containing 5ml of LB and 5μL of 37.5mg/mL kanamycin, to selectively remove cells not containing a kanamycin resistance gene. The tube was incubated at 37°C overnight.

Synthetic Plasmid Miniprep

The Miniprep of *E. coli* allowed for the template and recombinent plasmids to be extracted from the *E. coli* cell cultures. This was done by following the unmodified manufacturer instructions given for the QIAprep Spin Miniprep Kit.(Qiagen, 2021)

Glycerol Stocks

The following method was carried out next to a blue flame to maintain sterility. For *E. coli*, 0.7mL of overnight culture was mixed with 0.3mL of 50% sterile glycerol to achieve a final glycerol concentration of 15%. However, for *P. pastoris* the final optical density at 600nm (OD_{600}) needed to be between 50 and 100 (approximately 2.5×10^9 to 5×10^9 cells/mL). This was done by first measuring the OD_{600} of the overnight culture at a 1 in 50 dilution (in YPD) using a photometer, then multiplying the reading by 50. Then, the culture was centrifuged for 8 minutes at 3200g in a centrifuge. Next, the supernatant was discarded and calculations were made for the volumes of YPD and glycerol needed for a final glycerol concentration of 15% and a final OD_{600} of 75 based on the original measurement. For both stocks, 1mL of the mixture was transferred to a 2mL cryogenic tube and stored at -80°C.

3.3 Protein Expression in *P. Pastoris*

Starting with an overnight culture of *P. pastoris* in BMGY shaking at 30°C, a 100μL sample was taken to measure the optical density at 600nm (OD_{600}) using a photometer, and a 1mL of BGMY as a blank. As *P. pastoris* grows to high cell densities, a 1 in 100 dilution was performed using BMGY to ensure the OD falls within the range of the photometer. The reading was then multiplied by 100. After that, the remaining contents of the tube were centrifuged for 8 minutes at 3200g. A 300μL sample of the supernatant was taken as a control of protein expression at 0 hours, and the remaining supernatant was discarded. The pellet was then re-suspended in BMMY medium, to promote protein expression over cell growth. The tube was placed back in the shaking 30°C incubator for a further 72 hours, adding 25μL of pure methanol at 24 and 48 hours to sustain protein growth. To study protein expression over time, 300μL culture samples were removed at 24,48 and 72 hours and centrifuged for 5 minutes at 3200g, to obtain a pellet and a supernatant. These were then stored in separate eppendorf tubes at -20°C.(ThermoFisher, 2020)

3.4 SDS PAGE and Western Blot

To analyse the proteins expressed by *P. pastoris*, SDS PAGE and western blotting was used. These methods allowed for the proteins to be separated by their molecular weights.

First, the samples were prepared for running on a gel. For the supernatant, 40μL of sample was mixed with 10μL 5X SDS-PAGE sample buffer and incubated at 100°C for 10 minutes, later using 20μL per well. For the *P. pastoris* pellet, the method suggested by V Kushnirov was used (Kushnirov, 2000). The pellet was first re-suspended in 5mL of 1X PBS then 100μL of this suspension was transferred to a 1.5mL Eppendorf tube and centrifuged at max speed for 5 minutes in a microcentrifuge. The supernatant was discarded and the pellet was re-suspended in 100 μL of milliQ water. Then, an alkali lysis was performed using 100 μL of 0.2M Sodium Hydroxide, to dissolve the cell wall and free the cell contents. After incubating for 5 minutes at room temperature, the tube was centrifuged at maximum speed for 5 minutes, and the supernatant was discarded. The pellet was then re-suspended in 50μL 5X SDS-PAGE sample buffer with reducing agent and incubated at 100°C for 10 minutes, to denature proteins. After a final centrifugation at maximum speed for a further 5 minutes, 6-8 μL of the supernatant were added to each well.

Then, the gels were made using the Bio-Rad gel casting stands. These gels were made according to the Bio-Rad guide, with a 4% stacking gel and a 12.5% Tris-HCL resolving gel, details of reagents used can be found in Appendix A. Once the gels were set, again following the Bio-Rad guide, the gels were loaded into an electrophoresis tank filled with a 1X Tris running buffer. Before running, the protein expression samples were loaded into the gels along with PageRuler Prestained Protein Ladder (ThermoFisher, 2021b), full ladder can be found in Appendix C, and a pure, commercial recombinent protein sample as a control. Using a constant amperage of 25 mAmps per gel, the gels were run for about 60 minutes until the sample dyes had migrated to the bottom. ThermoFisher's SimplyBlue™ SafeStain (ThermoFisher, 2021c) was then used on one of the gels according to the microwave staining protocol.(Bio-Rad, 2021a)

To view the proteins with a higher sensitivity, western blotting was used. A transfer buffer containing 1.14% glycine, 0.303% Tris, 0.1% SDS and 20% methanol in 1L was used. A PVDF membrane was pre-wetted in methanol for 30 seconds followed by milliQ water for 2 minutes and finally left to soak in the transfer buffer, tweezers were always used whenever the membrane was handled to avoid protein contamination. From this point, the Mini Trans-Blot Cell by Bio-Rad was used (Bio-Rad, 2021b). 3MM paper and fiber pads were also soaked in transfer buffer prior to assembly. The sandwich was assembled as follows:

1. Cassette, with the gray side down, was placed on a clean surface.
2. One prewetted fiber pad was placed on the gray side of the cassette.
3. A sheet of 3MM paper was placed on the fiber pad.
4. One SDS PAGE gel was placed on the 3MM paper.
5. The prewetted membrane was placed on the gel.
6. The sandwich was completed by placing a piece of 3MM paper on the membrane.
7. The last fiber pad was placed on the sandwich.
8. The cassette was closed and placed into the module, with the black lid towards the black part of the module.

With the sandwich formed, the module was then placed into the electrophoresis tank filled with transfer buffer. The tank was placed in ice to reduce overheating, along with the blue cooling pack placed inside the tank. At a constant voltage of 90 Volts, the transfer was run for 70 minutes. TBS-T (0.05%) (1x TBS and 0.05% v/v Tween-20) was used to rinse the membrane after disassembling the transfer. About 10mL of blocking buffer, 5% skimmed milk in TBS-T (0.05%), was used to block the membrane at 4°C overnight. TBS-T (0.05%) was again used to wash the membrane.

A hepatitis E, HEV, to mouse antibody was used as the primary antibody. This primary antibody was diluted in 10mL blocking buffer to a final concentration of 1μg/mL and used on the membrane to incubate for two hours at room temperature whilst rocking. The membrane was rinsed twice with TBS-T (0.05%) then washed three times for 5 minutes each in TBS-T (0.05%). Similar to the primary antibody, the secondary antibody, mouse to rabbit, was diluted in blocking buffer and used to incubate the membrane for one hour while rocking. Again, the membrane was rinsed twice with TBS-T (0.05%) then washed three times for 5 minutes each in TBS-T (0.05%) followed by two additional two minute washes in milliQ water. Finally, the membrane was incubated in 5mL of BCIP for 10 minutes to an hour until the blot developed.

3.5 Primer Design for Gibson Components

The primers used to amplify the fragments for Gibson reaction had two different functions:

- To anneal to complementary regions and initiate DNA amplification
- To add overhangs which are complementary to the fragments that require assembly

The 3 fragments needing to be assembled are the 5' *HAC1* fragment, 3' *HAC1* fragment and the synthetic pKanB$_{v2}$ plasmid backbone. One of the main reason pKanB$_{v2}$ was chosen is because it contains the kanamycin resistance gene, allowing any cells containing the plasmid to survive in the presence of kanamycin. A full sequence of the pKanB$_{v2}$ plasmid can be found in Appendix E. The reason behind the two separate fragments of *HAC1* was that the intron between the two exons had to be removed, to effectively obtain the spliced version of the gene. Therefore, three forward and three reverse primers were needed, as seen in figure 1:

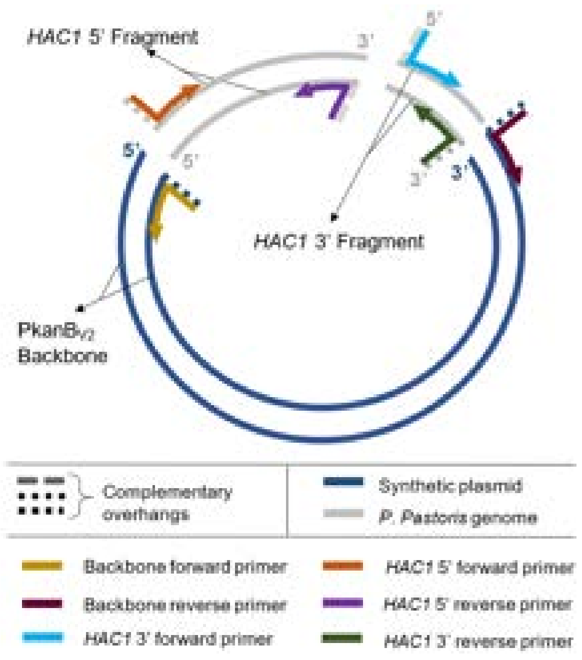

Figure 1: 3-part Gibson Assembly outline with components and primers

To design the primers, Benchling was used. The aim was to:

- Keep the GC content of each oligonucleotide betweeen 40% and 60%, to ensure primer stability. As hydrogen bonding is stronger between the G and C bases, if GC content was 60%, this would promote primer dimer formation.
- Terminate the 3' end of the primer with a GC sequence (GC clamp), to promote binding (ThermoFisher, 2019).

After design, the Tm calculator from the NEB website was used to verify that the annealing temperature of the annealing part of each primer pair was similar. In addition, the Oligo analysis tool IDT was used to check for the presence of any secondary structures, which could yield to poor or no yield of the product, due to a lower primer availability (Biosoft, 2021).

The sequences of the primers used, as well as their specifications can be found in Appendix B.

3.6 Polymerase Chain Reaction (PCR)

Two different approaches were later explored:

- A three-part assembly of the different fragments
- A two-part assembly, where the *HAC1* fragments are joined prior to the assembly

The following PCR techniques were therefore used:

3.6.1 Routine PCR

To amplify fragments, the following protocol was used. As this step required a high-fidelity enzyme, Phusion components were substituted with Q5 components in various runs to compare effectiveness of both enzymes.

Table 1: Reaction Setup for Routine PCR (NEB, 2021d), (NEB, 2021c)

Component	Quantity (μL)	Final Concentration
5X Phusion/Q5 Reaction Buffer	10	1X
Nuclease-free Water	Top up to 50	-
10 mM dNTPs	1	200 μM
10 μM Forward Primer	2.5	0.5 μM
10 μM Reverse Primer	2.5	0.5 μM
Template DNA	variable	1 pg-10 ng for Plasmid DNA; 50 ng- 250 ng for Genomic DNA
Phusion/Q5 DNA Polymerase	0.5	1 unit per 50 μL reaction

Table 2: Thermocycling Conditions for Routine PCR (NEB, 2021d), (NEB, 2021c)

Step	Temperature (°C)	Time (s)
Initial Denaturation	98	30
25–35 Cycles	98 T_a=50–72 72	5-10 10-30 20-30/kb
Final Extension	72	300-600
Hold	4-10	∞

Alterations to the standard protocol were occasionally required to yield improved results. These are outlined in section 3.6.3.

3.6.2 Overlap Extension PCR

Overlap extension was applied, in order to assess if a two part assembly would make the subsequent Gibson reaction more successful. The process of Overlap extension, as well as exact conditions used are outlined in Appendix D.1. The aim was to join the *HAC1* 5' fragment to the *HAC1* 3' fragment, and then add one overhang to each end of the joined DNA, forming sticky ends which were complementary to the ones found on the plasmid backbone.

3.6.3 Troubleshooting Methods

General Troubleshooting

The following reagent modifications were used for troubleshooting:

- Betaine: Add 10 μL for a 50 μL reaction mixture
- DMSO: Working in the fume hood, add 2.5 μL for a 50 μL reaction mixture
- Altering reagent amounts, e.g. decreasing primer concentration

Touchdown PCR

For touchdown PCR, the reaction was set up as outlined in table 1. The thermocycling conditions outlined in table

2 were followed, with the only exception being that the T_a was decreased by 1 °C every cycle.

Gradient PCR

Gradient PCR was used to assess the effects of the annealing temperature on primer dimer formation. Specifically, the same reaction mixture as set out in table 1 was prepared in bulk and aliquoted into PCR tubes. Then each tube was assigned a different annealing temperature within ± 3°C of the annealing temperature calculated on the NEB website, using the thermocycler.

3.7 Fragment Preparation for Gibson Assembly

3.7.1 Backbone Treatment

Dpn1 was used to treat the backbone fragment produced from the PCR reaction of pKanB$_{v2}$. This was done by pipetting 1μL of Dpn1 into the 50μL PCR product of pKanB$_{v2}$ and leaving to incubate at 37°C overnight. The purpose of this was to digest methylated GATC sites, which helps to remove cell-derived plasmid template left over in the PCR sample.(Leonard and Barnhart, 2021)

3.7.2 Gel Electrophoresis

Gel electrophoresis was used to analyse the size of DNA fragments. Agarose gels were prepared using a w/v percentage solution of agarose to TAE (40mM Tris-acetate, 1mM EDTA), varying between 0.8% and 1.5% depending on the size of fragment being analysed. By applying heat, the mixture was melted so that the agarose was completely dissolved. A gel tray was placed into the casting apparatus and either 2.5μL or 5μL of SYBR Safe DNA Gel Stain was pipetted in depending on if the tray was small or large respectively. Depending on the number of wells needed, an appropriately sized comb was inserted into the tray and the agarose gel was poured to sufficiently cover the comb so that wells form. The mixture inside the tray was stirred and then left to cool until solidified.

With the gel formed, it was ready to be transferred to the electrophoresis tank. Enough TAE running buffer was added so that the gel was covered. 5μL of each DNA samples were mixed with 1μL of 6X gel loading dye, then this mixture was transferred to a well in the gel using a pipette. Additionally, Hyperladder 1kb and 100bp DNA ladder were run with each gel to verify the size of each band (ThermoFisher, 2021a)(MeridianBiosciences, 2021). At a constant voltage of 100 Volts, the gel was run for about 45 minutes until the dye had migrated an appropriate distance.(Lee et al., 2012)

Making sure the power supply was turned off, the gel was removed from the tank and placed into a gel imaging system. When the UV light setting was used, the bands could be visualised and the image was captured. To analyse these bands, references for the ladders were required as shown in Appendix C.

3.7.3 DNA Purification

Two different methods of DNA purification were used through this report, gel extraction and Clean & Concentrator®-5.

Gel Extraction

Gel extraction followed the same steps as section 3.7.2 but instead the entire sample was loaded rather than just 5μL. From this point, the Zymoclean™ Gel DNA Recovery Kit was used. When following the instructions, maximum times on intervals were used and 11μL of milliQ water was used to elute the DNA.(ZymoResearch, 2021b)

Clean and Concentrator

DNA Clean & Concentrator®-5 kit by Zymo Research allows for DNA extraction without going through the process of running a gel. When following the instructions, a 5:1 ratio of DNA Binding Buffer to sample was used and 11μL of milliQ water was used to elute the DNA. (ZymoResearch, 2021a)

The concentration of each DNA solution was measured by adding 1μL to the BioDrop machine.

3.8 Gibson Assembly

Gibson assembly is the single stage DNA cloning method proposed by Gibson et al, previously discussed in section 2 (Gibson et al., 2009). Gibson assembly mastermix was made in bulk and aliquoted into 15μL volumes inside PCR tubes (components can be found in Appendix A). On ice, equimolar amounts of each fragment were added to the Gibson assembly mastermix, 100ng of which was composed of the pKanB$_{v2}$ backbone fragment. This was then left to incubate in a thermocycler for 60 minutes at 50°C, ensuring that the reaction mixture was only placed in the machine once it had reached 50°C. After the reaction, the mixture was stored at -20°C. Some troubleshooting methods that were used included using a 1:3:5 (plasmid backbone:*HAC1* 5':*HAC1* 3') molar ratio and using a total volume of PCR fragments less than 20% of the overall reaction volume.(NEB, 2021b)

3.9 E. Coli Transformation

To store and replicate the plasmid cloned from Gibson assembly, *E. coli* transformation was used. Specifically, commercial *E. coli* DH5α competent cells were used. These steps were conducted next to a blue flame for sterility. Tubes of cells were supplied in 50μL volumes but were left to thaw for 10 minutes and split into two volumes, 25μL each. Between 0.5μL and 2μL of the Gibson reaction product was added to the competent cells, as well as a separate positive control containing pKanB$_{v2}$, these were carefully mixed with 4 flicks of the tube and no vortexing. The mixtures were then left to incubate on ice for 30 minutes, followed by a 30 second heat shock at exactly 42°C and then back onto ice for a further two minutes without mixing at any point. 475μL of room temperature SOC medium was then pipetted into the *E. coli* mixture. For one hour, the mixture was then left to incubate whilst shaking at 37°C. Once incubation had completed, the culture was centrifuged at max speed for one minute in a microcentrifuge. About 300μL of the supernatant was discarded and the pellet was re-suspended in the remaining supernatant. Finally, the mixture was spread onto an LB agar plate containing kanamycin, to selectively remove cells not containing a kanamycin resistance gene, and left to incubate overnight at 37°C.(Froger and Hall, 2007)

3.10 Recombinent Plasmid Verification

Colony PCR

After incubating overnight, and after colonies had grown to a visible size, a colony PCR was run to verify and identify the presence of the correct recombinent plasmid in the colonies. Firstly, the PCR reaction mixture was prepared as follows:

Table 3: Reaction Setup for Colony PCR (Mastropietro, Aw, and M.Polizzi, 2021)(SigmaAldrich, 2021)

Component	Quantity (μL)	
RedTaq Readymix	10	-
Nuclease-free Water	8	-
10 μM Forward Primer (*AOX1*)	2.5	0.5 μM
10 μM Reverse Primer (*AOX1*)	2.5	0.5 μM

Under a sterile atmosphere, the colonies were streaked one by one using a sterile pipette tip. This tip was then streaked onto a fresh plate, and then used to transfer the cells to the PCR tubes (the fresh plate was incubated and used to prepare overnight cultures for glycerol stocks as outlined in section 3.2).
The following thermocycling conditions were used:

Table 4: Thermocycling Conditions for Colony PCR (NEB, 2021a)

Step	Temperature (°C)	Time (s)
Initial Denaturation	94	600
25–35 Cycles	94 T_a=53 72	30 30 60/kb
Final Extension	72	300-600
Hold	4-10	∞

Finally, the PCR mixture was run on a 0.8% agarose gel, as outlined in section 3.7.2, to verify the size of the plasmid.
Sequencing
Having already prepared an overnight culture of the cloned *E. coli* to prepare glycerol stocks, the remainder of the culture is used to mini prep the plasmid as outlined in section 3.2. The obtained plasmid was then sent to sequencing following the instructions for the TubeSeq service provided by Eurofins Genomics, sending both the forward and reverse *AOX1* primers.(EurofinsGenomics, 2021) The results were analysed to assess their similarity to the original spliced *HAC1* gene using the MAFFT algorithm of the alignment tool on Benchling.

4 Results and Discussion

4.1 Protein Expression in *P. Pastoris*

Initially, protein expression of hepatitis E virus (HEV) in *P. pastoris* was analysed to verify that there was a bottleneck issue within the cells. This was done using the methods outlined in sections 3.3 and 3.4. As can be seen in figure 2, the stained SDS PAGE gel does not clearly show the proteins. Samples from the pellet are unclear due to endogenous proteins being produced in the cell and samples from the supernatant are not visible because the concentrations are too low. To solve this issue, western blotting was used so that the HEV proteins could be directly amplified, allowing them to be more visible.

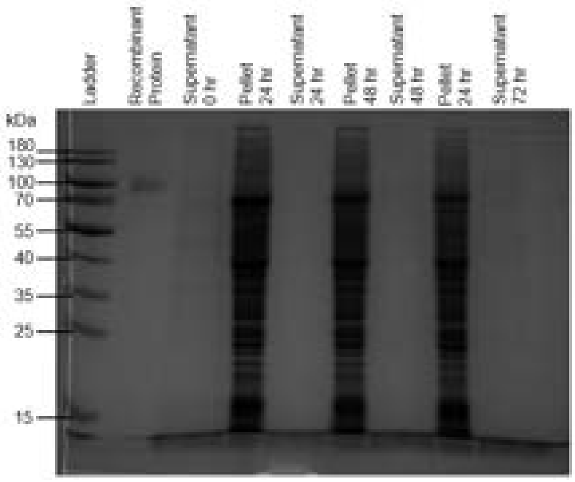

Figure 2: Stained SDS PAGE gel of HEV expression samples, of both supernatant and pellet, at 0, 24, 48 and 72 hour intervals after expression

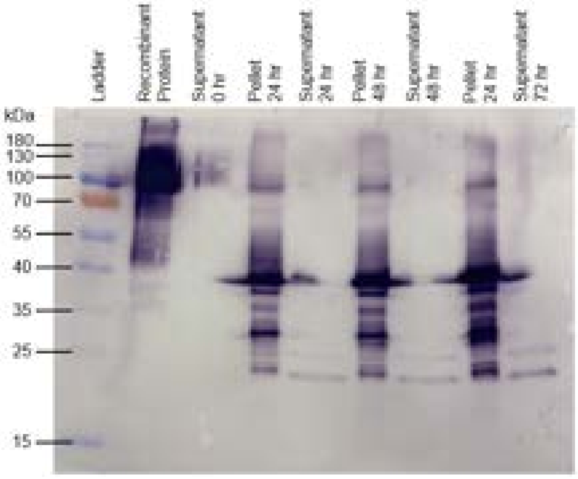

Figure 3: Western blot of HEV expression samples, of both supernatant and pellet, at 0, 24, 48 and 72 hour intervals after expression

Figure 3 shows the western blot of the HEV samples. For the supernatant, there are distinct bands, of similar intensity, at about 20 kDa at 24, 48 and 72 hours but there is no band at 0 hours. 23 kDa is the expected size of the recombinant HEV E2 capsid protein (Mazalovska and Kouokam, 2020), which then implies that initially there was no HEV protein in the supernatant, then at 24 hours HEV proteins had been secreted. However, the supernatant at 48 hours and 72 hours had similar bands suggesting that a minimal amount of the protein was secreted after the initial 24 hour period. It should be noted that there was a band at about 120 kDa in the 0 hour supernatant sample but not in the later samples, this was likely due to spillage from the recombinant protein lane. For the pellet lanes, bands at about 30 kDa and 40 kDa can be seen with increasing intensity as time progresses from 24 hours to 72 hours. Bands at these sizes are significantly more intense than at the expected 20 kDa because a signal peptide (α-mating factor), about 10 kDa in size, has to be attached to the HEV protein before it can be excreted from the cell(Lin-Cereghino et al., 2013), resulting in a 30 kDa structure, and dimerized proteins are also formed at a size of 40 kDa. Having increasing intensity within the pellets tells us that the rate at which proteins are being formed within the cell is greater than the rate at which the proteins are being secreted from the cell. One way that this could be mitigated would be by changing the reaction conditions to reduce the rate of protein formation, however, a potentially more effective solution would be to increase the protein secretion of the cell.

4.2 PCR Troubleshooting and Optimisation

4.2.1 Plasmid Modification

The synthetic plasmid backbone was initally extracted from an overnight *E. coli* culture using the method outlined in section 3.2 and a concentration of 168 ng/μL was measured using the BioDrop. However, following the routine PCR to add overhangs and amplify the backbone for Gibson assembly, an agarose gel revealed that the fragment amplified was 3000 base pairs (bp) instead of the expected 4000 bp, as seen in figure 4:

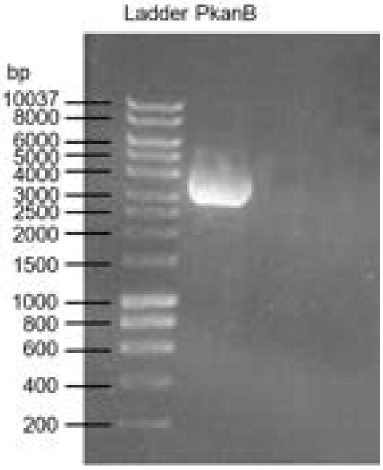

Figure 4: 0.8% Agarose gel containing a sample of the pKanB routine PCR mixture carried out at 58°C

When verifying that the primers designed did not have any other regions of homology on the plasmid, it was identified that the initally chosen pKanB plasmid contained two AOX1 terminators, one before and one after the Kanamycin resistance gene. As the AOX1 terminator was chosen to be the splicing site, it meant that instead of the full plasmid backbone being amplified, polymerisation ended at the first AOX1 terminator, instead of at the second one. It then follows that, the sequence in between the two terminators, including the Kanamycin resistance gene, was deleted. This rendered the existing primer and plasmid combination unsuitable for use, as without the Kanamycin resistance, it would not be possible to screen the *E. coli* clones after transformation.

To resolve this issue, a new splicing location could be selected, and new primers would then be designed, or one of the two AOX1 terminators could be removed. As this issue was previously encountered in the Polizzi lab, a supply of this plasmid with the excess AOX1 terminator removed, pKanB$_{v2}$, was provided.

4.3 Fragment Preparation

Initial PCRs for all fragments were run in parallel as outlined in section 3.6.1, using Phusion DNA Polymerase. The annealing temperature was set to 59°C (T$_a$ for pKanB$_v$2, *HAC1 5'* and *HAC1 3'* were calculated as 61°C, 63°C and 60°C respectively), to ensure that all forward and reverse primers can anneal (Bio-Rad, 2021c) . 0.5μL of genomic DNA (54ng) and 3.5μL (9ng) of plasmid DNA were used. However, when a 0.8% agarose gel was run after the reaction, no bands were observed, (results not shown) indicating that nothing had amplified. To address this, the PCR was repeated using Phusion DNA Polymerase, with the following adjustments:

- Betaine was used (10 μL). Betaine aids the amplification of GC-rich sequences by preventing the formation of secondary structures that inhibit polymerase action (Henke et al., 1997). Although all targets had a GC content below 60%, Betaine was still thought to help.
- The annealing temperature was reduced to 58°C, to encourage both reverse and forward primers to bind. T$_a$ should not be reduced further, as this would cause non-specific binding of primers on the template (Bio-Rad, 2021c).
- The volume of genomic DNA added was increased from 0.5μL to 2.0μL (54ng to 216ng). Although the original amount used lay within the protocol's accepted range (50ng-250ng), it was very close to the lower limit. By increasing the DNA template within the acceptable range, the probability of the primer binding to the template, instead of forming primer dimers, increased.
- A negative control was run for each of the fragment PCRs.

The results of the second PCR can be seen below:

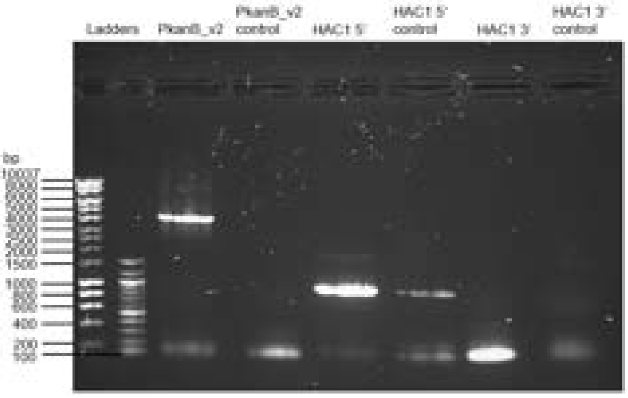

Figure 5: 0.8% Agarose gel with samples and controls following fragment amplification PCR (58 °C, with 216 ng genomic DNA/10ng of plasmid and Betaine)

The expected sizes of the fragments are:

Table 5: DNA Fragment Sizes for Gibson

pKanB$_{V2}$	4277 bp
HAC1 5'	916 bp
HAC1 3'	119 bp

For the plasmid backbone: The presence of a band at ∼4000 bp indicates that the fragment amplified has the correct size. The lack of a band at that size in the control lane indicates that nothing else from the mixture has amplified, and therefore, the 4000bp band is in fact the correct fragment. The bands at 100bp present in both lanes are thought to be primer dimers, as the oligonucleotides used for the PCR are 50bp long.

For *HAC1* 5': A band at 900bp can be seen, which suggests that the fragment amplified has the correct size, however, a fainter band at the same size can be seen in the control lane. This could suggest that the primers are binding to another mixture component and amplifying something of the same size. However, a manual error was made when pipetting, which meant that the control was contaminated with a small amount of genomic DNA, which, in the presence of the correct primers and dNTPs, was amplified. Therefore, it was concluded that the fragment amplified was indeed correct. As was the case with the plasmid backbone, both the *HAC1* 5' and its control have primer dimer bands at 100 bp. In spite of this, the band appears to be fainter in the *HAC1* 5' lane than in the control lane. This is because more DNA was present in the *HAC1* 5' mixture, compared to the control, which only had trace amounts due to contamination. The presence of more DNA effectively decreased the concentration of primers, which increased the probability of the primers annealing, instead of forming dimers.

For *HAC1* 3': As this fragment has a similar size as the primer dimers formed, the bands of the *HAC1* 3' lane and the control lane are at the same size. Therefore, it was concluded that the band in the *HAC1* 3' lane likely contained a mixture of the fragment of interest and primer dimers. Since this band was much more intense than the one in the control lane, the conclusion drawn was that the dimer concentration was sufficiently lower than the concentration of the fragment of interest.

Considering the above, the fragments were gel extracted as described in section 3.7.3. The concentrations obtained were 55ng/μL, 125 ng/μL and 59ng/μL for the plasmid backbone, *HAC1* 5' and *HAC1* 3' respectively.

4.4 Gibson Assembly

Initially, the Gibson assembly procedure outlined in section 3.8 was unsuccessful with no colonies forming after transformation into *E. coli*, suggesting that the desired plasmid was not being formed. There were two main expected reasons for this formation not taking place, either one of the required fragments was missing in the solution before assembly or due to the small size of the *HAC1* 3' DNA fragment, the probability of annealing was too low. Therefore, troubleshooting was applied to both the fragment formation and the Gibson assembly conditions in an attempt to resolve the issue.

In previous preparations for the *HAC1* 3' DNA fragment, it was unclear if the sample contained the actual fragment or whether it was majorly dominated by the presence of primer dimers as bands of the same size were appearing in both the sample and the negative control as shown in figure 5. To try and improve the efficiency of the PCR, three troubleshooting methods were used from section 3.6.3: addition of DMSO to the reaction mixture, decrease of primer concentration and gradient PCR. DMSO disrupts secondary structure formation and is particularly useful in templates with high GC content (Hardjasa et al., 2010). Decreasing primer concentration increases the chances of primers annealing to the template DNA, as opposed to them forming primer dimers (Bio-Rad, 2021c). Use of gradient PCR then allows for multiple annealing temperatures to be tested, in this case temperatures of 56°C, 58°C, 60°C and 62°C were assessed. As can be seen in figure 6, the negative controls for temperatures of 58°C and above still showed some amount of primer dimer formation, in spite of this, the band in the 56°C negative control is near invisible suggesting the 56°C sample band to be near pure *HAC1* 3'.

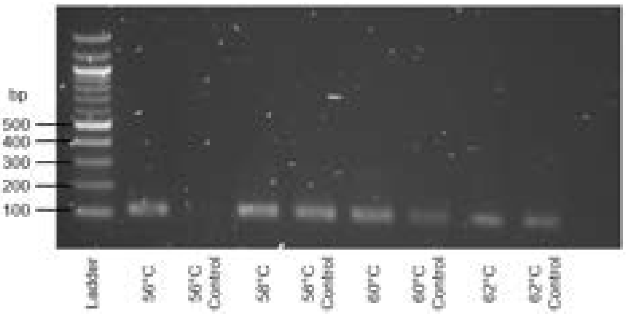

Figure 6: 0.8% Agarose gel with samples and controls from the *HAC1* 3' gradient PCR carried out at intervals between 56-62°C

In addition to the *HAC1* 3' preparation modifications, a different method of DNA purification was used. Initially, gel extraction was used to purify DNA fragments with relatively good resulting concentrations of about 60ng/μL. However, in an attempt to increase yield of DNA, Clean & Concentrator®-5 was used instead, as detailed in section 3.7.3. After performing the new method of purification, the concentrations obtained were 130 ng/μL, 98ng/μL and 92 ng/μL for the Plasmid backbone, *HAC1* 5' and *HAC1* 3' respectively .

Whilst the aforementioned troubleshooting method could have improved the Gibson assembly success rate enough, troubleshooting of the assembly conditions directly was performed to ensure the desired plasmid was produced. This was done by modifying the molar ratio of fragments used to 1:3:5 (plasmid backbone:*HAC1* 5':*HAC1* 3') and reducing the volume of fragments used to below 20% of the overall volume, as detailed in section 3.8. These changes reduce dilution of the mastermix and the issues caused by having varying fragment sizes.

It should be noted that overlap extension was considered as an alternative method, and would have been employed if the above failed to provide results. This would allow for the *HAC1* 3' and 5' fragments to bind prior to the Gibson assembly, mitigating the fragment size issue.

4.5 pKanB$_{v2}$-*HAC1* Analysis

After the Gibosn assembly had been performed, the resulting plasmid was transformed into *E. coli* according to section 3.9. Both the positive control and the transformations formed from 0.5μL and 1μL of Gibson assembly product successfully grew colonies, however, the transformation formed from 2μL of Gibson assembly product failed to grow any colonies. 10 colonies were chosen from the successful plates and colony PCR was performed on them as covered in section 3.10.

Figures 7 and 8 show the results of the colony PCR. The most notable bands formed from these PCRs are the ones at about 1200 bp and 300 bp. This is because when you analyse the size of DNA expected from colony PCR on either pKanB$_{v2}$-*HAC1* or pKanB$_{v2}$, with the *AOX1* reverse and forward primers, the resulting sizes are 1174 bp and 285 bp respectively. It can then be concluded that colonies 17, 19, 25 and 26 most likely contain the desired pKanB$_{v2}$-*HAC1* plasmid, which is less than half the success rate stated by Gibson et al (Gibson et al., 2009). All remaining colonies could have formed due to containing the original pKanB$_{v2}$, however this is unlikely to be the case for all colonies as some of the bands lie at slightly differing sizes. The fainter bands seen below 200 bp are most likely primer dimers.

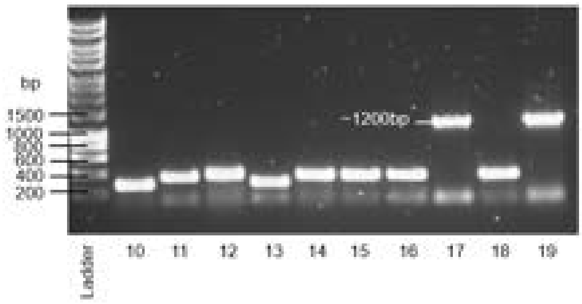

Figure 7: 0.8% Agarose gel following colony PCR. Pictured are colonies 10 to 19 from *E. coli* transformation using 0.5μL of Gibson assembly product

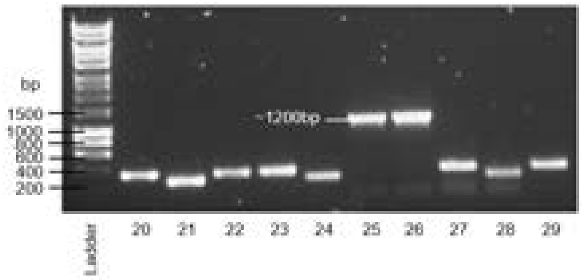

Figure 8: 0.8% Agarose gel following colony PCR. Pictured are colonies 20 to 29 from *E. coli* transformation using 1μL of Gibson assembly product

Whilst the colony PCR gives a fairly good estimation of how successful the plasmid formation was, it was necessary to further verify that the assembled plasmid was the desired pKanB$_{v2}$-*HAC1* plasmid. This was done by sending the plasmids for sequencing as detailed in section 3.10. The resulting sequences can be found in Appendix E. Results of the sequencing revealed that all colonies contained the spliced *HAC1* gene.

Once the sequences were received, the Alignment tool on Benchling was used to further assess the plasmid's match with the spliced *HAC1* gene (Benchling, 2021). Specifically, the MAFFT algorithm was used, which uses Fast Fourier Transforms for rapid multiple sequence alignment (Katoh, 2002). For each of the four colonies, the pair of sense and anti-sense DNA strands (each amplified using the forward and reverse AOX1 primers respectively) were aligned with the spliced *HAC1* gene. The % match for each strand was then given, together with the number of mismatches. These can be found in Appendix E. Following this, manual inspection was used to locate the mismatches, and identify if any of them occurred within the *HAC1* gene. This would be undesired, as mismatches or mutations could affect the amino acid sequence produced during translation of the gene in *P. pastoris.* Fortunately, none of the mismatches observed in all sequences was within the *HAC1* gene. Therefore, it was concluded that all of the recombinent plasmids could be linearised and transformed into *P. pastoris.* Despite this, it would be best to proceed with DNA from the colony which had the best overall % match, which was Colony 25.

5 Conclusions

5.1 Protein Expression in *P.* Pastoris

It was identified that high amounts of HEV VLPs remained in the pellet for up to 72hrs after expression was induced, causing lower yields in the supernatant. This indicates that the secretory pathway of *P. pastoris* could be the bottleneck responsible, confirming the motivation for using *HAC1* to induce the UPR (Guerfal et al., 2010).

5.2 PCR Optimisation

The use of Betaine and DMSO as additives in routine PCR was found to significantly reduce the formation of primer dimers, aiding amplification of targets. In addition, the use of Gradient PCR allowed for the optimal annealing temperature of *HAC1* 3' to be determined. It was found that an annealing temperature of 3-4 °C lower than the melting temperature of the primer pair was ideal, which is consistent with literature (Borah, 2011) . The ideal PCR conditions can be found in Appendix D.2.

5.3 Gibson Reaction and Transformation

The successful reaction was achieved with a 1:3:5 ratio of plasmid backbone: *HAC1* 5': *HAC1* 3', and the cumulative volume of fragments being less than 20% of the total reaction mixture.

Clean and concentrator was found to be a more effective method of DNA purification when compared to gel extraction, as higher concentrations of DNA were obtained. However, as clean and concentrator is considered to be less accurate by isolating any DNA and not necessarily the desired DNA fragment, prior PCR reactions need to be optimal to ensure sufficient amounts of the desired DNA are in the mixture.

Transformation of commercial *E. coli* DH5α competent cells was found to be equally successful with both 0.5 and 1.0 μ L, allowing for the use of lower volumes if the process was carried out in industrial scale in the future, to potentially reduce cost.

5.4 pKanB$_{v2}$-*H*AC1

As verified by the sequencing results, the pKanB$_{v2}$-*HAC1* plasmid had been sucessfully formed through the Gibson assembly reaction. Subsequent analysis through sequencing and the Benchling alignment function revealed that all colonies of interest had the correct plasmid, with the pairwise identities of the sequences ranging from 98.4% to 99.8%, when the MAFFT algorithm was used.

To further verify the success of plasmid formation, the plasmid should be linearised with a suitable restriction enzyme (PmeI), followed by gel electrophoresis to verify that the length of the linear DNA is the same as that of the plasmid, and that the reaction had no effect on the rest of the backbone.

5.5 Next Steps

The immediate next step would be to linearise the pKanB$_{v2}$-*HAC1* plasmid (so that it can integrate into the genome) and transform into *P. pastoris.* Following that, protein expression should be carried out as laid out in section 3.3 and the results of the expression yield should be compared to that without the plasmid. It is worth mentioning that the conditions for protein expression might also require adjustment, as optimal conditions pre-plasmid could differ from new optimal conditions. This methodology could then be further extrapolated into other *P. pastoris* protein expression systems, such as expression of different VLPs.

6 Acknowledgements

Many thanks to Giuliana Mastropietro for providing us with irreplaceable guidance and support throughout the project, as well as all the other members of the Polizzi lab for their support.

References

Ahmad, Mudassar et al. (2014). “Protein expression in Pichia pastoris: recent achievements and perspectives for heterologous protein production”. In: *Applied Microbiology and Biotechnology* 98.12, pp. 5301–5317. DOI: `10.1007/s00253-014-5732-5`.

Benchling (2021). *Multiple Sequence Alignment.* URL: `https://www.benchling.com/alignments/`.

Bio-Rad (2021a). *A guide to polyacrylamide gel electrophoresis and detection.* URL: `https://www.bio-rad.com/webroot/web/pdf/lsr/literature/Bulletin_6040.pdf`.

— (2021b). *Mini Trans-Blot Cell.* URL: `https://www.bio-rad.com/en-uk/product/mini-trans-blot-cell?ID=589ca8f7-5751-487a-a453-571ee8cc8b7e`.

— (2021c). *PCR Troubleshooting.* URL: `https://rb.gy/qxpwor`.

Biosoft, Premier (2021). *PCR Primer Design Guidelines.* URL: `http://www.premierbiosoft.com/tech_notes/PCR_Primer_Design.html`.

Borah, P (2011). “Primer designing for PCR”. In: *Science Vision* 11.3, pp. 134–136. URL: `http://shorturl.at/iuyTX`.

EurofinsGenomics (2021). *TubeSeq Service - Most Powerful DNA Sequencing.* URL: `https://eurofinsgenomics.eu/en/custom-dna-sequencing/eurofins-services/tubeseq-service/`.

Froger, Alexandrine and James E. Hall (2007). “Transformation of Plasmid DNA into E. coli Using the Heat Shock Method”. In: *Journal of Visualized Experiments* 6. DOI: `10.3791/253`.

Gibson, Daniel G et al. (2009). “Enzymatic assembly of DNA molecules up to several hundred kilobases”. In: *Nature Methods* 6.5, pp. 343–345.

Guerfal, Mouna et al. (2010). “The HAC1 gene from Pichia pastoris: characterization and effect of its overexpression on the production of secreted, surface displayed and membrane proteins”. In: *Microbial Cell Factories* 9.1. DOI: `10.1186/1475-2859-9-49`.

Hardjasa, Amelia et al. (2010). “Investigating the Effects of DMSO on PCR Fidelity Using a Restriction Digest-Based Method”. In: *Journal of Experimental Microbiology and Immunology (JEMI)* 14, pp. 161–164.

Henke, W. et al. (1997). “Betaine Improves the PCR Amplification of GC-Rich DNA Sequences”. In: *Nucleic Acids Research* 25.19, pp. 3957–3958. DOI: `10.1093/nar/25.19.3957`.

Hilgarth, Roland S. and Thomas M. Lanigan (2020). “Optimization of overlap extension PCR for efficient transgene construction”. In: *MethodsX* 7, p. 100759. DOI: `10.1016/j.mex.2019.12.001`.

Katoh, K. (2002). “MAFFT: a novel method for rapid multiple sequence alignment based on fast Fourier transform”. In: *Nucleic Acids Research* 30.14, pp. 3059–3066. DOI: `10.1093/nar/gkf436`.

Kushnirov, Vitaly V. (2000). “Rapid and reliable protein extraction from yeast”. In: *Yeast* 16.9, pp. 857–860. DOI: `10.1002/1097-0061(20000630)16:9<857::aid-yea561>3.0.co;2-b`.

Lee, Pei Yun et al. (2012). “Agarose Gel Electrophoresis for the Separation of DNA Fragments”. In: *Journal of Visualized Experiments* 62. DOI: `10.3791/3923`.

Leonard, Sean and Craig Barnhart (2021). *Dpn I digestion.* URL: `https://barricklab.org/twiki/bin/view/Lab/ProtocolsDpnIDigestion`.

Lin-Cereghino, Geoff P. et al. (2013). “The effect of α-mating factor secretion signal mutations on recombinant protein expression in Pichia pastoris”. In: *Gene* 519.2, pp. 311–317. DOI: `10.1016/j.gene.2013.01.062`.

Mastropietro, Giuliana, Rochelle Aw, and Karen M.Polizzi (2021). “Expression of proteins in Pichia pastoris”. In: *Methods in Enzymology* 660, pp. 53–80. URL: `https://doi.org/10.1016/bs.mie.2021.07.004`.

Mazalovska, Milena and J. Calvin Kouokam (2020). “Progress in the Production of Virus-Like Particles for Vaccination against Hepatitis E Virus”. In: *Viruses* 12.8, p. 826. DOI: `10.3390/v12080826`.

MeridianBiosciences (2021). *HyperLadder™ 1kb.* URL: `https://www.bioline.com/hyperladder-1kb.html`.

NEB (2021a). *Colony PCR.* URL: `https://tinyurl.com/yck79pdr`.

— (2021b). *Gibson Assembly® Protocol (E5510).* URL: `https://international.neb.com/protocols/2012/12/11/gibson-assembly-protocol-e5510`.

— (2021c). *PCR Protocol for Phusion® High-Fidelity DNA Polymerase.* URL: `https://international.neb.com/protocols/0001/01/01/pcr-protocol-m0530`.

— (2021d). *PCR Using Q5® High-Fidelity DNA Polymerase.* URL: `https://international.neb.com/protocols/2013/12/13/pcr-using-q5-high-fidelity-dna-polymerase-m0491`.

Nooraei, Saghi et al. (2021). “Virus-like particles: preparation, immunogenicity and their roles as nanovaccines and drug nanocarriers”. In: *Journal of Nanobiotechnology* 19.1. DOI: `10.1186/s12951-021-00806-7`.

Qiagen (2021). *QIAprep Spin Miniprep Kit.* URL: `https://www.qiagen.com/us/products/discovery-and-translational-research/dna-rna-purification/dna-purification/plasmid-dna/qiaprep-spin-miniprep-kit/`.

SigmaAldrich (2021). *REDTaq® ReadyMix™ PCR Reaction Mix.* URL: `https://tinyurl.com/3j5vp6bp`.

ThermoFisher (2019). *Primer Design Tips.* URL: `shorturl.at/oCG12`.

— (2020). *Pichia Expression Kit.* URL: `https://rb.gy/sehycy`.

— (2021a). *100 bp DNA Ladder.* URL: `https://rb.gy/04p8l0`.

— (2021b). *PageRuler™ Prestained Protein Ladder, 10 to 180 kDa.* URL: `https://www.thermofisher.com/order/catalog/product/26616`.

— (2021c). *SimplyBlue SafeStain User Guide.* URL: `https://rb.gy/33pq4w`.

Vicente, Tiago et al. (2011). “Large-scale production and purification of VLP-based vaccines”. In: *Journal of Invertebrate Pathology* 107, S42–S48. DOI: `10.1016/j.jip.2011.05.004`.

Whyteside, Graham et al. (2011). “Activation of the unfolded protein response in Pichia pastoris requires splicing of a HAC1 mRNA intron and retention of the C-terminal tail of Hac1p”. In: *FEBS Letters* 585.7, pp. 1037–1041. DOI: `10.1016/j.febslet.2011.02.036`.

ZymoResearch (2021a). *DNA Clean & Concentrator®-5.* URL: `https://files.zymoresearch.com/protocols/_d4003t_d4003_d4004_d4013_d4014_dna_clean_concentrator_-5.pdf`.

— (2021b). *Zymoclean™ Gel DNA Recovery Kit.* URL: `https://files.zymoresearch.com/protocols/_d4001t_d4001_d4002_d4007_d4008_zymoclean_gel_dna_recovery_kit.pdf`.

Spreading of Silicone Oil on 1D and 2D multiaxial wrinkled surfaces

Mihai-Andru Angheliu[1] **and Beckett Marshall**[1]

[1]Department of Chemical Engineering, Imperial College London, SW7 2AZ
Corresponding authors: mihai-andru.angheliu18@imperial.ac.uk, beckett.marshall18@imperial.ac.uk

---

Abstract:

This paper assesses the effect of specific surface topography of various PDMS samples on the spreading of a silicone droplet and quantifies the associated wettability and the disagreement between empirical and theoretical findings. This study utilises buckling instability of bilayers through 1D and 2D sequential wrinkling processes. To achieve various topographies, 1D wrinkled surfaces were replicated, and a second-generation wrinkle was applied at an angle to achieve various shapes. The wetting of the surfaces was analysed, and the corresponding data was fitted to an empirical power law and the Tanner's law. It was found that the rate of spreading for 1D wrinkled surfaces and flat surfaces was faster than the 2D multiaxial surfaces that were investigated. The shapes of these 2D topographies hugely impacted the rates of spreading, and it was found that the "sand dune" shapes had the highest spreading, whereas the transitional shapes had the lowest.

Key words: 1D monoaxial/2D multiaxial wrinkles, Buckling, Contact angle, Droplet spreading, Wettability

1. Introduction

Over the years, biological systems have been optimised to adapt to their natural environment. Micro- and nanoscale topographies host an array of properties depending on their morphology. These include anti-microbial resistance, surface adhesion, iridescence, and surface wetting and spreading. These are commonly displayed in nature in various animals, insects, and plants. Gecko's feet utilise hierarchical morphology for adhesion (Cai et al, 2014), morpho butterflies have nanostructures that create iridescent colours (Giraldo et al, 2016), and lotus leaves have micro or nanostructures that form a waxy surface which shows super-hydrophobicity and is self-cleaning (Kim et al, 2018).

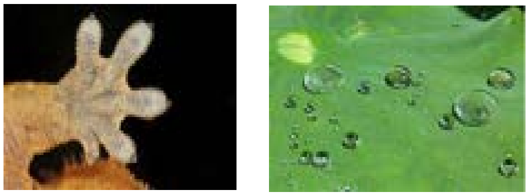

Figure 1: *Images of a) the nanostructures on a gecko's foot and b) the wetting properties of a lotus leaf*

Utilising the properties of nanostructures can make vital inroads into solving common problems. This report focuses on the wetting and spreading properties of droplets on nanostructured topographies. These findings can then be applied to problems associated with car windscreens, painting walls, and keeping solar panels clean amongst other applications. Previous studies have explored wetting properties on irregular rough surfaces, but with the advancement of technology it is now possible to manufacture surfaces with precise morphologies using the superposition of two wrinkles and study the wetting process at the microscopic level. Therefore, it is now possible to precisely analyse the effect of various surface morphologies on wetting and spreading.

There are several existing methods detailing how to produce accurate nanoscale surfaces including scanning lithography and photolithography. However, both methods are expensive and difficult to carry out on a large scale (Guo, 2007). Previous reports have shown how surface wrinkling can yield unidimensional and multidimensional periodical patterns. Surface wrinkling makes use of the mechanical buckling instabilities of various materials to produce sinusoidal waves on the surface. When these waves are superimposed onto each other they produce nanostructures that emulate those found in nature. Wrinkling is more cost efficient and can be utilised on larger scales and hence it was considered the best option to use in this study. This paper aims to analyse the effect of specific multiaxial patterns on droplet spreading on horizontal and inclined surfaces.

2. Background

2.1. The Theory of Wrinkling

Wrinkling utilises the mechanical buckling instabilities in layered soft materials. Plasma oxidation of polydimethylsiloxane (PDMS) elastomers produces a stiff layer on the surface resulting in a bilayer. The basic structure of the PDMS polymer is composed of -O-Si(CH_3)$_2$- units. The result of oxidising this surface using a plasma is that the PDMS develops silanol groups (-OH) at the expense of methyl groups. This creates a more hydrophilic surface (Walters et al, 2017). Subject to a uniaxial compressive strain, a mismatch in buckling instability between the PDMS and the stiff oxidised surface occurs producing a sinusoidal wrinkled surface in the process (Genzer et al, 2006).

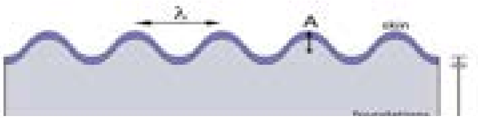

Figure 2: *A schematic of the wrinkled PDMS surface*

At low deformations (strain $\epsilon \lesssim 10\%$), the wavelength and amplitude of the sinusoidal surface profile are described by the following equations (Allen, 2014):

$$\lambda = 2\pi h \left(\frac{\bar{E}_f}{3\bar{E}_s}\right)^{1/3} \tag{1}$$

$$A = h\left(\frac{\epsilon}{\epsilon_c} - 1\right)^{\frac{1}{2}} \tag{2}$$

Here h is the stiff layer thickness, $\bar{E}_f$ and $\bar{E}_s$ are the plane strain moduli of the film and substrate, and ϵ is the applied strain and ϵ_c is the critical strain of the PDMS substrate. To trigger the buckling instability a critical strain must be exceeded which is given by:

$$\epsilon_c = \frac{1}{4}\left(\frac{3\bar{E}_s}{\bar{E}_f}\right)^{2/3} \tag{3}$$

Within the strain limit $\epsilon \lesssim 10\%$, the amplitude depends on the strain only and hence the wavelength and amplitude are decoupled in surface patterning. However, at higher deformations, the wrinkling wavelength also becomes strain dependent and hence yields the following equations:

$$\lambda_{HD} = \frac{\lambda}{(1+\epsilon)(1+\xi)^{\frac{1}{3}}} \tag{4}$$

$$A_{HD} = \frac{A}{(1+\epsilon)^{\frac{1}{2}}(1+\xi)^{\frac{1}{3}}} \tag{5}$$

Where $\xi = 5\epsilon(1+\epsilon)/32$, which accounts for the nonlinearity of the stress-strain relationship of the PDMS in the finite deformation regime. These wrinkling techniques produce a 1D topography and such sequential 2D wrinkling enables the production of multiaxial topographies. To produce a 2D structure, the original 1D surface is duplicated onto new PDMS to provide a structure without the stiff oxidised layer. The second layer is then formed by the same method as for the 1D master but applying the strain at various angles to achieve the multi-axial 2D morphologies. These 2D morphologies are described in terms of the wavelength and amplitudes of the first- and second-generation waves (Pellegrino, 2020).

$$w = A_{\parallel}\cos\left(\frac{k_{\parallel}x_{\parallel}}{\sqrt{2}}\right) + A_{\perp}\cos\left(\frac{k_{\perp}x_{\perp}}{\sqrt{2}}\right) \tag{6}$$

$$k_{\parallel/\perp} = \frac{2\pi}{\lambda_{\parallel/\perp}} \tag{7}$$

Where A_(‖/⊥) represents the amplitudes of 1st /2nd generation wrinkles and λ_(‖/⊥) represents the wavelength of the 1st /2nd generation wrinkles.

The spherical cap approximation is used to effectively model the macroscopic shape by approximating the droplet to be spherical. Utilising this, the apparent contact angle, drop thickness *h(t),* and the radius *R(t)* are related by the following equations (De Gennes, 1985):

$$h = \frac{1}{2}R\theta_a \tag{8}$$

$$\frac{\pi}{2}hR^2 = \Omega \tag{9}$$

Here Ω represents the droplet volume and is assumed to be constant. This effectively assumes the effect of evaporation to be negligible. Equations 8 and 9 are valid in the case where $\theta_a \ll 1$ which is the most important regime in complete droplet spreading. Combining equations 8 and 9 gives us an expression for the apparent contact angles in terms of the radius and the droplet volume.

$$\theta_a = \frac{\Omega}{R^3} \tag{10}$$

Previous experiments have shown that *R(t)* increases quickly at the beginning and then starts to slow down. This data is often represented in terms of the wetting area by an empirical power law:

$$\pi R^2(t) \cong t^n \Omega^p \tag{11}$$

The exponents n and p are to be found experimentally, and hence one of the objectives of this study was to fit the data to a power law and obtain values for n and p and compare those with literature values. Equations for both n and p can be derived by combing the spherical cap approximation with Tanner's law. Tanner's law is an equation that quantifies the rate of spreading in terms of the surface tension γ, viscosity η and apparent contact angle θ_a (Delgadino et al, 2021).

$$U = \frac{dR}{dt} \cong \frac{\gamma}{\eta}\theta_a^m \cong kV^*\theta_a^m \tag{12}$$

Here kV^* is chosen to be the metric for the wettability characteristic of a surface-droplet system. By utilising the spherical cap approximation and substituting equation 10, θ_a can be eliminated.

$$\frac{dR}{dt} \cong kV^*\left(\frac{\Omega}{R^3}\right)^m \tag{13}$$

Therefore, the spreading law becomes:

$$R^{3m+1} \cong kV^* t \Omega^m \tag{14}$$

It is therefore determined that:

$$n = \frac{2}{3m+1} \tag{15}$$

$$p = \frac{2m}{3m+1} \tag{16}$$

The p* parameter represents the theoretical p exponent of the Power Law that can be calculated in terms of m exponent of the Tanner Law, using equation 16. A similar n* could be potentially calculated, using the same process (eq. 15). However, because n is the exponent of the time variable, and it is desired to obtain the kV* parameter independent of time, the empirical n is taken as a reference value, from which m and thus p* are calculated. In the ideal case, all three exponents should satisfy all the equations that link them. Because of experimental errors and the fact that the laws used are empirical and not theoretical, one exponent must be chosen as the reference from which the other can be calculated.

The difference between the empirical p and the calculated p* parameters quantifies the disagreement between the two empirical laws, and the uncertainty which could be used to calculate other thermodynamic parameters. It is expressed as a percentage, and it is desired to be as small as possible.

There are two wetting regimes that explain the interactions between the droplets and the surface: the Wenzel model and the Cassie-Baxter model.

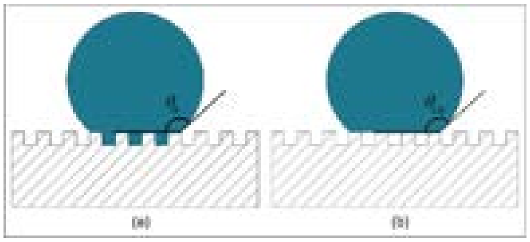

Figure 3: *Image of a) the Wenzel model and b) the Cassie-Baxter model*

The Wenzel model is used when droplets fill all the microchannels of the surface, whereas the Cassie-Baxter describes a rough surface where the droplets spread on top of the surfaces' wrinkles, leaving pockets of air under the fluid that does not penetrate the pores (Erbil, 2014). These regimes affect the empirical apparent contact angle. The theoretical apparent contact angle, θ_y, of a liquid droplet on a flat solid surface is given by the Young's equation (He et al, 2003) which states that:

$$\cos(\theta_y) = \frac{\gamma_{SV} - \gamma_{SL}}{\gamma_{LV}} \tag{17}$$

Where γ_{SV}, γ_{SL} and γ_{LV} are the surface tensions of the solid-vapour, solid-liquid and liquid-vapour interfaces. Wenzel's theory states that in the case where the droplet fills the depressions in the roughness, the apparent theoretical contact angle is given by:

$$\cos(\theta_a^{W,eq}) = \varphi_s \cos(\theta_y^{eq}) \tag{18}$$

Whereas for the Cassie-Baxter regime, the apparent theoretical contact angle is given by:

$$cos(\theta_a^{CB,eq}) = -1 + \varphi_s(cos(\theta_y^{eq}) + 1) \tag{19}$$

Where φ_s is the ratio of the projected wetted area (including microscopic perturbations) to the flat wetted surface area.

3. Methodology

3.1. Sample preparation

PDMS samples were prepared by mixing a silicone elastomer with a curing agent in a 10-to-1 ratio. This solution was thoroughly mixed then degassed for 15 minutes under vacuum. The degassed solution was then cast onto a glass plate at room temperature and then thermally cured in a convection oven at T = 75C for 3 hours. Once the sample was cooked, PDMS coupons were made by cutting the sample into 4.5cm x 5.5cm slabs.

3.2. 1st Generation Wrinkle Methodology

The pre-prepared PDMS samples were clamped onto a strain-stage and a pre-strain, ϵ, was applied by stretching the sample. The pre-strain was constant at 20% of the original length of the PDMS sample. The surface of the stretched sample was oxidised by plasma exposure using a plasma chamber. The plasma chamber was operating at a nominal power of 70W, a pressure of 0.2 mBar, and an exposure time of 7 minutes. After the exposure time had passed, the 20% strain was unloaded slowly resulting in a buckling of the surface of the PDMS. These conditions resulted in a wavelength of 2 microns and so was kept constant throughout the production of the 1D surfaces (Bayley et al, 2014).

3.3. Surface replication

Before 2D sequential wrinkling can take place, the original 1D master needs to be replicated onto a fresh PDMS coupon with no stiff oxidised layer. Firstly, the 1D master is coated with octadecyl trichlorosilane (OTS). A PDMS frame is the cut and applied to the surface of the coated 1D master. Liquid PDMS is casted into the PDMS frame and then cured for 1 hour at 75C. Once cooked, the PDMS frame can be peeled off producing a replication of the original 1D master.

3.4. 2D Sequential Wrinkling

To superimpose a second-generation wrinkle at a specific angle to the first-generation wrinkle, a square sample of the 1D replica was cut out a specific angle to the first-generation wrinkle. Using the strain-stage, a 20% strain was applied at an angle to the 1st generation wrinkled and oxidised in the plasma chamber at 70W and 2 mBar for exposure times between 2 – 7mins. These times varied to ensure the second-generation wrinkle didn't dominate the first-generation wrinkle.

__Figure 4:__ 3D AFM images of our (a) 1D and (b) 2D wrinkled surfaces

3.5. Wetting

The first set of experiments had the goal to explore the impact of surface morphologies on droplet spreading. This was analysed by dropping a volume of 0.5 µL of silicone oil onto the surface of the horizontal PDMS samples. The spreading was then observed under a Basler microscope using a 4x magnification and taking photos every 0.5s for 60 seconds. The images were transferred to ImageJ where the longitudinal and latitudinal diameters were measured. Using these lengths, the wetted area was calculated, plotted against time and fitted using the power law to quantify the wettability of the surface-droplet system.

After the spreading process was analysed, a new set of experiments were completed, where the flow rate of droplets on different inclined surfaces was explored. The distance travelled by the droplet was fixed to 0.5cm, while the inclination angles were varied from 30 to 90. The time taken by the droplet to reach the end line was measured to assess the influence of surface topography and of gravity on the flow rate of a droplet.

4. Results

4.1. 1D surface droplet wetting and spreading

The 1D wrinkled surface sample used to explore the spreading process and mechanism of silicone oil droplets had a first-generation wavelength of 2 µm. The surface topography of the sample can clearly be seen in figure 5. Figure 5a displays the surface as viewed using an optical microscope, whereas figures 1b and 1c show the 1D wrinkled surface as 2D and 3D AFM images. These figures were also used to calculate the wavelengths of the wrinkles and had an error of only 1% which is considered negligible.

Figure 5: (a) Optical microscope image of the 1D-wrinkled surface, showing channels in darker green and peaks in lighter green. (b) 2D AFM image showing the channels in black and hills in yellow. (c) 3D AFM image showing the sinusoidal profile of the surface, with amplitudes of around 0.24 µm and wavelengths of around 0.2 µm.

For the wetting experiment, the 1D surface droplet spreading was compared to the one of the flat surface. In figure 6, it can be clearly seen the difference in the shapes of the droplet once the spreading has started. On the 1D surface, the droplet followed an ellipsoidal shape. Whereas on the flat surface, the droplet followed a perfectly spherical shape. Therefore, the spreading process on the uniaxial sinusoidal grating was anisotropic whereas on the flat surface, the spreading is isotropic (Kusumaatmaja et al, 2008).

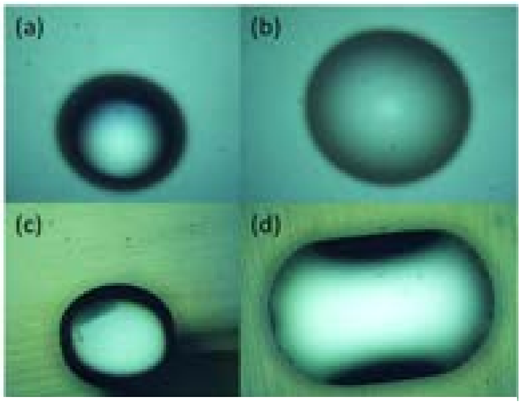

***Figure 6:** (a) Initial droplet on flat surface. (b) Perfect circular droplet at the end of the spreading process. (c) Initial droplet on 1D wrinkled surface. (d) Completely spread ellipsoidal droplet on 1D surface.*

The ellipsoidal shape is explained by the fact that the droplet front flows faster along channels of the wrinkles and slower across the hills of the wrinkles, thus the wrinkles minimising the free energy of the surface-droplet system. This was confirmed by plotting the longitudinal (major axis) and latitudinal (minor axis) diameters of the ellipse against time, as can be seen in figure 8a and 8b. The spreading rate of the droplet in the longitudinal direction (along the wrinkles) was higher on the 1D wrinkled surface than on the flat surface. However, the opposite trend happened for the latitudinal spreading rate (across the wrinkles), with the latitudinal spreading rate of the droplet on the flat surface being higher. It is important to notice that the longitudinal and latitudinal diameters of the droplet on the flat surface were almost equal, as expected for a perfect circular shape.

The overall effect of the two directional flows can be summarised by analysing the wetted surface (figure 8c). As the difference in longitudinal spread is much greater than the one in the latitudinal spread, the wetted surface of the droplet on the 1D surface is greater. Therefore, the sinusoidal grating surface has a higher wettability and hydrophilicity than the flat surface.

It is important to notice that the flat surface and the 1D surface were replicas of pure PDMS as layer, which is inherently hydrophobic (Jahangiri et al, 2020). The overall result would be a greater attraction between this material and the hydrophobic droplet where the wrinkles of the 1D surface increase the rate of spreading and making it anisotropic.

4.1. 2D surface droplet wetting and spreading

After following the methodology to obtain multiaxial wrinkled surfaces (2D wrinkled surfaces), the resulted wrinkles transitioned from a perfect "sand dune" shape at lower angles (20º) to a "beads-on-a-string" structure (45º) and a perfect "pearl" shape at higher angles (90º) (Zhao et al, 2007). When the 3D images of the surfaces were analysed, it was concluded that the perfect pearl shapes of the 90º wrinkled surfaces look more like a "checkerboard", with the walls of the wrinkles turning into sharp peaks and the floors presenting regular wells.

Figure 7 compares the light microscope images with the 3D AFM images, clearly showing a few characteristics of the surface topography. The first-generation wrinkles were dominated by the second-

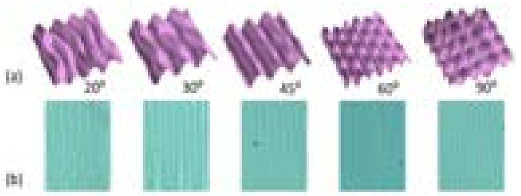

***Figure 7:** (a) 3D AFM images of multiaxial wrinkled surfaces, with increasing angle (20º to 90º) between the two wrinkle generations. The wrinkle's topography changes from a zigzag shape to a "chess-board" like shape. (b) Light microscope images of the wrinkles, showing the same change in shape.*

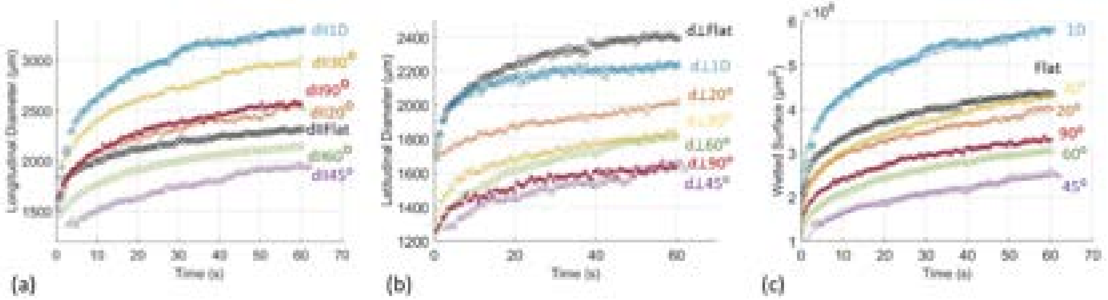

__Figure 8.__ (a) Longitudinal diameter (major axis of droplet) against time. (b) Latitudinal diameter (minor axis of droplet) against time. (c) Wetted surface data points and power law (continuous coloured curves) fitting the experimental data against time.

generation wrinkles, meaning that the effect of the first-generation would vaguely be seen as gaps in the walls of the wrinkles. As the compression angle between generations was increased, the gaps in the walls became larger. The second-generation wrinkles gave the overall shape of the channels. However, as the angle between generation was increased, the floors of the channels gained deeper wells at the intersection of opposite wall gaps. This changing topography affected the rates of droplet spreading in the longitudinal and latitudinal directions.

The second-generation wrinkles' wavelengths varied from 2.4 μm to 3.7 μm, with a measurement error of approximately 0.2 μm. This difference from the desired wavelength of 2 μm would slightly affect the wetting experiments. This happened due to difficulties in keeping the oxidation plasma at constant pressure and because the second-generation oxidised layer would cover the surface of the wrinkled replica, hence the samples had to be exposed to different doses such that the desired topography could be analysed. To analyse the effect of the second-generation wavelength, further experiments should be conducted with surfaces with constant compression angles, but exposed to various doses, to achieve the same topography at different scales.

From figure 8a and 8b it can be concluded that the spreading process on a 2D wrinkled surface will always be slower than on a 1D surface, with the wetted surface of the sinusoidal grating sample being the highest (figure 4c). The longitudinal diameter of the droplets on 2D surfaces with the two generations of wrinkles at lower angles tended to be bigger than at higher angles. Therefore, the sand dune shape is superior for droplet spreading along the wrinkles. The checkerboard (90⁰ compression angle) almost reached these high spreading rates along the wrinkles, but the transitional shapes (45⁰ and 60⁰ compression angle) gave a slower longitudinal spreading. A similar trend can be seen in the latitudinal diameter growth over time. However, the checkerboard surface had a much lower latitudinal spread than the sand dunes and even than the 60⁰ transitional surface.

The overall effect of the surface topography was determined by the change in wetted area over time. The 1D sample remained the best surface for fastest spreading, followed by the flat surface, lower angled 2D surfaces (30⁰ and 20⁰), and then by the higher angled ones (90⁰, 60⁰ and 45⁰). Hence, a monoaxial sinusoidal grating topography would be more wettable when in contact with silicone oil droplets than the flat case, while the multiaxial wrinkled topography would be less wettable than both. From a wettability perspective, the sand dunes outlines are followed by the pearl, and transitional shapes respectively. These 2D samples had an external layer of oxidised PDMS, presenting silanol groups that are hydrophilic and protect the underneath layers from any external factors (Corma et al, 1998). This explains why their wettability is lower when hydrophobic droplets are poured, as the attraction forces between them are weak.

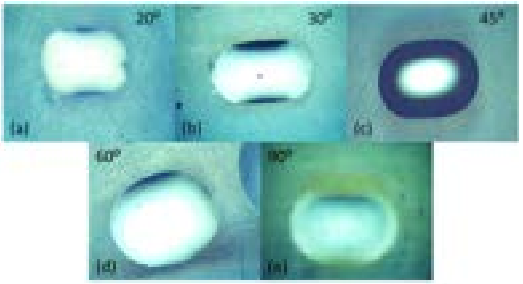

***Figure 9:** Optical microscope images of 0.5 μL droplets spreading on 2D multiaxial wrinkled surfaces, at different angles between wrinkle generations.*

At the macroscopic level, the droplets reached equilibrium shapes that oscillated between spherical to ellipsoidal. In figure 9 it can be seen how the shape of the droplet changed from ellipsoidal at 20⁰ (figure 9a), to elongated-ellipsoidal at 30⁰ (figure

9b). Then the equilibrium droplet shape transitioned back to almost spherical at 45° and 60° (figure 9c and 9d) while the topography of the surfaces shifted from sand dune to pearl, and finally reaching again the elongated-ellipsoidal shape at 90° (figure 9e). It was established that the greatest wetted surface occurred for the elongated ellipsoidal shape, with the second-generation wrinkles impacting most the spreading process along the creases.

4.2. Surface and wetting properties

It was concluded that the droplet spreading followed the Wenzel spreading regime model. This was because it was observed that during the spreading process, the fluid flows along the channels made by the wrinkles and fills them in the process. Therefore, the wrinkles could not have been seen under the droplet (figure 10). Using the Wenzel model equation, the theoretical contact angle (Young's contact angle) can be calculated and then used further to calculate additional properties of the surface-droplet system.

To quantify the wettability of the surface-droplet system and to verify the validity of combining equations 11 and 12 together, the kV* and p* parameters were calculated. The parameter p* was further processed to calculate p_{error} as a percentage. Table 1 summarises all the calculated exponents and parameters.

Figure 10: *In both images, the wrinkles are completely invisible under the droplet, proving that the spreading process follows the Wenzel regime. (a) Droplet flow across the wrinkles. The fluid first fills the channel before moving across the walls to the next wrinkle, in the latitudinal direction to continue the spreading process. (b) Droplet flow along the channel. The fluid fills the channel at a high rate in the longitudinal direction of the spreading process.*

It can be clearly seen that kV* was greater with faster spreading rates, proving that the material-droplet system has a larger wettability with bigger kV* values. For the 1D surface and flat surface, kV* was much bigger than for the 2D surfaces. This was due to the hydrophobicity of the sample and droplet, which increased the spreading rate as a result of stronger attractions between the molecules. Moreover, the wrinkles on the 1D surface increased the surface tension of the material, and thus it increased the V* term in the kV* parameter, which is directly proportional to the surface tension.

The sand dune wrinkles resulted in higher kV*, close to the one for the flat surface, even though the hydrophobic droplet spread over a hydrophilic master. Hence, having sand dunes in general would greatly increase the wettability of a surface, regardless of whether it is in contact with a hydrophilic or hydrophobic liquid.

Table 1. *Wettability parameters of the surface-droplet system analysed in the experiments.*

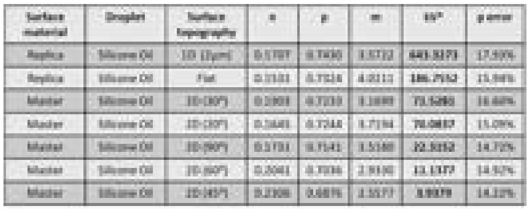

Surface material	Droplet	Surface topography	n	p	m	kV*	p error
Replica	Silicone Oil	1D (2µm)	0.1707	0.7430	3.5712	443.3171	17.59%
Replica	Silicone Oil	Flat	0.1531	0.7324	4.0211	186.7552	15.94%
Master	Silicone Oil	2D (30°)	0.1901	0.7233	3.1899	73.5280	16.66%
Master	Silicone Oil	2D (30°)	0.1681	0.7244	1.7194	78.0837	15.09%
Master	Silicone Oil	2D (90°)	0.1731	0.7141	1.5580	22.5152	14.72%
Master	Silicone Oil	2D (60°)	0.2041	0.7036	2.9100	13.1377	14.92%
Master	Silicone Oil	2D (45°)	0.2306	0.6876	2.1577	3.9379	14.22%

The p_{error} was approximately 16%. This is small and shows the agreement between the two laws (equations 11 and 12) and the other approximations that were used to calculate the parameters. Despite this, additional experiments finding the contact angle and the n and p exponents in terms of m (equations 15 and 16) should be completed to confirm this conclusion.

Our results can be confirmed by the work of other researchers and Tanner himself, where he obtained a value of the n exponent to be 0.21 and a value of the p exponent to be 0.66 (Tanner, 1979). Our results showed the value of n to vary between 0.15 and 0.23 and the value of the p exponent to be approximately 0.71. Therefore, our results were in line with previous studies.

4.3. Inclined surface droplet flow experiment

Figure 11 reviews the distances travelled by 2 µL droplets on 2D multiaxial wrinkled surfaces inclined at 30°, 60° and 90° angles. The first part of the process was dominated by the spreading mechanism, and the data points were fitted by a power law. However, as time passes and the droplet reached the equilibrium shape, gravity dominated the flow, and the power law transitioned into a linear relationship.

The linear segments of the curves are almost parallel to each other, meaning that the topography of the surface did not influence the droplet flow after the equilibrium state had been reached. To validate these results, additional experiments need to be

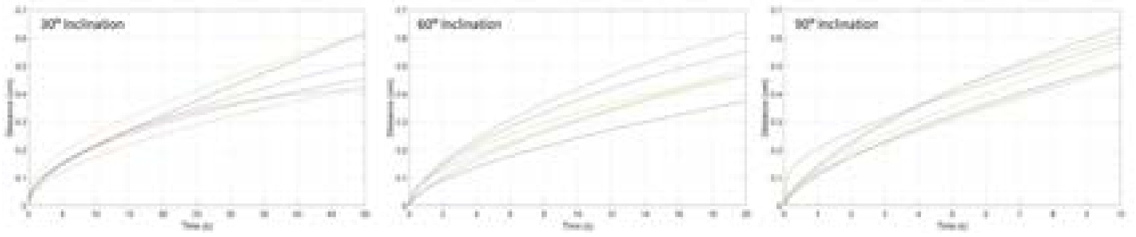

Figure 11: *Plot of distance travelled by the silicone-oil droplet against time, over the 2D multiaxial wrinkled surfaces. The following colours are assigned to the surfaces: black (flat), orange (20º), yellow (30º), purple (45º), green (60º) and red (90º).*

completed to determine the relationship between droplet flowrate, surface topography and droplet fluid. As the inclination angle was increased, the spreading effect was minimized, and an increasing proportion of the spreading process was dominated by gravitational effects. This can be seen in figure 11 in the case of 90º inclination, where the power law part of the graph is insignificant when compared to the linear law part.

5. Discussion

The trends in spreading can be explained at the microscopical level, by analysing the structures of the channels floors and walls (wrinkles). On the 2D multiaxial surfaces, the second generation establishes the overall topography, setting the width of the channels. The first generation affects mostly the walls, creating gaps that increase in size as the multiaxial angle is increased (from 20º to 90º).

The trends in spreading can be explained at the microscopical level, by analysing the structures of the channels floors and walls (wrinkles). On the 2D multiaxial surfaces, the second generation establishes the overall topography, setting the width of the channels. The first generation affects mostly the walls, creating gaps that increase in size as the multiaxial angle is increased (from 20º to 90º).

Figure 12 shows the gaps in the walls as dotted lines in the continuous walls made by the second wrinkle generation. The sand dunes (smaller multiaxial angle samples) have a flat floor and almost no gaps in the walls. The flow of liquid along this channel is the fastest, filling the channels quickly. This also increases the flow rate in the latitudinal direction (across the walls of the wrinkles) as the nearby channels are overflowing.

As the angle between the two generations of wrinkles is increased, the opposite gaps in walls shift from being out of phase to facing each other. Initially this process straightens the channel shape, making it similar to the 1D uniaxial wrinkles. However, when crossing into the transitional surfaces' region, deep wells in the floor and tall peaks on the wall start to form. The resulted checkerboard shape constricts the flow along the channel, as the fluid must fill the wells. At the same time, the wells also decrease the latitudinal spread because it is harder for the fluid to overcome the walls and after it fills a well, it spreads immediately to the next well along the channel. Hence, very deep wells (2D 90º surface) can lead to guided spreads along the wrinkles, as the fluid is mostly spreading in this direction. This can be explained by the elongated ellipsoidal shapes that a droplet has on a 2D 90º surface. All these effects explain the oscillation in the droplet shapes as the multiaxial angle is increased.

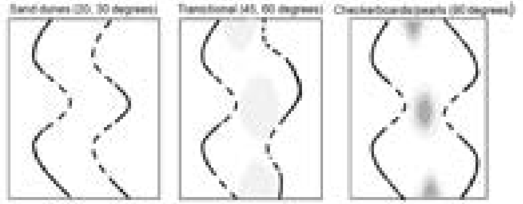

Figure 12: *The microscale schematic of a wrinkle's topography. The dotted lines represent gaps in the walls, while the light-grey and dark-grey ellipses represent shallow and deep wells respectively.*

The wettability properties are representative for a system of two materials, the wrinkled sample, and the droplet. For the all the experiments, the 1D and flat surfaces are assumed to be hydrophobic because they are replicas covered by the PDMS polymer, while the 2D surfaces are hydrophilic because they are covered by the oxidised PDMS. When interacting with the hydrophobic droplet, it is normal to obtain higher wetted areas for the system of two hydrophobic materials (1D and flat). If water would have been used, the trend would have been reversed, making the 2D surfaces the best in terms of wettability and the 1D surface the worst. Seeing the great effect of wrinkles on the spreading process, it is assumed that the roughness of the surfaces would keep the current trend in 2D surface wettability when water is used, the change in solid-liquid surface tension due to roughness being independent from the one due to solid material type.

In general, for this kind of spreading experiments, where the surface can also be glass or the droplets can be water, the n and p exponents are around the same values (De Gennes, 1895). In previous research work, the n exponent for water on glass was found to be around 0.22 (Lelah et al, 1981), varying with the surrounding temperature from 0.16 to 0.32 (Hyypia, 1948). All the values we obtained are well included within this range even though silicone oil was used on PDMS, thus proving that all types of droplets should give similar exponent values for their power laws. To validate this, further experiments can be done by changing the droplet liquid and the surface material.

Small differences in the exponent values result in big differences in the kV* parameter and thus, the wettability of the system. Two different solid materials, droplets or surface topographies would give similar n and p exponents, but a significant difference in the wettability characteristic.

The developed theory can be continued with other experiments that would improve the description of wetting processes and would even allow one to calculate important thermodynamic properties like the surface free energy and surface tensions. Our experiment managed to approximate the contact angles so that one would not need to measure it experimentally. This represents the novelty of our project and an easy approach to find contact angles. To be confirmed, separate experiments must be done where the contact angle is measured empirically and then compared to the values calculated using our method (Chung et al, 2007). It is important to notice here that the time taken by the droplet to reach equilibrium must be measured so that the power law can give the exact theoretical contact angle (Young's contact angle).

With Young's angle, and more data like the surface tensions between PDMS and air or silicone oil and air, one can find the free energy of a specific wrinkled surface and the surface tension between the liquid and the surrounding vapour. The following equation summarise the mathematical model used to calculate these properties:

$$\frac{E}{R_0 \pi \sigma} = -\left(cos\theta_y\right) f_1 + f_3 + Bo f_3 \qquad (20)$$

Bo represents the Bond number, and it is calculated in terms of the initial droplet radius R_0, specific weights of liquid and air and the surface tension between liquid and vapor σ. The f_i terms are auxiliary nondimensional functions that depends only on the minor and major axis of the spread droplet, and θ_y is the Young's contact angle (which is related to the surface tensions) (Lubarda et al, 2011).

6. Conclusion

The goal of the project was to simulate wetting processes that occur in nature on artificially tuned surface topographies, with the goal of influencing the droplet spreading and the unidirectional flow on the samples. In nature, the surfaces have much complicated features that could theoretical be created in labs using expensive methods. For this reason, this study analysed the wetting processes on easy to build 1D monoaxial wrinkled and 2D multiaxial wrinkled surfaces. The obtained results provide an overall idea of how microscopic perturbations of a surface would affect the spreading rates and direction of a droplet and so can be used as the base for future and more complex experiments.

Buckling instability models were utilised to create wrinkled surfaces of a known wavelength and amplitude. For the 2D multiaxial wrinkled surfaces, two generations of wrinkles were superimposed to create complex shapes (sand dunes, transitional or checkerboards). In total, enough surfaces were fabricated to draw strong conclusions about the direct influence of topographies on wetting processes and to quantify effects on wetting.

Silicone oil droplets were utilised for the wetting process because it does not evaporate quickly and can be better analysed with the theoretical approximations that were utilised. This created a surface-droplet system with the replica or master samples on which the spreading took place. For this reason, the properties that were further calculated are specific to the system and will change if one of the two components of the system is replaced. It is recommended to repeat these experiments with the replicas replaced by masters to compare the 2D surface-droplet systems with the 1D systems of the same surface material (oxidised hydrophilic PDMS).

Proving that the spreading process followed the Wenzel regime, and fitting data points using a novel theory based on combining two empirical laws and approximations, the wettability and apparent contact angles of the system was quantified by the kV* parameter. A p* parameter was calculated to check the validity of the theory. These results can be utilised for future research to calculate other thermodynamic properties. The droplet spreading on the 1D wrinkled and flat surfaces was the fastest, obtaining the highest kV* parameter for these two surface-droplet systems. This was expected to happen to do the higher attraction that exists between the hydrophobic replica surface and hydrophobic oil droplet. The hydrophilic 2D multiaxial surfaces resulted in lower wettability properties. However, the sand dune topographies reached the performances of the hydrophobic flat surface, proving that small deformations of a surface can greatly impact the wetting process. It is recommended to do more experiments to find empirically the apparent contact angles of the droplets when spreading on these surfaces and compare them with the ones calculated theoretically. This way, the agreement between the laws that we combined to create a new mathematical model to describe the wetting process can be confirmed.

Even though trends in the flow rate of droplet on inclined surfaces were seen (spreading affecting the first part of the process, gravity affecting the second part), more experiments should be done to clearly differentiate between the specific effects on the flow of surface-droplet systems. An improvement to our experiment would be to analyse the droplet flowing for a fixed amount time, and not a fixed distance.

There are many real-world applications for these materials, for example stopping the deposition of dirt, bacteria or water droplets on car windscreens, solar panels or building walls. After more experiments are completed to confirm the developed theory, and with all the parameters that were obtained in this study, more complex surfaces can be tuned to affect the wetting process in our advantage in a plenty of other applications.

Acknowledgements

We would like to express our gratitude to Dr. Luca Pellegrino, for all the support and guidance we received throughout the course of the project.

References

Giraldo, M.A. and Stavenga, D.G., 2016. *Journal of Comparative Physiology A*, *202*(5), pp.381-388.

Kim, W., Kim, D., Park, S., Lee, D., Hyun, H. and Kim, J., 2018. *Journal of industrial and engineering chemistry*, *61*, pp.39-52

Cai, L., Mei, H., Wang, W.B., Wang, H. and Dai, Z.D., 2014. In *Applied Mechanics and Materials* (Vol. 461, pp. 284-290). Trans Tech Publications Ltd.

Guo, L.J., 2007. *Advanced materials*, *19*(4), pp.495-513.

Allen, H.G., 2013. Elsevier.

Pellegrino, L., Khodaparast, S. and Cabral, J.T., 2020. *Soft matter*, *16*(3), pp.595-603.

Waters, L.J., Finch, C.V., Bhuiyan, A.M.H., Hemming, K. and Mitchell, J.C., 2017.. *Journal of pharmaceutical analysis*, *7*(5), pp.338-342.

Genzer, J. and Groenewold, J., 2006. *Soft Matter*, *2*(4), pp.310-323.

De Gennes, P.G., 1985. Wetting: statics and dynamics. *Reviews of modern physics*, *57*(3), p.827.

Delgadino, M.G. and Mellet, A., 2021.. *Communications on Pure and Applied Mathematics*, *74*(3), pp.507-543.

Erbil, H.Y., 2014.: A review. *Surface Science Reports*, *69*(4), pp.325-365.

Bayley, F.A., Liao, J.L., Stavrinou, P.N., Chiche, A. and Cabral, J.T., 2014.. *Soft matter*, *10*(8), pp.1155-1166.

He, B., Patankar, N.A. and Lee, J., 2003. *Langmuir*, *19*(12), pp.4999-5003. !!!!!!!!!!!

Jahangiri, F., Hakala, T. and Jokinen, V., 2020., 24(1), pp.1-11.

Corma, A. and Kumar, D., 1998., 117, pp.201-222.

Tanner, L.H., 1979. *Journal of Physics D: Applied Physics*, 12(9), p.1473.

Lelah, M.D. and Marmur, A., 1981. *Journal of Colloid and Interface Science*, 82(2), pp.518-525.

Hyypia, J., 1948. *Analytical Chemistry*, 20(11), pp.1039-1043.

Lubarda, V.A. and Talke, K.A., 2011. *Langmuir*, 27(17), pp.10705-10713.

Kusumaatmaja, H., Vrancken, R.J., Bastiaansen, C.W.M. and Yeomans, J.M., 2008. *Langmuir*, *24*(14), pp.7299-7308.

Zhao, Y., Lu, Q., Li, M. and Li, X., 2007. *Langmuir*, *23*(11), pp.6212-6217.

Chung, J.Y., Youngblood, J.P. and Stafford, C.M., 2007. *Soft Matter*, *3*(9), pp.1163-1169.

Development of the MILP Approach to Plant Layout Optimisation, Applied to the HDA Process

Nicholas Goh and Isobel Melvin

Department of Chemical Engineering, Imperial College London, U.K.

Abstract

A well-designed plant layout has the potential to mitigate the extent of plant damage and fatalities in the event of an accident. Extensive research on computer-aided plant layout optimisation has been done since the 1990s, especially using mixed-integer linear programming (MILP), and ongoing research continues to increase modelling complexity to make for more insightful modelling. Through the HDA process as a case study, this study looked to demonstrate a novel method of allowing for the MILP optimisation of plant layout on a non-rectangular plot area. The study also proposed a new framework for the simultaneous optimisation of process design and plant layout based upon design parameter interactions with Dow's Fire and Explosion Index. Aspen Plus V11 was used to model the HDA process for data collection, and the MILP optimiser was developed in Python with CPLEX as the solver. The results of the study showed that being able to model non-rectangular plot areas can reduce plant layout costs by 10% in the HDA process plant as well as improving the safety of the plant. Moreover, the proposed framework suggested that the total cost of a plant could be minimised by operating the reactor at a lower pressure, with possible savings of £1.8 million from potential accidents shown for the HDA case study.

1 Introduction

1.1 Background

Plant layout has been a subject of increasing interest in the chemical industry since the late 1970s, following events such as Flixborough that have highlighted glaring safety issues that could have been mitigated through considerations of equipment placement, amongst other factors [1]. A recent study by Kidam and Hurme showed that the most common type of design error leading to accidents was poor layout [2]. The UK Health Safety Executive (HSE) has issued Codes of Practices to ensure stringent safety standards are met, setting out technical guidelines for factors such as inherent safety, domino effect, fires, and explosions [3]. However, increased safety is often achieved through higher expenditure - increased inter-unit spacing may incur greater land and piping costs, while the inclusion of safety devices can lead to increased capital cost. The need to achieve as low as reasonably possible (ALARP) risks at minimum costs have provided the chemical industry with a financial incentive to optimise plant layout.

Early attempts at optimising process plant layout were based on quadratic assignment problems (QAP) and graph-theoretic approaches [4]. Heuristics and minimum separation distances between process units were developed following the aforementioned approaches. However, the latter two were limited in effectiveness - heuristics were unable to guarantee global optimality, and engineering judgement was required for the implementations of separation distances for process plants of varying sizes. Ranking techniques such as the hazardous area classification, which ranks units based on leak potential, have been used to inform plant layout as a substitute for hard minimum separation distances [5]. The Mond Index and Dow's Fire and Explosion Index (F&EI) have also been popular methods for determining fire and explosion hazards in a plant, taking into account the size of a unit and the materials a unit processes to give a clearer approximation of exposure radius in case of an event [6].

There has been extensive work done on conducting computer-aided plant layout optimisation using mixed integer programming (MIP) techniques. Penteado & Ciric suggested a mixed integer nonlinear programming (MINLP) approach to minimise the objective function (cost of layout) that included financial risk, quantified through expected losses in major accidents [7]. Patsiazis et al. proposed a mixed integer linear programming (MILP) approach to plant layout optimisation with a similar objective function but with piping arranged in a rectilinear configuration [8]. Low introduced realistic estimations for the cost of pumping and piping in his 2D MILP plant optimisation problem [9]. Ejeh et al. explored sensible considerations for the MILP multi-floor process plant problem by incorporating floor construction costs and vertical pumping costs into the objective function [10]. Moreover, Han et.al considered the direct risk to humans and equipment by assigning risk zones in a chemical plant based on the placements of process units around the plant [11]. The aforementioned works have largely considered fire and explosion as primary hazards, but there have also been other studies such as Diaz-Ovalle et al.'s work on comparing deterministic and stochastic approaches to solving layout problems with toxic release considerations [12]. MILP approaches have been favoured by many studies for safe process layout optimisation as nonlinear approaches are much more difficult and computationally expensive to solve [1].

Many of the works in MILP plant layout optimisation have focused on plot areas that are rectangular. However, existing literature have not explored the accommodation of non-rectangular plot areas for plant layout in great detail, such as for the retrofitting of new equipment on a non-rectangular space. Besides this, there has not been detailed literature in the quantification of realistic cost savings between using minimum separation distances with hazard indices as plant safety considerations. There has been great interest and effort in developing an effective framework for simultaneous plant design and layout, such as by Barbosa-Povoa [5]. However, there has yet to be an optimum method for such a problem due to the sheer complexity of the problem.

1.2 Aims

The aim of this study is threefold. Firstly, a comparison will be done to quantify the effectiveness of minimum separation distance-based plant layout guidelines against hazard indices as safety considerations in rectangular plot areas. Secondly, the practicality and usefulness of modelling non-rectangular plot areas are assessed. Finally, a proof-of-concept for a new, iterative framework for the simultaneous design of a process and its layout will be explored in order to reduce the overall cost of a chemical plant and maximise safety. This study will look to demonstrate the findings through a case study, implementing MILP single-floor plant layout optimisation on a HDA process plant that produces benzene.

1.3 HDA Process

Benzene is a common industrial chemical used for the production of plastics, resins and dyes [13]. It is produced naturally by volcanoes and forest fires but the HDA process is commonly used for industrial production of benzene. The HDA process was chosen as the case study due to its usage as a common learning tool in chemical process design around the world, such as in *The Conceptual Design of Chemical Processes* by Douglas [14]. Results from this study will be aimed to be adapted for supporting classroom exploration of plant layout and optimisation.

The reactions involved in the HDA process include the main reaction, which produces benzene, and a side reaction that consumes benzene to produce diphenyl:

$$\text{Toluene} + \text{Hydrogen} \longrightarrow \text{Benzene} + \text{Methane} \tag{1}$$

$$2\,\text{Benzene} \longleftrightarrow \text{Hydrogen} + \text{Diphenyl} \tag{2}$$

2 Methodology and Data Collection

To achieve the aims discussed, the following procedure has been designed, breaking down the overall problem into sub-components. They are as follows:

1. Creating a realistic flowsheet of the HDA process on Aspen Plus V11.
2. Grouping flowsheet items into unit blocks, before sizing and costing them with Aspen Economic Analyser
3. Determining the connections between unit blocks.
4. Determining damage factors and exposure radii
5. Determining desired shapes for available plant layout area.
6. Optimising the placement of unit blocks using a MILP optimiser from the collected data.

.

2.1 Aspen Data Collection

Using the design specifications found in Douglas' textbook as a point of reference [14], a flowsheet for the HDA process was developed on Aspen Plus V11. The specifications are as follows:

1. Toluene to benzene conversion of 75%, benzene to diphenyl conversion of 3%
2. Benzene product purity $\geq$ 0.9997
3. Benzene production rate of 265 kmolhr^{-1}
4. Pure liquid toluene feed at 1atm and 25°C
5. Hydrogen gas feed at 37.8°C and 37.4atm with a composition of 95% hydrogen, 5% methane
6. Hydrogen to aromatics ratio of 5 at the reactor inlet to prevent coking
7. Reactor outlet temperature $\leq$ 1300 F to prevent hydrocracking reactions
8. Reactor effluent quenched to to 1150 F to prevent coking

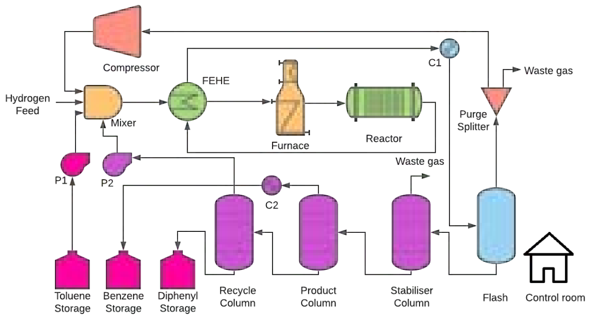

Figure 1: *Flowsheet of the HDA Process Designed on Aspen Plus V11*

The final flowsheet, shown in Figure 1, consisted of 14 process units and three storage tanks, with two recycle streams for recycling toluene and hydrogen. After the mixing of the pressurised fresh feed and recycle streams, the reactor feed stream was heated in series to 621°C by a feed-effluent heat exchanger (FEHE) and then a furnace. The reactor outlet stream was then cooled through the FEHE and C1 to 38°C and was flashed at that temperature. 30% of the flashed vapour, rich in methane and hydrogen, was purged and the remaining was passed through a compressor before being recycled. The liquid from the flash was passed through a series of distillation columns. The Stabiliser column removed the remaining trace amounts of hydrogen and methane. The Product column collected the benzene product, before the Recycle column isolated the diphenyl from the toluene, with the latter being recycled after being passed through P2. Hydrogen was assumed to be obtained from a shared pipeline in a chemical industrial cluster, hence no storage tank for hydrogen was included.

To reduce the computational time of the optimisation software, certain flowsheet items were grouped together to form a unit block (the term unit from here on shall refer to the unit block). The grouping of flowsheet items, displayed in Table 1, and determination of whether a unit is considered a pertinent unit had been done with engineering judgement and guidance from the Dow's F&EI Hazard Classification Guide [15]. Additionally, a control room was added to make the problem more realistic.

Aspen Economic Analyser was used to determine the size and installation cost of most of the flowsheet items. For those units unable to be sized or costed, the methods for sizing and costing the units are listed as follows:

1. The furnace's size and cost were determined from a manufacturer's brochure for an 18MW furnace [16].
2. The dimensions of the 3 storage tanks were calculated based on the assumption that there is sufficient volume to store 5 days worth of toluene, benzene and diphenyl at a 2:1 length:width ratio. The cost of the storage tanks was calculated by combining the capital cost of the tanks (costed using Guthrie's cost correlation) and the financial value of the chemical contents in the tank [14].
3. The control room was assumed to be a building with a length and width of 15m, with its cost of £4,054 per m^2 determined through industrial cost estimates [17].

A rectangular area just large enough to accommodate all of a unit's constituent flowsheeting items was determined as the base dimension for unit blocks. An additional 2m were added to the length and width of this base dimension to arrive at the final dimensions of the unit - the additional spacing was to account for space necessary for access, steelwork, etc. In the case of an event that causes unit damage, there are costs associated with the removal of the damaged unit, in addition to the installation cost. These were taken into consideration through a factor of 1.4, based on engineering judgement, that was applied to the unit installation cost to arrive at the unit replacement cost. There were 8 connections modelled in total between unit blocks as listed in Table 2.

2.2 Python Model

The MILP optimiser was built on Python, utilising the PuLP linear programming modeler to call upon IBM ILOG's CPLEX solver for providing the solution to the MILP problem at hand. CPLEX uses the branch-and-cut algorithm, which combines the cutting-plane method with the branch-and-bound algorithm to obtain solutions more quickly. Given the convex nature of the problem, a global optimum is guaranteed to be found.

The continuous decision variables to be determined by the programme were the x and y coordinates of the centre of the units, which will be used to calculate other continuous variables such as total rectilinear distance between units. An array of binary decision variables were also determined by the programme to inform decisions such as plant area utilised and location of units relative to each other. The full list of binary decision variables is detailed in the Supplementary Information file.

2.3 Data Collection of Safety Parameters

Safety considerations for plant layout have been considered in two ways - through the F&EI hazard index analysis and minimum separation distances.

The minimum separation distances between each unit were determined using typical spacing for plant equipment under fire circumstances derived from CCPS, Guidelines for Facility Siting and Layout [6]. The minimum separation distances for the units is detailed in the Supplementary Information file.

The F&EI was chosen as the quantitative representation of loss potential due to its accuracy and wide use in industrial plant safety evaluation [18]. Another reason for using the F&EI is because it provides empirical relationships between design parameters and loss potential, making possible the simultaneous process design and layout optimisation framework proposed in this paper. Fire and Explosion Risk Analysis was done on the pertinent units as per the guidance from the Dow's F&EI Hazard Classification Guide, with the damage factor (DF) and the exposure radius (De) of pertinent units being the desired values to be calculated [15].

Damage factors are important for the calculation of collateral costs due to explosion. Note that the De represents a radial distance from the centre of a pertinent unit. As the x and y coordinates of units are decision variables in the problem, the calculation of radial distances between units is not a trivial matter. To account for this, a factor of $\sqrt{2}$ was multiplied to the De as this represented the maximum deviation of rectilinear distances from true radial distances. Section 3.2 discussed the difference in objective functions due to this modification to De. The values for DF and De are summarised in Table 3.

2.4 Risk Tolerance

To quantify the loss potential on an annual basis, a sensible approximation of the frequency of accidents or events on process units is necessary. Industry risk tolerance criteria were used as a point of reference for the estimating the frequency of accidents since it indicates how often companies in industry are expecting an accident to occur [19]. For

Table 1: *Unit Block Specifications*

Unit	Flowsheet items included	Pertinent?	Dimensions (m)	Replacement cost (£)	No. of worker	% Time at unit
Furnace	Furnace, Mixer	Yes	7.0x16.0	778,820	2	0.1
Reactor	Reactor, FEHE	Yes	7.6 x 5.8	1,243,620	3	0.1
Flash	C1, Flash	No	4.0 x 4.0	763,840	2	0.1
Comp	Compressor, Purge Splitter	No	14.0 x 14.0	3,426,640	3	0.1
Distil	Stabiliser, Product, Recycle Columns, C2, P2	Yes	8 .0x 80	4,308,640	4	0.1
Store	Toluene, Benzene, Diphenyl Storage, P1	Yes	22.0 x 12.0	5,151,768	2	0.1
Ctrlroom	Control Room	No	15.0 x 15.0	1,227,010	10	0.375

Table 2: *Connection Specifications between units*

Connection	From	To
1	Furnace	Reactor
2	Reactor	Flash
3	Flash	Comp
4	Flash	Distil
5	Comp	Furnace
6	Distil	Store
7	Store	Furnace
8	Distil	Furnace

Table 3: *Exposure Radii and Damage Factors for the Pertinent Units*

Pertinent Units	Exposure Radius (m)	Damage Factor
Furnace	28.8	0.75
Reactor	40.4	0.82
Distil	35.4	0.77
Store	45.0	0.82

a conservative estimate, 1 accident every 1000 years was chosen as the frequency of accidents.

In the event of an accident, there is a possibility of the loss of human life. As such, this risk must be quantified and taken into consideration in the optimisation problem as a cost in the objective function. The UK Treasury sets the value of prevented fatality (VPF) as £2,000,000. For this study, a VPF of £10,000,000 was assumed for a more conservative number [20]. The occupancy of each units was calculated by Equation 3.

$$\text{Occupancy} = N_w \times t_p \tag{3}$$

Where N_w is the number of workers at the unit and t_p is the percentage of time the workers are present at the unit. These values were approximated for each unit and are tabulated in Table 1.

2.5 Cost of Piping and Pumping

Low had derived a set of equations that allows for the annualised cost of piping and pumping to be calculated from fluid flow properties [9]. The required fluid flow properties are velocities, flow rates, viscosities, densities and number of pipes between units. Velocities of gases and liquid were assumed to be 30ms^{-1} and 3ms^{-1}, respectively. The other fluid flow properties were determined from the HDA stream table generated by Aspen. An annualised factor of 0.1102 was calculated, assuming a plant lifetime of 25 years and a typical interest rate of 10%, and is used to annualise the cost of the piping and pumping.

2.6 Cost of Land and Road Paving

The plant was assumed to be situated in Teesside for the purpose of this optimisation problem. According to data from Colliers, land in Teesside for industrial purposes is priced at £62 per m^2 [21]. It was also assumed that the control room is connected to every other unit by a 4m wide rectilinear gravel path, allowing for vehicular and human movement. The road paving cost was estimated at £35 per m^2 [22]. These costs were multiplied by the annualised factor of 0.1102 to give an annualised cost for land and road paving.

2.7 Proposed Framework for Simultaneous Process Design and Layout Optimisation

Changing design parameters such as temperature and pressure can lead to changes in equipment requirements and safety. This can lead to a change in plant layout and plant cost. The following iterative approach has been designed to quantify how design parameters can directly affect the capital cost and F&EI of a pertinent unit, which will subsequently inform the optimum plant layout:

1. Selecting a design parameter in a pertinent unit to vary.
2. Identifying applicable penalties (in the context of F&EI analysis) that can change due to varying the design parameter
3. Iteratively calculate any changes in the De, DF & cost/size of pertinent unit over the range of design parameter values.
4. Iteratively inputting the range of De, DF and cost/size of pertinent unit into the optimiser and observing any changes to the objective function and plant layout.

To show a proof of concept of this approach, the pressure of the reactor flowsheet item is selected as the design parameter observed and is varied between 10 bar and 50 bar from the original 34.47 bar specified in Douglas [14]. To ensure that the conversions in the reactor and design parameters of other process units remain constant, the volume of the reactor was adjusted using Equation 4 derived from the ideal gas law. This ensures the reactant residence time in the reactor remains constant, maintaining reactor conversion. The molar flow rate and temperature in the reactor were assumed to be constant.

$$\frac{P1}{V2} = \frac{P2}{V1} \tag{4}$$

Where P denotes reactor pressure and V denotes reactor volume. Changes in pressure affect the pressure penalty term in the Special Process Hazards in the F&EI analysis, leading to changes in De and DF. The size and cost of the reactor at each pressure were recalculated using Aspen Economic Analyser. These new values are tabulated in Table 4. With all other model inputs remaining constant, the new De, DF, size and cost of the reactor were inputted into the optimisation problem.

2.8 Mathematical Formulation of MILP Problem Objective Function

Two different objective functions were used in this study depending on the scenario desired, and the objective functions are as follow:

$$min \sum_{i} \sum_{j \neq i} TTC_{i,j} + \sum_{i} MPPD_i, \ \forall i = 1, ...N \quad \forall j = i, .., N-1 \tag{5}$$

$$min \sum_{i} \sum_{j \neq i} TTC_{i,j} + \sum_{i} MPPD_i + LC, \ \forall i = 1, ...N \quad \forall j = i, .., N-1 \tag{6}$$

Note that the optimisation problem is a single objective function problem, hence the two objective functions are never active simultaneously. Objective Function 1, shown in Equation 5, minimises the cost of connection between units and the maximum probable property damage (MPPD). Objective Function 2, shown in Equation 6, minimises the same variables with an additional land cost term, LC, to be minimised. The cost of connection includes pumping costs, piping costs and road paving costs. The MPPD was calculated by considering the total annualised cost of capital and collateral damage if all the pertinent units were to simultaneously explode, including the cost of human life. Costs due to collateral damage from pertinent unit explosions are assumed to increase linearly with decreasing inter-unit distance. The detailed formulation for MPPD can be found in the Supplementary Information file.

2.9 Constraints

2.9.1 General Constraints

The following constraints were implemented alongside the objective function to provide a solution to the MILP problem:

1. Equipment orientation constraints
2. Non-overlapping constraints
3. Layout constraint
4. Distance constraint
5. Cost of connection constraints (both piping/pumping and road)
6. Land-use constraint
7. Fire and explosion exposure constraint.

In the land-use constraint, two methods of area calculation (the fixed and unfixed aspect ratio method) were proposed and are best described through an example. A square plot of land with sides of 100m is divided into a *100×100* grid by the optimiser. With the fixed aspect ratio method of area calculation, the optimiser tries to find the smallest $n \times n$ area to fit the units in. This will result in only square areas to be considered. With the free aspect ratio method, the optimiser looks for the smallest $n_1 \times n_2$ combination, with n_1 and n_2 being able to be different numbers. This effectively allows for rectangular plot areas to be modelled, albeit with the drawback of greater computational time.

It is important to note that all distances between units are calculated as rectilinear distances instead of radial distances as modelling radial distances would result in a non-linear problem. Rectilinear distances are practical for modelling piping length, but lead to problems when estimating radial distances between units for fire and explosion exposure damage calculations.

Most of the constraints have been derived directly from Low's work, and their full mathematical formulation can be found in the Supplementary Information file [9]. This study applied novel modifications specifically to the layout and cost of connection constraints which will be discussed below.

2.10 Layout Constraints

This study utilised several methods of imposing layout constraints depending on the layout shape desired, and the different methods are for rectangular shapes, convex shapes and non-convex shapes.

For a typical square or rectangular layout, the layout can easily be defined by imposing an upper bound and a lower bound , ensuring that no part of the unit exceeds these limits. These constraints are described in Equations 7 - 10.

$$x_i \geq \frac{l_i}{2} \quad \forall \, i \tag{7}$$

$$y_i \geq \frac{d_i}{2} \quad \forall \, i \tag{8}$$

$$x_i \leq \frac{l_i}{2} + X^{max} \quad \forall \, i \tag{9}$$

$$y_i \leq \frac{y_i}{2} + Y^{max} \quad \forall \, i \tag{10}$$

Low explored the need for making possible a method for modelling a non-rectangular plant layout [9]. There are useful applications for such a method, such as optimising plant layout around existing equipment or if an irregular-shaped plot of land is available for use. Mateus sought to

Table 4: *Changes in Reactor Specifications from Changes in Operating Pressure*

Pressure (bar)	Diameter (m)	Length (m)	Reinstallation Cost (£)	DF	DE (m)
10.00	2.29	3.66	650,860	0.80	36.71
20.00	1.98	3.66	884,380	0.80	38.56
30.00	1.83	3.66	1,181,740	0.81	39.92
34.47	1.80	3.66	1,243,620	0.82	40.40
40.00	1.68	3.66	1,462,160	0.83	41.28
50.00	1.68	3.66	1,592,640	0.83	41.62

add rectangular pseudo-equipment items in fixed positions, effectively constraining a larger rectangular plot into a shape with multiple right angles [4]. However, it does not allow for the modelling of plant layouts with non-right angled vertices. This paper proposes a novel method of allowing rectangular items to be modelled on plant layouts with non-right angled vertices such as triangles and pentagons. A stark limitation to this set of constraints is that only a convex plant layout can be modelled.

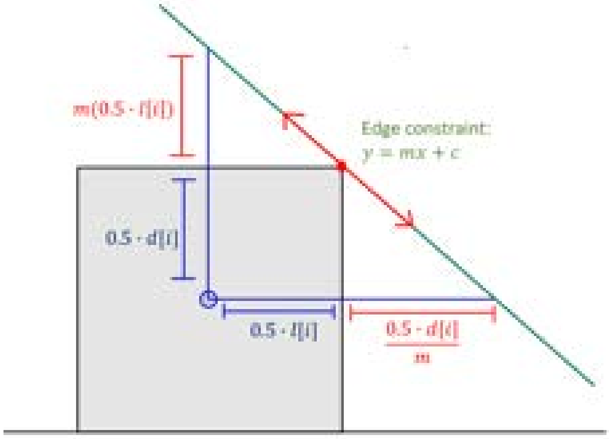

Figure 2: *Demonstration of the Application of Non-Rectangular Layout Constraint*

Consider a square unit with position *(x,y)* of length and width of *(l,d)* that needs to be placed as close as possible to the edge of a pentagon-shaped plant area. Given the vertices of the plant area, edges of the plant area can be represented as linear constraints denoted by $y = mx+c$, with m being a negative gradient in the case of Figure 2.

$$y_i + 0.5d_i + |m|\frac{l_i}{2} \leq mx_i + c, \quad c > 0 \quad \forall\, i \tag{11}$$

$$y_i - 0.5d_i - |m|\frac{l_i}{2} \geq mx_i + c, \quad c \leq 0 \quad \forall\, i \tag{12}$$

For the square unit to be as close as possible to the edge, the coordinate of the top right corner of the square needs to activate the edge constraint. Imagine a triangle originating from the centre of the unit with edges reaching vertically and horizontally until it meets the edge constraint. The vertical length of the triangle will be defined by $0.5d_i + m(0.5l_i)$, while the horizontal length is defined by $0.5l_i + m(0.5d_i)$. To ensure the top right corner of the square is allowed to always meet the edge constraint, this imaginary triangle has to 'slide' along the edge constraint. Equations 11 and 12 are applied in addition to Equations 7 - 10 to achieve this. The constraints have been formulated such that the same concept can also be applied to positive and zero gradient edge constraints.

Given the convex requirements of the shapes, any vertical edges would need to occur at the largest or smallest x coordinates of the plant area. Equations 7-10 ensures the implementation of the vertical constraints, avoiding the need to deal with infinite gradients in Equations 11 and 12.

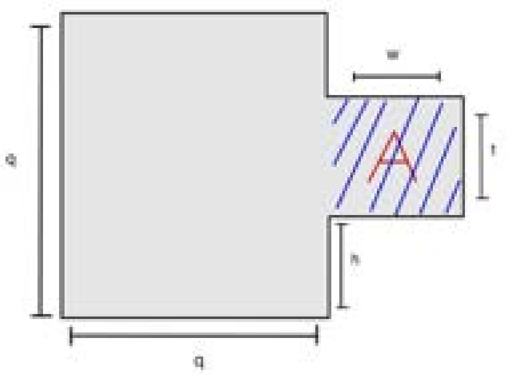

Figure 3: *Demonstration of the Application of Non-Convex Layout Constraint*

A general set of constraints for non-convex layouts is significantly more challenging, but can certainly be done on a case-by-case basis as shown by Mateus [4]. The set of constraints below describes an alternative method to how a 'T'-shaped plot area, shown in Figure 3, can be formulated:

$$y_i + 0.5d_i \leq qG1_i + (h+t)(1-G1_i) \quad \forall\, i \tag{13}$$

$$x_i + 0.5l_i \leq qG1_i + (q+w)(1-G1_i) \quad \forall\, i \tag{14}$$

$$y_i - 0.5d_i \geq h(1-G1_i) \quad \forall\, i \tag{15}$$

$$x_i - 0.5l_i \geq 0 \quad \forall\, i \tag{16}$$

As the 'T' shape is non convex, simple straight line constraints cannot be used as it will result in conflicts between feasible regions. Equations 13 to 16 allow for a tail portion to be added to a square of dimensions $q \times q$ through the use of the binary variable *G1*. For instance, when *G1=0*, the edges of unit blocks are allowed to enter region A (denoted by $h+t$ and $q+w$).

Equations 13 to 16 allows for the movement of the 'tail' along the right edge of the square, hence by adjusting the value of h, an 'L' shape can easily be constructed as well.

2.11 Cost of Connection Constraints

The cost of connection constraint was defined by Low to include the sum of the pumping cost and piping cost between process units [9]. Since the control room contains no piping to any process units there was no cost of connection considered. However, formulating the problem in this manner automatically places the control room as far away from the process units as possible due its high occupancy, and is only subjected to land cost limitations. To make the problem more realistic, it was assumed that a rectilinear road would be built to each unit from the control room. The distance of the control room to the units is defined by the distance constraints. Hence, the total cost of connections (TCC) is now defined by the Equation 17:

$$TCC_{i,j} = \sum_{i,j,i<j} C_{i,j} D_{i,j} + \sum_{i,i \neq ctrl} R_c D_i^{ctrl} \tag{17}$$

Where $C_{i,j}$ is the cost of piping and connection as defined by Low, $D_{i,j}$ is the rectilinear distance between unit i and j, R_c is the road cost, D_i^{ctrl} is the distance between the control room and all other units i that are not the control room.

2.12 Summary of Cases Analysed

A series of case studies of plant layout optimisation with different sets of activated constraints and objective functions were analysed to achieve the aims outlined in Section 1.2. In all the cases, the storage tanks were fixed to the bottom-left of the plot area, assuming that it is the most convenient location for tankers to collect the products or replenish raw materials. They are as follows:

1. Case 1 (Section 3.2) - Objective Function 1 was considered, quantifying the extent of the underestimation of objective function due to exposure radius being modelled as a rectilinear distance
2. Case 2 (Section 3.3) - Objective Function 2 was considered, comparing the effectiveness of fixed and unfixed aspect ratio methods for land area modelling
3. Case 3 (Section 3.4) - Objective Function 2 was considered, investigating the effectiveness of minimum separation distance in plant layout optimisation
4. Case 4 (Section 3.5) - Objective Function 1 was considered, demonstrating the practical applications of modelling a non-rectangular plot area
5. Case 5 (Section 3.6) - Demonstration of proposed framework for the simultaneous plant design and process plant layout, with Objective Function 2 considered.

3 Results and Discussion

3.1 General Observations

Table 5 provides a legend for Figures 4 to 8 in this section. It was interesting to note that the compressor, flash, furnace and reactor were placed close to each other in all of the cases, despite the latter two being pertinent units which carried the risk of causing damage to its surroundings. Upon closer inspection, it was observed that the connections between them (Connections 1,2,3 and 5, as defined in Table 2) carry gaseous process fluids. As the density of vapour is lower, this resulted in a larger pumping cost and hence required a larger pipe diameter, hence increasing the cost of connection. The optimiser placed these units closer to each other to save on the cost of connection in favour of reducing MPPD.

Table 5: *Legend Depicting Process Units for Figures 4 - 8*

Number	Unit
1	Furnace
2	Reactor
3	Flash
4	Compressor
5	Distil
6	Store
7	Control Room

Another observation was that the cost of road paving was significantly lower than the total cost of connection, at about 7-10% of the total connection costs in all of the cases. This appeared to be a sensible estimate, as it was expected for the cost of pumping and piping to be much greater than the cost of road paving.

3.2 Case 1

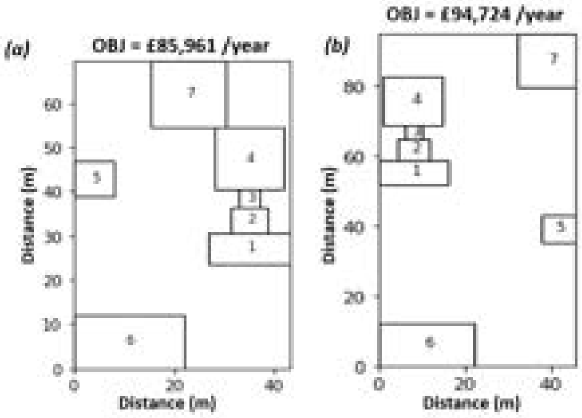

Figure 4: *Results of Layout for Case 1: (a) does not include the $\sqrt{2}$ Adjustment Factor; (b) includes the $\sqrt{2}$ Adjustment Factor*

In Case 1, the optimiser was given no restrictions on the land area available for use and Objective Function 1 was considered. Figure 4 depicts the results of the optimisation.

There was an approximately 10% increase in the objective function between Case 1a, which did not consider the $\sqrt{2}$ adjustment to exposure radius, and Case 1b, which did. This was expected as the model now overestimates the exposure radius by approximately 40%. Also as expected, Case 1a placed the process units much nearer to pertinent units than in Case 1b. This is because the radial distances between the units for event damage calculation was perceived by the programme to be further than it actually was, and it can be demonstrated through the following example.

In Case 1a, the control room's radial distance from the reactor was 30.8m, well within the reactor exposure radius of 40.4m. However, their rectilinear distance was 40.4m, hence the programme did not actually recognise that the control room was placed in a hazardous location. In Case 1b after the $\sqrt{2}$ adjustments, the control room was now a rectilinear 57.2m and a radial 40.6m distance away from the reactor, placing it outside the true reactor exposure area and effectively saving the lives of the plant operators in the control room in case of a reactor explosion. This example illustrated the importance of applying the $\sqrt{2}$ adjustment for creating a safer and more conservative model for plant layout.

3.3 Case 2

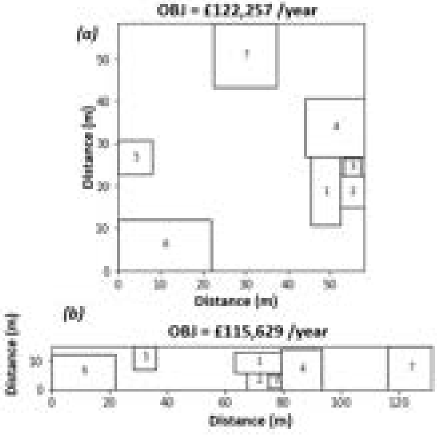

Figure 5: *Results of Layout Using the (a)Fixed and (b)Unfixed Aspect Ratio Methods for Land Area Calculation*

In Case 2, the optimiser was given a *150×150* square plot of land to place the units in. Case 2a and 2b implemented the fixed and unfixed aspect ratio methods, respectively, in deciding the final land area utilised. Objective Function 2 was considered. Figure 5 depicts the results from the optimisation.

When allowed to select the aspect ratio, the optimiser preferred to set out the plant in a long, rectangular configuration, leading to a 5% saving in total objective function cost compared to when a fixed aspect ratio was implemented. Placing units in this rectangular configuration increased the cost of connection and MPPD, but this was outweighed by the benefit of a 42% reduction in land cost. It should be noted that there was an increase of computational time from about 20 seconds to about 15 minutes - if the HDA plant was to be modelled in greater detail with more unit blocks, the computational time can increase greatly with only marginal reduction in objective function.

On the other hand, the cost of land used, assuming the plant will be built in Teesside, is quite low compared to the rest of the UK. At higher land costs, it will be expected that the effect of allowing for rectangular plant layouts can lead to greater cost savings compared to square layouts.

3.4 Case 3

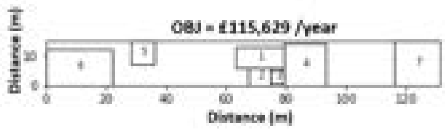

Figure 6: *Results of Layout Using the Unfixed Aspect Ratio Method for Land Area Calculation With Minimum Separation Distance Constraints Applied*

Case 3 examined the effects of adding minimum separation distance considerations to Cases 1 and 2 on the value of the overall objective function. For each of the cases, application of minimum separation distances led to an increase in overall cost of 48% or more. It was observed that the large increase in connection costs and land cost was only rewarded with a relatively modest reduction in MPPD.

Figure 6 depicted the addition of minimum separation distance considerations on Case 2b. A reduction of £6,783 in MPPD was observed, and was offsetted by a £53,349 and £22,929 increase in connection costs and land cost, respectively. Since the guidelines for minimum separation distances were fixed without considering the scale of the process, the possibility of underestimation, or in this case overestimation, of required separation distance was to be expected. For the HDA plant layout, it could be concluded that applying minimum separation distances will lead to an over-conversative plant layout by placing units further away than realistically required, therefore incurring additional costs greater than what the value of damage mitigated.

3.5 Case 4

In Case 4, the optimiser was given three shapes of plant area to optimise plant layout, shown in Figure 7. They are a *50×50* square plant area, a T-shaped plot area made up of a *50×50* square area and a *20×20* square, and a pentagon plot area made up of a *50×50* square area with an isosceles triangle on top. Objective Function 1 was used as non-rectangular plot areas could not be calculated with the land area formulation utilised in this study.

In both non-square plant areas, it was observed that the

Figure 7: *Results of Layout for a Square(a), T-shape(b), and Pentagon-shape(c) plant*

optimiser attempted to place the control room into the extra space available. This was a practical decision as the control room is arguably the most valuable unit on the plant, with its high human occupancy. Modelling of plant layout as a 'T' and a pentagon, respectively, allowed for a 9.1% and 8.1% reduction in total costs, with a high reduction in MPPD costs of 23.0% and 20.0% being countered by only a marginal increase of 4.0% and 2.4% in connection costs.

In industry, not all available plant areas are laid out in perfect rectangular shapes. Case 4 has shown the practical incentives, both financial and in terms of safety, of being able to model non-rectangular plot areas using the layout constraints proposed in this paper.

3.6 Case 5

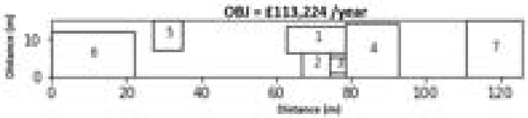

Figure 8: *Results of Layout, Operating the Reactor at a Pressure of 10 bar*

The unfixed aspect ratio method of area calculation and adjustment for exposure radius was applied to Case 5 without considering minimum separation distances, essentially replicating Case 2b with different inputs for reactor parameters. Table 6 illustrates the results of the optimisation from varying the operating pressure of the reactor.

In terms of layout, the positions of the units for the 6 simulations were all virtually identical to each other, appearing much like Figure 8 except for some very minor movement in their *x* and *y* coordinates. However, it could be seen that the total cost of layout was reduced at lower reactor operating pressures. This suggested an optimised plant configuration has been achieved, but reduction in pressure allowed for cost savings from other factors. Connection costs remained largely constant throughout the comparison, with the largest and smallest values varying by only 0.3%. This was mainly due to the fact that it was the dominating cost in the objective function and any significant changes to the plant configuration would result in a higher total cost. Land cost only increases marginally with increasing pressure as units are only spread out very marginally due to the increased risk of explosion.

Table 6: *Results of Varying Operating Pressure on the Costs of Layout*

Pressure (bar)	Connection Cost (£/year)	MPPD (£/year)	Land Cost (£/year)	Total (£/year)
10	61,423	38,972	12,830	113,224
20	61,539	39,382	13,212	114,133
30	61,560	40,241	13,404	115,204
34	61,483	40,743	13,404	115,629
40	61,610	41,226	13,595	116,431
50	61,544	41,592	13,595	116,731

The primary contributor to the reduction in total cost was from the decreased cost of damage to the units surrounding the reactor. As the collateral damage was calculated based on the extent to which a nearby unit was within the exposure radius of the reactor, a reduction in reactor exposure radius will lead to decreased damage to the units within the exposure radius of the reactor, namely the compressor, furnace and flash. It was also noted from the results that at higher pressures, MPPD cost increased at a slower rate. This corresponded to the fact that the pressure penalty from the special process hazards in the F&EI analysis approaches a plateau at higher pressure.

This analysis has suggested that by choosing to operate the reactor at 10 bar rather than 34.47 bar, there is a potential for savings of £1.8 million in the case that an event occurs, all without needing to significantly change the overall configuration of the flowsheet. This value of savings was calculated from the decrease in MPPD costs considering a catastrophic event occurs every 1000 years.

4 Conclusion

In this study, the HDA process was modelled in Aspen Plus V11 to collect realistic input data for the optimisation of the HDA plant layout. Novel layout constraints, which permitted the modelling of non-rectangular convex plot shapes, and a framework for simultaneous plant design and layout optimisation were introduced in this study. These were applied to constraints and considerations in existing literature, which allowed for insightful case studies to be conducted.

Case 1 highlighted the importance of including an adjustment factor for the implementation of exposure radius in a MILP layout optimiser, which if ignored could lead to a 10% underestimation of true cost of layout. Case 2 demonstrated that allowing for variable aspect ratios in land area determination can lead to a more meaningful representation of true land area used, with a potential 5% cost saving albeit with an exponential increase in computational time. Case 3 revealed the overly conservative nature of minimum separation distances when applied to the modelled HDA process, forcing an unnecessary increase in objective function of at least 48%. Case 4 showed that there is a financial and also safety-related incentive in being able to model non-rectangular plot shapes, allowing for up to 9.1% reduction in overall costs in the examples shown above. Finally, Case 5 illustrated a proof of concept of the proposed framework, suggesting that the total objective function could be minimised by lowering the reactor operating pressure to 10 bars without significant movement of unit blocks whilst providing a potential cost saving of £1.8 million.

There are several improvements that could be made in future works as extensions to this study. Firstly, distances for connection could be reformulated such that pipes would be modelled to start on the edges of the units rather than the centre since piping on process plants does not start from and end at the centre of each process unit. Secondly, a way of developing area approximation for non-rectangular plot areas should be developed such that land costs can be incorporated into such plot shapes. Further work should also be done to simplify how non-convex plant areas can be modelled. Finally, a solution should be developed for reducing the long computational time when implementing non-fixed aspect ratio land area calculation. This is to allow for more detailed modelling of the HDA process, such as breaking down the 'Distil' unit block into its individual constituent flowsheet items. As for the framework for simultaneous design and layout optimisation, more in-depth studies can be conducted in determining the effectiveness of the approach. Other parameters in different process units should be varied to see if large cost savings can be achieved. It should also be investigated how the framework can be extended methodically from the varying of a single design parameter to varying multiple parameters to allow for a more flexible tool.

5 Acknowledgements

We would like to thank Ms Mariana Monteiro for her support and guidance, especially for the modelling of the HDA process on Aspen.

References

[1] Jung S. *Facility Sitting and Layout Optimisation Based on Process Safety*. 2010.

[2] Kidam K. and Hurme M. *Design as a contributor to chemical process accidents*. 2012.

[3] HSE. *Plant Layout*. 2021. URL: https://www.hse.gov.uk/comah/sragtech/techmeasplantlay.htm.

[4] Mateus R. *Optimisation of the Facility Layout Problem*. 2000.

[5] Barbosa-Povoa A.P., Mateus R., and Novais A.Q. *Optimal Design and Layout of Industrial Facilities: A Simultaneous Approach*. 2002.

[6] Lees F. *Lees' Loss Prevention in the Process Industries*. Elsevier Science Technology, 2012. ISBN: 9780123971890.

[7] Penteado F.D. and Ciric A. *An MINLP Approach for Safe Process Plant Layout*. 1996.

[8] Patsiatzis D.I. *Optimal Process Plant Layout using Mathematical Programming*. 2003.

[9] Low C.C. *Minimising the plot size of carbon capture plant: Layout optimisation considering cost and safety factors*. 2021.

[10] Ejeh J.O., Liu S.S., and Papageorgioua L.G. *Optimal Multi-floor Process Plant Layout with Production Sections*. 2018.

[11] Han K., Cho S., and Yoon E.S. *Optimal layout of a chemical process plant to minimize the risk to humans*. 2013.

[12] Diaz C.O. et al. *A Comparison of Deterministic and Stochastic Approaches to Solve the Facility Layout Problem with Toxic Releases*. 2009.

[13] Wisconsin Department of Health Services. *Benzene*. 2018. URL: https://www.dhs.wisconsin.gov/chemical/benzene.htm.

[14] Douglas J.M. *Conceptual Design of Chemical Processes*. McGraw-Hill, 1988. ISBN: 9780070177628.

[15] AICHE. *Dow's Fire Explosion Index Hazard Classification Guide, 7th Edition Data*. CCPS of the American Institute of Chemical Engineers, 1994. ISBN: 978-0-8169-0623-9.

[16] Babcock Wanson. *BWR Firetube Steam Boiler*. 2017. URL: https://r6n7c4f7.rocketcdn.me/wp-content/uploads/sites/56/2018/09/BWR-Firetube-Steam-Boiler-Brochure.pdf.

[17] User Centred Design Services Inc. *Cost Estimate for a New State of the Art Control Room*. 2015. URL: https://mycontrolroom.com/cost-estimate-new-state-art-control-room/.

[18] Wang R. et al. *An Industrial Area Layout Optimization Method Based on Dow's Fire & Explosion Index Method*. 2017.

[19] AICHE. *Industry Risk Tolerance Criteria Data*. CCPS of the American Institute of Chemical Engineers, 2001. ISBN: 978-0-8169-0811-0.

[20] Dolan P. and Jenkins P. *Estimating the monetary value of the deaths prevented from the UK Covid-19 lockdown when it was decided upon – and the value of "flattening the curve"*. 2020.

[21] Colliers. *UK Industrial Rents Map*. 2021. URL: https://www.colliers.com/en-gb/services/industrial-logistics/industrial-rents-map.

[22] Tradesmen Costs. *Tarmac Driveway Cost: 2021 Price Comparison UK*. 2021. URL: https://tradesmencosts.co.uk/tarmac-driveway/.

Evaluation of equilibrium and kinetics to assess the feasibility of a novel process for the direct reduction of iron with hydrogen

Nicole Ching, Maria Starikova
Department of Chemical Engineering, Imperial College London

Abstract

This paper will explore the potential feasibility of the Zero Emissions Steel TechnologY (ZESTY) process proposed by Calix in their recent press release. Calix aim to reimagine the production of iron through the direct reduction of iron ore with green hydrogen at lower temperatures. Through the development of an ASPEN Plus model the equilibrium of the process was explored and by varying temperatures and flows, it was concluded that the process will be feasible on an equilibrium level. Fuelling profiles were suggested to improve conversions and remain at low hydrogen flow inputs. Through varying several parameters, the optimum solution for the ASPEN Plus model was found to be using FP3, $\mathrm{n_{in,H_2}} = 2550$ mol $\mathrm{s^{-1}}$, $\mathrm{T_{in,H_2}} = 700°\mathrm{C}$ and $\mathrm{T_{S,14}} = 800°\mathrm{C}$, which was used with the kinetics model built on MATLAB. This kinetics model only modelled the reaction of wustite to iron given it is agreed in literature that this is the slowest step. It demonstrated at the operating condition of the optimal ASPEN Plus solution, a reactor diameter of 5m and reactor height of 7.16m would be necessary to achieve 85% conversion of wustite to iron. Given a few more meters would be necessary for the two other reactions, this is perfectly reasonable given the Calix reactors are typically 10-50m long. In order to operate within Calix ZESTY reactors desired range of 600-800°C with FP3, the reactor length increases by 7.3 times. It would be recommended to operate at the upper limit of this range. The most optimum condition would be operating isothermally at 800°C where the reactor length is 6.39m. This would require a complicated heating profile but it would be ideal to operate as close to this optimum as possible.

Keywords: Iron ore, ASPEN Plus, kinetics, equilibrium

1 Introduction

Iron and steel industry is vital to today's economy due to sectors, such as construction, transportation and defense industry etc. (Deloitte, 2017), relying heavily on steel production. As the world continues to grow and less developed countries become more technologically advanced, the world demand for iron and steel will keep increasing, therefore, forcing the supply to increase. Currently the global production of crude steel sits at 1878 million tonnes in 2021 (WorldSteel, 2021*b*), with China producing 56.7%,, and IEA predicts a 50% increase in global demand by 2050 (IEA, 2020).

One of the main concerns with the iron and steel industry is how highly energy and emissions intensive it is, in 2020 it was responsible for 7% (2.6 Gt CO2) of total emissions and 8% of global energy demand (IEA, 2020). Therefore, with the rise of climate change coupled with the increase in demand, it is vital to find new solutions for iron production process in order to stay aligned with the Paris Agreement. There are currently 2 main routes for steel manufacturing: blast furnace-basic oxygen furnace (BF-BOF) and electric arc furnace (EAF) route. BF-BOF route produces around 70% of the global steel production (WorldSteel, 2021*a*) with emission intensity of 1870 $\mathrm{kgCO_2}$/tls (Sarkar et al., 2018), of which 61% can be attributed to the blast furnace (Pardo and Moya, 2013). Although EAF is a viable and popular alternative which bypasses the blast furnace, it does not produce high enough grade steel for the demand (He and Wang, 2017). Thus the focus should be on finding an alternative route for the production of iron to reduce it's emissions.

Due to the serious problems surrounding the iron and steel industry there have been many different routes suggested in literature. These include electrowining (Wiencke et al., 2018), carbon capture and storage (CCS) with BF-BOF, direct reduction of iron ore (DRI) with hydrogen, natural gas or CCS (Rechberger et al., 2020). The latter is predicted to play an essential role in reducing CO2 emissions and will account for around 20% of low carbon technologies in 2030 (currently 0% in 2021) (IEA, 2021).

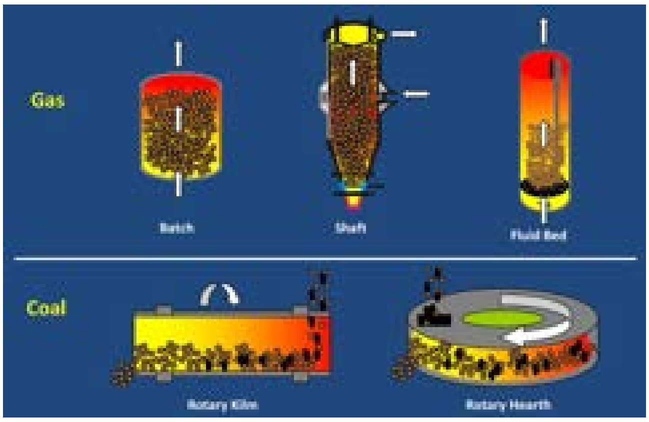

Figure 1: Types of DRI used in iron production industry (iima, n.d.)

Currently the industry has several different DRI processes

(Figure 1), most common being the gas based shaft furnace (MIDREX Process). The previously mentioned process utilises natural gas by passing it through catalyst tubes to convert it to hydrogen and carbon monoxide gas. These gases then act as reducing-gas flowing up the column encountering the downward falling iron ore, which is reduced to iron through a series of reactions (Atsushi et al., 2010). This process produces large amounts of CO2 combined with other various gases (H2O, H2, CH4, CO), making the capturing of carbon extremely difficult and cost heavy.

Calix has partnered with Imperial College London to tackle this issue and reimagine the DRI route with hydrogen. Their Zero Emissions Steel TechnologY (ZESTY) project entails the used of a specially heated kiln/reactor column, with either a fuel or electricity, to tackle the iron industry emissions and the theoretical theoretical minimum hydrogen use of 54 kg per tonne of iron (Calix, 2021). This report will focus on the exploration of the feasibility of the proposed process. It will explore how parameters such as temperature and flow affect the conversions of the reactions as well as the reactor column sizing through the use of ASPEN Plus and MATLAB.

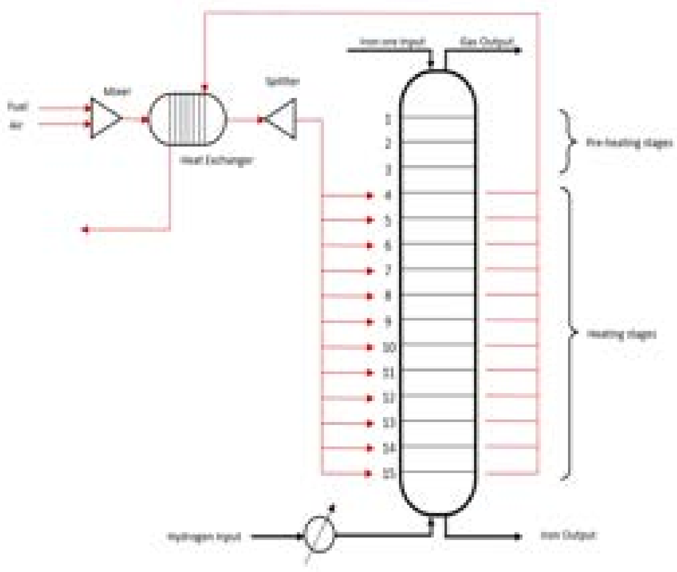

Figure 3: Simplified P&ID of ASPEN Plus model

2 Methodology

2.1 ASPEN Plus

ASPEN Plus simulation of iron ore reduction with hydrogen was built based on a previous cement simulation produced within the department of Imperial College London for Calix adn was modified to represent this process. It was highly important to investigate the effect of temperature and hydrogen flow on the iron output selectivities as well as the equilibrium effects.

The model consists of 3 pre-heating stages and 12 heating stage (Figure 3). This was designed to fit with Calix's available reactors. The kiln was modeled in stages to better map the temperature and composition profiles and to allow equilibrium to shift with varying temperatures.

2.1.1 Reactions

All modelled reactions in the ASPEN Plus are shown below (Eq. 4, Eq. 5, Eq. 6) (Spreitzer and Schenk, 2019). Reaction properties can be found in Table 1, where reaction 1 is identified as exothermic and reactions 2 and 3 are endothermic. The overall reaction is considered to be endothermic an therefore will require an input of heat.

$$\text{Reaction 1}: 3Fe_2O_3 + H_2 \rightarrow 2Fe_3O_4 + H_2O \tag{4}$$

$$\text{Reaction 2}: Fe_3O_4 + H_2 \rightarrow 3FeO + H_2O \tag{5}$$

$$\text{Reaction 3}: FeO + H_2 \rightarrow Fe + H_2O \tag{6}$$

2.1.2 Individual Stages

Stages 4-15 are represented in Figure 2 and the simplified description can be found in 2. The RGibbs reactor models multiphase chemical equilibrium through minimising Gibbs free energy of reactions. A restricted equilibrium was enforced with Eq. 4 - Eq. 6, to ensure no other reaction would occur. Each RGibbs reactor (R-1) was operated at 1 bar and the temperature would be determined by ASPEN based on the heat duty transferred from the combustion RGibbs (BURNER1). Stages 1-3 are similar to stages 4-15 (Figure 2) however there is no burner as no extra heat is supplied.

2.1.3 Fuel Heating

Heating throughout the reactor, stages 4-15, is conducted using natural gas as fuel, with the composition of methane (92.42% w/w), nitrogen (3.67% w/w), ethane (3.02% w/w), carbon dioxide (0.78% w/w), propane (0.11% w/w) (Agency, 2016). Before combustion, the fuel is mixed with air, at 25°C in the proportion of an excess oxygen level of 2% (from theoretical of 2 moles of oxygen per 1 mole of methane) to achieve optimum efficiency (Steinberg, 2013). This is computed with a DESIGNSPEC, called COMBAIR. The composition of air used: oxygen (79% mol/mol), nitrogen (21% mol/mol). The mixture is then heated to 500°C with flue gases of the combustion process using a HEATX heat exchanger in ASPEN Plus. This is done to utilise excess heat from flue gases and ensure more heat is available for the reactions. The heated mixture is then split into 12 stream, using a FSplit, where the splitting ratio can be controlled.

The proportioned fuel then enters another combustion RGibbs reactor (BURNER1), which is set to react at

Reaction	$\Delta_r H_{900^\circ C}$/kJ	Equilibrium constant
(4)	-6.02	$K_{1,H_2} = \exp\left(\frac{362}{T(K)} + 10.32\right) \quad (1)$
(5)	+42.64	$K_{2,H_2} = \exp\left(\frac{-8580}{T(K)} + 8.98\right) \quad (2)$
(6)	+17.61	$K_{3,H_2} = \exp\left(\frac{-2070}{T(K)} + 1.3\right) \quad (3)$

Table 1: Heat of reactions (Patisson, 2020) and equilibrium constants (Hara et al., 1974)

1.15 bar and 1200°C. This RGibbs reactor calculates phase equilibrium and chemical equilibrium, therefore unrestricted unlike the previous one. The main reaction happening in this block is Eq. 7, where methane reacts with oxygen to produce carbon dioxide.

$$CH_4 + 2O_2 \rightarrow CO_2 + 2H_2O + \text{Heat} \tag{7}$$

2.1.4 Importants Parameters

The main controlled variables can be found in Table 3. n_{in,Fe_2O_3} is primarily set to 300 mol/s in order to achieve an outflow of iron similar to a typical iron blast furnace (2880 tonnes of iron daily (Britannica, 2019)). n_{in,H_2} is varied to reach the desired conversions. $T_{S,14}$ was set a variable in order to have a fair comparison between simulation runs. It allows the user to evaluate the fuel needed to reach a desire temperature but also allows to see the effect of fuel splitting on the column at similar temperatures. T_{in,H_2} is used to not only compare it's effects on the column but also to evaluate the heat required to heat the hydrogen to the desired temperature in comparison to input of fuel in terms of pricing.

The main tools of comparisons consist of selectivity of iron, Eq. 8, conversion of hydrogen, Eq. 9 and ratio of hydrogen used per iron produced, Eq. 10.

$$\text{Selectivity of Iron} = S_{iro} = \frac{\text{Iron flow out}}{\text{Hematite flow in}} \tag{8}$$

$$\text{Conversion of Hydrogen} = X_{hyd} = \frac{\Delta\text{Hydrogen flow}}{\text{Hydrogen flow in}} \tag{9}$$

$$\begin{aligned}\text{Ratio of } H_2 \text{ per Fe} = \text{R (kg of } H_2\text{/ton of Fe)} \\ = \frac{\text{Hydrogen flow in}}{\text{Iron flow out}}\end{aligned} \tag{10}$$

2.2 Kinetics Model

The kinetics of the last reaction converting wustite to iron has been established by most researchers as the rate-limiting step due to the dense iron product layer that hinders the diffusion of the reducing agent file:///C:/Users/nicol/Downloads/materials-14-07540.pdf . Hence, only this final step will be kinetically modelled in this preliminary analysis. The random pore model was chosen to build the kinetic model for this reaction. Unlike the grain and order-of-reaction models, it can model an increase of reaction rate with conversion to a maximum before decreasing, which is what is observed experimentally. Muwanguzi et al. (2017) tried to fit the grain, volumetric and random pore model to their experimental data and found the most success with the latter. It is also more suitable for small particles, like those to be used in the Calix ZESTY reducer, compared to those such as the shrinking core model that model larger particles with larger intra-particle diffusion effects.

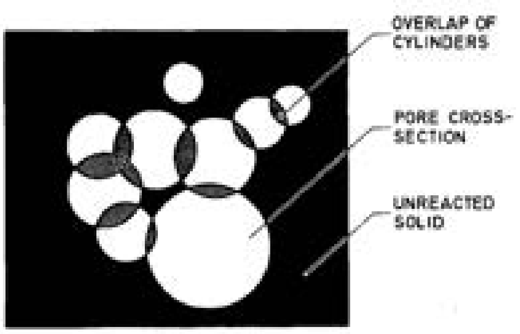

Figure 4: Overlapping of pores (Bhatia and Perlmutter, 1980)

The random pore model assumes a constant sized particle, with a fixed number of fixed length, randomly oriented pores. They initially grow radially, increasing available surface area for reaction. However, as they continue to grow, the pores start to overlap and surface area is lost as depicted in Figure 4. The equation describing this model

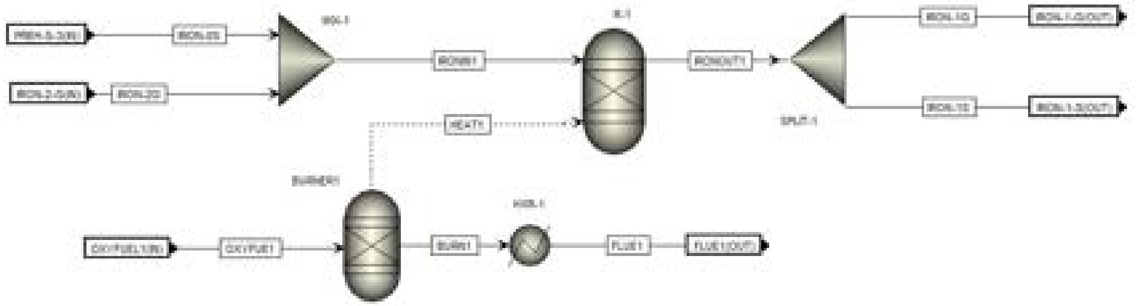

Figure 2: Configuration of a heated stage in ASPEN Plus

ASPEN Plus Name	Block Name	Description of Function
MIX-1	Mixer	Mixes the gas and solid flows evenly
SPLIT-1	SSplit	Splits the mixed stream into gas and solids
HXR-1	Heater	Heats the flue gas stream to appropriate temperatures and pressure to simulate real flue gas
R-1	RGibbs	Simulates reduction equilibrium reactions under constant conditions
BURNER1	RGibbs	Combustion of fuel and the energy is used to heat up the R-1

Table 2: Description of units in the ASPEN Plus simulation, based on Figure 2

Symbol	Unit	Description
n_{in,Fe_2O_3}	kmol/sec	Molar flow of hematite into the system
n_{in,H_2}	kmol/sec	Molar flow of hydrogen into the system
T_{in,H_2}	°C	Temperature of hydrogen flowing into the system
$T_{S,14}$	°C	Temperature of stage 14

Table 3: Main controlled variables in ASPEN simulation

is shown below:

$$\frac{dX}{dt} = \frac{S_0([H_2] - \frac{[H_2O]}{K})}{1-\epsilon_0} \frac{k_s\sqrt{1-\Psi\ln(1-X)}}{1+\frac{\beta\alpha}{\Psi}[\sqrt{1-\Psi\ln(1-X)}-1]} \tag{13}$$

X is conversion of wustite, so the rate of conversion depends on itself, the concentration of hydrogen, [H_2], the concentration of water and vapour, [H_2O]. Alongside these variables, there are also temperature dependent constants including K_{3,H_2}, the equilibrium constant, k_s, the rate constant per unit area for rate of conversion and $D_{s,O}$, the diffusivity of oxygen ions through the product layer. k_s and $D_{s,O}$ are important in the Biot number, β, which is a dimensionless ratio of the rates of chemical reaction to diffusion through the solid product. If diffusion is limiting, β is larger making the rate of conversion slower. Key particle properties to this equation include initial porosity η_0, initial specific surface area S_0 and L_0, total length of the whole pore system per unit volume. ψ is a structural parameter characterising the inital degree of overlap of pores. When ψ is small, the rate of conversion decreases with conversion, without increasing first, because the pore system was not very overlapped to start with. Hence, as conversion increases, the pores increase in size but lose surface area as the increase in overlapping of pores dominates. Finally, V_{FeO} is the molar volume of wustite and α is the ratio of molar volume of product, Fe to reactant, FeO.

2.2.1 Counter-flow reactor column model

The equilibrium data from the ASPEN model was used to find K_{3,H_2} as a function of temperature to input into Eq 13. Particle properties obtained from literature (Liu et al., 2014) were used: $L_0 = 7.5 \times 10^{12}$ m^{-2}, $S_0 = 2.5 \times 10^6$ m^{-1}, $\epsilon_0 = 0.6$. Functions for k_s and $D_{s,O}$ were taken from the same source as $1 \times 10^{-7}\exp[-90\ (\text{kJmol}^{-1})/RT(\text{K})]\ (\text{m}^2\text{s}^{-1})$ and $7 \times 10^{-6}\exp[-62\ (\text{kJmol}^{-1})/RT\ (°\text{C})]\ (\text{m}^4\text{mol}^{-1}\text{s}^{-1})$ respectively. Molar volumes were found by dividing molar mass (gmol^{-1}) by density (gm^{-3}), giving a value of V_{FeO} of 1.2516×10^{-5} m^{3}mol^{-1} and α of 0.563. The aim is to calculate the length of reactor required to reach the equilibrium achieved in the ASPEN model. To do so, a counter-current reactor model with the kinetics described by Eq. 13 was built to model the flowrate profiles of wustite and hydrogen (Eq. 11 and Eq. 12) on MATLAB.

It can be seen that 6 new variables are required to solve these molar flowrate differential equations: $n_{FeO,0}$, the initial molar flowrate of wustite, $n_{H_{2},0}$, the initial molar flowrate of hydrogen, $v_{T,0}$, the volumetric flowrate of gas, A, the cross-sectional area of the reactor, and u_{solids}, the velocity of the falling wustite particles. $n_{FeO,0}$ is 600 mols^{-1} as per the stochiometry, the amount of wustite produced is two time the amount of hematite fed in. $n_{H_{2},0}$ can be chosen as done so in the ASPEN model runs and the corresponding volumetric flowrate, $v_{T,0}$, can be found from ASPEN too. A was set to 100 m^2 which corresponds to five 5m diameter Calix ZESTY reactors in parallel while u_{solids} was set to 1 ms$^-$1 which was suggested in Calix's patent (Sceats et al., 2019).

3 Results & Discussion

3.1 ASPEN Plus

To better comprehend the model, it is important to understand the placement of the reactions occurring within the reactor. Using Figure 5, where stages 4-15 are evenly heated, reaction profiles can be determined. Due to the drop of Hematite to 0 after the first stage, it can be determined that reaction 1 (Eq. 4) occurs fully within this stage. As mentioned in Section 2.1.1, reaction 1 is exothermic meaning that the reaction performs more favorably in at lower temperatures. $K_{1,H_2} = 49738$ at 450°C is extremely high, therefore this aligns with hematite theoretically reacting completely. This phenomena was also witnessed by Wagner et al. (2008).

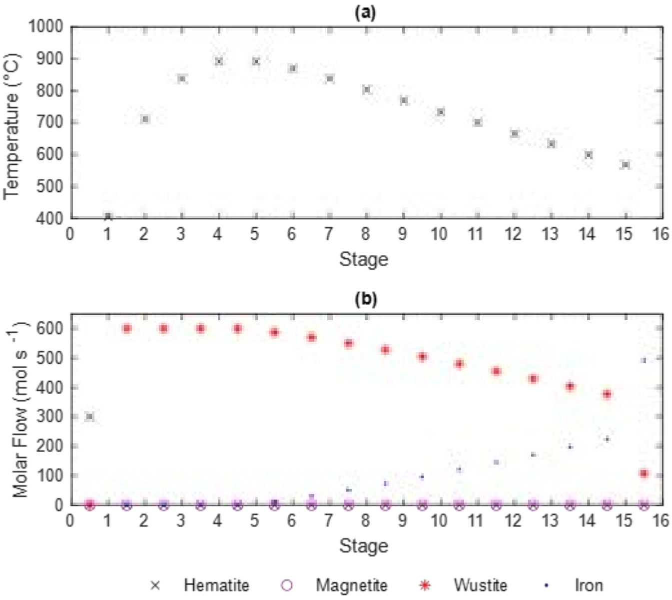

Figure 5: n_{in,Fe_2O_3}=2.55 $kmol\ s^{-1}$, T_{in,H_2}=600°C, $T_{S,14}$=600°C: (a) Temperature Profile (b) Molar flows of hematite, magnetite, wustite and iron.

$$\frac{dn_{FeO}}{dz} = \frac{n_{FeO,0}}{u_{solids}} \frac{S_0(\frac{n_{H_2}}{v_{T,0}} - \frac{n_{H_2,0}-n_{H_2}}{v_{T,0}K})}{1-\epsilon_0} \frac{k_s\sqrt{1-\Psi\ln(1-\frac{(n_{FeO,0}-n_{Fe,O})}{n_{FeO,0}})}}{1+\frac{\beta\alpha}{\Psi}\left[\sqrt{1-\Psi\ln(1-\frac{(n_{FeO,0}-n_{Fe,O})}{n_{FeO,0}})}-1\right]} \tag{11}$$

$$\frac{dn_{H_2}}{dz} = -\frac{n_{FeO,0}A}{v_{T,0}} \frac{S_0(\frac{n_{H_2}}{v_{T,0}} - \frac{n_{H_2,0}-n_{H_2}}{v_{T,0}K})}{1-\epsilon_0} \frac{k_s\sqrt{1-\Psi\ln(1-\frac{(n_{FeO,0}-n_{Fe,O})}{n_{FeO,0}})}}{1+\frac{\beta\alpha}{\Psi}\left[\sqrt{1-\Psi\ln(1-\frac{(n_{FeO,0}-n_{Fe,O})}{n_{FeO,0}})}-1\right]} \tag{12}$$

However, no magnetite is formed at any stage thus reaction 2 (Eq. 5) occurs completely to wustite within the first stage. This is interesting due to the temperature of solids leaving the first stage only being 459°C, which is lower than the rest of the column where reaction 2 (Eq. 6) occurs. We would expect the equilibrium of reaction 2 to be similar to reaction 3 as Wagner et al. (2008) witnessed both of the reactions are still observed at 800°C. When looking at literature equilibrium constant (Table 1), $K_{2H2} = 0.064$ and $K_{3H2} = 0.21$ @ 450°C, it is clear that at this temperature the reactions do not go to completion thus agreeing with results Wagner et al. (2008) found. Experiments were conducted on the ASPEN model and then the equilibrium constants were plotted against literature values (Figure 6. There is a large discretionary between the two at all temperature ranges. As RGibbs reactors uses the minimum Gibbs free energy method to calculate the extent of the reaction, it can be theorised that the activity coefficient used by ASPEN is simplified. This is an area to explore outside the scope of the project to confirm the equilibrium constants experimentally and implement into ASPEN Plus if found to be different. Nonetheless, Figure 6 explains the absence of magnetite within the reactor as it would all react at such temperatures.

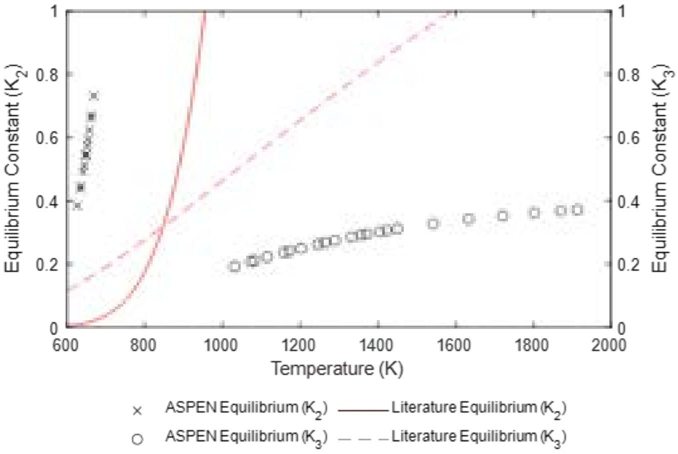

Figure 6: Equilibrium profiles of reaction 2 and 3

From Figure 6 it is also reasonable to say that reaction 3 is the most limited reaction by equilibrium, which is also observed by Chen et al. (2015). Therefore, reaction 3 is the most prominent reaction within the ASPEN Plus model, with most of the conversion occurring at stage 15 due to the high inflow of pure hydrogen. (Figure 5). Thereafter, the only way to induce furthe reaction is to shift the equilibrium through an increase in temperature thus it is vital to heat the column.

Figure 5 represents data for $n_{in,H_2} = 2850$ mol/sec, $T_{in,H_2} = T_{S,14} = 600$°C and has selectivity and efficiency of 0.926 and 91.8 kg of H_2/Tonne of Fe respectively. At first glance the selectivity and temperature profiles are sufficient, as the temperatures do not reach the melting point of iron. However, the theoretical efficiency that Calix is trying to reach is 53.7 kg of hydrogen per tonnes of iron, which is much lower than the previously mentioned efficiency. Thus the process has to be optimised.

3.1.1 Hydrogen flow Dependence

The impact of hydrogen flow on extent of reaction has been investigated in literature (Tsay et al., 1976) (Chen et al., 2015) (Xing et al., 2019). A strong correlation was found where an increase in hydrogen shifts increases the conversion of oxygen due to the ratio $\frac{H_2O}{H_2}$ being further below the equilibrium constant. Hence, more can react before the equilibrium constant is reached. This aligns with results found through the ASPEN Plus model (Figure 7). However, high hydrogen flows result in higher excess of hydrogen and therefore further away from theoretical efficiency ratio. This should be avoided as much as possible as higher gas flows can results in higher operating costs as well as capital costs.

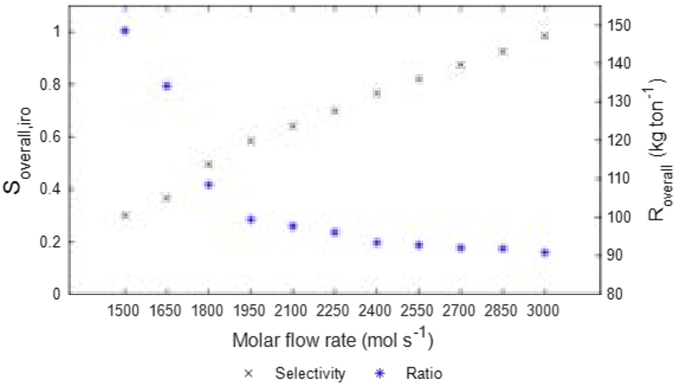

Figure 7: Selectivities and ratio of hydrogen per iron produced with varying hydrogen flow in at $T_{s,14} = 600$°C, $T_{in,H_2} = 600$°C

3.1.2 Temperature Dependence

As previously mentioned, one of the methods to improve the equilibrium is to increase the temperature in the column, however it is important to keep it low enough to prevent iron from melting. Temperature effect on the reduction reactions has been the subject of many papers in the past (Chen et al., 2018) (Turkdogan and Vinters, 1971) (Chen et al., 2015), with all reaching the consensus of higher conversion at higher temperatures.

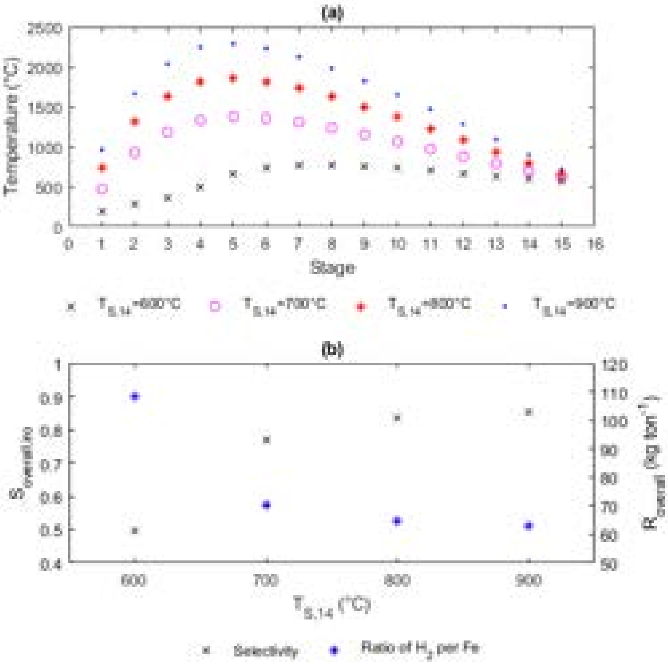

Figure 8: $n_{in,Fe_2O_3} = 1.8$kmol s^{-1}, T_{in,H_2}=600°C: (a) Temperature profiles (b) Selectivity and Ratio of H_2 per Fe of varying $T_{S,14}$ between 600°C and 900°C

Figure 8 shows the variation of $T_{S,14}$. As the temperature is varied from 600°C to 900°C, the selectivity improves by 72%. This is a significant improvement and clearly shows the impact of temperature on this process. Higher temperatures require higher amount of fuel to be supplied, in this case the mass flow of fuel increases by 420%. Thus it is vital to compare the costs of fuel relative to other costs in the future to identify if the trad-off is worth it. Referencing back to the temperature profiles of these results, $T_{S,14} = 800°C$ and $T_{S,14} = 900°C$ both exceed the melting point of iron, in stages 2-10, and are therefore infeasible. Nonetheless, the improvement with increasing temperature still stands and solutions to operating at temperatures as high as possible without melting the iron will be presented further on in the paper.

3.1.3 Fuelling Profiles (FP)

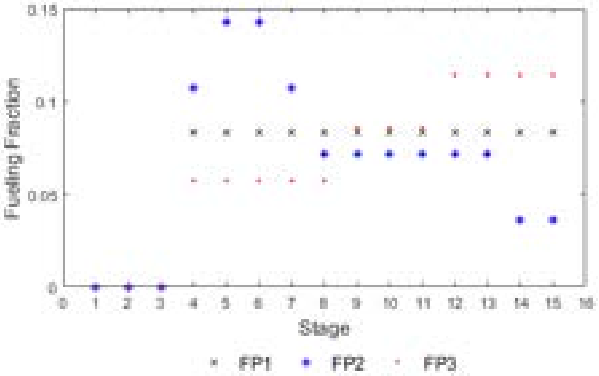

Figure 9: Fuelling Profiles used in ASPEN model

For cases reported above, FP1 (Figure 9) was used to ensure a fair comparison through equal heating of stages 4-15. However, as states in Section 3.1.2, this profile has its cons. One is that at lower stage 14 temperatures the temperatures throughout the rest of the column are too low, which causes low conversion. FP2 would theoretically solve the problem as the stages at the top of the column would receive more heat and therefore the equilibrium would be pushed further.

Figure 10 explores FP2 with varying molar flows of hydrogen. From Figure 10 (b), FP2 increases the selectivity of iron by 32% and the ratio of hydrogen to iron by 24% (at n_{in,Fe_2O_3}=2250molsec^{-1}), which is a vital improvement. Less hydrogen would be need to achieve the same amount of iron. This is due to the temperature in the top of the column being higher (Figure 10 (a)) therefore increasing the equilibrium constant of the reaction and subsequently the conversion of oxygen. However, when using with higher temperatures of stage 14, like 800°C, the temperatures at the top of the column exceed the melting point of iron. Thus FP2 can can only be used at low input temperatures to improve the process.

FP3 explores the possibility of reducing the ratio of fuelling at the top of the column allowing high temperatures at the bottom, increasing the rate of reaction where the majority of conversion occurs. This therefore reduces the column size. Figure 11 shows the how FP1 compares to FP3 and the run specifications can be found in Table 3.1.3. Run 1 and Run 2 were done to compared how the hydrogen inlet temperature would affect the temperature profiles, selectivity and ratio efficiency of the process with the new fuelling profile. The goal was to create a fuelling profile that would increase the selectivity and decrease the ratio efficiency at higher inlet temperatures to aid the kinetic at stage 15. From Figure 11 it can be seen that Run 2 resulted in extremely high temperatures, reaching past the melting point of iron, and Run 1 provided low selectivities and high ratio efficiencies. Run 3, however provided a middle ground and was found to be the most optimum set of results. It eliminated the extremely high temperatures, like Run 2, and reached higher selectivities and lower ratio efficiencies than Run 1. Therefore, fuelling profiles of higher input at the bottom of the column are more beneficial and would benefit greatly the kinetics, which will be discussed in Section 3.2.

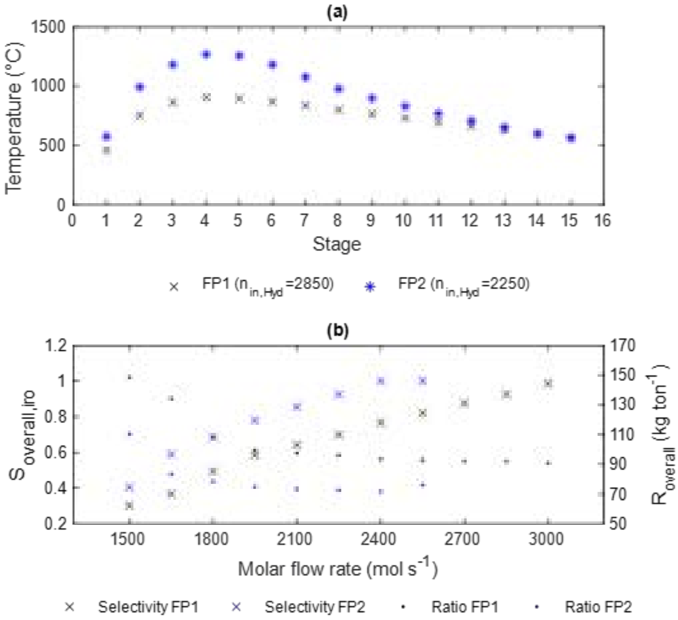

Figure 10: T_{in,H_2}=600°C & $T_{S,14}$=600°C: (a) Temperature Profiles of results of $S_{overall,iro}$ $\tilde{0}.92$ (b) Selectivity and Ratio of H_2 per Fe for Fuelling profiles 1 & 2

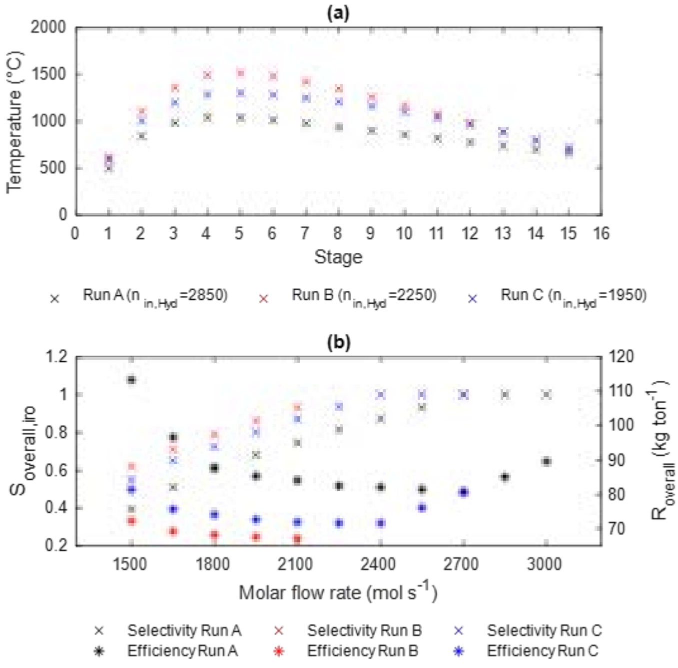

Figure 11: (a) Temperature Profiles of hydrogen flows (mol s^{-1}) which give $S_{overall,iro} = 0.93$ (b) Selectivity and Ratio of H_2 per Fe for Fuelling profiles 1 & 2

Run	FP	$T_{S,14}$ (°C)	T_{in,H_2} (°C)
A	1	700	700
B	1	800	700
C	3	800	700

3.2 Kinetics

The kinetics modelling was only for stages 5-15 of the ASPEN model as they are the stages where the reaction of wustite to iron take place. ode45 was used in MATLAB to numerically solve this equation for each stage as they each had a different temperature. It is worth noting that this is a simplification and the Calix ZESTY reactor will probably have a more continuous temperature profile so the mass balances would need to be solved in conjunction with a heat balance equation. The ASPEN run with $T_{S,14} = 800°C$, $n_{in,H_2} = 2250mols^{-1}$ and FP3 was modelled kinetically given it was found to be the most optimal. The results are shown as the coloured line in Figure 12. This demonstrates a required reactor length of 7.16m. Stages 1-4 will a few more metres, to account for reaction 1 and 2 which were not considered in this model. Calix's patent states a typical reactor length of 10 to 50 metres, therefore the results obtained are ideal. The bottom stage, Stage 15 (in red), was discovered to comprise 87.4% of the total reactor length. This is expected given the majority of conversion takes place in the stage and it is the stage at the lowest temperature resulting in lower values of k_s and D_s and therefore slower kinetics.

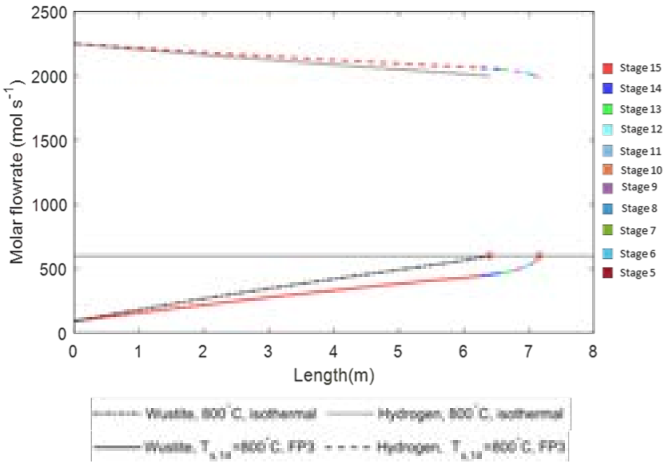

Figure 12: Wustite and Hydrogen molar flowrate profiles for the $T_{S,14} = 800°C$, FP3 and 800°c, isothermal case

Calix's ZESTY reactor would be aiming to operate within the temperature range of 600 and 800°C (Calix, 2021). The $T_{S,14} = 800°C$, $n_{in,H_2} = 2250mols^{-1}$, FP3 does not stay within this temperature range as temperature varies from 758°C to 1150°C. The ASPEN run $T_{S,14} = 600°C$, $n_{in,H_2} = 2700mols^{-1}$, FP3 does caries between 567°C and 899°C, achieving a similar conversion at temperatures much closer to Calix's desired temperature range. It was therefore modelled as displayed in Figure 13 alongside the $T_{S,14} = 800°C$, FP3 case for comparison. It is clear that the reactor length is significantly longer at 52.24m, this is 7.3 times larger than the $T_{S,14} = 800°C$, FP3 run. There is a significant trade off in reducing temperatures on the length of reactor required to achieve the same conversion. In addition, a higher flowrate of hydrogen is required.

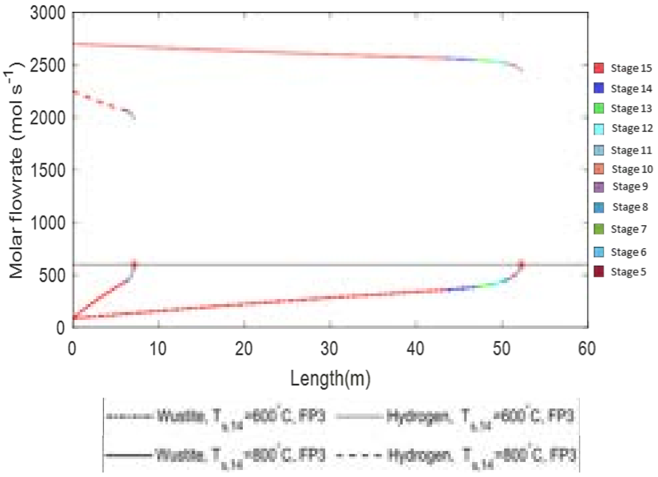

Figure 13: Wustite and Hydrogen molar flowrate profiles for the $T_{S,14} = 600°C$, FP3 and $T_{S,14} = 800°C$, FP3 case

Another option would be to operate the whole reactor at the upper limit of Calix's temperature range i.e. 800°C. As temperature clearly favours both equilibrium and kinetics, it logically follows to maximise it given the trade off of operational costs from increased energy input is much smaller than that of the increased capital cost from a length that is almost an order of magnitude larger. This isothermal reactor's flowrate profile is shown in Figure 12 in black. It actually requires a lower reactor length (6.39m) than $T_{S,14} = 800°C$, $n_{in,H_2} = 2250\ mols^{-1}$, FP3 as the temperature at the bottom stage, $T_{S,15}$, is at 800°C rather than 758°C and as discussed previously, this accounts for the majority of the reactor length so having faster kinetics in this stage offsets the slower kinetics in the previously hotter stages. However, keeping the reactor isothermal would require a complicated heating profile.

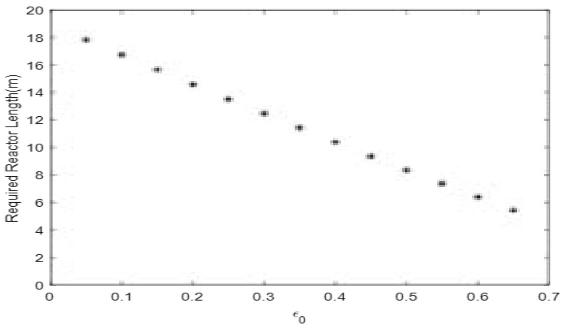

Figure 14: Impact of the porosity, ϵ_0, on the required length of reactor

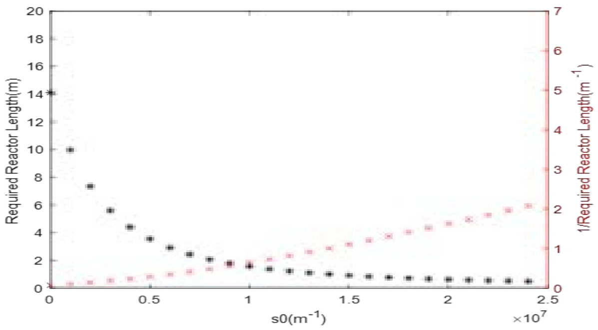

Figure 15: Impact of specific surface area, S_0, on the required length of reactor

Particle properties have a significant presence in the random pore model equation. However, ore particles can have a wide spectrum of values for these. Hence, a sensitivity analysis has been conducted to investigate the effect of varying these. Figure 14 illustrates the impact of varying the porosity of the particle. It isn't quite linear but there is approximately a 2 metre increase for every 0.1 decrease in porosity. This marginal change is quite low which fortunately means the the reactor length remain in a feasible range. Figure 15 illustrates the impact of ranging S_0 from $2.5*10^3$ to $2.5*10^7$ in black, which is the range of possible values that iron ore can have (Bhatti et al., 2021) and it can be seen that it is non-linear. This is logical given conversion rate as depicted in Eq. 13 is proportional to S_0. Therefore, the length required to achieve a given conversion is roughly inversely proportional to it.It can be seen in red in Figure 15 it is not exactly inversely proportional as if it was, plotting the inverse of reactor length against S_0 would be linear. This is due to the fact S_0 is not simply multiplying X and the structural parameter ψ is also dependent on it. Despite this inverse-natured behaviour, even at the lowest possible specific surface area of iron ore, the reactor length is still only 14.11m which is well within a reasonable length range of a Calix ZESTY reactor.

4 Conclusion

From the ASPEN Plus and kinetics model, it can be concluded that the proposed process of direct reduction of iron ore with hydrogen will be feasible in terms of equilibrium and kinetics. ASPEN Plus model explored the temperature and flow dependencies of the process and found data to support favourable conditions for the process, such as higher temperatures reduce the flow of hydrogen required. Fuelling profiles were also suggested to eliminate the risk of reaching the melting point of iron at the top of the column, settling on higher fuelling fractions at the bottom of the column. Although further experimental data will need to be obtained to solidify the results from the model, the general trends for improving the process will remain the same.

The kinetics model showed that the reactor dimensions necessary to achieve a production or iron that would typically be produced in a blast furnace, are very reasonable and within the range of Calix's typical reactor sizes. There is a significant trade-off between decreasing the temperature and increasing the reactor length to achieve the same conversion. The influence of temperature on reactor length is also much greater than that of any of the particle properties. It is therefore recommended to operate at as high a temperature as possible while staying within Calix ZESTY reactor's desired temperature range.

5 Outlook/Future Work

Due to this study being only the preliminary stage of the journey to finalising this process, there are a number of potential improvements that can be made to the models. The ASPEN Plus model equilibrium values should be compared to experimental data for the reaction equilibrium to confirm the validity of values used. If there is a significant difference, the experimental equilibrium data can be input into ASPEN Plus model instead to get more representative values of equilibrium conversions. Despite a change in the absolute values, the positive correlation between temperature and conversion and input hydrogen flow and conversion will remain true. Structural properties of iron ore particles that will be used in the actual process should also be experimentally determined to increase the accuracy of the kinetics model.

Another key improvement to be made is developing a fluid dynamics model of the process. Currently, velocity of the falling solid particles are set to 1 ms^{-1}. However, this velocity is not a true independent variable as it must satisfy two other equations. The first is simply, in order to satisfy the output molar flowrate of iron, the particles must be moving at a certain velocity through the reactor. This will depend on the cross-sectional area, the void fraction of the reactor, the density and iron composition of the particles. The second is the relationship between gas velocity and solid particle velocity due to the drag force of the gas acting on the solid. These extra contraints can be added to the equilibrium and kinetics model to find the feasible operating points.

Once the above parameters are obtained, implementing the kinetics model within ASPEN Plus will be vital to completing an accurate economical analysis of the process. This will entail capital and OPEX costs of the process. A particular area of interest will be the analysis of the green hydrogen industry and the future of it's production. With the pricing of green hydrogen likely to decrease when it is widely commercially available, this process will most likely to be a viable solution for the iron industry.

References

Agency, E. (2016), 'Material comparators for end-of-waste decisions. fuels: natural gas', `https://assets.publishing.service.gov.uk/government/uploads/system/uploads/attachment_data/file/545567/Material_comparators_for_fuels_-_natural_gas.pdf`. (Accessed on 12/10/2021).

Atsushi, M., Uemura, H. and Sakaguchi, T. (2010), 'Midrex processes', *Kobelco Technology Review* **29**, 50–57.

Bhatia, S. K. and Perlmutter, D. D. (1980), 'A random pore model for fluid-solid reactions: I. isothermal, kinetic control', *AIChE Journal* **26**(3), 379–386.
URL: *https://aiche.onlinelibrary.wiley.com/doi/abs/10.1002/aic.690260308*

Bhatti, Z. A., Qureshi, K., Bhatti, I., Ashraf, R. F. and Maitlo, G. (2021), 'Arsenic (iii) removal from aqueous water by indigenous iron ore adsorbent from balochistan province of pakistan', *Mehran University Research Journal Of Engineering & Technology* **40**(1), 16–30.

Britannica, T. E. o. E. (2019), *Blast furnace — metallurgy.*
URL: *https://www.britannica.com/technology/blast-furnace*

Calix (2021), 'Calix files a new patent for zero emissions iron and steel'.
URL: *https://www.calix.global/co2-mitigation-focus-area/new-patent-for-zero-emissions-iron-and-steel/*

Chen, F., Mohassab, Y., Jiang, T. and Sohn, H. Y. (2015), 'Hydrogen reduction kinetics of hematite concentrate particles relevant to a novel flash ironmaking process', *Metallurgical and Materials Transactions B* **46**(3), 1133–1145.

Chen, Z., Dang, J., Hu, X. and Yan, H. (2018), 'Reduction kinetics of hematite powder in hydrogen atmosphere at moderate temperatures', *Metals* **8**(10), 751.

Deloitte (2017), 'Iron and steel industry report — deloitte cis — manufacturing', `https://www2.deloitte.com/am/en/pages/manufacturing/articles/iron-and-steel-industry-report.html`. (Accessed on 12/09/2021).

Hara, Y., Tsuchiya, M. and Kondo, S.-i. (1974), 'Intraparticle temperature of iron-oxide pellet during the reduction', *Tetsu-to-Hagané* **60**(9), 1261–1270.

He, K. and Wang, L. (2017), 'A review of energy use and energy-efficient technologies for the iron and steel industry', *Renewable and Sustainable Energy Reviews* **70**, 1022–1039.

IEA (2020), 'Iron and steel technology roadmap - towards more sustainable steelmaking', `https://iea.blob.core.windows.net/assets/eb0c8ec1-3665-4959-97d0-187ceca189a8/Iron_and_Steel_Technology_Roadmap.pdf`. (Accessed on 12/09/2021).

IEA (2021), 'Net zero by 2050 - a roadmap for the global energy sector', `https://iea.blob.core.windows.net/assets/deebef5d-0c34-4539-9d0c-10b13d840027/NetZeroby2050-ARoadmapfortheGlobalEnergySector_CORR.pdf`. (Accessed on 12/10/2021).

iima (n.d.), 'Dri production — international iron metallics association', `https://www.metallics.org/dri-production.html`. (Accessed on 12/10/2021).

Liu, W., Lim, J. Y., Saucedo, M. A., Hayhurst, A. N., Scott, S. A. and Dennis, J. (2014), 'Kinetics of the reduction of wüstite by hydrogen and carbon monoxide for the chemical looping production of hydrogen', *Chemical Engineering Science* **120**, 149–166.

Muwanguzi, A. J., Alevanau, A., Byaruhanga, J. K. et al. (2017), 'Application of different models for the prediction of the kinetics of direct reduction of natural iron ores', *Geomaterials* **7**(04), 117.

Pardo, N. and Moya, J. A. (2013), 'Prospective scenarios on energy efficiency and co2 emissions in the european iron & steel industry', *Energy* **54**, 113–128.

Patisson, F. (2020), 'Hydrogen ironmaking: How it works', *Metals* **10**(7), 922.

Rechberger, K., Spanlang, A., Sasiain Conde, A., Wolfmeir, H. and Harris, C. (2020), 'Green hydrogen-based direct reduction for low-carbon steelmaking', *steel research international* **91**(11), 2000110.

Sarkar, S., Bhattacharya, R., Roy, G. G. and Sen, P. K. (2018), 'Modeling midrex based process configurations for energy and emission analysis', *steel research international* **89**(2), 1700248.

Sceats, M., Hodgson, P., Vincent, A., Thomsen, S., Gill, M. and Rennie, D. (2019), 'A flash calciner'.

Spreitzer, D. and Schenk, J. (2019), 'Reduction of iron oxides with hydrogen—a review', *steel research international* **90**(10), 1900108.

Steinberg, B. (2013), ‘What is the air fuel ratio effect on combustion efficiency?’, `https://sagemetering.com/combustion-efficiency/air-fuel-ratio-effect-on-combustion-efficiency/`. (Accessed on 12/10/2021).

Tsay, Q., Ray, W. and Szekely, J. (1976), ‘The modeling of hematite reduction with hydrogen plus carbon monoxide mixtures: Part ii. the direct reduction process in a shaft furnace arrangement’, *AIChE Journal* **22**(6), 1072–1079.

Turkdogan, E. and Vinters, J. (1971), ‘Gaseous reduction of iron oxides: Part i. reduction of hematite in hydrogen’, *Metallurgical and Materials Transactions B* **2**(11), 3175–3188.

Wagner, D., Devisme, O., Patisson, F. and Ablitzer, D. (2008), ‘A laboratory study of the reduction of iron oxides by hydrogen’, *arXiv preprint arXiv:0803.2831* .

Wiencke, J., Lavelaine, H., Panteix, P.-J., Petitjean, C. and Rapin, C. (2018), ‘Electrolysis of iron in a molten oxide electrolyte’, *Journal of Applied Electrochemistry* **48**(1), 115–126.

WorldSteel (2021*a*), ‘Sustainable steel: At the core of green economy’, `https://www.worldsteel.org/en/dam/jcr:5b246502-df29-4d8b-92bb-afb2dc27ed4f/Sustainable-steel-at-the-core-of-a-green-economy.pdf`. (Accessed on 12/09/2021).

WorldSteel (2021*b*), ‘World steel in figures 2021’, `https://www.worldsteel.org/en/dam/jcr:976723ed-74b3-47b4-92f6-81b6a452b86e/World%2520Steel%2520in%2520Figures%25202021.pdf`. (Accessed on 12/09/2021).

Xing, L.-Y., Zou, Z.-S., Qu, Y.-X., Shao, L. and Zou, J.-Q. (2019), ‘Gas–solid reduction behavior of in-flight fine hematite ore particles by hydrogen’, *steel research international* **90**(1), 1800311.

Optimisation of Machine Learning Models for Drug Discovery

Friedrich Hastedt, Kurt Reynolds

Department of Chemical Engineering, Imperial College London, South Kensington

Abstract

Optimisation of protein-ligand docking models is a major bottleneck in the process of virtual screening in computational drug discovery. Stochastic methods play an important role in solving the highly non-convex optimisation problems encountered in this field which contain no derivative information about the objective function. Herein, we present the results of using a variety of algorithms which include swarm intelligence and evolutionary elements to optimise docking functions. Novel hybridised algorithms have been proposed and their performance was analysed on a machine learning model for drug discovery (DeepDock). Prior to that, the user-input parameters were tuned to a set of relevant benchmarking functions which are representative of the model. The hybridised algorithms were found to outperform conventional techniques on a variety of benchmarking functions. However, the algorithms were seen to prematurely converge on the model. This was attributed to the mismatch in exploitation and exploration capabilities, overfitting parameters to benchmarking functions and unfavourable algorithm heuristics. Nevertheless, the hybridised algorithms are powerful and are expected to perform well on different optimisation problems.

1 Introduction

Computational methods are playing a larger role than ever in drug design. In the past, molecules needed to be synthesised, and analysed using experimental methods: a time-consuming and expensive process. Computational methods allow quick, inexpensive screening of entire libraries of compounds and their respective targets without the need for chemical synthesis or labour-intensive steps. However, the screening and prediction of binding conformations for drug design is not a trivial one. It is imperative for the computational method to be robust and accurate in order to compete with experimental drug discovery procedures [1].

An example of this is DeepDock, a docking method based on artificial intelligence. It uses geometric deep learning for molecular docking, reverse and forward screening in drug design [2]. DeepDock learns a statistical potential based on the estimated distance between the individual atoms of a ligand and the surface mesh of a target protein. The optimal conformation of the ligand is found at the minimum of the statistical potential. In order to precisely predict the binding of the ligand-protein complexes, optimisation techniques are employed.

For this paper, an array of optimisation algorithms have been curated and tested inside DeepDock with the aim of improving the overall performance of the optimisation step. The paper is split into several sections. Within Section 2, the problem is defined and the modelling approach is outlined. The stochastic techniques, which were explored as part of the research and implemented in DeepDock are briefly highlighted in Section 3. Algorithms are developed further as hybridised models in 4. The performance of each benchmarked algorithm on DeepDock is assessed in 5.

2 Preliminaries

2.1 Problem Formulation

Currently, DeepDock's optimisation uses a differential evolution algorithm (imported from the scipy library [3]) which is capable of consistently screening ligands containing up to 10 rotatable bonds successfully. Nevertheless, the algorithm fails to converge for most instances above this value.

By using more efficient optimisation algorithms, DeepDock will be capable of successfully screening ligands containing more rotatable bonds with higher precision in a shorter time frame.

2.2 Modelling Approach

Computing optimal protein-ligand binding conformations is computationally expensive and time-consuming. Therefore, initial algorithms were tested and tuned to a range of benchmarking functions (see Supplementary Information (SI)), which are relatively faster to evaluate. Algorithms which performed well on a range of benchmarking functions in n^{th} dimensional space (n = 2, 5, 10) were considered to be tested on the DeepDock model.

Hybridisation of well-performing algorithms was also considered.

To tune algorithms to the topographies encountered in DeepDock's optimisation step, information about the topographies must be acquired. To do so, two methods were employed:

1. Performances of algorithms tested on DeepDock were compared with the performances on a variety of benchmarking functions. If algorithms performed similarly on DeepDock and a benchmarking function, it is indicative that the two have similar topographies.
2. The DeepDock-computed functions were plotted in lower dimensions; 2 variables were changed at a time while all other variables were kept constant. The plotted surfaces were visually compared to test function landscapes.

Test functions which resembled similar landscapes to DeepDock-computed functions were considered as alternatives.

3 Stochastic Techniques

The nature of the optimisation problems encountered when predicting binding conformations favours the use of derivative-free optimisation techniques [4]. This is because no information about the gradient of the objective function is known. Furthermore, the use of deterministic methods is discouraged. As the topography of the objective function is expected to be highly non-convex, it would be likely for the algorithm to settle in a local optima.

Instead, stochastic methods will be employed. Stochasticity introduces randomness in the optimisation approach. This decreases the likelihood of premature convergence. In this section, different stochastic algorithms that will be used are outlined and explained.(Pseudo-code for each algorithm is available in SI file.)

3.1 Swarm Intelligence

Swarm intelligence algorithms (SIA) deal with the collective behaviour of individuals that interact with each other and their environment through decentralised control. Local information of the individual is exchanged with another, thus no prior information is required about intrinsic properties of the problem. SIA are inspired either by nature (school of fish, flock of birds) or by artificial intelligence [5].

Particle Swarm Optimisation (PSO)

In PSO, a population (swarm) of candidate solutions (individuals) are randomly initialised across the search space. At each iteration of the algorithm, each particle is perturbed by a small distance according to its velocity across the search space. The direction in which a particle will travel is influenced by the entire swarm's globally best position, the particle's own best-known position and a stochastic factor to increase the exploration of the search space [6].

Firefly Algorithm (FA)

FA was first introduced by Yang [7] and it works similarly to PSO in the sense that a population of candidate solutions (fireflies) exhibit behaviour analogously to particles in a swarm. Fireflies are attracted to, and move towards, better candidate solutions. The key difference from PSO is that in FA, fireflies become exponentially less attracted to other candidate solutions as the distance between the two becomes greater. The analogy to nature is that fireflies' light intensity decreases with distance. It has been applied to many types of problems and has been observed to be very powerful [8].

Artificial Bee Colony (ABC)

Also inspired by nature, particularly by the foraging behaviour of honeybees, is the ABC algorithm. The honeybees are split up into employer, onlooker and scout bees. After initialisation, the employer bees will search the close vicinity of known points (food sources) and evaluate their fitness. Onlooker bees will follow the employer bees to their food source probabilistically. In other words, the higher the fitness value of a food source, the more bees will explore its close vicinity. If a food source is poor, it will be abandoned and a scout bee will move to a new point in the search domain [9]. The generation of new points is governed by Eq. 3.1 , where ϕ_i is a random number from $\sim U(0,1)$ for the i^{th} dimension and $x_{k,i}$ is a random food source k.

$$x_{new,i} = x_{old,i} + \phi_i \cdot (x_{old,i} - x_{k,i}) \tag{3.1}$$

3.2 Evolutionary Algorithms (EA)

These types of algorithms are inspired by Darwin's theory of biological evolution. The three fundamental principles applied in evolutionary algorithms consist of natural selection, crossover and mutation. In the selection stage, parents from the population are chosen. During crossover, information between parents is exchanged to create offspring. Finally, the offspring can be mutated based on probability P.

Genetic Algorithm (GA)

Genetic algorithms are one of the most popular application of the evolutionary strategy. The first genetic algorithm was coded in strings of bits (0 and 1s), however it can be equally applied to a continuous search space. The algorithm operates on a population of N individuals, which are initialised over the search space. M number of parents are selected from the population, either by randomness or elitism (best individuals within the population have a higher probability to be chosen) [10]. 2 out of M parents will mate to produce offspring. The mating process requires a crossover operator. For bit strings, common ones are the k-point and uniform operator. As the decision variables are within a continuous domain, the Simulated Binary Crossover was utilised [11] as shown in Eq. 3.2,

$$\begin{aligned} c_1 &= 0.5 \cdot ((p_1 + p_2) - \beta \mid p_1 - p_2 \mid) \\ c_2 &= 0.5 \cdot ((p_1 + p_2) - \beta \mid p_1 + p_2 \mid) \end{aligned} \tag{3.2}$$

where p_i and c_i refer to the i^{th} parent and child, respectively. Finally, after all M parents have mated, the individuals within the population will be replaced by the offspring.

Differential Evolution (DE)

DE is a similar algorithm to the genetic algorithm constructed by Storn et. al. [12]. The main difference lies in the crossover stage. In DE, multiple individuals are used to create an offspring with mutation constant F (Eq. 3.3). Greedy selection between the offspring and individual k is performed to decide if k will be replaced by the offspring.

$$x_n = a_n + F \cdot (b_n - c_n) \tag{3.3}$$

where a_n, b_n and c_n, are the n^{th} dimensional coordinates for randomly chosen individuals a, b, c.

3.3 Simulated Annealing (SA)

SA is inspired by the thermodynamics of metallurgical annealing. In comparison to all other aforementioned algorithms, SA operates on a single point instead of a population of points. The candidate solution is moved randomly in the search space. To be precise, the probability p that the solution will move to a given location is dependent on the fitness of the given location relative to the current solution, and a time-varying parameter, T (temperature) [10]. From $t = 0$, T is large, which allows larger steps to be taken. This however may not result in an improved candidate solution. The approach facilitates "hillclimbing" and therefore, the candidate can escape local optima. As time goes on, T decreases according to a temperature schedule, causing the acceptance probability of new locations to decrease, especially if those locations result in a worse candidate solution (see Eq. 3.4).

$$p := \begin{Bmatrix} 1 & if\ f(x_{old}) > f(x_{new}) \\ else & \exp\left(-\frac{f(x_{old}) - f(x_{new})}{T}\right) \end{Bmatrix} \tag{3.4}$$

It is to be noted that the candidate solution is always updated when there is an improvement in the objective function value, regardless of T.

4 Algorithm Development

4.1 Hybridised Algorithms

The algorithms presented in this section were constructed after identifying the most promising stochastic techniques (see Section 5.2).

4.1.1 Mayfly Algorithm (MA)

A novel technique is the mayfly algorithm inspired by the flight behaviour and mating process of mayflies, first published in 2020 by Zervoudakis [13]. MA effectively combines features of the particle swarm, genetic and firefly algorithms. The algorithm is outlined in Alg. 1.

Algorithm 1 Mayfly Algorithm

```
Initialize:
Randomly spawn $n$ male/female mayflies from uniform distribution: $x(i) \leftarrow U\ (lb, ub)$
Initialise velocity $v(i,d) \leftarrow 0$, $i = 1, \ldots, n$
Calculate fitness $f(x(i)) \leftarrow$ objective function
while Termination Criteria not met do
    for Female i = 0 to n do
        Calculate distance $dt(i)$ between fireflies
        Update velocity of female:
        $v(i,d) \leftarrow g(dt, f(x, mal), f(x, fem))$
        Update position $z(i) \leftarrow x(i) + v(i,d)$
        Update fitness $f(x(i)) \leftarrow f(z(i)$
    for Male i = 0 to n do
        Perform operations similar to female
    for Offspring j = 0 to $n_{offspring}$ do
        Crossover female and male j:
        $x(j, child) \leftarrow g(x(j, mal), x(j, fem))$
        Mutate children based on $p_{mut}$
    Merge offspring with female/male pop
    Sort populations and reduce size to $n$
```

Zervoudakis demonstrated that MA consistently outperforms GA, PSO and FA on a large set of benchmarking functions. The only disadvantage to MA is the large number of parameters that need to be tuned.

4.1.2 Local Search EA - HGA & HDE

The evolutionary techniques lack local information about the objective function which can be improved by employing local search methods. The LS method used in this report was the Nelder-Mead method, also known as Downhill Simplex [14]. The Simplex method was implemented for both the GA and DE such that it is called upon whenever there is an improvement in the global fitness after a full iteration on the generation.

In addition to the LS method, the genetic algorithm was modified into a steady state genetic algorithm (SSGA); see Alg. 2. The difference between GA and the former is that there are no generations in SSGA. Instead, for each iteration, two parents are removed from the population and produce two children. The best two individuals out of the parents and children are added back to the population. [15]. The competition of the parents with their respective offspring will ensure that the diversity within the population stays high [16] in order to counteract early convergence.

Algorithm 2 Local Search - SSGA (HGA)

```
Initialize:
Randomly spawn $n$ individuals from uniform distribution: $x(i) \leftarrow U\ (lb, ub)$
Calculate fitness $f(x(i)) \leftarrow$ objective function
while Termination Criteria not met do
    Pick parents $p_1, p_2 \leftarrow$ tournament of $m$
    Perform Crossover on parents (Eq. 3.2)
    Mutate pair of children by $p_{mut}$
    Calculate distance of children & parents:
    Perform deterministic crowding [16]:
    if $f(child) < f(parent)$ then
        Replace parent with child
    if $f(child) < f(best, pop)$ then
        Perform SIMPLEX search
        Obtain local best result $l(best)$
        Replace $f(best, pop)$ with $l(best)$
        Update population with $l(best)$
```

4.1.3 Improved Firefly (IFA)

The standard Firefly Algorithm contains a monotonously decreasing parameter, α, which represents the magnitude of the stochastic contribution to fireflies' movements. A hybridisation of this algorithm includes a dynamic α which is reactive to how the algorithm is performing [17]:

$$\alpha = \alpha_{max} - (\alpha_{max} - \alpha_{min}) \cdot \frac{I_{max} - I_{mean}}{I_{max} - I_{min}} \tag{4.1}$$

Where I_{max}, I_{mean}, and I_{min} are the maximum, the average and the minimum intensities of the solutions.

Additionally, an evolutionary element has been added to the original FA. As shown in Alg 3, two populations exists and only the fittest fireflies from both populations survive.

Algorithm 3 Improved Firefly Algorithm

```
Initialize:
Randomly spawn $n$ fireflies from uniform distribution: $x(i) \leftarrow U\ (lb, ub)$
Calculate light intensity: $I(i) \leftarrow f(x(i))$
while Termination Criteria not met do
    Initialise second population
    for each firefly i=0 to n do
        for each firefly j $\neq$ i do
            if I(j) > I(i) then
                Calculate distance $r(i, j)$
                Determine attractiveness $\beta$:
                $\beta \leftarrow \beta_{min} \cdot \exp(-\gamma \cdot r(i, j))$
                Move firefly i towards j:
                $v(i) \leftarrow x(i) + g(\beta, \alpha)$
                Evaluate $I(v)$
                if $I(v) < I(x)$ then
                    Update firefly $i$
    Merge populations and sort by intensity
    Reduce population size to n
    Apply Eq. 4.1 to adjust $\alpha$
```

4.2 Hyperparameter Tuning

Using recommended parameters for stochastic methods allows each algorithm to perform reasonably well on a range of problems. Nevertheless, the performance can be elevated by optimising the user-input parameters to the algorithm. Parameters were tuned for the hybridised techniques. As mentioned in Section 2, to avoid long CPU run times (30 min per run), the tuning was done on benchmarking functions with a similar behaviour and topography to the DeepDock model. Two effective methods of doing this were utilised:

1. Logical parameters such as the social and cognitive coefficients in MA can be tuned intuitively to find the optimal balance between function exploration and exploitation.

2. Abstract parameters with less intuitive effects were tuned with a grid search method [18]. The best combination of parameters is given by the lowest objective function value and std. deviation.

Table 1: Peformance of Algorithms on Benchmarking Functions

Algorithms		*DE*		*FA*		*GA*	
Functions	*f*(x)*	Mean	Std. Dev.	Mean	Std. Dev.	Mean	Std. Dev.
2-D Beale	0.0	0.0	0.0	1.0E-10	1.1E-10	5.5E-33	1.1E-32
2-D Goldstein	3.0	3.0	1.8E-15	3.0	1.2E-08	3.0	0.0
5-D Rosenbrock	0.0	4.2E-3	1.5E-03	3.2E-02	2.4E-03	3.1E-02	1.8E-02
10-D Rosenbrock	0.0	6.2	7.8E-01	2.8	3.1E-01	1.5	5.7E-01
10-D Rastrigin	0.0	2.5	1.9	2.8	1.2	2.5E-04	1.4E-04
10-D Ackley	0.0	2.6E-02	3.2E-02	5.7E-04	1.6E-04	2.4E-04	1.1E-03
Algorithms		*PSO*		*ABC*		*SA*	
Functions	*f*(x)*	Mean	Std. Dev.	Mean	Std. Dev.	Mean	Std. Dev.
2-D Beale	0.0	2.2E-03	4.3E-03	1.8E-19	1.9E-19	6.8E-05	3.9E-05
2-D Goldstein	3.0	3.0	3.3E-15	3.0	1.4E-15	3.0	1.7E-03
5-D Rosenbrock	0.0	3.1	1.4	9.3E-16	1.1E-15	4.1	1.7
10-D Rosenbrock	0.0	68.1	32.3	6.6	2.1	52.1	8.9
10-D Rastrigin	0.0	30.2	2.9	2.6	1.3	33.7	8.0
10-D Ackley	0.0	2.0	4.2E-01	4.6E-01	5.6E-01	3.7	1.8E-01

5 Results & Discussion

5.1 Algorithm Benchmarking

All stochastic techniques presented in Section 3 were tested on the benchmarking functions in N-dimensions (see SI file). These results are shown in Table 1 and in Fig. 1a, for the 10-D Rosenbrock. Each algorithm was run 5 times for a maximum of 100,000 function evaluations per run. The upper limit on function evaluations was imposed to capture both the efficiency and accuracy of the algorithm. A tolerance limit of 2.5E-2 was instated for which algorithms can be said to converge even though there is still a numerical error remaining (the numerical error would vanish with more function evaluations). Standard deviation and mean, shown as a transparent area and a solid line in Fig. 1a, were chosen as representative metrics, as they are indicative of the robustness of the algorithm.

It can be observed that all algorithms converged on the global optima for the 2-D Goldstein-Price function. This can be also be said for the 2-D Beale function, where all optimal solutions fall within the tolerance coupled with low standard deviations.

As the DeepDock model is hyper-dimensional, it is important to assess the performance in more than 2 dimensions. Deterioration in performance can be first spotted for the 5-D Rosenbrock function. An increase in the number of decision variables, leads to an exponential growth of the search space. Both the PSO and SA algorithm are seen to prematurely converge as they fail to effectively screen the search domain. For SA, this is the case as there is no information about other points in the search space such as in the population based algorithms. Furthermore, once the temperature T has cooled down, no worse points than the current point will be accepted and the algorithm will converge. For PSO, particles will converge to the best point in the swarm after a certain number of iterations. If no improvement in the objective function is found during the convergence stage, the algorithm will terminate and therefore it is prone to premature convergence.

Increasing the dimensionality further to 10-D, the performance of the remaining algorithms worsens. This can be explained in similar fashion to the PSO algorithm.

The values recorded for the mean and standard deviation indicate that GA, DE and FA are the most robust, hinting at a slight superiority of evolutionary algorithm heuristics. On the other hand, PSO and SA have the largest mean and standard deviation values for the given number of runs.

5.2 Initial Test on DeepDock Model

The tested algorithms were used on DeepDock to optimise a random protein. It was decided to use a protein with a low number of rotational bonds. In other words, the objective function will have a lower number of decision variables and thus, the optimisation process is easier. The 2yge protein from the CASF-2016 with 4 rotatable bonds was chosen. The first 15000 function evaluations have been plotted on the x-axis against the mean objective function value for an average of 4 runs, with a horizontal dashed line indicating the final objective value of DeepDock's original optimisation algorithm (Fig. 1b).

It can be seen that none of the preliminary, unhybridised algorithms performed as well as Deep-

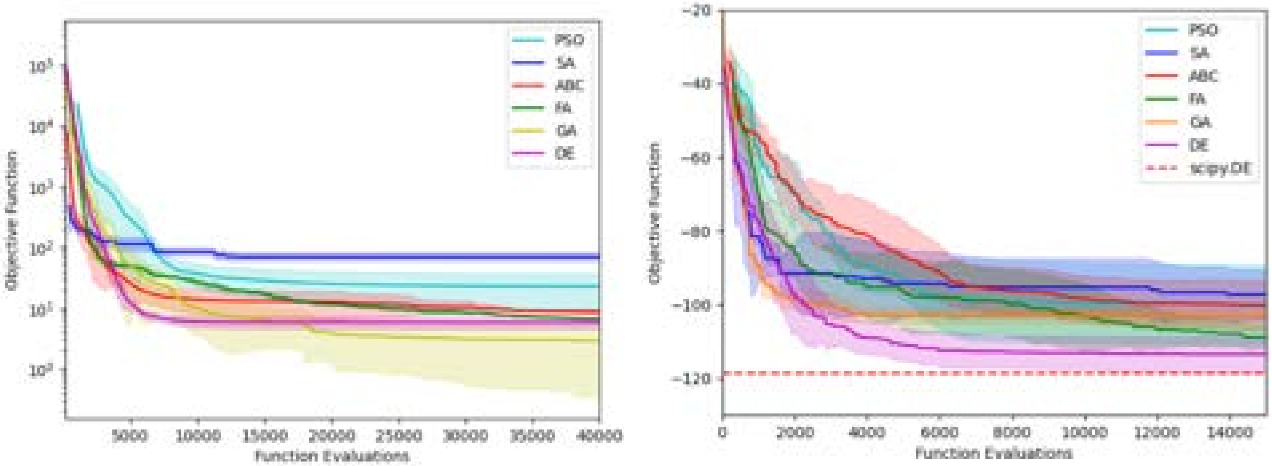

(a) Benchmarking on 10-D Rosenbrock

(b) Initial Test on DeepDock

Figure 1: Performance of Stochastic Techniques

Dock's original differential evolution algorithm (from the scipy library), and most of them converged into local optima. Nevertheless, some algorithms performed better than others. As expected from the initial benchmarking, the SA and PSO algorithms did poorly. Additionally, the best performing algorithms on the benchmark functions can be seen to be the most capable on the DeepDock model. Thus, initial benchmarking can be used as a screening process before deploying the algorithms on the model. It is interesting to note that the FA is the only algorithm which keeps on improving consistently after 12000 evaluations.

The imperative need for more efficient and robust optimisation algorithms becomes clear after analysing the preliminary results. This can be achieved by combining the most powerful features of different algorithms by hybridisation. As DE, GA and FA performed the best, these algorithms were considered for hybridisation as reported in Section 4.1.

5.3 Visualising Model Topography

As outlined in Section 2.2, information about DeepDock's topography in 2-D will be of assistance during parameter tuning. Fig. 2 and Fig 3b are plots of a DeepDock optimisation problem, where all dimensions except 2 have been fixed to their corresponding value at the global optimum. The remaining 2 dimensions are kept as variables.

Fig. 2 is a plot of how objective function varies with Cartesian coordinates. The surface is flat with a sharp peak at the optimum which shows the importance of the Cartesian coordinates in this problem; if the protein is not physically close enough to the ligand, docking is essentially impossible. Similar results were found for the Euler angles of ligand rotation (Fig. 3a)

Fig. 3b is a plot of how objective function varies with bond rotation. The surface is a steep valley-like structure with multi-modal optima. This means that certain less important bonds - likely attached to relatively small groups - can rotate without interfering with docking while other more important bonds need a specific orientation to enable docking.

These plots closely resemble the Easom and Michalewicz benchmarking functions (see SI). For hybridisation and further parameter tuning, algorithms have been benchmarked on these functions as they more closely represent the model.

It is worth mentioning that algorithms might be improved with a search-space reduction (SSR) technique for "Easom-like" topographies. The novel-SSR in [19] was implemented but no improvement in the performance of the algorithms was found.

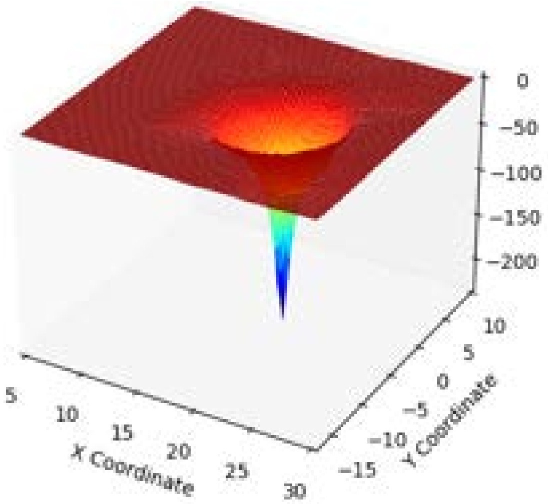

Figure 2: Topography of Cartesian Coordinates

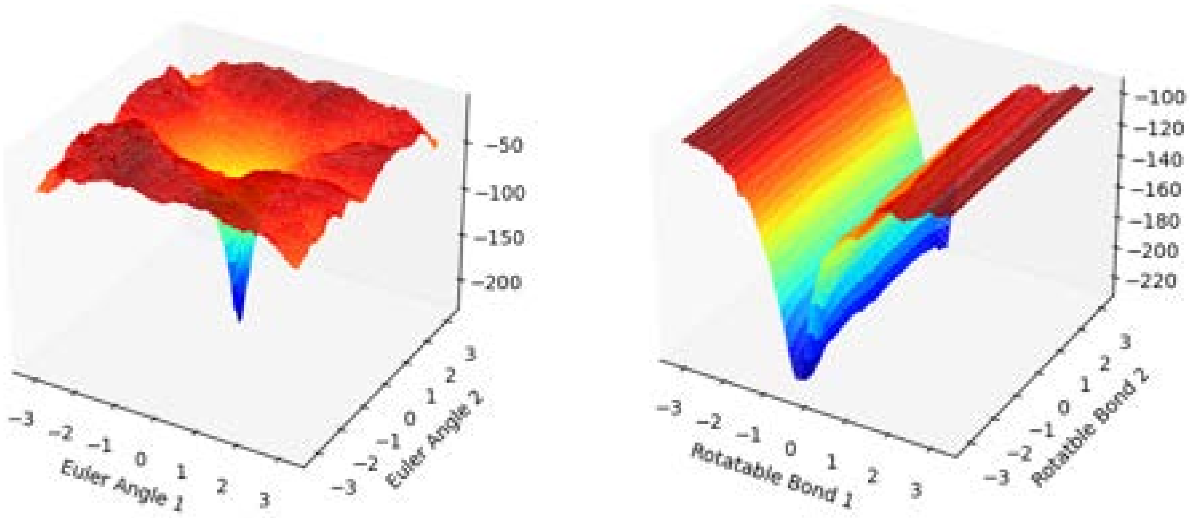

(a) Euler Angles

(b) Bond Rotation

Figure 3: Topography of DeepDock Model

5.4 Parameter Selection

Table 2 depict the user-defined parameters for the algorithms presented in Section 4.1. These parameters were used for all further testing on the benchmarking functions and the DeepDock model. There are three different classifications for the parameters:

First, the flight coefficients for MA and IFA guide the velocity and position vectors of the particles in the swarm. They play an important rule for both maintaining diversity within the swarm and for exploring promising regions in the search space.
The genetic parameters relate to operations that govern the mating and mutation process for pairs of parents and children.
Lastly, the stochastic parameters introduce randomness in the algorithms. They are comparable to the mutation rate F_{mut} in the evolutionary algorithms.

The approach outlined in Section 4 worked well for algorithms with no more than 5 input parameters. However, for the the MA algorithm, it was proven to be infeasible to alter all 9 parameters individually. A more sophisticated method should be employed for future work such as Bayesian optimisation [20].

Table 2: List of Parameters

Swarm Algorithms	*Mayfly Algorithm*	*Improved Firefly Algorithm*
Parameters	$n = 52$; $F_{mut} = 0.01$; $c_{grav} = 0.75$ $p = 1$; $g_1 = 1.3$; $g_2 = 1.5$ $\beta = 2$; $r_{dance} = 1.5$; $r_{flight} = 1.5$	$n = 25$; $\alpha_{min} = 2.0\text{E-}4$; $\alpha_{max} = 1.0\text{E-}3$ $\gamma = 3.0\text{E-}3$; $\beta = 2.24$
Explanation	**Flight Coefficients**: Gravity (c_{grav}), Social (p), Cognitive (g_1, g_2), Weighting (β) **Genetic Parameters**: Population Size (n), Mutation rate (F_{mut}) **Stochastic Parameters**: Random flight of mayflies (r_{dance}, r_{flight})	**Flight Coefficients**: Attraction of fireflies (γ), Weighting (β) **Stochastic Parameters**: Random flight of fireflies ($\alpha_{min}, \alpha_{max}$)
Evolutionary EA	*Local search - GA*	*Local search - DE*
Parameters	$n = 50$, $N_{selection} = 3$ $F_{mut} = 0.01$; $\eta = 3$	$n = 100$; $CR = 0.85$; $F_{mut} = 0.01$
Explanation	**Genetic Parameters**: Mutation Rate (F_{mut}), Crossover Weight (η) **Other Parameters**: Population Size (n), Tournament ($N_{selection}$)	**Genetic Parameters**: Mutation Rate (F_{mut}), Crossover (CR)

Table 3: Performance of Hybridised Algorithms on Benchmarking Functions

Algorithms		*IFA*			*MA*		
Functions	*f*(x)*	Mean	Standard Dev.	Compared to scipy.DE	Mean	Standard Dev.	Compared to scipy.DE
10-D Easom	-1	-1	1.6E-8	=	-1	5.0E-17	=
10-D Michalewicz	-9.66	-8.80	7.5E-1	-	-9.65	1.7E-2	+
20-D Rastrigin	0	33.8	12.8	+	1.7E-10	2.6E-10	++
20-D Rosenbrock	0	13.9	4.4	-	3.7	7.9E-1	+
		HGA			*HDE*		
10-D Easom	-1	-1	5E-10	=	-1	9.2E-12	=
10-D Michalewicz	-9.66	-9.58	7.5E-2	+	-9.43	1.5E-1	=
20-D Rastrigin	0	2.0E-9	3.5E-9	++	20.5	7.8	+
20-D Rosenbrock	0	1.4E-5	1.5E-5	++	1.6	2.2	+

5.5 Hybrid Algorithm Benchmarking

Similar to Section 5.1, the hybridised algorithms were benchmarked. As outlined in Section 5.3, good performance on the Easom and Michalewicz functions should be indicative of the algorithm's performance on the DeepDock model. Moreover, the algorithms were tested on the 20-D Rosenbrock and Rastrigin functions in order to represent the higher dimensionality encountered in the model. Algorithms were run for 100,000 function evaluations and the mean/standard deviation metrics were computed for a number of 5 runs.

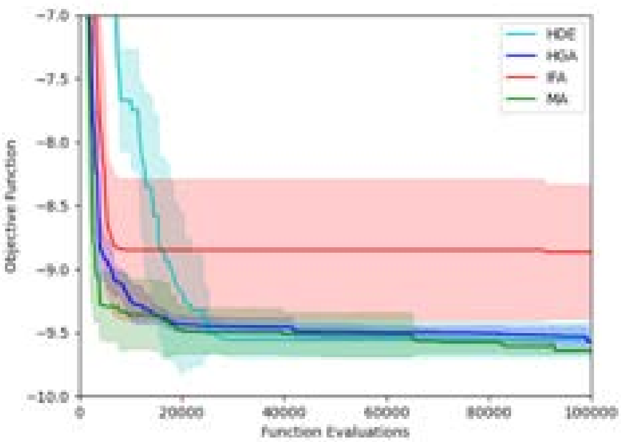

Figure 4: Hybrid algorithms on 10-D Michalewicz

The metrics are shown in Figure 4 and Table 3. The results were compared to scipy.DE, with a ++, +, = and − representing a much better, better, comparable and worse performance, respectively.

It was found that the IFA under-performed in comparison to the other algorithms. This suggests that the elitism heuristic employed when merging and reducing the population size (Lines 15-16 in Alg. 3) might reduce the exploration capabilities of the algorithm. It is seen to be the least robust with the highest standard deviation which might be attributed to the smaller population size n (Tab. 2). On the other hand, HDE, HGA and MA outperformed the scipy.DE on almost all benchmarking functions. Particularly, the HGA shows a large improvement over the GA in Tab 1. Hence, the local search implementation can be considered successful. MA also performed well, with large improvements over the standard PSO and FA algorithms. Thus, the combination of swarm intelligence with evolutionary heuristics (as outlined in Alg. 1) proves to be an interesting field for further research.

5.6 Performance Analysis on DeepDock

Figure 5 depicts the performance on the DeepDock model for a case study of 4 different proteins. No standard deviation was included in the Figure as the random number generator was seeded for reproducibility purposes. The dotted line represents the final value that DeepDock's original optimisation algorithm (Scipy's Differential Evolution) converges to when run on the same protein with the same seed. The red dot shows the point of termination of the algorithm.

A key observation is that the algorithms perform well on problems with a lower number of dimensions. In Fig. 5a all algorithms outperformed the scipy DE and managed to reach the global optima in less function evaluations. However, as the dimensionality increases, the algorithms begin to converge prematurely whereas the scipy DE successfully converges on the global optima.

Another noteworthy observation is that the outcome of benchmarking had very little correlation to performance on DeepDock. Hybrid algorithms which vastly outperformed scipy.DE in benchmarking compared similarly or worse when used for protein docking. Furthermore, MA which was found to perform excellently in Section 5.5, performs the worst in Figures 5b & 5d.

These findings seem counter-intuitive at first and may be explained by considering the following:

1. **Unsuitable Benchmarking Functions:**

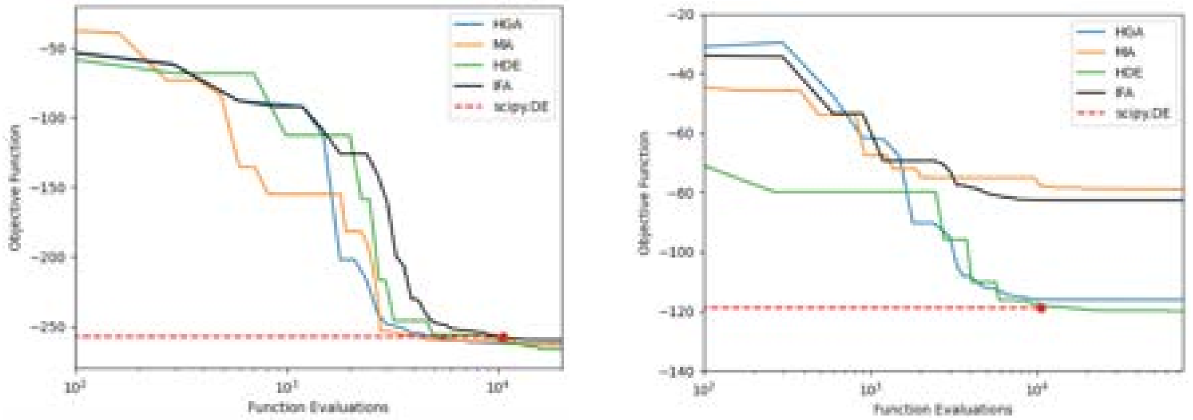

(a) 4 Rotatable Bonds (b) 5 Rotatable Bonds

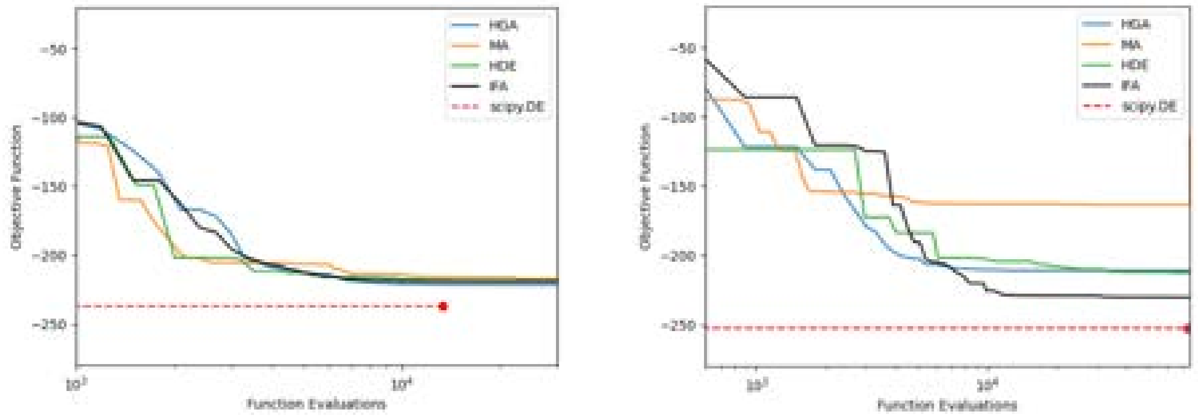

(c) 7 Rotatable Bonds (d) 8 Rotatable Bonds

Figure 5: Performance of Hybrid Algorithms on DeepDock

Based on the results, an inference can be made that the benchmarking functions were not representative of the DeepDock model. The hybrid algorithms may have been tuned too finely during parameter selection and may have been overfitted to the benchmarks which would hinder performance when optimising functions with different characteristics. The scipy.DE was not tuned to these functions which could explain the better performance.

2. **Exploitation vs Exploration**

Specifically, the balance between exploitation and exploration becomes sub-optimal when parameters are overfitted or when unsuitable benchmarks are used. Imbalanced algorithms may either become computationally expensive and have excessive run times caused by over-exploration of the function, or prematurely converge to local optima.

3. **Algorithmic Differences**

The scipy DE algorithm makes use of a strategy known as "best1bin". This means that the best point in the population is perturbed linearly by two other random points. The difference to Eq. 3.3 would be that a_n is replaced by the best point. This perturbation allows for larger jumps in the search space i.e. improved exploration. The hybridised techniques on the other hand, especially IFA and MA, will locate a good point in the search space and search a closer vicinity for an improvement. If there is no better point in the vicinity, it will converge. Thus, if the DeepDock model has optima which are far apart in the hyper-dimensional search space, the hybridised algorithms will fail to explore the different regions. The benchmarking functions on the other hand generally exhibit an "improving search directory". In other words, locating a good point in the search space will aid the algorithm towards the global optima.

Following up from this, the "best1bin" was implemented in order to verify the hypothesis and it was confirmed that the strategy improves the algorithm's performance on the model, but reduces the speed of convergence on benchmarking functions.

6 Conclusion

In this report, results of using various stochastic methods to solve protein docking optimisation problems are presented. Basic swarm intelligent and evolutionary algorithms have been hybridised and upgraded along with local search techniques to elevate the optimisation performance of DeepDock – a method of predicting binding conformations of ligands to proteins based on geometrical deep learning. Two of the best performing algorithms include:

IFA – a swarm intelligence algorithm upgraded with improved loop efficiency and dynamic stochastic features which assess performance during optimisation and alter stochasticity accordingly.

HGA – A non-generational steady state genetic algorithm with an embedded simplex solver providing local search capabilities.

Protein docking functions were visualised in 2-D so that similar known functions which resemble these visualisations could be used as suitable benchmarks on which to perform hyperparameter tuning. After tuning using grid searches, algorithms were used on DeepDock and their performances were compared with each other and with DeepDock's current optimisation technique scipy.DE. On proteins containing relatively few rotatable bonds, and hence in problems of lower dimensions, hybrid algorithms were able to outperform scipy.DE by finding more optimal solutions while using fewer function evaluations. However, when the dimensionality of the problem increases, hybrid algorithms begin to underperform and often prematurely converge to local optima.

To build upon the findings of this project, algorithms such as MA which contain too many parameters to be holistically tuned by grid searches could be optimised using a higher dimensional method such as Bayesian Optimisation. This would increase such algorithms' performances on protein docking optimisation problems.

In addition, using benchmarks which more closely resemble DeepDock's optimisation problems would result in more suitable parameters to be chosen. Alternatively, a subset of functions produced by DeepDock could be used as a training set for hyperparameter tuning. Bayesian Optimisation could then be used to find optimal parameters for each algorithm.

This project is heavily focused on swarm intelligence and evolutionary algorithms but gives little attention to statistical methods. One strategy to highlight is the CMA-ES technique. This technique makes use of a covariant matrix. Covariance is similar to learning second-order information about the objective function [21].

Link to python files: https://github.com/KurtReynolds2000/researchproject/tree/main

References

[1] Lengauer T, Rarey M. Computational methods for biomolecular docking. Current Opinion in Structural Biology. 1996 6;6:402-6.

[2] Oscar-Mendez L, et all. A geometric deep learning approach to predict 2 binding conformations of bioactive molecules; 2019.

[3] Community S. Scipy Differential Evolution;. https://docs.scipy.org/doc/scipy/reference/generated/scipy.optimize.differential_evolution.html.

[4] Larson J, Menickelly M, Wild SM. Derivative-free optimization methods. Acta Numerica. 2019 5;28:287-404.

[5] Dorigo M, Birattari M. Swarm intelligence. Scholarpedia. 2007;2(9):1462. Revision #138640.

[6] Sanyal S. An Introduction to Particle Swarm Optimisation Algorithm; 2021.

[7] Yang XS. Firefly Algorithms for Multimodal Optimization. In: Watanabe O, Zeugmann T, editors. Stochastic Algorithms: Foundations and Applications. Berlin, Heidelberg: Springer Berlin Heidelberg; 2009. p. 169-78.

[8] Kumar V, Kumar D. A Systematic Review on Firefly Algorithm: Past, Present, and Future. Archives of Computational Methods in Engineering. 2021 6;28:3269-91.

[9] Karaboga D. Artificial bee colony algorithm. Scholarpedia. 2010;5(3):6915. Revision #91003.

[10] Fouskakis D, Draper D. Stochastic Optimization: a Review. International Statistical Review. 2002;70:315-49. Available from: http://www.ams.ucsc.edu/draper.

[11] Deb K, Agrawal RB. Simulated Binary Crossover for Continuous Search Space Kalya nmoy D eb' Ram B hushan A gr awal; 1995.

[12] Storn R, Price K. Differential Evolution-A Simple and Efficient Heuristic for Global Optimization over Continuous Spaces. Journal of Global Optimization. 1997;11:341-59.

[13] Zervoudakis K, Tsafarakis S. A mayfly optimization algorithm. Computers & Industrial Engineering. 2020;145:106559. Available from: https://www.sciencedirect.com/science/article/pii/S036083522030293X.

[14] Singer S, Nelder J. Nelder-Mead algorithm. Scholarpedia. 2009;4(7):2928. Revision #91557.

[15] GeeksforGeeks. Steady State Genetic Algorithm (SSGA); 2021. https://www.geeksforgeeks.org/steady-state-genetic-algorithm-ssga/.

[16] LOZANO M, HERRERA F, CANO J. Replacement strategies to preserve useful diversity in steady-state genetic algorithms. Information Sciences. 2008 12;178:4421-33.

[17] Khan WA, Hamadneh NN, Tilahun SL, Ngnotchouye JMT. A Review and Comparative Study of Firefly Algorithm and its Modified Versions. InTech; 2016.

[18] Jordan J. Hyperparameter tuning for machine learning models; 2017. https://www.jeremyjordan.me/hyperparameter-tuning/.

[19] Aeidapu M, Sushnigdha G. A novel search space reduction optimization algorithm. Soft Computing. 2021 07;25:1-28.

[20] Frazier PI. A Tutorial on Bayesian Optimization; 2018.

[21] Hansen N. The CMA Evolution Strategy: A Tutorial; 2016.

Analysis of Carbon Capture Readiness for Backup Diesel Generator Power Stations in the United Kingdom

Haiyang Jiang, Yichen Huang

Department of Chemical Engineering, Imperial College London, U.K.

Abstract

MEA-based post-combustion carbon capture is a promising technology to mitigate greenhouse gas (GHG) emissions. This paper assessed carbon capture readiness for the United Kingdom domestic backup diesel generator power station of net capacity from $5MW_e$ to $30MW_e$. The modelling and simulation of the carbon capture process with 90% capture efficiency are carried out on Aspen Plus V11. Two cooling technologies, forced-draft cooling towers (FDCT) and seawater heat exchangers (SHE) were designed, and a comparison between their impact on carbon capture and storage (CCS) plants size was presented. It was found that carbon capture plant size per MW_e decreased from $111m^2\ MW_e^{-1}$ at 5MW to $42\ m^2\ MW_e^{-1}$ at $30MW_e^{-1}$ when FDCT acts as the cooling system. Similarly, this value decreased from $128m^2\ MW_e^{-1}$ at 5MW to $54.7\ m^2\ MW_e^{-1}$ at $30MW_e^{-1}$ for the SHE scenario.

1 Introduction

With the greenhouse effect intensifying due to the rising carbon dioxide (CO_2) emissions worldwide, the Paris Agreement was first proposed at COP21 (United Nations Climate Change Conference 2015), where governments agreed to work towards a world average temperature rise below the pre-industrial revolution level of 2°C, with a target of 1.5°C. However, a continuing gap in CO_2 reductions was pointed out in the recent COP26 summit (UNFCCC, 2021). Thus, it is foreseeable that a series of stricter regulatory measures will be put in place to ensure that the average temperature rise does not exceed 1.5°C. In addition, the United Kingdom (UK) has been the first major economy to pass the net zero emissions law, which requires it to bring all greenhouse gas emissions to be net-zero by 2050 (GOV.UK, 2019). This has promoted the development of decarbonisation in energy industries. Due to the intermittency of clean energy and requirements of peak shaving, it is vital to have backup power stations. Large capacity combined cycle gas turbines (CCGTs) retrofitted with CCS modules can be employed in urban areas with heavy electricity demand. While there has been an amount of research on decarbonisation for large scale power stations (Sterkhov, et al., 2021) (Schnellmann, et al., 2019), little study has been carried out regarding the CCS for small-scale power plants due to the unclarified emission legislation on small backup generators (GOV.UK, 2016). However, it is inevitable for the UK government to consider the decarbonisation of backup power stations in order to achieve the net-zero emissions target. Therefore, the study on CCS for small capacity diesel generators will be carried out. In addition, the energy penalty and land footprint requirements will be addressed in this report to ensure the CCS is commercially feasible under future carbon capture readiness (CCR) policies.

2 Background

2.1 Post-Combustion Capture

Although green energy has developed rapidly in this decade, thermal power plants will play a key role in electricity generation in the short future because the energy sector cannot be changed overnight. Nevertheless, combustion power plants contribute to the most CO_2 emission, CCS technique makes it feasible to operate thermal power plants synergistically with clean energy under zero-carbon policies. Three types of CCS have gained much attention, including pre-combustion capture, oxy-combustion and post-combustion capture (PCC). Among them, PCC has been viewed as the most promising technique where the exhaust gas from power plants is decarbonised through the CCS process before discharging to the atmosphere. For this reason, it can be retrofitted easily without radical changes on existing power plants (Wang, et al., 2011). Therefore, this is the most economically feasible method for existing power plants.

2.2 Amine Based Solvents

Separation is the most energy-consuming part of the entire process. Davison's work shows that it takes around 80% total cost of CCS (Davison, 2007). Thus, it is essential to choose an appropriate method. Amine-based chemical absorption is most applied to a PCC process because of its reliability and efficiency, despite a high regeneration energy consumption. Monoethanolamine (MEA), diethanolamine (DEA) and triethanolamine (TEA) are available for CO_2 treating. Primary amine is the most thermal unstable when compared with the secondary and tertiary amines. However, this thermal instability merits that MEA has favored kinetics which leads to a higher CO_2 capture efficiency than the others.

In addition MEA is the one most developed amine solvents by far, which has low cost in comparison with DEA and TEA. Admittedly, MEA solvent has inevitable shortcomings at the same time, including corrosion, thermal degradation and high enthalpy of reaction (Rochelle, 2012). Regardless these drawbacks, it still is the most developed and economy feasible solvent. Therefore, this paper is particularly interested at the feasibility of using MEA as a solvent for carbon capture processes in terms of capture efficiency and regeneration energy.

2.3 Diesel Engines

With renewable energy development, backup power stations are becoming increasingly crucial to ensure that energy supplies can be met even when wind turbines and solar panels are not working. Commonly, gas plants have been the most significant part of the reserve due to their large capacity, but the cost to keep it online is high. Compared to this, diesel generators are cheaper and more responsive to switch on and off, which makes them more suitable for providing backup power to nuclear power plants, industrial districts or government offices in the case of an emergency power cut. Based on the demand for diesel power stations and considering the severe pollution emitted by this type of generator, it is foreseeable that carbon emission regulation will become gradually strict and CCR will not only focused on the large-scale power plants in the future.

2.4 Carbon Capture Readiness

The present CCR predominantly emphasises that several evaluations are required prior to constructing large-scale combustion power plants (above 300 MW) from technical and economic perspectives (GOV.UK, 2009). While the CCR is well developed for large capacity power plants, little CCR has been carried out for small-capacity, not to mention CCR for backup diesel power stations.

The land footprint is a key focus in CCR, and numerous studies have been carried out relating to this. In this report, attention will be focused on the small-scale diesel power stations' land footprint. Of this, the following aspects are taken into consideration: 1) carbon capture equipment (including absorber, stripper, heat exchanger, knock-out drum, condenser and direct contact cooler). 2) cooling system. 3) minimum safety distance consideration.

3 Methodology

In this paper, CCS plants have been designed retrofitting to backup power stations in the UK with electricity capacity between 5-30MW$_e$. Generic diesel generators supply the electricity from these stations.

3.1 Exhaust Gas Composition

The composition of exhaust gas from diesel generators are summarised in Table 1. Composition depends on the operating conditions of fuel mixing, combustion chamber condition, air quality; therefore, it will vary between distinctive stations. However, to simplify the analysis, these values are assumed to be invariant throughout this paper. Exhaust gas flow rate is chosen such that amount of CO_2 pre-capture is 960kgMWh^{-1} based on data provided by EIA (EIA, 2021).

Table 1: Exhaust gas composition on molar basis before pre-capture

Component	H_2O	CO_2	O_2	N_2
Molar Composition	11%	12%	9%	67%

CO, NO_x and SO_x are not to present in this analysis. This is because the sum of all these compounds relative composition value is approximately 1mol%, which does not count much in the exhaust gas.

3.2 Reaction Mechanism

Electrolyte NRTL is chosen as the thermodynamic model to deal with non-ideal liquid phase equilibrium, which is contributed by massive, charged compounds. Vapor phase under high pressure can be described accurately by RK equation of state. The above information was implemented into the rate-based model in Aspen Plus V11 to carry out the simulation.

The chemistry of the CO_2-H_2O-MEA system consists of 5 equilibrium reactions (Jana & De, 2014):

$$2H_2O \leftrightarrow H_3O^+ + OH^- \tag{1}$$

$$CO_2 + 2H_2O \leftrightarrow H_3O^+ + HCO_3^- \tag{2}$$

$$HCO_3^- + H_2O \leftrightarrow H_3O^+ + CO_3^{2-} \tag{3}$$

$$MEAH^+ + H_2O \leftrightarrow MEA + H_3O^+ \tag{4}$$

$$MEACOO^- + H_2O \leftrightarrow MEA + HCO_3^- \tag{5}$$

Reaction 1 is water hydrolysis. Reaction 2 is hydro-carbonate formation with water. Reaction 3 represents hydro-carbonate dissociation, while Reaction 4 & 5 are amine deprotonation and protonation, respectively.

The kinetically controlled reactions consist of 4 reactions which are listed below:

$$CO_2 + OH^- \rightarrow HCO_3^- \tag{6}$$

$$HCO_3^- \rightarrow CO_2 + OH^- \tag{7}$$

$$MEA + CO_2 + H_2O \leftrightarrow MEACOO^- + H_3O^+ \tag{8}$$

$$MEACOO^- + H_3O^+ \leftrightarrow MEA + CO_2 + H_2O \tag{9}$$

Where Reaction 8 describes the formation of carbamate; Reaction 9 is the regeneration of amine.

Aspen build-in equations could estimate temperature-dependent equilibrium constants for Reaction 1 to 5:

$$\ln(K) = A + \frac{B}{T} + Cln(T) + DT \tag{10}$$

Table 2: Coefficients in built-in equations of K (Jana & De, 2014)

	A	B	C	D
1	132.8990	-13445.9	-22.4773	0
2	231.465439	-12092.1	-36.7816	0
3	216.050446	-12431.7	-35.4819	0
4	-3.038325	-7008.37	0	-0.00313
5	-0.52135	-2545.53	0	0

Kinetic controlled rates of Reactions 6 to 9 are in the form of reduced power-law expression stated below:

$$r = kT^n \exp\left(\frac{-E}{RT}\right)\prod_{i=1}^{n}(x_i y_i)^{a_i} \tag{11}$$

Table 3: Kinetic parameters for rate-controlled reactions (Aspen Plus., 2008)

	k	E/(kJ*kmol^-1)
6	4.32e13	55433.8
7	2.38e17	123223.0
8	9.77e10	41236.7
9	3.23e19	65500.5

3.3 Process Description

The process simulated with Aspen Plus V11 is the model of CCS plants, where flowsheet is illustrated in Figure 1.

This process starts with a stream of exhaust gas leaving the power station. Next, the exhaust gas is cooled by passing through a direct contact cooler (DCC) with counter-current cooling water before entering an absorber, where the absorption of CO2 into MEA solvent occurs. CO2 depleted flue gas then exits from the top. Meanwhile, CO2-rich amine stream leaves absorber as bottom product. It is then pumped through a rich/lean heat exchanger into a stripper. The stripping column liberates CO2 from the amine solvent, and CO2 vapour flows into a condenser. Subsequently, the condensed CO2 stream is fed into a knock-out drum where the remaining liquid can be separated to yield a higher purity CO2 product.

Overall CO2 capture efficiency achieves 90% for this plant.

3.3.1 Rate-Based Setting

Parameters for rate-based model set-up in RadFrac blocks are referenced from the book of Madeddu (Madeddu, et al., 2018):

- Reaction condition factor is 0.9
- Film discretisation ratio is 10
- Interface area is 1.2
- Liquid phase resistance to discretise film with 5 discretisation points
- Gas-phase film resistance is to consider the film.

3.3.2 Blower

The blower raised exhaust gas pressure by 10kPa to overcome frictional pressure drop in gas pipeline. The pressurized gas then enters DCC.

3.3.3 Direct Contact Cooler (DCC)

DCC acts as a pre-cooler to lower down exhaust gas temperature. This column is packed with random structure

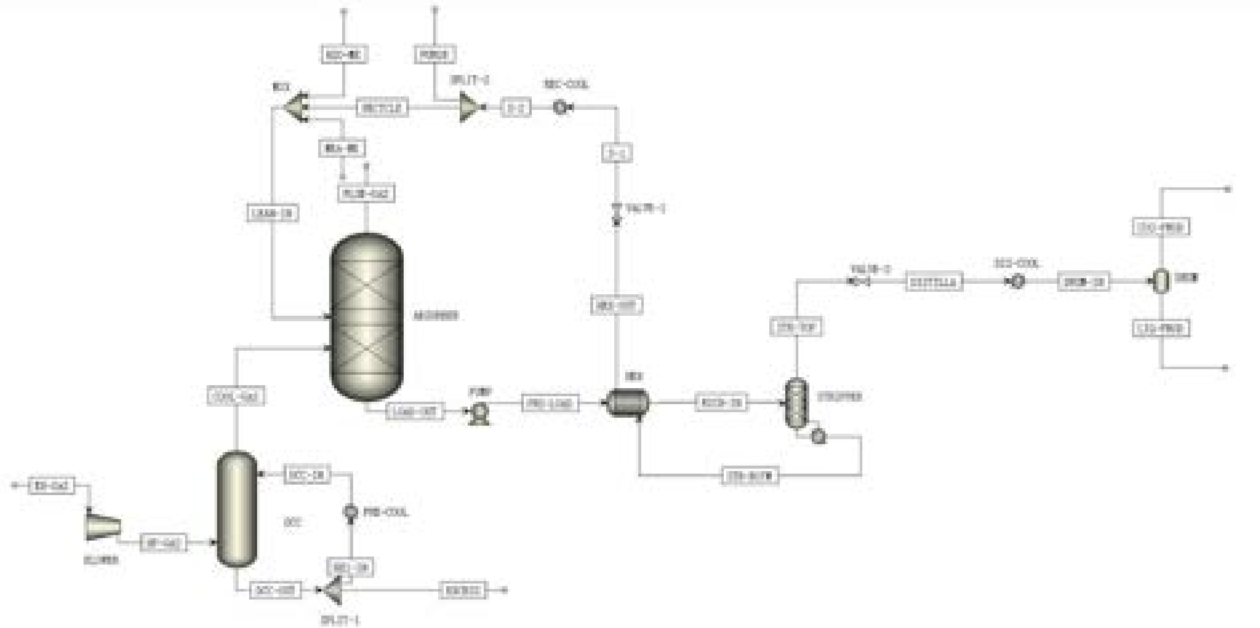

Figure 1: Process flow diagram of amine-based post-combustion carbon dioxide capture process, retrofitted to a diesel power plant

of 16 mm PALL rings. Low-temperature water stream drops down from tower top then contacts with the hot gas rise from this column's bottom. Then cool gas leaves DCC with an excess amount of water due to condensation, which needs to be removed by a splitter to recirculate the rest.

3.3.4 Absorber

The absorbing column is modelled by RadFrac block with an operating condition at 76kPa and 303K. Packing materials with a large surface area and suitability for the capture process ensure a good absorbing ability. As a results, selection of column internal structured packing is Sulzer MELLAPAK^{TM} 250Y (Sulzer Chemtech Ltd, Winterthur, 2010). Cooled exhaust gas is fed into bottom of the absorber, which contacts lean solvent entering top of the column. Regarding solvent flow, extensive study and research have stated 30wt% is an appropriate value for MEA concentration (Puxty, et al., 2009). Lean loading value is fixed at 0.23, which lies in the range literature often reports (Alie, et al., 2005). Combining two values could give minimum CO2 regeneration energy.

Column dimension is optimised by the sensitivity analysis method. Absorber diameter has little effect on absorbing ability, while infeasible hydraulic might be reported if a too small diameter is employed. Therefore, the stage with the highest vapour flow rate is selected as a base stage to determine a minimum diameter.

3.3.5 Rich/Lean Heat Exchanger

This component raises stripper feed temperature to 395K by utilising heat in recycled stripper bottom products. The designing equation is below:

$$Q = U * A * \Delta T_{LM} \tag{12}$$

The minimum temperature approach is selected as 5K. It is designed as a shell and tube heat exchanger (STHE) as it is the most common type of heat exchanger in the industry (Shah & Sekulic, 2003) and has a wide range of operating temperatures and pressures.

3.3.6 Stripper

Similarly to the absorber, stripper model is RadFrac block, internal packing material Sulzer MELLAPAK^{TM} 250Y. Pre-heated stream is fed into top stage of stripping column. Liquid falls to reboiler where low-pressure steam (LP steam) is injected to help reverse reaction, desorbing CO_2. Distillate stream enters a knock-out drum operating at 293K and 1atm, which helps separate CO_2 from H_2O. Meanwhile, regenerated amine solvent leaves the column as bottom product.

The reboiler is designed as a kettle operating at 405K. As previously mentioned in part 3.3.4, the choice of lean loading and MEA mass fraction promises a minimum reboiler energy consumption (Soltani, et al., 2017). Moreover, through sensitivity analysis, stripping column height variation from 3.5m to 6.5m, the value of minimum energy consumption in reboiler is found to be 4.20GJton^{-1}CO$_2$. In literature, it was reported as 4.00GJton^{-1}CO$_2$ using 30wt% MEA to capture CO2, and they had a high level of similarity (Soltani, et al., 2017).

3.4 Cooling System

From Figure 1, heat must be removed from utility water circulating in coolers of this CCS plant. Cooling duty can be estimated by conducting an energy balance around one block:

$$\dot{q}_i = \dot{m}_{i,f} c_{pf} \left(T_{i,f1} - T_{i,f2}\right) \\ = \dot{m}_{i,c} c_{pc} \left(T_{i,c1} - T_{i,c2}\right) \quad (13)$$

Where T represents the temperature, f means the process fluid, c indicates the cooling water, and subscript 1,2 means inlet and outlet conditions. In addition, the index i denotes cooling blocks which are DCC coolers (DCC), recycle cooler (RC) and condenser cooler (CC). Plant-wide cooling duty (q) and cooling water flow rate ($\dot{m}_c$) is therefore as below:

$$\dot{q} = \sum_{i=DCC}^{CC} \dot{q}_i \quad (14)$$

$$\dot{m}_c = \frac{\dot{q}}{c_{pc} * (T_{c2} - T_{c1})} \quad (15)$$

3.4.1 Forced-Draft Cooling Tower (FDCT)

A counter-current forced-draft cooling tower (FDCT) have been designed for scenarios in which the sea or lakes are not approachable in the vicinity of CCS plant location. A fan is installed to blow cool air into the cooling tower. Aspen simulation of cooling towers is in RadFrac block using equilibrium calculation with Murphree efficiency at each stage. Structured packing is selected as plastic Koch-Glitch's FLEXIPAC@-2Y.

Regarding cooling tower operations, an average ambient temperature was chosen as 282K (Jaganmohan, 2021). Considering the circulation water cooling range is 293K to 288K, temperature approach is thus 6K. The cooling tower was designed to consist of 10 cells, and each could draw 30% of the maximum load of air. This design merits that if some cells failed to work, they could be replaced; meanwhile, the rest can still remove heat from cooling water.

Equation (16) approximates base area (A_{CT}) of a cooling tower (G. B. Hill, et al., 2013):

$$A_{CT} = \frac{\dot{m}_c}{F_{loading}} * F_{CR} * F_{AP} * F_{AT} \quad (16)$$

As mentioned previously, liquid loading factor ($F_{loading}$), cooling range factor (F_{CR}), temperature approach factor (F_{AP}), ambient temperature factor (F_{AT}) can all be read from design plots (Figure A.3.4.1 and A.3.5.1 in (G. B. Hill, et al., 2013). The base area calculated with this equation is compared against the value obtained from Aspen simulation. A maximum 7% difference is found among all 6 cases of net capacity in this paper.

3.4.2 Seawater Heat Exchanger (SHE)

An alternative way to cool down plant circulation water is using a shell and tube heat exchanger, where seawater could be utilised as a 'cold stream' if the capture plants' location is in coastal region. Aspen simulation of a SHE is carried out in shell and tube heat exchanger block. Minimum temperature approach is 3K. The cold stream is North Sea water, roughly 3.5wt% is contributed by dissolved NaCl, and temperature is approximately 279K. By specifying outlet 'hot stream' temperature, outlet seawater temperature will rise to 290K. Similarly to cooling towers, multiple STHE in parallel are designed to construct this cooling system. STHE has comparative advantages of two points, low in construction cost and easy in cleaning and dissembling.

3.5 Plant Layout

It is noticed that the actual plant layout is normally much larger than simulated dimensions due to the safety distance limitations between each column. Although the carbon capture process is comparatively low-risk, it still has potential explosive or leakage hazards. Thus, CCS plants should comply with safety distance regulation, which is shown in Figure 2 and Figure 3 separately. All distances are given in meters (m), CP represents codes of practice implemented, and NM means no minimum spacing requirements.

While the non-rectangular shape of plant is generally applied in practice, nevertheless for the ease of calculation and comparison, rectangular layouts are designed in this report according to the following steps. Firstly, the column with the largest diameter is located, which is DCC in this process. Secondly, two sides of a rectangle can be fixed after that by drawing two perpendicular tangent lines of DCC. Thirdly, arrange all other process equipment in a sequence similar to the process flow diagram. Thirdly, add cooling system close to the rectangular side under process units. It is noted that, the location of cooling system can be changed to design an optimised layout. Since at least one side length of this rectangle is dominated by cooling system dimensions. Finally, space all units according to the safety distance requirements. Therefore, the other side length will be regulated by the position of the knock-out drum or the cooling system.

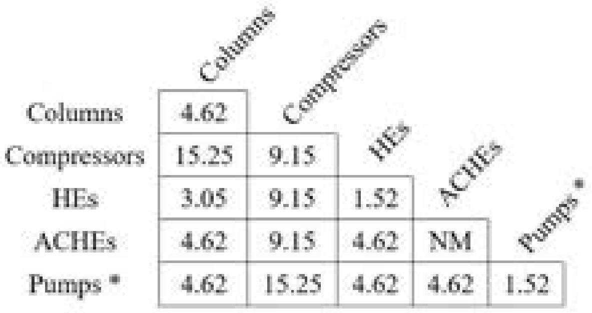

	Columns	Compressors	HEs	ACHEs	Pumps *
Columns	4.62				
Compressors	15.25	9.15			
HEs	3.05	9.15	1.52		
ACHEs	4.62	9.15	4.62	NM	
Pumps *	4.62	15.25	4.62	4.62	1.52

Figure 2: Safety distance limitation (Industrial Risk Insurers, 1991)
Pumps* : The safety distance between high hazard pumps.

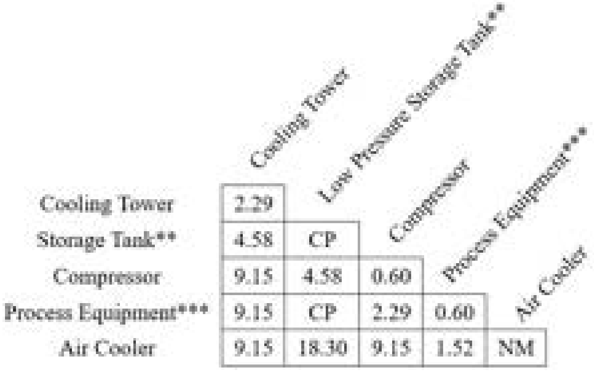

	Cooling Tower	Low Pressure Storage Tank**	Compressor	Process Equipment***	Air Cooler
Cooling Tower	2.29				
Storage Tank**	4.58	CP			
Compressor	9.15	4.58	0.60		
Process Equipment***	9.15	CP	2.29	0.60	
Air Cooler	9.15	18.30	9.15	1.52	NM

Figure 3: Separation distance (Aisyah, 2021)
Storage Tank**: Low-pressure storage tank (less than 1 bar)
Process Equipment***: High flash point

4 Results and Discussion

4.1 Effect of Capacity on Plant Size

An example plant plot in which the CCS is retrofitted to a diesel power station with 30 MW capacity is shown in Figure 4. The cooling system is chosen to be FDCT in this case. Although compression trains play an essential role in practice, their land footprint is not considered in our plots since this report's primary focus is on the carbon capture process. The CCS plant layout has been simplified to a rectangular shape to facilitate comparisons, and the optimisation has been done manually.

In Figure 5, the relationship between the CCS footprint and its capacity is displayed. Comparing two types of cooling systems shows clearly that the SHE requires more area than FDCT at the same capacity. In addition, the slope of the SHE curve is slightly steeper than that of FDCT, which means the footprint's gap will be enlarged for larger-scale power plants. This trend is reliable since the fact that seawater heat exchangers require more heat exchange areas compared with cooling towers. Although some previous works have non-linear trending (Florin & Fennell, 2010), a linear relation is observed in this report based on the following two reasons. On the one hand, the size of columns (DCC, absorber and stripper) increases with the capacity to deal with higher flow rates; however, this growth contributes negligible plant area since plant size is predominantly controlled by the cooling system and safety distances for small-scale power stations. On the other hand, replace one column with multiple smaller columns always increases the footprint requirement. In small capacity cases, the flow rate is able to be handled by one column within its size constraint, so it is unnecessary to replace it with several smaller columns. Thus, no step increase in plant size, which leads to a linear plot. The land footprint of CCS plants can be divided into three major parts, as mentioned in section 2.4, which are equipment, cooling system and safety distance.

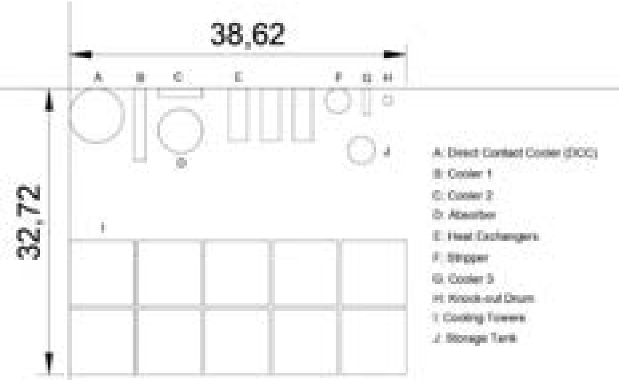

Figure 4: Layout of amine-based post-combustion CCS, retrofitted to a diesel power station with 30MW capacity

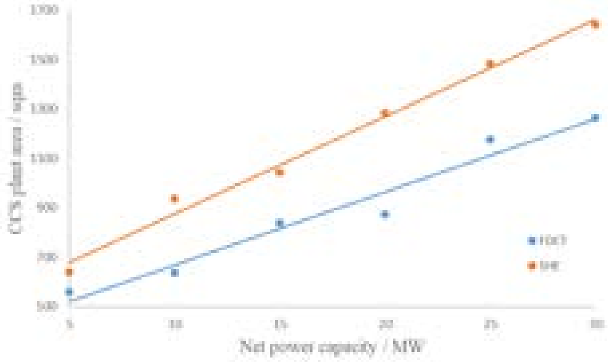

Figure 5: Effect of capacity on CCS plant size

In Figure 6, percentage of area taken up by each sector is compared for the scenario deploying cooling towers. As can be seen, safety distance is predominant in small-scale CCS. It contributes half of the total area for 30 MW

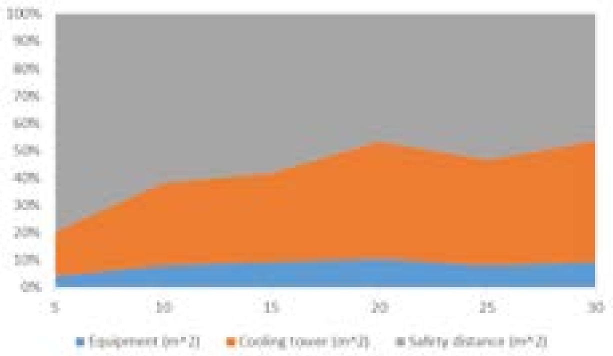

Figure 6: Percentage of the area taken by each sector

scenario, and this ratio grows to 80% at 5MW. Therefore, this ratio will keep growing when capacity is decreasing since safety distances are fixed. By contrast, the cooling tower area increases proportionally with capacity.

The specific footprint, measuring footprint requirement per MW_e capacity, is shown in Figure 7 for FDCT cooling system. Manual optimisation brings about fluctuations in the plot. 111.7 m^2MW^{-1} specific footprint is observed at 5 MW capacity. In contrast, this value declines to $42.1m^2MW^{-1}$ for 30 MW. It shows that less land footprint is required per unit of generation as the plant's capacity raises. It is worthy to notice that the specific area falls rapidly from 5MW to 10MW, after that the rate of decreasing slows down, eventually, it reaches a steady state. Thus, a power law correlation for specific footprint is predicted with an asymptote line at $37.2m^2MW^{-1}$.

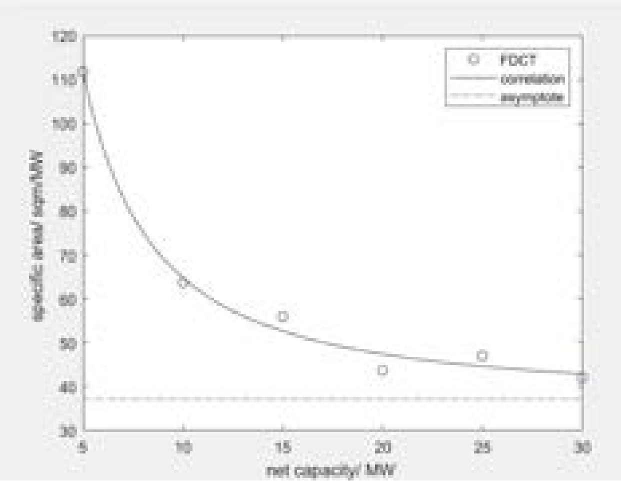

Figure 7: Effect of capacity on specific CCS plant size

This plot is compared with the previous work from Frewin and Fennell (Frewin, et al., 2020). In their work, the specific plot size decreases from about $28m^2MW^{-1}$ to around $25m^2MW^{-1}$ when net capacity increases from 300MW to 1500MW, and it remains steady with further increase to 2200MW. Figure 7 has resembled correlations, where the steady value is $37.2m^2MW^{-1}$. This large gap can be understood as following reasons.

First of all, in this report, all plant layouts were optimised manually resulting in an oversized footprint. Other than doing manually, the optimum footprint was designed by optimisation program in Frewin and Fennell's work. Consequently, all specific plot sizes are higher than minimum values.

The second reason is within cooling systems. The flexible number of cooling cells helps constructing a better plant layout. However, the quantity of cells is fixed in this report, which limits the performance of optimisations.

Finally, the asymptote line is obtained based on a current situation that number of columns are fixed within all scenarios below 30MW. However, it is necessary to have additional columns when the diameter exceeds the constraint which is normally found in large-scale power plants. Meanwhile, the effect of safety distance limitation is weakened as shown in Figure 6 with the raise of capacity. Therefore, the total plot size will be dominated by equipment area at large capacity scenario. The effect of increase in net capacity will outweigh the effect on plant area brought up by capacity variation. Therefore, a negative step change in specific plant layout takes place when additional columns installed. As the increase of capacity, the number of additional columns will increase and will integrate negative step changes to form a staggered curve finally. That is one possible reason for a downward movement of an asymptote line.

4.2 Simulation Performance

4.2.1 Choice of Lean Loading and Validation

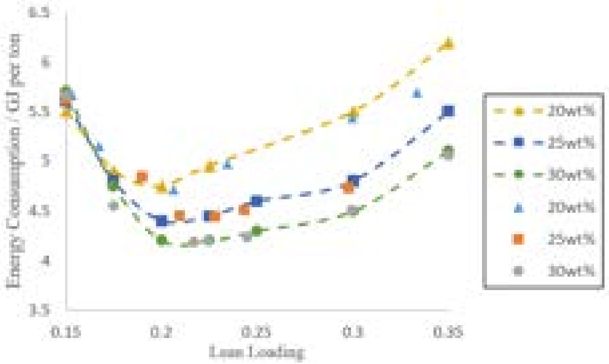

Figure 8: Energy consumption at CO_2 composition 4mol% by varying MEA mass fraction

Simulation of this capture process was run with lean loading (θ)values ranging from 0.15 to 0.35 (Bui, et al., 2018), meanwhile, holding amine solvent mass fraction as an invariant at 30wt%. It was found that minimum simulation reboiler consumption is $4.20GJton^{-1}CO_2$ which performed a high level of similarity with literature value 4.00GJton^{-1}CO$_2$ (Soltani, et al., 2017) with CO$_2$ lean loading at 0.229. To test the validity of this data, multiple testing simulations were carried out by varying exhaust gas flow rate and streams parameters (θ, MEA mass fraction, CO$_2$ molar composition). The result is illustrated in Figure 8. The dash plots represent minimum energy consumption based on the optimisation program (Soltani, et al., 2017), and symbols are results of testing simulations. Turning points of both data sets locate around 0.21-0.23. It is worth noticing that the testing reboiler consumption with parameters 0.225, 30wt% hit the bottom of the graph around 4.21GJton^{-1}CO$_2$. Reading the graph further shows that lean loading rate plays a secondary role in regeneration energy consumption, and amine solvent concentration poses a more significant effect on that. As mass fraction increase from 20wt% to 30wt%, the location of minimum energy also starts shifting towards right gradually. Corresponding lean loading values also increase from about 0.20 to 0.23. The breakdown of reboiler regeneration energy consumption is illustrated below:

$$\Delta H_{reg} = q_{vap} + q_{sen} + q_{desorb,CO_2} \tag{17}$$

q_{vap} means latent water heat of vaporisation, q_{sen} is sensible energy requirement to rise amine solvent temperature to that of reboiler, and q_{desrob,CO_2} represents energy of CO$_2$ desorbing from MEA. Sum of all these terms gives regeneration energy ΔH_{reg}.

It is necessary to mention that MEA and water flow rate both decrease when lean loading value increase. As a result, when the value of θ is lower, the process stream needs a higher amount of latent energy to produce more water vapour. This explains why regeneration energy consumption increase when θ drops from 0.23 to 0.15. At higher lean loading values, latent heat of water vaporisation is more negligible while q_{sen} contribute to regeneration energy consumption significantly. When streams MEA solvent flow rate is low, most MEACOO$^-$ ions leave stripper's bottom; therefore, CO$_2$ captured will be lower than specification. To maintain a degree of capture at 90%, more sensible heat must be supplied to keep the temperature of amine, amine complex ions same as that of reboiler. This is the reason behind the upward trend of plots when 0.23 to 0.35 is the region of θ. This is persuasive enough to convince that lean loading rate (θ) at 0.23 is a value that could be applied to most carbon capture scenarios to get optimal reboiler energy consumption when 30wt% MEA is selected as solvent.

4.1.2 Energy Consumption

The stripping column is the most energy-consuming component in capture plant discussed in this paper. Normalised energy penalty (ΔE_{loss}) is a key index to assess the impact of the CCS plant on the power station.

$$\Delta E_{loss} = \Delta H_{reg} * \dot{m}_{CO_2} * \eta_k \tag{18}$$

Where $\dot{m}_{CO_2}$ is mass of CO$_2$ produced when 1 MWh electricity is generated, η_k is CO$_2$ recovery efficiency. Table 4 compares the energy penalty of 3 types of power plants, all at 90% capture efficiency:

Table 4: Energy penalty of different types of power plant

Energy Penalty in GJ/MWh		
Coal-fire	CCGT	Diesel Generator
2.33	1.5	3.67

The results tell that diesel power station CCS incurs a considerable energy penalty, 1.6 times that of a fire plant and 2.5 times that of a gas turbine.

Energy penalty is not a burden to power stations as it could be powered by residual heat flows from diesel engines. Diesel generators have a maximum electrical efficiency of about 35% (Wheeler, 2017). The rest amount of heat was dissipated by engine cooling. Therefore, LP steam (about 433K) formed in the cooling process can be injected into the reboiler directly without an external heat source.

5 Conclusion

The post-combustion CCS process using 30wt% MEA as solvents retrofitted to various capacities of diesel power stations from 5MW$_e$ to 30MW$_e$ has been simulated and analysed in this paper. Two cooling scenarios were proposed to assess the impact on the total plant area plots, including seawater heat exchanger (SHE) and forced-draft cooling tower (FDCT). It concludes that CCS plant size increases linearly with the power station capacity for both technologies. However, the area required for the SHE scenario is constantly higher than that of FDCT. Despite the fact that SHE requires a larger footprint, it is still a better technique for coastal CCS when considering the safety issue caused by strong wind and the cost of replacing the cooling unit due to seawater corrosion. On the other hand, despite small-scale CCS being technically achievable by using residual heat from diesel engines to compensate large energy penalty, an enormous specific footprint at 5MW is observed, which results in a tremendous unit cost. In conclusion, CCR should be renewed carefully when the capacity is less than 20MW, and for the value above that a specific area at $43.7\mathrm{m}^2\mathrm{MW}^{-1}$ should be set aside.

Reference

Alie, C., Backham, L., Croiset, E. & Douglas, P. L., 2005. Simulation of CO2 capture using MEA scrubbing: a flowsheet decomposition method. *Energy Conversion and Management*, pp. 475-487.

Aspen Plus., 2008. *Rate Based model of the CO2 capture process by MEA using Aspen Plus.,* Cambridge, MA, USA: Aspen Technology Inc.

Bui, M. et al., 2018. Carbon capture and storage: the way forward. *Energy & Environmental Science*, pp. 1062-1176.

Davison, J., 2007. Performance and costs of power plants with capture and storage of CO2. *Energy*, pp. 1163-1176.

EIA, 2021. *How much carbon dioxide is produced per kilowatthour of U.S. electricity generation?.* [Online]
Available at: https://www.eia.gov/tools/faqs/faq.php?id=74&t=11
[Accessed 6 12 2021].

Florin, N. & Fennell, P., 2010. *Assessment of the validity of 'Approximate minimum land footprint for some types of CO2 capture plant',* London: United Kindom Department of Energy & Climate Change.

Frewin, J. M., Fennell, P. S., Tighe, C. J. & Low, C. C., 2020. Minimising the Plot Size of CCS Plant: Process Design and Intensification.

G. B. Hill, E. J. Pring & Osborn, P. D., 2013. *Cooling Towers Principles and Practice.* 3rd ed. s.l.:Elsevier Science.

GOV.UK, 2009. *Carbon Capture Readiness (CCR).* [Online]
Available at: https://assets.publishing.service.gov.uk/government/uploads/system/uploads/attachment_data/file/43609/Carbon_capture_readiness_-_guidance.pdf
[Accessed 6 12 2021].

GOV.UK, 2016. *Consultation on reducing emissions from Medium Combustion Plants and Generators to improve air quality.* [Online]
Available at: https://consult.defra.gov.uk/airquality/medium-combustion-plant-and-controls-on-generators/supporting_documents/161221%20Amended%20Condoc%20%20published.pdf
[Accessed 1 12 2021].

GOV.UK, 2019. *UK becomes first major economy to pass net zero emissions law.* [Online]
Available at: https://www.gov.uk/government/news/uk-becomes-first-major-economy-to-pass-net-zero-emissions-law
[Accessed 30 11 2021].

Jaganmohan, M., 2021. *Monthly average daily temperatures in the United Kingdom (UK) from 2015 to 2021.* [Online]
Available at: https://www.statista.com/statistics/322658/monthly-average-daily-temperatures-in-the-united-kingdom-uk/
[Accessed 6 12 2021].

Jana, K. & De, S., 2014. Biomass Integrated Combined Power Plant with Post Combustion Co2 Capture – Performance Study by ASPEN Plus®. *Energy Procedia.*

Madeddu, C., Errico, M. & Baratti, R., 2018. *CO2 Capture by Reactive Absorption-Stripping: Modeling, Analysis and Design.* s.l.:s.n.

Puxty, G. et al., 2009. Carbon Dioxide Postcombustion Capture: A Novel Screening Study of the Carbon Dioxide Absorption Performance of 76 Amines. *Environmental Science & Technology*, p. 6427–6433.

Rochelle, G. T., 2012. Thermal degradation of amines for CO2 capture. *Current Opinion in Chemical Engineering*, pp. 183-190.

Schnellmann, M. A., Chyong, C. K., Reiner, D. M. & Scott, S. A., 2019. *Deploying gas power with CCS: The role of operational flexibility, merit order and the future energy system,* s.l.: s.n.

Shah, R. K. & Sekulic, D. P., 2003. *Fundamentals of Heat Exchanger Design.* s.l.:s.n.

Soltani, S. M., Fennell, P. S. & Mac Dowell, N., 2017. A parametric study of CO2 capture from gas-fired power plants using monoethanolamine (MEA). *International Journal of Greenhouse Gas Control*, pp. 321-328.

Sterkhov, K., Khokhlov, D., Zaichenko, M. & Pleshanov, K., 2021. *A zero carbon emission CCGT power plant and an existing steam power station modernization scheme,* s.l.: s.n.

Sulzer Chemtech Ltd, Winterthur, 2010. *Structured Packings for Distillation, Absorption and Reactive Distillation.* [Online]
Available at: http://www.rcprocess.se/bdh_filearea/Sulzer_Kuhni/Structured_Packings.pdf
[Accessed 11 12 2021].

UNFCCC, 2021. *COP26 Reaches Consensus on Key Actions to Address Climate Change.* [Online]
Available at: https://unfccc.int/news/cop26-reaches-consensus-on-key-actions-to-address-climate-change
[Accessed 30 11 2021].

Wang, M. et al., 2011. Post-combustion CO2 capture with chemical absorption: A state-of-the-art review. *Chemical Engineering Research and Design*, pp. 1609-1624.

Wheeler, K. R., 2017. *Efficient Operation of Diesel Generator Sets in Remote Conditions.* [Online]
Available at: http://hdl.handle.net/10919/78374
[Accessed 12 12 2021].

The Effect of pH on Peptide Solubilities and Batch Crystallisation

Ruiyan Gao, You Cheng

Department of Chemical Engineering, Imperial College London, South Kensington Campus, London SW7 2AZ, U.K.

Abstract

Peptides as building blocks for many therapeutic compounds has complexities in their physical-chemical properties. With interest in the effect of pH on peptide solubility and crystallisation behaviour, glycine as one of the simplest and most common fragments in peptides is investigated in this work together with diglycine. The solubility of both species appears to have a dramatic increase at extreme pH and minor fluctuation in the middle. With experimentally determined solubilities under different pH, batch crystallisation was conducted in both neutral and acidic conditions. A significant decrease in induction time was found in both glycine and diglycine crystallisation in addition of acid. Samples of crystallisation were then examined under the microscope and smaller but higher number of crystals were found in acidic condition. The crystallisation observations are in accord with Classical Nucleation Theory. In addition, different glycine crystal structure is observed under acidic condition. In comparison to previous works, the different crystal structure was believed to be γ-glycine instead of α-glycine in neutral condition.

Key Words: Glycine, Diglycine, pH, Solubility, Crystallisation, Induction Time

1. Introduction

The physical and chemical properties of biomolecules have drawn more attention because of their wide applications in chemical, pharmaceutical and food industries, especially for drug discovery (Xia, et al., 2008). More than 7000 naturally existing peptides were identified. 500 of them were discovered with therapeutic function and 155 of them have already been applied in clinical treatment (Negahdaripour, et al., 2019). Since peptides can bind to the specific cell surface receptors, leading to its selectivity and efficacy of signal indication, they have been proven to play a crucial role in human physiology Additionally, the protein is composed of at least 20 peptides which means its molecule size is much larger than that of peptides. Hence, compared with peptide-based therapeutics, both the complexity and cost for the manufacture of protein-based biopharmaceutics are much higher. Therefore, peptide-based therapeutics is of importance and prevalence due to its safety, tolerability, efficacy and lower operating cost (Fosgerau & Hoffmann, 2015).

The purification of peptides is essential before delivering as drug active pharmaceutical ingredient (API) to patients. However, alternative purification technologies are being investigated because not only it is challenging for multi-step chromatography to handle the concentration of peptides beyond 5g/L, but also over 80% of consumption in peptide-based products manufacture comes from the downstream process. Since the crystals are considered as the purest and most stable state of a substance which facilitates isolation, formulation and storage, crystallisation is proposed as the better alternative for downstream bioprocess (Li, et al., 2020). Moreover, the historical evidence such as the crystallisation of microbial lipase from concentrated broth done by Jacobsen and batch crystallisation of antigen-binding fragment FabC225 conducted by Hekmat can also support the feasibility of crystallisation (Jacobsen, et al., 1998) (Hebel, et al., 2013). For designing a rational crystallisation process, solubilities of peptides under various conditions should be examined. Although the solubility can be calculated from thermodynamic data of pure components, it is difficult to obtain these values since the activity coefficients of components in the solution are hard to determine (Mohan, et al., 2002). Therefore, the common path for obtaining solubilities is still by exhaustive experiments.

Several research related to factors influencing crystallisation performance such as the stirring speed, supersaturation ratios and pH shifts have been done. As for stirring speed, Zwietering's correlation can be used to determine the minimum speed required for uniform suspension of solids in the mixture and the correlation is shown below (Ibrahim, et al., 2012).

$$N_{js} = S\left(\frac{g(\rho_S-\rho_L)d_p}{\rho_L}\right)^{0.45}\frac{\nu^{0.1}X^{0.13}}{{d_p}^{0.25}D^{0.85}} \qquad (1)$$

The supersaturation ratio is the driving force for crystal nucleation and growth, which plays a significant role in the crystal size distribution and morphology of crystals formed. For the low value of supersaturation ratio under cooling crystallisation, the rate of growth is faster than that of nucleation, resulting in a longer induction time and a larger size of crystals. The opposite phenomenon is observed when the supersaturation ratio is high (Mettler-Toledo, 2021). Researchers also found the pH environments can affect the solubility of peptides due to zwitterions formed in the aqueous state. The anti-solvent crystallisation with hydrochloric acid was carried out which shows a larger pH shift leads to a reduction in the induction time (Jansens & Horst, 2006). Therefore, in this project, the aim is to combine these two previous works and reduce the induction time with cooling crystallisation under different pH conditions when the supersaturation ratio is low.

Peptides is a short chain of amino acids, linking via peptide bonds. All twenty amino acids are zwitterions since they have at least one amino group accepting the proton to obtain a positive charge and at least one carboxyl group donating the proton to yield a negative charge, shown as the following equation.

$$HOOC - CR - NH_{2(aq)} \rightleftharpoons {}^{-}OOC - CR - NH_{3\,(aq)}^{+} \quad (2)$$

They have different properties due to unique side-chain R groups which lead them to range from basic to acidic and from hydrophilic to hydrophobic (Bischoff & Schlüter, 2012). Consequently, for better understanding the nature and behaviour of complex peptides, this research starts with the fundamental amino acid, glycine, and its oligopeptide as a baseline. The main objective is to measure the solubilities of glycine and glycylglycine (diglycine) under the pH range from 4 to 9 at the temperature range from 10 °C to 35 °C. These results would reveal how the thermodynamic behaviour of peptides is affected by the pH environment, and an appropriate framework for the crystallisation of the peptides was also proposed.

2. Methodology

2.1. Material

Glycine (Lot: SLCH2838) and diglycine (Lot: SLBZ1949) were both purchased from Sigma and used without further purification. Hydrochloric acid with volumetric fraction 37% (Lot: 18E154017) and sodium hydroxide solids (Lot: 16A080020) were analytical grade and obtained from VWR Chemicals. Both were used to provide different pH environments, but simultaneous addition of both acid and base was avoided to prevent salts formation. In this project, solvents with pH=1, 2, 3, 4, 5, 6, 6.5, 7, 9, 11, 12 and 13 were prepared. The pH values of solutions were measured before and after the addition of peptides since peptides are zwitterion. Deionized water was obtained from a Millipore-Q system in the analytical lab.

2.2. Calibration Curve

According to Beer-Lambert's Law, the absorbance is proportional to the concentration of the solution, shown in the following formula (Swinehart, 1962):

$$A = \varepsilon \ell c \quad (3)$$

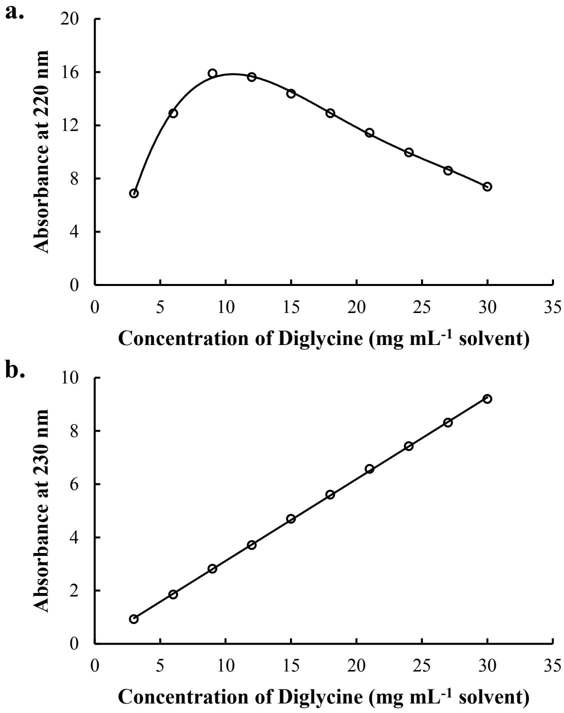

Figure 1. a. The absorbance at 220 nm against the concentration of diglycine; **b.** The absorbance at 230 nm against the concentration of diglycine.

Therefore, ultraviolet (UV) spectroscopy was used to detect the amount of glycine and diglycine dissolved in the solvent, since the peptide bond has a strong absorption peak at 190 nm. However, in practice, the peak was set in the range of 200 to 230 nm for detectors (Hamrníková, et al., 1998). Therefore, the calibration curve for each peptide solution is constructed by measuring the absorbance of known concentrations in the range of 200 to 230 nm. Beer-Lambert's law is only valid for the low concentration range and the overall function of the absorbance against the concentration at a certain wavelength presents a concave function. Taking the absorbance at 220 nm for diglycine as an example which is shown in Figure 1.a, it is likely to have two possible concentrations under the same value of absorbance.

Hence, after the stock solution is prepared, the concentrations of testing samples were diluted into a feasible range, typically from 0 mg mL^{-1} to 30 mg mL^{-1}, and the appropriate wavelength was chosen so that the absorbance is linearly increasing with respect to the selected concentration range, like Figure 1.b. Additionally, the difference between absorbances of two adjacent diluted concentrations should be large enough to avoid an extensive change due to the small fluctuation in absorbance.

2.3. Solubility Measurement

For ensuring the solubility has reached its dissolution equilibrium, an excess amount of peptide, typically approximately 400 mg, was added into 1 mL solvent prepared by using hydrochloric acid or sodium hydroxide. At a specific temperature, solubility measurements of 12 pH conditions were carried out. After testing samples were prepared, they were set in Thermo Mix HCM100-Pro with mixing frequency 1000 rpm at a desired temperature. The shaking time was at least 40 hours to make sure the solution equilibrium was achieved (Lu, et al., 2006). Then, the solution and residual solids were separated by centrifugation. To obtain the solubility of the sample, its supernatant was diluted into the selected range indicated in the calibration curve to prevent extrapolation. Finally, the diluted solution was tested at least 4 times with UV spectroscopy from ThermoFisher with modelling of NanoDrop One and its averaged absorbance was taken to calculate the solubility. Since the solubility of peptides decreases as the temperature drops, for investigation on temperatures below the room temperature, the solution was pre-cooled to avoid crystallisation inside the vials. There was no precaution for the operating temperature above the room temperature.

2.4. Batch Crystallisation

After collecting solubility data for different pH and temperatures, the cooling peptide batch crystallisation was carried out. In this project, how pH environment, especially in the acidic condition, affects the characteristics of crystallisation was investigated. Therefore, the only variable manipulated was the pH value of solvent used. Prior to the examination of pH effect on crystallisation, other operating factors were optimised such as the supersaturation ratio, rotation speed and cooling intervals to obtain an acceptable induction time, usually within 50 minutes. After a few trial experiments, the rotation speed for all batch crystallisations was set to be 150 rpm and the baseline temperature for glycine and diglycine were chosen to be 12.5 °C and 10 °C respectively. The supersaturation ratio for glycine was around 1.18 and that for diglycine was approximately 1.38 because of longer chains (Manimekalai & Selvarajan, 2015).

The stock solutions were prepared in advance and heated at 50 °C for 5 hours with stirring speed of 420 rpm until solids were fully dissolved. Its concentration was calculated by multiplying the supersaturation ratio with the baseline solubility. The timer and the camera were started when the solution was transferred into the vessel and the agitator was turned on. The plastic plugs on the top of the vessel were hermetically sealed to prevent the solvent from evaporating during the experiment. The photos of the vessel were captured every two minutes to get an accurate induction time. The sample was taken continuously at the time interval of 10 minutes before the nucleation started and sampling volume was kept less than 0.2 mL to reduce the influence on the volume of the stock solution. As the solution began to get turbid, the sampling frequency was increased to create a smooth concentration profile. After the concentration of the sample reached the baseline solubility for at least three consecutive samples, the batch crystallisation was terminated. In addition, to examine the morphology and growth of the crystals formed, the suspension samples were withdrawn from the vessel and observed under the microscope at the beginning and end of crystallisation.

Figure 2. Three consecutive captures of crystalliser from 20 to 24 minutes with 2-minute interval.

3. Result and Discussion

3.1. Glycine and Glycylglycine Solubility

Experiment was conducted on dissolving glycine in DI water at 25 °C. The concentration data was collected on 24, 40 and 48 hours. Solution concentration at 24 hours was 2% lower than that at 40 hours and no difference was found between 40- and 48-hour samples. The concentration of glycine stopped increasing at 40 hours which reached the dissolution equilibrium. Therefore, the concentration was measured at 40 hours to attain accurate solubility values.

The solubility values for glycine and diglycine as a function of temperature was plotted as shown in Figure 3. The experimental solubility of glycine at 25 °C in this work has 10.6% of deviation for glycine and 3.3%

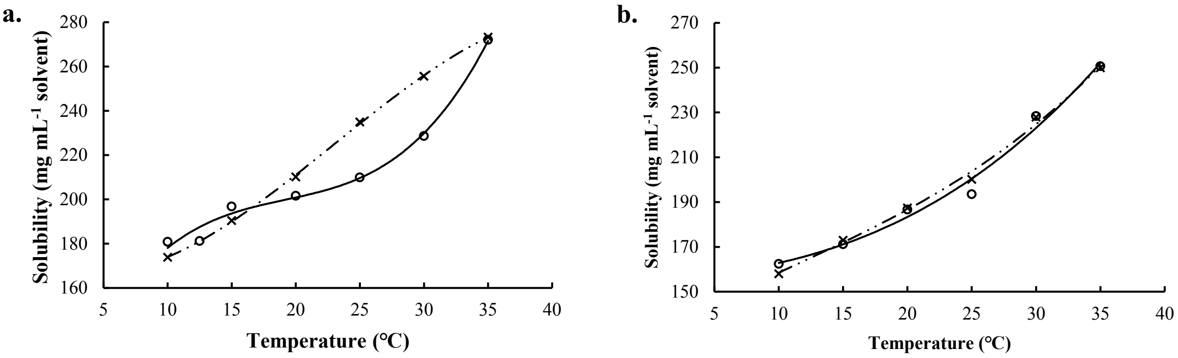

Figure 3. a. Glycine solubility against temperature graph: ○, this work; ×, reference; b. Diglycine solubility against temperature graph: ○, this work; ×, reference. (Guo, et al., 2021)

for diglycine compared to previous work (Guo, et al., 2021), which can be the difference in sampling and characterisation method. An experiment was done on comparison of centrifugation and membrane filtration method for the same sample. A minor deviation of 2.7% was found between two sampling methods, but centrifuge sampling has a lower deviation between each sample and was used for the following experiments. Further comparisons of solubility to other works are provided in Table 1. The solubility data were in accordance with previous works (Lu, et al., 2006) from Table 1 which proved the accuracy and validity of solubility measurements.

Table 1. Solubilities of glycine and diglycine at 25 °C from various work.

Peptides	Solubility (mg mL^{-1})	Reference
Glycine	209.93	This work
	235	(Guo, et al., 2021)
	206.41	(Lu, et al., 2006)
Diglycine	193.52	This work
	200.17	(Guo, et al., 2021)
	201.10	(Lu, et al., 2006)

The solubility values for glycine and diglycine under different pH was measured and plotted in Figure 4. The glycine solubility shows a dramatic increase at extreme pH values. Fluctuation of solubility from pH = 5 to pH = 8 suggests a relatively minor effect of pH on glycine solubility. The pH effect on glycine solubility from this work agrees with the results from Xia et al. (Xia, et al., 2008) where the lowest solubility value (200.92 mg ml^{-1}) appears at the point that is the closest to glycine pI value of 5.9 (Christensen, et al., 1968). Result of the solubility dependence on pH for diglycine shows a similar trend as shown in Figure 4.b.

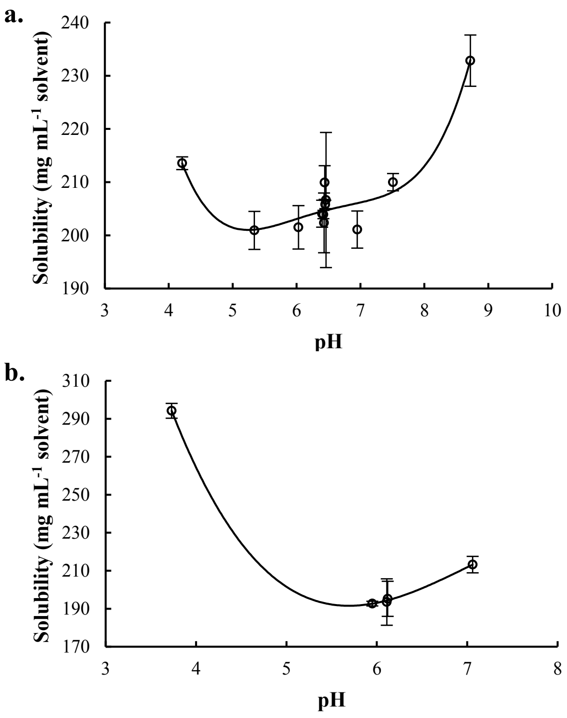

Figure 4. a. Glycine solubility against pH at 25 °C; **b.** Diglycine solubility against pH at 25 °C.

For simplification, HX is used to represent the peptides that undergo the deprotonation twice. As the pH value shifts from one extreme to the other, the following reactions occur:

$$H_2X^+ \rightleftharpoons H^+ + HX \qquad K_{a1} = \frac{[H^+][HX]}{[H_2X^+]} \tag{4}$$

$$HX \rightleftharpoons H^+ + X^- \qquad K_{a2} = \frac{[H^+][X^-]}{[HX]} \tag{5}$$

$$HX_{(s)} \rightleftharpoons HX_{(aq)} \qquad S_0 = [HX] \tag{6}$$

Since the solubility at a particular pH takes all the species dissolved in the aqueous phase into account, the formula for measuring the solubility is shown below:

$$S = [HX] + [H_2X^+] + [X^-] \tag{7}$$

The amount of cation or anion dissolved in the aqueous phase will increase when the acid or base is added, since $-COO^-$ group acts as a weak base which can attract the excess protons, shown as Equation (8) and $-NH_3^+$ is a weak acid which donates the proton to hydroxides, displayed as Equation (9).

$$^{-}OOC-CR-NH_{3}^{+}{}_{(aq)}+H^{+}\rightleftharpoons HOOC-CR-NH_{3}^{+}{}_{(aq)} \quad (8)$$

$$^{-}OOC-CR-NH_{3}^{+}{}_{(aq)}+OH^{-}\rightleftharpoons {}^{-}OOC-CR-NH_{2(aq)}+H_{2}O \quad (9)$$

Therefore, the solubility of peptides must be enhanced due to the addition of acid or base. Moreover, by using the Henderson-Hasselbalch equation, the solubility dependency on pH can be predicted and further support the results above. The derivation of the formula is shown below (Avdeef, 2007).

$$S=[HX]+\frac{[H^+][HX]}{K_{a1}}+\frac{K_{a2}[HX]}{[H^+]}$$

$$=S_0\left(1+\frac{[H^+]}{K_{a1}}+\frac{K_{a2}}{[H^+]}\right)$$

$$=S_0(1+10^{pK_{a1}-pH}+10^{-pK_{a2}+pH})$$

After taking the logarithm for both sides:

$$logS=logS_0+log(1+10^{pK_{a1}-pH}+10^{-pK_{a2}+pH}) \quad (10)$$

S_0 represents as the solubility in DI water without any addition of acid or base at a certain temperature. The comparison between the calculated and experimental result for glycine under 25 °C is presented in Figure 5, and the values for pK_{a1} and pK_{a2} are taken as 2.34 and 9.6 respectively (Max, et al., 1998).

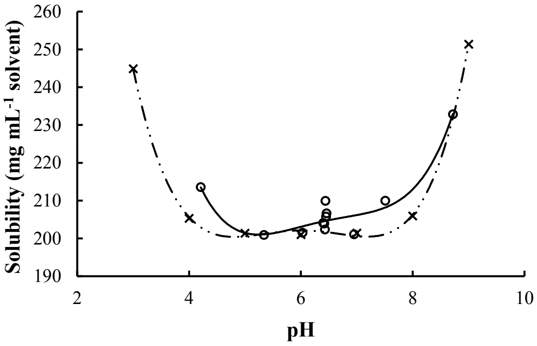

Figure 5. ○, glycine solubility vs. pH curve at 25 °C; ×, Theoretical solubility calculated from Hendersen-Hasselbalch equation.

However, there are deviations between the calculated results and that from experiments. In the Henderson-Hasselbalch equation, the activity coefficients of ions are considered as 1 which is not accurate in reality due to the shielding effect (Anon., 2021). After considering the effect of activity coefficients, the new expressions for two pKa values are shown below:

$$pK_{a1}'=pK_{a1}-log\frac{\gamma_{HX}}{\gamma_{H_2X+}}$$

$$pK_{a2}'=pK_{a2}-log\frac{\gamma_{X-}}{\gamma_{HX}}$$

In addition, the solubility predicted by the Henderson-Hasselbalch equation with pH range beyond pKa values shows steeper increase over 1000 which is not realistic for peptides.

3.2. Glycine and Diglycine Batch Crystallisation

The objective of batch crystallisation was to reach nucleation within 50 minutes and investigate the induction time and crystallisation concentration profile at different pH conditions. The temperature profile shown in Figure 6 was controlled by setting solution preparation temperature at 50 °C and batch crystallisation temperature at 12.5 °C. Supersaturation value was calculated from previous experimental solubility values and kept around 1.18 for consistency. Impeller rotation speed was controlled at 150 rpm to reduce shear rate difference which would cause difference in homogenous and heterogenous nucleation rate (Ploß & Mersmann, 1989).

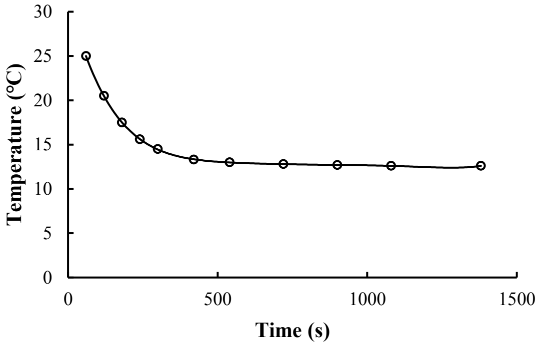

Figure 6. Temperature profile for glycine crystallisation.

Figure 7.a shows the concentration of glycine under both neutral and acidic conditions started to decrease before 30 minutes and reached plateau within 2 hours. Significant decrease of induction time was observed for glycine crystallisation at lower pH value. From camera captures, the induction time for neutral condition was obtained at 22 min and for acidic condition was 10 min.

Similar batch crystallisation was also done on diglycine (Figure 7.b). Diglycine is a larger molecule, for small particle sizes, supersaturation is described by following equation (Senoo & White, 2017).

$$ln\left(\frac{c_r}{c^*}\right)=\frac{2M\sigma}{n_iRT\rho_sr} \quad (11)$$

Therefore, with larger molecular weight the crystallisation for diglycine requires a higher

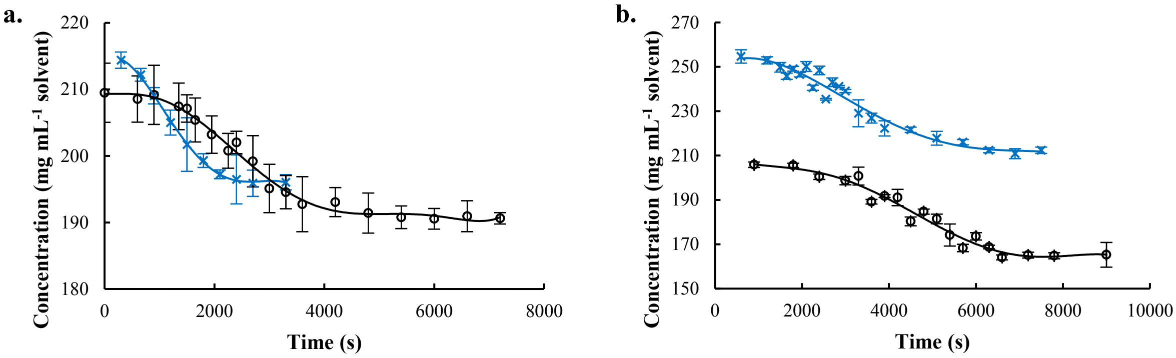

Figure 7. a. Glycine crystallisation concentration profile: ○, glycine with water supersaturation of 1.186; ×, glycine in 1M HCl solution with supersaturation of 1.177; **b.** Diglycine crystallisation concentration profile: ○, diglycine with water supersaturation of 1.383; ×, diglycine in 1M HCl solution with supersaturation of 1.377. The line is for guidance only.

supersaturation value. For consistency, the batch crystallisation of diglycine were conducted at supersaturation around 1.38. The induction time of diglycine crystallisation was found to be decreased from 32 minutes in neutral condition to 22 minutes in acidic condition.

Batch crystallisation operations for both peptides appear to have similar shape of concentration profile. The concentration decrease at the start of nucleation shows concave shape whereas approaching the concentration plateau, concentration profile has a convex shape. Both concave and convex shapes are mainly due to the change in solution supersaturation during crystallisation process. The primary nucleation of homogeneous mixture was slow at the beginning of crystallisation, but once the nucleation started, secondary nucleation was introduced. With high supersaturation, the nucleation rate increased resulting in a concave shape in concentration profile. Additionally, the convex shape of concentration profile was due to the low supersaturation toward the end of crystallisation where the solution was approaching dissolution equilibrium at the crystallisation temperature.

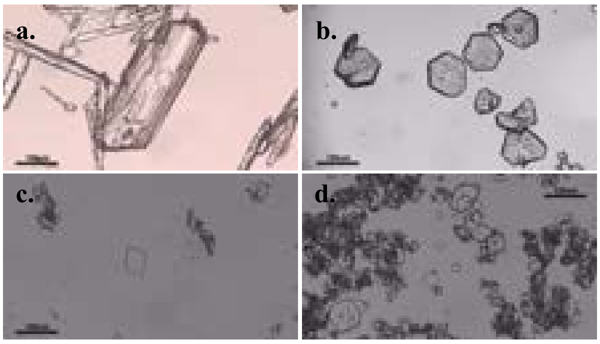

Figure 8. a. Glycine crystal in neutral condition; **b.** Glycine crystal in acidic condition; **c.** Diglycine crystal in neutral condition; **d.** Diglycine crystal in acidic condition.

The samples from batch were observed under the microscope to examine the crystal formation. Crystal images from Figure 8 shows that the crystals formed in neutral condition were larger than the crystals in acidic condition. More crystal glomeration was also observed in acidic condition. These observations indicated a higher nucleation rate for glycine in acidic condition.

A comparison of crystal shape under the microscope is shown in Figure 8. The crystal shape formed in acidic condition was prismatic where in neutral condition the crystals were more tubular or needle-like. This may suggest more γ-glycine formed instead of α-glycine (Srinivasan, 2008). However, the observation under microscope was not eligible to accurately describe crystal habit, further investigation on crystal structure is required with X-ray diffraction (Vesga, et al., 2019). Similarly, the crystallisation sample under microscope also shows more glomeration under acidic condition as shown in Figure 8.d. In contrast to glycine crystals, there was no obvious crystal structure change for diglycine varying the pH of solution. Although the difference between α-diglycine and β-diglycine crystal structure is minor, mainly difference in angles, further examination should be conducted with X-ray diffraction to give quantitative result on diglycine morphology.

Although the microscopic capture was not qualified to accurately determine the crystal habit, γ-glycine formation was predicted according to the previous studies. Two ends of tubular-shaped α-glycine were identified as the carboxyl and amino groups, the presence of hydrogen ion inhibits the bonding on both ends. Hence, with reduced growth on c-axis, glycine formation is dominated by its γ form (Han, et al., 2012).

The decrease in crystal size observed under acidic condition was explained by Classical Nucleation Theory (Davey & Garside, 2006). With the addition of HCl, the number of ions increases in solution. Rearranging Equation (11), with the same supersaturation ratio, the crystal particle radius is inversely proportional to n_i, the number of ions present in solution, hence smaller crystals formed in acidic solution.

$$r = \frac{2M\sigma}{n_i RT\rho_s ln\left(\frac{c_r}{c^*}\right)} \tag{12}$$

In Classical Nucleation Theory, the Gibbs free energy for nucleation with volume and surface contribution is proposed as

$$\Delta G_r = -\frac{4}{3}\pi r^3 \Delta G_v + 4\pi r^2 \sigma_{SL} \tag{13}$$

At critical nucleus size r_{crit}, ΔG_r is at its maximum, which is derived as

$$\Delta G_{crit} = \frac{4}{3}\pi r_{crit}^2 \sigma_{SL} \tag{14}$$

For a homogenous primary nucleation, nucleation rate, J can be described by Arrhenius rate with Gibbs free energy at ΔG_{crit}.

$$J = Fexp\left(-\frac{\frac{4}{3}\pi r_{crit}^2 \sigma_{SL}}{kT}\right) \tag{15}$$

Mullins proposed that the crystallisation induction time is inversely proportional to the nucleation rate (Söhnel & Mullin, 1988). From above derivation, the following relation between induction time and crystal size is proposed.

$$\frac{1}{t_i} \propto exp(-r_{crit}^2) \tag{16}$$

A decrease in crystal size results in a decrease in induction time, which is in accord with the experimental results from this work. As the nucleation rate is increased, the number of crystals is increased. With increasing number of crystals, the effect of attrition needs to be considered. Collision between crystals or with impeller created smaller particles which promoted secondary nucleation. From the microscopic pictures, several crystals grew on the chipped edges of other crystals. This explains the glomeration in batches with higher nucleation rates.

4. Conclusion

The primary objective is to investigate the solubility of glycine and diglycine at different pH and further batch crystallising behaviour according to the existing theories. The solubility of both species investigated shows the lowest solubility at pH closest to their pI value. A significant increase of solubility was observed at extreme pH investigated, which is in accord with Henderson-Hasselbalch equation theoretical calculation suggests. However, the Henderson-Hasselbalch equation predicts an even steeper increase of solubility beyond peptides' pKa point, further investigation on more extreme pH can be conducted to compare with the theory.

Batch crystallisation on both glycine and diglycine were subsequently investigated under different pH circumstances. The concentration profile proved the effect of supersaturation as major driving force of in crystallisation process. With supersaturation, shear rate and temperature profile controlled, induction time for crystallisation under acidic condition dropped significantly. The Classical Nucleation Theory was introduced and proved that for increased number of ions present in solution causes the increase of nucleation rate hence reduced induction time.

Microscopic captures for batch crystallisation were examined to further prove the increase of glomeration and decrease in particle size in acidic conditions. Although different crystal shape was observed for glycine crystallisation under acidic condition, which was believed to be transformation from α- to γ-glycine, the conclusion cannot be drawn without quantitative result from product characterisation methods. Therefore, further X-Ray diffraction can be conducted on product from crystallisation to provide accurate scientific evidence of different crystal habit presence under acidic condition.

5. Acknowledgement

The authors would like to express their sincere gratitude to Hamish Mitchell, a responsible and resourceful PhD student at Imperial College London, for his instructive advice and wholehearted support on this project and his sweat to set up the equipment.

Nomenclature

Symbol	Definition	Unit
A	Absorbance	-
c	Concentration of solution	mg mL^{-1} solvent
c_r	Solubility at particle size r	mg mL^{-1} solvent
c^*	Equilibrium solubility at temperature T	mg mL^{-1} solvent
D	Impeller Diameter	m
d_p	Particle diameter	m
g	Gravitational acceleration	m s^{-2}
ΔG	Gibbs free energy	J
J	Nucleation rate	m^{-3} s^{-1}
k	Boltzmann constant	m^{2} kg s^{-2} K^{-1}
K_a	Acid dissociation constant	mol dm^{-3}
ℓ	Optical path length	cm
M	Molecular weight	g mol^{-1}
n_i	Ions formed in the electrolyte/solution	-
N_{js}	Just suspended speed	rpm
R	Ideal gas constant	J K^{-1} mol^{-1}
r	Particle radius	m
S	Zwietering's N_{js} constant	-
T	Temperature	K
t_i	Induction time	s
X	Zwietering's mass ratio percent	-

Greek characters

Symbol	Definition	Units
ε	Proportionality constant	mol^{-1} dm^{3} cm^{-1}
ν	Kinematic viscosity	m^{2} s^{-1}
π	Mathematical constant	-
ρ_L	Liquid density	kg m^{-3}
ρ_S	Solid density	kg m^{-3}
σ	Interfacial free energy	J m^{-2}

References

Anon., 2021. *Reachdevices.com.* [Online]
Available at:
http://www.reachdevices.com/Protein/pKa_explanation.html
[Accessed 15 12 2021].

Avdeef, A., 2007. Solubility of sparingly-soluble ionizable drugs. *Advanced Drug Delivery Reviews,* 59(7), pp. 568-590.

Bischoff, R. & Schlüter, H., 2012. Amino acids: Chemistry, functionality and selected non-enzymatic post-translational modifications. *Journal of Proteomics,* 75(8), pp. 2275-2296.

Christensen, J. J., Oscarson, J. L. & Izatt, R. M., 1968. Thermodynamics of proton ionization in dilute aqueous solution. X. .DELTA.G.deg. (pK), .DELTA.H.deg., and .DELTA.S.deg. values for proton ionization from several monosubstituted carboxylic acids at 10, 25, and 40.deg.. *Journal of the American Chemical Society,* 90(22), pp. 5949-5953.

Davey, R. J. & Garside, J., 2006. *From molecules to crystallizers.* Oxford: Oxford University Press.

Fosgerau, K. & Hoffmann, T., 2015. Peptide therapeutics: current status and future directions. *Drug Discovery Today,* 20(1), pp. 122-128.

Guo, M. et al., 2021. The effect of chain length and side chains on the solubility of peptides in water from 278.15K to 313.15K: A case study in glycine homopeptides and dipeptides.

Hamrníková, I., Mikšík, I., Uhrová, M. & Deyl, Z., 1998. Ultraviolet detector response of glycine and alanine homopeptides: Some specific features in capillary electrophoresis. *Analytica Chimica Acta,* 372(1-2), pp. 257-272.

Han, G., Chow, P. S. & Tan, R. B. H., 2012. Direct Comparison of α- and γ-Glycine Growth Rates in Acidic and Basic Solutions: New Insights into Glycine Polymorphism. *Crystal Growth & Design,* 12(5), pp. 2213-2220.

Hebel, D., Huber, S., Stanislawsk, B. & D. H., 2013. Stirred batch crystallization of a therapeutic antibody fragment. *Journal of Biotechnology,* 166(4), pp. 206-211.

Ibrahim, S., Jasnin, S. N., Wong, S. D. & Baker, I. F., 2012. Zwietering's Equation for the Suspension of Porous Particles and the Use of Curved Blade

Impellers. *International Journal of Chemical Engineering,* Volume 2012, pp. 1-13.

Jacobsen, C., Garside, J. & Hoare, M., 1998. Nucleation and growth of microbial lipase crystals from clarified concentrated fermentation broths. *Biotechnology and Bioengineering,* 57(6), pp. 666-675.

Jansens, P. & Horst, J. t., 2006. *BIWIC 2006.* Amsterdam [etc.]: IOS Press.

Li, X. et al., 2020. Protein crystal occurrence domains in selective protein crystallisation for bio-separation. *CrystEngComm,* 22(27), pp. 4566-4572.

Lu, J., Wang, X.-J., Yang, X. & Ching, C.-B., 2006. Solubilities of Glycine and Its Oligopeptides in Aqueous Solutions. *Journal of Chemical & Engineering Data,* 51(5), pp. 1593-1596.

Manimekalai, P. & Selvarajan, P., 2015. Nucleation kinetics, growth and studies of diglycine magnesium. *Journal of Chemical and Pharmaceutical Research,* 7(7), pp. 691-696.

Max, J.-J., Trudel, M. & Chapados, C., 1998. Infrared Titration of Aqueous Glycine. *Applied Spectroscopy,* 52(2), pp. 226-233.

Mettler-Toledo, 2021. *Supersaturation and Crystallization.* [Online]
Available at:
https://www.mt.com/gb/en/home/applications/L1_AutoChem_Applications/L2_Crystallization/Supersaturation_Application.html
[Accessed 12 Dec. 2021].

Mohan, R., Lorenz, H. & Myerson, A. S., 2002. Solubility Measurement Using Differential Scanning Calorimetry. *Industrial & Engineering Chemistry Research,* 41(19), pp. 4854-4862.

Negahdaripour, M. et al., 2019. Selected application of peptide molecules as pharmaceutical agents and in cosmeceuticals. *Expert Opinion on Biological Therapy,* 19(12), pp. 1275-1287.

Ploß, R. & Mersmann, A., 1989. A new model of the effect of stirring intensity on the rate of secondary nucleation. *Chemical Engineering & Technology - CET,* 12(1), pp. 137-146.

Senoo, S. & White, A., 2017. Analysis and design of wet-steam stages. *Advances in Steam Turbines for Modern Power Plants,* pp. 165-218.

Söhnel, O. & Mullin, J. W., 1988. Interpretation of crystallization induction periods. *Journal of Colloid and Interface Science,* 123(1), pp. 43-50.

Srinivasan, K., 2008. Crystal growth of α and γ glycine polymorphs and their polymorphic phase transformations. *Journal of Crystal Growth,* 311(1), pp. 156-162.

Swinehart, D. F., 1962. The Beer-Lambert Law. *Journal of Chemical Education,* 39(7), p. 333.

Vesga, M. J. et al., 2019. Conundrum of γ glycine nucleation revisited: to stir or not to stir?. *CrystEngComm,* 21(13), pp. 2234-2243.

Xia, Y., Xiujuan, W. & Bun, C. C., 2008. Solubility of Form α and Form γ of Glycine in Aqueous Solutions. *Journal of Chemical & Engineering Data,* 53(5), pp. 1133-1137.

The Study of Minimising Backmixing in Continuous Protein Crystallisation

Christopher Chan & Roshan Sivabalan

Department of Chemical Engineering, Imperial College London, UK

Abstract

For a continuous oscillatory flow reactor, this paper does not only investigate the effect of backmixing by manipulating mixing conditions (amplitude and frequency), but also studies how backmixing can be reduced by using different mixing pieces. The severity of backmixing was determined by observing the changes in concentration of samples obtained by each stream in the experimental setup. Results from experiments conducted with colours show that lower flow rate ratios, lower frequency, and lower amplitude results in lower backmixing which is expected as there is less oscillatory turbulence generated due to poorer mixing conditions. Furthermore, results from experiments conducted with protein and precipitate solutions have shown identical trends to colours whereby the poorest mixing condition (7.9mm amplitude, 0.02Hz frequency) gave a time averaged protein concentration of 69.75 mg/ml. This is the mixing condition with the least amount of backmixing among all setups with a concentration drop of less than 6%. Lastly, the addition of Venturi valves in the T-piece setup reduced backmixing significantly in comparison to the Y-piece and T-piece with a protein stream concentration drop of less than 2%.

1 Introduction

The global protein therapeutics market is currently experiencing a rapid development as the market is predicted to hit an astonishing value of $217,591 million [1] by year 2023, and this is due to a steep rise in both demand and awareness with respect to protein therapeutics. However, the sharp increase in demand has resulted in a bottleneck in protein downstream purification with a heavy reliance on column chromatography that involves expensive preliminary purification steps, putting intense pressure on manufacturers to achieve high yield and purity.

Recently, alternate purification techniques have become one of the most researched areas as it is vital in many manufacturing processes especially in the pharmaceutical industry. Crystallisation is one of the most effective purification processes available and it is widely used in many industries such as food, chemical manufacturing, and pharmaceutical industry. It involves the conversion of a solid crystalline phase from a liquid solution. As of today, one of the most important uses of protein crystallisation is in structural biology where structures of large crystals with high purity can be determined using X-ray crystallography. When compared to chromatography, crystallisation has demonstrated to be a effective method in purifying proteins as it produces protein crystals with enhanced stability [2]. Protein crystallisation is a lucrative alternative as it not only offers low operating and capital costs, but it also has the potential to crucially minimise the number of steps required in the downstream process [3]. Furthermore, protein crystallisation brings many benefits such as foreseeable properties of dissolution in terms of drug delivery [4], improved formulation, and better storage. It is also reported that some protein crystallisation processes involving β-amylase were able to achieve recovery yields as high as 95% [5].

Despite having numerous advantages, protein crystallisation remains a challenge especially for large, complex 3D protein structures. It has been suggested that there is no comprehensive thesis based on the high complexity of protein crystallisation as the knowledge and understanding of this process is not derived from theoretical intuition but mainly based on data from experiments. Also, in terms of potential firms wanting to enter the market, factors such as strict government policies and high cost have acted as the main barriers to entry for businesses and has therefore constricted market growth.

In the current pharmaceutical industry, the usual mode of purification is via batch crystallisation whereby the crystal product from the batch system is collected only once and then end of the batch run. On the other hand, continuous crystallisation is considered to be an ideal alternative due to its advantages in terms of flexible scaling-up procedures, refined efficiency, and easier control of the process [6]. Intensive research regarding the use of oscillatory flow for continuous protein crystallisation has been carried out to investigate the influence of mixing conditions and shear rate on crystal sizes, crystal growth, and nucleation rate. When executed properly, the optimal amount of agitation will not only result in reduced collision between crystals and the crystalliser wall, but also produces a good suspension of crystals due to favourable mixing conditions [7]. However, the implementation of oscillatory flow induces a backward flow that causes backmixing in the supply streams, resulting in a decreased nucleation rate and hence less crystals formed.

Furthermore, there is no literature focused on reducing the effect of backmixing on continuous crystallisation of proteins. This paper focuses on finding optimal methods to reduce backmixing in the continuous crystallisation of lysozyme using oscillatory flow.

2 Theory

2.1 Crystallisation Phase Diagram

Figure 1 below illustrates the phase diagram for a typical crystallisation process [8].

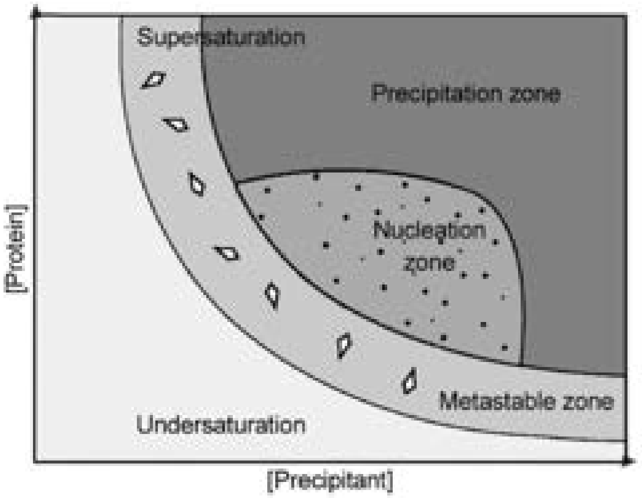

Figure 1: Phase Diagram of A Protein Crystallisation Experiment

For protein crystallisation, it is optimal to operate under two main zones. Firstly, the metastable zone where there is crystal growth, and no nucleation of new proteins is occurring. Secondly, the nucleation zone where nucleation of proteins is heavily promoted, and new crystal nuclei is produced. It is also important to note that if there is an excessive increase in supersaturation, the precipitation zone is reached whereby amorphous crystals (or poorly crystalline structures) is produced. Also, no formation of new crystal nuclei will be observed at the undersaturation zone.

2.2 Heterogeneous Nucleation

Nucleation can be classified into two types, namely primary and secondary nucleation. Primary nucleation involves the process of nucleation in the absence of crystals whereas secondary nucleation involves nucleation that occurs in the presence of crystals.

Primary nucleation is broken down into two types, namely heterogeneous and homogeneous nucleation. Heterogeneous nucleation involves the formation of crystals using an insoluble material whereas homogeneous nucleation involves the formation of crystals purely due to the phenomena of supersaturation.

For protein crystallisation, it is recommended to use heterogeneous nucleation as it has been proven that the formation of crystals occur with lower supersaturation and induction time due to the presence of inorganic crystals (also known as seeds) [9]. Equation 1 outlines the rate of homogeneous nucleation, J.

$$J = F.exp(\frac{-16\pi\sigma^3 v^2}{3k^3 T^3 (lnS)^2}) \tag{1}$$

2.3 Supersaturation Ratio

Supersaturation is the phenomena where a solution contains more solute than is theoretically allowed by its equilibrium solubility. This is a physical state that is not at equilibrium and is thermodynamically unstable. Supersaturation is often measured by the supersaturation ratio which is the protein concentration to at time, t over equilibrium protein concentration; as shown in Equation 2.

$$S = \frac{c_t}{c^*} \tag{2}$$

2.4 Backmixing

The occurrence of backmixing suggests a backwards flow against the direction of the principal stream, resulting in a portion of substance moving back relative to a fixed point. Furthermore, it has been proposed that the driving force of backmixing is the generation of turbulence from a moving automobile [10]. For the case of protein crystallisation via oscillatory flow, this phenomena is inevitable and could be detrimental to the overall process output. A significant portion of the research involved investigating the effect of different mixing conditions on the effect of backmixing experienced by the streams in the experimental setup. This was done because minimising backmixing was the key priority as backmixing has severe effects on nucleation, and by extension, crystallisation. If backmixing was to be severe, this would result in a decrease in the initial supersaturation ratio, which would subsequently lead to a decrease in nucleation rate as expressed in equation 1. To investigate the severity of backmixing, the change in concentration of the sample at fixed points must be known and can be found using calibration curves plotted using the concept of the Beer-Lambert Law.

2.5 Beer-Lambert Law

In a medium where monochromatic light is transmitted through it with an intensity, I and at an incident intensity of I_o, the transmittance (T) of the solution can be described as the ratio of I over I_o via Equation 3 stated below with values ranging between 0 to 1.

$$T = \frac{I}{I_o} \times 100\% \quad (3)$$

Furthermore, Equation 4 below expresses the logarithmic relationship between T and the absorbance of the medium (A).

$$A = -log_{10}T \quad (4)$$

An absorbance value of 1 corresponds to T being 10%, whereas an absorbance of 0 is achieved if T is 100%. It is important to note that both T and A do not have units and are therefore dimensionless quantities.

The Beer-Lambert Law details the absorbance of a particular material using a linear relationship involving the following factors and is expressed by Equation 5 below:

1. Optical Path Length, l (cm)
2. Molar Absorption Coefficient, ε ($cm^{-1}M^{-1}$)
3. Molar Concentration, c (M)

$$A = l\varepsilon c \quad (5)$$

The optical path length represents the length of the cuvette for the absorbance measuring equipment. Throughout all the experiments, the value of l in the UV-Vis spectrophotometer was set to 1cm when conducting absorbance measurements. The molar absorption coefficient is a sample dependent property that tells how well the material attenuates light at a given wavelength. As the Beer-Lambert Law describes a linear relationship between the absorbance and concentration, values of ε can be obtained through the gradient of a typical calibration curve. Section 3.3 provides evidence of this linear dependence as a linear calibration curve of absorbance against concentration was plotted using a line of best fit with high values of determination coefficient (R^2).

3 Experimental Methodology

3.1 Setup & Method

In this investigation, the research is broken up into two main parts. Preliminary research was conducted with colours in order to get an initial estimate of the ideal mixing conditions which was later used in the second part of the experiment - to crystallise the lysozyme protein out using a sodium chloride precipitate solution. The reason this was done is threefold. Firstly, natural dyes are cheaper and more accessible than proteins. This meant that multiple experimental runs could be conducted without any concern regarding the amount of materials that were available. Secondly, dyes were employed as it is easier to visually observe the effect of backmixing as the extent of backmixing is related to the intensity of the green colour in each stream. Lastly, it is predicted that the trends and results obtained from the work done with colours is transferable to the second part of the experiment; investigating backmixing in proteins.This is theorised as coloured water and dissolved lysozyme have similar physical properties of density and viscosity. The experiments were later repeated with proteins to confirm the hypothesis regarding the validity of using this method (assuming that the data and trends are transferable).

For the experimental setup, two syringes first filled with different coloured diluted dyes (blue & yellow) were attached to electronic pumps as shown in Figure 2. Different conditions were then used to identify how the rate of backmixing changes with these conditions; these conditions being flow rate ratios, frequency, amplitude and the mixing pieces. After the experimentation with colours was completed, a similar setup was used to investigate crystallisation with the syringes being filled with the protein and the sodium chloride precipitate solutions respectively. For both experiments, the absorbance was measured using a UV-Vis spectrophotometer, $Nanodrop - One^c$. Finding the corresponding concentration requires the use of calibration curves for both natural dye and lysozyme which is explained in section 3.3.

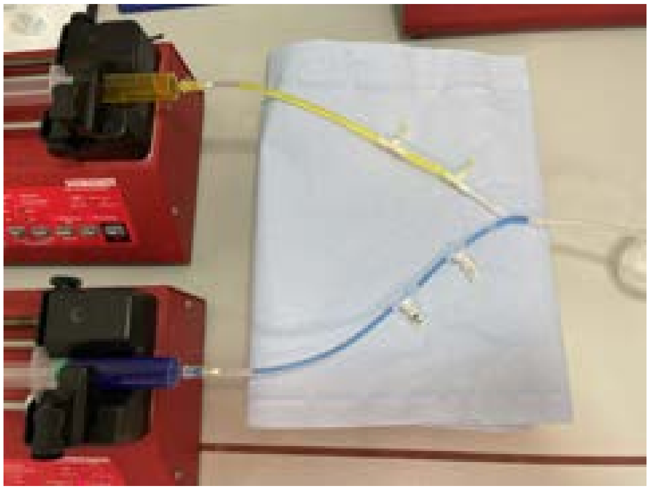

Figure 2: Experimental Setup with Diluted Dyes

3.2 Materials

Natural dye (liquid food colouring) was purchased for the preliminary experiment. It is imperative that the composition of the different chemical substances in both the blue and yellow dye remain exactly the same. As a UV-Vis spectrophotometer was used to measure composition and concentration of the samples, the coloured dyes must comprise of the same chemical substances at the same composition as a control. This ensures that the only thing measured by the spectrophotometer is the change in yellow composition. For protein crystallisation, three solutions were prepared – protein solution, buffer solution and precipitate solution. The buffer solution was prepared by mixing 1.6406g of sodium acetate with 200ml of water and 12ml of pure acetic acid to produce a sodium acetate buffer solution with a concentration of 0.1M and a pH value of 4. Next, the sodium chloride precipitate solution was prepared by mixing 4g of sodium chloride in 50ml of buffer solution to obtain a precipitate solution with a concentration of 80mg/ml buffer. Lastly, the protein solution of concentration of 73.6mg/ml buffer were prepared by dissolving 736mg of lysozyme in 10ml of buffer solution. The proposed concentrations for the protein and precipitate solutions are suggested in literature whereby it allows an initial supersaturation ratio of 10 to be achieved, and this may result in high nucleation rates at the start of the experiment [7].

3.3 Calibration Curves

The Beer-Lambert equation is used to predict the concentration of a given sample using the measured absorbance obtained by a spectrophotometer. The equation proposes a linear relationship between the absorbance values obtained from the spectrophotometer and the concentration of a sample at a defined wavelength. However, in order to make full use of this equation, that relationship must be plotted for both colours and proteins.

As such, calibration graphs were plotted as shown in Figure 3. This is done using different test concentrations of the desired sample that is measured in the spectrophotometer. However, due to the nature of the sample being a mixture of two separate coloured water samples, compositions were used instead of concentrations as the concentrations of the chemical substances in these natural dyes were not available. Multiple samples were prepared ranging from a mixture with 10% blue dye - 90% yellow dye to 90% blue dye - 10% yellow dye. This produces a range of samples with varying shades of green going from most blue (least yellow) to most yellow (most blue). For the purposes of this experiment, only the composition of yellow dye in each stream was measured. Hence, the absorbance values were taken from a wavelength of 430nm as results from the UV-Vis spectrophotometer indicate the highest peak for yellow colour at that specific wavelength.

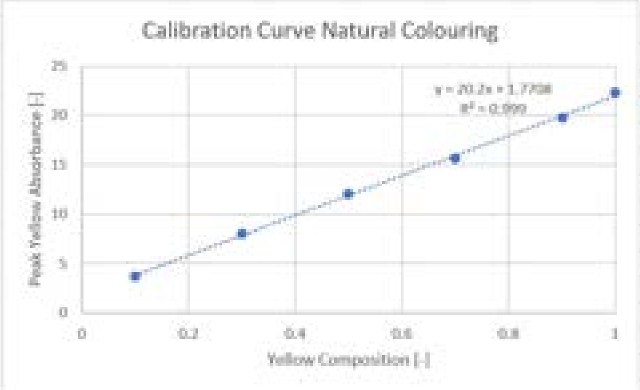

Figure 3: Calibration Curve for Colours

For the measurement of protein concentrations, a similar calibration graph is plotted. However, it is done in a different method – with concentrations instead of compositions. Test samples with known concentrations were prepared and measured using the spectrophotometer. Absorbance values at a wavelength of 280nm were measured and with the calibration curve the concentration of any sample can be obtained.

3.4 Sampling Technique

In order to investigate the extent of backmixing occurring in each individual stream, the composition (in the case of colours) or concentration (in the case of proteins) of the samples collected near the mixing point must be found by obtaining absorbance values through the spectrophotometer. In an ideal world, a clean sample is needed in order to obtain an accurate measurement for the composition/concentration to investigate the extent of backmixing at a specific point along the tubes in the experimental setup.

As it would be very difficult to achieve that, the proposed method of sampling included the usage of reservoirs at each sampling location. These reservoirs were built into the the tubes in the experimental setup and were covered with syringes in order to prevent the formation of air bubbles inside the tubes as shown in Figure 4.

The samples were withdrawn directly using a pipette through the reservoirs in order to minimise the extent of backmixing caused by the withdrawal process. Other methods were employed to obtain samples such as using the syringe attached to the reservoir to withdraw a larger volume into the reservoir which was then collected with a pipette. However, this brought about severe backmixing purely due to this sampling technique.

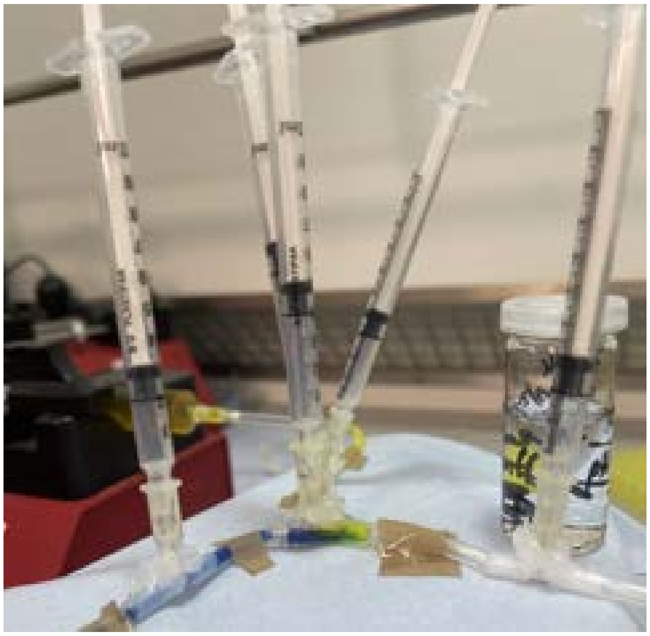

Figure 4: Setup with Reservoirs and Syringes

3.5 Time Averaged Concentration (T.A.C.)

As mentioned in section 3.4, the nature of the setup may result in inaccurate measurements as the sampling technique may induce some backmixing. The introduction of reservoirs and syringes helped reduce the severity of this problem. However, in order to further reduce the error caused by the sampling technique, all values of concentration were averaged after 24 minutes as majority of the results show a trend where the graph tends to plateau after 24 minutes. From this, time averaged concentrations ($< x >$) were computed in order to obtain a more accurate idea of the extent of backmixing that each stream experiences when the variables that are discussed in section 4 are manipulated.

Figure 5 outlines how the composition of yellow dye varies significantly at the outlet at different sampling times. Although this data set was not used, it outlines a clear picture of how the sampling method could heavily influence the compositions/concentrations of the samples which proved that the use of $< x >$ were necessary.

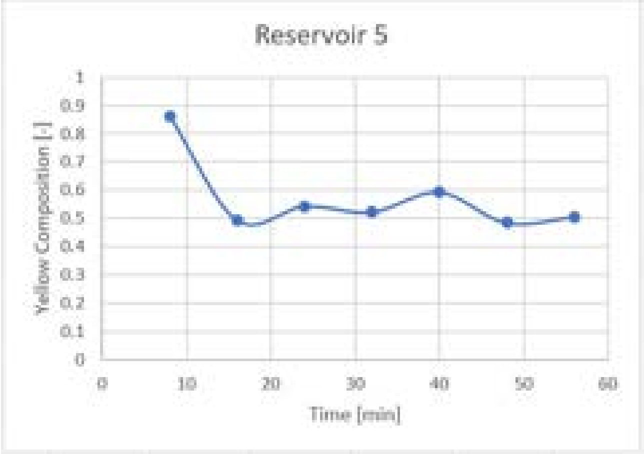

Figure 5: Varying Compositions of Yellow Dye in the Outlet Stream

4 Results

As mentioned previously, the experiment being conducted in two different phases; with the data from the first phase (backmixing in colours) being used to aid the decisions made to investigate the variables in the second phase of the experiment (backmixing in protein and buffer solutions and continuous crystallisation of lysozyme).

4.1 Investigation with Natural Dyes - Colours

The initial method of determining the severity of backmixing effect was to find the concentration of green colour after the blue and yellow colour streams have mixed. However, an important thing to note down is the fact that the process is simply the mixing of two water streams consisting of food dye, and no reaction occurred which will produce any molecule that will reflect green light.

Ratio	Blue Stream Flow rate [ml/min]	Yellow Stream Flow rate [ml/min]
1.00	0.05	0.05
2.00	0.05	0.10
4.00	0.05	0.20
8.00	0.05	0.40

Table 1: Experimental Conditions for when Flow rate ratio is Varied in Investigating Backmixing

4.2 Experimentation with Colours

In the past, experiments regarding continuous protein crystallisation where a ratio of 1 for the protein and precipitate flow rates were used. Therefore, the ratio of flow rates for both pumps were manipulated to study the effect of backmixing. The flow rate of the blue colour stream was kept at 0.05 ml/min throughout all 4 experiments, whereas the yellow colour stream was varied according to the proposed ratios of 1,2,4, and 8. The conditions experimented with are outlined in Table 1.

According to Figure 6, it is shown that there is backmixing of yellow into the blue stream at reservoir 2 with values of $< x_{yellow} >$ increasing from 0 to 0.06. The large increase in $< x_{yellow} >$ in both reservoirs 4 and 5 is expected as the yellow colour stream flow rate is increasing. Therefore, a flow rate ratio of 1 is implemented for future protein experiments as it gives the least backmixing effect and hence the initial supersaturation ratio will not be greatly affected.

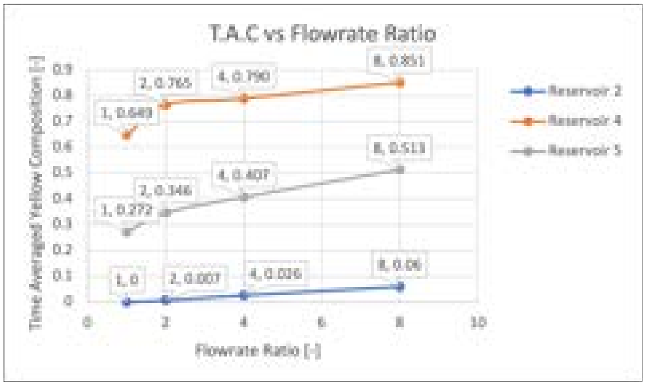

Figure 6: Effect of Different Flow Rate Ratios on Backmixing

The effect of backmixing was investigated further by varying the frequency of both colour streams. As shown in Figure 6, an increase in flow rate ratios escalates the effect of backmixing in both colour streams. Therefore, in this experiment, not only was the amplitude (x_o) kept constant at 9.61mm, but the ratio of the colour stream flow rates was also maintained at 1. Table 2 summarises the conditions for

Ratio	Amplitude [mm]	Frequency [mHz]	Reynolds Number
1.00	9.61	5.52	6.11
1.00	9.61	6.90	6.16
1.00	9.61	13.70	6.42

Table 2: Experimental Conditions for when Frequency is Varied in Investigating Backmixing

each experiment, with the only variable affecting Reynolds Number (Re) being frequency.

The overall trend observed in Figure 7 where minor changes of $< x_{yellow} >$ shown throughout reservoir 4 and 5 stipulates that despite the clear indication that there is backmixing from the blue stream into the yellow stream, the consequences upon backmixing is only considered to be minor. An improvement to the experiment is to investigate higher frequencies as experiments in protein crystallisation conducted previously have shown that an increase in frequency as big as 0.5Hz resulted in shorter nucleation time and faster crystal growth because of higher shear rates being induced [11].

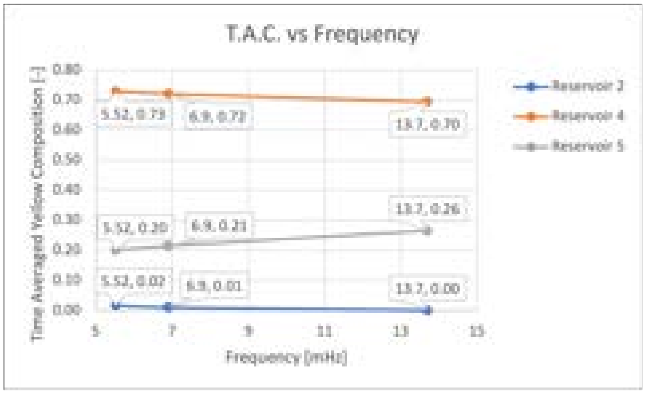

Figure 7: Effect of Varying Frequency on Backmixing with Constant Amplitudes and Flow Rate Ratios

Research has shown that the change in amplitude for oscillatory flow can affect both the crystal size distribution and nucleation rate of proteins. Therefore, the effect of backmixing was investigated by manipulating the amplitude of both colour streams. Table 3 shows the experimental conditions for the amplitude experiment.

From Figure 8, the results show an intense backmixing effect from the blue stream into the yellow stream as frequency increases, causing $< x_{yellow} >$ in reservoir 4 to drop from 0.86 to 0.71. Hence, a lower x_o value is used for future protein experiments to reduce backmixing which will affect the nucleation rate.

Ratio	Amplitude [mm]	Frequency [mHz]	Reynolds Number
1.00	9.61	5.50	2.13
1.00	15.10	5.50	3.36
1.00	20.70	5.50	4.56

Table 3: Experimental Conditions for when Amplitude is Varied in Investigating Backmixing

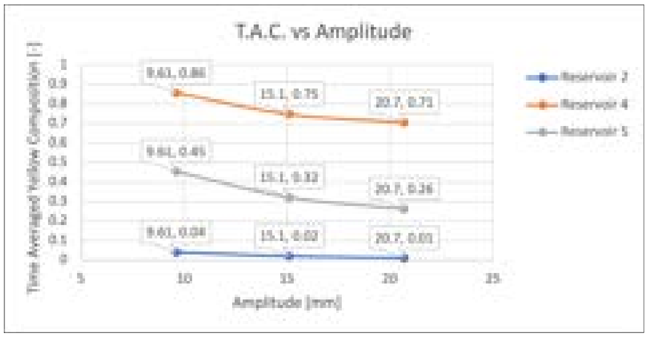

Figure 8: Effect of Varying Amplitude on Backmixing with Constant Frequency and Flow Rate Ratios

4.3 Investigation with Proteins

The first part of the experiment was designed to have a preliminary overview of how backmixing can be controlled and minimised. As mentioned in section 3.1, these conditions were later replicated with proteins and it was found to have the same effect as the investigation with colours revealed.

From the first part of the experiment, it was concluded that the most ideal conditions for minimising backmixing are when the flow rate ratio is kept at 1 and with lower frequency and amplitude. This is expected as the turbulence generated from these conditions is also reduced which results in lower eddy current diffusion leading to minimal backmixing in both stream. However, past research has indicated that increasing frequency and amplitude can have significant impacts on nucleation rates for proteins [7]. As such, the next steps involved further investigating different frequencies on the rate of backmixing as well as the crystal size distribution obtained from the continuous crystallisation process. In addition, different setups were experimented with to investigate the improvements to the crystals that were being collected and observed under a microscope.

A number of tests were conducted to confirm that the ideal conditions for minimised backmixing were at a flow rate ratio of 1 with low flow rates and it was revealed that the results matched the hypothesis where it was assumed that the trends observed when the mixing was conducted with colours would be the same for proteins. Next, the effect of manipulating frequency and amplitude. Figures 9 and 10 outline the trends observed with multiple runs being conducted.

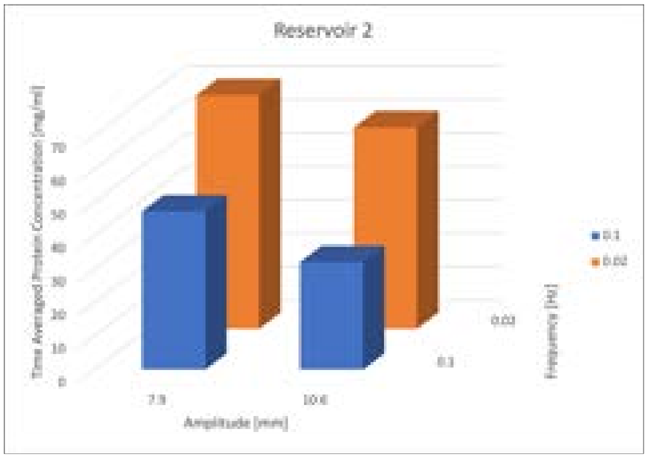

Figure 9: Effect of Varying Frequency and Amplitude on Backmixing in the Protein Stream

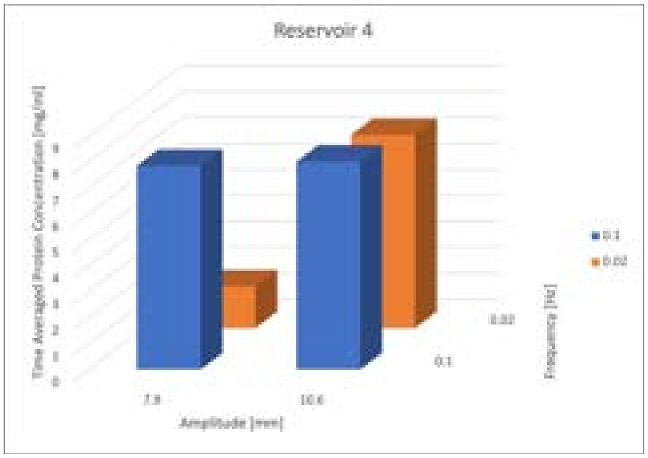

Figure 10: Effect of Varying Frequency and Amplitude on backmixing in the Precipitate Stream

From Figure 9, a higher protein concentration indicates that there is minimal backmixing, as reservoir 2 is attached to the protein stream. From this we can once again conclude that the results from the first part of the experiment were indeed transferable to the second part of the experiment. From Figure 10, it is evident that backmixing increases with increased frequency as the protein concentration in reservoir 4 which is located near the precipitate stream increases.

4.4 Investigation with Experimental Setups

With the first and second parts of the experiment being concluded, it is clear that a set of ideal conditions have been identified for minimising backmixing and that these conditions are transferable to proteins from the investigation with natural dyes (colours).

The final step was to investigate the robustness of different setups. Three setups were built; a Y-Piece setup, a T-Piece Setup, and a Double-Venturi Valve Setup. The structure and dimensions of these setups are shown in the images below.

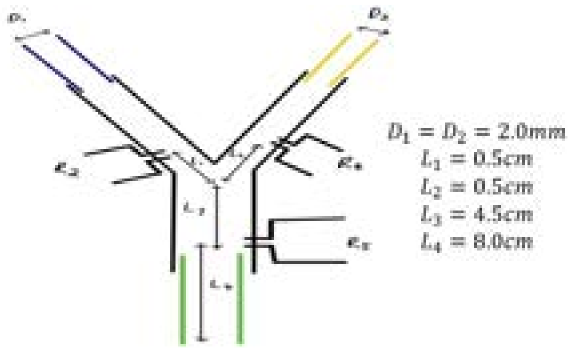

Figure 11: Y-Piece Setup Sketch

Figure 12: Y-Piece Setup

The Y-Piece setup was used early on in the first part of the experiment. It was selected as it is commonly used when experiments related to mixing are conducted. The reservoirs (R2, R4 and R5) are used as points of sample collection and the mixing point (where the two different streams coalesce) is at the middle of the Y-Piece.

The next setup that was used in the protein crystallisation investigation was the incorporation of the T-Piece. Unlike the Y-Piece which conservatively guides the mixing process due to its ”Y” shape, the usage of the T-Piece results in more ”aggressive” type of mixing as the streams combine head on at higher velocities. This is believed to enhance mixing and therefore nucleation rate[12]. Just like the Y-Piece, the reservoirs are set up in similar locations.

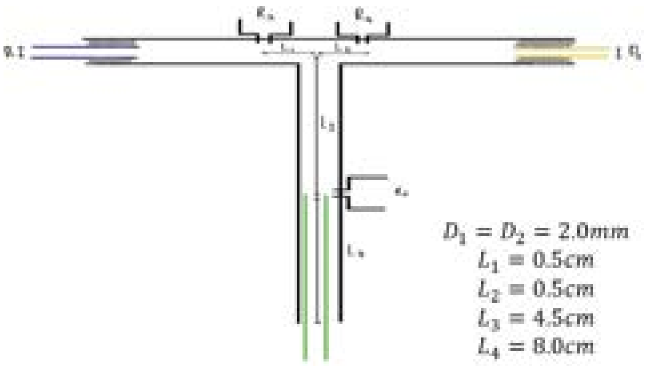

Figure 13: T-Piece Setup Sketch

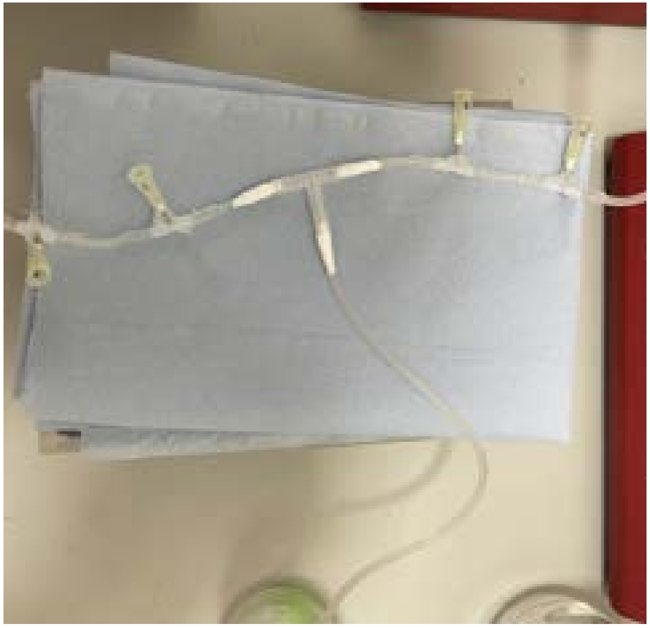

Figure 14: T-Piece Setup

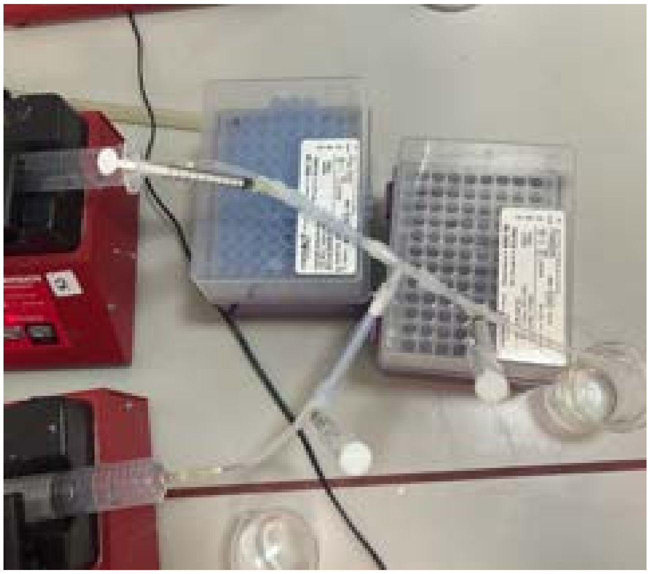

Figure 15: Double Venturi Setup

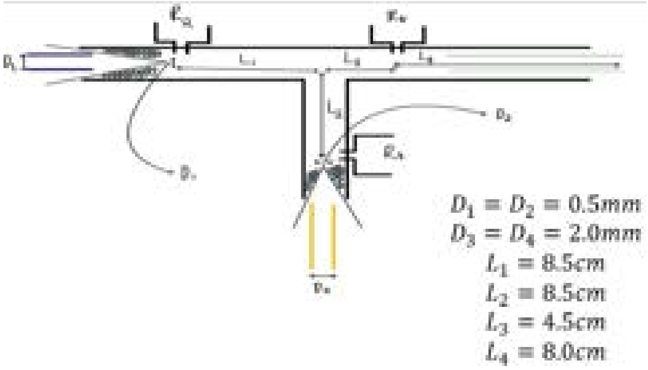

Figure 16: Double Venturi Sketch

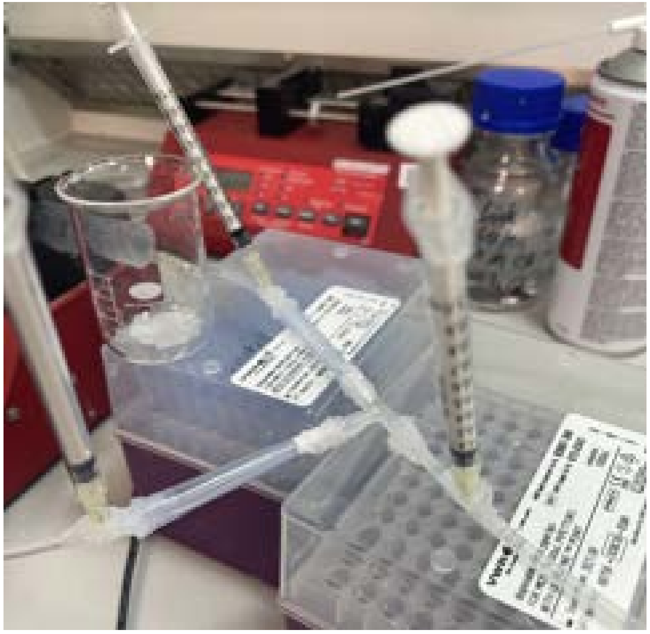

Figure 17: Different View of the Double Venturi Setup

The final step of this part of the experiment is the usage of Double Venturi ”Valves”. Pipette tips were built in to the setup to mimic the behaviour of Venturi valves. This setup was inspired by the Venturi valve and was built to inhibit backmixing even further as the diameter of the ”valve” is a lot smaller than that of previous experiments. It is thought to generate higher velocities at the Venturi throat which inhibits the movement of backward flows that might occur due to pressure drops [13].

4.5 Crystal Size Distribution

Samples of the protein product effluent for all 3 experimental setups were taken at the tube end for Crystal Size Distribution analysis. Each sample was centrifuged to ensure all solid crystals formed would sediment at the bottom of the Eppendorf tube. Crystal images of each sample were then taken after 32 minutes using Olympus CX41 light microscope and is shown below in Figures 18, 19 and 20.

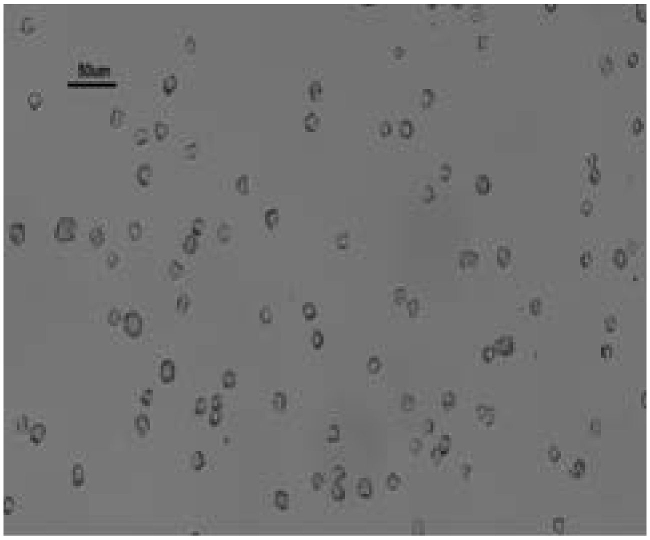

Figure 18: Lysozyme Crystals Observed With the Y-Piece Setup

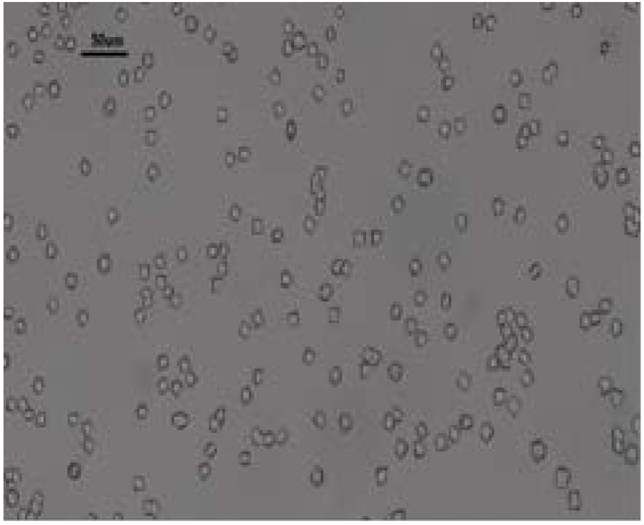

Figure 19: Lysozyme Crystals Observed With the Y-Piece Setup

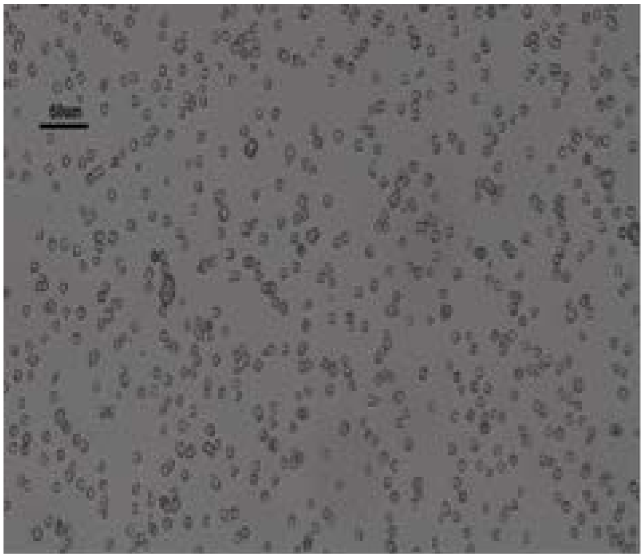

Figure 20: Lysozyme Crystals Observed With the Y-Piece Setup

Setup	**T-Piece**	**T-Piece**	**Venturi Valves**
T.A.C. Reservoir 5 [mg/ml]	28.47 ± 1.28	29.57 ± 1.25	31.59 ± 0.57
T.A.C. Tube End [mg/ml]	26.43 ± 1.21	2.56 ± 1.01	29.27 ± 0.26
Difference	1.74 ± 1.28	2.01 ± 1.25	2.31 ± 0.57

Table 4: Experimental Conditions for when Amplitude is Varied in Investigating Backmixing

Upon observation, it can be seen that the crystals generated for all three images are uniformly distributed with no breakages, indicating no sign of agglomeration with optimal oscillating conditions. This is due to the fact that more intense oscillations would cause the protein crystals to experience higher shear rates, resulting in higher breakage rates [11]. Among the 3 crystal images, the T-piece mixing setup with the 2 Venturi valves produced the largest number of crystals formed. This observation can be further supported from Table 4 where the drop in $< x_{protein} >$ from Reservoir 5 to the tube end for this setup is the largest (2.31mg/ml) in comparison to both T-piece and Y-piece mixing as the nucleation rate is the highest. In addition to the above, as discussed previously in Section 4.4, the number of crystals formed via T-piece mixing is more than Y-piece mixing because of the enhanced mixing that T-piece allows especially for the formation of smaller crystalline particles.

5 Experimental Improvements

Improvements can and must be made to further investigate the effect of backmixing and the process of continuous crystallisation. One suggested improvement relates to the setup itself. The experiments that were carried out, were conducted with setups that were built from scratch. As such, these setups had very short life spans and were susceptible to relatively quick wear and tear. This not only resulted in a lot of time being spent making new setups, but also caused the results to be less accurate than they would have been due to leaks that occasionally occurred. Another issue with these setups is that the sampling technique had initially severely induced backmixing on its own. The sampling technique involved withdrawing a sample using the syringe that was attached to the reservoirs. The process of withdrawal had induced backmixing, but this was later resolved as smaller pipettes were used to directly obtain a sample by inserting it through the reservoirs. In addition, the sampling technique often led to air bubbles appearing inside the tube due to the pressure difference between the surrounding environment and the contents of the tube.

Furthermore, an improvement to the CSD section is to use protein-staining dyes such as methylene blue (MB). It has been suggested that dye molecules such as MB are able to diffuse through protein structures like lysozyme that are porous via a detergent-like mechanism [14]. Figure 21 below shows that the addition of MB into lysozyme solution which allows the differentiation of lysozyme crystals stained in blue from the other crystal nuclei formed.

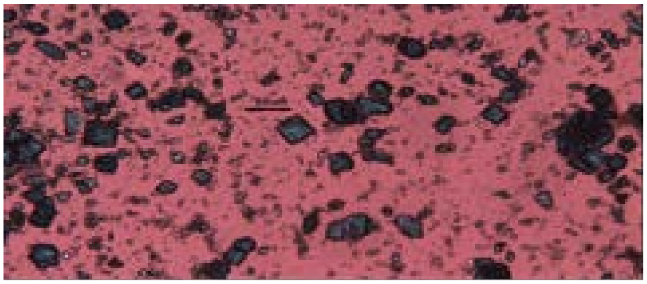

Figure 21: Lysozyme Crystals Stained with Methylene Blue Solution

6 Conclusion

In this study, the aim was to not only identify the severity of backmixing through manipulation of different oscillatory flow mixing conditions, but to also to determine the optimum mixing piece that minimises such effects. The results presented from the protein experiments indicates that backmixing can be reduced upon a flow rate ratio of 1 coupled with lower frequencies and amplitudes, for which the decrease in $< x_{protein} >$ in Reservoir 2 was a mere 5%, as compared with reservoirs with higher frequencies and amplitudes. While an enhanced mixing effect was observed upon utilisation of the T-piece, as supported by previous literature, an enhanced backmixing effect was also observed. This has not been established in literature thus far, and hence additional experiments should be conducted to investigate this thoroughly. Implementation of Venturi valves into the mixing piece was identified as a promising supplementary tool towards the reduction of backmixing in continuous protein crystallisation, equipping future industrial strategies towards large-scale procedures. It is clear that further work in this area would be essential towards the implementation of continuous protein crystallisation under optimal conditions.

References

[1] Anon (2021) Protein Therapeutics Market Set to Reach $217,591 Million by 2023. [Online]. 2021. Alliedmarketresearch.com. Available from: https://www.alliedmarketresearch.com/press-release/protein-therapeutics-market.html [Accessed: 16 December 2021].

[2] Sumant, O. and Shaikh, S., 2021. Protein Therapeutics Market Size, Share — Industry Analysis - 2023. [online] Allied Market Research. Available at: https://www.alliedmarketresearch.com/protein-therapeutics-market

[3] McPherson, Alexander., 2021. Introduction to protein crystallization. [online] Science Direct. Available at: https://www.sciencedirect.com/science/article/pii/S1046202304001094

[4] Influence of Mixing Intensity on Lysozyme Crystallization in a Meso Oscillatory Flow Reactor Filipa Castro, António Ferreira, José A. Teixeira, and Fernando Rocha Crystal Growth Design 2018 18 (10), 5940-5946

[5] [Lee, E. K.; Kim, W. (2003) 'Protein Crystallization for Large-Scale Bioseparation. In Isolation and Purification of Proteins']

[6] Wang et al. (2017) 'Recent Progress of Continuous Crystallisation'

[7] Neugebauer, P.; Khinast, J. G. (2015) 'Continuous Crystallization of Proteins in a Tubular Plug-Flow Crystallizer. Cryst. Growth Des'

[8] Schacherl, M. (2021) 2021. Available from: https://www.researchgate.net/figure/Phase-diagram-of-a-protein-crystallization-experiment-Crystals-can-only-form-when-the_fig7_311989637

[9] McPherson, A. and Shlichta, P., 2021. Facilitation of the growth of protein crystals by heterogeneous/epitaxial nucleation. [online] ScienceDirect. Available at: ¡https://www.sciencedirect.com/science/article/pii/0022024887902247¿

[10] Xu et al. (2005) 'Interstage Backmixing for Single-Phase Systems in Compartmented, Agitated Columns: Design Correlations'

[11] Yang et al. (2018) 'Continuous protein crystallisation platform and process: Case of lysozyme'

[12] Iversen et al. (2008) 'Comparison of T-piece and concentric mixing systems for continuous flow synthesis of anatase nanoparticles in supercritical isopropanol/water'

[13] Huang et al. (2012) 'Backmixing Characterization of a Bubble Column with Short Venturi Throats by Multipoint Internal Tracer Injections'

[14] McPherson, A. Larson, S. B. (2018) 'Acta Cryst'

CAR T-Cell Therapy Supply Chain: Cost-Benefit Analysis of Fresh versus Cryogenic Transport and Storage

Liang, Jiazhao and Mak, Long Hei Frederick

Department of Chemical Engineering, Imperial College London, U.K.

Abstract The major challenge in commercialisation of Chimeric Antigen Receptor (CAR) T-cell therapy is to establish a cost-effective global supply chain. CAR T-cell therapies is time sensitive on two folds: the short 'vein to vein' time is required for terminally ill patients and the transportation of samples between facilities due to the short shelf life of CAR T-cells. The more costly cryogenic transportation and storage can overcome logistical challenges as it accommodates shipping delays, eliminates time constraints during transportation and provides flexibility in scheduling manufacturing slot leading to a lower capital cost for manufacturing. Although the less costly fresh transportation is prone to unpredictable events during transportation, a fixed delivery mode should be adopted to account for the uncertainty in the demand profile. Mixed Integer Linear Program models can play an important role in cost benefit analysis to compare fresh and cryogenic supply chain network. Finally, in response to the growing demand of CAR T-cell therapy, cryogenic storage will be a crucial part in the development of allogeneic therapy.

Keywords: CAR T-cell therapy, cost-benefit analysis, cryogenic, fresh, supply chain, autologous, MILP, optimisation

1. Introduction

Chimeric Antigen Receptor (CAR) T-cell therapy is a complex and innovative immunotherapy. The process involves collecting a patient's T-cells from their blood samples and genetically modifying the patient's T-cells to express the CAR which can recognise and target a specific protein on the cancer cells. (Miliotou & Papadopoulou, 2018) Autologous cell therapies require the patient to obtain CAR T-cells from their blood whereas allogeneic cell therapies rely on a single source of cells to treat many patients. (Farid & Jenkins, 2017)

The development of CAR T-cell therapy has been a breakthrough for these patients who suffer from relapsed or refractory B-cell acute lymphoblastic leukaemia (ALL). Several large clinical trials of CAR T-cell therapy have demonstrated complete remission rates can be as high as 68% to 93%. (Zhang, 2020) Currently, the U.S. Food and Drug Administration (FDA) and European Medicines Agency (EMA) have approved 5 CAR T-cell therapy. In 2017, Kymriah™ of Novartis became the first approved CD19-targeting CAR T-cell immunotherapy that was available to patients up to 25 years of age with ALL. (Kymriah, 2017) (Kymriah EPAR, 2018) Subsequently, between 2017 to 2020, FDA and EMA approved Kite Pharma's Yescarta™ for treatment of large B-cell lymphoma, and Tecartus™ for treatment of mantle cell lymphoma (MCL) and ALL. (Yescarta, 17) (Yescarta, 2018) (Tecartus, 2020) (Tecartus EPAR, 2020) Bristol Myers Squibb developed Breyanzi™, treatment for large B-cell lymphoma, and was proved by the FDA in 2021. (Breyanzi, 2021) Most recently, Abecma™, also developed by Bristol Myer Squibb, was proved by the FDA and EMA, in March 2021 and August 2021 respectively. Abecma™ is a B-cell maturation antigen-targeting immunotherapy that treats patients with advanced multiple myeloma. (Abecma, 2021) (Abecma EPAR, 2021)

The commercialisation of CAR T-cell therapy faces major challenges due to the complex manufacturing process and supply chain network. The listed prices for a single CAR T-cell therapy range between $373,000 to $475,000. (Borgert, 2021) Autologous therapy treats each patient's cell production as one batch, which contributes to the high manufacturing cost. (I.B. Wall, 2013)This leads to the hesitation to utilise CAR T-cell therapy for early-stage patients and patients abandoning the therapy due to the financial burden. The cost of the treatments needs to be minimised to ensure the accessibility of the therapy. (Borgert, 2021)

The manufacture and distribution of T-cell therapy are time-sensitive on two folds: the 'vein to vein' time and the transportation of samples between facilities due to the short shelf life of CAR T-cells. Firstly, patients are most concerned about the 'vein to vein' time, often defined as the total return time (TRT) between the leukapheresis to the administration of the therapy. (Papanthanasious, Stamatis, Farid, Titchener-Hooker, & Shah, 2020) The progression of cancerous diseases is unpredictable and may worsen rapidly, end-stage patients may become ineligible for treatment. (Ghosh & Gheorghe, 2019)Thus, companies continuously explore opportunities to reduce TRT to ensure the patient can receive treatment within a reasonable timeframe. Secondly, the relatively short shelf life of fresh T-cells poses challenges to coordinating manufacturing slots and distribution networks. Patients must have manufacturing slots available and reserved for them before undergoing leukapheresis. (Tyagarajan, Schmitt, Acker, & Rutjens, 2019) In addition, any delays during transportation will disrupt the manufacturing schedule and affect the production of all therapies. (Sonnenberg, 2019) CAR T-cell can be cryopreserved at -150°C for up to 15 months. This provides the flexibility that allows the procedure to meet the patient's needs rather than those of the manufacturing site, accommodate shipping delays and eliminate time constraints during transportation. The establishment of a global cold supply chain network is also crucial for the development of allogeneic therapy. (Tyagarajan, Schmitt, Acker, & Rutjens, 2019)

In this paper, a Mixed Integer Linear Programming (MILP) formulation is developed to conduct a cost-benefit analysis of fresh and cryogenic transport and storage under different maximum TRT allowed.

2. Background

Due to the patient specific nature of CART therapy, it creates unprecedented challenges in terms of manufacturing and logistics when compared to other pharmaceutical products. The one-to-one model of autologous CART therapy inherently limits process scale-up which eventually leads to the high treatment cost. Moreover, the short shelf-life and instable properties of CART cells further increases the risk of failure of the supply chain (Panch, et al., 2019). Uncertainty in demand also adds more complexity to the supply chain because production could not be simply scaled up to meet the extra demand. As a result, the application of CART at large scale is still very limited currently.

A successful CART therapy supply chain should have the following criteria (BCG, n.d.):

- Short and predictable return time
- Low failure rate at manufacturing
- High efficacy at treatment
- Low treatment costs for patients

The autologous CAR T-cell therapy supply chain involves 5 major steps, namely leukapheresis, storage, manufacturing, quality control, and hospital treatment, as shown in Figure 1. Thorough planning and patient scheduling are needed to deliver CAR T-cell therapy quickly and at an affordable cost.

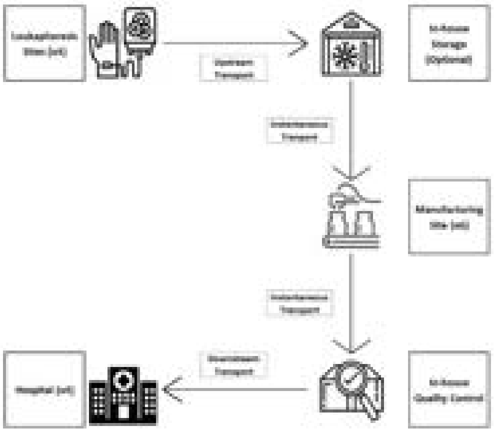

Figure 1. Process Flow Diagram of the Production of Autologous CAR T Drugs

1. Leukapheresis

The adoptive cell technology (ACT) in autologous CAR T-cell therapy requires patients' T-cells as raw material for the manufacturing of CAR T drugs. Whereas for allogeneic CAR T-cell therapy, T-cells are collected from regular blood donors at this stage. For autologous therapies, patients are connected to a leukapheresis machine which could separate and collect T-cells from patient's blood to produce an enriched leukapheresis product known as the leukopak (HemaCare, n.d.). The remaining blood will be returned to the patient's blood circulation via a vein on the other arm (Caltag Medsystems, n.d.). Typically, a target volume of 10-20L of blood is processed by the leukapheresis machine to deliver a leukopak of 100-500ml (EMJ, 2020). Within 24 hours after the extraction process, the leukapheresis product will be frozen and shipped either fresh (-80 °C) or cryogenic (-180 °C) (Papanthanasious, Stamatis, Farid, Titchener-Hooker, & Shah, 2020).

2. Upstream Transport

The leukopak will be transported in either a fresh or cryogenic state to the storage facility co-located to the manufacturing site. In our model, both fresh and cryogenic transport times are strictly limited to 3 days.

The unit transport costs of upstream and downstream cryogenic transportation are given by TrakCel Ltd. a market-leading software developer for advanced therapy supply chains. Since the data only includes the costs of one- or two-day delivery, we estimated the cost for three-day delivery in this study. Literature results show that the transport cost curve as a function of delivery time is negatively accelerated (Tavasszy, Ruijgrok, & Davydenko, 2012). This can be explained by the phenomenon of diminishing marginal returns and thus, the transport costs are modelled with the power law.

For the cost of fresh transport, it is assumed to be 50% of that of cryogenic transport. The cost is modelled in such a way for simplicity.

3. Storage (Optional)

Once the leukopak arrives at the manufacturing site, it will have the option of temporary storage in a freezer or entering the production lines directly. T-cells could be stored temporarily so that it allows flexibility to the production schedule, especially when busy manufacturing sites are constantly running at their full capacity. Cryopreservation is a process that suppresses the formation of intracellular ice crystals and could avoid cell damage during the process (Heubinger, et al., 2016). The cells will be cooled down to a very low temperature by liquid nitrogen. Typically, 10-14 days of cryogenic transport plus storage lead time can still maintain the good quality of the T-cells (Papanthanasious, Stamatis, Farid, Titchener-Hooker, & Shah, 2020). On the other hand, the lead time for fresh transport plus storage should be as short as possible because beyond 24 hours after the extraction, the T-cell viability could drop as much as half of its original amount, depending on the storage temperature (Tyagarajan, Schmitt, Acker, & Rutjens, 2019). In our model, the time for fresh and cryogenic storage is strictly limited to 3 and 10 days respectively.

Our choice of equipment for cryopreservation is the Thermo Scientific CE8120, a device that requires liquid nitrogen and electricity for freezing and can maintain a stable temperature at -185°C (Thermo Fisher Scientific, 2014). The cryogenic storage cost was broken down into 5 categories: capital cost, energy cost, liquid nitrogen cost, labour cost and maintenance cost. It is assumed that energy cost and liquid nitrogen cost are variable costs that vary against the number of leukopak at storage, whereas the other three costs are fixed.

The cost of fresh storage is expected to be lower than that of cryogenic storage because fresh storage does not require LN2 and consumes less electricity for cooling. Hence, for simplicity purposes, the total fresh storage cost is assumed to be the half of that of cryogenic storage.

4. Manufacturing & Quality Control

The manufacturing of CAR T drugs is the most time-consuming step throughout the supply chain. The first two steps are activation and expansion of T-cells (Skorka, Ostapinska, Malesa, & Giannopoulos, 2020). Next, transduction takes place and the leukapheresis products will be cultured in a bioreactor in the presence of a viral vector encoding CAR. The gene transfer would allow the expression of chimeric antigen receptors on the surface of the T-cells. The CAR receptor will be able to identify specific antigens on tumour cells. CD19 is the typically targeted antigen in CAR T-cell therapy for haematological cancers because CD-19 is not expressed in any healthy cells except B-cells, making it an ideal targeted antigen for CAR T-cell therapy (Frost & Sullivan, 2018). Finally, the genetically modified T-cells will be left in the bioreactor for another 9 to 11 days for the expansion of cell culture. The product will be concentrated into a smaller volume and will be suitable for blood infusion (Levine, Miskin, Wonnacott, & Keir, 2017). It is assumed that at the current technological level, the manufacturing of CAR T-cells would require a total of 13 days on average (Bernardi, et al., 2021). Following the completion of the production of CAR T-cell, the quality of the final products will be accessed during the quality control procedures at the manufacturing site and is assumed to spend 1 day.

Both the unit manufacturing and quality control cost are obtained from TrakCel Ltd. The exact values are proprietary information and cannot be disclosed.

5. Downstream Transport

Like upstream transport, the CAR T-cells will be cryopreserved and transported to the hospital within 3 days. The costs are also estimated similarly as the upstream transport.

6. Medical Administration at Hospital

Patients will receive the treatment once the CAR T-cell arrives at the hospital. Prior to the administration of CART, patients must be given chemotherapy to lower their immune cell count so that CAR T cells will have a higher chance of activation and could fight cancer effectively (American Cancer Society, n.d.).

3. Methods

The following model is constructed on the Python 3.7.1 and PYOMO 6.1.2 platform. In this study, the CPLEX 20.1.0.0 solver is used to solve the mixed-integer linear programming (MILP) problem because the solver is one of the most efficient commercial optimisation tools available in the market (Miltenberger, 2015). The model in this study is constructed with reference to previous research done by Dr Maria Papathanasiou's group.

The CAR T-cell therapy supply chain is comprised of 5 nodes namely, leukapheresis site, storage site, manufacturing site, quality control, and hospital. It is assumed that 4 leukapheresis sites, 6 manufacturing sites and 4 hospitals are available in the model, as shown in Figure 2. Details of these nodes are summarised in Table 1.

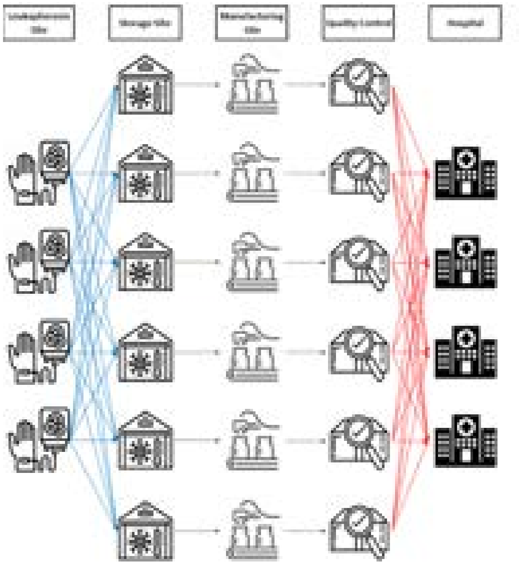

Figure 2. Supply Chain Network of Autologous CART Therapy

Node	Location	Capacity
Leukapheresis sites		
c_1	London	8 patients/day
c_2	Glasgow	
c_3	Manchester	
c_4	Birmingham	
Manufacturing sites including co-located storage and quality control		
m_1	UK/Stevenage	4 parallel lines
m_2	EU/Berlin	31 parallel lines
m_3	EU/Belgium	10 parallel lines
m_4	USA/Pennsylvania	4 parallel lines
m_5	USA/Virginia	31 parallel lines
m_6	UK/Glasgow	10 parallel lines
Hospitals		
h_1	London	No upper limit
h_2	Glasgow	
h_3	Manchester	
h_4	Birmingham	

Table 1. Overview of Locations and Capacities of Different Nodes

The objective of the optimisation problem is to minimise the average cost per therapy over a time horizon of a quarter of a year. Meanwhile, the supply chain must fulfil various constraints ranging from maximum TRT, production capacity, and material balances. Detailed mathematical equations could be found in Table 3. The decision variables of the problem include:

- Assignment of each therapy to a manufacturing site
- Decision if storage is used and duration for storage
- Time for upstream and downstream transport

The supply chain network is assessed for the demand scenario of 200 patients per year and at different maximum allowable TRT. The financial performance of fresh transport and storage was also compared with cryogenic transport and storage. Please refer to Table 2 for the detailed description of scenarios assessed in this report.

Scenario	Upstream Transportation	Downstream Transportation	Storage	Upstream Transportation /Storage Mode	Max TRT
1-8	Up to 3 days	Up to 3 days	Up to 10 days	Cryogenic	17-23,28
9-15	Up to 3 days	Up to 3 days	Up to 3 days	Fresh	17-23
16-21	1 day	Up to 3 days	Up to 3 days	Fresh	17-22
22-26	2 days	Up to 3 days	Up to 3 days	Fresh	18-22
27-30	3 days	Up to 3 days	Up to 3 days	Fresh	19-22

Table 2. Different Scenarios Assessed

Index	**Mathematical Formulation**	**Description**
Objective function		
(1)	$\min TOTCOST = \sum_p CTM_P + \sum_p CQC_P + \sum_p TTC_P + \sum_p CSTOR_P$	Minimise the total cost of therapies
(2)	$CTM_p = \frac{NT \cdot \sum_m E1(CIM_m + CVM_m)}{NP} , \forall p$	Manufacturing cost for each therapy
(3)	$\sum_p CQC_p = NP \cdot CostQ_p$	Total quality control cost of all therapy
(4)	$TTC_P = \sum_{c,m,j,t} Y1_{p,c,m,j,t} \cdot U1_{c,m,j} + \sum_{m,h,k,t} Y2_{p,m,h,k,t} \cdot U2_{m,h,k} , \forall p$	Transport Cost of for each therapy between leukapheresis site/ hospital and manufacturing site
(5)	$CSTOR_P = CostS_{FC} + \sum_{m,d,t} S1_{p,m,d,t} \cdot TSTOR_d \cdot CostS_{daily} , \forall p$	Storage cost of each therapy
Constraints		
(6)	$INC_{p,c,t} = OUTC_{p,c,t+TLS} , \forall p,c,t$ $INS_{p,m,d,t} = OUTS_{p,m,d,t+TSTOR_d} , \forall p,m,d,t$ $INM_{p,m,t} = OUTM_{p,m,t+TM+TQC} , \forall p,m,t$	Sample balances at leukapheresis, storage and manufacturing site
(7)	$LSR_{p,c,m,j,t} = LSA_{p,c,m,j,t+TT1_j} , \forall p,c,m,j,t$ $FTD_{p,m,h,k,t} = MSO_{p,m,h,k,t+TT2_k} , \forall p,m,h,k,t$	Transport constraints
(8)	$OUTC_{p,c,t} = \sum_{m,j} LSR_{p,c,m,j,t} , \forall p,c,t$ $INM_{p,m,t} = \sum_d OUTS_{p,m,d,t} , \forall p,m,t$ $OUTM_{p,m,t} = \sum_{h,k} MSO_{p,m,h,k,t} , \forall p,m,t$ $INH_{p,h,t} = \sum_{m,k} FTD_{p,m,h,k,t} , \forall p,h,t$	The samples leaving a node at time *t* that are equal to patient samples arrives at the succeeding node under transport mode *j*/*k* at time *t*.
(9)	$\sum_{c,j} LSA_{p,c,m,j,t} = \sum_d INS_{p,m,d,t} , \forall p,m,t$	The option to store therapy sample at the manufacturing facility at the given time
(10)	$CAP_{m,t} = FCAP_m - \sum_p INM_{p,m,t} , \forall p,m,t$ $\sum_p INM_{p,m,t} - \sum_p OUTM_{p,m,t} \leq CAP_{m,t} , \forall p,m,t$	The capacity of each manufacturing site at any given time do not exceed the available capacity
(11)	$X1_{c,m} \leq E1_m , \forall c,m$ $X2_{m,h} \leq E1_m , \forall m,h$	Matches are only made with existing manufacturing facilities
(12)	$\sum_{c,m,j,t} Y1_{p,c,m,j,t} \leq 1 , \forall p,c,m,j,t$ $\sum_{m,h,k,t} Y2_{p,m,h,k,t} \leq 1 , \forall p,m,h,k,t$ $\sum_{m,d,t} S1_{p,m,d,t} \leq \sum_{c,m,j,t} Y1_{p,c,m,j,t} , \forall p$	Ensures only one transport mode can be selected for each journey and one storage delay mode for each therapy
(13)	$\sum_{m,k,t} Y2_{p,m,h1,k,t} \leq \sum_t INC_{p,c1,t} \times t , \forall p$	Ensure a match is only made between a leukapheresis site

	$\sum_{m,k,t} Y2_{p,m,h2,k,t} \leq \sum_{t} INC_{p,c2,t} \times t \ ,\forall p$ $\sum_{m,k,t} Y2_{p,m,h3,k,t} \leq \sum_{t} INC_{p,c3,t} \times t \ ,\forall p$ $\sum_{m,k,t} Y2_{p,m,h4,k,t} \leq \sum_{t} INC_{p,c4,t} \times t \ ,\forall p$	and its corresponding co-located hospital
(14)	$\sum_{p,ht} INH_{p,h,t} = NP \ ,\forall p,h,t$	Demand constraint
(15)	$Y1_{p,c,m,j,t} \leq X1_{c,m} \ ,\forall p,c,m,j,t$ $Y2_{p,m,h,k,t} \leq X2_{m,h} \ ,\forall p,m,h,k,t$	Therapies can be transferred between nodes if and only if a match between the corresponding facilities has been previously made
(16)	$LSR_{p,c,m,j,t} \geq Y1_{p,c,m,j,t} \times FMIN \ ,\forall p,c,m,j,t$ $LSR_{p,c,m,j,t} \leq Y1_{p,c,m,j,t} \times FMAX \ ,\forall p,c,m,j,t$ $MSO_{p,m,h,k,t} \geq Y2_{p,m,h,k,t} \times FMIN,\forall p,m,h,k,t$ $MSO_{p,m,k,j,t} \leq Y2_{p,m,h,k,t} \times FMAX,\forall p,m,h,k,t$ $INS_{p,m,d,t} \geq S1_{p,m,d,t} \times FMIN \ ,\forall p,m,d,t$ $INS_{p,m,d,t} \leq S1_{p,m,d,t} \times FMAX \ ,\forall p,m,d,t$	Ensures a minimum and maximum flow of material exists for a transportation link and a storage site to be established
(17)	$STT_p = \sum_{c,t} INC_{p,c,t} \times t \ ,\forall p$ $CTT_p = \sum_{h,t} INH_{p,h,t} \times t \ ,\forall p$	The time point when a patient checks into a leukapheresis site and when therapy is delivered to the hospital
(18)	$STT_p \leq CTT_p \ ,\forall p$ $TRT_p = CTT_p - STT_p \leq 17 \ ,\forall p$	The TRT of therapy is less than or equal to 17 days. (can change up to 28 days depending on various scenarios.)
(19) Fresh Only	$LCTT_p = \sum_{c,t} OUTC_{p,c,t} \times t \ ,\forall p$ $AMTT_p = \sum_{h,t} INM_{p,m,t} \times t \ ,\forall p$	The time point when a therapy leaves the leukapheresis site and when therapy is delivered to the manufacturing site
(20) Fresh Only	$STT_p \leq CTT_p \ ,\forall p$ $STMTT_p = AMTT_p - LCTT_p \leq 4 \ ,\forall p$	The upstream delivery time for fresh transportation is less than or equal to 4 days.
Additional Calculations		
(19)	$DURM_{p,m,t} = \sum_{t} INM_{p,m,t-1} - \sum_{t} OUTM_{p,m,t} + OUT_{p,m,t} \ ,\forall p,m,t$	The manufacturing time of therapy in each facility. $DURM_{p,m,t}$ takes the value 1 only for the time points that the therapy is being manufactured.
(20)	$RATIO_{m,t} = \frac{\sum_p DURM_{p,m,t}}{FCAP_m} \ ,\forall m,t$	Percentage of the utilisation of manufacturing site at a given time
(21)	$ATRT = \frac{\sum_p TRT_p}{NP}$	Average return time of all the therapies

Table 3. Equations for Objective Function and Constraints

4. Results

The data and python code for all scenarios investigated in this section can be made available upon request.

4.1 Average Cost per Therapy and Average TRT

Scenario 1-8: Cryogenic Transport and Storage

Figure 3 illustrates the result of scenarios 1-8 in terms of the average therapy cost and average TRT. The average cost of cryogenic transportation and storage decreases exponentially from \$146491.52 to \$143177.77 between 17 to 23 days maximum TRT. It should be noted between 23 and 27 days maximum TRT, the average cost of therapy plateaus at \$143177.77 and the delivery modes and storage delays remain the same. Beyond 28 days maximum TRT, the average cost of therapy decreases significantly to \$83260.51. Figure 4 illustrates the breakdown of cost between 23 and 28 maximum TRT. Notably, the average cost of manufacturing halves from \$120307.87 to \$60153.94.

As illustrated in Figure 3, the average TRT increases accordingly from the constraint of maximum TRT 17 to

21 days. However, beyond 21 days maximum TRT, the average TRT plateaus at 21 days. An increase in average TRT can be observed at 28 days maximum TRT.

Scenario 9-15: Fresh Transport and Storage

Figure 5 illustrates the cost of fresh transportation and storage which decreases exponentially from $144448.70 to $141957.57 between 17 to 22 days maximum TRT. As the TRT constraint is further relaxed beyond 22 days, the average cost per therapy plateaus because the problem is already constrained to 22 days (max 4 days upstream, 3 days downstream).

Between 17 to 21 days maximum TRT, the average TRT increases with the constraint. However, it plateaus at 21 days beyond 21 days maximum TRT.

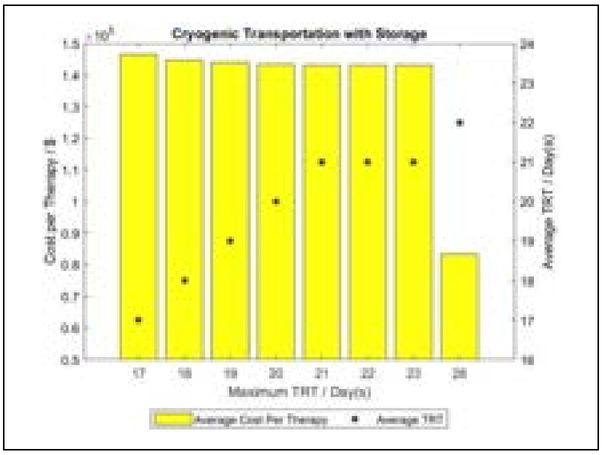

Figure 3. Average therapy cost (bar plots) and average return time (scatter plots) considering different maximum total return time allowed for cryogenic transportation with storage.

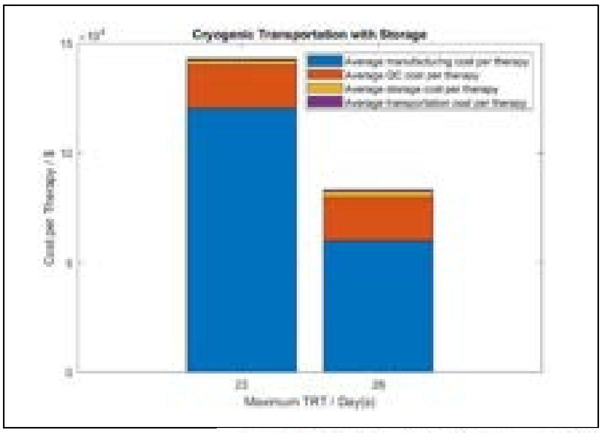

Figure 4. Cost breakdown of cryogenic transportation with storage for investigated scenarios of 23 and 28 maximum total return time.

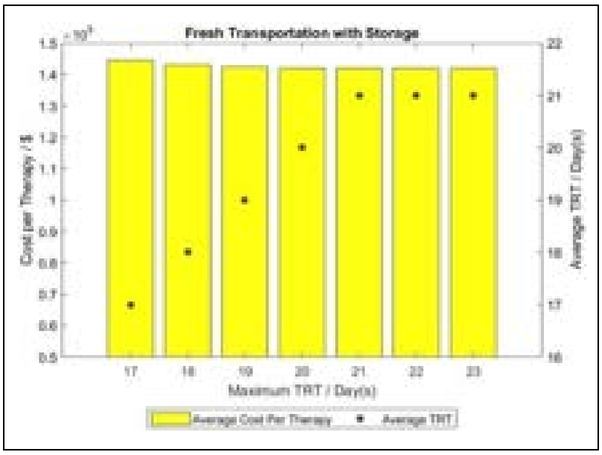

Figure 5. Average therapy cost (bar plots) and average return time (scatter plots) considering different maximum total return time allowed for fresh transportation with storage.

Scenario 16-30: Fixed Upstream Delivery Time

From Figure 6, in all the three cases of scenarios 16-30, the transportation cost decreases exponentially with increasing maximum TRT allowed. In general, the 2-day fixed upstream delivery mode has the highest usage of storage facility thus the highest storage cost. It should be noted that the manufacturing cost and quality control cost remains at $120307.87 and $19788.00 respectively, therefore it is not included in the chart to highlight the difference in transportation and storage cost.

Figure 6 also shows that the average TRT increases with the constraint initially. However, the average TRT plateau at 19, 20 and 21 days for 1, 2 and 3 days fixed upstream transportation respectively.

4.2 Distribution of TRT (Scenario 1-8)

Figure 7 illustrates the distribution of TRT of each therapy at 21, 22, 23 and 28 days maximum TRT for cryogenic transport and storage. As the TRT constraint is relaxed, the variation increases. For scenarios of 21, 22 and 23 days maximum TRT, most of the therapy has a TRT of 21 days with a few expectations. A statistical mode of 21 days TRT is observed. However, for scenarios of 28 days maximum TRT, the distribution is skewed and have a higher standard deviation of TRT of each therapy.

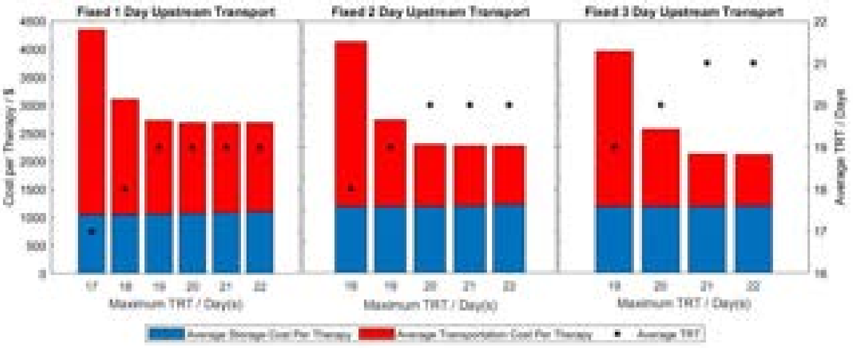

Figure 6. Comparison of average storage cost and transportation cost of fresh transportation with storage given a fixed upstream transport mode considering different maximum total return time.

Figure 7. Distribution of total return time of each therapy at 21, 22, 23 and 28 Days maximum total return time for cryogenic transport and storage

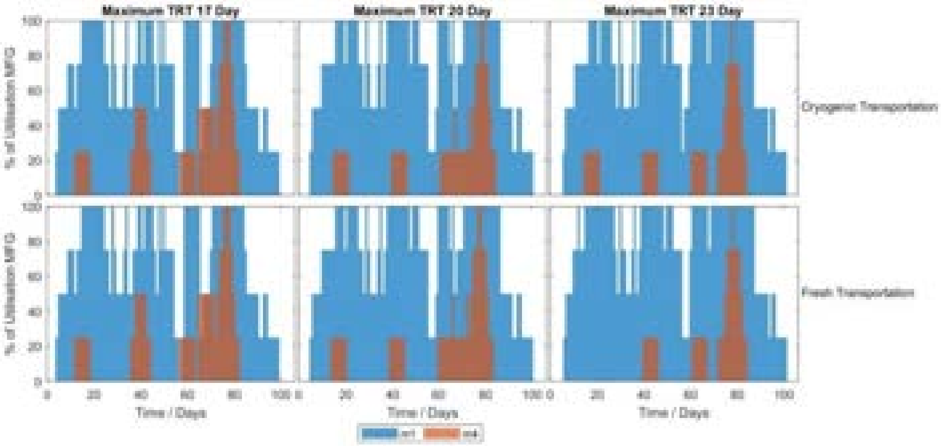

Figure 8. Comparison of percentage of utilisation of manufacturing site (MFG) at each time point for cryogenic transportation with storage and fresh transportation with storage considering 17, 20 and 23 maximum total return time allowed.

4.3 Utilisation of Production Capacity

The percentage of utilisation of each manufacturing site against time is plotted in Figure 8. Two manufacturing sites are established: Stevenage facility, UK (m_1) and Pennsylvania, USA (m_4). Most of the production will take place at the former site.

5. Discussion

5.1 Average Cost per Therapy and Average TRT

Scenario 1-8: Cryogenic Transport and Storage

The major advantage of cryopreservation is that it provides additional flexibility for manufacturing and allow production to focus on one plant. This is only useful when the max TRT constraint has a low requirement, and the production capacity of the cheapest facility has a high production capacity.

A significant drop in the average cost of therapy is observed when 28 days of maximum total return time is allowed. The manufacturing cost halves as only one manufacturing site is used instead of two so that a large sum of capital cost could be saved. Increase usage of storage supports the scheduling which focuses production in one facility. In the case of 28 days of max TRT, the median return time is 21 days. The average return time is acceptable in today's standard because typical CART vein-to-vein time takes around 3-4 weeks in reality (Ghosh & Gheorghe, 2019). Nevertheless, this does not account for the variation in the actual TRT and will be further discussed in Section 5.2.

Scenario 9-15: Fresh Transport and Storage

The decrease of therapy cost by relaxing turnaround time constraints is largely hindered by the short lifetime of fresh T-cells. At low maximum turnaround time, fresh storage gives rise to a slightly lower therapy cost due to the lower cost in fresh transportation and storage. Fresh transport is a cheaper option in general because of its low cooling requirement. Hence, fresh transport is a more viable option financially particularly when TRT constraint has a short time.

Scenario 16-30: Fixed Upstream Delivery Time

In real-life settings, it is hard for manufacturers to accurately predict the demand profile of therapy. Hence, it would be reasonable for drug companies to adopt the same type of delivery and the same delivery time for every therapy. The cost of therapy in this realistic case (scenario 16-30) is compared with that of the idealised, the most optimised scenarios (scenario 9-15). Table 4 shows the % increase of average therapy cost of the realistic case compared to the idealised case. Overall, the fixed delivery modes only increase the therapy cost by a small margin of no more than 0.79%. The transport cost is increased but it only accounts for a very small share in terms of the total therapy cost. It is thus reasonable for CAR T-cell manufacturers to fix all delivery times for every therapy so that they could cope with the uncertainties in demand, despite costing slightly more than the most optimised scenarios.

The performances of the three delivery modes are compared internally within scenarios 16-30. The most cost-effective upstream delivery mode depends on the maximum TRT constraint and is summarised in Table 5.

Max TRT (days)	Fixed 1 Day	Fixed 2 Days	Fixed 3 Days
17	0.00%	/	/
18	0.03%	0.42%	/
19	0.23%	0.03%	0.79%
20	0.47%	0.01%	0.18%
21	0.57%	0.10%	0.01%
22	0.58%	0.12%	0.01%

Table 4. % Difference of Therapy Cost between Realistic and Idealised Case

Max TRT (days)	Fixed 1 Day	Fixed 2 Days	Fixed 3 Days
17	✓		
18	✓		
19		✓	
20		✓	
21			✓
22			✓

Table 5. The Most Cost-Effective Choices for different Max TRT

5.2 Distribution of TRT of Each Therapy (Scenario 1-8)

The variation of TRT of each therapy with cryogenic storage is measured in terms of standard deviation (SD) and is summarised in Table 6. As the max TRT constraint is relaxed, the SD of the TRT of each therapy increases. This implies that some of the patients would have to wait longer to receive their medical administration. It could trigger ethical concerns as most of the patients are in life-threatening conditions and early treatment could potentially make a huge difference to the efficacy of treatment. Some of the patients will be significantly disadvantaged if they receive their medication later than expected (the average TRT). It is believed that the SD of 2.71 days from max TRT 28 is unacceptable and delivering CAR T-cell therapy with such a high uncertainty in TRT is not a viable option.

TRT 21	TRT 22	TRT 23	TRT 28
0.24	0.40	0.44	2.71

Table 6. Standard Deviations of the Distribution of TRT (Days)

5.3 Utilisation of Production Capacity

As described in Section 4.3, the two manufacturing facilities, m_1 and m_4 are the most favourable options amongst all available production plants because both have the lowest manufacturing costs of $23136.13 per day. Between the two, m1 is more favourable than m_4 since m_1 is in England while m_4 is in the US. m_1's proximity to leukapheresis sites and hospitals could greatly reduce transport costs and hence lower the overall therapy cost. Travelling distance is one of the dominant factors that affects the transport cost.

6. Conclusions

Fresh transport and storage are generally a cheaper option for the CAR T-cell therapy supply chain with a very limiting TRT constraint; while cryopreservation is better when TRT constraint has a longer allowable time. Although 28 days TRT with cryogenic storage has the lowest therapy cost among all scenarios assessed in this study, such a method is not recommended due to the high variation in TRT of therapy. With the assumptions in our model and the available facilities in the supply chain, it could be concluded that fresh transport and storage is a better option than cryopreservation. This conclusion is drawn in consideration of mainly two factors, the average cost of therapy and the standard deviation of the average TRT of each therapy.

Furthermore, keeping all delivery time to a constant number of days should be adopted to account for the uncertainty in the demand profile. The financial performances of fixed upstream delivery modes are evaluated. The cost per therapy only increases by a small percentage compared to the most optimised case. Therefore, the constant delivery time should be implemented. The exact delivery time to be used depends on the max TRT constraint that we set.

Finally, from the results of the utilisation profile at each plant, it could be shown that the utilisation of the UK Stevenage could lower the manufacturing cost. The next best option for manufacturing will be the Pennsylvania (US) facility. The production of CAR T-cells experiences economies of scale due to the capital-intensive nature of the CAR T-cell manufacturing industry. As more production processes are focused on a single facility, the average cost of therapy could be lowered by averaging out the fixed cost from manufacturing. Thus, researchers should concentrate on process scale-up instead of scale-out to improve the cost-effectiveness of CAR T-cell manufacturing processes.

7. Outlook

In this study, the average cost per therapy is considered as the only objective function. However, there are other aspects of the supply chain that should be taken into consideration for the scheduling of each therapy. For example, the mean and the standard deviation of therapy TRT should also be treated as other objective functions for minimisation. This would formulate a multi-objective optimisation (MOO) problem and could be solved by advanced techniques such as the weighted sum method and ε-constraint method.

Further studies regarding the supply chain of the allogeneic CAR T-cell therapy supply chain should be conducted to evaluate its financial performance compared with autologous CAR T-cell therapy. Allogeneic CAR T-cell therapy is a process that utilises T-cells from regular blood donors instead of from patients' blood so that universal T-cell drugs could be produced and will be readily available for medical administration (LONCAR, 2018). Cryogenic storage is expected to play a crucial role in allogeneic therapy because the CAR T-cell must be stored for days or even weeks before they are ordered for treatment. It is important to understand the feasibility of applying cryogenic storage in allogeneic CAR T-cell therapy in terms of the technical and financial aspects.

Another opportunity of T-cell therapy is its application beyond oncology such as autoimmune disorders and viral infections, and SARS-CoV-2 (Zmievskaya, et al., 2021). The wide application of CAR T-cell therapy could potentially provide patients with an alternative treatment method for their deadly diseases.

8. Nomenclature

Indices	
c	Leukapheresis sites
h	Hospitals
j	Upstream transport mode
k	Downstream transport mode
d	Delay mode
m	Manufacturing Site
p	Patients
t	Time points
Parameters	
$TOTCOST$	The total cost of all therapies p
CIM_m	Capital investment for manufacturing site m
CQC_p	In house quality control cost for therapy p
CVM_m	Fixed variable cost for manufacturing facility m
$TT1_j$	Transport time from leukapheresis to manufacturing site via transport mode j
$TT2_k$	Transport time from manufacturing site m to hospital h via transport mode k
$U1_{c,m,j}$	Unit transport cost from leukapheresis site c to manufacturing site m via transport mode j
$U2_{m,h,k}$	Unit transport cost from manufacturing site m to hospital h via transport mode k
$CostQ_p$	Quality control cost per therapies p
$CostS_{FC}$	Fixed cost of storage facility
$CostS_{daily}$	Variable cost of storage facility
$FCAP_m$	Total capacity of manufacturing site m
$INC_{p,c,t}$	Demand therapy p arriving for leukapheresis c at time t
$FMIN$	Minimum flow
$FMAX$	Maximum flow
NP	Number of therapies
NT	Number of time points
TLS	Duration of leukapheresis
$TSTOR_d$	Storage time via delay mode d
$TMFE$	Duration of manufacturing
TQC	Duration of quality control
TAD	Duration of administration
Variables	
CTM_p	Total manufacturing cost of therapy p
TTC_p	Total transport cost per therapy p
$OUTC_{p,c,t}$	Therapy p leaving leukapheresis site c at time t
$LSR_{p,c,m,j,t}$	Therapy p that is leaving leukapheresis site c and is transported to manufacturing site m via transport mode j at time t
$LSA_{p,c,m,j,t}$	Therapy p that left leukapheresis site c arriving at manufacturing site m via transport mode j at time t
$INS_{p,m,d,t}$	Therapy p arriving at manufacturing site m with a delay mode d at time t
$OUTS_{p,m,d,t}$	Therapy p leaving at manufacturing site m with a delay mode d at time t
$INM_{p,m,t}$	Therapy p arriving at manufacturing site m at time t
$OUTM_{p,m,t}$	Therapy p leaving manufacturing site m at time t
$MSO_{p,m,h,k,t}$	Therapy p leaving manufacturing site m and is transported to hospital h via transport mode k at time t
$FTD_{p,m,h,k,t}$	Final therapy that left from manufacturing site m arriving at hospital h via transport mode k at time t
$INH_{p,h,t}$	Therapy p arriving hospital h at time t
$DURM_{p,m,t}$	1 only for the time points t at which a therapy p is manufactured in facility m; 0 otherwise
$RATIO_{m,t}$	Percentage of utilisation of manufacturing site m at time t
$CAP_{m,t}$	Capacity of manufacturing facility m at time t
STT_p	Starting time of treatment for patient p
CTT_p	Completion time of treatment for patient p
$LCTT_p$	Starting time of upstream delivery for patient p
$AMTT_p$	Completion time of upstream delivery for patient p
$STMTT_p$	Duration of upstream delivery for patient p
TRT_p	Total return time of therapy p
$ATRT$	Average return time of all the therapies
$E1_m$	1 if manufacturing facility m is established; 0 otherwise
$X1_{c,m}$	1 if a match between leukapheresis site c and manufacturing facility m is established; 0 otherwise
$X2_{m,h}$	1 if a match between manufacturing facility m and hospital h is established; 0 otherwise
$Y1_{p,c,m,j,t}$	1 if sample p is transferred from leukapheresis site c to manufacturing facility m via transport mode j at time t; 0 otherwise
$Y2_{p,m,h,k,t}$	1 if sample p is transferred from manufacturing facility m to hospital h via transport mode k at time t; 0 otherwise
$S1_{p,m,d,t}$	1 if therapy p enters manufacturing facility m after being stored for d days at time t; 0 otherwise

9. Acknowledgements

We would like to express our heartfelt gratitude to Niki Triantafyllou and Andrea Bernardi for their patience, guidance, and insight over the course of this project.

10. References

Abecma. (2021). Retrieved from U.S. Food and Drug Administration (FDA): https://www.fda.gov/vaccines-blood-biologics/abecma-idecabtagene-vicleucel

Abecma EPAR. (2021). Retrieved from European Medicines Agency (EMA): https://www.ema.europa.eu/en/medicines/human/EPAR/abecma

American Cancer Society. (n.d.). *CAR T-cell Therapy and Its Side Effects*. Retrieved December 08, 2021, from https://www.cancer.org/treatment/treatments-and-side-effects/treatment-types/immunotherapy/car-t-cell1.html

BCG. (n.d.). *The Digital Edge in CAR T-Cell Manufacturing and Delivery*. Retrieved December 08, 2021, from https://www.bcg.com/publications/2021/car-t-cell-therapy-digital-supply-chain

Bernardi, A., Sarkis, M., Triantafyllou, N., Lakelin, M., Shah, N., & Papathanasiou, M. (2021). Assessment of intermediate storage and distribution. *Computers & Chemical Engineering, 157*.

Borgert, R. (2021). Improving Outcomes and Mitigating Costs Associated With CAR T-Cell Therapy . *Optimizing the Value of CAR T-Cell Therapy: Managed Care Considerations From Recent Clinical Findings, Volume 27, Issue 13*.

Breyanzi. (2021). Retrieved from U.S. Food and Drug Administration (FDA): https://www.fda.gov/vaccines-blood-biologics/cellular-gene-therapy-products/breyanzi-lisocabtagene-maraleucel

Caltag Medsystems. (n.d.). *What is Leukapheresis?* Retrieved December 08, 2021, from https://www.caltagmedsystems.co.uk/information/what-is-leukapheresis/

EMJ. (2020). *CAR-T: FROM BED TO BENCH AND BACK AGAIN*. Retrieved December 08, 2021, from https://www.emjreviews.com/hematology/symposium/car-t-from-bed-to-bench-and-back-again/

Farid, S. S., & Jenkins, M. J. (2017). Bioprocesses for Cell Therapies. In E. L. Günter Jagschies, *Biopharmaceutical Processing: Development, Design, and Implementation of Manufacturing Processes* (pp. 899-930). Elsevier.

Frost & Sullivan. (2018). *The Global Immuno-oncology Therapeutics Market— Adoptive T-cell Therapies, Forecast to 2022.*

Ghosh, A., & Gheorghe, D. (2019). *CAR T-Cell Therapies: Current Limitations & Future Opportunities.* Retrieved from Cell and Gene: https://www.cellandgene.com/doc/car-t-cell-therapies-current-limitations-future-opportunities-0001

HemaCare. (n.d.). *Leukopak*. Retrieved December 08, 2021, from https://www.hemacare.com/product/leukopak/

Heubinger, J., Han, H.-M., Hofnagel, O., Vetter, I., Bastiaens, P., & Grabenbauer, M. (2016). Direct Measurement of Water States in Cryopreserved Cells Reveals. *Biophysical Journal, 110*, 840-849.

I.B. Wall, D. B. (2013). Commercial manufacture of cell therapies. *Standardisation in Cell and Tissue Engineering :Methods and Protocols*, 212-239, 239a.

Kymriah. (2017). Retrieved from U.S. Food and Drug Administration (FDA): https://www.fda.gov/news-events/press-announcements/fda-approval-brings-first-gene-therapy-united-states

Kymriah EPAR. (2018). Retrieved from European Medicines Agency (EMA): https://www.ema.europa.eu/en/medicines/human/EPAR/kymriah

Levine, B., Miskin, J., Wonnacott, K., & Keir, C. (2017). Global Manufacturing of CAR T Cell Therapy. *Molecular Therapy: Methods & Clinical Development, 4*.

Miliotou, A. N., & Papadopoulou, L. C. (2018). CAR T-cell Therapy: A New Era in Cancer Immunotherapy. *Current Pharmaceutical Biotechnology, Volume 19*, 5-18.

Miltenberger, M. (2015, September 28). *Introduction to the SCIP Optimization Suite.* Retrieved December 10, 2021, from http://co-at-work.zib.de/berlin2015/files/introduction_to_SCIP_Opt_Suite.pdf

Panch, S., Srivastava, S., Elavia, N., McManus, A., Liu, S., Jin, P., . . . Stroncek, D. (2019). Effect of Cryopreservation on Autologous Chimeric Antigen Receptor T Cell Characteristics. *Molecular Therapy, 27*(7), 1275-1285.

Papanthanasious, M., Stamatis, C., Farid, S., Titchener-Hooker, N., & Shah, N. (2020). Autologous CAR T-cell therapies supply chain: challenges and opportunities? *Cancer Gene Therapy, 27*, 799-809.

Skorka, K., Ostapinska, K., Malesa, A., & Giannopoulos, K. (2020). The Application of CAR-T Cells in Haematological Malignancies. *Archivum Immunologiae et Therapiae Experimentalis*.

Sonnenberg, S. (2019). *Managing the Complexity of the Supply Chain for Cell and Gene Therapies.* Retrieved from pharma's almanac: https://www.pharmasalmanac.com/articles/managing-the-complexity-of-the-supply-chain-for-cell-and-gene-therapies

Tavasszy, L., Ruijgrok, K., & Davydenko, I. (2012). INCORPORATING LOGISTICS IN FREIGHT TRANSPORTATION MODELS: STATE OF THE ART AND RESEARCH OPPORTUNITIES. *Transport Reviews*.

Tecartus. (2020). Retrieved from U.S. Food and Drug Administration (FDA): https://www.fda.gov/vaccines-blood-biologics/cellular-gene-therapy-products/tecartus-brexucabtagene-autoleucel

Tecartus EPAR. (2020). Retrieved from European Medicines Agency (EMA): https://www.ema.europa.eu/en/medicines/human/EPAR/tecartus

Thermo Fisher Scientific. (2014). *Thermo Scientific CryoExtra High-Efficiency Cryogenic Storage.* Retrieved December 10, 2021, from https://www.thermofisher.com/document-connect/document-connect.html?url=https%3A%2F%2Fassets.thermofisher.com%2FTFS-Assets%2FLED%2Fbrochures%2FCryoExtra-Bro-0414.pdf

Tyagarajan, S., Schmitt, D., Acker, C., & Rutjens, E. (2019). *Autologous cryopreserved leukapheresis cellular material for chimeric antigen receptor–T cell manufacture.* East Hanover: Novartis Pharmaceuticals Corporation.

Yescarta. (17). Retrieved from U.S. Food and Drug Administration (FDA): https://www.fda.gov/vaccines-blood-biologics/cellular-gene-therapy-products/yescarta-axicabtagene-ciloleucel

Yescarta. (2018). Retrieved from European Medicines Agency (EMA): https://www.ema.europa.eu/en/medicines/human/EPAR/yescarta

Zhang, e. a. (2020). Efficacy and safety of anti-CD19 CAR T-cell therapy in 110 patients with B-cell acute lymphoblastic leukemia with high-risk features. *Blood Adv (2020) 4 (10)*, 2325–2338.

Virus Mimicking Nanoparticles for Intracellular Delivery

Suthinee Phanuvatsuk and Tudor-Octavian Sîrbu

Department of Chemical Engineering, Imperial College London, U.K.

Abstract. Polymers represent a valuable alternative for drug or gene delivery, being cheaper and safer than their viral counterparts, yet lacking their efficiency. This comes primarily from the bottleneck of endosomal escape, polymers not having naturally evolved to overcome this intracellular barrier. In this study 8 cationic polymers were investigated for their pH responsiveness and their endosomal escape capacity was assessed. Three showed promising results and were further investigated for their temperature, time and concentration dependence. Dynamic Light Scattering (DLS) measurements were performed for Particle Size and Zeta Potential. One of the polymers investigated showed the prospective of being employed as a drug delivery vehicle having great efficiency, as well as minimising the safety risks.

Keywords: pH-responsive polymers, endosomal escape, intracellular delivery, DLS Characterisation

---

1 Introduction

Modern day advancements with drug delivery technology have seen an increasing interest with the application of polymers. Polymers play a fundamental role in many new successful developments into novel drug delivery systems[1].

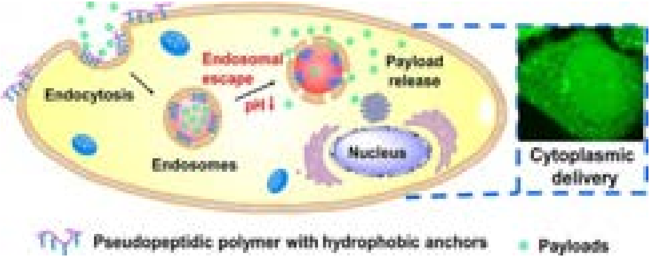

Figure 1: Intracellular trafficking of drug-polymer complexes [2]

Production and ease of synthesis has made the topic of these bio-inspired non-viral vectors an important area in advancing the field of gene therapy[3]. Efficient release of endocytosed materials into the cytoplasm of disease treating drug is also of interest for big pharmaceuticals. The tuneable release of hydrophobic and hydrophilic drugs and the controlled release of therapeutic agents in the body has allowed polymers to be tailored for specific cargo. By influencing the design of polymers, they can also be engineered to exert distinct biological functions during intracellular release and targeted delivery[4]. For pH-responsive polymers which is the focus of this study, the mechanism works by internalizing the polymer-drug conjugate by endocytosis. The acidification of early endosomes causes a shift in the hydrophobic or hydrophilic balance of the polymer, which then enables it to become membrane disruptive. This ultimately causes the release of the drug into the cytosol which is further diffused to the site of action[5].

The use of polymers spans from Polyethylene glycol (PEG) which is used from creams, tablet lubricants and plasticizers to Poly(amino acids) in the formation of micelles and liposomes[6]. Short interfering RNA si(RNA) has shown to be successful in treating triple negative breast cancer demonstrating the importance of research into encapsulating potential of the liposome coating[7]. Despite this, biomacromolecules have limited clinical use due to the difficulty of transport across the plasma membrane. There is a certain limitation to modulating intracellular pathway; like drugs used in chemotherapy which aside from cytotoxicity are inefficient due to non-specific distribution in the bloodstream [8]. Therefore, there is a critical need for drug delivering agents capable of transporting different sized therapeutic payloads to desired intracellular sites. Unfortunately, intracellular delivery of macromolecules remains a challenge[9].

Nonetheless, research into this field has seen several successes from stimuli-responsive smart polymers capable of responding to external stimulus to pH-responsive polymers overcoming intracellular delivery barriers. PP-polymers, which are anionic pH-responsive have shown to be very capable of targeted delivery[10]. Cationic polyethyleneimine[11] has also shown to mediate gene delivery through the proton sponge effect but does suffer from cytotoxicity and low transduction efficiencies[12]. Regardless, cationic lipid and cationic polymers still hold far greater potential in human gene therapy compared to any other polymers due to the ability to form lipoplexes/polyplexes[13]. Felgner [14] was the first to report the use of cationic lipids in 1987 and from then, it has been the most widely studied[15]. This was owing to its high delivery efficiency[16][17]. However, lipid-based gene delivery does have its pitfalls including difficulty in reproducibly fabricating DNA-liposomes complexes and colloidal stability[18]. Consequently, the focus has now been shifted to cationic polymers due to its ability to maintain biocompatibility and stable formulation alongside ease of manufacturing[19]. Following from the works of those before, this research therefore seeks to investigate eight novel cationic polymers to determine its potential in drug delivery and human gene therapy.

2 Methodology

2.1 Materials

Sodium phosphate dibasic, sodium citrate dihydrate and sodium chloride were purchased from Sigma-Aldrich (Dorset, U.K.). Defibrillated sheep red blood cells (RBCs) was purchased from TCS Biosciences (Buckingham, U.K.) and renewed every two weeks.

2.2 Polymers

The polymers studied in this paper were synthesized within the research group. Their structure is presented in *Table **1***. Each polymer has been given an index number which will be used throughout the report. In addition, details about the constituent copolymers and the monomers from which they were derived are given in the Supplementary Information document, if valuable for anyone involved in organic synthesis.

As of interest for the study, a series of features were extracted from the chemical formulas before experiments were carried out. A key characteristic for all polymers was the existence of the methyl polyethylene glycol (mPEG) and the presence of the polycaprolactone (PCL), a hydrophobic group. The former was known to enhance the breakage of membranes whilst the latter made sure the combination of both ensured biocompatibility and biodegradability[20]. The cationic character is given through a secondary amine group which enhanced the membrane breakage through the proton sponge effect. Out of the 8 polymers there were two polymers (2 and 5) which had random arrangements as opposed to the more encountered repeating units. Polymers 1 and 8 also had the same structure but were synthesised via two different routes.

2.3 Haemolysis

The buffer solutions were prepared from 100mM di-sodium phosphate (pH range: 7.4-5.5) and 100mM trisodium citrate dihydrate (pH range: 5.0-4.5) adjusted with 2M HCl solution using a pH meter. This specific pH range mimics the environmental conditions encountered during intracellular cell movement through early endosomes (pH: 6.0-6.8), late endosomes (pH: ~5.5) and lysosomes (pH: ~4.5) [22]. The RBC membranes were modelled as endosomal membranes. The membrane disruptive activity of the polymers was studied using a previously established haemolysis assay[23]. The RBCs were washed at least three times with 150mM NaCl solution and resuspended in buffer solution at pH 7.4. Negative and positive controls were also prepared by resuspending RBCs in buffer alone and deionized water, respectively. The samples were placed in a shaking water bath at 37°C for 1h, and then centrifuged at 3500 RPM for 3 min. The supernatant was removed, and its absorbance was measured using a Genesys 10S UV-Vis Spectrophotometer (Thermo Fisher Scientific, USA), and the percentages of haemolysis were determined. The number of lysed RBCs up to a concentration of 2.64×10^8 RBCs mL^{-1} is shown to be proportional to the absorbance of haemoglobin solution [23]. Each test was performed in triplicates. In the case of the temperature and time dependent assays, a single pH of 6.5 was chosen to reflect early endosomal conditions. The 0°C temperature was maintained using an icebox, for 40°C the water bath was employed, whereas the 22°C temperature was the room temperature the samples were set at.

2.4 Dynamic Light Scattering (DLS)

The hydrodynamic diameter, size distribution and zeta potential of three selected polymers were investigated at pH 6.5 and 7.4 by dynamic light scattering using an Anton Paar Litesizer 500 Particle Size Analyzer. Before the measurement the samples were filtered through 0.45 µm filters. The working temperature was 25°C. In the case of the particle size measurements, a disposable cuvette was employed, with the measurement angle set to automatic and with 6 repeats for each run. In the case of the zeta potential measurements, the approximation method selected was Smoluchowski with 20 repeats for each run.

Table 1: The chemical structures of the polymers studied (1)-(8)

Index	**Chemical Structure**
1	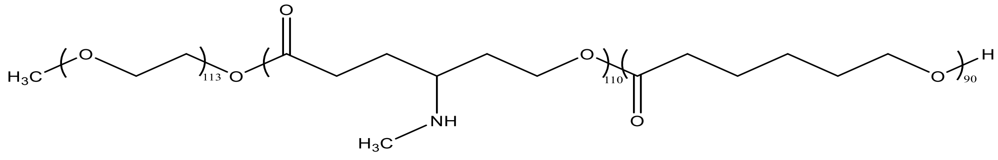
2	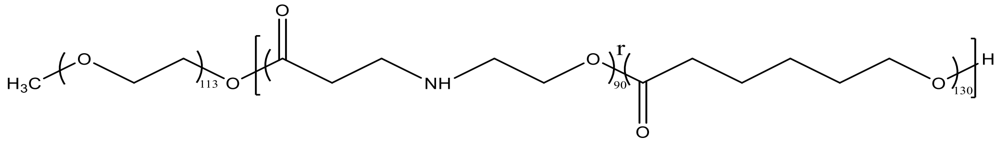
3	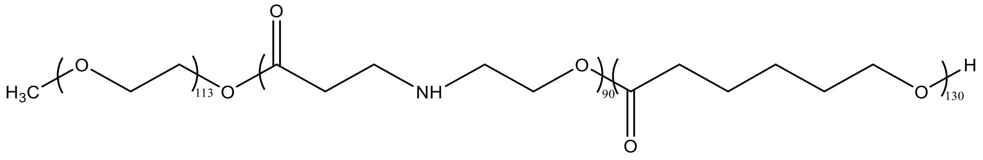
4	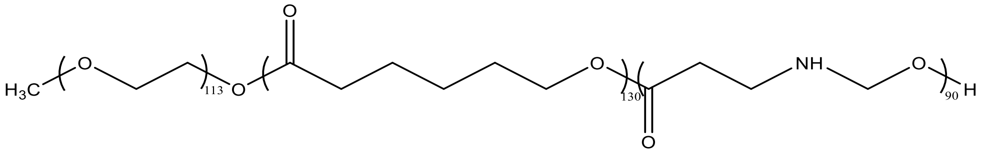
5	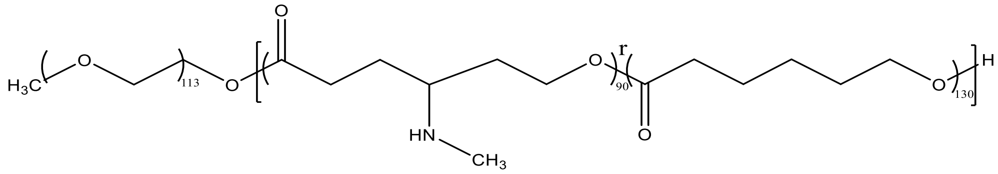
6	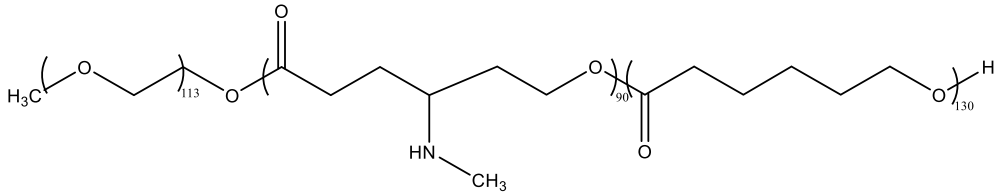
7	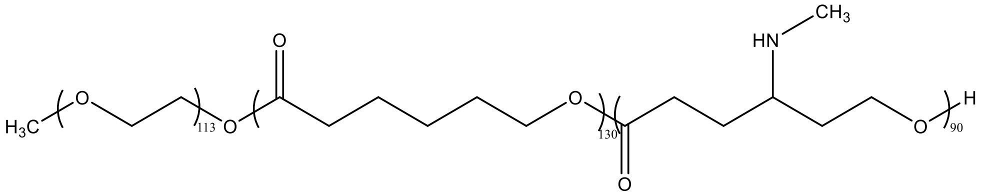
8	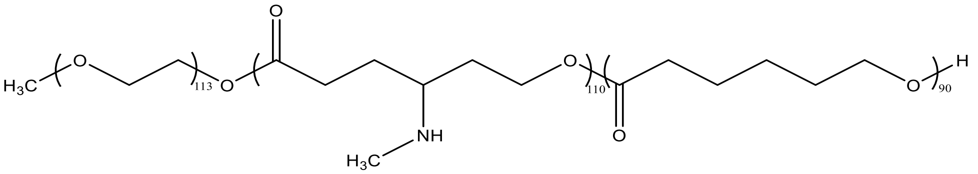

3 Results and Discussion

3.1 Haemolysis Assay

3.1.1 pH dependent haemolysis

The polymers were firstly screened via a pH dependent haemolysis assay in order to assess their responsiveness. The results of this experiment are shown in *Figure 2*.

Reduced lysis was obtained for polymer 1, with its peak being at around 40% alongside polymer 7 which showed almost no haemolysis.

In the case of polymers 3 and 4, their maximum haemolysis was observed at pH 5.5, with otherwise negligible activity. This pH corresponded with the lysosomal pH range, where an escape would be inefficient due to the hydrolytic enzymes present in lysosomes which would degrade the drug-polymer complex [22].

Polymer 6 displayed a higher haemolysis in comparison to the polymers already described. It had a pH higher of around 6 corresponding to the range for early endosomal release. However, as observed in the figure, its behaviour is not consistent, with a significant decrease taking place at pH 6.5. Due to this unusual trend, the assay was rerun, but the same shape was obtained. This raised the issue of stability for this polymer, as even small changes of pH can lead to considerable changes in haemolysis.

For polymer 5 a plateau can be observed at a pH above 5.5 with a haemolysis value of around 80%. This consistency in the pH range is beneficial for the endosomal escape, however it remaining constant even at the physiological pH of 7-7.4 raises issues regarding its possible cytotoxicity.

Two experiments were performed for polymer 8 due to the unexpected value at pH 5.

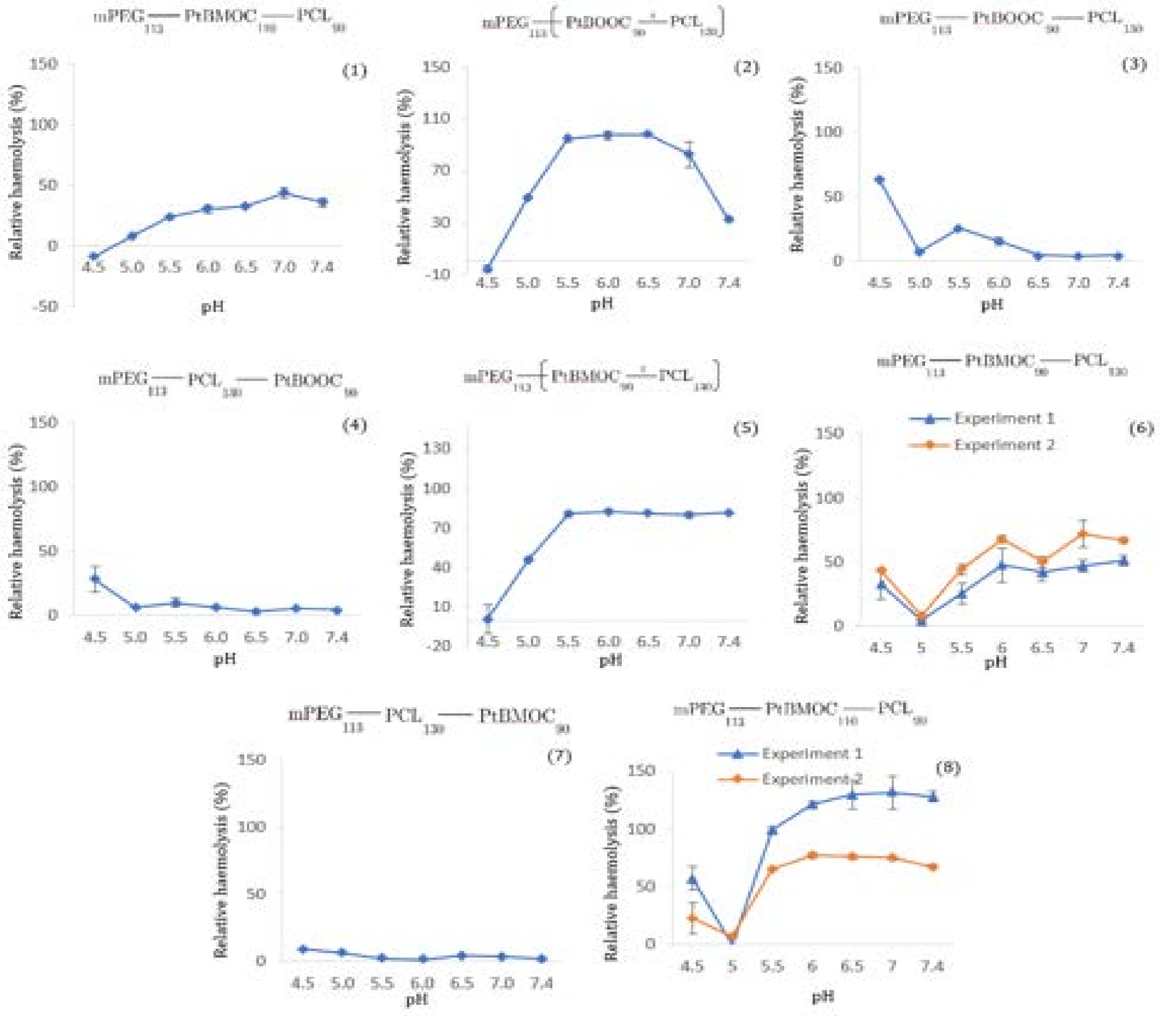

***Figure 2*:** pH dependent haemolysis for polymers 1-8

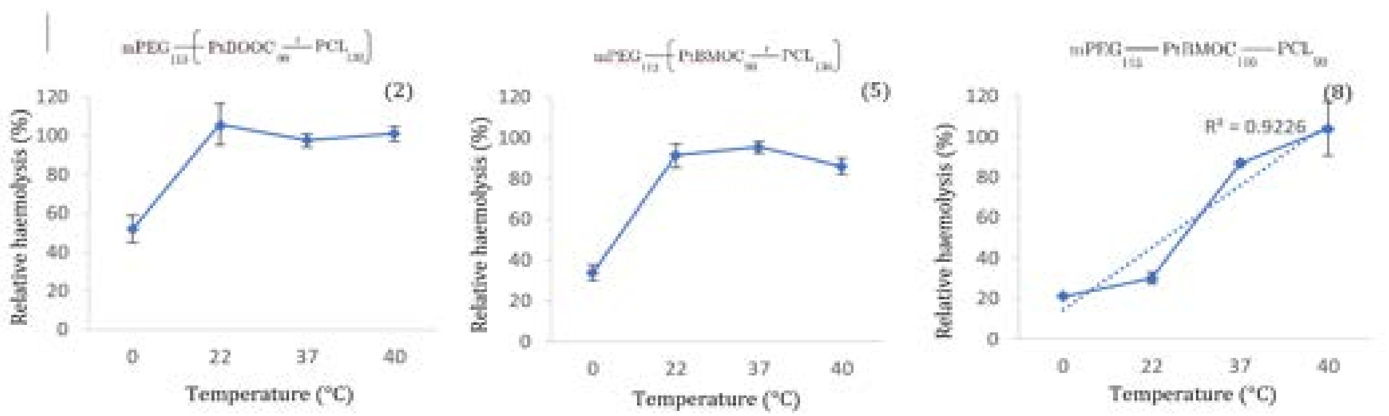

***Figure 3*: Temperature dependent haemolysis for polymers (2), (5), (8) at pH 6.5**

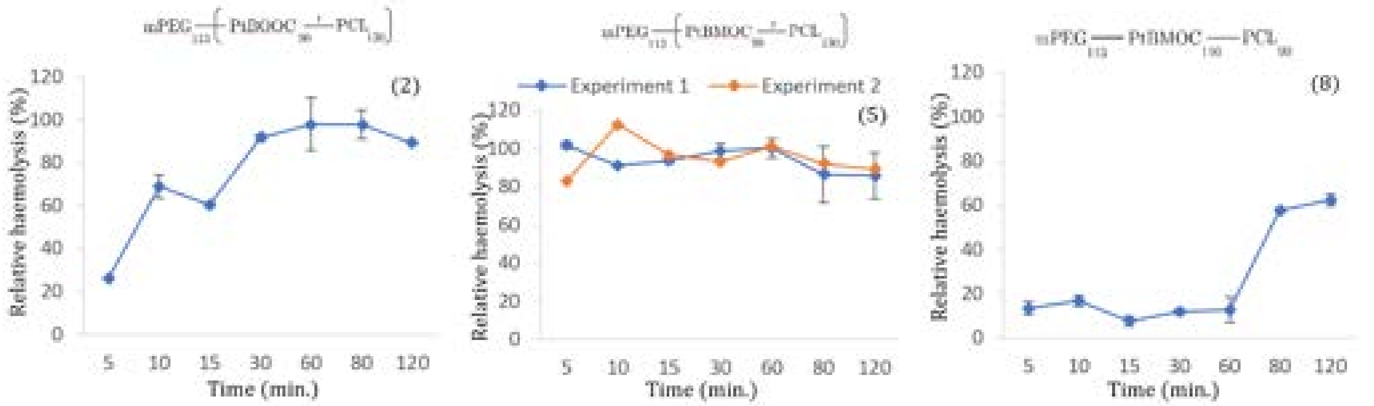

***Figure 4*: Time dependent haemolysis for polymers (2), (5), (8) at pH 6.5**

The results showed similar trends with a plateau being reached after pH 5.5. The haemolytic activity at endosomal pH was desirable but the high haemolysis at pH 7.4 raised issues of cytotoxicity similar to polymer 5. The difference in haemolysis for the two runs can be explained by the quality of the blood used in experiment 1, which was around 1.5 weeks old compared with the fresh blood used for experiment 2. Therefore, a third experiment may be required to assess the true haemolysis value this polymer could generate.

The best pH responsiveness was observed for polymer 2, which showed constant high haemolysis of up to 97.8% throughout the pH range characteristic of early endosomes. In addition to that, the haemolysis was also significantly lower at the physiological pH compared with polymers 5 and 8. This result shows high potential as both lysosomal degradation and cytotoxicity can be avoided.

After this initial screening, based on the observations above, three polymers: 2, 5 and 8 were selected for further research.

3.1.2 Temperature-dependent haemolysis

The temperature dependence of the top performing polymers in the pH dependence assay was assessed at 4 different temperatures: 0°C, 22°C, 37°C and 40°C. The temperature range of 0 to 40°C was chosen to model the environmental conditions at physiological temperature 36-38°C and during a possible fever from 38-40°C. The results are shown in ***Figure 3***. Overall, the results show a general positive trend with activity increasing with temperature. This was in line with literature which states high temperatures make disruption likely as a consequence of increasing kinetic [24].

Polymers 2 and 5 demonstrated very sensitive temperature changes from 0 to 22°C with its haemolytic activity increasing 60 and 50%

respectively, whereas Polymer 8 exhibit less of a sensitiveness increasing by just 10%. Nonetheless, Polymer 8 does exhibit an interesting linear trend with an $R^2 = 0.9226$ alongside a much more sensitiveness in the temperature range of 22 to 37°C. From 37-40°C only Polymer 5 showed a slight decrease of activity by 10%.

Overall, this gives generally positive results of how sensitive these are to temperature, having possible applications in different physiological scenarios, for example during a fever [25].

3.1.3 Time-dependent haemolysis

The time dependence of the top three polymers were assessed. The kinetic of haemolytic activity was investigated at pH 6.5. The time range of 5 to 120 minutes was chosen to replicate the transport of potential therapeutic agents from early endosomes to lysosomes. Studies suggests that endocytosed materials are usually trafficked within several hours. The results are shown in ***Figure 4***.

Polymer 8 displayed low haemolytic activities until 60 minutes and increased by almost 60% at 80 minutes. Whereas Polymers 2 and 5 demonstrated a much more gradual changes of haemolytic activities. Both also gave high haemolysis values of close to 100%. For polymer 5, experiments were rerun due to a discrepancy of the values before 15 minutes. The results demonstrated a consistency as a whole so the possibility of an error arising due to the close proximity of time was high.

Overall, since all Polymers showed signs of disruption in the time range investigated, with membrane disruption taking place before evolution of endosomes to lysosomes. It demonstrated a potential for drug and gene delivery. There is also a potential for further research of Polymers 2 and 5 to see if it could exhibit controllable release depending on the therapeutic drug. Areas like continuous and steady release could be investigated [26].

3.1.4 Concentration-dependent haemolysis

The relative haemolytic activity of the best performing pH dependent polymer was investigated again with a further variation of three new concentrations of 0.5mg/ml, 0.25mg/ml and 0.125mg/ml. The results of Polymer 2 can be seen in ***Figure 5***.

All concentrations exhibit roughly similar trends showing very high haemolytic activities of close to 100% at pH 6-6.5. Even with concentrations decreasing, the haemolytic value still managed to remain remarkably high. There was also no noticeable activity at physiological pH of 7.4. Moving forward, this could potentially offer a possibility of a lower concentration of polymer used during encapsulation.

Another interesting trend that was observed was a shift in the maximum value of Haemolysis from 6.5 to 6 as the concentration was decreased. This is something that could potentially be manipulated and employed in areas of study like tumour targeting where an acidic pH is required [27].

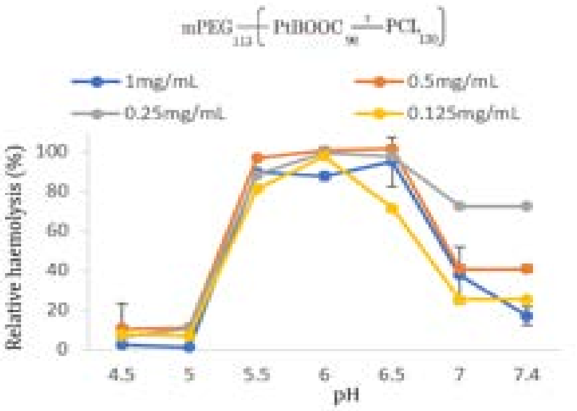

Figure 5**:** Concentration dependent haemolysis for polymer (2) throughout the pH range

3.2DLS Measurements

The DLS Measurements for the top three performing polymers were run at pH 6.5 and pH 7.4 in order to mimic the endosomal and the physiological conditions.

3.2.1 Particle Size

Considering that the measurements are performed on cationic polymers, an increase in particle size with a decrease in pH is expected due to the protonation of the cationic sites.

Table 2: Dynamic Light Scattering (DLS) Measurement results

	Particle Size	**Polydispersity Index**	**Zeta Potential**	**Standard Deviation**
Pol.2 pH=6.5	168.416 nm	7.350%	-0.6807 mV	7.7976 mV
Pol.2 pH=7.4	188.740 nm	10.985%	1.5172 mV	3.7696 mV
Pol.5 pH=6.5	172.205 nm	23.672%	6.7793 mV	6.0009 mV
Pol.5 pH=7.4	137.273 nm	10.895%	2.3315 mV	4.5871 mV
Pol.8 pH=6.5	362.930 nm	10.135%	7.6089 mV	5.3361 mV
Pol.8 pH=7.4	198.545 nm	12.552%	-0.4704 mV	1.4794 mV

This trend is observed for polymers 5 and 8. In the case of polymer 2 there was a slight decrease in particle size. This may be due to a measurement error or to some structural feature. By comparison, in the case of the polymer 2, the cationic centre is situated in the backbone while for the polymers 5 and 8, it was situated in the side chain. This could mean there was steric hindrance for polymer 2. To fully clarify this abnormality, the pKas of all the polymers must be determined; measurements that weren't possible at the moment of the study.

The values for Polydispersity Index (PDI) are in the order of 0.1-0.25 which is lower than the threshold of 0.3 often considered in literature for classifying samples as either mono or polydisperse [28]. Consequently, all the samples can be considered as monodisperse. The particle size distribution for the samples presented can be consulted in the Supplementary Material. The requirement for monodispersed particles is due to their capacity of releasing the drug slower compared with polydisperse particles [28] .

3.2.2 Zeta Potential

The Zeta Potential measurements also follows the expected behaviour for cationic polymers with mostly positive values. Still, the negative values obtained for polymer 2 at pH 6.5 and polymer 8 at pH 7.4 have to be explained by further investigations. Nonetheless, the range of values measured did fall between the -10mV to +10mV range where polymers are considered as weakly ionizing [29]. This may raise an issue of colloidal stability as well as drug binding, since most studies suggest that a value in the range of -30 to 30mV was desirable [29].

4 Conclusion

This study demonstrated that there is potential in using polymers especially cationic ones as drug/gene delivery vehicles. Polymer 2 showed encouraging results with very high haemolysis in the pH range characteristic of early endosomes and no haemolytic activity at physiological pH. It also exhibited stability in the temperature range above 22°C and increased its activity progressively in the time assay, proving that steady release of the attached drugs is achievable. It's sensitiveness to pH could also be manipulated to target acidic cancerous tumours. All these features, in addition to a modular chemical structure which comprises both hydrophilic and hydrophobic groups set this polymer on the top priority list for future research. The other two polymers studied also have potential for specific applications, but their concerning high haemolysis at physiological pH must be assessed.

5 Further research

For establishing if polymer 2 could be a good candidate for clinical trials, further characterisation is required. More specifically, the binding of the polymer with the drug/gene of interest, cell specificity, and the capacity of releasing the payload. Its ability to overcome extracellular barriers like stability and survival in the blood stream should also be investigated alongside its cytotoxicity that may be induced by the amines following the proton sponge mechanism[21]. Further study could also be placed on its random repeating structure, something that is not commonly seen in literature [1]. Since polymer 2 managed such a high efficiency, it might be worth looking into these types of copolymers in the future.

6 Acknowledgements

We would like to thank PhD student Xinyu Lu for synthesizing the polymers and helping with their structural characterization and offer our upmost gratitude to PhD student Gabriella Morisson for her support and useful discussions throughout the whole project. And finally, to Dr. Rongjun Chen for his expertise in the subject providing us with invaluable feedback.

References

[1] Y. Sung and S. Kim, "Recent advances in polymeric drug delivery systems", *Biomaterials Research*, vol. 24, no. 1, 2020. Available: 10.1186/s40824-020-00190-7.

[2]S. Chen, S. Wang, M. Kopytynski, M. Bachelet and R. Chen, "Membrane-Anchoring, Comb-Like Pseudopeptides for Efficient, pH-Mediated Membrane Destabilization and Intracellular Delivery", *ACS Applied Materials & Interfaces*, vol. 9, no. 9, pp. 8021-8029, 2017. Available: 10.1021/acsami.7b00498.

[3]G. Vilar, J. Tulla-Puche and F. Albericio, "Polymers and Drug Delivery Systems", *Current Drug Delivery*, vol. 9, no. 4, pp. 367-394, 2012. Available: 10.2174/156720112801323053 [Accessed 12 December 2021].

[4]W. Gao, J. Chan and O. Farokhzad, "pH-Responsive Nanoparticles for Drug Delivery", *Molecular Pharmaceutics*, vol. 7, no. 6, pp. 1913-1920, 2010. Available: 10.1021/mp100253e [Accessed 5 December 2021].

[5]N. Deirram, C. Zhang, S. Kermaniyan, A. Johnston and G. Such, "pH-Responsive Polymer Nanoparticles for Drug Delivery", *Macromolecular Rapid Communications*, vol. 40, no. 10, p. 1800917, 2019. Available: 10.1002/marc.201800917 [Accessed 6 December 2021].

[6]A. D’souza and R. Shegokar, "Polyethylene glycol (PEG): a versatile polymer for pharmaceutical applications", *Expert Opinion on Drug Delivery*, vol. 13, no. 9, pp. 1257-1275, 2016. Available: 10.1080/17425247.2016.1182485 [Accessed 5 December 2021].

[7]D. Hattab and A. Bakhtiar, "Bioengineered siRNA-Based Nanoplatforms Targeting Molecular Signaling Pathways for the Treatment of Triple Negative Breast Cancer: Preclinical and Clinical Advancements", *Pharmaceutics*, vol. 12, no. 10, p. 929, 2020. Available: 10.3390/pharmaceutics12100929 [Accessed 4 December 2021].

[8]E. Pérez-Herrero and A. Fernández-Medarde, "Advanced targeted therapies in cancer: Drug nanocarriers, the future of chemotherapy", *European Journal of Pharmaceutics and Biopharmaceutics*, vol. 93, pp. 52-79, 2015. Available: 10.1016/j.ejpb.2015.03.018 [Accessed 4 December 2021].

[9] C. Englert et al., "Pharmapolymers in the 21st century: Synthetic polymers in drug delivery applications", *Progress in Polymer Science*, vol. 87, pp. 107-164, 2018. Available: 10.1016/j.progpolymsci.2018.07.005 [Accessed 7 December 2021].

[10] W. Liechty, R. Chen, F. Farzaneh, M. Tavassoli and N. Slater, "Synthetic pH-Responsive Polymers for

Protein Transduction", *Advanced Materials*, vol. 21, no. 3839, pp. 3910-3914, 2009. Available: 10.1002/adma.200901733 [Accessed 2 December 2021].

[11] O. Boussif et al., "A versatile vector for gene and oligonucleotide transfer into cells in culture and in vivo: polyethylenimine.", *Proceedings of the National Academy of Sciences*, vol. 92, no. 16, pp. 7297-7301, 1995. Available: 10.1073/pnas.92.16.7297 [Accessed 6 December 2021].

[12] D. Fischer, Y. Li, B. Ahlemeyer, J. Krieglstein and T. Kissel, "In vitro cytotoxicity testing of polycations: influence of polymer structure on cell viability and hemolysis", *Biomaterials*, vol. 24, no. 7, pp. 1121-1131, 2003. Available: 10.1016/s0142-9612(02)00445-3 [Accessed 2 December 2021].

[13] A. Elouahabi and J. Ruysschaert, "Formation and Intracellular Trafficking of Lipoplexes and Polyplexes", *Molecular Therapy*, vol. 11, no. 3, pp. 336-347, 2005. Available: 10.1016/j.ymthe.2004.12.006 [Accessed 5 December 2021].

[14] P. Felgner et al., "Lipofection: a highly efficient, lipid-mediated DNA-transfection procedure.", *Proceedings of the National Academy of Sciences*, vol. 84, no. 21, pp. 7413-7417, 1987. Available: 10.1073/pnas.84.21.7413 [Accessed 8 December 2021].

[15] J. Zabner, "Cationic lipids used in gene transfer", *Advanced Drug Delivery Reviews*, vol. 27, no. 1, pp. 17-28, 1997. Available: 10.1016/s0169-409x(97)00019-7 [Accessed 4 December 2021].

[16] J. Ruysschaert et al., "A Novel Cationic Amphiphile for Transfection of Mammalian Cells", *Biochemical and Biophysical Research Communications*, vol. 203, no. 3, pp. 1622-1628, 1994. Available: 10.1006/bbrc.1994.2372 [Accessed 5 December 2021].

[17] F. Sakurai et al., "Effect of DNA/liposome mixing ratio on the physicochemical characteristics, cellular uptake and intracellular trafficking of plasmid DNA/cationic liposome complexes and subsequent gene expression", *Journal of Controlled Release*, vol. 66, no. 2-3, pp. 255-269, 2000. Available: 10.1016/s0168-3659(99)00280-1 [Accessed 6 December 2021].

[18] M. Filion and N. Phillips, "Major limitations in the use of cationic liposomes for DNA delivery", *International Journal of Pharmaceutics*, vol. 162, no. 1-2, pp. 159-170, 1998. Available: 10.1016/s0378-5173(97)00423-7 [Accessed 4 December 2021].

[19] O. Boussif et al., "A versatile vector for gene and oligonucleotide transfer into cells in culture and in vivo: polyethylenimine.", *Proceedings of the National Academy of Sciences*, vol. 92, no. 16, pp. 7297-7301, 1995. Available: 10.1073/pnas.92.16.7297 [Accessed 3 December 2021].

[20] P. Grossen, D. Witzigmann, S. Sieber and J. Huwyler, "PEG-PCL-based nanomedicines: A biodegradable drug delivery system and its application", *Journal of Controlled Release*, vol. 260, pp. 46-60, 2017. Available: 10.1016/j.jconrel.2017.05.028 [Accessed 10 December 2021].

[21]B. J.-P, "The Proton Sponge: a Trick to Enter Cells the Viruses Did Not Exploit", *Chimia*, 1997. [Accessed 12 December 2021]. – proton sponge effect

[22] Y. Hu, E. Dammer, R. Ren and G. Wang, "The endosomal-lysosomal system: from acidification and cargo sorting to neurodegeneration", *Translational Neurodegeneration*, vol. 4, no. 1, 2015. Available: 10.1186/s40035-015-0041-1 [Accessed 8 December 2021].

[23]R. Chen, S. Khormaee, M. Eccleston and N. Slater, "The role of hydrophobic amino acid grafts in the enhancement of membrane-disruptive activity of pH-responsive pseudo-peptides", *Biomaterials*, vol. 30, no. 10, pp. 1954-1961, 2009. Available: 10.1016/j.biomaterials.2008.12.036.

[24] P. Quinn, "Effects of temperature on cell membranes", *Symphosia of the Society for Experimental Biology*, 1998. Available: https://pubmed.ncbi.nlm.nih.gov/3077859/. [Accessed 4 December 2021].

[25]S. Fitzpatrick, L. Fitzpatrick, A. Thakur, M. Mazumder and H. Sheardown, "Temperature-sensitive polymers for drug delivery", *Expert Review of Medical Devices*, vol. 9, no. 4, pp. 339-351, 2012. Available: 10.1586/erd.12.24 [Accessed 4 December 2021].

[26] N. Kamaly, B. Yameen, J. Wu and O. Farokhzad, "Degradable Controlled-Release Polymers and Polymeric Nanoparticles: Mechanisms of Controlling Drug Release", *Chemical Reviews*, vol. 116, no. 4, pp.

2602-2663, 2016. Available: 10.1021/acs.chemrev.5b00346 [Accessed 5 December 2021].

[27] J. Heuts, W. Jiskoot, F. Ossendorp and K. van der Maaden, "Cationic Nanoparticle-Based Cancer Vaccines", *Pharmaceutics*, vol. 13, no. 5, p. 596, 2021. Available: 10.3390/pharmaceutics13050596 [Accessed 6 December 2021].

[28] Q. Xu et al., "Preparation of Monodisperse Biodegradable Polymer Microparticles Using a Microfluidic Flow-Focusing Device for Controlled Drug Delivery", *Small*, vol. 5, no. 13, pp. 1575-1581, 2009. Available: 10.1002/smll.200801855.)

[29J. Clogston and A. Patri, "Zeta Potential Measurement", *Methods in Molecular Biology*, pp. 63-70, 2010. Available: 10.1007/978-1-60327-198-1_6 [Accessed 4 December 2021].

In Situ ATR-FTIR Spectroscopic Study of CO_2 Sorption in Type II Porous Liquid

Berlin Lie and Nicholas Emilio Sutjiono
Department of Chemical Engineering, Imperial College London, U.K.

ABSTRACT: One of the recent developments that could aid in carbon capture processes is the concept of porous liquids, which are liquids that possess permanent porosity. This study utilized in situ ATR-FTIR spectroscopy to investigate the CO_2 sorption of Type 2 Porous Liquids (PLs), specifically 10% and 20% w/v of scrambled 3^3:13^3 cage in four different solvents (2'-Hydroxyacetophenone, Methyl Salicylate, 2,4-Dichlorotoluene, and 4-(Trifluoromethoxy) benzyl alcohol) at pressures of 2 up to 40 bar. Swelling and shift of solvents' characteristic bands towards a higher wavenumber were observed indicating interaction between CO_2 and PLs. CO_2 uptake showed a positive correlation with pressure. Upon comparing the CO_2 uptake of the PLs with the neat solvents, no increase in the amount of sorbed CO_2 was observed when increasing cage concentration. CO_2 sorption of porous liquids was instead found to be lower than that of its neat solvents in most cases. This is the first study where a decrease in uptake was reported when a cage was added to a solvent when forming a porous liquid. The implications of these results were discussed and perhaps this will allow a better understanding and design of these Type 2 porous liquids for carbon capture applications.

1. INTRODUCTION

With the ongoing rise in CO_2 levels in the atmosphere, there is a need for new and more efficient Carbon Capture and Storage (CCS) methods and materials. Despite the fact that a variety of CCS strategies have been proposed, absorption and adsorption are still thought to be attractive methods.[1,2] Amine solutions like monoethanolamine and diethanolamine (MEA/DEA) are widely considered the industry standard for absorption-based CCS, due to their ability to reversibly absorb CO_2. By heating the solution, CO_2 may be liberated, facilitating reuse of the absorbent. However, this technology is not without its faults, most notably the high energy cost of regeneration.[3] Adsorption, on the other hand, drastically decreases the energy required for the regeneration as the sorption only occurs on the interface of the solid/liquid.[4] Solid porous materials such as zeolites, and metal organic frameworks have been of interest for this method as they offer void spaces that enhance mass transport. However, the problem with porous solids is their inability to flow which makes them cumbersome to handle at the industrial scale.[5]

O'Reilly *et al.*[6] introduced the concept of porous liquids in 2007. Conventionally, liquids are viewed as a continuum which do not exhibit porosity. Porous liquids, conversely, achieve such porosity within the liquid either through natural or artificial means (solid doping). In so doing, porous liquids offer an opportunity to leverage the fluidity of orthodox absorption technologies coupled with the cheaper adsorption/regeneration of traditional solid adsorption. This offers superior capabilities in regeneration and reuse, making porous liquids highly suitable for integration into continuous processes.[7] An in depth understanding of the adsorption and chemical interactions between CO_2 and the porous liquids is essential to model these systems to optimise the performance of these processes.

Porous liquids (PLs) are categorized into three different types (Figure 1).[6] Type 1 are liquids that can exhibit porosity without any solid doping as they inherently organise to form rigid, hollow frames that can maintain their integrity. Type 2 are vacant molecular hosts dissolved in sterically hindered solvents and Type 3 are molecular frameworks that are dispersed in the solvent. Several studies on the CO_2 uptake have been done on Type 1 PLs. Zhou *et al.*[8] studied the melting of a Zeolitic Imidazolate Framework (ZIF)-based Type 1 PL. The study showed that a molten ZIF-76 and ZIF-76-mbim was able to reversibly adsorb 4 wt% and 7 wt% of CO_2 respectively. The problem with Type 1 PLs is that the synthesis requires harsh conditions and often leads to low yields.[9] Because of the cost and environmental risks associated with Type 1 PLs, they have gained less traction towards large scale utilisation.

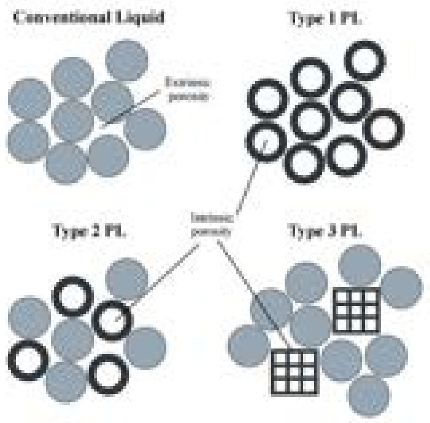

Figure 1. Schematic representation of molecules in conventional liquid (only consist of extrinsic porosity) and different types of porous liquids (possess intrinsic porosity within the molecules)

Numerous studies have shown that dispersing molecular frameworks in a solvent by creating a Type 3 PL increases CO_2 adsorption significantly. Shan *et al.*[10] investigated a Type 3 PL with ZIF-8 dispersed in an ionic liquid ([DBU-PEG] [NTf_2]) as the solvent. The CO_2 adsorption was reported to increase 4.7 times for a 30 wt% ZIF-8 dispersed in the solvent as compared to the pure solvent. This reveals the potential of these porous liquids.

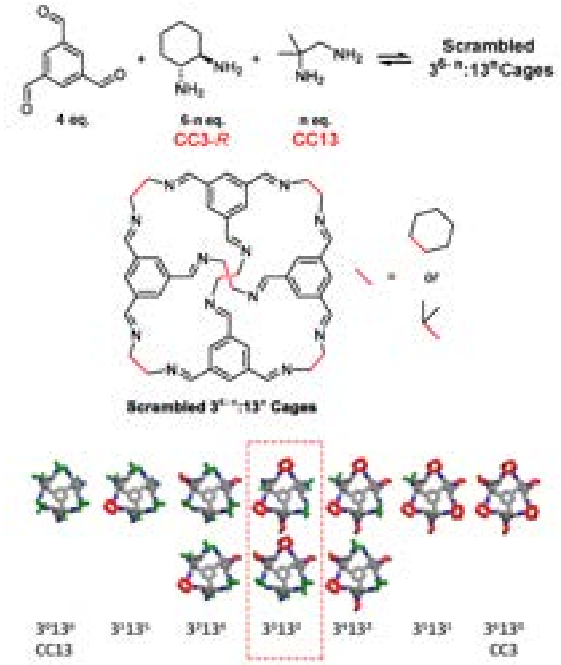

Figure 2. Structure of scrambled $3^{6-n}:3^{n}$ cage for Type 2 Porous Liquids, where *n* represents the equivalents of the CC13 diamine that were used. The red dotted box highlights the scrambled structure for $n = 3$ (scrambled $3^3:13^3$ cage)[11]

Giri *et al.*[12] discovered that a combination of CC3 and CC13 scrambled cages is highly soluble in perchloropropene (PCP) forming a Type 2 PL. The combination of CC3 and CC13 in a ratio of 3 : 3 mixture forming Scrambled $3^3:13^3$ cage (Figure 2) was found to be more soluble in the solvent than using CC3 and CC13 cage individually. Gas uptake measurements were then taken for this PL and was found to result in a 3-fold increase on the CO_2 sorption compared to the solvent alone.[11] However, a big problem with this PL is PCP is highly toxic. In search of more benign PLs, Kearsey *et al.*[13] developed a high throughput workflow to discover more Type 2 PLs. They tested several different bulky solvents such as 2'-Hydroxyacetophenone, Methyl Salicylate, 4-(Trifluoromethoxy) benzyl alcohol, and 2,4-Dichlorotoluene with a variety of scrambled cages. It was reported that all the solvents had significant methane and xenon uptake when Scrambled $3^3:13^3$ was added, showing the adsorption potential of these Type 2 PLs. However, unlike Type 1 and Type 3 PLs, minimal research has been done on the CO_2 sorption of these Type 2 PLs.

Fourier Transform Infrared (FTIR) spectroscopy has been proven to be robust in providing valuable insight of molecular interactions.[14-16] It measures the transition between vibrational energy levels from when IR light interacts with the sample. As CO_2 vibrational modes (antisymmetric stretching at 2335 cm^{-1} and bending mode at 655 cm^{-1}) are IR active, this allows FTIR spectroscopy to detect the presence of CO_2 in a sample. FTIR spectroscopy reveals physical effects such as swelling occurring on a sample as well as specific chemical interactions between CO_2 and a samples' functional groups under high pressure systems.[17] One of the commonly used FTIR modes is the Attenuated Total Reflection (ATR) mode which takes advantage of the total internal reflection that occurs at the interface between the ATR crystal and the sample.[18] At the interface an evanescent wave of infrared light penetrates through a thin layer of the sample which has a very short path length. This allows ATR mode to overcome the challenges faced by transmission mode which has a relatively long path length and could cause the CO_2 absorbance to be offscale.[19] ATR mode allows the spectra to be measured at a proper range for quantitative measurements. Another key benefit is measuring thin samples in ATR mode requires minimal preparation, allowing samples to be analysed in their native states.[20]

The aim of this paper is to investigate the CO_2 sorption in Type 2 PLs by utilizing ATR-FTIR spectroscopy. Swelling of the PLs upon subjection to CO_2 will also be quantitatively measured. Finally, the CO_2 uptake of the PLs will be compared against their neat solvents.

2. MATERIALS AND METHODS

2.1 Type 2 Porous Liquid Samples

The Type 2 PLs studied for this work were formed by dissolving two different concentrations (10% and 20% w/v) of Scrambled $3^3:13^3$ cages (CC3_13) in four different solvents: 2'-Hydroxyacetophenone (HAP), Methyl Salicylate (MS), 2,4-Dichlorotoluene (DCT), and 4-(Trifluoromethoxy)benzyl alcohol (TBA). As a reference point, CO_2 uptake in neat solvents (without the addition of CC3_13 cages) were also studied. In the rest of this report, PLs are referenced as SOLVENTS + % CC3_13 (e.g., HAP + 10% CC3_13 means 10% w/v of Scrambled $3^3:13^3$ cages in 2'-Hydroxyacetophenone solvent). All the samples were provided externally by Department of Chemistry, Faculty of Natural Science, Imperial College London.

2.2 ATR-FTIR Spectroscopy

An EQUINOX 55 FTIR spectrometer (Bruker, Germany) with a mercury-cadmium-telluride (MCT) detector was used to collect the ATR-FTIR Spectra. Golden Gate ATR accessories (Specac, UK) with two top plates (diamond and germanium crystals) were used. Samples were placed on top of the crystal surface and kept at a constant temperature of 25 °C during the measurements.

CO_2 was introduced at a range of 2 to 40 bar by a HiP syringe pump (Model: 62-6-10) to a custom designed high-pressure cell (Figure 3). The CO_2 pressure was monitored using an inline Honeywell pressure gauge (Model: LM). To prevent CO_2 leakage, a Teflon O-ring was used, and the high-pressure cell was clamped. 64 background and 64 sample scans were performed for all measurements at a resolution of 4 cm^{-1} across a spectral range of 3900-600 cm^{-1}. In order to ensure that equilibrium has reached, the FTIR spectra for each sample at each pressure were taken at 5 minutes intervals until the peak absorbance remained constant.

2.3 Refractometer

CETI prisma bench top analogue refractometer (Medline Scientific) was used to determine the refractive indices of all the samples. Samples were kept

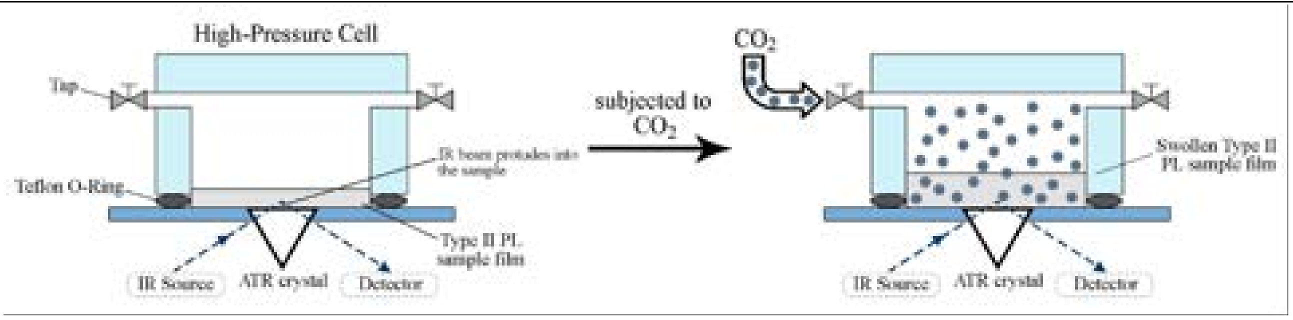

Figure 3. Schematic diagram of the custom designed high-pressure cell setup for the ATR-FTIR spectrometer and the swelling of Type II porous liquid film when subjected to CO_2

at constant temperature of 25 °C using a temperature bath. Three measurements of refractive index were taken for each sample and the arithmetic average is used.

2.4 Quantitative Analysis

The Beer-Lambert law (Eq. 1) states that the absorbance (A) is proportional to the molar absorptivity (ε), concentration (c), and the optical path length (l). In ATR mode, the optical path length is equal to the effective thickness of the sample for unpolarized light ($d_{\mathrm{e,u}}$).

$$A = \varepsilon \, c \, d_{\mathrm{e,u}} \tag{1}$$

In unpolarized light, the effective thickness is taken as the arithmetic average of the effective thickness for the s-polarized ($d_{\mathrm{e,s}}$) and p-polarized light ($d_{\mathrm{e,p}}$) (Eq. 2).

$$d_{\mathrm{e,u}} = \frac{1}{2}(d_{\mathrm{e,s}} + d_{\mathrm{e,p}}) \tag{2}$$

$d_{\mathrm{e,s}}$ and $d_{\mathrm{e,p}}$ are related to the refractive indices of the ATR crystal (n_1) and sample (n_2), wavelength of the incidence beam (λ), and angle of incidence (θ) (Eq. 3 and 4 respectively).[21]

$$d_{\mathrm{e,s}} = \frac{\lambda n_1 n_2 \cos\theta}{\pi(n_1^2 - n_2^2)\sqrt{n_1^2 \sin^2\theta - n_2^2}} \tag{3}$$

$$d_{\mathrm{e,p}} = [\lambda n_1 n_2 \cos\theta \, (2n_1^2 \sin^2\theta - n_2^2)]/[\pi(n_1^2 - n_2^2) \\ \{(n_1^2 + n_2^2)\sin^2\theta - n_2^2\}(n_1^2 \sin^2\theta - n_2^2)^{1/2}] \tag{4}$$

By substituting Eq. 3 and 4 into Eq. 2, the effective thickness for unpolarized light ($d_{\mathrm{e,u}}$) is obtained (Eq. 5)

$$d_{\mathrm{e,u}} = \left[\lambda n_{2,1} \cos\theta \, (3\sin^2\theta - 2n_{2,1}^2 + n_{2,1}^2 \sin^2\theta\right]/ \\ [2\pi(1 - n_{2,1}^2)\{(1 + n_{2,1}^2 \sin^2\theta - n_{2,1}^2)\} \\ (n_1^2 \sin^2\theta - n_2^2)^{1/2}\,] \tag{5}$$

where $n_{2,1} = n_2 / n_1$ = ratio between the refractive index of sample and ATR-crystal.

3. RESULTS AND DISCUSSION

3.1 FTIR Spectroscopic Analysis of Type 2 Porous Liquids

The FTIR spectra of the neat solvents and PLs prior to subjection of CO_2 are analysed. Several characteristics bands of neat solvents are selected for further analysis of this paper. The chosen characteristics bands are summarised in Table 1. Full spectra of neat solvents can be found in SI.1. There are distinct differences between the spectra of the PLs and the neat solvents. To confirm the presence of the CC3_13 cages in the solvent, spectral subtraction of the neat solvents from their corresponding PLs with 20% w/v CC3_13 spectra are analysed. The resulting spectra are expected to correspond to the bands of the CC3_13 cage. The scrambled cage's spectra resulting from the spectral subtraction of each PL is shown on Figure 4. While each solvent produces a marginally different scrambled cage spectrum, this is to be expected since the cage's spectra is obtained indirectly via spectral subtraction. Nevertheless, there are several distinct bands that are common to all four spectra that can be identified. Bands appearing in the 2800-3000 cm^{-1} region and 1640 cm^{-1} corresponds to alkane C-H stretching and the imine (C=N) stretching respectively. The spectra are also compared to the literature data of CC3 and CC13 cage and found to be very similar.[22,23] While C-N stretching and aromatic ring

Table 1. Characteristic bands of selected functional group in neat solvents

Peak (cm^{-1})	Functional Group
805	C-Cl stretching in (DCT)
833	C-Cl stretching in (DCT)
1150	C-F stretching in (TBA)
1635	Ketone (C=O stretching) (HAP)
1671	Ester (C=O stretching) (MS)

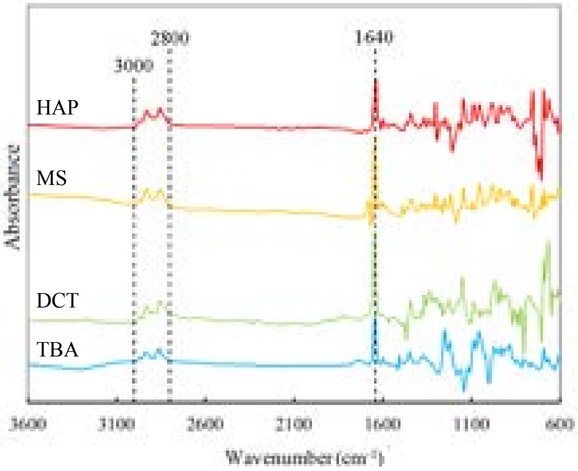

Figure 4. FTIR spectra of scrambled CC3_13 cage. The spectra shown are the results of spectral subtraction of neat solvents (HAP, MS, DCT and TBA) from their corresponding PLs with 20% w/v CC3_13

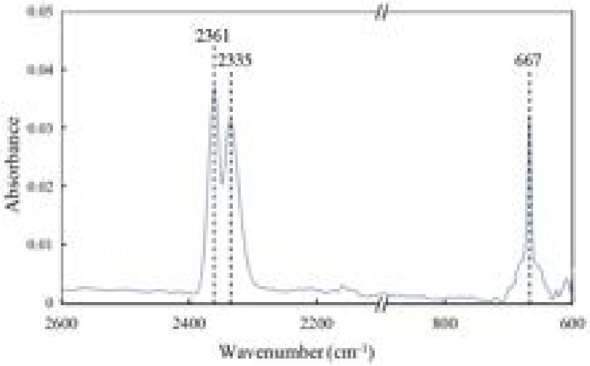

Figure 5. FTIR spectrum of pure gaseous CO_2 at 55 bar. Peak at 667 cm^{-1} corresponds to the bending mode while 2335 and 2361 cm^{-1} correspond to the P and R branches of antisymmetric stretching mode respectively.

stretching bands are reported in literature, our results failed to clearly exhibit these bands, likely due to the indirect means through which the cage spectra was obtained.

3.2 FTIR Spectroscopic Analysis of CO_2

CO_2 is a three atoms centrosymmetric molecule, meaning it has four vibrational modes: symmetric stretching, antisymmetric stretching and two bending modes. However only the antisymmetric stretching and bending modes are IR active. The ATR-FTIR spectra of CO_2 are displayed in Figure 5. Due to the rotational-vibrational coupling, the antisymmetric stretching (v_3) mode splits into P and R branches located at 2335 cm^{-1} and 2361 cm^{-1} respectively. In the absence of external field, the bending modes (v_2) are two-fold degenerate as the bending modes only differ in the plane of their bending (orthogonal to each other).[24] Thus, the two bending modes correspond to the same wavenumber resulting in one peak at 667 cm^{-1}.

3.3 FTIR Spectroscopic Analysis of CO_2 in Type 2 Porous Liquids

Once exposed to CO_2, several changes are observed in all the PLs' and neat solvents' spectra. As expected, the peaks within the regions associated with the CO_2 antisymmetric stretching (v_3) and bending (v_2) mode appear indicating the presence of CO_2. Spectra of HAP + 20% w/v CC3_13 subjected to increasing CO_2 pressure is shown in Figure 6. It is observed that the peak corresponding to the CO_2 v_3 mode are slightly shifted to a lower wavenumber of 2335 cm^{-1} compared to that of pure gaseous CO_2. This indicates that the CO_2 is dissolved within the PLs. Similar shifts are also observed in other PLs and the neat solvents (see SI.2). PLs made using MS had a v_3 peak that occurred at a wavenumber of 2336 cm^{-1}, while PLs made with TBA and DCT had a v_3 peak occurring at 2338 and 2334 cm^{-1} respectively. A slight shoulder (at 2323 cm^{-1}) on the right-hand side of the CO_2 antisymmetric stretching band also appears. This shoulder signifies the coupling of the antisymmetric stretch and bending mode ((v_3 + v_2) − v_2 hot band).[25] A small peak corresponding to the antisymmetric stretching of C_{13} isotopes of CO_2 is also present at 2272 cm^{-1}, where the shift comes from the difference in mass of the isotope.

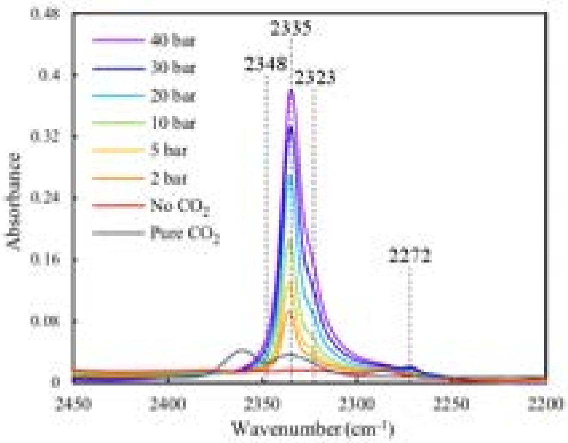

Figure 6. FTIR spectra of HAP + 20% w/v CC3_13 in increasing CO_2 pressure (prior to CO_2 subjection up to 40 bar of CO_2). FTIR spectrum of pure gaseous CO_2 at 55 bar is displayed as comparison.

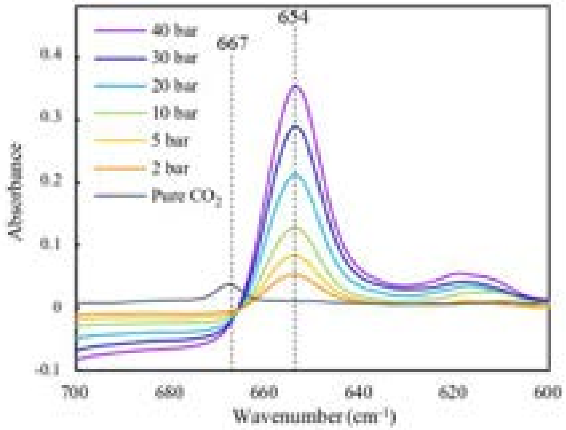

Figure 7. FTIR spectral subtraction of neat HAP prior to CO_2 subjection from neat HAP subjected to different pressure of CO_2 (2 to 40 bar). Negative absorbance is observed as a result of spectral subtraction. FTIR spectrum of pure gaseous CO_2 at 55 bar is displayed as comparison.

It is challenging to analyse the v_2 bands of CO_2 due to some degree of overlap with the solvents' bands. Hence, spectral subtraction of the neat solvents prior to CO_2 subjection from those subjected to CO_2 was performed. This results in spectra of sorbed CO_2 without any overlap with the solvents' bands. Similar to the v_3 mode, there are noticeable shifts of the v_2 peak to 654, 653, 658 and 657 cm^{-1} for HAP, MS, TBA and DCT respectively compared to pure CO_2 (Figure 7). This signifies the presence of interactions between CO_2 and solvents.[17] Previous studies have shown that there is a splitting of the v_2 band in polymers and ionic liquids when subjected to high pressure CO_2.[25,26] This is due to the removal of the double degeneracy of the in-plane and out-of-plane bending mode of CO_2 as a result of Lewis acid−base interactions of CO_2 with functional groups of the polymers such as the carbonyl group. One would expect there to be similar effects to be seen in these solvents as they also possess functional groups that could interact with CO_2 (e.g., ketone in HAP). Surprisingly, only one distinct peak of v_2 band is observed in all the solvents (see SI.3). This indicates that the interactions between CO_2 and the solvent

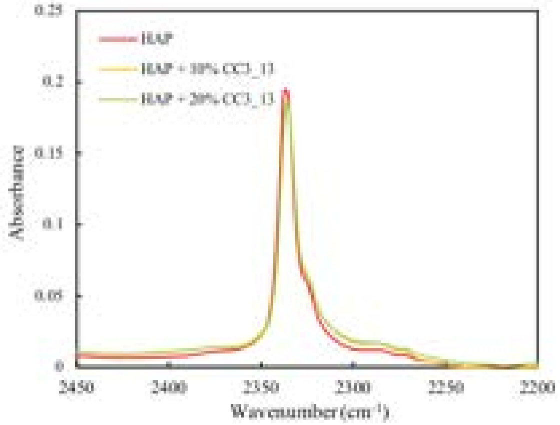

Figure 8. FTIR spectra of CO_2 antisymmetric stretching region of HAP in different cage concentration (neat solvents, 10% and 20% w/v CC3_13) subjected to10 bar of CO_2.

may be too weak to cause splitting to occur. To eliminate the issue of overlapping spectra between the PLs and the ν_2 band of CO_2, we employ spectral subtraction again. Similar to the neat solvents, the PLs with 10% and 20% w/v cage only shows one distinct peak (see SI.3), again, suggesting that the interactions may be too weak to cause splitting of the peaks to occur.

It is also important to analyse how the spectra changes as CO_2 pressure rises. As can be seen from Figure 6 and Figure 7, the ν_3 and ν_2 absorbance bands intensify when samples are subjected to increasing pressure of CO_2 (from 2 to 40 bar), suggesting higher concentrations of CO_2. This trend is also observed in all other neat solvents as well as PLs (see SI.3).

When the PLs are subjected to CO_2, one would expect there to be an increase in the CO_2 absorbance compared to their neat solvents. The scrambled cage offers free volume which ought to enhance the mass transport. However, the expected increase was not observed when 10% and 20% w/v CC3_13 is added to the solvents (Figure 8). Instead, no significant changes are observed in the ν_3 absorbance peaks (other solvents exhibit similar trend, see SI.4). While the absorbance does not indicate the exact concentration of CO_2, it provides a good first estimate. The concentration of sorbed CO_2 will be discussed further in section 3.5.

3.4 Swelling of Type 2 Porous Liquids

There is noticeable reduction and slight shifts in the peak of the functional groups' bands as the CO_2 pressure rises as seen on Figure 9. Upon exposing the samples to CO_2, the CO_2 supresses the intermolecular interaction within the solvents. For instance, due to the presence of CO_2,

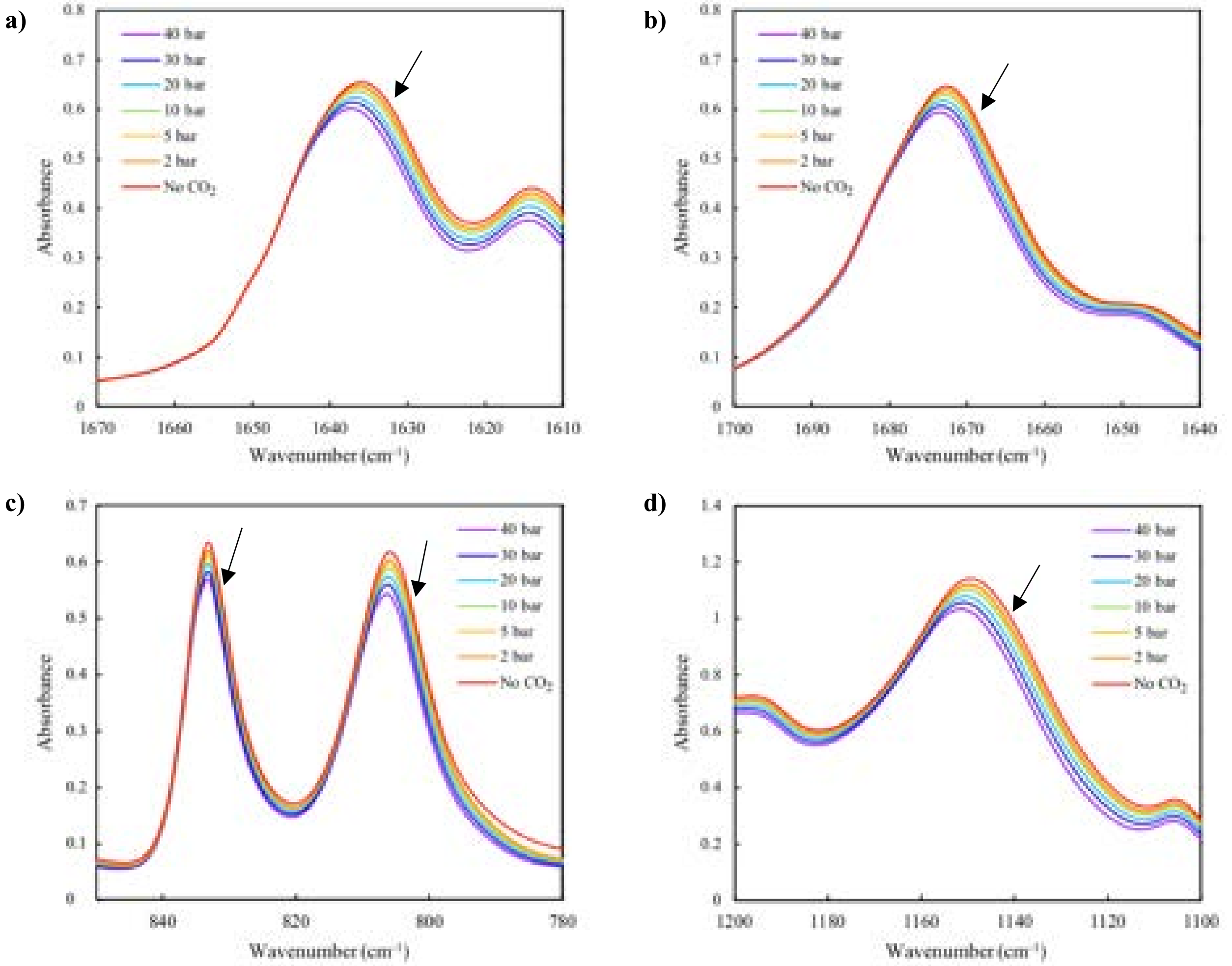

Figure 9. Comparison of FTIR spectra for 20% w/v CC3_13 in **a)** HAP **b)** MS **c)** DCT and **d)** TBA in their functional group peak regions as tabulated in Table 1. For each solvent, absorbance prior to any CO_2 introduction is compared to the absorbance as CO_2 pressure increases from 2 to 40 bar. Arrows indicate the direction of intensity change with increasing CO_2 pressure

the carbonyl group (C=O) in HAP interacts less with other C=O groups. As a result, the characteristics band's peaks shift to the higher wavenumber region. As the amount of sorbed CO_2 increases, the volume of the PL rises. This phenomenon is known as swelling,[25] which is reflected by the decrease in the peaks that corresponds to the PLs. Similar trend is also observed in all the neat solvents and PLs sample (see SI.5).

The swelling is quantified by incorporating Beer−Lambert law equation as described by Flichy *et al.*[27] As concentration is inversely proportional to volume, the relationship between swelling, *S,* and the concentration of porous liquid is defined as:

$$\frac{c_0}{c} = \frac{V + \Delta V}{V} = 1 + \frac{\Delta V}{V} = 1 + S \qquad (6)$$

where c_0 and c are the concentrations of PL prior to and during CO_2 exposure, V and $V+\Delta V$ are the volume of PL prior to and during CO_2 exposure. By substituting c_0 and c from the Beer-Lambert law (eq. 1) to equation 6, the equation for swelling is obtained:

$$S = \frac{A_0}{A} \cdot \frac{d_{\mathrm{e,u}}}{d_{\mathrm{e,u}_0}} - 1 \qquad (7)$$

As the refractive index of the ATR crystal (n_1), wavelength of the incidence beam (λ) and angle of incidence (θ) do not change, the changes between $d_{\mathrm{e,u}}$ and $d_{\mathrm{e,u}_0}$ are solely due to the change of the refractive index of the sample (n_2). However, Flichy *et. al.*[27] and Ewing *et al.*[25] asserts that increasing CO_2 pressure up to 100 bar only has a marginal influence on the refractive index, and by extension the effective thickness. Applying this reasoning, we can treat the refractive indices and effective thicknesses as invariant in the swelling calculations, and Eq. 7 can be simplified as:

$$S = \frac{A_0}{A} - 1 \qquad (8)$$

The functional group's characteristic bands in each solvent are used to calculate the swelling of the neat solvents and PLs. The swelling of different concentrations of the scrambled cage in PLs and their corresponding neat solvents, across all pressure conditions (prior to CO_2 subjection up to 40 bar of CO_2) are shown in Figure 10. Again, increase in CO_2 pressure results in higher swelling in all PLs. It can also be observed that increasing CC3_13 cage concentration results in a higher degree of swelling for both TBA and DCT. However, in HAP and MS no clear trend is observed. For instance, at low pressures HAP + 20% CC3_13 has the highest swelling percentage, but at higher pressures (20 to 40 bar) neat HAP solvent has a higher degree of swelling, while HAP + 10% CC3_13 consistently has the lowest degree of swelling across the studied pressure. In contrast, MS + 20% CC3_13 has the lowest degree of swelling across all pressures. At low pressures MS + 10% has the highest degree of swelling, but again at high pressures (30 and 40 bar) the neat solvent, MS turns out to have the highest degree of swelling.

3.5 Angle of Incidence and Refractive Indices

$D_{\mathrm{e,u}}$ for diamond (n_1 = 2.417)[28] and germanium (n_1 = 4.0026)[29] ATR crystals were first calculated using Eq. 1. Distilled water (n_2 = 1.333)[28] was chosen as the sample. As the concentration at 25 ˚C (c = 55.34 mol dm^{-3}) and the molar absorptivity at the O-H bending

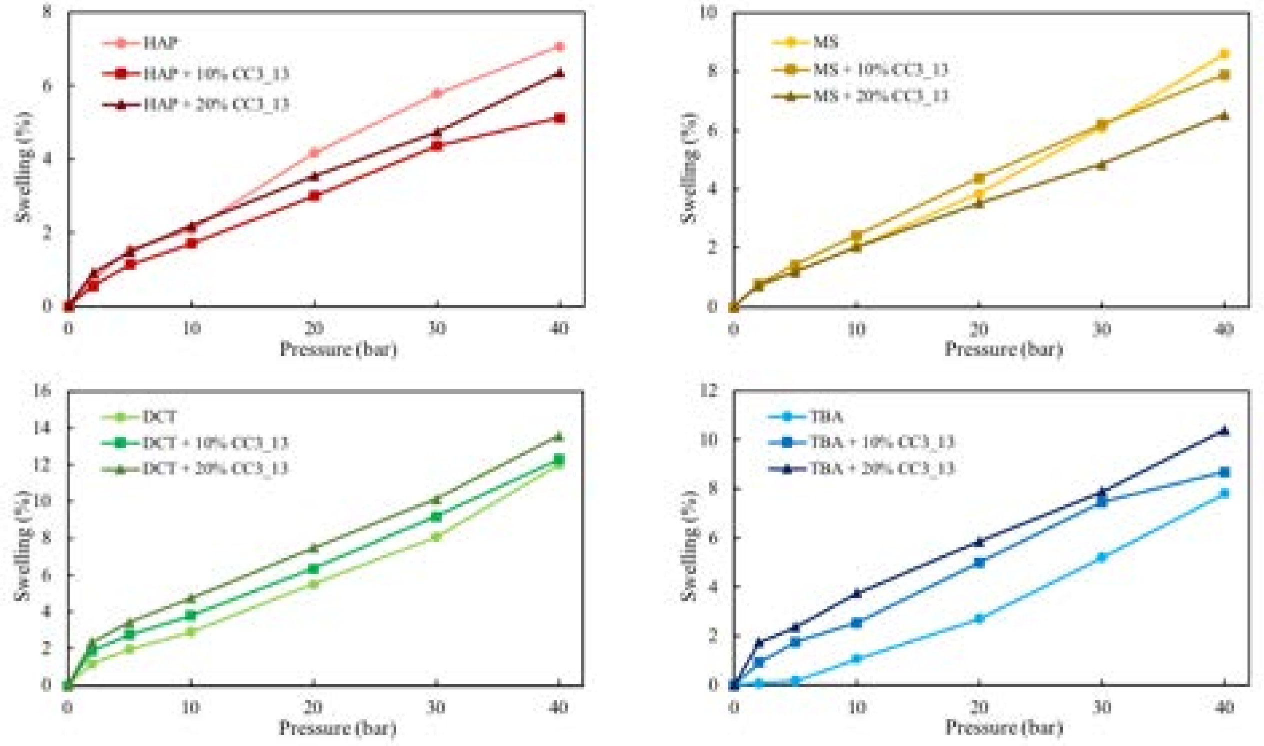

Figure 10. Percentage of swelling of neat solvents and PLs in different pressure of CO_2 (prior to any CO_2 introduction up to 40 bar of CO_2). Values are obtained from the change of absorbance of their characteristic functional group bands assuming no change in refractive indices of sample. Circles are the data for neat solvents, squares for 10% w/v CC3_13 and triangles for 20% w/v of CC3_13

mode band (ε = 21.8 dm^3 mol^{-1} cm^{-1})[30] are known. The corresponding absorbance of the bending band of water (1643.5 cm^{-1}) was obtained from the ATR-FTIR spectra. $d_{e,u}$ is found to be 1.55 µm for diamond and 0.32 µm for germanium. Using Eq. 5, we were able to determine $\theta_{diamond}$ and $\theta_{germanium}$ as 44.7° and 43.9° respectively.

These values of θ are used to determine the refractive indices of the Type 2 PLs at ambient conditions. Since the molar absorptivity and the concentrations of the samples are constant, therefore the equation for the ratio of absorbance in diamond and germanium ATR-crystal (Eq. 9) can be derived from the Beer-Lambert Law (Eq.1).

$$\frac{A_{\mathrm{d}}}{A_{\mathrm{Ge}}} = \frac{d_{\mathrm{e,u_d}}}{d_{\mathrm{e,u_{Ge}}}} \qquad (9)$$

For the three remaining unknowns (n_2, $d_{\mathrm{e,u_d}}$ and $d_{\mathrm{e,u_{Ge}}}$), there exists three simultaneous equations (Eq. 5 (diamond), Eq. 5 (germanium), and Eq.9), hence all variables can be solved, and n_2 can be obtained. However, upon solving these equations, it is found that the refractive indices vary noticeably with wavenumbers. This dependence of refractive index on wavenumber, particularly around the fingerprint region is in agreement with other studies.[31] Therefore, to obtain more accurate results, experimental measurements of the refractive indices of the samples are conducted using a refractometer. It is reported in the literature that the refractive indices for the neat solvents are 1.558[32], 1.534[33], 1.546[34], and 1.449[35] for HAP, MS, DCT and TBA respectively. The refractive indices of the neat solvents measured using the refractometer are then compared and found to be in good agreement with literature with less than 0.35% error. The value of refractive indices tabulated in Table 2 are used for the subsequent calculation for CO$_2$ concentrations.

Table 2. Value of refractive indices of all samples taken from refractometer at 25 °C

Solvent	Refractive Index		
	Neat	10% CC3_13	20% CC3_13
HAP	1.557	1.571	1.581
MS	1.533	1.544	1.552
DCT	1.544	1.552	1.561
TBA	1.444	1.462	1.476

3.6 Concentration of CO$_2$ in Type 2 Porous Liquids

The concentration of sorbed CO$_2$ in PLs is calculated by using Beer-Lambert law (Eq. 1). ε is assumed to be equal to the molar absorptivity for CO$_2$ in H$_2$O (0.89 × 10^6 cm^2·mol^{-1}).[36] $d_{e,u}$ for each samples is calculated using Eq. 5 from the refractive indices tabulated in Table 2. Hence the CO$_2$ concentration in mol per unit volume can be obtained from the absorbance of the v_3 peak. The concentration can be converted into mol per unit mass by incorporating the swelling, S calculated in section 3.4 and the density, ρ of the samples (eq. 10).

$$c_{\mathrm{w}} = c_{\mathrm{v}} \cdot \frac{(1+S)}{\rho} \qquad (10)$$

where c_w is the concentration in mol per unit mass and c_v is the concentration in mol per unit volume. The density of neat solvents and 20% w/v CC3_13 PLs were taken from literature, while the densities of 10% w/v CC3_13 PLs are estimated from linear interpolation

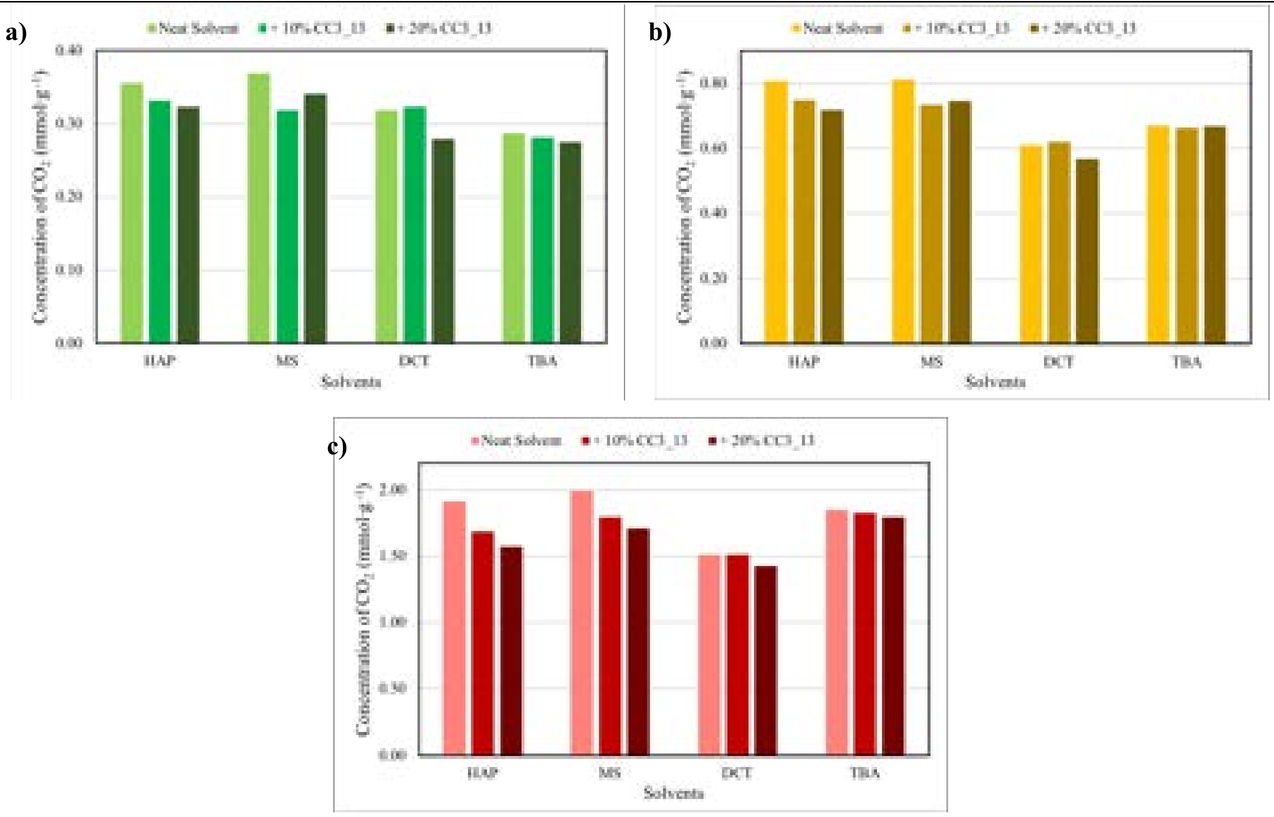

Figure 11. Concentration of CO$_2$ uptake in neat solvents (HAP, MS, DCT, and TBA) and PLs in 10% and 20% w/v CC3_13 cage concentrations at **a)** low pressure (2 bar), **b)** moderate pressure (10 bar), and **c)** high pressure (40 bar) of CO$_2$

Table 3. Density used for calculations for all samples

Solvent	Density ($g \cdot cm^{-3}$)		
	Neat	10% CC3_13	20% CC3_13[13]
HAP	1.131[32]	1.078	1.024
MS	1.174[33]	1.149	1.124
DCT	1.246[34]	1.217	1.187
TBA	1.326[35]	1.295	1.265

between those from neat solvents and 20% w/v CC3_13 PLs. The densities used in the calculation are tabulated in Table 3. As mentioned in section 3.3, the absorbance bands corresponding to CO_2 in all the neat solvents and PLs intensify when subjected to increasing pressure of CO_2, suggesting higher concentrations of CO_2. Figure 11 compares the CO_2 uptake across different solvents at low (2 bar), moderate (10 bar) and high pressure (40 bar) (CO_2 uptake for 5, 20, and 30 bar can be found in SI.6). Kearsey *et al.*[13] studied the methane uptake of these PLs and showed that for the neat solvents, the CH_4 uptake is in the order of MS>HAP>DCT>TBA. With the addition of 20% w/v CC3_13 the order changes to HAP>MS>TBA>DCT. When CO_2 is introduced, our results show that the PLs performed in a similar order. The CO_2 uptakes in PLs made with HAP and MS are predominantly seemed to perform slightly better than the other two solvents across all pressure, while in general DCT shows the lowest CO_2 uptake. It is observed that at low pressure, TBA exhibits the lowest CO_2 uptakes compared to other solvents. However, as pressure increases, TBA appears to exhibit a better CO_2 uptake.

It is essential to look at how PLs perform compared to the neat solvents. In theory, adding the CC3_13 cage offers void spaces in the liquid and should enhance the mass transport of CO_2. However, there is no increase in CO_2 sorption with the addition of cage. In fact, the concentrations of CO_2 are even decreasing in most cases. This is contrary to what is expected as it was previously reported that these solvents have shown significant increase in CH_4 and xenon uptake when CC3_13 cage was added.[13] Nevertheless, studies reported that the CH_4 uptake in neat solvents is in the order of μmol/g while Figure 11 shows that the uptake for pure solvent is in the order of 10^{-1} mmol/g. This indicates that the neat solvents have a significantly higher uptake in CO_2 compared to that of CH_4. Hence the addition of cage may not exhibit pronounce effect in the CO_2 uptake. A possible explanation would be due to the quadrupole moment of the CO_2 molecules. CO_2 has strong electric dipoles on both ends and may act as acid or base and interact with the functional groups in the solvent. CH_4, on the other hand, has very weak quadrupole moments which means that they are less likely to exhibit interaction with the solvent molecules. It has already been shown in the previous section that there are shifts in the wavenumber of v_2 and v_3 bands of CO_2 and characteristics bands of the solvents when samples are subjected to CO_2 indicating the presence of interactions.

Another possible explanation is the concept of forced intrusion.[38] HAP, MS, DCT and TBA were chosen as solvents for Type 2 PLs as they offer the bulkiness which provides steric hindrance to prevent them to enter the pores of the cage. However, most studies for these PLs were done in ambient or very low pressure (0.5 bar). At high pressure, there is higher chance that the solvents are 'forced' to enter the pores of the cage. Thus, occupying the space which is meant to sorb CO_2.

A study by Yin *et al.*[37] used electrostatic potential analysis to show that the interaction between CO_2 and the scrambled cage. It was found that the interactions are the strongest when CO_2 is located at the window of the cage. The oxygen atoms of CO_2 could form hydrogen bonds with the hydrogen atoms located in the positively charged region of the cage window. As the solvent molecules also contain electron-donating functional groups, this means that CO_2 possibly needs to compete with solvent molecules to occupy the adsorption sites of the cage.

When cage concentration is increased to 20% w/v, the concentration of CO_2 plateau or decreases further. A similar effect was also reported in the study for xenon uptake. When the cage concentration was increased from 14 to 24% in TBA, the gas evolution was shown to plateau or even decrease. The study speculated that it could be due to the increase in the viscosity of PLs when cage concentration is increased, which affects the xenon diffusion into the PLs. Hence viscosity is likely to be one of the reasons to why the gas uptake also decreased in our case of CO_2.

It is interesting to note that all the changes in the CO_2 uptakes when cage concentration increased is not substantial. Although general decreases were observed, but this is not always true. For instance, at 2 bar, MS + 20% CC3_13 showed increase in CO_2 uptake compared to MS + 10% CC3_13 (Figure 11.a)). At 10 bar, DCT + 10% CC3_13 also exhibits slight increase in the amount of sorbed CO_2 compared to the neat DCT solvent (Figure 11.b)). Therefore, a more accurate method of analysis needed to be done to quantify the CO_2 sorption.

4. CONCLUSIONS AND FUTURE WORK

The aim of this paper is to investigate the CO_2 sorption in Type 2 PLs, specifically scrambled 3^3:13^3 cage in 4 different types of solvent (HAP, MS, DCT and TBA) at pressure of up to 40 bar by utilizing ATR-FTIR spectroscopy.

Firstly, the FTIR spectra of neat solvents were obtained to identify characteristic bands of each solvent which were used in swelling calculation. The spectral subtraction of solvents from its respective PLs was done to confirm the presence of the scrambled cage. Next, the spectrum of pure CO_2 was also obtained to compare the peaks of the v_3 antisymmetric stretching and the v_2 bending mode of CO_2.

The FTIR spectra of the PLs subjected to CO_2 reveals a peak around the CO_2 v_3 band region indicating presence of CO_2 in the PLs. Spectral subtraction was required to eliminate the issue of overlapping spectra between the PLs and the v_2 band of CO_2. All solvents and PLs showed positive correlation in peak intensity of both the v_3 and v_2 bands and CO_2 pressure, indicating an increase in CO_2 uptake with increasing pressure. It was found that both the v_2 peak and the v_3 peak in the PLs had a shift towards the lower wavenumber when compared to that of pure gaseous CO_2 indicating potential interaction.

This method also successfully quantified the swelling of PLs when CO_2 was introduced, which was showed from the decrease of PLs' characteristics bands. The results showed that swelling increases in all PLs and neat solvents as CO_2 pressure was increased. In addition to the swelling, a slight shift towards higher wavenumber was also observed. This was thought to signify the suppression of intermolecular interaction between the functional group in the solvents due the presence of CO_2..

Finally, the concentration of CO_2 in the PLs were calculated and compared to the results of their corresponding neat solvents. Contrary to what expected, the addition of CC3_13 into the solvents did not show any increase in CO_2 uptake. Although general decrease in CO_2 uptake was observed when concentration of cage is increased, the change is not substantial and does not hold true for every cases.

Several reasons on the worsening of Type 2 PLs performance have been speculated. First, the CO_2 uptake of the neat solvents are good to start with, compared to those for CH_4 uptake from other studies, hence adding the cage may not exhibit any meaningful effect in CO_2 uptakes. This is due to the quadrupole moment of CO_2 which may exhibit interactions with the solvents. Second, forced intrusion may have occurred at high pressure where the solvent molecules could have entered the pore of the cage. Third, CO_2 may need to compete with solvent molecules to occupy the adsorption sites at the cage window. Finally, the increase in viscosity of the PLs could possibly negatively affect the diffusion of CO_2 into PLs.

While ATR-FTIR Spectroscopy provides a high level preliminary assessment on the CO_2 sorption in Type 2 Porous Liquid, further studies are still required. Computational calculations and molecular simulations such as molecular dynamics simulation are required to fully understand the interactions between CO_2, the solvents, and the cage, causing them to behave this way. Further research on the effect of high pressure and viscosity in gas uptake of porous liquid should also be conducted to verify the reasons of the unexpected performance of these PLs.

▪ ACKNOWLEDGEMENTS

Invaluable assistance offered by Evgeny Kovalev throughout the research are gratefully acknowledged. The authors also wish to thank Dr. Benjamin D. Egleston for the insights and samples prepared. Finally, the authors would like to express their utmost gratitude to Professor Sergei G. Kazarian for providing indispensable support and guidance.

▪ REFERENCES

1. Danaci, D.; Bui, M.; Mac Dowell, N.; Petit, C. Exploring the Limits of Adsorption-based CO_2 Capture Using MOFs with PVSA – From Molecular Design to Process Economics. *Molecular Systems Design & Engineering* **2020**, *5*, 212-231.
2. Kiani, A.; Jiang, K.; Feron, P. Techno-Economic Assessment for CO2 Capture from Air Using a Conventional Liquid-Based Absorption Process. *Frontiers in Energy Research* **2020**, *8*, 92
3. Joseph C. G.; Shane Q. Y.; Daud W. M. A. W. Carbon Dioxide Sequestration: A Review on the Current Techniques and the Way Forward. *Malaysian Journal of Chemistry* **2020**, *22(2)*, 1-21.
4. Zhang, W.; Liu, H.; Sun, Y.; Cakstins, J.; Sun, C.; Snape, C. E. Parametric Study on the Regeneration Heat Requirement of an Amine-Based Solid Adsorbent Process for Post-Combustion Carbon Capture. *Applied Energy* **2016**, *168*, 394-405.
5. Ahmad, M. Z.; Fuoco, A. Porous liquids – Future for CO_2 Capture and Separation? *Current Research in Green and Sustainable Chemistry* **2021**, *4*, 100070.
6. O'Reilly, N.; Giri, N.; James, S. L. Porous Liquids. *Chem. Eur J.* **2007**, 3020-3025.
7. Favre, E.; Svendsen, H. F. Membrane Contactors for Intensified Post-Combustion Carbon Dioxide Capture by Gas–Liquid Absorption Processes. *Journal of Membrane Science* **2012**, *407-408*, 1-7.
8. Zhou, C.; Longley, L.; Krajnc, A.; Smales, G. J.; Qiao, A.; Erucar, I.; Doherty, C. M.; Thornton, A. W.; Hill, A. J.; Ashling, C. W.; Qazvini, O. T.; Lee, S. J.; Chater, P. A.; Terrill, N. J.; Smith, A. J.; Yue, Y.; Mali, G.; Keen, D. A.; Telfer, S. G.; Bennett, T. D. Metal-Organic Framework Glasses with Permanent Accessible Porosity. *Nature Communications* **2018**, *9*, 5042-9.
9. Gao Y. Synthesis and Characterization of Porous Liquids. Master's Thesis, University of Tennessee, **2016**. https://trace.tennessee.edu/utk_gradthes/4287
10. Shan, W.; Fulvio, P. F.; Kong, L.; Schott, J. A.; Do-Thanh, C.; Tian, T.; Hu, X.; Mahurin, S. M.; Xing, H.; Dai, S. New Class of Type III Porous Liquids: A Promising Platform for Rational Adjustment of Gas Sorption Behavior. *ACS Applied Materials & Interfaces* **2018**, *10*, 32-36.
11. Greenaway, R. L.; Holden, D.; Eden, E. G. B.; Stephenson, A.; Yong, C. W.; Bennison, M. J.; Hasell, T.; Briggs, M. E.; James, S. L.; Cooper, A. I. Understanding Gas Capacity, Guest Selectivity, and Diffusion in Porous Liquids. *Chemical Science* **2017**, *8*, 2640-2651.
12. Giri, N.; Del Pópolo, M. G.; Melaugh, G.; Greenaway, R. L.; Rätzke, K.; Koschine, T.; Pison, L.; Gomes, M. F. C.; Cooper, A. I.; James, S. L. Liquids with Permanent Porosity. *Nature* **2015**, *527*, 216-220.
13. Kearsey, R. J.; Alston, B. M.; Briggs, M. E.; Greenaway, R. L.; Cooper, A. I. Accelerated Robotic Discovery of Type II Porous Liquids. *Chemical Science* **2019**, *10*, 9454-9465.
14. Alben, J. O.; Bare, G. H. Fourier Transform Infrared Spectroscopic Study of Molecular Interactions in Hemoglobin. *Applied Optics* **1978**, *17*, 2985-2990.
15. Ovchinnikov, O. V.; Evtukhova, A. V.; Kondratenko, T. S.; Smirnov, M. S.; Khokhlov, V. Y.; Erina, O. V. Manifestation of Intermolecular Interactions in FTIR Spectra of Methylene Blue Molecules. *Vibrational Spectroscopy* **2016**, *86*, 181-189.
16. Kamieńska-Piotrowicz, E.; Dziewulska, K.; Stangret, J. An Effective Method for Studying Intermolecular Interactions in Binary Liquids with Hydrogen Bonds; FTIR Spectra and Ab Initio Calculations in the N-Methylformamide−Methanol System. *The Journal of Physical Chemistry. B* **2010**, *114*, 5810-5818.
17. Kazarian, S. G.; Vincent, M. F.; Bright, F. V.; Liotta, C. L.; Eckert, C. A. Specific Intermolecular Interaction of

Carbon Dioxide with Polymers. *Journal of the American Chemical Society* **1996**, *118*, 1729-1736.

18. Ewing, A. V.; Kazarian, S. G. Current Trends and Opportunities for the Applications of In Situ Vibrational Spectroscopy to Investigate the Supercritical Fluid Processing of Polymers. *The Journal of Supercritical Fluids* **2018**, *134*, 88-95.
19. Kazarian, S. G. Polymers and Supercritical Fluids: Opportunities for Vibrational Spectroscopy. *Macromolecular Symposia.* **2002**, *184*, 215-228.
20. FTIR Spectroscopy: Attenuated Total Reflectance (ATR). http://cmdis.rpi.edu/sites/default/files/ATR_FTIR.pdf (accessed 8 December, 2021).
21. Milošević, M. *Internal Reflection and ATR Spectroscopy;* Chemical analysis; Wiley: Hoboken, N.J, 2012; Vol. 176, pp 79-80.
22. Lucero J. M. Porous Organic Cage CC2 and CC3 Crystals: Nucleation and Growth Studies. Ph.D. Dissertation, Colorado School of Mines, **2020.** https://hdl.handle.net/11124/174071
23. Song, Q.; Jiang, S.; Hasell, T.; Liu, M.; Sun, S.; Cheetham, A. K.; Sivaniah, E.; Cooper, A. I. Molecular Sieves: Porous Organic Cage Thin Films and Molecular-Sieving Membranes. *Advanced Materials* **2016**, *28*, 2652.
24. Gartner, T. A.; Barclay, A. A.; McKellar, R.; Moazzen-Ahmadi, N. Symmetry Breaking of the Bending Mode of CO_2 in the Presence of Ar. *Physical Chemistry Chemical Physics: PCCP* **2020**, *22*, 21488-21493.
25. Ewing, A. V.; Gabrienko, A. A.; Semikolenov, S. V.; Dubkov, K. A.; Kazarian, S. G. How Do Intermolecular Interactions Affect Swelling of Polyketones with a Differing Number of Carbonyl Groups? An In Situ ATR-FTIR Spectroscopic Study of CO_2 Sorption in Polymers. *Journal of Physical Chemistry. C* **2015**, *119*, 431-440.
26. Kazarian, S. G.; Briscoe, B. J.; Welton, T. Combining Ionic Liquids and Supercritical Fluids: In Situ ATR-IR Study of CO_2 Dissolved in Two Ionic Liquids at High Pressures. *Chemical Communications* **2000**, 2047-2048.
27. Flichy, N. M. B.; Kazarian, S. G.; Lawrence, C. J.; Briscoe, B. J. An ATR−IR Study of Poly (Dimethylsiloxane) under High-Pressure Carbon Dioxide: Simultaneous Measurement of Sorption and Swelling. *The Journal of Physical Chemistry. B* **2002**, *106*, 754-759.
28. A. Zajac; E. Hecht *Optics;* Pearson Higher Education: 2003.
29. Crystran. Germanium (Ge). https://www.crystran.co.uk/optical-materials/germanium-ge (accessed 8 December, 2021).
30. Venyaminov, S. Y.; Prendergast, F. G. Water (H_2O and D_2O) Molar Absorptivity in the 1000-4000 cm^{-1} Range and Quantitative Infrared Spectroscopy of Aqueous Solutions. *Analytical Biochemistry* **1997**, *248*, 234-245.
31. Averett, L. A.; Griffiths, P. R.; Nishikida, K. Effective Path Length in Attenuated Total Reflection Spectroscopy. *Analytical Chemistry* **2008**, *80*, 3045-3049.
32. Sigma Aldrich. 2′-Hydroxyacetophenone. https://www.sigmaaldrich.com/GB/en/product/aldrich/h18607 (accessed 8 December, 2021).
33. Sigma Aldrich. Methyl Salicylate. https://www.sigmaaldrich.com/GB/en/product/aldrich/240826 (accessed 8 December, 2021).
34. Sigma Aldrich. 2,4-Dichlorotoluene. https://www.sigmaaldrich.com/GB/en/product/aldrich/145009 (accessed 8 December, 2021).
35. Sigma Aldrich. 4-(Trifluoromethoxy)benzyl alcohol. https://www.sigmaaldrich.com/GB/en/product/aldrich/370614 (accessed 8 December, 2021).
36. Maiella, P. G.; Schoppelrei, J. W.; Brill, T. B. Spectroscopy of Hydrothermal Reactions. Part XI: Infrared Absorptivity of CO_2 and N_2O in Water at Elevated Temperature and Pressure. *Applied Spectroscopy* **1999**, *53*, 351-355.
37. Yin, J.; Fu, W.; Zhang, J.; Ran, H.; Lv, N.; Chao, Y.; Li, H.; Zhu, W.; Liu, H.; Li, H. Unraveling the Mechanism of CO_2 Capture and Separation by Porous Liquids. *RSC Advances* **2020**, *1*, 4276-42717.
38. Fraux, G.; Coudert, F.; Boutin, A.; Fuchs, A. H. Forced Intrusion of Water and Aqueous Solutions in Microporous Materials: From Fundamental Thermodynamics to Energy Storage Devices. *Chemical Society Reviews* **2017**, *46*, 7421-7437.

Reproducible Perovskite Layer Fabrication Achieved by Automatic Antisolvent Dispensing

Dylan Ooi and Leandro Guerra Guerrero
Department of Chemical Engineering, Imperial College London, U.K.

Abstract: Organic-inorganic halide perovskites are a promising type of semiconductor which could begin replacing predominantly silicon-based devices soon. However, there are some associated challenges due to the current lack of understanding of synthesis and degradation mechanisms leading to required improvements in the reproducibility of methods and device stability. This study aims to tackle the former of the two by implementing an automatic dispenser during spin coating of perovskite layers to mitigate human error in such a critical step of the synthesis process that is currently manually done. Furthermore, a comprehensive methodology has been developed and optimisation of parameters such as antisolvent dispensing time and rate executed. Two perovskite compositions were analysed: $(FAPbI)_{1.53}(MAPbBr_3)_{0.01}$, and $Cs_{0.1}(FAPbI)_{1.53}(MAPbBr_3)_{0.31}$ with PCEs (Power Conversion Efficiency) of >20% reported in the literature. In both cases, the perovskite was deposited onto a fluorine doped tin oxide coated substrate and spin coated with diethyl ether and chlorobenzene, respectively. Perovskite layers were characterized by using visual inspection, ultraviolet–visible spectroscopy, x-ray crystallography, and scanning electron microscope. Analysis found that the triple cation perovskite produced smaller grains and rougher surface morphology, but lower pinholes density compared to the double cation perovskite. It was identified that the optimum dispensing conditions for the double cation was a needle diameter 2.16 mm for 1.5 s and for the triple cation a needle of 1.68 mm for 0.3 s.

Keywords: Perovskites, Semiconductors, Antisolvent, Crystallisation, Spin coating, Automatic dispensing

Introduction

Organic-inorganic metal halide perovskites promise a cheap and highly efficient alternative for numerous technologies within photovoltaics and photocatalysis. Relatively low investments have caused the performance of perovskite solar cells, beginning at conversion efficiencies of 3.8% in 2009 (Kojima, Teshima, Shirai and Miyasaka, 2009), to increase to a current record of 25.8% in 2021 (Min et al., 2021) quickly approaching the current relatively stagnant record efficiency of 26.7% in single-junction silicon cells (Yamamoto, Yoshikawa, Uzu and Adachi, 2018). This emerging technology has become an area of extreme interest in the field of semi-conductor solid state physics. The rapid improvement of the performance of perovskite devices can be credited to optimisation of fabrication methods, chemical compositions, and phase stabilisation methods (Yoo et al., 2021).

In addition, these high efficiencies are feasible due to multiple favourable properties exhibited by perovskites such as high absorption coefficients, long charge carrier diffusion lengths and low exciton binding energies. Likewise, their naturally abundant raw materials and low fabrication temperatures yield low production costs thus promising shorter payback times if implemented compared to the expensive methods for synthesis of silicon cells (Taylor et al., 2021). Nevertheless, whilst perovskites can clearly push semiconductor utilising technologies to the next level there are many complications that arise. The main issues arise from the lack of existing understanding of the synthesis and degradation mechanisms of the perovskite layer (Saliba et al., 2018).

Several methods for deposition of perovskite layers exist such as inkjet printing and thermal evaporation however the most prevalent to date has been spin coating. It is worth noting that this is only in research as issues arise with the scalability of spin coating. This method consists of the addition of an antisolvent to a perovskite precursor solution to commence the crystallisation process upon removal of the relevant solvent. It has been found that the characteristics of the crucial antisolvent deposition step determine the behaviour of crystallisation (Paek et al., 2017).

Such characteristics include antisolvent type, volume, and delay of deposition which in turn influence the crystal growth and film formation produced differently depending on perovskite composition. The crystal morphology is paramount to the efficiency of all semiconductor devices. The effectiveness of two step antisolvent deposition has been previously explored however the increased complexity resulted in inferior efficiencies (Xiao et al., 2014).

Furthermore, the antisolvent deposition is usually done manually. in research laboratories, adding to the uncertainty of parameters through human error. This is an area that must be focused on to improve reproducibility of high efficiency perovskite layers. Discovery of high efficiencies hence requires optimisation of complex fabrication techniques which can only be replicated if provided with comprehensive methodologies.

Unfortunately, to this day there is still lack of focus in this area resulting in only a few groups being capable of producing near record efficiency devices as well as huge discrepancies in results. For example, Gosh et al. have reported antisolvent volumes between 100 and 900 µL as well as delay for deposition between 2 and 30 seconds with PSCs greater than 17%. (Ghosh, Mishra and Singh, 2020) Overall, these large efficiency gaps and contradictory results create confusion, drastically slowing down progress in the field.

The aim of this work is to address the current lack of reproducible methods for high efficiency perovskite devices by providing an exhaustive methodology which incorporates the use of an automatic dispenser to minimise human error. We convey a full methodology that addresses common issues experienced whilst providing expertise from practice. Moreover, we detail the steps required to optimise the parameters of the automatic dispenser to yield optimal perovskite layers. We hope that these results encourage future publishers to give emphasis to their methods and explore the automation of crucial steps within the antisolvent deposition step of spin coating to bridge the efficiency gap that currently exists and therefore accelerate progress.

Background

Perovskites

Perovskites are materials that exhibit the same crystal structure as the naturally occurring mineral calcium titanium oxide. This structure can be achieved using a large variety of elements which yields flexibility with regards to their material characteristics. Generally, their chemical formula follows the structure ABX_3 where A and B are cations whilst X is anionic oxides or halogens. (Fabbri et al., 2014). Most perovskites are semiconductors meaning that their conductivity is between that of an insulator and a conductor dependent on temperature. This property comes from the difference in energy between the valence and conduction bands of the material also known as the band gap. When an electron in the valence band is given sufficient energy, it becomes excited and moves to the conduction band where it can participate in conduction. It is important to note that the band gap of a material is the minimum energy that can be supplied to the electron otherwise it will not be excited. This minimum energy means that there exists a specific wavelength at which each perovskite begins to absorb light called the absorption onset. The specific band gap of a material can be calculated using the following equation,

$$Band\ gap = \frac{1240}{\lambda} \qquad (1)$$

Where λ is the absorption onset wavelength [nm].

Perovskites have been reported to possess high absorption coefficients thus light is readily absorbed and unlikely to traverse through the material without being absorbed. (Lee et al., 2012) Beer Lambert's law can be utilised to calculate absorbance from transmittance as follows,

$$Absorbance = 2 - \log(\%Transmittance) \quad (2)$$

Recombination

Minimising recombination within perovskite films continues to be one of the biggest challenges for maximising their efficiency. Recombination is essentially the opposite process to electron excitation; it is when an electron in the conduction band combines with a hole. There exist three types of recombination: non-radiative, radiative, and Auger (Honsberg and Bowden, 2021). Radiative recombination, most dominant in direct bandgap semiconductors, emits a photon of equivalent energy to the bandgap of the perovskite. Recombination through defects occurs when an electron in the conduction band is trapped within a different energy state provided by a defect in the film and recombines with a hole before it can escape back. This type of recombination can be minimised through minimisation of defects such as pinholes in the perovskite film. Auger recombination is analogous to radiative recombination however in this case the energy released is passed to a neighbouring electron in the conduction band which eventually returns to its original excited energy state. In summary, the relative magnitudes of these types of recombination are dependent on the material properties and film morphology but any recombination within applications like photovoltaics and photocatalysis is extremely undesirable as it reduces the number of excited electrons available for conduction.

Antisolvents

The application of antisolvents to the perovskite precursor is integral to the resulting morphology of the perovskite film. Antisolvents are fluids that create instantaneous supersaturation conditions within a solution due to its simultaneous high miscibility with the solvent and not dissolving the solute (Ghosh, Mishra and Singh, 2020). This commences the crystallisation of the perovskite film through complex solvent interactions.

Applications

The effectiveness of perovskite films can be quantified through application in photovoltaics and photocatalysis. Whilst there are a multitude of different factors involved in the observed efficiencies, this can still provide a great indicator on the feasibility of their use.

A solar cell is a device which can directly convert solar energy (photons) to electrical current. It is made up of two main components including a material which can absorb light (usually a semiconductor) and a path for the excited electrons to dissipate energy then return to the cell. The efficiency of a solar cell can be calculated as follows,

$$h = \frac{V_{OC} \cdot I_{SC} \cdot FF}{P_{IN}} \quad (3)$$

Where V_{OC} is open circuit voltage [V], I_{SC} is short circuit current [A], FF is fill factor and P_{IN} is input power [1 kW/m^2].

The Shockley Queisser (SQ) limit is the maximum theoretical efficiency that a single p-n junction solar cell can have assuming loss only occurs due to radiative recombination. An ideal cell has a band gap of 1.4 eV which corresponds to an SQ limit of 33.7% (Shockley and Queisser, 1961). Silicon only has a band gap of 1.1 eV whilst perovskite compositions can be adjusted to bring their respective band gap as close to the ideal value as possible.

Materials and Methodology

As a baseline for optimisation, two perovskite compositions and methods were chosen due to their high reported PCE's of over 20%. Yoo et al's method was used to synthesise a double cation perovskite (Yoo et al., 2021) and Saliba et al's method was used to synthesise a triple cation perovskite (Saliba et al., 2018).

Materials

Chemical	**Purity**	**Producer**
PbI2	99.0%	Sigma-Aldich
FAI	>99.9%	Greatcell Solar
MACl	>99.8%	Greatcell Solar
PbBr2	98.0%	Sigma-Aldich
MABr	>99.9%	Greatcell Solar
CsI	99.0%	Sigma-Aldich
Diethyl Ether anhydrous	99.0%	TCI Europe
Chlorobenzene anhydrous	99.8%	Scientific Laboratory Supplies Ltd

Table 1. List of all chemicals used throughout the experiment

An extensive list of all chemical materials and their manufacturing properties is provided in Table 1. With regards to the experimental methodology, a Laurell Technologies' Universal Dispenser (UD-3) spin coater was used for all perovskite deposition steps. The synthesis of perovskite solutions, deposition steps and annealing are carried out in a nitrogen filled glovebox with water and oxygen concentrations < 0.5 ppm. To ensure a constant nitrogen atmosphere, a constant circulation was imposed in the glovebox.

Substrate Preparation

Glass covered with fluorine doped tin oxide (FTO) was used for deposition of the perovskite layers. The substrates were cut into 2cmx2cm squares, labelled on the non-FTO side with a diamond-tipped pen, and carefully placed into staining jars. To ensure the FTO was completely contaminant free a three-step cleaning process was carried out using an ultrasonic cleaner. Each step ran for 15 minutes on the full setting, thoroughly rinsing between steps, and was executed in the following order:

1. Hellmanex solution (2%)
2. Acetone
3. Isopropyl Alcohol (IPA)

Afterwards, the clean FTO substrates were removed from the staining jars, dried using pressurised air and placed into a UV-ozone cleaner for 20 minutes. Upon removal from the UV-ozone cleaner the substrates were utilised for spin coating immediately.

Perovskite Precursor Solutions

Both perovskite precursor solutions were made up using three base solutions. These were prepared as follows:

1. $FAPbI_3$ (1.53M) synthesis
   a. Mix 1.53 M PbI_2, 1.4 M FAI, and 0.5 M MACl.
   b. Dissolve in 2 mL of DMF: DMSO = 4:1
2. $MAPbBr_3$ (1.53M) synthesis
   a. Mix 1.53 M $PbBr_2$, and 1.4 M MABr.
   b. Dissolve in 2 mL of DMF: DMSO = 4:1
3. CsI (1.50M) synthesis
   a. Dissolve 1.5 M of CsI in 2 mL of DMF: DMSO = 4:1

The double cation composition used was $(FAPbI)_{1.53}(MAPbBr_3)_{0.01}$ which was made up by mixing $FAPbI_3$ with 0.8 vol% $MAPbBr_3$. The triple

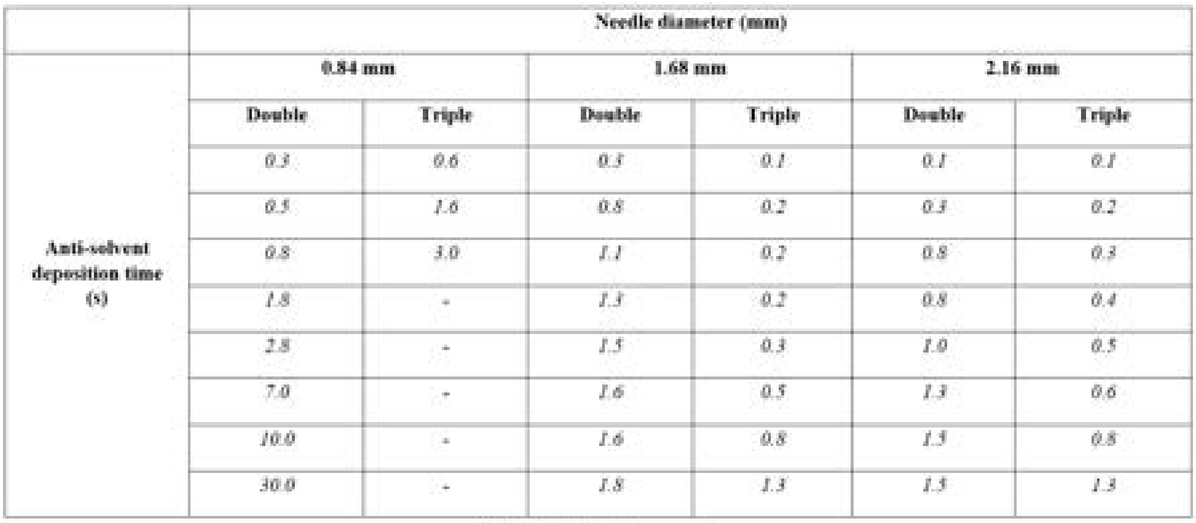

	Needle diameter (mm)					
	0.84 mm		1.68 mm		2.16 mm	
	Double	Triple	Double	Triple	Double	Triple
Anti-solvent deposition time (s)	0.3	0.6	0.3	0.1	0.1	0.1
	0.5	1.6	0.8	0.2	0.3	0.2
	0.8	3.0	1.1	0.2	0.8	0.3
	1.8	-	1.3	0.2	0.8	0.4
	2.8	-	1.5	0.3	1.0	0.5
	7.0	-	1.6	0.5	1.3	0.6
	10.0	-	1.6	0.8	1.5	0.8
	30.0	-	1.8	1.3	1.5	1.3

Table 2. List of all experiments ran

cation composition used was $Cs_{0.1}(FAPbI)_{1.53}(MAPbBr_3)_{0.31}$ which was made up by mixing FaPbI3 with MaPbBr3 in a 5:1 volume ratio and further adding a 5 vol% of the CsI solution. It is important to note that before mixing the base solutions, one should filter them to ensure no particles or grains are present in the perovskite precursor which can be detrimental to film quality.

Perovskite Film Spin Coating

The perovskite precursor solution was heated on a hotplate to 50 °C before deposition of antisolvent on the FTO substrate. The FTO substrate was placed on to the chuck of the spin coater, and 100µl of the heated perovskite solution was dripped on to the FTO substrate. The spin coater was then loaded with the appropriate antisolvent for each perovskite:

1. Diethyl ether for the double cation perovskite
2. Chlorobenzene for the triple cation perovskite

Equally, the individual steps for the spin coating program were taken from the papers (Yoo et al., 2021) and (Saliba et al., 2018) as a baseline for optimisation. Vacuum was then applied to the FTO substrate, and the appropriate deposition and spin coating program was run for the perovskite. The following initial programs were used:

Double cation perovskite spin coating steps:

1. 1000 rpm for 10 s with 2000 rpm ramp
2. 5000 rpm for 10 s with 2000 rpm ramp
3. Deposit diethyl ether for 0.3 s at 5000 rpm
4. 5000 rpm for 20 s at 2000 rpm ramp
5. Anneal on hot plate at 100 °C for 60 minutes

Triple cation perovskite spin coating steps:

1. 1000 rpm for 10 s with 200 rpm ramp
2. 6000 rpm for 15s with 2000 rpm ramp
3. Deposit chlorobenzene for 0.3 s at 6000 rpm
4. 6000 rpm for 5 s at 2000 rpm ramp
5. Anneal on hot plate at 100 °C for 60 minutes

In between deposition runs, the spin coater was opened, and the glovebox purged for 20 s. This was to ensure that the evaporated antisolvent did not start crystallization of the next sample prematurely.

In this report, two variables of the spin coating process were optimised:

1. Antisolvent dispensing time
2. Deposition needle diameter

Where experiments ran are shown in Table 2. To prevent dripping of the antisolvent from the needle, the recommended suck back and speed settings were used on the spin coater as described in the corresponding user manual. (Laurell Technologies Corporation, 2012)

Immediately after spin coating, the substrates were placed on a hot plate at 100 °C for one hour for thermal annealing.

Device Characterisation

Five main methods of characterisation were used to compare the quality of the perovskite layers:

1. Visual inspection and Photographs
2. Ultraviolet–Visible spectroscopy (UV-Vis)
3. Photoluminescence (PL)
4. X-ray diffraction (XRD)
5. Scanning electron microscope (SEM)

Visual Inspection and Photographs

Visual inspection was utilised for preliminary characterisation of the perovskite layers by analysis of colour, haziness, and uniformity. The perovskite layers deposited on FTO layers were photographed. This was used in tandem with SEM images to evaluate perovskite layers.

Ultraviolet-visible Spectroscopy

UV-Vis was used to measure the transmittance of the perovskite layers and quantify the band gap of the deposited layer.

Each sample was gently placed into the spectrometer using tweezers to avoid damage to the integrity of the layers. The latch is adjusted such that the light hits the surface of the perovskite perpendicularly. The UV-Vis was then run between a wavelength range of 400 – 1000 nm. The sampling interval used was 1.0 nm, with a scan speed of medium. Lastly, a slit width of 1.0 nm was set.

Photoluminescence

Photoluminescence (PL) spectra of the perovskite layers deposited on FTO substrate were obtained at ambient environment by a photoluminescence spectrometer (FLS1000, Edinburgh Instruments) using a 450 W ozone free continuous xenon arc lamp as excitation source. An excitation wavelength of 405 nm, bandwidth of 5 nm, and a long-pass filter (495 nm cut-off wavelength) was used. The PL emission was measured using a bandwidth of 5 nm, dwell time of 0.1 s, and spectral resolution of 1 nm.

X-ray Diffraction

A PANalytical X'Pert Pro Driffractometer was used to measure XRD diffraction spectra of the perovskite layer at 40 kV and 40 mA. The 2θ range of 10-40 degrees in steps of 0.05 degrees was carried out.

SEM Imaging

SEM images were obtained using a Gemini LEO 1525 field emission scanning electron microscope (5 kV accelerating voltage). Prior to imaging all samples were coated with 10 nm chromium.

Optimisation of Spin Coater

To keep runs of depositions consistent, the dispensing pressure of the spin coater was calibrated for each needle. The goal of calibrating the needle was to obtain the optimum stream when depositing, characterised by:

1. No excess dispensing such that the antisolvent splashes off the FTO substrate.
2. Consistent stream of antisolvent during dispensing, with no sputtering.
3. No premature dripping of the antisolvent before dispensing
4. No dripping of the antisolvent after dispensing

Figure 1. Photograph of the 8 experiments on double cation perovskite using the 2.16 mm needle, with deposition times from left to right: 0.1s, 0.3s, 0.8s, 0.8s, 1.3s, 1.5s, 1.5s, 1.0s.

By increasing dispensing pressure, the dispensing stream would come out stronger, giving a consistent stream and avoiding sputtering. However, using a dispensing pressure too high would cause excessive splashing, and therefore wash away the perovskite layer. It was found that the needles are sensitive to small changes in pressure, therefore one optimum pressure was identified for each needle. Results of the corresponding pressure used for each needle diameter size are presented in Table 3.

Needle Diameter (mm)	Pressure Selected (Pa)
0.84	26,200
1.68	30,300
2.16	13,100

Table 3. Pressure selected for the needles chosen

To ensure no antisolvent would drip before or after dispensing, needles were firmly screwed in until tight. The latch of the automatic dispenser should also be carefully closed to ensure no antisolvent drips when closing the lid.

Results and Discussion

To determine the optimum deposition time and needle size for each composition of perovskite, the range of layers were characterised through various techniques.

Optimising Antisolvent Deposition Time

Initial analysis by visual inspection of the different perovskite films was carried out to find the optimal antisolvent deposition time. This allowed ruling out of poorest quality perovskite layers without having to run further analysis on them. Figure 1 shows double cation perovskites spin coated with the 2.16 mm needle for a range of deposition times. Visually, the ideal perovskite layer should exhibit minimal scratches or drip marks as this indicates that there are less defects which minimises the degree of recombination. Likewise, the layer should be uniform with a shiny metal-like coat of dark colour showing the perovskite precursor has crystallised uniformly at the surface meaning reflectance is minimised and more light can be absorbed by the semiconductor.

Taking Figure 1 as an example, samples 1 and 2 can be immediately ruled out as almost no crystallization has occurred seen by the lack of a dark film over the slide. Sample 3 was ruled out due to the hazy colour of the perovskite layer which arises from poor surface morphology, leaving samples 4 through 8 to be viable candidates to be further analysed through UV-Vis spectroscopy.

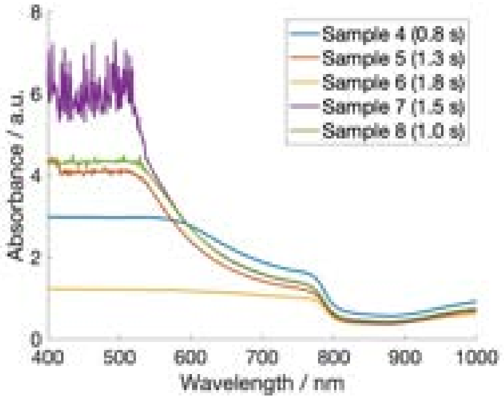

Figure 2. Absorbance curve for samples 4-8 for double cation perovskite composition with the 2.16 mm needle.

The absorption spectra of samples 4 to 8 for double cation composition using the 2.16 mm needle are shown in Figure 2. This was calculated using equation 2 and transmittance data obtained.

Figure 2 shows that the absorption onset for all four samples occurs at the same wavelength. This is expected since the films are composed of the same perovskite composition and thus equivalent band gap. However, it is evident that sample 7 has the largest difference in absorbance at the absorption onset from Figure 3 as well as largest overall absorbance at shorter wavelengths such as 500 nm from Figure 2. This implies that, based on visual inspection and UV-Vis analysis, sample 7 is the highest quality layer synthesised as it can absorb light most effectively.

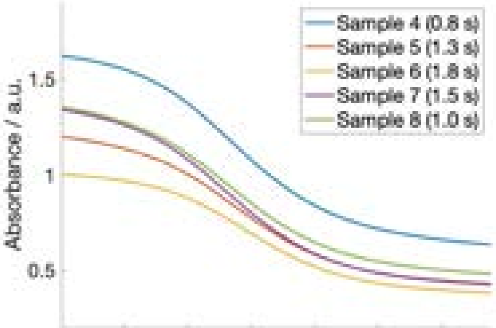

Figure 3. Absorption onset curve for samples 4-8 for double cation perovskite composition with the 2.16 mm needle.

In addition, SEM was used alongside UV-Vis to characterize devices and determine the optimal variable conditions. The SEM images for the perovskite films were directly compared to gain deeper insight into their crystalline structures. Two main degrees of magnification were used in the analysis: 10,000x (10kx), and 50,000x (50kx). The 10kx SEM images were used to identify the pinhole distribution within the film, whilst the 50kx images allowed clearer examination of average grain size and surface roughness.

Characteristics of a good crystal morphology for perovskite layers are:

1. No (or few) pinholes
2. Large grain size
3. Smooth surface

Pinholes are formed primarily during the crystallization step, which is highly dependent on the speed and uniformity of deposition of antisolvent during spin coating. An uneven distribution of antisolvent will cause regions to have incomplete crystallisation of the perovskite precursor to the perovskite, forming pinholes.

Pinholes are undesirable due to the sensitivity of the perovskite layer to moisture in the air. These pinholes facilitate the diffusion of moisture which can degrade the perovskite layer, leading to poor device performance and low PCEs. (Ono et al., 2015) Pinholes formed in the perovskite layer will also contribute to a higher surface recombination rate for holes, leading to a lower PCE (Masood et al., 2020).

Kim & Park showed that larger grain sizes corresponded to a higher PCE (Kim and Park, 2014). Therefore, this experiment aimed to produce large grain sizes. Liao et al. suggests that the formation of large grains is largely dependent on the temperature of the perovskite precursor (Liao et al., 2020). The theory is that the high temperature “provides the necessary driving force for the phase change” (Liao et al., 2020), resulting in more rapid crystal formation and larger grain sizes. Since the temperature of the perovskite precursor was not varied in this experiment, this could serve as an area of further investigation in future studies.

Figure 4 compares samples 4 (Figure 4a) and 7 (Figure 4b) in the 10kx magnification scale. Based off the SEM results, sample 4 showed a pinhole density of 0.014 pinholes per μm^2, while sample 7 showed a pinhole density of 0.004 pinholes per μm^2. This suggests that a greater needle size (and thus stream diameter) provides a more uniform distribution of antisolvent, which leads to the

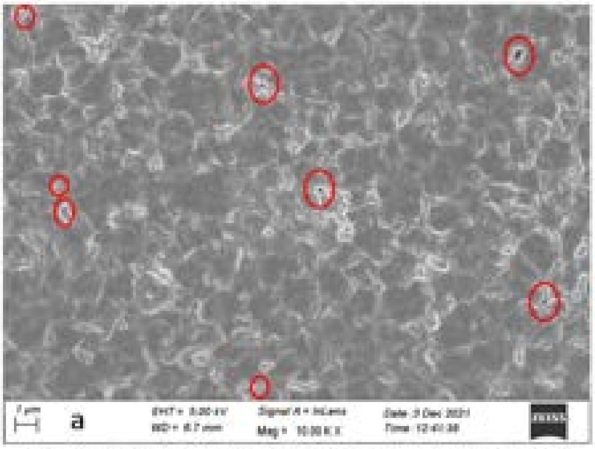

Figure 4a. Sample 4 (0.8s deposition) at 10000x magnification

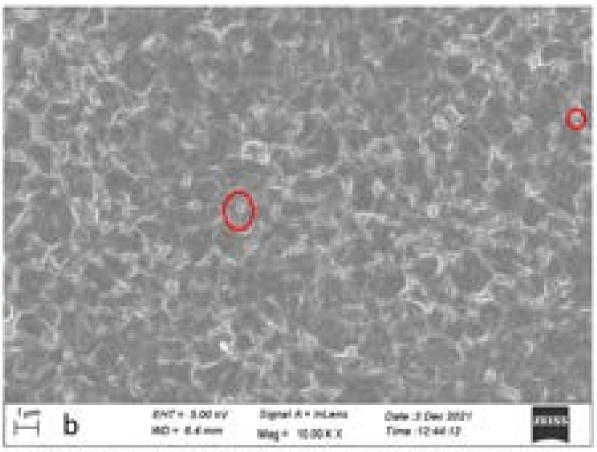

Figure 4b. Sample 7 (1.5s deposition) at 10000x magnification

formation of less pinholes. Comparison of sample 7 to the other samples (5, 6 and 8) revealed a similar trend, illustrating that a deposition time of 1.5 s is optimal using the 2.16 mm needle for the double cation perovskite.

This suggests that a deposition time <1.5s deposits too little antisolvent causing incomplete formation of the perovskite layer and thus more pinholes. While a deposition time >1.5s deposits too much antisolvent, washing away the perovskite precursor and causing non-uniform crystallization, forming pinholes too.

Next, samples were also compared in the 50kx magnification range to identify average grain size and surface roughness clearly as the 10kx magnification proved too wide. However, comparison between images showed similar grain size values with an average of 870 mm. This suggests that antisolvent deposition time does not have a large impact on the grain size formed during crystallisation. This is backed up by Liao et al. which suggest that grain sizes are largely dictated by the temperature of the perovskite precursor (Liao et al., 2020). Since the temperature of the perovskite was kept constant throughout experiments, this should not be a surprising result.

Overall, based on visual inspection, UV-Vis, and SEM images, it was determined that a deposition time of 1.5 s was optimum for the formation of the double cation perovskite layer using the 2.16 mm needle. An identical methodology was carried out for other needle sizes, and the triple cation. Table 4 shows the optimum deposition time for each needle and perovskite combination.

	Double cation		Triple cation	
	1.68 mm	2.16 mm	1.68 mm	2.16 mm
Optimum deposition time (s)	1.5	1.5	0.5	0.3

Table 4. Optimum deposition time for each needle and perovskite composition

The 0.84 mm needle produced extremely poor perovskite layers for composition over a variety of antisolvent dispensing times. Its small deposition surface area gave a narrow stream that in turn washed away the perovskite precursor thus leading to large areas where no crystallisation occurred. Utilisation of this needle proved to be much more difficult hence greatly decreasing the reproducibility of any results. The needle was deemed unsuitable and discarded from further investigation.

By using UV-Vis and SEM imaging as described earlier, it was identified that double cation perovskite layers formed with the 2.16 mm needle at 1.5 s deposition outperformed the 1.68 mm needle for a 1.5 s deposition. What is interesting to note is that the 1.68 mm needle formed perovskite layers with significantly more pinholes than the 2.16 mm needle.

In the case of the triple cation, minimal pinholes were seen for all perovskite layers. This suggests that the caesium ion stabilizes the perovskite layer better than the double cation perovskite, leading to less pinholes being formed. Figure 5 shows the 10kx magnification for the triple cation ran with the 2.16 mm needle for 0.5 s, where no pinholes were observed.

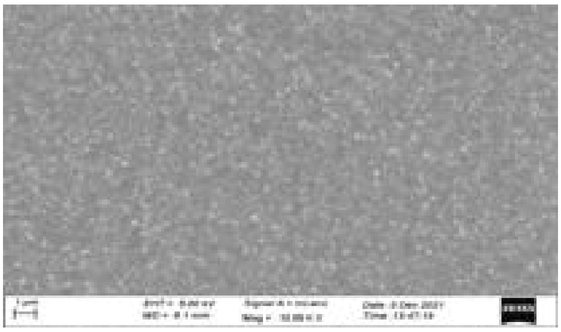

Figure 5. SEM image of triple cation with the 2.16 mm needle for 0.5s

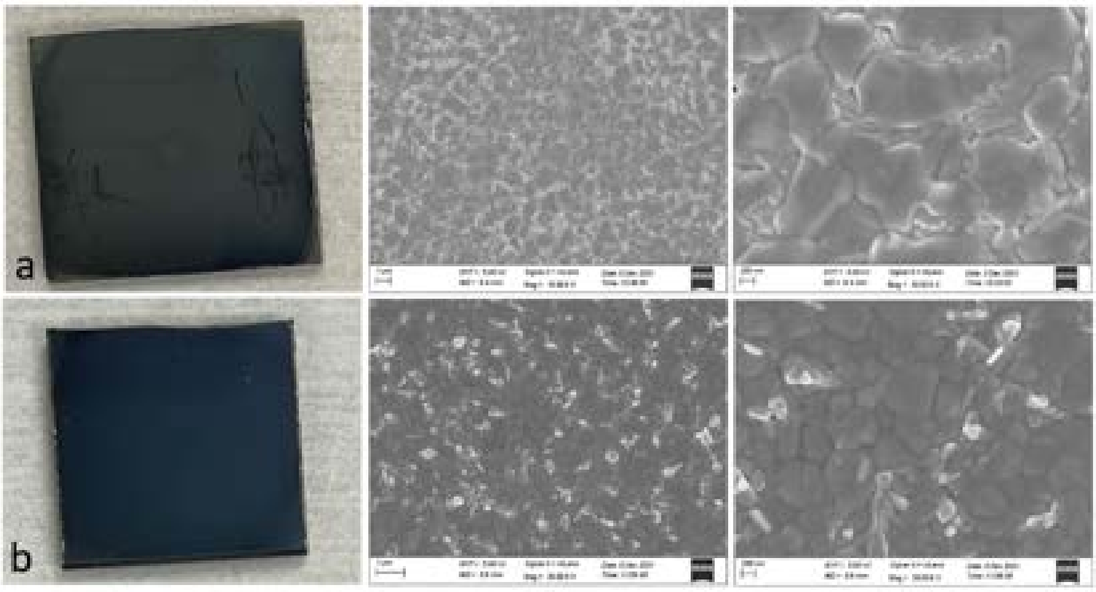

Figure 6a. Double cation perovskite with 2.16 mm needle for 1.5s **Figure 6b.** Triple cation perovskite with 1.68mm needle for 0.3s

Comparison Between Perovskite Compositions

Overall, the optimum needle size and deposition time was found for both perovskite composition to be:

1. Double cation: 2.16 mm needle for 1.5 s
2. Triple cation: 1.68 mm needle for 0.3 s

Figure 7 shows the absorption and photoluminescence (PL) spectra for both perovskite film compositions studied. For each composition, the absorption onset matched with the position of PL maxima. One difference between the two compositions is that the absorption onset is shifted between perovskite compositions due to addition of caesium increasing the corresponding semiconductor bandgap hence higher minimum photon wavelength is required to excite the electrons from the valence band to the conduction band. The bandgaps for the two perovskite compositions were calculated to be 1.55 eV and 1.62 eV using equation (1) for the double cation and triple cation, respectively.

It is important to consider reflectance for analysis of this absorption data as it may lead to misleading results. Similarly, the smaller PL peaks are due to the lamp from the equipment and not the perovskites. The difference in baseline heights that can be observed at higher wavelengths such as 900 nm conveys a clear difference in the reflectance on the two perovskite films. This concept is further explored by reviewing photographic evidence and SEM images as these give a clearer idea of the difference in surface morphology.

The PL curves are obtained from light re-emitted by the semiconductor due to radiative recombination. Figure 6 shows the perovskite sample as well as SEM images side by side, comparing the optimum settings for both the double and triple cation compositions. The triple cation had an average grain size of 430 mm while the double cation had an average grain size of 870 mm. The double cation composition formed perovskite layers with considerably larger grain sizes.

X-ray diffraction patterns (XRD) corresponding to the best perovskite layers for each composition are shown in Figure 8. The angle at which each peak exists corresponds to different crystal planes present within a perovskite structure. The relevant phases present have been identified and matched to their resultant peaks. The characteristic

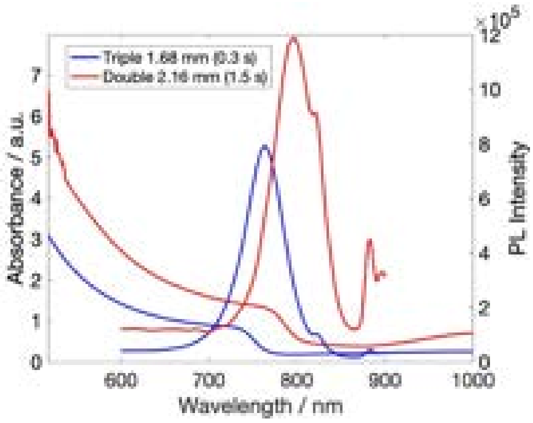

Figure 7. Absorption and photoluminescence spectra for optimum perovskite layers

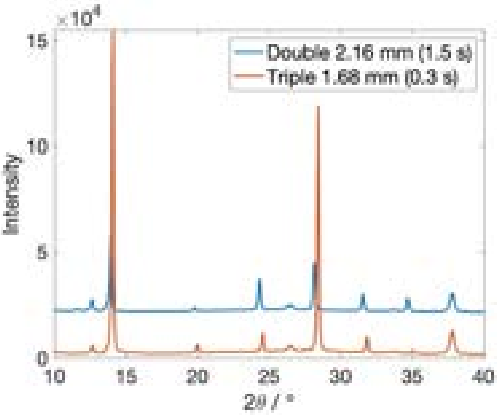

Figure 8. X-ray diffraction spectra for optimum perovskite layers

peaks present for each composition with varying antisolvent dispensing times were identical illustrating that perovskite crystal structure is independent of this and hence it is only necessary to show one perovskite layer per composition. Comparing the two diffraction patterns, both compositions exhibited very similar crystal structures however they differed with regards to intensity and placement. Peak intensity is dependent on plane thickness mainly thus the larger peaks at 14 and 28 degrees exhibited by the triple cation perovskite suggest that this composition possesses thicker α-phase FAPbI crystal planes. Likewise, the triple cation perovskite has its peaks for the α-phase of FAPbI all shifted to the right which shows that it has a different distance between these crystal planes compared to the double cation perovskite. Whilst the x-ray diffraction patterns show a difference between the size and spacing between the crystal phases in both perovskite compositions it proves that they both similar crystal structure. This proves that the automatic dispensing of antisolvent upon the perovskite precursor solutions has yielded the correct morphology regardless of the composition utilised. However, it is important to note that the peak present at 13 degrees appearing due to PbI_2 is undesirable meaning it should be minimised as much as possible. Decreasing storage time of the perovskite precursor and time before analysis of samples could help achieve this.

Not all peaks arise from the perovskite film. The peaks at 26 and 38 degrees come from the FTO layer on the glass substrate.

Devices

Perovskite layers were deposited on smaller FTO substrates, and solar cells were built with their respective performance quantified. Important parameters such as the short circuit current density, open circuit voltage, and fill factor were measured to calculate the power conversion efficiency. The noteworthy results are presented in Table 5.

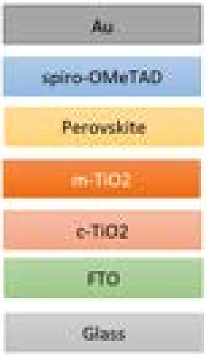

Figure 9. Structure of the solar cells

	Jsc (mA/cm2)	Voc [V]	FF	PCE [%]
Triple cation				
Reverse	-24	1.1	0.61	**15**
Normal	-23	1.0	0.57	13
Double cation				
Reverse	-21	1.0	0.51	**11**
Normal	-21	1.0	0.28	5.6

Table 5. Solar cell tests ran for the best perovskite layers

The highest power conversion efficiencies observed for the devices were 15% and 11% for the triple and double cation perovskite layers, respectively.

Both solar cells were constructed using a conventional structure (n-i-p), illustrated in Figure 9. Building solar cells and testing their efficiencies are not within the scope of this study, however this result proves that the synthesised perovskite layers can be applied as semiconductors in real solar cells.

Conclusions

Ultimately, the optimisation of variables for the synthesis of reproducible perovskite film layers for two different precursor compositions was carried out through the implementation of an automatic dispenser during spin coating.

The variables investigated proved to be specific to perovskite compositions yielding specific optimum results with regards to antisolvent dispensing time and needle diameter size. The use of a combination of film characterisation techniques including visual inspection, UV-Vis spectroscopy, and SEM images allowed for analysis of absorbance and crystal structure. This led to the discovery that for the double cation ($(FAPbI)_{1.53}(MAPbBr_3)_{0.01}$) 1.5 s antisolvent deposition time with the 2.16 mm diameter needle was optimal whilst the triple cation ($Cs_{0.1}(FAPbI)_{1.53}(MAPbBr_3)_{0.31}$) 0.3 s antisolvent deposition time with the 1.68 mm diameter needle was optimal. On the other hand, the 0.84 mm diameter needle yielded extremely poor perovskite layers giving an insight to the limit of size that is feasible. The significant difference between layer quality with regards to antisolvent dispensing time clearly conveys the sensitivity of perovskite film production and thus the difficulty associated with producing high efficiency devices. Similarly, there exist numerous other factors outside of parameter optimisation that can greatly impact perovskite layer quality due to the method consisting of multiple critical steps as well as degradation of the precursor.

Moreover, comparing the two compositions the triple cation exhibited a much lower pinhole density whilst the double cation had larger grains on average. Whilst the X-ray diffraction patterns showed similar crystal planes present within the two perovskites, the composition influenced the band gap and resulted in a difference of 70 meV.

The application of perovskite layers in solar cells using the corresponding optimal parameters was also investigated. This proved the feasibility of utilising the methodology found to produce electrical current. The highest obtained PCEs for solar cells was 15% and 11% for the triple and double cation compositions, respectively.

There are several future developments that could be explored for further improvement of reproducibility of perovskite film layer synthesis.

Most importantly, investigation of the repeatability of results would be greatly impactful. Whilst this report covers the optimisation of parameters no repeats were taken leading to the increased possibility of errors. Proving the ability to consistently produce identical crystal morphologies would be a huge step forward towards the possibility of commercial implementation of perovskite technologies in industry as it would speed up progress in developments and reassure investors.

Acknowledgements

We would like to express our gratitude towards everyone who helped throughout the duration of this study. Particularly, Dr Matyas Daboczi for all his support and training provided allowing us to use the spin coater and different characterisation techniques.

References

Kojima, A., Teshima, K., Shirai, Y. and Miyasaka, T., 2009. Organometal Halide Perovskites as Visible-Light Sensitizers for Photovoltaic Cells. Journal of the American Chemical Society, 131(17), pp.6050-6051.

Yamamoto, K., Yoshikawa, K., Uzu, H. and Adachi, D., 2018. High-efficiency heterojunction crystalline Si solar cells. Japanese Journal of Applied Physics, 57(8S3), pp.08RB20.

Min, H., Lee, D., Kim, J., Kim, G., Lee, K., Kim, J., Paik, M., Kim, Y., Kim, K., Kim, M., Shin, T. and Il Seok, S., 2021. Perovskite solar cells with atomically coherent interlayers on SnO2 electrodes. Nature, 598(7881), pp.444-450.

Laurell Technologies Corporation,, L., 2021. UNIVERSAL DISPENSER UD-3 MANUAL. p.4.

Yoo, J., Seo, G., Chua, M., Park, T., Lu, Y., Rotermund, F., Kim, Y., Moon, C., Jeon, N., Correa-Baena, J., Bulović, V., Shin, S., Bawendi, M. and Seo, J., 2021. Efficient perovskite solar cells via improved carrier management. Nature, 590(7847), pp.587-593.

Shockley, W. and Queisser, H., 1961. Detailed Balance Limit of Efficiency of p-n Junction Solar Cells. Journal of Applied Physics, 32(3), pp.510-519.

Saliba, M., Correa-Baena, J., Wolff, C., Stolterfoht, M., Phung, N., Albrecht, S., Neher, D. and Abate, A., 2018. How to Make over 20% Efficient Perovskite Solar Cells in Regular (n–i–p) and Inverted (p–i–n) Architectures. Chemistry of Materials, 30(13), pp.4193-4201.

Paek, S., Schouwink, P., Athanasopoulou, E., Cho, K., Grancini, G., Lee, Y., Zhang, Y., Stellacci, F., Nazeeruddin, M. and Gao, P., 2017. From Nano- to Micrometer Scale: The Role of Antisolvent Treatment on High Performance Perovskite Solar Cells. Chemistry of Materials, 29(8), pp.3490-3498.

Xiao, M., Huang, F., Huang, W., Dkhissi, Y., Zhu, Y., Etheridge, J., Gray-Weale, A., Bach, U., Cheng, Y. and Spiccia, L., 2014. A Fast Deposition-Crystallization Procedure for Highly Efficient Lead Iodide Perovskite Thin-Film Solar Cells. Angewandte Chemie International Edition, 53(37), pp.9898-9903.

Ghosh, S., Mishra, S. and Singh, T., 2020. Antisolvents in Perovskite Solar Cells: Importance, Issues, and Alternatives. Advanced Materials Interfaces, 7(18), p.2000950.

Fabbri, E., Habereder, A., Waltar, K., Kötz, R. and Schmidt, T., 2014. Developments and perspectives of oxide-based catalysts for the oxygen evolution reaction. Catal. Sci. Technol., 4(11), pp.3800-3821.

Lee, M., Teuscher, J., Miyasaka, T., Murakami, T. and Snaith, H., 2012. Efficient Hybrid Solar Cells Based on Meso-Superstructured Organometal Halide Perovskites. Science, 338(6107), pp.643-647.

Honsberg, C. and Bowden, S., 2021. Types of Recombination | PVEducation. [online] Pveducation.org. Available at: <https://www.pveducation.org/pvcdrom/pn-junctions/types-of-recombination> [Accessed 12 December 2021].

Ghosh, S., Mishra, S. and Singh, T., 2020. Antisolvents in Perovskite Solar Cells: Importance, Issues, and Alternatives. Advanced Materials Interfaces, 7(18), p.2000950.

Ono, L., Raga, S., Remeika, M., Winchester, A., Gabe, A. and Qi, Y., 2015. Pinhole-free hole transport layers significantly improve the stability of MAPbI3-based perovskite solar cells under operating conditions. Journal of Materials Chemistry A, 3(30), pp.15451-15456.

Masood, M., Qudsia, S., Hadadian, M., Weinberger, C., Nyman, M., Ahläng, C., Dahlström, S., Liu, M., Vivo, P., Österbacka, R. and Smått, J., 2020. Investigation of Well-Defined Pinholes in TiO2 Electron Selective Layers Used in Planar Heterojunction Perovskite Solar Cells. Nanomaterials, 10(1), p.181.

Kim, H. and Park, N., 2014. Parameters Affecting I–V Hysteresis of CH3NH3PbI3 Perovskite Solar Cells: Effects of Perovskite Crystal Size and Mesoporous TiO2 Layer. The Journal of Physical Chemistry Letters, 5(17), pp.2927-2934.

Liao, K., Li, C., Xie, L., Yuan, Y., Wang, S., Cao, Z., Ding, L. and Hao, F., 2020. Hot-Casting Large-Grain Perovskite Film for Efficient Solar Cells: Film Formation and Device Performance. Nano-Micro Letters, 12(1)

Techno-Economic Analysis of Redox Flow Batteries for Grid Scale Energy Storage

Final Year Research Project

Zhang Chunwan, Nam Kyungmin

ABSTRACT

Aqueous organic redox flow battery (AORFB) is an energy storage system which exploits redox reactions of cheap and abundant organic active species. Unlike other energy storage technologies such as lithium-ion battery and other redox flow batteries, its low material costs, non-toxicity, and non-flammability give it strong competitive advantages. However, the crossover of active species and degradation of active species are the barrier for commercialization of AORFBs as they contribute to the capacity decay. Furthermore, since their contribution on the costs is heavily dependent on the operating conditions, membrane and active species used, there are difficulties in carrying out accurate techno-economic analysis especially when calculating the maintenance cost by electrolyte replacement. Here, we report a mathematical model which integrates crossover and degradation of active species in the cost calculation. It is applicable to any RFB with various membranes and active species. Furthermore, the model will provide a guideline for the properties of future membranes and active species.

Key words. Aqueous organic redox flow battery, Techno-economic analysis, Crossover, Degradation

1. Introduction

With the growing demand and the dropping costs for renewable energy, the proportion of it in the total energy consumption is dramatically growing. In 2020, despite the COVID-19 pandemic, more than 260 GW of renewable energy capacity was added, exceeding the expansion in 2019 by more than 50% (1). Amongst all the types of renewable energies, solar and wind are currently the most prominent sources accounting for more than 50% of total installed renewable energy capacity(1). However, their intermittent nature imposed a problem of instability when it comes to the incorporation with the existing grid, and it has prevented the widespread use of renewable energies. With the expectation that this problem can be mitigated by energy storage technology, substantial efforts have been concentrated into developing more cost-effective and efficient energy storage technology (2).

There are various energy storage technologies such as pumped hydroelectrical, compressed air, and flying wheel. Nevertheless, the battery, the first systematic device for storing energy, is one of the most commonly viable technologies due to its site's high efficiency, scalability, and ease of operation(3). Amongst the diverse battery technologies, lithium-Ion battery dominates the energy storage market for portable devices, EVs, and smart grid facilities, with its market value of $40.5 billion in 2020 (4). But its high maintenance cost, limited availability of lithium, and safety limitations promote the interest in developing alternative electrochemical energy storage systems. Redox Flow Batteries (RFBs) are regarded as a promising alternative. RFBs contain electrodes, electrolytes, and ion-permeable membrane which separates redox-active species on the cathode from the anode. The liquid electrolytes of two redox-active species are separately stored in two storage tanks and are pumped into the cell when the cell is being charged or discharged. RFBs have advantages of low fire risk due to its non-flammability, high design flexibility due to decoupled power and energy systems. Furthermore, because of the virtually unlimited capacity, RFBs can be used for large-scale energy storage with their long operational lifetimes (>10,000 cycles, 10 – 20 years) (5)(6).

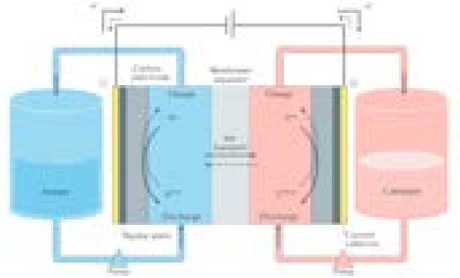

Fig. 1. Basic principles of redox flow batteries(6)

2. Background

Vanadium redox flow battery (VRFB), the most developed and commercially utilized RFB in the market, uses vanadium ions of different valences on each side of the cell. It was firstly introduced by Skyllas-Kazacos et al. in 1985, and has been experimented and developed with large-scale filed testing since 1996(7). Currently, VRFB is widely available in the global market (e.g. Japan, China, Germany), and the largest plant is located in China with 200 MW/800MWH invested by UniEnergy Technologies(8). As only vanadium ions are used in VRFB, it has high-capacity retention, stability and the low capacity decay as self-discharge can be naturally recovered. However, the development of VRFB is limited by the relatively low energy density (20-60 Wh/L) (9), high cost of vanadium ($27/kg), corrosivity due to acidic solution and the low solubility of vanadium in the electrolyte (10). The US Department of Energy estimated that the cost of utility-scale electricity delivery should be less than $150/kWh to be commercially feasible(11), however, VRFB systems are expected to cost $200 – 295/kWh, which is higher expenses than $150/kWh (12).

$$\begin{aligned}&\text{Anolyte:} \quad \mathrm{V}^{3+} + e^- \leftrightarrows V^{2+} \ (-0.255V)\\&\text{Catholyte:} \quad \mathrm{VO}_2^+ + 2H^+ + e^- \leftrightarrows VO^{2+} + H_2O \ (+0.991V)\end{aligned}$$

To tackle these challenges of VRFB, other aqueous RFBs were studied such as the zinc-bromine redox flow battery (ZFB), the polysulfide-bromine redox flow battery (PSFB), and aqueous-organic redox flow battery (AORFB). Among these technologies, low-cost AORFBs have been extensively studied with a big potential to grow as a next generation of green energy storage RFB because of its competitive advantages for large-scale energy storage. Firstly, the cost is low where aqueous electrolyte contains only water, cheap inorganic supporting electrolyte (e.g. KOH) and organic active species with high abundance. Secondly, the utilization of organic redox-active materials drives the high energy density and structure tunability due to the high oxidation and reduction redox potentials among a wide range of organic materials. Thirdly, AORFB also has effective power operation and high energy efficiency because of the highly conductive aqueous electrolyte and well-developed ion-selective membranes. B. Huskinson et al. (2014) demonstrated that the use of organic active species, anthraquinone, can dramatically reduce the costs (13) and in the subsequent year, K. Lin et al. (2015) showed the stability and performance of quinone-based derivatives and ferricyanide redox-active species in alkaline RFBs(14), promoting the potential of quinone derivative AORFB into the energy storage market. However, the degradation of organic active species due to its chemical instability still is a major obstacle preventing commercialization of AORFB, and the development of more stable redox species and regeneration techniques are needed.

Although the stability of redox-active species is important, the study on the ion-exchange membrane is also essential since ionic resistance and net electrolyte transport depend on it. Hence, chemical stability, capacity retention, and the lifetime of the battery(15) is affected by the membrane. A recent study by R. Tan et al. (2020) reported the new approach to design novel hydrophilic microporous membranes (e.g. AO-PIM-1) and their performances of high energy efficiency and capacity retention in AORFBs(16).

The techno-economic model from past literature is not suitable to assess AORFB since organic active species degrade rapidly, causing electrolyte replacement costs. Hence, this paper attempts to build the mathematical model which can evaluate the overall cost structure for the any RFB by integrating the impact of crossover and degradation on the costs. For the base case study, the provided literature data and the obtained experimental data on DPPEAQ-ferricyanide AORFB will be used to assess its performances (e.g. capacity retention) and optimal operating conditions. Through sensitivity analysis on properties of the active species and membranes, the necessary criteria for the commercialization will be identified in order to provide a guideline for the future development.

3. Methodology

Amongst various active species of quinone-derivatives, DPPEAQ-Ferricyanide systems are chosen for the analysis, and for the base case, the rated power of 1MW with the discharge time, E/P, of 10 hours are used(2).

$$\begin{aligned}&\text{Anolyte:} \quad \mathrm{DPPEAQ}^{2-} + 2e^- \leftrightarrows DPPEAQ^{4-} \ (-0.47V)\\&\text{Catholyte:} \quad \mathrm{Fe(CN)}_6^{3-} + e^- \leftrightarrows Fe(CN)_6{}^{4-} \ (+0.51V)\end{aligned}$$

The techno-economic model for AORFB covers the costs in the power and energy subsystems to calculate the overall system costs (C_{system}) with a linear cost function. The power cost is costs of cells and stack and the energy cost is the costs of electrolytes and tank.

$$C_{system} = P \cdot c_{power} + E \cdot c_{energy} \tag{1}$$

Furthermore, the relationship between membrane and performance of AORFB is analysed through capacity degradation modelling and sensitivity analysis.

3.1. Electrochemical Modelling

The electrochemical modelling is carried out to determine the operating condition of AORFB. Based on the correlation between the cell voltage and current density explained by Ohm's law, the target value of cell discharge voltage is selected from the charge and discharged model(17):

$$U_{cell}(SOC) = OCV(SOC) - R \cdot A_{cell} \cdot i(SOC) \tag{2}$$

$$R = \frac{ASR}{A_{cell}} \tag{3}$$

The cell voltage (Ucell) is determined by the current density (i) and in the base case energy storage system of 10MWh, current density of 1 kAm-2 is used. Area specific resistance (ASR) is converted into Ohmic resistance for the cell voltage calculation. All other parameters in Equation (2) are assumed to be constant for the AORFB, as shown below:

Table 1. Technical configurations of DPPEAQ-Ferricyanide AORFB

Parameter	**Value**	**Units**
Temperature (T)	298	K
Maximum state of charge ($\mathrm{SOC}_{\mathrm{max}}$)	0.8	-
Minimum state of charge ($\mathrm{SOC}_{\mathrm{min}}$)	0.2	-
State of charge (SOC)	0.5(17)	-
Open circuit voltage (OCV at SOC=0.5)	1.02(33)	V
Active cell area ($\mathrm{A}_{\mathrm{cell}}$)	2.7	m^2
Ohmic resistance of AO-PIM battery (R)	0.0278(16)	mΩ

The average SOC value of 0.5 is chosen from the SOC range between SOCmax and SOCmin. It is based on the assumption that the SOC and current density have a linear relationship within the selected range(17). OCV at SOC=0.5 was obtained from the experiment done in the literature(33). Ohmic resistance depends on the membrane and cell testing conditions such as temperature. For the base case, the ohmic resistance of the AO-PIM membrane is used for the battery[16]

3.2. Power Cost Model

Total number of cells (n) is calculated by division of total power of the system (P) 1MW by power generated by 1 cell (P_{cell}). P_{cell} is calculated based on the results of electrochemical modelling.

$$n = \frac{P}{P_{cell}} = \frac{P}{U_{cell} \cdot i \cdot A_{cell}} \tag{4}$$

As the power cost is a stack cost or in other words capital cost in building cells, the power cost model consists of the costs of cell components (e.g. membranes, felt electrodes, bipolar plates (BPP)) and expenses in practical installation (e.g. stack assembly, cables). The cost of cell components is calculated with a central unit: the number of the stack (n_{stack}), which is equal to the total number of cells (n) divided by the number of cells in one stack (n_{cell}).

$$n_{\text{stack}} = \frac{n}{n_{\text{cell}}} \tag{5}$$

With the assumption of 75 cells per stack (ncell= 75 cells), the total number of stacks is calculated for certain rated power (total power discharged by the system). Subsequently, the number of specific components in the AORFBs is determined, as shown below.

$$n_{\text{membrane}} = n \tag{6}$$

$$n_{\text{felt}} = n_{\text{gasket}} = 2n \tag{7}$$

$$n_{\text{BPP}} = n_{\text{stack}} + n \tag{8}$$

$$n_{\text{stack frame}} = n_{\text{stack}} + n \tag{9}$$

$$n_{\text{current collector}} = 2n_{\text{stack}} \tag{10}$$

where n_i and C_i represent the number and corresponding cost of each component i in the battery. Power cost is calculated by Equation (10), and specific power cost can be expressed in the units of \$/kW by dividing the cost with the power capacity.

$$C_{\text{power}} = \Sigma n_{\text{i}} C_{\text{i}} \tag{11}$$

$$c_{\text{power}} = \frac{C_{\text{power}}}{P} \tag{12}$$

Table 2. Costs of components in the power system(18),(19)

Component	**Cost (C_i)**	**Units**
C(BPP)	615.74	$/unit
C(Felt)	184.72	$/unit
C(Frame + Gasket)	228.05	$/unit
C(Membrane)	1231.47	$/unit
C(Converter)	114025.09	$
C(PCS)	57012.54	$
C(Current collector)	3420.75	$/stack
C(Connections)	4561	$
C(Stack, Assembling)	30159.64	$

Cost in €is converted to $ by the division with 0.877.

3.3. Energy Cost Model

The energy model includes the cost in the electrolyte ($C_{electrolyte}$), tank (C_{tank}), and electrolyte replacement ($C_{electrolyte\ replacement}$) of AORFBs:

$$C_{\text{energy}} = C_{\text{electrolyte}} + C_{\text{tank}} + C_{\text{electrolyte replacement}} \tag{13}$$

$$c_{\text{energy}} = \frac{C_{\text{energy}}}{E} \tag{14}$$

Specific energy cost is expressed in the units of \$/kWh by dividing the cost with the energy capacity.

3.3.1. Volume of Electrolyte

The cost in both electrolyte ($C_{eletrolyte}$) and tank (C_{tank}) are directly dependent on the amount of electrolyte. Therefore, the volume of electrolyte (V) is calculated, as shown below:

$$V = \frac{E}{U_{cell} \cdot SOC_{range} \cdot \left(\frac{F\Sigma z_i c_i}{3600}\right)} \tag{15}$$

Where E represents energy capacity, F is Faraday's constant, z_i and c_i are the number of electrons equivalent and the molar concentration for each active species i in the cell, and the SOC range is the difference between SOC_{max} and SOC_{min} (17). Concentrations of DPPEAQ and Ferricyanide are determined to be 0.5M and 0.4M below their maximum solubilities(20)and the energy capacity of 10MWh is used following the specification of the base case where the rated power is 1MW and the discharge time is 10 hours. As the calculated V is the volume for one side of the battery, the volume of catholyte and anolyte are separately calculated.

3.3.2. Electrolyte Cost

The electrolyte cost includes the cost of active species (Ferricyanide, DPPEAQ), as well as the expenses in solvent, additives, and electrolyte fabrication.

$$\begin{aligned} C_{\text{electrolyte}} = {} & C_{\text{active species 1}} + C_{\text{active species 2}} \\ & + C_{\text{solvent}} + C_{\text{additive 1}} + C_{\text{electrolyte replacement}} \end{aligned} \tag{16}$$

$$\begin{aligned} C_{\text{electrolyte}} = {} & \Sigma V_{\text{i}} \cdot (M_{\text{active species 1}} \cdot c_{\text{i}} \cdot C_{\text{active species 1}} \\ & + M_{\text{solvent}} \cdot c_{\text{solvent}} \cdot C_{\text{solvent}} + M_{\text{additive}} \cdot c_{\text{additive}} \cdot C_{\text{additive 1}} \\ & + C_{\text{electrolyte replacement}}) \end{aligned} \tag{17}$$

where M_i represents the molar mass of each species i. The costs of additive and electrolyte fabrication are assumed to be negligible.

3.3.3. Tank Cost

The tank cost is calculated based on the volume of tank, with $\$/m^{3(24)}$. It is assumed that the volume of tank is equivalent to the total volume of electrolyte used in cathode and anode.

Table 3. Inputs for the electrolyte and tank cost calculation

Input parameter	Species	Value	Units
Concentration of i (c_i)	DPPEAQ	0.5	mol/L
	$K_4Fe(CN)_6$	0.4	mol/L
	KOH	0.1	mol/L
Unit price of species i (C_i)	DPPEAQ	2.39(21)	\$/kg
	$K_4Fe(CN)_6$	0.65(22)	\$/kg
	KOH	0.82(23)	\$/kg
Tank cost (C_{tank})	Polyethene	155	\$/m^3

3.3.4. Electrolyte Replacement Cost

Ideally, the membrane in the battery is selective only to potassium ion, which moves from anode to cathode during discharge to complete the electrical circuit. However, in the real battery, membrane cannot be selective only to the potassium ion. The active species such as ferricyanide and DPPEAQ, irreversibly crossover through the membrane leading to self-discharge and capacity fade. Furthermore, the degradation of active species through spontaneous reduction of ferricyanide and DPPEAQ reduces the capacity of the battery with time. As a result, electrolytes are needed to be replaced regularly during the lifetime of the battery. Equation (18)(34) calculates the crossover rate by concentration difference and electric potential difference as the driving forces. To validate whether the mathematical model is accurate enough to be used in the analysis, the calculated crossover rates are compared with the experimental data.

$$J_i = -\frac{D_i}{L}\frac{z_i f \Delta\psi}{e^{z_i f \Delta\psi}-1}\left(c_i^{S2} e^{z_i f \Delta\psi} - c_i^{S1}\right) \tag{18}$$

$$\bigtriangledown\left(\varepsilon \bigtriangledown\left(\psi^m\right)\right) = -\rho_e = -F\sum_{i=1}^{k} z_i c_i^m \tag{19}$$

The effective diffusion coefficient, Di, can be calculated from the diffusion data of the active species against alkaline solvent from Tan R. et al (16). and the Fick's law. Equation (20) represents a rearranged Fick's law equation, where L represents membrane thickness, c_i^j represents concentration of species i in species i in electrolyte j. S1 represents the species i rich electrolyte and S2 represents i deficient electrolyte. Since the crossover rate is very low, it can be assumed that c_i^{S1} is constant at the initial concentration and c_i^{S2} is 0.

$$D_\mathrm{i} = \frac{J_i \cdot L}{c_i^{S1} - c_i^{S2}} \tag{20}$$

The capacity fade rates by degradation ($r_{d,i0}$) of ferricyanide and DPPEAQ are obtained from the paper published by David G. et al.(25)The corresponding value of DPPEAQ is 0.02 %/day and that of ferricyanide is 7.5 %/day (25) (26). With the assumption that the energy storage system should maintain above 80% of the original capacity, the total cost is expected to be dominated by ferricyanide replacement costs due to its' degradation through reversible spontaneous reduction (26). Therefore, it is assumed that there is no other irreversible side reaction, hence, the capacity decay due to ferricyanide degradation can be fully recovered by oxidation. In the case of DPPEAQ, it is assumed that degraded species can be regenerated to the fraction (fregen,i) of 0.947 by electrochemical regeneration (27). at pH 13 where there is almost no nucleophilic decomposition (28). Subsequently, the capacity fade rates by degradation is recalculated to be $r_{d,i}$ in the Equation (22).

Daily capacity losses by the crossover of each species ($r_{c,i}$) are calculated separately and the days needed to replace the electrolyte for each active species i (d_i) in each tank are calculated subsequently to obtain annualised electrolyte replacement cost ($C_{\text{Electrolyte replacement}}$) during the 10 years of the lifetime of the battery (λ)(2).

Here, we assume that regular and partial replacement is done throughout the lifetime of the system so that the system can maintain nearly constant capacity of 1MW/10MWh. The alternative to this method will be replacement of electrolyte only when there is a capacity decay more than 20%.

$$r_{\mathrm{c,i}} = \frac{J_i \cdot A \cdot n_{\mathrm{cell}}}{c_i^{S1} \cdot V_i} \cdot 24 \cdot 3600 \tag{21}$$

$$r_{\mathrm{d,i}} = r_{\mathrm{c,i0}} \cdot f_{\mathrm{regen,i}} \tag{22}$$

$$d_{\mathrm{i}} = \frac{0.2}{r_{\mathrm{c,i}} + r_{\mathrm{d,i}}} \tag{23}$$

$$C_{\text{electrolyte replacement}} = \sum C_{\text{electrolyte,i}} \cdot \frac{365}{d_i} \cdot \lambda \tag{24}$$

Table 4. Inputs for the electrolyte replacement cost calculation

Input parameter	Species	Value	Units
Concentration of i (c_i)	DPPEAQ	0.5	mol/L
	$K_4Fe(CN)_6$	0.4	mol/L
Capacity fade by degradation	DPPEAQ	0.02	%/day
	$K_4Fe(CN)_6$	7.5(25,26)	%/day
Lifetime of the system (λ)		10(2)	years

4. Result & Discussion

4.1. Base Case

4.1.1. Base Case: Electrochemical Modelling

The costs of a 1MW/10MWh DPPEAQ-ferricyanide energy storage system with defined specification in Section 3 is calculated through MATLAB. With the membrane AO-PIM-1, the discharge voltage of 0.945 V is yielded by the electrochemical modelling.

4.1.2. Base Case: Power Cost

The 1MW system requires 392 cells in 6 stacks. The total power cost is $1,506,000 resulting in a specific power cost 1,506 $/kW, which is very close to the recently reported power cost of RFBs. Kendall M et al. estimated that the specific power cost for RFBs will be around 1,493 $ /kW for 1MW/4MWh system in 2020(29). Meanwhile, Adam Z. et al. (30) reported that the key performance target of the power cost for grid-storage application is expected to reach 1,500 $/kW, which is approximately equal to the calculated value through mathematical model in this paper.

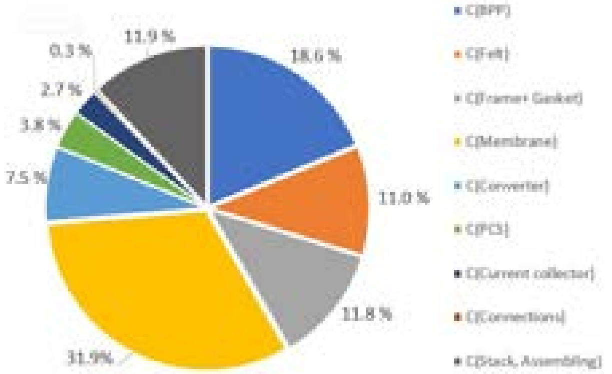

Fig. 2. Composition of power cost for base case

As shown in Figure (2), the cost structure for the AORFB power system was estimated. The highest expense component is the membrane, with 31.9% of the overall cost. Subsequently, another two high-cost sources are BPP and Frame, which account for 18.6% and 11.8% respectively.

4.1.3. Validation of mathematical diffusion model

Validating the accuracy of mathematical diffusion model is vital in calculating electrolyte replacement cost, which is attributed to crossover and degradation of active species.The validity of the mathematical model is tested using the experimental data of ferricyanide and DHAQ instead of DPPEAQ, as the experimental data for DPPEAQ is not available and they are close quinone derivatives.

The Table (5,6) compares the diffusion rates calculated using the mathematical model with the experimental data obtained by Tan R. et al.(16). It shows that the crossover rate of DHAQ calculated through the mathematical model, is very close to the experimental data, validating that the mathematical model is accurate. Therefore, it is assumed that the model is applicable to DPPEAQ. However, it failed to give similar crossover rate of ferricyanide. This is because there are other factors affecting the diffusion of ferricyanide in the real battery condition while the model only considers the diffusion facilitated by concentration difference and the electric potential. For instance, in the alkaline solution, the AO-PIM-1 become negatively charged and there will be a charge repulsion between negatively charged ferricyanide ions and the membrane. Furthermore, in the real battery, there will be a competitive diffusion of ions in the electrolyte through the micropores in the membrane. The more abundant, smaller, and positively charged potassium ions are likely to win the diffusion competition. Hence, crossover rate of ferricyanide is calculated differently using the experimental data under battery condition and linearity of Fick's law instead of calculating diffusion coefficient and using the mathematical model.

Table 5. Test result of the mathematical model for AO-PIM-1

Diffusion rate through AO-PIM-1 [mol/m^2h]			
	Experiment	**Model**	**Comments**
$K_4Fe(CN)_6$	0.000148	0.001142305	10-fold difference
DHAQ	<0.00084	0.00068937	Acceptable

Table 6. Test result of the mathematical model for Nafion 212

Diffusion rate through Nafion 212 [mol/m^2h]			
	Experiment	**Model**	**Comments**
$K_4Fe(CN)_6$	0.000637	0.0118	20-fold difference
DHAQ	0.00084-0.00167	0.000259	Acceptable

$$J_{\text{ferricyanide,base case}} = J_{\text{ferricyanide,exp}} \cdot \frac{\Delta c_{\text{ferricyanide,base case}}}{\Delta c_{\text{ferricyanide,exp}}} = 4J_{\text{ferricyanide,exp}} \quad (25)$$

In the paper published by Tan R.(16) et al concentration of ferricyanide is 0.1M while the concentration used in this study is 0.4M.

4.1.4. Base Case: Energy Cost Model

The total energy cost of the system is $1,078,400, giving specific cost of 107.84 $/kWh with the specification given in the section 3.3. It can be spotted that the DPPEAQ-Ferricyanide energy storage system has lower specific energy cost than the estimated cost of 177.7 $/kWh of all-vanadium RFBs in 2020$_{(26)}$.

Figure (3) illustrates the composition of energy cost. The expenditure on active species DPPEAQ (46.4%) and electrolyte replacement (25%) are dominating in the DPPEAQ-Ferricyanide energy storage cost system. The energy cost will be the greatest determinant factor that decides the viability of AORFB since the cost of active species varies within a wide range. With the lab -scale cost of DPPEAQ, this system will not be viable due to its high energy cost, however with the mass production the cost of DPPEAQ can decrease significantly (21). For the base case calculation, regular and partial replacement of electrolyte was assumed throughout the lifetime of the system to maintain nearly constant capacity of 1MW/10MWh, however, if we assume that electrolyte is only replaced when there is a capacity decay more than 20%, the specific energy cost will be further reduced to 80.7$/kWh.

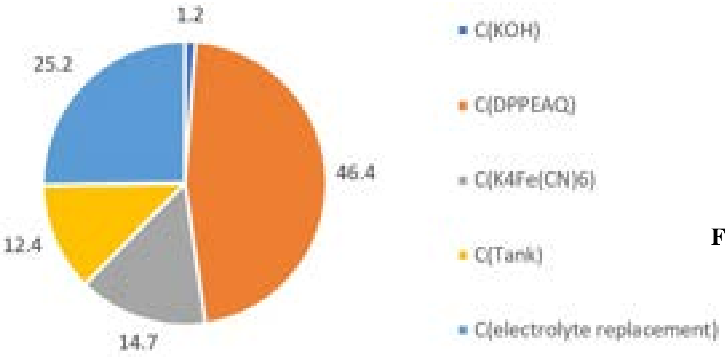

Fig. 3. Composition of energy cost for base case

4.1.5. Base Case: Total Cost

With the specific energy cost of 107.84 $/kWh and specific power cost of 1506 $/kW, the total cost is calculated to be $2,584,467 for the 1MW/10MWh DPPEAQ-Ferricyanide system with the operating conditions in the section 3.1. Since total cost depends on the size of the energy storage system, it is converted into specific cost of 258 $/kWh for easy comparison with other technologies.

4.1.6. Optimal operating point

Figure (4) shows that the higher the current density, the lower the power cost since high current density reduces the number of cells and stacks needed for the system. Figure (5) shows that specific energy cost initially drops with the increase in current density until around 1000 A/m2, however, it increases afterwards due to the increase in cost tank and initial electrolyte cost. This is because the increase in current density decreases the cell voltage which affects electrolyte volume.

Before the current density 1400 A/m2 of the power cost is greater than the energy cost, however, at the operating condition of this system where current density is 1000 A/m2 the power cost is around 1.4 times greater than the energy cost. In the Figure(6), it is found that at around 3300 A/m2, the total cost can be minimised at $1,859,993(186 $/kWh) which is 28% reduction in the total cost is very close to the target price of US department of energy which is 150$/kWh. At this point the specific energy cost is 121 $/kWh and specific power cost is 643 $/kW, which is less than a half the value before. However, further reduction in the cost was found to be possible with the assumption that there is no electrolyte replacement at all until the capacity of the system reduces to 80%. In this case, the specific energy cost will be 106.53 $/kWh while the specific power cost is the same making the total cost of $1,709,110 (170.9 $/kWh).

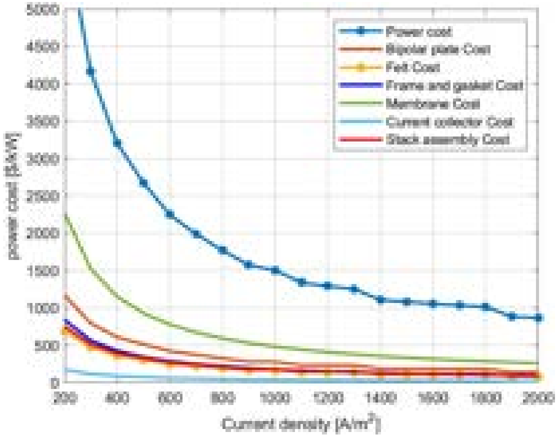

Fig. 4. Specific power cost against current density

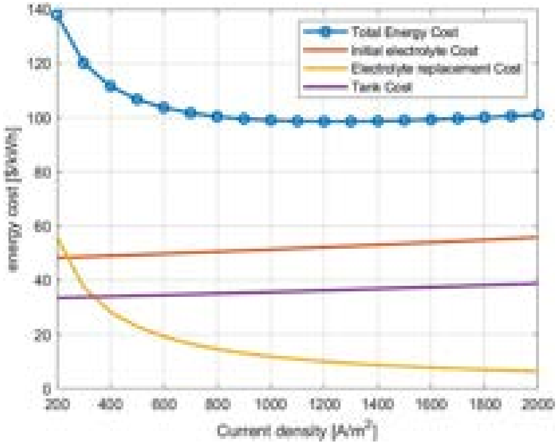

Fig. 5. Specific energy cost against current density

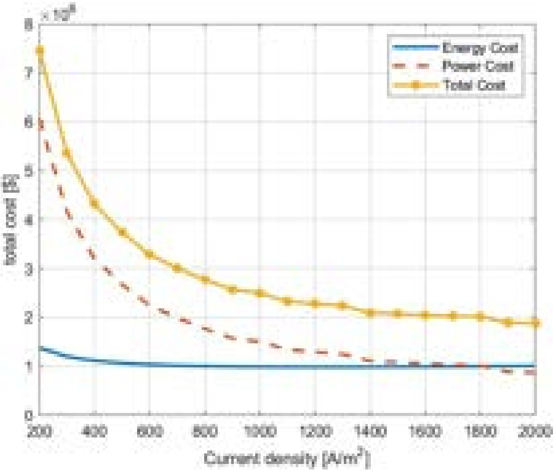

Fig. 6. Total cost against current density

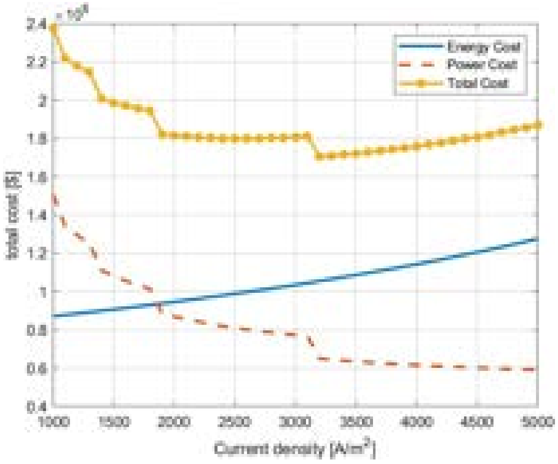

Fig. 7. Total cost against current density higher than 1000 A/m^2

4.2. Sensitivity Analysis

4.2.1. Membrane Performance

Two membranes: AO-PIM-1, which was used in base study, and the Nafion 212 were compared through the developed model. AO-PIM-1 is a membrane which is based on the hydrophilic polymers of intrinsic microporosity (PIM) with hydrophilic and ionizable amidoxime functional groups (AO). Nafion 212 is a widely used ion-exchange membrane made of poly(perfluorosulfonic acid). It selectively allows potassium ions to pass through due to its acidic sulfonic groups. Overall, it was shown by R. Tan et al. that AO-PIM-1 surpasses Nafion 212 in terms of ion selectivity when its AO-groups are well functionalised (12).

Different membranes have different diffusion coefficients which affect the crossover rates and hence the electrolyte replacement cost. To purely investigate the impact of membrane selectivity on the system performance, it is assumed that there is no degradation of active species, and the electrolyte replacement costs are solely dependent on the crossover of the active species. Under such an assumption, the crossover of ferricyanide was 100 times larger than that of DPPEAQ, accounting 95.7% of the total electrolyte replacement. Therefore, in the following analysis, it is assumed that there is negligible crossover of DPPEAQ and only the crossover rate of ferricyanide is varied to see how the selectivity of membrane can affect the energy cost.

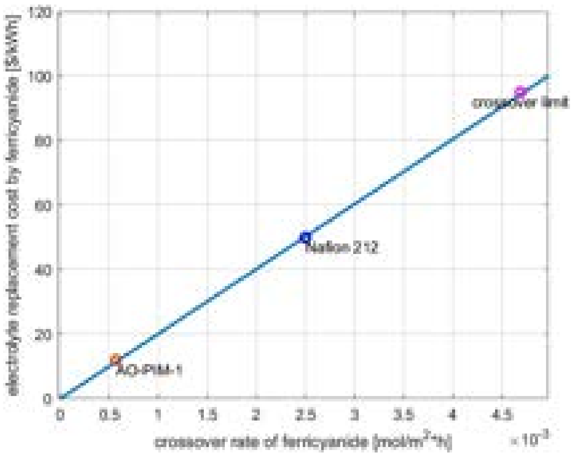

Fig. 8. Electrolyte replacement cost due to ferricyanide crossover rate

The crossover limit,in Figure (8), represents the crossover rate of ferricyanide that can cause capacity reduction by 20% within the system lifetime and it is a minimum requirement for the membrane. The crossover limit for other active species can be calculated using the inequality constraint below:

$$0.2 > \frac{(J_i \cdot 24) \cdot A_{cell} \cdot n}{c_i \cdot V_i} \cdot (LT \cdot 365) \tag{26}$$

Due to the linear relationship between crossover rate and the diffusion coefficient, the electrolyte cost increases linearly with the crossover rate at the gradient of 20 $/kWh per 0.001 mol/^{2}h. Even though two example membranes showed crossover rate below the limit, AO-PIM-1 shows a 5 times greater selectivity and 4.16 times lower electrolyte replacement cost than Nafion-212 membrane. The higher selectivity of AO-PIM-1 membrane is attributed to its narrow molecular-sized microporosity and the charge repulsion between active species and negatively charged AO-PIM-1 membrane in the alkaline solution.

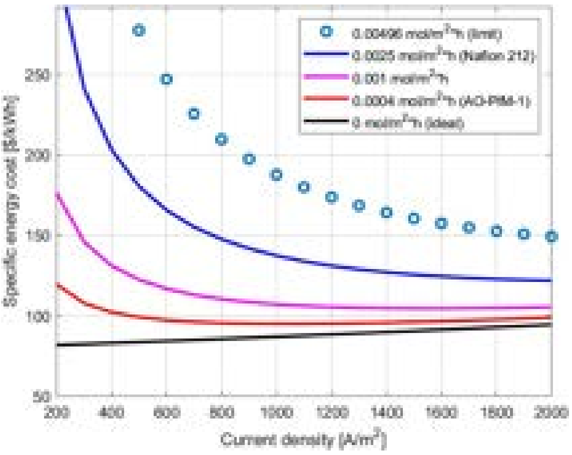

Fig. 9. Impact of crossover rate on specific energy cost

When specific energy costs of system are plotted against crossover rates, it is spotted that AO-PIM-1 has a very high selectivity that it behaves siumilar to the perfectly selective membrane. On the other hand, Nafion 212 membrane showed a very poor selectivity. It should be noted that for membranes with poor selectivity and crossover rate higher than 0.001 mol/m^{2}h, the use of higher current density can reduce the specific energy cost. This is because the use of higher current density reduces the total area of the membrane used in the cell.

The selectivity is not the only property of the membrane which affects the cost of the battery system. The area specific resistance (ASR) of membrane is another factor that can affect the power cost as it may change the number of cells needed for a given power capacity of the system as shown in the section 3.1. ASR of AO-PIM-1 is $0.75\Omega - cm^2$ while that of Nafion-212 is $0.45\Omega - cm^2$ and the ASR difference of them leads the cell numbers to be different by 12 and increase in specific power cost by 21 $/kW. When this is plotted in the Figure (10), it seems like they do not have significant difference in their specific power costs as two curves almost overlap with each other. However, it should be noted that a small difference in specific power cost can actually cause a large difference in total cost. The stair like shapes of the curves are due to rounding up of stack number and some components which only cost per stack. Since Figure (10) was not good enough to visualize the future goal of ASR, the Figure (11) was plotted and it was found that if a membrane has ASR close to $0.1\Omega - cm^2$ it will behave just like an ideal membrane. It also was found that curves have unfavourable convexity and the convexity becomes more significant when ASR is high. In case of AO-PIM-1, it should be noted that its ASR may vary from 0.75 up to 10 with the degree of AO-functionality (12). This is because the AO-group generates water channels for fast ion transport (12). It is recommended to keep AO-functionality as high as possible so that ASR and the power cost can be kept low as well.

The Figure (12,13) show that the impact of membrane cost on the power cost and total cost is also significant as it is the most expensive component within the cell. Currently the price of the membrane is set around 456 $/m2, however, it is expected to be decreased when there is a mass production of the membrane. In case where the cost is 200 \$/m2, total cost reduction of \$271008 is expected and this will reduce the specific total cost to 143.8 \$/kWh which is below the target cost of 150\$/kWh.

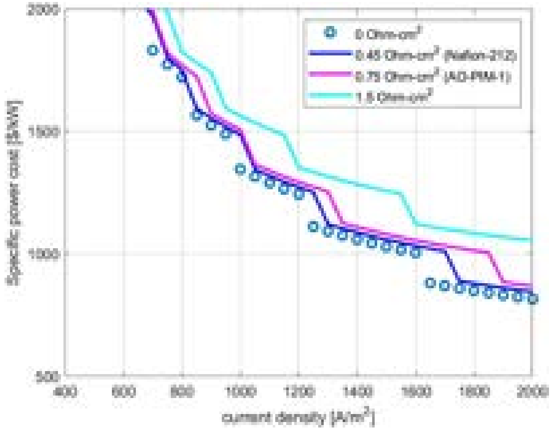

Fig. 10. Impact of ASR on specific power cost

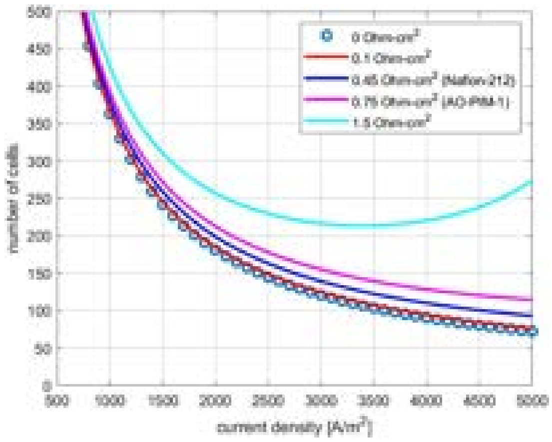

Fig. 11. Impact of ASR on number of cells

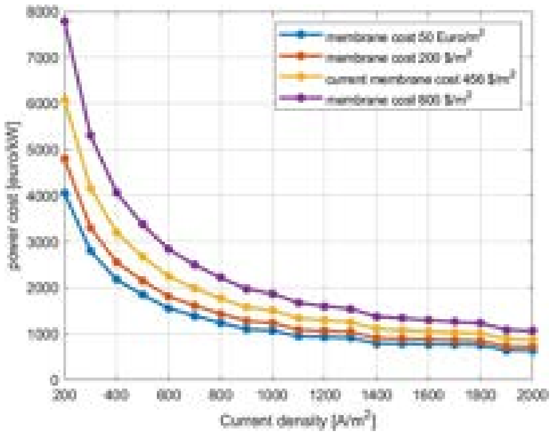

Fig. 12. Impact of membrane cost on specific power cost

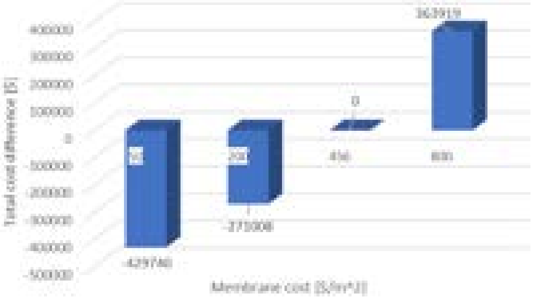

Fig. 13. Impact of membrane cost on total cost

4.2.2. Degradation of Active Species

As it was seen above, the selectivity of AO-PIM membrane is high enough that the crossover itself will not cause capacity decay below 80% during the lifetime of the battery system. However, the capacity degradation led by unstable active species is an obstacle to AORFBs commercialization.

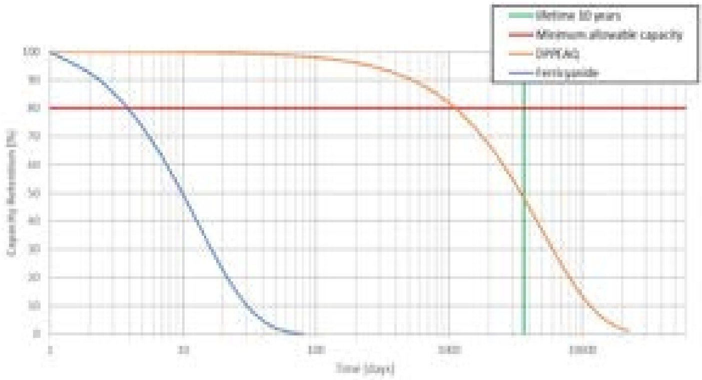

Fig. 14. Capacity retention of DPPEAQ and Ferricyanide against time

The Figure (14) shows capacity retention of the two active species without regeneration technology. The capacity on the side of ferricyanide will be reduced to allowable minimum capacity of 80% within 3 days while DPPEAQ can last till 1150 days. Since the electrolyte replacement cost takes up 25% of the energy cost, if regeneration technology can maintain capacity above 80% during the 10 years of system lifetime, there will be a great reduction in the total cost. The stability goal of active species will be having the capacity retention curve above the intersection point of minimum allowable capacity and lifetime lines. Capacity fade by degradation occurs either by active species' spontaneous redox reaction leading to self-discharge or side reaction of active species such as dimerization. There are existing mitigating techniques such as structural modification, oxidisation and rebalancing the state of charge. However, the chemical stability of active species itself is still very important.

The Figure (15,16) shows the required fraction regeneration as an intersection point of degradation curve and the lifetime line. It depicts that the greater the stability the less fractions are required to be regenerated. For the system with 10 years lifetime, the stability goal of the active species will be 0.005%/day. In case of viable DPPEAQ-ferricyanide system, where the capacity is retained above 80% during its lifetime, the required fraction regeneration is 73% for DPPEAQ and 99.96% for ferricyanide. Knowing that DPPEAQ being a comparatively stable quinone-based active species, further research on the more stable operating conditions, development of more stable active species and effective recovery technology are needed.

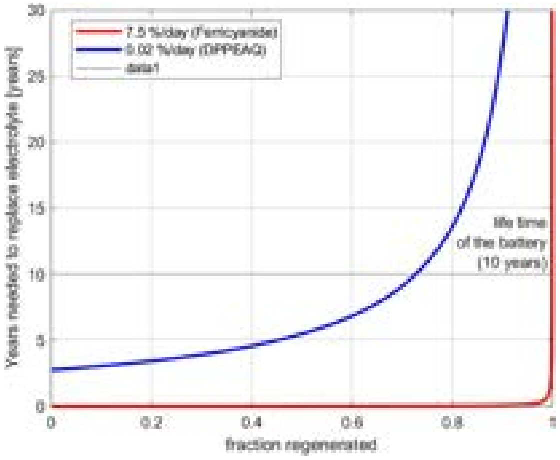

Fig. 15. Years to replace electrolyte for DPPEAQ-Ferricyanide

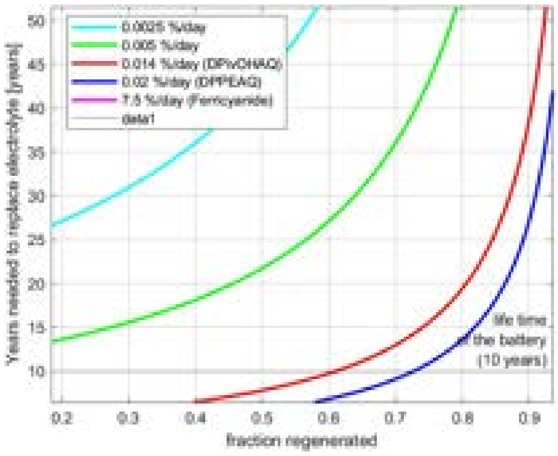

Fig. 16. Years to replace electrolyte for various species

5. Conclusion & Outlook

In conclusion, the objectives of this study were achieved. The developed mathematical model can be applied to any RFB. With this model, various active species and membranes can be tested for their viability. Through the base case study on DPPEAQ-ferricyanide AORFB, the model was successfully validated by calculating the costs within the expected range of values and that is comparable with the costs of other RFBs found in other literature. Furthermore, at optimal operating current density of 3300 A/m2, the specific power cost and energy cost was found to be 643 $/kW and 121 $/kWh resulting in the total cost of $ 1859993(186$/kWh). With different maintenance regulation it was identified that further reduction to $1709110 (170 $/kWh) is possible showing that it can successfully compete with the all-vanadium redox flow battery which has the specific total cost of 200 – 295$/kWh. Overall, DPPEAQ-Ferricyanide system is not only competitive against RFBs such as all-vanadium RFB but also other technology such as lithium-ion battery, however, its costs still have to be reduced to achieve the target of 150$/kWh through further reduction in material cost such as membrane cost and active species cost and by solving the degradation problem of active species. It should be noted that the competitiveness is ensured when the active species' degradation problem is solved by regenerating 73% of degenerated DPPEAQ and 99.96% of degenerated ferricyanide. Since there are past work on the regeneration technology on DHAQ, regenerating 94.7%, this goal of regeneration technology seems possible in near future (35).

With the mathematical model, sensitivity analysis was also successfully carried out to find out the required performance of membrane and active species. The inequality constraint was found to set the crossover limit for any RFBs. This can be used to test the viability of any membranes for their selectivity. For exemplar membranes, it was found out that AO-PIM-1 surpasses Nafion 212. AO-PIM-1 showed negligible crossover rates of DPPEAQ and ferricyanide that its curve on the specific energy cost against current density graph is very close to the ideal membrane where there is no crossover. For area-specific resistance, the goal of $0.1\Omega - cm^2$ was found as a guideline for the future membrane. It is recommended for AO-PIM-1 to maintain degree of functionality its hydrophilic group as high as possible as low degree can possibly increase ASR above $3\Omega - cm^2$ which is the starting point where the power cost significantly start to increase for a high current density. It also should be noted that the membrane is most expensive component in the cell and the cost reduction on the membrane will play a key role in reducing the total cost of the system. For the degradation of active species, it was found that regeneration technology and development of chemically very stable active species are the greatest obstacle to the commercialization of AORFB. Even for the stable chemical, DPPEAQ, it still required 73% of degraded species to be recovered. The viable future organic active species should have the degradation rate of 0.005%/day or lower for the lifetime of 10 years.

In future, improvement can be done on the mathematical model to include the impact of other factors on the cost and performance of the RFBs such as the competitive diffusion, side reactions of active species, membrane swelling and aging effect of membrane. By doing so the model will be able to provide more accurate and sophisticated results. Furthermore, more constraints can be added to the GAMS model to automatically screen non-viable active species out of the wide range of candidates. As the model developed can be used for any RFB, various types of systems can be studied, and compared.

References

[1] RENEWABLE CAPACITY STATISTICS 2021 STATISTIQUES DE CAPACITÉ RENOUVELABLE ESTADÍSTICAS DE CAPACIDAD RENOVABLE (n.d.). [online]
[2]Soloveichik, G.L. (2015). Flow Batteries: Current Status and Trends. Chemical Reviews, 115(20), pp.11533–11558.
[3]Dunn, B., Kamath, H. and Tarascon, J.-M. . (2011). Electrical Energy Storage for the Grid: A Battery of Choices. Science, [online] 334(6058), pp.928–935.
[4] Statista. (n.d.). Projected lithium-ion battery market size worldwide. [online] Available at: https://www.statista.com/statistics/1011187/projected-global-lithium-ion-battery-market-size/.
[5] Dunn, B., Kamath, H. Tarascon, J. M. Electrical energy storage for the grid: a battery of choices. Science 334, 928–935 (2011).
[6] Park, M., Ryu, J., Wang, W. and Cho, J. (2016). Material design and engineering of next-generation flow-battery technologies. Nature Reviews Materials, 2(1).
[7] Sum, E.; Skyllas-Kazacos, M. A study of the V(II)/V(III) redox couple for redox flow cell applications. J. Power Sources 1985, 15, 179–190.
[8] Vanadium Redox Flow Batteries: A Review Oriented to Fluid-Dynamic Optimization Iñigo Aramendia 1,* , Unai Fernandez-Gamiz 1 , Adrian Martinez-San-Vicente 1 , Ekaitz Zulueta 2 and Jose Manuel Lopez-Guede 2.
[9] Rahman, F. and Skyllas-Kazacos, M. (2009). Vanadium redox battery: Positive half-cell electrolyte studies. Journal of Power Sources, 189(2), pp.1212–1219.

[10] Chemicool.com. (2017). Periodic Table of Elements and Chemistry. [online] Available at: http://www.chemicool.com/.

[11] Moseley, P. T.; Garche, J. (2014) Electrochemical Energy Storage for Renewable Sources and Grid Balancing, 1st ed.; Elsevier: Amsterdam.

[12] Mongird, K., Fotedar, V., Viswanathan, V., Koritarov, V., Balducci, P., Hadjerioua, B. and Alam, J. (2019). Energy Storage Technology and Cost Characterization Report. [online]

[13] Huskinson, B., Marshak, M.P., Suh, C., Er, S., Gerhardt, M.R., Galvin, C.J., Chen, X., Aspuru-Guzik, A., Gordon, R.G. and Aziz, M.J. (2014). A metal-free organic–inorganic aqueous flow battery. Nature, 505(7482), pp.195–198.

[14] Lin, K.; Chen, Q.; Gerhardt, M. R.; Tong, L.; Kim, S. B.; Eisenach, L.; Valle, A. W.; Hardee, D.; Gordon, R. G.; Aziz, M. J.; Marshak, M. P. (2015) Alkaline quinone flow battery. Science, 349, 1529 1532.

[15] Gubler, L. (2019). Membranes and separators for redox flow batteries. Current Opinion in Electrochemistry, [online] 18, pp.31–36.

[16] Tan, R., Wang, A., Malpass-Evans, R., Williams, R., Zhao, E.W., Liu, T., Ye, C., Zhou, X., Darwich, B.P., Fan, Z., Turcani, L., Jackson, E., Chen, L., Chong, S.Y., Li, T., Jelfs, K.E., Cooper, A.I., Brandon, N.P., Grey, C.P. and McKeown, N.B. (2019). Hydrophilic microporous membranes for selective ion separation and flow-battery energy storage. Nature Materials, 19(2) 195–202.

[17] Noack, J., Wietschel, L., Roznyatovskaya, N., Pinkwart, K. and Tübke, J. (2016). Techno-Economic Modeling and Analysis of Redox Flow Battery Systems. Energies, 9(8), p.627.

[18] Minke, C., Kunz, U. and Turek, T. (2017). Techno-economic assessment of novel vanadium redox flow batteries with large-area cells. Journal of Power Sources, 361, pp.105–114.

[19] www.exchangerates.org.uk. (n.d.). US Dollar to Euro Spot Exchange Rates for 2020. [online]

[20] Kwabi, D.G., Lin, K., Ji, Y., Kerr, E.F., Goulet, M.-A., De Porcellinis, D., Tabor, D.P., Pollack, D.A., Aspuru-Guzik, A., Gordon, R.G. and Aziz, M.J. (2018). Alkaline Quinone Flow Battery with Long Lifetime at pH 12. Joule, [online] 2(9), pp.1894–1906.

[21] Minke, C., Kunz, U. and Turek, T. (2017). Techno-economic assessment of novel vanadium redox flow batteries with large-area cells. Journal of Power Sources, 361, pp.105–114.

[22] www.alibaba.com. (n.d.). High Purity Potassium Ferrocyanide Used In The Production Of Wine And Citric Acid - Buy Potassium Ferrocyanide,Potassium Ferrocyanide Used In The Production Of Wine And Citric Acid,High Purity Potassium Ferrocyanide Used In The Production Of Wine And Citric Acid Product on Alibaba.com. [online]

[23] www.alibaba.com. (n.d.). Industrial Potassium Hydroxide Price - Buy High Quality Potassium Hydroxide,Potassium Hydroxide Price Per Ton,Potassium Hydroxide 90 Product on Alibaba.com. [online]

[24] www.plastic-mart.com. (n.d.). Vertical Plastic Water Tanks | Liquid Storage Tanks. [online]

[25] Kwabi, D.G., Ji, Y. and Aziz, M.J. (2020). Electrolyte Lifetime in Aqueous Organic Redox Flow Batteries: A Critical Review. Chemical Reviews, 120(14), pp.6467–6489.

[26] Goulet, M.-A., Aziz, M., John, H. and Paulson, A. (2018). Flow Battery Molecular Reactant Stability Determined by Symmetric Cell Cycling Methods. Journal of The Electrochemical Society, [online] 165(7), pp.1466–1477.

[27] Jing, Y., Zhao, E.W., Goulet, M.-A., Bahari, M., Fell, E., Jin, S., Davoodi, A., Jónsson, E., Wu, M., Grey, C., Gordon, R. and Aziz, M. (2021). Electrochemical Regeneration of Anthraquinones for Lifetime Extension in Flow Batteries. chemrxiv.org. [online]

[28] Luo, J., Hu, B., Hu, M., Zhao, Y. and Liu, T.L. (2019). Status and Prospects of Organic Redox Flow Batteries toward Sustainable Energy Storage. ACS Energy Letters, 4(9), pp.2220–2240.

[29] Mongird, K., Viswanathan, V., Alam, J., Vartanian, C., Sprenkle, V., Northwest, P. and Baxter, R. (2020). 2020 Grid Energy Storage Technology Cost and Performance Assessment. [online]

[30] Weber, A.Z., Mench, M.M., Meyers, J.P., Ross, P.N., Gostick, J.T. and Liu, Q. (2011). Redox flow batteries: a review. Journal of Applied Electrochemistry, 41(10), pp.1137–1164.

[31] Feldman, D., Ramasamy, V., Fu, R., Ramdas, A., Desai, J. and Margolis, R. (2021). U.S. Solar Photovoltaic System and Energy Storage Cost Benchmark: Q1 2020. [online]

[32] Flow Battery Capacity Fade and Power Density with Aqueous-Soluble Organics. (2020). [online]

[33] DSpace Angular Universal. (n.d.). dr.lib.iastate.edu. [online]

[34] Yuan, J., Pan, Z.-Z., Jin, Y., Qiu, Q., Zhang, C., Zhao, Y. and Li, Y. (2021). Membranes in non-aqueous redox flow battery: A review. Journal of Power Sources, 500, p.229983.

[35] Yan, J., Eavan, Z., Marc-antoni ,G.,Meisam, B.,Eric, F., Shijian, J., Ali, D. et al. (2021). Electrochemical Regeneration of Anthraquinones for Lifetime Extension in Flow Batteries.

Supply Side Optimization of Short-Term Electricity Market Contracts

Alessandro Nardello and Soma Bulyaki
Department of Chemical Engineering, Imperial College London, U.K.

Abstract

Increasing amounts of variable renewable energies (VREs) and electrification of energy necessitates an ever-increasing amount of grid flexibility. This flexibility is increasingly being provided by distributed energy resources (DERs). This paper presents a novel framework for DERs aggregators in the UK short-term operating market (STOR) to determine by optimization the utilization price of a generating unit to contract, with the main objective being to maximizing total annual revenue. An initial data analysis was carried out in MATLAB, to determine the number of expected STOR calls a site would receive at each utilization price. This data was then used to run an MINLP model in GAMS to determine optimal generation to contract and hence total revenue at each utilization price. Results were compared the real-life scenario of £170/MWh utilization price. Sensitivity analysis was then carried out on the most impactful variables to better contextualize the results. The two most suitable solutions were found to be 600 £/MWh with 1500 kW contracted generation, which represents a total site revenue increase of 50% and 193£/MWh with 903.868 kW contracted generation, with a 5% increase in total site revenue.

Table 1: Nomenclature

Parameters	
d(i)	Site demand
G_{max}	Maximum generation the site can offer
KS(i)	Number of STOR calls in each demand bin
ah(i)	Site availability hours in each demand bin
gac	Availability price in £/MWh
guc	Utilization price in £/MWh
fc	Fuel price £/MWh
Ls	Duration of STOR call
Variables	
Z	Total annual revenue
TAR	Total annual availability revenue
TUR	Total annual utilization revenue
TGFC	Total generated fuel costs
TPs	Total penalties
X	Generation to offer
XACT(i)	Actual delivered generation
YP(i)	Binary variable indicating if a penalty was issued

1. Introduction

As electricity and power sectors across the world decarbonize, grid systems will have to become more flexible to cope with the intermittent nature of variable renewable energies (VREs), the inflexibility of nuclear power, and changes to peak demand due to electrification of energy (Strbac, Pudjianto, and Djanic, 2018). To ensure the careful balance of supply and demand, existing systems will need to be adapted. An important tool will be distributed energy resources (DERs), small-scale power generation or storage technologies, which provide increased flexibility to the grid (Hirth, 2017). Inclusion of DERs in wholesale electricity markets provides a variety of benefits, such as lower prices for consumers as a result of lower competition, and more importantly higher grid flexibility (FERC, 2021). In the UK, DERs are already being used by the National Grid (NG) in the Short-Term

Operating Reserve (STOR). STOR is one of the balancing mechanisms (BM) used by NG to ensure supply and demand are always met (National Grid, 2016). STOR balances supply and demand by providing additional generation or demand reduction (DR). This paper will focus on generation, although literature regarding DR is briefly considered. As penetration of intermittent renewable energies increases, DERs will play a more prominent role in balancing supply and demand as electricity generation becomes segmented into 2 main markets— a long term centralized market, for baseload generation, and a short-term decentralized market (Gramlich, 2019). In the US, DERs will only open to wholesale markets in 2022, following Federal Electricity Regulatory Committee (FERC) Order No. 2222. As this is a new and growing avenue in the US, there has been little analysis done, but the DER market is expected to follow 4% cumulative annual growth rate (CAGR) over the next 5 years to reach a cumulative 387 GW (Wood Mackenzie, 2021). Thus, as the STOR will continue to play a larger part in the electricity sector of the UK, it is important to analyse possibilities from a DER investor point of view. This paper builds upon research performed by Rai et al (2021). which established the amount of additional generation a DER could offer based on non-linear optimization rather than following heuristics-- the method most frequently employed currently. By using settlement data for the past 5 years, it is possible to create a novel framework to estimate the number of STOR calls a site would receive each year based on its utilization price. Hence, a range of utilization variables can be considered to maximize site revenue. The novelty of this paper is the framework it establishes to estimate number of STOR calls, as well as the determination of the optimal utilization price (sometimes referred to as simply 'price' from here on) in a STOR contract to maximize site revenue.

1.1 Background

Efficient electricity markets are crucial to the transition to a low carbon energy system (Corneli, Gimon, and Pierpont, 2019). DERs are essential in guaranteeing market efficiency, as they reduce consumer prices and increase competition, along with providing much needed stability (FERC, 2020). As DERs gain market share and renewable energies with near-zero fuel costs become more popular, short term, decentralized markets will increasingly shape overall energy policy, and the future of long-term central markets is much less clear (Silva-Rodriguez et al, 2020). It is estimated that DERs and energy storage systems (ESS) will take up 50% of the UK's electricity flex-up volume by 2025, compared to about 30% in 2020 (Fuergy, 2020). In the UK BM generation is provided primarily by gas and diesel generators, although battery and demand response are becoming increasingly popular (National Grid, 2021). Wide scale growth is projected across the DER sector. Specifically, grid-related battery storage is expected to grow at 30% CAGR through 2030 worldwide (U.S. Department of Energy, 2020). Forecasting demand is becoming more difficult due to increased penetration of intermittent technologies, which will increase the importance of balancing mechanisms such as STOR (Misconel, Zöphel, and Möst, 2021). To ensure continued growth of DERs and hence, electricity market stability, strong financing development and operations plans need to be considered (Cramton, 2017). The novelty of this paper is the site focused, DER investor point of view taken, which is necessary to consider ensuring implementability of short-term markets.

The electricity planning market in the UK is divided into 30-minute windows, called settlement periods (SPs). Integration of DERs into energy markets is performed by aggregators, who operate a portfolio of DERs and who will then contract with NG directly (National Grid, 2021). For this analysis, the site investigated is considered the only DER in an aggregator portfolio and thus contracts directly with the NG. Contracts with the NG specify the availability windows during which a site must be prepared to receive a STOR call. The contracts also specify the amount of electricity which must be delivered in the event of a STOR call. If the site fails to provide the specified amount of generation, it will incur a financial penalty. When a mismatch of supply and demand results in the NG putting out STOR calls, it will call contracts from lowest utilization prices to highest such that system cost is minimized. An example STOR day is shown in figure 1.

1.2 Literature Review

There are numerous studies which emphasize the importance of DERs to future electricity systems, and on the economic potential of DR in short term markets. This research adds to the body of literature by being the first to develop a tool to estimate the number of STOR calls a DER can expect, as well as considering an optimal utilization price to offer such that total site revenue is maximized.

Rai, Oluleye, and Hawkes (2021) consider the optimal generation to for a site to offer at a fixed utilization price to maximize site revenue. By using a MINLP model which considers existing site demand in detail, Rai et al. (2021) provides a strong basis for investigating DER revenue in the STOR market. This research builds off the MINLP model employed in Rai et. al (2021) to investigate the optimal generation to contract across a range of utilization prices.

Kirkerud, Nagel, & Bolkesjø (2021) consider the economic impact potential of DR in northern Europe using the energy model BALMOREL. While this is an important result, the paper primarily considers the future system potential rather than employing a site-based approach grounded in the present day, which is essential to develop financing plans which ensure feasibility of future systems.

Corneli, Gimon, & Pierpont (2019) lay out a vision of a design of electricity markets that would enable a smooth transition to low carbon networks. In the paper, they identify short-term markets and DERs as crucial infrastructure to the overall market design, which in their eyes, includes a large decentralized short-term market and a centralized long-term market to serve as baseload generation. The work carried out by these authors emphasizes the importance of conducting further research but fails to consider a financial assessment strategy. While this paper does not present a framework for full scale economic analysis of DERs, it does provide a novel framework to assess economic potential of DERs in a short-term market which is paramount to future economic assessments.

2. Methods

The case study was conducted in a 3-part process: data analysis, optimization modelling, and sensitivity analysis.

2.1 Data Analysis

The entire site demand from 2018 in half-hour periods was provided by KiwiPower and subsequently analysed. To receive accurate findings for peak load, a 25-bin characterization method from Rai et. al (2021) was applied. Hence, each SP is mapped to a corresponding demand. The current authors used data from Elexon portal containing info regarding all STOR calls made from 2018-2019 (~170,000 data points) (Elexon, 2021). This information contained date, SP, utilization price, and SO Flag (a T or F classification for whether the STOR call was completed, T means it was), as well as other extraneous information. The dataset did not contain information regarding the availability price. In each SP, there may be multiple STOR calls made, depending on the level of capacity required to balance the system. Thus, for each SP there are a range of utilization prices at which calls were made. To determine the number of calls one site will receive, the utilization price data first needs to be reduced

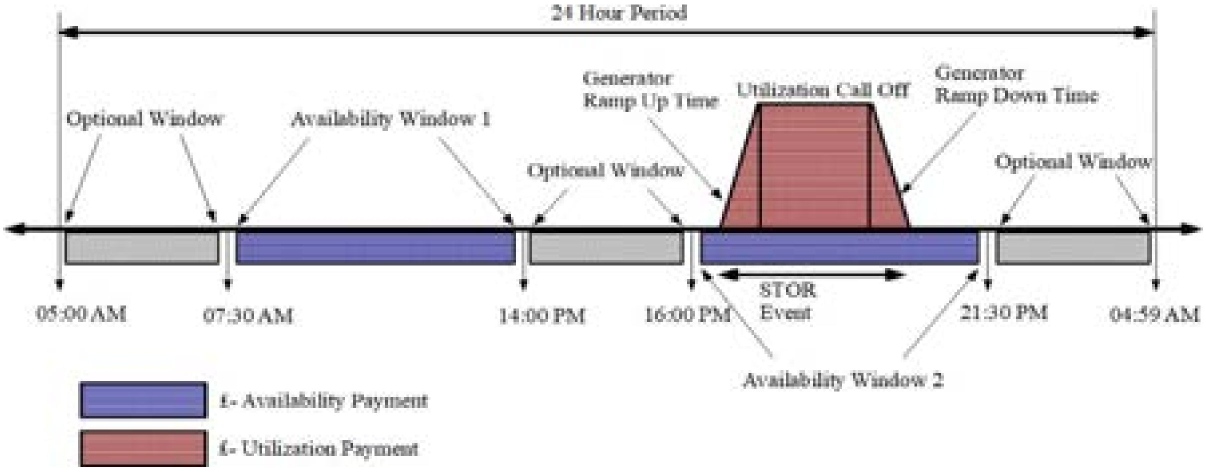

Figure 1: Example STOR day

to one utilization price point per SP. Using MATLAB code, the maximum price of STOR call made in each SP was extracted. This reduced set is henceforth referred to as the STOR price index. The maximum price of the STOR index was set as the maximum of test prices, and a minimum test price was chosen based on site fuel costs. 25 data points were chosen in this range. To determine the number of STOR calls at each price point, the test price was compared to the price index. The key assumption in this analysis is that if a test price is lower than the index price of a given SP, the site would receive a STOR call in that SP. Where consecutive SP would have each independently incurred a STOR call, these were considered to be 1 call, as the average length of a STOR call is assumed to be greater than 30 min. This analysis was carried out by a MATLAB script which returned the number of STOR calls which would have taken place in each bin (25 data points).

Once the expected number of calls were determined, a mixed integer non-linear programming model, implemented in GAMS, was used to calculate contracted generation for a certain utilization price mitigating the penalty costs that might incur, hence maximizing total revenue. The model was identical to that used by Rai. et. al. (2021), as are the problem statement, solution strategy and mathematical formulation that follow. However, this paper uses this strategy not only to determine the optimal generation to offer but also to apply it to a range of utilization prices, thus providing newfound insight into the field.

2.2 Optimization Model

The optimization model is adapted from Rai et al. (2021)

2.2.1 Problem Statement

Given:

- Generator capacity: Maximum generation capacity of the generator at a site participating in STOR.
- The energy demand of the site: A HH site demand data for the whole year
- Utilisation revenue: The contracted revenue obtained for electricity generated by the site and exported to the grid during grid STOR utilisation calls by the SO.
- Availability cost: The contracted revenue for the availability of the site generator during potential STOR call periods.
- Fuel cost: The cost of fuel for electricity generation during utilisation calls.
- The total number of availability hours in a STOR year.
- The average duration of STOR dispatch call by the SO.
- Penalty cost for under or no delivery of electricity by the site during utilisation call. (i.e., the penalty when a call cannot be served because site demand is too high to enable sufficient export of electricity to the grid to meet the contracted STOR capacity).
- The total number of grid dispatch calls in a year.

Determine:

- Optimal capacity of the generating unit at a site that can be offered for STOR to the SO by an aggregator.

Subject to:

- Maximum electricity generation capacity of the site generator constraint.
- Site STOR generation capacity limits due to uncertain site demand.
- Actual electricity generation capacity delivered by the generator constraint.

In order to:

- Maximise site revenue (comprising of both availability and utilisation revenue of site generator)
- Minimise penalty costs incurred either by no or under-delivery of electricity during grid dispatch call.

2.2.2 Solution Strategy for MINLP

A deterministic DICOPT MINLP approach is used and implemented in GAMS, to calculate the optimal generation capacity a site should offer, by using the expected STOR calls determined previously in MATLAB. The contracted generation leads directly to the calculation of total revenue generated by the site.

2.2.3 Formulation

There are two constraints introduced to the model.

$$X \leq G_{max} \qquad [1]$$

Where *X* stands for amount of generation to offer, with a constraint applied, that it cannot exceed G_{max},, the maximum generation the site can offer, which is equal to1500 kW, and

$$XACT(i) \leq G_{max} - d(i) \qquad [2]$$

Where *XACT(i)* is the actual delivered generator capacity, that cannot go above the max generation less the site demand, *d(i)*. (i) stands for the 25 different bins or scenarios, in which the site demand was separated into.

The objective function of the model is maximizing *Z*, that stands for the total annual revenue for the unique utilization prices. The total revenue is calculated using the following equation:

$$Z = TAR + TUR - TGFC\ - TPs \quad [3]$$

Where, *TAR, TUR, TGFC* and *TPs* stand for total availability revenue, total utilization revenue, total generated fuel costs originating from the operation of the generator when a STOR call is made and the total penalties, which apply when the contracted generation is not met, respectively.

The total availability revenue is calculated by summing all the availability revenues through each of the 25 scenarios. The number of availability hours the generator was available for, *ah(i)*, is multiplied by, *X*, and by *gac,* or the availability price, which is taken as a constant throughout the use of the model. Considering that the availability price has one of the biggest impacts on the model, a sensitivity analysis was carried out, which is discussed in detail in **Section 3.3.2** of the paper.

$$TAR = \ \sum_{i=1}^{n} ah(i) * gac * X \quad [4]$$

The total utilization revenue is formulated as *XACT(i)* being multiplied by the utilization price, *guc*, the duration of the STOR call, *Ls*, taken to be constant 1.66 hours, and *Ks(i)*, the number of STOR calls in each demand bin, estimated by the MATLAB code described in the previous section. To get the total annual result, the multiplication is summed over all the 25 scenarios.

$$TUR = \ \sum_{1}^{i} XACT(i) * guc * Ls * Ks(i) \quad [5]$$

The costs, stemming from the operation of the generator during a STOR even is calculated as the previous calculation, in equation [5], but is altered by using the price of fuel, instead of utilization.

$$TGFC = \ \sum_{1}^{i} XACT(i) * fc * Ls * Ks(i) \quad [6]$$

Penalties are issued when a contractor fails to deliver the amount of generation agreed upon. The total costs penalties annually are calculated as:

$$TPs = \sum_{1}^{i}((224 * gac * X) - \big(160 * gac * XACT(i)\big) * Ks(i) * YP(i). \qquad [7]$$

where *YP(i)* is indicating whether a penalty incurred or not.

The next step was to make use of the model for a wide range of utilization prices, in order to recognize a general behaviour of the total revenue depending on the chosen utilization price, and determine an optimal solution, so that the objective function can be maximized.

2.3 Sensitivity Analysis

Sensitivity analysis is done to demonstrate the impact of non-quantifiable variables and the volatility of the STOR market and fuel prices.

3. Results

The results presented are conducted for a real-life case study to add value to the model and involve a highly data driven approach to ensure maximum rigor.

3.1 Data Analysis

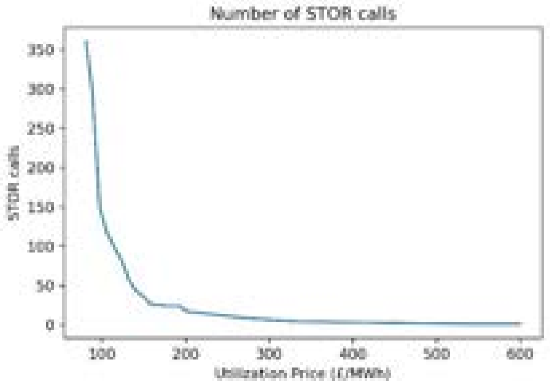

Figure 2. STOR call vs Utilization Price

Figure 2 shows the number of STOR calls a site receives decreases exponentially when utilization price increases. This is a logical result given the system design to minimize total cost.

The maximum price of a STOR call in 2018 was £180 / MWh, thus this was the maximum utilization price considered in the remainder of the analysis. Given a fuel cost of £80/MWh, the minimum price chosen was £81/MWh to ensure operation feasibility. 25 price points were considered across this range to ensure smooth results. STOR calls were determined for all 5 years and examination of these results revealed that, averaged across all prices, the number of calls in 2018 was 66% higher than the 5-year average. A sample of calls across 5 years is provided in table 2. The analysis suggested that in 2018, at a utilization price of £170/MWh there should be 25 STOR calls. Compared to the 23 STOR calls received by the site in 2018, this shows that while imperfect, the analysis conducted was sensible and the optimization model will provide results with real world meaning.

Table 2: Selected Data Analysis Results

Expected calls at £170/MWh 2015 - 2020								
Year	2015	2016	2017	2018	2019	2020	AVG	'18 Real
E[Calls]	14	22	20	25	7	10	16.3	23

3.2 Modelling

As shown in figure 3, total site revenue is maximized at the highest utilization price, with a revenue increase of 50% compared to the base case of £170/MWh. Total revenue is strongly dependent on availability revenue, as demonstrated by the strong correlation between the blue and green lines in the figure below, whereas utilization revenue only weakly affects total revenue.

Figure 3. 2018 Breakdown

The importance of availability revenue is characterized by the increasing amount of generation which can be contracted at higher utilization prices, as decreased likelihood of receiving a call leads to a lower chance of incurring a penalty, and any increase in total penalties is heavily outweighed by the increase in availability revenue. To further investigate the utilization revenue, an operating revenue is defined as utilization revenue less generated fuel costs and presented in figure 5. At low utilization prices the high utilization revenue is quickly eroded by the high fuel costs. Operating revenue quickly increases and reaches a maximum at £193/MWh, corresponding to the local optimum shown in figure 3.

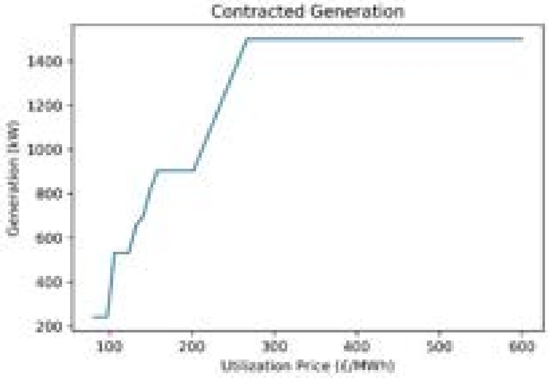

Figure 4. Generation vs Utilization Price

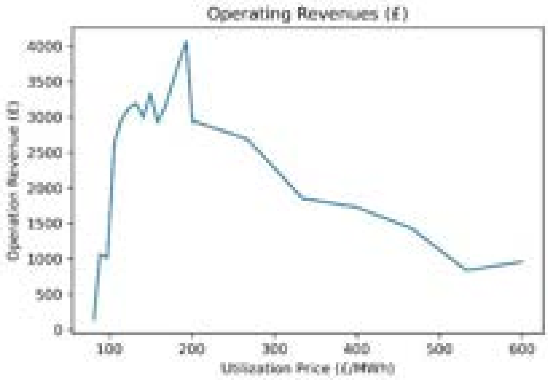

Figure 5. Operating revenue vs Utilization Price

3.3 Sensitivity Analysis

To ensure the accuracy of these findings, a sensitivity analysis was performed on fuel costs, availability price, and number of STOR calls received, as these were identified as the most impactful parameters.

3.3.1 Fuel Costs

The site investigated runs a CGCT to generate its power which makes it susceptible to the unpredictable natural gas market. For a broad scope, fuel costs were varied by +- 50%. Figure 6 shows that fuel price has noticeable effect on revenue at lower utilization prices, while it has a negligible impact on high utilization prices. This result creates additional merit for the high-price-low-calls strategy, as it would insulate the site from volatile fuel prices. The same logic would apply in terms of avoiding any increases in carbon pricing which are likely to ensue as the transition towards a low-carbon economy intensifies. The reduced risk which results from low calls should increase attractiveness to investors.

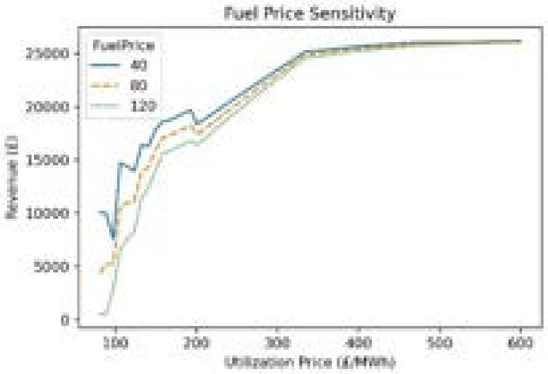

Figure 6. Fuel Sensitivity Analysis

3.3.2 Availability Price

The analysis conducted thus far has assumed that availability price remains constant, hence it is always beneficial to increase utilization price to generate more availability revenue. In the data analysed, there was no information regarding the availability price of individual contracts, but it is reasonable to speculate that as utilization price increases, availability price decreases, as the grid and supplier know that higher prices lead to less calls and prevent farming of availability revenue. Figure 7 highlights the importance of availability revenue in total revenue, as in all 3 cases, revenue is maximized at higher utilization prices. A more detailed analysis of availability price should be conducted, although this is beyond the scope of the current paper.

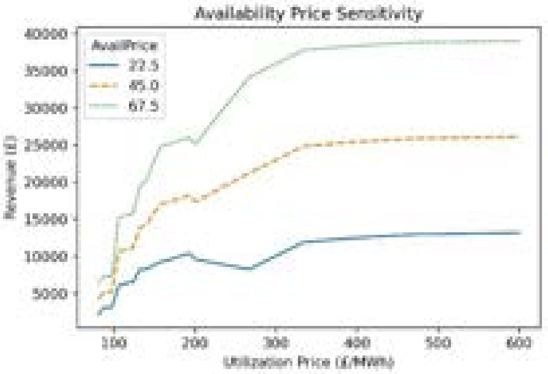

Figure 7. Availability Sensitivity

3.3.3 Number of STOR calls

The analysis conducted to estimate the number of STOR calls received focused on the year 2018. However, number of calls that a site will receive in a year is difficult to predict, so it is important to consider the impact that a change in number of calls would have on site revenue. As previously mentioned, the number of STOR calls received in 2018 was well above the average. The optimization model was re-run using the estimated number of STOR calls the site would have received in 2020, as this presents more recent results with numbers more representative of the average year. As figure 8 shows, having fewer calls is beneficial to site revenue. This additional information strengthens the value of previous results, as the analysis was conducted in a high-risk situation. More rigorous analysis would involve changing the number of STOR calls for a fixed utilization price and a fixed generation. This would, however, involve modifying the optimization model, which is outside the scope of this report.

Figure 8. STOR Call Sensitivity

3.4 Limitations

The analysis presented thus far has several limitations, primarily the assumptions made and the use of historical data. The key underlying assumption of this analysis is that the contract offer would always be accepted by the NG. In reality, the tender process is highly competitive and dependent on both the utilization price and availability price, which was assumed to be constant. Additionally, the analysis was carried out with the use of historic data. Data analysis revealed there is significant yearly variation in the number of STOR calls, and site demand will also show yearly variations, although to a lesser extent. The ongoing change in this sector makes it even more difficult to predict future behaviour.

4. Conclusions

This paper presents a novel framework for estimating number of STOR calls a DER will receive in a STOR year by performing rigorous analysis on real-life data sets. It also presents a novel method to maximize site revenue, by finding an optimal utilization price for DER aggregators, thus recommending contracted generation, by making use of mixed integer non-linear programming (MINLP) model. Results indicate two possible ways to go about maximizing income: one that incorporates both utilization and availability revenue, resulting in a local optimum corresponding to a 5% increase in revenue. The alternative method explored in this report is a global optimum, a model which relies almost solely on availability revenue and corresponds to a 50% increase in overall revenue for the site.

The MINLP model was implemented in GAMS. The model was used for testing across a wide range of contract prices. We assumed that if a test utilization price was less than the corresponding index price in a given SP, the site would receive a call. The results found have been, a local optimum of 193£/kWh that relies on a balanced share of both availability and utilization revenue, lowered by the associated penalties, and a global optimum of 600£/kWh, the highest call price to occur, which mostly relied on availability revenue, hence minimizing penalty costs, and having a decreased share of utilization revenue.

The most influential parameters of the model were the cost of fuel, availability price, and the number of STOR calls made in one year at certain contracted prices. Thus, sensitivity analysis was carried on these parameters. A method of +-50% was utilised on the first two factors, warranted by the ever-fluctuating nature of the natural gas industry, which the generation is reliant on, and the lack of real-life data of availability price dependence on contracted price. Number of STOR call analysis was done using data from 2020 which better represented the 5-year average and used more recent data, providing a more accurate real-life presentation.

Future work would include gathering real life data of the actual number STOR calls taking place at certain utilization prices and investigating the dependence of availability pricing on said utilization prices.

5. Acknowledgements

The authors would like to thank Ussama Rai for guidance during the project and help in obtaining the data necessary to carry out this analysis.

References

Aggarwal, S. and Orvis, R., 2019. Wholesale Electricity Market Design for Rapid Decarbonization: Visions for the Future. [online] San Francisco: Energy Innovation. Available at: <https://energyinnovation.org/wp-content/uploads/2019/06/Wholesale-Electricity-Market-Design-For-Rapid-Decarbonization-Visions-For-The-Future.pdf> [Accessed 12 November 2021].

Bloess, A., Schill, W. and Zerrahn, A., 2018. Power-to-heat for renewable energy integration: A review of technologies, modelling approaches, and flexibility potentials. Applied Energy, 212, pp.1611-1626.

Corneli, S., Gimon, E. and Pierpont, B., 2019. Wholesale electricity market design for rapid decarbonization. [online] San Francisco: Energy Innovation. Available at: <https://energyinnovation.org/wp-content/uploads/2019/06/Wholesale-Electricity-Market-Design-For-Rapid-Decarbonization-Long-Term-Markets-Working-WIth-Short-Term-Energy-Markets.pdf> [Accessed 15 November 2021].

Cramton, P., 2017. Electricity market design. Oxford Review of Economic Policy, 33(4), pp.589-612.

European Network of Transmission System Operators for Electricity, 2015. Market Design for Demand Side Response.

Federal Energy Regulatory Commission, 2020. FERC Order No. 2222: A New Day for Distributed Energy Resources. Washington, DC.

Fuergy.com. 2021. Get ready for a modern energy era: Distributed energy resources and microgrids. [online] Available at:

<https://www.fuergy.com/blog/der-and-microgrids> [Accessed 13 December 2021].

Gramlich, R., 2019. Wholesale Electricity Market Design for Rapid Decarbonization: A Decentralized Markets Approach. San Francisco.

Hirth, L., 2017. The European Electricity Market Model EMMA. [online] Neon Neue Energieökonomik GmbH. Available at: <https://neon.energy/emma-documentation.pdf> [Accessed 11 December 2021].

Heitkoetter, W., Schyska, B., Schmidt, D., Medjroubi, W., Vogt, T. and Agert, C., 2021. Assessment of the regionalised demand response potential in Germany using an open-source tool and dataset. Advances in Applied Energy, 1, p.100001.

Johnson, M., 2017. Controlling and optimizing resilient distributed energy resources and microgrids with a demand-side operation platform. The Electricity Journal, 30(4), pp.12-15.

Kirkerud, J., Nagel, N. and Bolkesjø, T., 2021. The role of demand response in the future renewable northern European energy system. Energy, 235, p.121336.

Maribu, K., Firestone, R., Marnay, C. and Siddiqui, A., 2007. Distributed energy resources market diffusion model. Energy Policy, 35(9), pp.4471-4484.

Markets and Markets, 2021. Distributed Energy Resource Management System Market by Application (Solar PV, Wind, Energy Storage, CHP, EV Charging), Software (Analytics, Management & Control, VPP), End User (Industrial, Commercial, Residential), and Region - Global Forecast to 2026. [online] Available at: <https://www.marketsandmarkets.com/Market-Reports/distributed-energy-resource-management-system-market-256436187.html> [Accessed 12 December 2021].

Misconel, S., Zöphel, C. and Möst, D., 2021. Assessing the value of demand response in a decarbonized energy system – A large-scale model application. Applied Energy, 299, p.117326.

Müller, F. and Jansen, B., 2019. Large-scale demonstration of precise demand response provided by residential heat pumps. Applied Energy, 239, pp.836-845.

Philpott, A. and Pettersen, E., 2006. Optimizing Demand-Side Bids in Day-Ahead Electricity Markets. IEEE Transactions on Power Systems, 21(2), pp.488-498.

Rai, U., Oluleye, G. and Hawkes, A., 2021. An optimisation model to determine the capacity of a distributed energy resource to contract with a balancing services aggregator. Applied Energy, 306, p.117984.

Silva-Rodriguez, L., Sanjab, A., Fumagalli, E. and Gibescu, M., 2020. Short Term Electricity Market Designs: Identified Challenges and Promising Solutions. ArVix, [online] Available at: <https://arxiv.org/pdf/2011.04587.pdf> [Accessed 9 December 2021].

Sperber, E., Frey, U. and Bertsch, V., 2020. Reduced-order models for assessing demand response with heat pumps – Insights from the German energy system. Energy and Buildings, 223, p.110144.

Strbac, G., Pudjianto, D. and Djapic, P., 2018. Market Framework for Distributed Energy Resourcesbased Network Services. [online] National Grid PLC. Available at: <https://www.nationalgrid.com/sites/default/files/documents/NG%20-%20Power%20Potential%20ICL%20SDRC%209.3.pdf> [Accessed 12 December 2021].

U.S. Department of Energy, 2020. Energy Storage Grand Challenge: Energy Storage Market Report. Washington D.C.

Wood Mackenzie, 2020. United States distributed energy resources outlook: DER installations and forecasts 2016-2025E. [online] Available at: <https://www.woodmac.com/our-expertise/focus/Power--Renewables/der-outlook-us-2020/> [Accessed 2 November 2021].

Zhang, L., Good, N. and Mancarella, P., 2019. Building-to-grid flexibility: Modelling and assessment metrics for residential demand response from heat pump aggregations. Applied Energy, 233-234, pp.709-723.

Real-time optimisation of a simulated CCS pilot plant using gaussian processes and bayesian optimisation methods

Abdullahi Elmi, Ahmed Massli
Imperial College London

December 16, 2021

Abstract

Carbon Capture and Storage (CCS) is a key climate change mitigation strategy that has the potential to play a significant role in supporting the transition to net zero. As with all processes, there are cost pressures as a result of competition and process disturbances that need to be dealt with. Real-time optimisation is an online model-based optimisation approach that uses process measurements to adapt to disturbance sand process changes. In this paper, a cutting-edge modifier adaptation algorithm developed by Del Rio Chanona et al incorporating Gaussian processes,trust region methods and bayesian optimisation is bench-marked on a simple example problem before being applied to Imperial's CCS Pilot Plant. Key insights about the algorithm and its performance relative to more established MA algorithms are obtained. The algorithm is then evaluated on a model of the pilot plant, taking another step closer to an implementation on the real plant.

1 Introduction

Greenhouse gas emissions resulting from energy generation account for 95% of CO_2 emissions in the UK Hammond & Spargo (2014). Over the last decade, as more countries have committed to stronger climate targets, Carbon capture and storage (CCS) has matured as a key climate change mitigation strategy to assist with society's transition to low carbon energy generation. Consequently, there has been a rapid growth in the number of CCS projects being implemented worldwide with investment doubling in the last 10 years OECD (2016).

A key question that arises when operating a CCS Plant is how to identify the optimal operating conditions for a given steady state whilst satisfying all safety and environmental constraints.

Process optimization is an important tool that allows maximal benefit to be derived from chemical processes whilst ensuring they operate safely and meet environmental regulations. Advancements such as the availability of flowsheet simulators and improved algorithms applicable to non-linear systems led to the development of a new frontier in process optimisation - Real time optimization Barrett et al. (2018).

Real-time optimization is a model based approach using current process information to predict optimal operating points for the next RTO interval. The particular benefit of RTO in addressing the difficulties with plant-model mismatch is that it utilises real-time process information to compensate for model uncertainty.

Traditionally, a "two-step approach" is taken whereby the inaccurate process model is optimised with deviations between predicted and measured parameters used to iteratively improve the model parametersChen & Joseph (2002). The key challenge associated with this approach is the model is often unable to converge to the true plant optimum due to insufficient flexibility within the problem to ensure KKT matching between the model and plant. Chachuat et al. (2008).

To tackle the issue of mismatch between the model and plant optimum, an approach called Modifer-adaptation (MA) was proposed by Marchetti et al (2016) Marchetti et al. (2016). In basic MA, tailored correction terms or 'modifiers' are introduced to the cost and constraint functions to ensure matching of the plant NCO upon convergence. However, this approach can be quite costly as it requires more plant evaluations to estimate cost and constraint gradients from the process measurements, which are often noisy, adding further difficulty.

Ferreira et al recently proposed the use of Gaussian processes (GPs) trained on previous plant data as modifiers in the MA optimisation scheme Ferreira et al. (2018). This was developed further by del Rio Chanona et al Chanona et al. (2021) who introduced trust regions and acquisition functions from Bayesian optimization to MA schemes. This allows the use of an established and well developed convergence theory that provides sufficient conditions for local optimality. This local approach maintains an accurate guess of the real optimization problem within a defined trust region that is iteratively adapted as the algorithm progresses. Acquisition functions such as LCB and EI attempt greater exploration within the feasible region - and when implemented on various examples were found to reach the optimum faster.

In this paper, the focus is on analysing the performance of various RTO schemes in terms of accuracy and convergence speed. Moreover, attempts will be made to compare the performance of these schemes with a simpler model then on a more complex real-life problem. The initial section will focus on the application of these schemes to a simple example problem as described in Chanona et al. (2021). The latter section will describe an implementation of MA-GP and trust region algorithms on an Aspen simulation of Imperial College's Carbon capture plant with the hope of providing insights and guidance to aid in future implementation on the real plant.

2 Preliminaries

2.1 Problem Formulation

Optimization of a plant steady state can be formulated as the following NLP:

$$\min_{u \in U} G_0^p(u) := g_0(u, y^p(u)), \tag{1}$$

$$s.t. G_i^p(u) := g_i(u, y^p(u)) \leq 0, \tag{2}$$

$$i = 1 ... n_g$$

where $u \in \ R^{n_u}$ is the vector of input variables, $y^p \in R^{n_y}$ is the vector of output variables, $g_0 : R^{n_u} \times R^{n_y} \Rightarrow \ R$ and $g_i : R^{n_u} \times \ R^{n_y} \Rightarrow \ R \ i = 1...n_g$

denote the cost and inequality constraint functions respectively and $\cup \subseteq \ R^{n_u}$ is the feasible set of input points. The superscript $(.)^p$ denotes a plant parameter. Typically as the plant equation is not known a priori, optimization is carried out on a model of the plant $y(u, \theta)$ where $\theta \in \ R^{n_\theta}$ is a vector of adjustable model parameters:

$$\min_{u \in U} G_0(u) := g_0(u, y(u, \theta))$$
$$s.t. G_i(u) := g_i(u, y(u, \theta)) \leq 0$$
$$i = 1 ... n_g$$

In the case of plant-model mismatch or process disturbances, the solutions to optimization problems 1 and 2 would not match. The two-step approach attempts to rectify this by iteratively updating the model parameter based on plant measurements to reduce this plant-model mismatch. This allows the model-based optimization problem to be driven to converge at the true plant optimum. However, as mentioned previously, this is not guaranteed to approach the plant optimum.

Modifier adaptation uses first-order correction terms to the cost and constraint functions to enable matching of the NCO of the plant upon convergence Marchetti et al. (2016). These first order correction terms are computed by methods such as finite forward differences and thus are costly as this requires more plant evaluations. The optimal inputs in a classic MA scheme are obtained by solving the following optimization problem:

$$u^{k+1} \in argmin G_0(u) + (\lambda_{\delta G_0}^k)^T u \tag{3}$$

$$s.t. G_i(u) + \epsilon_{\delta G_i}^k + \lambda_{\delta G_0}^k)^T (u - u_k) \leq 0 \qquad i = 1 ... n_g \tag{4}$$

where $\epsilon_{\delta G_i \in \ R}^k$ are zeroth-order modifiers for the constraints and $\lambda_{\delta G_0}^k$ are first-order modifiers for the cost and constraints. These are modified at each iteration and ensure that a KKT point for the model-based optimization problem is also a KKT point for the plant.

2.2 Gaussian Processes

GPs are a regression method based on kernel methods that use available input-output data to approximate an unknown function.Their use is machine learning was popularised by Rasmussen et al and for a more detailed introduction the reader is referred to this source **?** .

Consider an unknown noisy function $f : R^n \Rightarrow R, y = f(u) + \nu \ N(0, \sigma_v^2)$. Given n_p input-output pairs, the dataset generated by f is denoted as $U = [u_1, u_2, ..u_n] \in R^{nxn^p}$ and $y = [y_1, y_2, ..y_n]^T$. $\nu \ N(0, \sigma_v^2$ denotes a Gaussian noise with zero mean and variance σ_v^2. A GP is fully specified by a mean vector μ and a covariance matrix K which takes into account correlations between the function values at different points.

There are many potential choices for the covariance matrix however in this paper the squared-exponential (SE) Kernel is utilised as it is known to predict smooth functions well: $k(u, u') := \sigma^2 exp(-0.5(u - u')^T \Lambda (u - u'))$ where $\Lambda = diag(\Lambda_1, \lambda_2 ... \lambda_n)$ is a scaling matrix that contains the length scales for each dimension. The hyperparameters $\Psi = [c \sigma_n \sigma_v \lambda_1 ... \lambda_n]$ for a given input-output data set are inferred using maximum likelihood estimation. This entails maximising the log-likelihood (or minimising the negative log-likelihood).

The log-likelihood function is defined as: $\mathcal{L}(\Psi) := -\frac{1}{2}(y - 1c)^T K(U)^{-1}(y - 1c)$ where $K_{ij} := k(u_i, u_j) + \sigma_v^2 \delta_{ij}$ and δ_{ij} is Kronecker's delta function. The GPs prediction at u and the uncertainty associated with this prediction $ffgf$ can then be computed using the posterior mean μ_f and variance σ_f^2 functions respectively which are written as follows:

$$\mu_f ; = r(u, U) K(U)^{-1} y + c \tag{5}$$

$$\sigma_f^2 := \sigma_n^2 - r(u, U) K(U)^{-1} r(u, U)^T, \tag{6}$$

$$r(u, U) := [k(u, u_1 .. k(u, u_N] \tag{7}$$

The basic MA-based optimisation problem in equation (3) can now be reformulated as such:

$$u^{k+1} \in [argmin G_0(u) + (\mu_{\delta G_0}^k)](u) \tag{8}$$

$$s.t. [G_i(u) + \mu_{\delta G_i}^k](u) \leq 0, i = 1 ... n_g \tag{9}$$

Where $\mu_{\delta G_i}^k$ denotes the mean of the GP trained on the input-output data set $[U^k, \delta G_i^k]$ and δG_i^k contains information about the mismatch between the model and plant $\delta G_i^k := G_i - G_i^p$.

The use of a GP modifier to predict the mismatch is appealing as it comprises zeroth- and first order correction terms for the costs and constraints, as well as second-order corrections of the curvature. This is beneficial as it facilitates the enforcement of model adequacy conditions for modifier adaptation - model KKT points being equivalent to plant KKT points.

2.3 Trust region methods

Trust region algorithms are an alternative approach to the classic line search algorithms preferred in the past. In trust region methods at a potential solution u^* to an optimization problem, an approximate model can be created which is only "trusted" to model the true solution within a neighborhood or "region" of u^*. In essence the trust region constrains the size of the predicted step at a given iterate.

Δ^k is the trust-region radius for the predicted step d^{k+1}

The ratio of the actual improvement of objective function compared to the models prediction is defined as ρ^{k+1}:

$$\rho^{k+1} = \frac{G_0^p(u^k) - G_0^p(u^{k+1})}{[G_0 + \mu^k_{\delta G_0}](u^k)] - [G_0 + \mu^k_{\delta G_0}](u^{k+1})]} \quad (10)$$

If $\rho^{k+1} = 1$ the model is accurate but if $\rho^{k+1} \ll 1$, it is very inaccurate and the current iterate must be rejected.

Trust region methods are reliant on an algorithm which iteratively determines how to adapt trust region size and whether or not steps can be accepted. These decisions are taken using pre-determined trust region parameters: $\gamma_{red}, \gamma_{inc}, \eta_1 and \eta_2$. The trust region is adapted iteratively and shrinks or expands depending on the level of accuracy of the model.

to illustrate this approach the MA optimization problem in equation(3):

$$d^{k+1} \in argmin[G_0 + (\mu^k_{\delta G_0})^T](u^k + d) \quad (11)$$

$$s.t.[G_i + \mu^k_{\delta G_0}](u^k + d) \quad (12)$$

$$||d|| \leq \Delta^k, u^k + d \in \cup \quad (13)$$

where Δ^k is the trust-region radius for the predicted step $d^{k+1} \in \Re^{n_u}$.

The accuracy of the model at a given iterate k is determined by calculating ρ^{k+1}, a ratio of the actual plant improvement to predicted improvement:

where the model is deemed to be fairly accurate for $\rho^{k+1} \simeq 1$ and inaccurate for $\rho^{k+1} \ll 1$. The trust region is thus expanded whenever the accuracy ratio is high and reduced when it is low. There are a number of trust region parameters utilised for decision making when implementing algorithms: η_1,η_2, γ_{red},γ_{inc}. These parameters can be varied and will be explained in more detail when discussing the algorithm (section).

2.4 Lower Confidence Bound

Acquisition functions can be interpreted as calculating an expected loss/benefit associated with evaluating a function f at a point x. The point with the lowest expected loss (or highest benefit) is then selected as the sampling point.They are very beneficial as they enable exploration within the trust region. A number of acquisition functions exist including expected improvement,probability of improvement and entropy search however the focus in this paper is on implementing the Lower confidence bound acquisition function:

$$\mathcal{A}[\mu_f, \sigma_f](u) := \mu_f(u) - \beta\sigma_f(u) \quad (14)$$

where β can be seen as an exploration weight.

3 Methodology

3.1 Model Parameter Adaptation

The "two step approach" is a well-established optimization that is heavily utilised in industry. The downside of this approach are that the model-based optimisation problem often fails to reach the plant optimum in the presence of structural mismatch however it is utilised in this paper to act as a bench mark for case study 1. This approach also requires a good estimation of the plant model equations which is in practise very difficult to achieve particularly in larger systems such as a CCS plant.

3.2 Modifier adaptation

Modifier adaptation schemes are able to handle considerable plant model-mismatch mismatch by directly adapting the cost and constraint functions using zero and first-order modifiers which correct the mismatch between the model and plant. For any RTO scheme to be successful the gradients and values of the constraint and cost function for the model-based optimisation problem must match those of the plant. This problem is formulated as above in equation(x). The major challenge associated with this is the estimation of plant gradients from noisy data and the repeated plant evaluations required in this approach makes it costly.

3.3 Modifier adaptation with GP

To overcome the costly plant evaluations required in the basic MA scheme, Ferreira et al proposed the use of GPs to model the mismatch between the plant and model **?**. A useful property of modifiers computed by GPs is their ability to act as both zero and first-order correction terms.

The basic MA-based optimisation problem in equation (X) can now be reformulated as such:

$$u^{k+1} \in [argminG_0(u) + (\mu^k_{\delta G_0})](u) \quad (15)$$

$$s.t.[G_i(u) + \mu^k_{\delta G_i}](u) \leq 0, i = 1...n_g \tag{16}$$

Where $\mu^k_{\delta G_i}$ denotes the mean of the GP trained on the input-output data set $[U^k,\delta G_i^k]$ and δG_i^k contains information about the mismatch between the model and plant $\delta G_i^k := G_i - G_i^p$. The use of a GP modifier to predict the mismatch is appealing as it comprises zeroth- and first order correction terms for the costs and constraints, as well as second-order corrections of the curvature. This is beneficial as it facilitates the enforcement of model adequacy conditions for modifier adaptation - model KKT points being equivalent to plant KKT points.

Trust region algorithms are reliable, can be applied to non-convex approximate models and have strong convergence properties.

3.4 MA-GP with trust region methods

Del Rio Chanona et al (2018) developed an extension to the GP-MA problem [equation (8)] by introducing trust region methods as described above. The algorithm developed by del RIo Chanona et al (2021) is reproduced as Algorithm 1 below:

Algorithm 1 Modifier adaptation with Gaussian process, trust region and acquisition function

```
Input:
(1) initial data sets $(U^0, \delta G_i^0)$, $i = 0...n_g$:
(2) GP modifiers trained on initial data: $\mu^k_{\delta G_i}$
(3) initial operating point: $u_0$
(4) trust-region parameters: $0 < \Delta^0 < \Delta^{max}$,
$0 < \eta_1 < \eta_2 \leq 1$ and $\gamma_{red}, \gamma_{inc}$
(5) subset of unrelaxable constraints $UC \subseteq [1...n_g]$
Repeat: for k = 0,1..n
    1. Solve modified optimization problem (equation (11)) - $d^{k+1}$
    2. Obtain process cost and constraint values
       - $G_i^p(u^k + d^{k+1}), i = 0..n_g$
    3. Check infeasibility
       if either modified NLP is infeasible
       or if $G_i^p(u^k + d^{k+1}) > 0$
       for any i:$\Delta^{k+1} \leftarrow [\gamma_{red}, 1]$,
       $u^{k+1} \leftarrow u^k$ (reject step) and go to Step 7
    4. Compute Merit function (Equation (10))
    5. Update trust region
       if $\rho^{k+1} > \eta_2 \wedge ||d^{k+1}|| = \Delta^0$:
       $\Delta^{k+1} \leftarrow \gamma_{inc}\Delta^k$,
       $u^{k+1} \leftarrow u^k + d^{k+1}$ (accept)
       Else if $\rho^{k+1} < \eta_1$:
       $\Delta^{k+1} \leftarrow \gamma_{red}\Delta^k$,
       $u^{k+1} \leftarrow u^k$ (reject)
       Else: $\Delta^{k+1} \leftarrow \gamma_{red}\Delta^k$,
       $u^{k+1} \leftarrow u^k + d^{k+1}(accept)$
    6. Update input data
    7. Retrain GPs
```

The steps of the algorithm will be briefly explained below as it is utilised in both case studies that will be presented in this report. After initialising the optimization problem and selecting suitable trust region parameters, the GP modifiers must be obtained by training on the input data set. The modified NLP can them be solved to identify the best set within the initial trust region. The true cost and constraint values for this point are then obtained from the plant to confirm there are no constraint violations. In the event of a constraint violation the algorithm skips to step 6. If the NLP is feasible, the accuracy of the model is ascertained by computing the merit function and comparing to trust region parameters as stated in section x. If the model is accurate enough, the step is accepted. (Note: The trust region is only increased in size if the current step is at the boundary of the trust region). Otherwise, the algorithm backtracks by rejecting the step and reducing the size of the trust region. In the final two steps, the initial data is updated with the latest values and the GPs are retrained.

The NLP solved in this algorithm can be either ... LCB with or without exploration

4 Case Study 1 - Simple Example

To develop intuition of the various RTO algorithms that were later applied to the ICCS Pilot Plant a simpler model with a known optimum was selected - one KKT point at the coordinates $[0.36, -0.39]$. A comparison of the various algorithms on this simpler system was conducted to validate the performance of the cutting-edge RTO algorithm proposed by Del Rio Chanona et al (2021) prior to implementation on the CCS plant.

4.1 Problem Initialisation

The problem is stated as below:

$$\min_{u\in[-2,2]^2} G_0(u,\theta) := u_1^2 + u_2^2 + \theta_1 u_1 u_2 \tag{17}$$

$$G_1(u,\theta) := 1 - u_1 + u_2^2 + \theta_2 u_1 \leq 0 \tag{18}$$

$$\theta^p := [1,2] \tag{19}$$

$$\theta^m := [0,0] \tag{20}$$

This NLP demonstrates a clear plant-model mismatch and is non-linear thus this is a good initial problem to test the effectiveness and accuracy of the various MA algorithms that were coded in python.

To enable results for all case studies to be compared, the same 5 initial data points within the feasible range were selected. For the Basic MA scheme, finite forward differences were utilised to compute the plant gradients at each point.

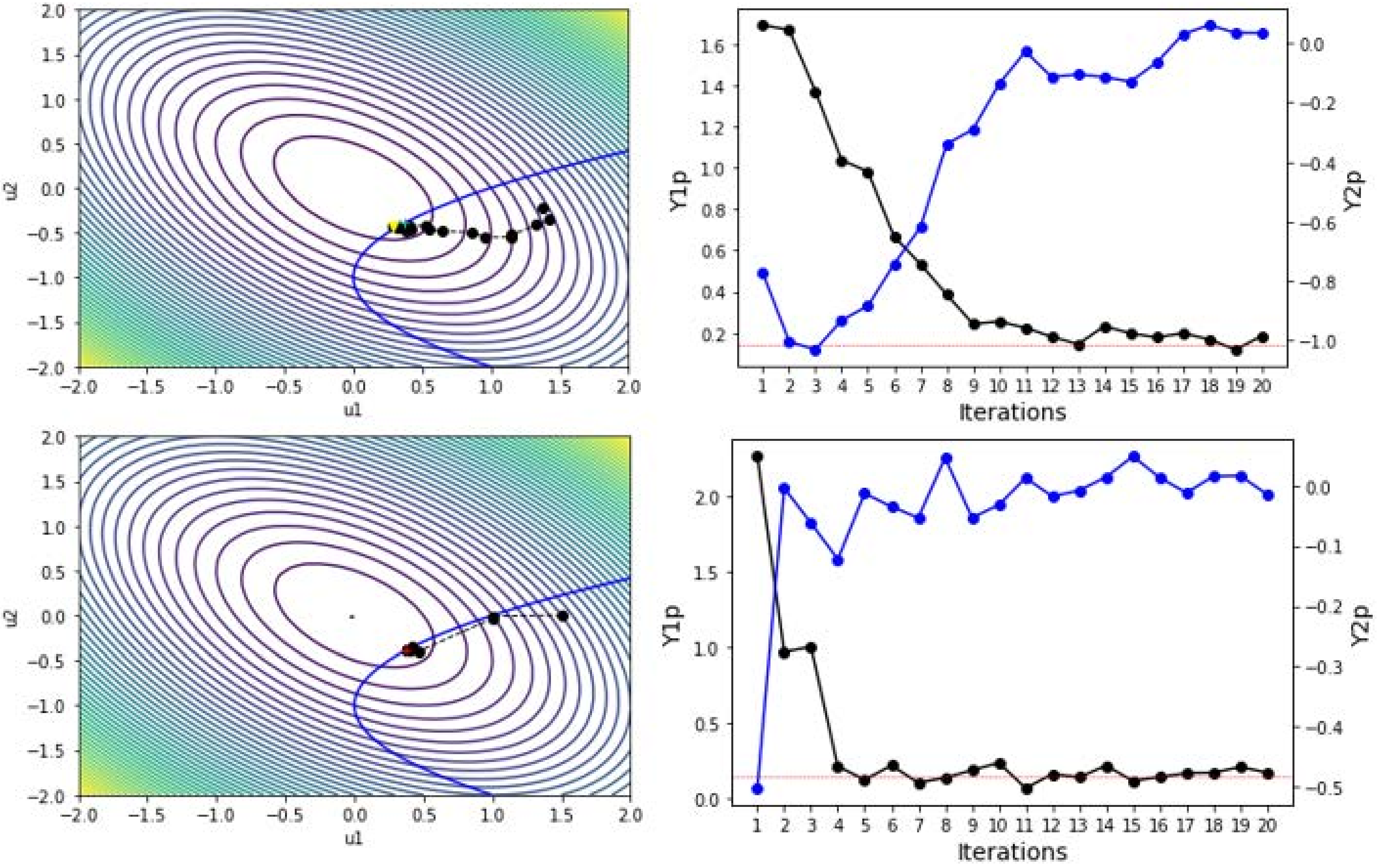

Figure 1: RTO for Case Study 1: The black contours on the 2 left graphs show the objective function .the constraint function is shown as the thick blue line . RTO iterates are plotted with a black line with black circular markers. The black line on the right two graphs depicts the progress of the objective function and the blue shows the constraint value at each iteration

In GP-based algorithms the hyperparameters were trained by minimizing the negative log-likelihood using the SLSQP solver in the scipy minimze package in python. A multi-start scheme was implemented which initialised the solver from various starting points to avoid the risk of being stuck at a local optimum. This fairly simplistic approach yielded GPs that accurately predicted the objective function and mismatch. The cost G_0 and constraint G_i measurements are assumed to have a known Gaussian noise with zero mean and variance of $\sigma^2_{G_0} = \sigma^2_{G_1} = 10^{-3}$

4.2 Results

Comparison of trajectory for GP MA and MA shows that addition of GP reduces the number of iterations to reach the optimum. The optimum is reached within 5 iterations after which point the algorithm fluctuates due to the presence of process noise. This is an expected result as GP is known to be able to handle noisy data well. This is a beneficial as it confirms that the integration of GP in RTO algorithms is a useful approach that can enable an NLP to reach the optimum faster with fewer function evaluations.

Following this result, Algorithm 1 was implemented on the example function to validate the benefits of introducing trust regions and acquisition functions. This algorithm was also coded in python utilised the same GP function as in the GP-MA optimisation problem. This enables direct comparison of the relative benefit introduced by the algorithm.

In both cases, it is clear to see that when initialising from the same point the algorithm is able to direct the problem towards the optimum in fewer steps (about 3). There is also a notable decrease in the influence of noise when the algorithm is implemented.

Overall, it can also be seen that there is little discrepancy between the performance of the algorithm with and without the LCB acquisition function. This suggests that sufficient exploration is carried out using trust-region methods alone. This was observed with a fairly large initial trust region.The LCB problem is highly dependent on the exploration weight chosen as can be seen in figures 3. When exploration weight is increased from 0 to 1 there is a small but noticeable increase in speed of convergence, there are also fewer constraint violations. However, as shown in the figure when it is increased to 2.5 there are significantly more constraint violations and the optimization problem takes longer to approach the neighborhood of the optimum. This appears to be because a high exploration weight makes the algorithm more op-

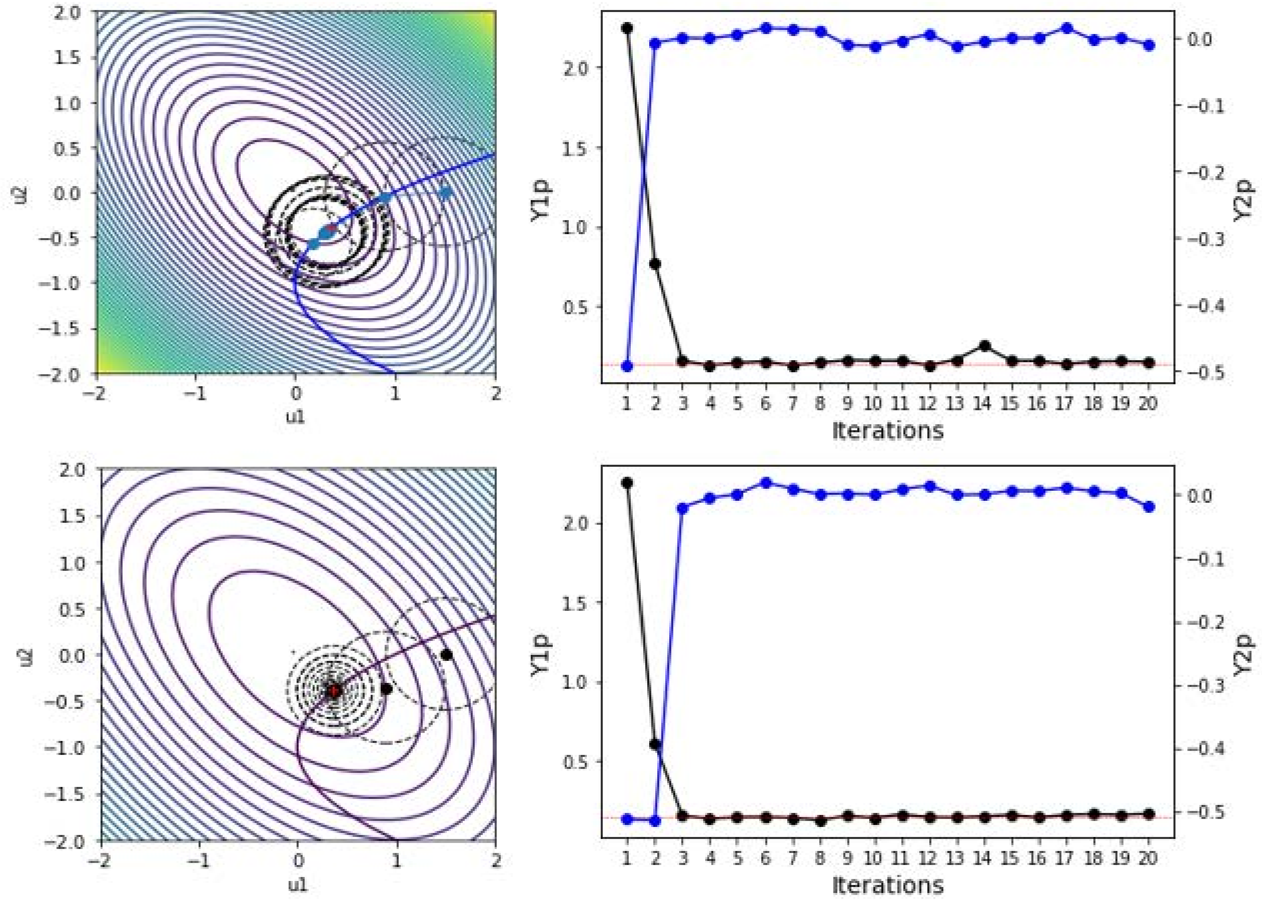

Figure 2: Case Study 1: The Black contours on the 2 left graphs show the objective function .the constraint function is shown as the curve through the graph .The top 2 graphs are the implementation of algorithm 1 without exploration.The bottom 2 graphs are the implementation of algorithm 1 with exploration (LCB,β=1.2). The iterations are presented with black and turquoise points surrounded by ellipsoidal trust regions. Dashed Orange line at the bottom of the scatter graphs represents the optimal point for the operating region. The Blue scatter corresponds to the plant constraint whilst the Black scatter is the plant objective.

timistic and liable to explore a wider range of points despite being on the right trajectory towards the optimum. This indicates that careful choice of Beta is required to ensure the NLP does not significantly violate the constraints and to balance the risk and reward associated with exploration. Another important insight obtained from this is the importance of selecting the right trust region - when a significantly more conservative trust region was selected, as expected, the optimization problem took longer to reach the true optimum.

5 Case Study 2

The aim of the project is to implement the RTO algorithms on the ICCS Pilot Plant (Imperial college Carbon capture pilot plant) to minimize the cost of operation whilst ensuring CO_2 emissions remain below a set target. An Aspen flowsheet was created to emulate the base case for the pilot plant - further detail can be obtained in Dong (2017).

Aspen Plus was selected as the simulation environment as it readily provides thermodynamic property data allowing the heat duties and other properties to be easily approximated. It also allows complex models to be built accurately without the requirement to build exhaustive The detailed Process Flow Diagram (PFD) of the PP was created by the company TPI before construction of the PP. The PFD provides the basis for the convergence of the Aspen simulation. Initially the set up of the flowsheet without a recycle stream but modelled the 2nd inlet stream to the absorber as closely as possible to the expected recycle stream from the PFD. Once the flowsheet adjusted to counteract the convergence issues, the recycle stream from the stripper to the absorber is set up.

The pilot plant has a solution of approximately 20% Monothanolamine (MEA mass fraction) that loops around the plant in a figure 8 configuration see figure 5 ,CO_2 is first capture in the absorber the flows to the stripper where the CO_2 is released in the stripper by heating the solution to regenerate the MEA solution. To maximise simulation accuracy Aspen rate based models are implemented in the RadFrac blocks rather than the equilibrium based calculations to closely replicate the stripper and absorber columns in the pilot plant see **?** for more information.

the price of CO_2 is expected to be around £42 per ton according to OECD (2016). The power plant

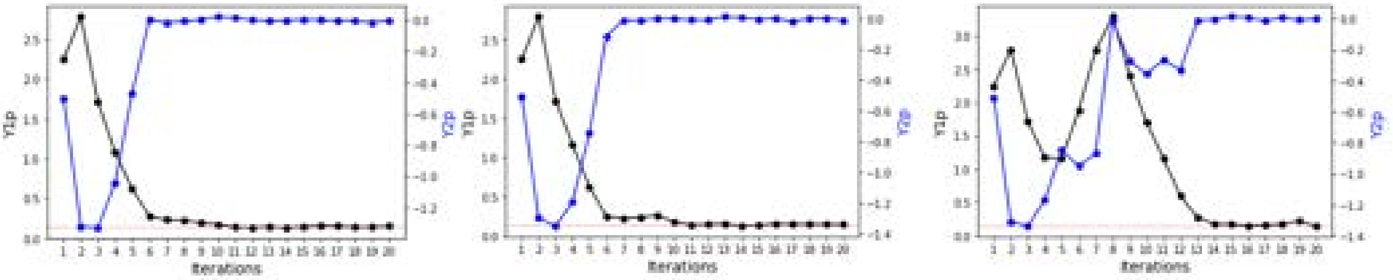

Figure 3: Case Study 1: Plots of Objective function and Cost function when implementing Algorithm 1 with LCB. From left to right, the exploration weight is varied between 0, 1 and 2.5. The cost function is plotted as a black line with black dots and the constraint function is plotted as a blue line with blue dots.

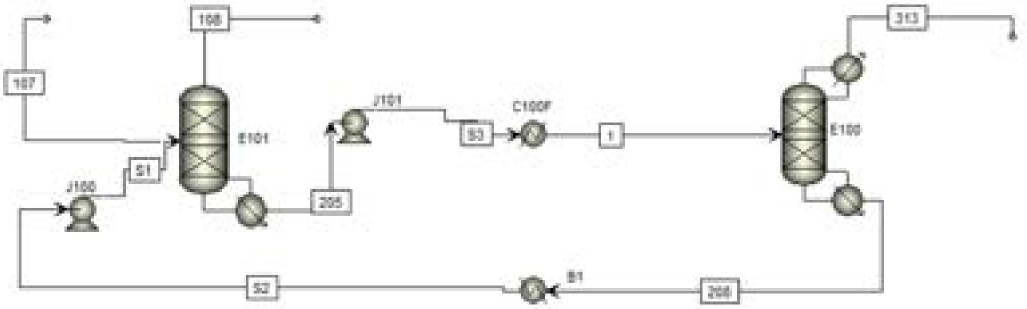

Figure 4: Model created in Aspen Plus to act as a testing environment for Algorithms prior to implementation on pilot plant

efficiency is estimated to be the same as the UK average being 53%Ecofys (2014). It is assumed that the heat required to generate steam is fixed and equal to the latent heat of vaporisation of water , according to of Standards & Technology (1996) $\Delta h_{vap} = 2065.8\text{kJ/kg}$. the price of electricity is estimated to be around £50 per MWh from the UK electricity wholesale prices Ofgem (n.d.).

5.1 Problem Initialisation

$$\min_{u \in U} G_0(u) := 0.0152F_{steam} - 0.0413F_{CO_2} + 6.16 * 10^{-5}(F_{pumpJ101} + F_{pumpJ100}) \tag{21}$$

$$G_1(u) := x_{outlet,CO2} - 0.02 \leq 0$$

$$F_{steam} = f(u_{reb})$$

$$F_{CO2} = f(u_{reb}, u_{bottoms})$$

$$F_{pumps(j101/100)} = f(u_{reb}, u_{bottoms})$$

$$u_{bottoms} \in [1100, 1350]$$

$$u_{reb} \in [300, 320]$$

For the second case study, the 2 decision variables chosen for the system are reboiler duty (reb) of the stripper column and the bottoms flowrate (bottoms) of the absorber because they have an immediate impact on the cost and the lean gas purity. The expected noise is modeled to have a $\sigma = 0.001$ for both the reb and bottoms in the objective function .The expected noise is modeled to have a $\sigma = 0.0001$ for both the reb and bottoms in the constraint function.The trust region parameters are chosen to allow a full step with maximum trust region radius which could not break the Aspen simulation. The trust region parameters of the decision variables are seen on the table below .The typical trust region parameters $\eta_1 = 0.2$, $\eta_2 = 0.8$ and $\gamma_{red} = 0.8$, $\gamma_{inc} = 1.2$ are used from this point on wards.

Table 1: Trust region parameters for decision variables

Symbol	u$_{bottoms}/kghr^{-1}$	u$_{reb}/MJhr^{-1}$
Δ^0	25	1
Δ^{max}	50	2

5.2 Results

The objective function is slightly nonlinear in the graph above in figure 2, this is due to the noise present in the system.

Since the objective function behaves linearly it can be inferred there aren't any stationary points within the range explored in this case study. The lowest value in our system was calculated by running 1000 different points within the range and locating the lowest value which is [0.439] at [300.17,1102.54]. it is imperative to highlight the fact that the constraint is far from the lowest value so it is inactive throughout all the iterations. both algorithms start have the same initial data and parameters. the scatter graphs show that python stops iterating once it reaches the lower

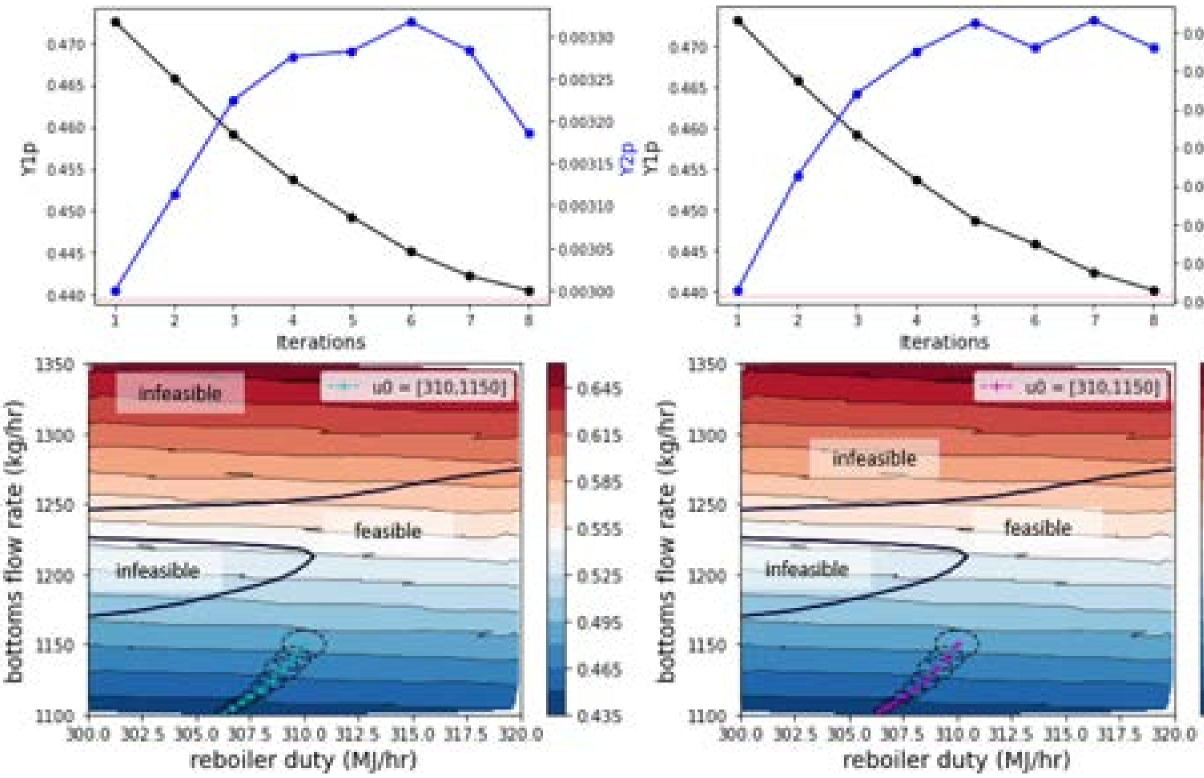

Figure 5: Case Study 2: The contours on the bottom 2 graphs show a decrease in a moderately linear manner from red to blue.constraint is shown in the black curves through the figure.The left 2 graphs are the implementation of algorithm 1 without exploration.The right 2 graphs are the implementation of algorithm 1 with exploration (LCB,β=1.2). The iterations are presented with magenta and cyan points surrounded by ellipsoidal trust regions. the feasible and infeasible regions are also highlighted.Dashed Orange line at the bottom of the scatter graphs represents the lowest value within operating region. The Blue scatter corresponds to the plant constraint whilst the Black scatter is the plant objective.

end of the bottoms flowrate as it would iterate outside the range of input values. but the aspen model struggles to converge outside of the range so the run was stopped, due to this it is known which algorithm operates more effectively.both algorithms iterate towards the direction of decreasing objective function.

6 Conclusions

This paper aimed to build-on previous work Del Rio Chanona et al (2021) on a cutting-edge MA and trust-region-based algorithm. Attempts were first made in case study 1 to develop an intuition of the more MA schemes on an example problem.

This approach also enabled algorithms developed in python to be validated on a simple model prior to implementation on the key CCS problem. Some key insights obtained included: 1) A well-trained GP is a major factor in reducing convergence time and dealing with process noise, 2) Trust region parameters need to be carefully chosen to balance risk and exploration, 3) The most promising algorithms for implementation on the pilot plant were Algorithm 1 with and without LCB, 4) The LCB acquisition function can improve performance when compared to the case without exploration but the Beta parameter needs to be well-tuned to prevent significant deviations from the optimum and slower convergence.

In the second case study it was proven that despite utilising a model-free GP approach for the constraint - the algorithm was able to consistently move in the direction of improving function value. The results were very similar with exploration (LCB) and without.

7 Outlook

A key area of investigation in future work would be to expand the operating region of the Aspen model. As mentioned previously, the convergence issues encountered with the model limited the search space to an area where the problem became almost unconstrained.

As a result, despite observing a decreasing function value it was not possible to confirm whether the algorithms reached a stable optimum. Once this is achieved an interface between the pilot plant and the python algorithm needs to be developed to enable application on the ICCS Pilot Plant.

Furthermore, as the analysis in this paper was conducted with a fixed price of electricity and a carbon price - a sensitivity analysis would be beneficial to understand how the optimum varies in different conditions. Marchetti et al. (2016)

References

Barrett, J., Cooper, T., Hammond, G. P. & Pidgeon, N. (2018), 'Industrial energy, materials and products: Uk decarbonisation challenges and opportunities', *Applied Thermal Engineering* **136**, 643–656.

Chachuat, B., Marchetti, A. & Bonvin, D. (2008), 'Process optimization via constraints adaptation', *Journal of Process Control* **18**, 244–257.

Chanona, E. A. R., Petsagkourakis, P., Bradford, E., Graciano, J. E. & Chachuat, B. (2021), 'Real-time optimization meets bayesian optimization and derivative-free optimization: A tale of modifier adaptation', *Computers and Chemical Engineering* **147**.

Chen, C. Y. & Joseph, B. (2002), 'On-line optimization using a two-phase approach: an application study', *Industrial and Engineering Chemistry Research* **26**, 1924–1930.
URL: *https://pubs.acs.org/doi/pdf/10.1021/ie00069a034*

Dong, L. (2017), 'Viability of simulator for use in operator training and model based control on a carbon capture process'.

Ecofys (2014), 'International comparison of fossil power efficiency and co2 intensity'.

Ferreira, T. D. A., Shukla, H. A., Faulwasser, T., Jones, C. N. & Bonvin, D. (2018), 'Real-time optimization of uncertain process systems via modifier adaptation and gaussian processes', *2018 European Control Conference, ECC 2018* pp. 465–470.
URL: *https://www.researchgate.net/publication/329510908*

Hammond, G. P. & Spargo, J. (2014), 'The prospects for coal-fired power plants with carbon capture and storage: A uk perspective', *Energy Conversion and Management* **86**, 476–489.

Marchetti, A. G., François, G., Faulwasser, T. & Bonvin, D. (2016), 'Modifier adaptation for real-time optimization—methods and applications', *Processes 2016, Vol. 4, Page 55* **4**, 55.

OECD (2016), 'Effective carbon rates on energy'.

of Standards, N. I. & Technology (1996), 'Nist chemistry webbook'.

Ofgem (n.d.), 'Wholesale$_energy_markets_in_2015'$.
URL:

Ion-Conductive Metal Organic Frameworks as Membrane Separators in Zinc-Vanadium Sulphide Batteries

Marius Kornovan and Koray Araz
Department of Chemical Engineering, Imperial College London, U.K.

Abstract

Rechargeable aqueous Zinc-ion batteries (ZIBs) have been under the attention of researchers since 1980 because of Zinc's high abundance, low cost, high energy storage capacity, and environmental friendliness, but have failed to transition from the lab to commercial production. Much effort has been devoted to the exploration of suitable anode and cathode materials for this technology, but very little attention has been paid to finding a suitable membrane which would act as the separator for the battery. Metal Organic Frameworks (MOFs), a class of porous crystalline materials made up of ligands and a central metal ion cluster, could be the answer to the issues present in ZiBs. The focus of this paper is to compare how the alteration of the number of carboxyl functional groups in the ligands of the MOFs, affects the conductivity and performance of the Zn-VS_2 batteries.

Introduction

We are moving towards a new revolution in the energy industry. The climate change crisis is swooping the world unprecedently and new, sustainable technologies have never been in greater demand. As humans are moving from fossil fuel-based energy, we need different energy storage technologies that would power our phones, laptops and electric vehicles (EVs). A big challenge is energy density and since fossil fuels offer such and incredible energy density (Petrol-46MJ/kg), we need to develop a viable alternative.

Currently, the Lithium-ion battery (LIB) market is the largest in sustainable energy storage, capped at over $44B as of 2021 (Springfield, 2020). Despite the success of LIB there are great limitations to this technology associated with its uneven distribution around the world and scarce of source. The lack of environmental friendliness linked to the extraction of this metal, undermines the sustainability of LIBs. Adding the numerous safety issues encountered with this technology such as high toxicity and increased flammability, motivated us to search for alternatives.

Background

An interesting metal that is believed to have great potential of breaking into the energy storage market in the coming decades is Zinc and more specifically it's use in Zinc ion batteries (ZiBs). The key drivers in choosing to focus on this metal are its high abundance (at least 4 times more abundant than Li low redox potential (-0.76 vs SHE) and good chemical stability in aqueous systems. (Abundance, 2021). These make Zn a low cost more eco-friendly alternative to Li since the extraction doesn't require electrolysis. The ZiBs have a high theoretical capacity (820 mA g-1) and offer a two-electron transfer mechanism in electrochemical reactions. And for the taste of environmentalists, Zn is easily recyclable.

To ensure fast diffusion and excellent insertion/extraction of a multivalent ion like Zn^{2+} (diameter - 0.74 A), we chose Vanadium Sulphide (VS_2) as the cathode for our batteries. Vanadium compounds have been under the spotlight in battery research due to their multivalency and open framework crystal structures, which provide high theoretical capacity and a long cycling life. VS_2's structure is composed of a vanadium layer surrounded by two sulphur layers, with an interlayer spacing of 5.67 A. Some VS_2 devices have been reported to deliver 190.3 mA h/g spec cap when used with 1M $ZnSO_4$ electrolyte. Other papers state that certain battery configurations which used VS_2 reached ~80% of initial specific capacity after 2000 cycles (He, 2017).

Despite all the advantages linked to using Zn as the anode in batteries, there are many problems with the metal which contributed to limiting the research and development of rechargeable ZiBs and slowed their transition from the lab to large scale commercial production. Zinc suffers from the formation of non-uniform Zn crystals on the anode, which evolve to dendrides. This usually starts with a decrease in performance, followed by a short circuit. It is crucial to prevent the formation of dendrides as it may lead to risks of fire and explosion.

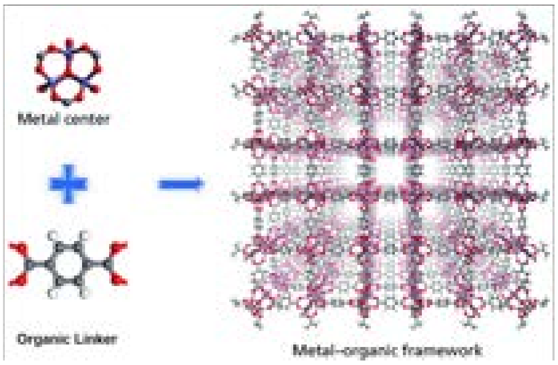

Figure 1: Metal Organic Frameworks (Bell, nd)

Fortunately, in 1990 a scientist named Yaghi defined a new type of materials – Metallic Organic

Frameworks (MOFs).(Hailan, nd) MOFs are a class of porous crystalline materials. Made up of two main components: organic linkers and metal ions, they are synthesized by bonding organic ligands to a central metal ion cluster such as $ZrClO.8H_2O$ via coordination bonds (Wei, 2021) Figure 1 shows the structure of a typical metal organic framework. The skeleton and physical characteristics are largely driven by the ligands used, synthesis method and reaction conditions (Wei, 2021). MOFs are known to have high specific surface area, low-density well-defined pore size distribution and very high porosity. All these characteristics can be designed and controlled.

MOFs can solve the issues of Zn metal anodes. The framework has an abundance of active sites in its structure. This helps to homogenise the Zn^{2+} flux and promote uniform Zn deposition, reducing the issues associated with dendride formation on the anode. Furthermore, the transport of Zn^{2+} can be controlled thanks to the open channels inside the MOF structure. (Wei, 2021) (Yuan, 2018) (Zou, nd).

UiO-66, a new type of MOF, offers a relatively highly conductive structure and an easy lab scale synthesis pattern that can be further investigated for the use of these separators. Consisting of H_2Bdc ligands attached to the Zirconium metal node, UiO-66 utilizes the highly conductive nature of the carboxylic functional groups to create coordination complexes that offers strategic ion transport channels (Wang, 2018)

Methods

Synthesis of UiO-66 and its derivatives

To investigate the ionic conductivity, battery performance, and activation energy by varying ligands coordinated to the MOF membranes, telephtalic acid, trimesic acid, pyromellitic acid, and 3-sulfobenzioc acid were coordinated to the zirconium metal cluster. The chemical drawings of these ligands can be seen in Figure 2 below.

Telephtalic Acid	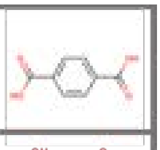
Trimesic Acid	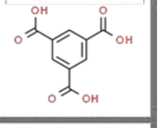
Pyromelitic Acid	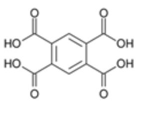
3-Sulphobenzoic Acid + Na⁺	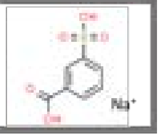

Figure 2 shows the chemical structures of each ligand used (Merck, nd)

When combined with zirconium chloride octahydrate ($ZrClO.8H_2O$), these ligands would respectively form a MOF membrane with one carboxyl, two carboxyl, three carboxyl, and a carboxyl attached with a sulfate group coordinated to the zirconium metal. Pre-dissolved in a hydrochloric acid and glacial acetic acid solution, zirconium chloride octahydrate was mixed with each ligand dissolved in anhydrous dimethyl formamide (DMF) at a molar ratio of 1:1.4. The resulting solution was placed in the oven at 100 °C for 2 hours to form the coordinated MOF gels.

Subsequently, the obtained gels were dissolved in DMF and centrifuged for 10 minutes at 7000 rpm to ensure a faster separation of the gels from the solvent than would've been achieved by gravity separation. The DMF solvent was discarded, and the gels were put through two more cycles of washing and centrifugation. 3 subsequent washing cycles with Ethanol followed.

The resulting product was dried in a vacuum oven at 100 C for 48 hours to ensure complete dehydration. The dried samples were grinded using a pestle and mortar to obtain a fine powder. Prior to pelletisation, the dried products were bound with polytetrafluoroethylene (PTFE) agent. This was done to reduce brittleness of samples during the pelletisation process and avoid formation of cracks. The PTFE and the MOF powder were mixed at a 20:80 weight ratio. The mixture was dissolved into a homogeneous suspension using Isopropyl Alcohol (IPA). Using a heat gun, the mixture was dried to form a thick paste. The paste was covered with wind paper and rolled as a thin sheet. The resulting sheet was dried in a vacuum oven at 100 °C for 2 days. The sheets were cut in a disc shape and pelletized using mechanical pressure of 15 tons. The desired MOF membrane pellets were obtained.

Ionic Conductivity and Energies of Activation

The ionic conductivities and the activation energies of the MOF membranes were analyzed using Electrochemical Impedance Spectroscopy (EIS). Pellets were left in distilled water overnight prior to the EIS analysis. Using a Randles equivalent circuit model, the EIS analysis was run first at room temperature, then repeated at temperatures between 30 °C to 80 °C with 10 °C increments. Figure 3 shows the equivalent circuit model used for the EIS analysis, where R_s represents the Ohmic resistance and R_{ct} represents the membrane resistance of the samples (Sekar, 2020). Z-Fit analysis was carried out to find the resistance of each membrane. The Ohmic resistance for each membrane was assumed to be negligible because of its relatively low value when compared to the membrane resistance.

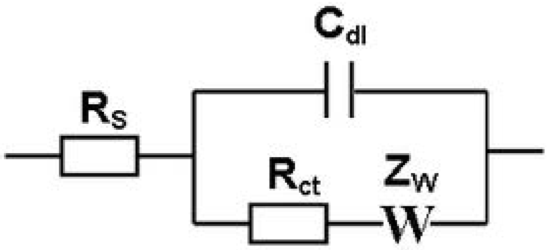

Figure 3 shows the Nyquist plots used in the EIS analysis. (Sekar, 2020)

The real impedance against the imaginary impedance was plotted for all the samples at varying temperatures. The ionic conductivities were calculated using Equation 1 where σ is the ionic conductivity, L is the thickness of the membrane, R is the membrane resistance, and A is the membrane's surface area (Porcarelli, nd):

$$\sigma = \frac{L}{R * A} \quad (1)$$

Furthermore, once the ionic conductivities of the samples were calculated, the Arrhenius plots of each sample were plotted. Through the plots, the activation energies of the MOF membranes were also obtained through the Vogel-Tamnar-Futel Equation (Equation (2)) where R is the gas constant, T is temperature in Kelvins. (Porcarelli, nd)

$$\log \sigma = -\frac{E_a}{R}\frac{1}{T - T_o} \quad (1)$$

Battery Performance

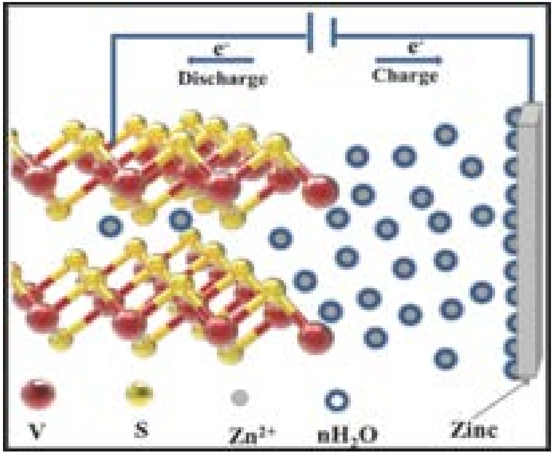

Figure 4: Diagram of a VS||Zn battery (He, 2017)

The charging/discharging capacities of the samples were tested to further investigate how the varying ligand groups contained in the membrane, affects the performance of the battery. A mixture of VS_2 (80%), carbon, PTFE, and titanium was used as the cathode. Zinc metal was used as the anode. Figure 4 shows the diagram of the Zn||VS batteries used. Prior to the charging/discharging cycles, MOF pellets were soaked in a 1M $ZnSO_4$ solution for 1 day. The batteries were compressed and put in the charging/discharging station, where it ran for 100 cycles.

A common metric that is widely used for the analysis of Battery Performance is Coulombic Efficiency (CE). CE represents the current efficiency and describes the charge efficiency by which the electrons are transferred in the cell (Yaghi, 2021)

The electrochemical equations used in this report are laid out below (He, 2017).

a) *Cathode:*

(1) $VS_2 + 0.09\,Zn^{2+} + + 0.18\,e^- \leftrightarrow Zn_{0.09}VS_2$

(2) $Zn_{0.09}VS_2 + 0.14\,Zn^{2+} + 0.28\,e^- \leftrightarrow Zn_{0.23}VS_2$

a) *Anode:*

(3) $Zn^{2+} + 2e^- \leftrightarrow Zn$

Results

Characteristics

Each sample was analysed with XRD analysis to better understand their structures

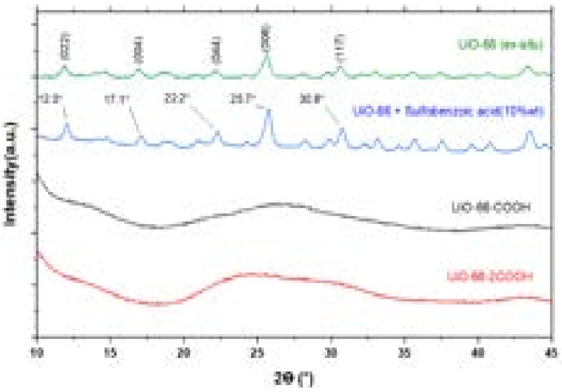

Figure 5 shows the XRD peaks of the samples.

Figure 5 shows sharp and well-defined peaks for the samples of UiO-66 and mix of UiO-66 + 3-sulphobenzoic acid. This indicates that the two samples acquired a crystallographic structure and since they have matching peaks, they have very similar morphology. The main peaks were observed at 12.0°, 17.1°, 22.2°, 25.7° and 30.8° with crystal configurations (022), (004, (044), (006) and (117) respectively in the Raman plots. However, the bottom two graphs which correspond to UiO-66-COOH and UiO-66-2COOH show smooth curves with almost no sharp peaks. This confirms that these two samples did not form a crystalline structure and formed amorphous structures instead.

To further analyse the contents of the samples, FTIR spectra were done on each sample. Figure 6 shows the FTIR analysis of the 4 samples.

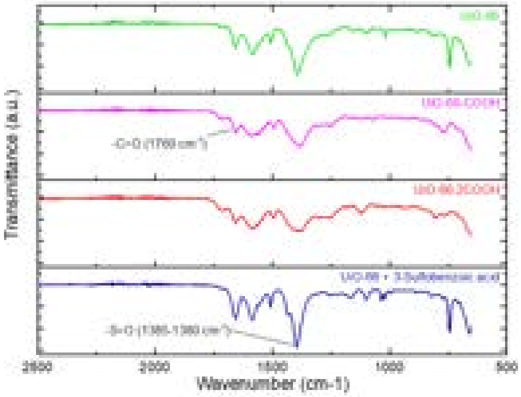

Figure 6: FTIR curves of the 4 samples

For all the samples, the spectra show the characteristic -CH_2=CH saturated double bond peak around 1650-1566 cm^{-1}. Additionally, each sample shows a strong peak around 1760 cm^{-1}, where the C=O bond in the carboxylic group is expected. This evidently confirms the coordination of carboxyl groups in all the samples analysed. When compared to the other samples, UiO-66 + sulphate group shows a significant peak around 1415-1380 cm^{-1} where -S=O stretching occurs. As all the samples also contains C-H bonds which peaks mediumly around 1385-1380 cm^{-1}, a peak around the same range as the S=O stretching is present. However, compared to the other samples, UiO-66 + sulphate group shows a very strong peak which is expected for a sulphate group coordinated to the ligand. Therefore, the FTIR spectra further confirms the existence of the sulphate groups in the sample (Wang, 2018).

Electrochemical Properties

After the synthesis of UiO-66, UiO-66-COOH, UiO-66-2COOH, and UiO-66 + sulphate group, each sample was analysed using EIS. When using any type of solid-sate electrolytes, ionic conductivity is a prominent parameter. Using a Randles Cell with Walburg Impedance equivalent circuit scheme, each samples' impedance values were graphed, and their membrane resistances were calculated. Figure XX shows UiO-66-COOH's impedance values with ranging temperatures from 30ºC to 80ºC. As expected, each sample became more conductive with increasing temperatures.

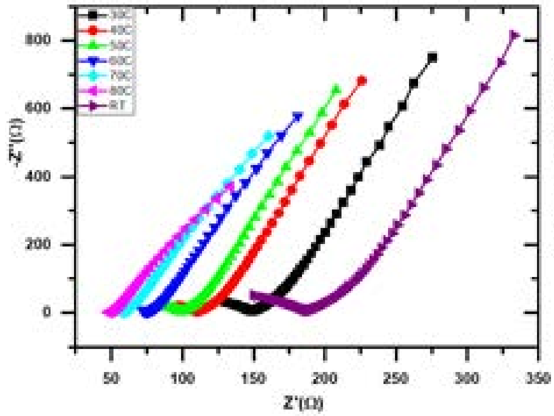

Figure 7: UiO-66-COOHs' ionic conductivities at temperatures ranging from 30ºC to 80ºC.

By analysing the correlation between UiO-66, UiO-66-COOH, and UiO-66-2COOH, the ionic conductivities of each sample increased with the additional carboxyl group attached to the ligand. At all temperatures, UiO-66-2COOH attains higher ionic conductivity values, followed by UiO-66-COOH, and UiO-66. Figure 8 shows the Arrhenius plots for our 4 samples.

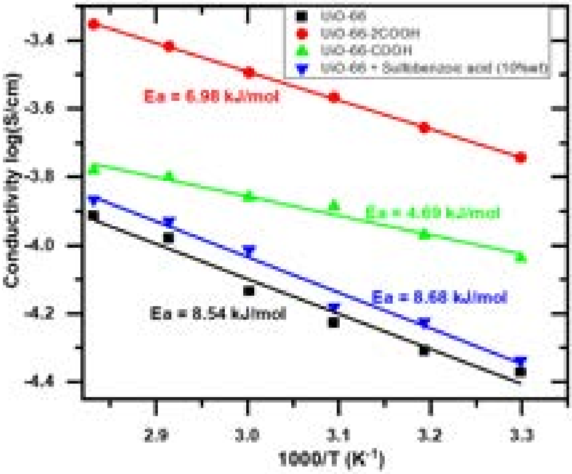

Figure 8: The Arrhenius plots of the 4 samples.

With each additional carboxylic group coordinated to the metal, the ionic conductivity has increased. For example, UiO-66 showed a conductivity value of 1.2 x 10^{-4} (S/cm) at 80°C, whereas at the same temperature, UiO-66-2COOH showed a conductivity value of 4.4 x 10^{-5} (S/cm), almost 3.6 times greater than the control sample.

Even with the low levels (10%wt) of sulphate group present in the MOF, it can be clearly seen that the addition of the sulphate groups has increased the ionic conductivity. Almost at all temperatures, the mix with the sulphate group outperforms UiO-66. This is due to the additional sulphate group contained in the ligand. This additional group creates a more conductive ion transport channel within the membrane and improves the ionic conductivity.

By using the VTF equation, the samples' energies of activation were calculated for UiO-66, UiO-66-COOH, and UiO-66-2COOH. As UiO-66 + sulphate group offers a different chemical structure and a different functional group, the activation energy analysis was done on the ligands with the same functional groups. Activation energies of the samples obtained by the VTF equation indicates the energy barrier each sample has for ion transport through their frameworks. Both UiO-66-COOH and UiO-66-2COOH attained low values of activation energies of 4.69 kJ/mol and 6.98 kJ/mol, respectively when compared to UiO-66 at 8.54 kJ/mol.

Battery Performance

The cycling performances of UiO-66, UiO-66-COOH, UiO-66-2COOH and UiO-66 + sulphate group were tested using galvanostatic measurements at a current density of 500 mA g^{-1} in the potential range of 0.2 – 1.1 V at room temperature.

Figure 9 below shows the charge/discharge curves for the four different MOFs. The UiO-66 membrane delivered an initial discharge and charge capacities of 71.2 and 26.7 mAh/g, respectively, and an initial coulombic efficiency (CE) of 35%. The UiO-66-COOH pellet provided 193.2 and 49.9 mAh/g of discharge and charge capacities and CE of 25.8%, when UiO-66-2COOH showed an initial performance of 297.7 and 93.8 mAh/g respectively, resulting in a CE of 31.5%. At the same time, the UiO-66 + sulphate group sample performed at an initial CE of 32.7% and charge/discharge of 112.1 and 36.7 mAh/g. An initial overview suggests that UiO-66-2COOH had the highest initial output, despite a low initial CE.

The Coulombic Efficiencies after 100 cycles reached 97.5%, 93.2%, 96.2% and 98.8% for UiO-66, UiO-66-COOH, UiO-66-2COOH and UiO-66 + 3-sulfobenzoic acid, respectively.

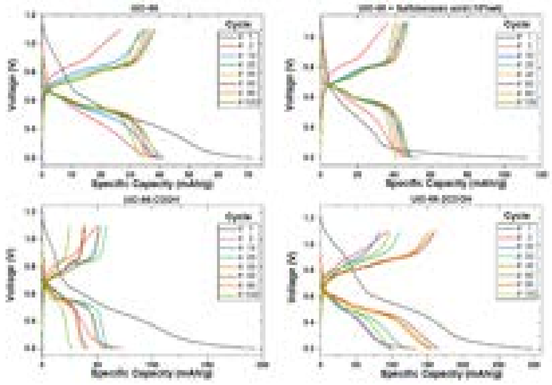

Figure 9: Galvanostatic Charge/Discharge curves for each battery

The galvanostatic charge-discharge (GCD) curves in Figure 10 display the oxidation/reduction plateaus for vanadium redox conversion due to the possible insertion/extraction of Zn2+ inside the battery system.

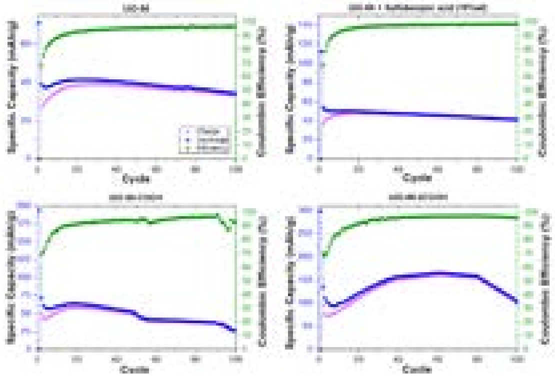

Figure 10: Specific Capacity and Coulombic efficiency with number of cycles for each membrane

Discussion

Characteristics

As shown in the results section, UiO-66-COOH and UiO-66-2COOH failed to form a crystalline structure. This was most probably because of the palletisation and the grinding of the powders. Excess grinding has caused the powders to lose their crystalline structures. These results may have also caused by the reaction rates and the temperature needed for reaction. As the synthesis methods for UiO-66 were used for both UiO-66-COOH and UiO-66-2COOH, there may have been some lack of reaction temperature which may have altered the crystalline nucleation during the synthesis.

Ionic Conductivity

Metal Organic Frameworks allows ion transport through the existence of coordination complexes formed between the metals and the ligands attached to the central metal (Xie, nd). Each ligand used for the MOF samples UiO-66, UiO-66-COOH, UiO-66-2COOH, and UiO-66-SO3Na, contain 2 carboxylic groups, 3 carboxylic groups, 4 carboxylic groups, and a sulphate group in addition to the one carboxylic group attached to the benzene in each ligand.

When new functional groups were added to the zirconium metal node, new means of ion transport were created. Both functional groups, carboxyl and sulphate groups, are highly conductive. With their conductive structure, these functional groups coordinate to the metal node and create a conjugation pathway between neighbouring complexes. This allows easy and controlled ion transfer through the metal organic framework. As discussed in the Results section above, each new functional group added increased the conductivities of the samples.

This is also shown with each sample's activation energies. Activation Energies talk about the energy barrier for ion transport through the metal organic framework. Confirming the EIS results for our samples, both UiO-66-COOH and UiO-66-2COOH attained low values of activation energies compared to UiO-66. This also further confirms the existence better ionic transport channels within these derivative structures. A difference could also be caused by the morphologies of the structures. Both UIO-66-COOH and UiO-66-2COOH have an amorphous structure and lower activation energies whereas UiO-66 has a crystalline structure and similar activation energies. However, to better understand this difference in morphologies, further analysis, such as running the same calculations with both amorphous and crystalline structures of these samples, will be required.

Battery Performance

It can be seen in Figure 10 that the charging and discharging curves for all samples go through a specific capacity maximum after the initial cycles. This can be related to the gradual activation of the electrodes (Zhang, 2015). It can also be observed that the gap between charging and discharging curves decreases with the number of cycles, which results in an increase in Coulombic Efficiency.

The fact that the discharge curve in Figure 10 is always above the charge one indicates a certain degree of polarization linked to electrochemical performance (Prakas, nd).

The reason for a low initial CE could be attributed to a high degree of electrochemical irreversibility, the formation of Solid Electrolyte Interface (SEI) layers linked to the decomposition of the electrolyte and adverse side reactions (Li, 2020). Other reasons for the decreasing specific capacities could be linked to the passivation of the anode due to corrosion. This leads to a surface passivation layer (ZnO, $Zn(OH)_2$ and zincates) and increases the impedance of batteries.

The charge/discharge capacities for UiO-66, UiO-66-COOH and mix of UiO-66 with sulphobenzoic acid strictly saw an increase until cycle 20, followed a decrease in capacity. The charge/discharge capacities for UiO-66-2COOH increased until cycle 60, and then began decreasing. UiO-66 and mix with sulphobenzoic acid showed the most stable trends in the battery performance tests. This could be linked to the successful formation of crystallographic structures in the two samples and the structured pores that offer more reliable ion transport channels. The VS_2 cathode provides excellent Zn^{2+} ion extraction/insertion dynamics during the discharge/charge process (Zhang, 2015)

Conclusions

Metal Organic Frameworks promise a reliable future on clean, stable energy storage. UiO-66, a metal organic framework with Zirconium metal attached to H_2Bdc ligands, is a type of these membranes that offers a prominent ion transport pathway. This paper focused on improving the ways that UiO-66 transfer ions through its channels by adding new functional groups to the metal organic framework. As hypothesized earlier on, it was expected that with each new functional groups added to the Zirconium framework, the membranes would create new, stronger ion channel pathways and they would achieve a higher value of ionic conductivity. As a result, UiO-66-2COOH, having 2 additional carboxylic groups attached to it offered the highest ionic conductivity followed by UiO-66-COOH. The addition of a sulphate group also developed new ways of ion transport and increased the ionic conductivity of UiO-66. As for battery performance, all membranes performed well in the battery performance tests, reaching a high Coulombic Efficiency (CE) after the first 100 cycles.

UiO-66 and the mix of 3-sulfobenzoic acid showed the most stable trends in the battery performance tests. It can be said with certainty that the cell with UiO-66-2COOH showed the highest initial discharge capacity when compared to the other membranes.

For further research, a study of morphologies and how the amorphous or crystalline structure would affect the ways of ion transport is needed for further investigation. Additionally, new ligands with new functional groups can be tested and analysed.

Acknowledgements

We would like to thank PhD. Rui Tan for mentoring and supporting us throughout this research project.

References

“(PDF) Super Soft All-Ethylene Oxide Polymer Electrolyte for Safe All-Solid Lithium Batteries.” *ResearchGate*, https://www.researchgate.net/publication/291420588_Super_Soft_All-Ethylene_Oxide_Polymer_Electrolyte_for_Safe_All-Solid_Lithium_Batteries.

“Abundance of Elements in Earth's Crust.” *Wikipedia*, Wikimedia Foundation, 5 Nov. 2021, https://en.wikipedia.org/wiki/Abundance_of_elements_in_Earth%27s_crust.

“Abundance of Elements in Earth's Crust.” *Wikipedia*, Wikimedia Foundation, 5 Nov. 2021, https://en.wikipedia.org/wiki/Abundance_of_elements_in_Earth%27s_crust.

“Basics of Electrochemical Impedance Spectroscopy.” *Basics of EIS: Electrochemical Research-Impedance*, https://www.gamry.com/application-notes/EIS/basics-of-electrochemical-impedance-spectroscopy/.

Bell, David S. *The Promise of Metal–Organic Frameworks for Use in Liquid* ...https://www.researchgate.net/publication/325824373_The_Promise_of_Metal-Organic_Frameworks_for_Use_in_Liquid_Chromatography.

Berger, Michael. “What Is a MOF (Metal Organic Framework)?” *Nanotechnology*, 2 July 2021, https://www.nanowerk.com/mof-metal-organic-framework.php.

Berger, Michael. “What Is a MOF (Metal Organic Framework)?” *Nanotechnology*, 2 July 2021, https://www.nanowerk.com/mof-metal-organic-framework.php.

Cuia, Yanhui, et al. “Quasi-Solid Single Zn-Ion Conductor with High Conductivity Enabling Dendrite-Free Zn Metal Anode.” *Energy Storage Materials*, Elsevier, 7 Jan. 2020, https://reader.elsevier.com/reader/sd/pii/S2405829720300039?token=CE9B431CD859C7377620ED3B4FA8170352D82C324F1963CA27BC259DAD6B9D5D399A685555303C68DF47EF6914286E65&originRegion=eu-west-1&originCreation=20211129221241.

Hailan Lee. “Hydrothermal Synthesis of a Metal-Organic Framework Containing Large Rectangular Channels.” *ACS Publications*, https://pubs.acs.org/doi/abs/10.1021/ja00146a033.

He, Pan, et al. “Layered VS2 Nanosheet-Based Aqueous Zn Ion Battery Cathode.” *Wiley Online Library*, John Wiley & Sons, Ltd, 6 Jan. 2017, https://onlinelibrary.wiley.com/doi/10.1002/aenm.201601920.

He, Pan, et al. “Layered VS2 Nanosheet-Based Aqueous Zn Ion Battery Cathode.” *Wiley Online Library*, John Wiley & Sons, Ltd, 6 Jan. 2017, https://onlinelibrary.wiley.com/doi/10.1002/aenm.201601920.

Li, Xin, et al. “Review on Comprehending and Enhancing the Initial Coulombic Efficiency of Anode Materials in Lithium-Ion/Sodium-Ion Batteries.” *Nano Energy*, Elsevier, 25 July 2020, https://www.sciencedirect.com/science/article/pii/S2211285520307217.

“Merck.” *Merck | United Kingdom*, https://www.sigmaaldrich.com/GB/en.

Pracas, Samanta. “Metal–Organic Framework-Derived Sea-Cucumber-like fes2@c Nanorods with Outstanding Pseudocapacitive Na-Ion Storage Properties.” *ACS Publications*, https://pubs.acs.org/doi/ipdf/10.1021/acsaem.8b01239.

Sebastian Anthony - Aug 18, 2016 12:52 pm UTC. “Tesla Model S Battery Bursts into Flames, Car ‘Totally Destroyed’ in 5 Minutes.” *Ars Technica*, 18 Aug. 2016, https://arstechnica.com/cars/2016/08/tesla-model-s-france-battery-fire/.

Sekar, Narendran, and Ramaraja Ramasamy. “Figure 2: (a) Representation of Randles Circuit, (b) Its Characteristic...” *ResearchGate*, 30 Sept. 2020, https://www.researchgate.net/figure/a-Representation-of-Randles-circuit-b-its-characteristic-Nyquist-plot-c-Randles_fig15_257651671.

Springfield, Cary. “The Outlook for the Global Battery Market.” *International Banker*, 5 Oct. 2021, https://internationalbanker.com/brokerage/the-outlook-for-the-global-battery-market/#:~:text=A%20March%202021%20report%20from,%2444.2%20billion%20to%20%2494.4%20billion.

Wang, Zhinan, et al. “Covalently Linked Metal–Organic Framework (Mof)-Polymer All-Solid-State Electrolyte Membranes for Room Temperature High Performance Lithium Batteries.” *Journal of Materials Chemistry A*, The Royal Society of Chemistry, 15 Aug. 2018, https://pubs.rsc.org/en/content/articlelanding/2018/ta/c8ta05642k.

Wang, Zhinan, et al. “Covalently Linked Metal–Organic Framework (Mof)-Polymer All-Solid-State Electrolyte Membranes for Room Temperature High Performance Lithium Batteries.” *Journal of Materials Chemistry A*, The Royal Society of Chemistry, 15 Aug. 2018, https://pubs.rsc.org/en/content/articlelanding/2018/ta/c8ta05642k.

Wei, Chuanliang, et al. “Metal-Organic Frameworks and Their Derivatives in Stable Zn Metal Anodes for Aqueous Zn-Ion Batteries.” *ChemPhysMater*, Elsevier, 26 Oct. 2021, https://www.sciencedirect.com/science/article/pii/S2772571521000036.

Xie, Lilia. “Electrically Conductive Metal–Organic Frameworks.” *ACS Publications*, https://pubs.acs.org/doi/abs/10.1021/acs.chemrev.9b00766.

Yaghi, O.M., and Hailan Li. “BU-808C: Coulombic and Energy Efficiency with the Battery.” *Battery University*, 4 Nov. 2021, https://batteryuniversity.com/article/bu-808c-coulombic-and-energy-efficiency-with-the-battery#:~:text=Coulombic%20efficiency%20(CE)%2C%20also,battery%20over%20a%20full%20cycle.

Yuan, Shuai, et al. “Stable Metal–Organic Frameworks: Design, Synthesis, and Applications.” *Wiley Online Library*, John Wiley & Sons, Ltd, 12 Feb. 2018, https://onlinelibrary.wiley.com/doi/10.1002/adma.201704303.

Zhang, Kai, et al. “Fese2 Microspheres as a High-Performance Anode Material for Na-Ion Batteries.” *Wiley Online Library*, John Wiley & Sons, Ltd, 20 Apr. 2015, https://onlinelibrary.wiley.com/doi/abs/10.1002/adma.201500196.

Zou, Ruiqanq, et al. “Metal–Organic Framework-Based Materials for Energy Conversion and Storage.” *ACS Publications*, https://pubs.acs.org/doi/10.1021/acsenergylett.9b02625.

Factors that affect Relaxation time of Shake-Gels

Yuzi Hong, Tongyu Zhao

Department of Chemical Engineering, Imperial College London, U.K

Abstract

The aqueous mixture of colloidal silica nanoparticles and polyethylene oxide (PEO) undergoes notable solidification when external shear is applied. It transits from semi-transparent liquid to opaque solid and returns to the liquid state after the shear is removed for a period. This project aims at understanding the relaxation process of solidified colloidal silica nanoparticles and polyethylene oxide (PEO) mixture through a parametric study. We selected 3 parameters that might affect the relaxation: PEO concentration, silica concentration and temperature. The process was monitored by taking viscosity readings over time with a rheometer, using different samples.

The nature of the mechanism itself was evaluated by studying their common trends in the changes in viscosity. According to the data obtained, all the factors that we considered have strong impacts on relaxation time. We discussed the effect of each of them by comparing their relaxation processes and relaxation times. Our results demonstrated that silica-PEO gel could only be formed within a certain polymer/silica concentration range, and the relaxation of silica-PEO gel is a first-order process that can be speeded up by increasing temperature, using a moderate PEO concentration and a moderate silica concentration. Future improvements, such as methods that can confirm our findings, were also proposed.

Keywords: Shake-gels, Interface, Particle, Polymers, Rheology, Polyethylene oxide (PEO), Relaxation time

1 Introduction

Some mixtures of colloids and polyethylene oxide (PEO) are known to have unique rheologic properties. Apart from typical non-Newtonian behaviours, these suspensions undergo reversible gelation when subjected to external forces. For example, under vigorous shaking, the mixture of disc-shaped clay particles (laponite) and PEO changes its states of matter. In the first stage, it transforms from a semi-transparent watery fluid into a non-transparent solid with high elasticity and viscosity[1]. When the shaking stops, the suspension enters the second stage and slowly returns to its original, watery state. Such mixtures with these unique properties are called ‘shake-gel’, and the two major stages are known as gelation (watery fluid to gel) and relaxation (gel to watery fluid).

The reversibility of this phenomenon has received the attention of many researchers. Several works of literature have been published containing in-depth studies about the mechanisms behind these transitions and methods to control them. The process is governed by the extend of particle adsorption and polymer bridging. The latter refers to adsorption between PEO molecules. Under equilibrium (i.e., not subject to external shear), the PEO particles tend to form random coils, with few silica molecules physically adsorbed to each coil. The bonds between PEO and silica molecules are weak, leading to a dynamic equilibrium with continuous breakage and formation of the bonds. Although adsorption and desorption occur constantly, the overall number of adsorbed molecules is small. Thus, the mixture appears to be in a liquid state. The PEO coils are stretched and deformed when subject to external forces, exposing more active sites susceptible to adsorption. So, polymer bridging is enhanced, and the polymer chain captures more silica molecules. The amount of adsorption is more significant than desorption. As a result, a network of 3D assemblies is formed.

The mixture's viscosity increases as the chains of immobilised particles intertwine across the suspension. Therefore, significant gelation, or shear-thickening behaviour, is observed. An increase in applied shear leads to a greater deformation, resulting in more active sites produced and thus favours the aggregation. When shaking stops, the deformation of PEO chains cannot be sustained. As a result, the thermal energy prevails, and desorption is favoured, causing the system to gradually relax to its equilibrium stage (i.e., liquid state). The process can be controlled by intervening or enhancing bond formation between the molecules. Many previous studies have proposed methods to control gelation, such as introducing soluble chemicals and surfactants[1] or changing the conditions (e.g., pH; temperature; particles size). However, it is often mentioned that many of these studies focused on the gelation stage[234]. At the same time, the analysis of the relaxation process is relatively limited and was sometimes performed ‘by observation’ [5] instead of using organised quantified measurements.

A new formulation of shake-gel has been discovered recently[6]. It consists of PEO nanoparticles and colloidal silica (SiO_2). The latter refers to the aqueous suspension of fine, spherical amorphous, and non-porous silica particles. Although it shows similarities in behaviours under shearing, the mixture is less rigid than the gels made from laponite and PEO and has different gelation/relaxation profiles[5]. The results and properties obtained from other shake-gels do not apply to this colloidal silica-PEO suspension, and it should be tested independently. Different researches on how different physical variables (such as PEO concentration, shear rate, temperature.)[2] affect the gelation process have been conducted for this particular mixture. However, the relaxation process of this suspension has not yet been studied, and the knowledge gap should be filled to provide relevant data and aid future research. Therefore, our primary goal is to gather information and evaluate the relaxation process.

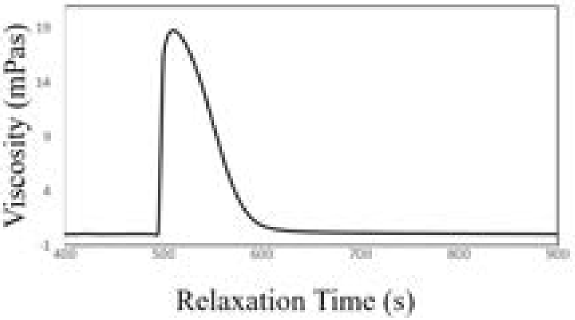

Figure 1. Typical viscosity profile with rapid gelation followed by relaxation. The gelation takes place from 495s to 515s, and the relaxation takes place from 515s to 890s. After the 890s, the sample is at its equilibrium state.

We carried out experiments by recording the viscosity of samples with different compositions subject to changes in the conditions. This paper reports the measurements of relaxation time under different conditions. Furthermore, we analysed and assessed the effects of temperature and particle concentrations (both PEO concentration and silica concentration) on relaxation time. These data help us better understand the characteristics of this aqueous mixture of PEO and silica and the mechanism of its relaxation. We believe the insights are helpful for the industrial application of shake-gels in the future.

2 Experimental

2.1 Materials

This study has two major components used for making shake-gels: silica (LUDOX) solutions and polyethylene oxide (PEO).

LUDOX® TM-50 colloidal silica was purchased from Sigma-Aldrich with 50 wt.% suspension in water. The molecular weight is 60.08 g/mol. The density is 1.4 g/ml at 25°C. The pH is around 9.0, measured with pH paper manufactured by Fisher Scientific (No. 10333501), with an applicable range from7.0 to 10.0. Poly (ethylene oxide) was also obtained from Sigma-Aldrich. It is a solid powder with an average molecular weight of about 900,000Da. The batch number is Lot#MKBS9423V. It contains 200-500 ppm BHT as an inhibitor.

Deionised water obtained from the Millipore-Q System in the analytical lab from the Department of Chemical Engineering, Imperial College London, was used to dissolve PEO clusters before being mixed with silica suspension.

The pH values of the overall mixture were measured with the same batch of pH paper used on colloidal silica samples.

2.2 Solution Formulation Design

According to results from H. Collini et al.[2] and various materials, shake gels only exist for PEO within 0.25-0.50 wt% and silica within 15-35 wt%. No gel is formed below the lower boundary, in which only a weak shear thickening effect is seen. By contrast, permanent gels form above the upper boundary. Formulations designed were based on these ranges to observe all behaviours. PEO concentration was designed from 0.05 wt% to 0.70 wt%, while Silica concentration is controlled from 15 wt% to 35 wt%.

2.3 Sample Preparation

Deionised water was used for solution preparation and suspension of silica and PEO molecules.

All samples were made from the same procedure, with a total mass of 100g. Deionised water and PEO powder were weighed respectively, according to corresponding formulation compositions designed. PEO powder is added slowly into water under constant stirring with no external heating to prevent the formation of bubbles and agglomeration. LUDOX was then measured and well mixed with previous solutions slowly to produce the final solutions, with their pH-controlled within 9.5-10.0. All solutions were left to relax into a liquid state for 24 hours before conducting experiments. All samples made were tested within two weeks to avoid any changes in the compositions.

From Collini et.al[2], all solutions were made from the same batch of materials to minimise deviations of relaxation time for one formulation. This helped to produce more accurate trends.

2.4 Viscosity Measurement

The viscosity of samples was measured through Thermo Scientific HAAKE MARS 60 Rheometer as a function of time. Since the viscosity of most samples changed significantly when forming gels, a cone and plate geometry with a 2-degree cone angle was chosen for all experiments except for samples that were unable to form gels or thicken under shear. In addition, a concentric cylinder system was preferred for very low viscosity samples to obtain more accurate viscosities.

Initially, the temperature of the instrument was allowed to equilibrate for 120s. Then, the initial shear rate was set at 0.1 s^{-1} for 100s. Viscosity measured from this condition can be considered as the viscosity of the original liquid state sample, which is then used to compare with values relaxed after high shearing. Then 1000 s^{-1} shear rate for 500s was applied to make sure samples form gels on the measuring plate. At the last stage, 0.1 s^{-1} shear rate was applied immediately, and the rheometer recorded the change in viscosity until fully relaxed as a function of time. Time differences calculated between the viscosity of the initial and fully relaxed state were regarded as relaxation time.

3 Results & Discussion

3.1 Phase Behaviours

All samples were in a liquid state before shaking or sheared. 0.1 wt% PEO with 25 wt% Silica showed a weak shear thickening effect in (E-2). For the same 25 wt% Silica, 0.3 wt%, 0.4 wt% and 0.5 wt% PEO were also displayed as (C-2), (B-2) and (A-2) respectively, and all these samples performed shake-gel effects well in Figure.2.

By contrast, (D-2) and (F-2) demonstrated different results. This is due to a large difference in the silica weight percentage of the two samples. The former had agglomeration, while the latter only had a weak thickening effect, both after appropriate shaking.

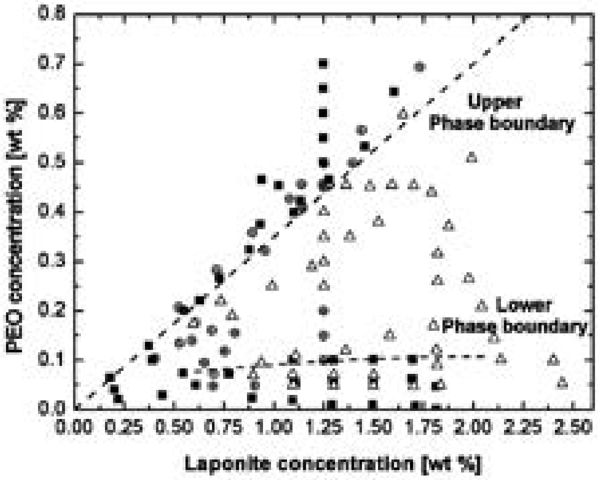

Figure 3. Phase behaviour of laponite/PEO 'shake-gels' results from Zebrowski[5], shake gels formed by vigorous shaking

In Figure.3, the open triangles represent shake-gels that can form after shearing. The circles represent samples that only show the shear-thickening effect and increased viscosity but do not form a gel. Last, the solid squares represent mixtures that have no effect even upon the application of large shear.

Results obtained were nearly consistent with Zebrowski[5] in Figure. 3, which stated that PEO range

Figure 2. Visual observation of relaxation. (A-1) 0.5% PEO, 25% Silica, before shaking, (A-2) after shaking, (B-1) 0.4% PEO, 25% Silica, before shaking, (B-2) after shaking, (C-1) 0.3% PEO, 25% Silica, before shaking, (C-2) after shaking, (D-1) 0.4% PEO, 35% Silica, before shaking, (D-2) after shaking, (E-1) 0.1% PEO, 25% Silica, before shaking, (E-2) after shaking, (F-1) 0.4% PEO, 15% Silica, before shaking, (F-2) after shaking.

from 0.1-0.5 wt% and Silica range from 15-35 wt% show effective shake-gels. Therefore, relaxation time can be analysed by a rheometer to give viscosity changes.

3.2 Effects of PEO Concentration on relaxation time

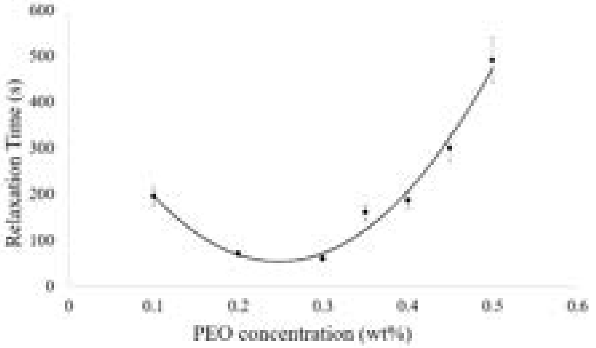

Figure 4. Average relaxation time (s) against PEO concentration (0.1 wt% to 0.5 wt%) with silica concentration 25 wt%, under 25ºC

Other factors were kept constant to investigate the effect of changing PEO concentration on relaxation time. The samples were prepared with their silica concentration (25 wt%) fixed while their PEO concentrations were varied from 0.05 wt% to 1.0 wt%. All measurements were taken under 25°C, and their relaxation time was calculated using the procedure stated in Section 2.4. Figure.4 shows the empirical relationship between PEO concentrations and relaxation time. It should be noted that only readings between 0.1 wt% and 0.5 wt% were used for plotting because data out of this range were considered less reliable. When the concentration was higher than 0.5 wt%, the relaxation time was usually longer than 10 minutes. Considering that the rheometer was not air-tight and only 0.4 ml sample was used for each set of readings, it is highly probable that the viscosity measurements beyond 10 minutes were affected by water evaporation. Therefore, it was decided that reading for higher concentrations should not be used for this part of the analysis. No significant gelation was observed for samples with PEO concentrations less than 0.1 wt%. For example, when the mixture with 0.05 wt% PEO was shaken, it did not undergo solidification despite its notable increase in turbidity. Therefore, any analysis on relaxation would be futile.

The result shows a quadratic correlation between polymer concentration and relaxation time, and the latter reaches a minimum when concentration is around 0.25 wt%. From 0.1 wt% to 0.3 wt%, the relaxation time decreases from 195s to 60s, equivalent to a percentage decrease of 69.23%. However, for higher concentration, the correlation between relaxation time and mass percentage of PEO become strongly positive. From 0.3 wt% to 0.5 wt%, the relaxation time decreases from 60 s to 491s. It can be seen from Figure 4. that the profile is almost symmetric. The relaxation time at 0.4 wt% is 186 s which is very similar to that at 0.2 % (195s). The extrapolated quadratic trendline suggests a more precise estimation of minimum relaxation time. According to its formula, the predicted slowest relaxation would occur at 0.25 wt% with a value of 53.10s.

Because relaxation is the reversed process of gelation, samples that relax slowly are likely to have short gelation times. An intuitive approach would be treating relaxation time as an indicator for silica-PEO complex stability: long relaxation time means high stability, so gelation should be rapid as the formation of such complex is favoured and vice versa. Therefore, the relaxation profile should be precisely the opposite of the gelation profile (i.e., at a specific PEO concentration, the gelation graph peaks when the relaxation graph reaches its minimum). This is true when comparing the general trend in Figure.4 (decrease then increase) with the gelation time profile obtained by H. Collini et al.[2]. It should be noticed that the latter used a higher shear rate of 1600 s^{-1}, which might be the reason these two graphs do not align perfectly.

There have been explanations proposed to explain the observations regarding gelation times[2], which are also helpful for analysing the relaxation process: At low PEO concentrations (<0.1 wt%), the mixture is said to be over-saturated with silica particles[7]. The number of PEO molecules is small, so when shear is applied, the number of PEO-silica complexes is also tiny. There is no gelation because the PEO-silica chains are overwhelmed by free silica molecules. Therefore, although changes in turbidity were observed, the suspension remained in the liquid state. When the PEO concentration is high enough to make gelation feasible (>0.1 wt%), the number of PEO molecules is large enough to produce robust and elastic 3D assemblies supporting the entire gel structure. However, as the concentration increased even more (towards 0.25 wt%), silica particles started to run into shortage. As a result, the gelation was slowed down because the lack of available silica particles reduced the probability of PEO-silica adsorption. More time was required to achieve complete gelation, which means a decrease in relaxation time. For even higher PEO concentrations (0.25 wt% to 0.5 wt%), the adsorption sites released from the deformation of PEO coils were more likely to attract other PEO molecules rather than free silica particles. Polymer bridging outweighed PEO-silica adsorption, and it sped up the gelation process, which led to an increase in relaxation time.

At extreme high PEO concentrations, the bridging effect was strong enough to produce irreversible, permanent gels[2]. In conclusion, the changes in relaxation time under different PEO concentrations were caused by the changes in the stability of the gel structure.

3.3 Effects of Silica Concentration

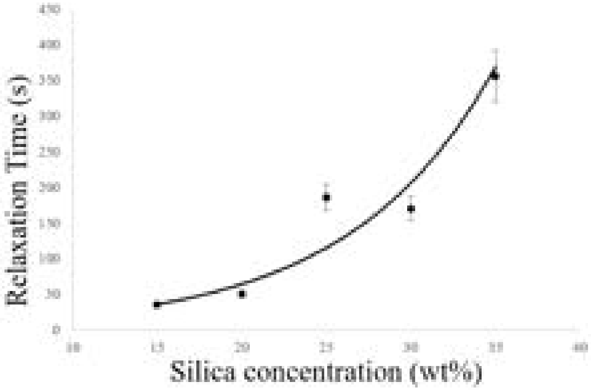

Figure 5. Average relaxation time (s) against silica concentration (15 wt% to 35 wt%) with PEO concentration fixed at 0.4 wt%, under 25°C

Samples with their silica mass percentage were varied between 15 wt% and 35 wt% are prepared, with their PEO concentrations kept constant at 0.4 wt%. All results were obtained under 25°C. Concentrations beyond 35 wt% were not studied because their relaxation times were too long and were affected by water evaporation. A similar reason applied for concentrations lower than 15 wt%, where relaxation times were too short. The results were plotted in Figure.5. There is a strong positive correlation between silica concentration and relaxation time. Within this range, any increase in silica concentration leads to a rise in relaxation time, and the impact is more significant for higher silica concentrations.

Slow relaxations indicate stable gels. Using higher silica concentration is, in fact, the introduction of molecules that contributes to assemblies' formation. On the other hand, lowering silica concentration is equivalent to replacing those contributing particles with water molecules, undermining the gel structure by reducing the probability of successful adsorption. This explains the rise in relaxation times as the silica concentration increases. It is noticed that the relaxation profile in Figure.5 is highly similar to the right half (from 0.3 wt% to 0.5 wt%) of Figure.4 from section 2.2, which visualises the effect of changing PEO concentrations. A possible cause may be that both silica and PEO molecules are essential for the cross-linked network of complexes, so introducing either would result in a more stable solid structure that can be reflected by a long relaxation time. Considering that all results used in this section were obtained from samples with 0.4 wt%, it can be concluded that increasing silica concentration has similar, but not necessarily identical, effects as increasing PEO concentration as long as the other is kept constant.

Therefore, according to Figure.5, if silica concentration is increased further, longer relaxation times are expected and finally lead to a formation of permanent gels, as reported by many other pieces of literature[8]. However, when the concentration is too high, the mixture no longer exhibits shake-gel behaviours (i.e., gelation would not be observed). As discussed in section 2.1, when the silica/polymer number ratio is too large, the PEO-silica chains are overwhelmed by free silica molecules; thus, they cannot support the gel structure. Similar predictions can be made for lowering the silica concentration: a decrease in relaxation time followed by loss of shake-gel properties because the samples are too diluted with water. This prediction can be confirmed by other studies[2].

3.4 Effects of Temperature on relaxation time

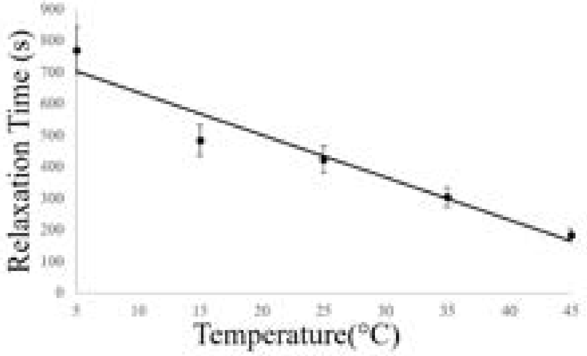

Figure 6. Average relaxation time (s) against temperature (5 °C to 45 °C) with PEO concentration fixed at 0.4 wt% and silica concentration fixed at 25 wt%.

With PEO concentration 0.5 wt% and silica concentration 25 wt%, the relaxation times of the same sample under different temperatures (from 5°C to 45°C) are recorded and plotted in Figure.6. As the temperature increases, the relaxation time decreases approximately linearly. Due to time constraints, experiments with temperatures outside this range were not carried out. Increasing temperature gives rise to kinetic energy, thus causing vibration of the molecules. The rate of desorption is higher because of two reasons. Firstly, the breakage of silica-PEO bonds happens faster because the movements of both molecules have become more vigorous. Secondly, since the PEO molecules have high kinetic energy, they return to their original, random coil, shape at a higher rate and 'squeeze' the silica particles out of the active sites. Such behaviours of PEO molecules and the method for modelling them have been discussed in other studies[9].

Similar trends were observed for gelation time[2], indicating that high temperatures also favour gelation. It may seem contradictory to our results as relaxation/gelation time have been treated as an indicator for gel stability. Nevertheless, the reason for faster gelation time is that the movement of particles increases the chance of adsorption when external shear is applied. Besides, in our experiments, no significant differences were observed when comparing the viscosities of the relaxed sample under different temperatures (i.e., the final viscosity readings of each experiment.). Therefore, high temperatures were merely speeding up the relaxation without altering its nature, similar to the effect of adding catalysts to a chemical reaction. Temperature plays a crucial role in both solidification and relaxation mechanisms and should always be considered, especially for future industrial applications.

3.5 Effects of PEO Molecular Weight on relaxation time

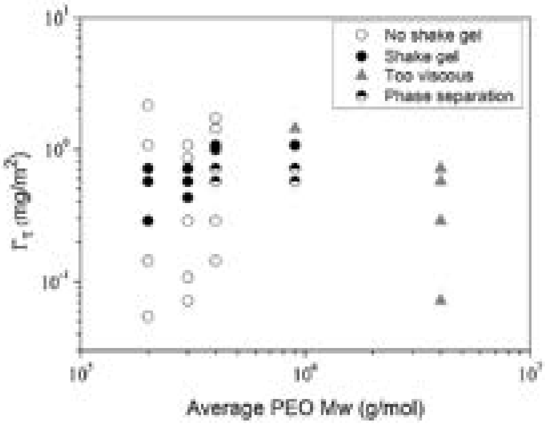

Figure 7. Effect of varying the molecular weight of the PEO on the phase behaviour of the PEO-laponite (laponite concentration 2%)[2].

From the results of Collini et.al[2] and Mar[6], low molecular weight polymers usually need full shaking for at least 10 mins to form a weak gel. The reason is that bridging formation between particles is much harder due to the shorter length of polymer chains. Also, they think the range of concentrations is quite independent of the PEO molecular weight to which the shake gel is formed, as shown in Figure.7. A shake gel can be formed when the PEO concentration ranges between 0.5 and 1 mg/m^2.

The relaxation time of higher molecular weight was longer[6] because PEO polymer with longer chains can attach onto silica at more points, connect with more particles, and form stronger networks. Consequently, the binding between PEO and silica nanoparticles are more stable.

PEO Molecular weights of 900,000 g/mol and 2000,000 g/mol were used to investigate the relaxation process of shake gels in this study. 0.5 wt% was preferred as it was the highest concentration for 900,000 g/mol PEO to stay in a liquid or transition state between liquid and gel. For concentrations above 0.5 wt%, permanent gels were discovered in previous results. It was evident that the molecular weight of 2000,000 g/mol PEO formed permanent gel at 0.5 wt%. Therefore, it was hard to conduct further relaxation time analysis by the rheometer. This means that relaxation time can only be analysed for PEO with a molecular weight that can form liquids, not permanent gel.

3.6 Effects of pH on relaxation time

pH is an essential factor that affects the adsorption amount of PEO of other particles and may also influence the adsorption state of polymers[14]. Also, pH determines the charge and zeta potential of silica nanoparticles. Zeta potential is the potential difference between the dispersion medium and the stationary layer of fluid attached to the dispersed particle. The shake gel relates to the electrical repulsion between silica nanoparticles, which will influence the aggregation-dispersion of silica.

HCl and NaOH were chosen to change the pH of samples[14]. For pH below 7.0, the bridging effect was too strong and induced cloudy suspensions. Relaxation time for samples made for pH of 8.4 was longer than pH 9.4. While for pH between 9.5 and 10.0, the relaxation time was nearly the same. No shear thickening effect occurred when pH was greater than 10 since the sample itself was a permanent gel.

3.7 Relaxation orders

A function of logarithm viscosity over time was used to investigate relaxation orders for each formulation. From the modelling of A.A. Lukichev[3], a first-order relaxation process shows a smooth curve: linearity and stationarity. While a second-order shows a damped oscillation. Through his equations and trends, the relaxation orders of all samples can be determined easily.

$\varphi(t)$ is the normalised first-order relaxation function (RF):

$$\varphi(t) = exp - \frac{t}{\tau}$$

where τ is the relaxation time or time constant, this parameter determines the rate of change of the relaxation function.

PEO concentrations from 0.1 wt% to 0.4 wt% with Silica concentration fixed at 25 wt% showed obvious smooth curves respectively in Figure.8, and the slope of log viscosity over time before reaching complete relaxation was nearly constant, demonstrating the first order of relaxation processes. As a result, linear trendlines were drawn, and slope calculated were used for further analysis later.

From 0.45 wt% and onwards, functions performed slightly different from lower concentrations. A weak maximum can be seen for 0.45 wt%, and relaxation function slope first increased for 75s, then decreased with time. The gel formed under high shears relaxed very slowly after 50s for 0.5 wt%. Linear trendlines were also drawn for 0.45 wt% and 0.5 wt% to analyse further and maintain the consistency of the data analysis method. However, their gradients obtained do not represent reality.

One of the reasons that 0.5 wt% performed differently was that samples had gel and liquid mixture even after 24h made, other than only liquids. Therefore, when shear decreased after 500s, some gels could not relax back, then the final level of 0.5 wt% was higher than other samples. Another reason for 0.45 wt% and 0.5 wt% behaving in this way was equipment error. The rheometer was supposed to need some time to transfer to low shearing immediately before measuring its viscosity. As a result, inaccurate data at the beginning of the relaxation process can be ignored.

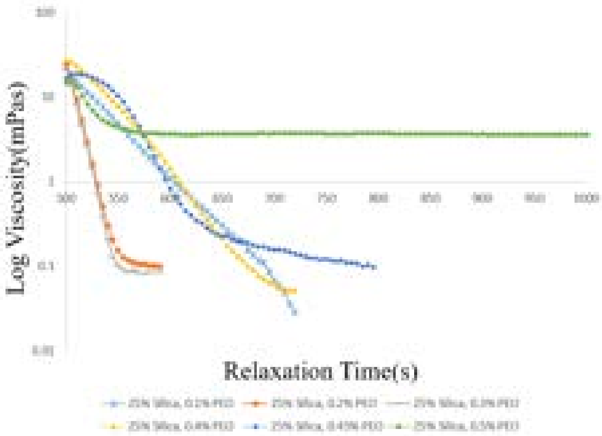

Figure 8. Average Log Viscosity (mPas) against time, with silica concentration fixed at 25 wt% and PEO concentration range from 0.1 wt% to 0.5 wt%, under 25ºC

Similarly, Silica concentrations from 15 wt% to 35 wt% all showed first-order relaxations and were analysed with linear trendlines. However, 35 wt% Silica concentration had a maximum in relaxation as well, and it is evident that the linear trendline does not fit the smooth curve very well. A significant error in this trendline and its slope was not used to show the general trend. Figure.9 also show that for 15-35 wt% silica concentrations, higher wt% requires a longer relaxation time.

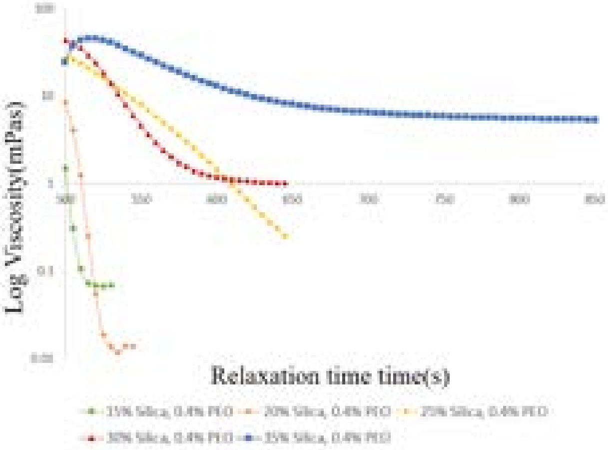

Figure 9. Average Log Viscosity (mPas) against time, with PEO concentration fixed at 0.4 wt% and silica concentration range from 15 wt% to 35 wt%, under 25ºC

Slopes obtained from linear trendlines were plotted with PEO concentrations and Silica concentrations respectively, then quadratic polynomial trendlines were predicted as shown in Figure.8 and Figure.9. In Figure.8, a minimum at approximately 0.25 wt% with a gradient of about -0.048 represented 0.25 wt% PEO concentration had the steepest slope and fastest relaxation speed. This is only suitable for PEO concentrations that can form a shake-gel.

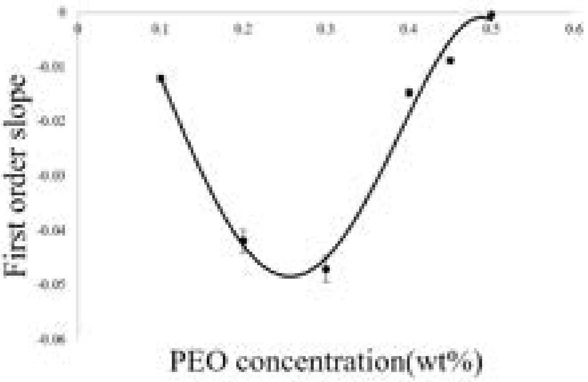

Figure 10. Average first order straight trendline slope (s) against PEO concentration (0.1 wt% to 0.5 wt%) with silica concentration fixed at 25 wt%, under 25ºC

In contrast, the quadratic trendline of Silica concentration also demonstrated a maximum of around 26 wt% Silica with 0.4 wt% PEO concentration, as shown in Figure.11. This shows a positive gradient as silica concentration goes up, and tells that as Silica concentrations increase, linear trendlines have smaller gradients showing a longer relaxation time. Since qualified data points were limited, these two graphs only demonstrate the general trends. The reason for this trend is more bridging formed with large amount of Silica molecules.

However, only a general trend is shown in Figure. 11. More data points experiments should be carried out for more detailed results and functions.

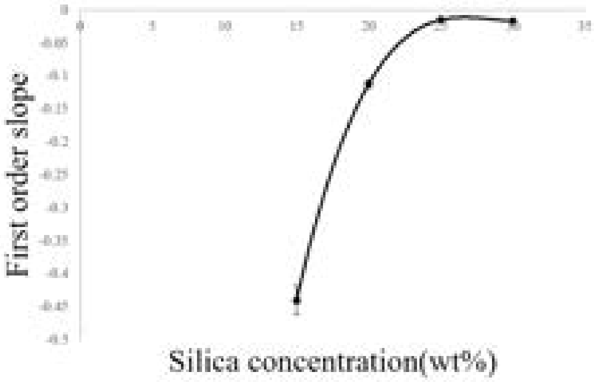

Figure 11. Average first order straight trendline slope (s) against silica concentration (15 wt% to 30 wt%) with PEO concentration fixed at 0.4 wt%, under 25ºC

3.8 Half-Life

The relaxation curve of viscosity over time can be considered as an exponential curve. Half-life is the time required for exactly half of the entities to decay on average, such as radioactive atoms.

For a first-order reaction, the half-life of a reactant is independent of its initial concentration and depends solely on the reaction rate constant, k. This model can be applied to relaxation processes since the mathematical models are nearly identical.

Exponential decay equations were obtained by setting exponential trendlines for each sample.

The half-life for a first-order relaxation process was calculated by

$$t_{\frac{1}{2}} = \frac{ln(2)}{\tau}$$

where τ is the relaxation constant and always a positive number, in this situation, is the coefficient of time for exponential.

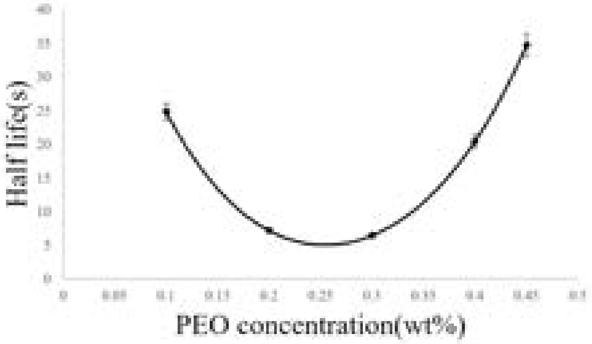

Figure 12. Average Half-life (s) against PEO concentration (0.1 wt% to 0.45 wt%) with silica concentration fixed at 25 wt%, under 25 ºC

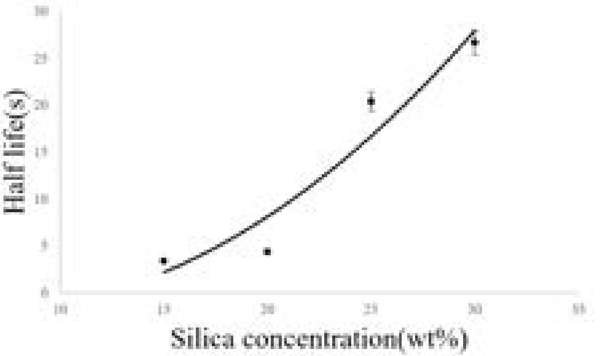

Figure 13. Average Half-life (s) against silica concentration (15 wt% to 30 wt%) with PEO concentration fixed at 0.4 wt%, under 25ºC

The half-life for different PEO concentrations and Silica concentrations were plotted in Figure.12 and Figure.13. Their trends both matched with first-order slope trends and showed similar conclusions about relaxation time. There is a minimum point in Figure.12, 0.25 wt% PEO had the shortest Half-life among all test samples.

4 Conclusions

Specific range concentrations of two main materials, silica solutions (15 wt%-35 wt%) and polyethylene oxide (0.1 wt%-0.5 wt%) can perform a great shake-gel effect, and the corresponding relaxation processes were analysed. In this study, we found that the relaxation time of shake-gels will be affected by concentrations of both Silica and PEO, temperature, the molecular weight of PEO, and pH of sample solutions made. Long or short relaxation time will apply to different functional products in the future. It is hard to decide which relaxation speed is more preferred. If this technology is used in engine oil and helps prevent accidents, slow relaxation speed should be focused on more.

A minimum relaxation time of PEO concentration obtained around 0.25 wt% is well-matched with the trend of results from Collini et.al[2] which stated a peak in gelation time, assuming the bond or bridges forming or breaking speed is nearly constant. Also, it was very significant that relaxation time increases as Silica concentration rises. As an essential factor, temperature leads to lower relaxation times as it goes up since bonds are easier to break, and the kinetic energy of molecules is high. pH between 8.0 and 10.0 can show shake gels, and lower pH in this range has a longer relaxation time. The best performance of shake-gel is pH between 9.5 and 10.0. Furthermore, all our samples performed the first order of relaxation process and modelled to have an exponential rate of decrease of logarithm viscosity.

The effects of molecular weight of PEO on relaxation time was not well-defined from our results due to the direct formation of permanent gels for Mv=2000,000 g/mol. In addition, a polydisperse polymer of average molecular weight 900,000 by blending high and low molecular weight for appropriate concentrations should be carried on with more experiments.

Other measuring methods of viscosity change with a function of time should be tried in the future, such as viscometer. Additionally, new methods of using analytical tools to get more precise viscosities can be discovered or developed.

5 Acknowledgement

We gratefully acknowledge the technical support from Prof. Paul Luckham for valuable discussions and Shawn Lew Jin Hau for practical help.

References

[1] Can, V. and Okay, O., 2005. Shake gels based on Laponite–PEO mixtures: effect of polymer molecular weight. *Designed Monomers and Polymers*, 8(5), pp.453-462. https://doi.org/10.1163/1568555054937917

[2] Collini, H., Mohr, M., Luckham, P., Shan, J. and Russell, A., 2018. The effects of polymer concentration, shear rate and temperature on the gelation time of aqueous Silica-Poly(ethylene-oxide) “Shake-gels”. *Journal of Colloid and Interface Science*, 517, pp.1-8. https://doi.org/10.1016/j.jcis.2018.01.094

[3] Lukichev, A., 2020. Classification of relaxation processes. Generalised equation yielding new relaxation functions. *Journal of Physics and Chemistry of Solids*, 145, p.109539. https://doi.org/10.1016/J.JPCS.2020.109539

[4] Saito, Y., Hirose, Y. and Otsubo, Y., 2011. Effect of poly(ethylene oxide) on the rheological behavior of silica suspensions. *Rheologica Acta*, 50(3), pp.291-301. https://link.springer.com/article/10.1007/s00397-010-0523-0

[5] Zebrowski, J., Prasad, V., Zhang, W., Walker, L. and Weitz, D., 2003. Shake-gels: shear-induced gelation of laponite–PEO mixtures. *Colloids and Surfaces A: Physicochemical and Engineering Aspects*, 213(2-3), pp.189-197. https://doi.org/10.1016/S0927-7757(02)00512-5

[6] Mar Ramos-Tejada, M. and Luckham, P., 2015. Shaken but not stirred: The formation of reversible particle – polymer gels under shear. *Colloids and Surfaces A: Physicochemical and Engineering Aspects*, 471, pp.164-169. https://doi.org/10.1016/J.COLSURFA.2015.02.021

[7] Yan, F., Ye, L. and Qiu, D., 2016. Effect of particle/polymer number ratio on the structure and dynamics of complex between large polymer and nanoparticle. *Colloids and Surfaces A: Physicochemical and Engineering Aspects*, 507, pp.67-75. https://doi.org/10.1016/j.colsurfa.2016.07.080

[8] Liu, S., Lafuma, F. and Audebert, R., 1994. Rheological behavior of moderately concentrated silica suspensions in the presence of adsorbed poly (ethylene oxide). *Colloid & Polymer Science*, 272(2), pp.196-203. https://link.springer.com/article/10.1007/BF00658848

[9] Eshuis, A. and Mijnlieff, P., 1986. Dynamics of poly (ethylene oxide) chains in water. *Polymer*, 27(12), pp.1951-1957. https://doi.org/10.1016/0032-3861(86)90188-6

[10] Deepak Selvakumar, R. & Dhinakaran, S. (2017) Effective viscosity of nanofluids — A modified Krieger–Dougherty model based on particle size distribution (PSD) analysis. *Journal of Molecular Liquids.* 225 20-27. Available from: https://dx.doi.org/10.1016/j.molliq.2016.10.137. Available from: doi: 10.1016/j.molliq.2016.10.137.

[11] Kawasaki, S. & Kobayashi, M. (2018) Affirmation of the effect of pH on shake-gel and shear thickening of a mixed suspension of polyethylene oxide and silica nanoparticles. *Colloids and Surfaces. A, Physicochemical and Engineering Aspects.* 537 236-242. Available from: https://dx.doi.org/10.1016/j.colsurfa.2017.10.033. Available from: doi: 10.1016/j.colsurfa.2017.10.033.

[12] Yi, H. (2021) *Shear-induced Gelation of Aqueous Colloidal Silica Suspensions in the Presence of Poly (ethylene oxide).*

[13] Zhang, Q. & Archer, L. A. (2002) Poly(ethylene oxide)/Silica Nanocomposites: Structure and Rheology. *Langmuir.* 18 (26), 10435-10442. Available from: http://dx.doi.org/10.1021/la026338j. Available from: doi: 10.1021/la026338j.

[14] Huang, Y. & Kobayashi, M. (2020) *Direct Observation of Relaxation of Aqueous Shake-*

Investigating the Effects of N, P Co-doped Porous Carbon Materials with Ni Single Atom Catalysts for the Electrochemical Reduction of CO_2

Shavaiz Mir and Lynn Moe

Department of Chemical Engineering, Imperial College London, U.K.

Abstract

Carbon Capture, Utilisation and Storage (CCUS) technologies have been determined to be an inevitable part of limiting global warming levels according to the Paris Agreement. The electrochemical CO_2 reduction reaction (CO_2RR) has the potential to sustainably produce fuels and other commercial chemicals by using water and renewable energy sources. Heteroatom-doped carbon materials with metal-coordinated active sites have emerged as an interesting field of study as they have proved to be affordable and effective catalysts for the CO_2RR, overcoming previous limitations such as high costs and energy requirements. In this paper, porous materials with good catalytic performance have been synthesised using a simple experimental procedure which can be scaled up to industrial applications. XPS, BET analysis and Raman spectroscopy were employed to characterise the materials, while electrochemical testing shows that Ni-coordinated TAP materials in particular can achieve $CO:H_2$ selectivity ratios as high as 94:1, while P-doping has the potential to produce longer chain carbon products such as 2-propanol.

Introduction

The level of CO_2 in the atmosphere has been steadily increasing since the Industrial Revolution, reaching a monthly average of 419 ppm in 2021, a record high in the last 2 million years.[1] It is almost certain that the increase of CO_2 and the warming of the atmosphere is due to human influence. The IPCC has reported that each of the last four decades has been successively warmer than any other decade since 1850.[2] Global surface temperature in the 2011–2020 decade was 1.09 °C higher than in 1850–1900 (from 0.95 to 1.20 °C), and since 1970, has increased at a rate higher than in any other 50-year period during the last 2000 years.[2] To tackle the issue of global warming, the Paris Agreement was signed in 2015, with the goal of limiting global warming to well below 2, preferably 1.5 degrees Celsius.[3] The IPCC has reported that all pathways that limit warming to 1.5 °C by 2100 with no or limited overshoot requires the implementation of some form of carbon dioxide removal.[4]

Increasing global energy demand is a significant contributor of greenhouse gas. Global energy related CO_2 emissions reached 33.5 Gt in 2018,[5] with the power sector accounting for nearly 40%.[6] While 84.3% of global primary energy comes from fossil fuels,[7] energy consumption is expected to increase 50% by 2050.[8] Carbon Capture, Utilisation and Storage (CCUS) technologies will play an important role in supporting the power transition from fossil fuels to clean energy.[5] These technologies include storing the CO_2 separated from exhaust gases in carbon sinks and utilising it as the source material to produce alternative carbon-based materials.

Among different CCUS technologies, the electrochemical CO_2 reduction reaction (CO_2RR) has the potential to sustainably produce commodity carbon-based chemicals and synthetic fuels by using renewable sources of electricity to power the reaction between captured CO_2 and water.[9,10] The low cost of production for some products provides the financial incentive to produce them from CO_2RR instead of direct purchase from the market. The market price of some of these products and their levelised cost of production from CO_2 are compared in *Figure 1*.[11] Furthermore, surplus energy from intermittent sources such as solar and wind can be stored by this process in the form of carbon-based fuels.[10]

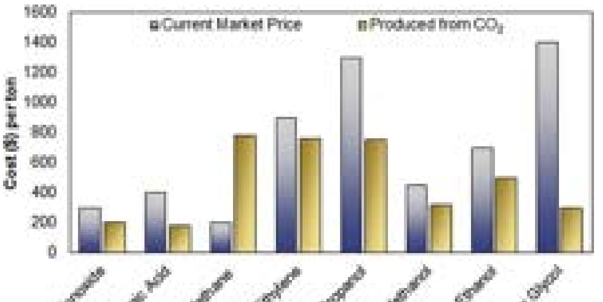

Figure 1: Current market price and levelised cost of production from CO_2 for some carbon-based products; ethylene glycol shows the highest profit margin, followed by propanol (adapted from Bushuyev et al.)[11]

Metal catalysts have been well-studied as effective catalysts for the CO_2RR. One of the most interesting catalysts is metallic copper, owing to its ability to reduce CO_2 into 16 different carbon products such as ethylene and ethanol.[12] This is because the intermediate binding energy of CO on Cu allows effective C-C coupling to take place, producing longer chain carbon products, while preventing catalyst poisoning.[13] However, the low selectivity of Cu, which would lead to high separation costs of the desired product, and the requirement of a high overpotential to drive the rate of reaction limit the use of Cu as a suitable catalyst for industrial scale production.[14]

The production of CO can be accompanied by H_2 to form syngas, which can be converted to synthetic fuels such as methanol via the Fischer-Tropsch process.[15] Electrochemical reduction of CO_2 toward CO is also a less restricted mechanism as it has a relatively simple pathway involving the transfer of only two electrons and two protons.[10] This electrochemical reaction is commonly carried out using precious metals such as gold and silver, as this group of catalysts has demonstrated the largest efficiencies for the CO_2RR toward CO.[10,16,17] However, the use of precious metal catalysts is not optimal in developing affordable industrial scale electrolysers due to the high cost and low availability of such metals in nature.

Carbon materials derived from graphene have recently emerged as promising electrocatalysts for the CO_2RR owing to their large specific surface area and superior electrical conductivity.[18] They are also a cheaper and more environmentally friendly alternative to metallic catalysts. In addition, they exhibit high-temperature stability and resistance to acids and bases, while having a tailorable porous structure which allows for significant catalytic activity and high selectivity.[19] The electronic properties of such carbon materials can be further tuned by doping the structure with heteroatoms such as nitrogen and phosphorus. Nitrogen-doped carbons have been widely studied for the CO_2RR as N-containing groups have a Lewis base character, facilitating the adsorption and reaction of acidic CO_2 molecules on the catalyst surface.[20] This doping process can give rise to several different nitrogen moieties such as pyridinic, pyrrolic and graphitic N species, which can all behave as active sites (*Figure 2*).

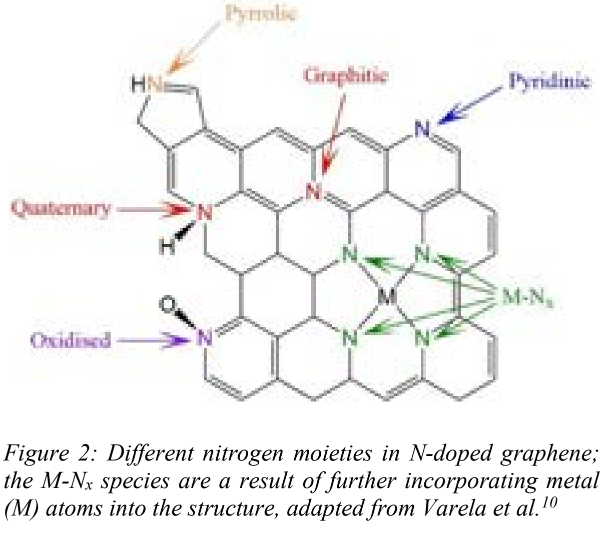

Figure 2: Different nitrogen moieties in N-doped graphene; the M-N_x species are a result of further incorporating metal (M) atoms into the structure, adapted from Varela et al.[10]

In 2015, Varela et al. showed for the first time that catalytic activity with respect to CO_2RR could be significantly improved by incorporating non-precious transition metal atoms into N-doped carbon materials.[21] These materials are a type of single-atom-catalyst (SAC) where the efficiency of metal-atom utilisation reaches almost 100%. The metal atoms are also highly dispersed, which results in a high active site density.[22] These metal-nitrogen-carbon (MNC) materials are comparable to Au or Ag catalysts at low overpotentials in terms of mass activity as well as selectivity toward CO. Furthermore, a strong enough interaction between CO and the metal atom may also allow certain MNC catalysts to further protonate the CO, potentially forming hydrocarbon molecules.[21] The reduction of CO_2 into CO (Equation 1) is often coupled by a competing hydrogen evolution reaction (Equation 2), as shown below.[10]

$$CO_2 + 2H^+ + 2e^- \rightarrow CO + H_2O \qquad (1)$$
$$E_0 = -0.11 \text{ V vs. RHE}$$

$$2H^+ + 2e^- \rightarrow H_2 \qquad (2)$$
$$E_0 = 0 \text{ V vs. RHE}$$

The transition metals commonly used in MNCs include Mn, Fe, Co, Ni and Cu, to name only a few. Among the catalysts mentioned, the nickel-coordinated "NiNC" catalyst showed the most favourable CO_2RR selectivity toward CO, especially at higher overpotentials and current densities. This has been attributed to the Ni-N_x sites having favourable energetics for CO_2 adsorption and reduction to CO via the pathway shown in *Figure 3*. At the same time, these sites bind weakly to *H species (where * represents a reaction intermediate), discouraging the hydrogen evolution reaction (HER) which also occurs at the cathode.[10] Using NiNC catalysts for CO_2 reduction has become a growing area of interest, with recent studies achieving either excellent selectivities (represented by Faradaic Efficiency) or activities (represented by current density) toward CO, as shown in *Table 1*.

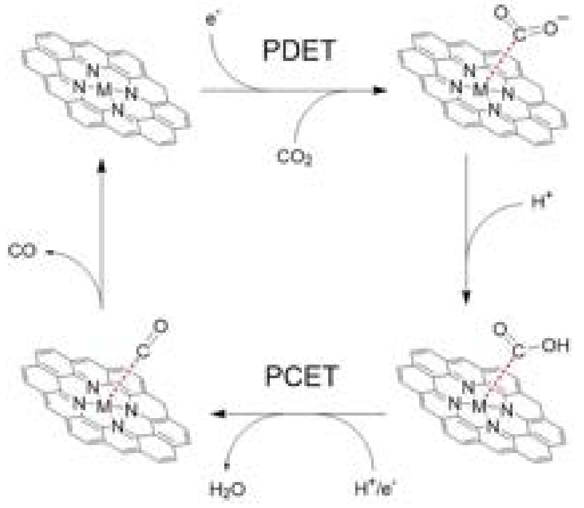

Figure 3: Mechanistic pathway for CO_2 electroreduction to CO on MNC materials, adapted from Varela et al.[10]

Co-doping porous carbon structures with nitrogen and other heteroatoms has been widely reported to increase the activity of the oxygen reduction reaction (ORR), but their synergistic effects on the CO_2RR have only recently begun to be explored.[26,27] The oxophilic character of phosphorus in particular can promote the oxygen-bridged adsorption of CO_2. Metallic phosphorus-rich compounds have also been shown to be able to reduce CO_2 into C_2^+ products, such as the formation of 1-butanol (C_4) using a copper phosphide catalyst.[28] Nickel phosphide materials have been well-studied as they can reduce CO_2 to methyl glyoxal (C_3) and 2,3-furandiol (C_4) at very low potentials.[29] The Ni and P atoms are respectively able to create partial positive and negative sites on the catalyst surface, helping to stabilise multiple transition states and lower the energy barriers, which leads to C-C coupling.[30] This provides a logical incentive to test the catalytic performance of Ni, P co-doped graphene on CO_2RR, as the catalytic performance of nickel phosphides may be reproduced by coordinating Ni atoms onto P-containing active sites. Nevertheless, the insertion of phosphorus into C-N lattices, as well as the evaluation of their performance in electrochemical scenarios, has yet to be explored in depth. Therefore, in this work, we aim to construct N, P-doped Ni single atom catalysts and study their performance and selectivity in the electrochemical CO_2RR.

Table 1: Catalytic performances of recent NiNC materials from literature (a CuNC example has also been given for comparison)

Metal SAC	**Carbon Support**	**Product Formed**	**Max Faradaic Efficiency (%)**	**Potential at Max FE (V_{RHE})**	**Current Density at max FE (mA cm^{-2})**
Nickel	Dicyandiamide[23]	CO	99	-0.81	28.6
Nickel	Ketjen600EC[14]	CO	87	-0.7	100
Nickel	Dicyandiamide, urea, glucose[24]	CO	92	-0.68	10.2
Nickel	Dicyandiamide, 2-methylimidazole[20]	CO	97	-0.9	41.5
Copper	N-doped graphene (commercial)[25]	C_2H_5OH	25	-1.0	8

Experimental Procedure

Synthesis. Nitrogen-doped carbon materials were prepared using triaminopyrimidine (TAP) as the starting monomer as it contributes both carbon and nitrogen atoms. Solid TAP powder (97% Sigma Aldrich) was mechanically mixed with magnesium chloride hexahydrate (99% Sigma Aldrich) in a 1:8 mass ratio using a pestle and mortar. The mixture was pyrolysed in a ceramic crucible at 900 °C for 1 h with a heating rate of 5 °C min^{-1} under N_2 atmosphere. The resulting material was then crushed to a fine powder and washed with 2M HCl (prepared by dilution of 37% fuming HCl, Merck) for 24 h to remove the remaining salt phase, then filtered and rinsed thoroughly with distilled water before being dried at 80 °C in a vacuum oven for another 24 h. This material is labelled "TAP-900".

The N, P co-doped carbon was prepared by pyrolysis of a cross-linked precursor containing TAP and phosphonitrilic chloride trimer (PNCl), following a previous study.[31] Namely, 1.25 g of TAP (0.01 mol) was mechanically mixed with 3.48 g of PNCl (99% Sigma Aldrich, 0.01 mol) in a pestle and mortar, and the mixture was pyrolysed at 300 °C for 1 h with a heating rate of 5 °C min^{-1} under N_2 atmosphere. The cross-linked precursor obtained was labelled as "PNC-300" and mechanically mixed with magnesium chloride hexahydrate in a 1:8 mass ratio. The mixture was then pyrolysed at 900 °C in the same fashion as TAP-900, washed with 2M HCl and vacuum dried at 80 °C before being labelled as "PNC-900".

Metal Coordination. Ni-coordinated materials were prepared by a wet impregnation method as previously reported in literature.[32] 60 mg of TAP-900 was first dispersed in 75 mL methanol. Then, a 75 mL solution of 25 x 10^{-3}M $NiCl_2$ in methanol (prepared from $NiCl_2.6H_2O$, 98% Sigma Aldrich) was added and the mixture subjected to reflux for 24 h at 85 °C. Afterwards, the mixture was filtered and rinsed with methanol, then washed with 0.5M H_2SO_4 (95-98% Sigma Aldrich) for 24 h to remove any aggregated Ni species that were not coordinated into the matrix. This was filtered again and rinsed thoroughly with distilled water, then vacuum dried at 80 °C for 24 h before finally being labelled as "TAP-900-Ni". The procedure was repeated using 60 mg of previously synthesised PNC-900 instead of TAP-900 to obtain "PNC-900-Ni".

Electrochemical tests. Electrochemical testing was performed without iR correction using an AUTOLAB PGSTAT302N potentiostat. NOVA 2.1.4 software was employed to set the procedures for cyclic voltammetry (CV), chronoamperometry (CA) and chronopotentiometry (CP) measurements. Gas diffusion electrodes (GDEs) were prepared for each of the catalysts using an ink-based method for catalyst deposition which consists of catalyst powder, a solvent and a non-volatile ionomer.[33] In this procedure, 12 mg of each catalyst powder was mixed in a pestle and mortar with 40 mg of polytetrafluoroethylene (PTFE), which serves as a hydrophobic agent.[33] The mixture was dispersed in 10 mL of isopropanol solvent by 10 minutes of sonication to obtain the catalyst ink, which was then air-brushed onto Sigracet 39BB carbon fibre paper using a spray gun. A 2 x 1.5 cm rectangle was cut out and drop-casted with 200 µL of 1 wt% Sustainion ionomer (prepared from Sustainion® XA-9 Alkaline Ionomer 5% in ethanol) to obtain the final working electrode. The mass loading per surface area for each of the catalysts on carbon paper is given in *Table 2*.

Table 2: Mass loading per surface area of carbon fibre paper for the catalysts tested

Catalyst	**Mass loading (mg cm^{-2})**
TAP-900	0.154
PNC-900	0.140
TAP-900-Ni	0.214
PNC-900-Ni	0.077

0.5 M KOH electrolyte (99.995% Suprapur®) was saturated with CO_2 (≥99.99998% BIP® Plus, Air Products) prior to each run by 30 minutes of purging. Testing of catalysts was conducted in an electrolyser using a three-electrode GDE configuration with an $Ag/AgCl_{sat}$ reference electrode (stored in saturated KCl solution) and nickel foam as counter electrode (*Figure 4*). The potentials were therefore measured vs. $Ag/AgCl_{sat}$ and later converted to reversible hydrogen electrode (RHE) potential by the Nernst equation at pH 7.2 for CO_2 saturated 0.5 M KOH solution.[34,35]

$$E_{RHE} = E_{Ag/AgCl} + 0.059\, pH + E^0_{Ag/AgCl}$$

Where $E^0_{Ag/AgCl}$ = 0.1976 V at 25 °C.

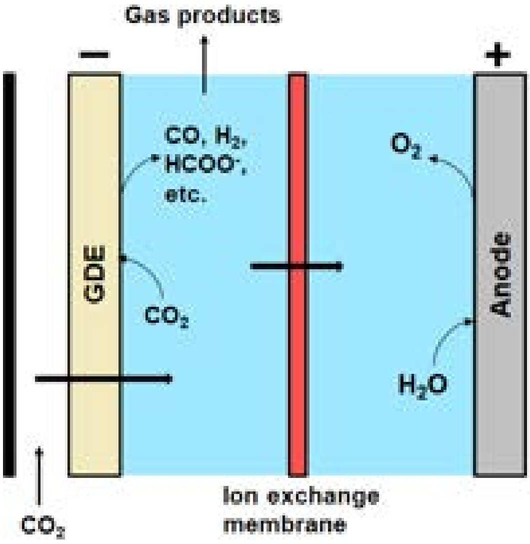

Figure 4: Schematic of electrolyser in three-electrode GDE configuration, adapted from Rabiee et al.[33]

A CV procedure at 50 mV s^{-1} for 20 cycles between 0 to -1.0 $V_{Ag/AgCl}$ (0.622 to -0.378 V_{RHE}) was first performed for each catalyst to stabilise the catalyst surface. This was followed by five CA procedures at -0.88, -1.08, -1.28, -1.48 and -1.68 V_{RHE}, each measured over 1 h. Throughout each run, four gas samples were taken (at 5 minutes after start time, and every 15 minutes afterwards) for GC analysis using an SRI 8610C gas chromatograph. At the end of each run, the cathode-side liquid electrolyte was collected for HPLC analysis using an Agilent Technologies 1260 Infinity II LC system.

The partial current I_i and the partial current density j_i of a CO_2RR product i are given by the equations:

$$I_i = \dot{n}_i . z_i . F \tag{3}$$

$$j_i = \frac{I_i}{S} \tag{4}$$

Where $\dot{n}_i$ is the molar flowrate of product i as given by GC or HPLC, z_i is the number of moles of electrons involved per mole of product i formed, F is the Faraday constant (96485 C mol^{-1}) and S is the active surface area of the working electrode (1 cm^2 in every case). The Faradaic efficiency (%) of product i is given by the following equation, where I_{total} is the total current averaged over the readings taken when the gas samples were extracted:

$$FE_i = \frac{I_i}{I_{total}} . 100\% \tag{4}$$

Material characterisation. X-ray Photoelectron Spectroscopy (XPS) was performed in a Thermo Fisher K-Alpha XPS system. All spectra were charge corrected to the carbon C1s peak at 284.8 eV and analysed using Avantage software. The pyrolysed materials were degassed in situ at 200 °C for 16 h before conducting N_2 sorption isotherms at 77 K in a Micromeritics 3Flex system within the relative pressure range of 0.0002–0.03 to deduce the Brunauer-Emmett-Teller (BET) surface area. The pore size distribution was calculated by heterogeneous surface-2D-NLDFT_Carbon_N2_77 method from the same isotherms on Saieus software (v3). An inVia Renishaw confocal Raman microscope was operated with an incident laser beam at 532 nm, focused through a 50x objective (Leica), for the collection of Raman spectra.

Results and Discussion

Characterisation results. XPS measurements were conducted to investigate the bonding environment and weight composition of heteroatoms on the catalyst surface at various stages during the synthesis.[9] The samples analysed include TAP and PNCl monomers for reference data; PNC-300 to investigate the bonding in the cross-linked precursor; TAP-900 and PNC-900 to confirm the successful doping of N and P heteroatoms into the final structure. The high-resolution spectra for C1s and N1s were analysed for all samples to confirm the overall structure, while the P2p spectra was further explored for the phosphorus-containing materials. The O1s spectra were also analysed to aid with cross-referencing.

The C1s spectra for TAP-900 (*Figure 5a*) and PNC-900 (*Figure 5c*) both show similar results. The large peak at 284.8 eV can be assigned to the main sp^2-hybridised C-C bonding present in both graphene-like materials.[36] Smaller peaks detected around 285.8 eV and 287 eV correspond respectively to C-N bonding at the nitrogen-doped active sites and C-O bonding due to oxidation at high pyrolysis temperatures.[37,38] The N1s spectra for TAP-900 (*Figure 5b*) and PNC-900 (*Figure 5d*) show three main peaks at 398.31 (pyridinic N), 399.59 (pyrrolic N) and 400.8 (graphitic N), with TAP-900 displaying a fourth peak at 402 eV for small amounts of oxidised N species.[38,39]

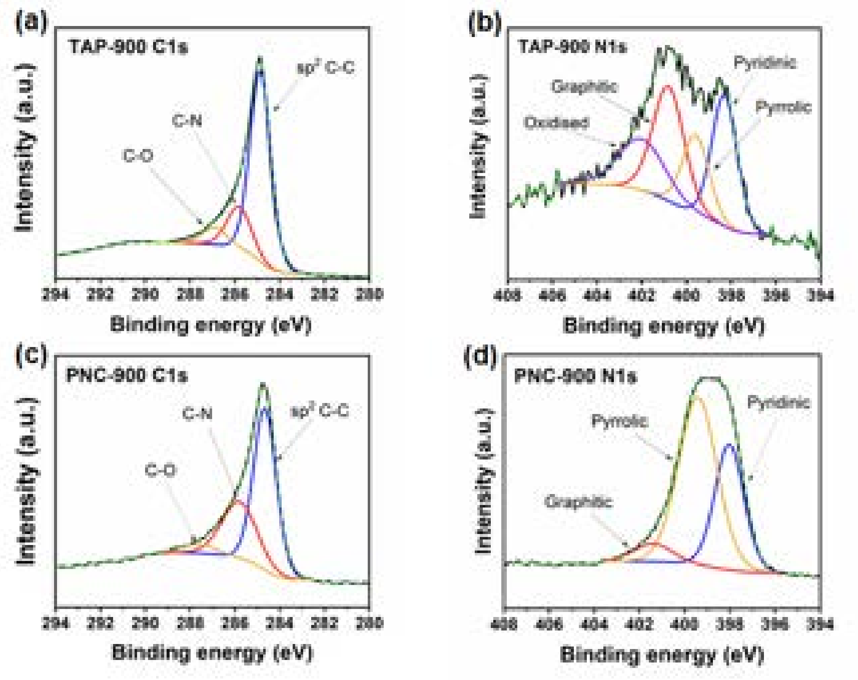

Figure 5: High-resolution (a) C1s and (b) N1s spectra of TAP-900; (c) C1s and (d) N1s spectra of PNC-900, as analysed by XPS

The P2p spectra for PNCl, PNC-300 and PNC-900 all show doublet peaks due to spin-orbit splitting. This gives rise to separate P2p3 and P2p1 peaks being present in a 2:1 ratio for the same bonding environment.[40] Each sample only had one doublet peak, where the P2p3 binding energy lies in the 133.31 to 133.77 eV range (*Figure 6*). The peak for PNCl is naturally attributed to P-N bonding, while no extra peaks can be observed for PNC-300 and PNC-900, suggesting that the same bonding environment is present. It is known from literature that PNC materials synthesised from PNCl and DPT (a similar monomer to TAP) also showed binding energy values of ~133 eV, which have been attributed to the P environment in the backbone of –[PNR]$_n$– polymer chains, where the R group was also connected by a P-N bond.[31] This suggests that P atoms were successfully incorporated into the matrix via bonding with pyridinic or pyrrolic N atoms. However, other literature sources report a possible P-C binding motif at 133.4 eV,[38] as well as P-O bonding in the 133.4–133.9 eV range.[41,42] The O1s spectra for PNC-300 and PNC-900 show two peaks, corresponding to C=O and C-O/P-O bonding, with an extra peak from PNC-900 that could be due to P-O-C bonding[38,43]. Further characterisation would be required to ascertain the exact environment of P atoms due to the close proximity of P-N, P-C and P-O binding energies reported in literature.

The results from XPS analysis were then used to tabulate the composition by weight of each heteroatom in the different catalyst materials in *Table 3* by comparison of the peak areas for the different spectra shown by each material.

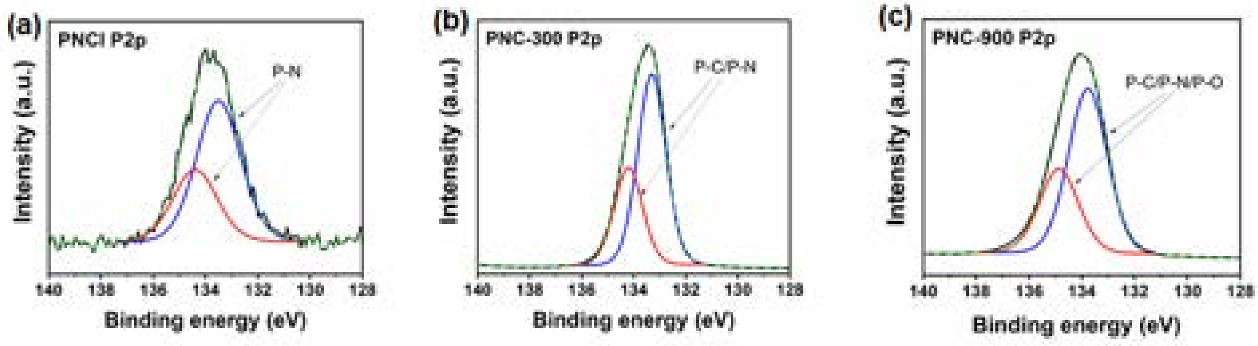

Figure 6: High-resolution P2p spectra of (a) PNCl, (b) PNC-300 and (c) PNC-900

Table 3: Weight composition of each heteroatom in TAP-900 and PNC-900 as analysed by XPS

Catalyst	C (wt%)	N (wt%)	P (wt%)	O (wt%)	Cl (wt%)
TAP-900	92.94	4.46	-	2.6	-
PNC-900	32.2	18.8	24.72	20.3	3.88

The surface area and porosity of the materials was studied through BET analysis, as these properties can influence the accessibility of metal atoms into the active sites as well as the conductivity of the matrix.[44] TAP-900 and PNC-900 both showed type Ib isotherms containing micropores and narrow mesopores (*Figure 7a*). The presence of micropores in the range of 8-12 Å is confirmed by the pore size distribution (*Figure 7b*). These features resemble the ones observed in C_2N covalent organic materials; reported initially by Mahmood et al.,[45] which have been demonstrated to provide a very suitable coordination environment for single and dual atom catalysts.[46,47] The existence of mesopores in the 20-30 Å range can be attributed to the use of $MgCl_2$ as a porogen for ionothermal templating, which has been shown to be able to create pore sizes of 30 Å in similar nitrogen-doped carbon materials.[48]

The combination of high specific surface area (SSA) of 3030 m^2 g^{-1} and large total pore volume (TPV) of 2.74 cm^3 g^{-1} in TAP-900 suggests good mass transport properties and confirms the high accessibility of nitrogen moieties for the coordination of metallic species.[44] These features therefore make the prepared materials suitable as CO_2RR catalysts, where the transport of CO_2 onto the active sites directly influences the overall performance. PNC-900 shows a lower SSA of 656 m^2 g^{-1} and TPV of 0.58 cm^3 g^{-1}. This can be attributed to the higher bond strength of P=N compared to C=N, which leads to lower degradation of the cross-linked precursor.[49]

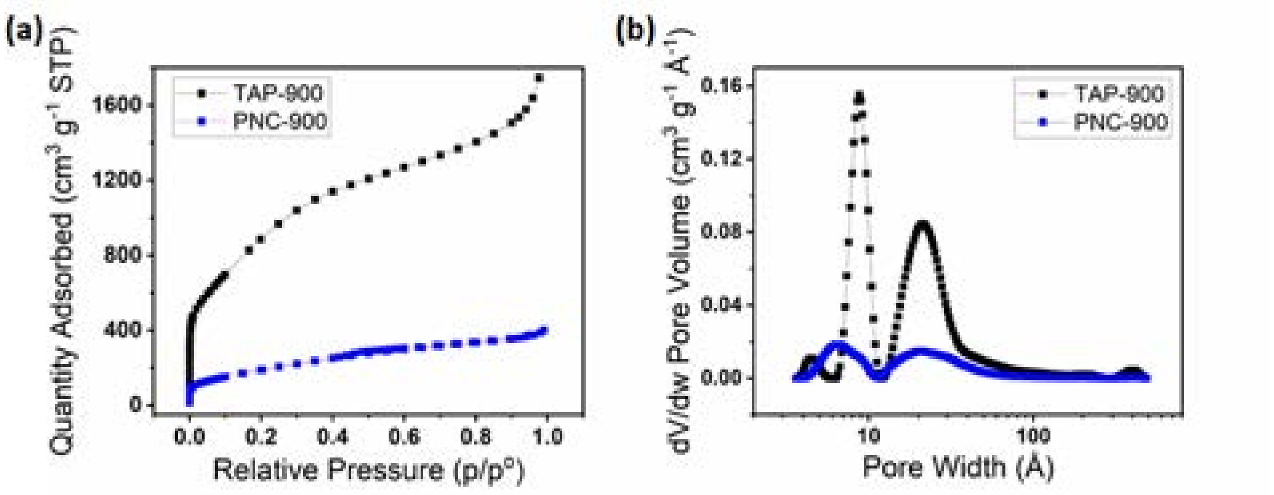

Figure 7: (a) N_2 sorption isotherm, and (b) Pore size distribution for TAP-900 and PNC-900

Raman spectra for TAP-900 and PNC-900 show similar results (*Figure 8*). The D and G bands appearing at 1340 cm^{-1} and 1580 cm^{-1} represent the defects in the graphene-like structure and the graphene structure itself, respectively. The D-to-G peak intensity ratios are similar for both materials, suggesting similar defect densities.[50]

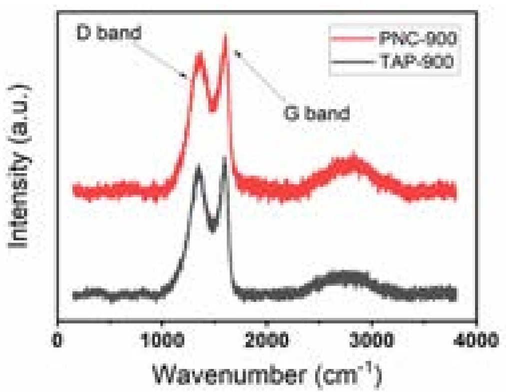

Figure 8: Raman spectra of TAP-900 and PNC-900

Electrochemical testing results. Each of the four catalysts (TAP-900, PNC-900, TAP-900-Ni and PNC-900-Ni) was used as the working electrode in an electrolyser with GDE configuration to test their catalytic performance. Chronoamperometry measurements were carried out to test the dependence of current density and CO_2RR product distribution on the applied potential, as well as the stability of the catalysts over 1 h. The results in *Figure 9* show that the current density increases with the applied potential. More current fluctuation is also observed at higher potentials, which can be attributed to more gaseous products being formed, hence disturbing the charge flow. The current remains stable at lower potentials for all catalysts, but a sudden decrease can be observed at -1.68 V_{RHE} for TAP-900-Ni. This fact could be due to mass transport limitations, owing to the catalyst surface becoming poisoned as more gas molecules are adsorbed at high potentials. Both Ni-coordinated materials display higher current densities than their uncoordinated counterparts, in agreement with other MNCs reported in literature.[10,14,19]

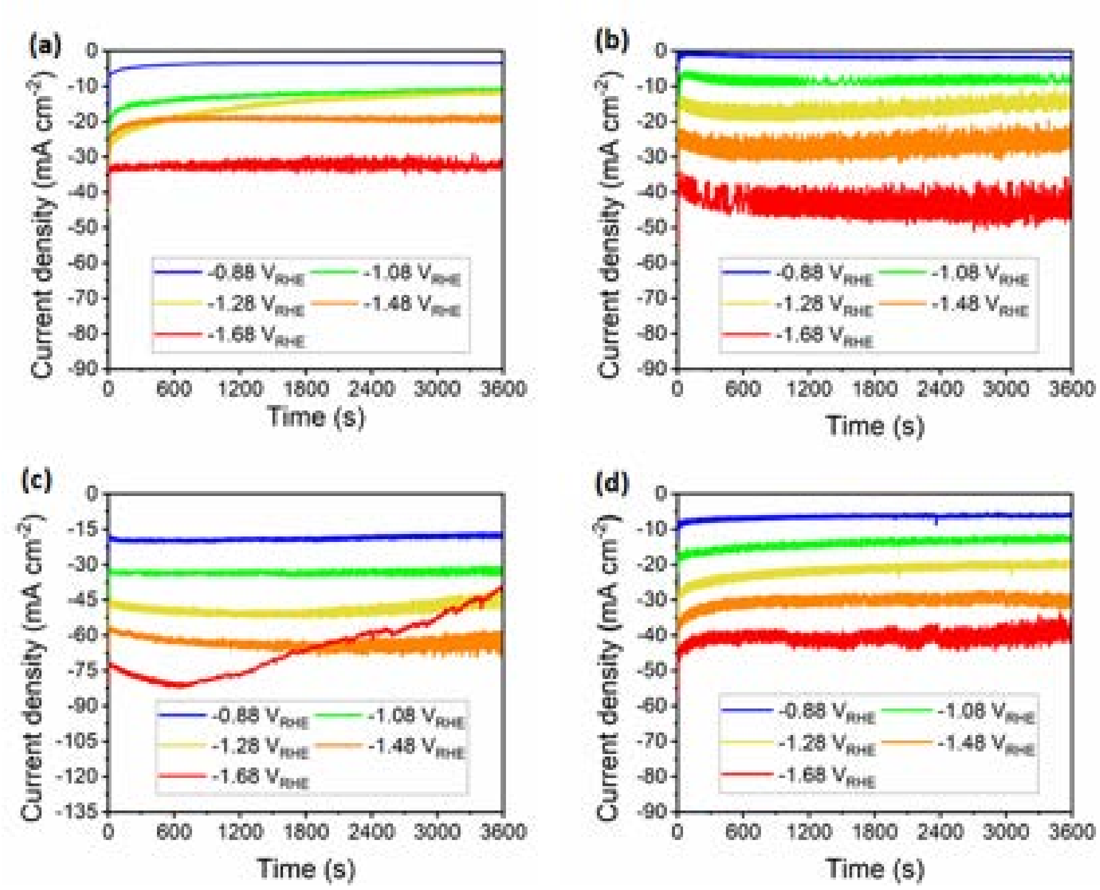

Figure 9: Chronoamperometry results for (a) TAP-900, (b) PNC-900, (c) TAP-900-Ni, and (d) PNC-900-Ni, taken over 1 h runs

The partial current densities of CO and H_2 obtained during the CA measurements were calculated from GC analysis. The results in *Figure 10a* show that the H_2 partial current increases with applied potential, regardless of the catalyst. However, TAP-900-Ni and PNC-900-Ni gave the lowest H_2 partial currents, suggesting that nickel coordination contributes to suppressing the HER. This can be explained by computational free energy diagrams in literature, where Ni possesses one of the highest energy barriers for *H formation.[10,21]

Figure 10b shows that CO partial current densities reached a maximum around -1.48 V_{RHE} before dropping off at higher potentials, possibly due to catalyst poisoning. Both Ni-coordinated materials displayed much better activities toward CO than their uncoordinated counterparts which showed negligible CO_2RR activity. These findings agree with density functional theory (DFT) calculations in literature, which state that the weak binding of *CO to Ni-N_x-C sites is responsible for the fast desorption and therefore high CO production rate of NiNCs.[10,21] Both P-doped materials displayed higher H_2 partial currents and lower CO partial currents than their undoped counterparts. Increased H_2 production is likely due to P atoms facilitating the HER by reducing the free energy change required for *H adsorption, as reported in literature.[51] The decrease in CO production may be due to this increased competition for active sites, as well as the much lower porosity of PNC-900 compared to TAP-900, where mass transport limitations become a major factor.

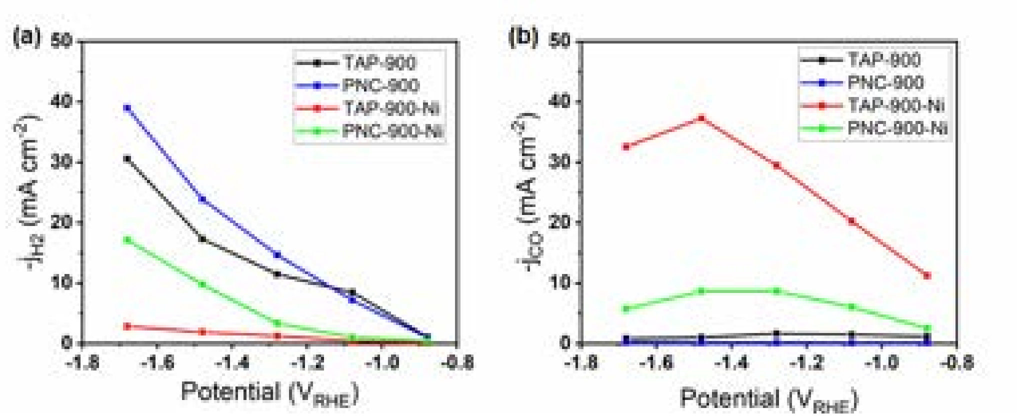

Figure 10: (a) H_2 and (b) CO partial current densities as obtained from gas chromatography analysis

The Faradaic Efficiency (FE) for each product was calculated from their composition as analysed by chromatography. All of the results showed increased FE_{H2} as the potential increases, resulting in the decrease of FE_{CO}. TAP-900 serves as a reference catalyst as it has no additionally doped P or Ni (*Figure 11a*). H_2 was the major product at every potential tested. A variety of CO_2RR products, namely CO, formate, acetate and trace amounts of 2-propanol were formed. This can be attributed to different nitrogen species functioning as active sites, as reported in literature.

The result from PNC-900 (*Figure 11b*) also showed that H_2 is the major product, with the selectivity ratio of CO to H_2 being as little as 1:191 at -1.68 V_{RHE}, the lowest among all the catalysts tested. P-doping facilitates the HER as discussed before, which competes with the CO_2RR and results in a decreased CO production. However, it is also worth noting that PNC-900 had a FE of 0.775% toward 2-propanol (C_3), more than twice the FE shown by TAP-900 at the same potential. This implies that the implementation of phosphorus into the carbon network does contribute to producing longer chain carbon products from CO_2RR.

Doping TAP-900 with Ni has shown significant increase in selectivity toward CO while severely hindering the HER (*Figure 11c*). For every potential tested, CO has become the major product and the selectivity ratio of CO to H_2 has increased to as high as 94:1 at -0.88 V_{RHE}, the highest out of all the tested catalysts. Compared to the TAP-900 at -1.68 V_{RHE}, TAP-900-Ni has an almost 17-fold greater FE_{CO} value (2.8% vs 45.9%). As previously discussed, this can be attributed to the high energy barrier of HER and weak binding of CO on Ni-coordinated active sites.

PNC-900-Ni gave CO as the major product at lower potentials, while H_2 becomes the major product at higher potentials (*Figure 11d*). Compared to PNC-900, a 27-fold improvement of FE_{CO} (0.6% vs 15.7% at -1.68 V_{RHE}), showing that the Ni atom is again the primary factor for the trend observed. Compared to TAP-900-Ni, PNC-900-Ni has a much higher selectivity of H_2, which can once again be attributed to the presence of phosphorus atoms.

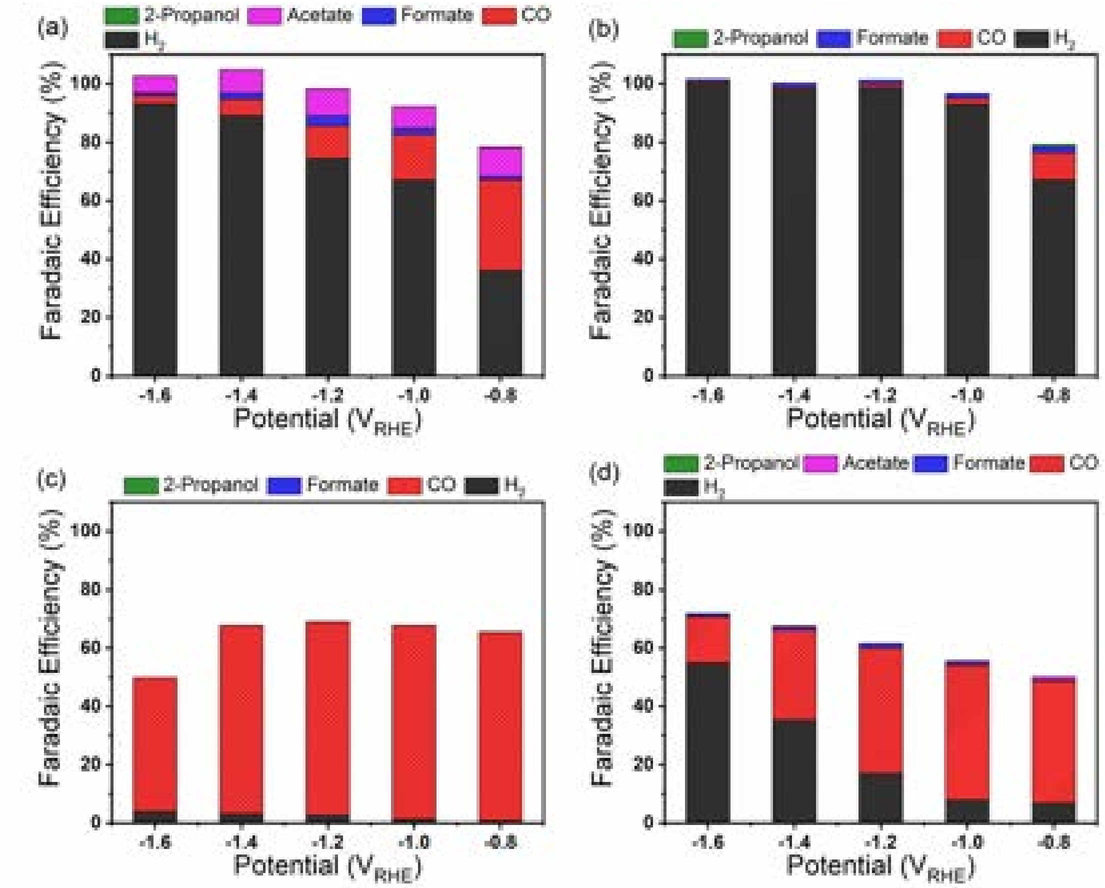

Figure 11: Faradaic Efficiencies for CO_2RR products obtained by (a) TAP-900, (b) PNC-900, (c) TAP-900-Ni, and (d) PNC-900-Ni

Some products formed using TAP-900 and PNC-900 showed total FE values beyond 100%. This is likely due to inherent experimental error while collecting the measurements. On the other hand, TAP-900-Ni and PNC-900-Ni showed total FEs of no more than 72%. The cause was suspected to be the migration of liquid CO_2RR products through the ion exchange membrane into the anodic chamber, from which the electrolyte was not analysed by HPLC.[52]

To the best of our knowledge, the FE of 0.775% toward 2-propanol shown by PNC-900 is better than state-of-the-art metallic Cu catalysts which gave a maximum value of 0.74%.[53] The CO:H_2 selectivity ratio of TAP-900-Ni also exceeds 89:1, the best reported value for NiNCs in literature at the time of writing.[21] The increased performance of our catalyst could be due to the combination of high porosity and electrode preparation technique. The large SSA and TPV allow Ni atoms to be coordinated fully into the matrix, maximising catalyst activity. The PTFE in the catalyst ink creates a superhydrophobic but aerophilic electrode surface which hinders the HER and enhances CO_2 adsorption, while air-brushing forms a thick uniform catalyst layer, preventing the electrolyte from coming into contact with the carbon fibre paper where significant HER can take place.[32]

Conclusion

In summary, we have synthesised novel nitrogen-doped carbon materials with different chemical compositions through the pyrolysis of N, P-containing organic molecules, and their metallic counterparts by low-temperature metal coordination. The performance of these materials as catalysts for CO_2RR was tested using an electrolyser in GDE configuration. Results showed that although doping with phosphorus increases the HER activity, it can promote the formation of 2-propanol. Conversely, doping with Ni significantly reduces HER and increases activity and selectivity toward CO. The maximum CO:H_2 selectivity ratio of 94:1 was achieved at -0.88 V_{RHE} by TAP-900-Ni, with a CO Faradaic efficiency of 65%, partial current density of 11.3 mA cm^{-2} and a catalyst loading of 0.214 mg cm^{-2}. Characterisation techniques such as XPS, BET and Raman spectroscopy were employed to confirm the physical structure of the catalyst materials before nickel coordination. TAP-900 was determined to be extremely porous compared to similar materials in literature. The large SSA and TPV created by employing $MgCl_2.6H_2O$ as a porogen resulted in a highly accessible structure with good mass transport and conductive properties.

To better understand the effect of phosphorus on CO_2RR, further studies can focus on investigating different molar ratios of TAP to the phosphorus monomer during synthesis. Different metals can also be coordinated into the matrix. High-resolution TEM or XAS can be conducted to investigate the distribution of Ni atoms. Ni bonding and composition after metal coordination can be further analysed by XPS or ICP. DFT calculations can also be carried out to gain a deeper insight into possible new mechanism pathways for 2-propanol formation.

Furthermore, repeats of the experiment can be carried out at higher catalyst loadings to remove low catalyst loading as a limiting factor on the CO_2RR. The CA measurements for TAP-900-Ni and PNC-900-Ni should be repeated in the GDE configuration to validate the results and also to analyse the liquid products in the anodic electrolyte. The flow electrolyser can also be operated in the membrane electrode assembly (MEA) configuration to see how the catalysts perform at higher current densities of industrial relevance. Stability tests can be further conducted at different potentials and longer durations to investigate the durability of the catalyst against CO poisoning and degradation.

Acknowledgements

We would like to express our gratitude to Angus Pedersen and Dr Hossein Yadegari for their kind assistance with the BET analysis and Raman spectroscopy, respectively. We would also like to thank Dr Jesús B. Hermida for the XPS measurements and Dr Saurav C. Sarma for assistance with the electrochemical testing, and their support and guidance throughout the whole project.

References

[1] Lindsey, R. (2020) *Climate Change: Atmospheric Carbon Dioxide.* https://www.climate.gov/news-features/understanding-climate/climate-change-atmospheric-carbon-dioxide [Accessed 15 Dec 2021].
[2] IPCC. (2021) *Climate Change 2021 : The Physical Science Basis : Summary for Policymakers.*
[3] United Nations. (2015) *Paris Agreement.*
[4] IPCC. (2021) *Climate Change 2021; The Physical Science Basis. Working Group I contribution to the Sixth Assessment Report of the Intergovernmental Panel on Climate Change. Part 2 - Chapter 4-7.*
[5] IEA. (2021) Global Energy Review: CO2 Emissions in 2020. https://www.iea.org/articles/global-energy-review-co2-emissions-in-2020.
[6] IEA. (2020) *The role of CCUS in low-carbon power systems.* Paris, OECD Publishing.
[7] Ritchie, H. & Roser, M. (2020) *Energy mix.* https://ourworldindata.org/energy-mix [Accessed 15 Dec 2021].
[8] EIA Projects Nearly 50% Increase in World Energy Usage by 2050, Led by Growth in Asia. (2020) *Energy and Power.* 17 (15), https://www.eia.gov/todayinenergy/detail.php?id=41433.
[9] Ju, W. et al. (2017) *Nature Communications.* 8 (1), 1-9. 10.1038/s41467-017-01035-z.
[10] Varela, A. S. et al. (2019) *ACS Catalysis.* 9 (8), 7270-7284. 10.1021/acscatal.9b01405.
[11] Bushuyev, O. S. et al. (2018) *Joule.* 2 (5), 825-832. 10.1016/j.joule.2017.09.003.
[12] Kuhl, K. P. et al. (2012) *Energy & Environmental Science.* 5 (5), 7050. 10.1039/c2ee21234j.
[13] Nitopi, S. et al. (2019) *Chemical Reviews.* 119 (12), 7610-7672. 10.1021/acs.chemrev.8b00705.
[14] Möller, T. et al. (2019) *Energy & Environmental Science.* 12 (2), 640-647. 10.1039/C8EE02662A.
[15] Dry, M. E. (2002) *Journal of Chemical Technology and Biotechnology (1986).* 77 (1), 43-50. 10.1002/jctb.527.
[16] Lu, Q. et al. (2014) *Nature Communications.* 5 (1), 3242. 10.1038/ncomms4242.
[17] Zhu, W. et al. (2013) *Journal of the American Chemical Society.* 135 (45), 16833-16836. 10.1021/ja409445p.

[18] Hu, H. et al. (2021) *Chemical Engineering Journal (Lausanne, Switzerland : 1996).* 425 130587. 10.1016/j.cej.2021.130587.
[19] Duan, X. et al. (2017) *Advanced Materials (Weinheim).* 29 (41), n/a. 10.1002/adma.201701784.
[20] Lu, P. et al. (2019) *Applied Catalysis. B, Environmental.* 241 113-119. 10.1016/j.apcatb.2018.09.025.
[21] Varela, A. S. et al. (2015) *Angewandte Chemie (International Ed.).* 54 (37), 10758-10762. 10.1002/anie.201502099.
[22] Huang, L. et al. (2021) *Composites. Part B, Engineering.* 220 108986. 10.1016/j.compositesb.2021.108986.
[23] Li, X. et al. (2017) *Journal of the American Chemical Society.* 139 (42), 14889-14892. 10.1021/jacs.7b09074.
[24] Bi, W. et al. (2018) *Advanced Materials (Weinheim).* 30 (18), 1706617-n/a. 10.1002/adma.201706617.
[25] Dongare, S., Singh, N. & Bhunia, H. (2021) *Journal of CO2 Utilization.* 44 10.1016/j.jcou.2020.101382.
[26] Choi, C. H., Park, S. H. & Woo, S. I. (2012) *ACS Nano.* 6 (8), 7084-7091. 10.1021/nn3021234.
[27] Sun, X. et al. (2021) *Angewandte Chemie (International Ed.).* 60 (44), 23614-23618. 10.1002/anie.202110433.
[28] Choi, M. et al. (2021) *ACS Energy Letters.* 6 (6), 2090-2095. 10.1021/acsenergylett.1c00723.
[29] Calvinho, K. U. D. et al. (2018) *Energy & Environmental Science.* 11 (9), 2550-2559. 10.1039/C8EE00936H.
[30] Banerjee, S. et al. (2021) *ACS Catalysis.* 11 (18), 11706-11715. 10.1021/acscatal.1c03639.
[31] Zhang, W. et al. (2018) *Angewandte Chemie (International Ed.).* 57 (31), 9764-9769. 10.1002/anie.201805279.
[32] Mehmood, A. et al. (2018) *Advanced Energy Materials.* 8 (9), 1701771-n/a. 10.1002/aenm.201701771.
[33] Rabiee, H. et al. (2021) *Energy & Environmental Science.* 14 (4), 1959-28. 10.1039/d0ee03756g.
[34] Wang, L., Lee, C. & Schmuki, P. (2013) *Journal of Materials Chemistry. A, Materials for Energy and Sustainability.* 1 (2), 212. 10.1039/c2ta00431c.
[35] Liu, M. et al. (2016) *Nature (London).* 537 (7620), 382-386. 10.1038/nature19060.
[36] Wan, Y., Hu, Y. & Zhou, W. (2021) *The Science of the Total Environment.* 151502. 10.1016/j.scitotenv.2021.151502.
[37] Maddi, C. et al. (2018) *Scientific Reports.* 8 (1), 3247-13. 10.1038/s41598-018-21639-9.
[38] Ozturk, A. & Bayrakceken Yurtcan, A. (2021) *Journal of Solid State Chemistry.* 296 121972. 10.1016/j.jssc.2021.121972.
[39] Ren, G. et al. (2020) *Journal of Electroanalytical Chemistry (Lausanne, Switzerland).* 877 10.1016/j.jelechem.2020.114732.
[40] Moulder, J. F. & Chastain, J. (1992) *Handbook of X-ray photoelectron spectroscopy.* Eden Prairie, Minn, Perkin-Elmer.
[41] Lei, W. et al. (2018) *ACS Catalysis.* 8 (3), 2464-2472. 10.1021/acscatal.7b02739.
[42] Ren, G. et al. (2018) *ACS Sustainable Chemistry & Engineering.* 6 (12), 16032-16038. 10.1021/acssuschemeng.8b02170.
[43] Ahmad, M. W. et al. (2021) *ACS Applied Energy Materials.* 4 (11), 12177-12190. 10.1021/acsaem.1c01790.
[44] Pampel, J. et al. (2017) *Materials Horizons.* 4 (3), 493-501. 10.1039/C6MH00592F.
[45] Mahmood, J. et al. (2015) *Nature Communications.* 6 (1), 6486. 10.1038/ncomms7486.
[46] Zhang, X. et al. (2018) *Journal of Materials Chemistry. A, Materials for Energy and Sustainability.* 6 (24), 11446-11452. 10.1039/C8TA03302A.
[47] Pedersen, A. et al. (2021) *Advanced Energy Materials.* 2102715. 10.1002/aenm.202102715.
[48] Huang, Y. et al. (2011) *Journal of Colloid and Interface Science.* 363 (1), 193-198. 10.1016/j.jcis.2011.07.065.
[49] Azoulay, A. et al. (2020) *Journal of Materials Chemistry. A, Materials for Energy and Sustainability.* 8 (17), 8752-8760. 10.1039/D0TA03162C.
[50] Mohan, V. B., Jayaraman, K. & Bhattacharyya, D. (2020) *Solid State Communications.* 320 114004. 10.1016/j.ssc.2020.114004.
[51] Qu, K. et al. (2017) *ACS Nano.* 11 (7), 7293-7300. 10.1021/acsnano.7b03290.
[52] Rabinowitz, J. A. & Kanan, M. W. (2020) *Nature Communications.* 11 (1), 5231. 10.1038/s41467-020-19135-8.
[53] Ting, L. R. L. et al. (2020) *Angewandte Chemie (International Ed.).* 59 (47), 21072-21079. 10.1002/anie.202008289.

Study of Charged Vesicles Fusion for Microreactor Development

Zichen Fan and Yue Zheng

Department of Chemical Engineering, Imperial College London, U.K.

Abstract

The study of artificial cells to mimic characteristics of biological cells is a growing interest of research. Artificial cellular systems provide solid foundations for diverse applications across from medical to environment fields, and one motivation of constructing artificial cells is the development of microreactor. In the context of bottom-up synthetic biology, initiated by a fusion process, liposomes can act as microreactors when they interact and the encapsulated contents react. Hence the fusion mechanism between liposomes have been extensively explored. In this work, a charge-mediated phospholipid-based vesicles fusion system was developed between DOTAP and DOPG, and the fusion process was monitored by fluorescence spectroscopy. Lipid mixing of vesicles were successfully proved by NBD-PE and Liss Rhod-PE FRET-based assays and dynamic light scattering (DLS) measurements, and content mixing of the substances loaded in vesicles was verified by a calcein quenching assay, which also demonstrated that DOPE enhances the rate of fusion. In addition, the fusogenic feature of phospholipid DOPE during fusion was investigated. The DLS results showed a critical concentration of 30 mol% DOPE is necessary to drive the fusion process. In summary, this work provides the potential for artificial microreactor development, and the fusion system developed here can be applied to further research on drug delivery system and biosensors.

Key words: Charge-mediated vesicles fusion; Artificial cell; Microreactor; Phospholipid; Förster resonance energy transfer (FRET); Dynamic light scattering (DLS)

1 Introduction

Artificial cells are synthetic confined structures that encapsulate biological compartments such as DNA, proteins, enzymes and can mimic the functions of living cells (Du and Webb, 2011). In the context of synthetic biology, the study of artificial cells has been a burgeoning field for comprehension and recreation of biological processes. As a tool to investigate biological mechanisms, artificial cells are beneficial because of their less complexities than living cells and the abilities to be programmed and controlled easily (Salehi-Reyhani et al., 2017), hence provide models for various potential applications. Among these diverse applications of artificial cells, the development of biosensors is a promising one. They can be constructed from stimuli responsive protocells that release bioactive contents when there is a change in environment such as light (Jayaraman et al., 2018), temperature (Jia et al., 2019), magnetic field (Finkler and Ott, 2019), and as well as biological signals such as an increase in glucose concentration (Chen et al., 2018). The applications in medical therapies of artificial cell have also been extensively researched, and progresses were made including treatment for port-wine stains (Rikihisa et al., 2017), synthesis of anticancer proteins (Krinsky et al., 2018), multiple sclerosis therapies (Nuzzo and Picone, 2021).

Until far, there are two primary approaches to generate an artificial cell: top-down and bottom-up. The top-down approach constructs artificial cells by reducing the complexity of real cells down to simplified ones, while the bottom up approach creates artificial cells from non-living building blocks (Xu et al., 2016). Top-down techniques are less favourable due to the complexity of a biological cell, as undesired consequences are likely to arise when one compartment is impacted by the programming of another in the cells (Xu et al., 2016).Therefore, bottom-up approach is often used to build synthetic cells, and possible starting materials includes proteins, polymers, vesicles and water-in-oil droplets (Martino et al., 2012). Lipid-based vesicles, also known as liposomes, win other choices over in the construction of artificial cell membranes. Liposomes are membrane bound cavities which inner aqueous contents are segregated with the external medium (Sato and Takinoue, 2019). Phospholipids have the ability to form stable bilayers due to the amphiphilic properties. Since biological cell membranes are also composed of these lipid building blocks, phospholipid-based structures are highly biocompatible and biomimetic to imitate key features of living cells (Elani et al., 2014). DNA, proteins, organelles, therapeutic materials and other bioactive molecules can be encapsulated inside liposomes, producing structures with a membrane resembling biological cells.

Based on lamellarity, liposomes can be categorized into two categories: unilamellar vesicles with only one lipid bilayer, and multilamellar vesicles that have more than one bilayers (van Swaay and deMello, 2013). Based on different sizes, unilamellar vesicles are then classified into three classes: small unilamellar vesicles (SUVs, <100 nm), large unilamellar vesicles (LUVs, 100-1000 nm) and giant unilamellar vesicles (GUVs, >1000 nm) (van Swaay and deMello, 2013). A range of techniques can be used to generate vesicles, such as extrusion for SUVs and LUVs, electroformation and phase transfer for GUVs (Elani et al., 2014). Following these procedures, vesicles with desired sizes can be produced and used in further research including the development of microreactors.

Microreactors are confined spaces where reactions can happen. (Ehrfeld et al. 2005). Biological cells are natural and complex microreactors that host numerous necessary reactions to keep organelles alive, whereas in the area of synthetic biology, vesicles can perform as reaction platforms (Elani et al., 2014). One feature that needs to be incorporate into microreactors and artificial cells is membrane fusion. Being a ubiquitous process among living cells, fusion refers to the destabilization of the lipid membranes of two vesicles which are in close contact and the promotion of mixing both vesicle membranes and their inner contents (Elani et al., 2013). A variety of biological mechanisms are dominated by membrane fusion for example exocytosis (Salaün et al., 2004). In recent decades, the fusion process has been extensively studied due to its potential in biological technologies, and it provides advanced innovations in targeted drug delivery. For example, an ATP-responsive drug delivery system was developed by the fusion of two lipid vesicles loading ATP and doxorubicin (DOX) respectively to enhance anticancer efficacy (Mo et al., 2014). To expand the biomimetic scope for the development of bioreactors, the fusion process in artificial systems has to be imitated and programmed.

However, for a fusion process to happen, energy barriers needs to be overcome (Mondal Roy and Sarkar, 2011). Electrostatic force was used as the driving force for a fusion between oppositely charged phospholipids DOTAP and DOPG at a pH value of 7.4 (Li et al., 2019). Due to the low reproducibility, a zwitterionic 1,2-dioleoyl-sn-glycero-3-phosphoethanolamine (DOPE) phospholipid was added to the network and investigated in this project for better fusion process. Owing to the conical molecular shape, DOPE has been proven to be a helper lipid and a fusogen during membrane fusion process (Mochizuki et al., 2013, Kleusch et al., 2012, Kolasinac et al., 2018). Since DOPE behaves more fusogenic at acidic conditions due to the transformation to a nonlamellar hexagonal-II arrangement (Jinturkar and Misra, 2011, Simoes et al., 2004), herein, the fusion process was run and monitored in buffer solutions at pH 5.0.

In this work, the fusion process driven by cationic DOTAP and anionic DOPG was studied. The relationship between DOPE concentration in the lipid bilayer and the fusion process was investigated. Film rehydrating and extrusion techniques were used to generate charged LUVs followed by freeze-thawing. Fluorescence spectroscopy was carried out to perform the lipid and content mixing assays. Lipid mixing assays were performed by monitoring of emission spectra and measurement of fluorescence intensity of Förster resonance energy transfer (FRET) donor NBD-PE and acceptor Liss Rhod-PE (Rh-PE). The rationale behind this assay is because the emission wavelength (λ_{em} = 530 nm) of NBD-PE is close to the excitation wavelength of Rh-PE (λ_{ex} = 560 nm) (Fig.1). When these two fluorophores are in close contact, NBD-PE at excited state will transfer the energy to excite the nearby Rh-PE instead of releasing a photon, therefore the fluorescence of NBD-PE is quenched and only at Rh-PE's emission wavelength will observe an fluorescence (Maier et al., 2002).

Fluorescence quenching for calcein by $CuCl_2$ was performed for content mixing. In addition, LUVs were subjected to dynamic light scattering (DLS) for size distribution and zeta potential. A charge-mediated LUV fusion system has been developed, providing the basis for the construction of a bio-microreactor and future research directions in this topic.

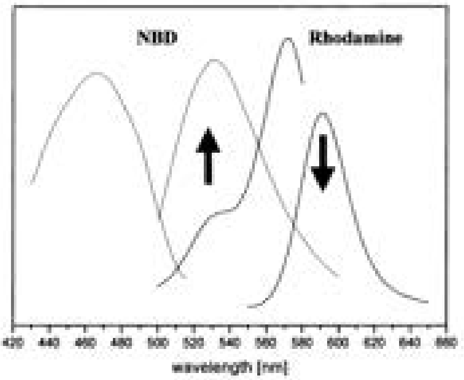

Figure 1. The emission spectrum of NBD-PE overlapping the excitation spectrum of Rh-PE leading to a quenching in NBD-Rh florescence intensity. Image taken from Maier et al., 2002.

2 Reagent and Methods

2.1 Reagents and instruments

1,2-dioleoyl-3-trimethylammonium-propane (DOTAP), 1,2-dioleoyl-sn-glycero-3-phospho-(1'-rac-glycerol) (DOPG), 1,2-dioleoyl-sn-glycero-3-phosphoethanolamine (DOPE), 1,2-dipalmitoyl-sn-glycero-3-phosphoethanolamine-N-(7-nitro-2-1,3-benzoxadiazol-4-yl) (NBD-PE) and 1,2-dioleoyl-sn-glycero-3-phosphoethanolamine-N-(lissamine rhodamine B sulfonyl) (Liss-Rhod PE) were purchased from Avanti Polar Lipids (UK). 4-(2-hydroxyethyl)-1-piperazineethanesulfonic acid (HEPES), chloroform, hydrochloric acid (HCl), potassium sulphate (K_2SO_4), sucrose, calcein, $CuCl_2$, Sephadex G-50 and Triton X100 were purchased from Sigma-Aldrich (UK).

Large unilamellar vesicles (LUVs) were prepared using Avanti Mini-Extruder (Avanti Polar Lipids, UK) with Nuclepore™ Polycarbonate Track-Etched Membranes (Cytiva Whatman™, UK). Fluorescence intensities and spectra were recorded on a Cary Eclipse Fluorometer (Agilent Technologies, USA) using Nunc™ MicroWell™ 96-Well Flat-Bottom Microplates (ThermoFisher Scientific, UK). Dynamic light scattering technique was carried by Zetasizer Ultra (Malvern Panalytical, UK).

2.2 Preparation of buffer solutions

Four buffer solutions were prepared，listed in Table 1. The pH of the buffers was adjusted by 0.1M HCl.

Table 1. Buffer solutions used in this work.

Buffer	Composition
A	20mM HEPES, 25mM K2SO4
B	1mM calcein, 20mM HEPES, 25mM K2SO4, 500mM sucrose
C	1mM CuCl2, 20mM HEPES, 25mM K2SO4, 500mM sucrose
D	20mM HEPES, 25mM K2SO4, 500mM sucrose

2.3 Generation of LUVs

2.3.1 Lipid film preparation

Lyophilised powder stocks were dissolved in chloroform to 25 mg/ml concentration for DOTAP, DOPG, DOPC and DOPE phospholipids. The aliquots of these phospholipid stocks and commercially available NBD-PE and Liss Rhod-PE (Rh-PE) phospholipid stocks of 1 mg/ml concentration were used to formulate desired mixtures with different lipid molar ratios as listed in Table 2 and Table 3.

To produce a phospholipid film, chloroform was evaporated under a mild stream of nitrogen until a thin layer of phospholipids formed on the inner surface of the glass vial. The vials were then left in a vacuum desiccator overnight for thorough drying. Rehydrating the lipid films with corresponding buffer solutions (Table 2, Table 3), lipid mixtures with concentration of 7 mg/ml and 5 mg/ml for lipid mixing and content mixing respectively were prepared.

Table 2. Phospholipid compositions and buffer solutions for lipid mixing assays.

Sample group	**Catinoic lipid composition (%)**					**Anionic lipid composition (%)**		
	DOTAP	DOPE	DOPC	NBD-PE	Rh-PE	DOPG	DOPE	DOPC
1	30	0	69	0.5	0.5	30	0	70
2	30	10	59	0.5	0.5	30	10	60
3	30	20	49	0.5	0.5	30	20	50
4	30	25	44	0.5	0.5	30	25	45
5	30	30	39	0.5	0.5	30	30	40
6	**Neutral lipid composition - 100 DOPC**							

Notes: 1) All samples were rehydrated with buffer solution A;
2) Mixing of the cationic & anionic lipids in sample group 1 is referred to DOTAP/DOPG mixed LUV in this paper; mixing of the cationic & anionic lipids in sample groups 2-5 is referred to DOTAP/DOPG/DOPE mixed LUV;
3) For each experiment, the control group was the mixing of the cationic lipid from Sample 1-5 with the neurtal lipid sample 6 and is referred to DOTAP/DOPC mixed LUV.

Table 3. Phospholipid compositions and buffer solutions for content mixing assays.

Sample	**Catinoic lipid composition (%)**			**Sample**	**Anionic lipid composition (%)**		
	DOTAP	DOPE	DOPC		DOPG	DOPE	DOPC
7	30	0	70	**11**	30	0	70
8	30	30	40	**12**	30	30	40
9	**Neutral lipid composition (%) - 100 DOPC**						
10	**Neutral lipid composition (%) - 100 DOPC**						

Notes: 1) Sample 7&8&9 were rehydrated with buffer solution B, Sample 10&11&12 were rehydrated with buffer solution C;
2) Mixing of sample7&11 is referred to DOTAP/DOPG mixed LUV; mixing of sample 8&12 is referred to DOTAP/DOPG/DOPE mixed LUV in this paper;
3) Control groups were mixing of sample 9 &11/12 (referred to DOPG/DOPC mixed LUV) and mixing of sample 9&10 (referred to DOPC/DOPC mixed LUV).

2.3.2 Extrusion

The lipids for content mixing assays were vortexed for 3 min and underwent 5 freeze-thaw cycles to form vesicles and encapsulate the calcein and buffer solution inside them, while the ones for lipid mixing assays were vortexed only. The lipids were then extruded 13 times through polycarbonate membranes with pore size of 0.8 µm, 0.2 µm and 0.1 µm sequentially to form LUVs with diameters at 100 nm.

2.3.3 Size exclusion chromatography

Following extrusion, size exclusion chromatography was performed to separate the external unencapsulated calcein from the vesicles containing encapsulated calcein. The column for size exclusion chromatography was prepared by dissolving 400 mg Sephadex G-50 in buffer solution D and left in oven at 65 °C for 1 hour. The resin was poured into a column and became ready to be used after being settled for 30 min. The extruded vesicles were added to the column and left to absorb into it. The vesicles were purified by adding buffer D gradually to the column and collecting the eluted fractions (Fig. S5). The surfactant Triton was introduced to the fractions containing vesicles to prove a successful encapsulation of calcein, as it permeates the lipid bilayer of vesicles and releases the loaded contents.

2.4 Lipid Mixing Assay

Förster resonance energy transfer (FRET)-based assay was carried out to measure the change in the fluorescence intensity of the NBD-PE fluorophore in LUVs. For mixing experiment, 20 µl of DOTAP LUVs and 20 µl of DOPG LUVs were mixed and diluted in 100 µl of buffer A. Meanwhile, 20 µl of DOTAP LUVs were added to 20 µl of DOPC LUVs in 100 µl of buffer A for control purpose. Fluorescence intensities of these mixed LUVs were measured as triplicate repeats for 1200s at NBD-PE's excitation and emission wavelength ($\lambda_{ex}/\lambda_{em}$ = 466/530 nm) at room temperature, with a voltage of 600 V, an average time of 0.5 seconds and excitation/emission filters of 10 nm/5 nm respectively. All raw intensities obtained were normalised to reduce influence from surroundings as well as clearing representing the overall tendency using following formula

$$F_{normalised} = \frac{I - I_{min}}{I_{max} - I_{min}} \tag{1}$$

where I is intensity, I_{max} and I_{min} are the maximum intensity and the minimum intensity during whole measurement period, all in units a.u.

2.5 Emission spectra of Rh-PE

As the FRET-based lipid mixing assay verified the fusogenic property of DOPE, fluorescence emission spectra of Rh-PE were collected from LUVs with varying DOPE contents to evaluate the relation between the DOPE concentration and the fusion process. For each DOPE concentration, 100 µl of DOTAP LUVs were diluted in 600 µl of buffer A, and 100 µl of DOTAP LUVs and 100 µl of DOPG LUVs were mixed and diluted in 500 µl of the same buffer. Spectra were measured as triplicate repeats from 140 µl of DOTAP and DOTAP/DOPG mixed LUVs. Samples were excited at NBD-PE's excitation wavelength of 466 nm, and emission spectra were recorded from 500 nm to 700 nm covering the emission wavelength of both NBD-PE and Rh-PE. The voltage was set at 600 V, and excitation/emission filters were both 5nm.

2.6 Dynamic Light Scattering

Dynamic light scattering (DLS) analysis was performed for size distribution and zeta potential measurements of DOTAP and DOPG LUVs at time zero, and DOTAP/DOPG and DOPC/DOPC mixed LUVs samples 5 hours after mixing. Each liposome samples was diluted to 1 mg/ml with buffer A and measured in triplicate repeats at room temperature.

2.7 Content Mixing Assay

A volume of 40 µl of purified DOTAP LUVs containing encapsulated calcein and 40 µl of DOPG LUVs containing encapsulated $CuCl_2$ were mixed and diluted in 160 µl of buffer D. The same procedures were carried for DOPG/DOPC and DOPC/DOPC Mix LUVs control preparations. For all samples, fluorescence intensities were measured in triplicate repeats for 20 minutes at calcein's excitation and emission wavelength ($\lambda_{ex}/\lambda_{em}$ = 495/515 nm) at room temperature, with a voltage of 600 V, an average time of 0.1 minutes, a cycle time of 0.5 minutes, and both excitation/emission filters of 5 nm. Data was processed using Eq.1.

3 Results and Discussion

To evaluate the LUV fusion, lipid mixing assay was conducted. Firstly, change in fluorescence intensity was detected for samples of DOTAP/DOPG/DOPE, and DOTAP/DOPG mixed LUVs to compare with DOTAP/DOPC control group.

The fluorescence intensity of the FRET-pair donor NBD-PE was measured for DOTAP/DOPG mixed LUVs with and without 30% DOPE. The fluorescence intensity of NBD-PE is expected to increase if fusion happens, as an increase in the distance between the fluorophores will unpair the NBD-Rh FRET-pair upon LUV fusion. NBD-PE will therefore emit photons instead of exciting Rh-PE, hence being detected by the fluorescence spectrometer. The results of this assay is shown in Fig. 3(a) and Fig.3(b).

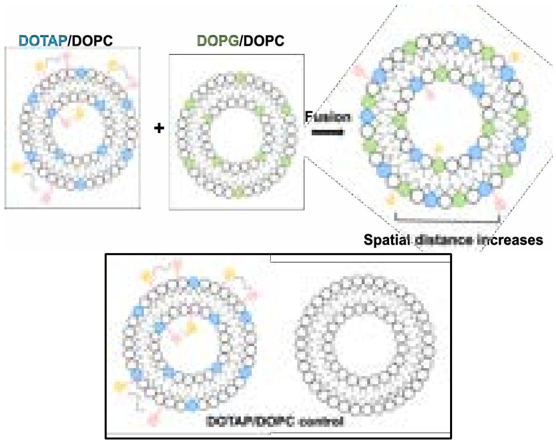

Figure 2. Schematic diagram displays lipid mixing with control experiments. Oppositely charged DOTAP (blue) with FRET pairs (NBD-PE and Liss Rhod-PE) and DOPG (green) LUVs fuse, making spatial distance between FRET pairs increasing. DOPC liposomes are shown in white.

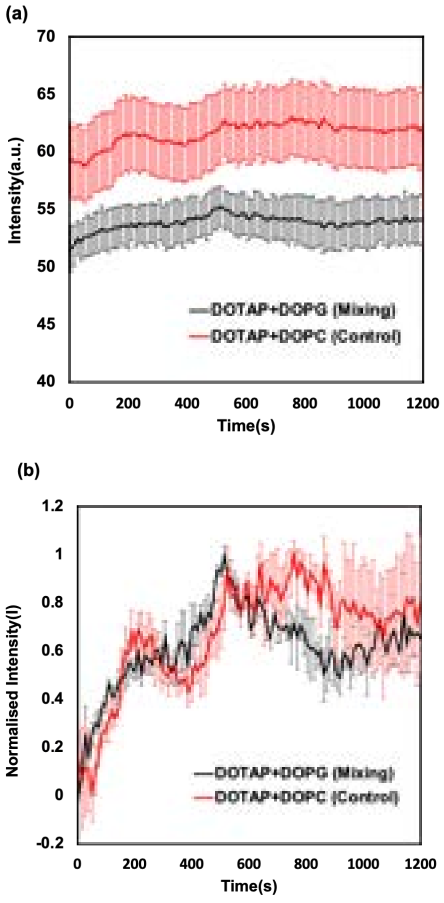

Figure 3. In fusogenic conditions, the fluorescence intensity of FRET-pair NBE-PE increases, alluding to successful fusion of LUVs. Fluorescence intensity changes for DOTAP/DOPG/30% DOPE mixed LUVs and DOTAP/DOPE/DOPC control LUVs are shown in (a) before data normalisation and (b) after normalisation. (Error bars stands for 1 s.d., calculated from n=6)

As seen from the Fig.3(a), the NBD-PE fluorescence intensity increases over time for both fusion and control samples, indicating that the FRET-pair is disassembled due to fusion. This trend can be observed better in Fig.3(b) as a general increasing trend is found, which could indicate that the lipid vesicles were fusing. Once the charged and DOPE-doped LUVs were mixed together, approximately from 0 to 600s, the fluorescence intensity of NBD-PE kept increasing. This indicates a fusion between the oppositely charged DOTAP and DOPG vesicles. The further observed flat trend after 600s could be a result of negatively charged DOPG liposomes reacting with fused liposomes, where the fusion process was nearly closing to end. This was shown in Table 4 of zeta-potential values.

For LUVs without DOPE, the fluorescence variation is shown in Fig.4. From Fig.4(a) shows there is barely a difference between initial intensities between mixing and control experiments. With the control group keeping consistent, it can be seen from Fig.4(b) that the normalised intensity of mixing group is steeply decreasing during 0 to 600 s, which is not a sign of NBD-PE being dequenched. However, from 600 to 1000 s, the normalised intensity begins to display an increasing trend. One possible reason here is that hemi-fusion could happen at the intermediate stage, hence leading to a short-period of increasing in fluorescence intensity from the transient spatial separation between FRET pairs, after which the structure continued to disassociate back to segregated vesicles. This is shown by size of mixing vesicles in Table 4.

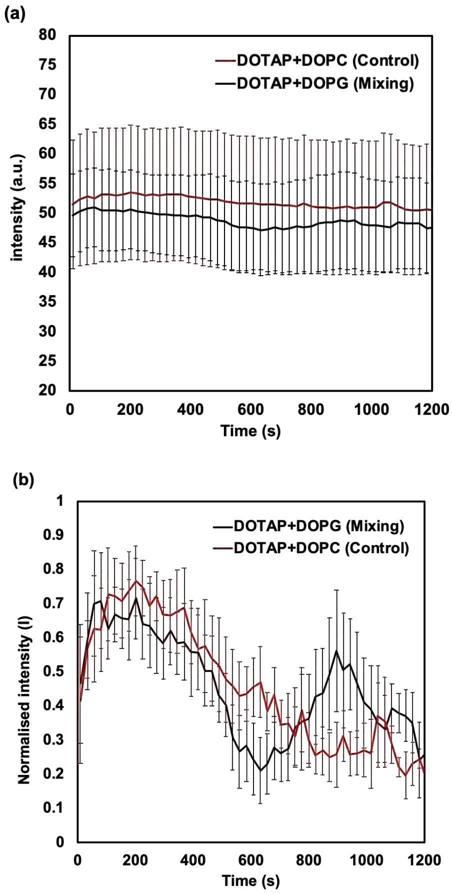

Figure 4. In non-fusogenic conditions, the fluorescence intensity of FRET-pair NBE-PE does not increase as expected, comparing with Fig.3. The overall tendency suggests possibility of other intermediate states or short-period of fusion process existing. Fluorescence intensity changes for DOTAP/DOPG mixed LUVs and DOTAP/DOPC control LUVs are shown in (a) before data normalisation and (b) after normalisation. (Error bars stands for 1 s.d., calculated from n=6)

Therefore, according to the lipid mixing assay, when the LUV system is supplied with DOPE, a more prominent increase could be detected in N BD fluorescence alluding to fusion between LUVs.

The results for fluorescence intensity can be influenced greatly by the sensitivity of the instruments used. It is possible that the increase in NBD-PE fluorescence is too low to be detected using the fluorimeter. Also, there could be photobleaching of NBD-PE happening during the measurement, where the shorter the cycle time taken for each round, the more likely photobleaching would appear resulting in increases in intensities for both mixing and control samples. As fluorophores could undergo the fluorescence process by excitation for several times, they can produce the signal repeatedly (ThermoFisher Scientific, n.d.). This can make the assay unstable and uncertain to measure the short increase in fluorescence of unpaired NBD composing FRET-pair.

To further evaluate the lipid mixing of fusogenic LUVs, one can also measure the decrease of fluorescence intensity of the FRET-pair acceptor Rh-PE upon LUV fusion. The measurement was taken by exciting the samples at the excitation wavelength of NBD-PE (466 nm) while recording the emission spectra of Rh-PE (590 nm). The experiment was done to figure out if the Rh-PE fluorescence intensity decreases in relation to the increasing DOPE concentration, as being hypothesed that more DOPE in the LUV system increases chances of LUV fusion.

Fluorophores were kept at 1 mg/ml for all samples to avoid the influence of dilution. The effect of dilution on peak intensities is shown in Fig.S2 and Fig.S3 in Supplementary.

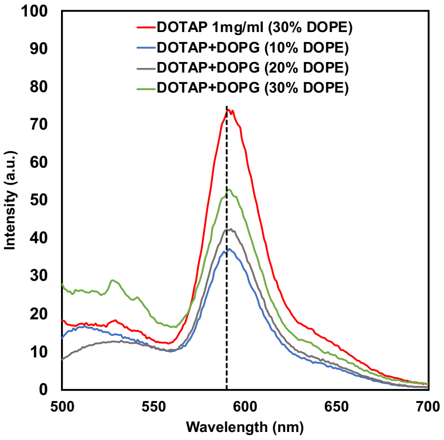

Figure 5. The emission spectra compares peak intensities at 590 nm (Rh-PE emission wavelength) among fusogenic samples containing DOPE mol% ranging from 10 to 30 mol%. The data were measured after 40 minutes of mixing. The emission detected decreases with DOPE mol% reduced.

Fig. 5 shows the emission spectra of fusogenic samples composed of 10 to 30 mol% DOPE, including control group of DOTAP/DOPE/DOPC (refer to DOTAP 1mg/ml). It is expected that with fusion occurring, the spatial distance between FRET pairs would increase hence less energy is transferred from NBD-PE to excite Rh-PE, which means a decrease in peak emission intensity at Rh-PE emission wavelength would be obtained as a loss of FRET pair.

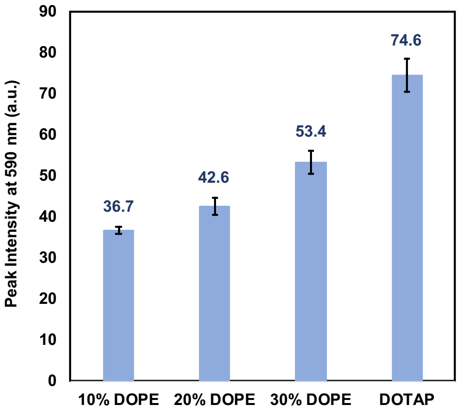

Figure 6. The chart provides further information on exact values of peak emission intensities detected at 590 nm with DOPE mol% from 10 to 30 mol%. (Error bars stands for 1 s.d., calculated from n=3)

However, Fig.5 provides an opposite result to expectation. The actual emission intensity detected at 590 nm decreases with the mol% of DOPE. From Fig.6, a relatively great decrease in emission intensity around 20 a.u. from control group DOTAP (1 mg/ml) to mixing LUVs with 30 mol% DOPE is detected, which successfully proves that fusion happens. According to previous research by Ma et al. (2013), it was found that the fusion potential between negatively charged and neutral fluid liposomes can be highly improved by DOPE. The extent of fusion (%) calculated is increasing with mol% DOPE. However, the stability of mixing structures is affected by many factors including temperature, pH, and also charged property of lipids. Hence the opposite trend observed in Fig.5 and Fig. 6 may be explained by the cationic liposome DOTAP influencing the potential of DOPE enhancing fusion. On the other hand, the difference between emission intensities from 10 to 30 mol% is relatively small, which means the mixing samples might be at initial stages of association, protrusion or hemi-fusion, hence not approaching to fusion. In further research, it is necessary to do emission measurements after different time periods and with different composition of charged lipids.

Next, dynamic light scattering (DLS) technique was used to measure size distribution. Fig. 7 shows the size population profile for charged liposomes DOTAP, DOPG and DOTAP/DOPG/DOPE(30%) mixed LUVs. Both DOTAP and DOPG LUVs have similar size profiles due to extrusion, with peak sizes appearing at 163 nm and 148 nm respectively. These sizes are larger than expected after extrusion through a 100 nm membrane, which might be a consequence of aggregation of charged liposomes in buffer and presence of multilayer structure of liposomes (Li et al., 2019).

For the samples containing mixed fusogenic liposomes, two peaks at size=102 nm and 261 nm are observed. The shift toward the larger fraction of 16.4% population of the mixed LUV samples indicates possible fusion as there is an increase in size of the vesicles. The smaller peak size of 102 nm with lower fraction of 7.2% population could have been resulted from the formation of micelles of DOPE or mixed micelles of DOPE and DOPC. Instead of forming a bilayer structure, the polar region of lipids tends to be in contact with aqueous environment while non-polar tails region does not favour the interaction shown in Fig.8. A combination of DOPE and DOPC promotes the formation of mixed micelles with DOPE at a lower critical micelle concentration (CMC) value (Cui et al., 2014). However, it requires further investigation into CMC for DOPE in DOTAP/DOPC mixtures. To test this hypothesis, cryogenic transmission electron microscopy (Cryo-TEM) technique can be applied to research what aggregating structures these samples form.

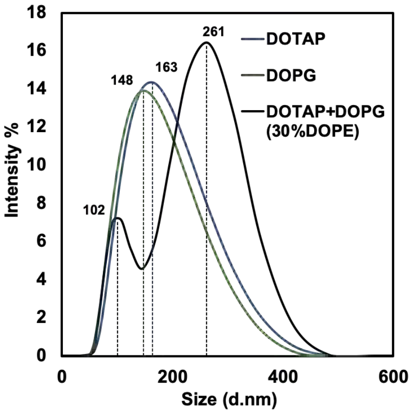

Figure 7. When oppositely charged LUVs containing DOPE are mixed, they increase in size over time. DLS results show the population of sizes for charged LUVs DOTAP, DOPG and DOTAP/DOPG/DOPE mixed LUVs after 5 hours.

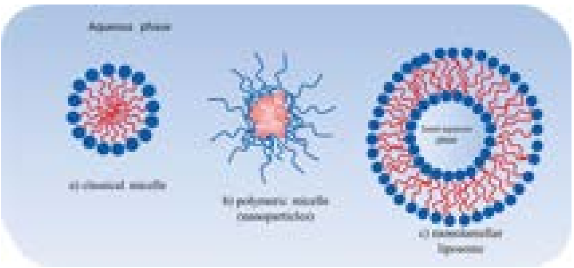

Figure 8. Scheme showing different aggregation of lipids (a) shows structure of classical micelle, with hydrophilic heads facing aqueous solvent, while tails towards inner region. (b) shows structure of polymeric micelle, with core-shell aggregation of head groups. (c) shows normal bilayer liposome with monolamellar structure. Image taken from Falsini. and Ristori., 2016.

According to Putta et al., (2016), 30% DOPE is within the safe range when forming lamellar structures, However, there is a possibility that higher mol% DOPE can destabilise the lamellar structure without being stabilised by negatively-charged lipids hence interfering with formulation of fusogenic LUVs, and therefore affecting their fusing process with other LUV species (Ma et al., 2013). It is also suggested that a mixture with DOPE content less than 50 mol% is more suitable for mimicking bacterial membranes (Hamai et al., 2006). Hence no molar concentration over 30% DOPE was tested in this work.

Fig. 9 shows the comparison of the size distributions for LUVs with different DOPE concentrations after being mixed for 5 hours. And a summary of peak sizes for each sample is shown in Table 4. The control groups used in this case was DOPC/DOPC and DOTAP/DOPG without DOPE. Based on these results, it can be concluded that LUV fusion was happening only in condition where oppositely charged LUVs containing 30 mol% DOPE were mixed. There is no significant increase in LUV sizes from 0 to 25 mol% of DOPE, and no obvious trend can be found below 30% DOPE added, which suggests a certain concentration within 25% to 30% could be the critical point for fusion to carry out.

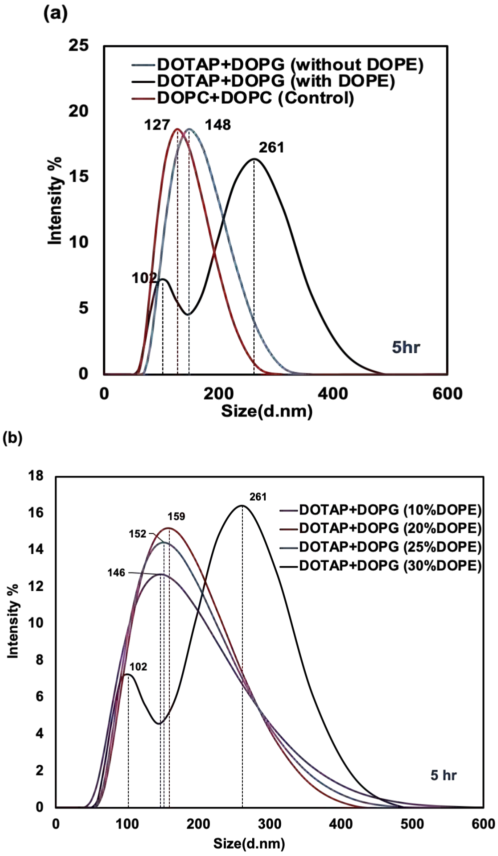

Figure 9. (a) shows comparison of DLS results for mixed LUVs with and without (30mol%) DOPE after 5 hours. No obvious changes in size population and peak sizes appear for samples without DOPE, suggesting no fusion happening. (b) shows comparison of DLS results for mixed LUVs with different DOPE concentrations from 10% to 30mol%. No general trend can be concluded. Only one peak size is observed for DOPE concentration below 30%.

Table 4. Comparison of LUV sizes for each population studied.

	No. of Peaks	Peak size (nm)	Fraction(%)
DOTAP	1	163	14.3
DOPG	1	148	13.9
No DOPE	1	148	18.6
10% DOPE	1	146	12.7
20% DOPE	1	159	15.2
25% DOPE	1	152	14.4
30% DOPE	2	102	16.4
		261	7.2

It is also essential to determine zeta potential to study the flocculation process which is favoured by fusion events. Zeta potential is a key physical property of particle which measures the electrical charge. This is related to electrostatic repulsion between positively charged or negatively charged particles, which enables the particles to segregate (Feng and Huang, 2001; Kumar et al., 2004).

The classifications of stability from zeta potential values are shown in Table 5. The mean zeta potentials of the LUV fusion and control samples used were shown in Table 6. Both DOTAP and DOPG liposomes are at a relatively stable state, not forming aggregates which is probably due to them being charged and electrostatically repelling one another, therefore inhibiting the association. On the other hand, when the oppositely charged vesicles are mixed, they attract and move towards each other, promoting vesicle association and eventual fusion if the attraction is sufficient. As shown in Table 6, after DOTAP and DOPG liposomes were mixed, the mean zeta potential value is nearly zero. This can indicate that the mixed LUVs are at an unstable state and can perform rapid flocculation which favours fusion as a pre-step.

What is interesting here is that the mean zeta potential of mixed oppositely charged LUVs without DOPE is more positive than that of samples containing 30% DOPE. This could indicate that the latter sample is at a more unstable state, but the zeta potential difference between these samples might not be significant enough to conclude that it is the case. It is also expected that with higher concentration of the fusogenic DOPE, the mean zeta potential would become closing to zero. Due to instrument maintenance issues, it was not possible to carry zeta potential measurements with various DOPE concentrations, therefore further experiments should be continued to studying the relationship between zeta potential and the LUV DOPE composition.

Table 5. Stability of colloid depending on zeta potential. Information taken from Kumar and Dixit., 2017.

Zeta Potential (mV)	Stability behavior
0 to ±5	Rapid coagulation or flocculation
±10 to ±30	Incipient instability
±30 to ±40	Moderate stability
±40 to ±60	Good stability
>61	Excellent stability

Table 6. Mean zeta potentials of charged liposomes and mixed liposomes after 5 hours, clarified with stability from Table 5 (Error bars stands for 1 s.d., calculated from n=3).

	Zeta Potential (mV)	Stability
DOTAP	+24.5±2.2	Incipient instability
DOPG	-48.6±1.5	Good stability
DOTAP+DOPG (WIthout DOPE)	+4.9±1.4	Rapid coagulation or flocculation
DOTAP+DOPG (with 30% DOPE)	+2.1±1.5	Rapid coagulation or flocculation

Proving lipid fusion happening, content mixing assay was then conducted. Fluorescence intensity was measured for DOTAP/DOPG/DOPE mixed LUVs, to compare with DOPG/DOPC control group 1 and DOPC /DOPC as control group 2.

Calcein and $CuCl_2$ molecules were encapsulated in DOTAP and DOPG LUVs separately. In theory, when fusion happens, the content inside mixed LUVs are in contact with each other, where calcein is strongly quenched by $CuCl_2$ to generate a decrease in fluorescence intensity of calcein.

It was tested if the inner contents of LUVs mix upon fusion. For LUVs containing 30% DOPE, the fluorescence change is shown in Fig. 11. The fluorescence intensity of calcein in mixed fusogenic LUV samples shows a gradually decreasing tendency, which is a result of calcein being quenched by $CuCl_2$. However, the two control groups did not act as constantly as in expectations. After t=5 min, both control group 1 and 2 are observed quickly declining to their minimum intensities at approximately 22 a.u. and 15 a.u. respectively (numbers refer to Fig.S4 in supplemantory). These values are both below the calcein fluorescence intensity of the fusogenic sample group. This reveals that there might be leakage during fusion, which the inner LUV calcein was released outside the vesicles and quenched by $CuCl_2$ in the surrounding solution. To evaluate this, DLS measurements could be taken to check: the contents could only react by leakage if no change in vesicle size is observed. This could also show whether the fast decreasing rate of calcein fluorescence intensity was due to passive leakage or not. Previous research also suggests that copper ions might interact with the lipid membrane hence disrupting vesicle formation (Jiang et al., 2018), which could be a reason that the production of stable LUVs for control experiments failed.

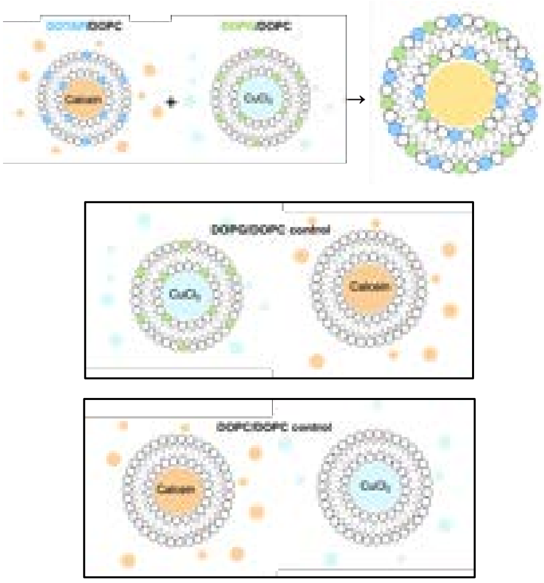

Figure 10. Scheme of content mixing with control experiments. The LUVs shown are positively charged DOTAP (blue) with calcein encapsulated, and negatively charged DOPG (green) with $CuCl_2$ encapsulated. DOPC liposomes are shown in white. Oppositely charged LUVs fuse and calcein is quenched by $CuCl_2$.

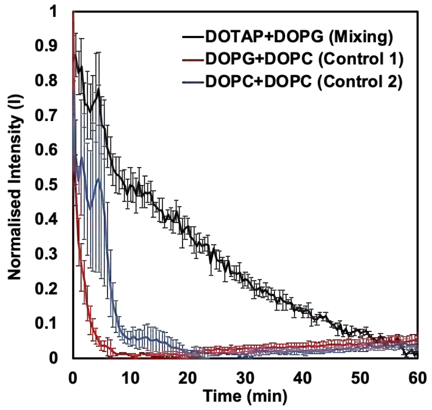

Figure 11. In fusogenic conditions, the fluorescence intensity of calcein decreases, deducing successful fusion of LUVs. Fluorescence intensity changes for DOTAP/DOPG/DOPE mixed LUVs and DOTAP/DOPE/DOPC control LUVs are shown after normalisation. (Error bars stands for 1 s.d., calculated from n=3)

Further experiments were carried out to investigate the effect of DOPE on content mixing through fusion. From Fig.12, the decreasing rate of mixed LUVs with DOPE is much higher than that of LUVs without DOPE, which is consistent with conclusion obtained previously from lipid mixing experiment that DOPE does drive the fusion to progress and improve the rate of fusion. In this case, under fusogenic condition, as there is large variation of approximately 76 a.u. in initial intensities at t=0 between control and mixed LUVs (refer to Fig.S5 in supplementary), it is suggested that simultaneously after the initiation of fusion process, quenching could happen quite quickly before the samples being taken to measurement.

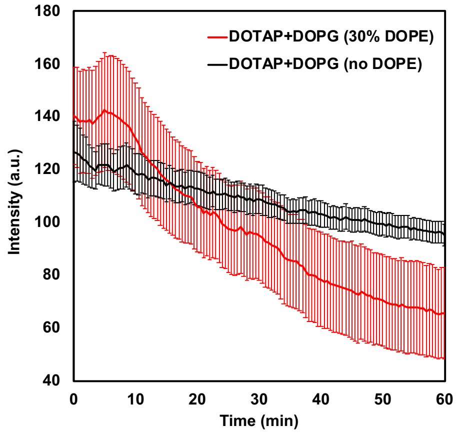

Figure 12. The figure shows comparison of fluorescence intensity of calcein for mixed LUVs with and without (30mol%) DOPE during 60 minutes. The decreasing rate of DOTAP/DOPG/DOPE is much faster than that of DOTAP/DOPG LUVs, which means the former fusion rate is higher. (Error bars stands for 1 s.d., calculated from n=6)

4 Troubleshooting

When size exclusion chromatography was used for the purification of DOPC LUVs loaded with 1 mM calcein, no separated colour bands were observed which could have led to the incorrect collection of the elution fraction. What is more, this phenomenon can also be a result of unsuccessful encapsulation of calcein molecules into DOPC vesicles. The purification process was repeated using both HEPES buffer solutions of pH 5.0 and pH 7.4. The change in pH did not improve the purification of 1 mM calcein loaded LUVs.

To investigate this issue, Rh-PE dye was used to label the DOPC LUVs to better identify where the purified LUV band is present in the column. After LUV collection, 6% v/v Triton X-100 was introduced as a detergent to test whether calcein were encapsulated. The images of LUV purification with and without Rh-PE labelling could be found in Fig.S6 in Supplementary.

Three concentrations of 1mM, 10 mM, and 50 mM were tested in this work, but only for LUVs loaded with 50 mM calcein, a significant increase in calcein fluorescence intensity is observed after addition of Triton (Fig. 13). Hence this certifies that the previous failure in control experiments was due to inefficient encapsulation of calcein.

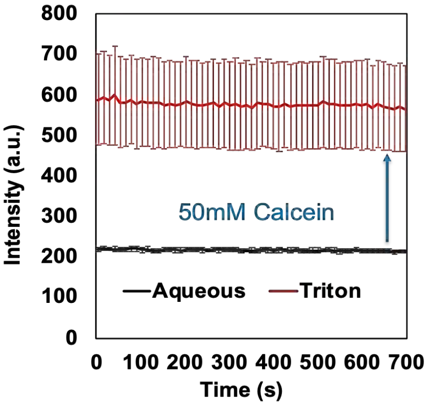

Figure 13. Fluorescence intensity change of calcein was detected before and after adding Triton to purified LUVs. For LUVs loaded with 50 mM calcein, it shows an increase over 400 a.u., meaning calcein encapsulation is successful.

Calcein will self-quench when its concentration exceeds 70 mM (Patel, Tscheka and Heerklotz, 2009), so 50 mM is within the range. However, to use 50 mM of calcein, equimolar of $CuCl_2$ is required to quench it which is not feasible due to the possible copper ion interactions with membranes leading to destabilisation as mentioned in previous discussion. Additional research is required on seeking for substitute buffer capable of quenching calcein instead of $CuCl_2$.

5 Conclusion and Outlook

The main objective of this project is to study oppositely charged LUV fusion in the context of their lipid and content mixing. The study investigated the influence of fusogenic phospholipid DOPE in LUV populations consisting of positively charged DOTAP containing LUVs and negatively charged DOPG containing LUVs.

To evaluate fusion, lipid mixing experiments were conducted first. The fluorescence assay on NBE-PE and Rh-PE verified an increase in the spatial distance between fluorophores attached on membrane due to the fusion between charged vesicles with 30 mol% DOPE, which was further proved by the emission spectra of Rh-PE. It also revealed that there is a positive correlation between Rh-PE emission intensity and DOPE concentration, which can be a result of instability of DOPE.

These results were also supported by DLS technique. It successfully proved that oppositely charged LUVs were fusing by their increment in size upon mixing, only when the LUVs contained fusogenic 30 mol% DOPE phospholipid. Without sufficient content of DOPE being added (below 30 mol%), although charged liposomes managed to associate and form neutral mean zeta potential, no significant change in LUV size was observed, meaning fusion would not occur.

In content mixing experiment, the fluorescence assay on calcein and its quencher $CuCl_2$ showed a decreasing intensity for mixing liposomes, which is a proof of cargo mixing taking place. However, the failure in control groups made it hard to compare and conclude the conditions for content mixing. This could be due to passive leakage of calcein and its being quenched by copper ions in the surroundings.

Furthermore, to solve the issues with calcein encapsulation into DOPC, calcein release experiments with detergent Triton were carried out and the results showed that the approximate minimum concentration that should be used for calcein encapsulation is 50 mM. However, such a high concentration of calcein would require an equivalent molar concentration of $CuCl_2$ which is too high and possibly causes damage to the lipid membrane, resulting in no LUV formation during extrusion. Hence a different content mixing strategy should be proposed.

To improve the accuracy and reliability of results, microfluidic technology can be applied to get more uniform size population of vesicles. And mixed LUVs can be detected with fluorescence intensity change of both fluorophores after different time periods, which helps observation of complete fusion process. In addition, Cryo-TEM microscopy can be referred to obtain the morphologic mixing status of LUVs.

In conclusion, this project provided a fundamental base for artificial microreactor development, and could be applied to further research on drug delivery system, including investigation into effects of different factor as pH, temperature and light signals on fusion process as well as encapsulating enzyme reaction. In future, the optimised conditions for LUV fusion would be applied for generation of a microreactor that is capable of producing chemical or enzymatic reactions due to separated compartmental fusing upon stimuli.

Acknowledgements

We appreciate Greta Zubaite for her generous support and help throughout the research. We would also express our gratitude to all the members in Membrane Biophysics Group at Imperial College London, especially Claudia Contini, Yizhao Yang, Matthew Allen, Ignacio Gispert Contamina, Aileen Cooney and Karen Zhu for their constructive suggestions towards this project.

References

Chen, Z., Wang, J., Sun, W., Archibong, E., kahkoska, A. R., Zhang, X., Lu, Y., Ligler, F. S., Buse, J. B. & Gu, Z. 2018. Synthetic beta cells for fusion-mediated dynamic insulin secretion. Nat Chem Biol, 14, 86-93.

Cui, L. & Kittipongpittaya, K., Mcclements, D., Decker, E. 2014. Impact of Phosphoethanolamine Reverse Micelles on Lipid Oxidation in Bulk Oils. Journal of Oil & Fat Industries. 91. 1931-1937. 10.1007/s11746-014-2544-9.

Du, C. & Webb, C. 2011. Cellular systems. Comprehensive biotechnology.

Elani, Y., Gee, A., Law, R. V., Ces, O. 2013. Engineering multi-compartment vesicle networks. Chemical science, 4.

Elani, Y., Law, R. V., Ces, O. 2014. Vesicle-based artificial cells as chemical microreactors with spatially segregated reaction pathways. Nat commun, 5, 5305.

Falsini, S. and Ristori, S., 2016. Lipoplexes from Non-viral Cationic Vectors: DOTAP-DOPE Liposomes and Gemini Micelles. [online] Springer Link. Available at: <https://link.springer.com/protocol/10.1007/978-1-4939-3718-9_3> [Accessed 12 December 2021].

Feng, S., Huang, G., 2001. Effects of emulsifiers on the controlled release of paclitaxel (Taxol) from nanospheres of biodegradable polymers. J. Control. Release. 71 (1), 5369.

Hamai, C., Yang, T., Kataoka, S., Cremer, P. and Musser, S., 2006. Effect of Average Phospholipid Curvature on Supported Bilayer Formation on Glass by Vesicle Fusion. Biophysical Journal, 90(4), pp.1241-1248.

Jayaraman, P., Yeoh, J. W., Jayaraman, S., Teh, A. Y., Zhang, J. & Poh, C. L. 2018. Cell-Free Optogenetic Gene Expression System. ACS Synth Biol, 7, 986-994.

Jia, H., Heymann, M., Hartel, T., Kai, L., Schwille, P. 2019. Temperature-sensitive protein expression in protocells. Chem Commun (Camb), 55, 6421-6424.

Jiang, X., Zhang, J., Zhou, B., Li, P., Hu, X., Zhu, Z., Tan, Y., Chang, C., Lü, J. and Song, B., 2018. Anomalous behavior of membrane fluidity caused by copper-copper bond coupled phospholipids. Scientific Reports, 8(1). [online] Available at: <https://www.nature.com/articles/s41598-018-32322-4>[Accessed 12 December 2021].

Jinturkar, K. A., Misra, A. 2011. Challenges and Opportunities in Gene Delivery. Challenges in Delivery of Therapeutic Genomics and Proteomics.

Kleusch, C., Hersch, N., Hoffmann, B., Merkel, R., Csiszar, A. 2012. Fluorescent lipids: functional parts of fusogenic liposomes and tools for cell membrane labeling and visualization. Molecules, 17, 1055-73.

Kolasinac, R., Kleusch, C., Braun, T., Merkel, R., Csiszar, A. 2018. Deciphering the Functional Composition of Fusogenic Liposomes. Int J Mol Sci, 19.

Krinsky, N., Kaduri, M., Zinger, A., Shainsky-Roitman, J., Goldfeder, M., Benhar, I., Hershkovitz, D., Schroeder, A. 2018. Synthetic Cells Synthesize Therapeutic Proteins inside Tumors. Adv Healthc Mater, 7, e1701163.

Kumar, A., Dixit, C. K. 2017. "Methods for characterization of nanoparticles". Advances in Nanomedicine for the Delivery of Therapeutic Nucleic Acids. pp. 43–58. doi:10.1016/B978-0-08-100557-6.00003-1. ISBN 9780081005576.

Kumar, M.N.R., Sameti, M., Mohapatra, S.S., Kong, X., Lockey, R.F., Bakowsky, U., et al., 2004. Cationic silica nanoparticles as gene carriers: synthesis, characterization and transfection efficiency in vitro and in vivo. J. Nanosci. Nanotechnol. 4 (7), 876881.

Li, Q., Elani, Y. Ces, O. 2019 Engineering Fusogenic Membranes as Functional Compartments in Vesicle Microreactors.

Ma, Y., Wang, Z., Zhao, T., Lu, T., Rutao Wang, R., Mei, Q. and Chen, T., 2013. Enhanced bactericidal potency of nanoliposomes by modification of the fusion activity between liposomes and bacterium. International Journal of Nanomedicine, p.2351.

Maier, O., Oberle, V., Hoekstar, D. 2002. Fluorescent lipid probes: some properties and applications (a review). Chemistry and Physics of Lipids, 116, 3-18.

Martino, C., Kim, S.H., Horsfall, L., Abbaspourrad, A., Rosser, S. J., Cooper, J., Weitz, D. A. 2012. Protein Expression, Aggregation, and Triggered Release from Polymersomes as Artificial Cell-like Structures. Angewandte Chemie, 124, 6522-6526.

Mo, R., Jiang, T., Gu, Z. 2014. Enhanced anticancer efficacy by ATP-mediated liposomal drug delivery. Angew Chem Int Ed Engl, 53, 5815-20.

Mochizuki, S., Kanegae, N., Nishina, K., Kamikawa, Y., Koiwai, K., Masunaga, H. & Sakurai, K. 2013. The role of the helper lipid dioleoylphosphatidylethanolamine (DOPE) for DNA transfection cooperating with a cationic lipid bearing ethylenediamine. Biochim Biophys Acta, 1828, 412-8.

Mondal Roy, S., Sarkar M. 2011. Membrane fusion induced by small molecules and ions. J Lipids, 2011, 528784.

Nuzzo, D., Picone, P. 2021. Multiple Sclerosis: Focus on Extracellular and Artificial Vesicles, Nanoparticles as Potential Therapeutic Approaches. Int J Mol Sci, 22.

Patel, H., Tscheka, C., Heerklotz, H. 2009. "Characterizing vesicle leakage by fluorescence lifetime measurements". Soft Matter. 5 (15): 2849–2851. Bibcode:2009SMat....5.2849P. doi:10.1039/B908524F.

Putta, P., Rankenberg, J., Korver, R., van Wijk, R., Munnik, T., Testerink, C., Kooijman, E. 2016. Phosphatidic acid binding proteins display differential binding as a function of membrane curvature stress and chemical properties:. Biochimica et Biophysica Acta (BBA) Biomembranes. 1858. 10.1016/j.bbamem.2016.07.014.

Rikihisa, N., Watanabe, S., Saito, Y., Sakai, H. 2017. Artificial Red Blood Cells as Potential Photosensitizers in Dye Laser Treatment Against Port-Wine Stains. J Funct Biomater, 8.

Salaün, C., James, D. J., Chamberlain, L. H. 2004. Lipid Rafts and the Regulation of Exocytosis. Traffic, 5, 255-264.

Salehi-Reyhani, A., Ces, O., Elani, Y. 2017. Artificial cell mimics as simplified models for the study of cell biology. Exp Biol Med (Maywood), 242, 1309-1317.

Sato, Y., Takinoue, M. 2019. Creation of Artificial Cell-Like Structures Promoted by Microfluidics Technologies. Micromachines (Basel), 10.

Simoes, S., Moreira, J. N., Fonseca, C., Duzgunes, N., De Lima, M. C. 2004. On the formulation of pH-sensitive liposomes with long circulation times. Adv Drug Deliv Rev, 56, 947-65.

Thermofisher.com. n.d. Photobleaching Principles | Thermo Fisher Scientific - UK. [online] Available at: <https://www.thermofisher.com/uk/en/home/life-science/cell-analysis/cell-analysis-learning-center/molecular-probes-school-of-fluorescence/fluorescence-basics/fluorescence-fundamentals/photobleaching-principles.html> [Accessed 13 December 2021].

Van Swaay, D., Demello, A. 2013. Microfluidic methods for forming liposomes. Lab Chip, 13, 752-67.

Xu, C., Hu, S., Chen, X. 2016. Artificial cells: from basic science to applications. Mater Today (Kidlington), 19, 516-532.

Design of a Red Blood Cell-derived Nanoparticle System to Efficiently Target Cancer Cells

Paolo Biondi and Purav Choudhury
Department of Chemical Engineering, Imperial College London, U.K.

Abstract A red blood cell vesicle (RBCV) nanoparticle drug delivery system was synthesised to efficiently target cancer cells via the enhanced permeability and retention effect. This was achieved by producing RBCVs, and loading them with fluorescein, coating with a pH-responsive PLP-NDA18% polymer and incorporating cholesterol. The average particle size of RBCVs was below 200nm, which was confirmed using a Zetasizer. Encapsulation efficiencies and drug release were also measured. The highest encapsulation efficiency obtained was 16.74±0.4%, and the largest difference in drug release after 24 hours between endosomal pH 6 and physiological pH 7.4 was 24.00%. Hemolysis assay showed that PLP-NDA18% displays maximum membrane destabilisation at endosomal pH and minimum membrane destabilisation at physiological pH. This is desirable to reduce cytotoxicity and enhance the targeting of cancer cells. Overall, this study shows that RBCVs can be utilised to successfully encapsulate hydrophilic drugs for intracellular drug delivery, with the potential for further improvement in the future.

1 Introduction

Over the past 60 years, the development of vaccines and antibiotics has sharply reduced mortality from infectious diseases, and improvements in the prevention of cardiovascular diseases mean that in 134 of 183 countries cancer is the first or second leading cause of premature death (CP, E and BW, 2020). Common treatment strategies include surgery, immunotherapy, radiotherapy and chemotherapy. A mixture of treatments is sometimes utilised, such as chemoradiotherapy, combining chemotherapy and radiotherapy, which can increase effectiveness (Kimberly D. Miller *et al.*, 2019). Chemotherapeutic drugs however face problems such as opsonisation, non-specific cytotoxicity, accumulation in vital organs and rapid clearance by the reticuloendothelial system. Additionally, driver mutations in cancer cells can lead to drug resistance resulting in chemotherapeutic drugs becoming ineffective (Chen and Chang, 2019). Therefore, research and development of new drug delivery systems are critical.

Drug delivery systems are designed to transport therapeutic drugs to specific target cells, minimising interactions with non-specific cells or organs (Erin B. Lavik *et al.*, 2013). Nanoparticle technology has been important for drug delivery since particles of diameter between 100-200nm have been shown to accumulate in tumour cells due to the enhanced permeability and retention effect (Carlotta Pucci *et al.*, 2019). A current well-established nanoparticle technique is the use of liposomes, coated by a synthetic polymer PEG, to encapsulate and deliver cancer drugs. Coating with PEG is termed PEGylation and is used due to its biocompatibility and stealth-like properties, an ability to evade the immune system and increase circulation time. The hydrophilic polymers in PEG hide the liposome nanoparticles behind a hydration layer to decrease macrophage uptake (Verhoef and Anchordoquy, 2013). However, there have been growing reports over immune responses against PEG, and of multiple administrations leading to antibody resistance. Therefore, there has been a shift in focus into biomimicry and encapsulating cancer drugs with naturally derived materials, with a particular interest in using red blood cells. Creating a nanoparticle drug delivery system by encapsulating drugs into red blood cell membranes is beneficial due to biocompatibility, long circulation time and ease of production (Ronnie H Fang *et al.*, 2018)

In this study, the use of red blood cell membranes for drug delivery will be investigated, and a fixed concentration of fluorescein will be used as a model drug, with defibrinated sheep blood used to obtain red blood cell membranes. Ghost red blood cells will be produced, membranes with intracellular contents removed, then fluorescein will be loaded in-situ during the production of red blood cell vesicles (RBCVs). To achieve a pH-dependent drug release, the RBCVs were coated with polymer PLP-NDA 18%, and different amounts of cholesterol were incorporated to increase rigidity and control drug release. The first main objective of the study is to maximise the encapsulation efficiencies of fluorescein loading into the RBCVs. The second main objective of the study is to minimise payload release at physiological pH and maintain payload release at a high level at endosomal pH, which will be tested by measuring drug release over 24 hours. This is to ensure that the drug will only be released when it reaches cancer cells and is engulfed by endosomes at endosomal pH. Encapsulation and release will be varied through testing the effect of the number of extrusions during RBCV formation, incubation time pre-RBCV formation and through the incorporation of different amounts of cholesterol. Additionally, hydrodynamic diameter, polydispersity index and zeta potential are to be measured to characterise the drug delivery systems produced. Also, the pH responsiveness of PLP-NDA 18% was evaluated through hemolysis assay.

2 Background

The development and application of red blood cells for use in drug delivery systems has risen dramatically in recent years, due to the excellent biocompatibility, biodegradability and long circulating half-life of 100-120 days, compared to around 10 hours for PEG-modified liposomes (Muzykantov, 2011).

Various studies have been performed to assess encapsulation efficiencies and payload release of different drugs into RBCV systems. A study by (Aryal *et al.*, 2013) loaded doxorubicin into RBCVs and achieved low encapsulation efficiencies between 0.9-1.8%. In the study during RBCV formation, the samples were extruded through a 100-nm polycarbonate porous membrane 11 times. In our study, we will be testing 5, 15 and 25 extrusion repetitions to assess its impact on encapsulation efficiency and payload release, as the mechanical force during extrusion can promote fluorescein to pass through the lipid bilayer of the RBCV membrane, increasing encapsulation (Qing Xia *et al.*, 2019). A study by (Wang and Huang, 2003) investigated encapsulating protein into liposomes, which showed that increasing incubation time up to 2 hours increased encapsulation and then plateaued. This principle can be applied to produce RBCV drug delivery systems, where ghost cells will be mixed with fluorescein solution and then incubated for 1, 2 and 3 hours before forming RBCVs. During the incubation, fluorescein can passively pass through the lipid bilayer of the membrane and start loading before the vesicles are produced, potentially increasing encapsulation.

The incorporation of cholesterol into the lipid bilayer membrane increases membrane rigidity and reduces membrane permeability (Rongjun Chen, 2019). A study by (Maria-Lucia Briuglia *et al.*, 2015) using liposomes showed that by increasing the amount of cholesterol added, the encapsulation efficiencies of hydrophilic drugs decreased. Therefore, cholesterol will be incorporated pre and post RBCV formation to investigate its effect on encapsulation. A paper by (Asli Astarci *et al.*, 2009) tested the encapsulation and release profiles of celecoxib in liposomes. It was found that adding cholesterol lowered encapsulation and significantly lowered payload release. Celecoxib is a hydrophobic drug, therefore, adding cholesterol, which is also hydrophobic, reduced encapsulation. In our study, fluorescein was loaded to investigate the influence of loading hydrophilic drugs into RBCV systems.

There is a literature gap for designing a drug delivery system that combines red blood cell membranes, a pH-responsive polymer, such as PLP-NDA 18%, and cholesterol. The objective of this research is to design an RBCV drug delivery system to improve cancer drug delivery treatment. By investigating different parameters such as number of extrusions, incubation time pre-RBCV formation and cholesterol content, the optimum configuration can be determined to optimise encapsulation efficiencies of cancer drugs, whilst keeping a good balance between high payload release at endosomal pH, and a low payload release at physiological pH.

3 Methods

3.1 Materials

Sodium chloride, potassium chloride, potassium chloride, disodium hydrogen phosphate, monopotassium phosphate, fluorescein sodium salt, ethylenediaminetetraacetic acid (EDTA), Triton X-100 and cholesterol were purchased from Sigma-Aldrich. On the other hand, chloroform was purchased from VWR. Defibrinated sheep blood was purchased from TCS Biosciences Ltd. Lastly, polymer (PLP-NDA 18%) was provided by Nikki Henry (Ph.D. student, Imperial College London).

3.2 Methods

3.2.1 Preparing RBCs and RBCVs

To prepare red blood cell ghost cells (GCs), 5 ml of defibrinated sheep blood was centrifuged for 4 minutes at 4000 rpm and 4°C. The supernatant was then removed and replaced by 5 ml 1x PBS buffer to wash the RBCs. The washing step was repeated three times. Thereafter, the supernatant was removed and replaced by 4.5 ml of 0.2 mM EDTA solution and 0.5 ml 10x PBS buffer. This was centrifuged for 7 minutes at 12100 rpm and 4°C and repeated 7 times. The ghost cells were then washed one last time with 5 ml 1x PBS buffer. The supernatant was removed, and the final volume was made up to 5 ml with 1x PBS buffer. The final 5 ml sample of ghost cells was then stored at 4°C. Multiple test tubes were used to obtain larger volumes of ghost cells.

To obtain red blood cell-derived vesicles (RBCVs), GCs were sonicated with an ultrasonic disintegrator for 10 mins at 100 W, 50% amplitude, 1 s on, 1 s off. Thereafter, the sonicated GCs were extruded through a 0.2 μm membrane using an extruder at 1 bar pressure to obtain RBCVs, which were then stored at 4°C.

3.2.2 Drug loading and polymer coating

Fluorescein-loaded GCs were prepared in situ by mixing GCs with fluorescein stock solution (fluorescein dissolved in 1x PBS buffer) using sonication and extrusion, as described in the previous section, to load fluorescein at a fixed concentration of 0.125 mg/ml. The RBCVs were coated with polymer by adding PLP-NDA 18% stock solution (PLP-NDA18% dissolved in 1x PBS buffer) to it and incubating in a water bath for 1 hour at 37°C and 100 rpm. The coated RBCVs were then stored overnight at 4°C.

3.2.3 Cholesterol incorporation

Two different concentrations of cholesterol were incorporated: 5% and 10% by volume. This was achieved by dissolving 150 mg of cholesterol in 3 ml chloroform to make a stock solution. The stock solution was then mixed with two different samples of ghost cells to achieve 5% and 10% concentration using a round bottom flask and heating for 30 minutes at 37°C over an oil bath to fully evaporate the chloroform.

3.2.4 Dynamic light scattering (DLS) and zeta potential

A dynamic light scattering (DLS) instrument (Zetasizer) was used to find the surface charge (zeta potential) and average particle size. Before measurement, a 0.45 μm membrane was used to filter the samples, and each sample was measured 3 times in a 10 mm diameter cuvette at 25°C at a 90° angle.

3.2.5 Quantitative measurement of fluorescein

A plate reader, emission filter at 500-550 nm and excitation filter at 475 nm (blue) were used to measure the fluorescence intensity of the model drug fluorescein. The fluorescein intensity was used to calculate the fluorescein concentration using standard calibration curves shown in Figures SI 1 and SI 2, with $R^2 = 0.9838$ and $R^2 = 0.9968$, respectively.

3.2.6 Fluorescein encapsulation and release

Fluorescence intensity was measured before and after purification to calculate encapsulation efficiency as seen in Equation 1. Firstly 50 µl of the coated RBCV samples were mixed with 50 µl of 0.1% (v/v) Triton X-100 in microplates, then incubated in a water bath for 10 minutes at 37°C. The fluorescence intensity was then measured. Then, the original samples were centrifuged for 10 minutes at 4°C and 1000 rpm and resuspended with 1x PBS to remove excess drug and polymer, purifying the samples. 50 µl of the respective purified samples were mixed with 50 µl of 0.1% (v/v) Triton X-100 in microplates, then incubated in a water bath for 10 minutes at 37°C. The fluorescence intensity was then measured again. To calculate the encapsulation efficiency, Equation 1 was used:

$$\text{Encapsulation efficiency } \% = \frac{m_l}{m_o} * 100 \ (1)$$

where m_o is the weight of fluorescein added to the RBCVs, and m_l is the weight of fluorescein encapsulated in the RBCVs.

Release fluorescence intensity for fluorescein loaded RBCVs was measured after purification. To adjust the pH of the samples to 6 and 7.4, HCl solution (0.2M) was added. The adjusted samples were then added to dialysis tubes and immersed in 1x PBS buffer at the corresponding pH of the sample. The samples were then incubated in a water bath at 37°C at 100 rpm for 24 hours. At 1, 2, 3, 4, 5 and 24 hour time intervals, 100 µl of the sample on the outside of the dialysis tubes were extracted, and the fluorescence intensity was measured. This volume was replaced with 100 µl of 1X PBS buffer at the corresponding pH. The fluorescein released from the RBCVs was then calculated using Equation 2:

$$\text{Relative release } \% = \frac{m_r}{m_t} * 100 \ (2)$$

where m_r us the weight of fluorescein released, and m_t is the weight of fluorescein the RBCV after purification.

3.2.7 Hemolysis assay of PLP-NDA18%

Unloaded RBCV samples were coated with polymer a day before performing hemolysis assay. To remove the excess polymer, the samples were centrifuged for 10 minutes at 4°C and 10,000 rpm. The supernatant (polymer) was then removed and replaced by either the pH 5.5, 6.0, 6.5, 7.0 and 7.4 PBS buffer or the pH 5.0 citrate buffer. Defibrinated sheep blood was then centrifuged for 3 minutes at 3500 rpm, and the supernatant was removed. 150mM NaCl solution was used to wash the RBCs 3 times. 400 µl of the RBCV samples were added to 100 µl of washed RBCs, at the different pHs. Positive and negative control samples were produced by adding water or the correct pH buffer, respectively, to the RBCs instead of adding the RBCV samples. The samples produced were then incubated in a water bath for 1 hour at 120 rpm and 37°C, followed by centrifugation for 3 minutes at 3500 rpm. The supernatant of each sample was extracted, and the absorbance was measured in a plate reader, at a 560 nm wavelength. Using the absorbance, the relative hemolysis was calculated as shown in Equation 3:

$$\text{Relative hemolysis } \% = \frac{\text{Abs} - \text{Abs}^-}{\text{Abs}^+} * 100 \ (3)$$

where Abs is the absorbance of the supernatant, Abs^- is the absorbance of the negative control and Abs^+ is the absorbance of the positive control.

3.2.8 Statistical analysis

All data points were repeated in triplicates (n=3), and student's t-test was used to determine if the difference in results were significant, where $p<0.05$ indicates the results are significantly different.

4 Results

4.1 Characterisation of RBCVs

The characterisation of RBCV systems was investigated to confirm the successful production of RBCVs. As seen in Table 1, average particle size and polydispersity index (PDI) were measured for different samples using a Litesizer to perform dynamic light scattering (DLS). During DLS, a laser is targeted at the sample particles. The light scattered from different particles combines to create a fluctuating intensity signal, which is used to create an autocorrelation function, to extract a translation diffusion coefficient. The average particle size can then be obtained via the Stokes-Einstein equation. The smaller the particles, the higher the diffusion rate and more rapid fluctuations in scattered light, leading to a more rapid correlation decay function (Dynamic Light Scattering DLS, 2021).

RBCV sizing is critical because a diameter between 30nm and 200nm ensures that nanoparticles are long-circulating and accumulate inside tumour tissues (Alexandre Albanese *et al.*, 2012). Tumours contain large fenestrations between the endothelial cells of blood vessels formed by angiogenesis, described as being leaky and more permeable. Nanoparticles of size 100-200nm can extravasate through vascular fenestrations within tumours, targeting the tumour via the enhanced permeability and retention effect (EPR), and escaping macrophage uptake in the liver and the spleen, enhancing circulation time (Elvin Blanco *et al.*, 2015).

In this study, the RBCV samples were all below 200nm, which shows that the sonication and extrusion techniques had successfully formed the RBCVs and

Table 1. Particle sizes polydispersity index (PDI) and zeta potential of different samples. Loading was done 0.125 mg/ml fluorescein and coated with 1 mg/ml PLP-NDA18%.

		Size (nm)	PDI	Zeta potential (mV)
Uncoated	Empty RBCV	140.21±2.84	0.23±0.02	-14.8±0.3
	Loaded RBCV	173.71±1.32	0.18±0.02	-14.1±0.4
Coated	Loaded RBCV	187.65±2.45	0.21±0.03	-16.6±0.3
	Loaded RBCV + Cholesterol	198.97±0.84	0.22±0.02	-16.3±0.2

decreased sample sizes as desired. Table 1 shows that uncoated and unloaded RBCV had the smallest average size at 140.21±2.84 nm, which increased to 173.71±1.32 nm when loaded. Coating the RBCVs with PLP-NDA 18% increased average particle size to 187.65±2.45 nm. This increase can be attributed to the comb-like structure of the polymer, which consists of long NDA alkyl chains grafted onto the carboxylic acid groups along the backbone of a linear pseudopeptide (Rongjun Chen *et al.*, 2017).

The addition of 5% (v/v) cholesterol further increased the average particle size to 198.97±0.84 nm. This agrees with literature that focused on liposomes where adding cholesterol increased size to a greater extent than just by coating with polymer. The introduction of cholesterol increases the rigidity of the bilayered lipid membrane and changes the interaction between PLP-NDA 18% coated and the membrane. Cholesterol could reduce the insertion of the long hydrophobic NDA chains into the membrane, increasing the hydrophobicity of the membrane surface. This results in more hydrophobic interaction between the membrane and polymer to occur on the membrane surface, rather than translocation through the membrane, leading to a slight increase in average particle size as displayed (Siyuan Chen and Rongjun Chen, 2016). PDI is a measure of the particle size distribution, which varied from 0.18±0.02 to 0.23±0.02. PDI values of around 0.2 or below are acceptable for use in polymer incorporated nanoparticle drug delivery (Danaei *et al.*, 2018).

Zeta potential was investigated to estimate the surface charge of the RBCV samples. The lipid bilayer membrane of an RBC contains embedded sialylated glycoproteins, creating a repulsive electric potential. This gives RBCs a negative zeta potential. Literature data measured this to be -13.7mV for human RBCs (Heloise Pöckel Fernandes *et al.*, 2011). From Table 1, zeta potential varied between -14.1 to -16.6 mV agreeing with the literature data, suggesting that surface proteins are successfully maintained. Coating loaded RBCVs made the surface charge more negative, from 14.1±0.4 mV to -16.6±0.3 mV, as the polymer contains negatively charged carboxylate groups. The addition of cholesterol had no significant effect on the zeta potential compared to coated without cholesterol ($p<0.05$ in a student's t-test). Cholesterol is an amphipathic module, comprised of a hydroxyl group polar head, with the rest of the molecule being non-polar, making the molecule overall non-polar (LabXchange, 2020). Therefore, the insignificant change in zeta from -16.6±0.3 mV to -16.3±0.2 mV is expected. All tested samples had a negative surface charge which is critical because nanoparticles with a positive charge can cause blood clotting and hemolysis in the blood (De Jong and Borm, 2008).

Overall, the average particle sizes of the samples tested remained below 200nm, which is desired for effective drug delivery. The zeta potential values were all negative and within an expected range, confirming that RBCVs were successfully produced, PLP-NDA 18% coated the RBCVs, and that 5% (v/v) cholesterol was incorporated as intended.

4.2 Hemolysis assay and polymer coating

PLP-NDA 18% was used to coat the RBCVs throughout the study. PLP-NDA 18% is formed via grafting hydrophobic decylamine (NDA) onto the pendant carboxylate groups along the backbone of poly (L-lysine isophthalamide), PLP, a pseudopeptide. This results in a comb-like structure, with the long hydrophobic NDA chains acting as hydrophobic membrane anchors, increasing polymer hydrophobicity (Rongjun Chen *et al.*, 2017). PLP-NDA 18% was chosen in preference to the linear PLP due to the enhanced cell membrane destabilising ability at endosomal pH and increased hydrophobicity that is added with the NDA chains.

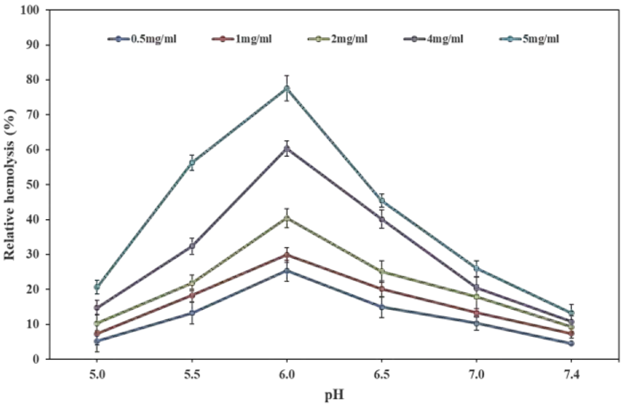

Figure 1. Hemolysis assay of RBCs for different PLP-NDA18% concentrations.

RBCVs containing the payload drug enter the body into the blood, which is maintained at physiological pH, between pH 7.35 to 7.45. When the RBCV system reaches the target drug tumour, the RBCV is engulfed by endosomes and enters the tumour cells via a process called endocytosis. The pH gradually decreases, and the payload is released via endosomal escape into the cytoplasm of cancerous cell lines, which occurs at

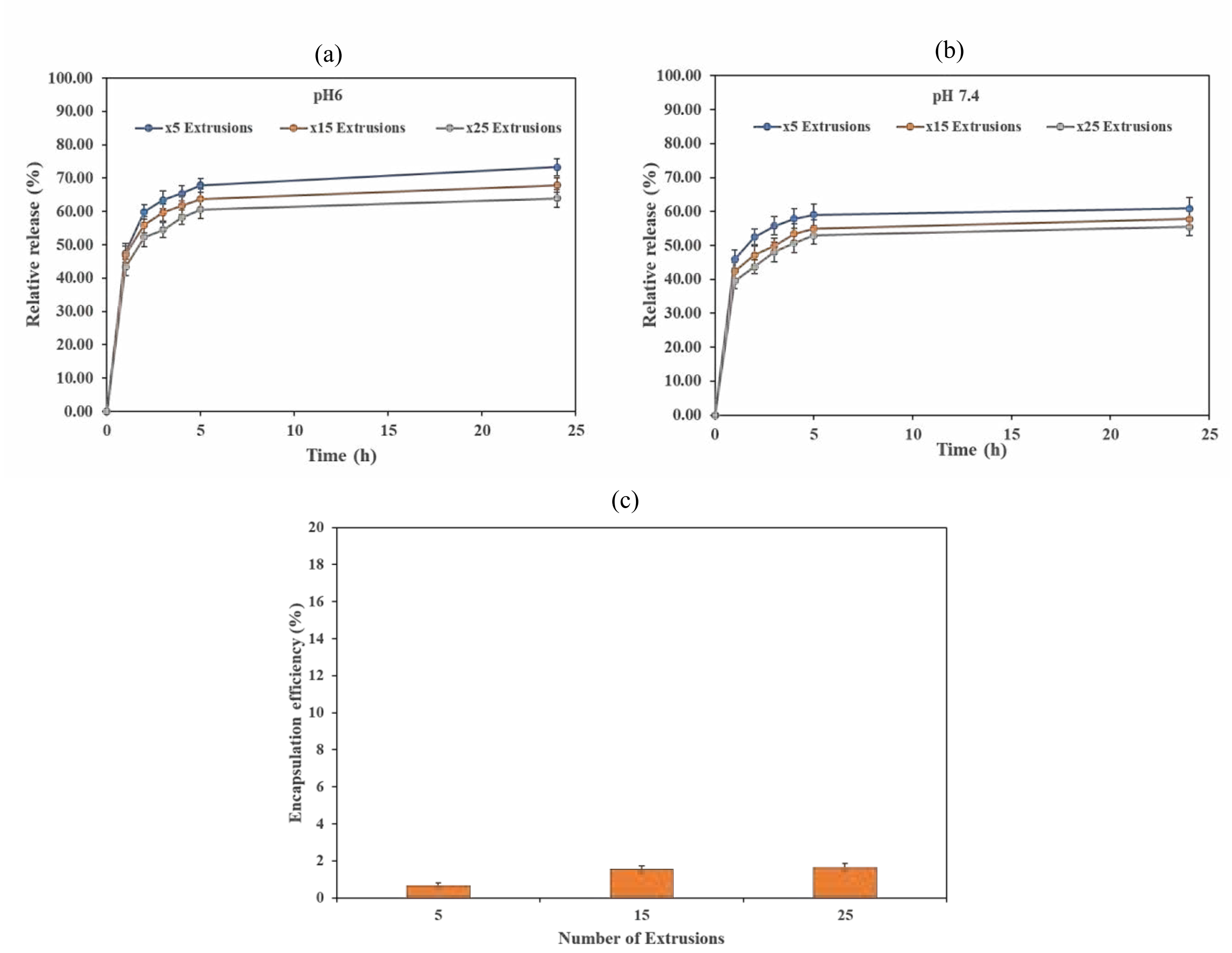

Figure 2. (a) Release at pH 6 varying extrusions. (b) Release at pH 7.4 varying extrusions. (c) Encapsulation efficiency at pH 7.4 varying extrusions.

endosomal pH around 6.5 to 5.5 (Oh and Park, 2014). Therefore, it is desirable to coat the RBCVs with a polymer that is highly pH-sensitive and displays low membrane destabilisation at physiological pH. However, high membrane destabilisation at endosomal pH is desired to ensure the drug is only released at the target cancer cells. Literature shows that PLP-NDA 18% also presents another benefit: cell membrane destabilisation occurs via the polymer-mediated pore formation mechanism, reducing cytotoxicity (Rongjun Chen *et al.*, 2017).

In this study, RBCV membranes produced were used as a model for mimicking endosomal membranes to investigate the cell membrane disruptive activity of PLP-NDA 18% by performing hemolysis assay. A pH range of 5.0 to 7.4 was used to assess the polymer activity over the full endocytic pathway. The red blood cell disruption percentage and the amount of haemoglobin released can be quantified to measure the extent that PLP-NDA 18% causes RBC membrane destabilisation (Evans *et al.*, 2013). The results of the study are displayed in Figure 1, with five concentrations of polymer coating tested.

For all concentrations of polymer coating, the relative hemolysis was lowest at pH 7.4, which is desired to minimise payload release at physiological pH. At pH 5, the carboxylate groups may protonate causing an increase in hydrophobic interactions and aggregation (Rongjun Chen *et al.*, 2017), then precipitation, which could limit cell membrane disruption and explain why there was also low relative hemolysis at this acidic pH. For each respective concentration of polymer coating, there was an increase in relative hemolysis observed in the endosomal pH range of 5.5 to 6.5, with the maximum relative hemolysis at pH 6, indicating maximum cell membrane destabilisation at pH 6. 25.34±3.14%, 29.85±2.10%, 40.42±2.71%, 60.34±2.24% and 77.54±3.64% relative hemolysis was achieved at pH6 for 0.5mg/ml, 1mg/ml, 2mg/ml, 4mg/ml and 5mg/ml polymer coating concentrations, respectively. This behaviour exhibited by the polymer is expected and optimum to ensure low payload release at physiological pH in the blood but maximum payload release at target cancer cells. Going forward in the study encapsulation efficiencies will be measured at ph 7.4, and release profiles will be investigated at both physiological pH 7.4 and endosomal pH 6.

4.3 Number of extrusions

Extrusion is a technique used to reduce the size of vesicles and fuse them, which has several advantages over other methods; it yields vesicles with homogeneous size distributions; it is reproducible; it is rapid; and it is

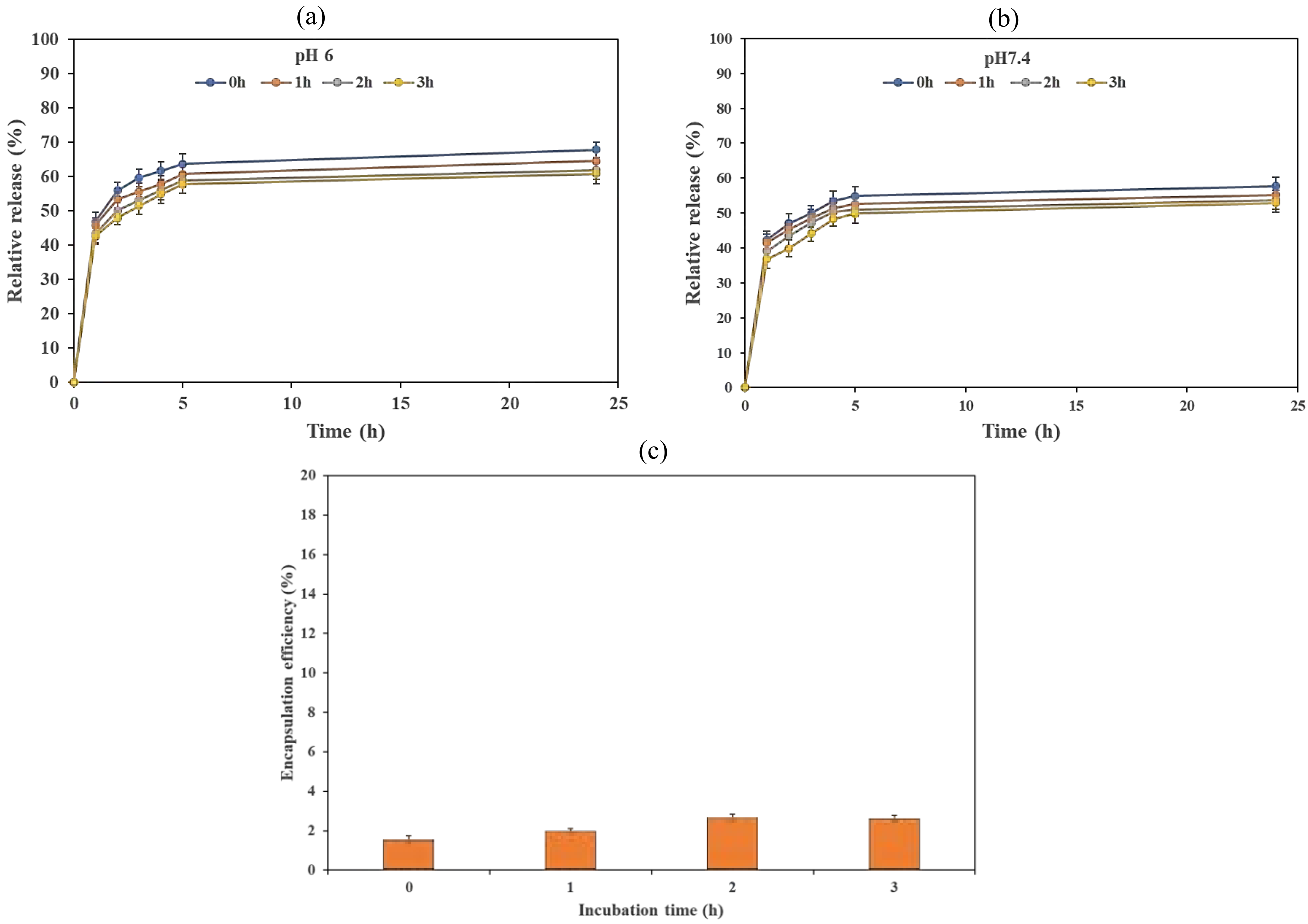

Figure 3. (a) Release at pH 6 varying incubation time. (b) Release at pH 7.4 varying incubation time. (c) Encapsulation efficiency at pH 7.4 varying incubation time.

a relatively gentle process. Changing the number of extrusion cycles was tested because it influences the mean diameter and size distribution of the vesicles produced, which can affect the relative release and encapsulation efficiency (Berger *et al.*, 2001).

Figure 2 (c) shows the effect of changing the number of extrusions on encapsulation efficiency. In general, encapsulation efficiency increased with an increasing number of extrusions. According to literature, extrusion reduces the size of the vesicles and causes a narrow size distribution, which leads to better interactions between the vesicles and the drug, leading to better encapsulation (Colletier *et al.*, 2002). By increasing the number of extrusions from 5 to 15, the encapsulation efficiency increased by about three times. This was a significant increase, with $p<0.05$ in a student's t-test. However, there was a plateau when extrusion repetitions were increased from 15 to 25. The encapsulation efficiency does not change significantly beyond a certain number of extrusions because the sample gets adsorbed in the filter inside the extruder (Colletier *et al.*, 2002).

Looking at drug release, at both pHs, increasing the number of extrusions decreased relative drug release. This is because smaller vesicles lead to better interactions between the payload and vesicles, which makes it harder for the drug to be released. A high encapsulation efficiency at pH 7.4 is desirable as this indicates that more fluorescein is loaded into the vesicles. On the other hand, a high relative payload release at pH 6 is desirable as this is the endosomal pH, while at physiological pH 7.4 a low payload release is favourable. 15 extrusions provided the best balance of increasing encapsulation efficiency, decreasing release at pH 7.4 and maintaining a relatively high release at pH 6. This was therefore used in the subsequent sections. Comparing Figures 2 (a) and 2 (b), the release at pH 7.4 is not significantly lower than the release at pH 6. Therefore, other parameters were varied to increase this difference and further increase encapsulation.

4.4 Incubation time

Before sonication and extrusion, ghost cells and fluorescein solution were incubated at 37°C for 1, 2 and 3 hours, with the results shown in Figures 3 (a), (b) and (c). As shown in Figure 3 (c), increasing incubation time generally improves encapsulation efficiency. This is because incubating provides an opportunity for fluorescein to passively diffuse into the GCs (Shariat, 2014). Increasing incubation time from 0 to 2 hours improved encapsulation efficiency significantly from 1.55±0.18% to 2.54±0.16% ($p<0.05$ in a student's t-test). This is an improvement from just 15 extrusions with no incubation discussed in section 3(extrusions). Beyond 2 hours incubation, however, the amount of drug encapsulated reached a plateau because a dynamic equilibrium between free and loaded drug was achieved, and there was a limited inner volume in the GCs (Shariat, 2014).

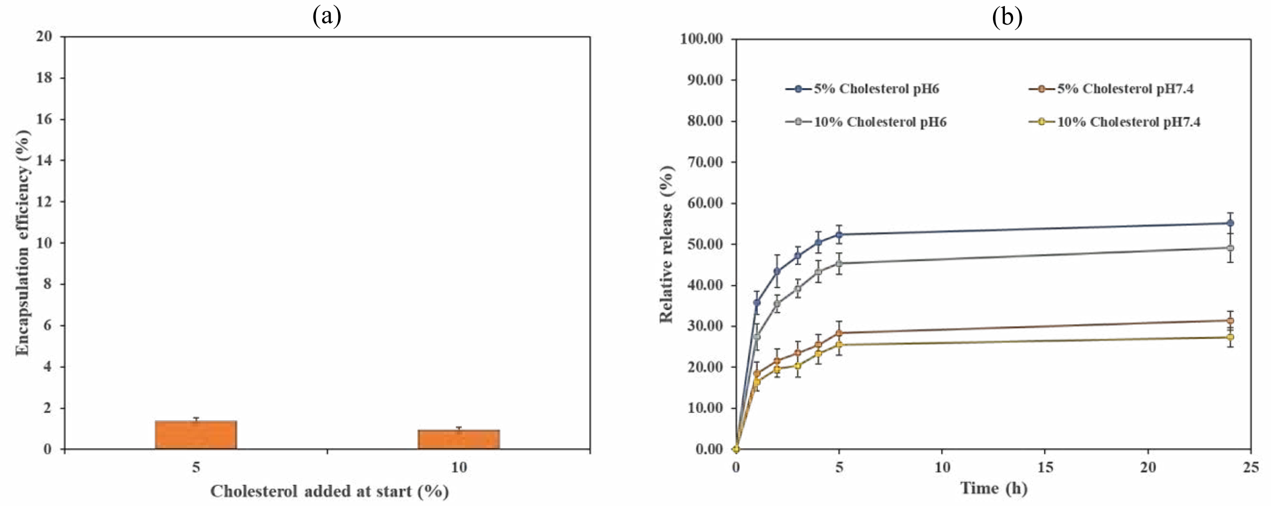

Figure 4. (a) Effect of adding 5 and 10% (v/v) cholesterol pre-RBCV formation on encapsulation efficiency. (b) Effect of adding 5 and 10% (v/v) cholesterol pre-RBCV formation on release.

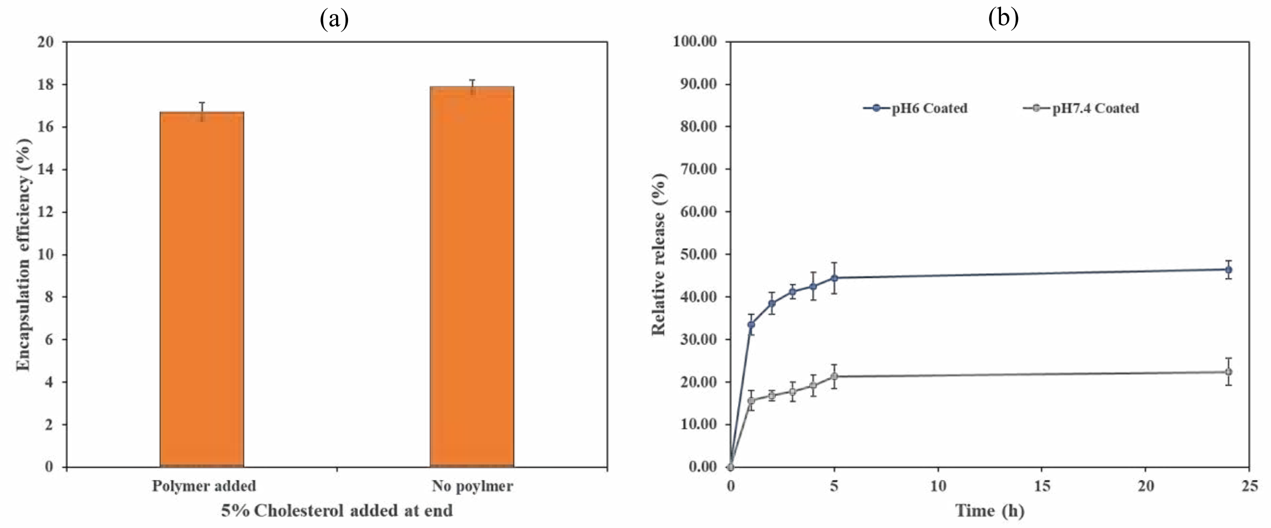

Figure 5. (a) Effect of adding 5% cholesterol (v/v) post-RBCV formation on polymer coated and uncoated encapsulation efficiency. (b) Effect of adding 5% cholesterol post-RBCV formation on release.

For payload release, at both pHs, increasing the incubation time decreased relative drug release, albeit very slightly. For 2 hour incubation compared to no incubation, release after 24 hours decreased by 4.01% at pH 7.4 and by 6.00% at pH 6. This change in the release was not significant, with p>0.05 in a student's t-test. Therefore, in subsequent experiments, 2h incubation was incorporated because it improved the encapsulation efficiency at pH 7.4 and did not lead cause a very large drop in relative release at pH 6. Incubating further led to no additional improvement in encapsulation efficiency and lowered the release slightly more.

Within a given incubation time, the relative release was slightly higher at endosomal conditions (pH 6) compared to physiological conditions (pH 7.4) On average, the release was 7.35% higher at pH 6. This difference is similar to that obtained in section 3. Therefore, cholesterol was incorporated to increase the difference in release at pH 6 and pH 7.4 and to further improve encapsulation efficiency.

4.5 Cholesterol incorporation

The effect of incorporating cholesterol, a rigid system of 4 fused hydrocarbon rings with a polar hydroxyl head (Rongjun Chen, 2019), was investigated. Incorporating cholesterol into RBCV systems can help maintain structural integrity and fluidity of the membrane, providing mechanical stability and decreasing permeability to small water-soluble molecules (Rongjun Chen, 2019). Cholesterol can dissolve within the bilayered lipid membrane and increase the packing density of lipid molecules. This effectively fills in the spaces of the membranes, making the bilayer less permeable (Mohammed *et al.*, 2004).

Firstly, 5 and 10% (v/v) cholesterol were added to the RBCs and then sonicated and extruded, forming RBCVs. From Figure 4 (a), the encapsulation efficiencies achieved were 1.39±0.14% and 0.95±0.13% for 5 and 10% cholesterol, respectively, which is lower than the 2.60±0.15% achieved previously with 15 extrusions and 2 hours of incubation. A previous study looking at loading ibuprofen showed that increasing cholesterol content reduced the encapsulation efficiencies of the drug (Mohammed *et al.*, 2004). In our study, adding 5% cholesterol significantly reduced efficiencies and 10% even more so (student t-test $p<0.05$), agreeing with the literature. Cholesterol reduces membrane permeability and potentially reduces how much fluorescein can pass through the RBC membrane during in situ loading with sonication and extrusion, reducing encapsulation efficiencies. According to Figure 4 (b), the difference in the release between pH 6 and pH 7.4 after 24 hours was 23.71% and 21.81% for 5 and 10% cholesterol, respectively. This is a significantly larger difference compared to those obtained in sections x and x. 5% cholesterol gave a higher encapsulation efficiency and larger difference in release than 10% cholesterol. Therefore, 5% cholesterol is better for drug delivery.

Although drug release was improved by adding cholesterol at the start, encapsulation efficiencies remained low, so the effect of incorporating 5% cholesterol at the end, post-RBCV formation, was investigated. From Figure 5 (a), the encapsulation efficiencies increased dramatically to 16.74±0.4% and 17.92±0.3% for polymer-coated and uncoated samples, respectively. One sample was coated and one was uncoated to test if the polymer was responsible for low encapsulation obtained in previous sections. Interestingly, the higher encapsulations shown in Figure 5 (a) indicated the polymer was not responsible for low encapsulation. Similar to improving encapsulation, cholesterol incorporation at the end improved release behaviour as seen in Figure 5 (b). The difference in payload release between pH 6 and pH 7.4 after 24 hours was 24%, the largest difference achieved so far. Therefore, it was determined that adding 5% cholesterol at the end provided the best encapsulation efficiencies and release profiles.

5 Conclusion

An encouraging RBCV nanoparticle system that incorporates pH-responsive PLP-NDA18% and cholesterol has been successfully designed for intracellular drug delivery. The system was optimised to maintain an average particle size under 200nm. This enhances the permeability and retention effect to effectively target cancer cells. Hemolysis assay was performed to show that PLP-NDA18% allows for maximum payload release at endosomal pH 6 and minimum release at physiological pH 7.4. It was found that using 15 extrusions, 2 hour incubation pre-RBCV formation and 5% cholesterol incorporation post-RBCV formation resulted in the most optimum drug delivery system. Using this combination of techniques, an encapsulation efficiency of 16.74±0.4% was achieved. Performing 15 extrusions and 2 hour incubation improved encapsulation and release behaviour, albeit very slightly. However, combining this with the addition of 5% cholesterol at the end was critical and led to the most dramatic increase in encapsulation efficiency of all parameters varied. It also improved the release profiles the most because the largest difference in the release after 24 hours between pH 6 and pH 7.4 was achieved; there was a 24% higher release at pH 6 than at pH 7.4. This ensures that more payload is released at endosomal conditions than at physiological conditions, which is essential to reduce cytotoxicity and improve targeted drug release.

In the future, this study can be built upon to further increase encapsulation efficiencies and release behaviour. In this study, a fixed concentration of 0.125 mg/ml of fluorescein was loaded into the RBCVs, which could be varied in the future. Fluorescein is a hydrophilic drug; however, more research could be done into loading hydrophobic drugs to assess the interaction with cholesterol. Additionally, fluorescein was loaded in situ, although, other methods could be investigated. For example, post-harvest loading, where the drug is added into empty RBCVs after sonication and extrusion, could potentially increase encapsulation since the free drug has more vesicles to enter and isn't disrupted by the mechanical force during extrusion. Also, active loading, which utilises a pH gradient, could be tested to investigate any benefit over passive loading (in situ and post-harvest).

6 Acknowledgements

We would like to thank Dr Rongjun Chen for allowing us to use the laboratory and his continuous support and guidance. We also wish to thank Nikki Henry for training us and guiding us throughout the project. We want to also thank the whole research group for always being there to help and answer questions.

7 References

Alexandre Albanese et al., 2012. *The Effect of Nanoparticle Size, Shape, and Surface Chemistry on Biological Systems*. [online] Annual Reviews. Available at: https://www.annualreviews.org/doi/10.1146/annurev-bioeng-071811-150124

Aryal, S, *et al.*, 2013. *Erythrocyte membrane-cloaked polymeric nanoparticles for controlled drug loading and release*. [online] Available at: https://pubmed.ncbi.nlm.nih.gov/23409747/

Asli Astarci et al., 2009. *Celecoxib-loaded liposomes: Effect of cholesterol on encapsulation and in vitro release characteristics*. [online] Available at: https://www.researchgate.net/publication/38077043_Celecoxib-loaded_liposomes_Effect_of_cholesterol_on_encapsulation_and_in_vitro_release_characteristics

Berger et al., N., 2001. *Filter extrusion of liposomes using different devices: comparison of liposome size, encapsulation efficiency, and process characteristics*. [online] Available at: http://file.yizimg.com/553/2010041611223136.pdf

Carlotta Pucci et al., 2019. *Innovative approaches for cancer treatment: current perspectives and new challenges*. [online] Available at: https://www.ncbi.nlm.nih.gov/pmc/articles/PMC6753017/

Chen, S. and Chang, J., 2019. *New Insights into Mechanisms of Cisplatin Resistance: From Tumor Cell to Microenvironment*. [online] Available at: https://www.ncbi.nlm.nih.gov/pmc/articles/PMC6747329/

Colletier et al., J., 2002. *Protein encapsulation in liposomes: efficiency depends on interactions between protein and phospholipid bilayer.*. [online] Available at: https://bmcbiotechnol.biomedcentral.com/articles/10.1186/1472-6750-2-9

CP, W., E and BW, 2020. *World Cancer Report: Cancer Research for Cancer Prevention*. [online] Publications.iarc.fr. Available at: https://publications.iarc.fr/Non-Series-Publications/World-Cancer-Reports/World-Cancer-Report-Cancer-Research-For-Cancer-Prevention-2020

Danaei et al., M., 2018. Impact of Particle Size and Polydispersity Index on the Clinical Applications of Lipidic Nanocarrier Systems. *Pharmaceutics*, 10(2), p.57.

De Jong, W. and Borm, P., 2008. *Drug delivery and nanoparticles:applications and hazards*. [online] Available at: https://pubmed.ncbi.nlm.nih.gov/18686775/

Elvin Blanco *et al.*, 2015. *Principles of nanoparticle design for overcoming biological barriers to drug delivery*. [online] Available at: https://www.ncbi.nlm.nih.gov/pmc/articles/PMC4978509/

Erin B. Lavik et al., 2013. *Drug Delivery System*. [online] ScienceDirect. Available at: https://www.sciencedirect.com/topics/nursing-and-health-professions/drug-delivery-system

Evans, B., *et al.*, 2013. *Ex Vivo Red Blood Cell Hemolysis Assay for the Evaluation of pH-responsive Endosomolytic Agents for Cytosolic Delivery of Biomacromolecular Drugs*. [online] Available at: https://www.ncbi.nlm.nih.gov/pmc/articles/PMC3626231/

Heloise Pöckel Fernandes *et al.*, 2011. *Electrical properties of the red blood cell membrane and immunohematological investigation*. [online] Available at: https://www.ncbi.nlm.nih.gov/pmc/articles/PMC3415751/

Kimberly D. Miller *et al.*, 2019. *Cancer treatment and survivorship statistics*. [online] ACS Journals. Available at: https://acsjournals.onlinelibrary.wiley.com/doi/10.3322/caac.21565

Labxchange.org. 2020. *Cholesterol modulates membrane fluidity*. [online] Available at: https://www.labxchange.org/library/items/lb:LabXchange:53ad14be:html:1

Malvernpanalytical.com. 2021. *Dynamic Light Scattering DLS*. [online] Available at: https://www.malvernpanalytical.com/en/products/technology/light-scattering/dynamic-light-scattering

Maria-Lucia Briuglia *et al.*, 2015. *Influence of cholesterol on liposome stability and on in vitro drug release*. [online] Available at: https://pure.strath.ac.uk/ws/portalfiles/portal/41419242/Briuglia_etal_DDTR_2015_Influence_of_cholesterol_on_liposome_stability.pdf

Mohammed, A., *et al.*, 2004. *Liposome formulation of poorly water soluble drugs: optimisation of drug loading and ESEM analysis of stability*. [online] Available at: https://www.sciencedirect.com/science/article/abs/pii/S0378517304004491

Muzykantov, V., 2011. *Drug delivery by red blood cells: vascular carriers designed by Mother Nature*. [online] Available at: https://www.ncbi.nlm.nih.gov/pmc/articles/PMC2844929/

Oh, N. and Park, J., 2014. *Endocytosis and exocytosis of nanoparticles in mammalian cells*. [online] Available at: https://www.dovepress.com/getfile.php?fileID=19906

Qing Xia *et al.*, 2019. *Red blood cell membrane-camouflaged nanoparticles: a novel drug delivery system for antitumor application*. [online] Available at: https://www.sciencedirect.com/science/article/pii/S2211383518307202

Rongjun Chen *et al.*, 2017. *Membrane-Anchoring, Comb-Like Pseudopeptides for Efficient, pH-Mediated Membrane Destabilization and Intracellular Delivery*. [online] ACS Publications. Available at: https://pubs.acs.org/doi/abs/10.1021/acsami.7b00498

Rongjun Chen, 2019, Lecture 9/10: Cell membranes and transport, Lecture notes, Biochemistry CENG 95014, Imperial College

Ronnie H Fang et al., 2018. *Cell Membrane Coating Nanotechnology*. [online] Available at: https://pubmed.ncbi.nlm.nih.gov/29582476/

Sheyda Shariat, S., 2014. *Optimization of a Method to Prepare Liposomes Containing HER2/Neu- Derived Peptide as a Vaccine Delivery System for Breast Cancer*. [online] PubMed Central (PMC). Available at: https://www.ncbi.nlm.nih.gov/pmc/articles/PMC3977049/

Siyuan Chen and Rongjun Chen, 2016. *A Virus-Mimicking, Endosomolytic Liposomal System for Efficient, pH-Triggered Intracellular Drug Delivery*. [online] Available at: https://pubs.acs.org/doi/pdf/10.1021/acsami.6b05041

Verhoef, J. and Anchordoquy, T., 2013. *Questioning the Use of PEGylation for Drug Delivery*. [online] Available at: https://www.ncbi.nlm.nih.gov/pmc/articles/PMC4051498/

Wang, C. and Huang, Y., 2003. *Encapsulating Protein into Preformed Liposomes by Ethanol-Destabilized Method*. [online] Available at: https://www.tandfonline.com/doi/pdf/10.1081/BIO-120023160

Dynamic Geographical Prioritisation of Scarce COVID-19 Vaccines within a Country

Mustafa Fazlani and Tom Valenduc
Department of Chemical Engineering, Imperial College London, U.K.

Abstract

This work presents an initial study of optimal inter-regional vaccine distribution strategies for the UK during the COVID-19 pandemic. This investigation arises because of the distinct epidemiological paths observed during the pandemic between different regions of the UK. A novel non-linear programming (NLP) model is presented to optimize decision-making regarding distribution of scarce vaccines between regions. The model's aim of minimising the effects of the pandemic through vaccinations is evaluated by certain key performance indicators (KPIs) including total deaths, total cost and a normalised death spread. The model contains a new SEI(HQ)R(D) epidemiology model, an adaption of the widely used SEIR model, as well as supply chain constraints such as manufacturing and transportation constraints to distribute vaccines. Official statistical epidemiological data available for the UK is used from the 2nd of October 2020 to the 23rd of October 2020 to calculate key parameters and initialise the model. Results from distribution found that an ineffective vaccine rollout could result in 70% more total deaths after 20 weeks. For inhomogeneous pandemics, it is important to minimise total deaths to save lives by allocating vaccines to the more affected regions. For homogeneous pandemics, vaccine allocation proportional to population in each region is an adequate approximation for minimising total deaths. Overall, this paper shows that regional vaccine prioritisation should be leveraged with other vaccination prioritisation strategies, such as age groups, for mass vaccination campaigns.

Key words: COVID-19 Pandemic, Regional Vaccine Prioritisation, Epidemiology Model, Vaccine Supply Chain

1. Introduction

The current coronavirus, SARS-CoV-2 (COVID-19), pandemic emerged as the cause of severe respiratory infections in Wuhan, China in 2019 and spread globally at an unprecedent rate in 2020. With at least over 5 million confirmed related deaths worldwide as of November 2021 (World Health Organization, 2021), and untold effects on the global economy (Jones, Palumbo, and Brown, 2021), many countries have implemented different strategies to reduce the impact of COVID-19. One of the most effective strategies has been an aggressive vaccination roll-out policy, for example in Israel, the US, and the UK (Sandmann and Jit, 2021). However, the urgent demand for these vaccines has caused large vaccine shortages during the pandemic, exacerbated by a lack of essential ingredients and appropriate production facilities. Additionally, the majority of vaccines have been and are allocated to high income countries with prevailing deals with drug manufacturers (Feinmann, 2021). Therefore, many low-income countries have been unable to get proper access to the necessary vaccines. These shortages have resulted in particular interest towards developing vaccine programmes that provide an effective allocation of this scarce resource. The UK have taken a priority group approach to maximise the benefits of the vaccine for individuals, for instance large priority has been placed on age, underlying health conditions, as well as health care workers due to their increased transmission and health risks from COVID-19 (Joint Committee on Vaccination and Immunisation, 2020).

In the UK, the intensity of the pandemic has varied substantially between different regions. The three-tier approach implemented in October 2020 exemplifies this (Walker, Elgot and Pidd, 2020). However, little emphasis has been placed on regional allocation prioritisation, where vaccines are allocated dependent on the extent of the pandemic in different regions. The objective of this paper is thus to use GAMS modelling to investigate regional vaccine distribution prioritisation between 3 regions of the UK to mitigate the effects of the pandemic.

2. Background

Vaccine prioritisation is a crucial research topic due to the scarcity of COVID-19 vaccines during the beginning stages of a vaccination program. Prioritisation can be broken down into many demographics, the main areas of COVID-19 prioritisation research (Saadi et al., 2021) have been age-group vaccine prioritisation (Campos et al., 2021), occupational (Babus, Das and Lee, 2020) , and social interaction prioritisation (Chen et al., 2021). AB Hogan et al. (2020) find that seniors should be prioritised to minimise deaths when there is limited supply (<20% of the population). While Shim (2021) recommends vaccinating seniors and high transmitting individuals simultaneously, to minimise deaths, years of life lost, and infections. Several studies can be found where geographic vaccine prioritisation has been considered. Wrigley-Field et al. (2021) analysed prioritisation using historical data and statistical modelling to study vaccine prioritisation based on age and race, and more specifically age and geography, and found that targeting different geographies avert more deaths.

Mathematical modelling of an epidemiology model was used, for real world application and prediction in geographical prioritisation. Several studies focus on country allocation prioritisation (Castonguay et al., 2020). AB Hogan et al. (2020) focused on geographical vaccine allocation between countries and found the most efficient approach to vaccine distribution is according to population size to avert more deaths globally (WHO's allocation rule). However, for an individual country it is better to take all vaccines until herd immunity is achieved.

This study focuses on a central government allocating vaccines to regions within a single country, which removes the conflict in strategy between jurisdictions. Fuady et al. (2021) used an SIQRD model and static vaccine allocation to compare the effect on infections of vaccine allocation to regions in Indonesia with the highest infection rates compared to WHO's allocation rule. This report fills a gap in research on regional vaccine allocation, since a novel NLP model with an adapted SEIR epidemiology model is developed to dynamically assign vaccines to aid governmental decisions, and several objectives are explored to identify the best regional vaccine allocation strategy that should be taken.

Vaccine prioritisation and vaccine supply chain models are commonly separate model. Soria-Arguello et al. (2021) developed a mixed integer linear program (MILP) supply chain vaccine allocation model based around a given demand, and constraints on manufacturing, and storage. Where vaccines are allocated based on minimising supply chain costs.

In this paper, a first attempt is made at coupling both a vaccine supply chain model with an epidemiology model, aiming to allocate vaccines without a set demand. Aiming to optimise epidemiological criteria and not solely supply chain costs while still considering supply chain constraints (e.g., manufacturing, and cold storage).

3. Methods

3.1 Preliminary

Three regions in the UK are considered: Northeast, Northwest, and Yorkshire and the Humber. Initial values for daily cases, daily admissions, beds occupied, and deaths were obtained for 2nd October 2020, the start date of the model (UK Government, 2021).

The final aim is to develop a vaccine distribution model, which requires the development of both an epidemiology and supply chain model.

3.2 Epidemiology Model

For the spread of the disease, an adapted form of the popular SEIR model is used (Ferguson et al 1996). In this case, there are 7 subgroups of the population for each region: Susceptible, Exposed, Infected, Quarantined, Hospitalised, Recovered, Dead (SEI(HQ)R(D)). Figure 1 is a diagram representing the SEI(HQ)R(D) model. Diffusion is then added for susceptible, exposed, and infected populations as these groups may travel between regions. An assumption in the model is the total population is fixed: the normal death rate equals the birth rate, and people cannot move out of the three regions or into the three regions from other areas.
For simplicity, only one vaccine dose is implemented.

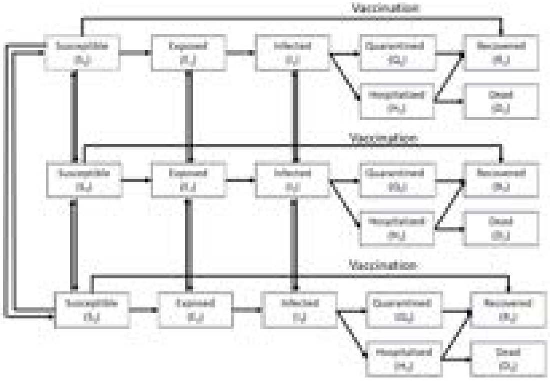

Figure 1. Simplified SEI(HQ)R(D) for 3 regions

Vaccines have been implemented into the model using a certain efficacy (ε_1). When a susceptible member of the population receives a vaccination, if effective they will immediately be recovered, or if ineffective they will become exposed at the same rate they would if they were not vaccinated.

Vaccines available are scaled to the proportion of susceptible population to overall population. This returns the number of vaccines administered to the susceptible population, assuming vaccines are distributed to each population group proportional to the population size. This is since, in reality, the available weekly vaccines are distributed to each of the subgroups of the population. Vaccination of exposed and infected groups are neglected due to the relatively small size of the population group. Similarly for quarantined and hospitalised since they would not be getting vaccinated.

Table 1 presents a system of differential equations to calculate the value of differential variables (e.g., dead, recovered, hospitalised, infected) as well as the rate of transfer between each region. The differentials represent the mass balances for each of the subgroups of the population, this is extended to each of the 3 regions.

Table 1. Epidemiology Equations

$$\frac{d\mathbf{S}}{dt} = -k_s \cdot \mathbf{S} \cdot \frac{\mathbf{I}}{\mathbf{N}} - \left(\mathbf{V_1} \cdot k_s \cdot (1-\varepsilon_1) \cdot \frac{\mathbf{I}}{\mathbf{N}} + V_1 \cdot \varepsilon_1\right) \cdot \frac{\mathbf{S}}{\mathbf{N}} + \mathbf{DfS} \tag{1}$$

$$\frac{d\mathbf{E}}{dt} = k_s \cdot \mathbf{S} \cdot \frac{\mathbf{I}}{\mathbf{N}} - k_E \cdot \mathbf{E} + \left(\mathbf{V_1} \cdot k_s \cdot (1-\varepsilon_1) \cdot \frac{\mathbf{I}}{\mathbf{N}}\right) \cdot \frac{\mathbf{S}}{\mathbf{N}} + \mathbf{DfE} \tag{2}$$

$$\frac{d\mathbf{I}}{dt} = k_E \cdot \mathbf{E} - k_I \cdot \mathbf{I} + \mathbf{DfI} \tag{3}$$

$$\frac{d\mathbf{H}}{dt} = Ratio_H \cdot k_I \cdot \mathbf{I} - k_H \cdot \mathbf{H} \tag{4}$$

$$\frac{d\mathbf{Q}}{dt} = (1 - Ratio_H) \cdot k_I \cdot \mathbf{I} - k_q \cdot \mathbf{Q} \tag{5}$$

$$\frac{d\mathbf{D}}{dt} = Ratio_D \cdot k_H \cdot \mathbf{H} \tag{6}$$

$$\frac{d\mathbf{R}}{dt} = (1 - Ratio_D) \cdot k_H \cdot \mathbf{H} + k_q \cdot \mathbf{Q} + \boldsymbol{V_1} \cdot \varepsilon_1 \cdot \frac{\mathbf{S}}{\mathbf{N}} \tag{7}$$

Table 2. Parameter values for Vaccine Distribution Model

Symbol	Parameter	Value	Source
k_S	Rate constant of susceptible becoming exposed (person·day^{-1})	0.3487	RMSE Predictions
k_E	Rate constant of exposed becoming infected (day^{-1})	0.25	Assuming 4-day latent period
k_I	Rate constant of infected either being hospitalized or quarantining (day^{-1})	0.25	Assuming 8-day incubation period
k_H	Rate constant of hospitalized either recovering or dying (day^{-1})	0.1080	RMSE Predictions
k_q	Rate constant of quarantined recovering (day^{-1})	0.125	Assuming 8-day quarantine
$Ratio_H$	Ratio of infected becoming hospitalized to quarantining	0.0535	RMSE Predictions
$Ratio_D$	Ratio of hospitalized dying to recovering	0.1907	RMSE Predictions
N_i	Total population in region i		
N_1		2,669,941	
N_2		7,341,196	Literature (UK Government, 2021)
N_3		5,502,967	
V_1	Total vaccinations given out in each week		Found from supply chain
ε_1	Efficacy of vaccine	0.95	Literature (Institute for Health Metrics and Evaluation, 2021)
DfX	Diffusion of X into region (X = (S,E,I))	0	Set for analysis

3.2.1 Finding Model Parameters

Values of the model parameters as shown in Table 2 were either obtained from literature or calculated by running a simulation with known COVID-19 data from the 2nd of October 2020 to the 23rd of October 2020.

With the epidemiology equations, and known data for daily cases, daily admissions, hospital beds occupied and daily deaths a root mean square error function (RMSE) is developed:

$$\text{RMSE} = \left(\sum_{\mathrm{i}} \frac{(\mathbf{x_i} - \hat{\mathbf{x}}_\mathbf{i})^2}{\mathbf{N_i}}\right)^{\frac{1}{2}} \tag{8}$$

Where $\mathrm{x_i}$ and $\hat{\mathrm{x}}_\mathrm{i}$ are the known and predicted values of cases, admissions, beds, or deaths respectively. N_i is the order of magnitude of the values, included to ensure appropriate weighting of errors of each. By running an epidemiology model and minimising this RMSE, estimates of the model parameters are obtained.

Parameters are assumed to maintain a fixed value which can be used to approximate future pandemic trajectory. However, they should be a function of a range of factors such as time, age, and ethnicity.

3.2.2 Discretising of Epidemiology Model

There are explicit and implicit methods used in numerical analysis to discretise and approximate solutions of differential equations. Explicit methods use the current state of a system to approximate subsequent states whereas implicit methods use both the current and subsequent states. Implicit solvers require more computational power but have greater numerical stability using larger time steps (Flow 3D, 2021). 7-day time-steps were preferred for vaccine allocation as the supply chain model used runs on a 7-day time step, and smaller timesteps assume unrealistic flexibility in the supply chain of vaccines. A 4th order explicit Runge-Kutta method was initially proposed. However, due to the stiffness in the susceptible differential equation, instability was identified for timesteps larger than 4 days. An implicit Euler was then implemented, yielding stability for the desired 7-day time-period at the cost of inaccuracy in approximations, relative to the 4th order Runge-Kutta method. Therefore, a 2nd order implicit method has been implemented as shown in equation 9, as it was identified to be the optimum between simplicity, accuracy, stability, and a lower amount of computational power will be needed relative to higher order implicit methods.

$$\mathbf{x_{t+dt}} = dt \cdot \frac{1}{2} \cdot \left(\frac{d\mathbf{x}}{dt_{(t=t)}} + \frac{d\mathbf{x}}{dt_{(t=t+1))}}\right) \tag{9}$$

3.3 Supply Chain Model

The supply chain model used is a simplified version of the one used in 'Optimizing COVID-19 vaccine supply chain network in England' (Zhu and Ye, 2020). The four-tier distribution network consists of: (a) 1 manufacturing/national storage facility, (b) 3 regional warehouse storage facilities, (c) 26 local storage facilities and (d) 26 clusters of recipient locations (places of vaccine administration e.g., pharmacies). Each stage of the distribution network has a limited capacity with time delays present for production and storage. This limits the total number of vaccines available for a given week.

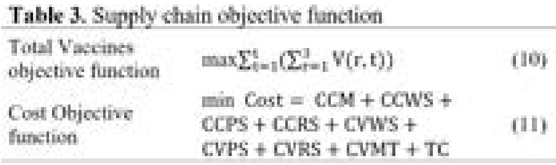

Table 3. Supply chain objective function

Total Vaccines objective function	$\max\sum_{t=1}^{t}(\sum_{r=1}^{3} V(r,t))$	(10)
Cost Objective function	min Cost = CCM + CCWS + CCPS + CCRS + CVWS + CVPS + CVRS + CVMT + TC	(11)

In this mixed-integer linear program (MILP) model, a sequential optimisation approach is adopted.

Initially, the first objective function, equation 10, is maximised. This maximises the total number of vaccines administrated across the three regions for a specified time-period. Then the number of vaccines is bounded, and cost is minimised, as shown in equation 11. The total cost includes: (a) CCM, the total capital cost of manufacturing facility (b) CCWS, CCPS, CCRS, the total capital cost of regional, local, and recipient storage respectively (c) CVWS, CVPS, CVRS, the total variable cost of regional, local, and recipient storage for each type of vaccines and (d) CVMT,TC which are total variable costs of manufacturing and transporting each vaccine (Zhu and Ye, 2020).The minimum cost for a certain number of vaccines to be administrated is then obtained.

Once this optimisation sequence is run, the weekly total vaccinations are obtained and can then be inputted into the vaccine distribution nonlinear program (NLP).

Redistribution of vaccines between different administration points across regions, and the movement of personnel to administer vaccines is assumed to be feasible. This assumption allows the value of total weekly vaccines found from running the supply chain model to be used and re-allocated in the vaccine distribution model.

3.4 Vaccine Distribution

The vaccine distribution consists of the epidemiology model as well as the output of total weekly vaccines from the supply chain model. 3 different vaccine distribution strategies were analysed for different regional allocation scenarios, these are highlighted in table 4.

Table 4. Vaccine distribution strategies

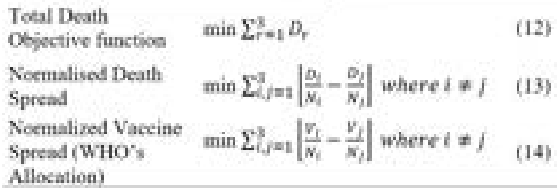

Total Death Objective function	$\min \sum_{r=1}^{3} D_r$	(12)
Normalised Death Spread	$\min \sum_{i,j=1}^{3} \left\lvert \frac{D_i}{N_i} - \frac{D_j}{N_j} \right\rvert$ *where* $i \neq j$	(13)
Normalized Vaccine Spread (WHO's Allocation)	$\min \sum_{i,j=1}^{3} \left\lvert \frac{V_i}{N_i} - \frac{V_j}{N_j} \right\rvert$ *where* $i \neq j$	(14)

As seen in equation 12, the first strategy is to minimise total number of deaths. For ethical reasons, further objective functions are explored. The second strategy in equation 13, minimises the normalised death spread: difference in deaths across regions normalised by their respective population. For an optimal solution to be found, sequential optimisation is performed. The normalised death spread is minimised, added as a constraint in the model, and then total deaths are minimised.

The final strategy is the minimisation of the normalised vaccine spread. This is also known as the WHO allocation rule, each region receives vaccines proportional to its population (Castonguay et al., 2020).

A 20-week timeframe is proposed as peak cases and hospitalisations occur before 20 weeks, and this reduces the computing time required to run the model relative to longer timeframes.

3.5 Finding Global Optima

Both MILP (supply chain) and NLP (vaccine distribution) models were solved using the Branch-And-Reduce Optimisation Navigator (BARON) solver. This was used to guarantee global optimality. While local solvers, such as CONOPT, and CPLEX could be implemented and run using personal computers, the Dept. of Chemical Engineering Linux Cluster (24 cores) was used to run longer simulations to obtain a global optimum. This enabled solutions to be found within 24 hours of the code being run.

3.6 Sensitivity analysis

Sensitivity analysis is done to demonstrate the importance of an accurate data set, to correctly predict epidemiological factors such as deaths, as well as achieving the correct optimal vaccine allocation.

4. Results and Discussion

4.1 Importance of Geographical Allocation

The importance of an efficient vaccine distribution can be illustrated by comparing two scenarios where the number of total weekly vaccines are constant, however the vaccines are distributed differently to each region. Figure 2 represents the optimal vaccine distribution for minimal deaths after 20 weeks. Figure 3 represents the least optimal vaccine allocation, which corresponds to the greatest number of total deaths.

As seen in table 5, total deaths are 70% higher with an ineffective vaccine distribution despite total vaccines being the same. Certain regions, that are at a later stage of the pandemic, should be prioritised to minimise deaths. In this case, Region 1 got the most vaccines despite having the smallest number of exposed and infected per total population. A good distribution model will allocate regions an optimal number of vaccines to minimise a certain key performance indicator (KPI), in this case, total deaths.

A large risk that can be implied from these results are the risks caused by inaccurate predictions. If an epidemiology model overestimates infections in a certain region, many vaccines will be allocated to that region. If another region then results in more infections, it will have less vaccines and the outcome could be catastrophic.

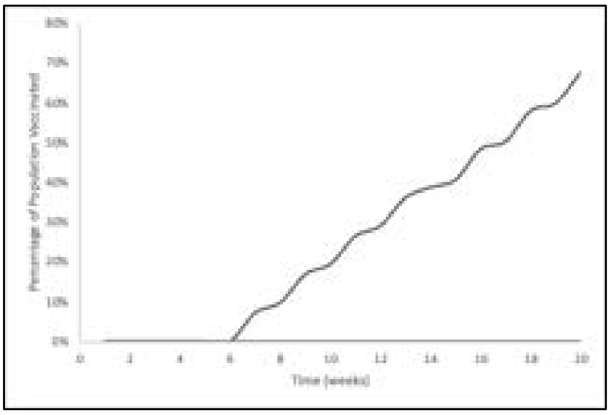

Figure 2. Inefficient 20-week vaccine distribution

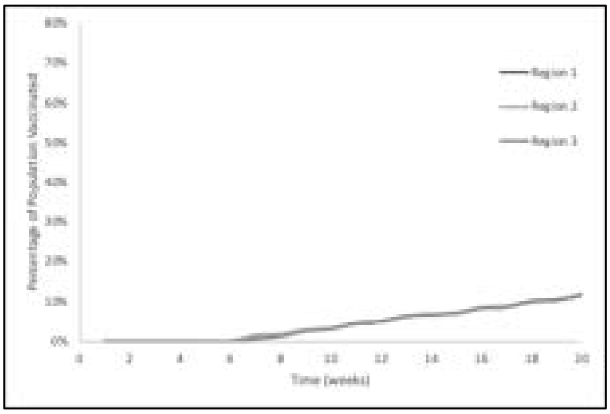

Figure 3. Efficient 20-week vaccine distribution

Table 5. Effect of Efficient Vaccine Distribution on Deaths

	Inefficient Distribution	Optimum Distribution
Total Deaths	59964	35655

The ineffective scenario above can be seen during the pandemic for country vaccine allocation. Less economically developed countries could be at a later stage in a pandemic however receive very little vaccines due to high costs and inequitable vaccine supply. To minimise global total deaths, developing countries should be supported with vaccines as early as possible, as seen with initiatives such as COVAX (COVAX, 2021).

4.2 Geographical allocation with respect to cost

For a pandemic such as COVID-19, costs of vaccine distribution can mostly be associated to the cost of buying vaccines from manufacturers, and certain other variable costs such as delivery, and technical assistance (COVAX Working Group, 2021). This is due to the lack of time to construct new facilities (e.g., manufacturing and storage), consequently countries must leverage their existing health system.

A pareto frontier in figure 4 has been developed to look at the trade-off between minimising variable costs, vs minimal total cumulative deaths between the 3 regions after 20 weeks.

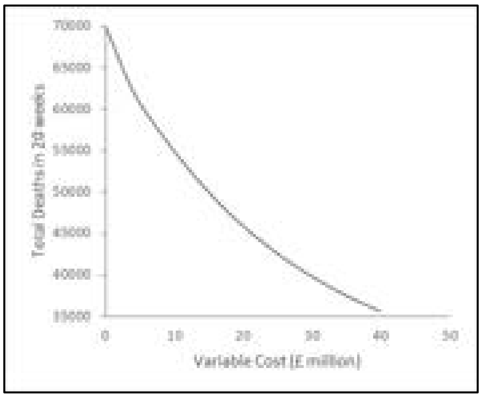

Figure 4. Pareto frontier of minimising variable costs to minimising total deaths after 20 weeks

As shown in figure 4, as costs increase, total deaths decrease. This can be explained by two phenomena's, the first and greatest effect is the increase in variable costs directly linked to more vaccines being distributed. Second, is observed at high variable costs once no more extra vaccines can be supplied, due to supply chain constraints, and is caused by optimal regional vaccine allocation for minimising total deaths.

As illustrated, total deaths can be significantly decreased with an increase in total vaccines in the system. The majority proportion of variable costs is associated to buying vaccines e.g. Pfizer vaccines are at £22 per dose (Kollewe, 2021). The UK treasury currently uses £2m as the value of a prevented fatality (VPF) (Dolan and Jenkins, 2020). Even at these high vaccine prices, 90909 vaccines would need to not save a single life for there to be a reason to not buy extra vaccines. The 1st phenomenon is thus a trivial demonstration of the importance of maximising the number of vaccines available in the vaccine program, as seen in many prior papers (AB Hogan et al., 2020).

Table 6. Minimising costs vs minimizing deaths for same total vaccines

Change in Total Deaths (In 20 weeks)	89
Change in Cost (£)	-114,000

The second phenomena, more relevant to this research paper, is the pareto frontier shows the importance of using other KPI's for optimising regional vaccine allocation. As seen in table 6, for the same number of total vaccines, when minimising total deaths instead of minimising cost over 89 lives are saved, at an increased variable cost of 114,100. These costs are associated to increased delivery distances, and higher storage costs. Using the same VPF evaluation, savings of over £178 million could be made for the UK government by minimising deaths rather than costs. This is since supply chain costs are negligible relative to the detrimental effects of the pandemic on the economy.

Costs are an important metric for effective planning, budgeting, and fundraising for the vaccine (COVAX Working Group, 2021). However, should not be used as the sole KPI to distribute vaccines, as this could have detrimental effects on a population's total deaths and the overall ability to recover from a pandemic.

4.3 Distribution Strategies

To compare different geographical vaccination allocation strategies, two scenarios are considered. Scenario 1 is based of real-life data for the regions starting on 2nd October 2020. In this case, all regions are at a similar stage of the pandemic as the infections are similar relative to their population size. This is referred to as a homogenous disease spread. A second scenario is introduced where the initial infectious and exposed populations in region 2 is reduced. Region 2 is hence in an earlier stage of the pandemic; this is considered an inhomogeneous disease spread. This inhomogeneity is shown in figure 5 where deaths in region 2 increase at a lower rate than region 1 and 3.

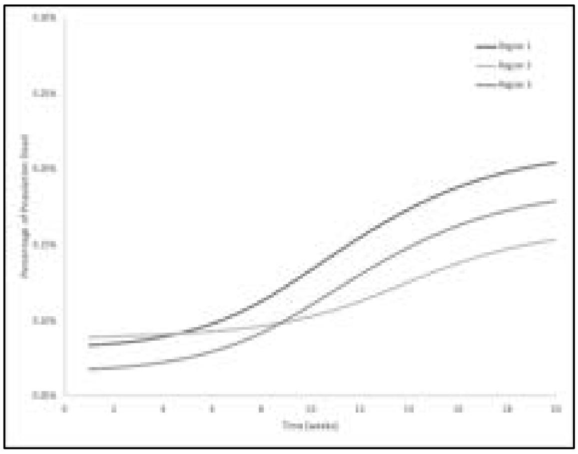

Figure 5. Inhomogeneous pandemic - vaccine allocation by minimising total death

It could be argued that total deaths aren't the most effective KPI when considering an effective vaccine rollout. Considering an average of deaths across the regions normalised by their respective population is another potential KPI. Minimising the sum of the differences between these values leads to the same death to population ratio for all regions.

The WHO allocation rule is commonly used in vaccine rollouts (Castonguay et al., 2020). Vaccines are given out according to population size. This method is simple to implement and doesn't rely on epidemiology modelling. This strategy could be used as a good approximation of minimising total death for inaccurate models, at least for homogeneous disease spreads. However, for inhomogeneous disease spreads it is important to leverage vaccine allocation using dynamic regional vaccine prioritisation.

As shown in table 7, for scenario 2, minimising total deaths results in 720 and 841 less deaths than minimising normalised death spread and normalised vaccine spread respectively. Due to the large discrepancy in total deaths, for inhomogeneous scenarios, minimising total deaths is an effective strategy.

Table 7. Difference in total death between a strategy and minimising total death

	Minimising Total Death	Minimising Normalised Death Spread	Minimising Normalised Vaccine Spread
Scenario 1	0	10	19
Scenario 2	0	720	841

In scenario 1, where the pandemic is homogeneous, all three strategies result in similar deaths. Therefore, minimising total deaths is not necessarily the best strategy, as we can be more lenient. It could be argued that minimising the normalised death spread is more ethical. As seen in figure 6, this strategy results in complete equality by result due to all regions having the same death to population ratio. Similarly, implementing the WHO allocation rule can be considered fairer than minimising total deaths as this results in complete equality of resource allocation while still maintaining similar total deaths to the minimum. It is for this reason that WHO's allocation strategy is a trusted strategy implemented globally but should only be so for homogeneous disease spread.

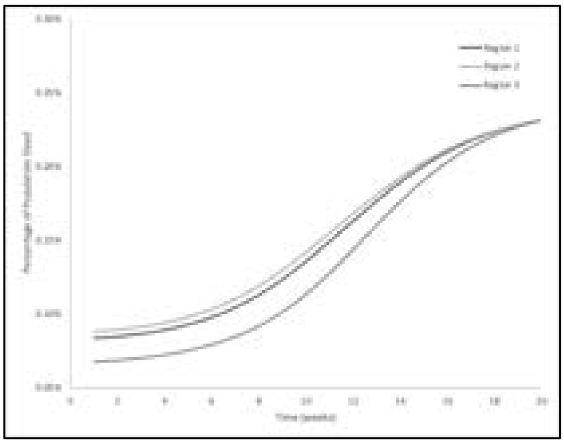

Figure 6. Homogeneous pandemic - vaccine allocation by minimising normalised death spread

4.4 Sensitivity Analysis

The model is developed using real-life covid data from the official UK website (UK Government, 2021). However, initialisation of the model requires predictions of number of infected as well as number of exposed in each region which can vary substantially.

4.1.1 Infections

Changing the number of initial infected population in each region has large effects on the total deaths of the regions as well as the peak hospitalisations when minimising total deaths, as shown in figure 7. A smaller initial infected population leads to lower total deaths and hospitalisations and vice versa for higher infected population levels. Therefore, accuracy on initialisation parameters is paramount to accurate epidemiology modelling. Many mathematical models have been developed to predict the number of infected (Vytla et al., 2021), with high levels of accuracy. Therefore, using such models in conjunction with the vaccine distribution model could lead to much higher levels of accuracy.

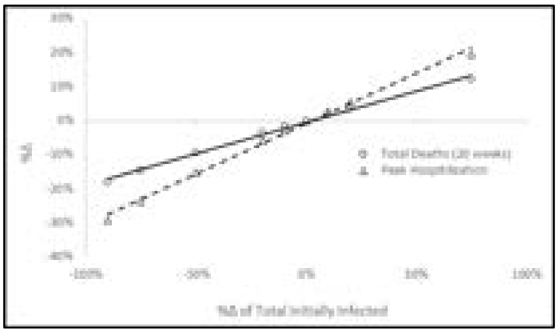

Figure 7. Percentage change vs percentage change of total initially infected (including all regions)

Additionally, accuracy will have a large impact on vaccine allocation. If a region is initialised with low infections, this will lead to lower allocation to said region. This risk was previously discussed in section 4.3.

Figure 7 also re-iterates the importance of adopting an aggressive vaccination program and infection reducing policies, as lower number of infected leads to less of the susceptible population becoming infected and potentially dying.

4.4.2 Exposed

Inaccuracy in the exposed population can have detrimental effects on total death and peak hospitalisation. Exposed populations are likely greater than the infected population due to COVID R values being greater than 1 (WHO, 2021). Therefore, percentage change in exposed population can lead to even greater effects on the total death and peak hospitalisation than can be said for equivalent percentage changes in infected.

Figure 7, and Figure 8 demonstrate the importance of early attempts to isolate cases of COVID-19. as even for initially small percentages of infected and exposed, the total deaths after 20 weeks only decrease by 30%. This is due to the high transmissivity and R number of COVID-19.

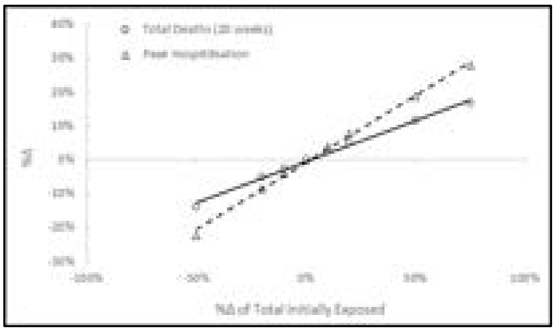

Figure 8. Percentage change vs percentage change of total initially exposed (including all regions)

5. Conclusions

This paper presented a novel model to optimise regional vaccine distribution while accounting for supply chain constraints. The importance of an effective distribution strategy is highlighted. Total deaths are found to be 70% higher with an ineffective vaccine distribution compared to an optimum despite total vaccines being the same. It is concluded that cost should be neglected when deriving vaccination strategies, since supply chain costs during a pandemic are negligible. Different strategies to define an optimum vaccine rollout were also explored. Minimisation of total deaths is the key strategy for inhomogeneous scenarios, as other strategies lead to much larger loss of life. Whereas when regions are at a similar stage of the pandemic, all three strategies showed comparable results, and other considerations, such as ethical arguments, should be considered when implementing a distribution strategy. Inaccurate epidemiology models lead to inefficient distribution of vaccines so in cases where an accurate epidemiology model cannot be produced, WHO's allocation rule can be followed, however this is only a good approximation of minimising total deaths when there is homogeneous disease spread.

Dynamic regional vaccine allocation within a country is not common in the literature. As well as this, the combination of a supply chain and epidemiology model is uncommon. Therefore, the findings of this research can have many future uses.

Further Research Scope

There are many interesting ways in which this research can be continued.

The vaccine distribution model allocated vaccines based on region and didn't consider demographics. Much of vaccine prioritisation is focused on age-group, occupation, and social contact prioritisation. Therefore, a regions population should be broken down into different demographics. Meaning the model parameters used will differ for different demographics (e.g. age groups, ethnicities, and genders). For example, the ratio of infected becoming hospitalised to quarantining would be much larger for older age groups. The UK allocated vaccines based on demographics (Joint Committee on Vaccination and Immunisation, 2020). However, ideally a combination of regional and demographic allocation would be implemented to minimise the KPI's in question. It would thus be noteworthy to see how important regional allocation is with demographics implemented into the model.

Improving the accuracy of the epidemiology model and supply chain model are paramount to developing a vaccine distribution model which can be used by government officials to make real decisions about effective vaccine allocation. For example, an approximation with the adapted SEIR model is that reinfections are not considered. An addition to the model could be implementing a reinfection rate out of the recovered sample size. Another improvement could be the implementation of different vaccines into the model with different efficacies, and double doses.

Research into other objective functions, to develop better strategies. An objective function which combines costs as well as health criteria could be developed. For example, combining supply chain costs and value of prevented fatality costs. However, the ethics and value of the VPF is a highly argued topic (Wolff, 2007), and thus this introduces large uncertainty in the objective function. For this reason, this has not been covered further in this paper. Other objective functions, such as minimisation of peak hospitalisation, or minimisation of infections could be used to investigate other health strategies.

Finally, coupling the epidemiology model with the supply chain model would be a good way to carry on this research. While this was done, our results are from sequential optimisation where the output of the supply chain model was inputted into the vaccine distribution model. An assumption that was made is that when vaccines arrive at local storage, they are free to move across any administration point in the three regions. Although this is a relatively feasible assumption for earlier stages in the vaccination program when there are little vaccines in supply, this is not the case further along during the vaccination program. With the coupled models, all supply chain constraints will stand.

While the coupled supply chain and epidemiology model was attempted, the computing power required to obtain a global optimum using BARON was large (running 24 cores for more than 48 hours). Due to time constraints in this research, the sequential optimisation method was used instead as a get around.

Acknowledgements

We would like to express a huge amount of gratitude towards Professor Benoit Chachuat and Dr Maria Papathanasiou for their continued insights, support, and encouragement throughout the project. Additionally, we would like to thank Dr. Dauda Ibrahim and Dr. Kyungjae Tak for their guidance and expertise.

References

AB Hogan, P Winskill, OJ Watson et al. 2020. *Modelling the allocation and impact of a COVID-19 vaccine*. Available at: < https://www.imperial.ac.uk/mrc-global-infectious-disease-analysis/covid-19/report-33-vaccine/> Imperial College London (25-09-2020). [Accessed 13 December 2021]

Babus, A., Das, S. and Lee, S., 2020. The Optimal Allocation of Covid-19 Vaccines.

Campos, E., Cysne, R., Madureira, A. and Mendes, G., 2021. Multi-generational SIR modeling: Determination of parameters, epidemiological forecasting and age-dependent vaccination policies. *Infectious Disease Modelling*, 6, pp.751-765.

Castonguay, F., Blackwood, J., Howerton, E., Shea, K., Sims, C. and Sanchirico, J., 2020. Spatial Allocation of Scarce COVID-19 Vaccines.

Chen, J., Hoops, S., Marathe, A., Mortveit, H., Lewis, B., Venkatramanan, S., Haddadan, A., Bhattacharya, P., Adiga, A., Vullikanti, A., Srinivasan, A., Wilson, M., Ehrlich, G., Fenster, M., Eubank, S., Barrett, C. and Marathe, M., 2021. Prioritizing allocation of COVID-19 vaccines based on social contacts increases vaccination effectiveness.

COVAX, 2021. *COVAX*. [online] Who.int. Available at: <https://www.who.int/initiatives/act-accelerator/covax> [Accessed 15 December 2021].

COVAX Working Group, 2021. *Costs of delivering COVID-19 vaccine in 92 AMC countries*. [online] World Health Organization. Available at: <https://www.who.int/docs/default-source/coronaviruse/act-accelerator/covax/costs-of-covid-19-vaccine-delivery-in-92amc_08.02.21.pdf> [Accessed 12 December 2021].

Feinmann, J., 2021. Covid-19: global vaccine production is a mess and shortages are down to more than just hoarding. *BMJ*, [online] p.n2375. Available at: <https://www.bmj.com/content/375/bmj.n2375> [Accessed 10 December 2021].

Flow 3D, 2021. *Implicit vs. Explicit Numerical Methods*. [online] FLOW-3D. Available at: <https://www.flow3d.com/resources/cfd-101/numerical-issues/implicit-versus-explicit-numerical-methods/> [Accessed 15 December 2021].

Fuady, A., Nuraini, N., Sukandar, K. and Lestari, B., 2021. Targeted Vaccine Allocation Could Increase the COVID-19 Vaccine Benefits Amidst Its Lack of Availability: A Mathematical Modeling Study in Indonesia. *Vaccines*, 9(5), p.462.

Institute for Health Metrics and Evaluation, 2021. *COVID-19 vaccine efficacy summary*. [online] Institute for Health Metrics and Evaluation. Available at: <https://www.healthdata.org/covid/covid-19-vaccine-efficacy-summary> [Accessed 11 December 2021].

Jones, L., Palumbo, D. and Brown, D., 2021. *Coronavirus: How the pandemic has changed the world economy*. [online] BBC News. Available at: <https://www.bbc.co.uk/news/business-51706225> [Accessed 10 December 2021].

Kollewe, J., 2021. *Covid-19 vaccines: the contracts, prices and profits*. [online] The Guardian. Available at: <https://www.theguardian.com/world/2021/aug/11/covid-19-vaccines-the-contracts-prices-and-profits> [Accessed 12 December 2021].

Saadi, N., Chi, Y., Ghosh, S., Eggo, R., McCarthy, C., Quaife, M., Dawa, J., Jit, M. and Vassall, A., 2021. Models of COVID-19 vaccine prioritisation: a systematic literature search and narrative review. *BMC Medicine*, 19(1).

Sandmann, F. and Jit, M., 2021. Rapid COVID-19 vaccine rollout: immense success but challenges ahead. *The Lancet Infectious Diseases*, [online] Available at: <https://www.thelancet.com/journals/laninf/article/PIIS1473-3099(21)00616-2/fulltext> [Accessed 10 December 2021].

Shim, E., 2021. Optimal Allocation of the Limited COVID-19 Vaccine Supply in South Korea. *Journal of Clinical Medicine*, 10(4), p.591.

Soria-Arguello, I., Torres-Escobar, R., Pérez-Vicente, H. and Perea-Rivera, T., 2021. A Proposal Mathematical Model for the Vaccine COVID-19 Distribution Network: A Case Study in Mexico. *Mathematical Problems in Engineering*, 2021, pp.1-11.

UK Government, 2021. *Joint Committee on Vaccination and Immunisation: advice on priority groups for COVID-19 vaccination, 30 December 2020*. [Accessed 10 December 2021].

UK Government, 2021. *UK Summary | Coronavirus (COVID-19) in the UK*. [online] Coronavirus.data.gov.uk. Available at: <https://coronavirus.data.gov.uk/> [Accessed 11 December 2021].

Vytla, V., Ramakuri, S., Peddi, A., Kalyan Srinivas, K. and Nithish Ragav, N., 2021. Mathematical Models for Predicting Covid-19 Pandemic: A Review. *Journal of Physics: Conference Series*, 1797(1), p.012009.

Walker, P., Elgot, J. and Pidd, H., 2020. *Boris Johnson unveils three-tier Covid restrictions for England*. [online] The Guardian. Available at: <https://www.theguardian.com/world/2020/oct/12/boris-johnson-unveils-three-tier-covid-restrictions-for-england> [Accessed 10 December 2021].

Wolff, J., 2007. *What is the value of preventing a fatality?*. [online] Available at: <https://sas-space.sas.ac.uk/664/1/J_Wolff_Fatality.pdf> [Accessed 15 December 2021].

World Health Organization, 2021. *Weekly epidemiological update on COVID-19 - 23 November 2021*. COVID-19 Weekly Epidemiological Update - Edition 67. [online] World Health Organization. Available at: <https://www.who.int/publications/m/item/weekly-epidemiological-update-on-covid-19---23-november-2021> [Accessed 10 December 2021].

Wrigley-Field, E., Kiang, M., Riley, A., Barbieri, M., Chen, Y., Duchowny, K., Matthay, E., Van Riper, D., Jegathesan, K., Bibbins-Domingo, K. and Leider, J., 2021. Geographically targeted COVID-19 vaccination is more equitable and averts more deaths than age-based thresholds alone. *Science Advances*, 7(40).

Zhu Y., Ye, J., 2020. Optimising COVID-19 Supply Chain Network in England. *Chemical Engineering Research Reports of the 4th year Research projects in the Department of Chemical Engineering at Imperial College London v3*, p.110.

Author Index

Linked to paper number

Supervisor Index

Linked to paper number